



NATIONAL RESEARCH CENTRE
"KURCHATOV INSTITUTE"

Petersburg Nuclear Physics Institute
named by B.P. Konstantinov



PNPI

High Energy Physics Division

MAIN SCIENTIFIC ACTIVITIES
2013–2018

GATCHINA
2019

Editor G.D. Alkhazov

ISBN 978-5-86763-435-3

© NRC “Kurchatov Institute” – PNPI, 2019

PREFACE

This edition presents a summary of the scientific activities of the High Energy Physics Division (HEPD) in the period 2013–2018. It can be considered as a continuation of the previous editions:

High Energy Physics Division. Main scientific activities 1971–1996, Gatchina (1997);

High Energy Physics Division. Main scientific activities 1997–2001, Gatchina (2002);

High Energy Physics Division. Main scientific activities 2002–2006, Gatchina (2007);

High Energy Physics Division. Main scientific activities 2007–2012, Gatchina (2013).

The main directions of the HEPD scientific activities are experimental studies in nuclear and particle physics at accelerators, as well as some applications of nuclear methods, in medicine in particular. As in the previous years, the HEPD strategy was, on one hand, to exploit in a maximal possible way the accelerator facilities available at NRC “Kurchatov Institute” – PNPI (PNPI) and, on the other hand, to maintain active international cooperation in fundamental research in the world’s most advanced accelerator centres. The PNPI 1-GeV proton synchrocyclotron with its proton, neutron, pion, and muon beams remains a valuable instrument for nuclear physics, for solid state physics, for medical applications, as well as for radiation studies of various materials and equipment. The medical 1 GeV proton beam was successfully used for neurosurgery. An important step in medical applications is related to the construction at PNPI of a new 80-MeV high-intensity proton cyclotron. This accelerator will be specialized on production of various radioactive isotopes, including production of generators of positron emitting isotopes for applications in the positron emission tomography. During the reviewed period, the HEPD participated in experiments at the leading accelerator centres: CERN, FNAL (USA), BNL (USA), PSI (Switzerland), DESY (Germany), GSI (Germany), FZ-Juelich (Germany), as well as at the accelerators in the Universities in Jyvaskyla (Finland), in Bonn (Germany), in Mainz (Germany), and at the accelerator at ITEP (Moscow). Our main efforts were concentrated on experiments at the Large Hadron Collider (LHC) at CERN. PNPI participates in all major collider experiments at the LHC: CMS, ATLAS, LHCb, ALICE with essential contributions to the design, construction, and maintenance of these experiments. The tremendous success of the LHC experiments is well known. More than 1 500 physics papers were published by the end of 2018. A great amount of new results have been obtained, crowned by the discovery of the Higgs boson. At present, PNPI participates in preparations for further studies at the LHC with the increased energy and intensity of the colliding beams. Very successful was also our traditional cooperation with the nuclear centre PSI in Switzerland, where we have a possibility to use the world’s best muon beams of the “meson factory”. Deep studies of the muon catalyzed dd - and dt -fusion, were followed by high precision measurements of the muon capture by protons and by light nuclei.

The future plans of the HEPD include participations in the experiments at the accelerator complex FAIR, which is under construction at GSI (Germany). We plan to create a special complex (project IRINA) at the high flux neutron reactor PIK at PNPI for studies of neutron-rich nuclei far from the stability region. Also, we are preparing a new experiment to perform a precision measurement of the proton charge radius on Mainz Microtron at the Johannes Gutenberg University in Mainz.

Alexey Vorobyev

Scientific adviser of the High Energy Physics Division,

Oleg Fedin

Head of the High Energy Physics Division



Status of the Accelerator
Facilities at PNPI

50 YEARS OF THE PNPI SYNCHROCYCLOTRON SC-1000

S.A. Artamonov, E.M. Ivanov, G.F. Mikheev, G.A. Riabov, G.D. Alkhazov

In the middle of 50s it was decided to build the world's largest synchrocyclotron with the proton energy 1 000 MeV (SC-1000) in the branch of the A.F. Ioffe Physical-Technical Institute (FTI) at Gatchina. In its design, installation and adjustment, the major participation was taken by the staff of D.V. Efremov Institute of Electrophysical Apparatus (JSC "NIIEFA") and FTI.

1. Brief historical overlook on the design and creation of the SC-1000

Despite the fact that a number SC were already operating in the world, the creation of the largest SC required to solve a number of new technical problems among which we would mark out the following:

1. Creation of the world's largest magnet with the pole 7 m in diameter, with the gap of 0.5 m, and the induction of the magnetic field of 1.9 T. The SC magnet, developed by JSC "NIIEFA", has the mass of 7 800 t, and it is still the largest magnet in the world with a one-piece pole.

2. The most serious problem was associated with creation of the high-frequency system of the SC-1000. In all synchrocyclotrons with lower energy, a half-wave scheme of the accelerating system with the capacitor at the end for frequency variation was used. However, in such a scheme it is possible to obtain a frequency overlap no more than a factor of two. In our case, it was necessary to cover the frequency range from 30 to 13 MHz, that is, the frequency variation by 2.3 times. This problem was solved by JSC "NIIEFA" engineers. In the scheme proposed by JSC "NIIEFA", a substantially inhomogeneous feeder line was used and along with the capacitors the inductance was included in the variator scheme.

3. Due to a large volume of the vacuum chamber (30 m³), new diffusion pumps with the capacity of 45 m³/s were designed.

During the construction of the accelerator, a lot of work was done to modernize and tune its systems.

1. Due to the large volume of the magnetic field and high tolerances to the field formation, for the first time in our country an automated system for magnetic measurements was developed. With the help of this system, the entire magnetic field topography (5 000 points) was measured within the 8 h. The system consists of the coordinate mechanism which allows the probe to be positioned at any point along the radius and azimuth, a nuclear magnetic resonance probe with automatic resonance frequency tuning, a thermo-stabilized Hall probe and a magnetic median plane meter. This system made it possible to form the SC magnetic field with unprecedented high tolerances. The same system was used for alignment of the extraction system to correct the magnetic field perturbation introduced by the magnetic channel [1].

2. The most serious problems took place under practical realization of the accelerating system of a new type. The great complexity of the high-frequency (HF) system did not allow it to be calculated or modeled. Therefore, the system was adjusted to the design parameters directly on the already installed full-scale system. After first tests it became obvious that the manufactured system was not operable because it could not provide the accelerating voltage in the needed frequency range. As a result of the numerous studies, test measurements and analyses, significant changes were introduced to the system. To increase the coefficient of the capacity overlapping, changes were made in the design of the inductive elements of the variator. In order to maintain stable excitation of the HF system in the all operation frequency range and to suppress parasitic transversal modes of dee oscillations, a static two-feeder feedback system was applied in the resonance system and a lamp generator was developed. According to the results of these developments, two author's certificates of the USSR were issued [2].

2. Start-up of the accelerator and the experimental program

After all preparatory work, on November 4, 1967, the physical start-up of the SC-1000 was performed by the 50th anniversary of the Great October. Unfortunately, as a result of the physical start-up, an incomplete energy of about 750 MeV was obtained at a low beam intensity. Despite the modest results of the physical

start-up, it showed that all SC systems are workable and the project can be realized. That is why the 50th anniversary of the SC-1000 was celebrated in 2017.

However, the physical program started only in the beginning of 1970 when the proton energy was increased to 1 000 MeV [3], and the extraction of the beam from the vacuum chamber and its transportation to the physicist's targets were performed.

1. The work on the improvement of the HF system for obtaining the design energy of 1 000 MeV was continued. To increase the capacity overlap, additional condenser packs connected to the dee *via* an additional inductance were introduced into the variator.

2. The intensity of the beam of the accelerated protons was significantly increased after introduction of a Penning-type ion source, which was used at the Dubna synchrocyclotron.

3. The standard extraction efficiency for synchrocyclotrons does not exceed 1–5% due to usage of the open ion source and poor quality of the internal beam. An analysis of the factors limiting the extraction efficiency was carried out. Computer simulations of a large number of particle trajectories in the accelerator were performed. On the basis of the carried out analyses, it was proposed to increase considerably the extraction efficiency without radical reconstruction of the accelerator by developing the extraction system with a wide-aperture magnetic channel and a regenerator. A careful correction of the disturbances introduced by the massive iron magnetic channel made it possible to obtain the record 30% extraction efficiency in agreement with the calculated prediction [4]. First beam lines of several dozen of meters to transport the proton beam from the accelerator hall through the shielding wall to the experimental hall were built up.

Finally, on February 27, 1970, as a result of the performed work, the State Commission license was issued for the SC operation. From that time the SC-1000 began to work on the physical experiment for 4 000–6 000 hours a year.

3. The accelerator improvements in parallel with the experimental program

Simultaneously with physical experiments, an intensive program was carried out to improve the beam parameters and to develop new experimental capabilities:

1. *Long burst operation system* [5]. To increase the effectiveness of electronic methods of registration, an original long burst operation system using a C-electrode was developed. Unlike similar systems, the SC-1000 uses a $\frac{3}{4}$ wave resonance line with ferrite frequency variation and synchronization of the C-voltage in frequency and phase with the main dee voltage. The use of a resonance scheme made it possible to reduce the C power supply and to increase the beam macro duty cycle from 1.4 to 50% and more. The originality of the technical solutions is confirmed by an author's certificate.

2. *Electrostatic focusing system in the SC centre* [6]. In the central region of the accelerator, a new three-electrode focusing system was put into operation to increase the vertical focusing and to compensate the space-charge forces that limit the accelerator intensity. The new focusing system made it possible to increase the intensity by about 5 times and to reach 3.5 μA beam inside the vacuum chamber, and the intensity of the extracted beam to 1 μA . The originality of the technical solutions is also confirmed by an author's certificate.

3. *New variator*. To improve the reliability of the accelerator and to facilitate the maintenance work of the HF system, new variator rotors with Al plates, manufactured at PNPI, were introduced instead of the old ones with stainless steel plates. After installation of the new variators, the accelerator operating time achieved 6 000 hours per year.

4. Experimental SC complex and beams

The experimental complex of the PNPI SC (Fig.) consists of the accelerator, buildings and experimental halls with the systems of engineering maintenance (power supplies, water cooling, ventilation), beam transport lines, biological protection, beam dampers and experimental installations.

The SC is installed in a round hall of 32 m in diameter. The thickness of the wall made of heavy concrete is ~ 8 m; the thickness of the floor is 4 m. Collimators in the concrete wall between the accelerator and the experimental halls allow to transport beams to experimental set-ups. In the proton mode of operation, the beam with an intensity of $\leq 10^{11} \text{ s}^{-1}$ can be transported to the experimental hall to experimental set-ups. Also,

the proton beam can be transported to specialized areas such as the laboratory for short-lived isotope investigation IRIS (full intensity beam) or the medical building for the patient treatment (low intensity well focused beam). In the meson mode of operation, the proton beam is directed onto a meson-production target which is installed in the accelerator hall behind a thick concrete wall. The proton beam lines are terminated by 4 m long iron beam dampers to cut down the background in the experimental hall. According to the operation regulation, the non-used collimators in the wall between the accelerator and the experimental halls are closed down by remote handling of iron blocks. This collimator shielding with the remote handling helps to decrease the background and the irradiation dose for the staff.

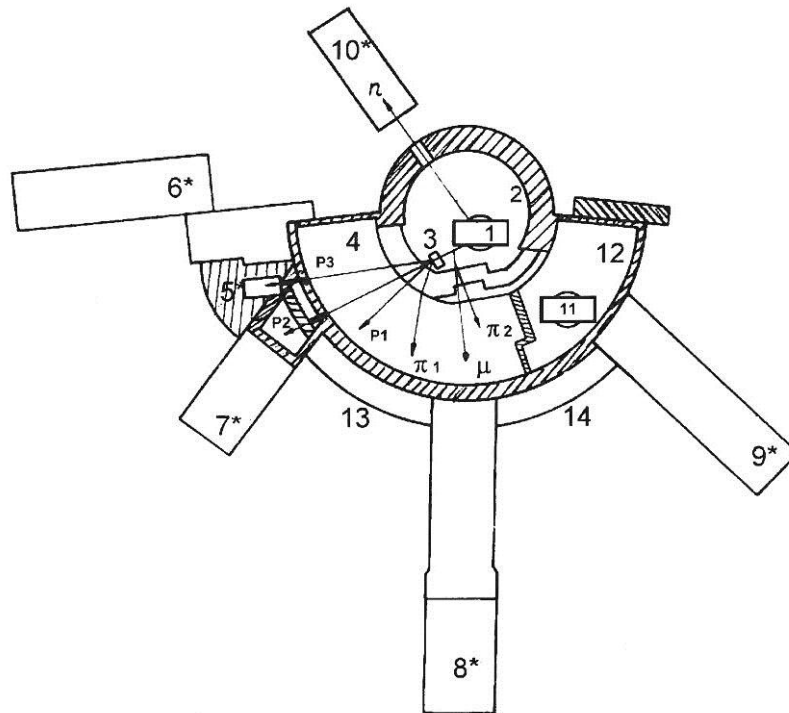


Fig. General view of the synchrocyclotron building complex and beam lines: 1 – the synchrocyclotron; 2 – the main hall; 3 – the beam distributing magnet SP-40; 4 – the experimental hall; 5 – the trap-damper of the proton beam; 6 – IRIS; 7 – the medicine annex; 8 – the block of technical maintenance; 9 – the computer centre; 10 – GNEIS; 11 – the isochronous cyclotron; 12 – the cyclotron hall; 13, 14 – the counting rooms. The blocks which were built after the synchrocyclotron start up are marked with *

Proton beams. Parameters of the proton beams are presented in Table 1.

Table 1

Proton beams

Particles	Energy, MeV	$\Delta E/E$, %	Intensity I , s^{-1}	Beam line	Notes
Protons	1 000	1	$6 \cdot 10^{12}$	P1, P2, P3	Main beam
		1	10^8	P2	Medical beam
		0.1	10^{10}	P2	Monochromatic beam
		1	10^{10}	–	Additional beam

The PNPI SC allows to accelerate protons only up to the fixed energy of 1 000 MeV. However, for some physical and applied researches, a variable energy beam is required. Such a beam was achieved by using a calibrated copper degrader with remote change of its thickness. This beam line consists of a degrader, collimators, a deflecting magnet to separate the beam from the background, and two doublets of quadrupole

lenses to focus the beam in the experimental hall. The parameters of the variable energy beam are presented in Table 1 for the main beam intensity of $3.0 \cdot 10^{12} \text{ s}^{-1}$. The parameters of the proton beam with variable energy are presented in Table 2, where I is the beam intensity and σ is the root mean square beam transversal size [7].

The variable energy proton beam was used for the fission cross-section measurements of heavy elements in the ISTC-1405 project and for radiation tests of electronics components.

Table 2

The parameters of the proton beam with variable energy

$E, \text{ MeV}$	$I, \text{ s}^{-1}$	$\Delta p/p, \%$	$\sigma_x, \text{ cm}$	$\sigma_z, \text{ cm}$
1000	$3.0 \cdot 10^{12}$	0.67	0.64	0.64
800	$1.675 \cdot 10^{10}$	1.27	0.690	1.547
600	$4.333 \cdot 10^9$	1.96	1.265	1.406
400	$1.393 \cdot 10^9$	3.29	2.265	1.442
200	$2.063 \cdot 10^8$	7.93	2.462	1.374
100	$4.600 \cdot 10^7$	12.27	3.627	1.368
60	$1.533 \cdot 10^7$	14.93	2.996	1.407

Meson beams [8]. All meson beams at the PNPI SC are generated at the same target installed in the accelerator hall behind a thick wall. It is possible to perform two experiments simultaneously. In total, there are three meson channels: π_1 channel, π_2 channel of lower energy and μ^- channel. Parameters of the meson beams are presented in Table 3. The π_1 channel selects π^\pm mesons generated in the forward direction. In this channel one can get beams with the maximum for the SC-1000 meson energy up to 700 MeV. The π_2 channel selects π^- mesons with the production angle of 60° . This channel provides pion beams with lower energy.

Table 3

Secondary particle beams

Particles	Momentum, MeV/c	$\Delta p/p, \%$	Intensity I , part./s	Beam line	Notes
π^+	450	6	10^6	π_1	Achromatic mode
π^-	450	6	$3 \cdot 10^5$		
π^-	250	2.5–12	10^5 – $5 \cdot 10^6$	π_2	Achromatic mode. “Surface” mesons
π^+	250	2.5–12	$3 \cdot 10^5$ – 10^7		
μ^+	29	12	$3 \cdot 10^4$		
μ^-	160	10	$9 \cdot 10^4$	μ	Separated beams
μ^+	170	10	$3 \cdot 10^5$		

At the π_2 channel, a special vacuum target can be installed to obtain the so called μ^+ “surface” mesons with the momentum of $\sim 29 \text{ MeV}/c$. The muon channel can provide separated μ^\pm mesons and an assortment of mixed π^- and μ^- -meson beams.

Neutron beam and neutron time-of-flight spectrometer GNEIS [9]. A one-turn deflection of the proton beam to the neutron production target generates on the target a short (7 ns) flush of neutrons with the intensity of $(2\text{--}3) \cdot 10^{14} \text{ s}^{-1}$. The time-of-flight (ToF) neutron spectrometer GNEIS has a 48.5 m flight base. Due to the high beam intensity and the short pulse duration, the spectrometer GNEIS is competitive with other well known spectrometers like WNP–LAMPF (Los-Alamos, USA), ORELA (Oak-ridge, England), and GELINA (Gel, Berlin). The neutron beam is used for investigations of neutron–nucleus interaction cross sections. The cross sections for inelastic neutron–nucleus interaction in the case of heavy nuclei were

measured in collaboration with Japan scientists in the frame of the ISTS-19-72 program and for tests of electronics components (see below).

Specialized experimental facilities and laboratories are located in the experimental hall and in the annexes.

High resolution magnetic spectrometer MAP [10] with the resolution of 10^{-3} is located in the experimental hall on the P1 beam line. Its effective use became possible after an invention of a way of monochromatization of the SC proton beam. With this spectrometer, an extensive series of researches on the study of the nuclear matter structure by means of elastic and quasi-elastic proton–nucleus scattering was performed.

The IRIS facility is aimed at investigations of short lived isotopes far from the β -stability line. New types of targets for a high production rate of rare isotopes were developed at the PNPI in collaboration with scientists from Italy, France, and Canada. The IRIS Laboratory is a well known world's research centre. This laboratory is working in cooperation with other centres, such as ISOLDE at CERN.

The proton therapy facility [11] was developed at the PNPI SC in collaboration with the Central Research Institute of Radiology and Surgery Technologies. The main peculiarity of the Gatchina facility is application of the 1 000-MeV proton beam for irradiation of intracranial targets in human brain. Up to now, more than 1 300 patients have been treated.

Universal testing centre for radiation resistance of electronics for the needs of space research, aviation and defense [12].

In the present time, more and more attention is paid to applied research. At the Gatchina SC together with the Institute of Space Instrument Engineering, a universal, single in Europe centre for the accelerated testing of radiation resistivity of electronics for aviation and space research was designed. The centre allows testing electronics on three sorts of the beam: on a proton beam with the energy 1 000 MeV, on a proton beam with a variable energy from 900 to 50 MeV and on a neutron beam with the spectrum repeating atmosphere neutrons. The neutron beam was developed on the basis of a one-turn beam deflection onto the internal target and due to modification of the GNEIS spectrometer. The centre is equipped with beam diagnostics systems, beam monitors, magnetic lenses, and dipole magnets and is controlled with the help of a computer. This centre has great potential in our country and evidently looks good at the international level.

5. Physics research at the PNPI synchrocyclotron

A large number of experiments on elementary particle physics and physics of atomic nuclei were carried out at the PNPI synchrocyclotron during the years of its operation. Here we will enumerate some of the performed experiments.

1. *Study of Pion–Nucleon Scattering in the Region of πN Resonances.* S.P. Kruglov, I.V. Lopatin, V.V. Sumachev *et al.* measured the differential cross sections of π^+p and π^-p elastic scattering with a high accuracy at twelve energies of incident pions in the range of 300 to 640 MeV using a liquid hydrogen target and a hodoscope detector consisting of 40 scintillation counters. More than three hundred cross-section data points were obtained with a statistical error of 2–5% and a systematic uncertainty about 2%. Using a dedicated polarized proton target and an experimental set-up including several arrays of magnetostrictive spark chambers and a multiplate carbon polarimeter built at PNPI, the polarization parameter P and spin-rotation parameters A and R were measured at several pion energies and several scattering angles. The obtained experimental data were used in new πp phase-shift analyses. Also, πd scattering and production of η mesons in $\pi^- p$ scattering were studied.

2. *Measurement of Polarization Parameters and Analysis of pp Elastic Scattering at 0.6–1.0 GeV.* V.G. Vovchenko, A.A. Zhdanov, A.V. Shvedchikov *et al.* studied the pp polarization P and the Wolfenstein polarization parameters D , R , and A at the proton energies of 650–970 MeV in a wide range of scattering angles. To perform such measurements, a proton beam polarized in all possible directions, vertical, horizontal, and longitudinal, was designed, and a liquid hydrogen target and a frozen spin polarized target were used. The detector set-up consisted of scintillation counters and polarimeters. Each polarimeter was made of two blocks of spark chambers and a carbon analyzer. The measured values of the polarization parameters were used in new pp phase-shift analyses.

3. *Study of πN and pN Interaction with a Hydrogen Bubble Chamber.* G.L. Sokolov, V.I. Medvedev, M.M. Makarov, V.V. Sarantsev *et al.* measured differential cross sections for pion and proton scattering on protons and neutrons in the 2π angular range in the energy range of the incident pions of 180–500 MeV and the incident protons of 500–1 000 MeV. A liquid hydrogen bubble chamber built at PNPI was used. The measurements were performed in 1972–1985 years, and as a result a wealth of information on πN and pN scattering was obtained.

4. *Small-Angle pp Scattering Studied with IKAR.* A.A. Vorobyov, G.A. Korolev, V.A. Schegelsky *et al.* investigated the differential cross section for pp scattering at small scattering angles in the energy interval from 600 to 1 000 MeV. The measurements were performed using a new experimental method suggested and worked out at PNPI based on a hydrogen-filled high-pressure ionization chamber IKAR. In these experiments, the “puzzle of Dutton” was solved and the validity of the dispersion relations in pp scattering at these energies was restored.

5. *Measurement of the Pion Mass with a Crystal Diffraction Spectrometer.* A.I. Smirnov, A.F. Mezentsev, A.A. Petrunin *et al.* measured with high precision the π^- mass using the crystal diffraction techniques developed at PNPI in the Neutron Research Division. A new experimental scheme was proposed, in which a proton beam produced pions in a meson production target, the produced pions were stopped in this target and pionic atoms were formed. Such an approach allowed to increase significantly the luminosity of the experiment. The measured pion mass, $m_{\pi^-} = 139\,565.7 \pm 1.7$ keV was the most precise value at that time (in 1976).

6. *Measurement of π^+ and K^+ Lifetime.* V.P. Koptev, S.M. Mikirtych'yants, G.V. Shcherbakov *et al.* performed precise measurements of the lifetimes of π^+ and K^+ mesons. The measurements were based on utilization of the periodic time microstructure of the proton beam, production of π^+ and K^+ mesons in a meson-production target, and detection of positive muons arising from the decay of π^+ and K^+ mesons stopped in this target. The determined π^+ - and K^+ -mesons lifetimes are: $\tau_{\pi^+} = 26.0361 \pm 0.0052$ ns and $\tau_{K^+} = 12.415 \pm 0.024$ ns. These measurements are among the most precision ones up to now.

7. *Measurement of the Subthreshold Kaon–Meson Production.* V.P. Koptev, S.M. Mikirtych'yants, G.V. Shcherbakov *et al.* performed also measurements of the “subthreshold” production of K^+ kaons in proton–nucleus interaction, that is production of kaons at energies 800–1 000 MeV not sufficient to produce kaons in free proton–nucleon interaction. The relatively large measured cross sections for subthreshold K -meson production were explained by a two-step mechanism: at first pions are produced in the target in pN interaction, and then these pions produce kaons in πN interaction in the same meson-production target.

8. *Crystal Optics of High-Energy Particles.* V.M. Samsonov, A.I. Smirnov, A.V. Khanzadeev *et al.* studied the process of capture of 1 GeV protons by a bent silicon crystal. An effect of the volume capture into the channeling regime by a bent crystal was discovered. It was demonstrated that the region where particles were captured into the channeling regime by a bent crystal was not limited to the region near the entry face but was distributed over the entire length of the crystal. As a result, the angular interval of the capture into the channeling regime was shown to be more than two orders of magnitude larger than the Lindhard angle.

9. *Proton Diffraction Scattering on Nuclei and Nuclear Matter Distributions.* A.A. Vorobyov, S.L. Belostotsky, G.D. Alkhazov *et al.* performed measurements of the differential cross sections for 1 GeV proton elastic scattering on a number of stable nuclei and determined the nuclear matter distributions from the measured cross sections. The proton energy of about 1 GeV has occurred to be optimal for studying the nuclear matter distributions since the mechanism of proton–nucleus scattering at this energy is simple and there exists an accurate theory of multiple scattering, which allows one to connect the measured cross sections with the nuclear density distributions under study. It was demonstrated that with this method it is possible to obtain information on the nuclear matter distributions with the accuracy comparable to that reached in studies of the nuclear charge distributions by the method of electron scattering.

10. *Elastic Diffraction Scattering of Protons on the Lightest Nuclei.* A.A. Vorobyov, G.A. Korolev, A.V. Khanzadeev *et al.* performed precise measurements of small-angle pd and $p^4\text{He}$ scattering at intermediate energies (700–1 000 MeV). The measurements were executed with the help of the hydrogen-filled high pressure ionization chamber IKAR.

11. *Study of the Nuclear Structure with Quasi-Elastic Proton Scattering at 1 GeV*. A.A. Vorobyov, Yu.V. Dotsenko, O.V. Miklukho *et al.* studied ($p, 2p$) and (p, np) reactions at $E_p = 1$ GeV with the help of a correlation two-arms missing mass spectrometer consisting of a magnetic spectrometer to register the scattered proton and a ToF spectrometer to register the knocked-out proton or neutron. With this approach, the shell structure of a large number of nuclei (from the light nucleus ${}^6\text{Li}$ to the heavy nucleus ${}^{208}\text{Pb}$) was investigated. Valuable information on the nuclear shell structure, including the inner proton and neutron shells, was obtained.

12. *Study of Muon-Catalyzed Fusion*. A.A. Vorobyov, G.G. Semenchuk, E.M. Maev *et al.* thoroughly studied the process of muon catalyzed dd - and dt -fusion. A new very efficient experimental approach to study the muon-catalyzed fusion was proposed. The new experimental method was based on a high-pressure hydrogen-filled ionization chamber. All principal parameters governing the process of the muon catalyzed dd - and dt -fusion were measured. The obtained results of investigations of the muon catalyzed fusion reactions constitute the up-to-date data base of these reactions and are used for testing the relevant theory.

13. *Nuclear Fragmentation Induced by 1 GeV Protons*. E.N. Volnin, A.A. Kotov, D.M. Seliverstov *et al.* studied fragmentation of middle-weight and heavy nuclei under action of 1 GeV protons. Energy spectra of light fragments (isotopes of He, Li, Be, and B) were measured with the help of a ToF quadrupole lens magnetic spectrometer. The fragments were registered in the focal plane of the spectrometer with the help of a surface barrier Si(Au) detector (which measured the fragments energy) and a thin ionization chamber (which measured dE/dx).

14. *Measurements of Cross Sections for Heavy Nuclei Fission Induced by Intermediate Energy Protons*. V.G. Vovchenko, A.A. Kotov, L.A. Vaishnena *et al.* for a number of heavy nuclei performed measurements of the total cross sections for fission induced by protons with the energy from 200 MeV to 1 GeV using a new method based on parallel plate avalanche counters.

15. *Investigation of the Mass, Angular and Energy Distributions of Fission Fragments*. G.E. Solyakin, A.V. Kravtsov, B.L. Gorshkov *et al.* performed measurements of the mass, angular and energy distributions of heavy fragments in fission of the ${}^{238}\text{U}$, ${}^{232}\text{Th}$, ${}^{209}\text{Bi}$, ${}^{197}\text{Au}$, ${}^{184}\text{W}$, and Sm nuclei induced by 1 GeV protons. The measurements were carried out with the help of the two-arm spectrometer PUSEK2 consisting of arrays of semiconductor detectors which allowed to determine the angular-velocity-energy correlations of the emitted fragments.

16. *Study of Exotic Nuclei at the Mass-Separator Complex IRIS*. E.Ye. Berlovich, Yu.N. Novikov, V.I. Tikhonov, A.A. Bykov, V.D. Vitman *et al.* performed investigations of properties of exotic nuclei at the mass-separator complex IRIS. More than 20 nuclei were identified for the first time at IRIS, a resonant structure of beta-strength functions was observed, masses of about 100 exotic nuclei were determined.

17. *Study of Exotic Nuclei at the Laser Complex IRIS*. E.Ye. Berlovich, G.D. Alkhozov, A.E. Barzakh, V.P. Denisov, V.N. Panteleev *et al.* performed laser spectroscopy investigations of exotic nuclei at the laser set-up IRIS built at PNPI. An efficient method of the resonance ionization spectroscopy was applied for the first time to study exotic nuclei. A new high-efficiency laser ion source was proposed and developed. More than 100 nuclei were studied at IRIS with the method of the laser spectroscopy.

18. *Study of Magnetic Properties of Substances with the μSR Method*. V.P. Koptev, S.I. Vorobyov, V.G. Scherbakov *et al.* performed investigations of magnetic properties of a number of substances using the muon spin rotation (μSR) method. Note that the PNPI μSR set-up located at the exit of the polarized muon channel of the PNPI synchrocyclotron is the only μSR installation in Russia.

19. *Studies at the Neutron beam Facility GNEIS*. G.A. Petrov, O.A. Scherbakov *et al.* performed investigations of the interaction of low-energy and intermediate energy neutrons with nuclei at the neutron-beam facility GNEIS. The neutron energy spectrum of the GNEIS beam resembles that of atmospheric neutrons in a wide energy range (from 1 to 1 000 MeV). This beam is effectively used for investigation of radiation hardness of the electronic components intended for aviation and for cosmos research.

Most of the investigations listed above were carried out for the first time, and new important results were obtained. Many investigations which were started at the PNPI synchrocyclotron were continued later at other high-energy accelerators in Russia and abroad. Scientists from other nuclear centres in Russia and foreign scientists (from Great Britain, France, Germany, Japan, Polish, and other countries) also took part in investigations at the PNPI accelerator.

Detailed information about the experiments performed at the PNPI synchrocyclotron can be found in the HEPD reports “Main scientific activities 1971–1996”, “Main scientific activities 1997–2001”, “Main scientific activities 2002–2006”, “Main scientific activities 2007–2012”, and in the present report “Main scientific activities 2013–2017”.

6. Present status of the SC-1000

Even now, after 50 years of successful operation, the Gatchina synchrocyclotron remains a valuable facility, especially for various studies in nuclear physics.

The proton energy of 1 GeV proved to be ideal for investigation of the nuclear structure with elastic and quasi-elastic proton scattering off nuclei.

A major part of the beam is provided now for the IRIS facility for production and studies of nuclei far from the nuclear stability region. The development of the laser ion source and the high temperature target allowed IRIS to be competitive with similar facilities like ISOLDE at CERN. An extensive experimental program is continued in the π beams. Further plans are associated with an increase in the resolution of the $\pi 1$ channel up to 0.2%.

The neutron ToF facility GNEIS is regularly used for studies of nuclear fission by resonance energy neutrons.

In recent years, a number of experiments have been carried out at the SC-1000 to study the channeling and deflection of the proton beam with the help of crystals. At CERN at the Large Hadron Collider it is planned to increase the luminosity. In this connection, experiments are carried out to eliminate the beam halo by means of a crystal–optic system developed at the PNPI.

Currently, a lot of attention is paid to applied researches. As in the previous years, the medical proton beam is effectively used for stereotaxic proton therapy.

Considerable amount of the beam time is provided for radiation tests on radiation resistance of electronics components for aviation and space research.

The μ SR experiments on the muon channel continue to play an important role in the experimental program at the SC to study new materials.

Many experimental methods were developed at PNPI and tested in the SC beams, before they were used in collaborative experiments at other accelerators (CERN, SACLAY, FNAL, PSI, GSI, DESY, BNL). This tradition is continued.

In conclusion, in spite of the reduction of the beam time down to 2 500 hours per year, the Gatchina SC remains an active and reliable accelerator allowing to carry out important physical and application programs.

7. Conclusion

The Synchrocyclotron is the basic PNPI set-up for nuclear and particles physics. Many PNPI physicists passed the school of experiments on the SC-1000 and then became well known in the world physical community.

Unique set-ups designed at the PNPI passed through the initial tune-up and tests at the SC-1000 and then were used at advanced accelerator centres of the entire world.

At the Gatchina accelerator, high precision properties of the elementary particles were obtained, which are included in the word reference books.

A large number of collaboration experiments were performed with other institutes from Russia, France, Germany, Japan, the USA, Italy, *etc.*

Since the start-up of the SC-1000 in 1970, a new generation of the intermediate-energy accelerators has appeared in the world. In particular, these are modernized synchrocyclotrons after cardinal reconstruction of all their systems and meson factories. Thanks to intensive and original improvements programs at the SC-1000, about the same beam intensities were obtained at the SC-1000, as in other synchrocyclotrons after their reconstruction. In spite of the fact that modern “meson factories” exceed considerably the PNPI SC in the beam intensity, nevertheless, due to some accelerator features, mainly due to the higher energy, which is important in a number of cases for experiments on proton, meson and neutron beams, and an extensive and

successful application program, there is a significant area for the research at the SC-1000 which is not overlapped by other facilities.

After 50 years of successful operation, the SC-1000 remains one of the active accelerators in Russia. At the present time, the SC-1000 is on operation about 2 500 hours per year. The SC is an multidisciplinary research facility of the institute, on the beams of which a wide range of fundamental and applied research is carried out. The accelerator beams are in demand and are used by many organizations and institutes of our country. There are good prospects for expanding the scope of the work on radiation tests of electronics, proton therapy, on study of rare radioactive isotopes, *etc.*

References

1. V.A. Eliseev, G.A. Riabov, I.I. Tkach, *Zh. Tekhn. Fiz.* **41**, 1787 (1971) [in Russian].
2. N.K. Abrossimov, D.G. Alkhazov, S.P. Dmitriev *et al.*, *Zh. Tekhn. Fiz.* **41**, 1222 (1971) [in Russian]; Certificate No. 270131 with the Priority Date of 28.04.1969. *Bull. Izobr.* **16**, 62 (1970).
3. N.K. Abrossimov, D.G. Alkhazov, S.P. Dmitriev *et al.*, *Zh. Tekhn. Fiz.* **41**, 1769 (1971) [in Russian]; *Sov. J. Techn. Phys.* **16**, No. 9, 1399 (1972) [in English].
4. N.K. Abrossimov, V.A. Eliseev, V.A. Volchenkov *et al.*, *Nucl. Instrum. Meth.* **126**, 221 (1975).
5. N.K. Abrossimov, A.G. Kotov, A.V. Kulikov *et al.*, in *Proc. of the 3 All-Union Conf. on Charged Particle Accelerators, Moscow, Russia, 2–4 Oct. 1972, Moscow*, **2**, 277 (1973); Certificate 370901 with the Priority Date of 20.07.1972.
6. N.K. Abrossimov, S.P. Dmitriev, A.V. Kulikov *et al.*, in *Proc. of the 6 All-Union Conference on Charged Particle Accelerators, Dubna, Russia, 11–13 Oct. 1978, Moscow*, **1**, 277 (1979).
7. S.A. Artamonov, E.M. Ivanov, N.A. Ivanov *et al.*, *Phys. Part. Nucl. Lett.* **14**, No. 1, 188 (2017); DOI 10.1134/S1547477117010046
8. N.K. Abrossimov, V.A. Volchenkov, V.A. Gordeev *et al.*, in *Proc. of the 8 All-Union Conf. on Charged Particle Accelerators, Protvino, Russia, 19–21 Oct. 1982, Dubna*, **2**, 90 (1983).
9. N.K. Abrossimov, G.Z. Borukhovich, A.B. Laptev *et al.*, *Nucl. Instr. Meth. A* **242**, 121 (1985).
10. G.D. Alkhazov, S.L. Belostotski, Certificate No. 582709 with the Priority Date of 3.05.1976. *Bull. Izobr.* **18**, 294 (1979).
11. N.K. Abrossimov, V.A. Volchenkov, V.A. Eliseev *et al.*, in *Proc. of the 8 All-Union Conf. on Charged Particle Accelerators, Protvino, Russia, 19–21 Oct. 1982, Dubna*, **2**, 94 (1983).
12. D.A. Amerikanov, S.A. Artamonov, E.M. Ivanov *et al.*, *Quest. Atom. Sci. Techn. Ser.: Phys. Radiat. Eff. Radio-Electron. Equipm.* **20**, 42 (2017).

STATUS OF THE PNPI H⁻ ISOCHRONOUS CYCLOTRON C-80

**D.A. Amerkanov, S.A. Artamonov, E.M. Ivanov, G.F. Mikheev, G.A. Riabov,
V.A. Tonkikh, V.I. Yurchenko and the accelerator staff
in collaboration with D.V. Efremov Institute of Electrophysical Apparatus:
A.V. Galchuck, Yu.N. Gavrish, S.V. Grigorenko, A.N. Kuzhlev, V.G. Mudrolyubov**

1. Introduction

Installation of the cyclotron system for acceleration of H⁻ ions at energies ranging from 40 up to 80 MeV has been completed in the PNPI. The cyclotron is intended for production of a wide assortment of radioisotopes including radiation generators (Sr–Rb, Ge–Ga) for medicine, proton therapy of ophthalmic diseases, tests of radioelectronic components for radiation resistance and studies in the field of nuclear physics and radiation material science.

In June 2016, physical start-up of the cyclotron was realized in the pulsed mode. To date, the beam of ~ 38 μA is obtained at the inner probe of the cyclotron, the extracted beam at the first diagnostic device being ~ 28 μA. The beam transport to the final diagnostic device of the beam line (~ 35 m long) practically without losses has been demonstrated. On November 8, 2016, the design parameters (80 MeV, 100 μA) of the cyclotron C-80 were obtained.

2. Purpose and main characteristics

The C-80 cyclotron system developed by specialists of PNPI and the D.V. Efremov Institute of Electrophysical Apparatus (JSC “NIEFA”) is intended for production of proton beams with energies ranging from 40 up to 80 MeV and the current of up to 100 μA. The beams with such parameters will be used to finalize the development of the technology for production of a wide assortment of radioisotopes for medicine including radiation generators and for commercial production of these radioisotopes [1, 2]. In the nearest future, the following works are planned: 1) building of a special line to form homogeneous proton beams of ultra-low intensity (10^7 – 10^9 s⁻¹) for proton therapy of ophthalmic diseases, 2) building of a test facility to carry out studies on the radiation resistance of radioelectronic equipment using intensive beams of protons and neutrons.

The cyclotron system equipment with the transport system of the accelerated proton beam to remote target stations is mounted in the experimental hall of building 2 and in its basement. The equipment of the cyclotron and that of the first section of the beam transport system is located on the ground floor (Fig. 1), the external injection system, the radio frequency (RF) generator and the system for the beam transport to three targets are mounted in the basement. The main characteristics of the cyclotron are given in Table.



Fig. 1. The C-80 cyclotron system

Table

Main characteristics of the cyclotron

System, parameter	Characteristic, value
Type of the accelerated particles	H^-
Type of the extracted particles	H^+
Pole diameter	2.05 m
Valley gap	386 mm
Hill gap (min)	163 mm
Number of sectors	4
Spiral angle (max)	65°
Magnetic field in the centre	1.352 T
Flatter (max)	0.025
Extraction radius	0.65–0.90 m
Beam energy – variable	40–80 MeV
Method	Stripping
Beam current	100 μA

The major unit of the cyclotron, its electromagnet, was designed using the model of the magnet of the synchrocyclotron operating in the PNPI, and further it was updated. Such a decision limited naturally the choice of engineering solutions when designing the cyclotron. The profile of the magnet poles was chosen as a result of 3D computer simulations of the entire magnet [3]. After manufacturing the sectors and the overlays on them, the final heights of the shims were refined in the course of full-scale magnetic measurements and calculations taking into account the actual magnetic permeabilities of the used iron. As a result, an isochronous magnetic field was formed with an accuracy of about 5 Gs. Such a field allows, as show simulations, to accelerate particles up to an energy of 80 MeV [4].

3. Tests and results

In the process of preliminary tests of the cyclotron, appreciable losses of the beam intensity in the cyclotron central region were observed. Measurements of the current with a three-electrode probe inside the cyclotron chamber demonstrated a noticeable beam shift relative to the median plane (Fig. 2).

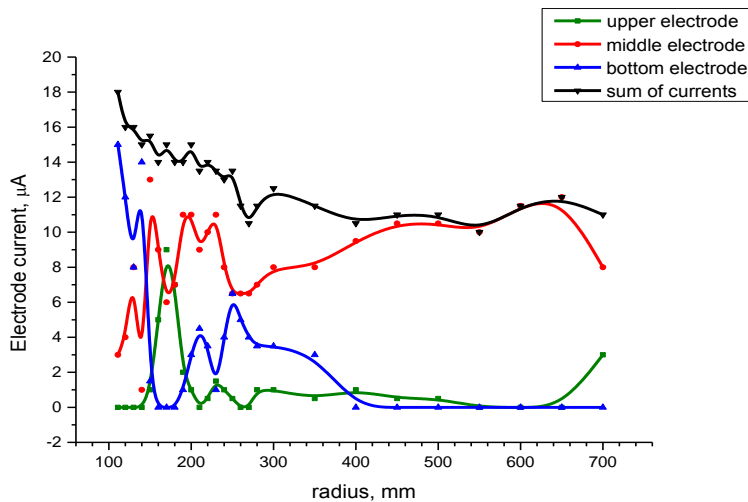


Fig. 2. Results of the current and beam position measurements in the process of acceleration

To establish the reason for such a behaviour of the beam, additional magnetic measurements were carried out, which showed that the actual field in the central region exceeded significantly the calculated one and the field formed prior the vacuum chamber assembly. The main reason for such a difference is due to magnetic properties of the stainless steel which was used as a material for the vacuum chamber. Figure 3 shows the difference (≤ 5 Gs) between the formed and isochronous magnetic fields before the vacuum chamber was installed in the gap of the magnet [4]. Figure 4 shows the difference between the resulting and isochronous magnetic fields after the vacuum chamber was installed in the gap of the magnet.

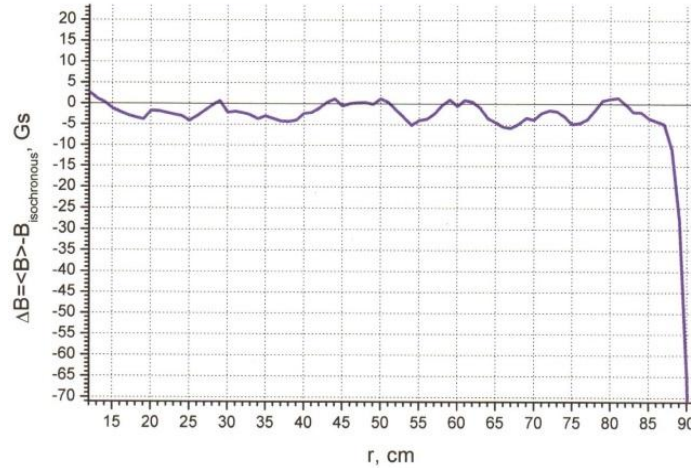


Fig. 3. Difference between the formed magnetic field and the calculated isochronous magnetic field (prior the vacuum chamber assembly)

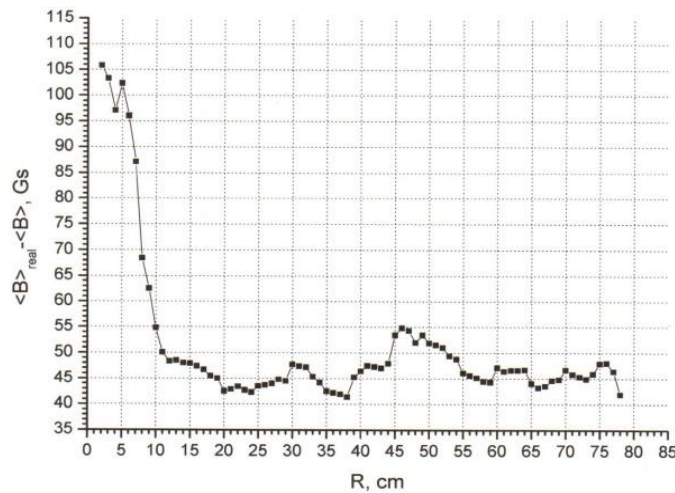


Fig. 4. Difference between the actual magnetic field and the formed isochronous magnetic field (after the assembly of the vacuum chamber)

Thus, the vacuum chamber perturbed the magnetic field by about 45 Gs at all cyclotron radii larger than 15 cm. The perturbation of the magnetic field by the chamber at small radii (< 15 cm) was much larger.

In addition, an analysis of the results obtained allowed us to suppose that large intensity losses result from the presence of a radial component of the magnetic field in the median plane [5]. Unfortunately, there are no means to measure a radial component of the magnetic field correctly for the actual geometry of the cyclotron central region. Apparently, this effect is due to the fact that during the installation of the systems of the axial injection and of the accelerating system, it was not possible to align the magnetic median plane with the output of the beam from the inflector with a sufficient accuracy.

The use of additional harmonic coils improved the situation not significantly due to their remote location from the central plane of the electromagnet. To place the coils closer to the median plane is impossible as the central region is limited in space, and the sizes of the channel that accepts the beam from the external injection system should be kept unchanged. Therefore, the only method to reduce the intensity losses of the accelerated beam is an experimental choice of the position, size and shape of additional magnetic elements (plugs, additional rings, *etc.*) located in the cyclotron central region.

The resonance acceleration system consists of two symmetrical quarter-wave resonators which are placed completely inside the vacuum chamber. The system is equipped with a capacitor for frequency tuning, an automatic frequency tuning trimmer and a RF probe. The operating frequency is 41.2 MHz, which corresponds to the 2nd harmonic of the ion revolution frequency. The normal value of the RF voltage amplitude is 60 kV. When manufacturing the vacuum chamber, a required rigidity of the covers was not provided, and this resulted in a smaller gap between them and in deformation of the resonator claddings in the process of pumping-down. This made necessary to change the vertical sizes of the dee stems and the resonator tanks, which required a subsequent radio technical tuning of the system. Under tests of the RF system at a high power level, an appreciable heating of a ceramic unit of the trimmer stem took place, which resulted in its subsequent destruction. This occurred due to a poor choice of the trimmer position in the tank of one of the resonators. A new unit was designed, manufactured and installed, which allowed to locate the trimmer outside of the resonator volume, and thus its heating was excluded.

The RF power supply system consists of a stabilization and control module and of a RF power amplifier. The stabilization and control module designed in the JSC "NIEFA" provided reliable operation in the process of generating 41.2 MHz operating frequency, tuning and stabilization of the natural frequency of the resonance system and the accelerating voltage amplitude.

The RF power amplifier designed and delivered by the coaxial power systems (CPS), Great Britain, should provide an output power of 80 kW at a frequency of 41.2 MHz. From the results of initial tests of this equipment in the operating modes, a pressing need for its fundamental updating was ascertained. Six additional fans, each of 0.25 kW, and additional partitions were installed; perforations were made in the available partitions, which provided an optimal distribution of air flows and the required thermal mode. The insulators used by the CPS firm in the final stage were completely replaced because of their systematic breakdowns. We detected and eliminated a number of errors in the circuitry, which did not allow to obtain the necessary stability of the output signal and prevented normal operation of the RF system:

- The high-voltage input of the final stage was redesigned, re-manufactured and newly installed; the leading-in power cable was replaced by a shorter one.
- The circuit of the transistor amplifiers power supply was modified, and one of the power supply units was replaced by a more powerful one.
- The voltage filters of the final stage anode were replaced.
- The fans power supply circuit providing an effective cooling of heated electronic components after switching off the amplifiers was modified.
- The switch-on time of the power supply system of the tube filaments was changed to improve their operation stability.
- The circuit-breaker for power supply input was replaced.
- Inspection of the cable inter-connections in the amplifier was conducted with subsequent their replacement where it was necessary, *etc.*

Works on updating the RF power amplifier slowed down considerably the completion of the commissioning works and demonstrated a pressing need for using our own efforts to design proper amplifiers for our cyclotrons.

The cyclotron is equipped with remotely-operated diagnostic probes intended to measure the beam current. In the process of the commissioning works, a high level of the RF noise was observed, which made difficult correct displaying of the beam current on the central monitor of the operator workstation. We managed to eliminate the observed noise by placing additional protection screens on the probe electrodes.

A distributed automatic control system was used. It consists of Mitsubishi and Fastwel IO controllers and computers, each being responsible for the control of one or several sub-systems of the cyclotron. The main unit of the control system is an industrial (host) computer, which inquires slave controllers and transmits

the information acquired to the computers of the operator's workstation; receives commands from the operator's workstation and performs their arbitration and distribution. The data exchange is realized *via* network interfaces. To ensure normal operation of the automated control system, there must be a reliable special grounding to provide electromagnetic compatibility of the cyclotron equipment. At the initial stage of the works, this grounding did not meet the requirements, which resulted in failures of several controllers and made us to prolong the time for carrying out the commissioning works.

The beam transport system of the C-80 cyclotron is intended to transport the extracted proton beam to final devices. Figure 5 shows the schematic of the beam transport system layout and elements of its equipment.

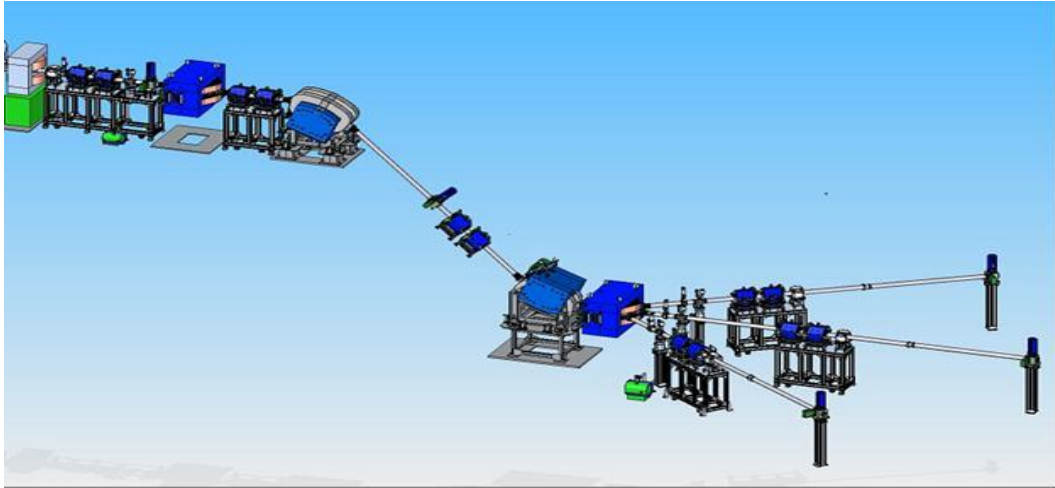


Fig. 5. Layout of the beam transport system

The first section of the beam transport system consisting of matching, correcting, switching and bending magnets, a doublet of quadrupole lenses and a beam diagnostics device is located in the experimental hall. The second section of the beam transport system comprising bending, switching and correcting magnets, quadrupole lenses doublets and a beam diagnostics device is housed in the basement of the experimental hall. Because of a rather large length of the inclined beam-line part between the bending magnets in the experimental hall and in its basement, the quadrupole lenses doublet and the diagnostic device are placed just in this beam-line.

In June 2016, a physical start-up of the C-80 cyclotron system was realized. The accelerator was started in the pulse mode at low currents of the accelerated beam to exclude strong activation of the equipment to make possible safe continuation of works in the cyclotron vacuum chamber, works with the components of the beam transport system, *etc.* When choosing the operating modes, available permissions granted by supervising authorities to carry out the commissioning works were taken into account. At this stage, a beam of $\sim 38 \mu\text{A}$ was obtained at the inner probe of the cyclotron. The extracted beam obtained at the first diagnostic device was $\sim 28 \mu\text{A}$. The beam transport practically without losses to the final diagnostic device of the beam transport system ($\sim 35 \text{ m}$) was demonstrated. Physical start-up was realized in the automated control mode under monitoring of all the systems of the cyclotron. On November 8, 2016, the designed parameters (80 MeV, 100 μA) of the C-80 cyclotron were obtained.

4. Conclusion

Our short-term plans include an increase of the maximum proton beam intensity by using reserves untapped so far:

- completion of works on optimization of the electromagnetic field in the cyclotron central area,
- increase of the injection current up to its specified value (from 900 up to 2 500 μA),
- use of the buncher potentialities with the anticipated effect of not less than two times higher current of the extracted beam (in the works on the physical start-up, the buncher installed in the external injection system line was not used).

The efforts listed above will guarantee stable maintenance of the design parameters of the C-80 cyclotron system and will offer opportunities for further increase of the accelerated proton beam intensity.

In the future, it is planned to carry out the following works:

- to engineer a local protection system for the cyclotron, the transport path and the target stations to ensure operation at the full beam intensity,
- to develop technologies of operation of the target stations at high beam intensity,
- to create a radiochemical complex with hot chambers for isolating the necessary isotopes and creating pharmaceuticals for medicine,
- to construct a special beam transport system for formation of precision proton beams for proton therapy of ophthalmic diseases,
- to build a test bench for carrying out radiation resistance of radio electronic products using intensive beams of protons and neutrons with an energy of 40–80 MeV,
- to optimize the beam transport system and to minimize the beam losses.

References

1. S.A. Artamonov, E.M. Ivanov, G.A. Ryabov *et al.*, *Probl. Atomic Sci. Technol.* No. 3 (91), 3–7 (2014).
2. P.V. Bogdanov, I.N. Vasilchenko, Yu.N. Gavrish *et al.*, in *Proc. of XXIII Russ. Particle Accelerator Conf. (RuPAC 2012)*, St. Petersburg, Russia, 24–28 Sept. 2012, Proc. Vol., pp. 106–108, <http://accelconf.web.cern.ch/accelconf/>
3. S.A. Artamonov, E.M. Ivanov, G.A. Riabov, N.A. Chernov, in *Proc. of RuPAC-2012*, St. Petersburg, Russia, 24–28 Sept. 2012, WEPPC015, pp. 475–477.
4. S.A. Artamonov, D.A. Amerkanov, G.I. Gorkin *et al.*, in *Proc. of XX Int. Conf. Beam Dynamics & Optimization, BDO-2014*, St. Petersburg, Russia, 30 June 30 – 4 July 2014, pp. 18–19.
5. G.A. Karamysheva, S.A. Kostromin, N.A. Morozov *et al.*, *Lett. to the ECHAY*, **11**, No. 6, 1232 (2014).



Elementary Particles Physics

SELECTED PHYSICS RESULTS FROM THE CMS EXPERIMENT AT THE LARGE HADRON COLLIDER

PNPI participants of the CMS Collaboration:

A.A. Vorobyev, V.T. Kim, Yu.M. Ivanov, V.L. Golovtsov, E.V. Kuznetsova, P.M. Levchenko,
V.A. Murzin, V.A. Oreshkin, L.A. Shchipunov, I.B. Smirnov, D.E. Sosnov, V.V. Sulimov,
L.N. Uvarov, S.A. Vavilov, S.S. Volkov, An.A. Vorobyev

1. Introduction

The CMS experiment [1] is one of the largest international scientific collaborations in history, involving about 4300 particle physicists, engineers, technicians, students and the support staff from 182 institutes in 42 countries.

Main physics goals of CMS are precision tests of the Standard Model (SM), electroweak boson physics, top quark physics, quantum chromodynamics (QCD), B physics, a search and study of the properties of the Higgs boson, and a search for physics beyond the SM (BSM): supersymmetric particles, gravitons, candidates for the cosmic dark matter, and a search for extra dimensions.

During 2013–2018, CMS obtained a big amount of physics results based on the Run-1 and Run-2 data. Run-1 included the data taken at $\sqrt{s} = 7$ and 8 TeV with an integrated luminosity of 5 and 20 fb^{-1} . Run-2 featured the centre-of-mass (c. m.) energy increased to 13 TeV and an increased instantaneous luminosity. The data taking was ended in December 2018 accumulating the total integrated luminosity of more than 160 fb^{-1} , as shown in Fig. 1. The combined dataset of Run-1 and Run-2 is the largest sample ever collected at a collider equivalent to about 5% of the total dataset that the Large Hadron Collider (LHC) is expected to deliver in its lifetime.

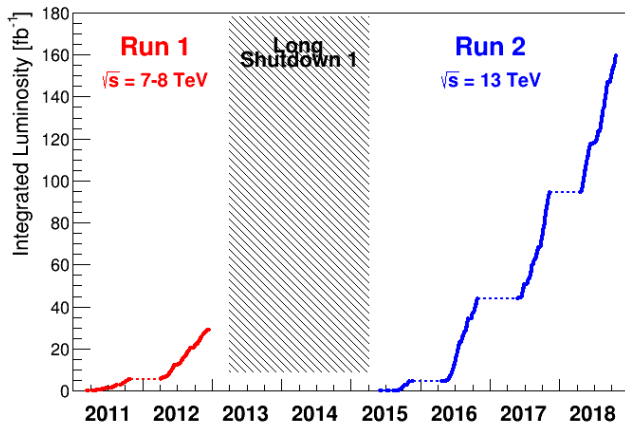


Fig. 1. Integrated proton–proton luminosity for LHC Run-1 (7 and 8 TeV) and Run-2 (13 TeV)

The results cover a wide assortment of topics and range from precision measurements of the Higgs boson and the SM processes to searches for rare decays and exotic phenomena. Some selected results are presented below: precision measurements of the QCD and electroweak processes cross sections, top quark production and top quark mass measurements, the SM parameters extraction (such as Cabibbo–Kobayashi–Maskawa (CKM) matrix elements), flavour physics including very rare B -meson decays, heavy quark resonance spectroscopy, and limits on BSM physics models. Two other crucial topics, the Higgs boson physics results and the electroweak vector boson fusion, are covered separately elsewhere in this volume.

3. Top physics

The LHC can sometimes be referred to as a “top quark factory” producing large numbers of these heavy particles thanks to high luminosity and high c. m. energy delivered by the LHC. Thus, we are now in the era of precision top quark measurements, where systematic sources of uncertainty dominate over the statistical uncertainties.

Figure 4 shows the inclusive top pair production cross section measured for the energies 5.02, 7, 8, and 13 TeV along with the theoretical prediction from the SM as a function of the c. m. energy. Good agreement with the SM prediction can be seen [4–7].

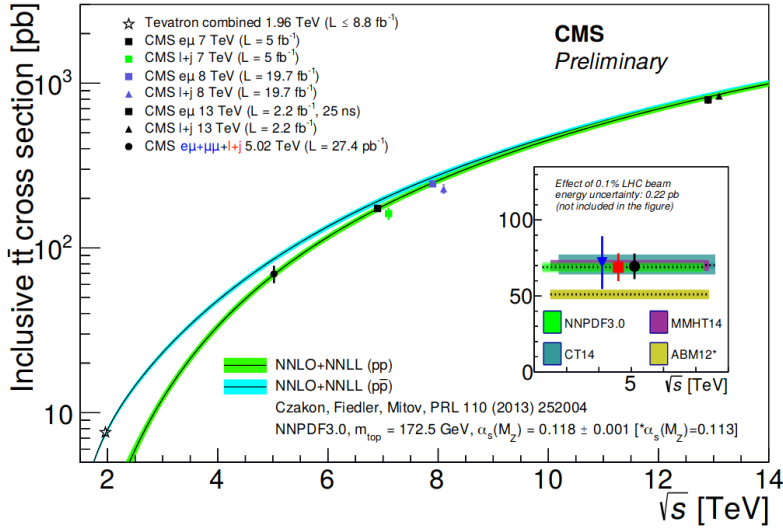


Fig. 4. Summary of the CMS measurements of the top-pair production cross-section as a function of the c. m. energy compared to the NNLO QCD calculation complemented with the next-to-next-to-leading logarithmic resummation (top++2.0) [4]

CMS also measured the differential cross sections for the top-pair production, which, aside from providing information about the process kinematics and offering sensitivity to the QCD fundamental parameters, allow for improvements in the background modelling to search for physics beyond the SM, in particular those involving signal processes for which the top–antitop quark pairs represent a significant source of background.

As the datasets grew, the top-pair production analyses became far less statistically limited. The dilepton channel [8] was the most statistically challenging, but it featured the least amount of background.

The differential cross sections were measured as a function of various kinematic observables of the top quarks, jets, and leptons of the event final state. The main challenge of the differential cross section measurement in this channel was to reconstruct the six components of the two neutrino momenta in the events, starting only from the measured E_T^{miss} component. To solve it, CMS used the kinematic reconstruction algorithm [9] based on the imposition of a set of kinematic constraints resulting from the fact that the missing transverse energy is originating from a pair of neutrinos, as well as constraints on the W boson and top-quark masses, on an ensemble of 100 data samples smeared artificially according to the detector resolution. This technique allowed to reconstruct the $t\bar{t}$ system with a 90% efficiency for the selected signal in both data and simulation. Moreover, considering events with highly boosted top quarks with the jet substructure technique helped to extend the kinematical reach up to the TeV scale.

Most of the measured differential cross sections are well modelled by theoretical predictions at next-to-leading order (NLO) QCD obtained using the POWHEG V2+PYTHIA 8, POWHEG V2+HERWIG++ and MADGRAPH interfaced to PYTHIA (MG5_aMC@NLO+PYTHIA 8 [FxFx]) Monte Carlo (MC) generators.

However, a set of transverse momentum distributions of the top quarks, leptons, b -jets, and $t\bar{t}$, $l\bar{l}$, and $b\bar{b}$ systems was observed to be significantly softer in the data than in the MC predictions both at 8 and 13 TeV, especially for POWHEG V2+PYTHIA 8. At the same time, the POWHEG V2+HERWIG++ simulation provides a better modelling of the top quark p_T distributions. This provides a valuable input for understanding and improvements of the MC description. The measured distribution of the azimuthal angle difference between the two leptons was used to put a constraint on the anomalous top-quark chromomagnetic moment, a feature

of some BSM models such as two-Higgs-doublet models, supersymmetry, technicolour, and top-quark compositeness models. The distribution of the difference in absolute rapidities between the top quark and top antiquark was used to extract the $t\bar{t}$ charge asymmetry for the first time at the c. m. energy of 13 TeV.

The inclusive single top-quark production was studied for four processes which can be defined at leading order in the SM: an exchange of a virtual W boson either in the t channel [10–12] or in the s channel [13], or the associated production of a top quark with a W boson [14] or a Z boson [15, 16]. Figure 5 demonstrates good agreement of the measured cross sections with the SM predictions for all the available LHC c. m. energies 5.02, 7, 8, and 13 TeV.

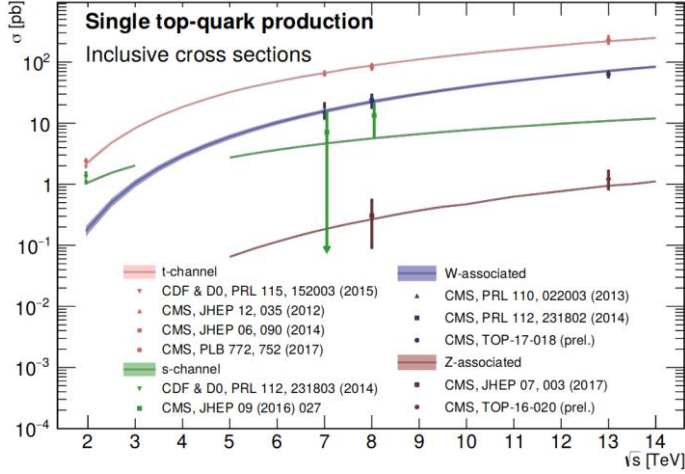


Fig. 5. Summary of the CMS (and Tevatron as in the legend) measurements of the inclusive single top-quark production cross section in the t - and s -channels, and in association with a W or Z boson. The measurements are compared to theoretical calculations based on approximate NNLO QCD accuracy, except for the Z -associated production that is based on MG5_AMC@NLO

The production rate of single top-quark processes is proportional to the square of the coupling at the Wtb production vertex. Hence, in the SM the measurement of the single top-quark production cross-sections allows for direct determination of the modulus of the CKM matrix element $|V_{tb}|$ [11]. This method relies on the assumption that the other two top-related CKM elements are much smaller, $|V_{ts}|, |V_{td}| \ll |V_{tb}|$, as well as that the Wtb interaction involves only the left-handed weak coupling (as postulated in the SM). However, in contrast to the indirect methods, no assumption is made about the number of quark generations or unitarity of the CKM matrix. Figure 6 shows a summary of the $|V_{tb}|$ determinations in CMS at various collision energies and channels. They all give a value $|V_{tb}| \approx 1$, as expected for the diagonal CKM element.

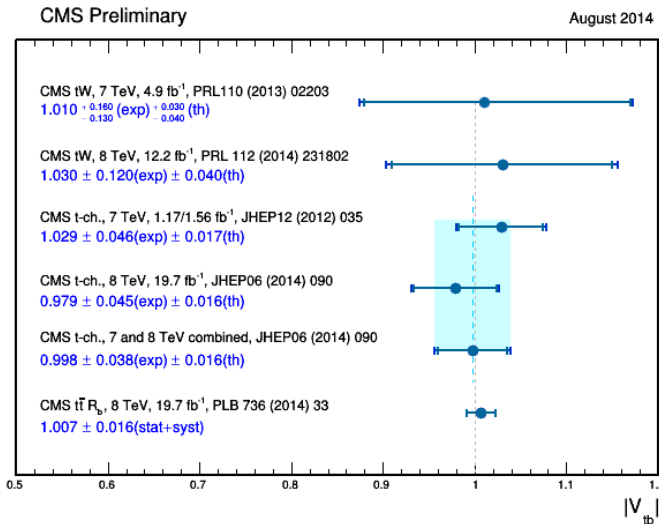


Fig. 6. Summary of $|V_{tb}|$ determinations by CMS from the single top quark production cross section and $\text{BR}(t \rightarrow b)$ [7]

Since the top quark does not hadronize, its polarization becomes directly accessible. The top lifetime is shorter than the depolarization scale, and the W boson is produced on-shell in the top-quark decay. Therefore,

the top-quark spin information is directly transferred to its decay products. A high purity sample of the t -channel events was used to measure the distribution of the angle between the muon from the top-quark decay and the polarization axis in the top quark's rest frame, θ_{μ}^* . The study is focused on the single muon decay channel as leptons have the highest spin-analysing power and the CMS detector has a very high muon identification efficiency. From this measurement, the top-quark spin asymmetry (A_{μ}) was extracted using a χ^2 -fit of the unfolded $\cos \theta_{\mu}^*$ distribution. The value of $A_{\mu} = 0.26 \pm 0.03$ (stat) ± 0.10 (syst) $= 0.26 \pm 0.11$ is compatible within 2.0 standard deviations with the SM prediction ($A_{\mu} = 0.44$) [17].

The top quark was also used in the studies of the flavour changing neutral current (FCNC). According to the Glashow–Iliopoulos–Maiani (GIM) mechanism, there is no tcZ coupling at the tree level in the SM, with loop effects further suppressed by the GIM cancellation. The previous world best limit was from the CMS

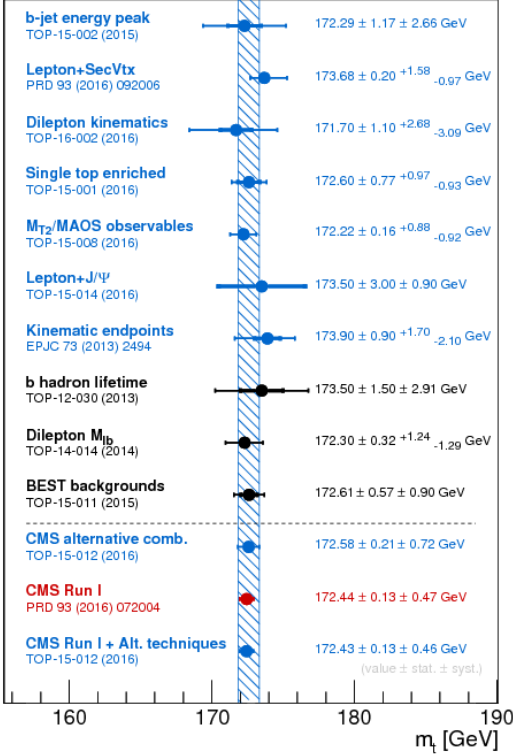


Fig. 7. Summary of the new CMS top-quark mass measurements and the results derived from their combination

Run-1 data [18]. The newer analysis [16] uses data of integrated luminosity of 19.7 fb^{-1} at $\sqrt{s} = 8 \text{ TeV}$. This analysis identifies the expected SM processes and provides searches for the FCNC interactions. Final states with three leptons (electrons or muons), large missing energy, and at least one jet are investigated. The signal is extracted from data by performing a simultaneous binned maximum-likelihood fit to the boosted decision tree discriminant distributions of the signal samples and a background-enriched control region. Event yields compatible with tZq SM production are observed, and the corresponding cross-section is measured to be 10_{-7}^{+8} fb , which is in agreement with the SM prediction of 8.2 fb . The data statistical uncertainty is dominant. The observed (expected) significance is 2.4 (1.8) standard deviations.

CMS also measured the top-quark mass, which plays important role in the SM, since the top quark, being the heaviest particle, participates in the dominant Higgs boson production mechanism. CMS provides the currently most accurate LHC number giving $m_t = 172.44 \pm 0.13$ (stat) ± 0.47 (syst) GeV/c^2 [19]. However, such a measurement achieves a complex systematic uncertainty regime mainly due to b -quark fragmentation. Therefore, alternative methods were developed by using, for example, the dilepton kinematic endpoint observable or the selection of charmonium states or charmed mesons originating from a b -hadron produced in one of the b -jets [20]. Figure 7 shows a summary of the traditional measurements, alternative methods and their combination.

4. B physics

The rare FCNC decay is a prominent channel to look for new physics, because it is forbidden in the SM at the tree level. On the other hand, virtual effects in loops make them complementary with direct searches for new physics. Since the SM effects are tiny, new physics, if present, could be competitive in magnitude. One of the important examples is the FCNC decay $B_s \rightarrow \mu^+\mu^-$. It was searched for during almost 30 years at many accelerators improving the sensitivity by five orders of magnitude before being observed by CMS and LHCb in November 2014 through a combination of their Run-1 datasets [21] with a statistical significance exceeding six standard deviations. The CMS result taken alone [22] corresponds to a statistical significance of 4.5 standard deviations. The found branching fractions for B_s^- - and B^0 -meson decays are in agreement with the expectations from the SM, as shown in Fig. 8. It was possible to achieve these results thanks to the excellent muon detection in the CMS detector.

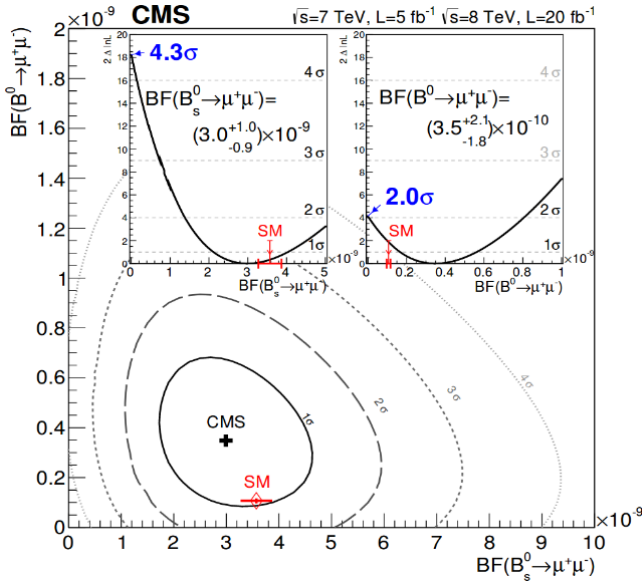


Fig. 8. Scan of the ratio of the joint likelihood for two branching fractions of the strange B meson and B^0 meson. As insets, the likelihood ratio scan for each of the branching fractions when the other is profiled together with other nuisance parameters; the significance at which the background-only hypothesis is rejected is also shown

5. Exotic spectroscopy

In recent years, the observation of many new states, with masses above the open-charm threshold that do not fit into the conventional quark model, has renewed interest in exotic quarkonium spectroscopy. For example, the $X(3872)$ resonance was discovered by the Belle experiment in 2003. Later it was rediscovered by other experiments, including CMS, and interpreted as charmonium $\chi_{c,1}(3872)$. Its analogues in the bottomonium sector, the $\chi_{b,J}(3P)$ states (with the angular momenta $J = 0, 1, 2$), were discovered by ATLAS in 2011 and observed by D0 and LHCb. Nevertheless, the experiments did not provide results for the mass splitting between the members of the $\chi_b(3P)$ system. At the same time, the bottomonia, composed of beauty quark–antiquark pairs bound to each other through the strong force, play a special role in our understanding of hadron formation, since the large quark mass allows important simplifications in the relevant theoretical calculations.

CMS performed [23] a search for $\chi_b(3P)$ through the radiative decay $\chi_b(3P) \rightarrow \Upsilon(3S)\gamma$, $\Upsilon(3S) \rightarrow \mu^+\mu^-$. Thanks to its excellent mass resolution of 2.2 MeV, CMS managed to resolve the two peaks corresponding to two states $\chi_{b,1}(3P)$ and $\chi_{b,2}(3P)$ with masses $M_1 = 10\,513.42 \pm 0.41$ (stat) ± 0.18 (syst) MeV/ c^2 and $M_2 = 10\,524.02 \pm 0.57$ (stat) ± 0.18 (syst) MeV/ c^2 with the mass difference $\Delta M = 10.60 \pm 0.64$ (stat) ± 0.17 (syst) MeV/ c^2 . The main challenge in this study was the low energy of photons, since their energy resolution in the electromagnetic calorimeter is decreasing with energy as $\sim 1/\sqrt{E_\gamma}$. To overcome that difficulty, the CMS analysis uses the photons that convert into e^+e^- pairs, which are reconstructed in the silicon tracker, instead of using electromagnetic calorimeter, with very high precision. It leads to two clear $\chi_b(nP)$ peaks in the resulting $\Upsilon(nS)\gamma$ invariant mass distributions. This comes at a price of necessity of a very large dataset. *In situ*, photon energy scale corrections were employed using the well known decay $\chi_{c,1} \rightarrow J/\psi\gamma \rightarrow \mu^+\mu^+\gamma$.

The measured distribution (Fig. 9) is well reproduced by the superposition of the two states $\chi_{b,1}(3P)$ and $\chi_{b,2}(3P)$, overlaid on a smooth continuum. This was the first time that the two states are individually observed. The new measurement is a step forward in completing the spin-dependent bottomonium spectroscopy diagram, and should significantly contribute to an improved understanding of the non-perturbative QCD processes that lead to the binding of quarks and gluons into hadrons.

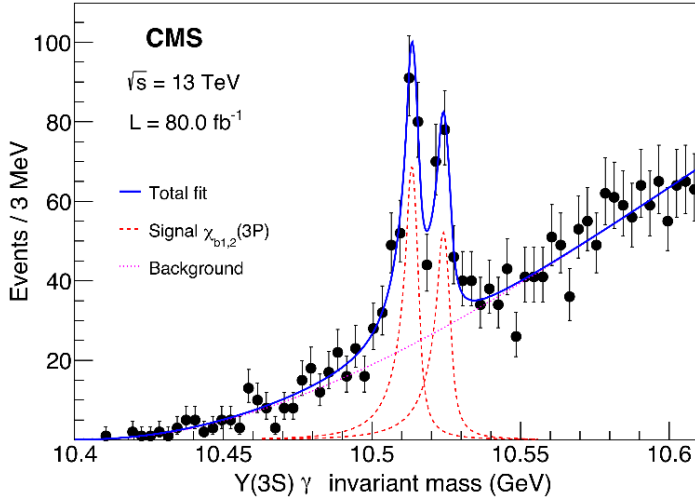


Fig. 9. The invariant mass distribution of the $\chi_{b,J}(3P) \rightarrow Y(3S)\gamma$ candidates. The vertical bars are statistical uncertainties. The curves represent the fitted contributions of the two signal peaks, the background, and their sum

6. Heavy ion physics

Heavy ions collisions provide another testing ground for QCD, in extreme conditions of very high temperature and very high density of particles, where quark–gluon plasma (QGP) might exist. CMS has a diverse set of observables to test and study this medium. The charged hadron multiplicity, low p_T inclusive hadron spectra, and elliptic flow provide collective properties of the system. Another set of observables, involving perturbative QCD (hard) probes, provide the “tomographic” information owing to the suppression phenomenon in nuclear interactions. Among the hard probes can be jets, high- p_T hadrons, heavy quarks, and quarkonia. The latter ones, the bound states of a quark and antiquark, are of special interest, since the theory of the QGP predicts a suppression dependent on the binding energy. The relative melting of the quarkonium states serves as an effective thermometer of the QGP.

While the charmonium states were previously extensively explored, the heavier bottomonium family, Y -family, was not. At the same time, the suppression is more dramatic for the bottomonium family. The $Y(3S)$ state has one of the lowest binding energies, around 200 MeV, and therefore close to the temperature T_C , a temperature near that of the deconfined QGP phase, around 150 to 190 MeV.

CMS is very well suited for studies of heavy ions collisions this way, thanks to the high-resolution silicon tracker detector and the high magnetic field of its solenoid. In particular, the good momentum resolution of the muon allows us to clearly resolve muon pairs from quarkonia (*e. g.*, the bottomonium family, Y) in the high-multiplicity environment of nucleus–nucleus collisions. CMS was the first experiment to successfully separate the signals of the three Y states in heavy-ion collisions [24] at $\sqrt{s} = 2.76$ TeV, establishing experimentally this sequential pattern of quarkonium suppression.

CMS has since updated and extended this result using additional data collected in 2011 for $\sqrt{s} = 2.76$ TeV and later for the 5.02 TeV heavy-ion runs, and the observation has a significance of greater than 5σ , the gold standard for claiming a discovery in high-energy physics [25, 26]. Figure 10 shows the dimuon invariant mass spectrum measured by CMS at the c. m. energy 5.02 TeV for the Pb–Pb collisions. The pp lineshape has been scaled by the mean number of individual nucleon–nucleon collisions, in order to give the expectation for the Pb–Pb collisions in the absence of nuclear effects. The data show a clear suppression in the yield of all three Y states, the more excited states being more suppressed.

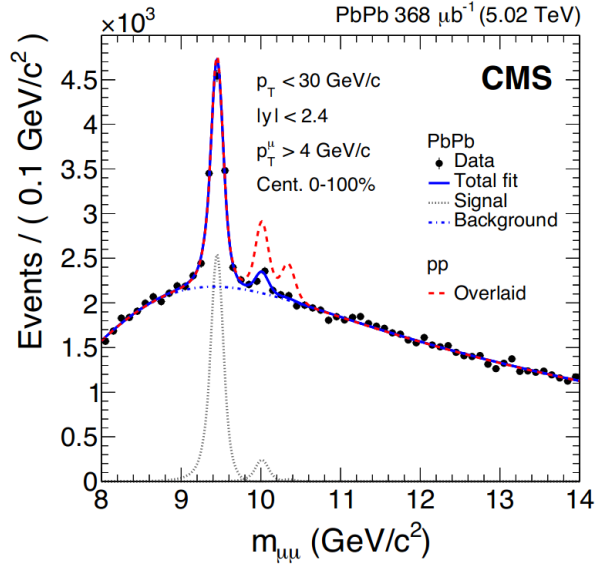


Fig. 10. Measured dimuon invariant mass distribution in Pb–Pb data [25]. The individual signal shapes of $\Upsilon(1S)$, $\Upsilon(2S)$, and $\Upsilon(3S)$ are shown with *dotted gray lines*. The *dashed red line* represents the pp signal shape added to the Pb–Pb background and normalized to the $\Upsilon(1S)$ mass peak in Pb–Pb

7. Beyond the Standard Model: supersymmetry and exotica

The CMS Collaboration pursued many generic searches to look for BSM physics under the broad category of supersymmetry, exotic resonances and dark matter. CMS has performed an extensive search for the SUSY particles (squarks, gluinos, charginos, neutralinos) in a broad parameter space considering benchmark scenarios including R -parity violating SUSY models. The larger datasets, higher collision energy and higher mass reach have motivated development and application of new analysis techniques in order to reconstruct the decay products of highly boosted bosons or top quarks. However, to date no signature of SUSY has been observed. Strongly produced superpartners of gluons and quarks, gluinos and squarks, have been excluded up to ~ 2 and ~ 1 TeV/c^2 , respectively.

The CMS resonance searches cover major theoretical models involving leptoquarks, RS gravitons, excited fermions, large extra dimensions, compositeness. In these searches, any signature of new particles would be quite evident in the reconstructed invariant mass distributions and hence the bumps over the SM predictions are looked for. However, to date no signature for new particles has been observed and limits are set accordingly on the respective models [27]. Exclusion bounds at 95% CL on mass scales are shown in Fig. 11.

CMS also performed a search for dark matter in the final states with invisible particles recoiling against visible states. Various topologies and kinematic variables were explored, including the jet substructure as a means of tagging heavy bosons [28]. No evidence for dark matter candidates has been found so far.

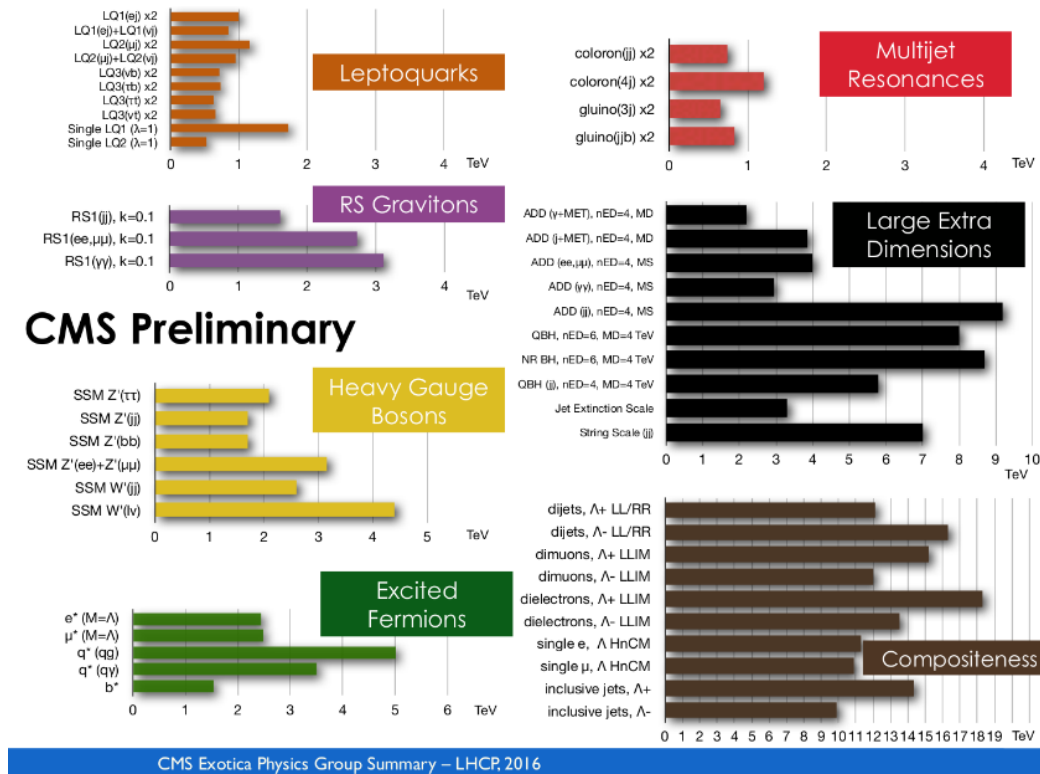


Fig. 11. CMS limits on different BSM models at 95% CL [27]

8. Conclusion

Thanks to excellent performance of the LHC and the CMS detector, a large number of important and unique physics results were obtained in 2013–2018.

The PNPI team was involved in the CMS project through design, production, maintenance [29], and upgrade [30] of the CMS endcap muon system, as well as in the data physics analysis, including the QCD and electroweak physics studies.

References

1. CMS Collaboration, JINST **3**, S08004 (2008), <https://doi.org/10.1088/1748-0221/3/08/S08004>
2. CMS Collaboration, <https://twiki.cern.ch/twiki/bin/viewfile/CMSPublic/PhysicsResultsCombined>
3. CMS Collaboration, Report No. CMS-PAS-SMP-15-004 (2015).
4. CMS Collaboration, <https://twiki.cern.ch/twiki/bin/view/CMSPublic/PhysicsResultsTOPSummaryFigures>
5. CMS Collaboration, EPJC **77**, 172 (2017).
6. CMS Collaboration, JHEP **09**, 051 (2017).
7. CMS Collaboration, JHEP **03**, 115 (2018).
8. CMS Collaboration, Report No. CMS-TOP-17-014, CERN (2018), <https://cds.cern.ch/record/2317191>
9. CMS Collaboration, Eur. Phys. J. C **75**, 542 (2015).
10. CMS Collaboration, JHEP **12**, 035 (2012).
11. CMS Collaboration, JHEP **06**, 090 (2014).
12. CMS Collaboration, Phys. Lett. B **772**, 752 (2017).
13. CMS Collaboration, JHEP **09**, 027 (2016).
14. CMS Collaboration, CMS Physics Analysis Summary CMS-PAS-TOP-17-018 (2017), <https://cds.cern.ch/record/2284831>

15. CMS Collaboration, Phys. Lett. B **779**, 358 (2018).
16. CMS Collaboration, JHEP **07**, 003 (2017).
17. CMS Collaboration, JHEP **04**, 073 (2016).
18. CMS Collaboration, Phys. Rev. Lett. **112**, 171802 (2014).
19. CMS Collaboration, Phys. Rev. D **93**, 072004 (2016).
20. CMS Collaboration, Report No. CMS-PAS-TOP-15-012 (2016).
21. CMS and LHCb Collaborations, Nature **522**, 68 (2015).
22. CMS Collaboration, Phys. Rev. Lett. **111**, 101804 (2013).
23. CMS Collaboration, Phys. Rev. Lett. **121**, 092002 (2018).
24. CMS Collaboration, Phys. Rev. Lett. **109**, 222301 (2012).
25. CMS Collaboration, Phys. Rev. Lett. **120**, 142301 (2018).
26. CMS Collaboration, JHEP **04**, 103 (2014).
27. CMS Collaboration,
https://twiki.cern.ch/twiki/bin/view/CMSPublic/SummaryPlotsEXO13TeV#ICHEP_2018
28. CMS Collaboration,
https://twiki.cern.ch/twiki/bin/view/CMSPublic/SummaryPlotsEXO13TeV#Dark_Matter_Summary_plots
29. A.A. Vorobyov, B.V. Bochin, S.A. Gets *et al.*, in *PNPI. High Energy Physics Division. Main Scientific Activities 2003–2012*, Gatchina, 2013, p. 24.
30. A.A. Vorobyev *et al.* *PNPI in the CMS Upgrade Program*, this volume, p. 210.

EXPERIMENT ATLAS AT THE LARGE HADRON COLLIDER

PNPI participants of the ATLAS Collaboration: A.E. Basalaev, A.E. Ezhilov, O.L. Fedin, M.P. Levchenko, V.P. Maleev, Yu.G. Naryshkin, V.A. Schegelsky, V.M. Solovyev

1. Introduction

ATLAS is a particle physics experiment at the Large Hadron Collider (LHC) at CERN which operates at unprecedented high energy of proton–proton collisions $\sqrt{s} = 13$ TeV. The purpose of the ATLAS experiment [1] is to investigate a wide range of physics including studies of the Standard Model (SM), searches for new physics beyond the Standard Model (BSM), like supersymmetry (SUSY), dark matter (DM), extra dimensions of space, new particles from the extended Higgs sector, study of hot and dense matter created in relativistic lead–lead collisions (quark–gluon plasma), *etc.* ATLAS is an international collaboration of about 3 000 physicists from 182 institutions and 38 countries.

PNPI participates in the ATLAS experiment from the very beginning of the conceptual detector design. Since the LHC started recording data, PNPI physicists are involved in many physics analyses carried out by the collaboration.

2. ATLAS detector

The ATLAS detector is shown in Fig. 1. ATLAS is over 25 m high, and almost 44 m long. It weighs approximately 7 000 t. ATLAS is built around the LHC beam pipe, 100 m underground. The main components of the ATLAS detector are an inner tracker, calorimeters, a muon system, and a magnet system. The ATLAS inner detector (ID) (see Fig. 1) is designed to reconstruct tracks of charged particles and to measure transverse momenta of the tracks with high resolution. It is located inside a solenoid which provides a 2T magnetic field. The detector elements closest to the beam are only about 5 cm from the beam axis. ID itself has a radius of 1.2 m and is 6.2 m long. ID is composed of three subsystems: silicon-based pixel and semiconductor tracker (SCT) detectors, and a gaseous drift tube transition radiation tracker (TRT). The PNPI team was involved in the construction and design of the end-caps of TRT. A new innermost pixel layer, the insertable B-layer (IBL), which was added during the shutdown between Run-1 and Run-2 around a new and thinner beam pipe, allows a more robust track reconstruction with better impact parameter resolution and more precise vertex reconstruction.

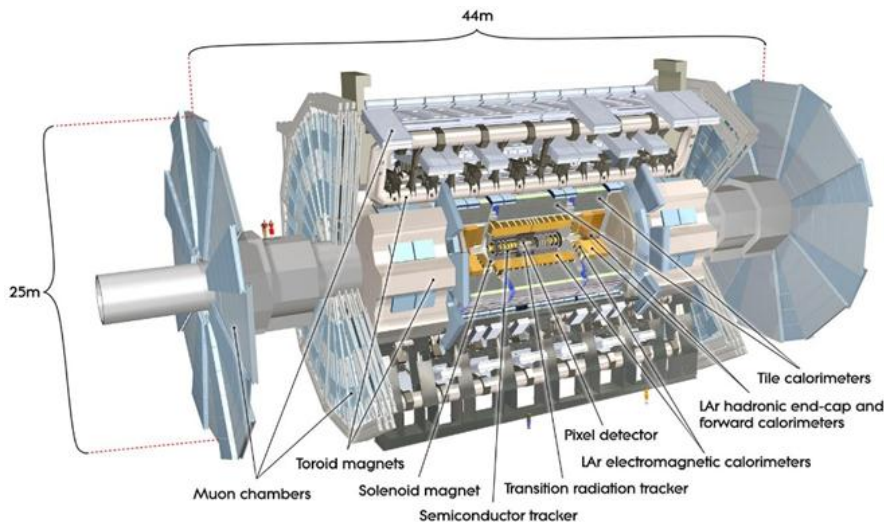


Fig. 1. ATLAS detector cut-away view. The beam pipe runs through the middle of the detector from left to right in the figure

ID is surrounded with a calorimeter system [2]. The calorimeter system is composed of the liquid argon electromagnetic calorimeters [3], the tile calorimeters [4], the liquid argon hadronic end-cap calorimeters, and the forward calorimeters (see Fig. 1). The fine granularity of the electromagnetic calorimeter in the region

matched to the ID is necessary for precision measurements of electrons and photons. The hadronic calorimeters are dedicated for the jet reconstruction and missing transverse energy measurements for which a coarser granularity is sufficient. The muon spectrometer [5] surrounds the calorimeters. The muon spectrometer measures the deflection of the muon tracks in the magnetic field produced by large superconducting air-core toroid magnets (one in the barrel and two in the end-caps) in the region $|\eta| < 2.7$. The spectrometer chambers are arranged in three cylindrical layers around the beam axis, while in the transition region and in the end-caps the chambers are installed in three planes perpendicular to the beam axis [6, 7]. The ATLAS detector provides a good track reconstruction and particle identification at very high luminosity (HL) of the order of $10^{34} \text{ cm}^{-2} \cdot \text{s}^{-1}$ and high pile-up (the average number of interactions per crossing is more than 40). The ATLAS track-finding algorithm first finds tracks in the pixel and SCT detectors and later adds TRT hits extending the tracks out to the calorimeter region. The track reconstruction algorithms employ local and global pattern recognition to identify a coherent pattern of hits corresponding to a track produced by a charged particle. An iterative track-fitting procedure is used to estimate the compatibility of the detector measurements with the track hypothesis and to compute the final track parameters [8]. The ATLAS trigger menu consists of over 2 000 trigger selection strategies [9]. The composition of the menu is driven by the physics goals of ATLAS and is constrained by the rate and bandwidth limitations of the detector, the trigger and data acquisition system, and offline computing.

3. Transition radiation tracker

One of the basic components of ID (Fig. 2) is TRT. TRT is a straw tracker composed of 298.304 carbon-fibre-reinforced Kapton straws, 4 mm in diameter, with $70 \mu\text{m}$ walls which are held at a potential of $-1\,530 \text{ V}$ with respect to a $30 \mu\text{m}$ diameter gold-plated tungsten wire in the center [10]. TRT has two different geometrical arrangements of straws. The barrel section, where 52.544 straws are aligned parallel to the direction of the beam axis, covers the radial region $560 < r < 1\,080 \text{ mm}$ and the longitudinal region $|z| < 712 \text{ mm}$ [11].

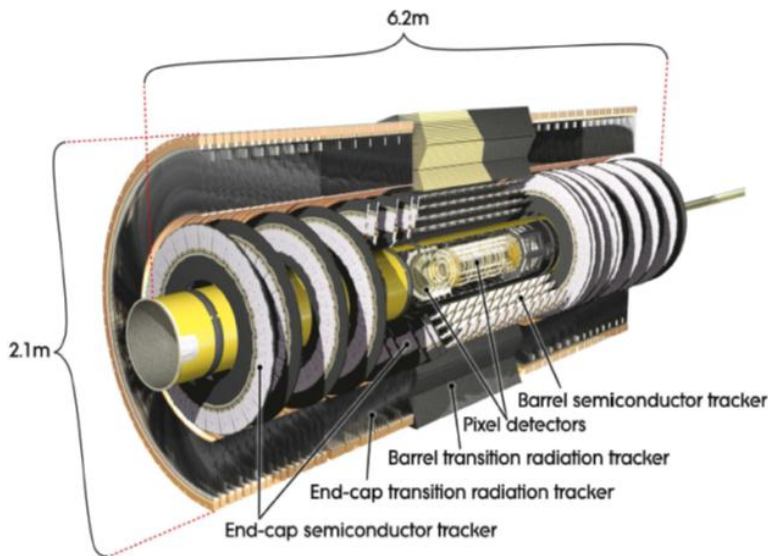


Fig. 2. View of the inner detector of the ATLAS detector

Two end-cap sections, each with 122.880 straws that are aligned perpendicular to the beam axis and point outwards in the radial direction, cover the regions $644 < r < 1\,004 \text{ mm}$, $827 < |z| < 2\,744 \text{ mm}$ [10], and $|\eta| < 2.0$, where η is the pseudorapidity.

At the beginning of the LHC and ATLAS operation, the only gas used in the TRT detector was a xenon-based gas mixture. However, due to large irreparable gas leaks which developed in the gas system, a part of the TRT detector is now flushed with a gas mixture composed primarily of much cheaper argon. The efficiency of TRT straws was larger than 96% and the track measurement accuracy was better than $120 \mu\text{m}$ for Run-1

data-taking period with 50 ns bunch spacing. During the Run-2 data-taking period with 25 ns bunch spacing, the track measurement accuracy is better than $130\ \mu\text{m}$. The straw efficiency and the position residual for the end-cap TRT are presented in Fig. 3.

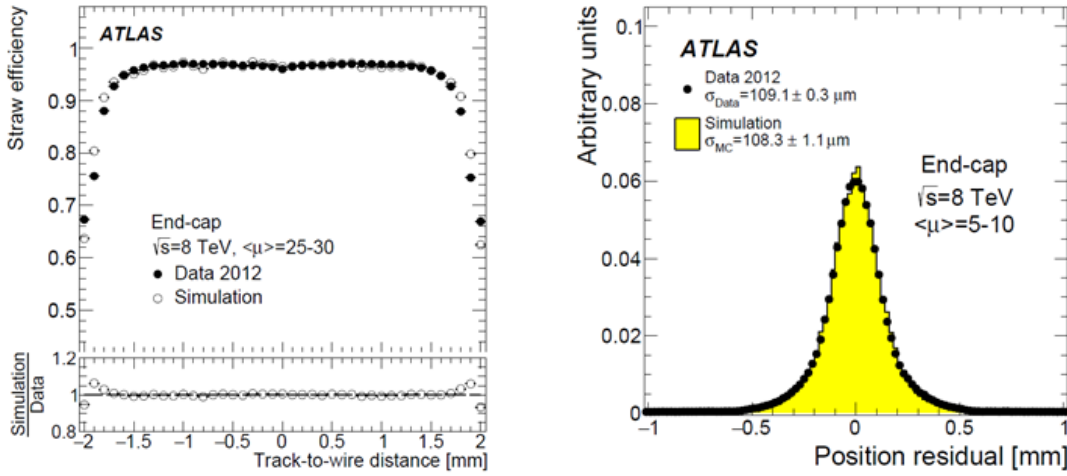


Fig. 3. Straw efficiency (left) in the end-cap wheels filled with a Xe-based mixture as a function of the track-to-wire distance in the data (solid circles) and simulation (open circles) for muons with $p_T > 30\ \text{GeV}$ from $Z \rightarrow \mu\mu$ events. Position residual distribution (right) in the TRT end-caps operating with a Xe-based gas mixture for muons with $p_T > 30\ \text{GeV}$

TRT is designed to operate in a high occupancy environment thanks to a large number of measurements (up to 30) provided by TRT along the reconstructed tracks. Figure 4 (left) shows the correlation between the TRT occupancy and the average number of collisions per bunch crossing (pile-up) $\langle \mu \rangle$ for the high- $\langle \mu \rangle$ LHC fill. The average TRT occupancy for $\langle \mu \rangle = 70$ is about 35% in these pp collisions and can even reach a level of 50% in some events due to large fluctuations of the number of primary collisions. The averaged straw track position measurement accuracy as a function of $\langle \mu \rangle$ for the TRT end-caps is also shown in Fig. 4 (right), where the data are compared with the simulation.

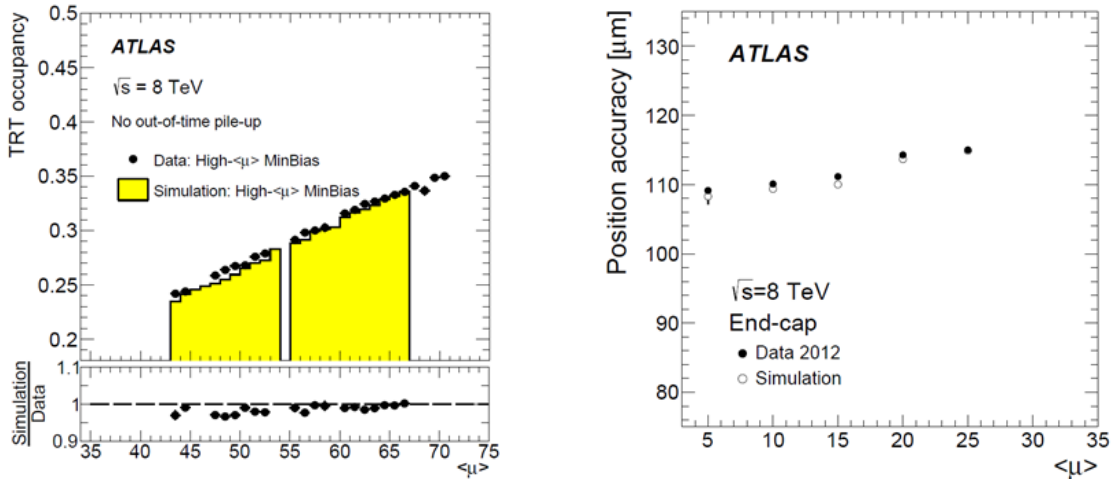


Fig. 4. TRT straw occupancy (left) as a function of $\langle \mu \rangle$ in the TRT from a special high $\langle \mu \rangle$ LHC fill (no pile-up from adjacent bunches) during the pp data-taking period in 2012 operating with a Xe-based gas mixture at $\sqrt{s} = 8\ \text{TeV}$, for data (solid circles) and simulation (filled histograms). Straw track position measurement accuracy (right) for muons with $p_T > 30\ \text{GeV}$ from $Z \rightarrow \mu^+\mu^-$ events in the TRT end-caps as a function of $\langle \mu \rangle$. Data (solid circles) and simulation (open circles) are shown for the 2012 running period operating with a Xe-based gas mixture and for an average value of pile-up $5 \leq \langle \mu \rangle \leq 30$

An important feature of TRT is the particle identification. The particle identification is based on transition radiation (TR), which arises when an ultrarelativistic charged particle crosses a boundary between the media with different dielectric constants [12]. The probability of a given particle to emit transition radiation is determined solely by its Lorentz γ -factor. In the X-ray energy range of the TR photons, this probability is a step-like function which rises from about zero to its maximum when the γ -factor changes from about 500 to 2000.

TRT was built to exploit this effect, in particular to distinguish between electrons and pions. For separating electrons from charged pions, the fraction of high threshold (6 keV) hits on a track can be used. As indicated in Fig. 5, the probability for generating a transition radiation photon and a subsequent high threshold hit is much higher for electrons than for pions. In this way, TRT separates electrons from pions over a momentum range between 1 and 150 GeV/c.

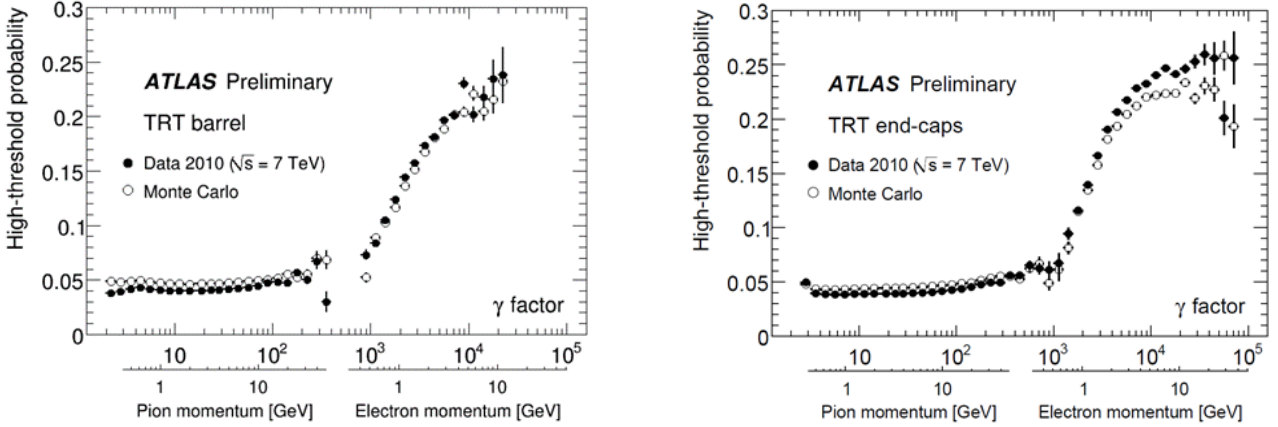


Fig. 5. Probability of a TRT high-threshold hit as a function γ -factor as measured in 7 TeV collision events for barrel (*left*) and end-cap (*right*)

Another way to separate different types of particles can be based on dE/dx measurements. Even though the TRT detector was not designed for this purpose and not equipped with amplitude measuring electronics, the TRT timing information based on the discriminators can be used for a particle identification, since the measured time over threshold (ToT) distribution correlates with the ionization deposit within the straws. For the purpose of dE/dx measurements, the ToT is defined as the time between the leading and trailing edges above the threshold. Figure 6 shows the ToT distributions for electron and pion candidates divided by the average transverse track path length inside the straw (*left*) and the track-averaged ToT distribution, as a function of the track momenta (*right*). The electron identification efficiency is 90%.

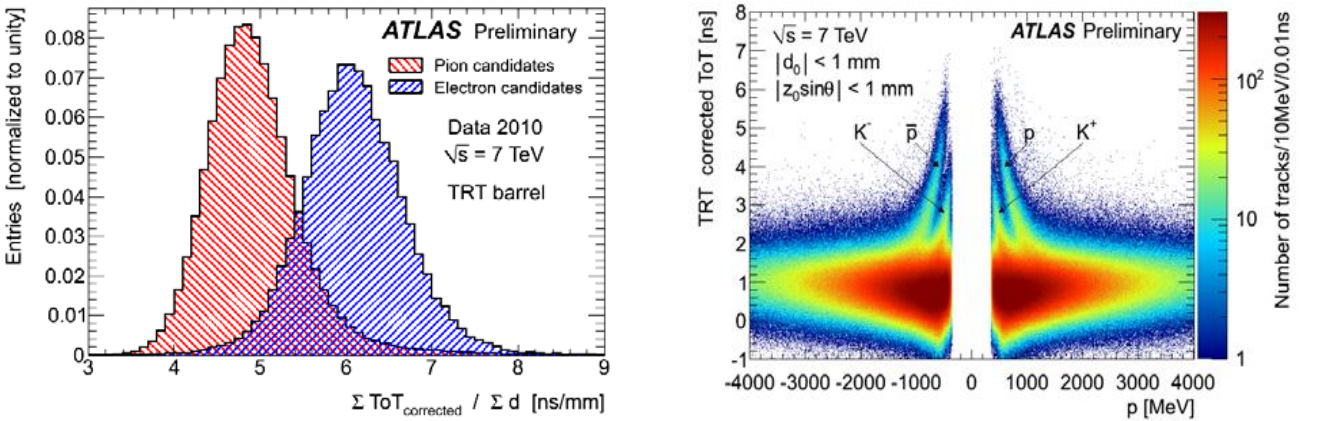


Fig. 6. The average time over threshold, divided by the average transverse track path length inside the straw (*left*) and the track-averaged ToT distribution, as a function of the track momenta (*right*)

4. Detector performance in Run-1 and Run-2

The ATLAS experiment at the LHC has been successfully taking data since the end of 2009, both in proton–proton collisions at the center of mass energies of 7, 8, and 13 TeV, and in heavy ion collisions. The luminosity recorded by the ATLAS detector during Run-1 (2010–2012) and the first part of Run-2 (2015–2017) is shown in Fig. 7 (*left*). In total, ATLAS has recorded data corresponding to about 25 fb^{-1} in Run-1 and 80 fb^{-1} in 2015–2017 of Run-2. The ATLAS data taking efficiency was very high – 93.3%. The instantaneous luminosity delivered by the LHC was increased from $0.5 \cdot 10^{33} \text{ cm}^{-2} \cdot \text{s}^{-1}$ in 2010 to $2.05 \cdot 10^{34} \text{ cm}^{-2} \cdot \text{s}^{-1}$ in 2017, which is higher than the initial design luminosity $10^{34} \text{ cm}^{-2} \cdot \text{s}^{-1}$. The pile-up dramatically increases with the luminosity, and it goes rapidly from the average 5–7 interactions in 2011 data to 37.5 in 2017 data, shown in Fig. 7 (*right*).

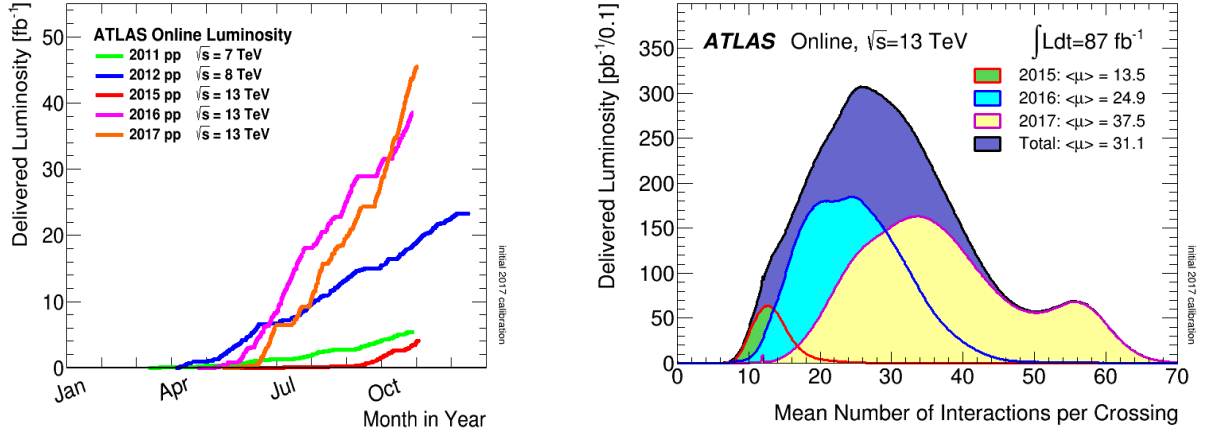


Fig. 7. Delivered luminosity by ATLAS experiment for different years of the data taking (*left*) and mean number of interactions per crossing (pile-up) for different years of Run-2 (*right*)

The detector performance was excellent even in the high pile-up conditions (~ 60). The performance of the reconstruction of the main physics objects was very good. The efficiency to reconstruct an electron associated with a good quality track varies from 97 to 99% between the end cap and barrel regions for electrons with $E_T > 15 \text{ GeV}$ [13]. Lower efficiencies (95%) are obtained in the calorimeter transition region. For very energetic electrons ($E_T > 80 \text{ GeV}$) the efficiency is $\sim 99\%$ over the whole η range. Identification of the prompt photons relies on the high granularity of the calorimeter system [14]. The photon identification efficiency increases from 53–64% (47–61%) for unconverted (converted) photons at $E_T \approx 10 \text{ GeV}$ to 88–92% (96–98%) for $E_T \geq 100 \text{ GeV}$. The ATLAS muon spectrometer performed very well, with an alignment precision of about $50 \mu\text{m}$ for both barrel and end-cap. The muon reconstruction efficiency is measured to be close to 99% over most of the covered phase space ($|\eta| < 2.5$ and $5 < p_T < 100 \text{ GeV}$).

5. Physics research at ATLAS

Based on the data recorded during Run-1 and Run-2, the ATLAS experiment has performed a wide range of physics analyses. A major achievement of ATLAS is the discovery of the SM Higgs boson [15]. Since then, the Higgs boson properties were studied in details. Different production mechanisms (VBF, ggF associated production: VH , $t\bar{t}H$) and different decay channels (e. g., $H \rightarrow \gamma\gamma$, $H \rightarrow ZZ^* \rightarrow 4l$, and $H \rightarrow \tau\tau$) were analyzed. The electroweak theory does not predict directly the Higgs mass. By combining the results obtained in the ATLAS and CMS experiments in Run-1 and Run-2 based on two high mass resolution and sensitive channels, $H \rightarrow \gamma\gamma$, $H \rightarrow ZZ^* \rightarrow 4l$, the Higgs mass was found to be 125.04 ± 0.24 (total) (± 0.21 (stat), ± 0.15 (syst)) GeV [16]. In the SM, the Higgs boson width is very precisely predicted once the Higgs boson mass is known. For a mass of 125.1 GeV, the Higgs boson has a very narrow width of 4.2 MeV. The upper limits on the total width of the Higgs boson are derived from fits to the mass spectra in the $H \rightarrow \gamma\gamma$ and

$H \rightarrow ZZ^* \rightarrow 4l$ decay channels under the assumption that there is no interference with background processes. In the $H \rightarrow \gamma\gamma$ channel, at the 95% CL limit of 5.0 (6.2) GeV is observed (expected) and in the $H \rightarrow ZZ^* \rightarrow 4l$ channel, at the 95% CL limit of 2.6 (6.2) GeV is observed (expected) [17]. The signal strength $\mu = (\sigma\text{BR})_{\text{obs}} / (\sigma\text{BR})_{\text{SM}}$, which is the observed product of the Higgs boson production cross section (σ) and its branching ratio (BR) in units of the corresponding SM values, is 1.17 ± 0.27 [18] in Run-1 and 0.99 ± 0.14 in Run-2 [19]. Studies of the spin, parity and couplings of the Higgs boson were studied as well [20]. The tensor structure of the HVV interaction in the spin-0 hypothesis was investigated using the $H \rightarrow ZZ^* \rightarrow 4l$ and $H \rightarrow WW^* \rightarrow e\nu\mu\nu$ decays [21].

Many features of the SM have been studied: cross sections of the SM processes, W -boson mass, properties of the Drell–Yan process, *etc.* [22–24]. However, as it is known, the SM cannot explain a number of phenomena, such as the baryon asymmetry, existence of DM, the hierarchy of particle masses and the interaction scale, *etc.*

Multiple searches for the BSM (or SM extensions) physics were performed, such as searches for SUSY, DM particles, a new particle from the extended Higgs sector, *etc.* SUSY is a theory that postulates a space-time symmetry which introduces a fermionic partner to every boson and vice versa identical in all quantum numbers other than spin. SUSY solves a number of still open questions in the SM. It provides a solution to the hierarchy problem, suggests the lightest supersymmetric particle as a possible candidate for DM and allows gauge coupling unification at high energies, which is not possible in the SM at any scale. Recent results of the ATLAS SUSY searches are reviewed in Refs. [25–27]. There is no indication of existence of SUSY particles up to the mass 2 TeV (gluino) and up to 1.2 TeV (lightest neutralino).

Some of the BSM theories extend, in particular, the Higgs sector of the SM. They include, *e. g.*, two Higgs doublet model – 2HDM, minimal super symmetric model – MSSM and its extension next to MSSM – NMSSM, Higgs triplet model – HTM, left right symmetric model – LRSM. In the frame of the 2HDM model, the second doublet is added to the SM, which leads to five new physics states: two CP -even h and H , CP -odd pseudoscalar A , and two charged H^+ and H^- . The Higgs sector of MSSM is a particular case of 2HDM (type II) and contains the same five physical states. In NMSSM, an addition singlet is added to MSSM, which leads to seven physical state: three CP -even H_1, H_2, H_3 , two CP -odd pseudoscalar A_1 and A_2 , and two charged H^+ and H^- . In HTM, a scalar triplet is added to the SM, which leads to seven new physical states.

All possible searches of new Higgs particles in many possible decay channels were done in the ATLAS experiment [28–30]. No new particles were found up to the mass 3 TeV, and limits on the production cross sections and model parameters were set.

The limits for heavy neutral CP -even Higgs boson H cross section varies from 4.3 pb (300 GeV) to 0.051 pb (3 TeV) for the gluon–gluon fusion production mechanism and changes from 1.1 pb (300 GeV) to 0.03 pb (3 TeV) for the vector boson fusion process.

One of the most appealing modern studies performed in ATLAS is a search for the DM particles. There is a strong evidence of the DM existence from astrophysical observations. DM particles are searched in direct, indirect and collider experiments. In the collider searches, there are several processes under study: the so-called “mono- X ” process, the associated production of DM particles with heavy quarks and searches for the “dark mediator” which mediates interaction between the SM particles and DM particles. The results are interpreted in the context of the effective field theories and simplified models. All these studies have been performed in the ATLAS experiment [31–33]. The analysis of dijet events excludes the mediator masses in the region from 1.25 to 2.8 TeV. The lower limit on the DM particle mass was set to 0.45 TeV in the mono- X channel. The search for the DM produced in association with heavy quarks excludes at 95% CL the mediator masses between 10 and 50 GeV for scalar mediators assuming couplings equal to unity and a DM mass of 1 GeV [34].

There are some other interesting studies in BSM physics on going in the ATLAS experiment, *e. g.*, searches for manifestation of extra dimensions [35]. If there were two or more extra space-time dimensions, then the gravity might, in fact, be just as strong as all other forces. Some models with extra dimensions predict existence of the microscopic black holes that could be detected by ATLAS [36]. Models with extra dimensions also predict a massive graviton – the particle which mediates gravity. There are several searches for the graviton carried out in the ATLAS experiment [36, 37]. Some of the SM extensions predict leptoquarks. Leptoquarks are hypothetical particles carrying both baryon (B) and lepton number (L). If leptoquarks are allowed to couple

to fermions within more than just one generation, they could induce four-fermion interactions causing flavour-changing neutral currents and lepton family-number violations. The search for leptoquarks is a part of the ATLAS physics program [38].

6. Summary

The ATLAS experiment successfully operated during Run-1 (2010–2012) and Run-2 (2015–2017) and continues collecting data till the end of Run-2 (2018). The ATLAS detector provides very high data taking efficiency. A lot of physics results have been obtained since the beginning of data taking in 2010 and published in about 738 papers and many more are still in the pipeline. The PNPI physicists team actively participates in many ATLAS physics analyses such as the SM physics studies: measurement of the angular coefficients in Z-boson events, measurement of the transverse momentum and ϕ_{η}^* distributions of Drell–Yan lepton pairs and Bose–Einstein correlation study, as well as searches for a new physics, such as new gauge Z'/Z^* , W'/W^* bosons, a DM particle candidate (WIMP) in mono-Z channel and new heavy neutral Higgs boson.

The forthcoming upgrades of the ATLAS experiment are divided into two phases, in step with the upgrades of the LHC. The Phase I upgrade and the Phase II (HL–LHC era) upgrade are planned correspondingly for the periods during the shutdown in 2019–2020 and shutdown in 2024–2026. During Phase I, it is planned to upgrade the muon system, which will allow to provide high precision muon track reconstruction and keep high trigger efficiency with low momentum threshold at high luminosity $2 \cdot 10^{34}$ – $5 \cdot 10^{34} \text{ cm}^{-2} \cdot \text{s}^{-1}$. The largest Phase I upgrade project for the ATLAS muon system is the replacement of the present first station in the forward regions with the so-called New Small Wheels [39]. Since 2014, PNPI participates in the Phase I upgrade program of the muon system and produces the largest of the strip thin gap chambers quadruplets.

The HL upgrade of the LHC Phase II is currently expected to begin operations in the second half of 2026, with a nominal-levelled instantaneous luminosity $5 \cdot 10^{34} \text{ cm}^{-2} \cdot \text{s}^{-1}$ corresponding to an average, $\langle \mu \rangle \approx 140$ inelastic pp collisions in each beam-crossing and delivering an integrated luminosity of around 250 fb^{-1} per year of operation. The entire tracking system of the ATLAS detector will be replaced by an all-silicon detector called inner tracker (ITK) [40]. PNPI is involved in the development of the cooling system for the ITK detector.

References

1. ATLAS Collaboration, G. Aad *et al.*, JINST **3**, S08003 (2008).
2. ATLAS Collaboration, A. Airapetian *et al.*, CERN-LHCC-96-40 (1996).
3. ATLAS Collaboration, CERN-LHCC-96-041 (1996).
4. ATLAS Collaboration, CERN-LHCC-96-042 (1996).
5. ATLAS Collaboration, CERN-LHCC-97-022 (1997).
6. ATLAS Collaboration, CERN-LHCC-97-019 (1997).
7. ATLAS Collaboration, CERN-LHCC-97-020 (1997).
8. ATLAS Collaboration, G. Aad *et al.*, arXiv: 0901.0512 (2009).
9. ATLAS Collaboration, PoS ICHEP2016 **282**, 244 (2016).
10. E. Abat *et al.*, JINST **3**, P02013 (2008).
11. E. Abat *et al.*, JINST **3**, P02014 (2008).
12. X. Artru, G.B. Yodh, G. Mennessier, Phys. Rev. D **12**, 1289 (1975).
13. ATLAS Collaboration, ATL-CONF-2016-024 (2016).
14. ATLAS Collaboration, ATL-PHYS-PUB-2016-014 (2016)
15. ATLAS Collaboration, G. Aad *et al.*, Phys.Lett. B **716**, 1 (2012).
16. Particle Data Group, C. Patrignani *et al.*, Chin. Phys. C **40**, 100001 (2016) and 2017 update.
17. ATLAS Collaboration, G. Aad *et al.*, Phys. Rev. D **90**, 052004 (2014).
18. ATLAS Collaboration, G. Aad *et al.*, Phys. Rev. D **90**, 112015 (2014).
19. ATLAS Collaboration, ATLAS-CONF-2017-045 (2017).
20. ATLAS Collaboration, G. Aad *et al.*, Eur. Phys. J. C **75**, No. 10, 476 (2015).
21. ATLAS Collaboration, ATL-CONF-2015-008 (2015).

22. ATLAS Collaboration, G. Aad *et al.*, JHEP **08**, 159 (2016).
23. ATLAS Collaboration, M. Aaboud *et al.*, CERN-EP-2016-305 (2016).
24. ATLAS Collaboration, M. Aaboud *et al.*, Eur. Phys. J. C **77**, No. 3, 144 (2017).
25. ATLAS Collaboration, M. Aaboud *et al.*, JHEP **09**, 084 (2017).
26. ATLAS Collaboration, M. Aaboud *et al.*, Eur. Phys. J. C **76**, No. 12, 683 (2016).
27. ATLAS Collaboration, M. Aaboud *et al.*, Eur. Phys. J. C **76**, No. 11, 585 (2016).
28. ATLAS Collaboration, G. Aad *et al.*, CERN-EP-2017-214 (2017).
29. ATLAS Collaboration, M. Aaboud *et al.*, Phys. Lett. B **759**, 555 (2016).
30. ATLAS Collaboration, G. Aad *et al.*, CERN-EP-2017-198 (2017).
31. ATLAS Collaboration, M. Aaboud *et al.*, CERN-EP-2017-166 (2017).
32. ATLAS Collaboration, G. Aad *et al.*, Eur. Phys. J. C **75**, No. 2, 92 (2015) .
33. ATLAS Collaboration, M. Aaboud *et al.*, arXiv:1703.09127 (2017).
34. ATLAS Collaboration, M. Aaboud *et al.*, Eur. Phys. J. C **78** 18 (2018).
35. ATLAS Collaboration, G. Aad *et al.*, Eur. Phys. J. C **74**, No. 12, 3134 (2014).
36. ATLAS Collaboration, G. Aad *et al.*, JHEP **08**, 103 (2014).
37. ATLAS Collaboration, M. Aaboud *et al.*, arXiv:1712.06386 (2017).
38. ATLAS Collaboration, M. Aaboud *et al.*, New J. Phys. **18**, No. 9, 093016 (2016).
39. ATLAS Collaboration, T. Kawamoto *et al.*, CERN-LHCC-2013-006 (2013).
40. ATLAS Collaboration, S. McMahon *et al.*, CERN-LHCC-2017-005 (2017).

EXPERIMENT LHCb AT THE LARGE HADRON COLLIDER

PNPI participants of the LHCb Collaboration:

G.D. Alkhazov, N.F. Bondar, A.D. Chubykin, A.A. Dzyuba, S.N. Kotryakhova, O.E. Maev, N.R. Sagidova, Yu.A. Shcheglov, A.A. Vorobyev

1. Introduction

LHCb is an international collaboration of more than 800 physicists from 62 institutions, who have designed, built and operated a collider detector at the CERN Large Hadron Collider (LHC).

Main physics goals are precision tests of the Standard Model (SM) in the heavy quark sector *via* studies of rare decays of heavy hadrons and constraining measurements of the parameters of the quark mixing matrix (Cabibbo–Kobayashi–Maskawa – CKM). Another goal of the LHCb experiment is the precision spectroscopy of heavy hadrons helping to understand the quantum chromodynamics (QCD) – the theory of the strong interaction.

During Run-1, the LHC was operated at the pp centre-of-mass energy of 7 and 8 TeV, and the LHCb experiment collected the experimental data corresponding to 1 and 2 fb^{-1} of an integrated luminosity, respectively. During Run-2, the LHC was operated at the pp centre-of-mass energy of 13 TeV, which allowed LHCb to collect the data sample corresponding to more than 6 fb^{-1} of an integrated luminosity.

PNPI was involved in the LHCb project through the design, construction, commissioning, and operation of the LHCb muon system. PNPI physicists took part in the data analysis, including QCD, charm and B physics studies. Among main LHCb physics results are the discovery of new heavy particles (including “exotic” particles), the high precision measurements of the parameters of the CKM matrix, the studies of rare decays of heavy hadrons, as well as the studies of the heavy hadrons spectroscopy. This report presents several LHCb results obtained in 2012–2018 years.

2. LHCb detector

The LHCb detector is a forward spectrometer [1]. The angular distribution for the charm and beauty hadrons, produced in collisions of high energy protons, is boosted into the forward direction, where the products of their decays are registered in the 10 to 250 mrad range of the polar angle. A schematic view of the LHCb experiment is presented in Fig. 1.

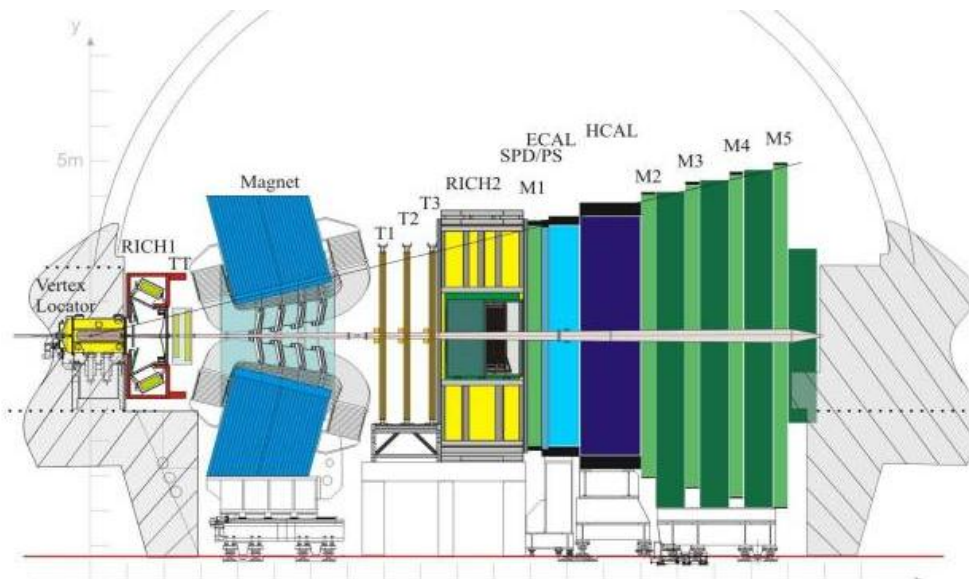


Fig. 1. Schematic view of the LHCb experiment

The LHCb detector is a single-arm forward spectrometer covering the pseudorapidity range $2 < \eta < 5$. The detector includes a high-precision tracking system comprising a silicon-strip vertex detector (vertex locator) surrounding the pp interaction region, a large-area silicon-strip detector (TT) located upstream of a dipole magnet with a bending power of about 4 Tm, and three stations of silicon-strip detectors and straw drift tubes placed downstream of the magnet (T1–T3). The tracking system provides a measurement of the momentum, p_{tot} , of charged particles with a relative uncertainty that varies from 0.5% at low momentum to 1.0% at 200 GeV/c. The minimum distance of a track to a primary vertex, the impact parameter, is measured with a resolution of $15 + 29 p_{\text{T}} \mu\text{m}$, where p_{T} is the component of the momentum transverse to the beam, in GeV/c. Different types of charged hadrons are distinguished using information from two ring-imaging Cherenkov detectors (RICH). Photons, electrons, and hadrons are identified by a calorimeter system consisting of scintillating-pad and preshower detectors (SPD/PS), an electromagnetic calorimeter (ECAL), and a hadronic calorimeter (HCAL). Muons are identified with a system composed of alternating layers of iron and multiwire proportional chambers (M1–M5). The online event selection is performed by a trigger, which consists of a hardware stage, based on information from the calorimeter and muon systems, followed by a software stage, which applies a full event reconstruction.

3. Discovery of new particles

The high rate of heavy hadrons produced in pp collisions provided by the LHC, together with the possibilities of precise tracking and particle identification in the LHCb detector, allows to discover new hadrons which contain heavy (c and b) quarks. Some of these hadrons correspond to the known scheme, for example baryons, others have an exotic nature.

In 2015, the LHCb experiment reported observation of the $\Xi_b^{\prime-}$ and Ξ_b^{*-} baryons [2], which were predicted by the quark model but were not seen before. The quark content of these two states is $\{bsd\}$, the difference being in the spin structure. In the $\Xi_b^{\prime-}$ state, the spins of the two lighter quarks point in the opposite direction to the spin of the b quark, whereas in the Ξ_b^{*-} state they are aligned. This difference makes the Ξ_b^{*-} a little heavier. The two new particles are observed through their decay into the ground state of Ξ_b^0 and a π^- . They both appear in the distribution of the $\Xi_b^0\pi^-$ invariant mass δm , with $\delta m = 0$ at the threshold (*left panel* of Fig. 2). The two peaks are clear observations of the $\Xi_b^{\prime-}$ and Ξ_b^{*-} baryons above the hatched red histogram representing the expected background. Both particles have extremely short lifetimes, as their decays are strong force driven, the Ξ_b^{*-} baryon having a shorter lifetime, which follows from the larger width of the corresponding peak. The results demonstrate an extraordinary precision of the LHCb experiment: the mass difference between the $\Xi_b^{\prime-}$ and Ξ_b^0 baryons is measured with an uncertainty of $0.02 \text{ MeV}/c^2$. By observing these particles and measuring their properties with such an accuracy, LHCb makes a stringent test of models of nonperturbative QCD.

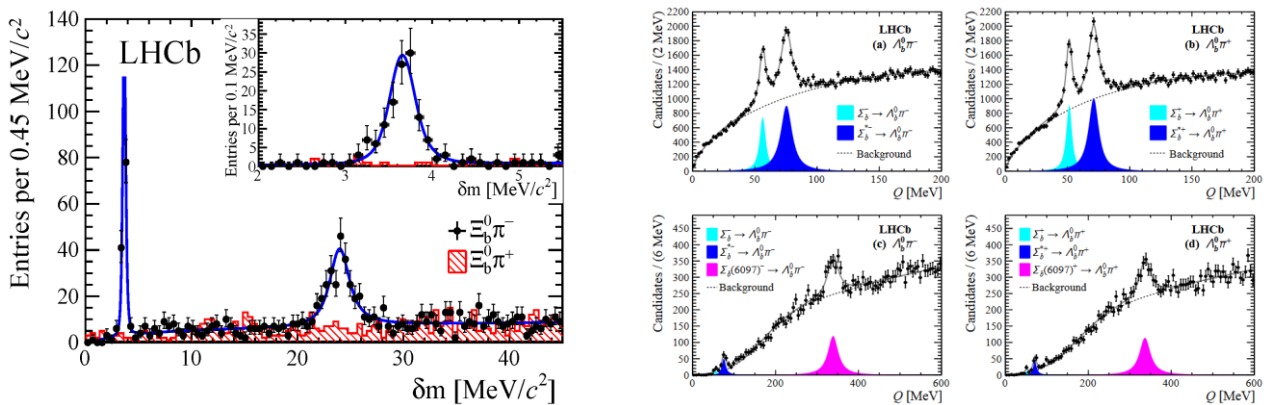


Fig. 2. The $\Xi_b^0\pi^-$ mass spectrum with the peaks corresponding to the $\Xi_b^{\prime-}$ and Ξ_b^{*-} baryons; the region of the $\Xi_b^{\prime-}$ is also presented with the zoom (*left panel*). Observation of the $\Sigma_b(6097)^+$ and $\Sigma_b(6097)^-$ in different channels; the lower images show the mass spectra over a wider range and with stricter selection requirements, $Q = m(\Lambda_b^0\pi^\pm) - m(\Lambda_b^0) - m(\pi^\pm)$ (*right panel*)

Another example of discovery abilities of the LHCb experiment is the observation of two new baryons named as $\Sigma_b(6097)^+$ and $\Sigma_b(6097)^-$ with the statistical significances of 12.7σ and 12.6σ , respectively [3]. Together with the two new Σ_b particles, the four known states were also found in the mass spectrum of the two-body system $\Lambda_b^0\pi^\pm$ (*right panel* of Fig. 2). These Σ_b particles manifest themselves as peaks above the smooth background, as shown in the image; on the x -axis, $Q = m(\Lambda_b^0\pi^\pm) - m(\Lambda_b^0) - m(\pi^\pm)$. The Λ_b^0 baryons are reconstructed *via* their decay $\Lambda_b^0 \rightarrow \Lambda_c^+\pi^-$, with the Λ_c^+ baryons in turn decaying to $p\bar{K}^+\pi^+$. The Σ_b family of resonances have $\{uub\}$ and $\{ddb\}$ for Σ_b^+ and Σ_b^- , respectively. In each of the upper plots of Fig. 2, there are two peaks clearly visible (*blue*) that are identified as the Σ_b^\pm and $\Sigma_b^{*\pm}$ baryons, which were observed previously by the CDF Collaboration and now confirmed by LHCb with the improvement in the precision on the particles properties by a factor of 5. Beyond these two particles, additional excited states, which are expected at higher masses, were found by LHCb. The $\Sigma_b(6097)^+$ and $\Sigma_b(6097)^-$ states are likely to be part of the same family of excited states of the Σ_b baryons. Theoretically, the family of excited Σ_b states whose mass is closer to that of the new observed particles is composed of five $\Sigma_b(1P)$ states, some of which may be difficult to observe experimentally. Since it is possible that the masses of different excited states may be similar, it cannot be excluded that the seen structures are superpositions of more than one state. A search for and study of these states will cast light on the internal mechanisms governing the dynamics of the strong force.

The exotic states are also available at LHCb. In 2014, the LHCb Collaboration published results on precise measurements of properties of the $Z(4430)^-$ particle which allow to determine unambiguously its exotic nature. It is hard to explain this state with the electric charge in the framework of the traditional quark model, *i. e.* as a mesonic or a baryonic state. The first evidence for the $Z(4430)^-$ particle was presented in 2008 by the Belle Collaboration, and now it is confirmed by LHCb in the analysis of about 25 200 $B^0 \rightarrow \psi' K\pi^-$, $\psi' \rightarrow \mu^+\mu^-$ decays with the data sample corresponding to an integrated luminosity of 3 fb^{-1} collected at $\sqrt{s} = 7$ and 8 TeV [4]. The significance of the $Z(4430)^-$ signal, which manifests itself as a large bump in the $\psi' \pi^-$ mass spectrum (*left panel* of Fig. 3) is overwhelming, at least 13.9σ . An amplitude analysis was performed. The $Z(4430)^-$ quantum numbers are determined to be $J^P = 1^+$ by ruling out $0^-, 1^-, 2^+$, and 2^- assignments at more than 9.7σ , confirming the evidence from Belle. The LHCb analysis established the resonant nature of the observed structure in the data, in this way proving unambiguously that $Z(4430)$ is really a particle. The corresponding Argand diagram is presented in the central panel of Fig. 3. The experimentally extracted real and imaginary part of the $Z(4430)$ amplitude follows the one expected from the Breit–Wigner distribution. The minimal quark content of the $Z(4430)$ state is $c\bar{c}d\bar{u}$. It is therefore a four-quark state or a two-quark plus two-antiquark state.

The exotic states could be also found as intermediate resonances appearing in decays of b hadrons. For example, the LHCb Collaboration presented an observation of four “exotic” particles decaying into a J/ψ and a ϕ mesons. Only one of these four states was well established before. The experimental results were based on a detailed many-dimensional analysis of the charged B^+ -meson decays into J/ψ , ϕ , and K^+ mesons using the full data sample collected during Run-1. The data could not be described by a model that contains only ordinary particles and require a large contribution from tetraquarks, as presented in Fig. 3.

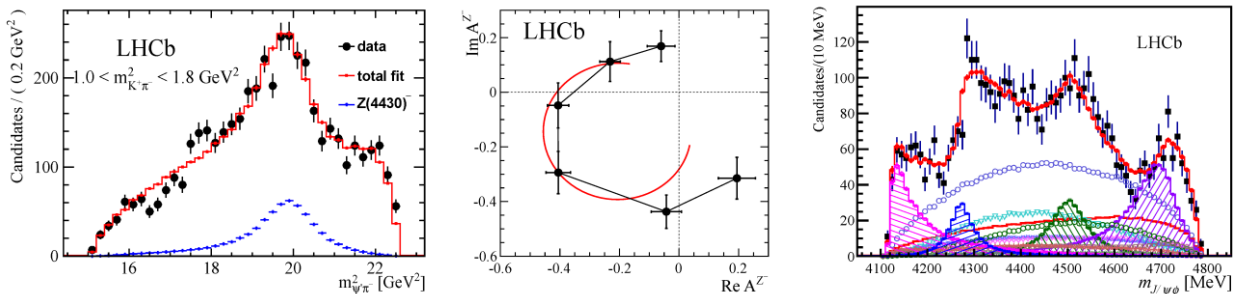


Fig. 3. The $\psi' \pi^-$ mass spectrum with the structure corresponding to the $Z(4430)^-$ tetraquark particle (*left panel*). Argand plot for the $Z(4430)^-$ amplitude (*central panel*). The result of the amplitude analysis of the $B^+ \rightarrow J/\psi' K^+ \phi$ decay projected into the $J/\psi \phi$ mass spectrum; tetraquark states are visible as peaking contributions (*right panel*)

The first observation of the $X(4274)$, $X(4500)$, and $X(4700)$ particles was announced by LHCb in 2017 [5]. Evidence at a level of 3.8σ for the $X(4140)$ particle near-threshold of the $J/\psi\phi$ mass peak was first reported by the CDF Collaboration and later was confirmed by the CMS and D0 Collaborations. Searches for this particle by the Belle and BaBar Collaborations gave negative results. The LHCb analysis yields a clear observation of $X(4140)$, and indicates a particle with the similar mass but larger width to the earlier measurements from CDF, CMS, and D0. It is important to emphasize that simple “bump-hunting” in the mass spectra is not sufficient to learn about the nature of such complicated hadronic structures. A multi-dimensional full amplitude analysis is crucial for the data interpretation, and it has allowed LHCb to characterize fully the particles and to determine their quantum numbers.

More information about observations of new baryons (doubly-charmed states, Ω_c^0 excited states, pentaquark states) is presented in a separate article in this report about main HEPD results.

4. Lifetime measurements

Due to the Lorentz boost for the relativistic particles produced in pp collisions at the LHC and due to the excellent tracking in the vertex region available at LHCb, the lifetime of the hadrons can be measured with high precision. In 2017, LHCb presented the result of a measurement of the Ω_c^0 -baryon lifetime, *i. e.* a particle composed of $\{css\}$ quarks [6]. The Ω_c^0 baryon was identified *via* $\Omega_b^- \rightarrow \Omega_c^0 \mu^- \bar{\nu}_\mu X$ decays, and then by means of the $\Omega_c^0 \rightarrow pK^- K^- \pi^+$ decay. The intercept region for the muon track and the reconstructed track of the Ω_c^0 candidate fixes the production point, while the intercept of the tracks from the $\Omega_c^0 \rightarrow pK^- K^- \pi^+$ decay fixes the decay point. The lifetime was evaluated from this information and from the momentum of the Ω_c^0 candidate. The decay-time distribution of the Ω_c^0 baryons reconstructed in the analysed sample was measured relative to that of the D^+ -meson decays. The lifetime of the D^+ meson is known to better than 1% precision. This approach allowed for significant reductions in the systematic uncertainty associated to the measurement. The measured Ω_c^0 decay-time distribution is presented in the left panel of Fig. 4. The “Fit” distribution is created with the lifetime parameter adjusted to fit the data in the best possible way, while the blue histogram shows the distribution produced using the world average Ω_c^0 lifetime, which turned out to be inconsistent with the LHCb data.

The measured lifetime value $268 \pm 24 \pm 10 \pm 2$ fs (here the first uncertainty is statistical, the second one is systematic and the third one comes from the uncertainty in the D^+ -meson lifetime) is nearly four times larger than the values measured by the previous experiments, as it is shown in the right panel of Fig. 4. The high production rate allowed to analyse about 1 000 Ω_c^0 -baryon decays, that is an order of magnitude larger sample than those used by the previous experiments. The lifetime measurements of the hadrons containing heavy quarks are sensitive to the internal structure and dynamics within those hadrons, and the LHCb precision measurement helps to understand how to incorporate QCD effects into the calculations used to describe the decays of baryons containing b or c quarks.

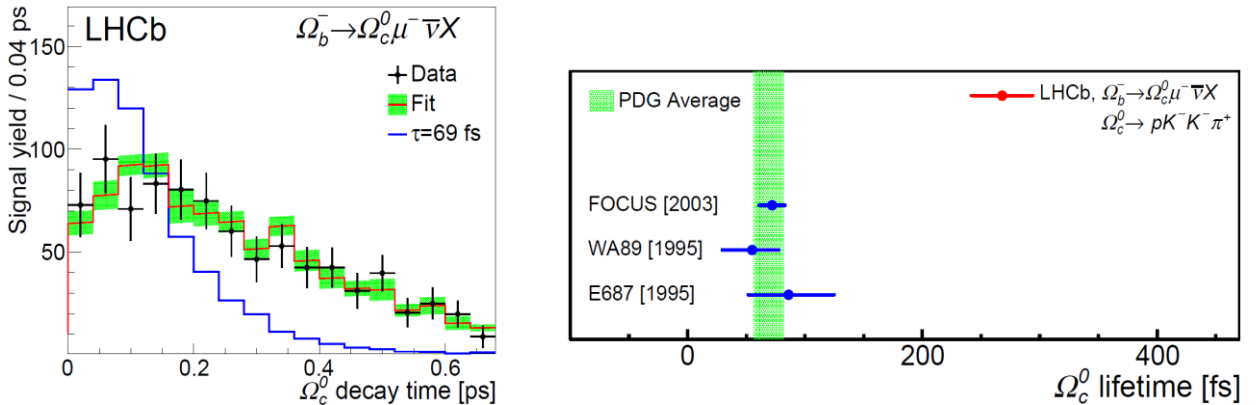


Fig. 4. The decay time spectrum for the Ω_c^0 baryon; experimental data are inconsistent with the previous world average (left panel). The comparison of the LHCb result and the previous determinations of the Ω_c^0 -baryon lifetime (right panel)

5. Observation of rare decays of heavy hadrons

One of the goals of the LHCb experiment is the search of rare decays of b and c hadrons. Many of them are interesting as new physics (NP) could enhance their probability. The search for the rare decays with dileptons in the final state is reported as a separate contribution in this book. In this section, we report about rare hadronic decays of the B meson family.

Studies of B -mesons decaying to baryonic final states were carried out since the late 1990s. It was quickly realized that the baryonic B decays differ from the mesonic decays since the two-body charmless decays are suppressed with respect to decays to multi-body final states. The B^0 -meson decay into a proton–antiproton pair was observed by LHCb in 2017 for the first time with a statistical significance of 5.3 standard deviations [7]. The image in the left panel of Fig. 5 shows the corresponding mass spectrum where the contribution of B^0 decaying into a proton–antiproton pair is clearly visible. The branching fraction is measured to be $(1.25 \pm 0.27_{\text{stat}} \pm 0.18_{\text{syst}}) \cdot 10^{-8}$. This decay is the rarest fully hadronic decay of the B meson ever observed. This observation provides a valuable input towards the understanding of the dynamics of the hadronic B decays and allows for a better scrutiny of the QCD models. In the future, with the analysis of additional data, it is hoped that the B_s^0 decay into this channel will be also observed.

Another interesting analysis was devoted for the search of the B_c^+ -meson decay into the charm D^0 and strange K^+ mesons. Surprisingly, LHCb found a signal [8]. The B_c^+ is the only meson consisting of two heavy quarks of different flavour, namely a b and a c quark. Unlike other B mesons, the b -quark decay accounts only for a small fraction of B_c^+ decays, with the c -quark decay accounting for the majority of them. The enhancement around the B_c^+ mass in the D^0 and K meson invariant mass spectrum is clearly visible (see *right panel* of Fig. 5). The contribution of the $B_c^+ \rightarrow D^0 K^+$ decay, shown as the red Gaussian distribution, is observed with a statistical significance of 5.1σ . The result is surprising because the measured decay rate is high compared to the theoretical predictions. It will be a challenge for the theoretical physicists to understand the origin of this disagreement. The $B_c^+ \rightarrow D^0 K^+$ decay proceeds predominantly through the penguin and annihilation decay diagrams, and the tree-level-amplitude decay $B_c^+ \rightarrow D^0 \pi^+$ has not been yet observed. This is the first observation of a B_c^+ decay dependent on such processes.

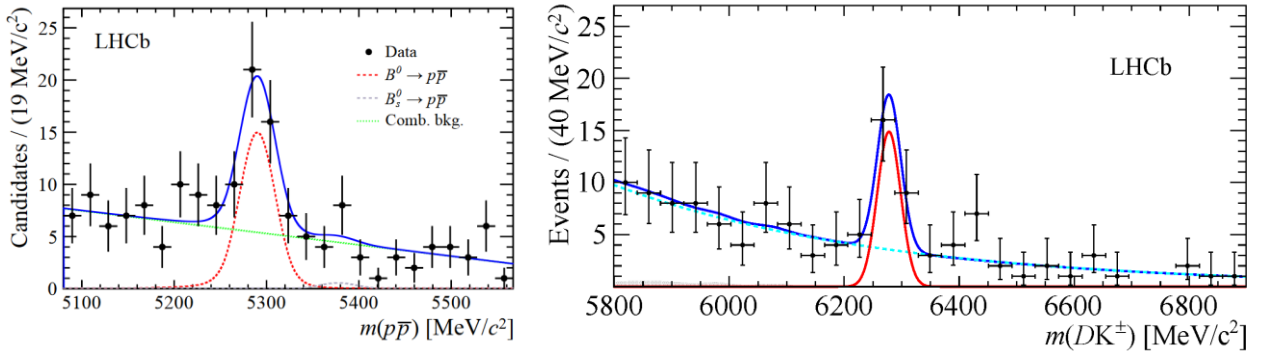


Fig. 5. The $p\bar{p}$ mass spectrum with the structure corresponding to the B^0 meson (*left panel*). The $D^0 K$ mass spectrum with the peak corresponding to the B_c^+ meson. The red Gaussian shows the contribution of the $B_c^+ \rightarrow D^0 K^+$ decay (*right panel*)

6. Precise determination of the parameters of the Cabibbo–Kobayashi–Maskawa matrix

In the SM, the CKM is a unitary 3×3 matrix which contains information on the strength of the flavour-changing weak interaction. The constraints of unitarity of the CKM matrix on the diagonal terms can be written as $\sum_i |V_{ik}|^2 = 1$, while for non-diagonal elements the relations of the type $\sum_k V_{ik} V_{jk}^* = 0$ must be met. The strategy of the search for NP in the CKM sector is based on precise measurements of the elements (or their combinations) of the quark mixing matrix and checking the unitarity conditions, as well as the consistency between measurements of different types for the same quantity. LHCb performed a number of such measurements in 2011–2018 for the b hadrons.

One of the parameters, which can be predicted with high accuracy in the framework of the SM is the γ angle of the unitarity triangle. This angle is related to the elements of the quark mixing matrix as $\gamma = \arg[-V_{ud}V_{ub}^*/V_{cd}V_{cb}^*]$. The uncertainty of theoretical predictions for γ is less than 10^{-7} as the tree level decays are involved. The γ angle can be determined in the measurement of the ratio between the favoured ($b \rightarrow cW$) and suppressed ($b \rightarrow uW$) amplitudes in weak decays of charged and neutral B mesons. For example, in 2016 several constraints on γ were measured by the LHCb Collaboration in the decays of B^0 mesons [9]. These measurements were combined, and an overall constraint on $\gamma = (72.2^{+6.8}_{-7.3})^\circ$ was determined (statistical and systematic uncertainties are also combined in this result). The constraints, which were measured in decays of different types, as well as the overall measurement are presented in the left panel of Fig. 6. The obtained result is in good agreement with the SM predictions, as well as with other measurements of the unitarity triangle parameters.

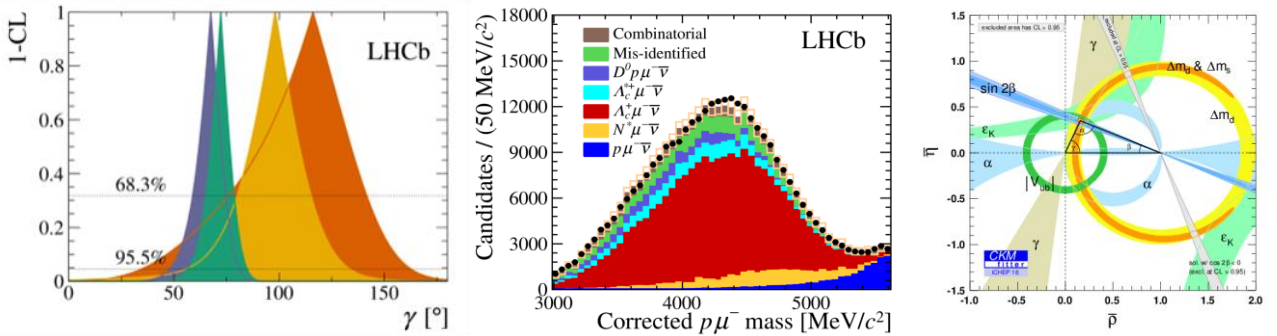


Fig. 6. The p -value spectra for the measurements of the γ angle: red, yellow and blue distributions correspond to different B mesons in the initial state (B_s^0 , B^0 , and B , respectively); the green one reflects the combination produced out of three constraints (*left panel*). The proton–muon mass spectrum for the reconstructed Λ_b^0 baryons corrected on its flight direction; the histograms of different colours demonstrate the contributions of different types (*central panel*). Recent experimental constraints on the unitarity triangle (*right panel*)

The V_{ub} element of the CKM matrix defines the probability of transitions between u and b quarks. This is the smallest element of the quark mixing matrix. The $|V_{ub}|$ parameter has been measured with the highest experimental uncertainty among all CKM elements. Moreover, the results of two type of measurements (inclusive and exclusive) performed on B -factories by Belle and BaBar Collaborations are inconsistent at more than three standard deviation level. In 2015, LHCb presented a new technique for the $|V_{ub}|$ parameter determination, which is based on measurements of the probability of the semimuonic decay of the Λ_b^0 baryon [10]. The decay $\Lambda_b^0 \rightarrow p\mu\bar{\mu}$ was observed for the first time. The registration of this rare decay was possible due to high integrated luminosity collected by LHCb. The events of this decay, due to its kinematical properties, populate the high proton–muon invariant masses in contrast to the other semimuonic Λ_b^0 decays with production of baryons heavier than proton (see *central panel* of Fig. 6). This allows to separate the signal channel from the background one. Using the results of the lattice QCD calculations and the experimental results on the parameters of the quark mixing matrix, a new absolute value for the $|V_{ub}|$ has been obtained: $|V_{cb}| = (3.27 \pm 0.15_{\text{exp}} \pm 0.16_{\text{LQCD}} \pm 0.06_{V_{cb}}) \cdot 10^{-3}$. The new result supports the results of the exclusive measurements of $|V_{ub}|$. The result of this measurement is in contradiction with the additional right-hand current based hypothesis (NP) involved to explain the difference occurred between the inclusive and exclusive techniques of the $|V_{ub}|$ determination. The obtained result also imposes constraints for the unitarity triangle.

The recent progress in the measurement of the properties of the unitarity triangle is demonstrated in the *right panel* of Fig. 6. The overall picture is self-consistent and is in good agreement with the SM expectations.

7. Search for CP violation in the heavy quark sector

One of the goals for the LHC experiments is a search of new phenomena to explain the so-called Baryon asymmetry of the Universe (BAU). According to the Sakharov's conditions, one of the requirements to explain BAU at the microscopic level is an additional source of violation of the combined charge conjugation parity (CP) symmetry. So far, the CP violation (CPV) has been observed for K and B mesons. The observed effects are theoretically related with the non-zero complex phase, which makes the CKM elements complex values. However, the CKM mechanism is insufficient to explain BAU and some additional CPV interaction is required. LHCb performs the CPV searches in heavy quark sector of the SM.

The SM has clear close-to-zero prediction for the CPV for the charm particles. One of the best channels to search for additional sources of the CPV in charm is the D^0 decay to the $K\pi$ final state. The initial matter-antimatter identity can be determined by the charge of the accompanying pion in the decay $D^{*+} \rightarrow D^0\pi^+$ or $D^{*-} \rightarrow D^0\pi^-$. The mixing effect (oscillation) appears as a decay-time dependence of the ratio R^\pm between the number of reconstructed “wrong-sign” (WS; $D^0 \rightarrow K^+\pi^-$) and “right-sign” (RS; $D^0 \rightarrow K^-\pi^+$) processes. The sign of R shows the flavour of the D^* meson. The comparison of the R^\pm distributions is a powerful tool to determine the parameters of the mixing of the neutral charm mesons. This approach also allows one to test all possible manifestations for neutral systems: direct one, CPV in mixing and CPV in the interference of decay and mixing. An example of the WS D^* decay is presented in the left panel of Fig. 7 [11]. The corresponding R^\pm spectra and their difference are presented in the central panel of Fig. 7. No CPV has been observed. Up to now, the results of the LHCb experiment are the most precise for the charm sector.

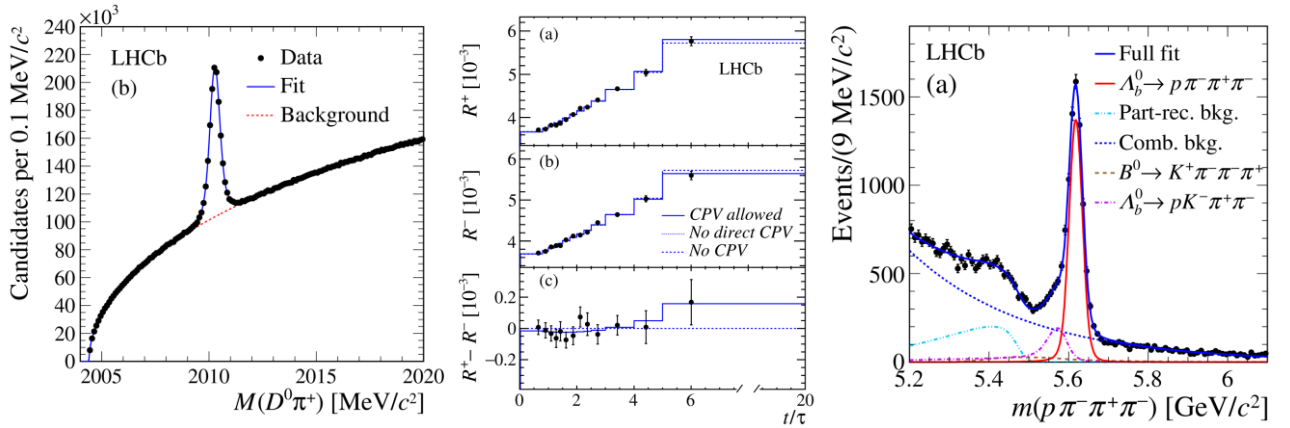


Fig. 7. $D\pi$ invariant mass spectrum for the WS combination (left panel). The ratio of the WS/RS yields as a function of the decay time; lines indicate the results of the fits, which are done under different hypotheses concerning CPV in the charm sector (central panel). $p\pi^-\pi^+\pi^-$ invariant mass distribution; the red line shows the contribution from the $\Lambda_b^0 \rightarrow p\pi^-\pi^+\pi^-$ decay (right panel)

In 2016, the LHCb experiment presented results of the analysis devoted to the $\Lambda_b^0 \rightarrow p\pi^-\pi^+\pi^-$ decay, in which the first evidence of the CPV for the baryons was found. LHCb reconstructed $6\,646 \pm 105$ candidates using the data sample collected during Run-1 of the LHC, which corresponds to 3 fb^{-1} of the integrated luminosity [12]. The signal from the decay of interest is presented in the right panel of Fig. 7. The $a_P^{T\text{-odd}}$ and $a_{CP}^{T\text{-odd}}$ observables were produced for different parts of the $\Lambda_b^0 \rightarrow p\pi^-\pi^+\pi^-$ decay phase space. The deviations of these observables from zero would indicate violation of the parity or CP symmetries. Two different phase space partitioning was tested. In both cases there were parts for which the evidence of the deviation of $a_P^{T\text{-odd}}$ and $a_{CP}^{T\text{-odd}}$ values from zero was observed. The statistical significance of the evidence consists of 3.3σ .

8. Direct search for new physics, electroweak, and top quark program

Besides the charm and beauty quark physics, the LHCb experiment carries an experimental program on direct searches for NP particles. Also, a part of the program is devoted to measurements in the electroweak and top quark sectors of the SM.

One example of direct searches for NP particles is the search for a dimuon resonance in the Y mass region. The LHCb detector has good sensitivity to light spin-zero particles produced by gluon–gluon fusion and decaying to a pair of opposite-sign muons, due to its capability of triggering on particles with small transverse momentum and to its high-precision spectrometer. No evidence for NP particles produced in pp collisions at \sqrt{s} of 7 and 8 TeV has been found for a signal in the mass range 5.5 to 15 GeV/ c^2 , and upper limits are set on the product of the production cross-section and the branching fraction to pairs of muons [13]. The limits are competitive with the most stringent ones over most of the mass region considered, and the first limits are set near the Y resonances.

For the electroweak sector of the SM, the LHCb Collaboration performed measurements of a fundamental SM parameter – the electroweak mixing angle (θ_w). This parameter quantifies the relative strengths of electromagnetism and the weak force. LHCb has measured the forward–backward asymmetry A_{FB} in the angular distribution of muons in the dimuon final states as a function of the dimuon mass for $\sqrt{s} = 7$ and 8 TeV [14]. The LHCb result of the effective $\sin^2\theta_w = 0.23142 \pm \pm 0.00073_{\text{stat}} \pm 0.00052_{\text{syst}} \pm 0.00056_{\text{theo}}$ is in very good agreement with the determinations from other experiments and is one of the most precise measurements obtained at a hadron collider.

The production of top quarks at hadron colliders represents an important test of the SM. The top quark is the heaviest known fundamental particle and its production and decay properties are sensitive to a number of parameters involved in physics models beyond the SM. So far, only general-purpose detectors such as ATLAS and CMS at LHC or CDF and D0 at Tevatron have observed direct top quarks. The unique forward acceptance of the LHCb detector allows a phase space inaccessible to be probed in ATLAS and CMS. Top-quark production in this region receives a higher contribution from quark–antiquark annihilation than in the central region. In addition, it probes the proton parton distribution functions at high values of the fraction of proton momentum carried by quarks or gluons, whose knowledge suffers from large uncertainties, which can be reduced by LHCb measurements. A large contribution from quark-initiated production also results in a larger expected charge asymmetry in the forward region than in the central region probed by ATLAS and CMS. The top pair production was measured by LHCb at the proton–proton collision energy of 13 TeV, where the production cross-section in the acceptance of the LHCb detector is expected to be ten times larger than it was at the lower Run-1 energies [15]. The higher cross-section allows LHCb to select a high-purity sample, in which the dilepton (μ and e) channel is partially reconstructed by requiring that a muon, an electron, and a b -jet are present in the event. The measured cross-sections within the LHCb acceptance does not contradict with predictions of the theoretical models.

9. Conclusion

The LHCb detector was performing well with a high data taking efficiency during Run-1 and Run-2. Many new physics results on different topics have been obtained. By the end of 2018, the number of publications reached 454. The data analysis will be continued as only a part of the collected data has been analyzed by now. During 2019–2020, the LHCb detector will be upgraded to be able to operate with five times higher luminosity after the start up of the LHC in 2021.

References

1. LHCb Collaboration, JINST **3**, S08005 (2008).
2. LHCb Collaboration, Phys. Rev. Lett. **114**, 062004 (2015).
3. LHCb Collaboration, Phys. Rev. Lett. **122**, 012001 (2019), arXiv:1809.07752.
4. LHCb Collaboration, Phys. Rev. D **92**, 112009 (2015).
5. LHCb Collaboration, Phys. Rev. Lett. **118**, 022003 (2017).
6. LHCb Collaboration, Phys. Rev. Lett. **121**, 092003 (2018).
7. LHCb Collaboration, Phys. Rev. Lett. **119**, 232001 (2017).
8. LHCb Collaboration, Phys. Rev. Lett. **118**, 111803 (2017).
9. LHCb Collaboration, JHEP **1808**, 176 (2018); JHEP **1612**, 087 (2016); JHEP **1608**, 137 (2016); JHEP **1606**, 131 (2016); Phys. Rev. D **93**, 112018 (2016).
10. LHCb Collaboration, Nat. Phys. **10**, 1038 (2015).
11. LHCb Collaboration, Phys. Rev. D **97**, 031101 (2018).
12. LHCb Collaboration, Nat. Phys. **13**, 391 (2017).
13. LHCb Collaboration, JHEP **1808**, 147 (2018).
14. LHCb Collaboration, JHEP **1511**, 190 (2015).
15. LHCb Collaboration, JHEP **1808**, 174 (2018).

OVERVIEW OF ALICE RESULTS

PNPI participants of the ALICE Collaboration:

Ya.A. Berdnikov, V.V. Ivanov, A.V. Khazadeev, E.L. Kryshen, M.V. Malaev,
V.N. Nikulin, Yu.G. Riabov, V.G. Ryabov, V.M. Samsonov, M.B. Zhalov

1. Introduction

ALICE (A Large Ion Collider Experiment) is aimed to study hot and dense quantum chromodynamic (QCD) matter produced in heavy ion collisions at the Large Hadron Collider (LHC) [1]. ALICE collected about 10 and 100 μb^{-1} of Pb–Pb collisions at $\sqrt{s_{NN}} = 2.76$ TeV during the first heavy ion runs in 2010 and 2011, respectively, and about 360 μb^{-1} at $\sqrt{s_{NN}} = 5.02$ TeV in 2015. In the beginning of 2013, the LHC delivered 30 nb^{-1} of p –Pb collisions at $\sqrt{s_{NN}} = 5.02$ TeV, important reference data for the Pb–Pb studies. Selected results based on these data samples are briefly summarized in the following.

2. Global properties

ALICE measurements of the global event observables indicate that the matter, produced in Pb–Pb collisions at the LHC, reveal even more extreme properties than at lower energies. The charged-particle density at mid rapidity amounts to $dN/d\eta \approx 2000$ in the most central Pb–Pb collisions at $\sqrt{s_{NN}} = 5.02$ TeV [2], by a factor of 2.6 higher than in central Au–Au collisions at the Relativistic Heavy Ion Collider (RHIC), Fig. 1, *left*. It corresponds to an initial energy density of about 18 GeV/fm^3 at a conventional value of 1 fm/c for the thermalization time [3], by a factor of 3.5 higher than in Au–Au collisions at the top energy of RHIC.

The measured slope of the direct photon spectrum, $T = 297 \pm 12$ (stat) ± 41 (syst) MeV for the 0–20% of the most central collisions (Fig. 1, *right*) suggests that the initial temperature of the produced medium goes well above the critical temperature of 150–160 MeV predicted for the deconfinement state transition by lattice QCD calculations [4].

The volume of the produced fireball, measured with two-pion Bose–Einstein correlations, increases by a factor of two from RHIC to LHC, while the matter lifetime, roughly proportional to the longitudinal dimension of the fireball, turns out to be more than 10 fm/c , 20% higher than at RHIC, in line with the hydrodynamic predictions [5] (Fig. 2).

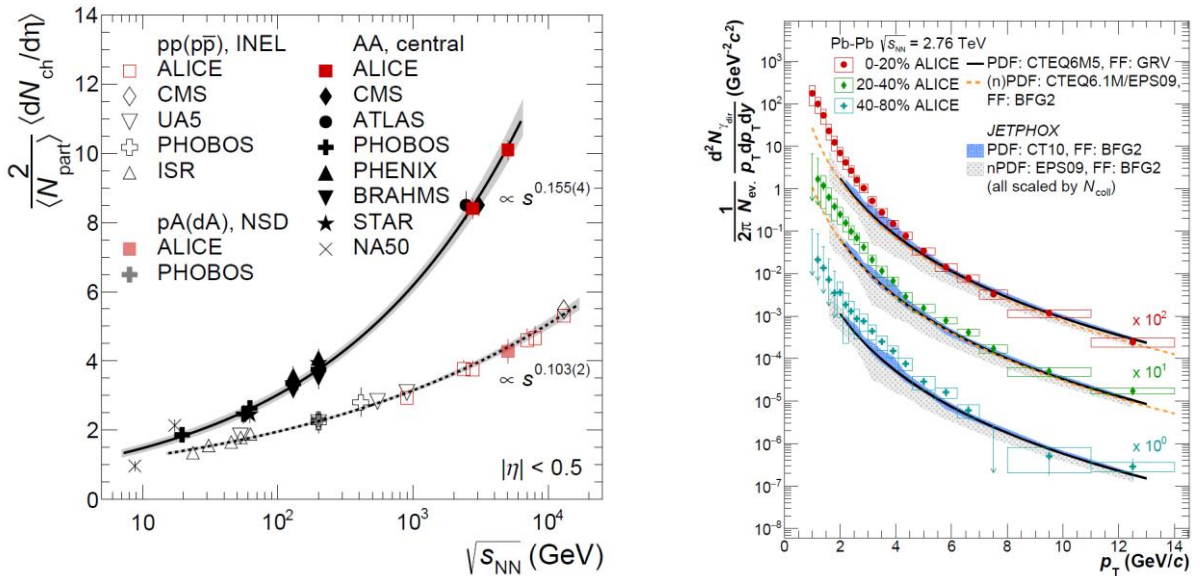


Fig. 1. Charged particle pseudorapidity density $dN_{\text{ch}}/d\eta$ per colliding nucleon pair versus the centre-of-mass energy for pp and AA collisions (*left*). Direct photon spectra in Pb–Pb collisions at $\sqrt{s_{NN}} = 2.76$ TeV compared to NLO pQCD predictions for the direct photon yield (*right*)

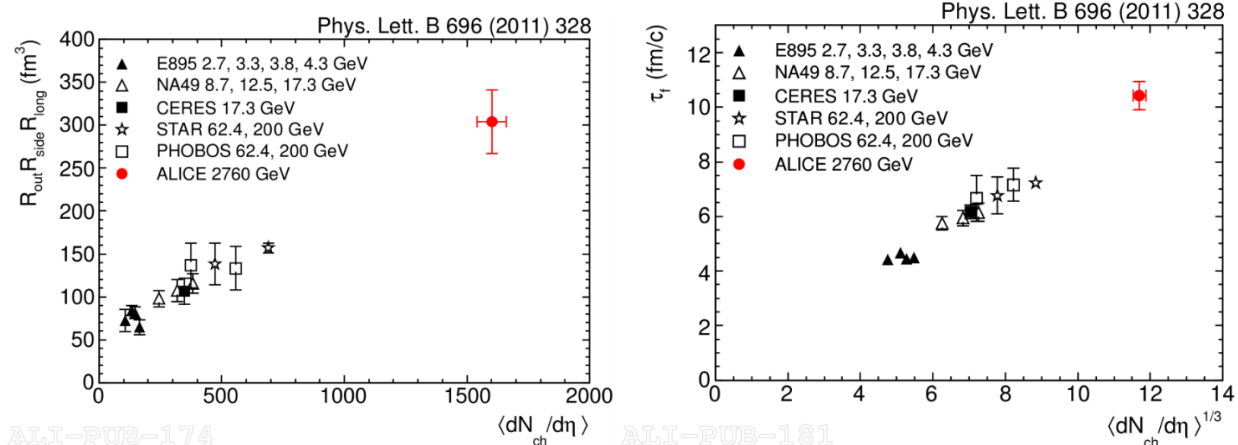


Fig. 2. Local freeze-out volume as measured by the identical pion interferometry at the LHC compared to central gold and lead collisions at lower energies (*left*). The system lifetime (decoupling time) compared to results from lower energies (*right*)

3. Anisotropic flow

Further constraints on the evolution of the produced medium come from the measurement of the momentum-space anisotropy (flow) which is quantified *via* the Fourier decomposition of azimuthal particle distributions. Large elliptic flow (or second Fourier coefficient, v_2), observed both at RHIC and LHC energies [6], appears to be consistent with the dynamics of an almost perfect liquid characterized by the shear viscosity to entropy density ratio η/s close to the lower bound of $1/4\pi$ from AdS/CFT (Fig. 3, *left*). Significant triangular flow (third Fourier coefficient, v_3), measured by ALICE [7], appears to be highly sensitive to the η/s ratio and initial state fluctuations providing promising tools to constrain hydrodynamic models. The best estimate for the η/s ratio was found to be about 0.2, a bit higher than at RHIC, indicating that the produced hot and dense matter might be going to approach an asymptotic freedom regime at higher collision energies.

Furthermore, the elliptic flow of identified particles reveals a clear mass ordering at low p_T [8], being explained by the strong collective dynamics of the medium (Fig. 3, *right*). However, the number of constituent quark (NCQ) scaling of the elliptic flow observed at RHIC and considered as a direct consequence of the coalescence hadronization mechanism, is not that good at the LHC energies.

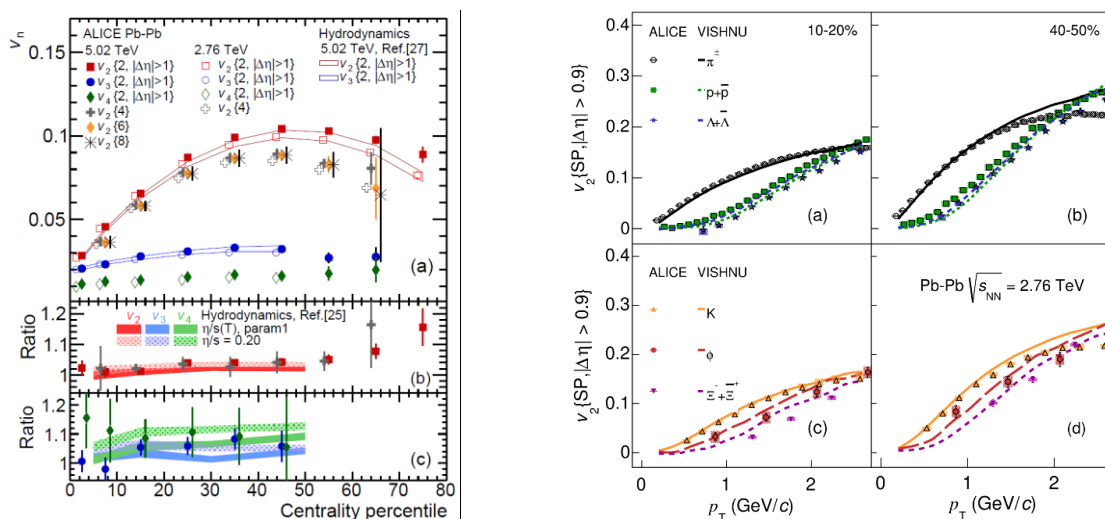


Fig. 3. Anisotropic flow of charged particles as a function of centrality compared to hydrodynamic calculations in Pb–Pb collisions at $\sqrt{s_{NN}} = 2.76$ TeV and 5.02 TeV [6] (*left*). Elliptic flow of identified particles compared to the VISHNU model [8] (*right*)

4. Particle spectra

ALICE measurements of the low-momentum proton, pion and kaon p_T spectra in central Pb–Pb collisions also agree with hydrodynamic predictions within 20% supporting the hydrodynamic interpretation of the data at the LHC [9] (Fig. 4, *left*). Hydro-inspired blast wave fits to these spectra allowed ALICE to extract the mean collective velocity of the transverse expansion, which was found to be about 65% of the speed of light, 10% higher than at RHIC and in good agreement with the observed tendency from the RHIC energy scan.

ALICE also measured integrated particle yields for various particle species. At lower energies, the yields were surprisingly well described in terms of a simple thermal model with a common chemical freeze-out temperature T_{ch} [10]. Thermal fits for 0–10% central collisions at the LHC provide $T_{\text{ch}} = 156 \pm 3$ MeV, lower than at RHIC (Fig. 4, *right*). Small deviations from the fit can be explained by the final-state interactions in the hadronic phase.

High- p_T hadrons, produced in hard interactions at early stages of heavy ion collisions, can be used as effective tomography probes of the produced medium. An energy loss of hard partons in the medium may result in a strong suppression of high- p_T hadrons (jet quenching), which was indeed observed at RHIC and quantified in terms of the nuclear modification factor R_{AA} (p_T spectra in AA collisions normalized to appropriately scaled pp spectra). The suppression of high- p_T hadrons appeared to be even stronger in central Pb–Pb collisions at the LHC with R_{AA} reaching the minimum of about 0.14 for $p_T \approx 6$ GeV/c [11] (Fig. 5, *left*). The slowly increasing high p_T behaviour of the nuclear suppression factor was successfully described within partonic transport models based on perturbative QCD [12].

High- p_T heavy flavour mesons serve as sensitive probes of the in-medium energy loss of charm and bottom quarks, which are expected to interact weaker than light quarks and gluons. However, the suppression for open heavy flavour D^0 , D^+ , and D^{*+} mesons reaches a factor of 5 at $p_T \approx 10$ GeV/c [13], almost as large as that observed for light hadrons (dominated by pions from gluon fragmentation), providing an indication of no strong colour charge or mass dependence of the in-medium energy loss (Fig. 5, *right*). The observed elliptic flow of prompt D^0 mesons is also comparable with v_2 of light hadrons [14], suggesting that the azimuthal anisotropy of the system is effectively transferred to charm quarks *via* multiple interactions in the medium.

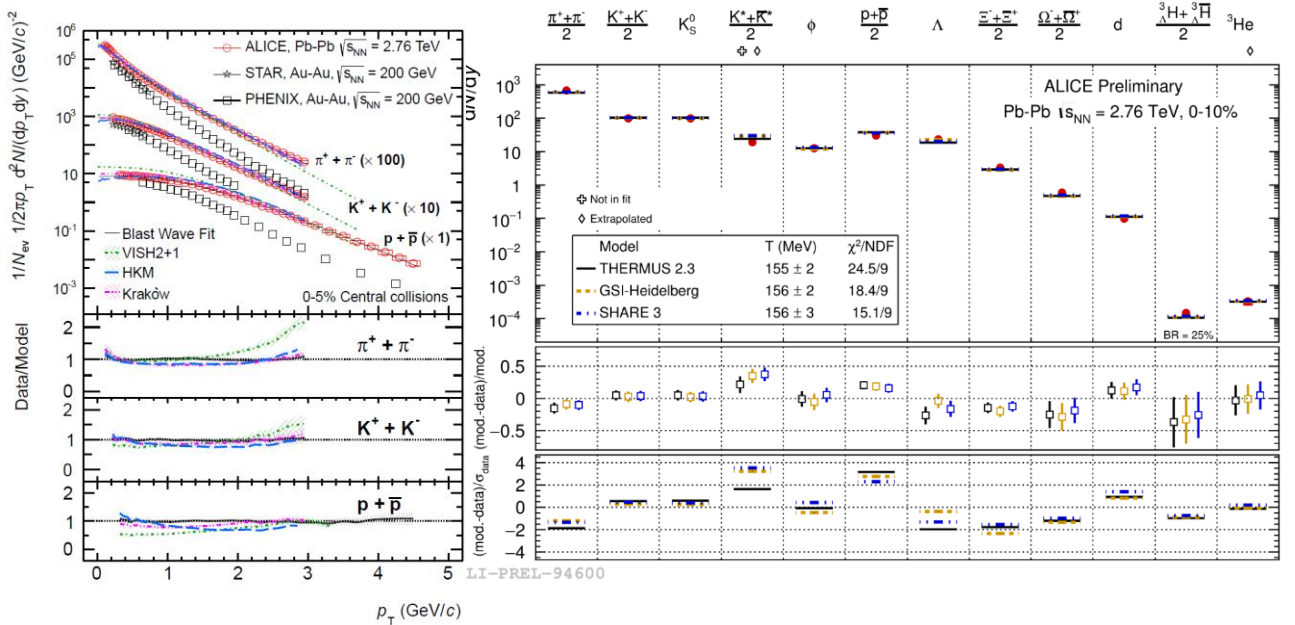


Fig. 4. Low-momentum proton, pion, and kaon p_T spectra in central Pb–Pb collisions in comparison with hydrodynamic predictions (*left*). Grand canonical thermal fit of integrated particle yields in 0–10% central Pb–Pb collisions (*right*)

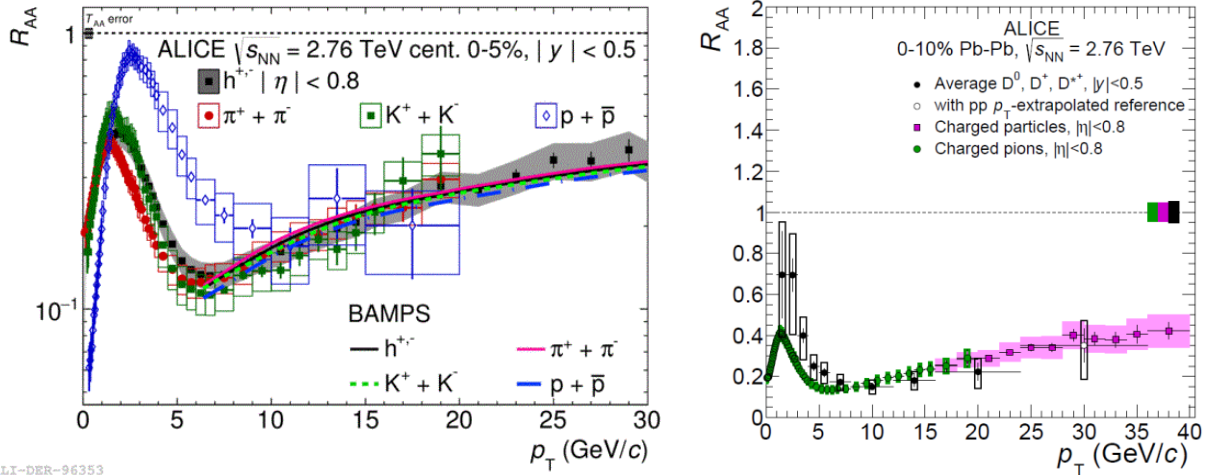


Fig. 5. R_{AA} of π , K , p and charged particles in central Pb–Pb collisions together with the BAMPs calculations [12] (*left*). Prompt D -meson R_{AA} (average of D^0 , D^+ , and D^{*+}) compared to the nuclear modification factors of pions and charged particles in central Pb–Pb collisions (*right*)

5. Charmonium suppression and flow

Suppression of hidden charm mesons due to colour-screening effects was one of the first signals predicted for formation of the deconfined phase and indeed observed at Super Proton Synchrotron (SPS) and RHIC. However, high abundance of charm quarks at the LHC may also result in an enhancement of bound $c\bar{c}$ states *via* regeneration in the thermalized quark–gluon plasma (QGP) medium. The J/ψ suppression, measured by ALICE versus the number of participants N_{part} , appeared to flatten at $\langle N_{\text{part}} \rangle \approx 100$, being much weaker than at RHIC for central collisions [15]. Such a centrality dependence and p_T differential studies, shown in Fig. 6 (*left*), suggest that $c\bar{c}$ regeneration processes indeed play an important role at the LHC energies. The observed non-zero elliptic flow for J/ψ in semicentral Pb–Pb collisions, shown in Fig. 6 (*right*), is also in favour of this picture [16].

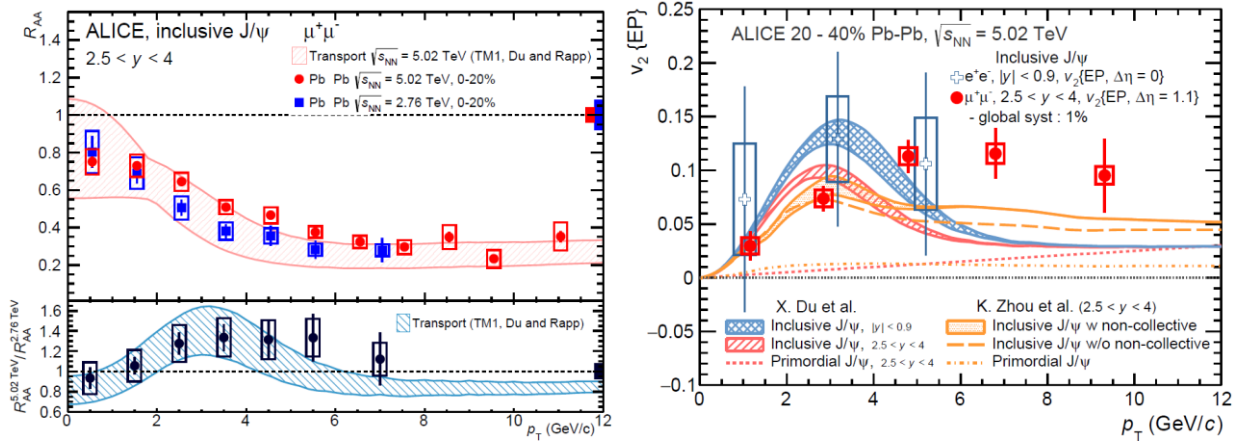


Fig. 6. Nuclear suppression factor for J/ψ at forward rapidity as a function of p_T in central Pb–Pb collisions (*left*). J/ψ elliptic flow at mid and forward rapidity as a function of p_T in semicentral Pb–Pb collisions at $\sqrt{s_{NN}} = 5.02$ TeV (*right*)

6. Ultrapерipheral collisions

J/ψ production was also measured at forward and mid rapidity in ultra-peripheral collisions (UPC), which are dominated by photon-induced reactions [17, 18]. In the leading order (LO) pQCD, the coherent J/ψ photoproduction cross section is proportional to the squared nuclear gluon density providing a direct tool to study poorly known gluon shadowing in nuclei at small $x \approx 10^{-3}$ – 10^{-2} , one of the most important initial state effects in heavy ion collisions. The ALICE measurements appear to be in good agreement with the leading twist approximation [19] and with a model that incorporates nuclear gluon shadowing according to EPS09LO global fits [20] (Fig. 7, *left*).

The ALICE experiment also discovered an excess in the yield of J/ψ at very low transverse momentum ($p_T < 0.3$ GeV/c) in peripheral hadronic Pb–Pb collisions [21]. The measured nuclear modification factor of J/ψ reaches about 7 in the 70–90% centrality class (Fig. 7, *right*). This excess at low p_T is remarkably similar to the shape of the p_T distribution of J/ψ coherently produced in ultraperipheral collisions. If confirmed, the observation of coherent J/ψ photoproduction in Pb–Pb collisions at impact parameters smaller than twice the nuclear radius opens new theoretical and experimental challenges and opportunities.

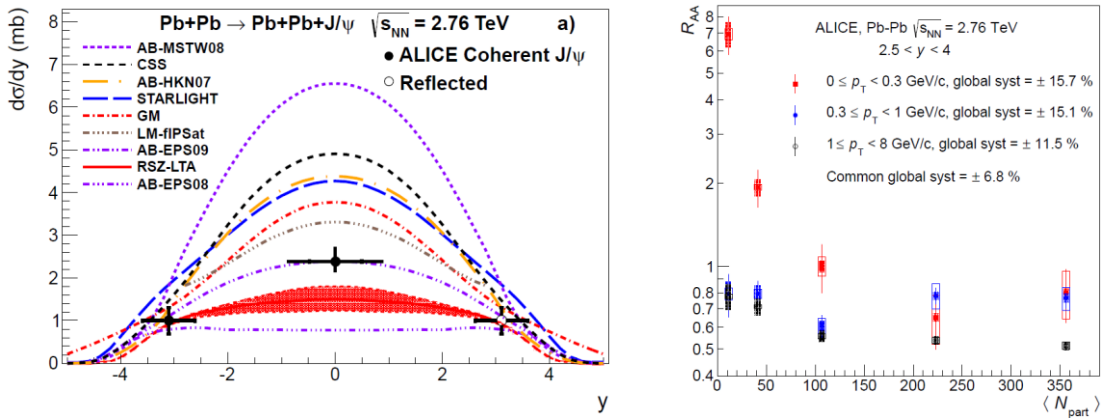


Fig. 7. Coherent J/ψ photoproduction cross section in ultraperipheral collisions compared to model predictions (*left*). Nuclear modification factor for J/ψ as a function of N_{part} in different p_T domains at forward rapidity (*right*)

7. Proton–lead results

Proton–nucleus collisions provide further tools to study initial and final state effects in cold nuclear matter and establish a baseline for the interpretation of heavy-ion results. The nuclear modification factor $R_{p\text{Pb}}$ of charged particles, shown in Fig. 8, *left*, is consistent with unity at transverse momentum above 2 GeV/c, indicating that the strong suppression of hadron production measured in Pb–Pb collisions at the LHC is not an initial state effect but is a consequence of jet quenching in hot QCD matter [22]. ALICE also measured the J/ψ suppression pattern in p –Pb collisions, an important baseline for interpretation of the J/ψ suppression in Pb–Pb collisions [23]. The results are in agreement with models incorporating EPS09 shadowing or coherent parton energy losses, while colour-glass condensate predictions are disfavoured by this measurement (Fig. 8, *right*).

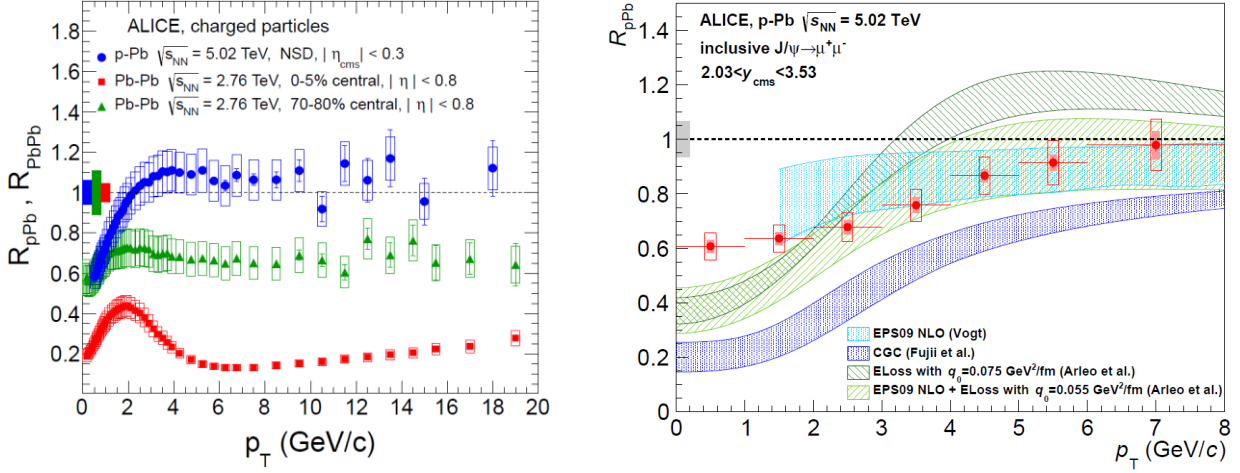


Fig. 8. Nuclear modification factor R_{pPb} as a function of p_T for charged particles in p -Pb collisions compared to R_{PbPb} in central and peripheral Pb-Pb collisions (*left*). Nuclear modification factor for J/ψ in p -Pb collisions compared to various model predictions (*right*)

Proton-lead collisions also appeared to be good for surprises. The analysis of two-particle angular correlations in high-multiplicity p -Pb collisions showed the presence of a ridge structure elongated in the pseudorapidity direction, the so-called near-side ridge. Subtraction of the correlation pattern for low-multiplicity events revealed a symmetric structure on the away side, the so called double-ridge, similar to the modulations caused by the elliptic flow in Pb-Pb [24] (Fig. 9, *left*). The dependence of v_2 coefficient, corresponding to these modulations, on p_T for identified particles exhibits a mass ordering pattern similar to Pb-Pb in agreement with hydrodynamic models [25] (Fig. 9, *right*). Other models attribute the effect to gluon saturation in Pb or to parton-induced final-state effects.

The ALICE experiment has also found persisting long-range correlation structures in J/ψ -hadron correlations in p -Pb collisions, reminiscent of the double ridge previously found in charged-particle correlations [26]. The corresponding second-order Fourier coefficient is found to be positive with a significance of about five, the magnitude being similar to the J/ψ v_2 coefficients measured in Pb-Pb collisions, suggesting a common mechanism at the origin of the J/ψ v_2 .

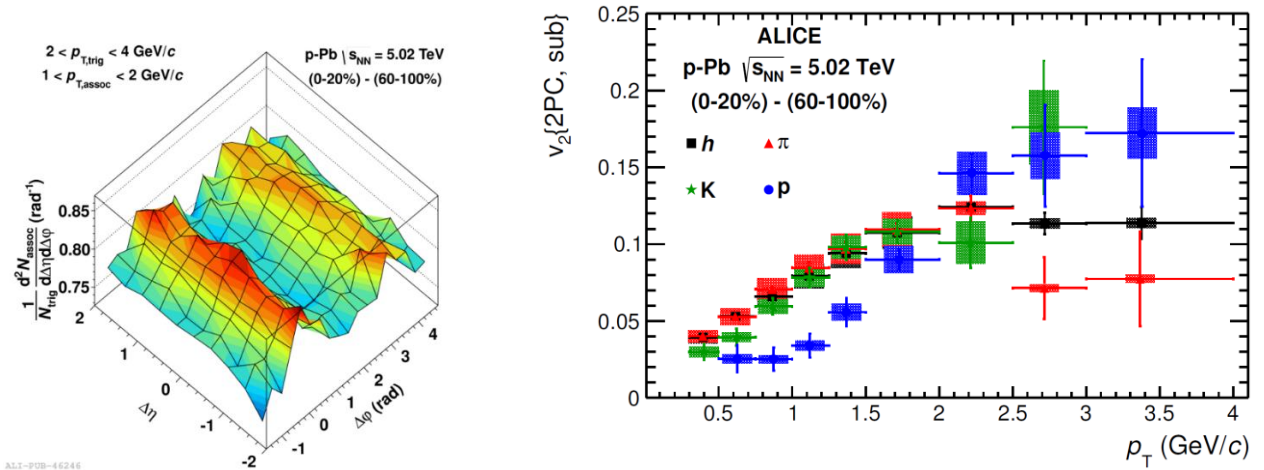


Fig. 9. Double ridge structure in the two-particle correlation function (*left*) and the elliptic flow for protons, pions, and kaons as a function of p_T (*right*) in high-multiplicity p -Pb collisions after subtraction of the low-multiplicity correlation pattern

8. Strangeness enhancement in proton–proton and proton–lead collisions

The enhancement of strangeness in heavy-ion collisions was one of the earliest proposed signals for the QGP because in a deconfined state the abundances of parton species should quickly reach their equilibrium values, resulting in a higher abundance of strangeness than is seen in proton–proton interactions.

The ALICE experiment discovered that the ratios of the strange hadron to light hadron yields in pp and p –Pb collisions grow with multiplicity, the growth being faster for multistrange hadrons [27]. Moreover, the relative strange hadron yields approach the values measured in central Pb–Pb collisions (Fig. 10). This measurement accompanied by the ridge discovery can be interpreted as another signature for formation of QGP like state in small collision systems.

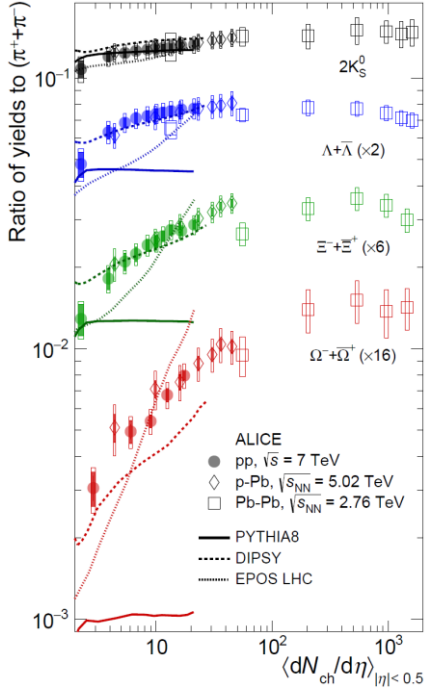


Fig. 10. Ratio of the strange particle yields to the charge pion yield as a function of the multiplicity in pp , p –Pb, and Pb–Pb collisions

9. CPT invariance checks

The CPT theorem, one of the most fundamental theorems of the quantum field theory, states that all laws of nature should be invariant under simultaneous transformations of the charge conjugation (C), the parity transformation (P), and the time reversal (T). The equality of particle and antiparticle masses, a direct consequence of this theorem, has been extensively tested for bosons in weak decays of neutral kaons in the KLOE experiment. In 2015, the ALICE experiment published results on deuteron, helium-3, antideuteron, and antihelium-3 in Pb–Pb collisions at 2.76 TeV [28]. The measured relative mass differences agree with zero within uncertainties of $\sim 3 \cdot 10^{-4}$ for deuteron/antideuteron and within $\sim 3 \cdot 10^{-3}$ for helium/antihelium (Fig. 11, *left*).

The obtained masses for nuclei and antinuclei were used to calculate the binding energy of those nuclei. The binding energy difference agrees with zero within the experimental uncertainty (Fig. 11, *right*). These results show that the effective nuclear forces are invariant under the CPT transformation.

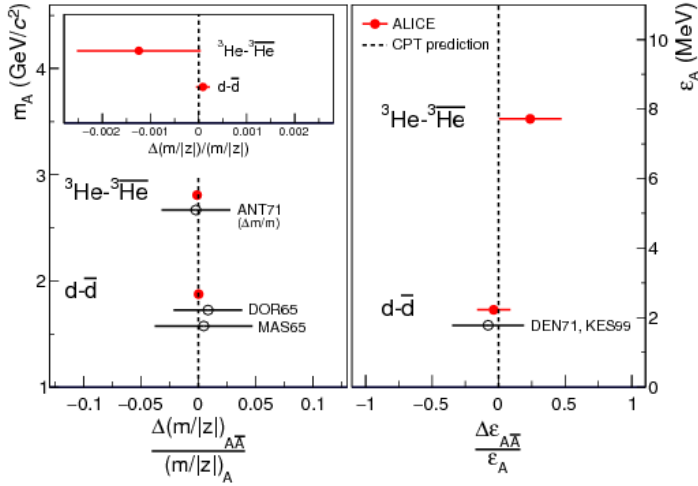


Fig. 11. Relative mass differences (*left*) and binding energy differences (*right*) for helium/antihelium and deuteron/antideuteron in Pb–Pb collisions at 2.76 TeV

10. Plans

In Run-3 and Run-4, after the Long Shutdown 2 of the LHC, the Pb–Pb luminosity of the collider will increase by a factor of 10. The ALICE experiment is going to focus on high precision measurements of heavy flavour hadrons, low-momentum quarkonia and low mass dileptons. These observables are characterised by a low signal-to-background ratio and require a large recorded sample of minimum bias events. The ALICE goal is to upgrade all detectors to readout all incoming events continuously and to increase the current statistics of minimum bias events by a factor of 100.

11. Conclusion

In conclusion, the ALICE Collaboration has obtained a wealth of interesting physics results from the heavy ion runs at the LHC revealing many new phenomena not observed at lower energies. ALICE is entering a charm era of precision measurements and is looking forward to new discoveries in pp , p –Pb, and Pb–Pb collisions in Run-3 and Run-4. PNPI participants reported ALICE results at various conferences and workshops, see, *e. g.*, [29–36], and made an important contribution to the overall success of the ALICE experiment.

References

1. K. Aamodt *et al.*, J. Instrum. **3**, S08002 (2008).
2. K. Aamodt *et al.*, Phys. Rev. Lett. **105**, 252301 (2010); J. Adam *et al.*, Phys. Rev. Lett. **116**, 222302 (2016).
3. J.D. Bjorken, Phys. Rev. D **27**, 140 (1983).
4. J. Adam *et al.*, Phys. Lett. B **754**, 235 (2016).
5. K. Aamodt *et al.*, Phys. Lett. B **696**, 328 (2011).
6. K. Aamodt *et al.*, Phys. Rev. Lett. **105**, 252302 (2010); J. Adam *et al.*, Phys. Rev. Lett. **116**, 132302 (2016).
7. B. Abelev *et al.*, Phys. Lett. B **719**, 18 (2013).
8. B. Abelev *et al.*, JHEP **1506**, 190 (2015).
9. B. Abelev *et al.*, Phys. Rev. Lett. **109**, 252301 (2012).
10. A. Andronic, P. Braun-Munzinger, J. Stachel, Phys. Lett. B **673**, 142 (2009).
11. K. Aamodt *et al.*, Phys. Lett. B **696**, 30 (2011); B. Abelev *et al.*, Phys. Rev. C **88**, 044910 (2013); J. Adam *et al.*, Phys. Rev. C **93**, 034913 (2016).
12. F. Senzel, O. Fochler, J. Uphoff *et al.*, Nucl. Phys. A **931**, 937 (2014).
13. B. Abelev *et al.*, JHEP **1209**, 112 (2012); J. Adam *et al.*, JHEP **1603**, 081 (2016).

14. B. Abelev *et al.*, Phys. Rev. Lett. **111**, 102301 (2013).
15. B. Abelev *et al.*, Phys. Rev. Lett. **109**, 072301 (2012); B. Abelev *et al.*, Phys. Lett. B **734**, 314 (2014); J. Adam *et al.*, Phys. Lett. B **766**, 212 (2017).
16. E. Abbas *et al.*, Phys. Rev. Lett. **111**, 162301 (2013); S. Acharya *et al.*, Phys. Rev. Lett. **119**, 242301 (2017).
17. B. Abelev *et al.*, Phys. Lett. B **718**, 1273 (2013).
18. E. Abbas *et al.*, Eur. Phys. J. C **73**, 2617 (2013).
19. V. Rebyakova, M. Strikman, M. Zhalov, Phys. Lett. B **710**, 647 (2012).
20. K.J. Eskola, H. Paukkunen, C.A. Salgado, JHEP **0904**, 065 (2009).
21. J. Adam *et al.*, Phys. Rev. Lett. **116**, 222301 (2016).
22. B. Abelev *et al.*, Phys. Rev. Lett. **110**, 082302 (2013).
23. B. Abelev *et al.*, JHEP **1402**, 073 (2014), J. Adam *et al.*, JHEP **1506**, 055 (2015).
24. B. Abelev *et al.*, Phys. Lett. B **719**, 29 (2013).
25. B. Abelev *et al.*, Phys. Lett. B **726**, 164 (2013).
26. S. Acharya *et al.*, arXiv:1709.06807.
27. J. Adam *et al.*, Nat. Phys. **13**, 535 (2017).
28. J. Adam *et al.*, Nat. Phys. **11**, 811 (2015).
29. E. Kryshen *et al.*, arXiv:1305.2804, LHC on the March Proc., PoS IHEP-LHC-2012, 002 (2012).
30. E. Kryshen *et al.*, arXiv:1306.1072, Rencontres de Moriond 2013 Proc. (2013).
31. E. Kryshen *et al.*, arXiv:1310.5819, NTHEP 2013 Proc. (2013).
32. E. Kryshen *et al.*, arXiv:1410.8192, PANIC 2014 Proc. DESY-PROC-2014-04/198 (2014).
33. E. Kryshen *et al.*, arXiv:1705.06872, QM2016 Proc., Nucl. Phys. A **967**, 273 (2017).
34. M. Malaev, V. Riabov, Yu. Riabov, V. Samsonov, Bull. Russ. Acad. Sci. Phys. **79**, 909 (2015).
35. M. Malaev *et al.*, AIP Conf. Proc. **1701**, 060014 (2016).
36. V. Riabov *et al.*, J. Phys. Conf. Ser. **798**, 012054 (2017).

HIGGS BOSON PROPERTIES STUDIED IN ATLAS AND CMS EXPERIMENTS

PNPI participants of the ATLAS Collaboration:

O.L. Fedin, A.E. Ezhilov, V.T. Grachev, M.P. Levchenko, V.P. Maleev, I.G. Naryshkin, V.A. Schegelsky, V.M. Solovyev

PNPI participants of the CMS Collaboration:

A.A. Vorobyev, V.T. Kim, Y.M. Ivanov, V.L. Golovtsov, E.V. Kuznetsova, P.M. Levchenko, V.A. Murzin, V.A. Oreshkin, I.B. Smirnov, V.V. Sulimov, L.N. Uvarov, S.A. Vavilov, An.A. Vorobyev

1. Introduction

The CMS and ATLAS experiments [1, 2], the most ambitious projects in high energy physics, demonstrated unique capabilities of extending the human knowledge in the fundamental elementary particle physics. The main result of these experiments is the discovery of the (Brout–Englert–)Higgs-boson made in 2012 [3, 4]. In the Standard Model (SM), the Higgs boson is the quantum of the fundamental scalar vacuum field responsible for the spontaneous electroweak symmetry breaking and for the origin of mass.

After the discovery of a particle consistent with the SM Higgs boson (H), the properties of this particle were studied using the full Run-1 (2011–2012) dataset and found to be consistent with the SM expectations. The mass was measured with a 0.2% precision [5], all tested alternatives to the 0^+ spin-parity assignment were rejected [6, 7], and the couplings were found to be consistent with the SM predictions with accuracies about 10% in the most favourable cases [8]. However, only the gluon fusion and vector boson fusion (VBF) production processes and the decays to bosons were clearly observed, with the decays to $\tau\tau$ pairs observed at the five standard deviations level only with a combination of the ATLAS and CMS results. Direct observations of the coupling to b and t quarks were lacking, the latter being only inferred from the gluon fusion loop induced Higgs production.

The Run-2 data taking period started in 2015 at an increased centre of mass energy of 13 TeV and an increased instantaneous luminosity, reaching $2 \cdot 10^{34} \text{ cm}^2 \cdot \text{s}^{-1}$, twice the Large Hadron Collider (LHC) design luminosity. Among the main goals of that data taking period were the discovery of the $t\bar{t}H$ production process, the observation of the decay $H \rightarrow b\bar{b}$ and precise measurements of the H boson properties in the decay channels involving bosons (WW , ZZ , and $\gamma\gamma$). The results presented here are based on either the data collected in 2015–2016, corresponding to an integrated luminosity about 35 fb^{-1} , or on the data collected between 2015 and 2017, corresponding to an integrated luminosity about 80 fb^{-1} .

At the LHC, the main production mode for the Higgs boson is the gluon fusion process, mostly mediated by a top quark loop. The predicted cross-section for the Higgs boson mass of 125 GeV is about 50 pb. Thanks to recent N³LO quantum chromodynamic (QCD) computations [9], the accuracy on the predicted cross-section is about 5%. The second most important production mode, with a cross-section of 3.7 pb, is the VBF process, which has a distinct signature of two scattered quarks in addition to the produced Higgs boson. The associated production of a Higgs boson with a vector boson W or Z (VH production) has a predicted cross-section of about 2 pb. Finally, the $t\bar{t}H$ production, which is sensitive at the tree level to the coupling between top quarks and H , has a predicted cross-section of 0.5 pb. This production mode benefits from the centre of mass energy increase from 8 to 13 TeV with a factor four increase in the predicted cross-section.

The dominant decay mode of the Higgs boson, with a predicted branching ratio of 58%, is to $b\bar{b}$ pairs. The other decay modes are $\tau\tau$ (6.2%), $c\bar{c}$ (2.9%), $\mu\mu$ (0.02%), WW^* (21%), ZZ^* (2.6%), gg (8.2%), $\gamma\gamma$ (0.2%), and $Z\gamma$ (0.15%). Details about the predicted cross-section and branching ratio values can be found in Ref. [10] and the references therein.

2. Observation of the $t\bar{t}H$ production

This production mode leads to a final state with $bbWW$ from the top quark decays to which the Higgs boson decay products are added. Different analyses are performed to target the different Higgs boson decay modes:

- $H \rightarrow b\bar{b}$ decay with the final state containing four b quarks. The hadronic, semi-leptonic or fully leptonic decays of the top quarks are selected. The main background arises from the processes $t\bar{t}b\bar{b}$ and $t\bar{t}c\bar{c}$, which are difficult to model. This channel also suffers from combinatorial background. The events are classified according to the number of jets and the b -tagging properties of the jets. The multivariate discriminants based on kinematical variables are trained for each category to enhance the signal over background separation. The signal yield is extracted from a global fit with the $t\bar{t}b\bar{b}$ and $t\bar{t}c\bar{c}$ background normalisations free in the fit. An excess over the background-only hypothesis is observed with a significance of 1.4 (ATLAS [11]) and 1.6 (CMS [12, 13]) standard deviations with the 2015–2016 dataset, in agreement with the expected sensitivity for the SM $t\bar{t}H$ production.
- $H \rightarrow WW$ or $H \rightarrow \tau\tau$ with the multi-leptons final state. The final states with two leptons (e or μ) of same sign (one from the Higgs boson decay and one from one of the top quark decays), or with three or four leptons (including up to one hadronic τ decay) are considered. The opposite sign two lepton events are not considered to avoid the large background from the $t\bar{t}$ production. The main irreducible backgrounds are the associated production of a vector boson W or Z with a $t\bar{t}$ pair and the diboson production processes. This channel also suffers from significant reducible backgrounds with non-prompt leptons (mostly from b -hadron decays) or with mismeasured lepton charge. Multivariate discriminants are trained to separate the signal from different background sources. An example is shown in Fig. 1a for the same sign 2μ final state in CMS data. The main systematic uncertainties are related to the background modelling, the total systematic uncertainty is being comparable to the statistical uncertainty obtained with the 2015–2016 dataset. The expected significance over the background-only hypothesis is 2.8 standard deviations. The observed excesses correspond to significances of 4.1 (ATLAS [14]) and 3.8 (CMS [15]) standard deviations. The measured signal yields are consistent with the SM expectations within approximately one standard deviation.
- $H \rightarrow \gamma\gamma$. This decay mode provides a clean mass peak but suffers from a low event rate. The main irreducible background is the $t\bar{t}\gamma\gamma$ production with other backgrounds coming from $\gamma\gamma$ pairs not associated to $t\bar{t}$, from non-prompt photon production and also from other H production modes. The ATLAS analysis [16], performed with the 2015–2017 dataset, separates events in all hadronic and leptonic regions. In each region, a neural network discriminant is trained using a mixture of data and simulation to define categories with varying signal over background ratio. In the most sensitive categories, the signal over background is around unity for $\gamma\gamma$ masses close to the Higgs boson mass. The signal is extracted from signal plus background fits to the $\gamma\gamma$ mass distribution with the background constrained by the mass sidebands. The observed (expected) significance is 4.1 (3.7) standard deviations. Figure 1b shows the combined $\gamma\gamma$ mass distribution, where the mass peak is clearly visible above the background. A similar search is performed by the CMS Collaboration using the 2015–2016 dataset [17].
- $H \rightarrow 4l$. This final state is clean but suffers from a low expected signal rate. It is used in the final combination although its expected sensitivity is significantly smaller than that for the channels discussed above.

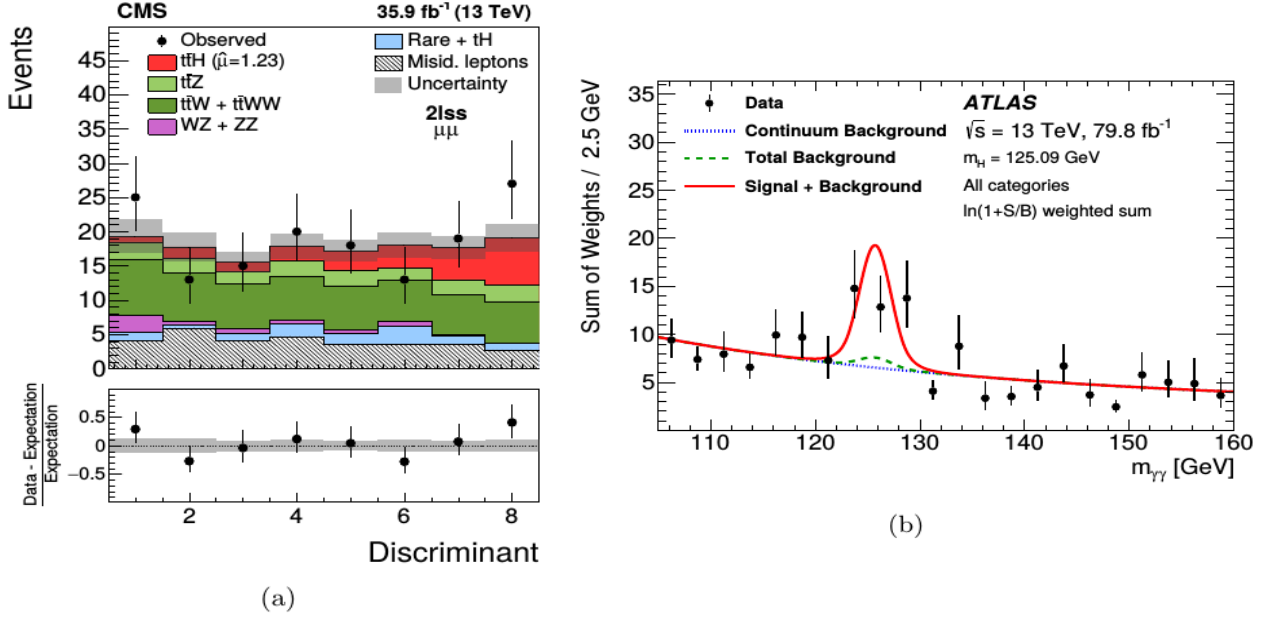


Fig. 1. Distributions of the multivariate discriminant in the two same-sign μ channel for the $t\bar{t}H$ CMS analysis [15] (a) and of the $\gamma\gamma$ invariant mass distribution in the $t\bar{t}H, H \rightarrow \gamma\gamma$ ATLAS analysis [16] (b)

Combining the different decay modes above, and also with the Run-1 data, the observed significance for the $t\bar{t}H$ observation is 6.3 (5.2) standard deviations for the ATLAS [16] (CMS [18]) analysis, in agreement with the expected significances (5.1 and 4.2 respectively). The ATLAS analysis sensitivity is higher because 2017 data are used for the $\gamma\gamma$ and $4l$ decay channels. The observed yield is 1.32 ± 0.27 ($1.26^{+0.31}_{-0.26}$) times the SM predictions from the ATLAS (CMS) analysis.

3. Observation of the decay $H \rightarrow b\bar{b}$

Despite that $H \rightarrow b\bar{b}$ is the dominant Higgs boson decay mode, its observation is difficult at the LHC, because of large background contamination. The most sensitive channel is based on the VH associated production, but $t\bar{t}H$, VBF [19], and gluon fusion at high Higgs boson transverse momentum [20] productions are also investigated.

The search of $H \rightarrow b\bar{b}$ with the VH production mode separates events according to the number of leptons (electrons or muons). Events with 0 leptons (but with missing transverse momentum) and two leptons target the ZH production, while events with one charged lepton target WH production. Two b -tagged jets are required. The main backgrounds arise from $V + \text{jets}$ (mostly $Vb\bar{b}$) and $t\bar{t}$ productions. In addition to b -tagging abilities, the main handles to separate signal and background are the $b\bar{b}$ invariant mass and kinematical variables like the transverse momentum of the V boson. Dedicated corrections are applied to the b -jet energy to optimise the invariant mass resolution. A multivariate discriminant is trained to separate signal from background in the different analysis categories. Control regions are also defined to constrain the normalisation of the $V + \text{jets}$ and $t\bar{t}$ backgrounds. The small background from multijet events is derived directly from data.

The main uncertainties are statistical uncertainties (data and Monte Carlo sample size), background modelling uncertainties, and uncertainties in b -tagging performance and in the jet energy scale. An important validation step is the search for the VZ production followed by $Z \rightarrow b\bar{b}$ decay, which looks like the signal except for the lower $b\bar{b}$ invariant mass. This process is observed at a rate consistent with SM expectations with a 20% accuracy. The expected sensitivity with the combined Run-1 and 2015–2017 dataset to the $VH, H \rightarrow b\bar{b}$ production is 5.1 (4.8) standard deviations for the ATLAS [21] (CMS [22]) analysis. The observed significance is 4.9 (4.8) for ATLAS (CMS).

Figure 2a shows the distribution of all events entering in the CMS analysis ordered by their signal over background ratio. An excess of events at large values of signal over background is clearly seen over the

background-only hypothesis, consistent with the expected signal from $VH, H \rightarrow b\bar{b}$. As a cross-check, a cut-based analysis is also performed. The $b\bar{b}$ invariant mass can then be investigated as the final discriminating variable. The result of this analysis is shown in Fig. 2b for the ATLAS analysis after all backgrounds but VZ production are subtracted. The VZ contribution, peaking at a mass near 90 GeV, is clearly visible. The VH production gives a significant excess of events at larger values of the $b\bar{b}$ invariant mass.

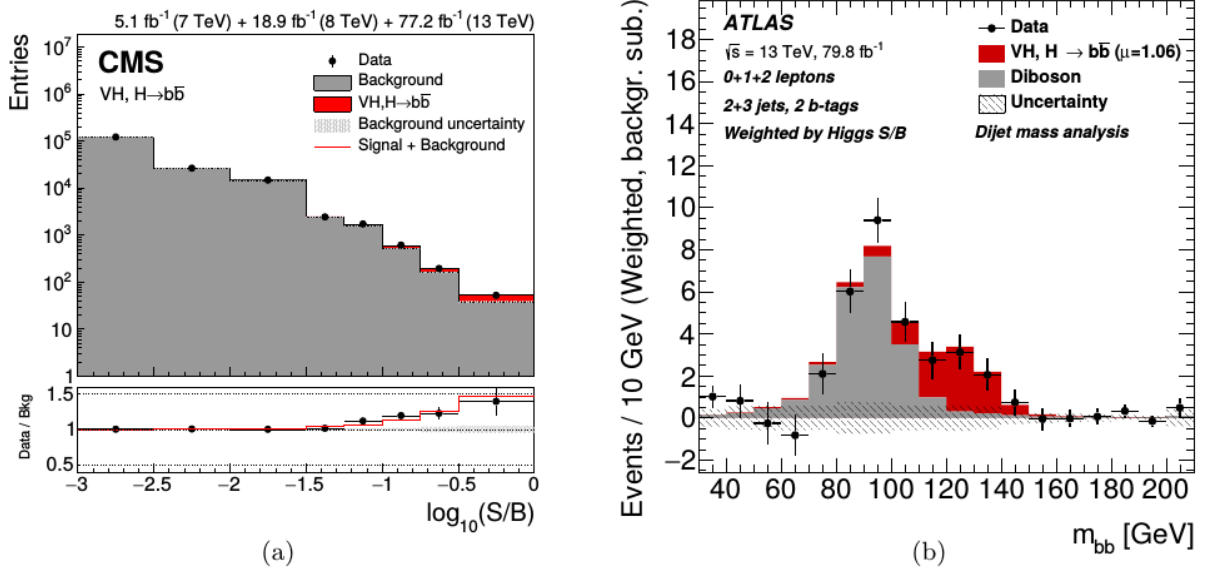


Fig. 2. Distributions of the signal over background ratio of the events selected in the CMS $VH, H \rightarrow b\bar{b}$ analysis [22] (a) and of the $b\bar{b}$ invariant mass for the cut-based ATLAS $VH, H \rightarrow b\bar{b}$ analysis [21] (b)

After combining the VH search with the searches in the other production modes, the $b\bar{b}$ decay mode is observed at a significance of 5.4 (5.6) standard deviations by the ATLAS (CMS) Collaboration. The yield of events compared to the SM predictions (assuming that the ratio of the different production modes is that predicted by the SM) is 1.01 ± 0.20 (1.04 ± 0.20) for the ATLAS (CMS) analysis, in excellent agreement with the expectations. The $VH, H \rightarrow b\bar{b}$ search, after combination with the other searches for the VH production in different decay modes, also provides an observation of the VH production.

4. Decays to leptons

4.1. Observation of the decay $H \rightarrow \tau\tau$

$H \rightarrow \tau\tau$ decays can be searched for using either leptonic or hadronic decay modes of the τ lepton. The invariant mass can be estimated using the missing transverse momentum measurement. The main background arises from the $Z/\gamma^* \rightarrow \tau\tau$ process, estimated from the simulation normalised in the dedicated control region. The simulation is also extensively validated using for instance a large sample of $Z/\gamma^* \rightarrow \mu\mu$ decays. Backgrounds from fake hadronic τ candidates are derived from data. Categories are defined according to the Higgs boson production, the most sensitive ones are the category targeting VBF production and the category targeting boosted H production *via* gluon fusion. The signal yield per production mode is extracted from fits of the $\tau\tau$ invariant mass distribution.

With the 2015–2016 dataset, the ATLAS [23] and CMS [24] experiments observed this decay mode at more than five standard deviations significance each. The total cross section (assuming the SM fractions for each production mode) in the $H \rightarrow \tau\tau$ decay channel is measured with an accuracy around 25% in each experiment and found to be consistent with the SM prediction. The ATLAS measurement for the cross-section times branching ratio to the $\tau\tau$ pair is 3.71 ± 0.59 (stat) $^{+0.87}_{-0.74}$ (syst) pb. CMS reports a measurement of the cross-section times branching ratio of $1.09^{+0.27}_{-0.26}$ times the SM expectation. Separate cross-section measurements for the gluon fusion and VBF production processes are also reported.

4.2. Search for the decay $H \rightarrow \mu\mu$

This channel allows one to probe the coupling to second generation fermions. The predicted branching ratio is about 0.02%. This channel has a low signal over background ratio with the background being largely dominated by the Drell–Yan process. Categories are defined targeting gluon fusion and VBF productions and also according to the expected di-muon mass resolution. The best category in CMS has a di-muon mass resolution of about 1.2 GeV. The expected sensitivity to the SM predicted rate is about one standard deviation. The observed limit at 95% confidence level is 2.9 times the SM expectation in the CMS analysis [25] based on 2015–2016 data combined with Run-1, and 2.1 times the SM expectation in the ATLAS analysis [26] using the 2015–2017 dataset.

5. Decays of Higgs bosons to bosons

5.1. $H \rightarrow WW^*$

This decay mode is searched for in the dilepton final state, the $e\mu$ channel being the most sensitive one. The Higgs boson mass cannot be reconstructed because of the two undetected neutrinos. The signal rate is large but the signal over background ratio is smaller than unity, even after dedicated kinematical selections. The main backgrounds from WW , $t\bar{t}$, and $W\gamma$ productions are normalised in dedicated control regions. Events are divided into categories sensitive to different production modes. The signal yields relative to the SM expectations are measured separately for gluon fusion and VBF production. The ATLAS results [27] are 12.6 ± 1.0 (stat) $_{-1.8}^{+1.9}$ (syst) pb and $0.5_{-0.23}^{+0.24}$ (stat) ± 0.18 (syst) pb for the cross-section times branching ratio for the gluon fusion and VBF productions, in agreement with SM expectations. The CMS results [28] on the ratio between the measured cross-sections and the SM predictions are $1.24_{-0.26}^{+0.20}$ for gluon fusion and $0.24_{-0.24}^{+0.74}$ for VBF production.

5.2. $H \rightarrow ZZ^*$

The experimental signature with four leptons (e or μ) in the final state is clean. The combined branching ratio is however small, and great care is made to optimise the reconstruction and identification of low transverse momentum leptons, especially electrons. The background arises mostly from the irreducible ZZ^* production estimated from the simulation with smaller reducible backgrounds from $t\bar{t}$ and $Z + \text{jets}$ processes with non-prompt leptons. Figure 3a shows the four-lepton mass distribution observed by ATLAS [29] with the 2015–2017 dataset. The data are divided in several categories (seven in this analysis) to optimise the sensitivity to the different production modes. The ATLAS analysis obtains a measurement of the ratio between the observed and predicted yields of $1.19_{-0.15}^{+0.16}$, where the main contribution to the uncertainty is the data statistical uncertainty. The CMS analysis [30] reported a signal yield relative to the SM prediction of $1.10_{-0.17}^{+0.19}$ with the 2017 dataset.

5.3. $H \rightarrow \gamma\gamma$

This channel offers a clear signature with a narrow mass peak over a smooth background. There is a large background mostly from continuum diphoton production, with the inclusive signal over background ratio being around a few percent. For this search, the invariant mass resolution is optimised and studied starting from samples of $Z \rightarrow ee$ events. Events are categorised according to the signal over background ratio and to the invariant mass resolution as well as according to the production modes to enhance the sensitivity. The overall signal yield compared to the SM prediction is measured to be $1.06_{-0.12}^{+0.14}$ by the ATLAS analysis [31] with the 2015–2017 dataset, while the CMS analysis [17] obtained a value of $1.18_{-0.14}^{+0.17}$ with the 2015–2016 dataset.

5.4. Higgs boson mass measurement

The Higgs boson mass can be measured using the high resolution ZZ^* and $\gamma\gamma$ final state. Combining the measurements in these two channels from 2015–2016 data and from Run-1, the ATLAS Collaboration reported a value of the Higgs boson mass of 124.97 ± 0.24 GeV [32] (with ± 0.19 GeV of statistical uncertainty and ± 0.13 GeV of systematic uncertainty, mainly from uncertainties in the photon energy scale). With the ZZ channel from 2015–2016 data, the CMS Collaboration reported a mass value of 125.26 ± 0.21 GeV [33]. At the same time, a direct upper limit on the decay width is set at 95% confidence level as 1.1 GeV. This is still far above the predicted width in the SM which is about 4 MeV (about 2.5 MeV with higher orders corrections up to N3LO [34]). A more model-dependent constraint on the Higgs boson width can be derived comparing the rate of $gg \rightarrow H^* \rightarrow ZZ^*$ events in the on-shell and off-shell Higgs mass regions. The ATLAS analysis with 2015–2016 data sets a model-dependent limit at 14.4 MeV on the decay width, at 95% confidence level [35].

5.5. Total and differential cross-section measurements of Higgs boson production with ZZ^* and $\gamma\gamma$ final states

The total cross-section can be measured with a small model dependence using the ZZ^* and $\gamma\gamma$ final states. With the 2015–2016 dataset, the ATLAS Collaboration reports a measurement of $57.0^{+6.0}_{-5.9}$ (stat) $^{+4.0}_{-3.8}$ (syst) pb [36], while the CMS analysis finds 61.1 ± 6.0 (stat) ± 3.7 (syst) pb [37]. These measurements are in good agreement with the SM expectation of 55.6 ± 2.5 pb.

Differential cross-sections as a function of several variables can also be measured in these channels. Figure 3b illustrates the measurement performed by CMS of the cross-section as a function of the transverse momentum of the Higgs boson [37]. The accuracies of the $\gamma\gamma$ and ZZ channels are comparable. At high transverse momentum, the $b\bar{b}$ analysis [20] is also used. The measured differential cross-section agrees with the state-of-the-art theoretical predictions over the full transverse momentum range. Similar results are also reported by the ATLAS Collaboration [29, 31].

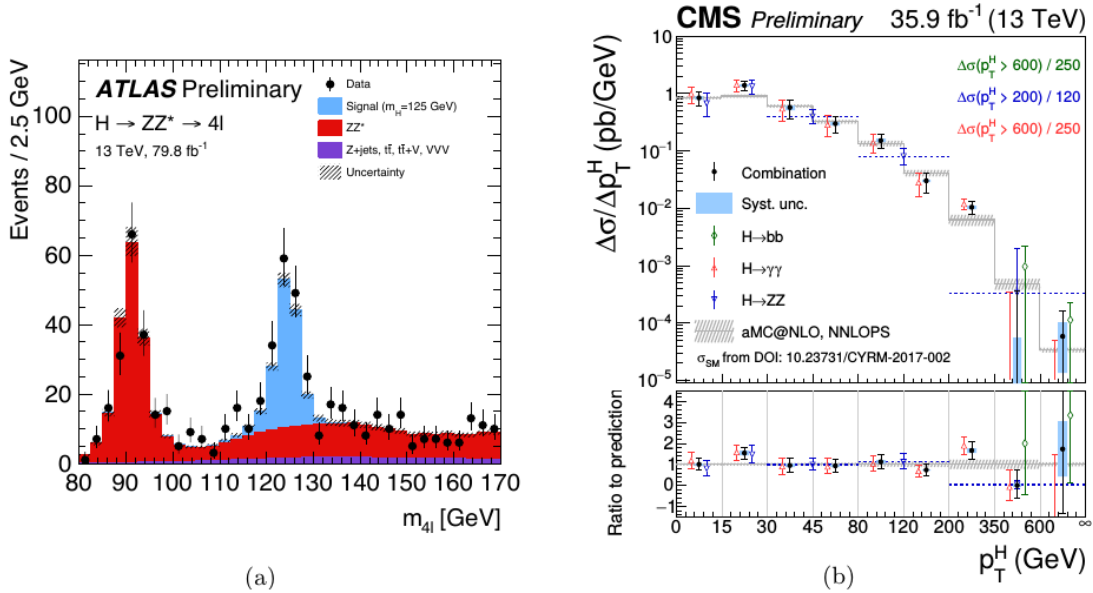


Fig. 3. Distributions of the four lepton invariant mass in the $H \rightarrow ZZ^*$ channel from the ATLAS experiment [29] (a) and measurement of the differential cross-section as a function of the Higgs boson transverse momentum with the CMS experiment [37] (b)

6. Constraints on the Higgs boson couplings

Studies of the Higgs boson couplings to probe physics beyond the SM can be achieved combining information from all the investigated production and decay modes. One framework used to report the Higgs coupling properties is the κ framework, in which the same coupling structure as in the SM is assumed and the couplings are just scaled by coupling modifiers κ_i . For channels involving loops, like the couplings between H and photons or gluons, the coupling strength can be either parameterised by an effective coupling scale factor or computed resolving the loop content with its SM particle content. In the latter case, the Higgs boson coupling to gluons is for instance mostly driven by the κ_t factor with a small contribution from κ_b and their interference. A detailed discussion of this framework and how the rates in each production mode and decay channel are modified can be found in Ref. [38]. Since the total width of the Higgs boson is not directly accessible at the LHC, some assumptions are needed to avoid the degeneracy between the κ scaling and the total width.

The combinations reported here are based on 2015–2016 data for most decay modes with the 2015–2017 dataset used for the ATLAS $H \rightarrow \gamma\gamma$ and $H \rightarrow ZZ^*$ channels, including the $t\bar{t}H$ production mode categories of these analyses. The CMS results are described in Ref. [39] and the ATLAS results in Ref. [40].

Figure 4a shows the constraints on the gluon and photon effective couplings from the CMS analyses assuming all the other couplings are like those predicted by the SM, thus probing new physics contributions to the loop mediated couplings of the Higgs boson to gluons and photons. The values are found consistent with the SM expectation of unity. Figure 4b shows the constraints on the effective couplings to fermions and bosons from the ATLAS analyses. All H bosons couplings to fermions are assumed to scale by the same factor κ_F and similarly for the couplings to bosons with the scale factor κ_V . Loops are resolved assuming the SM content and no other new physics contribution. The total Higgs boson width is also computed assuming rescaled SM contributions and no invisible or undetected decay modes. The data are consistent with the SM predictions. This figure also shows the constraints from each individual decay mode and how the combination allows one to obtain more stringent constraints.

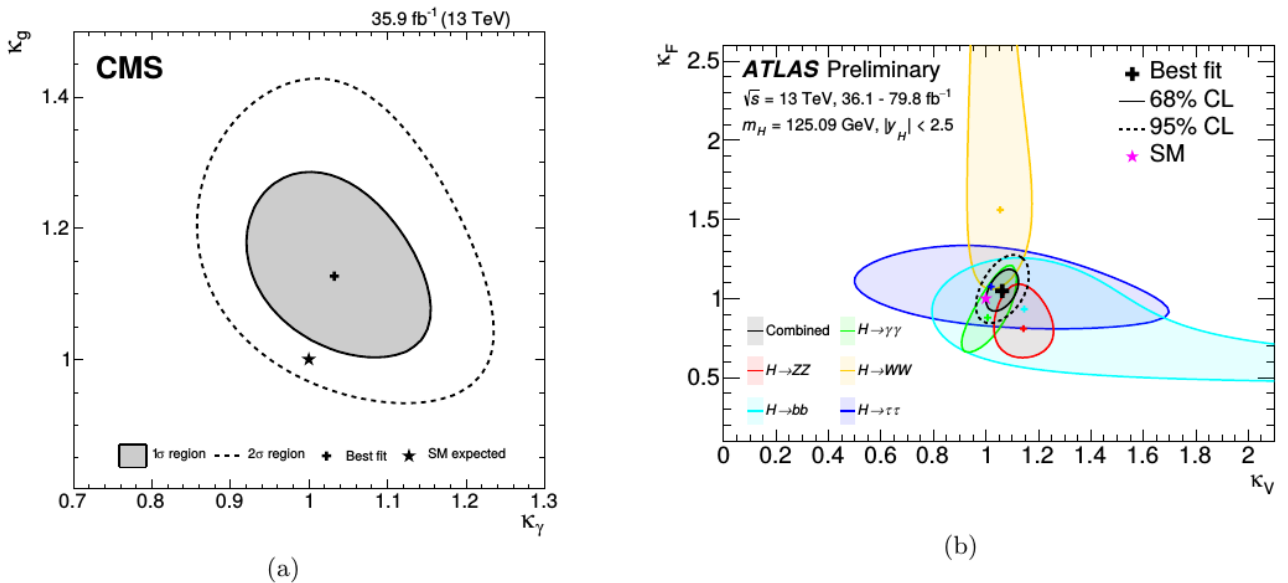


Fig. 4. Measurements of the effective couplings to photons and gluons in the CMS combined analysis [38] (a) and of the effective couplings to fermions and bosons in the ATLAS combined analysis [39] (b)

Figure 5a shows the measurements of all κ parameters achieved in the ATLAS analysis. Two different assumptions are shown. In the first one, it is that there is no invisible or undetected H decay mode. In the second one, a beyond SM contribution to the H decay width is allowed, but the parameter κ_Z and κ_W are restricted to be less than unity to break the degeneracy between coupling strengths and total width. This assumption is natural in several extensions of the SM, like for instance two Higgs doublets models where

the couplings to W and Z bosons are shared between the two neutral scalar bosons. The measurement of the $b\bar{b}$ decay mode has an important impact on all results since this decay mode drives the total Higgs boson width in the SM. In this case where effective couplings are used for photon and gluon couplings, the measurement of the $t\bar{t}H$ production mode is the only input that allows to constrain κ_t . The measured values are in good agreement with the SM predictions. The accuracy on the κ parameters varies between 10 and 20% and is already better than the combined Run-1 results from ATLAS and CMS. Analogously, Fig. 5b shows with similar assumptions how the rescaled couplings vary with the mass of the particle. The observed scaling agrees well with the SM predictions.

The ATLAS and CMS Collaborations also report results [29, 31, 39, 41] using a simplified template cross-section framework [10].

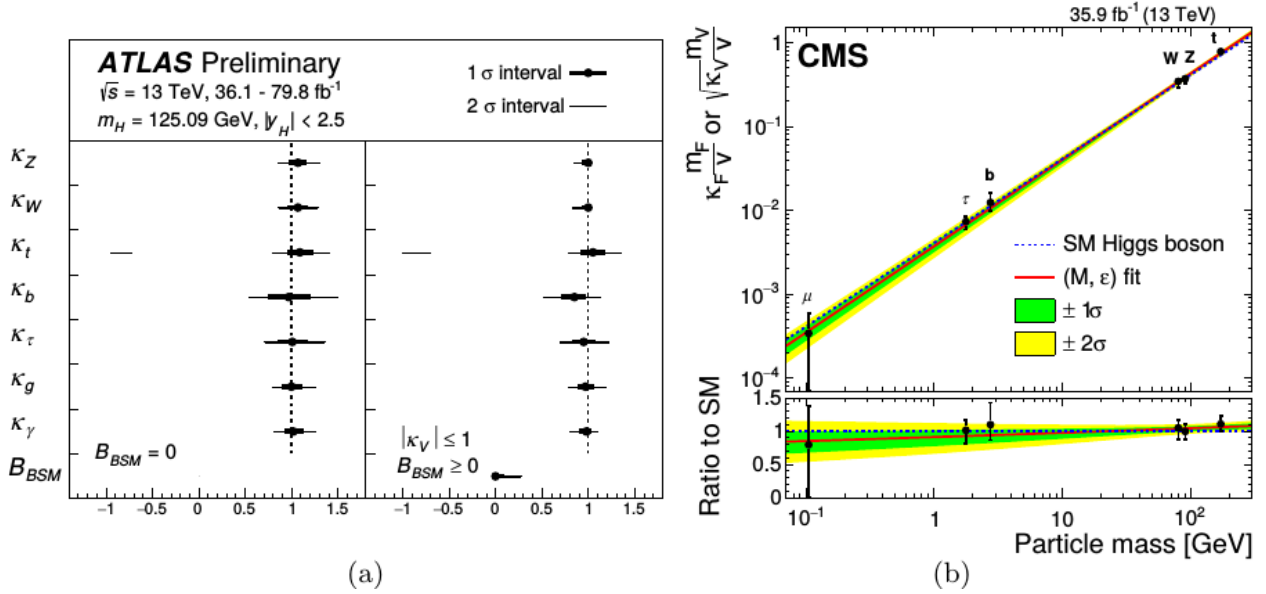


Fig. 5. Measurements of all κ coupling modifier parameters simultaneously for two different assumptions in the ATLAS combined analysis [39] (a) and of the scaling of the Higgs boson couplings as a function of the particle mass in the CMS analysis [38] (b)

7. Conclusion

Higgs boson studies based on the 35 to 80 fb^{-1} of proton–proton collision data recorded in Run-2 at the LHC by the ATLAS and CMS experiments have been reviewed. With this dataset, important milestones for the Higgs boson physics have been reached with observation of the $t\bar{t}H$ production and the $H \rightarrow b\bar{b}$ decay. The four main production processes and five main decay modes of the Higgs boson are now established. In addition, measurements involving bosons in the final state reached higher precision allowing quasi-model independent determination of the Higgs boson production differential cross-sections. Studies of the Higgs boson couplings using the combination of all investigated production and decay modes are reported with the accuracy on the coupling modifier parameters reaching 10 to 20%. The results are consistent within the current uncertainties with the SM expectations.

The PNPI teams made substantial contributions to the construction and maintenance of the CMS endcap muon system (the EMU system) and the ATLAS inner tracker (the TRT system), as well as to physics data analyses, which in their turns played an important role in the discovery of the Higgs boson and determination of its properties.

References

1. ATLAS Collaboration, JINST **3**, S08003 (2008).
2. CMS Collaboration, JINST **3**, S08004 (2008).
3. ATLAS Collaboration, Phys. Lett. B **716**, 1 (2012).
4. CMS Collaboration, Phys. Lett. B **716**, 30 (2012).
5. ATLAS and CMS Collaborations, Phys. Rev. Lett. **114**, 191803 (2015).
6. ATLAS Collaboration, Eur. Phys. J. C **75**, 476 (2015).
7. CMS Collaboration, Phys. Rev. D **92**, 012004 (2015).
8. ATLAS and CMS Collaborations, JHEP **1608**, 045 (2016).
9. C. Anastasiou *et al.*, Phys. Rev. Lett. **114**, 21200110 (2015).
10. LHC Higgs Cross Section Working Group, arXiv:1610.07922 [hep-ph].
11. ATLAS Collaboration, Phys. Rev. D **97**, 072016 (2018).
12. CMS Collaboration, CMS-HIG-17-026, CERN-EP-2018-065, arXiv:1804.03682 [hep-ex].
13. CMS Collaboration, JHEP **1806**, 101 (2018).
14. ATLAS Collaboration, Phys. Rev. D **97**, 072003 (2018).
15. CMS Collaboration, JHEP **1808**, 066 (2018).
16. ATLAS Collaboration, Phys. Lett. B **784**, 173 (2018).
17. CMS Collaboration, arXiv:1804.02716 [hep-ex].
18. CMS Collaboration, Phys. Rev. Lett. **120**, 231801 (2018).
19. ATLAS Collaboration, Phys. Rev. D **98**, 052003 (2018).
20. CMS Collaboration, Phys. Rev. Lett. **120**, 071802 (2018).
21. ATLAS Collaboration, Phys. Lett. B **786**, 59 (2018).
22. CMS Collaboration, Phys. Rev. Lett. **121**, 121801 (2018).
23. ATLAS Collaboration, ATLAS-CONF-2018-021, <https://cds.cern.ch/record/2621794>.
24. CMS Collaboration, Phys. Lett. B **779**, 283 (2018).
25. CMS Collaboration, arXiv:1807.06325 [hep-ex].
26. ATLAS Collaboration, ATLAS-CONF-2018-026, <https://cds.cern.ch/record/2628763>.
27. ATLAS Collaboration, arXiv:1808.09054 [hep-ex].
28. CMS Collaboration, arXiv:1806.05246 [hep-ex].
29. ATLAS Collaboration, ATLAS-CONF-2018-018, <https://cds.cern.ch/record/2621479>.
30. CMS Collaboration, CMS-PAS-HIG-18-001, <https://cds.cern.ch/record/2621419>.
31. ATLAS Collaboration, ATLAS-CONF-2018-028, <https://cds.cern.ch/record/2628771>.
32. ATLAS Collaboration, Phys. Lett. B **784**, 345 (2018).
33. CMS Collaboration, JHEP **1711**, 047 (2017).
34. V.T. Kim, Nucl. Phys. B Proc. Suppl. **198**, 223 (2010).
35. ATLAS Collaboration, arXiv:1808.01191 [hep-ex].
36. ATLAS Collaboration, Phys. Lett. B **786**, 114 (2018).
37. CMS Collaboration, CMS-PAS-HIG-17-028, <https://cds.cern.ch/record/2628757>.
38. LHC Higgs Cross Section Working Group, arXiv:1307.1347 [hep-ph].
39. CMS Collaboration, arXiv:1809.10733 [hep-ex].
40. ATLAS Collaboration, ATLAS-CONF-2018-031, <https://cds.cern.ch/record/2629412>.
41. ATLAS Collaboration, ATLAS-CONF-2017-047, <https://cds.cern.ch/record/2273854>.

DIJETS WITH LARGE RAPIDITY SEPARATION AT CMS

PNPI participants of the CMS Collaboration:

A.A. Vorobyev, Yu.M. Ivanov, V.T. Kim, A.Yu. Egorov, V.L. Golovtsov, E.V. Kuznetsova, P.M. Levchenko, V.A. Murzin, V.A. Oreshkin, I.B. Smirnov, D.E. Sosnov, V.V. Sulimov, L.N. Uvarov, S.A. Vavilov

1. Introduction

This paper presents a search for asymptotic Balitsky–Fadin–Kuraev–Lipatov (BFKL) effects at CMS in dijet events with large rapidity separation between jets in proton–proton collisions at 7 TeV. CMS data on cross-section ratios and azimuthal decorrelations for dijets with large rapidity separation between jets are compared with predictions of various Monte Carlo (MC) event generators based on the Dokshitzer–Gribov–Lipatov–Altarelli–Parisi (DGLAP) and BFKL evolutions. Note that quantum chromodynamics (QCD) is well tested in hard processes ($\sqrt{s} \gg p_T \gg \Lambda_{\text{QCD}}$) and the data are successfully described by perturbative QCD (pQCD) calculations within the framework of collinear factorization and the DGLAP evolution equations [1–5]. Parton–parton scattering at leading order in the strong coupling α_s produces two outgoing partons which are back-to-back in the azimuthal plane. The partons manifest themselves as a collimated stream of hadrons, which are observable jets. A deviation from the back-to-back configuration occurs if higher order parton contributions are considered, which can be described by the parton showers initiated by the initial and final partons in the scattering process. At high centre-of-mass energies a kinematical domain can be reached where semi-hard parton interactions ($\sqrt{s} \gg p_T \gg \Lambda_{\text{QCD}}$) play a substantial role. The asymptotic region, where $\sqrt{s} \rightarrow \infty$, is described by the BFKL equation [6–8].

2. Ratios of dijet production cross sections as a function of the rapidity separation between jets in proton–proton collisions at $\sqrt{s} = 7$ TeV

In the paper of A.H. Mueller and H. Navelet [9], the ratio of the cross-section for dijet production with the maximal rapidity separation (Mueller–Navelet (MN) pair) to the Born dijet production cross-section (MN K -factor) was calculated as a function of the rapidity separation $\Delta y = |y_1 - y_2|$. An exponential growth of the cross-section ratio with Δy was predicted in terms of the leading logarithm (LL) BFKL approach.

However, the Born dijet production cross-section is unmeasurable because one cannot kinematically exclude virtual corrections. The way to solve this problem was found by V. Kim and G. Pivovarov [10]: the Born cross-section should be replaced with the “exclusive” cross-section (exactly two jets with transverse momenta above a minimum value of $p_{T\text{min}}$ should be considered). The inclusive (two and more jets with $p_T > p_{T\text{min}}$ dijet production cross-section and the corresponding “ K -factor” were also calculated.

Measurements of dijet production in proton–proton collisions at $\sqrt{s} = 7$ TeV for jets with $p_T > 35$ GeV/ c and $|y| < 4.7$ using data collected with the CMS detector at the Large Hadron Collider in 2010 are presented in Ref. [11]. Here the inclusive dijet production cross-section is taken from events with at least two jets with $p_T > 35$ GeV/ c and $|y| < 4.7$, “exclusive” dijets are the subset of “inclusive” when there are exactly two jets in an event, and the MN cross-section is for jets with the maximal rapidity separation. The measured ratios R_{incl} and R_{MN} are inclusive and MN “ K -factors”, respectively.

The measured values of R_{incl} (Fig. 1, *left*) and R_{MN} (Fig. 1, *right*) are compared with predictions of various MC event generators: the LL DGLAP parton shower with various effects (colour coherence, dipole approximation) with LL BFKL elements (PYTHIA 6 tune Z2 [12–14], PYTHIA 8 tune 4C [15, 16] and HERWIG++ tune UE-7000-EE-3 [17, 18]) and the LL BFKL-motivated generators CASCADE [19] and HEJ+ARIADNE [20–22].

PYTHIA 6 and PYTHIA 8 predictions are in agreement with the data. HERWIG++ predictions lie higher than the data, especially for large Δy region. The LL BFKL-motivated MC generators predict a stronger rise of the ratios than in the data. A moderate rise of the ratios signs that BFKL effects for jets with $p_T > 35$ GeV/ c and $|y| < 4.7$ may be present in pp collisions at 7 TeV.

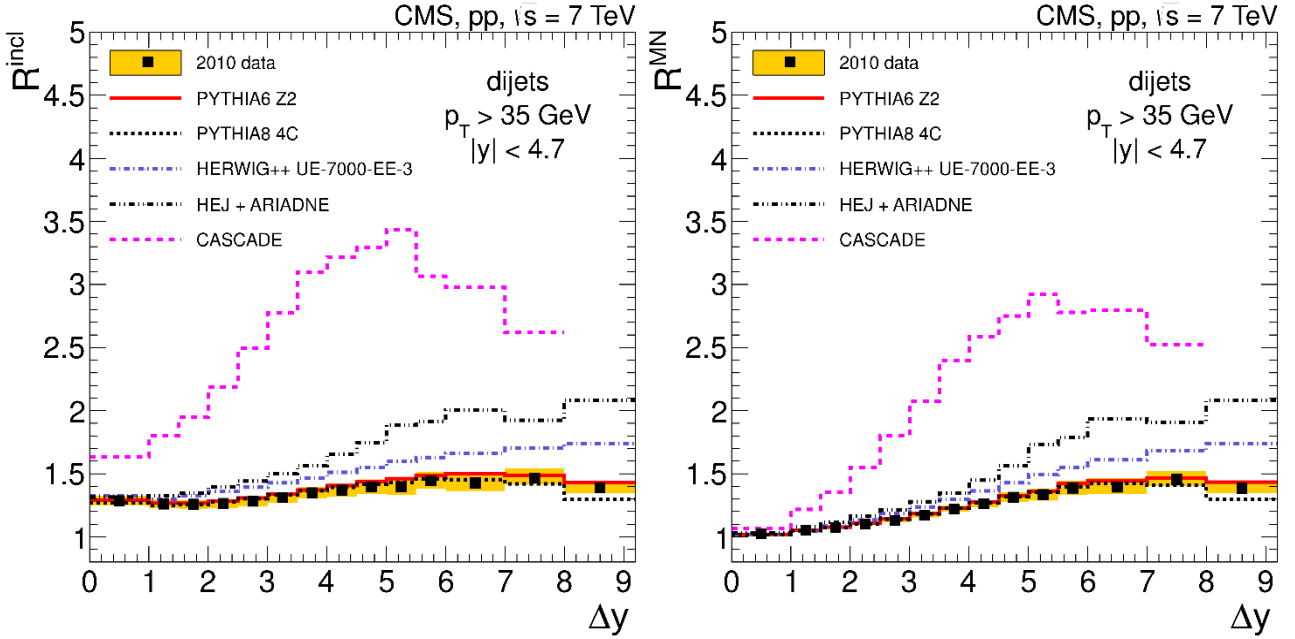


Fig. 1. Inclusive R_{incl} (left) and Mueller–Navelet R_{MN} (right) “ K -factors” as a function of the rapidity separation Δy between two jets in comparison with predictions of the PYTHIA 6, PYTHIA 8, HERWIG++, CASCADE, and HEJ+ARIADNE generators. The shaded band indicates the total systematic uncertainty in the data

3. Azimuthal decorrelation of jets widely separated in the rapidity in pp collisions at $\sqrt{s} = 7$ TeV

According to V. Del Duca, C. Schmidt, and W. Stirling [23, 24], the normalized cross-section for MN jets with $p_T > p_{T\text{min}}$ can be written as a Fourier series:

$$\frac{1}{\sigma} \frac{d\sigma}{d(\Delta\varphi)}(\Delta y, p_{T\text{min}}) = \frac{1}{2\pi} \left[1 + 2 \sum_{n=1}^{\infty} C_n(\Delta y, p_{T\text{min}}) \cos(n(\pi - \Delta\varphi)) \right],$$

where C_n , the Fourier coefficients, are the average cosines of the decorrelation angle, $(\pi - \Delta\varphi)$, and $C_n = \langle \cos n(\pi - \Delta\varphi) \rangle$, where $\Delta\varphi = \varphi_1 - \varphi_2$ is the difference between the azimuthal angles φ_1 and φ_2 of MN jets.

The average cosines C_1 , C_2 , and C_3 (Fig. 2) were measured in Ref. [25] for jets with $p_T > 35$ GeV/ c and $|y| < 4.7$ for pp collisions at $\sqrt{s} = 7$ TeV. The data and event selection are the same as in Ref. [11]. Also, in this paper the average cosine ratios C_2/C_1 and C_3/C_2 (Fig. 3) were measured as proposed in work [26]. The measured observables were compared with predictions of the LL DGLAP MC generators (PYTHIA 6 tune Z2 [12–14], PYTHIA 8 tune 4C [15, 16], and HERWIG++ tune UE-7000-EE-3 [17, 18]), the tree approximation MC generator SHERPA [27], the next-to-leading order (NLO) matrix element MC generator POWHEG [28–30] interfaced with the LL DGLAP-based PYTHIA 6 and PYTHIA 8 generators, the LL BFKL-motivated HEJ+ARIADNE generator [20–22], and next-to-leading logarithm (NLL) BFKL parton level analytical calculations [31].

The predictions of the LL DGLAP MC generator HERWIG++ show reasonable agreement with the data for average cosines, while for their ratios it cannot describe the data for $\Delta y \geq 5$. On the contrary, the LL DGLAP MC generators PYTHIA 6 and PYTHIA 8 have a reasonable description for the average cosine ratios from $\Delta y \geq 5$, while it cannot describe the average cosines. The results of the NLO matrix element MC generator POWHEG interfaced with the LL DGLAP-based parton shower of PYTHIA 6 and PYTHIA 8 show no better description of the measured observables than standalone results of PYTHIA 6 and PYTHIA 8. The tree multiparton approximation MC generator SHERPA also provides the same level of MC data description as PYTHIA 8. The LL BFKL-motivated MC generator HEJ+ARIADNE provides a stronger decorrelation than it is observed in the data. An analytical NLL BFKL calculation provides reasonable agreement with the data for $\Delta y \geq 4$.

All these facts (sensitivity to implementation of colour-coherence effects in different MC generators and reasonable data description by analytical NLL BFKL calculations) indicate that the given kinematic region (jets with $p_T > 35$ GeV/c and $\Delta y \geq 5$ at collision energy 7 TeV) may be beyond the domain described by the DGLAP approximation.

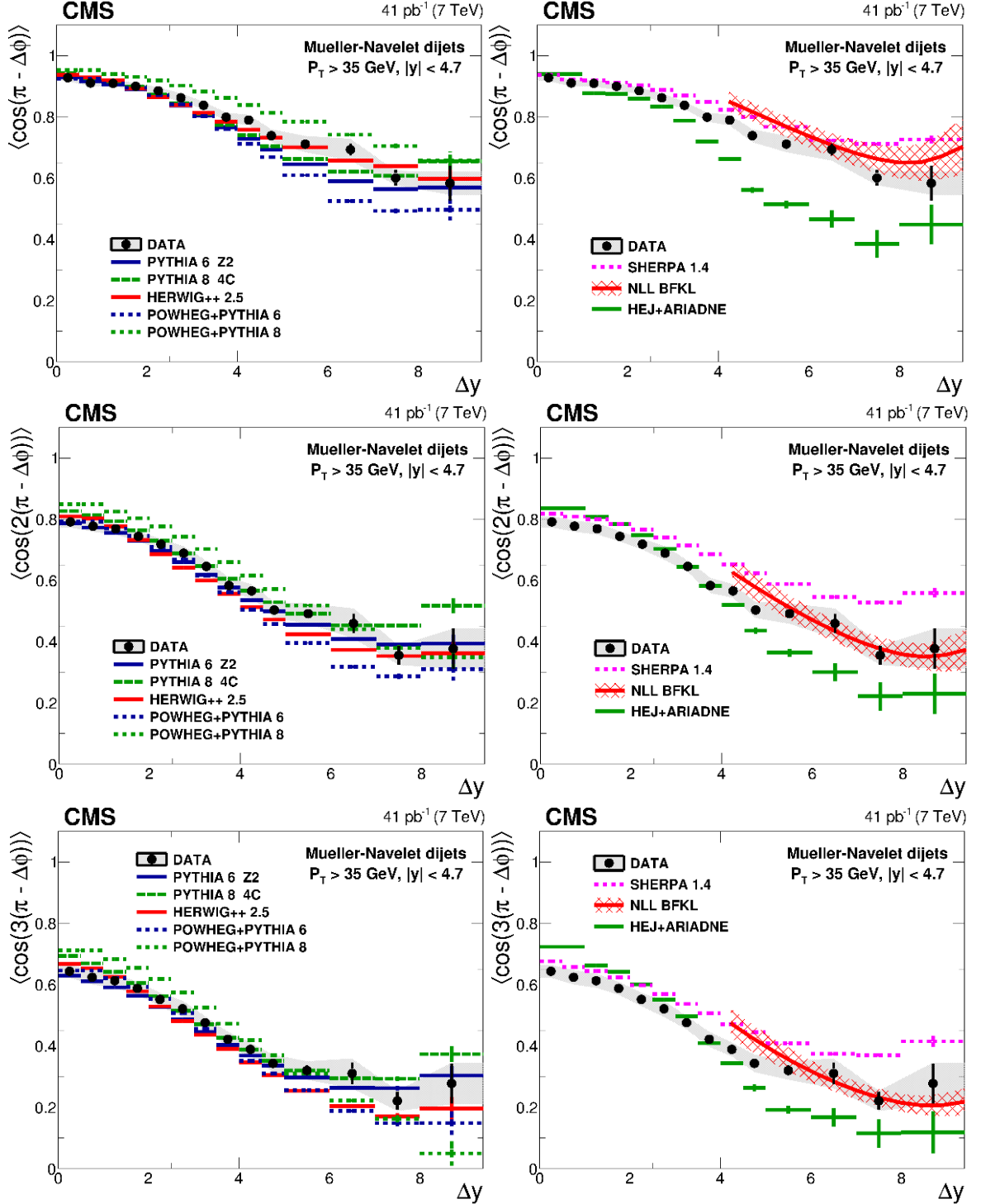


Fig. 2. Measured average cosines C_1 (top row), C_2 (middle row), and C_3 (bottom row) as a function of the rapidity separation Δy compared with the LL DGLAP MC generators and the NLO generator POWHEG (left column). Comparisons with the tree approximation MC generator SHERPA, the LL BFKL-motivated HEJ+ARIADNE generator, and analytical NLL BFKL parton level calculations ($4.0 < \Delta y < 9.4$) (right column). The shaded band indicates the total systematic uncertainty in the data

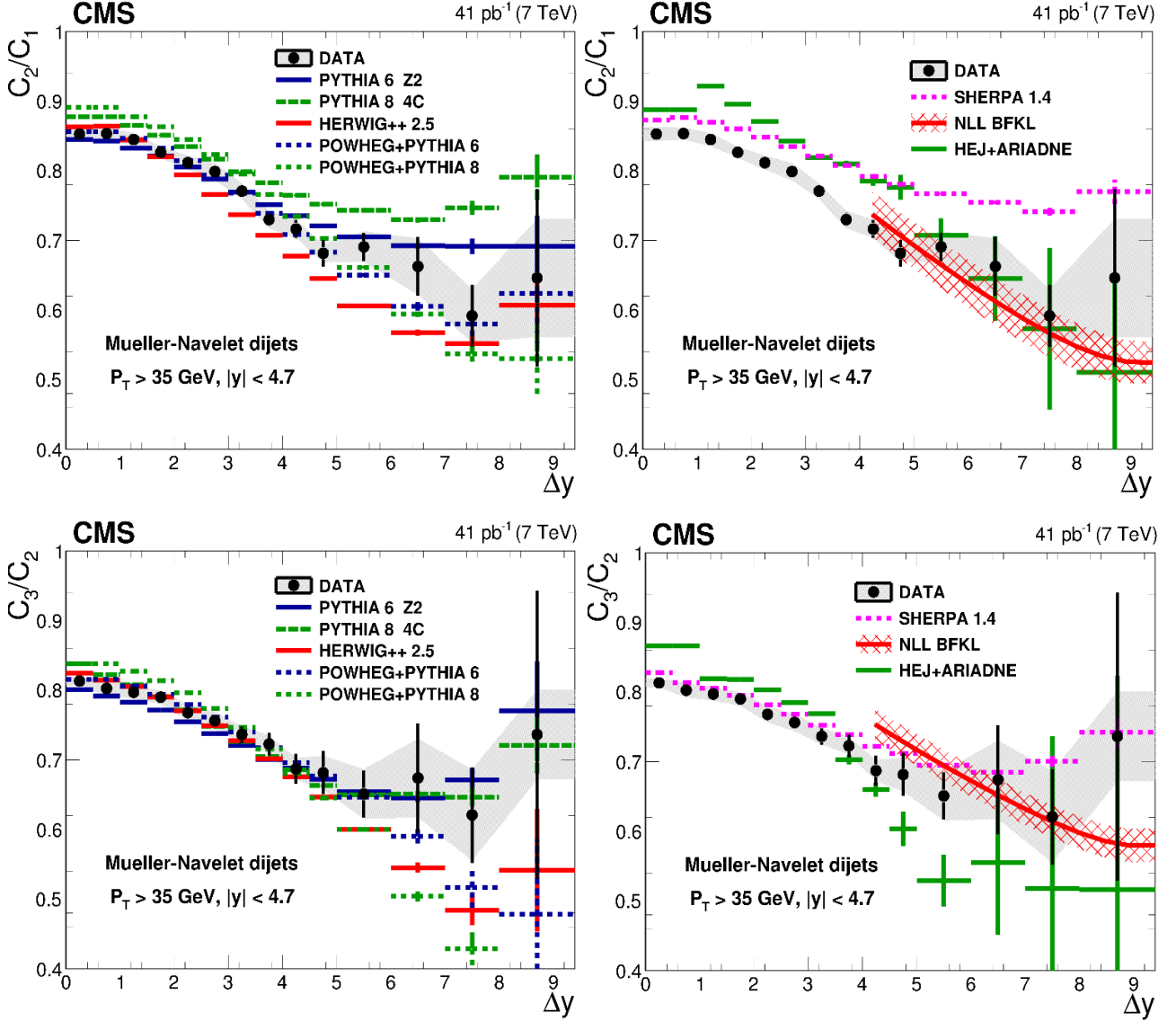


Fig. 3. Measured average cosine ratios C_2/C_1 (top) and C_3/C_2 (bottom) as a function of the rapidity separation Δy compared with the LL DGLAP MC generators and the NLO generator POWHEG (left column). Comparisons with the tree approximation MC generator SHERPA, the LL BFKL-motivated HEJ+ARIADNE generator, and analytical NLL BFKL parton level calculations (right column). The shaded band indicates the total systematic uncertainty in the data

4. Summary

A moderate rise is observed in the ratios of the dijet production cross sections (“K-factors”) as a function of rapidity separation between jets Δy . This observed behaviour is described by the LL DGLAP-based PYTHIA 6 and PYTHIA 8 MC generators. The other LL DGLAP-based HERWIG++ predictions for the dijet cross-section ratios lie significantly higher than the data. The LL BFKL-based MC predictions by the HEJ+ARIADNE generator have a stronger rise of the ratios than it is observed in the data.

As to dijet azimuthal decorrelations, there is a reasonable description of the average cosines by HERWIG++, while their ratios cannot be described with HERWIG++ for $\Delta y \geq 5$. On the contrary, PYTHIA 6 and PYTHIA 8 have a reasonable description for the average cosine ratios at $\Delta y \geq 5$, while it cannot describe the average cosines. The data description does not become better even if one can take the NLO matrix element MC generator POWHEG interfaced with the LL parton shower of PYTHIA 8. The tree multiparton approximation MC generator SHERPA also provides the same level of MC data description as PYTHIA 8.

The LL BFKL-based MC generator HEJ+ARIADNE predicts a stronger dijet azimuthal decorrelation than it is observed in the data, while an analytical NLL BFKL calculation shows reasonable agreement with the data.

Therefore, none of DGLAP-based generators can describe all of the CMS measured observables for dijets with large rapidity separation at 7 TeV. The fact that there is reasonable agreement only for particular observables for dijets with large rapidity separation for different LL DGLAP-based MC generators, may be explained by implemented into the generators various effects beyond the DGLAP evolution.

To conclude, the inability to describe the CMS measured observables for dijets with large rapidity separation between jets by DGLAP-based generators and at the same time good agreement of the NLL BFKL calculation with the dijet azimuthal decorrelations at 7 TeV mean that more pronounced signatures of BFKL effects can be expected at higher collision energies.

References

1. V.N. Gribov, L.N. Lipatov, Sov. J. Nucl. Phys. **15**, 438 (1972) [Yad. Fiz. **15**, 781 (1972)].
2. V.N. Gribov, L.N. Lipatov, Sov. J. Nucl. Phys. **15**, 675 (1972) [Yad. Fiz. **15**, 1218 (1972)].
3. L.N. Lipatov, Sov. J. Nucl. Phys. **20**, 94 (1975) [Yad. Fiz. **20**, 181 (1974)].
4. G. Altarelli, G. Parisi, Nucl. Phys. B **126**, 298 (1977).
5. Y.L. Dokshitzer, Sov. Phys. JETP **46**, 641 (1977) [Zh. Eksp. Teor. Fiz. **73**, 1216 (1977)].
6. E.A. Kuraev, L.N. Lipatov, V.S. Fadin, Sov. Phys. JETP **44**, 443 (1976) [Zh. Eksp. Teor. Fiz. **71**, 840 (1976)].
7. E.A. Kuraev, L.N. Lipatov, V.S. Fadin, Sov. Phys. JETP **45**, 199 (1977) [Zh. Eksp. Teor. Fiz. **72**, 377 (1977)].
8. I.I. Balitsky, L.N. Lipatov, Sov. J. Nucl. Phys. **28**, 822 (1978) [Yad. Fiz. **28**, 1597 (1978)].
9. A.H. Mueller, H. Navelet, Nucl. Phys. B **282**, 727 (1987).
10. V.T. Kim, G.B. Pivovarov, Phys. Rev. D **53**, 6 (1996).
11. CMS Collaboration, S. Chatrchyan *et al.*, Eur. Phys. J. C **72**, 2216 (2012).
12. T. Sjostrand, S. Mrenna, P.Z. Skands, JHEP **0605**, 026 (2006).
13. R. Field, arXiv:1010.3558 [hep-ph].
14. CMS Collaboration, S. Chatrchyan *et al.*, JHEP **1109**, 109 (2011).
15. T. Sjostrand, S. Mrenna, P.Z. Skands, Comput. Phys. Commun. **178**, 852 (2008).
16. R. Corke, T. Sjostrand, JHEP **1103**, 032 (2011).
17. M. Bahr *et al.*, Eur. Phys. J. C **58**, 639 (2008).
18. S. Gieseke *et al.*, arXiv:1102.1672 [hep-ph].
19. H. Jung *et al.*, Eur. Phys. J. C **70**, 1237 (2010).
20. J.R. Andersen, J.M. Smillie, JHEP **1106**, 010 (2011).
21. L. Lonnblad, Comput. Phys. Commun. **71**, 15 (1992).
22. J.R. Andersen, L. Lonnblad, J.M. Smillie, JHEP **1107**, 110 (2011).
23. V. Del Duca, C.R. Schmidt, Phys. Rev. D **49**, 177 (1994).
24. W.J. Stirling, Nucl. Phys. B **423**, 56 (1994).
25. CMS Collaboration, V. Khachatryan *et al.*, JHEP **1608**, 139 (2016).
26. A. Sabio Vera, F. Schwennsen, Nucl. Phys. B **776**, 170 (2007).
27. T. Gleisberg, S. Hoeche, F. Krauss *et al.*, JHEP **0902**, 007 (2009).
28. P. Nason, JHEP **0411**, 040 (2004).
29. S. Frixione, P. Nason, C. Oleari, JHEP **0711**, 070 (2007).
30. S. Alioli, P. Nason, C. Oleari, E. Re, JHEP **1006**, 043 (2010).
31. B. Duclou, L. Szymanowski, S. Wallon, Phys. Rev. Lett. **112**, 082003 (2014).

**THE ELECTROWEAK Z-BOSON PRODUCTION
WITH TWO ASSOCIATED JETS IN THE CMS EXPERIMENT
AT THE LARGE HADRON COLLIDER ENERGIES 7, 8, AND 13 TeV**

PNPI participants of the CMS Collaboration:

**A.A. Vorobyev, B.V. Bochin, S.A. Gets, V.L. Golovtsov, Yu.M. Ivanov, V.T. Kim, E.V. Kuznetsova,
P.M. Levchenko, V.A. Murzin, V.A. Oreshkin, L.A. Schipunov, I.B. Smirnov, V.V. Sulimov,
V.I. Tarakanov, L.N. Uvarov, S.A. Vavilov, S.S. Volkov, An.A. Vorobyev**

The CMS experiment has a large program of experimental study of electroweak theory, including vector-boson fusion (VBF) processes. One of the processes is the electroweak production of a Z boson associated with two jets coming from an electroweak vertices. The Feynman diagram is shown on Fig. 1a. This process was directly measured for the first time by the CMS experiment using pp collisions at $\sqrt{s} = 7$ TeV [1, 2]. Studies of this process were also performed at $\sqrt{s} = 8$ TeV [3] and 13 TeV [4], taking benefit both from the increased process cross section and increased integrated luminosity.

This process is interesting to study experimentally, because the non-abelian nature of the weak interactions can be directly observed, as it contains a triple gauge boson vertex. Moreover, existence of anomalous triple gauge couplings can be tested. Also, this process is the background to other VBF processes such as VBF Higgs production, with which it shares the following common experimental signatures: 1) the presence of two jets produced at high rapidities, these jets originating from the two outgoing quarks recoiled against virtual emission of W bosons (in the analysis, they are called tagging jets, since their presence is used to tag an event); 2) the suppressed quantum chromodynamic (QCD) radiation in the rapidity space between the tagging jets because of the absence of colour exchange in the process diagram. CMS has excellent capabilities for measuring such processes because of the hadronic forward calorimeter, an efficient tracking system, able to reconstruct events at high pile-up, as well as the muon system indispensable for muon channel of a Z-boson decay.

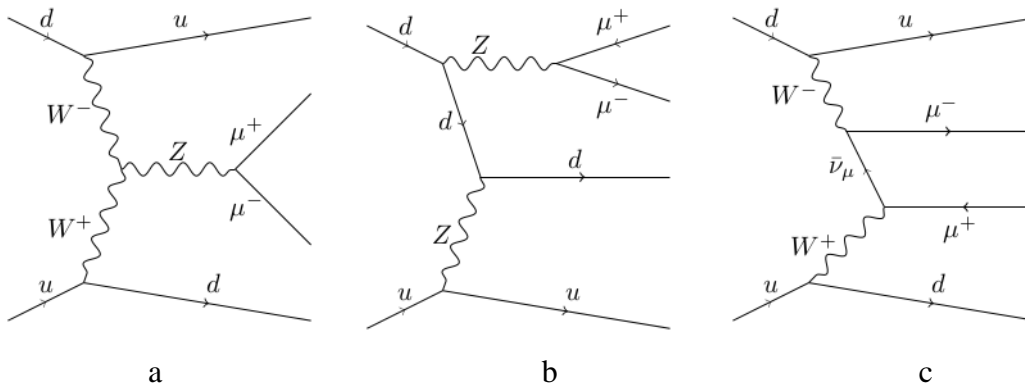


Fig. 1. Diagrams of electroweak production of two jets with a Z boson: a – vector boson fusion; b – Z-boson bremsstrahlung; c – multiperipheral production

The higher order correction in the form of initial and final state radiation as well as the underlying event strongly rely on various Monte Carlo (MC) generator models, making it an important source of input for MC development and tuning.

However, the Z production *via* VBF is not the only type of diagram that should be considered, since a Z boson can be produced also in bremsstrahlung (Fig. 1b), a process not sharing the mentioned experimental signatures, and in multiperipheral (non-resonant) production, which, although sharing the VBF characteristics, has its dilepton not originating from a Z-boson decay (Fig. 1c). As calculations show, the signal strength is significantly diminished through large negative interference with them, which is inherently related to cancellations that keep the electroweak theory renormalizable and unitary. Thus, contributions of these diagrams are considered as an indistinguishable background.

In contrast, the interference between the VBF Z production and QCD backgrounds, with contributions of order $\alpha_{\text{EWK}}^2 \alpha_{\text{QCD}}^2$, presented in Fig. 2, was shown to be small enough to be accounted for by including its value into the systematic uncertainty. This allows for the following analysis strategy. A prediction for the differential cross section of the Z-boson production is represented as an algebraic sum of a signal multiplied by a coefficient, signal strength modifier, and various QCD backgrounds, with the dominant one – the Drell–Yan plus jets production – also multiplied by its own strength modifier coefficient. Each term in the sum is obtained from a specific MC sample. Then this sum is fitted to the differential cross section measured for real data, the strength coefficients being free parameters. The measured cross sections are shown in Fig. 3 for 7, 8, and 13 TeV together with MC predictions for the signal and each type of background.

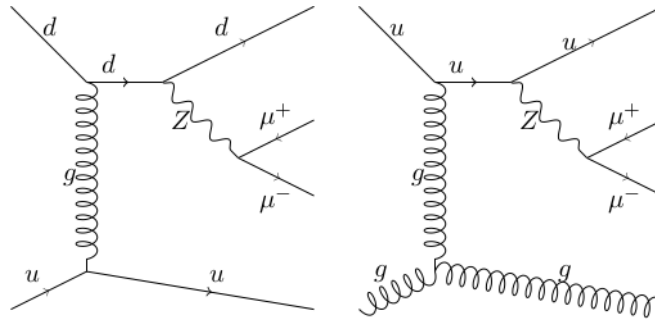


Fig. 2. Examples of diagrams of electroweak and QCD Z-boson production with two jets

Here, the differential cross section is measured as a function of the boosted decision tree (BDT) discriminant aimed at discriminating between signal and QCD background events. This discriminant is a function of certain kinematic event variables. Their choice is based on distinctive characteristics of the signal events such as: large rapidity separation between the tagging jets production (because of small-angle scattering of the two initial partons); larger invariant mass of the tagging jet pair (because of topological configuration and large p_T of the outgoing partons); a Z-boson candidate is expected to be produced centrally with respect to the tagging jets; the balance of the “Z boson – tagging jets” subsystem in the transverse momentum plane; absence of gluon jets in the signal (a special CMS quark/gluon jet discriminant is used).

The training of the BDT was based on MC events processed through full CMS detector simulation. In general, MC event generators that provided best possible accuracy while retaining positive event weights were employed for each event sample. Then the integrated cross sections were rescaled by the cross section found by NLO (next-to-leading order) or NLO + NLLA (next-to-leading logarithmic approximation) calculations, depending on the type of the background process. The interference between purely electroweak diagrams and Drell–Yan plus jets was taken into account either by generating a separate event sample where interference terms were included using a special configuration of the MadGraph generator, or by taking difference between the differential cross sections from event samples with interference effects turned on and samples without interference.

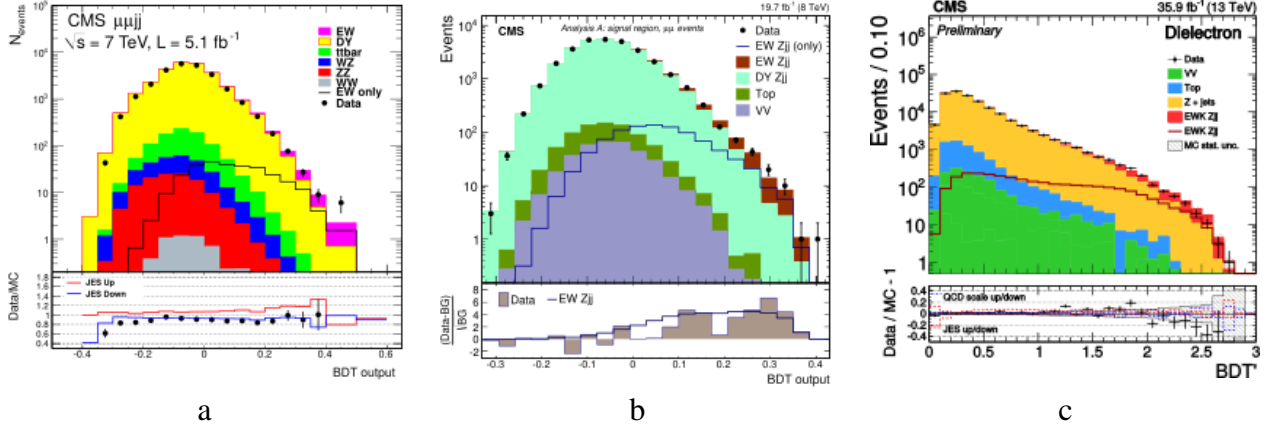


Fig. 3. Differential cross sections as functions of BDT multivariate discriminant for \sqrt{s} : a – 7 TeV; b – 8 TeV; c – 13 TeV

The measured cross section was obtained by multiplying the signal strength factor found from the fit by a leading order (LO) prediction obtained for the given phase space region. For $\sqrt{s} = 7$ TeV and an integrated luminosity of 5 fb^{-1} , the cross section was found to be $\sigma^{\text{EW}} = 154 \pm 24$ (stat) ± 46 (exp. syst) ± 27 (theo. syst) ± 3 (lum) fb. It is in good agreement with the theoretical prediction at the LO order obtained by VBFNLO 166 fb within systematic uncertainties. For $\sqrt{s} = 8$ TeV and an integrated luminosity of 19.7 fb^{-1} , the measured cross section was found to be $\sigma^{\text{EW}} = 174 \pm 15$ (stat) ± 40 (syst) fb, which is also in good agreement with the LO prediction 208 ± 18 fb. Finally, for $\sqrt{s} = 13$ TeV and an integrated luminosity of 35.9 fb^{-1} , $\sigma^{\text{EW}} = 552 \pm 19$ (stat) ± 55 (syst), which is in good agreement with the LO result of 543 fb. The last result has the best relative accuracy ever attained (around 10%) thanks to the increased signal cross section, due to the increased energy and increased integrated luminosity. The phase space limits corresponding to the measured integrated cross sections were set to attain optimal signal to background ratio. For 7 TeV, they were set to be 65, 40, and 600 GeV for leading jet transverse momentum, second leading jet transverse momentum and invariant mass of the tagging dijet, respectively. For 8 TeV, these numbers were set to 50, 30 and 200 GeV, respectively. For 13 TeV, they were set to 25, 25, and 120 GeV.

After the signal was established, events from the signal-enriched phase space region (where the contribution of signal events was comparable to that of background events) were used to study additional hadronic activity. Kinematic distributions of additional hadrons, not included into the tagging jets, as well as additional jets, beside the tagging ones, were measured. Two types of jets were used. The particle flow jets, commonly used in the CMS analysis, as well as the soft-track jets, clustered from the charged tracks, were used. The advantage of the latter type of jets is the better resilience against pile-up effects, because the calorimeter information is not used, as well as a lower limit on accessible transverse momentum. In general, good agreement between predictions of both the HERWIG++ shower model and the PYTHIA 8 shower model was obtained. For 13 TeV, the HERWIG shower exhibits better descriptions than PYTHIA at low values of additional jet transverse momentum, while the PYTHIA shower, on the contrary, does better at medium values.

The PNPI team was involved in the support of the CMS muon system and physics analysis.

References

1. CMS Collaboration, Report No. CMS PAS FSQ-12-019, CERN (2012).
2. CMS Collaboration, S. Chatrchyan *et al.*, JHEP **1310**, 062 (2013).
3. CMS Collaboration, V. Khachatryan *et al.*, Eur. Phys. J. C **75**, 66 (2015).
4. CMS Collaboration, A. Sirunyan *et al.*, Eur. Phys. J. C **78**, 589 (2018); arXiv:1712.09814 [hep-ex].

**MEASUREMENTS OF THE ANGULAR COEFFICIENTS IN Z-BOSON EVENTS
USING ELECTRON AND MUON PAIRS FROM THE DATA TAKEN AT $\sqrt{s} = 8$ TeV
WITH THE ATLAS DETECTOR**

**PNPI participants of the ATLAS Collaboration: A.E. Basalaev, A.E. Ezhilov, O.L. Fedin,
V.T. Grachev, M.P. Levchenko, V.P. Maleev, Yu.G. Naryshkin, V.A. Schegelsky, V.M. Solovyev**

1. Introduction

The Drell–Yan production of lepton pairs is a benchmark process at hadron colliders like the Large Hadron Collider (LHC). The production of Z bosons with subsequent leptonic decays has both a clean and readily identifiable signature and a large event rate. It is a key process for precision measurements of electroweak parameters, and also allows to probe various aspects of the strong interaction, including parton distribution functions (PDFs), the strong coupling constant α_s , and the behaviour of processes involving multiple scales. At all orders in quantum chromodynamics (QCD), the differential cross-section has the following general form:

$$\begin{aligned} \frac{d\sigma}{dp_T^Z dy^Z dm^Z d\cos\theta d\phi} &= \frac{3}{16\pi} \frac{d\sigma^{U+L}}{dp_T^Z dy^Z dm^Z} \times \\ &\times \left\{ (1 + \cos^2\theta) + \frac{1}{2} A_0 (1 - 3 \cos^2\theta) + A_1 \sin 2\theta \cos\phi + \right. \\ &+ \frac{1}{2} A_2 \sin^2\theta \cos 2\phi + A_3 \sin\theta \cos\phi + A_4 \cos\theta + \\ &\left. + A_5 \sin^2\theta \sin 2\phi + A_6 \sin 2\theta \sin\phi + A_7 \sin\theta \sin\phi \right\}, \end{aligned} \quad (1)$$

where p_T and y denote the transverse momentum and the rapidity of the Z boson in the laboratory frame and the angles θ and ϕ are the polar and azimuthal decay angles, respectively, of the leptons in the gauge boson rest frame. In this study, the Collins–Soper (CS) rest frame [1] most widely spread in measurements was used. The full five-dimensional differential cross-section is decomposed as a sum of nine harmonic polynomials, which depend on $\cos\theta$ and ϕ , multiplied by the corresponding helicity cross-sections that depend on the Z -boson transverse momentum, rapidity and invariant mass. The dimensionless angular coefficients $A_{0-7}(p_T^Z, y^Z, m^Z)$ represent ratios of helicity cross-sections with respect to the unpolarized one, σ^{U+L} .

PNPI physicists participate in inclusive measurements of the full set of eight A_i coefficients using charged lepton pairs (electrons or muons) from the Z decay. These results are based on 20.3 fb^{-1} of pp collisions data collected at $\sqrt{s} = 8$ TeV by the ATLAS experiment at the LHC. A detailed description of the ATLAS detector can be found in Ref. [2]. These measurements allow to probe perturbative QCD predictions at all orders of α_s complemented with parton showers and non-perturbative effects.

2. The moments method

The angular coefficients in Eq. (1) are not explicitly used as input to theoretical calculations nor in the Monte Carlo (MC) event generators. They can, however, be extracted from the shapes of the angular distributions with the moment method proposed in Ref. [3], owing to the orthogonality of the P_i polynomials. The weighed average of the angular distributions with respect to any specific polynomial isolates the average reference value or moment of its corresponding coefficient. The moment of a polynomial $P(\cos\theta, \phi)$ over a specific range of p_T^Z, y^Z , and m^Z is defined by

$$\langle P(\cos\theta, \phi) \rangle = \frac{\int P(\cos\theta, \phi) d\sigma(\cos\theta, \phi) d\cos\theta d\phi}{\int d\sigma(\cos\theta, \phi) d\cos\theta d\phi}.$$

The moment of each harmonic polynomial can be expressed as

$$\begin{aligned} \langle \frac{1}{2} (1 - 3 \cos^2 \theta) \rangle &= \frac{3}{20} \left(A_0 - \frac{2}{3} \right); & \langle \sin 2\theta \cos \phi \rangle &= \frac{1}{5} A_1; & \langle \sin^2 \theta \cos 2\phi \rangle &= \frac{1}{10} A_2; \\ \langle \sin \theta \cos \phi \rangle &= \frac{1}{4} A_3; & \langle \cos \theta \rangle &= \frac{1}{4} A_4; & \langle \sin^2 \theta \sin 2\phi \rangle &= \frac{1}{5} A_5; \\ \langle \sin 2\theta \sin \phi \rangle &= \frac{1}{5} A_6; & \langle \sin \theta \sin \phi \rangle &= \frac{1}{4} A_7. \end{aligned}$$

The moment method relies on integration over the full phase space of the angular distributions, it cannot be applied directly to data, but is used to compute all theoretical predictions.

3. Methodology of measurements

The polarization angular coefficients are extracted from the data by fitting templates of the P_i polynomial terms, defined by Eq. (1), to the reconstructed angular distributions. Each template is normalized by free parameters for its corresponding coefficient A_i , as well by an additional common parameter representing the unpolarized cross-section. All these parameters are defined independently in each bin of p_T^Z . To build the templates of the P_i polynomials, the reference coefficients A_{ref} for the signal MC sample are first calculated with the moments method. These are obtained in each of p_T^Z bins and also in each of y^Z bins for the y^Z -binned measurements. The information about the angular coefficients in the simulation is then available through the corresponding functional form of Eq. (1). Next, the MC event weights are divided by the value of this function on an event-by-event basis. When the MC events are weighed in this way, the angular distributions in the full phase space at the event generator level are flat. Effectively, all information about the Z -boson polarization is removed from the MC sample. The selection requirements, corrections, and event weights are then applied and finally nine separate template histograms are obtained after weighing by each of the P_i terms. The templates t_{ij} are thus three-dimensional distributions in the measured $\cos \theta$, ϕ , and p_T^{ll} variables. The sum of all signal templates normalized by their reference coefficients and unpolarized cross-sections agrees exactly with the three-dimensional reconstructed distribution expected for signal MC events. Templates T_B are also built for each of the multijet, top and electroweak, and non-fiducial Z -boson backgrounds.

The maximum likelihood fit is performed on the reconstructed data to determine the coefficients. The likelihood is built from the nominal templates and the varied ones reflecting the systematic uncertainties. A set of nuisance parameters (NPs) $\theta = \{\beta, \gamma\}$ is used to interpolate between them. These are constrained by the auxiliary probability density function and come in two categories:

1. Beta are the NPs representing experimental and theoretical uncertainties. Each β^m is constrained by unit Gaussian probability density functions $G(0|\beta^m, 1)$ and linearly interpolated between the nominal and varied templates. These are defined to have a nominal value of zero, with $\beta^m = \pm 1$ corresponding to $\pm 1\sigma$ for the systematic uncertainty under consideration.
2. Gamma are the NPs that handle systematic uncertainties from the limited size of the MC samples. For each bin n in the reconstructed distribution γ^n has a nominal value of one and normalizes the expected events in bin n of the templates. They are constrained by Poisson probability density functions $P(N_{\text{eff}}^n | \gamma^n N_{\text{eff}}^n)$, where N_{eff}^n is the effective number of MC events in bin n . The meaning of ‘‘effective’’ here refers to corrections applied to non-uniform event weights.

When all signal and background templates are summed over with their respective normalizations, the expected events N_{exp}^n in each bin n can be written as

$$N_{\text{exp}}^n(A, \sigma, \theta) = \left\{ \sum_{j=1}^{23} \sigma_j L \left[t_{8,j}(\beta) + \sum_{i=0}^7 A_{i,j} t_{i,j}(\beta) \right] + \sum_B^{\text{bkgs}} T_B(\beta) + T_{\text{Fakes}} \right\} \gamma^n.$$

The likelihood is the product of Poisson probabilities across all N_{bins} bins and of auxiliary constraints for each nuisance parameter β^m :

$$\mathcal{L}(A, \sigma, \theta | N_{\text{obs}}) = \prod_n^{N_{\text{bins}}} \{P(N_{\text{obs}}^n | N_{\text{exp}}^n(A, \sigma, \theta)) P(N_{\text{eff}}^n | \gamma^n N_{\text{eff}}^n)\} \prod_m^M G(0 | \beta^m, 1).$$

4. Data analysis

The data recorded with the ATLAS detector in 2012 for proton–proton collisions with a centre of mass energy of 8 TeV corresponding to the total integrated luminosity of 20.3 fb^{-1} were used for determination of the angular coefficients. The measurements were performed and splitted into three orthogonal channels, namely the ee_{CC} channel with two central electrons, the $\mu\mu_{\text{CC}}$ channel with two central muons and the ee_{CF} with one central and one forward electron. The selected events are required to be in the data-taking period in which the beams were stable and the detector was functioning well, and to contain a reconstructed primary vertex with at least three tracks with $p_{\text{T}} > 0.4 \text{ GeV}$.

Candidate ee_{CC} events are obtained using a logical “OR” of a dielectron trigger requiring two electron candidates with $p_{\text{T}} > 12 \text{ GeV}$ and of two high- p_{T} single-electron triggers (the main one corresponding to a p_{T} threshold of 24 GeV). The electron candidates are required to have $p_{\text{T}} > 25 \text{ GeV}$ and are reconstructed from clusters of energy in the electromagnetic calorimeter matched to inner detector tracks. The electron candidates must satisfy a set of “medium” selection criteria [4] which have been optimized for the level of pile-up present in the 2012 data. Candidate ee_{CF} events are obtained using the logical “OR” of the two high- p_{T} single-electron triggers used for the ee_{CC} events, as described above. The central electron candidate is required to have $p_{\text{T}} > 25 \text{ GeV}$. Because the expected background from multijet events is larger in this channel than in the ee_{CC} channel, the central electron candidate is required to satisfy a set of “tight” selection criteria. The forward electron candidate is required to have $p_{\text{T}} > 20 \text{ GeV}$ and to satisfy a set of “medium” selection criteria, based only on the shower shapes in the electromagnetic calorimeter since this region is outside the acceptance of the inner tracker. Candidate $\mu\mu_{\text{CC}}$ events are retained for the analysis using a logical “OR” of a dimuon trigger requiring two muon candidates with $p_{\text{T}} > 18 \text{ GeV}$ and 8 GeV , respectively, and of two high- p_{T} single-muon triggers (the main one corresponding to a p_{T} threshold of 24 GeV). Muon candidates are required to have $p_{\text{T}} > 25 \text{ GeV}$ and are identified as tracks in the inner detector which are matched and combined with the track segments in the muon spectrometer. The track-quality and longitudinal and transverse impact-parameter requirements are imposed for muon identification to suppress backgrounds, and to ensure that the muon candidates originate from a common primary pp interaction vertex. Events are required to contain exactly two leptons satisfying the above criteria. The lepton pairs with the invariant mass in a narrow range near the Z -boson mass pole ($80 < m_{ll} < 100 \text{ GeV}$) were selected to reduce the contribution from virtual photons. In this mass region, the background contribution is less than 0.5% for ee_{CC} and $\mu\mu_{\text{CC}}$ channels and at the level of 2% for the ee_{CF} channel. The background from lepton pairs is estimated using simulated samples and consists of lepton pairs from top-quark processes and from diboson production with a smaller fraction from $Z \rightarrow \tau\tau$ decays. Another source of the background, the so-called QCD background, appears when at least one of the leptons is produced in decays of hadrons containing heavy quarks (beauty or charm). The contribution of the QCD background was estimated from the obtained data.

Figure 1 shows the angular distributions, $\cos\theta_{\text{CS}}$ and ϕ_{CS} , for the three channels for the data, for the Z -boson signal MC sample, and for the main sources of background.

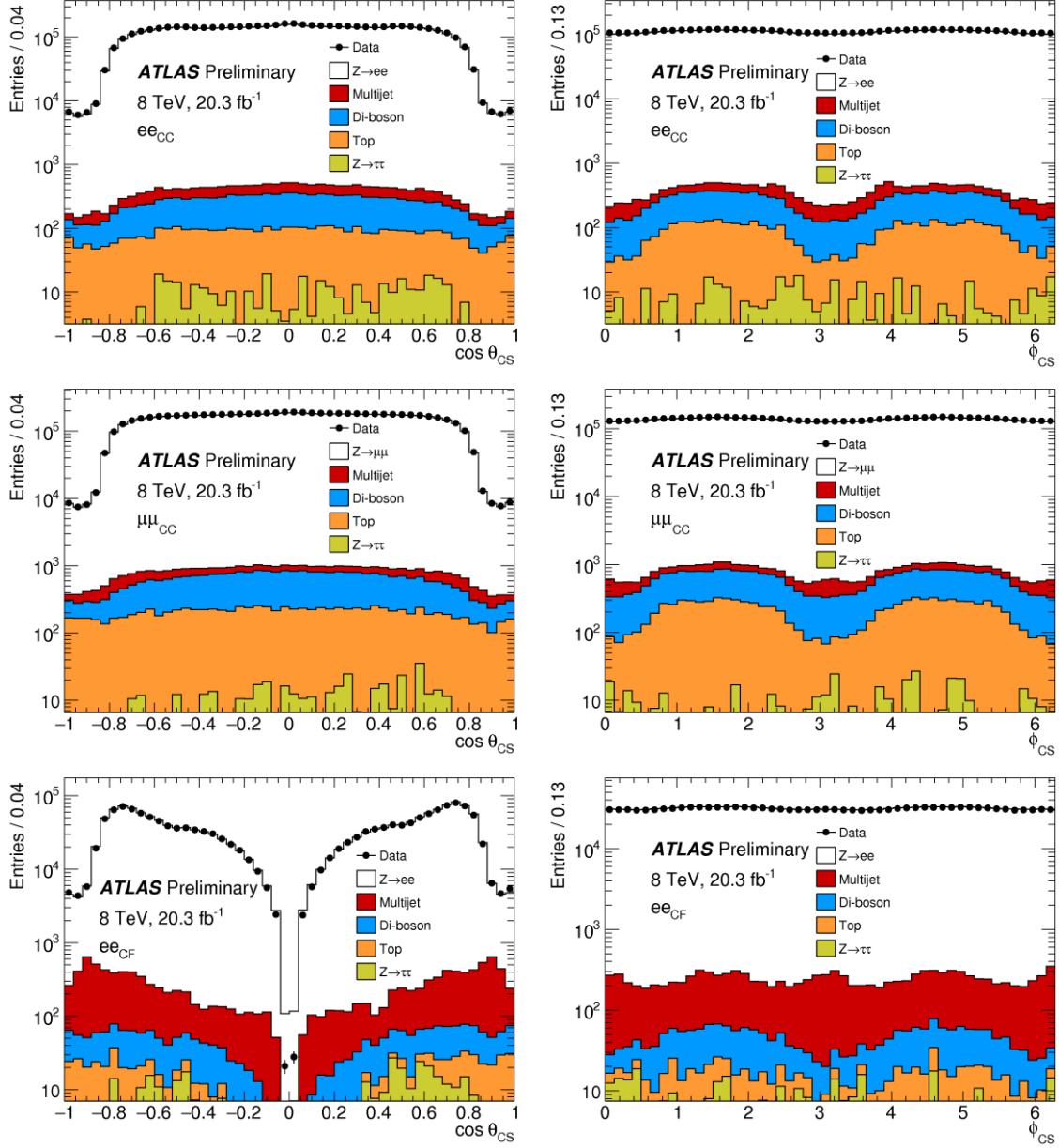


Fig. 1. The $\cos \theta_{CS}$ (left) and ϕ_{CS} (right) angular distributions, averaged over all Z -boson p_T , for the ee_{CC} (top), $\mu\mu_{CC}$ (middle), and ee_{CF} (bottom) channels [5]

5. Results in the individual and combined channels

The measurements were performed as for the full set of y^Z -integrated coefficients, so for the y^Z -dependent coefficients as a function of p_T^Z in the available y^Z bins. The combination of the ee_{CC} and $\mu\mu_{CC}$ channels is used for the y^Z -integrated measurements and the measurements in the first two y^Z bins, while the ee_{CF} channel is used for the measurements in the last y^Z bin. Figure 2 shows the y^Z -integrated measurements for all coefficients A_i and overlays of the y^Z -dependent A_i in each accessible y^Z bin. The A_1 and A_6 measurements are missing from the third y^Z bin since they are inaccessible in the projections used in the ee_{CF} channel. Also, a measurement of $A_0 - A_2$ is missing in this bin since A_0 and A_2 are accessible in different projections in the ee_{CF} channel. A large degree of correlation from bin to bin coupled with statistical fluctuations can lead to correlated deviations in the spectra, for example, near $p_T^Z = 40$ GeV for A_4 in the $2 < |y^Z| < 3.5$ bin and for A_1

in the $0 < |y^Z| < 1$ bin. Visually, the coefficients $A_{5,6,7}$ all show a trend towards non-zero positive values in the region with p_T^Z around 100 GeV.

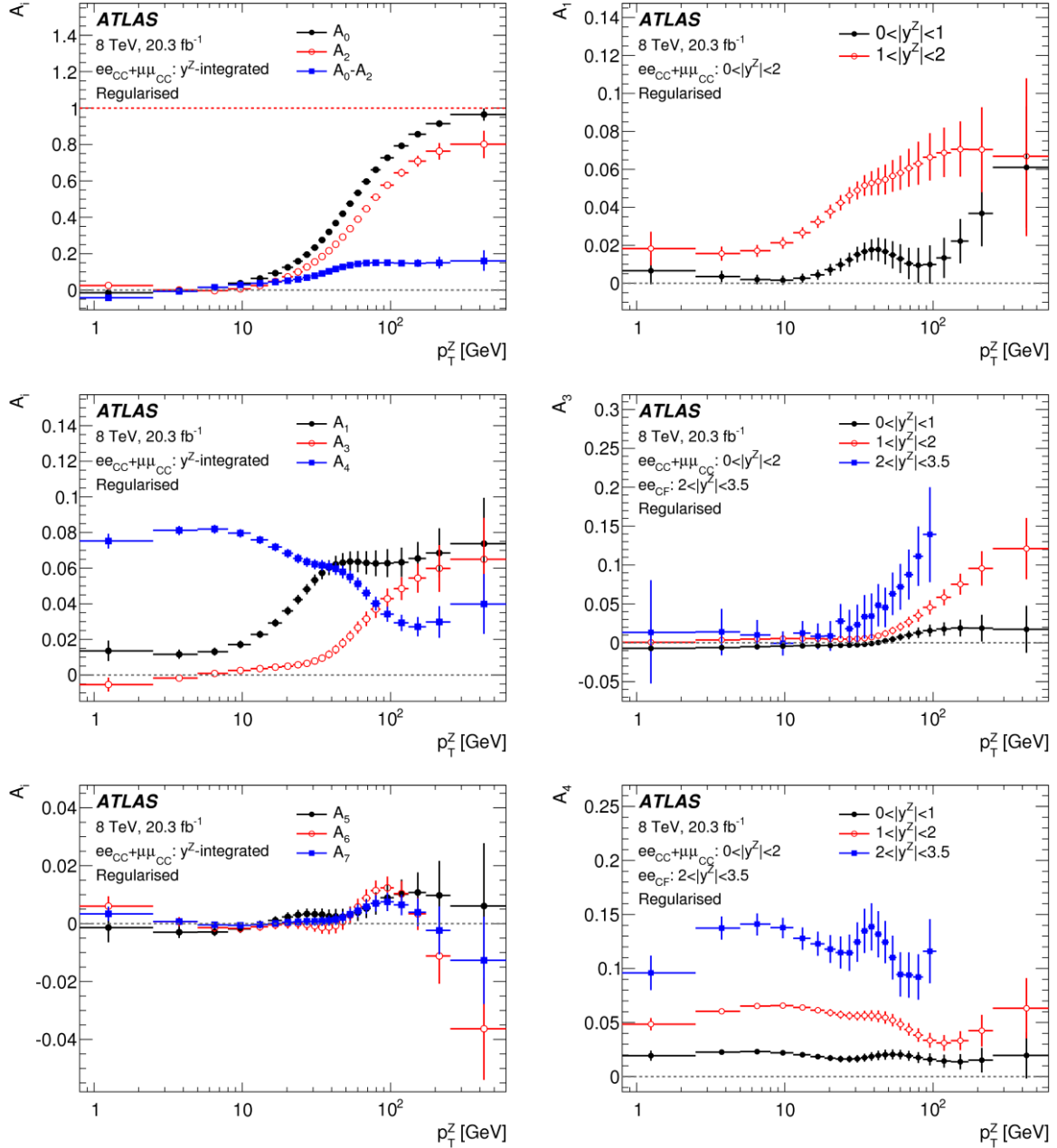


Fig. 2. Measurements of the angular coefficients in the y^Z -integrated and y^Z -binned configurations versus p_T^Z . Among the y^Z -integrated configurations, $A_{0,2}$, $A_0 - A_2$ (top left), $A_{1,3,4}$ (middle left), and $A_{5,6,7}$ (bottom left) are shown. The y^Z -binned A_i are overlaid in each accessible y^Z bin for A_1 (top right), A_3 (middle right), and A_4 (bottom right) [5]

6. Comparisons with theory predictions

The measurements are compared to the most precise fixed-order calculations currently available. The theoretical fixed-order QCD predictions for Z-boson production at NLO and NNLO were obtained with DYNNLO. It was also compared with FEWZ at NNLO. The agreement between the two generators was found within uncertainties. The calculations from DYNNLO are shown at NNLO for $p_T^Z > 2.5$ GeV. A_0 and A_2 are

the fractions of transverse and longitudinal polarization. The Lam–Tung relation predicts that $A_0 - A_2 = 0$ at NLO, but it can be violated at higher orders. For $p_T^Z > 50$ GeV significant deviations from zero are observed, as shown in Fig. 3 (*top left*). The deviation is about a factor of two larger than the predicted one. Since the impact of the PDF uncertainties on the calculations is very small, these deviations must be due to higher-order QCD effects. Coefficients $A_{5,6,7}$ are equal to 0 at NLO and show some non-zero behaviour at higher order of QCD mostly at high values of p_T^Z . The results visible in Fig. 3 (*top right* and *both bottom*) are consistent with the predictions. However, the calculations and the data are at the limit of the sensitivity. The coefficients $A_{5,6,7}$ are measured for the first time, and additional tests provide an evidence of a non zero value with a significance of three standard deviations.

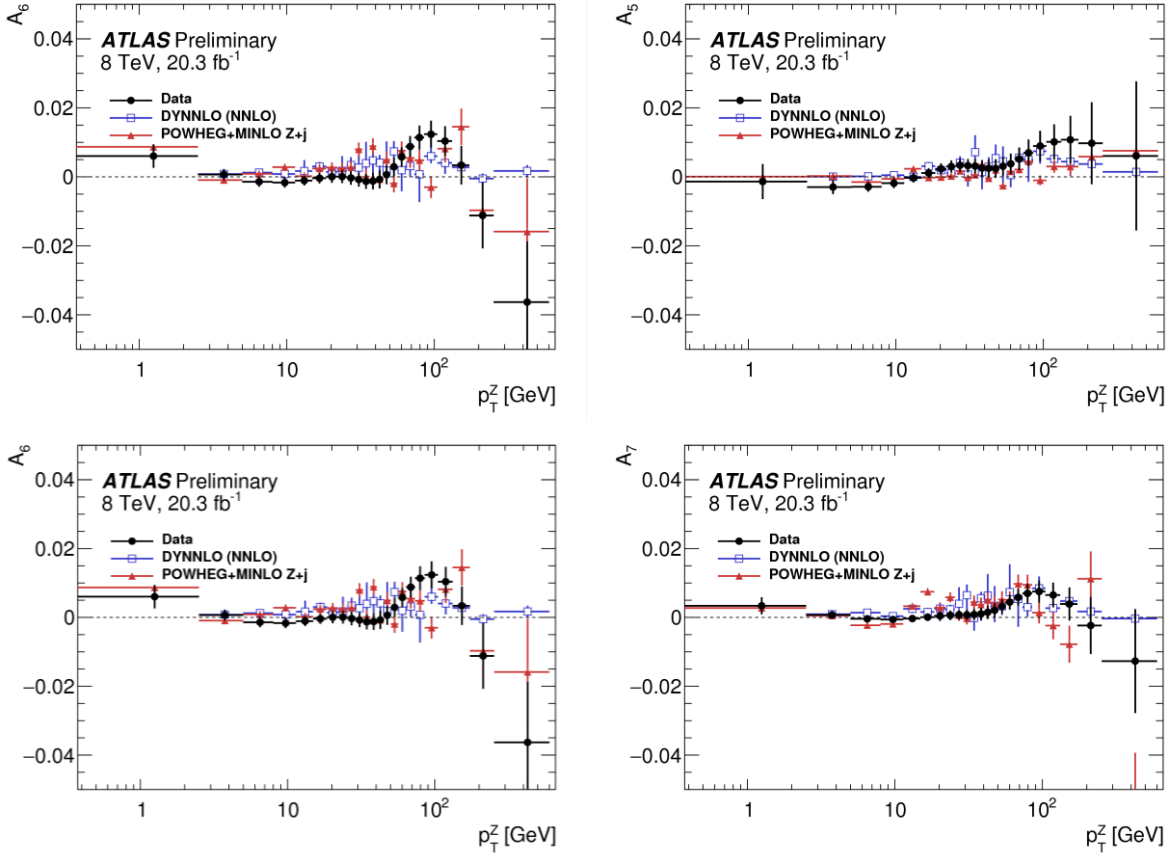


Fig. 3. Distributions of the angular coefficients $A_0 - A_2$ (*top left*), A_5 (*top right*), A_6 (*bottom left*), and A_7 (*bottom right*) as a function of p_T^Z [5]

7. Conclusion

The results of angular coefficients measurements are presented corresponding to 20.3 fb^{-1} of pp collisions data collected at $\sqrt{s} = 8 \text{ TeV}$ by the ATLAS experiment at the LHC. The measurements are performed as a function of p_T^Z over y^Z and in bins of y^Z , covering almost the full range of y^Z spanned by Z-boson production at $\sqrt{s} = 8 \text{ TeV}$.

The results compared to theoretical calculations and to predictions of MC generators are precise enough to probe QCD corrections beyond the formal accuracy of the calculations. A significant deviation from $O(\alpha_s^2)$ is observed for $A_0 - A_2$, indicating that higher-order QCD corrections are required to describe the data. The evidence at the 3σ level is found for the non-zero $A_{5,6,7}$ coefficients for the first time, consistent with the expectations from DYNNLO at $O(\alpha_s^2)$.

The measurements of the A_i coefficients, in particular through the correlation of the angular distributions with the lepton transverse momentum distributions, are thus an important ingredient to next steps in precision measurements of electroweak parameters at the LHC, such as the effective weak mixing angle $\sin^2\theta_W$ and the W -boson mass.

References

1. J.C. Collins, D.E. Soper, Phys. Rev. D **16**, 2219 (1977).
2. ATLAS Collaboration, JINST **3**, S08003 (2008).
3. E. Mirkes, J. Ohnemus, Phys. Rev. D **50**, 5692 (1994).
4. ATLAS Collaboration, ATLAS-CONF-2014-032.
5. ATLAS Collaboration, JHEP **1608**, 159 (2016).

SEARCH FOR DARK MATTER PARTICLES PRODUCED IN ASSOCIATION WITH A Z BOSON AT THE ATLAS DETECTOR

PNPI participants of the ATLAS Collaboration: A.E. Basalaev, A.E. Ezhilov, O.L. Fedin,
V.T. Grachev, M.P. Levchenko, V.P. Maleev, Yu.G. Naryshkin, V.A. Schegelsky, V.M. Solovyev

1. Introduction

Evidence from multiple independent astrophysical sources demonstrates that in addition to the known baryonic matter there is over five times as much of the so-called dark matter (DM) in the Universe, which interacts gravitationally, but is not known to interact *via* other forces [1]. Since most of astrophysical data come from the analysis of the electromagnetic radiation, there have been numerous attempts to explain the observed gravitational influence by non-luminous ordinary matter. However, all such hypothetical sources were found to be inconsistent with modern cosmological models of the Universe. Similarly, it was considered that the general relativity might break down on large scales, from galactic and above, where the DM influence is visible. Nevertheless, to date all proposed modified gravity theories fail to explain the available evidence better than the DM hypothesis. The current consensus [2] is, therefore, that DM should be of a non-baryonic origin and most probably consists of yet unknown particles. One of the most natural hypothesis is that it consists of weakly interacting massive particles (WIMPs), which being in thermal equilibrium in the early Universe would give the observed abundance of the dark matter. After the Universe cooled down below the WIMP mass, interactions of DM with the Standard Model (SM) particles became rare, allowing them to remain undetected.

Currently, there are many experiments searching for WIMPs of three main classes: direct detection, searching for recoils of WIMPs against the SM nuclei; indirect detection, searching for excesses above the expected background in cosmic rays indicating the DM–SM annihilation events; and collider experiments, searching for WIMPs production events associated with SM particles. The Large Hadron Collider (LHC), and in particular two of its experiments, ATLAS [3] and CMS [4], carry out leading DM collider searches thanks to the unprecedented centre-of-mass energy of $\sqrt{s} = 13$ TeV.

There are two main strategies used for collider searches at ATLAS. The production of DM particles can be inferred by a signature involving a missing transverse momentum E_T^{miss} (vector sum of the transverse momenta of all detected collision products with the opposite sign) when there is a SM particle from initial state radiation (ISR). For example, a vector boson, a photon, or a jet. The second strategy looks for a mediator connecting DM to the SM, which couples to light quarks and gluons and could produce a characteristic resonance in energetic dijet events.

PNPI physicists participate in the search for DM particles production associated with a Z boson. The analysis presented here is based on 36.1 fb^{-1} of proton–proton collision data collected with the ATLAS detector in 2015 and 2016 at a centre-of-mass energy of $\sqrt{s} = 13$ TeV [5].

2. Event selection

Since the detector does not register DM particles, events with a large missing transverse momentum and two oppositely charged electrons or muons consistent with a decay of a Z boson are selected in the analysis. The Z boson is required to be back-to-back with the E_T^{miss} to give a clear recoil signature.

Electron candidates are reconstructed from isolated energy deposits in the electromagnetic calorimeter, matched to inner detector tracks. Muon candidates are reconstructed from a combined fit of tracks independently found in the muon spectrometer and inner detector. Jets are reconstructed using the anti- k_t algorithm with a radius parameter $R = 0.4$. Basic kinematic cuts along with some additional selections are also applied to reduce the probability of misidentification of the reconstructed objects [5].

The invariant mass of a lepton pair is required to be in the range $76 \text{ GeV} < M_{ll} < 106 \text{ GeV}$ to reject background processes with two leptons that do not originate from the prompt decay of a Z boson (non-resonant- ll). Events are required to pass quality checks for errors in sub-detectors during recording.

A combination of a lower p_T threshold trigger with an isolation requirement and a higher p_T threshold trigger without any isolation requirement is used, yielding the trigger efficiency above 98%.

To suppress the non-resonant- ll background further, candidate events are required to have $E_T^{\text{miss}} > 90$ GeV and $E_T^{\text{miss}}/H_T > 0.6$, where H_T is calculated as the scalar sum of the p_T of the selected leptons and jets. E_T^{miss} is expected to be back-to-back with the Z boson. This is accounted for in the $\Delta\phi(Z, E_T^{\text{miss}})$ variable, which is required to be greater than 2.7 radians, and the selected leptons must be close to each other, which is ensured by a threshold on their angular separation. Any possible imbalance, implying the presence of fake E_T^{miss} , is accounted for by an upper threshold on the fraction of jets total p_T plus E_T^{miss} relative to the p_T of the lepton pair. Events are removed if they contain b -jets to suppress top-quark pair background. Events containing a third lepton with $p_T > 7$ GeV, satisfying looser identification requirements, are removed to suppress diboson background.

3. Modelling

The results were interpreted in terms of the so-called simplified DM models, where WIMP production is mediated by a vector or an axial-vector particle (mediator). The exclusion limits on the WIMP mass m_{DM} and the mediator mass m_{med} were set for fixed coupling constants of the mediator to quarks g_q and to WIMPs g_χ . The WIMP pair is produced through the s -channel exchange of an axial-vector or vector mediator. This choice provides a useful framework for comparison with direct detection experiments, which aim to observe recoils of DM particles against nuclei, they typically contain large volumes of scintillator and are situated deep underground to reduce background contamination. Furthermore, LHC searches can be more sensitive than direct searches to WIMP production in this particular model with an axial-vector mediator. The leading tree-level diagram for WIMP production is presented in

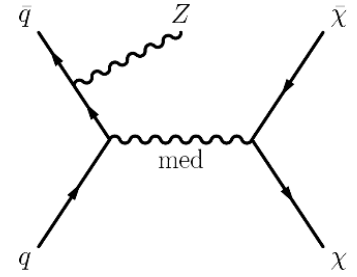


Fig. 1. Leading tree-level diagram for WIMP production in the simplified DM model [5]

Fig. 1. A Monte Carlo (MC) simulation of DM signal events with a vector and axial-vector mediator and fermionic WIMPs was performed for m_{med} and m_{DM} , ranging from 10 to 1 000 GeV. Following recommendations in Ref. [6], the coupling constants were set to $g_q = 0.25$ and $g_\chi = 1$, and the mediator width was set to be minimal, such that it decays only to DM or quarks.

4. Background estimation

The dominant background process (59%) is Z -boson pairs production, where one Z decays into a lepton–antilepton pair and another one into a neutrino–antineutrino pair. This background is estimated using MC simulation. Main uncertainties in it originate from the parton density function choice, the perturbative calculation, and the parton shower modelling. The other important background (25%) is simultaneous production of W and Z bosons, which is contributing if a lepton from the W -boson decay is undetected, or a τ -lepton decays hadronically. It is estimated from data using three-lepton control region. Main uncertainties consist of systematic uncertainties on the ratio of events in the control and signal region and statistical uncertainties on data. The non-resonant- ll background (8%) is estimated from data using the absence of signal in the $e\mu$ channel and the relative production rate of 1 : 1 : 2 for the ee , $\mu\mu$, and $e\mu$ channels. An $e\mu$ control region similar to the signal region is defined, and the background estimate for the ee and $\mu\mu$ signal regions is obtained from the number of $e\mu$ events in the control region after correcting for different acceptances and efficiencies. Main uncertainties consist of systematic uncertainties on the bias of the method and statistical uncertainties on data. The Z + jets background (8%) is estimated from data using a set of two uncorrelated variables, constructing four regions (one signal region, A, and three Z -enriched control regions, B, C, D) and using a relation $N_A = N_B \cdot N_C / N_D$ to estimate the yield in the signal region. The W + jets (estimated using the fake-factor method), three vector bosons, and top quark–antiquark pairs with a vector boson (estimated using MC simulation) backgrounds have minor contributions (less than $\sim 1\%$).

The observed and predicted E_T^{miss} distributions in the ee and $\mu\mu$ channels with a breakdown of contributions of each background are shown in Fig. 2. The observed data yields, the estimated background contributions, and the expectations for a single DM signal are shown in Table. No significant excess over the SM background expectation is observed.

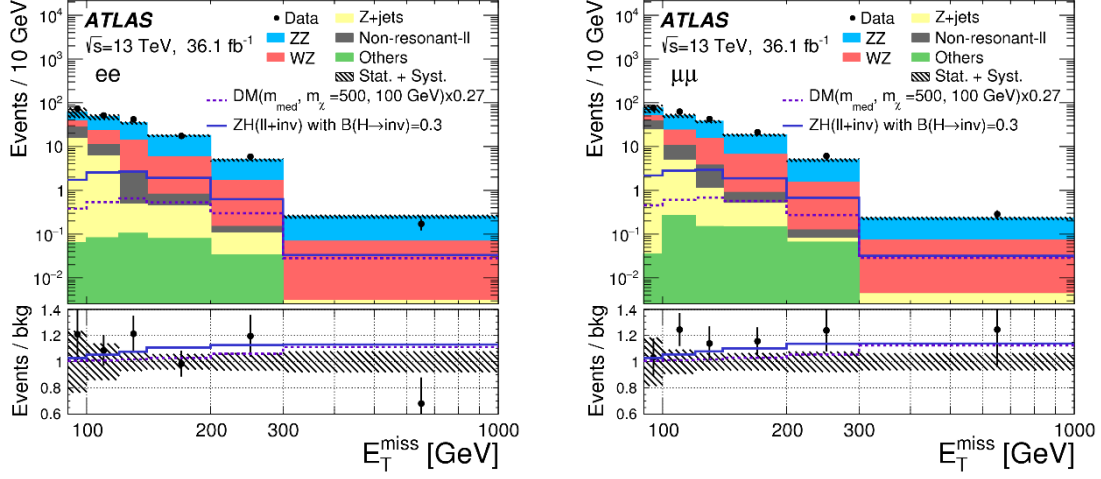


Fig. 2. Observed E_T^{miss} distribution in the ee (left) and $\mu\mu$ (right) channel (black points) compared to the background predictions (stacked histograms). The error band shows the total statistical and systematic uncertainty on the background prediction. The dashed purple line shows the DM signal prediction for $m_{\text{DM}} = 100$ GeV and $m_{\text{med}} = 500$ GeV case, scaled by the factor of 0.27 to the best-fit contribution [5]

Table

Observed data yields and expectations for the signal and background contributions after all selections applied*

Final State	ee	$\mu\mu$
Observed Data	437	497
Signal		
DM ($m_{\text{med}} = 500$ GeV, $m_{\chi} = 100$ GeV) $\times 0.27$	$10.8 \pm 0.3 \pm 0.8$	$11.1 \pm 0.3 \pm 0.8$
Backgrounds		
$qqZZ$	$212 \pm 3 \pm 15$	$221 \pm 3 \pm 17$
$ggZZ$	$18.9 \pm 0.3 \pm 11.2$	$19.3 \pm 0.3 \pm 11.4$
WZ	$106 \pm 2 \pm 6$	$113 \pm 3 \pm 5$
Z +jets	$30 \pm 1 \pm 28$	$37 \pm 1 \pm 19$
Non-resonant- ll	$30 \pm 4 \pm 2$	$33 \pm 4 \pm 2$
W +jets, VVV and $t\bar{t}V(V)$	$1.4 \pm 0.1 \pm 0.2$	$2.5 \pm 2.0 \pm 0.8$
Total Background	$399 \pm 6 \pm 34$	$426 \pm 6 \pm 28$

* To the right of each number, statistical and systematic uncertainties are shown, correspondingly. The DM signal expectation is presented, modelled in the framework of simplified models with $m_{\text{med}} = 500$ GeV and $m_{\text{DM}} = 100$ GeV scaled with a factor of 0.27 to the best-fit contribution. The background contributions are summed up from the W + jets, three vector bosons, and top quark–antiquark pairs with a vector boson [5].

5. Results

To evaluate the results of the experiment quantitatively, compatibility of the data and the signal-plus-background hypothesis is assessed using a statistical approach. A test statistic is defined using the profile likelihood ratio method [7]. The likelihood function is the product of all the Poisson probability density functions built in individual E_T^{miss} bins and final states. In each bin the observed number of events in data is represented by a Poisson probability density function with a mean equal to the sum of the predicted signal and background yields. The systematic uncertainties are incorporated as nuisance parameters constrained by auxiliary Gaussian functions. A frequentist approach with the CLs formalism [8] is then applied to set upper limits on the overall signal contribution, which is the parameter of interest left free in the test statistic.

The 95% CL DM exclusion limits in the two-dimensional phase space of the WIMP mass m_{DM} and the mediator mass m_{med} are presented in Fig. 3.

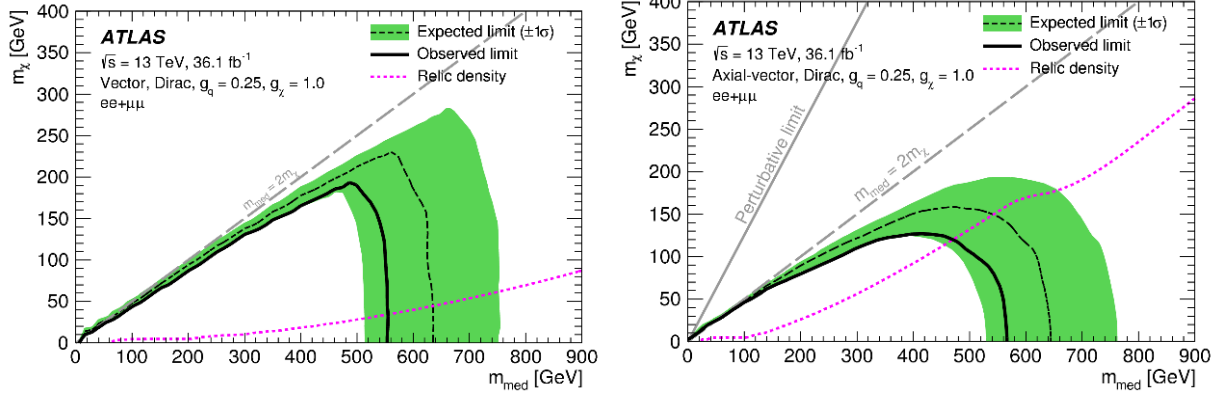


Fig. 3. DM exclusion limits in the two-dimensional phase space of WIMP mass m_{DM} vs mediator mass m_{med} for a fermionic WIMP, vector (*left*) or axial-vector (*right*) mediator with coupling constants of mediator to quarks and to DM $g_q = 0.25$ and $g_\chi = 1$, correspondingly. Regions bounded by the limit curves are excluded at the 95% CL [5]

6. Summary and prospects

There is an extensive program of DM searches performed by the ATLAS experiment. It encompasses the searches for signatures of DM production in events with $E_{\text{T}}^{\text{miss}}$ and a SM particle in ISR, as well as searches for a dark mediator in dijet events. No evidence of physics beyond the SM is observed so far. The results reported in terms of 95% CL DM exclusion limits in the two-dimensional phase space of WIMP mass m_{DM} and mediator mass m_{med} are presented in Fig. 4. Additionally, the limits translated into the cross section for scattering of a dark matter particle on a nucleon and compared with direct DM searches are shown in Fig. 5. The comparison demonstrates a greater sensitivity of ATLAS searches for an axial-vector mediator, and a greater sensitivity for a vector mediator in the range of low masses of a dark matter particle below a few GeV.

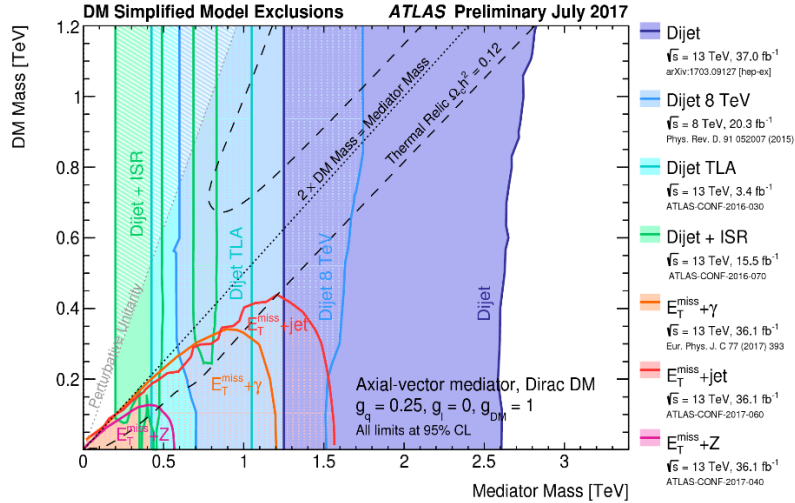


Fig. 4. DM exclusion limits in the two-dimensional phase space of WIMP mass m_{DM} vs mediator mass m_{med} for a fermionic WIMP, axial-vector mediator with coupling constants of mediator to quarks and to DM $g_q = 0.25$ and $g_\chi = 1$, correspondingly. Regions bounded by the limit curves are excluded at the 95% CL. Results are presented for the searches analyzing $E_{\text{T}}^{\text{miss}} + \gamma$, $E_{\text{T}}^{\text{miss}} + \text{jet}$, $E_{\text{T}}^{\text{miss}} + Z$, and dijet events. For dijets, results both at $\sqrt{s} = 13$ TeV and $\sqrt{s} = 8$ TeV are shown, as well as dijet trigger-level analysis, where the analysis is partially done online [9]

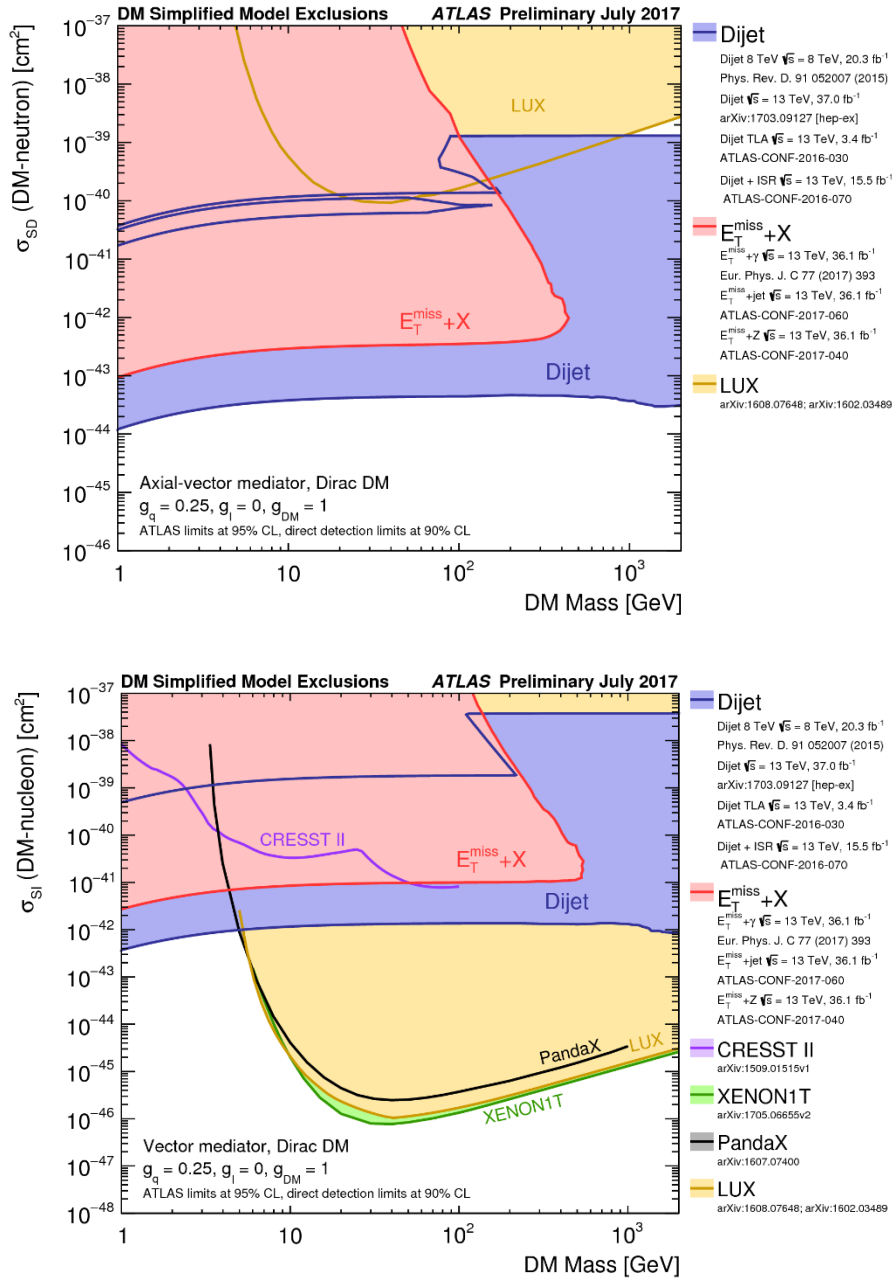


Fig. 5. The 95% CL limits on the WIMP and proton scattering cross section as a function of WIMP mass, obtained for simplified DM models with a vector mediator (*bottom*) and an axial-vector mediator (*top*). The pink area represents the combined limits from $E_T^{\text{miss}} + \text{SM}$ searches, the blue area represents the limits for dijet searches. Other curves, presented for comparison, are 90% CL limits for direct DM search experiments [10]

The LHC is expected to collect about 10 times more luminosity by 2035, which will provide a great increase in sensitivity for ATLAS searches. Combined with the fact that direct DM detection experiments will soon reach what is known as “neutrino floor” – the level of sensitivity at which the neutrino background from solar and other neutrinos becomes irreducible – the results of the ATLAS experiment, and of other collider searches will be crucial for further probing the WIMP hypothesis.

References

1. E. Komatsu *et al.*, *Astrophys. J. Suppl. Ser.* **192**, 18 (2011).
2. Particle Data Group, K.A. Olive *et al.*, *Chin. Phys. C* **38**, 090001 (2014).
3. ATLAS Collaboration, G. Aad *et al.*, *JINST* **3**, S08004 (2008).
4. CMS Collaboration, S. Chatrchyan *et al.*, *JINST* **3**, S08004 (2008).
5. ATLAS Collaboration, M. Aaboud *et al.*, *Phys. Lett. B* **776**, 318 (2018).
6. D. Abercrombie *et al.*, arXiv:1507.00966 [hep-ex].
7. A.L. Read, *J. Phys. G* **28**, 2693 (2002).
8. G. Busoni *et al.*, CERN-LPCC-2016-001, arXiv:1603.04156 [hep-ex].
9. ATLAS Collaboration, C. Alpigiani, ATL-PHYS-PROC-2017-112, arXiv:1708.09674 [hep-ex].
10. ATLAS Collaboration, M. Aaboud *et al.*, Summary Plots from the ATLAS Exotic Physics Group, <https://atlas.web.cern.ch/Atlas/GROUPS/PHYSICS/CombinedSummaryPlots/EXOTICS/index.html>

SEARCH FOR A NEW HEAVY GAUGE BOSON RESONANCE WITH THE ATLAS DETECTOR

PNPI participants of the ATLAS Collaboration: A.E. Basalaev, A.E. Ezhilov, O.L. Fedin, V.T. Grachev, M.P. Levchenko, V.P. Maleev, Yu.G. Naryshkin, V.A. Schegelsky, V.M. Solovyev

1. Introduction

Although the Standard Model (SM) of strong and electroweak interactions is remarkably consistent with particle physics observations to date, the high-energy proton–proton collisions at the Large Hadron Collider (LHC) at CERN provide new opportunities to search for physics beyond it. Many models of physics beyond the SM predict the existence of new spin-1 gauge bosons that could be discovered at the LHC. While the details of the models vary, conceptually these particles are heavier versions of the SM W and Z bosons and are generically called W' and Z' bosons.

PNPI physicists participate in searches for heavy gauge bosons and play a key role in the analyses of decays of these bosons into the final state with an electron. This article presents the most recent searches for W' and Z' bosons decaying into the $W' \rightarrow l\nu$ and $Z' \rightarrow ll$ channels. In the following, the term lepton (l) is used to refer to an electron or a muon. The analyses are based on 36.1 fb^{-1} of proton–proton collision data collected with the ATLAS detector in 2015 and 2016 at a centre-of-mass energy of $\sqrt{s} = 13 \text{ TeV}$. The results of the search for the W' bosons are interpreted in the context of the benchmark Sequential Standard Model (SSM) [1], in which the couplings of the SSM W' boson to fermions are assumed to be identical to those of the SM W boson. Models considered in the search for the Z' bosons include the Z' bosons of the E6-motivated [2, 3] theories as well as minimal models [4]. The SSM Z' boson [3] is also considered due to its inherent simplicity and usefulness as a benchmark model.

Previous searches for W' and Z' bosons were carried out in 2013–2016 by the ATLAS Collaboration with participation of PNPI physicists using proton–proton collision data collected at a centre-of-mass energy of $\sqrt{s} = 8 \text{ TeV}$ in 2012 [5, 6] and proton–proton collision data collected at $\sqrt{s} = 13 \text{ TeV}$ in 2015 [7, 8]. No significant deviation from the SM predictions was observed in these searches. Upper limits on the W' and Z' bosons cross-sections times branching ratios to leptons are set as functions of the W' and Z' masses. Analyses based on data corresponding to an integrated luminosity of 20.3 fb^{-1} taken at $\sqrt{s} = 8 \text{ TeV}$ set 95% confidence level (CL) lower limits on SSM W' mass of 3.24 TeV [5] and on SSM Z' mass of 2.90 TeV [6]. Based on 3.2 fb^{-1} of data collected at $\sqrt{s} = 13 \text{ TeV}$, 95% CL lower mass limits are 4.07 TeV for SSM W' [7] and 3.36 TeV for SSM Z' [8].

2. Search for a new heavy gauge boson resonance decaying into a charged lepton and a neutrino

The analysis uses events with a high transverse momentum (p_T) lepton and significant missing transverse momentum E_T^{miss} , which is the measure to infer the presence of the neutrino in the event as it escapes direct detection. The signal discriminant in this search is the transverse mass:

$$m_T = \sqrt{2p_T E_T^{\text{miss}}(1 - \cos \varphi_{l\nu})},$$

where $\varphi_{l\nu}$ is the azimuthal angle between the lepton p_T and the E_T^{miss} directions in the transverse plane.

A W' signal would appear as an excess of events above the SM background at high m_T . This background mainly arises from processes with at least one prompt final-state lepton, with the largest source being the charged-current Drell–Yan (DY) W boson production, where the W boson decays into an electron or muon and a neutrino. The second largest source is a top-quark pair and single-top-quark production, denoted in the following as “top-quark background”. Other non-negligible contributions are from the neutral-current DY (Z/γ^*) process, diboson production, as well as from events in which one final-state jet or photon satisfies the lepton selection criteria. The latter background component, referred to in the following as the multijet background, receives contributions from multijet, heavy-flavour quark and $\gamma + \text{jet}$ production. The multijet background is determined using a data-driven method, while the other backgrounds are modelled by Monte Carlo (MC) simulations.

The multijet background is estimated from data using the “matrix” method [9]. The first step of the matrix method is to calculate the fraction f of lepton candidates that pass the nominal lepton identification and isolation requirements (“tight”), with respect to a sample of “loose” lepton candidates in a background-enriched sample. These loosely selected candidates satisfy only a subset of the nominal criteria, which is stricter than the trigger requirements imposed. A potential contamination of prompt final-state leptons in the background-enriched sample is accounted for using MC simulation. In addition, the fraction r of real leptons in the sample of loose candidates satisfying the nominal requirements is used. This fraction is computed from MC simulation. The number of jets and photons misidentified as leptons ($N_T^{\text{Multi-jet}}$) in the total number of candidates passing the signal selection (N_T) is

$$N_T^{\text{Multi-jet}} = fN_F = \frac{f}{r-f}(r(N_L + N_T) - N_T),$$

where N_F is the number of fake leptons and N_L corresponds to leptons that pass the “loose” requirements but fail the nominal requirements.

The event reconstruction and selection for the W' boson search are described in detail in Ref. [9]. Figure 1 displays the m_T distributions for events satisfying all selection criteria in the electron and muon channels. As example, Fig. 1 also shows the expected signal distributions for three SSM W' -boson masses on top of the SM background. The effect of the momentum resolution is clearly visible when comparing the shapes of these three reconstructed SSM W' signals in the electron and muon channels. The middle panels of Fig. 1 show the ratio of the data to the SM predictions. The data are systematically above the predicted background at low m_T , but still within the total systematic uncertainty, which is dominated by the E_T^{miss} -related systematic uncertainties in this region. The bottom panels of Fig. 1 show the ratio of the data to the adjusted background that results from a common fit to the electron and muon channels within the statistical analysis described in Ref. [9]. This ratio agrees well with unity.

The compatibility between the data and the predicted background is evaluated with a profile-likelihood ratio test quantifying the probability that the background fluctuates to give a signal-like excess equal to or larger than what is observed. The likelihood functions in the ratio are products of Poisson probabilities over all bins in the transverse mass distribution (as shown in Fig. 1) and log-normal constraints for the variations in signal and background yields associated with systematic uncertainties. In the denominator of the likelihood ratio, the likelihood function is maximized assuming the presence of a signal above the expected background, and in the numerator assuming the background-only hypothesis. To model the signal, SSM W' templates binned in m_T are used for a series of SSM W' masses in the search range $150 \text{ GeV} \leq m_{W'} \leq 6000 \text{ GeV}$. Figure 1 displays a few examples of these templates. No significant excesses are observed in the data. The most significant excess is at $m_{W'} = 350 \text{ GeV}$ in the electron channel, with a local significance of 2.0σ . In the muon channel, the most significant excess is at high mass, with a maximum local significance of 1.8σ at $m_{W'} \approx 5 \text{ TeV}$. These excesses correspond to a global significance of 0.1σ in each channel when the look-elsewhere effect is taken into account.

Based on the above findings, upper limits on the cross-section for producing a SSM W' boson times its branching ratio to only one lepton generation ($\sigma \times \text{BR}$) are computed at the 95% CL as a function of the SSM W' -boson mass. The limits are calculated in a Bayesian analysis with a uniform positive prior probability distribution for $\sigma \times \text{BR}$. The observed upper limits are extracted by comparing data to the expected background and signal using SSM W' templates for a series of SSM W' masses in the range $150 \text{ GeV} \leq m_{W'} \leq 6000 \text{ GeV}$. The expected limits are derived from pseudoexperiments obtained from the estimated background distributions. The median of the distribution of the limits from the pseudo-experiments is taken as the expected limit, and 1σ and 2σ bands are defined as the ranges containing respectively 68 and 95% of the limits obtained with the pseudo-experiments. The 95% CL upper limits on $\sigma \times \text{BR}$ as a function of the SSM W' mass are shown in Fig. 2 for the combination of the electron and muon channels. The observed (expected) lower mass limit for a SSM W' boson is 5.1 (5.2) TeV for this combination. This corresponds to an improvement of approximately 1 TeV in mass reach compared to the previous ATLAS analysis [7], which was based on a subset of the data used in this analysis.

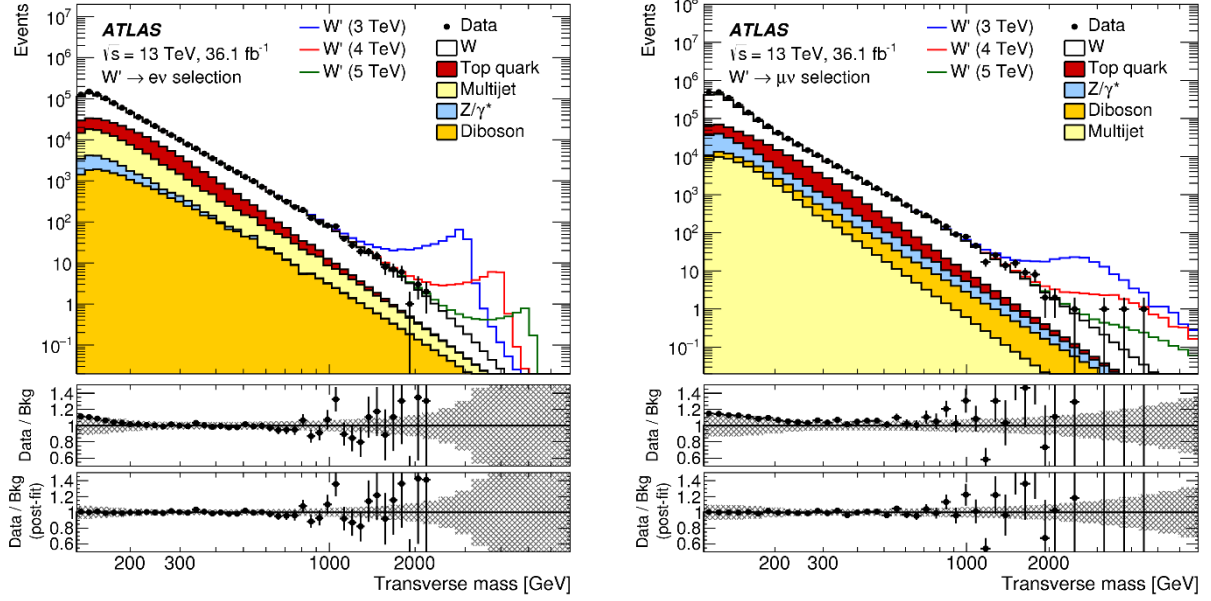


Fig. 1. Transverse mass distributions for events satisfying all selection criteria in the (*left*) electron and (*right*) muon channels. The distributions in data are compared to the stacked sum of all expected backgrounds. As examples, expected signal distributions for three different SSM W' -boson masses are shown on top of the SM prediction. The *middle panels* show the ratios of the data to the expected background, with vertical bars representing both data and MC statistical uncertainties. The *lower panels* show the ratios of the data to the adjusted expected background (“post-fit”) that results from the statistical analysis. The bands in the ratio plots indicate the total systematic uncertainty

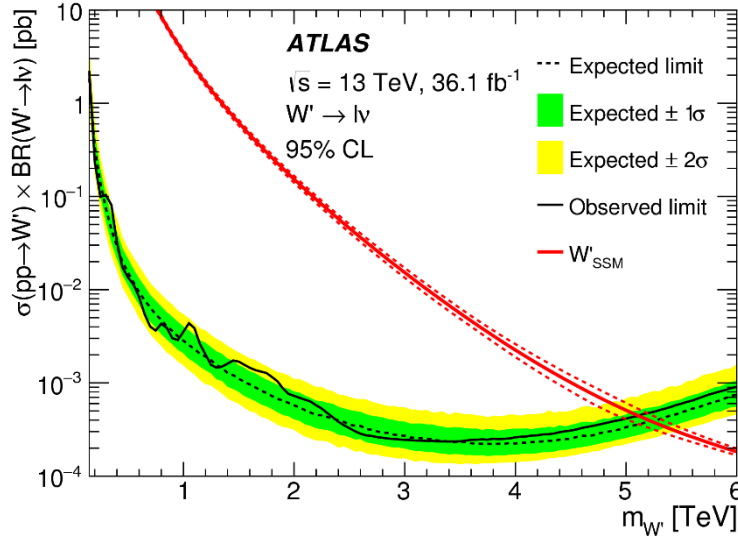


Fig. 2. Observed (*solid black line*) and expected (*dashed black line*) upper limits on cross-section times branching ratio ($\sigma \times \text{BR}$) as a function of the SSM W' -boson mass in the combined electron and muon channels. The 1σ (*green*) and 2σ (*yellow*) expected limit bands are also shown. The predicted $\sigma \times \text{BR}$ for SSM W' production is shown as a *red solid line*. For illustration, the uncertainties in $\sigma \times \text{BR}$ are also shown as *red dashed lines*

3. Search for a new heavy gauge boson resonance decaying into two charged leptons

The search utilizes the invariant mass spectra of the observed dielectron and dimuon final states as discriminating variables. The analysis and interpretation of these spectra rely primarily on simulated samples of signal and background processes. The interpretation is performed taking into account the expected shape of different signals in the dilepton mass distribution.

For both channels, the dominant and irreducible background is due to the Z/γ^* (DY) process, characterized by the same final state as the signal. Small contributions from top-quark pair and single top-quark production as well as diboson production are also present in both channels. The background from the above processes are modelled by MC simulations. An additional background arises from W + jets and multi-jet events from which at most one real lepton is produced. This background contributes to the selected samples due to having one or more jets satisfying the lepton selection criteria (the so called “fakes”). In the dimuon channel, contributions from W + jets and multi-jet production are found to be negligible, and therefore are not included in the expected yield. In the dielectron channel, the contributions from these processes are determined with a data-driven technique, the “matrix” method, similar to the one used in the W' search. In the first step, the probability f that a jet passing the “loose” selection satisfies the nominal (“tight”) electron selection criteria is evaluated using a background-enriched sample. The “loose” selection differs from the nominal one by the use of the loosened electron identification criteria and no isolation criterion. Residual contributions from processes with real electrons in the calculation of f are accounted for by using the MC simulated samples. In addition, the probability r that a real electron passing the loosened selection satisfies the nominal electron selection criteria is estimated from MC simulated DY samples. Then, in the second step these probabilities are used to estimate the level of contamination due to fakes in the selected sample of events. A more detailed description of this method is provided in Ref. [10].

The event reconstruction and selection for the Z' -boson search are described in detail in Ref. [10]. Figure 3 shows invariant mass distributions in the dielectron and dimuon channels. The expected Z'_χ signal for three mass hypotheses is also shown. This ratio agrees well with unity. The data, scrutinized using the log-likelihood ratio (LLR) test, show no significant excesses. The largest deviation from the background-only hypothesis using the LLR tests for a Z'_χ is observed at 2.37 TeV in the dielectron mass spectrum with a local significance of 2.5σ , but globally the excess is not significant.

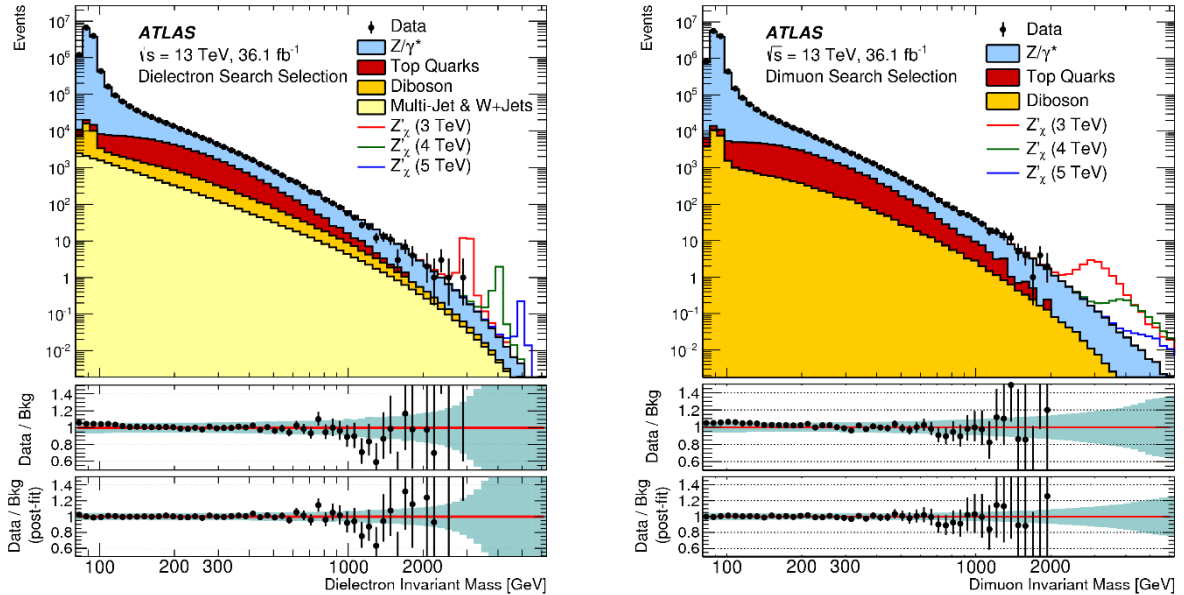


Fig. 3. Distributions of (left) dielectron and (right) dimuon reconstructed invariant mass after selection, for data and the SM background estimates as well as their ratio before and after marginalization. Selected Z'_χ signals with a pole mass of 3, 4, and 5 TeV are overlaid. The shaded band in the lower panels illustrates the total systematic uncertainty. The data points are shown together with their statistical uncertainty

Upper limits on the cross-section times branching ratio (σB) are set using Bayesian approach. Limit values obtained using the experimental data are quoted as the observed limits, while median values of the limits obtained from a large number of simulated experiments, where only SM background is present, are quoted as the expected limits. The upper limits on σB are interpreted as lower limits on the Z' pole mass using the relationship between the pole mass and the theoretical Z' cross-section.

Upper 95% CL limits on σB for Z' bosons are presented in Fig. 4. The upper limits on σB for Z' bosons start to weaken above a pole mass of ~ 3.5 TeV. The effect is more pronounced in the dilepton channel due to worse mass resolution than in the dielectron channel. The weakening is mainly due to the combined effect of a rapidly falling signal cross-section as the kinematic limit is approached, with an increasing proportion of the signal being produced off-shell in the low-mass tail, and the natural width of the resonance. The selection efficiency also starts to slowly decrease at very high pole masses, but this is a subdominant effect. The observed (expected) lower limits on the pole mass for a SSM Z' boson as well as Z'_χ and Z'_ψ bosons in E6-motivated theories are 4.5 (4.5), 4.1 (4.0), and 3.8 (3.7), respectively. This corresponds to an improvement of approximately 1 TeV in mass reach compared to the previous ATLAS analysis [8], which was based on a subset of the data used in this analysis.

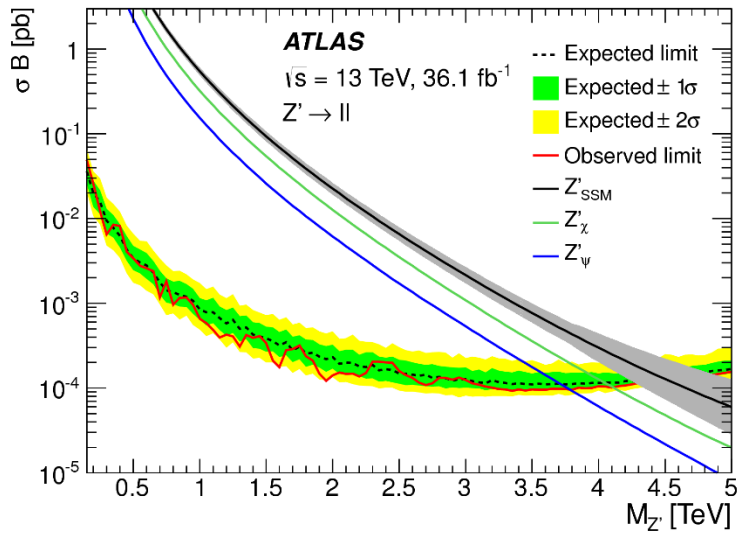


Fig. 4. Upper 95% CL limits on the Z' production cross-section times branching ratio to two leptons of a single flavour as a function of Z' pole mass ($M_{Z'}$). Results are shown for the combined dilepton channel. The signals theoretical uncertainties are shown as a band on the Z' SSM theory line for illustration purposes, but are not included in the σB limit calculation

4. Conclusion

The results of searches for a new heavy gauge boson resonance with the ATLAS detector are reported. The analyses use 36.1 fb^{-1} of $\sqrt{s} = 13$ TeV proton–proton collision data recorded by the ATLAS detector at the LHC in 2015 and 2016. Examining the transverse mass spectra of final states with one charged lepton and large missing transverse momentum and invariant mass spectra of final states with two charged leptons, no significant excesses above the expected SM background are observed. Exclusion limits at 95% CL are placed on the mass of benchmark SSM W' and Z' bosons, as well as Z'_χ and Z'_ψ bosons in E6-motivated theories. Masses for SSM W' bosons up to 5.1 TeV are excluded. Masses for SSM Z' boson, E6-motivated Z'_χ and Z'_ψ bosons up to 4.5, 4.1, and 3.8 TeV are excluded, respectively. These limits exceed previous limits from ATLAS, derived from similar analyses based on 3.2 fb^{-1} of $\sqrt{s} = 13$ TeV data, by approximately 1 TeV.

In 2017, the ATLAS experiment continued taking data. During this period about 47 fb^{-1} of proton–proton collision data was recorded at $\sqrt{s} = 13$ TeV. These data are being used to search for W' and Z' bosons at the moment. The full dataset collected by the ATLAS experiment during LHC Run-2 in 2015–2018 will allow either to discover new heavy gauge boson resonances or to significantly improve the exclusion limits reported in this article.

References

1. G. Altarelli, B. Mele, M. Ruiz-Altaba, *Z. Phys. C* **45**, 109 (1989).
2. D. London, J.L. Rosner, *Phys. Rev. D* **34**, 1530 (1986).
3. P. Langacker, *Rev. Mod. Phys.* **81**, 1199 (2009).
4. E. Salvioni, G. Villadoro, F. Zwirner, *JHEP* **11**, 068 (2009).
5. ATLAS Collaboration, G. Aad *et al.*, *JHEP* **09**, 037 (2014).
6. ATLAS Collaboration, G. Aad *et al.*, *Phys. Rev. D.* **90**, 052005 (2014).
7. ATLAS Collaboration, M. Aaboud *et al.*, *Phys. Lett. B* **762**, 334 (2016).
8. ATLAS Collaboration, M. Aaboud *et al.*, *Phys. Lett. B* **761**, 372 (2016).
9. ATLAS Collaboration, M. Aaboud *et al.*, *Eur. Phys. J. C* **78**, 401 (2018).
10. ATLAS Collaboration, M. Aaboud *et al.*, *JHEP* **10**, 182 (2017).

STUDY OF THE BOSE–EINSTEIN CORRELATIONS AT THE ATLAS DETECTOR

V.A. Schegelsky, M.G. Ryskin

1. Introduction

An effective tool to study the space-time structure of the production amplitude is to measure the Bose–Einstein correlations (BEC) between two identical particles produced in the inclusive hadron interaction, see, for example, Refs. [1–4]. The idea is as follows. To satisfy the Bose–Einstein statistics we have to sum up the amplitudes with all the permutations of the identical secondary bosons. After the permutation of two bosons (pions) the amplitude gets the factor e^{irq} , where the four-vector $q = p_2 - p_1$ is the difference between the pions momenta while $r = r_1 - r_2$ is the space separation between these pions. So the two particle cross section corresponding to the bare production amplitude $M(\dots r_1, r_2 \dots)$ becomes proportional to the factor $(1 + \langle e^{irq} \rangle)$:

$$\frac{E_1 E_2 d^2 \sigma}{d^3 p_1 d^3 p_2} = \frac{1}{2!} |M|^2 \langle 2 + 2e^{irq} \rangle = |M|^2 \langle 1 + e^{irq} \rangle. \quad (1)$$

The angle brackets $\langle \dots \rangle$ denote the averaging over r_1 and r_2 . Due to fast oscillations, the mean value of this exponent for a large q vanishes after integration over the $r_{1,2}$ coordinates. On the other hand, $\langle e^{irq} \rangle \rightarrow 1$ for a very low q , enlarging the cross section two times. So we have a peak at $q \rightarrow 0$, and the inverse width of the peak characterizes the size of the domain from which the pions were emitted.

To extract the effect, the measured Q spectrum

$$Q = \sqrt{-(p_1 - p_2)^2} \quad (2)$$

is compared with a similar one but without BEC. Q is the invariant mass of two BEC particles considered as massless. To be precise, we form the ratio

$$R(Q) = \frac{dN/dQ - dN_{\text{ref}}/dQ}{dN_{\text{ref}}/dQ}, \quad (3)$$

where dN/dQ is the two pion distribution integrated over all the variables except Q , and dN_{ref}/dQ is the distribution expected in the world without BEC. There are different ways to choose dN_{ref}/dQ . We may measure the $\pi^+\pi^-$ Q -distribution for non-identical pions; or we may change the sign of the three momentum of the second pion $\vec{p}_2 = -\vec{p}_2$ in the calculation of the Q value; and so on (*e. g.*, see the very first Large Hadron Collider (LHC) CMS BEC analysis [5]). For the conventional “one-radius” fit the simplest parametrization is commonly used:

$$R(Q) = \lambda e^{-RQ} + a + bQ. \quad (4)$$

The parameter $R = \bar{r}$ is the radius of the radiation area¹, λ can be called as a strength of BEC, and a and b describe the simplest background to BEC. The exponential form approximates the case when the radiation sources are uniformly distributed over the surface of the sphere with the radius \bar{r} . The values of R extracted from the data using one or another reasonable reference function dN_{ref}/dQ , are close to each other. Such an analysis of high energy proton–proton interactions at the LHC was performed by ATLAS [6], CMS [7], and ALICE [8]. For an analysis of lower energy data see, for example, the review in Ref. [4].

However, it was argued in Ref. [9] that the distribution of the coordinates of emission requires two scales as the secondaries produced in high energy hadron collisions may be radiated by small size sources distributed over a much larger area of the proton–proton interaction. To study this point experimentally, we re-analyse the existing ATLAS data on BEC at $\sqrt{s} = 0.9$ and 7 TeV fitting the $R(Q)$ distribution by the formula with two scales

$$R(Q) = \lambda e^{-R_1 Q} + (1 - \lambda) e^{-R_2 Q} + a + bQ. \quad (5)$$

¹ The “mean” radius, \bar{r} , is such that $e^{-\bar{r}Q}$ approximates the value of e^{irq} averaged over r .

Note that we do not introduce two parameters, λ_1 and λ_2 , but in agreement with Eq. (1) fix the sum $\lambda_1 + \lambda_2 = 1$; *i. e.* $\lambda_1 = \lambda$ and $\lambda_2 = 1 - \lambda$. We define $R1$ to be larger than $R2$. In such an approach $R2$ is the radius of radiation source, whereas $R1$ is the distance between two sources, *i. e.* full size of the radiation zone.

The ATLAS experiment set-up and the event selection are described in Ref. [6]. Here we just emphasize that a huge statistics is available in the LHC experiments (about 10^7 minimum bias events in the case of ATLAS at 7 TeV corresponding to more than 10^9 pairs of the same sign secondary hadrons) which allows to re-analyse the data with *two* scales and to study not just the size of the radiative domain but the structure of the hadron production process.

2. Two scales analysis

The “reference” distribution dN_{ref}/dQ was obtained by changing the sign of the three momentum of the second hadron $\vec{p}_2 = -\vec{p}_2$. In our reanalysis, the minimum bias data obtained by ATLAS at $\sqrt{s} = 0.9$ and 7 TeV were used. For the details of the experiment and the events selection see Ref. [6]. Here we consider all charged hadrons as pions and select the particles with transverse momentum $p_t > 0.1$ GeV in the pseudorapidity interval $|\eta| < 2.5$ observed in the central detector. In addition, single diffraction events were excluded by requirement that at least one particle was detected in each end-cap scintillator detector. The majority of the selected hadrons are pions.

The description of the data is shown in Fig. 1. In a traditional analysis one can see a quite interesting feature – the size of the radiation zone looks to be independent of the beam energy, at the same time the mean multiplicity is very much different. It might be an artifact because of a poor statistical quality of the experimental distribution data description. Recall that the value of the mean radius R is the same for the same particle density, $dN_{\text{ch}}/d\eta$ being independent of the colliding protons energy³. This effect was observed for the first time by the UA1 Collaboration in 1989 [10].

The quality of the fits with two different radii model is much better. The value of χ^2/n_{dof} turns out to be more than order of magnitude smaller than that in the conventional one scale fit (Eq. 4). In this analysis, the overall radiation zone size $R1$ has a strong dependence on the beam energy. At the same time, the source size is independent of the energy. As soon as the collected statistics becomes very high, one cannot expect good χ^2/n_{dof} in global fits, after integration over all parameters except the Q -value. In particular, there is a strong dependence on the multiplicity. The multiplicity distribution has an essential beam energy dependence. To exclude the influence of such dependencies, one should perform the data fitting in adequate small bins of the final state phase and get χ^2/n_{dof} more acceptable.

Qualitative features of the distributions at $\sqrt{s} = 900$ GeV are very similar to that at $\sqrt{s} = 7$ TeV, but the statistics at $\sqrt{s} = 7$ TeV is much higher. Therefore, below we will present detailed analysis results for 7 TeV only.

The dependencies of the mean radii, the correlation strengths $\lambda_{1,2}$ and the values of χ^2/n_{dof} on the particles multiplicity N_{ch} are shown in Fig. 2. The bin size is small enough where the parameters change has small influence on the fits statistical quality. One can see that the overall radiation zone size and the correlation strength have strong dependence on the particles multiplicity. The radiation source size is small and independent of the multiplicity. From the top right of Fig. 2 one may conclude that since for $N_{\text{ch}} < 15-20$ the correlation strength $\lambda_2 > 0.5$, each source radiates a small number ($< 15-20$) of particles. The high multiplicity BEC is dominated by pairs from different sources (the corresponding correlation strength is larger than 0.5). Recall that we have to keep the sum of these two correlation strength parameters to be 1. The nearly perfect χ^2/n_{dof} corresponds to the p -value of 0.25.

² This is not the only difference with Ref. [6]. In the publication [6], the unlike pairs distribution used as a reference with a huge influence of low mass resonances produced and the double ratio approach does not exclude this feature. Moreover, large regions in the Q -distributions have to be excluded making impossible to study the space structure of the radiation zone.

³ $dN_{\text{ch}}/d\eta$ should be used if experiments have different η acceptance. The ATLAS and CMS LHC experiments have nearly identical η acceptance, and the multiplicity distribution N_{ch} instead of the particle density may be used.

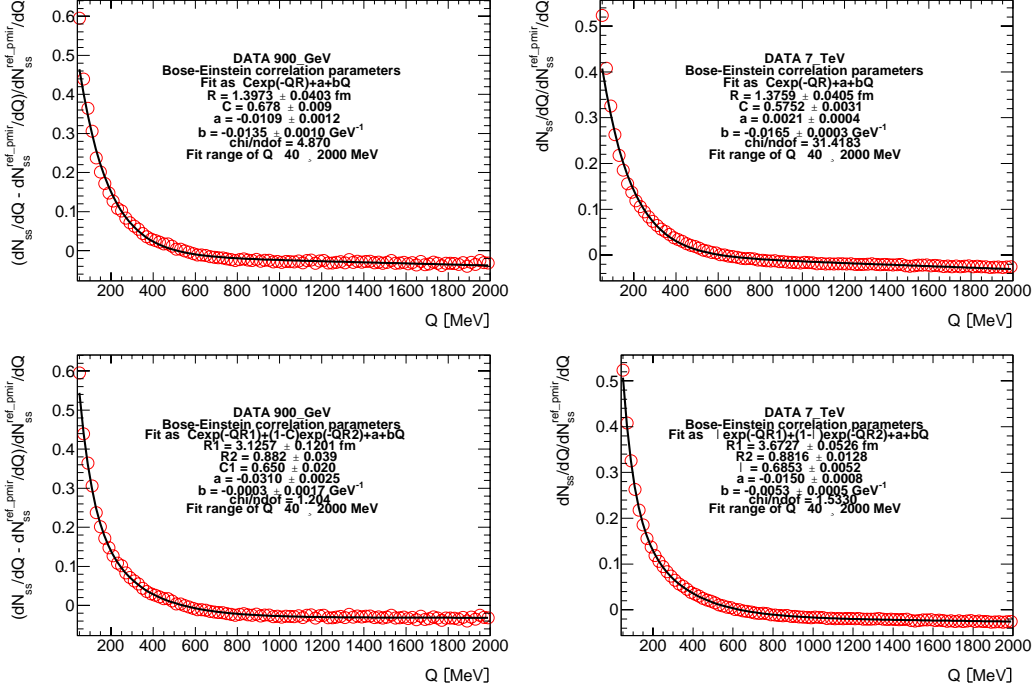


Fig. 1. One (top) and two (bottom) radii global fits of dR/dQ distributions at $\sqrt{s} = 900$ GeV (left) and 7 TeV (right)

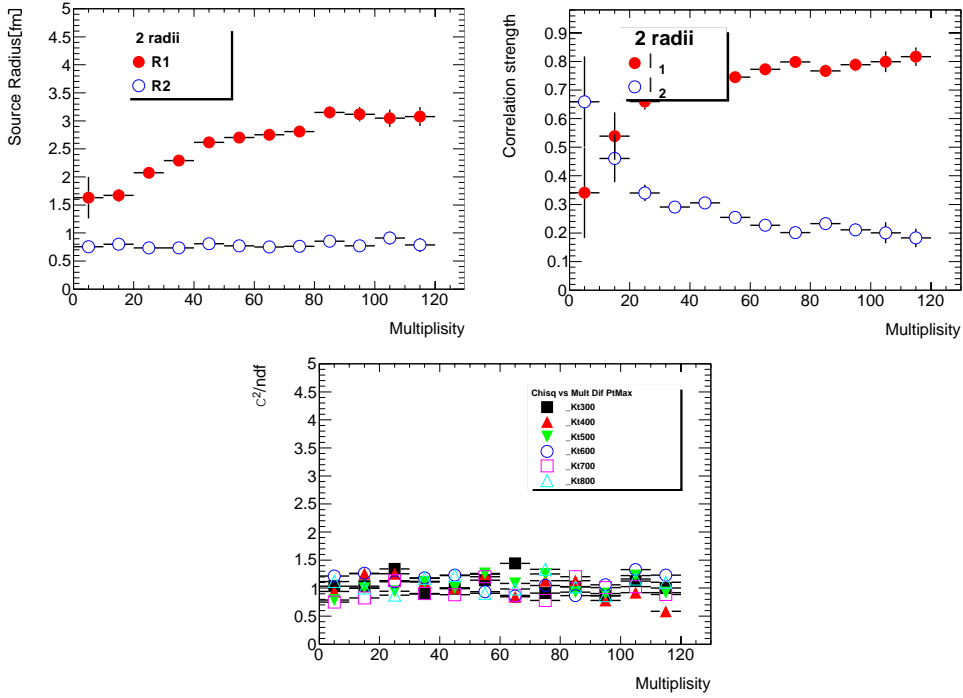


Fig. 2. Fit results with two radii correlation functions for the LHC energy 7 TeV: radiation source size (top left) and correlation strength (top right) as functions of the multiplicity integrated over k_t ; fits $\chi^2/ndof$ as a function of the multiplicity (bottom) in different bins of $k_t = |\vec{p}_{t1} + \vec{p}_t|/2$

Figure 3 shows the small radius $R2$ dependence on the mean transverse momentum $k_t = |\vec{p}_{t1} + \vec{p}_t|/2$ of a BEC pair. This is a typical picture for an interferometry measurement: the smaller the radiation wave length

($\sim 1/k_t$) – the smaller objects might be seen. The drop of $R1$ value might indicate on a screening at the large multiplicity, *i. e.* we do see only nearby sources.

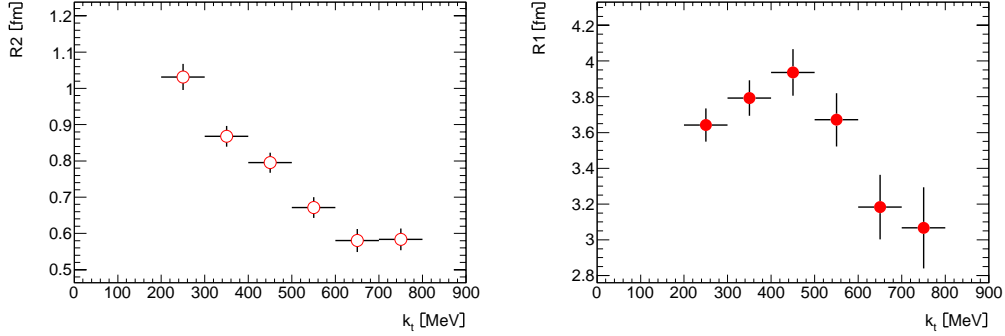


Fig. 3. Two radii BEC fits integrated over the multiplicity for the LHC energy 7 TeV, k_t dependences of radii $R2$ (left) and $R1$ (right)

3. Discussion

Following the original paper [9], where it was proposed to introduce a two scales description of BEC, we focus on the interpretation of the obtained result in terms of a multi-Pomeron approach. Here the “pomeron” denotes a subset of Feynman diagrams which provides the interaction across a large rapidity gap, and whose cross section does not decrease with energy. This may be the Balitsky–Fadin–Kuraev–Lipatov pomeron built of gluons [11] or the multiperipheral ladder diagrams based on the colourless hadron degrees of freedom. It was studied first by Amati *et al.* in Ref. [12]. In the case of general purpose Monte Carlo (MC) generators, such an elementary interaction is described by some hard subprocess supplemented by the backward Dokshitzer–Gribov–Lipatov–Altarelli–Parisi (DGLAP) evolution down to the low scale proton wave function. Each time we deal with a colourless object which in general can be decomposed in terms of the colourless (hadron) degrees of freedom⁴.

We have to emphasize that all the processes of multi-particle production can be described in terms of colourless objects – the incoming colourless hadron wave function, new colourless pairs produced from the vacuum fluctuations and the secondary colour dipoles (or more complicated but the colourless objects). That is, it can be reworded in terms of the colourless (hadron) degrees of freedom. Indeed, many years ago V.N. Gribov discussed the possibility to treat the pomeron as the high energy vacuum fluctuation which contains the $\ln s$ Feynman partons including the “wee” partons with low rapidities in the wave function of a fast hadron. See Ref. [14] where the space-time structure of the process was analysed in details.

However, the one-pomeron exchange is only the beginning of the story. Starting from the one-pomeron amplitude, the s -channel unitarity generates a sequence of multi-pomeron diagrams [15]. The simplest and the most important subset of such diagrams is given by the eikonal model. It corresponds to the expansion of the elastic amplitude (calculated at a fixed impact parameter b)

$$A(b, s) = i(1 - e^{-\Omega(b, s)/2}) \quad (6)$$

in powers of opacity $\Omega(b, s)$. Then the multi-particle production from one or few “cut” pomerons can be calculated with the help of the Abramovsky–Gribov–Kancheli (AGK) cutting rules [16].

Using the AGK rules it is easy to see that the mean number of the “cut” pomerons is $NP = \Omega(b, s)$. In particular, for the central pp collision at $\sqrt{s} = 7$ TeV based on the TOTEM elastic data [17] we expect $NP = \Omega(0, s) \approx 9$ [18]. Recall that according to AGK the particle density generated in the central rapidity interval is proportional to the number of the cut pomerons.

In the case of MC, the process analogous to the multi-pomeron exchange is generated *via* the multiple interaction (MI) option (see, *e. g.*, Ref. [19]).

⁴ In MC this is actually done *via* the hadronization algorithm, implemented, for example, as the Lund string [13].

That is in BEC we have to see at least two different radii – one corresponding to the correlation of two pions emitted from the same string/pomeron and another one caused by the observation of two pions radiated from two different strings/pomerons. The first radius is expected to be rather small. Its value is characterized by the value of the slope, α'_p of the pomeron trajectory or by the typical scale in the DGLAP evolution chain generated by the MC. However, since it is “measured” *via* the pion correlations (and a pion is not a point-like particle) it cannot be much smaller than the pion radius $R_\pi^2 \simeq 0.6 \text{ fm}^2$. The second radius should be larger. The space separation between different pomerons is of the order of two proton–proton interaction radii. The last can be evaluated through the total elastic slope B_{el} . The value of $B_{el} \simeq 20 \text{ GeV}^{-2}$ [17] corresponds to the mean value of $R_p \approx 2.2 \text{ fm}$ [20]. The results presented in Figs. 2 and 3 are in good agreement with the picture described above. Indeed, the small radius $R2$ practically does not depend on the multiplicity, that is on the number of “cut” pomerons in an event (*top left* of Fig. 2) and decreases with \vec{k}_t . When with \vec{k}_t increasing the resolution of our “femtoscope” improves, we observe $R2 \rightarrow R_\pi$ (*left* of Fig. 3). At low multiplicities we deal mainly with the events caused by the one pomeron exchange⁵, and here the contribution of the small radius component, $\lambda_2 = 1 - \lambda_1$, is large. At a larger N_{ch} , which corresponds to a larger number of pomerons N_P , the value of λ_2 decreases while λ_1 increases (*top right* of Fig. 2) since we have a larger combinatorial probability to observe two pions emitted from two different pomerons. The value of the large radius $R1$ increases with the multiplicity – selecting the events with a larger N_{ch} , *i. e.* with a larger N_P , we consider the configurations with a larger area where the wave functions of two incoming protons overlap. That is the pomerons are distributed over a larger area. For a low \vec{k}_t the value of $R1$ does not depend on \vec{k}_t but for a larger \vec{k}_t it starts to decrease (*right* of Fig. 3) – the events with a high transverse momenta (scales) are mainly concentrated in the central part of the collision area.

4. Conclusion

We have shown that the observed Q -distribution of identical pions is much better described by Eq. (5) with two different radii. This may indicate that secondaries are produced by some small size sources distributed over a much larger (of the order of the whole radiation size) domain. These sources may be considered as individual pomerons, or as minijets, or as colour strings between the jets which emit a “spray” of hadrons.

The main result of the present paper is the following. For the first time we observe that the secondaries in BEC are produced by a number of small size sources (hot spots) of the radius $R2 \approx R_\pi$ (or smaller) with a much larger separation $R1$ between the individual sources (hot spots). At last but not least, the value of the radius of a small size object is independent of the LHC energy, *i. e.* this object is a universal one.

For a low particle density $dN_{ch}/d\eta < 2$, the radiation area is smaller than the proton size – that is we deal with only one hot spot.

In terms of the quark–gluon plasma/liquid, that is in terms of collective degrees of freedom, our observation may be treated/interpreted as a hint in favour of a scenario where the hadronization of quark–gluon system passes *via* formation of a number of relatively small size colourless bubbles/drops which finally produce hadrons.

However, it should be noted that due to a small size ($R2$) of radiative sources the probability of this “hot spots” to overlap is rather small even in the case of a heavy ions collision, while the energy density inside each small size “hot spot” is large.

Having the particle identification, it would be interesting to perform the two scales BEC fit for the kaons and/or the protons in order to ascertain whether the space-time structure (BEC) of the production mechanism observed in this case is the same as that for the pions.

The next step is to study the two scales BEC in events with a high E_T jet and/or W/Z bosons.

Finally, looking for the two scales BEC in the events with a large rapidity gap (LRG) we expect to see a much smaller contribution of the large size component. Indeed, in the case of a pomeron interpretation observing the LRG we select the events without an additional pomeron exchange across the gap region. That

⁵ Of course, the distribution over the number of pomerons is washed out due to fluctuations in the particle densities produced by individual pomerons.

is the probability of a MI is suppressed and in the first approximation one may say that the large size component should be absent. To be more precise, we may observe some large size contribution corresponding to the multi-pomeron exchange in the pomeron–proton collision. However, the probability of the multi-pomeron interactions in pomeron–proton collisions should be smaller due to a smaller pomeron–proton cross section.

References

1. R. Hanbury-Brown, R.W. Twiss, *Phil. Mag.* **45**, 663 (1954); *Proc. Roy. Soc.* **242** A, 300 (1957); *ibid* **243** A, 291 (1957).
2. G. Goldhaber, W.B. Fowler, S. Goldhaber *et al.*, *Phys. Rev. Lett.* **3**, 181 (1959).
3. G.I. Kopylov, M.I. Podgoretskii, *Sov. J. Nucl. Phys.* **15**, 219 (1972); *Sov. J. Nucl. Phys.* **18**, 336 (1973).
4. G. Alexander, *Rep. Prog. Phys.* **66**, 481 (2003).
5. CMS Collaboration, V. Khachatryan *et al.*, *Phys. Rev. Lett.* **105**, 032001 (2010).
6. ATLAS Collaboration, G. Aad *et al.*, *Eur. Phys. J. C* **75**, 466 (2015).
7. CMS Collaboration, V. Khachatryan *et al.*, *JHEP* **1105**, 029 (2011).
8. ALICE Collaboration, K. Aamodiet *et al.*, *Phys. Rev. D* **84**, 112004 (2011).
9. V.A. Khoze, A.D. Martin, M.G. Ryskin, V.A. Schegelsky, *Eur. Phys. J. C* **76**, 193 (2016).
10. UA1 Collaboration, C. Albajar *et al.*, *Phys. Lett. B* **226**, 410 (1989).
11. B.L. Ioffe, V.S. Fadin, L.N. Lipatov, *Quantum chromodynamics: Perturbative and non-perturbative aspects*, Cambridge Univ. Pr., 2014.
12. D. Amati, A. Stanghellini, S. Fubini, *Nuovo Cim.* **26**, 896 (1962).
13. B. Andersson, G. Gustafson, C. Peterson, *Zh. Phys. C* **1**, 105 (1979); B. Andersson, G. Gustafson, G. Ingelman, T. Sjostrand, *Phys. Rept.* **97**, 31 (1983).
14. V.N. Gribov, *The Theory of Complex Angular Momenta*, Appendix A1, Cambridge Univ. Pr., 2003.
15. V.N. Gribov, *Sov. Phys. JETP* **26**, 414 (1968); *Zh. Eksp. Teor. Fiz.* **53**, 654 (1967).
16. V. Abramovsky, V.N. Gribov, O.V. Kancheli, *Sov. J. Nucl. Phys.* **18**, 308 (1964).
17. TOTEM Collaboration, G. Antchev *et al.*, *Europhys. Lett.* **101**, 21002 (2013).
18. M.G. Ryskin, A.D. Martin, V.A. Khoze, *Eur. Phys. J. C* **72**, 1937 (2012).
19. T. Sjostrand, S. Mrenna, P.Z. Skands, *Comput. Phys. Commun.* **178**, 852 (2008).
20. V.A. Schegelsky, A.D. Martin, M.G. Ryskin, V.A. Khoze, *Phys. Lett. B* **703**, 288 (2011).

STUDY OF RARE DECAYS OF B^0 AND B_s^0 MESONS IN THE LHCb EXPERIMENT

PNPI participants of the LHCb Collaboration:

G.D. Alkhazov, N.F. Bondar, A.D. Chubykin, A.A. Dzyuba, S.N. Kotryakhova, O.E. Maev,

Yu.A. Shcheglov, N.R. Sagidova, A.A. Vorobyev

1. Introduction

In the Standard Model (SM) of the particle physics, the decays of neutral beauty mesons B^0 into lepton pairs (with or without additional hadrons) in the final states proceed *via* the $b \rightarrow s$ or $b \rightarrow d$ flavour-changing neutral current (FCNC) transition. Such processes are suppressed as they are forbidden at the tree-level and can proceed *via* loop diagrams of the electroweak penguin or box types diagrams. In extensions of the SM, new particles may enter in competing processes and can significantly change the decay branching fraction and the angular distribution of the final-state particles. Thus, precision studies of such decays provide a natural test of the SM predictions and could provide evidence of new physics (NP).

PNPI group is involved in the LHCb project mainly through the design, construction, and operation of the LHCb muon system. Also, PNPI physicists take part in analyses of the experimental data related to studies of the rare B -meson decays. This report presents several LHCb results obtained in 2015–2017 years.

2. The $B_{(s)}^0 \rightarrow \mu^+\mu^-$ decays

In the SM, there are strict theoretical predictions for the B_s^0 and B^0 decays by the $\mu^+\mu^-$ channel. The time-integrated branching fractions of these loop-driven helicity suppressed processes are predicted to be $B(B_s^0 \rightarrow \mu^+\mu^-) = (3.65 \pm 0.23) \cdot 10^{-9}$ and $B(B^0 \rightarrow \mu^+\mu^-) = (1.06 \pm 0.09) \cdot 10^{-10}$, respectively, which makes them sensitive probes for NP. The first observation of the B_s^0 decay in the dimuon channel was reported in a combined analysis of the LHCb and CMS results. Recently, LHCb extended these studies by using a pp dataset corresponding to the integral luminosity of 4.4 fb^{-1} collected during Run-1 in 2011–2012 for the centre-of-mass energy 7 and 8 TeV and during Run-2 in 2015–2016 for 13 TeV [1].

The candidates for dimuon decays of B_s^0 were classified according to their mass and the output variable, a multivariate classifier based on a boosted decision tree (BDT), which is employed to separate the signal and the combinatorial background. The BDT was optimized using simulated samples of $B_s^0 \rightarrow \mu^+\mu^-$ events and the $b\bar{b} \rightarrow \mu^+\mu^-X$ events for the background. The BDT variable is constructed to be distributed uniformly in the range $[0, 1]$ for the signal, and to peak strongly at zero for the background. It has less than 5% residual correlation with the dimuon mass. The multivariate classifier makes a decision on the base of the kinematical parameters of the decay as well as on the isolation variables, which was new in this version of the analysis and allowed to increase the background suppression by approximately 50% for the $\text{BDT} > 0.25$.

An excess of the B_s^0 candidates over the expected background was observed with a significance of 7.8 standard deviations (σ), while the significance of the $B^0 \rightarrow \mu^+\mu^-$ signal is 1.6σ . The signal for the $\text{BDT} > 0.5$ requirement presented in Fig. 1 demonstrates a clear excess of the candidates in the B_s^0 mass range. The $B^+ \rightarrow J/\psi K^+$ and $B^0 \rightarrow K^+\pi^-$ decays have been used as normalization channels. Their yields, the efficiency ratios, and the f_s/f_d parameter, previously determined by LHCb, were used to determine the branching fraction of the $B_s^0 \rightarrow \mu^+\mu^-$ decay, which turns to be $(3 \pm 0.6_{-0.2}^{+0.3}) \cdot 10^{-9}$. The upper limit on the $B^0 \rightarrow \mu^+\mu^-$ decay was set with the CL_s method to be $3.4 \cdot 10^{-10}$ at 95% confidence level. These are the most precise measurements of these quantities to date. The results are in agreement with the SM predictions and tighten the existing constraints on possible NP contributions to these decays.

The mass eigenstates for the system of the B_s^0 meson and the corresponding antiparticle are characterized by the difference between their decay width $\Delta\Gamma = 0.082 \pm 0.007 \text{ ps}^{-1}$. Only the heavy state can decay into the $\mu^+\mu^-$ pair in the SM, but NP could violate this scenario. The first moment of the time dependent width distribution for the $B_s^0 \rightarrow \mu^+\mu^-$ decay, called the effective lifetime ($\tau_{\mu\mu}$), is sensitive to NP. The dependency of $\tau_{\mu\mu}$ on the B_s^0 -meson mean lifetime and $\Delta\Gamma$ includes the $A_{\Delta\Gamma}$ parameter, which has to be $A_{\Delta\Gamma} = 1$ for

the SM but could vary in the range $[-1, 1]$ for its extensions. Therefore, the measurement of the effective lifetime can be also used as a tool for NP searches.

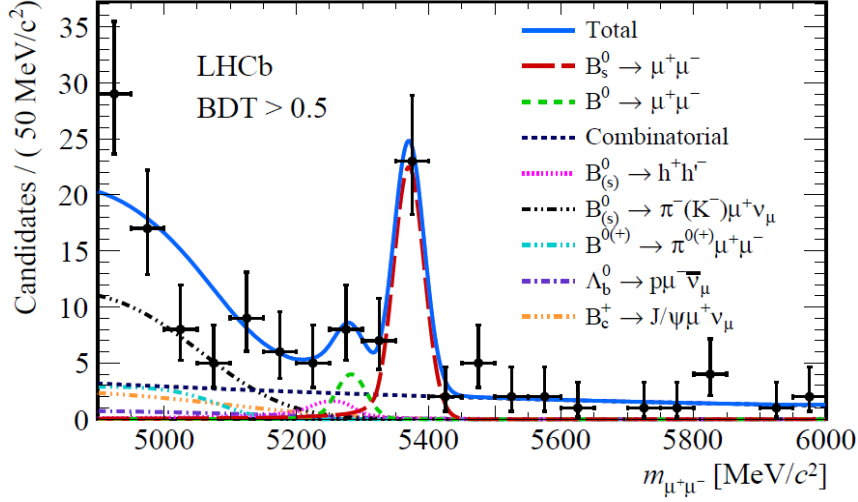


Fig. 1. The dimuon mass distribution for selected candidates with the $\text{BDT} > 0.5$ requirement

The selection efficiency and the BDT distribution for the $B_s^0 \rightarrow \mu^+\mu^-$ decays depend on the lifetime, which in turn depends on the model assumption (absence or presence of NP). This introduces a further model dependence in the measured time-integrated branching fraction. For the nominal $B(B_s^0 \rightarrow \mu^+\mu^-)$ value evaluation, the SM expectation (*i. e.* $A_{\Delta\Gamma} = 1$) was used. The deviations from this value by 4.6% and by 10.9% should occur if one chooses the $A_{\Delta\Gamma} = 0$ and $A_{\Delta\Gamma} = -1$ NP hypotheses, respectively.

The background subtraction for determination of $\tau_{\mu\mu}$ was done by the *sPlot* technique, using a fit to the dimuon mass distribution. Subsequently, a fit to the signal decay-time distribution is made with an exponential function multiplied by the acceptance function of the detector. Similar selection criteria to those applied in the branching fraction analysis were used for the B_s^0 -meson candidates, the main differences being a reduced dimuon mass window and the looser particle identification requirements on the muon candidates. A requirement of $\text{BDT} > 0.55$ was imposed instead of performing a fit in bins of BDT. This selection results in a final sample of 42 candidates. The variation of the trigger and the selection efficiencies with the decay time is corrected in the fit by introducing an acceptance function, determined from the simulated signal events that are weighted to match the properties of the events seen in the data. The control measurement of the effective lifetime in the $B^0 \rightarrow K^+\pi^-$ decay channel gave 1.52 ± 0.03 ps, where the uncertainty is statistical only. This measurement is consistent with the world average.

The background-subtracted $B_s^0 \rightarrow \mu^+\mu^-$ decay-time distribution together with the fit result is presented in Fig. 2. The fit result is $\tau_{\mu\mu} = 2.04 \pm 0.44 \pm 0.05$ ps, where the first uncertainty is statistical and the second is systematic. This measurement is consistent with the $A_{\Delta\Gamma} = 1$ (SM) hypothesis at the 1σ level. At the present statistics, this result impose a rather weak constraint on the $A_{\Delta\Gamma}$ value but this constraint could be tightened significantly with the datasets that LHCb is expected to collect in the coming years. Thus, the measurement of the rare dimuon decays of the B_s^0 mesons has become a discovery tool for NP searches.

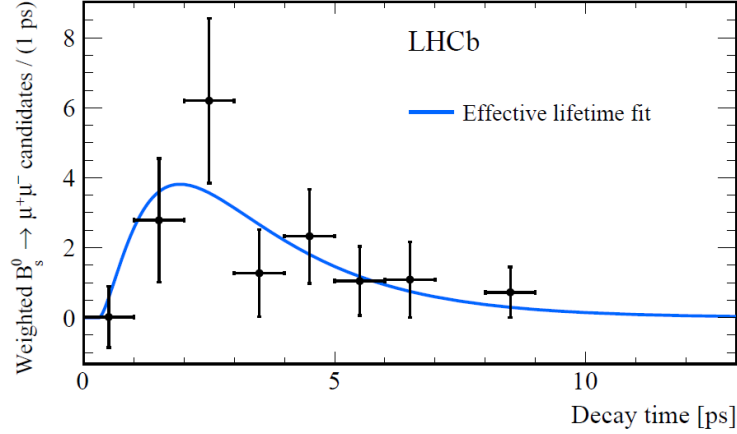


Fig. 2. The background-subtracted $B_s^0 \rightarrow \mu^+\mu^-$ decay-time distribution together with the result of the fit

3. Searches for the $B_{(s)}^0 \rightarrow \tau^+\tau^-$ decays

The decay of the neutral B mesons into the $\tau^+\tau^-$ final state is much more challenging from experimental point of view due to the short lifetime of the τ lepton. The current SM predictions for decays into a pair of τ leptons are $B(B_s^0 \rightarrow \tau^+\tau^-) = (7.73 \pm 0.49) \cdot 10^{-7}$ and $B(B^0 \rightarrow \tau^+\tau^-) = (2.22 \pm 0.19) \cdot 10^{-8}$, while the upper limit for the branching fraction $B(B^0 \rightarrow \tau^+\tau^-)$ determined experimentally by the BaBar Collaboration is $4.1 \cdot 10^{-3}$ (90% CL). No direct limits on $B(B_s^0 \rightarrow \tau^+\tau^-)$ have been established so far, though this branching fraction can be indirectly constrained to be less than 3 at 90% CL. Different scenario of NP such as leptoquarks, W'/Z' bosons, or a two-Higgs-doublet model can enhance the $B_{(s)}^0 \rightarrow \tau^+\tau^-$ branching fraction by several orders of magnitude with respect to the SM predictions.

The LHCb experiment was able to push down the limits for $B(B_{(s)}^0 \rightarrow \tau^+\tau^-)$ using the Run-1 dataset corresponding to the integral luminosity of 3 fb^{-1} [2]. The τ leptons were reconstructed through the hadronic decay $\tau^- \rightarrow \pi^+\pi^-\pi^-\nu_\tau$, which has a 9.3% branching fraction and dominantly proceeds through the chain of the hadronic resonances $\nu_\tau a_1(1260)^-$ at the first step and $a_1(1260)^- \rightarrow \rho\pi^-$ at the second step. Due to the final-state neutrinos, the $\tau^+\tau^-$ mass provides only a weak discrimination between the signal and the background, and it cannot be used to distinguish the B_s^0 decays from the B^0 decays. The number of signal candidates was obtained from a fit to the output of a neural network (NN) based multivariate classifier that uses several kinematic and topological variables as the input. The NN output is transformed to obtain a distribution for the signal over the range $[0.0, 1.0]$, while the background peaks towards zero. Data-driven methods are used to determine the signal and the background models. The overall selection efficiency determined using simulated $\tau^+\tau^-$ decays of B mesons is approximately $2.2 \cdot 10^{-5}$, including the geometrical acceptance.

The $B^0 \rightarrow D_s^+D^-$ decay is used as a control channel to check that the signal is not mismodelled in the simulation (Fig. 3). Ten variables are found to be slightly mismodelled and their distributions are corrected by weighting. The output of the neural network and its description with the model containing the background and the possible signal contribution is presented in Fig. 3. The fit procedure is validated with pseudo-experiments, and it is found to be unbiased. Negative values were allowed in the fitting. The fit gives a signal yields $-23_{-53}^{+63}(\text{stat})_{-40}^{+41}(\text{syst})$ for the $B_s^0 \rightarrow \tau^+\tau^-$ decay, $-15_{-56}^{+67}(\text{stat})_{-42}^{+44}(\text{syst})$ for the $B^0 \rightarrow \tau^+\tau^-$ decay. The signal yield obtained from the likelihood fit is translated into an upper limit using the CL_s method. The corresponding upper limits on the branching fractions are $B(B_s^0 \rightarrow \tau^+\tau^-) < 6.8 \cdot 10^{-3}$, which is the first experimental limit for this quantity, and $B(B^0 \rightarrow \tau^+\tau^-) = 2.1 \cdot 10^{-3}$, which constitutes a factor 2.6 improvement with respect to the previous result.

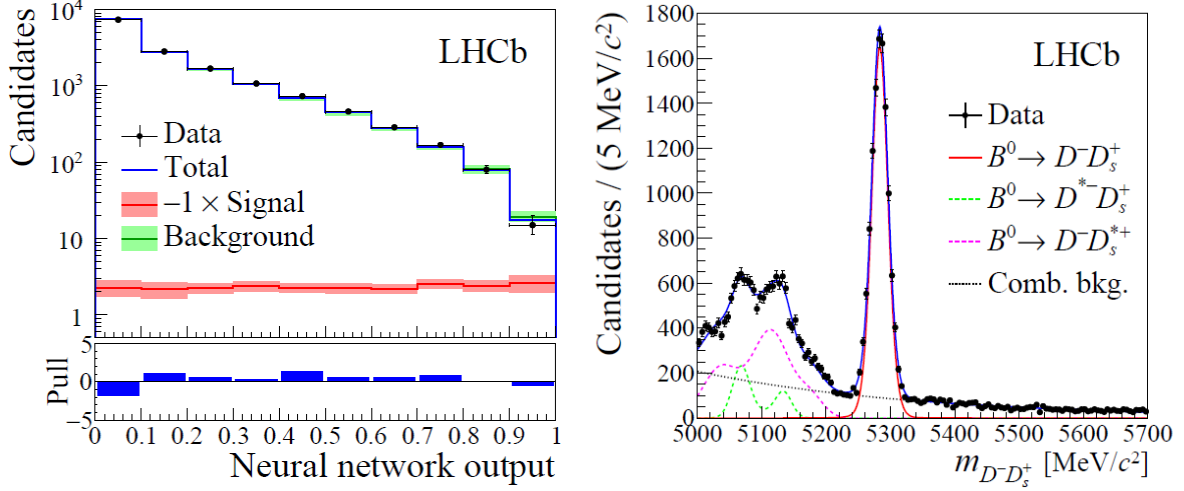


Fig. 3. Left panel – the distribution of the NN output in the signal region (black points), with the total fit result (blue line) and the background component (green line); the fitted $B_s^0 \rightarrow \tau^+\tau^-$ signal component is negative and is therefore shown multiplied by -1 (red line). Right panel – control channel

4. The angular analysis of the $B^0 \rightarrow K^{*0}\mu^+\mu^-$ decay

The three-body decays with dimuons are also the loop driven FCNC processes. The angular distribution of such decays can be predicted in the SM thus providing a powerful tool to search for NP. The LHCb experiment performed an angular analysis of the $B^0 \rightarrow K^{*0}\mu^+\mu^-$ decay followed by the $K^{*0} \rightarrow K^+\pi^-$ decay [3]. The Run-1 dataset corresponding to the integrated luminosity of 3 fb^{-1} was used in these studies. After some loose preselection requirements, the signal candidates were selected using a BDT trained with the $B^0 \rightarrow K^{*0}J/\psi(\rightarrow \mu^+\mu^-)$ decay data as a proxy for the signal events. The candidates from the upper mass sideband were used as a proxy for the background. The signal yield in the most interesting low invariant mass squared of the dimuon system region $1.1 < q^2 < 6.0 \text{ GeV}^2/c^4$ was found to be 624 ± 30 decay candidates. The non-resonant (non- J/ψ and non- $\psi(2S)$) part of the distribution for the full q^2 range is presented in Fig. 4.

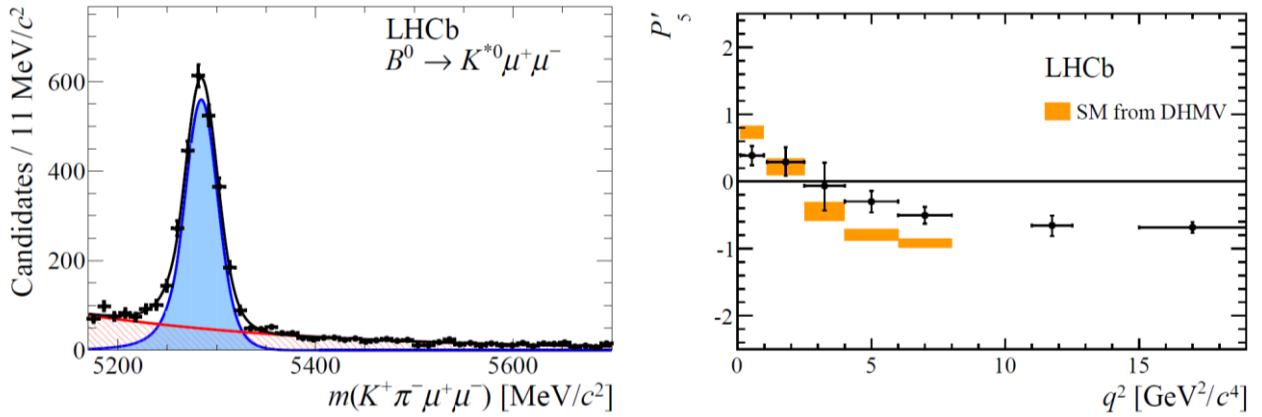


Fig. 4. Left panel – the mass distribution for the $B^0 \rightarrow K^{*0}\mu^+\mu^-$ decay candidates; overlaid are the projections of the total fitted distribution (black line) and the signal and background components; the signal is shown by the blue shaded area and the background by the red hatched area. Right panel – measured dimuon mass dependence for the P'_5 observable. The LHCb data are shown by the black points; the yellow bands are the SM predictions

The complete angular information from the decay is used to determine the CP -averaged observables and the CP asymmetries, taking account of possible contamination from decays with the $K^+\pi^-$ system in

an S -wave configuration. The angular observables and their correlations are reported in the bins of q^2 . A global fit is also performed to the complete set of the CP -averaged observables obtained from the maximum likelihood fit. Six complex decay amplitudes that describe the decay are extracted in the bins of q^2 . On their base the optimized angular observables could be produced. There is a particular interest in these observables because their theoretical prediction is much less dependent on understanding of the hadronic form-factors involved in turning a B meson into a K^* meson. These observables (named as P_{1-3} and $P'_{4,5,6,8}$) are therefore ideal for searching for the effects of new particles in this decay.

This fit indicates differences with predictions based on the SM at the level of 3.4 standard deviations. Mainly these deviations come from the $4 < q^2 < 8 \text{ GeV}^2/c^4$ region for the P'_5 observable (see Fig. 4). These differences could be explained by contributions from physics beyond the SM, or by an unexpectedly large hadronic effect that is not accounted for in the SM predictions.

5. Lepton universality test with dilepton decays of the b hadron

The SM predicts that the electroweak couplings of leptons to gauge bosons are independent of their flavor, and the model is referred to as exhibiting lepton universality (LU). The FCNC transitions provide a unique possibility to test LU for the electroweak loop driven transitions. If NP particles have different couplings with the leptons of different generations, a sizeable increase or decrease in the rate of some particular decays can be measured. The ratios of the type $R_H = \int [d\Gamma(H_b \rightarrow H\mu^+\mu^-)/dq^2] dq^2 / \int [d\Gamma(H_b \rightarrow He^+e^-)/dq^2] dq^2$, where H_b represents the b hadron and H represents the strange hadron, are sensitive probes for such effects. As an example, the R_{K^*} is expected to be close to unity in the SM for the $H_b = B^0$ and $H = K^{*0}$ case. Only a small deviation from the unit in the low- q^2 region is expected due to the phase-space effects.

The LHCb has performed the measurement of the double ratio of the branching fractions [4]. The ratio R_{K^*} determined in the two q^2 bins between zero and $6 \text{ GeV}^2/c^2$ is divided by the ratio R_{K^*} determined in the region of q^2 where the J/ψ resonance dominates. The experimental quantities relevant for the measurement are the yields and the reconstruction efficiencies of the four decays entering in the double ratio. Due to similarity between the experimental efficiencies of the non-resonant (low- q^2) and resonant (J/ψ) decay modes, many sources of the systematic uncertainty are substantially reduced. The decay of the J/ψ into dileptons is measured to be consistent with LU.

The experimental environment in which the LHCb detector operates leads to significant differences in the treatment of decays involving muons or electrons in the final state. Electrons emit a much larger amount of bremsstrahlung which, if not accounted for, would result in a significant degradation of the momentum resolution and consequently in a degradation of the B mass resolution. Though a dedicated bremsstrahlung recovery procedure is used to improve the electron momentum reconstruction, the corresponding mass resolution of the reconstructed B candidates is worse than that in the final states with muons, as the background contamination in the signal region is larger. The level of combinatorial background, arising from the accidental association of particles produced by different b - and c -hadron decays, is also higher in such channels due to a larger number of electron candidates. The result of the fit for the electron channel is presented in the *left panel* of Fig. 5. The statistics for the dielectron channel is the limiting factor for this measurement.

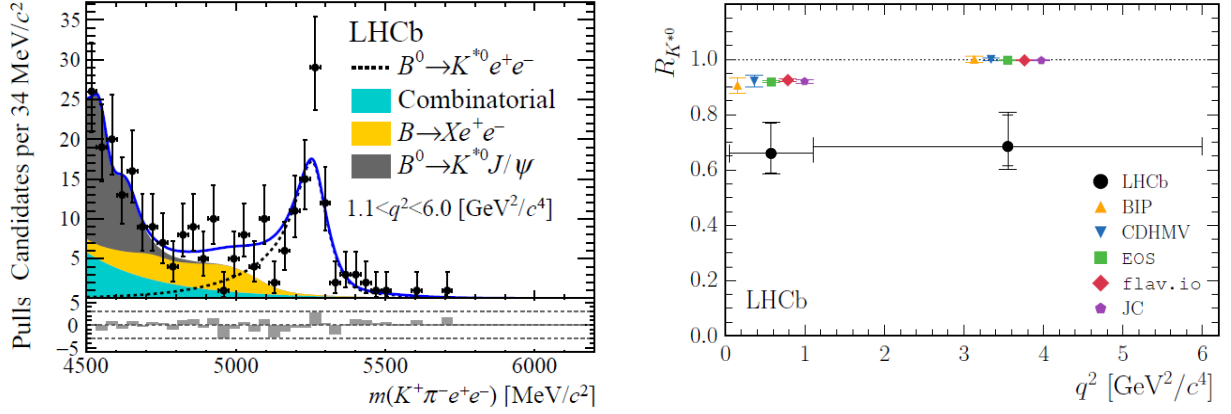


Fig. 5. The mass distribution for the $B^0 \rightarrow K^{*0} e^+ e^-$ decay candidates for the central q^2 mass bin (*left panel*). Comparison of the LHCb R_{K^*} measurements with the different SM predictions, which are displaced horizontally for presentation (*right panel*)

The obtained yields are corrected for the efficiency of selecting each decay mode. This correction is defined as the product of the geometrical acceptance of the detector, the complete reconstruction efficiency of all tracks, the trigger requirements, and the full set of kinematic, particle identification, and background rejection requirements. All efficiencies are determined using simulation that is tuned to the data and accounts for the bin migration in q^2 due to resolution (an order of several percent effect), final state radiation, and bremsstrahlung in the detector.

The results for the ratio R_{K^*} are presented in the right panel of Fig. 5, where they are compared with the available SM predictions. The obtained values are compatible with the previous measurements from the B factories. The incompatibility with the SM expectations is determined to be 2.1–2.3 and 2.4–2.5 standard deviations for the low- q^2 ($0.045 < q^2 < 1.1 \text{ GeV}^2/c^2$) and for the central- q^2 ($1.1 < q^2 < 6.0 \text{ GeV}^2/c^2$) regions, respectively, depending on the theory prediction used. The corresponding 95.4% confidence level intervals are [0.52, 0.89] and [0.53, 0.94], respectively.

6. Conclusion

The LHCb detector is the world leader in studies of the dilepton decays of the b hadron. Such decays, being strongly suppressed in the SM, offer an attractive area for search of the effects related with NP. In particular, presented in this report results on the $B_s^0 \rightarrow \mu^+ \mu^-$ decay impose a strong constraint on the Minimal Super Symmetry Model. The obtained results proved to be in impressive agreement with the SM. On the other hand, the studies of the angular distributions in the $B^0 \rightarrow K^{*0} \mu^+ \mu^-$ decay resulted in some hints (3.4σ) on possible deviations from predictions given by the SM. Also, the measured branching ratio of the $B^0 \rightarrow K^{*0} e^+ e^-$ and $B^0 \rightarrow K^{*0} \mu^+ \mu^-$ decays revealed a noticeable disagreement with the expectations on the basis of the SM, which might indicate a possible violation of lepton universality. In the future, LHCb plans to operate with five times higher luminosity that will further increase the potential for discoveries in this experiment.

Note that a crucial role in the dilepton studies plays the LHCb muon system designed and constructed with an active participation of PNPI. During Run-1 and Run-2, the PNPI group shared responsibility for operation of the muon system.

References

1. LHCb Collaboration, Phys. Rev. Lett. **118**, 191801 (2017).
2. LHCb Collaboration, Phys. Rev. Lett. **118**, 251802 (2017).
3. LHCb Collaboration, JHEP **02**, 104 (2016).
4. LHCb Collaboration, JHEP **08**, 055 (2017).

DISCOVERY OF NEW HEAVY CHARM BARYONS IN THE LHCb EXPERIMENT

PNPI participants of the LHCb Collaboration:

G.D. Alkhazov, N.F. Bondar, A.D. Chubykin, A.A. Dzyuba, S.N. Kotryakhova, O.E. Maev, N.R. Sagidova, Yu.A. Shcheglov, A.A. Vorobyev

1. Introduction

The LHCb experiment is exploiting unprecedented high rates of the charm and beauty hadrons produced in the forward direction ($2 < \eta < 5$). Therefore, the search for new baryons predicted by the quantum chromodynamic part of the Standard Model (SM) and new excited states of already discovered c and b baryons, as well as exotic (pentaquark) states, is a natural part of the LHCb physics program.

2. Observation of a doubly charmed baryon

All expected ground states of the baryons with the charm quantum number equal to 0 or 1 were observed in the past, while the baryons containing two c quarks, which form the isospin doublet ($\Xi_{cc}^{++} = ccu$ and $\Xi_{cc}^+ = ccd$) and the isospin singlet ($\Omega_{cc}^+ = ccs$) with $J^P = \frac{1}{2}^+$, were not reliably seen. Different theoretical models predicted the range of the mass for the iso-doublet to be between $3.5 \text{ GeV}/c^2$ and $3.7 \text{ GeV}/c^2$ with a few MeV/c^2 isospin splitting. The predictions for the lifetime of the Ξ_{cc}^+ baryon are in the range from 50 to 250 fs, and the lifetime of the Ξ_{cc}^{++} baryon is expected to be between 200 and 1 000 fs. The leading channels of the Ξ_{cc}^{++} baryon decay were predicted to be $\Lambda_c^+ K^- \pi^+ \pi^+$ and $\Xi_c^+ \pi^+$ (the corresponding Feynman diagrams are presented in Fig. 1).

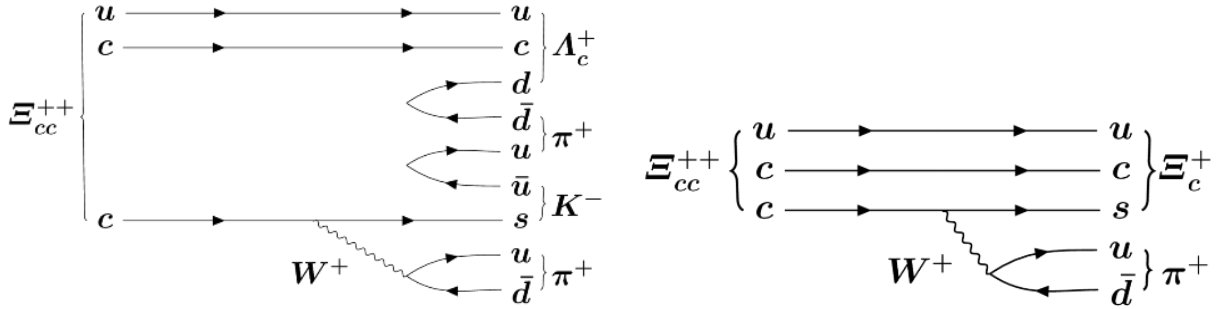


Fig. 1. Examples of the Feynman diagrams contributing to the decay channels of the Ξ_{cc}^{++} baryon

In the past, the SELEX Collaboration reported an experimental observation of the Ξ_{cc}^+ baryon with the mass of $3519 \pm 2 \text{ MeV}/c^2$ in the $\Lambda_c^+ K^- \pi^+$ decay channel (with a statistical significance of 6.3σ) and evidence for the $pD^+ K^-$ decay channel (4.8σ significance). These experimental results were based on very small statistics. Later, these measurements were not confirmed by the FOCUS, BaBar, Belle, and LHCb Collaborations. However, because the production environments for these experiments differ from that at SELEX which studied collisions of a hyperon beam on fixed nuclear targets, these null results do not exclude the original observations.

The LHCb experiment reported the first observation of the Ξ_{cc}^{++} baryon *via* the decay mode $\Lambda_c^+ K^- \pi^+ \pi^+$ with the Λ_c^+ baryon reconstructed in the $pK^- \pi^+$ final state [1]. This observation was based on an analysis of the proton–proton collision data collected at the centre-of-mass energy of 13 TeV corresponding to an integrated luminosity of 1.7 fb^{-1} (Run-2 data). It was also confirmed in an analysis of an additional sample of data collected by LHCb at 8 TeV (Run-1 data). A multivariate analysis based on the multilayer perception algorithm, trained with the simulated signal events and with a control sample of the data to represent the background, provided a 12σ significance for the peak in the $\Xi_{cc}^{++} \rightarrow \Lambda_c^+ K^- \pi^+ \pi^+$ decay channel for the 13 TeV dataset (Fig. 2). The local statistical significance of the peak in the 8 TeV sample is above 7σ , and its mass is consistent with that in the 13 TeV data sample. The signal yield in the Run-2 data set is by

a factor of three larger than that in the Run-1 sample, which is partially due to an increase of the baryon production cross section and partially due to a more effective technique performing the online event reconstruction. The events selected at the trigger level were transferred directly into the storage, and this allowed to increase the number of recorded candidates.

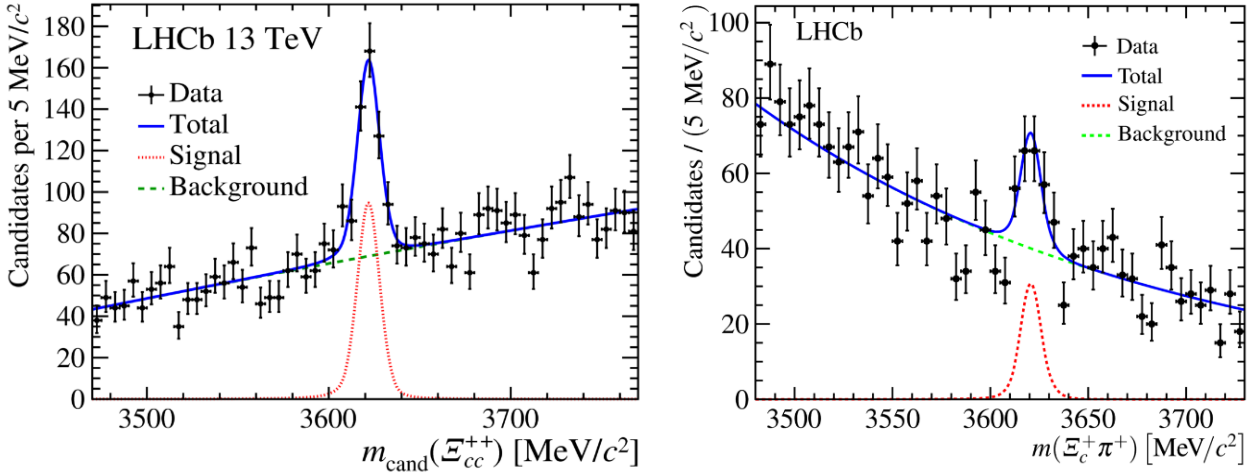


Fig. 2. Mass distributions for the $\Lambda_c^+ K^- \pi^+ \pi^+$ (left panel) and Ξ_{cc}^{++} (right panel) systems (the Run-2 data). The lines correspond to the fit to the experimental data

The measured mass of the Ξ_{cc}^{++} state is found to be $3621.40 \pm 0.70 \pm 0.27 \pm 0.14$ MeV/ c^2 , where the first uncertainty is statistical, the second is systematic and the last one is due to the limited knowledge of the Λ_c^+ mass. The peaking structure at the same mass region was also observed for the $\Xi_c^+ \pi^+$ decay channel [2] (see Fig. 2). The statistical significance of the observed peak is 5.9σ , and its mass is in good agreement with the measured value for the $\Lambda_c^+ K^- \pi^+ \pi^+$ decay channel (Fig. 3). The combination of these two measurements determines the Ξ_{cc}^{++} mass to be $3621.24 \pm 0.65 \pm 0.31$ MeV/ c^2 .

The lifetime of the observed Ξ_{cc}^{++} baryon was determined using the $\Lambda_b^0 \rightarrow \Lambda_c^+ \pi^- \pi^+ \pi^-$ decay as a control channel with the similar topology and the known lifetime. Such a technique leads to a reduced systematic uncertainty as it is only sensitive to the ratio of the decay-time acceptances determined with the simulations. The Ξ_{cc}^{++} lifetime is measured by performing a weighted, unbinned maximum-likelihood fit to the decay-time distribution of the selected sample of the doubly charmed baryons (Fig. 3). The measured lifetime proved to be $256 \pm 23 \pm 14$ fs [3], and it favours the smaller values in the range of the theoretical predictions. If the lifetime of the isospin partner state Ξ_{cc}^+ is shorter by a factor of 3 to 4 as predicted, it would be roughly 60–90 fs.

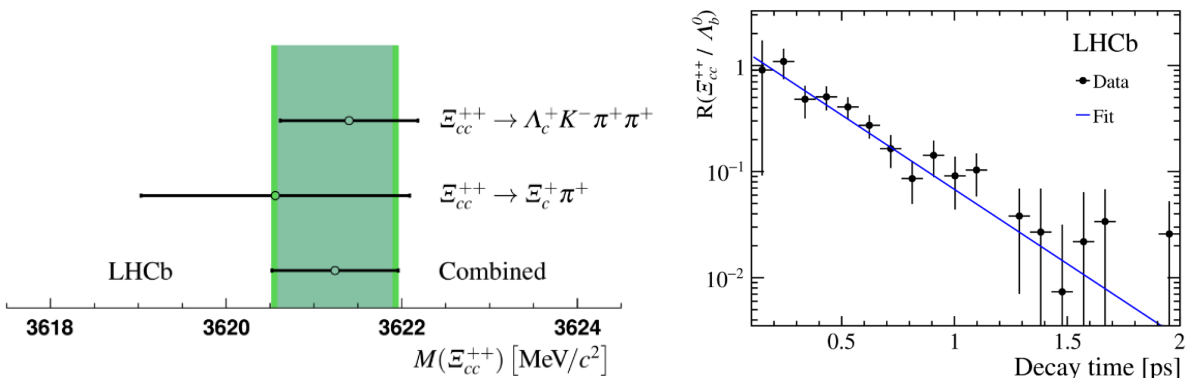


Fig. 3. The measured mass of the doubly charmed baryon for the $\Lambda_c^+ K^- \pi^+ \pi^+$ and $\Xi_c^+ \pi^+$ final states (left panel). The ratio of the decay-time distributions for the $\Xi_{cc}^{++} \rightarrow \Lambda_c^+ K^- \pi^+ \pi^+$ and $\Lambda_b^0 \rightarrow \Lambda_c^+ \pi^- \pi^+ \pi^-$ decays; the blue line corresponds to the best approximation made by the model which contains the Ξ_{cc}^{++} lifetime as a free parameter (right panel)

3. Observation of excited states of the Ω_c baryon

Till 2017, Ω_c remained the only baryon with no excited states observed. The observed Ω_c and $\Omega_c(2770)^0$ states, with the $c s s$ quark content, presumed to be $1/2^+$ and $3/2^+$ ground states. LHCb have performed searches for the excited states in the $\Xi_c^+ K^-$ decay channel. The candidates for the Ξ_c^+ baryon (reconstructed in the $p K^- \pi^+$ final state) were combined with the fourth track from a negatively charged kaon. The $\Xi_c^+ K^-$ mass distribution is shown in Fig. 4, where five narrow structures are observed [4].

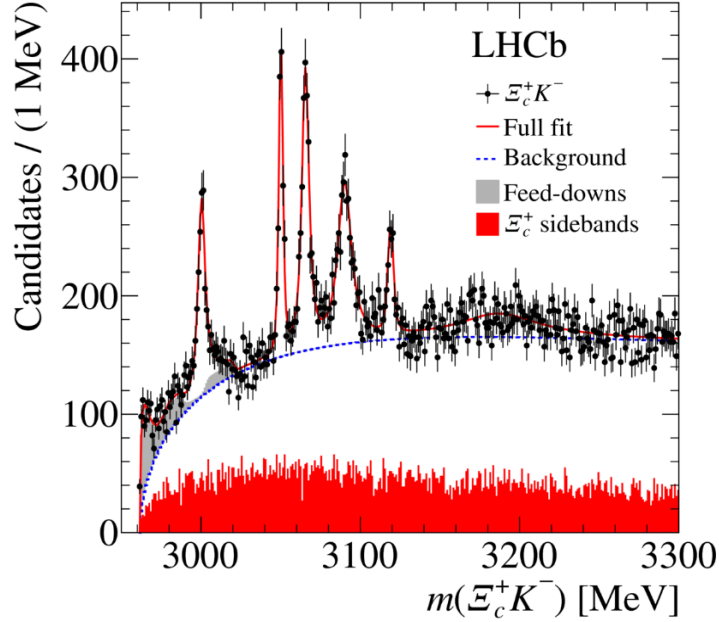


Fig. 4. Distribution of the reconstructed $\Xi_c^+ K^-$ invariant mass. The solid (red) curve shows the result of the fit, and the dashed (blue) line indicates the fitted background. The shaded (red) histogram shows the corresponding mass spectrum for the Ξ_c^+ sidebands, and the shaded (light gray) distributions indicate the feed-down from partially reconstructed resonances

No structure was observed for the corresponding mass spectra evaluated for the Ξ_c^+ sidebands as well as for the spectrum where the Ξ_c^+ candidate was combined with the kaon carrying the same charge. The absence of the corresponding feature in the control samples is consistent with the five structures being the resonant states. A binned χ^2 fit was performed to describe the $\Xi_c^+ K^-$ mass distribution in the range from the threshold to $3450 \text{ MeV}/c^2$. In addition to the background and to the narrow resonant contributions (approximated with the relativistic spin-zero Breit–Wigner distributions), three feed-down components for the $\Omega_c(3066)^0$, $\Omega_c(3090)^0$, and $\Omega_c(3119)^0$ resonances were observed. These states decay into $\Xi_c'^+ K^-$ with the $\Xi_c'^+$ decaying into $\Xi_c^+ \gamma$ (photons are not registered by LHCb). It is found that the fit improves if an additional broad Breit–Wigner function is included in the $3188 \text{ MeV}/c^2$ mass region. This broad structure may be due to a single resonance, due to superposition of several resonances, due to feed-down from the higher states, or due to some combination of the above. The parameters of the observed resonances are presented in Table.

Table

The results of the fit to the $\Xi_c^+ K^-$ distribution for the mass, width, yield, and significance for each of the resonances*

Resonance	Mass, MeV/ c^2	Width, MeV/ c^2	Yield	$N\sigma$	Feed down yield
$\Omega_c(3000)^0$	$3\,000.4 \pm 0.2 \pm 0.1 \pm 0.4$	$4.5 \pm 0.6 \pm 0.3$	$1\,300 \pm 100 \pm 80$	20.4	
$\Omega_c(3050)^0$	$3\,050.2 \pm 0.1 \pm 0.1 \pm 0.4$	$0.8 \pm 0.2 \pm 0.1$	$970 \pm 60 \pm 20$	20.4	
$\Omega_c(3066)^0$	$3\,065.6 \pm 0.1 \pm 0.3 \pm 0.4$	$3.5 \pm 0.4 \pm 0.2$	$1\,740 \pm 100 \pm 50$	23.9	$700 \pm 40 \pm 140$
$\Omega_c(3090)^0$	$3\,090.2 \pm 0.3 \pm 0.5 \pm 0.4$	$8.7 \pm 1.0 \pm 0.8$	$2\,000 \pm 140 \pm 130$	21.1	$220 \pm 60 \pm 90$
$\Omega_c(3119)^0$	$3\,119.1 \pm 0.3 \pm 0.9 \pm 0.4$	$1.1 \pm 0.8 \pm 0.4$	$480 \pm 70 \pm 30$	10.4	$190 \pm 70 \pm 20$
$\Omega_c(3188)^0$	$3\,188 \pm 5 \pm 13$	$30 \pm 15 \pm 11$	$1\,670 \pm 450 \pm 360$	6	

* The yields for the feed-down contributions of the $\Omega_c(3066)^0$, $\Omega_c(3090)^0$, and $\Omega_c(3119)^0$ resonances decaying into $\Xi_c^+ K^-$ final state with the partially reconstructed Ξ_c^+ are also presented.

This discovery leads to a wide theoretical discussion about the nature of the observed resonances. In some models, the narrowest of them are interpreted as pentaquark states. Further measurements of the corresponding quantum numbers of the observed resonances are certainly needed to provide information on their internal structure. Such information can be obtained from the study of possible three-body decays or when reconstructing these states in decays of beauty baryons.

4. Observation of pentaquarks with hidden charm

The states with the baryon number $B = 1$, which consist of four quarks and one antiquark (named *pentaquark* states) were predicted together with the introduction of the quark model itself, but the searches for such states formed by the light (u , d , and s) quarks gave controversial results. The first confirmation of existing of pentaquark hadrons was done by the LHCb experiment [5]. Two pentaquark states were observed in the decay of the Λ_b^0 baryon into the $J/\psi p K^-$ final state. The observation was done with the data sample corresponding to the integral luminosity of 3 fb^{-1} collected by the LHCb detector during Run-1 at $\sqrt{s} = 7$ and 8 TeV. Using the boosting decision tree method, LHCb has found $26\,007 \pm 166$ signal events at the background level of 5.4%. The band parallel to the $m^2(J/\psi p)$ -axis was observed at the corresponding Dalitz plot in addition to the contributions from the excited Λ baryons decaying into $p K^-$ (Fig. 5). The peak in the corresponding $J/\psi p$ mass distribution is also prominent (Fig. 5).

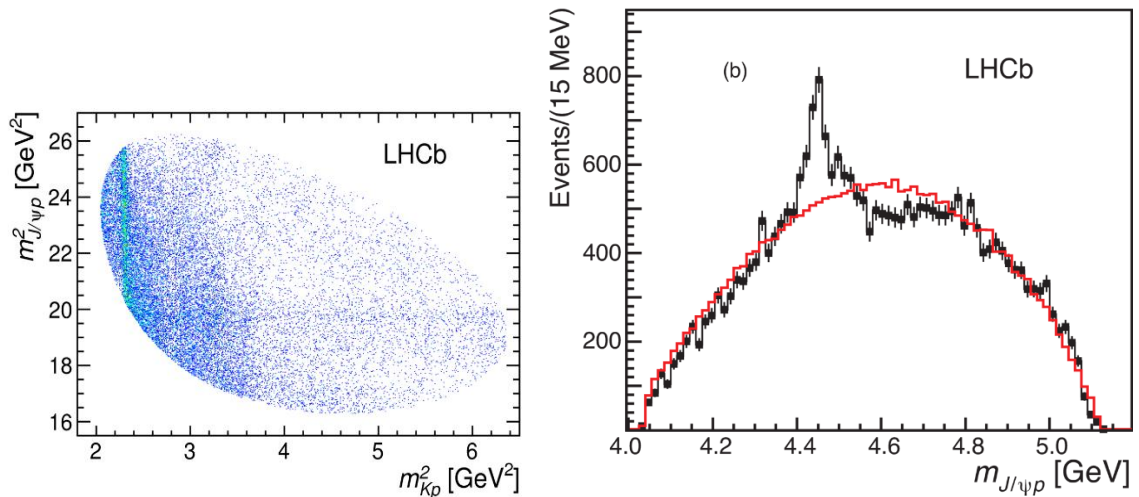


Fig. 5. Dalitz plot for the $\Lambda_b^0 \rightarrow J/\psi p K^-$ decay (left panel). Mass spectrum for the $J/\psi p$ system; the black points indicate the distribution for the data; the red histogram demonstrates the expectation of the three-body phase space model (right panel)

For the selected sample, a full five-dimensional amplitude analysis was performed under the helicity formalism. Two interfering decay sequences $\Lambda_b^0 \rightarrow J/\psi \Lambda$, $\Lambda \rightarrow p K^-$ and $\Lambda_b^0 \rightarrow K^- P_c^+$, $P_c^+ \rightarrow J/\psi p$ with the $J/\psi \rightarrow \mu^+ \mu^-$ in both cases were considered. Two independently developed fitting algorithms were used to establish contributions of the intermediate resonances. A reasonable agreement could be achieved when in addition to the known Λ resonances two pentaquark states were introduced. The lower mass state has the mass of $4380 \pm 8 \text{ MeV}/c^2$ and the width of $205 \pm 18 \text{ MeV}/c^2$, while the higher mass state has the mass of $4449.8 \pm 1.7 \text{ MeV}/c^2$ and the width of $39 \pm 5 \text{ MeV}/c^2$. The mass resolution is approximately $2.5 \text{ MeV}/c^2$ and does not affect the width determination. The agreement of the model which includes the pentaquark state is good in all selected $p K^-$ mass intervals (Fig. 6).

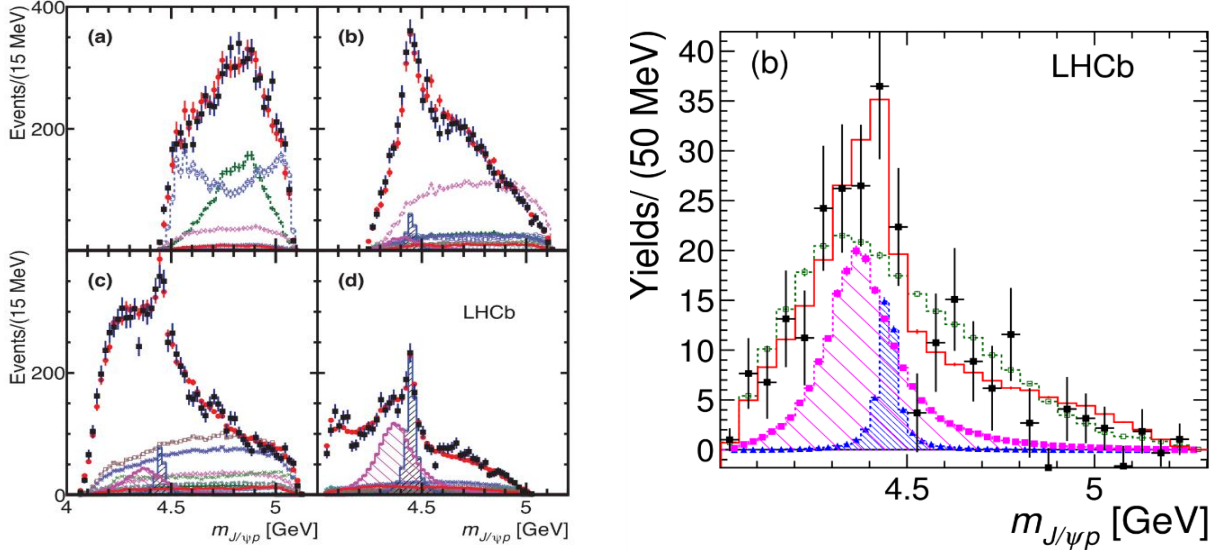


Fig. 6. Left panel – $m(J/\psi p)$ in various intervals of $m(Kp)$ for the fit with two P_c^+ states: $m(Kp) < 1.55 \text{ GeV}/c^2$ (a); $1.55 < m(Kp) < 1.70 \text{ GeV}/c^2$ (b); $1.70 < m(Kp) < 2.00 \text{ GeV}/c^2$ (c), $m(Kp) > 2.00 \text{ GeV}/c^2$ (d). The data are shown as *black squares* with error bars, while the *red circles* show the results of the fit. The *blue* and *purple histograms* show the two P_c^+ states. Right panel – background-subtracted data and fit projections onto $m(J/\psi p)$ for the $\Lambda_b^0 \rightarrow J/\psi p \pi^-$ decay in the $m(p\pi^-) > 1.8 \text{ GeV}/c^2$ region

The amplitude analysis allows to determine quantum numbers of the pentaquarks. The best fit combination finds P_c^+ states with J^P values of $3/2^-$ and $5/2^+$, for the lower and higher mass states, respectively. The combinations $(3/2^+, 5/2^-)$ and $(5/2^+, 3/2^-)$ also cannot be ruled out. Further evidence for the resonant character of the higher mass, narrower, P_c^+ state is obtained by viewing the evolution of the complex amplitude in the Argand diagram. The resulting Argand diagram is consistent with a rapid counter-clockwise change of the $P_c(4450)^+$ phase when its magnitude reaches the maximum, a behaviour characteristic of a resonance.

Further analysis [6] of the same data sample of the $\Lambda_b^0 \rightarrow J/\psi p K^-$ decays demonstrated at more than nine standard deviations that the decays cannot all be attributed to $K p$ resonant or nonresonant contributions in almost model-independent way. This analysis based on the Legendre expansion requires only minimal assumptions on the mass and spin of the $K p$ contribution, but no assumptions on their number, their resonant or nonresonant nature, or their lineshapes have been made. This analysis clearly suggests that the non- $K p$ contributions, which must be present in the data, can be either of the exotic hadron type, or due to rescattering effects among ordinary hadrons.

Different binding mechanisms of pentaquark states are possible. A possible explanation is heavy-light diquarks, examples of other mechanisms include a diquark–diquark–antiquark model, a diquark–triquark model, and a coupled channel model. Weakly bound “molecules” of a baryon plus a meson were also discussed. Models involving thresholds or “cusps” have been invoked to explain some exotic meson candidates *via* nonresonant scattering mechanisms. There is no threshold close to the lower mass state, and

for the higher mass states such structures arising from $\Lambda_c(2595)^+ \bar{D}$ re-scattering would have $1/2^+$ quantum numbers, which are disfavoured by the data.

The $\Lambda_b^0 \rightarrow J/\psi p \pi^-$ decay channel is singly Cabibbo suppressed with respect to the $\Lambda_b^0 \rightarrow J/\psi p K^-$ one. Instead of the Λ excitation, the nucleon resonances play a major role here. Moreover, in addition to the pentaquark states, another exotica, which decay into the $J/\psi \pi^-$ final state, can contribute. An example of such a tetraquark state is $Z_c(4200)^-$ previously observed in the $B^0 \rightarrow J/\psi K^+ \pi^-$ decay channel. The LHCb Run-1 data sample corresponding to the integrated luminosity of 3 fb^{-1} was used for the full amplitude analysis of this Λ_b^0 decay [7]. The signal yield is 1885 ± 50 , determined by an unbinned extended maximum likelihood fit to the mass spectrum.

The amplitude model based on the same formalism, which was used for the pentaquarks discovery, were developed to examine the presence of two P_c^+ states as well as for searching of the $Z_c(4200)^-$ one. As a base, a model with up to eleven N^* resonances decaying into $p \pi^-$ was used. If the $Z_c(4200)^-$ contribution is assumed to be negligible, adding the two P_c^+ states to a model without exotics yields a significance of 3.3σ . On the other hand, under the assumption that no P_c^+ states are produced, adding the $Z_c(4200)^-$ without exotics yields a significance of 3.2σ . Thus, there is clear evidence for the presence of exotic states for the decay of interest.

5. Conclusion

The LHCb experimental program is very successful in discovering new particles containing one or a pair of charm quarks, including pentaquarks with hidden charm. The PNPI analysis group participates in these investigations as a part of the Charm Physics Group.

References:

1. LHCb Collaboration, Phys. Rev. Lett. **119**, 112001 (2017).
2. LHCb Collaboration, Phys. Rev. Lett. **121**, 162001 (2018).
3. LHCb Collaboration, Phys. Rev. Lett. **121**, 052002 (2018).
4. LHCb Collaboration, Phys. Rev. Lett. **118**, 182001 (2017).
5. LHCb Collaboration, Phys. Rev. Lett. **115**, 072001 (2015).
6. LHCb Collaboration, Phys. Rev. Lett. **117**, 082002 (2016).
7. LHCb Collaboration, Phys. Rev. Lett. **117**, 082003 (2016).

PRODUCTION OF SHORT-LIVED HADRONIC RESONANCES IN Pb–Pb COLLISIONS AT $\sqrt{s_{NN}} = 2.76$ AND 5 TeV MEASURED BY THE ALICE EXPERIMENT AT THE LARGE HADRON COLLIDER

PNPI participants of the ALICE Collaboration:

Ya.A. Berdnikov, V.V. Ivanov, A.V. Khanzadeev, E.L. Kryshen, M.V. Malaev,
V.N. Nikulin, Yu.G. Riabov, V.G. Ryabov, V.M. Samsonov, M.B. Zhalov

1. Introduction

Ultrarelativistic heavy ion collisions are used to study properties of the strongly interacting matter under extreme conditions of high temperature and density. The interacting system produced in such collisions evolves through different stages, with the early partonic stage followed by hadronization. Properties of the early partonic phase are studied by measuring the angular and momentum distributions of particles produced in the final state. Hadronic interactions can significantly modify properties of the emitted particles, thus hiding properties of the early phase. Hence, understanding and proper description of the late hadronic phase plays an important role in correct interpretation of the experimental results.

Properties of the hadronic phase produced in high-energy heavy-ion collisions can be studied by measuring yields of short-lived resonances. Resonances with the lifetime comparable to that of the fireball are sensitive to rescattering and regeneration occurring in the dense partonic medium. Rescattering of the daughter particles with the surrounding hadrons changes the kinematics of the decay and some of the resonances can no longer be reconstructed. However, the counter-process of regeneration, in which pseudo-elastic scattering of hadrons results in production of resonances, tends to increase the yields. The cumulative effect depends on the lifetime of the hadronic phase and that of the resonance, as well as on details of the hadronic interactions, such as particle cross sections and medium density. Previous measurements at the Relativistic Heavy Ion Collider (RHIC) showed suppressed production of $K^*(892)^0$ [1] and $\Lambda(1520)$ [2], no effect for $\phi(1020)$ [3] and $\Sigma(1385)$ [2] and a hint of an enhancement for $\Delta^{++}(1232)$ [4, 5] in central Au + Au collisions at $\sqrt{s_{NN}} = 200$ GeV. These results are qualitatively consistent with expectations from rescattering and regeneration in the hadronic phase. With the start of the heavy-ion program at the Large Hadron Collider (LHC), similar measurements became possible at much higher collision energies.

2. Data analysis

The production of the resonances was measured at mid-rapidity ($|y| < 0.5$) in pp , p -Pb, and Pb–Pb collisions at different energies, $\sqrt{s_{NN}} = 2.76$ –5.02 TeV, using the data samples accumulated by the ALICE experiment at the LHC in 2010–2015. Detailed description of the ALICE detector can be found in Ref. [6]. The main detector subsystems used in the analysis are the V0 detectors, the inner tracking system (ITS), the time projection chamber (TPC) and the time-of-flight (ToF) detector. The minimum bias trigger was configured to obtain high efficiency for hadronic interactions by requiring signals in the V0 and/or in the silicon pixel detector, which constitutes two innermost layers of the ITS [7]. The collision centrality in p -Pb and Pb–Pb collisions is determined on the basis of the multiplicity measured by the V0 detector. Glauber-model simulations are used to estimate the average number of participants $\langle N_{\text{part}} \rangle$ and the number of binary inelastic nucleon–nucleon collisions $\langle N_{\text{coll}} \rangle$ for each selected centrality interval [8, 9].

The TPC is used to reconstruct charged particle tracks with the requirement that the track has crossed at least 70 read-out rows out of the maximum 159. Only high-quality tracks reconstructed with the TPC and ITS are selected for analysis; tracks are required to be matched to the primary vertex within 2 cm in the longitudinal direction and within 7σ in the transverse plane, where σ is $(0.0105 + 0.035/p_T^{1.1})$ cm for pp/p -Pb and $(0.0182 + 0.035/p_T^{1.01})$ cm for Pb–Pb, with p_T in units of GeV/ c . The primary vertex is required to be within ± 10 cm of the nominal interaction point along the beam axis. Tracks are required to have a minimum transverse momentum of 150 MeV/ c in a pseudorapidity range of $|\eta| < 0.8$. To be identified as charged pions, kaons or protons, the reconstructed tracks need to have specific ionisation energy loss dE/dx measured in the TPC within $2\sigma_{\text{TPC}}$ of the expected value. Particles with a signal in the ToF subsystem are

identified by requiring the ToF and dE/dx to be within $2\sigma_{\text{ToF}}$ and $5\sigma_{\text{TPC}}$ of the expected values, respectively. The value of σ_{TPC} is about 5% for isolated tracks and 6.5% for central Pb–Pb collisions. The typical value of σ_{ToF} is about 40 ps. For baryonic resonances, the intermediate weakly decaying daughters are identified using the decay topology cuts [10].

Basic characteristics of the measured resonances are presented in Table. The resonance yields for each p_T and centrality interval are measured by accumulating unlike-sign invariant mass distributions for each of the decay channels shown in the table. The combinatorial background is estimated using the like-sign pairs from the same events or using the mixed-event method where particle pairs are selected from different events with similar multiplicity and vertex location. Combinatorial background is then subtracted from the invariant mass distributions of unlike-sign pairs. The resulting invariant-mass distributions contain peaks from the resonance decays and the remaining background from jets and mis-reconstructed decays of other hadrons. Detailed Monte Carlo (MC) studies were performed to insure that the remaining background is a smooth function of mass and does not have peaked structures next to the resonance peaks. The resonance raw yields are determined from fits, the remaining background is described with the polynomial and the resonances are described with the Voigtian function, which takes into account the intrinsic relativistic Breit–Wigner shape of the produced resonances and the detector mass resolution estimated from simulations. The extracted raw yields are corrected for the detector acceptance and reconstruction efficiencies, which were estimated using a detailed GEANT 3.14 based MC simulation of the experimental set-up.

Table

Basic properties of the resonances

Resonance Parameter	$\rho(770)^0$	$K^*(892)^0$	$\Lambda(1520)$	$\Xi(1530)^0$	$\phi(1020)$
$c\tau$, fm/c	1.3	4.2	12.7	21.7	46.2
Decay channel	$\pi\pi$	$K\pi$	pK	$\pi\Xi$	KK
BR, %	~ 100	~ 100	22.5 ± 0.5	~ 100	48.9 ± 0.5

3. Particle ratios and properties of the hadronic phase

Figure 1 shows the ratio of integrated yields, $\rho(770)^0/\pi$, measured as a function of multiplicity in pp and Pb–Pb collisions at $\sqrt{s_{NN}} = 2.76$ TeV [11]. The meson $\rho(770)^0$ is a very short-lived resonance, its daughter particles are expected to interact with the surrounding hadrons thus affecting the measured yields. One can see that production of the $\rho(770)^0$ meson is suppressed going from pp to peripheral and then to central Pb–Pb collisions. The value of the ratio measured in central collisions is inconsistent with the prediction of the grand-canonical thermal model with a chemical freeze-out temperature of 156 MeV [12, 13]. However, the EPOS3 event generator [14], which includes the UrQMD [15, 16] afterburner to simulate the late hadronic cascade, describes the observed multiplicity dependence of the ratio. EPOS3 predicts a flat ratio when UrQMD is disabled in the simulation. The measurement is consistent with the loss of the $\rho(770)^0$ signal due to rescattering of the daughter pions in the hadronic phase.

Two panels in Fig. 2 show the $K^*(892)^0/K$ and $\phi(1020)/K$ ratios measured as a function of multiplicity in pp , p –Pb, and Pb–Pb collisions at different energies [17–20]. The $K^*(892)^0$ meson has about three times longer lifetime than $\rho(770)^0$ and yet it is only ~ 4.2 fm/c. Hence, one can expect similar effects for $K^*(892)^0$ as for $\rho(770)^0$. On the other hand, $\phi(1020)$ meson lives ten times longer than $K^*(892)^0$, and one can expect that it behaves as a quasi-stable particle. Indeed, the $\phi(1020)/K$ ratio does not change much and it is consistent between pp , p –Pb, and different centrality Pb–Pb collisions. At the same time, the $K^*(892)^0/K$ ratio, similar to the $\rho(770)^0/\pi$ ratio, exhibits a suppression from pp to central Pb–Pb collisions.

The ratio $K^*(892)^0/K$ in central Pb–Pb collisions is not consistent with the thermal model prediction [12]. The measured $K^*(892)^0/K$ ratio in Pb–Pb is compared to the EPOS3 calculation [14], which reasonably well reproduces the measured multiplicity dependence of the ratio. The observed behaviour of the ratios is in

agreement with expectations from rescattering of decay particles of very short-lived $K^*(892)^0$ in the hadronic phase, whereas the $\phi(1020)$ meson behaves as a stable particle because of its much longer lifetime.

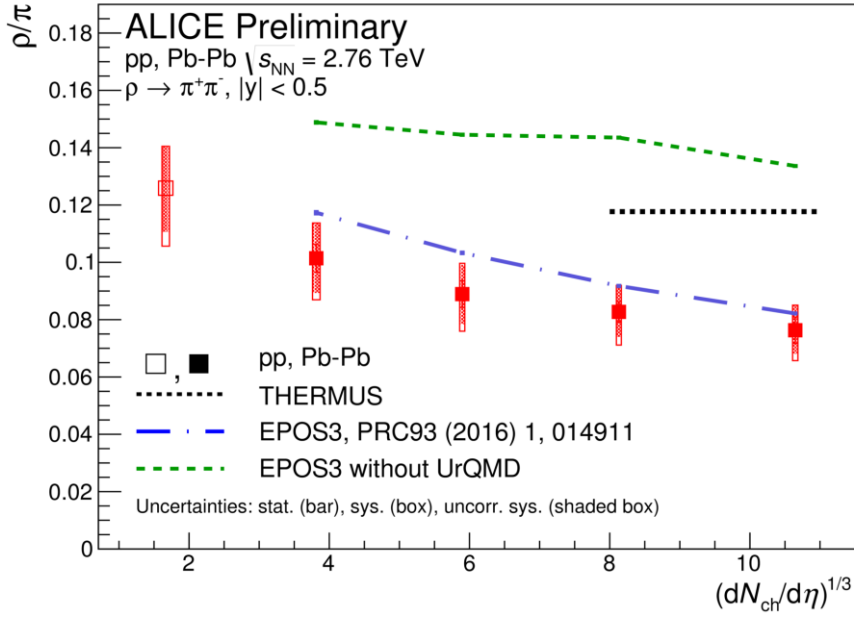


Fig. 1. Ratio of the integrated yields, $\rho(770)^0/\pi$, in pp and 0–20, 20–40, 40–60, 60–80% central Pb–Pb collisions at $\sqrt{s_{NN}} = 2.76$ TeV as a function of multiplicity [11]. The statistical uncertainties are shown as bars. The total and uncorrelated systematic uncertainties are shown with open and shaded boxes, respectively. The measurements are compared to the EPOS3 calculations [14] and the grand canonical thermal model prediction [12, 13]

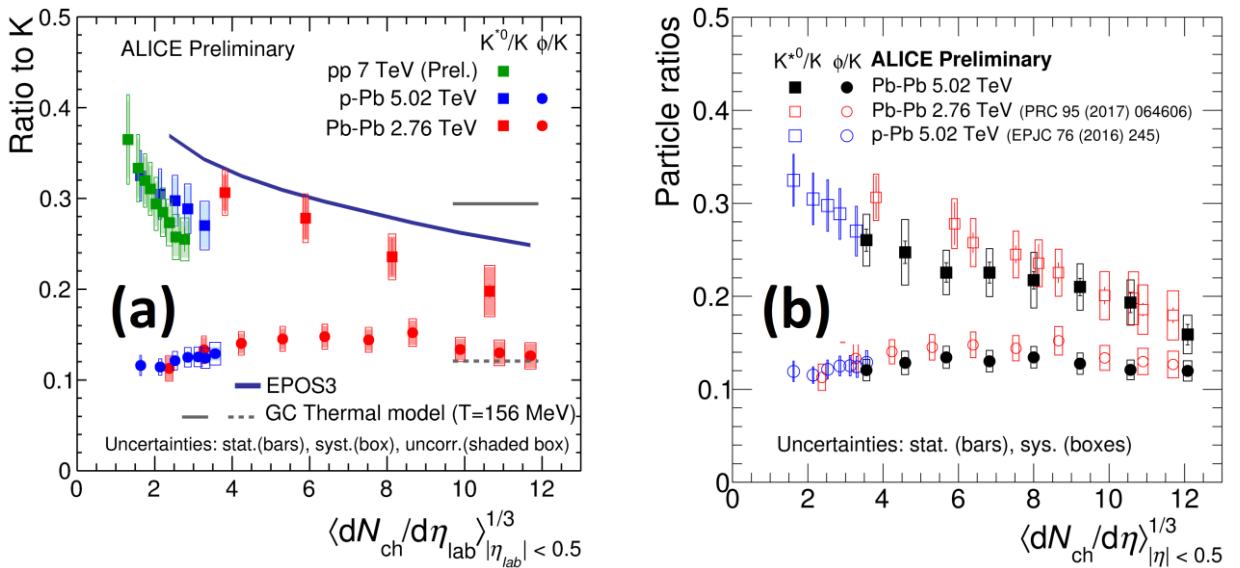


Fig. 2. Ratios of the integrated yields, $K^*(892)^0/K$ and $\phi(1020)/K$, in pp , p -Pb, and Pb–Pb collisions at different energies as a function of multiplicity [17–20]. The statistical uncertainties are shown as bars. The total and uncorrelated systematic uncertainties are shown with hollow and shaded boxes, respectively. The measurements are compared to the EPOS3 calculations [14] and the grand canonical thermal model prediction [12]

It is interesting to note that the multiplicity dependent measurements in pp and p -Pb collisions show a smooth transition of $K^*(892)^0/K$ ratio to peripheral Pb–Pb points, hinting at the possible presence of a finite-lifetime hadronic phase in the highest multiplicity collisions of small systems. The *right panel* in Fig. 2

also compares measurements performed at $\sqrt{s_{NN}} = 2.76$ TeV and 5.02 TeV. Within uncertainties, there is no energy dependence of the ratios.

Figure 3 shows results for the $\Lambda(1520)/\Lambda$ ratio measured in pp , p -Pb, and Pb-Pb collisions at different energies. $\Lambda(1520)$ lives ten times longer than $\rho(770)^0$, ~ 13 fm/c. The ratio stays constant in pp and different multiplicity p -Pb collisions. However, it becomes more and more suppressed going from peripheral to central Pb-Pb interactions. Similar to other short-lived resonances, the ratio in central collisions is not reproduced by thermal model predictions [21–23], the multiplicity dependence of the suppression is qualitatively reproduced by EPOS3 calculations [14], although absolute scaling is not matched by calculations. The LHC points are also consistent with previous measurements by STAR in Au + Au collisions at $\sqrt{s_{NN}} = 200$ GeV.

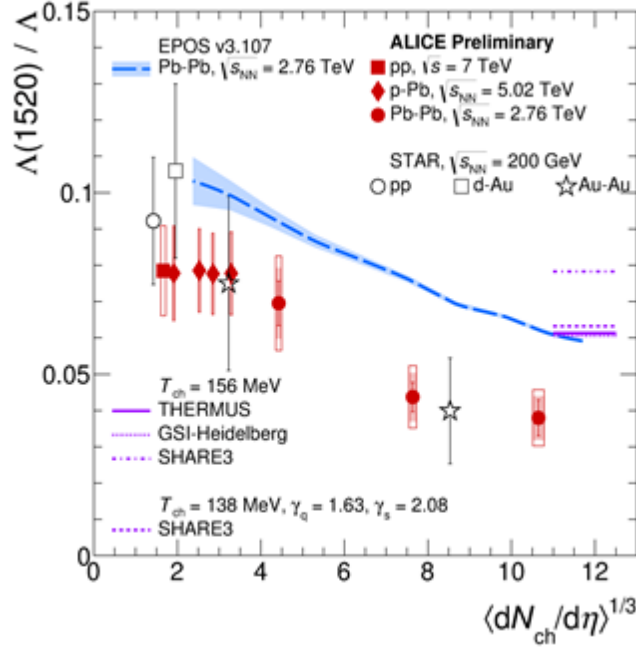


Fig. 3. Ratio of the integrated yields, $\Lambda(1520)/\Lambda$, in pp , d -Au, p -Pb, Au-Au, and Pb-Pb collisions at different energies as a function of multiplicity. The statistical uncertainties are shown as bars. The total and uncorrelated systematic uncertainties are shown with hollow and shaded boxes, respectively. The measurements in Pb-Pb collisions are compared to the EPOS3 calculations [14] and the grand canonical thermal model predictions [21–23]

Figure 4 shows the multiplicity dependence of the $\Xi(1530)^0/\Xi$ ratio in pp , p -Pb, and Pb-Pb collisions at different energies. The $\Xi(1530)^0$ baryon lives two times longer than $\Lambda(1520)$, for which we observed suppression. However, it lives two times shorter than $\phi(1020)$, for which we observed no multiplicity dependent effects. The ratio was measured with high precision in pp and p -Pb collisions, and in these systems the ratio stays constant. There is a hint of suppression observed in Pb-Pb collisions, although within large systematic uncertainties. Thermal models [12, 13, 21–23] overestimate the ratio in Pb-Pb, while PYTHIA 8 [24] and DPMJET [25] underestimate it in pp and p -Pb, respectively. The EPOS3 [14], which was very successful for other resonances does not predict a significant multiplicity dependence of the ratio in Pb-Pb collisions. Experimental uncertainties in the measurements of Pb-Pb collisions should be reduced in order to see multiplicity dependent effects.

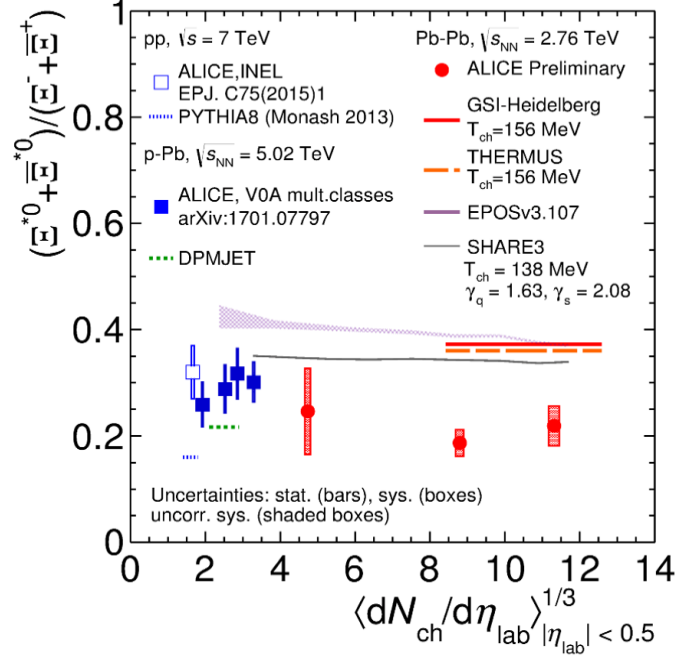


Fig. 4. Ratio of the integrated yields, $\Xi(1530)^0/\Xi$, in pp , p -Pb, and Pb-Pb collisions at different energies as a function of multiplicity. The statistical uncertainties are shown as bars. The total and uncorrelated systematic uncertainties are shown with open and shaded boxes, respectively. The measurements in Pb-Pb collisions are compared to the EPOS3 calculations [14] and the grand canonical thermal model predictions [12, 13, 21–23]. The measurements in pp and p -Pb are compared to the predictions of PYTHIA 8 [24] and DPMJET [25] event generators

4. Conclusion

The $\rho(770)^0/\pi$, $K^*(892)^0/K$, $\Lambda(1520)/\Lambda$, $\Xi(1530)^0/\Xi$, and $\phi(1020)/K$ ratios presented in this contribution show a close connection between the resonance lifetimes and their suppression in central Pb-Pb collisions at the LHC. A similar effect was previously observed at RHIC and can qualitatively be explained by rescattering of the daughter particles in the late hadronic phase. The shorter the resonance lifetime, the larger fraction of the resonances decays during this phase and the higher the probability for daughter particles to rescatter.

The $\rho(770)^0/\pi$, $K^*(892)^0/K$, $\Lambda(1520)/\Lambda$, $\Xi(1530)^0/\Xi$ ratios in central Pb-Pb collisions are not reproduced by thermal models with a chemical freeze-out temperature of 156 MeV. The multiplicity dependence of the ratios in Pb-Pb collisions is reasonably well reproduced by the EPOS3 event generator, which models the hadronic cascade with UrQMD. It supports rescattering in the hadronic phase as a driving force for the observed suppression. Several models relate the measured particle ratios to the temperature of chemical freezing and the hadronic phase lifetime [26, 27]. The lower limit for the hadronic phase lifetime is 2 fm/c [26, 27].

To summarize, the obtained results for Pb-Pb collisions support the existence of the hadronic phase which lasts long enough to cause a significant reduction of the reconstructed yields of short-lived resonances. Theoretical models that describe the full evolution of the interacting system should be able to describe the results obtained for short-lived resonances in order to be validated.

References

1. J. Adam *et al.*, Phys. Rev. C **71**, 064902 (2005).
2. B.I. Abelev *et al.*, Phys. Rev. Lett. **97**, 132301 (2006).
3. J. Adam *et al.*, Phys. Lett. B **612**, 181 (2005).
4. C. Markert, J. Phys. G **30**, S1313 (2004).
5. H.-B. Zhang, arXiv:nucl-ex/0403010 (2004).
6. K. Aamodt *et al.*, JINST **3**, S08002 (2008).
7. E. Abbas *et al.*, JINST **8**, P10016 (2008).
8. K. Aamodt *et al.*, Phys. Rev. Lett. **106**, 032301 (2011).
9. B. Abelev *et al.*, Phys. Rev. C **88**, 044909 (2013).
10. B. Abelev *et al.*, Phys. Lett. B **728**, 216 (2014).
11. V. Riabov *et al.*, J. Phys. Conf. Ser. **798**, 012054 (2017).
12. J. Stachel *et al.*, J. Phys.: Conf. Ser. **509**, 012019 (2014).
13. A. Andronic *et al.*, Phys. Lett. B **673**, 142 (2009), Erratum: Phys. Lett. B **678**, 516 (2009).
14. A. Knospe *et al.*, Phys. Rev. C **93**, 014911 (2016).
15. S.A. Bass *et al.*, Prog. Part. Nucl. Phys. **41**, 255 (1998).
16. M. Bleicher *et al.*, J. Phys. G **25**, 1859 (1999).
17. B. Abelev *et al.*, Phys. Rev. C **91**, 024609 (2015).
18. J. Adam *et al.*, Eur. Phys. J. C **76**, 245 (2016).
19. J. Adam *et al.*, Phys. Rev. C **95**, 064606 (2017).
20. M. Malaev *et al.*, AIP Conf. Proc. **1701**, 060014 (2016).
21. A. Andronic *et al.*, Nucl. Phys. A **772**, 167 (2006).
22. S. Wheaton *et al.*, J. Phys. G **31**, S1069 (2005).
23. M. Petran *et al.*, Comput. Phys. Commun. **185**, 2056 (2014).
24. T. Sjostrand *et al.*, Comput. Phys. Commun. **178**, 852 (2008).
25. S. Roesler *et al.*, arXiv:hep-ph/0012252 (2000).
26. G. Torrieri *et al.*, J. Phys. G **28**, 1911 (2002).
27. C. Markert *et al.*, arXiv:hep-ph/0206260v2 (2002).

LOW- x GLUON DENSITY IN NUCLEI FROM EXCLUSIVE CHARMONIUM PHOTOPRODUCTION IN ULTRAPERIPHERAL ION COLLISIONS AT THE LARGE HADRON COLLIDER

V.A. Guzey, E.L. Kryshen, M.B. Zhalov

1. Introduction

At the Large Hadron Collider (LHC), dedicated studies of different aspects of the quantum chromodynamics (QCD), which describes the strong interaction of quarks and gluons of the Standard Model (SM), constitute an important part of the physics program. Production of gauge bosons W , Z , direct photons, jets, dileptons, and heavy flavours in proton–proton (pp) and proton–nucleus (pA) scattering provides new information on parton (quark, gluon) densities in the proton and nuclei, parton fragmentation to hadrons, the strong coupling constant, and parton interactions with nuclear medium (in the pA case). In nucleus–nucleus (AA) collisions, hard probes are used to study properties of the produced quark–gluon plasma (QGP) and the interaction of colour charges with nuclear matter (jet quenching, jet substructure and correlations, charmonium and bottomonium suppression and regeneration, *etc.*). One of the key quantities in these studies is the collinear gluon density $g_A(x, \mu^2)$ in heavy nuclei at small x (x is the light-cone momentum fraction of the nuclear nucleon carried by the gluon, μ is the resolution scale). Knowledge of $g_A(x, \mu^2)$ is essential for QCD calculations of high-energy hard processes with nuclei since it characterizes the initial-state nuclear wave function. Parton densities in general – and $g_A(x, \mu^2)$ in particular – are non-perturbative quantities, which cannot be calculated from first principles of QCD. Hence, they are determined indirectly by fitting to experimental data employing the QCD factorization theorems and evolution equations. Several groups have performed such global QCD fits to the data on lepton deep inelastic scattering on fixed nuclear targets, on the nuclear Drell–Yan process, on inclusive production of pions in deuteron-gold scattering at Relativistic Heavy Ion Collider (RHIC), and hard pA scattering at the LHC and extracted nuclear parton distribution functions (nPDFs) (for recent development and references see Ref. [1]). It is found that $g_A(x, \mu^2)$ cannot be reliably constrained by such analyses owing to the limited kinematic coverage of the fixed-target data and the largely indirect access to $g_A(x, \mu^2)$ through the used observables. The uncertainty in $g_A(x, \mu^2)$ is especially large for small $x < 0.005$, where $g_A(x, \mu^2)$ is expected to be suppressed compared to the sum of the gluon densities in the nucleons by nuclear shadowing, $g_A(x, \mu^2) < A g_N(x, \mu^2)$.

The phenomenon of nuclear shadowing is well-established in hadron–nucleus and lepton–nucleus scattering at high energies. The suppression of the nuclear cross section compared to the sum of nucleon cross sections is explained in the Gribov–Glauber model as resulting from the destructive quantum-mechanical interference among the scattering amplitudes for the interaction with one, two, three, *etc.* nucleons of the nuclear target. The extension of this idea to QCD offers a dynamical model of nuclear shadowing allowing one to calculate $g_A(x, \mu^2)$ at small x in terms of the nuclear density and of the diffractive parton distribution functions of the proton [2]. Another theoretical approach to nPDFs at small x is based on the colour-glass condensate framework, which is an effective field theory of high-energy QCD, where nuclear shadowing is a consequence of multiple interactions of quark–antiquark dipoles with the nucleus colour field characterized by the saturation scale, which is predicted to determine universal properties of many-particle production in high-energy QCD. While these theoretical approaches make predictions for $g_A(x, \mu^2)$ with the theoretical uncertainty, which is noticeably smaller than that of the global QCD fits, the dynamics and magnitude of nuclear shadowing is a subject of debate and on-going research.

Only incremental and limited progress in constraining nPDFs at small x is expected in the course of the analysis of the LHC Run-2 data on hard processes in pA scattering. Therefore, it is topical to explore complimentary probes of small- x nPDFs at the LHC.

This contribution summarizes a series of our papers [3–10], where we demonstrated that the low- x nuclear gluon density can be constrained using the LHC data on exclusive charmonium (J/ψ , $\psi(2S)$) photoproduction in ultraperipheral nucleus–nucleus scattering. Our theoretical results are based on the data obtained by the ALICE Collaboration at the LHC, where the PNPI team plays a prominent role, notably in the data taking and analysis of the data on photo-induced reactions.

2. Heavy ion ultraperipheral collisions at the Large Hadron Collider

Collisions of ultrarelativistic ions at large impact parameters, when the strong interaction is suppressed and the ions interact electromagnetically *via* emission of quasi-real photons in the so-called ultraperipheral collisions (UPCs), give an opportunity to study photon–photon, photon–proton, and photon–nucleus scattering at unprecedentedly high energies [11]. As part of the LHC heavy ion program, it was realized by measuring exclusive photoproduction of charmonia (J/ψ and $\psi(2S)$ vector mesons) in Pb–Pb UPCs at $\sqrt{s_{NN}} = 2.76$ TeV by the ALICE [12–14] and CMS [15] Collaborations. In experiments, UPC events are characterized by an otherwise empty detector containing only two lepton tracks from a charmonium decay. Note that UPC measurements are continued and extended in Run-2 at the LHC.

The cross section of exclusive J/ψ photoproduction in AA UPCs reads:

$$\frac{d\sigma_{AA \rightarrow AAJ/\psi}(y)}{dy} = N_{\gamma/A}(y)\sigma_{\gamma A \rightarrow AJ/\psi}(y) + N_{\gamma/A}(-y)\sigma_{\gamma A \rightarrow AJ/\psi}(-y), \quad (1)$$

where y is the J/ψ rapidity; $N_{\gamma/A}(\omega)$ is the photon flux; $\sigma_{\gamma A \rightarrow AJ/\psi}(y)$ is the $\gamma A \rightarrow AJ/\psi$ cross section. The measured rapidity y determines the photon energy ω in the laboratory frame, $\omega = \frac{M_{J/\psi}}{2} e^{\pm y}$, where $M_{J/\psi} = 3.1$ GeV is the J/ψ mass. The value of the photon energy is ambiguous since both right-moving and left-moving ions can serve as photon sources and targets, see Eq. (1). However, this ambiguity is absent at central rapidities $y \approx 0$, when both terms in Eq. (1) are equal, and unimportant for large rapidities $|y| \geq 3$, when the lower ω contribution dominates. The photon flux $N_{\gamma/A}(\omega)$ can be calculated with reasonably high accuracy using the well-known QED Weizsacker–Williams method of equivalent photons for the electromagnetic field of relativistic charges. Note that the interference term in Eq. (1) makes a noticeable contribution only for very small values of the J/ψ transverse momentum and, hence, can be safely neglected.

In heavy ion physics, it is customary to quantify the results of nuclear influence on observables under study introducing the modification factor defined as the ratio of the cross section on the nuclear target and the appropriately normalized reference cross section on the nucleon target. In our analysis of J/ψ photoproduction in Pb–Pb UPC, we introduced the nuclear suppression factor, $S_{\text{Pb}}(x)$, [4, 5] as

$$S_{\text{Pb}}(x) = \left[\frac{\sigma_{\gamma\text{Pb} \rightarrow J/\psi\text{Pb}}^{\text{exp}}(W_{\gamma p})}{\sigma_{\gamma\text{Pb} \rightarrow J/\psi\text{Pb}}^{\text{IA}}(W_{\gamma p})} \right]^{1/2}, \quad (2)$$

where $x = \frac{M_{J/\psi}^2}{W_{\gamma p}^2}$, $W_{\gamma p}^2$ is the invariant photon–nucleus energy per nucleon. The denominator of Eq. (2) is the cross section calculated in the impulse approximation (IA):

$$\sigma_{\gamma\text{Pb} \rightarrow J/\psi\text{Pb}}^{\text{IA}}(W_{\gamma p}) = \frac{d\sigma_{\gamma p \rightarrow pJ/\psi}(W_{\gamma p}, t=0)}{dt} \Phi_A(t_{\min}). \quad (3)$$

Here $\frac{d\sigma_{\gamma p \rightarrow pJ/\psi}(W_{\gamma p}, t=0)}{dt}$ is the differential cross section at zero momentum transfer on the proton; $\Phi_A(t_{\min}) = \int_{t_{\min}}^{\infty} dt |F_A(t)|^2$, where $F_A(t)$ is the nucleus elastic form factor. While the IA cross section is theoretically defined, it can be reliably evaluated using the HERA and LHCb data on the $\gamma p \rightarrow pJ/\psi$ cross section and high-precision calculations or parameterizations of $F_A(t)$. Combining Eqs. (1–3), we determined $S_{\text{Pb}}(x)$ using the ALICE [12–14] and CMS [15] data. The results are shown by the filled squares and the circle in Fig. 1, which demonstrate that the nuclear cross section is significantly suppressed compared to its free proton counterpart.

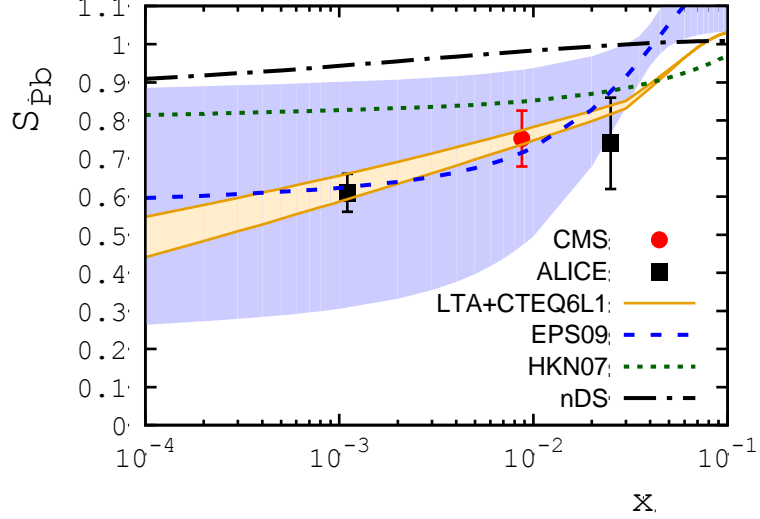


Fig. 1. The nuclear suppression factor $S_{\text{Pb}}(x)$ for coherent exclusive J/ψ photoproduction in Pb–Pb UPCs as a function of x : the values extracted from the ALICE and CMS measurement *vs* theoretical predictions

3. Constraints on small- x gluon density in heavy nuclei from exclusive coherent J/ψ photoproduction at the Large Hadron Collider

The nuclear factor $S_{\text{Pb}}(x)$ can be used to obtain new information on the gluon density $g_A(x, \mu^2)$ in heavy nuclei at small x . In the leading logarithmic approximation of perturbative QCD and in the non-relativistic approximation of the charmonium wave function, the cross section for J/ψ photoproduction on the proton is expressed in terms of the squared gluon density of the proton [16]:

$$\frac{d\sigma_{\gamma p \rightarrow p J/\psi}(W_{\gamma p}, t=0)}{dt} = C(\mu^2) |x g_p(x, \mu^2)|^2, \quad (4)$$

where $C(\mu^2)$ is proportional to the J/ψ leptonic decay width and the strong coupling constant squared, and is a certain kinematic function of $M_{J/\psi}$ the resolution scale is $\mu^2 = M_{J/\psi}^2/4 \approx 2.4 \text{ GeV}^2$. The expression in Eq. (4) receives corrections due to the real part and the non-forward kinematics of the exclusive $\gamma p \rightarrow p J/\psi$ amplitude, non-zero momentum of charm quarks in the J/ψ rest frame, higher-order QCD radiative corrections, and power-suppressed (higher-twist) corrections. They mostly affect $C(\mu^2)$ and suggest that the resolution scale μ^2 can be somewhat larger than $\mu^2 \approx 2.4 \text{ GeV}^2$. Therefore, in our analysis we took Eq. (4) at the face value and compared its predictions using a wide array of leading-order gluon densities in the proton to the HERA data on the $\gamma p \rightarrow p J/\psi$ cross section. We found that Eq. (4) works well and the data favours $\mu^2 \approx 3 \text{ GeV}^2$, see details in Ref. [4].

Further, we applied Eq. (4) to the $\gamma A \rightarrow A J/\psi$ process on a nuclear target and found [3, 6] that

$$\sigma_{\gamma A \rightarrow \frac{AJ}{\psi}}(W_{\gamma p}) = \frac{C_A(\mu^2)}{C_p(\mu^2)} \left[\frac{g_A(x, \mu^2)}{A g_p(x, \mu^2)} \right]^2 \sigma_{\gamma A \rightarrow \frac{AJ}{\psi}}^{\text{IA}}(W_{\gamma p}), \quad (5)$$

where the ratio $C_A(\mu^2)/C_p(\mu^2)$ takes into account a small (at the level of 5–10%) nuclear dependence of the normalization factor of $C(\mu^2)$; the last term is the impulse approximation cross section given by Eq. (3). Now, similarly to Eq. (2) we can theoretically define the nuclear suppression factor in the leading logarithmic approximation of pQCD. Using Eq. (5), one readily finds that

$$S_{\text{Pb}}(W_{\gamma p}) = \left[\frac{C_A(\mu^2)}{C_p(\mu^2)} \right]^{1/2} \frac{g_{\text{Pb}}(x, \mu^2)}{A g_p(x, \mu^2)} = \left[\frac{C_A(\mu^2)}{C_p(\mu^2)} \right]^{1/2} R_g(x, \mu^2). \quad (6)$$

Thus, on the one hand, $S_{\text{Pb}}(x)$ can be essentially model-independently extracted from the experimental data, see our discussion in Sect. 1. On the other hand, $S_{\text{Pb}}(x)$, apart from a numerically insignificant correction, is the ratio of the nuclear and proton gluon densities $R_g(x, \mu^2) = g_A(x, \mu^2)/A g_p(x, \mu^2)$.

As was explained in the Introduction, the nuclear gluon density $g_A(x, \mu^2)$ is extracted with large uncertainties by different groups using the global QCD fits to the available data; it has also been predicted by dynamical models of small- x nuclear PDFs. Theoretical predictions for $S_{\text{Pb}}(x)$ based on Eq. (6) are shown in Fig. 1: the curves labeled ‘‘EPS09’’, ‘‘HKN07’’, and ‘‘nDS’’ correspond to $R_g(x, \mu^2)$ obtained in Refs. [1], [17], and [18], respectively; the curve labeled ‘‘LTA+CTEQ6L1’’ is based on the leading twist approximation (LTA) model of Ref. [2]. The shaded bands, where given, show the theoretical uncertainty in the corresponding prediction. One can see in Fig. 1 that the LTA and EPS09 results provide a very good description of the values of $S_{\text{Pb}}(x)$, which we extracted from the ALICE and CMS UPC measurements. It allows us to conclude that the LHC data on coherent J/ψ photoproduction in Pb–Pb UPCs [12–15] give first almost model-independent evidence of large nuclear gluon shadowing down to $x \approx 10^{-3}$, which agrees well with the predictions of the leading twist nuclear shadowing model and the EPS09 nPDFs.

4. Complimentary probes of nuclear gluon density at small- x in UPCs at the Large Hadron Collider

Besides the coherent nuclear process, ALICE also measured incoherent J/ψ photoproduction in Pb–Pb UPCs, which is characterized by dissociation of the target nucleus $AA \rightarrow AX J/\psi$ [12]. The coherent and incoherent contributions were separated using their characteristic dependence on the J/ψ (final dilepton) transverse momentum p_T : while the coherent term has a sharp and narrow p_T dependence given by $|F_A(t \approx -p_T^2)|^2$, the incoherent contribution has a wide p_T spectrum. Similarly to the coherent case, gluon nuclear shadowing also affects and suppresses incoherent J/ψ photoproduction on nuclei at small x . Using the leading twist model of nuclear shadowing, we predicted that the nuclear suppression of the incoherent cross section $\sigma_{\gamma\text{Pb} \rightarrow X J/\psi}(W_{\gamma p})$ should be approximately as large as that in the coherent case [13–15]. It underestimates the experimentally measured cross section [12] and calls for further analysis.

Another opportunity to constrain $g_A(x, \mu^2)$ at small x is presented by UPCs accompanied by forward neutron emission due to electromagnetic excitation of one or both colliding ions by additional photon exchanges [6, 8]. They do not affect nuclear coherence, but modify the photon flux by pushing it towards smaller impact parameters. Thus, by measuring the UPC cross section in any two channels ($0nXn$ and $XnXn$ in the example below) corresponding to certain numbers of forward neutrons detected in zero-degree calorimeters (ZDCs), one has the possibility to separate the low- x and high- x contributions to the cross section by solving the following system of equations (compare to Eq. (1)):

$$\begin{aligned} \frac{d\sigma^{0nXn}}{dy} &= N_{\gamma/A}^{0nXn}(y) \sigma_{\gamma A \rightarrow AJ/\psi}(y) + N_{\gamma/A}^{0nXn}(-y) \sigma_{\gamma A \rightarrow AJ/\psi}(-y); \\ \frac{d\sigma^{XnXn}}{dy} &= N_{\gamma/A}^{XnXn}(y) \sigma_{\gamma A \rightarrow AJ/\psi}(y) + N_{\gamma/A}^{XnXn}(-y) \sigma_{\gamma A \rightarrow AJ/\psi}(-y). \end{aligned} \quad (7)$$

The $0nXn$ channel corresponds to at least one neutron detected in one ZDC and no neutrons in the other one; the $XnXn$ channels denotes the situation, when both ZDCs register at least one neutron. The corresponding photon fluxes are labeled by the respective superscripts.

One more opportunity to separate the low- x and high- x contributions to the cross section can be realized by measuring the incoherent photoproduction with detection of the $0nXn$ channel. In this case the neutrons are almost always emitted by the target nucleus, which means that the neutron and J/ψ directions are correlated: their opposite directions correspond to the high-energy photons. Thus, the use of this correlation allows one to probe $g_A(x, \mu^2)$ at very small values of x [6].

We also studied nuclear shadowing in photoproduction of ρ mesons on nuclei in Pb–Pb UPCs and showed that the available RHIC and LHC data can be described (Fig. 2) when one takes into account inelastic Gribov shadowing and modifications of the vector meson dominance model to enhance

the contribution of small transverse-size configurations in the photon [19]. The latter is a general observation, which can be tested by studying the number of wounded nucleons in inelastic photon–nucleus scattering [20].

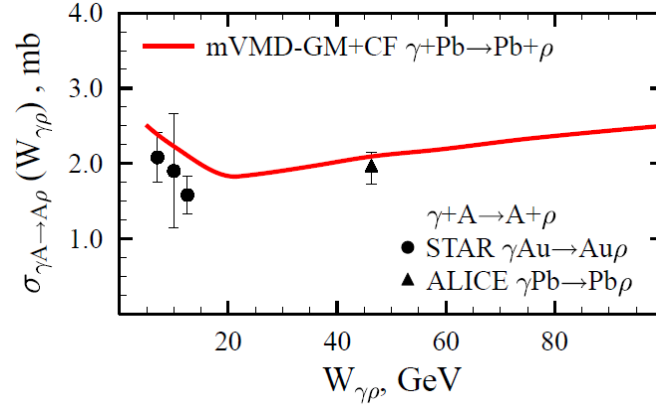


Fig. 2. Theoretical ρ -meson photoproduction cross section on Pb (calculated taking into account the Gribov–Glauber nuclear shadowing and the enhancement of small transverse size configurations in the photon wave function) is compared to the values extracted from STAR–RHIC and ALICE UPC data

The program of UPC measurements continues in Run-2 at the LHC; our predictions (Fig. 3) for the cross sections of photoproduction of light and heavy vector mesons on nuclei in the Run-2 kinematics are given in Ref. [8].

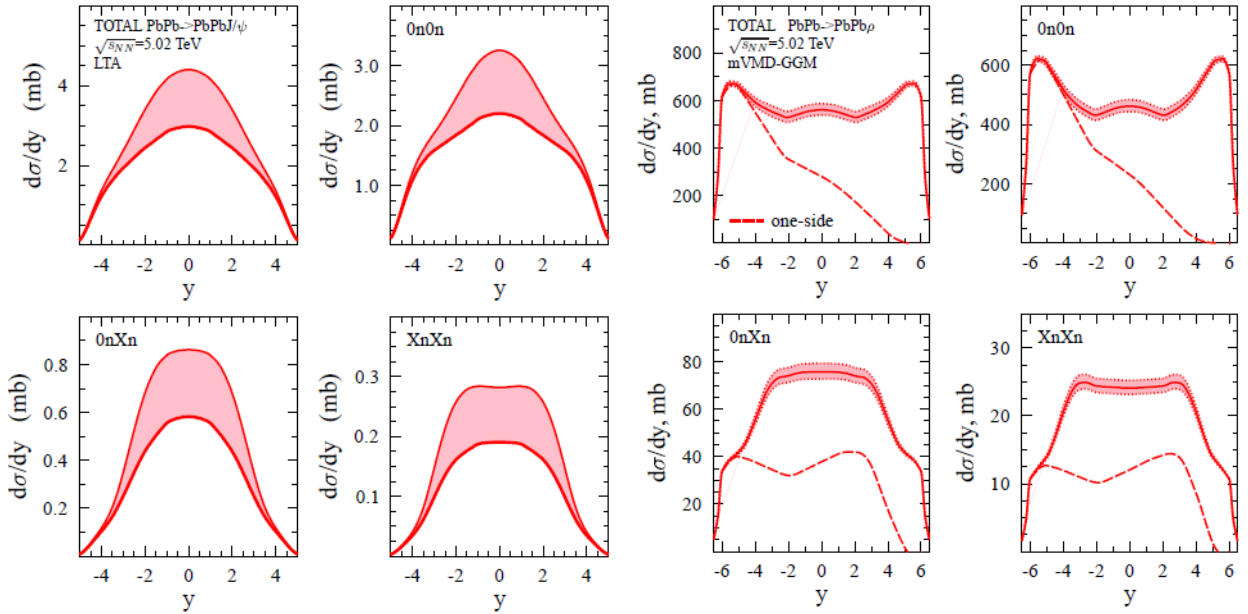


Fig. 3. Our predictions for the coherent ρ meson and charmonium photoproduction cross sections in Pb–Pb UPCs at energies $\sqrt{s_{NN}} = 5.02$ TeV (Run-2). The shaded area shows theoretical uncertainties. Predictions are given also for the coherent photoproduction accompanied by electromagnetic excitation of colliding nuclei with subsequent decay by neutrons

In addition, the ATLAS Collaboration also measured photoproduction of dijets on nuclei, which probes both $g_A(x, \mu^2)$ and the quark nPDFs at small and intermediate x and large μ . Requiring that the target nucleus stays intact allows one to study diffractive dijet photoproduction, which probes nuclear diffractive PDFs at small x and might shed some light on the open question of QCD factorization breaking in diffraction [21].

5. Conclusion

Over the last five years, the PNPI group has provided an important contribution to the theoretical support of the program of photon-induced processes at the LHC in terms of a steady stream of publications, conference and workshop presentations, and participation in planning of future measurements. This is especially topical because members of PNPI play a prominent role in the ALICE Collaboration and, in particular, in obtaining and analysing UPC data.

To summarize, we showed that the ALICE and CMS data on exclusive J/ψ photoproduction in Pb–Pb UPCs give first and weakly model-dependent evidence of large nuclear gluon shadowing: $R_g(x, \mu^2) = g_A(x, \mu^2)/A g_p(x, \mu^2) \approx 0.6$ at $x = 0.001$ and $\mu^2 = 3 \text{ GeV}^2$. It agrees with the predictions of the leading twist model of nuclear shadowing and the EPS09 nPDFs. While this result is important for constraining the gluon density in nuclei $g_A(x, \mu^2)$ at small x , it is a theoretical challenge to develop an unambiguous method to include the UPC data in global QCD fits of nPDFs. We also emphasized the importance and made predictions of the cross sections for incoherent J/ψ photoproduction on nuclei and UPCs accompanied by forward neutron emission in the LHC kinematics, including Run-2, which provide an access to $g_A(x, \mu^2)$ at even smaller values x . In Refs. [5, 9] we explained that the suppression of J/ψ photoproduction on nuclei leads both to the suppression of the gluon density in nuclei and broadening of the gluon distribution in the transverse plane by 5–11%. This results in a shift of the momentum transfer dependence towards smaller values of $|t|$ comparing to the dependence dictated by the nuclear form factor. Some evidence for such a shift is seen in the ALICE data.

References

1. K.J. Eskola, P. Paakkinen, H. Paukkunen, C.A. Salgado, *Eur. Phys. J. C* **77**, 163 (2017).
2. L. Frankfurt, V. Guzey, M. Strikman, *Phys. Rept.* **512**, 255 (2012).
3. V. Guzey, E. Kryshen, M. Strikman, M. Zhalov, *Phys. Lett. B* **726**, 290 (2013).
4. V. Guzey, M. Zhalov, *JHEP* **1310**, 207 (2013).
5. V. Guzey, M. Zhalov, *JHEP* **1402**, 046 (2014).
6. V. Guzey, M. Strikman, M. Zhalov, *Eur. Phys. J. C* **74**, 2942 (2014).
7. V.A. Guzey, M.B. Zhalov, *Bull. Russ. Acad. Sci. Phys.* **79**, No. 7, 912 (2015) [*Izv. Ross. Akad. Nauk Ser. Fiz.* **79**, No. 7, 1018 (2015)].
8. V. Guzey, E. Kryshen, M. Zhalov, *Phys. Rev. C* **93**, No. 5, 055206 (2016).
9. V.A. Guzey, M.B. Zhalov, *Bull. Russ. Acad. Sci. Phys.* **80**, No. 8, 970 (2016) [*Izv. Ross. Akad. Nauk Ser. Fiz.* **80**, No. 8, 1058 (2016)].
10. V. Guzey, M. Strikman, M. Zhalov, *Phys. Rev. C* **95**, No. 2, 025204 (2017).
11. A.J. Baltz *et al.*, *Phys. Rept.* **458**, 1 (2008).
12. ALICE Collaboration, E. Abbas *et al.*, *Eur. Phys. J. C* **73**, 2617 (2013).
13. ALICE Collaboration, B. Abelev *et al.*, *Phys. Lett. B* **718**, 1273 (2013).
14. ALICE Collaboration, J. Adam *et al.*, *Phys. Lett. B* **751**, 358 (2013).
15. CMS Collaboration, V. Khachatryan *et al.*, *Phys. Lett. B* **772**, 489 (2017).
16. M.G. Ryskin, *Zh. Phys. C* **57**, 89 (1993).
17. M. Hirai, S. Kumano, T.-H. Nagai, *Phys. Rev. C* **76**, 065207 (2007).
18. D. de Florian, R. Sassot, *Phys. Rev. D* **69**, 074028 (2004).
19. L. Frankfurt, V. Guzey, M. Strikman, M. Zhalov, *Phys. Lett. B* **752**, 51 (2016).
20. M. Alvioli, L. Frankfurt, V. Guzey *et al.*, *Phys. Lett. B* **767**, 450 (2017).
21. V. Guzey, M. Klasen, *JHEP* **1604**, 159 (2016).

COLLIMATION OF THE LARGE HADRON COLLIDER BEAMS WITH CRYSTALS

Yu.M. Ivanov, A.S. Denisov, Yu.A. Gavrikov, B.L. Gorshkov, M.A. Koznov, L.P. Lapina, L.G. Malyarenko, V.I. Murzin, L.F. Pavlova, V.V. Skorobogatov, L.A. Vaishnene

1. Introduction

The collimation system in the Large Hadron Collider (LHC) is designed to absorb the growing halo of the circulating beam to protect the accelerator components from damage and to reduce the background of the collider experiments. In the present collimation system (Fig. 1), primary collimators working as solid targets give angular kicks to halo particles increasing their impact parameters on the next large secondary collimators and absorbers. A solid target deflects particles due to Coulomb scattering, therefore, the maximum of the halo particle distribution stays at the absorber edge.

The collimation process can be improved by using a bent crystal as a primary collimator (Fig. 2). In this case, the crystal in the channeling regime deflects halo particles onto the absorber far from its edge, so the collimation efficiency increases due to reduction of particle scattering from the absorber back to the beam and due to suppression of inelastic interactions in the channeling crystal collimator. This is the basis for consideration of the crystal collimation capable to solve the beam loss problem for the high-luminosity upgrade (HL) of the LHC.

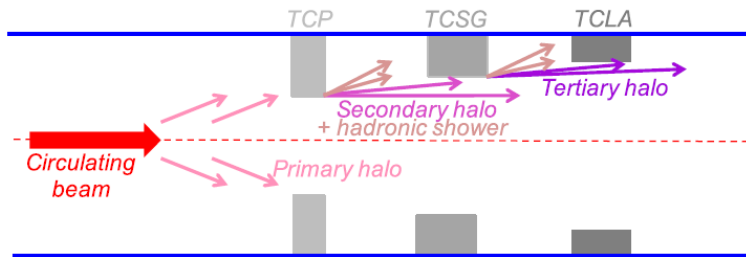


Fig. 1. Working principle of the present collimation system: TCP – primary collimator; TCSG – secondary collimator; TCLA – absorber

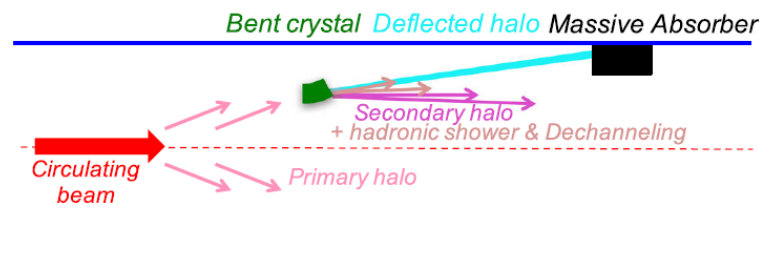


Fig. 2. Working principle of the crystal collimation system

2. Crystal collimation feasibility studies at the Super Proton Synchrotron (experiment UA9)

After an extensive investigation of the beam-crystal interaction at the Super Proton Synchrotron (SPS) H8 and H4 external beam lines in the frames of the H8-RD22 Collaboration in 2006–2008, in order to demonstrate the feasibility and advantages of the crystal-based collimation and to justify the design requirements for the LHC, the experiment UA9 was proposed and carried out at the CERN SPS in 2009–2018 [1–6]. PNPI scientists and engineers contributed significantly to the success of the UA9 Collaboration studies.

The experimental UA9 layout is shown in Fig. 3. It consists of several units located in the SPS tunnel in the accelerator pipe and near the pipe. It includes a scraper set before the collimation region, which is intended to block the multi-turn effect. In the beginning of the collimation region, several goniometers with different type crystals used alternately as a primary collimator are installed. After them goes a two-sided

collimator intended to align the UA9 elements relative to the beam orbit and to scan the deflected halo. In the end of the collimation region, there is a 60-cm-long tungsten absorber. A medipix pixel detector is mounted in one of the Roman Pots, it is used to observe the spatial distribution of the deflected particles. A few beam loss monitors (BLM) are mounted along the accelerator pipe, they are used to register secondary particles from interaction of the high energy beam with the set-up elements. In the first dispersive area downstream the absorber, a 10-cm-long tungsten scraper limiting the accelerator aperture is installed to detect off-momentum halo particles. Such particles, which have lost a part of the momentum in the crystal or in the absorber, may escape from the collimation area. At the high dispersion area, they undergo an additional displacement from the orbit and cross the scraper giving a signal in the nearest BLM.

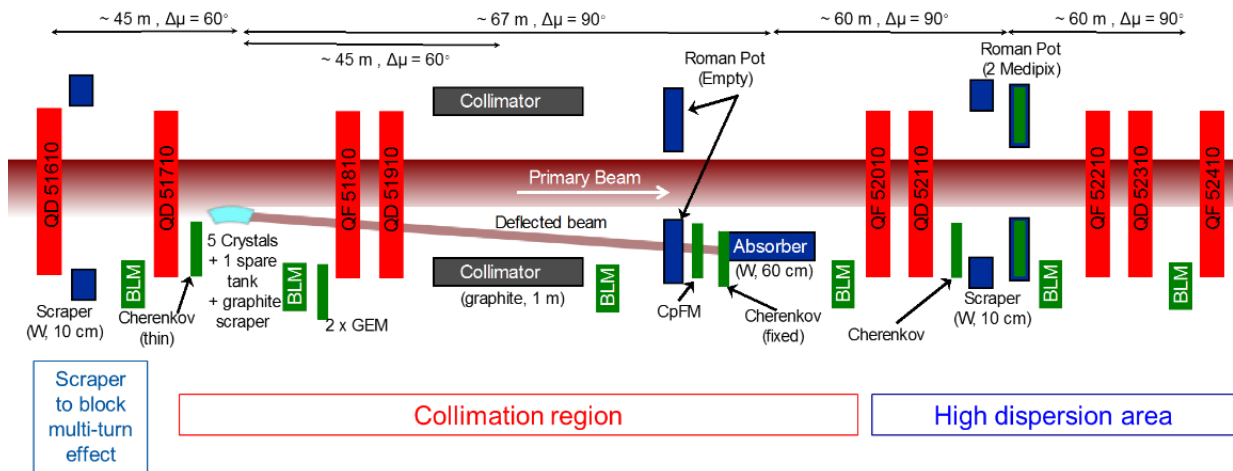


Fig. 3. Experimental UA9 layout in the SPS accelerator ring

Two series of bent silicon crystals were developed for the UA9 project – with anticlastic bending of (110) atomic planes and with quasi-mosaic (QM) bending of (111) planes. The first type crystals invented at Institute for High Energy Physics (IHEP) were produced by Istituto Nazionale di Fisica Nucleare (INFN), Fig. 4. The second type crystals were designed and produced by PNPI (Fig. 5). All crystals had the bending angle in the optimal range 150–200 μrad and the length along the beam from sub-millimeters to a few millimeters depending on the experimental task.

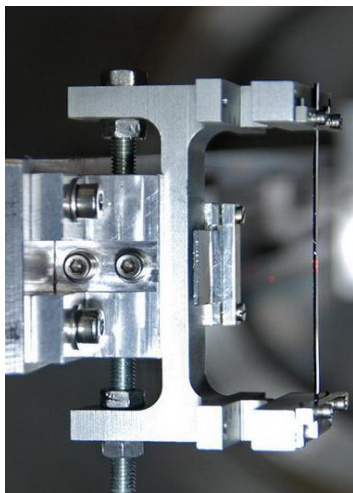


Fig. 4. Crystal with anticlastic bending (IHEP–INFN)

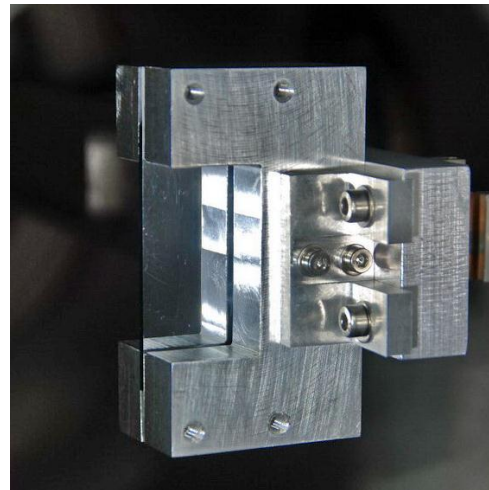


Fig. 5. Crystal with QM bending (PNPI)

The UA9 studies were performed in stored proton beams of 120 and 270 GeV/c momentum, typically with 10^9 – 10^{12} particles in a single bunch. Lead ion beams were used in the same range of the momentum per charge and with ten times less particles. In the storage mode, the beam lifetime ranged from a few minutes to 10 hours. The number of particles hitting the crystal was in the range of 10 – 10^3 protons per bunch of a few ns length. To increase the total intensity and the loss rate, four, eight or 52 bunches were used.

A typical response of the BLM to the angular scan of the crystal is shown in Fig. 6. In the minimum of the loss count, the fraction of the beam halo channeled by the crystal is maximal. With the best crystals, the reduction of the beam losses in the channeling state reached a factor of ~ 25 . A wide angular range of decreased beam losses to the right of the minimum is due to volume reflection of halo particles in the crystal. A typical image of the deflected halo obtained with the Medipix detector is shown in Fig. 7.

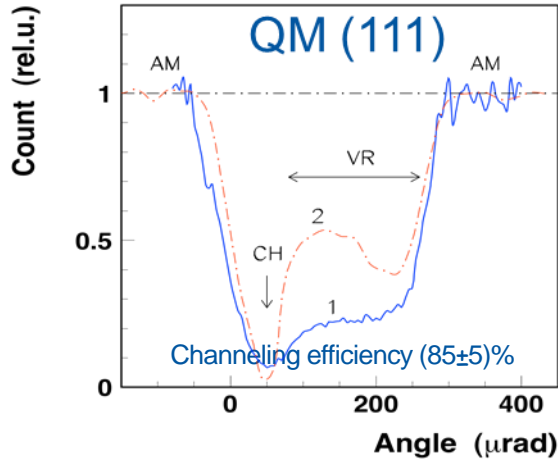


Fig. 6. BLM counts vs the angular position of the QM crystal (1); the number of inelastic interactions in the crystal vs the orientation angle obtained by simulations (2); AM – amorphous; CH – channeling; VR – volume reflection

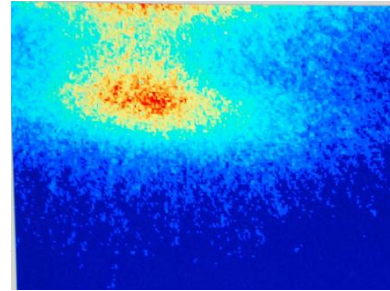


Fig. 7. Edge of the main beam and the beam channeled by the QM crystal registered with the Medipix detector

The channeling efficiency was studied through linear scanning with the collimator across the deflected beam. A typical result of such a scan is shown in Fig. 8. The deflected beam profile found from the scan is shown there below. The channeling efficiency was estimated to be $(85 \pm 5)\%$ for this QM crystal, for other crystals similar values were obtained.

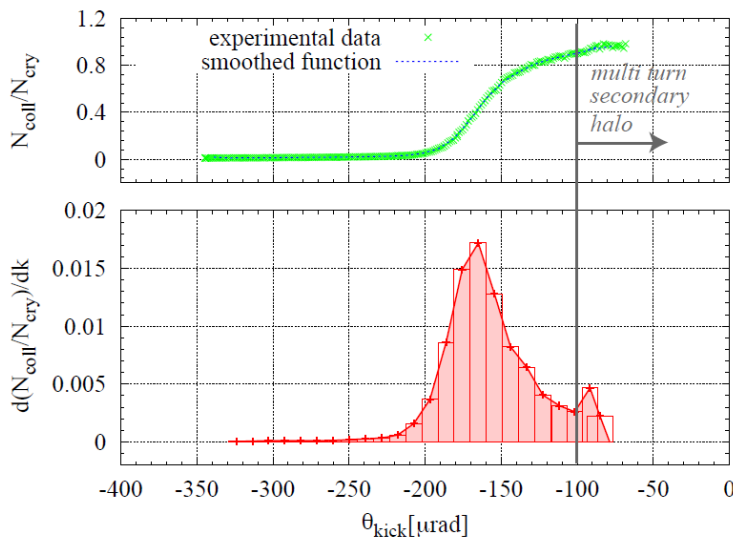


Fig. 8. The BLM signal during the collimator scan of the beam deflected by the QM crystal, plotted as a function of the collimator position (*top*); the numerical derivative of the BLM signal corresponding to the channeled beam profile; the collimator position is shown in the angular scale (*bottom*)

The effect from the off-momentum halo particles escaping the collimation region was investigated through the linear scanning with the scraper in the high-dispersion area. The off-momentum collimation leakage with a perfectly aligned crystal was found to be reduced by at least an order of magnitude.

A stored multi-bunched beam was used to measure beam losses in regions of the SPS ring far from the crystal (1 km and more downstream the crystal). It was found that the beam losses for the channeling orientation are few times smaller than those for the amorphous one.

Summarizing, the UA9 experiment has shown a strong reduction of the collimation leakage in the SPS accelerator ring working in the storage mode with the crystal primary collimator (deflector) under channeling conditions. This UA9 result has demonstrated the crystal collimation advantages with respect to the standard collimation scheme and stimulated an extension of studies from the SPS to the LHC.

3. Crystal collimation studies at the Large Hadron Collider in 2014–2016. Observation of channeling at LHC energies

The collimation system at the LHC is composed of 44 movable collimators per beam (Fig. 9). Two LHC insertion regions (IR) are dedicated to collimation: IR3 for momentum cleaning, *i. e.* removal of particles with a large energy offset; and IR7 for betatron cleaning, *i. e.* continuous controlled disposal of transverse halo particles. Each collimator insertion features a three-stage cleaning based on primary collimators (TCP), a secondary collimator (TCSG), and an absorber (TCLA) working in horizontal, vertical and skew planes. In this scheme, the energy carried by the beam halo intercepted by the TCPs is distributed over several collimators (*e. g.* 19 collimators are used in the betatron cleaning insertion). Dedicated collimators for protection of sensitive equipment (such as TCTP for the inner triplets), absorption of physics debris (TCL), and beam dump protection (TCSP) are present at specific locations of the machine.

In fact, the crystal collimation project in the LHC ring started in 2011 [7]. Its concept relies on steering of halo particles onto a single massive absorber per plane by using crystal channeling. Ideally, only one bent crystal per plane is needed, with an associated absorber of channeled particles. Bent crystals are placed at the edge of the beam envelope, as with the present TCPs, and they are angularly oriented to position the crystalline planes at the entry point parallel to the beam direction.

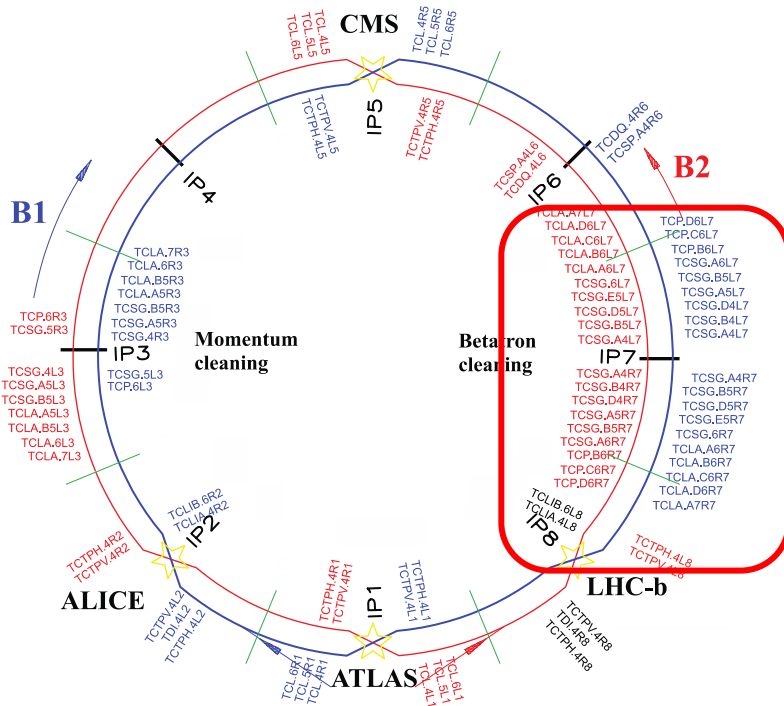


Fig. 9. Collimation layout in the LHC for both beams (B1 and B2). Area with the installed crystals is outlined by red

The main advantages of the crystal collimation system are a significant reduction of losses in IR7 and an important decrease of the machine impedance. The present collimation system takes about 90% of the resistive wall impedance of the LHC, which is mainly due to 19 collimators in IR7. Thus, a fewer number of collimators surrounding the beam in the case of crystal collimation would lead to a drastic reduction of the resistive wall impedance of the entire machine, improving this way the machine stability. The improved cleaning performance is reached mainly due to a reduced inelastic interaction rate at the crystal compared to TCPs. The crystal bending leads to large impact parameters on the absorber, increasing its effective length seen by the impacting particles and therefore reducing the number of out-scattered protons that could emerge with a significant energy offset.

The proposed plan was to install crystals close to the existing LHC primary collimators and to use the existing LHC secondary collimators as absorbers of the channeled halo particles (Fig. 10). The acceptance of the channeling process is very small at the LHC maximum energy. The critical angle is of the order of about $2.5 \mu\text{rad}$ at 7 TeV (*i. e.* the maximum angle with respect to the crystalline planes to undergo channeling). Thus, the location of crystals in the lattice of the machine has to provide an angular distribution of incident particles much smaller than the critical angle to ensure stable channeling. The crystal locations found through detailed simulations [8] allow to reach the angular distributions below $1 \mu\text{rad}$ at 7 TeV.

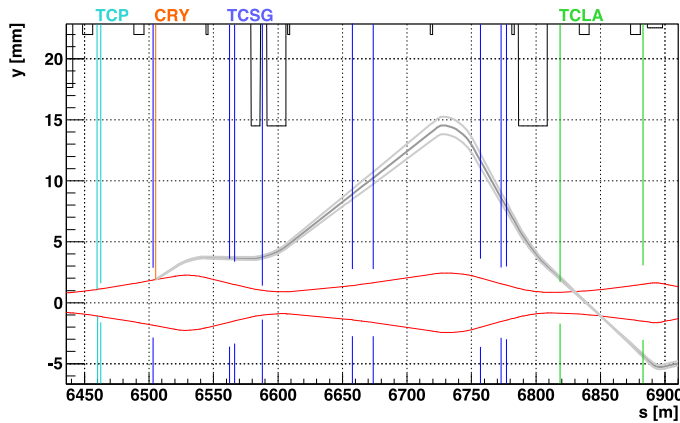


Fig. 10. Simulation of halo particles deflected by a crystal in the channeling regime at the LHC

In 2011–2013, the first generation of high precision piezo-goniometers with sub-microradian angular resolution (Fig. 11) were developed at CERN for horizontal and vertical crystal collimation tests at beam-1. An important feature of the goniometer design is its complete transparency for the normal LHC operations. This is ensured by a movable segment of the beam pipe that masks the crystal and the goniometer itself. It is remotely retracted only during special collimation tests, to allow the crystal insertion. The goniometers were mounted on standard collimation supports using the same fast plug-in technology, which ensures fast handling of the object in the tunnel.

The bending angle of the crystal should be such as to provide the maximal impact parameters of deflected halo particles with the collimator-absorbers while ensuring that the deflected halo remains at a safe distance from the beam pipe. The bending angle of the crystal for the LHC beam collimation was selected from these considerations to be $\alpha = 50 \mu\text{rad}$.

This bending angle can be realized with different crystal length L and consequently with different bending radius R , $L = \alpha R$. For channeling, the bending radius should exceed the critical value $R_c = pv/eE_{\text{max}}$, where E_{max} is the maximal strength of the planar electric field. For protons with 6.5 TeV/c momentum, R_c is equal to 11 m in the (110) silicon channels. The efficiency of proton channeling for the crystal with a given bending angle α , considering the possibility of their multiple passages through the crystal, is maximal when its bending radius R is in the range of $(3\div 10) R_c$. The length of the LHC crystals was chosen to be $L = 4 \text{ mm}$, that is their bending radius $R = 80 \text{ m} \approx 7 R_c$.



Fig. 11. One of the first piezo-goniometers for crystal collimation experiments at the LHC

Two types of crystals were prepared for the project. A silicon strip crystal bent along the (110) planes due to anticlastic deformation (Fig. 12) was developed at INFN and installed for the LHC beam collimation in the horizontal plane. A QM crystal bent along the (111) planes due to the QM effect (Fig. 13) was developed at PNPI and installed for the LHC collimation in the vertical plane. The bending devices for both crystals were made from titanium to reduce possible electron emission from them when LHC proton bunches pass the azimuths of their locations.

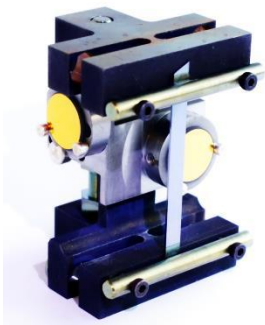


Fig. 12. Crystal STF76 with anticlastic bending designed and produced by INFN for LHC beam-1. It is used for collimation in the horizontal plane

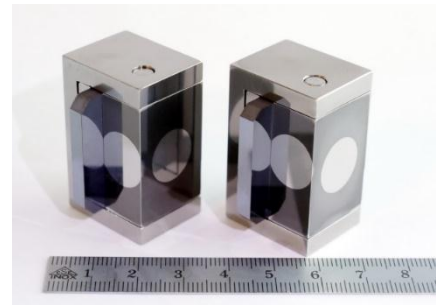


Fig. 13. Crystals QMP33 and QMP34 with QM bending designed and produced by PNPI for LHC beam-1. Crystal QMP34 was used for collimation in the vertical plane

During the long shutdown in 2014, the two crystals, STF76 and QMP34, were installed in the IR7 betatron cleaning insertion of beam-1, for horizontal and vertical collimation tests. They were placed on the external and top side of the machine, respectively. The first measurements with crystals started in 2015 and continued in 2016. In measurements, bent crystals were approached to the circulating beams to test their usage as a first stage in the crystal-based collimation system, both in proton and Pb ion beams. Tests were performed with protons at the injection energy (450 GeV) and at the flat top (6.5 TeV), and with ions at the injection energy (450 Z GeV). A reduction of losses immediately downstream of the crystals was observed in optimum channeling orientation, demonstrating for the first time particle channeling at these energies [9]. Typical results with 6.5 TeV protons at beam-1 are shown in Figs. 14 and 15. Measurements at the LHC confirmed the value of the bending angle determined after fabrication in the case of QMP34, but gave a larger value in the case of STF76, which revealed a problem with the bender design.

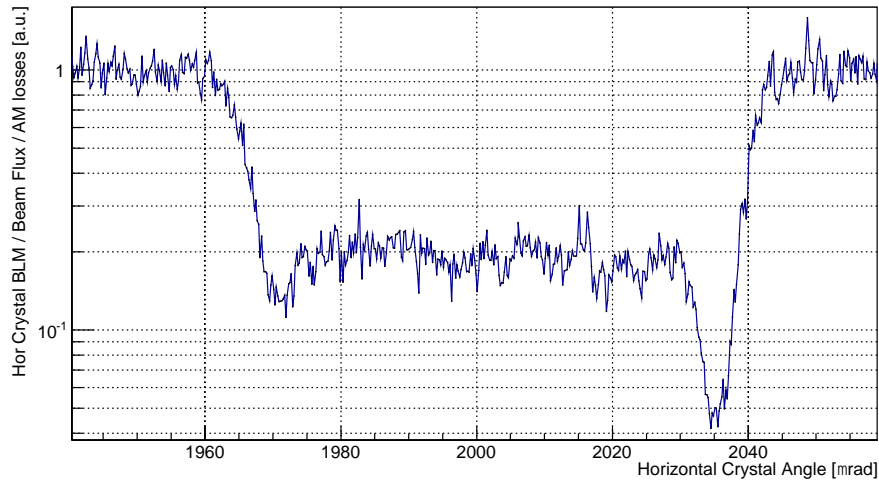


Fig. 14. Horizontal crystal angular scan for 6.5 TeV protons at the distance of 5.5σ from the axis of beam-1. The reduction factor is 26.9 in the channeling position

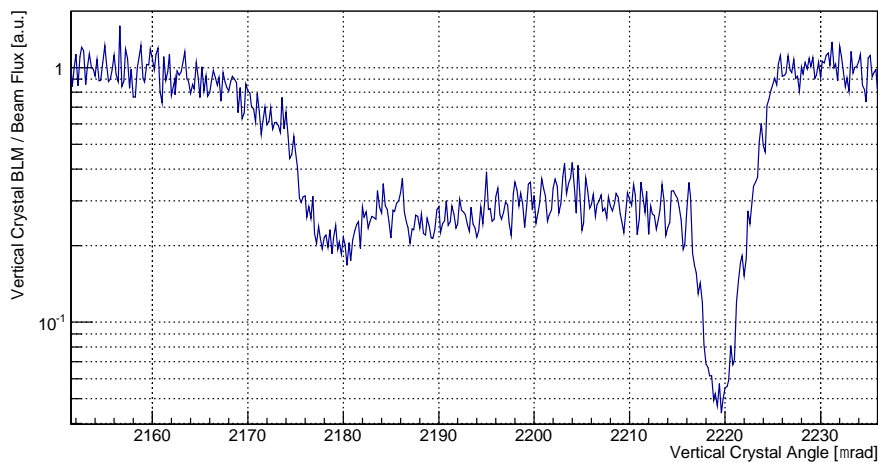


Fig. 15. Vertical crystal angular scan for 6.5 TeV protons at the distance of 5.5σ from the axis of beam-1. The reduction factor is 23.5 in the channeling position

4. Crystal collimation studies at the Large Hadron Collider in 2017–2018

In 2015–2016, an improved second generation of piezo-goniometers was developed at CERN for crystal collimation tests with LHC beam-2. In parallel, a new series of crystals with QM bending for installation in the new goniometers was designed and produced at PNPI (Fig. 16). Before using them at the LHC, all crystals were tested many times with SPS extracted beams and showed good stability. Finally, two of them, QMP52 and QMP53, were chosen for installation at the LHC.

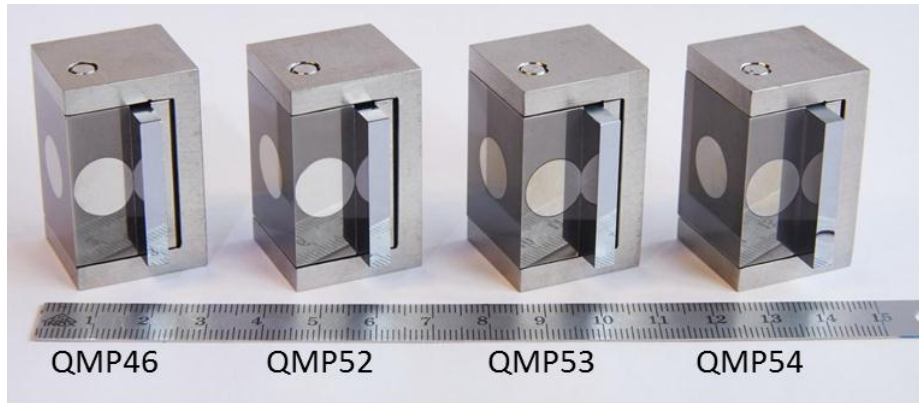


Fig. 16. Crystals with QM bending designed and produced at PNPI for crystal collimation tests in LHC beam-2. QMP52 and QMP53 crystals installed at the LHC

In 2017, detailed measurements with new crystals were performed. Scanning in a wide angular range made at the injection energy showed that crystal QMP52 installed in the horizontal collimation plane of LHC beam-2 is aligned too close to the crystal axis, so that channeling in skew planes becomes essential and modifies planar channeling in (111) planes (Fig. 17). It is seen from a comparison with the angular scan in the vertical collimation plane of LHC beam-2.

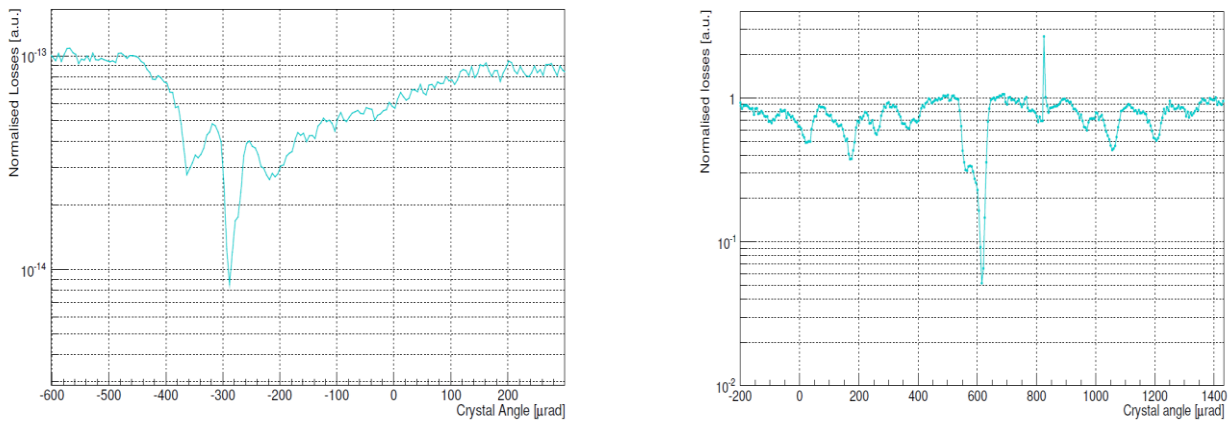


Fig. 17. Horizontal (*left*) and vertical (*right*) crystal angular scans in beam-2 at the injection energy. The losses are normalized to the beam flux and are shown as a function of the orientation angle [10]

In 2016–2017, a new series of bent crystals for the LHC was developed at PNPI and tested in external beams at the H8 SPS CERN. The crystals of this series have (110) channeling planes which are bent due to anticlastic effect with titanium holder specially designed to provide the required bending angle and a high mechanical and thermal stability (Fig. 18).



Fig. 18. Crystals TCP76 and TCP77 with anticlastic bending designed and produced at PNPI for crystal collimation tests in LHC beam-2. Crystal TCP76 installed at the LHC

In 2018, the best from them (TCP76) was installed in a specially prepared new piezo-goniometer, which was then mounted in the horizontal collimation plane of beam-2 instead of the goniometer with crystal QMP52. It provided a complete set of crystals for collimation studies with both LHC beams during 2018. The data analysis is in progress [11]. A series of improved crystals was produced at PNPI and tested in external beams at the H8 SPS CERN during 2018 (Fig. 19).



Fig. 19. A series of improved crystals ACP79, ACP80, ACP84, ACP85, ACP86 with anticlastic bending designed and produced at PNPI for the future HL LHC

5. Conclusion

To study the feasibility of crystal collimation, a test bench was arranged in the betatron cleaning insertion of the LHC using the present collimators to absorb deflected halo particles. Four crystals in the vertical and horizontal planes of both LHC beams were installed. Channeling was observed by means of crystal angular scans and collimator linear scans in proton, xenon and lead ion beams. The reduction of losses (between amorphous and channeling orientations) was evaluated during the angular scans and compared for all crystals tested at the LHC. The factors of 20 and 8 were measured in proton and ion beams, respectively.

The demonstration that the goniometers are reliable during the LHC ramp, in which both the linear and rotational stages were used to keep the crystal in channeling, was successfully achieved. Good understanding of the dynamics allowed us to determine the function for both rotational and linear stages, and the stability of the goniometers was adequate to obtain excellent results. This, together with the observation that channeling was reliably under control at the top energy where the critical angle was $2.5 \mu\text{rad}$, represents an important step towards the operational deployment of this technology.

The major peaks of the beam loss maps were reproduced in simulations. For the vertical plane, using the configuration where all the downstream collimators were closed to the nominal aperture, good agreement between the leakages in measurements and simulations was observed.

Cleaning measurements in lead beams showed a general improvement when crystal collimation was deployed. The results previously obtained in Xe beams were reproduced. By using existing collimators in

IR7, at settings tighter than their nominal ones but still operationally usable, the leakages at the IR7 magnets were improved by factors up to > 60 (at the first dispersive peak) and > 10 (at the second peak), which is remarkable. These measurements are important because demonstrate a promising potential of using bent crystals for ion cleaning at the LHC. A systematic study shows how a proper arrangement of several collimators (secondary collimators and absorbers) can reduce losses, as observed consistently in IR7 and IR3.

References

1. W. Scandale *et al.*, Phys. Lett. B **692**, 78 (2010).
2. W. Scandale *et al.*, JINST **6**, T10002 (2011).
3. W. Scandale *et al.*, Phys. Lett. B **703**, 547 (2011).
4. W. Scandale *et al.*, Phys. Lett. B **714**, 231 (2012).
5. W. Scandale *et al.*, Phys. Lett. B **726**, 182 (2013).
6. W. Scandale *et al.*, Phys. Lett. B **748**, 451 (2015).
7. LUA9 Collaboration, CERN-LHCC-2011-007 / LHCC-I-019 10/06/2011 (2011).
8. D. Mirarchi, CERN-THESIS-2015-099 (2015).
9. W. Scandale *et al.*, Phys. Lett. B **758**, 129 (2016).
10. R. Rossi, CERN-THESIS-2017-424 (2017).
11. Crystal Cleaning the LHC Beam, CERN Bull., Iss. 48–49 (2018).

EXPERIMENT D0: RECENT RESULTS AND JETS WITH LARGE RAPIDITY SEPARATION

PNPI participants of the D0 Collaboration:

G.D. Alkhazov, V.T. Kim, A.A. Lobodenko, P.V. Neustroev, G.Z. Odrant, V.A. Oreshkin, Yu.A. Shcheglov, L.N. Uvarov, S.L. Uvarov

1. Introduction

D0 is an international collaboration of about 670 physicists from 83 institutions, who have designed, built and operated a collider detector at the Fermilab Tevatron.

Main physics goals are precision tests of the Standard Model (SM), weak bosons physics, top-quark physics, quantum chromodynamics (QCD), B physics, a search for the Higgs boson, and a search for particles and forces beyond the SM: supersymmetric particles, gravitons, candidates for the cosmic dark matter, and a search for extra dimensions.

During Run-2, the Tevatron was operated at an increased $p\bar{p}$ centre-of-mass energy of 1.96 TeV. The luminosity was increased by a factor more than ten, to $\geq 10^{32} \text{ cm}^{-2} \cdot \text{s}^{-1}$. Originally, the Tevatron operation and the data taking were planned up to 2009. However, the Tevatron operation was extended to 2011. By the end of September 2011, the data taking was completed, and the Tevatron was shut down. The data, corresponding to about 11 fb^{-1} of an integrated luminosity, were collected by the D0 experiment. The analyses of the collected data will continue a few more years.

PNPI was involved in the D0 project through the design and programming of the electronic readout for mini drift tubes (50 000 channels) and operation of the forward muon system [1]. PNPI physicists took part in the data analysis, including QCD, B physics, and electroweak and new phenomena physics studies. Among recent D0 physics results are the top-quark mass, the $t\bar{t}$ forward–backward production asymmetry, the cross section for single top-quark production, the measurement of the weak mixing angle, the discovery of new resonances $X(5568)$ and $X(4140)$, and the study of the double parton interaction. This report presents several D0 results obtained in 2013–2017 years.

2. D0 detector

The Run-2 D0 detector (Fig. 1) [2] consists of a central tracking system, a liquid–argon/uranium sampling calorimeter and an iron toroid muon spectrometer. The central tracking system is composed of a silicon microstrip tracker (SMT) and a central fiber tracker, both located into a 2 T superconducting solenoidal magnet. The SMT detector has about 800 000 individual strips, and its design is optimized for tracking and vertexing capabilities allowing heavy flavour tagging. The calorimeter is longitudinally segmented into electromagnetic and hadronic layers and is housed into three cryostats. The muon system [3] resides beyond the calorimeter and consists of a layer of tracking detectors and scintillation counters before the toroidal magnet, followed by two similar layers after the toroid. Tracking in the muon system relies on wide or mini drift tubes, depending on the acceptance. The Run-2 D0 detector allows to work at the luminosity of $> 10^{32} \text{ cm}^{-2} \cdot \text{s}^{-1}$. The D0 detector is described in detail in Ref. [2]. The rapidity coverages of the tracks, muons and jets are $|\eta| < 2.4$, $|\eta| < 2.0$, and $|\eta| < 3.6$, respectively.

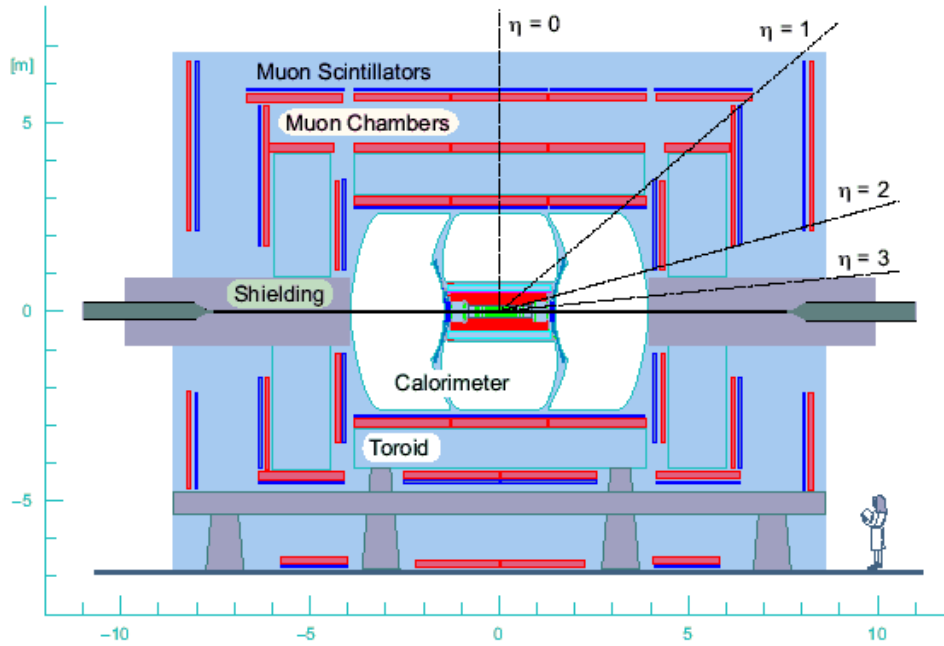


Fig. 1. Schematic view of the D0 detector

3. Top-quark pair production cross section and top-quark mass

The t quark, the heaviest particle known, was discovered at the Tevatron in 1995. Since then, the study of the top quark was one of important directions of investigations at D0. The top-quark mass is a fundamental SM parameter. It is related to other fundamental parameters, m_H and m_W , through radiative corrections. Namely, the loop diagrams that contain the top quark dominate among other loop diagrams which make the quantum correction to the masses of the W and H bosons. This provides a consistency check of the SM by comparing the direct measurement of the Higgs boson mass with the constraints derived from the top and W -boson masses. Since the top quark has the largest Yukawa coupling to Higgs, it may play a special role in electroweak symmetry breaking by governing the shape of the Higgs potential and thus may shed some light on the fundamental question of vacuum stability in our universe.

The top-quark pair production occurs *via* either quark–antiquark annihilation or gluon–gluon fusion. At the Tevatron, the former process comprises approximately 85% of the top–antitop production, and the latter about 15%, which is roughly the other way round at the Large Hadron Collider (LHC). Thus, the Tevatron result provides complementary information to the result of the LHC.

Different methods were used at D0 to derive the top-quark mass – the template method and the matrix element (ME) method. In the template method, the multivariate analysis (MVA) technique is used to construct a discriminant variable which is aimed at separating the signal events from various types of background. Templates of its distributions are built using Monte Carlo (MC) simulation for $t\bar{t}$ signal at different values of the top-quark mass m_t . A likelihood fit to the data determines the best signal template and thus m_t is found. Systematic uncertainties are also determined in the fit by introducing nuisance parameters for each source of systematic uncertainty. In the ME method, there is no need for MVA (except for the b -tagging one), which could distinguish signal from background, because an event-by-event probability is constructed as a function of m_t , making use of all reconstructed objects in the events. For that purpose the matrix elements, PDFs and transition functions which relate the parton-level kinematics to the jet-level, *e. g.* the parton p_T to the jet p_T , are used to construct the probability function employed in the likelihood fit. Because it uses the full kinematic information, the ME method offers the best statistical sensitivity. In both methods, by introducing another free parameter that corrects the jet energy scale (JES), the JES uncertainty is reduced by a factor of three with an *in situ* calibration which exploits the hadronic $W \rightarrow q\bar{q}$ decay by constraining the invariant mass of

the dijet system to be consistent with the mass of the W boson, $m_W = 80.4 \text{ GeV}/c^2$. This additional calibration was accessible only for the “jet + lepton” channel.

In the triggering and analysis, the event selection was done with high- p_T isolated leptons, high E_T multiple jets, a large missing energy E_T and displaced vertices for b -jets. Good momentum resolution is required for all objects, especially the jet energy scale should be known with high precision.

For the dilepton channel, using the template method the top-quark mass was obtained to be 173.32 ± 1.36 (stat) ± 0.85 (syst) GeV/c^2 [4]. To correct for the difference of p_T distributions of two neutrinos present in the event and the missing energy, a special event weight was introduced. The dominant systematic uncertainties come from the knowledge of the absolute JES ($0.47 \text{ GeV}/c^2$), its flavour-dependence ($0.36 \text{ GeV}/c^2$) and higher-order effects on the signal modelling ($0.33 \text{ GeV}/c^2$).

Alternatively, the ME technique was used to extract the top-quark mass in the dilepton channel 173.93 ± 1.61 (stat) ± 0.88 (syst) GeV/c^2 [5] and the “lepton + jets” channel [6]. In this measurement, the neutrino momenta are integrated out to overcome the challenge of the kinematically underconstrained system.

The combined result for the top-quark mass, obtained by the D0 and CDF Collaborations from the data of Run-1 and Run-2, is $m_t = 174.30 \pm 0.65 \text{ GeV}/c^2$ [7] (Fig. 2).

The mass that was presented so far comes from measuring what the top-quark decays into relying on MC predictions, and therefore sometimes called the MC mass. This is not necessarily the same as what we want

for the number that goes with the diagram. The more theoretically well defined quantity, the top-quark “pole mass” entering the top-quark propagator, was also measured by D0. It was determined using an indirect method, *i. e.* exploiting the dependence of the inclusive $t\bar{t}$ production cross section on the top-quark pole mass, as observed in the measurement, with the expected dependency obtained in perturbative QCD using a next-to-next-to-leading order cross-section calculation with the top++ program [8]. The determined top-quark pole mass is 172.8 ± 1.1 (theo) ± 3.2 (exp) GeV/c^2 [9].

For all the MC simulations involving the generation of top quarks, a top-quark mass of $m_t = 172.5 \text{ GeV}/c^2$ is used. In particular, assuming the top-quark mass is $172.5 \text{ GeV}/c^2$, the $t\bar{t}$ production cross section was measured to be $\sigma_{t\bar{t}} = 7.26 \pm 0.13$ (stat) $^{+0.57}_{-0.50}$ (syst) pb [9].

Another measurement of the pole mass was based on the unfolded differential cross sections measured as a function of the top-antitop invariant mass and transverse momentum of the top and antitop quarks. The result of 169.1 ± 1.1 (theo) ± 2.2 (exp) GeV/c^2 [10] shows an improvement in terms of experimental uncertainties with regard to the measurement based on the inclusive cross section.

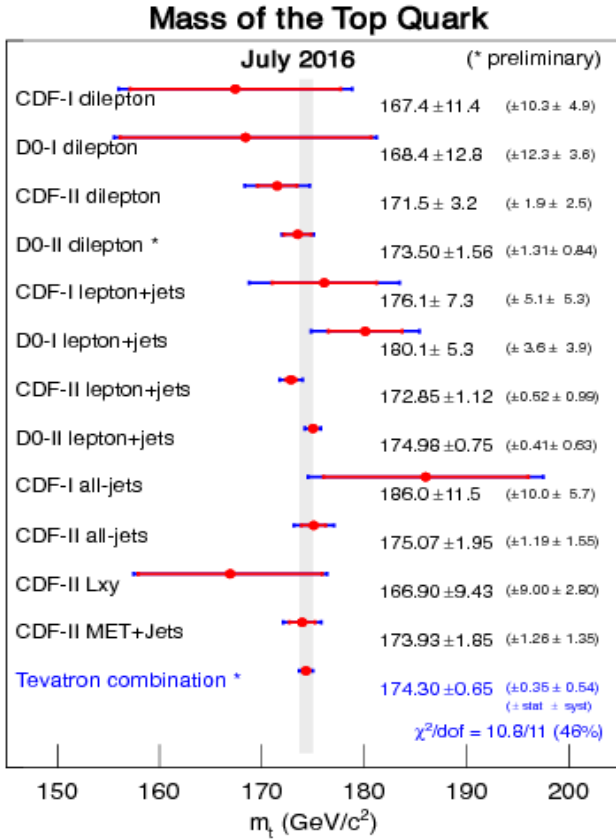


Fig. 2. Summary of the Tevatron top-quark mass measurements

4. Single top-quark production *via* the *s* channel and the CKM matrix element $|V_{tb}|$

Although the dominant production of the *t* quark is the top–antitop pair production *via* QCD, the single top production was also observed at D0. It proceeds *via* electroweak interaction of the *b* quark and the *W* boson. The single top production cross section is sensitive to the quark-mixing Cabibbo–Kobayashi–Maskawa (CKM) matrix element $|V_{tb}|$, without any assumption on the number of quark families or the unitarity of the CKM matrix. Thus it can serve as a probe for new phenomena such as a fourth generation of quarks.

The event selection in the search for single top quarks is similar to that for the search for top-quark pairs in the $l + \text{jets}$ mode.

The SM predicts the single top quark to have three different production processes: the *t* channel with the exchange of a virtual *W* boson, the *s* channel with the *W*-boson decaying into a top and antibottom quarks and the *Wt* channel with the associated production of a *W* boson and a top quark. The *t* channel is the dominant production channel and it was measured by D0 in 2011 using a data sample with an integrated luminosity 5.4 fb^{-1} . The latest achievement of D0 is the first observation of the *s*-channel single top-quark production [11]. In combination with the results obtained by the CDF experiment at the Tevatron, the cross sections were found to be $\sigma_t = 2.25^{+0.29}_{-0.31} \text{ pb}$ for the *t*-channel production and $\sigma_s = 1.29^{+0.26}_{-0.25} \text{ pb}$ for the *s*-channel production [12], with the significance of 6.3 standard deviations. A summary of the measurements is presented in Fig. 3.

The measurements are consistent with SM predictions calculated at next-to-leading order (NLO) in QCD, including next-to-next-to-leading logarithmic (NNLL) corrections. The SM single top-quark production cross section is directly sensitive to the square of the CKM matrix element $|V_{tb}|$, thus providing a measurement of $|V_{tb}|$, which describes the *Wtb* coupling. The value of V_{tb} was constrained in the interval $0.92 < |V_{tb}| \leq 1.0$ at 95% CL, which agrees with the SM.

5. Forward–backward asymmetry in $t\bar{t}$ production

The SM predicts the top-quark pairs produced at the Tevatron to be slightly forward–backward asymmetric as shown by NLO calculations. In other words, in the $t\bar{t}$ production, the top-quark tends to go in the side of the proton while the antitop quark is more likely to go to the side of the antiproton. This NLO QCD effect is present only for asymmetric initial states such as $q\bar{q}$ and qg , accessible in proton–antiproton collision at the Tevatron. Thus, the charge asymmetry translates into the forward–backward asymmetry at the Tevatron, which is not the case at the LHC for proton–proton collisions. Physics beyond the SM can affect the $t\bar{t}$ production mechanism and thus the asymmetry, as well as the top quark polarization. The polarization at the Tevatron and the LHC is expected to be different because of the difference in the initial states, which motivates the measurement of the top-quark and antitop-quark polarizations in the Tevatron data. D0 has recently measured these quantities with the full available data.

The $t\bar{t}$ production asymmetry is defined as

$$A^{t\bar{t}} = \frac{N(\Delta y_{t\bar{t}} > 0) - N(\Delta y_{t\bar{t}} < 0)}{N(\Delta y_{t\bar{t}} > 0) + N(\Delta y_{t\bar{t}} < 0)},$$

where $N(X)$ is the number of events in configuration X .

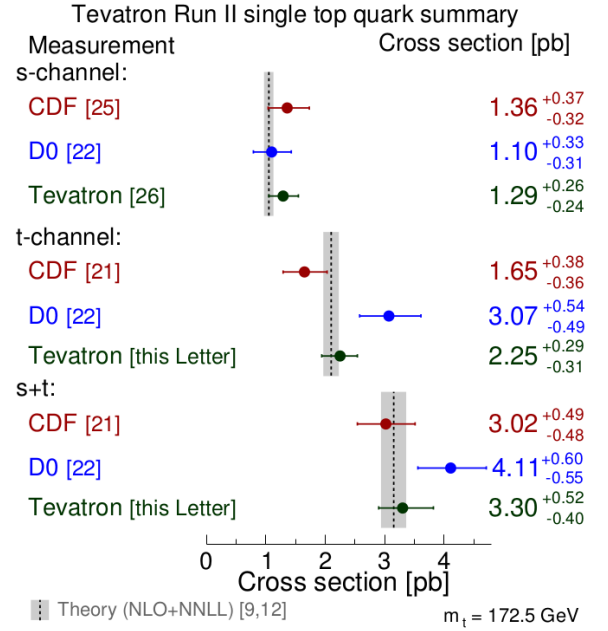


Fig. 3. Measured single top-quark production cross sections from the CDF and D0 Collaborations in different production channels and the Tevatron combinations of these analyses compared with the NLO + NNLL theoretical prediction

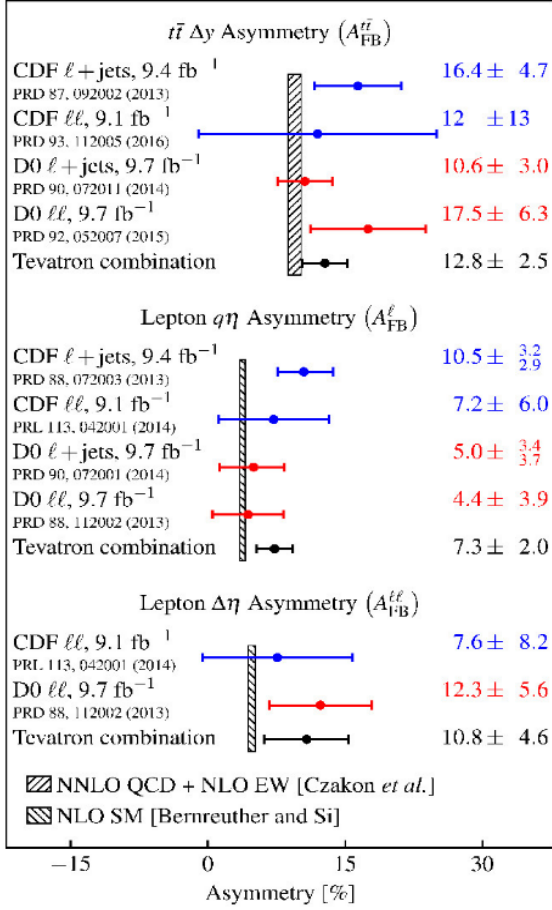


Fig. 4. $p\bar{p} \rightarrow t\bar{t}$ forward-backward asymmetry measurements and their combinations [13]

nonzero polarization. As top quarks decay before they hadronize, their spin properties are transferred to the decay products. Thus the top (antitop) polarization impacts the charged lepton. The obtained results are compatible with the SM, which predicts the polarization below the percent level.

6. W -boson and electron charge asymmetries in $W^{\pm} \rightarrow e^{\pm}\nu$ events

In $p\bar{p}$ collisions, W^{\pm} bosons are produced mainly in $u\bar{d}$ and $d\bar{u}$ annihilation, hence W^{+} and W^{-} are expected to be produced with a boost in the same direction of the incoming u and \bar{u} quarks, respectively. It is possible then to define the charge asymmetry as a function of the boson rapidity:

$$A(y_W) = \frac{(d\sigma^{+}/dy_W) - (d\sigma^{-}/dy_W)}{(d\sigma^{+}/dy_W) + (d\sigma^{-}/dy_W)} = \frac{u(x_p)\bar{d}(x_{\bar{p}}) - d(x_p)\bar{u}(x_{\bar{p}})}{u(x_p)\bar{d}(x_{\bar{p}}) + d(x_p)\bar{u}(x_{\bar{p}})},$$

which is then sensitive to u and d parton distribution functions (PDFs) $u(x_p)$ and $d(x_p)$. The W charge asymmetry was measured by D0 in 2014 [16], and a more recent analysis extracted information on the same quantities considering the electron charge asymmetry from $W^{\pm} \rightarrow e^{\pm}\nu$ decays [17]. The lepton charge asymmetry is a more straightforward observable since it is easier to determine and there is a strong correlation between the W boson rapidity distribution and the produced electron pseudorapidity distribution. The resulting lepton charge asymmetry is the convolution of the W production asymmetry and its characteristic $V-A$ subsequent decay. The recent analysis from D0 considers the full collected dataset and the improved lepton energy reconstruction and calibration, for electrons up to $|\eta| < 3.2$. The observed asymmetries were corrected for detector effects (unfolding), subtracted for the contribution from the expected background, and then

Analogously, the asymmetries of top decay products of the lepton (for semileptonic) or dilepton (for leptonic) top decay were also measured:

$$A^{\ell\bar{\ell}} = \frac{N(\Delta\eta > 0) - N(\Delta\eta < 0)}{N(\Delta\eta > 0) + N(\Delta\eta < 0)},$$

$$A^{\ell} = \frac{N(q \times \eta > 0) - N(q \times \eta < 0)}{N(q \times \eta > 0) + N(q \times \eta < 0)},$$

where η or $\Delta\eta$ are the lepton rapidity and dilepton rapidity difference, q is the sign of the lepton charge. A summary of D0 results, as well as the results combined with CDF using the best linear unbiased estimate method (BLUE), are shown in Fig. 4. They are all in good agreement with the SM expectations.

The top-quark polarization was measured [14, 15] in the top-quark rest frame through the angular distributions of the top-quark decay products relative to three axes: the beam axis, given by the direction of the proton beam; the helicity axis, given by the direction of the parent top or antitop quark; and the transverse axis, given as perpendicular to the production plane defined by the proton and parent quark directions. The SM predicts the top quarks produced at the Tevatron collider to be almost unpolarized, while models beyond the SM (BSM) that include a new parity-violating interaction, such as the model with axiglons, predict enhanced polarization. For the beam and transverse axes, the top-quark polarizations in $p\bar{p}$ collisions are expected to be larger than those for pp at the LHC, therefore offering greater sensitivity at the Tevatron to BSM models with

compared to theoretical predictions obtained using several combinations of generators and PDF sets, in different kinematic regions. Various regions were defined considering both symmetric and asymmetric requirements on the transverse energy of the electron and the missing transverse energy from the undetected neutrino. Fig. 5 (left) shows the measured asymmetry distribution obtained requiring electrons with the electron transverse energy threshold and missing transverse energy threshold equal to 25 GeV, compared to different predictions, while Fig. 5 (right) shows the difference of the same distribution and the MC@NLO + NNPDF2.3 predictions. This result represents the most precise lepton charge asymmetry to date and its contribution to the PDF knowledge in the Q^2-x region corresponding to the W production will have a strong impact on the upcoming W mass measurement issues.

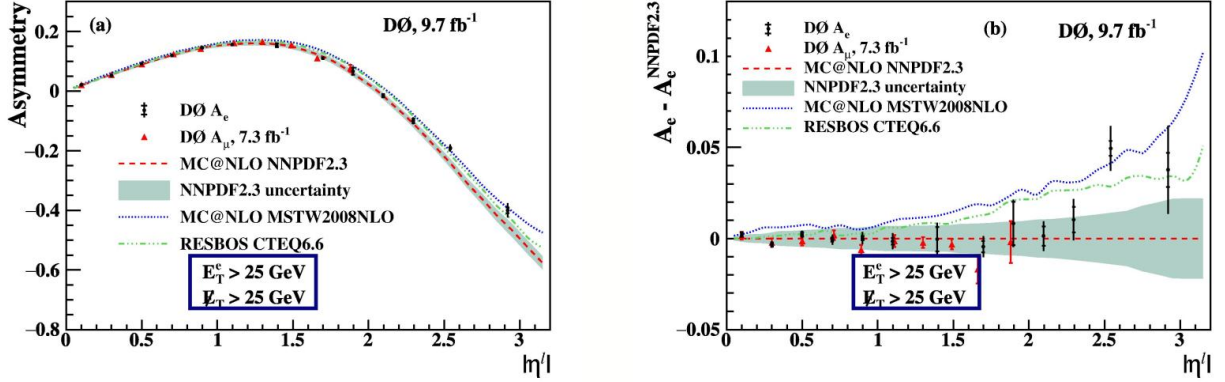


Fig. 5. Electron charge asymmetry observed in data as a function of the lepton pseudorapidity η^ℓ (left). Asymmetry difference with respect to the MC@NLO + NNPDF2.3 predictions for events with the electron transverse energy threshold and missing transverse energy threshold equal to 25 GeV (right)

7. Measurement of the W -boson mass

The Tevatron experiments CDF and D0 performed extremely precise measurements of the W mass, m_W , which along with the top mass provided a constraint on the allowed mass of the Higgs boson within the SM. The D0 Collaboration extracted the W -boson mass by considering W boson decays to an electron or a muon and a neutrino. The transverse momenta of the charged lepton and the neutrino are separately sensitive to m_W , while the transverse mass $m_T = \sqrt{2p_T^\ell p_T^\nu (1 - \cos\Delta\phi)}$ gives the best statistical sensitivity to m_W . The combined fit to these distributions relies on a high-precision lepton momentum calibration (better than a part of 10 000), an accurate calibration of the detector response to the initial-state radiation and the underlying event activity, and an accurate model of the longitudinal and transverse momenta of the W boson. The most recent D0 result based on half of the complete data set is $80.375 \pm 0.023 \text{ GeV}/c^2$ [18].

The W -boson mass measurement uncertainty is the limiting factor in our ability to tighten the constraints on new physics that couples to the EW sector. Therefore, improving the measurement of m_W is an important task. The conditions of the Tevatron collisions are well suited to the m_W measurement. The average number of additional interactions per event is small (< 10) and the majority of the W bosons are produced by valence quarks, whose momentum distributions are well constrained.

The analyses of the complete data sets are progressing towards the final measurements. The final measurements could improve the Tevatron m_W precision to $< 10 \text{ MeV}/c^2$, but will require the PDF uncertainties to be reduced to $O(5 \text{ MeV}/c^2)$. Such a reduction is possible if all the Tevatron measurements of the W -boson production charge asymmetry are incorporated in the constraints, and if the analyses are optimized to reduce PDF uncertainties.

8. Discovery of the $X(5568)$ resonance

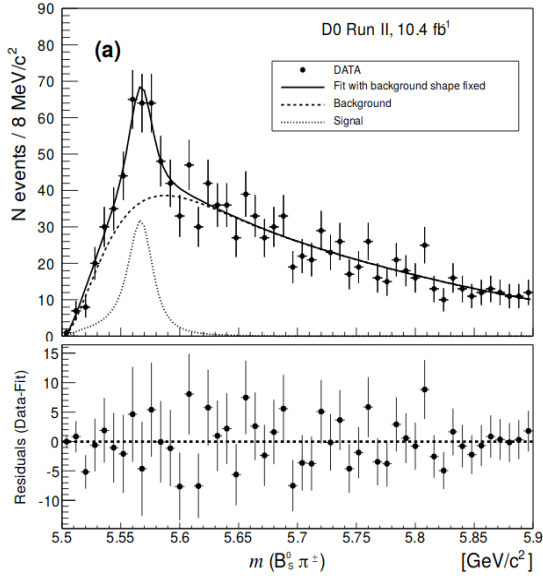


Fig. 6. The mass spectrum of the $B_s^0 \pi^\pm$ final state together with the background distribution and the fit results

The D0 Collaboration found evidence for a new state decaying into $B_s^0 + \pi^\pm$ with B -meson decaying either into J/ψ [19] (the hadronic decay) or into a pair of muons (the semileptonic decay) [20] based on a data sample of 10.4 fb^{-1} . The measured mass spectrum of the $B_s^0 \pi^\pm$ system is shown in Fig. 6. To suppress background in this spectrum, the $B_s^0 \pi^\pm$ system was required to have $p_T > 10 \text{ GeV}/c$. To further reduce background, a limit was imposed on the difference between the direction of the B_s^0 candidate and the pion to be $\Delta R = (\Delta\eta^2 + \Delta\phi^2) < 0.3$, where η is the pseudorapidity and ϕ is the azimuthal angle. An enhancement is seen near $5.57 \text{ GeV}/c^2$. To extract the signal parameters, the background was modeled with a smooth empirical function, while the signal was described with a Breit–Wigner parameterization. The fit yields the mass and width of $M_X = 5567.8 \pm 2.9 \text{ MeV}/c^2$, $\Gamma_X = 21.9 \pm 6.4 \text{ MeV}/c^2$, and the number of signal events of $N = 133 \pm 31$. As the measured width is significantly larger than the experimental mass resolution, one can infer that $X(5568) \rightarrow B_s^0 \pi^\pm$ is a strong decay. The significance of the signal is 6.1σ . The observed structure may be interpreted as a tetraquark state with four different valence quark flavours, b, s, u , and d .

9. Search for the $X(4140)$ and $X(4274)$ states in $BB^+ \rightarrow J/\psi \phi K^+$ decays

In 2009, the CDF Collaboration reported evidence for a narrow peak near threshold in the $BB^+ \rightarrow J/\psi \phi K^+$ system by studying decays of what was called $Y(4140)$. The search was later updated by processing a larger data-set, corresponding to an integrated luminosity of 6 fb^{-1} , yielding about 115 B^+ candidate decays.

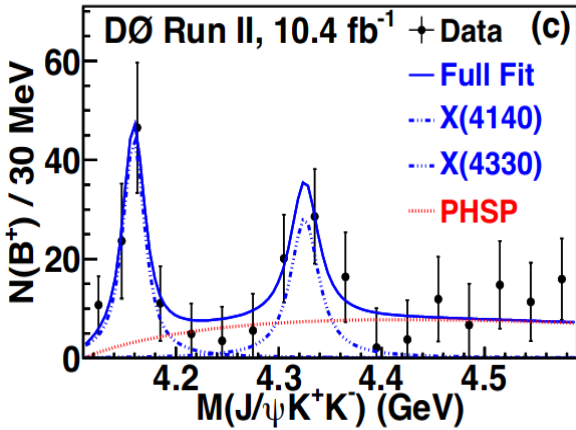


Fig. 7. B^+ yields as function ΔM and $J/\psi KK$ mass measured by D0. Fits to the data assuming two narrow structures and a phase space background are also shown

Since it decays into J/ψ and ϕ mesons, it has been suggested that this particle is composed of charm quarks and charm antiquarks, possibly even a four quark combination. The narrow structures inspired searches in other experiments.

The search performed by Belle in the two-photon process $\gamma\gamma \rightarrow J/\psi \phi$ found no significant structure near threshold but observed a narrow structure, which was named $X(4350)$, at $4350.6 + 4.6 \div 5.1 \text{ (stat)} \pm 0.7 \text{ (syst)} \text{ MeV}/c^2$. The LHCb Collaboration also reported no excess near threshold, in disagreement with the CDF observation at 2.4σ level. To resolve this controversy, the D0 Collaboration performed an analysis [21] of an integrated luminosity of 10.4 fb^{-1} in order to obtain the $J/\psi \phi K^+$ mass distribution corrected for detector efficiency and acceptance (Fig. 7).

The search performed by Belle in the two-photon process $\gamma\gamma \rightarrow J/\psi \phi$ found no significant structure near threshold but observed a narrow structure, which was named $X(4350)$, at $4350.6 + 4.6 \div 5.1 \text{ (stat)} \pm 0.7 \text{ (syst)} \text{ MeV}/c^2$. The LHCb Collaboration also reported no excess near threshold, in disagreement with the CDF observation at 2.4σ level. To resolve this controversy, the D0 Collaboration performed an analysis [21] of an integrated luminosity of 10.4 fb^{-1} in order to obtain the $J/\psi \phi K^+$ mass distribution corrected for detector efficiency and acceptance (Fig. 7).

A binned maximum-likelihood fit yielded 215 candidates. A structure near threshold was observed and its significance was estimated from a binned least-squared fit assuming a BW signal shape with unconstrained mass and width convoluted with the detector resolution. The background shape was given by the non-resonant three-body phase space continuum. The fit yielded 52 ± 19 signal events corresponding to a statistical

significance of 3.1σ . This excess was interpreted as the $X(4140)$ state. The data also supported the presence of a second structure around $4300 \text{ MeV}/c^2$, but it was not possible to reliably fit the data with an unconstrained width. The significance of the second structure was found to be 1.7σ by varying the width between 10 and 50 MeV.

10. Weak mixing parameter $\sin^2\theta'_{\text{eff}}$

The weak mixing constant $\sin^2\theta_W$ is one of the fundamental parameters of the SM. It describes the mixing of the coupling constants of the $SU(2) \times U(1)$ gauge group, and consequentially the relative strength of the axial-vector couplings g_A^f to the vector couplings g_V^f in neutral current interactions of a Z boson to fermions. At the Born level and in all orders of the on-shell renormalization scheme, the parameter is related to the W - and Z -boson masses as $\sin^2\theta_w = 1 - M_W^2/M_Z^2$. It is customary to define an effective value $\sin^2\theta_{\text{eff}}$ taking into account radiative corrections when considering the decay to a given fermion f :

$$\sin^2\theta'_{\text{eff}} = \frac{1}{4|Q_f|} \left(1 - \frac{g_V^f}{g_A^f} \right).$$

This is the quantity that was measured by the previous experiments LEP and SLD. The combined LEP and SLD average gives a value of 0.23149 ± 0.00016 . However, there is a tension between the two most precise individual measurements: the LEP b quark forward–backward charge asymmetry of 0.23221 ± 0.00029 and the SLD left–right polarization asymmetry of Z -boson production of 0.23098 ± 0.00026 differ by 3.2 standard deviations. Therefore, an independent determination of the effective weak mixing angle is an important precision test of the SM electroweak breaking mechanism.

In D0, it is determined from the Drell–Yan process $p\bar{p} \rightarrow Z/\gamma^* \rightarrow \ell^+\ell^-$ (where $\ell = e, \mu$) by measuring the forward–backward charge asymmetry,

$$A_{\text{FB}} = \frac{N_{\text{F}} - N_{\text{B}}}{N_{\text{F}} + N_{\text{B}}},$$

where N_{F} and N_{B} are the numbers of forward and backward events. The A_{FB} distribution, as a function of the invariant mass of the dilepton system measured from data, is compared with parameterized leading order simulation templates to extract $\sin^2\theta_{\text{eff}}$ at the Born-level. This extracted value is further translated to the effective mixing angle using certain schemes of the PDF algorithm and the NLO electroweak radiative corrections. The D0 Collaboration has achieved precise measurements of $\sin^2\theta_{\text{eff}}$ in $Z \rightarrow ee$ final states, with the full Tevatron Run-2 data [22]. The electron-channel result is $\sin^2\theta_{\text{eff}} = 0.23139 \pm 0.00043$ (stat) ± 0.00008 (syst) ± 0.00017 (PDF). The extraction from the muon channel gives $\sin^2\theta_{\text{eff}} = 0.23002 \pm 0.00059$ (stat) ± 0.00005 (syst) ± 0.00024 (PDF). After applying corrections related to different choice of PDF and difference in the methods applied for weak-interaction radiative corrections used at CDF and D0, the D0 results were combined with the CDF results using the BLUE method yielding a Tevatron combination value of $\sin^2\theta_{\text{eff}} = 0.23148 \pm 0.00027$ (stat) ± 0.00005 (syst) ± 0.00018 (PDF) [23].

This result represents the best precision from hadron colliders, nearly matching the best individual measurements from LEP-1 and SLD, as shown in Fig. 8. While not resolving the long-standing 3.2σ difference

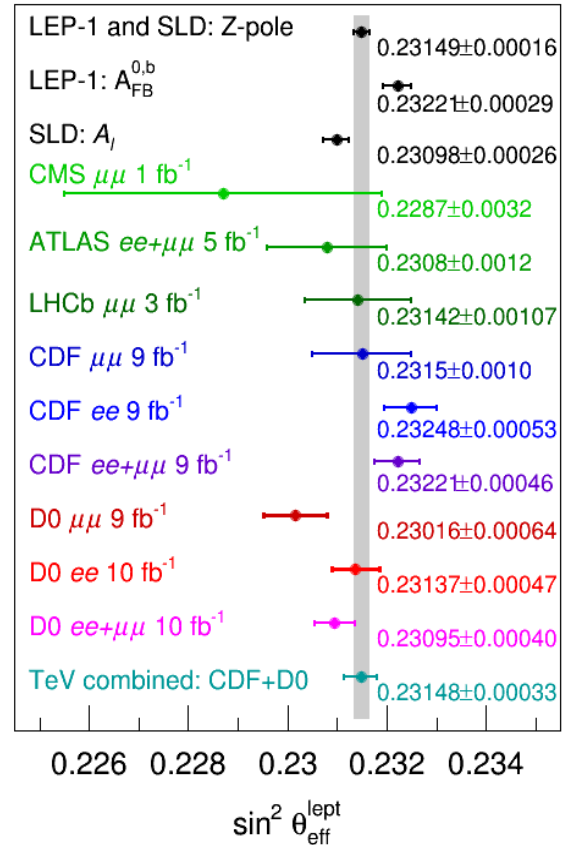


Fig. 8. The Tevatron combination of $\sin^2\theta_{\text{eff}}$ measurements and comparison to LEP/SLD and LHC experiments

between those results, the Tevatron value for $\sin^2\theta_{\text{eff}}$ perhaps removes some of the tension due to the fact that it falls squarely in the world average, and is consistent with both.

11. CP violation in $B^+ \rightarrow \mu^+ \nu \bar{D}^0$ decay

The motivation for studying this process was to try to explain the like-sign dimuon asymmetry measured previously by D0 [24]. The like-sign dimuon asymmetry is based on counting the numbers of events with two positively charged muons (N^{++}) and two negatively charged muons (N^{--}). The asymmetry is defined as $A = (N^{++} - N^{--}) / (N^{++} + N^{--})$. However, this value is raw in the sense that the detector effect may affect it.

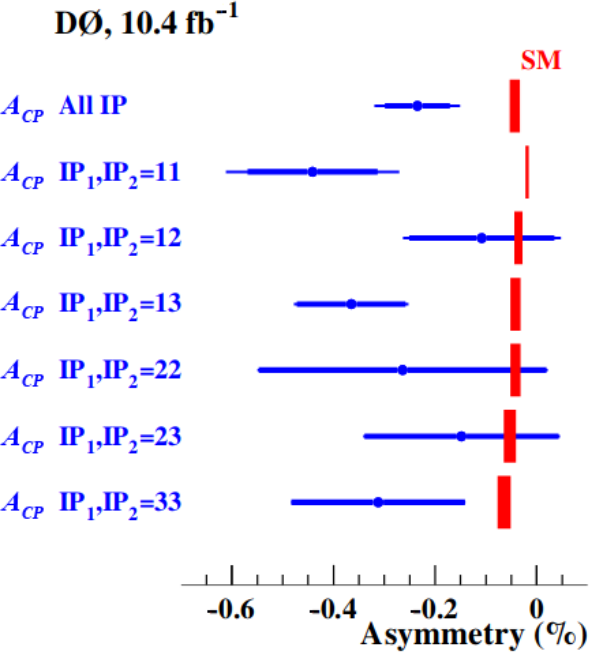


Fig. 9. Asymmetry A_{CP} measured in different muon impact parameter (IP) samples IP1 and IP2. The thick error bar for each measurement presents the statistical uncertainty, while the thin error bar shows the total uncertainty. The filled boxes show the SM prediction. The half width of each box corresponds to the theoretical uncertainty

So this value was corrected by subtracting detector-induced asymmetry. Systematic uncertainties are significantly reduced by reversing polarities of the toroidal and solenoidal magnetic fields every two weeks, which cancels first-order detector effects. As can be seen in Fig. 9, the asymmetry deviates from the SM expectation. The statistical significance is 3.6σ . An analogous quantity defined for a single muon was also measured. The measurement served as a closure test. In contrast to the dimuon measurement, no significant deviation from zero was found. The anomalously large CP -violating effect in the like-sign dimuon asymmetry could be explained by the presence of direct CP violation in semileptonic decays, such as $B^+ \rightarrow \mu^+ \nu \bar{D}^0$. The CP -violation charge asymmetry is defined [25] as

$$A^{\mu D^0} = \frac{\Gamma(B^- \rightarrow \mu^- \bar{\nu}_\mu D^0) - \Gamma(B^+ \rightarrow \mu^+ \nu_\mu \bar{D}^0)}{\Gamma(B^- \rightarrow \mu^- \bar{\nu}_\mu D^0) + \Gamma(B^+ \rightarrow \mu^+ \nu_\mu \bar{D}^0)}.$$

Again, the measurement is performed using the raw asymmetry based on the number of reconstructed decays and then corrected for detector effects and subtraction of decays of other type in this sample. The obtained asymmetry is $A^{\mu D^0} = [-0.14 \pm \pm 0.14 \text{ (stat)} \pm 0.14 \text{ (syst)}]\%$ [25]. This result is in agreement with the SM expectation of no CP violation in this decay.

12. Study of double parton interactions

Multiple parton interactions are important to describe a big variety of measurements, including track observables used in MC generators tuning. When one of the secondary parton interaction reaches a scale comparable to that of the hard scattering, and therefore produces detectable hadronic jets, such a process can be used to study experimentally the double parton scattering (DPS) using hadronic jet observables. The understanding of DPS is particularly relevant for the estimation of background in measurements of specific or rare physics channels, especially the ones involving jets in the final state. A good comprehension of the DPS dynamics is also a great help for the general phenomenology, with increasing importance for higher collision energies, and for the development of partonic models of hadrons. It is characterised by a parameter, called “effective DPI (double parton interaction) cross-section”, σ_{eff} , defined through the total DPI cross section σ_{DP} and the total γ + jet and dijet production cross sections $\sigma^{\gamma j}$ and σ^{jj} :

$$\sigma_{\text{DP}} = \frac{\sigma^{\gamma j} \sigma^{jj}}{\sigma_{\text{eff}}}.$$

The parameter σ_{eff} is related to the distance in the transverse plane between partons in the colliding nucleons and does not depend on the colliding energy. The method used in the recent D0 analyses employs fits to DPS-sensitive observables performed with two different templates, one for the background contribution and one for the signal (DPS). A comparison with results of previous measurements is shown in Fig. 10.

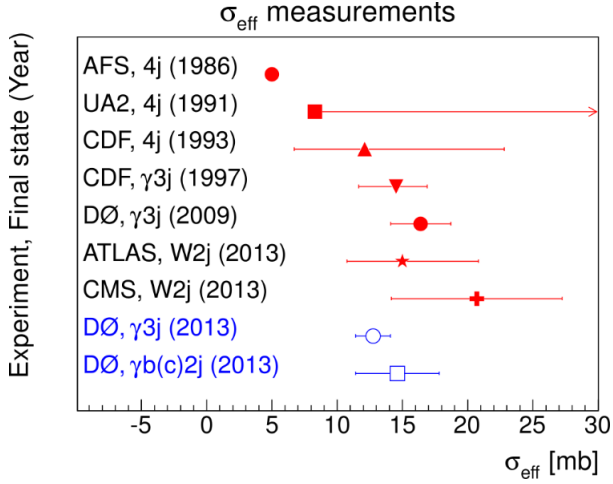


Fig. 10. Comparison of the previous measurements of σ_{eff} from various experiments with the current measurement in D0 [26]

13. Jets with large rapidity separation

Large rapidity separation between two measured jets in an event implies large values of partonic CM energy, thereby introducing an additional energy scale. This introduces the so-called large logarithms, which can be resummed using the Balitskii–Fadin–Kuraev–Lipatov (BFKL) equations, as was shown by L.N. Lipatov with collaborators [27].

During the years 2002 to 2011, the D0 experiment collected a significant amount of minimum bias data, which allows measurements at low jet transverse momentum threshold without bias from the jet trigger inefficiencies. Moreover, recent advances in the D0 jet energy scale correction include an additional correction based on single particle response, *i. e.* response of an individual particle within a jet. This correction is sensitive to the nature of the jet: a quark or a gluon type. Applied to MC samples, it enhances agreement between detector-simulated jet response and the jet response in real data, making it independent on the physics process of interest, be it Z-boson production, dijet production, or multi-jet production. The latter is the subject of the current analysis, where this improvement is important since the quark–gluon jet proportion changes quickly with jet p_T , as shown in Fig. 11.

This provides a unique opportunity for measuring the so-called dijet K factor, already measured at CMS [28] and dijet angular correlations, measured by D0 for Run-1 data [29] at 1.8 TeV and CMS [30] at 7 TeV at large rapidity separation and small jet transverse momentum threshold of 15 GeV, and thereby complementing its counterpart at the LHC with different measurement conditions, such as the CM energy, the transverse momentum threshold, the underlying event activity and the initial state of the interaction.

The dijet K factor is defined as a ratio of two differential cross sections, where the numerator is measured using all events with at least two jets above the p_T threshold, while the denominator is measured using exclusively two jet events, *i. e.* no additional jets

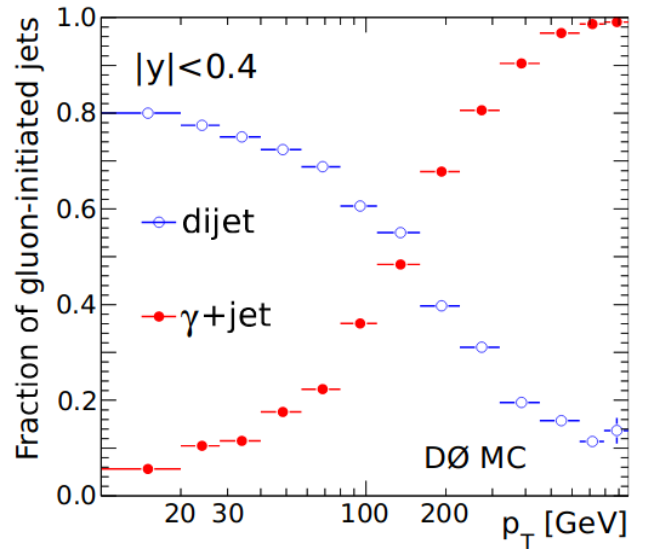


Fig. 11. Fraction of gluon-initiated jets in $\gamma + \text{jet}$ and dijet events in the central calorimeter

above p_T threshold are allowed. The cross sections are measured as a function of the maximal rapidity separation between a pair of jets. As can be seen in Fig. 12, predictions of various MC generators are quite diverse.

The BFKL-inspired MC generators are CASCADE and HEJ (High Energy Jets). CASCADE implements a CCFM-driven shower evolution, while HEJ complements the shower with an additional all-order resummation, taking into account hard wide-angle emissions missing in the shower-approach. HEJ is interfaced to the ARIADNE program to generate the parton shower and hadronisation. Both generators give higher values of the dijet K factor than the conventional generators PYTHIA 8 and HERWIG 7.1 (next version of HERWIG++). Although the PYTHIA 8 and HERWIG 7.1 generators use the Dokshitzer–Gribov–Lipatov–Altarelli–Parisi (DGLAP) equation for shower modeling, their predictions are somewhat different from each other. They implement some non-DGLAP features such as colour-coherence or soft interaction, which may also affect their predictions. HERWIG 7.1 gives higher magnitude of the dijet K factor. Its main distinguishing characteristic is the way the colour coherence effect is taken into account, namely the choice of the shower evolution variable. HERWIG 7.1 also includes a special model for soft interactions based on multi-Regge kinematics.

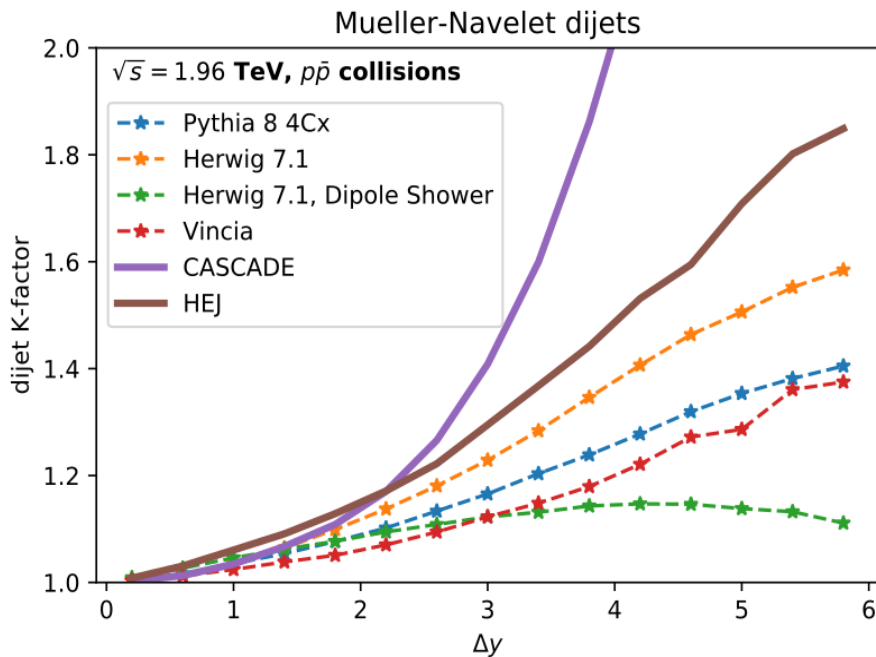


Fig. 12. Predictions of the Mueller–Navelet dijet K factor obtained using various MC generators: DGLAP-based generators PYTHIA 8 tune 4Cx, PYTHIA 8 with the VINCIA plugin, and HERWIG, as well as BFKL-inspired generators CASCADE and HEJ

On the other hand, the generators that use the dipole shower formalism, such as VINCIA, SHERPA, and HERWIG with dipole shower, demonstrate significantly smaller values of the dijet K factor. In general, the dijet K factor is sensitive to the physics approach behind the shower modeling. A comparison of their predictions with data might reveal some non-DGLAP features of the data. Currently, a physics analysis aimed at measuring dijet K factor is underway.

14. Conclusion

Although, the Tevatron was shut down in 2011, the D0 Collaboration still has a number of new interesting results in

- 1) top-quark physics that takes advantage of the unique proton–antiproton initial state;
- 2) heavy flavour physics and hadronic spectroscopy, namely it is able to discover new resonances containing b quarks;
- 3) QCD physics where the underlying event activity is different to that of the LHC due to different colliding energy and different types of the colliding particles.

The data analysis will be continued.

References

1. G.D. Alkhazov, V.L. Golovtsov, V.T. Kim *et al.*, in *PNPI. High Energy Physics Division. Main Scientific Activities 1997–2001*, Gatchina, 2002, p. 124.
2. D0 Collaboration, V.M. Abazov *et al.*, Nucl. Instr. Meth. A **565**, 463 (2006).
3. D0 Collaboration, V.M. Abazov *et al.*, Nucl. Instr. Meth. A **552**, 372 (2005).
4. D0 Collaboration, V.M. Abazov *et al.*, Phys. Lett. B **752**, 18 (2016).
5. D0 Collaboration, V.M. Abazov *et al.*, Phys. Rev. D **94**, 032004 (2016).
6. D0 Collaboration, V.M. Abazov *et al.*, Phys. Rev. D **91**, 112003 (2015).
7. CDF and D0 Collaborations, Tevatron Electroweak Working Group, arXiv:1608.01881.
8. M. Czakon, A. Mitov, Comput. Phys. Commun. **185**, 2930 (2014).
9. D0 Collaboration, V.M. Abazov *et al.*, Phys. Rev. D **94**, 092004 (2016).
10. D0 Collaboration, M. Czakon, P. Fiedler, D. Heymes, A. Mitov, D0 Note 6473-CONF (Sept. 2016), <http://inspirehep.net/record/1640868/>
11. D0 Collaboration, V.M. Abazov *et al.*, Phys. Rev. Lett. **112**, 231803 (2014).
12. CDF and D0 Collaborations, T.A. Aaltonen *et al.*, Phys. Rev. Lett. **115**, No. 15, 152003 (2015).
13. CDF and D0 Collaborations, T.A. Aaltonen *et al.*, Phys. Rev. Lett. **120**, No. 4, 042001 (2018).
14. D0 Collaboration, V.M. Abazov *et al.*, Phys. Rev. D **92**, 052007 (2015).
15. D0 Collaboration, V.M. Abazov *et al.*, Phys. Rev. D **95**, 011101 (2017).
16. D0 Collaboration, V.M. Abazov *et al.*, Phys. Rev. Lett. **112**, 151803 (2014).
17. D0 Collaboration, V.M. Abazov *et al.*, Phys. Rev. D **91**, 032007 (2015).
18. D0 Collaboration, V.M. Abazov *et al.*, Phys. Rev. D **89**, 012005 (2014).
19. D0 Collaboration, V.M. Abazov *et al.*, Phys. Rev. Lett. **117**, 022003 (2016).
20. D0 Collaboration, V.M. Abazov *et al.*, <https://arxiv.org/abs/1712.10176>
21. D0 Collaboration, V.M. Abazov *et al.*, Phys. Rev. Lett. **115**, 232001 (2015); D0 Collaboration, V.M. Abazov *et al.*, Phys. Rev. D **89**, 012004 (2014).
22. D0 Collaboration, V.M. Abazov *et al.*, Phys. Rev. Lett. **115**, 041801 (2015); The D0 Collaborations, D0note 6497-CONF, <https://www-d0.fnal.gov/Run2Physics/WWW/results/prelim/EW/E42/>
23. CDF and D0 Collaborations, T.A. Aaltonen *et al.*, Phys. Rev. D **97**, 112007 (2018).
24. D0 Collaboration, V.M. Abazov *et al.*, Phys. Rev. D **89**, No. 1, 012002 (2014).
25. D0 Collaboration, V.M. Abazov *et al.*, Phys. Rev. D **95**, 031101(R) (2017).
26. D0 Collaboration, V.M. Abazov *et al.*, Phys. Rev. D **89**, 072006 (2014).
27. L.N. Lipatov, Sov. J. Nucl. Phys. **23**, 338 (1976); E.A. Kuraev, L.N. Lipatov, V.S. Fadin, Sov. Phys. JETP **44**, 443 (1976), **45**, 199 (1977); Ya.Ya. Balitsky, L.N. Lipatov, Sov. J. Nucl. Phys. **28**, 822 (1978); L.N. Lipatov, Sov. Phys. JETP **63**, 904 (1986) 904; L.N. Lipatov, in *Perturbative QCD*, ed. A.H. Mueller, World Scientific, Singapore, 1989.
28. CMS Collaboration, S. Chatrchyan *et al.*, Eur. Phys. J. C **72**, 2216 (2012).
29. D0 Collaboration, S. Abachi *et al.*, Phys. Rev. Lett. **77**, 595 (1996).
30. CMS Collaboration, S. Chatrchyan *et al.*, JHEP **1608**, 139 (2016).

HIGH-ENERGY ASYMPTOTIC QUANTUM CHROMODYNAMIC EFFECTS AT COLLIDERS

V.T. Kim

1. Introduction

Quantum chromodynamics (QCD) being an essential ingredient of the Standard Model (SM) is well tested in hard processes when the transferred momentum is of the order of the total collision energy (Bjorken limit: $Q^2 \sim s \rightarrow \infty$). The cornerstones of perturbative QCD at this hard kinematic regime (QCD-improved parton model) are the factorization of inclusive hard processes and the Gribov–Lipatov–Altarelli–Parisi–Dokshitzer (GLAPD) evolution equation [1–5], which provide a basis for the successful QCD-improved parton model. The factorization theorem for inclusive hard processes with hadron(s) ensures that the inclusive cross section factorizes into the partonic subprocess cross section and the parton distribution function(s). The GLAPD evolution equation governs the $\log Q^2$ -dependence (at $Q^2 \rightarrow \infty$) of the inclusive hard process cross-sections at the fixed scaling variable $x = Q^2/s$.

Another important kinematic domain at high-energy is expected to be described by the BFKL-evolution (Balitsky–Fadin–Kuraev–Lipatov) [6–9], in the so called QCD Gribov–Regge limit, whereby $s \rightarrow \infty$ at fixed $Q^2 \gg \Lambda_{\text{QCD}}^2$. In the Gribov–Regge limit, the BFKL evolution in the leading logarithmic (LL) approximation governs $\log(1/x)$ evolution (at $x \rightarrow 0$). Note that the BFKL-evolution in the next-to-leading logarithmic (NLL) approximation [10–13], unlike the LL BFKL [6–9], partly includes the leading order (LO) GLAPD evolution with the running coupling constant, $\alpha_s(Q^2) = 4\pi/\beta_0 \log(Q^2/\Lambda_{\text{QCD}}^2)$.

Therefore, the LL BFKL and especially the NLL BFKL [10–13] are anticipated to be important theoretical tools for exploring the high-energy limit of QCD. In particular, this importance arises since the highest eigenvalue, ω^{max} , of the BFKL equation is related to the intercept of the pomeron, which in turn governs the high-energy asymptotics of the total cross-sections: $\sigma \sim (s/s_0)^{\alpha_{IP}-1} = (s/s_0)^{\omega^{\text{max}}}$, where the Regge parameter s_0 defines the approach to the asymptotic regime. The BFKL pomeron intercept in the LL turns out to be rather large: $\alpha_{IP} - 1 = \omega_{\text{LO}}^{\text{max}} = 12 \log 2 (\alpha_s/\pi) \simeq 0.54$ for $\alpha_s = 0.2$. The NLL corrections to the BFKL have been calculated in Refs. [10, 11], but the results in the $\overline{\text{MS}}$ scheme have a strong renormalization scale dependence. This scale ambiguity dependence is, in particular, due to large running coupling corrections. Naive application of the Brodsky–Lepage–Mackenzie (BLM) approach [14] for reduction of the scale ambiguity for the NLL BFKL prediction in $\overline{\text{MS}}$ scheme does not lead to a sensible result.

In Ref. [12], an approach has been formulated based on the asymptotic conformal properties of the theory generalizing the BLM optimal scale setting procedure [14] for non-Abelian cases, *i. e.*, for the processes which contain non-Abelian interactions in the leading order. The BLM optimal scale setting resumes the conformal-violating β_0 -terms into the running coupling in all orders of perturbation theory, thus preserving the conformal properties of the theory. It turns out [12] that the BLM procedure [14] within physical non-Abelian renormalization schemes [15, 16] eliminates the renormalization scale ambiguity of the NLL BFKL [10, 11]. (Hereafter, we will call the generalized BLM approach of Ref. [12] by BFKLP).

Strictly speaking, the integral kernel [10, 11] of the BFKL equation at NLL is not conformally invariant and, hence, one should use a more accurate method for its solution [17]. But in BFKLP approach [12], the dependence of the eigenvalue of the kernel from the gluon virtuality is extremely weak and, therefore, ω_{NLL} coincides basically with the eigenvalue [13].

Therefore, one of the striking features of the NLL BFKL analysis by BFKLP [12] is that the NLL value for the intercept of the BFKL pomeron, improved by the generalized BLM procedure, has a very weak dependence on the gluon virtuality Q^2 : $\alpha_{IP} - 1 = \omega_{\text{NLL}}^{\text{max}} \simeq 0.13\text{--}0.18$ at $Q^2 = 1\text{--}100 \text{ GeV}^2$ (Fig. 1). This agrees with the conventional Regge theory, where one expects universal intercept of the pomeron without any Q^2 -dependence. The obtained minor Q^2 -dependence leads to approximate conformal invariance.

Note that the BFKLP approach [12] generalizes the BLM procedure [14] for non-Abelian cases when the processes contain non-Abelian contributions at the LO, while the recent approaches in Refs. [18–20] and [21–24] generalize it for higher orders.

It is important that BFKLP approach [12] allows to use in the NLL BFKL many of celebrated features of LL BFKL [6–9], such as conformal invariance [17], using the fact that a source of conformal invariance violation is the running coupling.

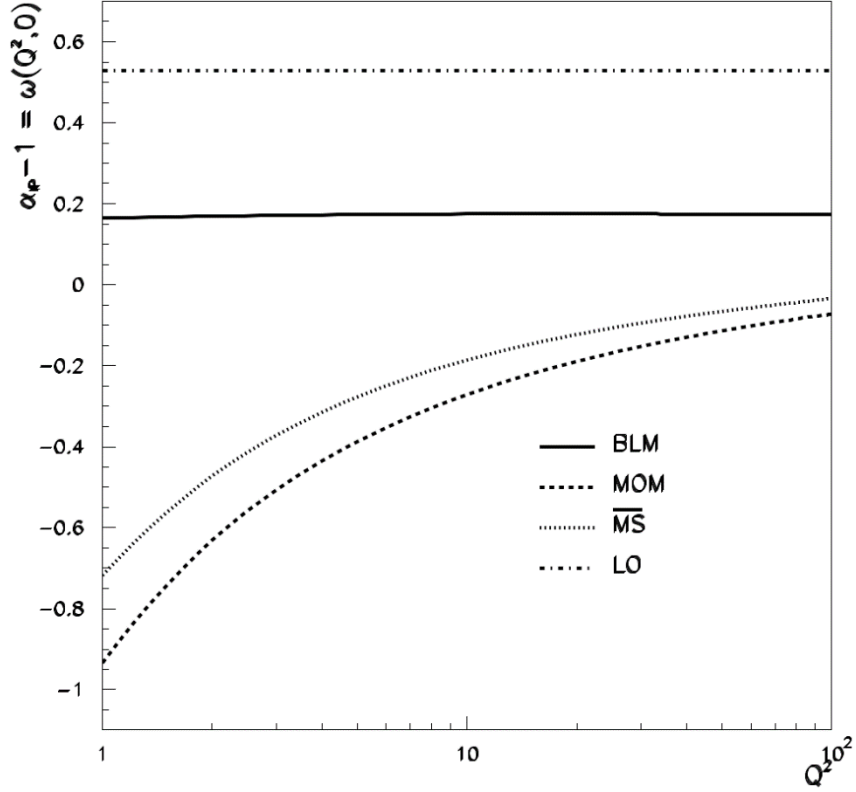


Fig. 1. The intercept of the BFKL pomeron in NLL $\alpha_{pP} - 1 = \omega_{\text{NLL}}^{\text{max}}$, improved by BFKLP [12], the generalized BLM approach for the non-Abelian case

2. BFKL for photon–photon collisions

As a phenomenological application of the NLL BFKL improved by BFKLP [12], the generalized BLM procedure, with its effective resummation of the conformal-violating β_0 -terms into the running coupling in all orders of the perturbation theory, one can consider scattering of highly virtual photons [25]. The LL BFKL application for highly virtual photon scattering was considered in Refs. [26–30].

Photon–photon collisions, particularly $\gamma^*\gamma^*$ processes, play a special role in QCD, since their analysis is under much better control than the calculation of lepton–hadron and hadron–hadron processes, which require the input of non-perturbative hadronic structure functions or wave functions. In addition, unitarization (screening) corrections due to multiple pomeron exchange should be less important for scattering of highly virtual photons (γ^*) than for hadronic collisions or real photon (γ) scattering [31].

The high-energy asymptotic behaviour of the $\gamma\gamma$ total cross section in quantum electrodynamics (QED) can be calculated [32–34] by an all-orders resummation of the leading logarithmic terms: $\sigma \sim \alpha^4 s^\omega$, $\omega = \frac{11}{32} \pi \alpha^2 \simeq \simeq 6 \cdot 10^{-5}$ (Fig. 2). However, the slowly rising asymptotic behaviour of the QED cross section is not apparent since large contributions come from other sources, such as the cut of the fermion-box contribution: $\sigma \sim \alpha^2(\log s)/s$ [35] (which although subleading in energy dependence, dominates the rising contributions by powers of the QED coupling constant) and QCD-driven processes (Fig. 3).

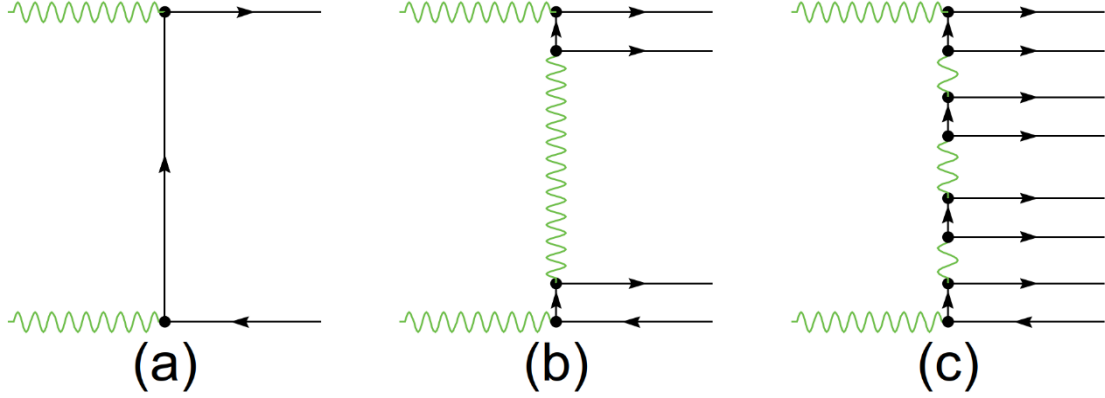


Fig. 2. Photon–photon collisions in QED: a – electron-box diagram $\sigma \sim \alpha^2(\log s)/s$; b – one-photon exchange diagram $\sigma \sim \alpha^4 s_0$; c – a typical higher-order diagram; its resummation leads to $\sigma \sim \alpha^4 s_0^\omega$, $\omega = \frac{11}{32} \pi \alpha^2$ [33]

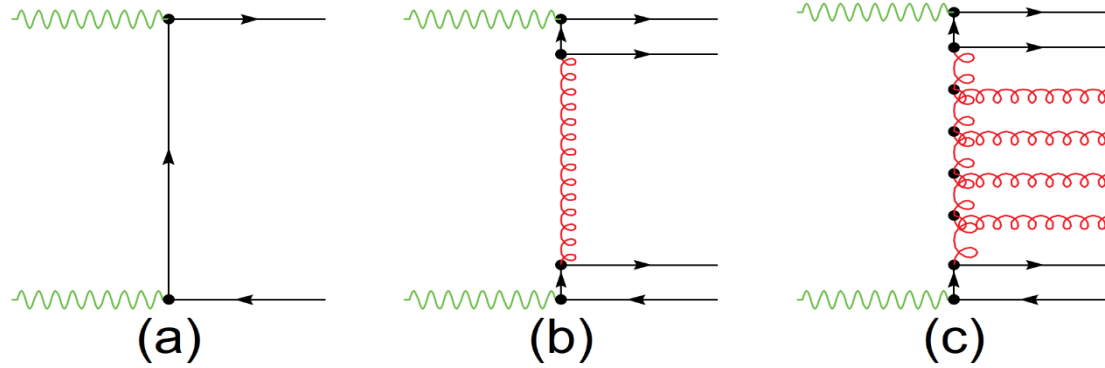


Fig. 3. High-energy photon–photon collisions in QCD: a – quark-box diagram $\sigma \sim \alpha^2(\log s)/s$; b – one-gluon exchange diagram $\sigma \sim \alpha^2 \alpha_s^2 s_0$; c – a typical higher-order diagram; its resummation leads to $\sigma \sim \alpha^2 \alpha_s^2 s_0^\omega$, $\omega_{LL} = 12 \ln 2(\alpha_s/\pi) \simeq 0.55$ [6–9] and $\omega_{NLL} = 0.13\text{--}0.18$ [12]

Figure 4 compares the LL and BLM scale-fixed NLL BFKL predictions $\sigma \sim \alpha^2 \alpha_s^2 S^\omega$ [25] with CERN LEP2 data from OPAL [36] and L3 [37]. The spread in the curves reflects the uncertainty in the choice of the Gribov–Regge scale parameter which defines the beginning of the asymptotic regime: $s_0 = Q^2$ to $4Q^2$ for LL and NLL BFKL, where Q^2 is the mean virtuality of the colliding photons. One can see in Fig. 4 that the agreement of the NLL BFKL predictions [25], improved by BFKLP [12], with the data is quite good. The sensitivity of the NLL BFKL results [25] to the Gribov–Regge parameter s_0 is much smaller than that in the case of the LL BFKL. The variation of the predictions in the value of s_0 reflects uncertainties from uncalculated subleading terms. The parametric variation of the LL BFKL predictions is so large that it can be, in fact, neither ruled out nor confirmed at the energy range of CERN LEP2.

The next-to-leading order (NLO) impact factor of the virtual photon, which is needed for complete NLL BFKL calculations, has become recently known [38–40]. However, it is still difficult to apply it for full NLL calculations of highly virtual photon cross sections. So, currently one can use LO impact factor of Ref. [33], assuming that the main energy-dependent NLL corrections come from the NLL BFKL subprocess rather than from the photon impact factors [25, 41].

The double-logarithmic DGLAP asymptotics related with $\log(Q_A^2/Q_B^2)$ -terms for the total photon–photon cross section was considered in Ref. [30] and found to be small for the CERN LEP2 kinematical region. The point is that most of the CERN LEP2 data [36, 37] are collected at the approximately equal virtualities of the colliding photons: $1/2 < Q_A^2/Q_B^2 < 2$. It should be stressed that the soft pomeron contribution to the $\gamma^*\gamma^*$ total cross section, if estimated within the vector-dominance model, is proportional to $\sigma_{\gamma^*\gamma^*} \sim (m_V^2/Q^2)^4 \sigma_{\gamma\gamma}$ and therefore suppressed for such highly virtual photons as those under consideration.

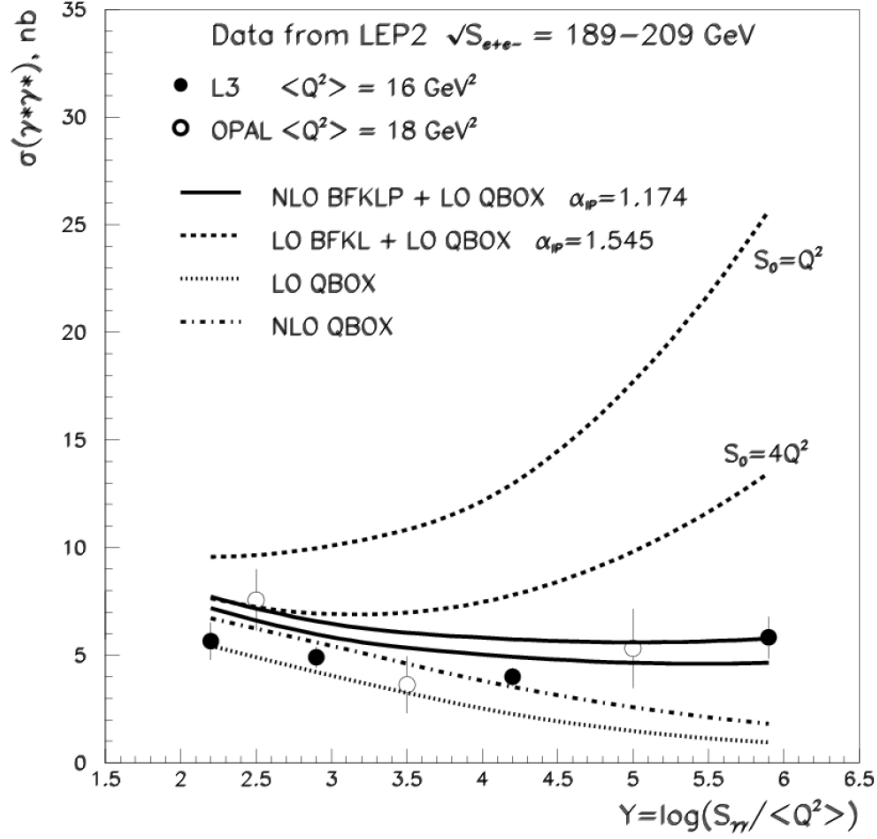


Fig. 4. The energy dependence of the total cross section for highly virtual photon–photon collisions predicted by the generalized BLM scale-fixed NLL BFKL [25] compared with OPAL [36] and L3 [37] data from LEP2 at CERN. The *solid dashed curves* correspond to the (N)LL BFKL predictions for two different choices of the Regge scale: $s_0 = Q^2$ for upper curves and $s_0 = 4Q^2$ for lower curves

We also note that to the NLL BFKL predictions [25, 41] improved by BFKLP [12] should be added for consistency quark and antiquark exchange contributions [42], which correspond to the secondary Reggeon exchange and should not play an important role at very high energies. On the other hand, at not very high energies such as at LEP2 they can yield a noticeable contribution [42].

The NLO quark-box contribution [43], which is leading in coupling constant counting and subleading in energy dependence, underestimates the L3 data point at $Y \equiv \log(s_{\gamma\gamma}/\langle Q^2 \rangle) = 6$ by 4 standard deviations. Indeed, the NLO quark-box contribution [43], calculated in massless approximation, can be scaled down from general considerations with the quark masses. For example, at leading order, the inclusion of masses to the quark-box diagram reduces its contribution by 10–15% [43]. Also, the one-gluon exchange added to the (N)LO quark-box contribution is not sufficient to describe the data at $Y = 6$ within 3–4 standard deviations.

To summarize this section, highly virtual photon–photon collisions provide a very unique opportunity to test high-energy asymptotics of QCD. The NLL BFKL predictions for the $\gamma^*\gamma^*$ total cross section improved by BFKLP approach [12] show good agreement with the data from OPAL [36] and L3 [37] at CERN LEP2. Nevertheless, it will be interesting to compare the presented results with forthcoming complete NLL BFKL calculations for highly virtual photon collisions.

3. BFKL predictions for jet production in hadron collisions

Experimental tests of BFKL predictions and the search for good observables of BFKL effects are very important to study the new high-energy domain of QCD.

The first LL BFKL calculations were applied for heavy quark production in photon collisions [9], deep inelastic lepton–nucleon scattering [44], heavy lepton-pair production [45] and high p_T hadron production [46–48] in hadronic collisions (see for a review Ref. [49]).

A proposal [50] to study the most forward and most backward in rapidity jets (Mueller–Navelet jets) in hadronic collisions was very promising since the BFKL effects could be very pronounced with increasing of the rapidity separation between Mueller–Navelet jets. Mueller–Navelet dijets is a special case of inclusive dijets [51], the latter are more suitable for jet tagging in limited rapidity coverage detectors. However, the K -factor for the Mueller–Navelet dijet production [50], which is the ratio of the Mueller–Navelet dijet cross section to the Born cross section for two jet production, cannot be experimentally measured. This is because the Born cross section is a purely theoretical quantity: *e. g.*, one cannot forbid by experimental conditions virtual corrections to the Born process.

So, other jet observables were suggested: dijet azimuthal angle decorrelations [51–55], single jet ratio at different collision energies [56], dijet ratio at different collision energies [57], *etc.* In Refs. [58, 59] there was proposed an analog of dijet K -factor: instead of the Born dijet cross section one can use the cross section for events when there are only two jets above $p_{T\min}$ ($p_{T\min}$ -veto on extra jets).

At Fermilab Tevatron, the D0 Collaboration has measured azimuthal angle decorrelations [60] and the ratio of the Mueller–Navelet dijet cross sections for Mueller–Navelet dijets at 1 800 and 630 GeV collision energies [61]. Unfortunately, those two measurements for Mueller–Navelet dijets are somewhat not consistent: the first one [60] shows no indication of BFKL evolution manifestation, while the second one [61] shows an overwhelming BFKL-like contribution.

The dijet “ K -factor” as a function of the rapidity separation was measured at Large Hadron Collider (LHC) Run-1 at 7 TeV by ATLAS (inverse “ K -factor”) [62] and CMS [63]. The ATLAS measurement [62] has less sensitivity to BFKL effects than the CMS one [63] due to a smaller range in the jet rapidity separation and larger values of $p_{T\min}$ (ATLAS: $\Delta y < 6$ and $p_{T\min} > 70$ GeV, versus CMS: $\Delta y < 9.4$ and $p_{T\min} > 35$ GeV). Figure 5 shows a comparison of CMS data [63] with predictions of various Monte Carlo (MC) event generators.

LL BFKL based MC generators CASCADE [64] and HEJ+ARIADNE [65] overestimate the CMS data [63]. The MC generators based on LL BFKL, which is designed for infinite energy, inherit its drawbacks at finite energy. So, this is not a big surprise that LL BFKL based MC generators do not describe the available data.

LL GLAPD based MC generator HERWIG++ [66] overshoots the data, while LL GLAPD PYTHIA 6 [67] and PYTHIA 8 [68] provide pretty good agreement with the data. However, both HERWIG++ and PYTHIA generators contain beyond GLAPD contributions, such as colour coherence, polar angle ordering, colour dipole approximation, *etc.* Those contributions are small corrections in GLAPD kinematical domain and often improve quality of data description. However, in BFKL domain those corrections are no longer valid, one has to use a proper tool: BFKL approach. One can see it in Fig. 5, instead of constant behaviour both LL GLAPD based MC generators HERWIG++ and PYTHIA yield a noticeable rise with increasing of the rapidity separation. Different implementations of those corrections provide a quite different behaviour for HERWIG++ and PYTHIA. Unfortunately, there is neither NLL BFKL generator nor pure GLAPD generator to confront with the data. So, one can check whether the description of the data by PYTHIA generators is accidental or not by testing other observables.

Indeed, CMS data [69] for azimuthal angle decorrelations of dijets as a function of the rapidity separation between jets show better overall description by HERWIG++ than PYTHIA. However, the best description provide analytical NLL BFKL calculations [70] improved by BFKLP [12].

Further progress in experimental tests of BFKL predictions would be related with LHC Run-2 and Run-3 data and with developments of BFKL MC generators by adopting the NLL BFKL corrections.

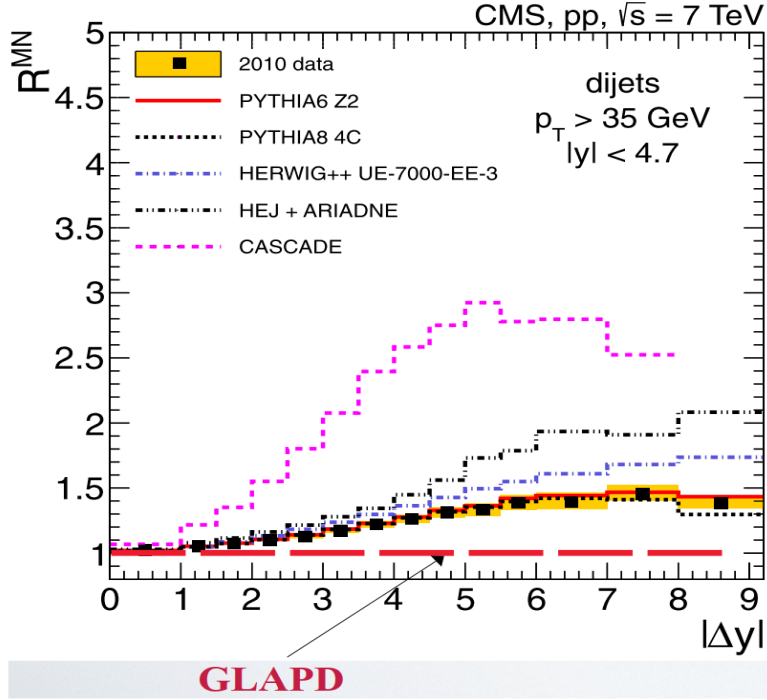


Fig. 5. Ratio of the Mueller–Navelet dijet production cross section over the two-jet cross section (dijet “ K -factor”) as a function of the rapidity separation between jets at the LHC: CMS data at 7 TeV versus predictions of GLAPD event generators with LL parton shower improved by beyond-GLAPD effects such as colour coherence, colour dipole approximation, *etc.*

4. Summary and outlooks

The BFKLP approach [12], the generalized BLM scale setting for the non-Abelian case, opens new windows for applications of NLL BFKL evolution to the high-energy phenomenology.

Highly virtual photon–photon collisions provide a very unique opportunity to test high-energy asymptotics of QCD. The NLL BFKL predictions [25, 41] for the $\gamma\gamma^*$ total cross section with LO photon impact factors and with the renormalization scale fixed by BFKLP approach [12] show good agreement with the data from the OPAL [36] and L3 [37] Collaborations at CERN LEP2. This is at the moment the most pronounced BFKL evolution manifestation in high energy phenomenology. Forthcoming complete NLL BFKL calculations for highly virtual photon collisions will shed light on the role of different ingredients of the NLL BFKL approach.

The LHC data at 7 TeV [69] on dijet production with wide rapidity separation between jets are in good agreement with analytical NLL BFKL calculations [70] improved by BFKLP [12]. Further progress in experimental tests of BFKL predictions for jet production will be related with LHC Run-2 and Run-3 data, as well as with the search of new observables for BFKL evolution manifestation. The progress requires also a development of BFKL MC generators by inclusion the NLL BFKL corrections.

References

1. V.N. Gribov, L.N. Lipatov, Sov. J. Nucl. Phys. **15**, 438 (1972) [Yad. Fiz. **15**, 781 (1972)].
2. V.N. Gribov, L.N. Lipatov, Sov. J. Nucl. Phys. **15**, 675 (1972) [Yad. Fiz. **15**, 1218 (1972)].
3. L.N. Lipatov, Sov. J. Nucl. Phys. **20**, 94 (1975) [Yad. Fiz. **20**, 181 (1974)].
4. G. Altarelli, G. Parisi, Nucl. Phys. B **126**, 298 (1977).
5. Y.L. Dokshitzer, Sov. Phys. JETP **46**, 641 (1977) [Zh. Eksp. Teor. Fiz. **73**, 1216 (1977)].
6. V.S. Fadin, E.A. Kuraev, L.N. Lipatov, Phys. Lett. B **60**, 50 (1975).
7. E.A. Kuraev, L.N. Lipatov, V.S. Fadin, Sov. Phys. JETP **44**, 443 (1976) [Zh. Eksp. Teor. Fiz. **71**, 840 (1976)].

8. E.A. Kuraev, L.N. Lipatov, V.S. Fadin, Sov. Phys. JETP **45**, 199 (1977) [Zh. Eksp. Teor. Fiz. **72**, 377 (1977)].
9. I.I. Balitsky, L.N. Lipatov, Sov. J. Nucl. Phys. **28**, 822 (1978) [Yad. Fiz. **28**, 1597 (1978)].
10. V. Fadin, L. Lipatov, Phys. Lett. B **429**, 127 (1998).
11. M. Ciafaloni, G. Camici, Phys. Lett. B **430**, 349 (1998).
12. S. Brodsky, V. Fadin, V. Kim *et al.*, JETP Lett. **70**, 155 (1999).
13. V.S. Fadin, V.T. Kim, L.N. Lipatov, G.B. Pivovarov, in *Proc. of the 35th PNPI Winter School on Nuclear and Particle Physics, St. Petersburg, Repino, Russia, 19–25 Febr., 2001*, arXiv:hep-ph/0207296.
14. S.J. Brodsky, G.P. Lepage, P.B. Mackenzie, Phys. Rev. D **28**, 228 (1983).
15. W. Celmaster, R.J. Gonsalves, Phys. Rev. Lett. **42**, 1435 (1979).
16. W. Celmaster, R.J. Gonsalves, Phys. Rev. D **20**, 1420 (1979).
17. L.N. Lipatov, Sov. Phys. JETP **63**, 904 (1986) [Zh. Eksp. Teor. Fiz. **90**, 1536 (1986)].
18. S.V. Mikhailov, JHEP **06**, 009 (2007).
19. A.L. Kataev, S.V. Mikhailov, Theor. Math. Phys. **170**, 139 (2012) [Teor. Mat. Fiz. **170**, 174 (2012)].
20. A.L. Kataev, S.V. Mikhailov, Phys. Rev. D **91**, 014007 (2015).
21. S.J. Brodsky, X.G. Wu, Phys. Rev. D **85**, 034038 (2012) [Erratum: Phys. Rev. D **86**, 079903 (2012)].
22. S.J. Brodsky, L. Di Giustino, Phys. Rev. D **86**, 085026 (2012).
23. M. Mojaza, S.J. Brodsky, X.-G. Wu, Phys. Rev. Lett. **110**, 192001 (2013).
24. S.J. Brodsky, M. Mojaza, X.-G. Wu, Phys. Rev. D **89**, 014027 (2014).
25. S.J. Brodsky, V.S. Fadin, V.T. Kim *et al.*, JETP Lett. **76**, 249 (2002) [Pisma Zh. Eksp. Teor. Fiz. **76**, 306 (2002)].
26. J. Bartels, A. De Roeck, H. Lotter, Phys. Lett. B **389**, 742 (1996).
27. S.J. Brodsky, F. Hautmann, D.E. Soper, Phys. Rev. Lett. **78**, 803 (1997) [Erratum: Phys. Rev. Lett. **79**, 3544 (1997)].
28. S.J. Brodsky, F. Hautmann, D.E. Soper, Phys. Rev. D **56**, 6957 (1997).
29. A. Bialas, W. Czyz, W. Florkowski, Eur. Phys. J. C **2**, 683 (1998).
30. M. Boonekamp, A. De Roeck, C. Royon, S. Wallon, Nucl. Phys. B **555**, 540 (1999).
31. V.P. Goncalves, M.S. Kugeratski, E.R. Cazaroto *et al.*, Eur. Phys. J. C **71**, 1779 (2011).
32. G.V. Frolov, V.N. Gribov, L.N. Lipatov, Phys. Lett. B **31**, 34 (1970).
33. V.N. Gribov, L.N. Lipatov, G.V. Frolov, Sov. J. Nucl. Phys. **12**, 543 (1971) [Yad. Fiz. **12**, 994 (1970)].
34. H. Cheng, T.T. Wu, Phys. Rev. D **1**, 2775 (1970).
35. V.M. Budnev, I.F. Ginzburg, G.V. Meledin, V.G. Serbo, Phys. Rept. C **15**, 181 (1975).
36. OPAL Collaboration, G. Abbiendi *et al.*, Eur. Phys. J. C **24**, 17 (2002).
37. L3 Collaboration, P. Achard *et al.*, Phys. Lett. B **531**, 39 (2002).
38. J. Bartels, A. Kyrieleis, Phys. Rev. D **70**, 114003 (2004).
39. I. Balitsky, G.A. Chirilli, Phys. Rev. D **83**, 031502 (2011).
40. I. Balitsky, G.A. Chirilli, Phys. Rev. D **87**, 014013 (2013).
41. F. Caporale, D.Yu. Ivanov, A. Papa, Eur. Phys. J. C **58**, 1 (2008).
42. J. Bartels, M. Lublinsky, JHEP **09**, 076 (2003).
43. M. Cacciari, V. Del Duca, S. Frixione, Z. Trocsanyi, JHEP **02**, 029 (2001).
44. L.V. Gribov, E.M. Levin, M.G. Ryskin, Nucl. Phys. B **188**, 555 (1981).
45. E.M. Levin, M.G. Ryskin, Yad. Fiz. **32**, 802 (1980).
46. M.G. Ryskin, Yad. Fiz. **32**, 259 (1980).
47. L.V. Gribov, E.M. Levin, M.G. Ryskin, Phys. Lett. B **100**, 173 (1981).
48. L.V. Gribov, E.M. Levin, M.G. Ryskin, Phys. Lett. B **121**, 65 (1983).
49. L.V. Gribov, E.M. Levin, M.G. Ryskin, Phys. Rept. C **100**, 1 (1983).
50. A.H. Mueller, H. Navelet, Nucl. Phys. B **282**, 727 (1987).
51. V.T. Kim, G.B. Pivovarov, Phys. Rev. D **53**, 6 (1996).
52. V. Del Duca, C.R. Schmidt, Phys. Rev. D **49**, 4510 (1994).
53. W.J. Stirling, Nucl. Phys. B **423**, 56 (1994).
54. A. Sabio Vera, Nucl. Phys. B **746**, 1 (2006).
55. A. Sabio Vera, F. Schwennsen, Nucl. Phys. B **776**, 170 (2007).

56. V.T. Kim, G.B. Pivovarov, Phys. Rev. D **57**, 1341 (1998).
57. L.H. Orr, W.J. Stirling, Phys. Lett. B **429**, 135 (1998).
58. V.B. Gavrilov, V.T. Kim, A.A. Krokhotin *et al.*, in *Proc. of the 15th Int. Seminar on High Energy Physics (QUARKS-2008)*, arXiv:hep-ph0901.1985.
59. V.B. Gavrilov, V.T. Kim, V.A. Murzin *et al.*, Nucl. Phys. Proc. Suppl. **245**, 153 (2013).
60. D0 Collaboration, S. Abachi *et al.*, Phys. Rev. Lett. **77**, 595 (1996).
61. D0 Collaboration, B. Abbott *et al.*, Phys. Rev. Lett. **84**, 5722 (2000).
62. ATLAS Collaboration, G. Aad *et al.*, JHEP **1109**, 053 (2011).
63. CMS Collaboration, S. Chatrchyan *et al.*, Eur. Phys. J. C **72**, 2216 (2012).
64. H. Jung, S. Baranov, M. Deak *et al.*, Eur. Phys. J. C **70**, 1237 (2010).
65. J.R. Andersen, L. Lonnblad, J.M. Smillie, JHEP **07**, 110 (2011).
66. M. Bahr *et al.*, Eur. Phys. J. C **58**, 639 (2008).
67. T. Sjostrand, S. Mrenna, P.Z. Skands, JHEP **05**, 026 (2006).
68. T. Sjostrand, S. Mrenna, P.Z. Skands, Comput. Phys. Commun. **178**, 852 (2008).
69. CMS Collaboration, V. Khachatryan *et al.*, JHEP **1608**, 139 (2016).
70. B. Duclou, L. Szymanowski, S. Wallon, Phys. Rev. Lett. **112**, 082003 (2014).

STUDY OF THE QUARK–GLUON PLASMA PROPERTIES BY PHENIX

PNPI participants of the PHENIX Collaboration:

V.V. Baublis, D.A. Ivanishchev, A.V. Khanzadeev, B.G. Komkov, D.O. Kotov,
M.V. Malaev, V.G. Riabov, Yu.G. Riabov, V.M. Samsonov

1. Introduction

The PHENIX experiment at the Relativistic Heavy Ion Collider (RHIC) finished data taking in 2016. However, the processing and analysis of the data samples accumulated by PHENIX in previous years is still ongoing. New results on different observables are regularly released by the collaboration and are published in highly rated scientific journals.

The main heritage of the PHENIX experiment is the discovery of the strongly coupled quark–gluon plasma (QGP) in central collisions of heavy ions, which was announced back in 2005 [1]. Since then, the main effort of the collaboration was directed towards a detailed study of the new state of matter using more differential and precise measurements. In this review, we present the most recent PHENIX results on the jet quenching and direct photon and charmonium production.

2. PHENIX experiment

The PHENIX experiment is one of the two large experiments at the RHIC, which started its regular operation in 2000 [2]. The experiment is conducted by the collaboration which consists of over a thousand scientists from 75 institutions and 14 countries. The main purpose of the PHENIX experiment is to study properties of the strongly interacting matter under extreme conditions of high temperature and density.

Schematic view of the experimental set-up is shown in Fig. 1. The detector is designed as a high rate and fine granularity apparatus that utilizes a variety of detector technologies to measure global characteristics of events, and to reconstruct hadrons, leptons and photons over a wide range of transverse momenta. The experimental set-up consists of two central arm spectrometers, each covering 90° in azimuth at midrapidity ($|\eta| < 0.35$), two forward muon spectrometers with full azimuthal coverage and a system of “global” detectors such as beam-beam counters and zero degree calorimeters. Each spectrometer provides very good momentum and spatial resolution and particle identification capabilities. The main subsystems of the central spectrometers are the central and forward silicon vertex detectors (VTX, FVTX), drift chambers, three layers of pad chamber (PC1, PC2, PC3), a Cherenkov detector (RICH), two time-of-flight systems (ToF-E and ToF-W) and an electromagnetic calorimeter (PbSc, PbGl). The muon spectrometers consist of three layers of tracking detectors (MuTr) and five layers of Iarocci tubes (MuID) intervened with muon filters made of steel plates for muon identification. The experiment has a data acquisition system, which operates at 5–7 kHz, and a multi-level triggering system to select rare observables.

PNPI participates in the PHENIX experiment since the moment it was announced. PNPI was responsible for the design and construction of the main detector of the central tracking system – multiwire focusing drift chambers [3, 4]. The chambers were successfully operated for sixteen years. Over 80% of all published scientific results of the collaboration were obtained using the drift chambers. After the PHENIX experiment finished data taking in 2016, specialists from PNPI continued to participate in physical analyses of the data collected in previous years.

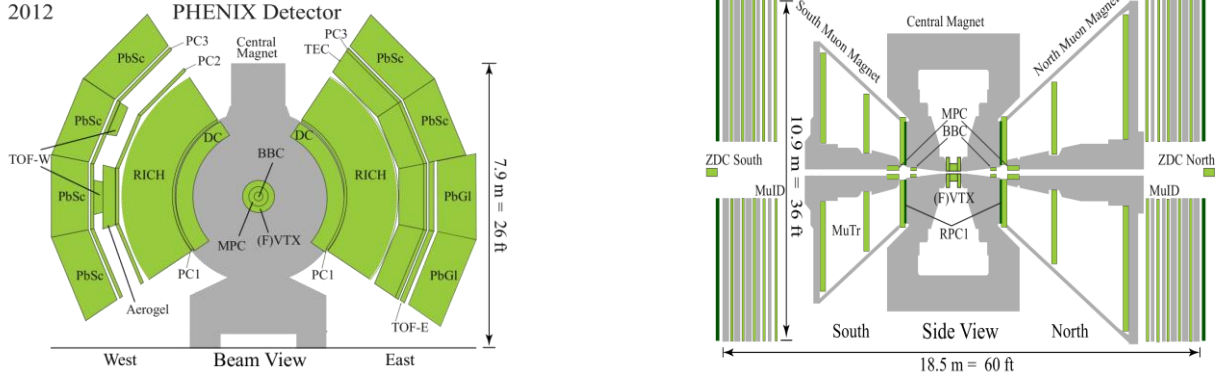


Fig. 1. Schematic view of the PHENIX experimental set-up in two projections

3. Production of hadrons at high transverse momenta

Hard scattered partons lose a significant part of their energy when traverse the medium produced in heavy ion collisions resulting in suppressed production of high- p_T hadrons or jet quenching. As a result, high- p_T hadrons and jets are a sensitive probe of opacity of the produced medium. Production of identified hadrons was measured in a wide transverse momentum range in proton–proton, proton–nucleus, and heavy-ion collisions [5–7]. The jet quenching effect in nuclear collisions is quantified with the nuclear modification factor R_{AA} , which is the ratio of the yields measured for the same particle in heavy ion and pp collisions and scaled by the corresponding number of inelastic nucleon–nucleon collisions, N_{coll} . The number of such collisions is not experimentally measured and is estimated using the Glauber model.

The nuclear modification factors, R_{pA} , measured for π^0 mesons in 0–20 and 60–84% central $p(d, {}^3\text{He}) + \text{Au}$ collisions at $\sqrt{s_{NN}} = 200$ GeV are shown in Fig. 2 as a function of the transverse momentum. In peripheral collisions, the nuclear modification factors are consistent with unity within uncertainties at $p_T > 2$ GeV/ c for all collision systems. However, in central collisions a clear hierarchy of the factors can be seen. In $p + \text{Au}$ collisions, production of π^0 mesons is strongly enhanced in the intermediate p_T range, $2 < p_T < 7$ GeV/ c , with a maximum at $p_T \approx 4\text{--}5$ GeV/ c . The enhancement, which is known as the Cronin effect, is less prominent in $d + \text{Au}$ collisions. Finally, in ${}^3\text{He} + \text{Au}$ collisions production of π^0 mesons is not enhanced, on the contrary it is slightly suppressed. At higher transverse momentum, production of π^0 mesons is suppressed by up to $\sim 50\%$ at $p_T \approx 20$ GeV/ c . The level of suppression is the same for three collision systems within uncertainties. This is the first time when suppression is observed for light hadrons in collisions of light and heavy nuclei. The origin of this suppression is not fully understood, it could be related to cold nuclear matter (CNM) effects, hadronic rescattering or parton energy loss. A detailed comparison to model predictions for all three systems is needed to clarify the situation.

PHENIX obtained new results for the nuclear modification factors in Au+Au collisions at $\sqrt{s_{NN}} = 200$ GeV [8, 9]. Figure 3 presents the R_{AA} factors measured for π^0 pions as a function of the transverse momentum at different centralities. Black and red points correspond to different data sets. The results are in very good agreement and fully confirm the previous findings. These figures illustrate the system size dependence of the hadron suppression. In peripheral collisions, production of neutral pions is slightly suppressed, the R_{AA} factor is equal to ~ 0.8 with practically no dependence on the transverse momentum. The suppression increases with centrality. In most central collisions, the suppression is the largest at 6–8 GeV/ c ($R_{AA} \approx 0.2$) and then decreases at higher and lower momenta. A similar behaviour was previously observed in Pb + Pb collisions at much higher energy of $\sqrt{s_{NN}} = 2.76$ TeV at the Large Hadron Collider (LHC) [10].

Another interesting question is the dependence of the jet quenching on the collision energy. Results of the beam energy scan at RHIC are presented in Fig. 4. The plot on the left shows the nuclear modification factors measured for π^0 pions in most central Cu + Cu collisions at $\sqrt{s_{NN}} = 22.4, 62.4,$ and 200 GeV [11].

At 200 and 62.4 GeV, the production of neutral pions is suppressed. At $\sqrt{s_{NN}} = 22.4$ GeV, one observes instead a significant enhancement.

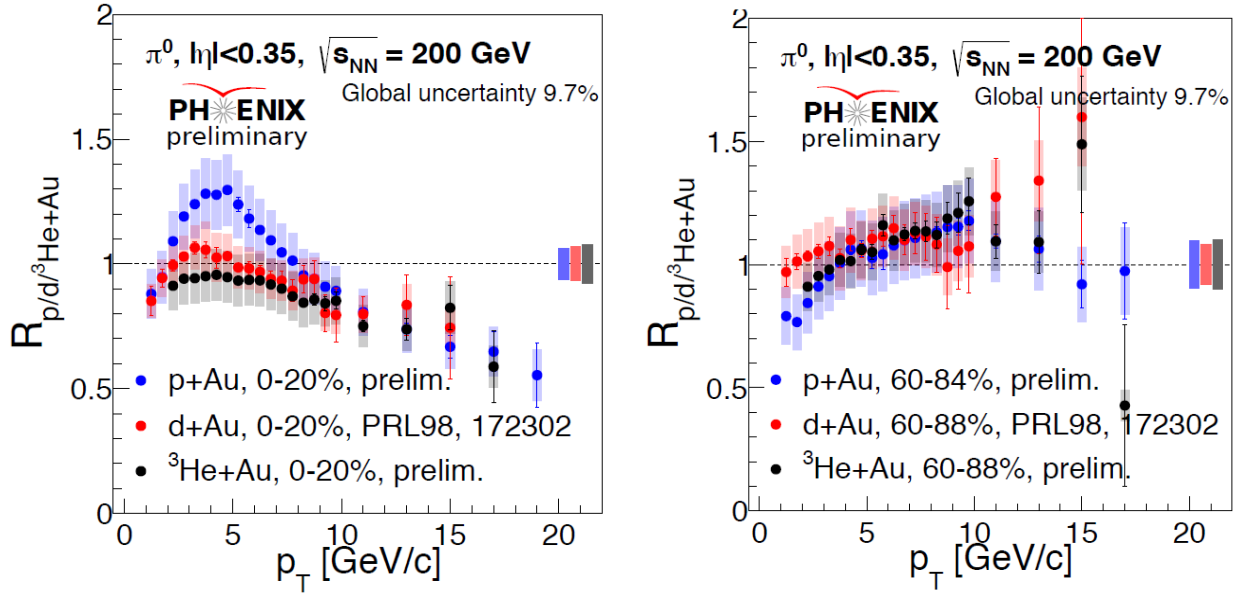


Fig. 2. The nuclear modification factors measured for π^0 mesons in 0–20% (left) and 60–84% (right) central $p(d, {}^3\text{He}) + \text{Au}$ collisions at $\sqrt{s_{NN}} = 200$ GeV

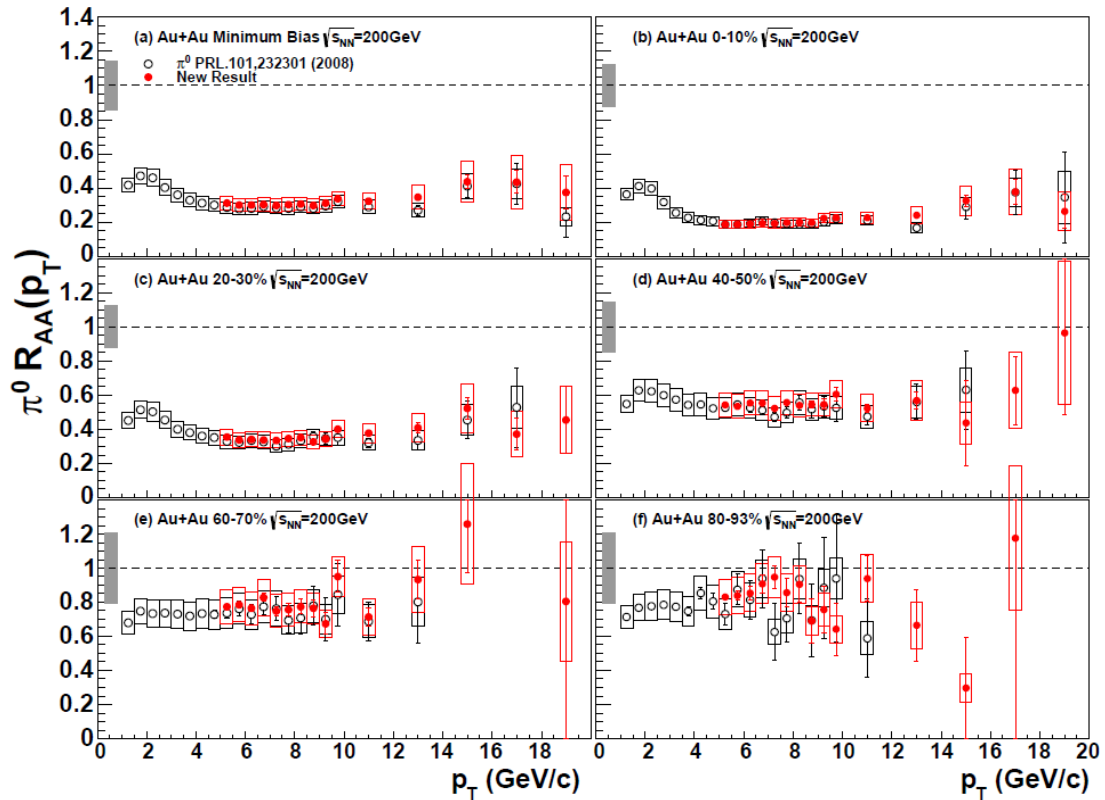


Fig. 3. The nuclear modification factors R_{AA} for π^0 mesons in Au + Au collisions at $\sqrt{s_{NN}} = 200$ GeV. The results are presented for different centrality bins

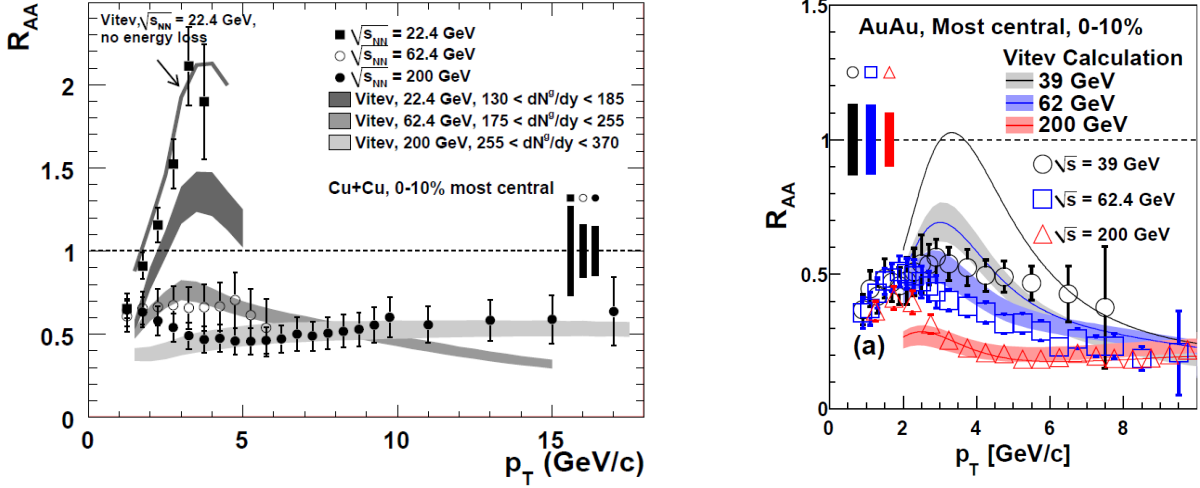


Fig. 4. The nuclear modification factors for π^0 mesons in Cu + Cu and Au + Au collisions at different energies as a function of the transverse momentum

The plot on the right shows the R_{AA} factors measured in central Au + Au collisions at $\sqrt{s_{NN}} = 39, 62.4,$ and 200 GeV with black, blue, and red markers [12]. One can see that at all collision energies the production of pions is significantly suppressed. This suppression at 39 and 62.4 GeV is the same at high transverse momentum. It means that in heavy ion collisions the enhancement takes over the suppression somewhere in the range of collision energies between 22.4 and 39 GeV. It is interesting to note that the lowest energy of 22.4 GeV is very close to the top Super Proton Synchrotron (SPS) energy, at which the suppression was not observed either.

A comparison of the nuclear modification factors measured for charged hadrons at the LHC in Pb + Pb collisions at $\sqrt{s_{NN}} = 2.76$ TeV [10] and for neutral pions in Au + Au collisions at $\sqrt{s_{NN}} = 200$ GeV shows that regardless of the difference by a factor of 14 in collision energies the measured factors are very close and they show very similar dependence on the transverse momentum in peripheral and central collisions.

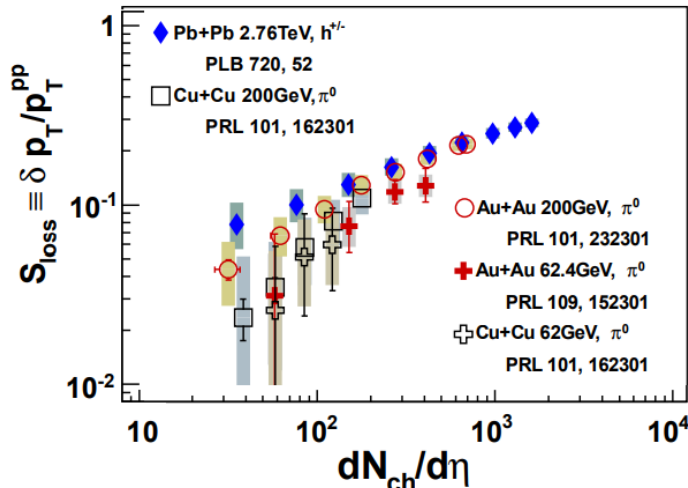


Fig. 5. Fractional momentum loss calculated with respect to $p + p$ reference at $p_T = 6$ GeV/c and shown as a function of the particle multiplicity

gradually increase with the multiplicity, and all the measured points independent of collision energy merge to one universal curve at large values of the particle multiplicity. One can also see that at the same energy the points corresponding to different colliding nuclei follow the same scaling, like black and red points obtained for Au + Au and Cu + Cu collisions at $\sqrt{s_{NN}} = 200$ GeV.

The similarity of the nuclear modification factors measured in heavy ion collisions at different energies indicates that this parameter is biased by the shapes of the particle production spectra at different energies. Instead, it was suggested to look at the fractional momentum loss [1].

Figure 5 shows the dependence of the fractional momentum loss on the charged particle multiplicity used as a measure of the energy density [13]. One can see that even though the R_{AA} values are very similar for different collision energies the fractional momentum losses are quite different. The momentum losses increase by 50% from central Au + Au collisions at $\sqrt{s_{NN}} = 200$ GeV to most central Pb + Pb collisions at $\sqrt{s_{NN}} = 2.76$ TeV and by a factor of 6 from $\sqrt{s_{NN}} = 62$ GeV to $\sqrt{s_{NN}} = 2.76$ TeV. The momentum losses

4. Direct photons

Direct photons are the photons emitted from the interaction region which do not originate from hadron decays. Such photons are produced at all stages of the collisions and can be used to constrain the time evolution of the medium. The strongly interacting medium produced in heavy ion collisions is transparent for photons, they leave the interaction region largely unaffected.

Figure 6 shows the nuclear modification factors measured for direct photons [14]. The plot on the top presents R_{dA} of direct photons in the minimum bias $d + Au$ collisions at $\sqrt{s_{NN}} = 200$ GeV. The plot on the bottom shows R_{AA} measured in most central Au + Au collisions at the same energy. Within uncertainties, R_{dA} and R_{AA} are consistent with unity in the whole range of measurements. The measured values of the factors can be quantitatively described by model calculations. Most of calculations for heavy ion collisions predict small suppression of direct photon production at high p_T values due to the isospin effect which originates from different photon production cross sections in $p + p$, $n + n$, and $p + n$ collisions. Modifications of the nuclear structure functions and plasma effects do not change much the predictions. In $d + Au$ collisions, model calculations with different combinations of standard CNM effects predict similar results consistent with the experimental data. The value of R_{dA} leaves room for the Cronin-like enhancement at intermediate p_T -values. The absence of significant suppression for high p_T direct photons in central Au + Au collisions was one of the most convincing arguments in favour of jet quenching as a main mechanism responsible for suppression of high- p_T hadron production.

Production of soft direct photons was measured in $p + p$ and Au + Au collisions at $\sqrt{s_{NN}} = 200$ GeV [15]. It was found that yields of soft photons in Au + Au collisions significantly exceed the yields in $p + p$ collisions scaled by the number of binary collisions at $p_T < 4$ GeV/c. The latest measurements at PHENIX are shown in Fig. 7. The measurements cover a wider p_T range; they provide finer centrality selections and higher precision. Blue points in the figure are for soft direct photon yields in Au + Au collisions, and green curves are the N_{coll} scaled $p + p$ results. For all centrality bins, one observes excessive yield of the photons. If

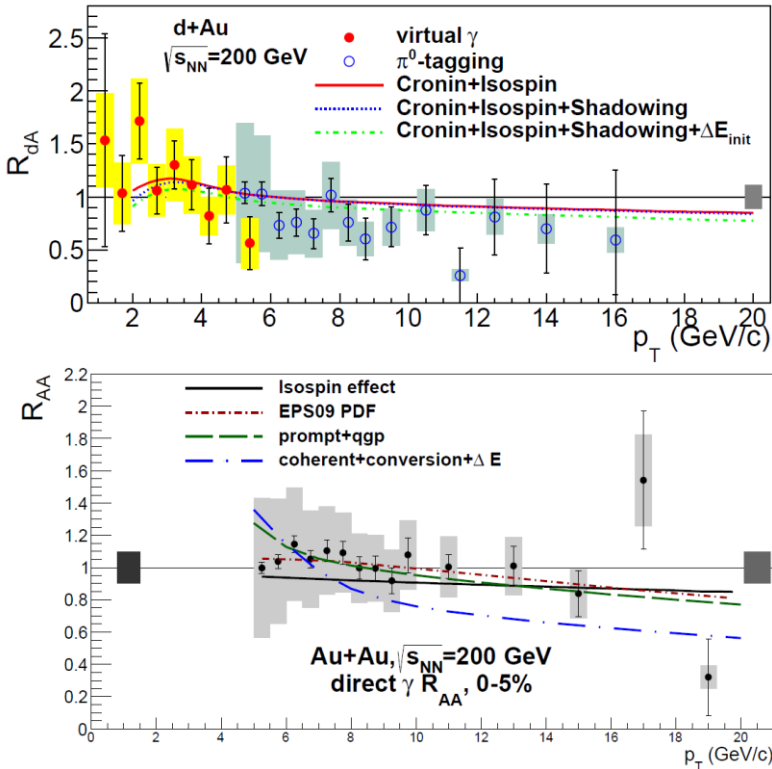


Fig. 6. The nuclear modification factors for direct photons in $d + Au$ (top) and Au + Au (bottom) collisions at $\sqrt{s_{NN}} = 200$ GeV. The measurements are compared to different model calculations

this excess yield is fitted to the exponential function, one gets values of the slope parameters equal to ~ 240 MeV with very weak centrality dependence. The excess of the photon yields scales with the number of participants, N_{part} , as N_{part}^α , where $\alpha = 1.48 \pm 0.08$ (stat) ± 0.04 (syst).

Most of theoretical models need to assume very early emission of direct photons from the interacting system when the temperature is still very high, in order to describe the large measured excessive yields.

The PHENIX experiment also has new measurements for direct photons momentum anisotropy at low momenta [16]. The top panel in Fig. 8 shows the dependence of the elliptic flow, v_2 , on the transverse momentum in Au + Au collisions at $\sqrt{s_{NN}} = 200$ GeV for different centrality bins. The panel on the bottom shows similar results for the triangular flow, v_3 . The flow was

measured using two different methods, the results are shown with green and red markers, and they agree very well in the overlap region. What is surprising is that the values of v_2 and v_3 measured for soft direct photons are very similar to the values previously measured for light hadrons. Similar to hadrons, the v_3 value shows only very weak dependence on the collision centrality. Large measured values of v_2 and v_3 similar to that for light hadrons present a serious challenge for theoretical models, which should assume late photon emission from the medium with relatively low temperature but well developed collective expansion. Observations of the large photon yields and the large flow are difficult to reconcile, and there is still no satisfactory model description of the two phenomena.

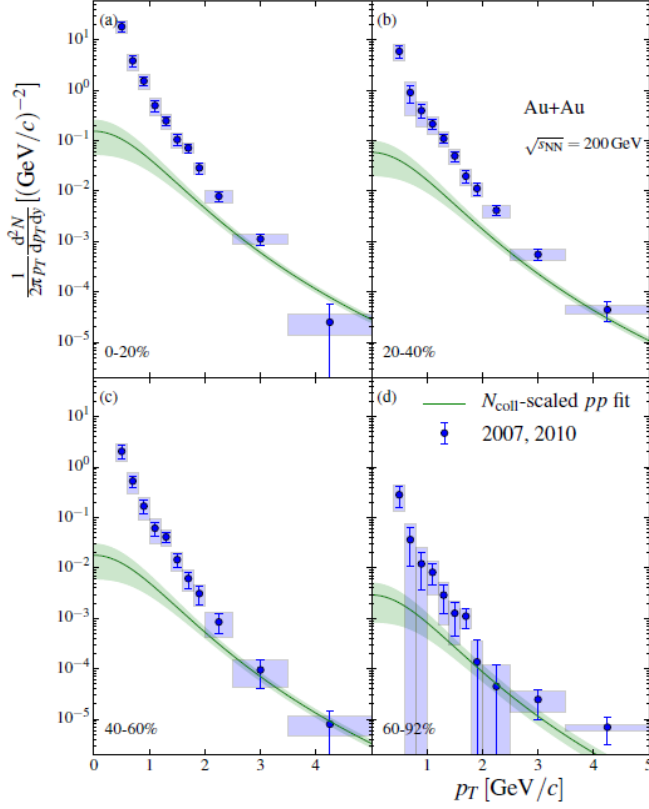


Fig. 7. Direct photon production spectra in Au + Au collisions at $\sqrt{s_{NN}} = 200$ GeV. The panels correspond to different centrality bins: 0–20, 20–40, 40–60, and 60–92%

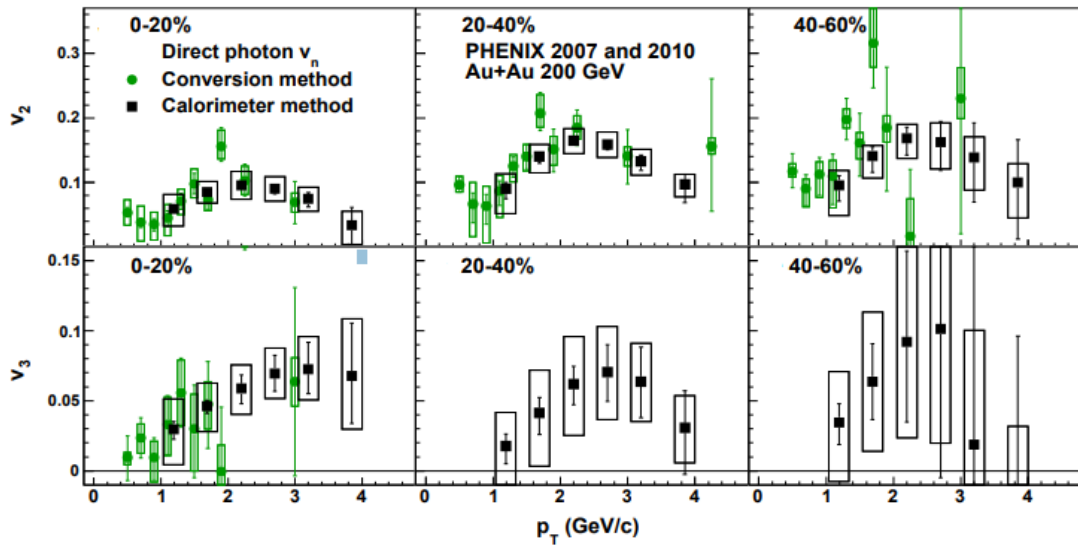


Fig. 8. The elliptic and triangular flows for soft direct photons in Au + Au collisions at $\sqrt{s_{NN}} = 200$ GeV

5. Charmonium in small systems

Originally, quarkonia, which are the bound states of c - \bar{c} and b - \bar{b} were considered as a golden signal of the QGP formation in heavy ion collisions [17]. These bound states have different radii and binding energies. With the onset of the Debye screening in plasma, the bound states with large radii would have to melt resulting in smaller measured final state yields. By studying the sequential melting of different quarkonia states, one could measure the temperature and other properties of the produced state of matter. Real life turned out to be more complicated. The charmonium suppression was indeed observed at SPS in CERN at collision energy of about $\sqrt{s_{NN}} \approx 20$ GeV. At much higher energies realized at RHIC and the LHC, one could expect formation of the hotter medium with larger probability of melting of the bound c - \bar{c} states. However, experiments showed the opposite trend. The suppression of J/Ψ production at RHIC turned out to be the same as at SPS, while suppression at the LHC turned out to be even smaller. These observations triggered multiple theoretical studies, which showed that many additional effects should be taken into account in order to reproduce the measurements. One of the main effects is the recombination of the open charm, which leads to an increase in the production of charmonium. The CNM effects, such as modification of parton distribution functions and co-mover dissociation, also play an important role.

PHENIX has new results on charmonium production (of J/Ψ and Ψ' mesons) in small systems: $p + p$, $p + \text{Al}$, $p + \text{Au}$, and ${}^3\text{He} + \text{Au}$ collisions at $\sqrt{s_{NN}} = 200$ GeV [18]. Measurements in $p + p$ are used as a baseline for heavier collision systems. The left panel in Fig. 9 shows the ratio of $\Psi' / J/\Psi$ values as measured in $p + A$ and $p + p$ collisions. The double ratio provides the means to cancel out some of the experimental systematic uncertainties. The ratio is presented as a function of the rapidity. Different colours correspond to different collision systems: blue points are for ${}^3\text{He} + \text{Au}$, red points are for $p + \text{Al}$, and black points are for $p(d) + \text{Au}$ collisions. One can see that the double ratio does not change in $p/d/{}^3\text{He}$ -going direction for all systems. However, in Au-going direction the ratio is suppressed by a factor of two.

It is well known that J/Ψ and Ψ' are the bound c - \bar{c} states with very different binding energies equal to 640 MeV for J/Ψ and only 50 MeV for Ψ' . This large difference in binding energies could be a reason for different suppression of these states if they scatter with the co-moving hadrons. To test this hypothesis, the right panel in Fig. 9 shows the same double ratio as a function of the co-mover particle density estimated using a multiphase transport (AMPT) model [19]. The PHENIX results are shown with the same colours as in the left panel. Additional points for p -Pb collisions at the LHC are shown with green and violet markers. One can see a clear correlation between the co-mover density and the observed level of suppression. It is crucial for theoretical models to understand the charmonium suppression due to the co-mover dissociation in order to correctly interpret the quarkonia results in $A + A$ collisions.

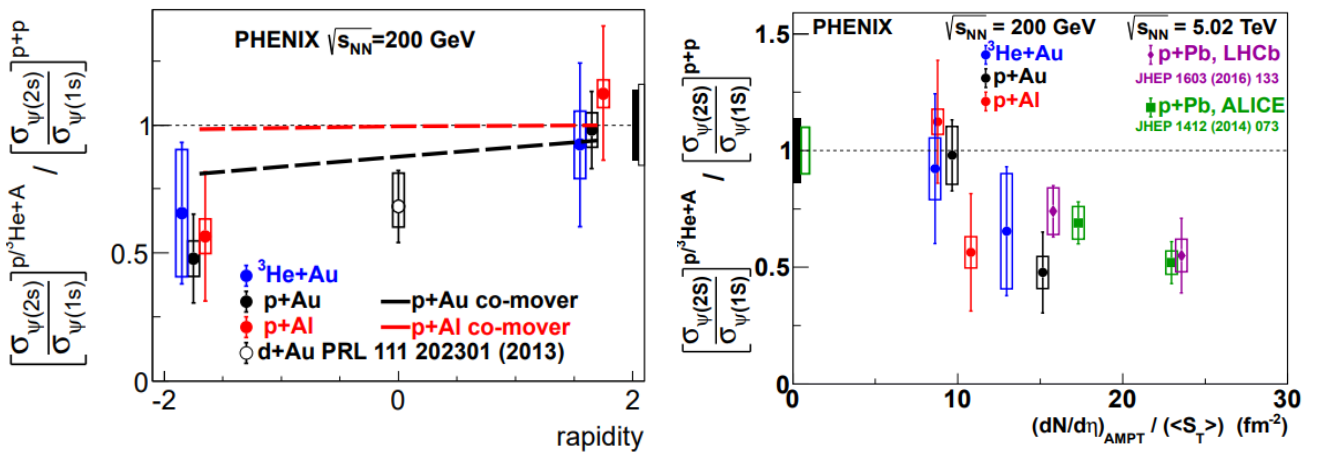


Fig. 9. The ratio of the ($\Psi' / J/\Psi$) values measured in $p + A$ and $p + p$ collisions at $\sqrt{s_{NN}} = 200$ GeV. The *left* and *right* panels show the dependence of the ratio on the particle rapidity and the co-mover density, respectively

6. Conclusion

The PHENIX experiment significantly contributed in the study of the hot and dense matter produced in central collisions of ultrarelativistic heavy nuclei. The results obtained by the collaboration were used to make a statement about the formation in such collisions of a new state of matter, the QGP. The collaboration continues to produce new results, which in close cooperation with the community of theoreticians are used to better understand the properties of the produced matter.

The main results of the PHENIX Collaboration were presented at several “Nucleus” conferences and International Session-Conferences of the Section of Nuclear Physics of the Physical Sciences Department of the Russian Academy of Sciences, which took place in the past decade. The results were also published in Russian scientific journals [20–29].

The PHENIX detector will be replaced with a new generation experimental set-up called sPHENIX [30], which should start taking data at RHIC in 2022.

References

1. K. Adcox *et al.*, Nucl. Phys. A **757**, 184 (2005).
2. K. Adcox *et al.*, NIM **499**, 469 (2003).
3. K. Adcox *et al.*, NIM **499**, 489 (2003).
4. V.G. Ryabov *et al.*, NIM A **419**, 363 (1998).
5. V. Riabov *et al.*, J. Phys. Conf. Ser. **675**, 022011 (2016).
6. V. Ryabov *et al.*, Nucl. Phys. A **774**, 735 (2006).
7. Yu. Riabov *et al.*, J. Phys. G **34**, 925 (2007).
8. A. Adare *et al.*, Phys. Rev. C **87**, 034911 (2013).
9. A. Adare *et al.*, Phys. Rev. Lett. **101**, 232301 (2008).
10. K. Aamodt *et al.*, Phys. Lett. B **969**, 30 (2011).
11. A. Adare *et al.*, Phys. Rev. Lett. **101**, 162301 (2008).
12. A. Adare *et al.*, Phys. Rev. Lett. **109**, 152301 (2012).
13. A. Adare *et al.*, Phys. Rev. C **93**, 024911 (2016).
14. A. Adare *et al.*, Phys. Rev. C **87**, 054907 (2013).
15. A. Adare *et al.*, Phys. Rev. C **91**, 064904 (2015).
16. A. Adare *et al.*, Phys. Rev. C **94**, 064901 (2016).
17. T. Matsui *et al.*, Phys. Lett. B **178**, 416 (1986).
18. A. Adare *et al.*, Phys. Rev. C **95**, 034904 (2017).
19. Z.W. Lin *et al.*, Phys. Rev. Lett. **89**, 152301 (2002).
20. D.A. Ivanishchev *et al.*, Bull. Russ. Acad. Sci. Phys. **81**, No. 10, 1181 (2017); Izv. Ross. Akad. Nauk Ser. Fiz. **81**, No. 10, 1321 (2017).
21. D.A. Ivanishchev *et al.*, Bull. Russ. Acad. Sci. Phys. **81**, No. 10, 1179 (2017); Izv. Ross. Akad. Nauk Ser. Fiz. **81**, No. 10, 1318 (2017).
22. D.A. Ivanishchev *et al.*, AIP Conf. Proc. **1701**, 100011 (2016).
23. M.V. Malaev *et al.*, Bull. Russ. Acad. Sci. Phys. **79**, No. 7, 909 (2015); Izv. Ross. Akad. Nauk Ser. Fiz. **79**, No. 7, 1015 (2015).
24. D.A. Ivanishchev *et al.*, Bull. Russ. Acad. Sci. Phys. **79**, No. 7, 921 (2015); Izv. Ross. Akad. Nauk Ser. Fiz. **79**, No. 7, 1028 (2015).
25. V.G. Riabov *et al.*, PoS Baldin ISHEPPXXII **078** (2015).
26. D.A. Ivanishchev *et al.*, Bull. Russ. Acad. Sci. Phys. **77**, 904 (2013); Izv. Ross. Akad. Nauk. **77**, 992 (2013).
27. D.A. Ivanishchev *et al.*, Bull. Russ. Acad. Sci. Phys. **77**, 900 (2013); Izv. Ross. Akad. Nauk. **77**, 988 (2013).
28. V.G. Riabov *et al.*, Phys. Atom. Nucl. **74**, 453 (2011); Yad. Fiz. **74**, 474 (2011).
29. V.G. Riabov *et al.*, Phys. Atom. Nucl. **72**, 509 (2009); Yad. Fiz. **72**, 545 (2009).
30. C. Aidala *et al.*, e-Print: arXiv:1207.6378 (2012).

JET QUENCHING IN ASYMMETRIC HEAVY-ION COLLISIONS (Cu + Au, $\sqrt{s_{NN}} = 200$ GeV) MEASURED BY THE PHENIX EXPERIMENT AT RELATIVISTIC HEAVY ION COLLIDER

PNPI participants of the PHENIX Collaboration:

V.V. Baublis, D.A. Ivanishchev, A.V. Khanzadeev, B.G. Komkov, D.O. Kotov, M.V. Malaev, V.G. Riabov, Yu.G. Riabov, V.M. Samsonov

1. Introduction

Production of quark–gluon plasma (QGP) has been established in central heavy-ion collisions at Relativistic Heavy Ion Collider (RHIC) [1–4] and the Large Hadron Collider (LHC) [5]. Jet quenching is one of the QGP signatures, which manifests itself in suppressed production of jets and leading hadrons at high transverse momentum relative to binary scaled yields measured in elementary pp collisions. The suppression is caused by softening of the production spectra in heavy-ion collisions due to the energy loss of the partons traversing the hot and dense medium produced in such collisions. Several theoretical models, such as parton quenching model (PQM) and Gyulassy–Levai–Vitev (GLV), were successful in description of the high- p_T suppression at RHIC. A comparison of model predictions to experimental data constrained the colour-charge density ($dN_g/dy \approx 1400$) and the transport coefficient ($\hat{q} \approx 13.2$ GeV²/fm) of the QGP [6, 7].

So far, jet quenching was experimentally observed only in central collisions of symmetric systems (Cu + Cu, Au + Au at RHIC; and Pb + Pb at the LHC). In 2012, RHIC for the first time delivered asymmetric collisions of heavy ions, Cu + Au at $\sqrt{s_{NN}} = 200$ GeV. In such collisions, the formed coloured medium provides a unique way to study the jet quenching. In central collision, the smaller nucleus is fully submerged in the larger one, thus reducing the contribution of nucleon–nucleon collisions in the low-density nuclear corona region. In non-central collisions, such interactions produce an asymmetric nuclear overlap region. This makes asymmetric collisions of heavy nuclei distinct and important for a systematic study of the parton energy loss, they can help to better constrain the input parameters of different theoretical models and to better understand the parton energy loss mechanism.

In this report, we present results on jet and leading hadron production in Cu + Au collisions at $\sqrt{s_{NN}} = 200$ GeV obtained by the PHENIX experiment [8] at RHIC. The results are discussed and compared to model predictions where available.

2. Experimental set-up and data analysis

The PHENIX detector is one of two large experiments that took data at RHIC. A detailed description of the PHENIX experimental set-up can be found elsewhere [8]. The PHENIX experimental set-up consists of two central and two forward spectrometers. The measurements presented in this report were obtained using the central spectrometers of the PHENIX detector, each covering 90° in azimuthal angle and $|\eta| < 0.35$ in pseudorapidity. The charged particle track reconstruction in PHENIX is performed with drift and three layers of pad chambers (DC/PC), which have high momentum and spatial resolution. The energy and coordinates of photons are measured using six lead-scintillator (PbSc) and two lead-glass (PbGl) sectors of the electromagnetic calorimeter (EMCal).

Jets are reconstructed using the anti- k_t algorithm [9] with the cone size $R = 0.2$ from charged particle tracks in DC/PC and electromagnetic clusters in the EMCal. The tracks are required to have the minimum p_T value of 0.5 GeV/ c and the clusters are required to have the minimum energy of 0.5 GeV. In order to avoid double counting of energy, the clusters associated with the reconstructed tracks are rejected.

To reject jets that are reconstructed from combinatoric particles, the reconstructed jets are required to have three or more constituents. The jet axis is required to be 0.05 units away in pseudorapidity and 0.12 units away in azimuth from the edge of the PHENIX detector to reject jets with mis-measured energy. A single mis-reconstructed track or EMCal cluster from a noisy tower can sometimes dominate the jet energy, and in order to reject such jets, the fraction of the jet's transverse momentum arising from the charged constituents was required to be between 0.2 and 0.7.

Jet spectra have previously been measured in a similar analysis using the anti- k_t algorithm with $R = 0.3$ in pp and $d + \text{Au}$ collisions in PHENIX [10–12]. In pp collisions, the results showed good agreement with perturbative quantum chromodynamic calculations, validating the jet reconstruction procedure. In the minimum bias $d + \text{Au}$ collisions, the jet rates were in line with geometric expectations. In the $\text{Cu} + \text{Au}$ analysis, the smaller cone size of $R = 0.2$ is used, constrained by the larger jet energy resolution and the higher rate of the underlying event fluctuations in the $\text{Cu} + \text{Au}$ collision system.

As there is no unique way to separate jets from soft background and jets from hard scattering, a data driven method was developed to estimate and statistically subtract fake jet contributions. For events where no jet is reconstructed, the position (η , ϕ) of tracks and the position (η , ϕ) of clusters are randomly shuffled. Jet reconstruction is performed in these shuffled tracks and clusters, which returns the estimated fake jet yield. The fake jet contribution is both p_T and centrality dependent with the contribution being large for central collisions and at low p_T . For the 0–20% centrality, it is 70% (93%) at 15 GeV/ c (23 GeV/ c).

After subtraction of the fake jets, the spectra are unfolded using the singular value decomposition (SVD) method [13] to correct for the detector effects and the centrality dependent underlying event fluctuations. The SVD unfolded results are cross-checked against the iterative Bayesian method [14], and the variation is included in the systematic uncertainty. The systematic uncertainty in the measured spectra and nuclear modification factors results from uncertainties in various sources. For most sources, the effects on the results are determined by repeating the analysis after varying the unfolding procedure, modifying the response matrix, or changing the jet selection criteria.

The procedure for π^0 -meson reconstruction which includes extraction of the raw π^0 yields and the estimation of corrections for the detector acceptance and reconstruction efficiency are described in Ref. [15]. Neutral pions are reconstructed with the EMCal in $\pi^0 \rightarrow \gamma\gamma$ decay channel separately for PbSc and PbGl subsystems. The acceptance and efficiency corrections are obtained using GEANT3 based Monte Carlo simulations. The systematic uncertainty of the measurements was estimated by varying different analysis parameters within their uncertainties. The main contribution comes from a possible mismatch of the calorimeter absolute energy scales in data and simulation. At high transverse momentum ($p_T > 10\text{--}15$ GeV/ c), a cluster merging effect gives a significant contribution to the total systematic uncertainty: two photons from high energy π^0 -meson decay have a small opening angle and are reconstructed in electromagnetic calorimeter as one photon. The neutral pion transverse momenta spectra measured in PbSc and PbGl are consistent within uncertainties, and the final results were obtained by averaging the PbSc and PbGl measurements.

3. Results

Figure 1 shows the per-event reconstructed jet yields [11, 12] and invariant transverse momentum spectra for π^0 mesons [16] in different centrality intervals of $\text{Cu} + \text{Au}$ collisions at $\sqrt{s_{NN}} = 200$ GeV. Measurements for jets and neutral pions were performed in a wide transverse momentum range up to 40 GeV/ c and 20 GeV/ c , respectively.

Collective effects in heavy ion collisions are studied with the so called nuclear modification factor R_{AA} , which is calculated as a ratio of particle yields measured in heavy ion and pp collisions and divided by the number of binary inelastic nucleon–nucleon collisions (N_{coll}).

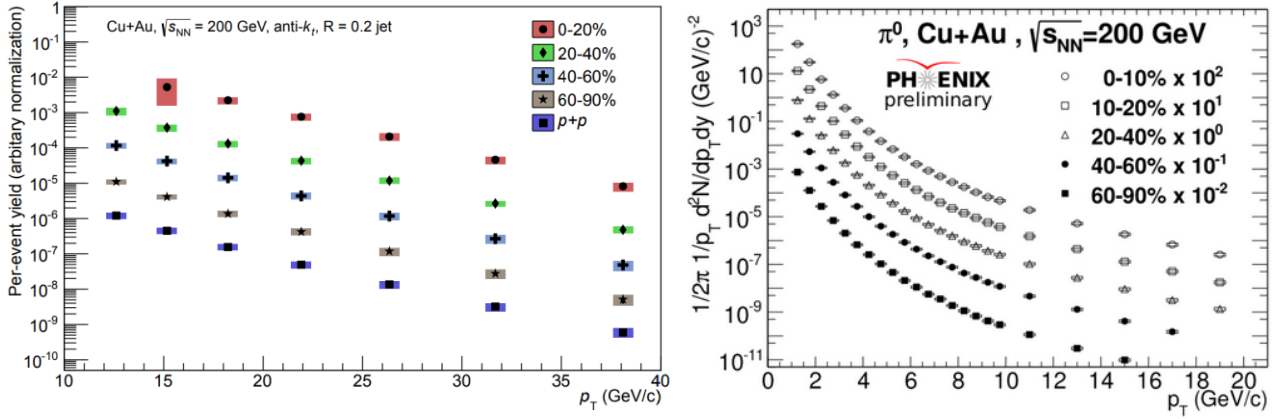


Fig. 1. Per-event reconstructed jet yields and invariant transverse momentum spectra for π^0 mesons obtained in Cu + Au collisions at $\sqrt{s_{NN}} = 200$ GeV by the PHENIX experiment

Figure 2 presents the nuclear modification factors R_{AA} for reconstructed jets obtained in Cu + Au collisions at $\sqrt{s_{NN}} = 200$ GeV [11, 12]. Jets are suppressed by a factor of 2 in central Cu + Au collisions. The suppression shows no p_T dependence. A weak momentum dependence of the jet suppression was observed at the LHC in Pb + Pb collisions at much higher energies [17]. The observed suppression gradually disappears towards peripheral collisions with a hint of enhancement in the 60–90% centrality interval.

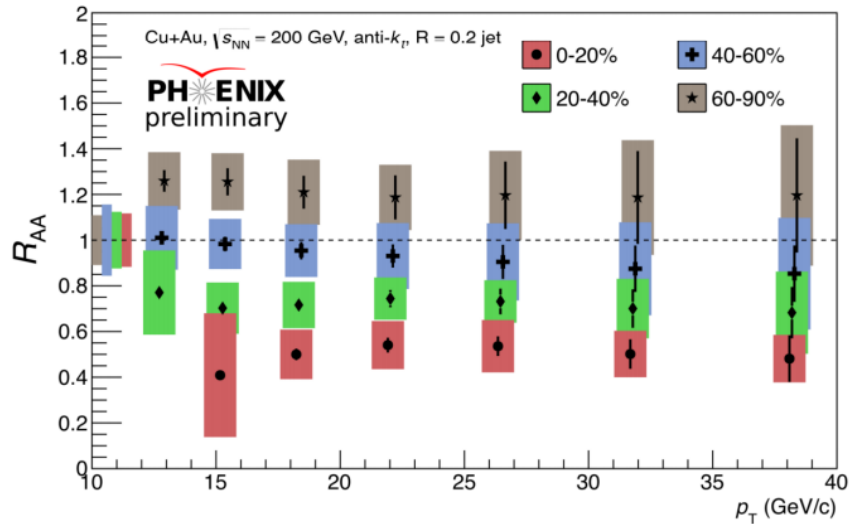


Fig. 2. Nuclear modification factors R_{AA} obtained for reconstructed jets in Cu + Au collisions at $\sqrt{s_{NN}} = 200$ GeV

Figure 3 presents p_T -integrated nuclear modification factors for reconstructed jets [11, 12] and π^0 mesons [16] in Cu + Au collisions at $\sqrt{s_{NN}} = 200$ GeV, respectively. The nuclear modification factors R_{AA} for the reconstructed jets were integrated in two p_T ranges: from 17 to 20 GeV/c and from 29 to 35 GeV/c. The nuclear modification factors R_{AA} for π^0 mesons were integrated in the momentum range $p_T > 10$ GeV/c.

The suppression pattern for π^0 mesons is similar in Cu + Au and Au + Au collisions for the number of participants $N_{part} > 50$. In more peripheral collisions and the number of participants $N_{part} < 50$, the production of π^0 mesons is less suppressed in Cu + Au than in Au + Au collisions. Both π^0 mesons and jets show a similar hint of enhancement in peripheral Cu + Au collisions at $\sqrt{s_{NN}} = 200$ GeV.

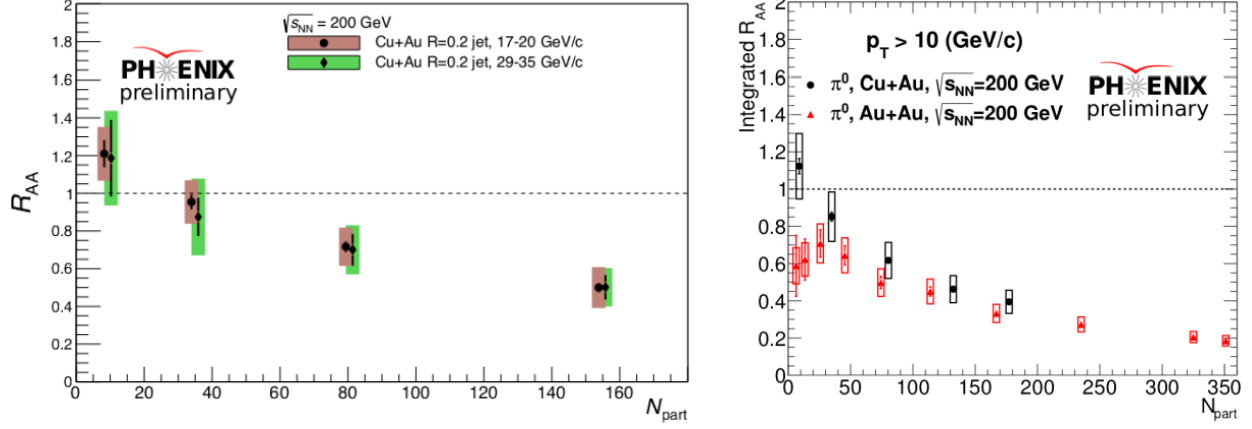


Fig. 3. Transverse momentum integrated nuclear modification factors R_{AA} for reconstructed jets and π^0 mesons obtained in Cu + Au and Au + Au collisions at $\sqrt{s_{NN}} = 200$ GeV

Model predictions for jet and leading hadron production in Cu + Au collisions at $\sqrt{s_{NN}} = 200$ GeV are very scarce. The only calculation currently available for jets comes from work [18]. Figure 4 shows soft collinear effective theory (SCET) with Glauber gluons model predictions (*red* and *black lines*) for the reconstructed jets nuclear modification factors R_{AA} obtained in the 0–20 and 40–60% central Cu + Au collisions. The model uses the coupling between the jets and the medium as an input parameter g , the calculations were performed for two values of this parameter: 2.0 and 2.2. As seen from the figures, the model predictions quantitatively agree with the experimental results.

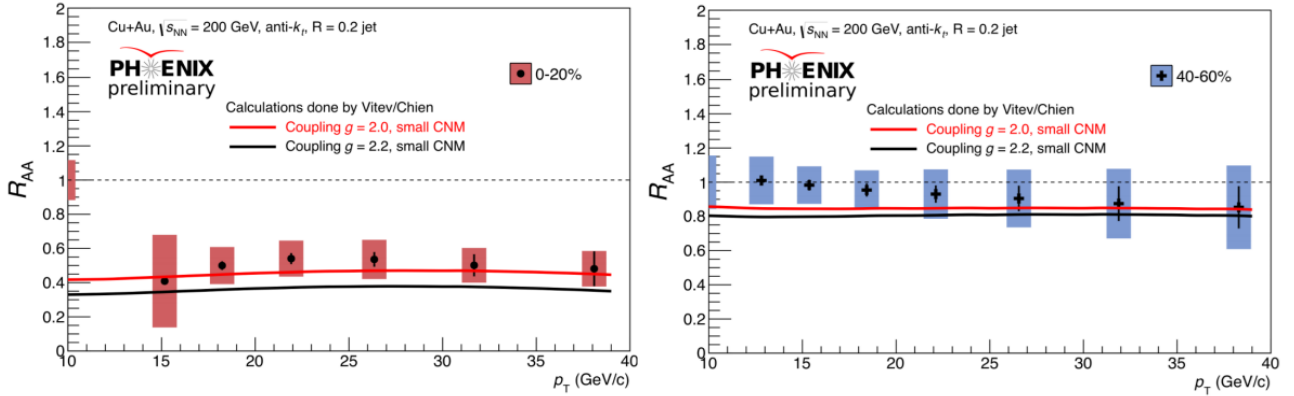


Fig. 4. SCET model predictions for reconstructed jets nuclear modification factors R_{AA} obtained in the 0–20 and 40–60% centralities of Cu + Au collisions at $\sqrt{s_{NN}} = 200$ GeV

4. Conclusion

The PHENIX experiment at RHIC has measured production and nuclear modification factors for reconstructed jets and π^0 mesons in Cu + Au collisions at $\sqrt{s_{NN}} = 200$ GeV. In central collisions, the production of jets and π^0 mesons is similarly suppressed by a factor of two. In peripheral collisions, there is a hint of enhancement for the two observables. Production of jets has not been yet measured in Au + Au collisions at the same energy. A comparison of the nuclear modification factors integrated for π^0 mesons at $p_T > 10$ GeV/c reveals a similar degree of suppression in Cu + Au and Au + Au collisions at the large number of participants, $N_{part} > 50$. However, at a smaller number of participants, production of π^0 mesons is enhanced in Cu + Au collisions while it is suppressed in the case of Au + Au collisions.

The nuclear modification factors measured for jets as a function of the transverse momentum in central and semicentral Cu + Au collisions at $\sqrt{s_{NN}} = 200$ GeV are well reproduced by the SCET model with

the value g of the coupling parameter between the jet and the medium equal to 2 and 2.2. There are no predictions for neutral pions available for comparison. The model calculations, which proved to be successful in description of jet quenching in Au + Au collisions at $\sqrt{s_{NN}} = 200$ GeV, should now be tested against experimental data in Cu + Au collisions.

References

1. PHENIX Collaboration, K. Adcox *et al.*, Nucl. Phys. A **757**, 184 (2005).
2. PHENIX Collaboration, Yu. Riabov *et al.*, J. Phys. G **34**, 925 (2007).
3. PHENIX Collaboration, V. Ryabov *et al.*, Nucl. Phys. A **774**, 735 (2006).
4. PHENIX Collaboration, D. Kotov *et al.*, J. Phys. Conf. Ser. **668**, 012017 (2015).
5. ALICE Collaboration, T. Gunji *et al.*, Nucl. Phys. A **956**, 11 (2016).
6. PHENIX Collaboration, A. Adare *et al.*, Phys. Rev. C **77**, 064907 (2008).
7. PHENIX Collaboration, A. Adare *et al.*, Phys. Rev. Lett. **101**, 232301 (2008).
8. K. Adcox *et al.*, Nucl. Instr. Meth. A **499** (2003).
9. M. Cacciari, G. P. Salam, G. Soyez, JHEP **04**, 063 (2007).
10. PHENIX Collaboration, A. Adare *et al.*, Phys. Rev. Lett. **116**, 122301 (2016).
11. PHENIX Collaboration, V. Riabov *et al.*, J. Phys. Conf. Ser. **675**, 022011 (2016).
12. PHENIX Collaboration, V. Riabov *et al.*, PoS BaldinISHEPPXXII **078**, (2015).
13. A. Hocker, V. Kartvelishvili, Nucl. Instrum. Meth. A **372**, 469 (1996).
14. G. D'Agostini, Nucl. Instrum. Meth. A **362**, 487 (1995).
15. PHENIX Collaboration S.S. Adler *et al.*, Phys. Rev. C **76**, 034904 (2007).
16. S. Zharko (for the PHENIX Collaboration), Nucl. Part. Phys. Proc. **289**, 113 (2017).
17. ALICE Collaboration, J. Adam *et al.*, Phys. Rev. B. **746**, 1 (2015).
18. Y.T. Chien, I. Vitev, JHEP **05**, 023 (2016).

HELICITY AMPLITUDE RATIOS FOR EXCLUSIVE ρ^0 -MESON ELECTROPRODUCTION ON TRANSVERSELY POLARIZED PROTONS

PNPI participants of the HERMES Collaboration:

S.L. Belostotski, G.E. Gavrilov, A.A. Izotov, A.Yu. Kisselev, P.V. Kravchenko,

S.I. Manaenkov, Yu.G. Naryshkin, D.O. Veretennikov, V.V. Vikhrov

1. Introduction

Exclusive electroproduction of vector mesons on nucleons gives information both on the reaction mechanisms and the nucleon structure [1]. Electroproduction at high energies can be considered to consist of three sub-processes: 1) the incident lepton emits a virtual photon γ^* , which dissociates into a quark–antiquark pair; 2) this $q\bar{q}$ pair interacts strongly with the nucleon; 3) the observed vector meson is formed from the scattered $q\bar{q}$ pair. In the Regge phenomenology, the interaction of $q\bar{q}$ pair with the nucleon proceeds through exchange of a pomeron or/and exchange of secondary reggeons. If quantum numbers of a particle lying on the Regge trajectory are $J^P = 0^+, 1^-, \text{etc.}$ (pomeron, ρ, f_2, \dots), the process is denoted as natural parity exchange (NPE). Alternatively, the case of $J^P = 0^+, 1^-, \text{etc.}$ (π, α_1, \dots) corresponds to unnatural parity exchange (UPE). In the framework of perturbative quantum chromodynamics valid at large photon virtuality Q^2 and high photon–nucleon centre-of-mass (CM) energy W , the nucleon structure can also be studied through hard exclusive meson production, as the process amplitude contains generalized parton distributions (GPDs) (see review [1]). However, the factorization property that permits to extract GPDs is rigorously proved only for the amplitudes $F_{01/20\pm 1/2}$ of longitudinal vector meson production by longitudinal virtual photons [2]. In the Goloskokov–Kroll (GK) model (see Ref. [3] and references therein), the validity of factorization is assumed for some other amplitudes in addition to $F_{01/20\pm 1/2}$, and this assumption is justified with a good description of existing data. The presented HERMES data can be well described in the GK model if the pion exchange is taken into account (see Ref. [4] and references therein). This means that the GPD-based approach should be modified at intermediate energies and momentum transfers.

All observables in vector-meson electroproduction can be expressed in terms of the helicity amplitudes in the CM system describing ρ^0 -meson production by a virtual photon. In particular, spin-density-matrix elements (SDMEs) are functions of the helicity-amplitude ratios (HARs). Therefore, HARs can be extracted from the data as was shown in Ref. [5]. For the first time, the HARs with the nucleon-helicity flip are obtained in the present analysis since the data on ρ^0 -meson production by the longitudinally polarized electrons (or positrons) on a transversely polarized hydrogen target are accumulated. The most recent HERMES results on the ρ^0 -meson production are published in Ref. [6], where more details can be found.

2. Spin-density-matrix elements and helicity amplitudes

The SDMEs are the Fourier coefficients in the angular distribution of the final-state particles. In the present paper, the formalism proposed in Ref. [7] for SDMEs is used. Any SDME can be expressed as a ratio of two sums of bilinear products of the helicity amplitudes and their conjugate quantities $F_{\nu\lambda'\mu\lambda}^*$. Here, $F_{\nu\lambda'\mu\lambda}$ is the helicity amplitude of the reaction $\gamma^*(\mu) + p(\lambda) \rightarrow \rho^0(\nu) + p(\lambda')$, where the particle helicities are given in parentheses. The helicity amplitude depends on W, Q^2 , and $t' = t - t_{\min}$, where t is the Mandelstam variable and $-t_{\min}$ represents the smallest kinematics allowed value of $-t$ at fixed W and Q^2 .

Any helicity amplitude can be decomposed into a sum of a NPE ($T_{\nu\lambda'\mu\lambda}$) and UPE ($U_{\nu\lambda'\mu\lambda}$) amplitudes: $F_{\nu\lambda'\mu\lambda} = T_{\nu\lambda'\mu\lambda} + U_{\nu\lambda'\mu\lambda}$, see for details Refs. [7, 8]. The amplitudes obey the symmetry relations hold due to parity conservation:

$$T_{\nu\lambda'\mu\lambda} = (-1)^{\mu-\nu} T_{-\nu\lambda'-\mu\lambda} = (-1)^{\lambda'-\lambda} T_{\nu-\lambda'\mu-\lambda}; \quad U_{\nu\lambda'\mu\lambda} = -(-1)^{\mu-\nu} U_{-\nu\lambda'-\mu\lambda} = -(-1)^{\lambda'-\lambda} U_{\nu-\lambda'\mu-\lambda}. \quad (1)$$

These symmetry properties of the helicity amplitudes permit to introduce the notation:

$$T_{\nu\mu}^{(1)} \equiv T_{\nu 1/2\mu 1/2}; U_{\nu\mu}^{(1)} \equiv U_{\nu 1/2\mu 1/2}; T_{\nu\mu}^{(2)} \equiv T_{\nu 1/2\mu -1/2}; U_{\nu\mu}^{(2)} \equiv U_{\nu 1/2\mu -1/2}. \quad (2)$$

All other amplitudes can be obtained using relations (1). The HARs extracted in the present analysis are defined for $n = 1, 2$ as $t_{\nu\mu}^{(n)} = T_{\nu\mu}^{(n)} / T_{00}^{(1)}$, $u_{\nu\mu}^{(n)} = U_{\nu\mu}^{(n)} / T_{00}^{(1)}$.

3. Experiment and data analysis

The data were accumulated with the HERMES spectrometer using the 27.6 GeV longitudinally polarized electron or positron beam of HERA and a gaseous hydrogen target. The HERMES set-up included a forward spectrometer [9], in which the scattered lepton and the produced hadrons were detected within an angular acceptance of ± 170 mrad horizontally and $\pm(40-140)$ mrad vertically. The tracking system had a momentum resolution of about 1.5% and an angular resolution of about 1 mrad. Lepton identification was accomplished using a transition-radiation detector, a preshower scintillator counter, and an electromagnetic calorimeter. The particle-identification system included also a dual-radiator ring-imaging Cherenkov detector [10] to identify hadrons. Combining the responses of the detectors in a likelihood method leads to an average lepton-identification efficiency of 98%, with a hadron contamination of less than 1%. The helicity of the beam was typically reversed every two months. The beam polarization was continuously measured by two Compton polarimeters [11, 12]. The average value of the beam polarization for the events used in the analysis is ± 0.30 with a 0.03 uncertainty. A small part of the data was collected with an unpolarized target and the main part with a transversely polarized target [13], for which the polarization direction was reversed every 60 to 180 s. The measured mean value of the target polarization was $\langle |P_T| \rangle = 0.72 \pm 0.06$ [14].

The ρ^0 mesons are produced and decay in the following exclusive reactions: $e + p \rightarrow e + p + \rho^0$ and $\rho^0 \rightarrow \pi^+ + \pi^-$. The event sample used in this analysis is practically the same as that used in Ref. [14]. The most important improvement is the application of a new tracking algorithm, which is based on a Kalman filter [15]. For the present analysis, the data are required to fulfil the following criteria:

1. The scattered lepton should have an energy larger than 3.5 GeV in order not to introduce effects from varying trigger threshold.
2. The longitudinal beam polarization is restricted to the interval $15\% < |P_T| < 80\%$.
3. Events with exactly two oppositely charged hadrons and one lepton with the same charge as the beam lepton are selected. All tracks are required to originate from the same vertex.
4. No calorimeter clusters are observed (no π^0 is detected).
5. The two pion invariant mass is required to obey $0.6 \text{ GeV} \leq M(\pi^+\pi^-) \leq 1.0 \text{ GeV}$.
6. The recoiling proton is not detected, but instead reconstructed through the missing energy. Taking into account the spectrometer resolution, the missing energy ΔE should lie in the interval $-1.0 \text{ GeV} < \Delta E < 0.8 \text{ GeV}$. Here, $\Delta E = (M_X^2 - M_p^2) / (2M_p)$, M_p is the proton mass and $M_X^2 = (p + q - p_{\pi^+} - p_{\pi^-})^2$ is the missing mass squared, where p, q, p_{π^+} , and p_{π^-} are the four momenta of the target nucleon, the virtual photon, and each of the two pions, respectively. The distribution of the missing energy, shown in Ref. [14], exhibits a clearly visible exclusive peak.
7. The kinematic constraints $Q^2 > 1.0 \text{ GeV}^2$, $6.3 \text{ GeV} > W > 3 \text{ GeV}$, $-t' < 0.4 \text{ GeV}^2$ are applied. After application of all these requirements, the data sample contains 8741 events. These data are referred to in the following as data in the ‘‘entire kinematic region’’. The applied constraints do not fully suppress the background. The exclusive sample contains contributions from double-diffractive processes, which should be neglected in the low ΔE region, from non-resonant $\pi^+\pi^-$ -pair production, which is of the order of 1–2% [14], from Δ -isobar excitation, which in the HERMES acceptance is less than 7% [14], and from semi-inclusive deep-inelastic scattering (SIDIS) events.

The presented results are not corrected for the former three processes, while a correction is applied for the SIDIS background. The shaded histogram of the missing energy ΔE (presented in Ref. [14]) shows

the SIDIS background obtained from a Pythia Monte Carlo (MC) simulation. It is normalized to the data in the region of $2 \text{ GeV} < \Delta E < 20 \text{ GeV}$. The simulation is used to determine the fraction of the SIDIS background under the exclusive peak. This fraction f_{bg} increases from 7 to 23% for increasing $-t'$ and amounts on average to 11%. A fit of the angular distribution of the SIDIS MC events under the exclusive peak is performed. The obtained function W_{bg} with no free parameters and the angular distribution W_{ρ} of the exclusive ρ^0 production are combined to give the total angular distribution $W_{\text{tot}} = (1 - f_{\text{bg}})W_{\rho} + f_{\text{bg}}W_{\text{bg}}$. The function W_{tot} is used in an unbinned maximum-likelihood method, the detector properties are taken into account by a MC simulation. The contribution of background from SIDIS events to the obtained amplitude ratios is considered as one of the main sources of systematic uncertainty. This uncertainty is calculated as the difference between the HARs obtained when f_{bg} is put equal to zero and the HARs extracted when the background corrections are taken into account.

4. Results

Using an unbinned maximum-likelihood method, the HARs are obtained from the 25-parameter fit in the entire kinematic region ($\langle W \rangle = 4.73 \text{ GeV}$, $\langle Q^2 \rangle = 1.93 \text{ GeV}^2$, $\langle -t' \rangle = 0.132 \text{ GeV}^2$). The result is shown in Fig. 1 with red points. While the phase of $u_{11}^{(1)}$ is fixed according to the results of Refs. [16, 17], the amplitude modulus is fit so that $\text{Re}[u_{11}^{(1)}]$ and $\text{Im}[u_{11}^{(1)}]$ represent the results for one parameter fit. The systematic uncertainty in $\text{Re}[u_{11}^{(1)}]$ and $\text{Im}[u_{11}^{(1)}]$ is much larger than the statistical one due to the large total experimental uncertainty in the $u_{11}^{(1)}$ phase. The value of $\text{Im}[u_{11}^{(1)}]$ represents the result of Ref. [5]; its error bar shows the total uncertainty. The shadowed area in Fig. 1 corresponds to ratios of amplitudes without the nucleon–helicity flip obtained here and earlier in work [5] for the unpolarized proton. All other ratios of the nucleon–helicity-flip amplitudes to $T_{00}^{(1)}$ are calculated for the first time. As can be seen in Fig. 1, all HARs except $t_{11}^{(1)}$, $t_{01}^{(1)}$, and $u_{11}^{(1)}$ are compatible with zero within two standard deviation of their total uncertainty. The HAR $t_{01}^{(1)}$ is responsible for the violation of the s -channel helicity-conservation approximation, while $u_{11}^{(1)}$ shows the role of UPE in ρ^0 -meson electroproduction.

The results of the theoretical predictions in the GK model [3, 18] are depicted in Fig. 1 with blue triangles and squares. In order to describe the presented HERMES data, the one-pion exchange (OPE) diagrams have to be included in addition to the handbag Feynman graphs containing the GPDs. Note that even the HARs compatible with zero are informative and can be used to fix the sign of the $\pi\rho$ form factor $g_{\pi\rho}(Q^2)$ in the OPE amplitude which is proportional to $g_{\pi\rho}(Q^2)/(t - m_{\pi}^2)$, where m_{π} denotes the π^0 mass. As seen in Fig. 1, the positive sign of the $\pi\rho$ form factor $g_{\pi\rho}(Q^2)$ (*triangles*) corresponds to the extracted HARs $u_{11}^{(2)}$ and $u_{10}^{(2)}$, that are sensitive to the sign, much better ($\chi^2/\text{ndf} = 1.8/4$) than the negative sign (*squares*) for which $\chi^2/\text{ndf} = 30.3/4$.

The most serious disagreement between the extracted HAR $\text{Im}[t_{11}^{(1)}]$ and that calculated in the GK model was already discussed in the previous HERMES work [5] and can be explained probably with the unsatisfactory description of the $q\bar{q}$ re-scattering from the proton in the GK model. As can be seen in Fig. 1, neither the phase nor the modulus of the amplitude ratio $u_{11}^{(1)}$ are described well in the GK model.

A comparison of the SDMEs directly obtained from the HERMES data in Refs. [8] and [14] to those calculated with the HARs extracted in the present analysis is performed in work [6], and good agreement is found. The correlation matrix for 25 parameters is taken into account for the calculation of the statistical uncertainty of the SDMEs in the Diehl representation [7] $u_{\mu\mu'}^{\text{vv}'}$, $n_{\mu\mu'}^{\text{vv}'}$, and $s_{\mu\mu'}^{\text{vv}'}$ obtained from the HARs. The SDMEs $n_{\mu\mu'}^{\text{vv}'}$ and $s_{\mu\mu'}^{\text{vv}'}$, presented in Figs. 2 and 3, have linear contributions of the small HARs $t_{\nu\mu}^{(2)}$ and $u_{\nu\mu}^{(2)}$, respectively. These SDMEs can only be extracted from measurements with a transversely polarized

target so that the nucleon–helicity-flip amplitude ratios $t_{\nu\mu}^{(2)}$ and $u_{\nu\mu}^{(2)}$ are extracted in Ref. [6] for the first time. The total uncertainty is the sum in quadrature of the statistical and the total systematic uncertainties.

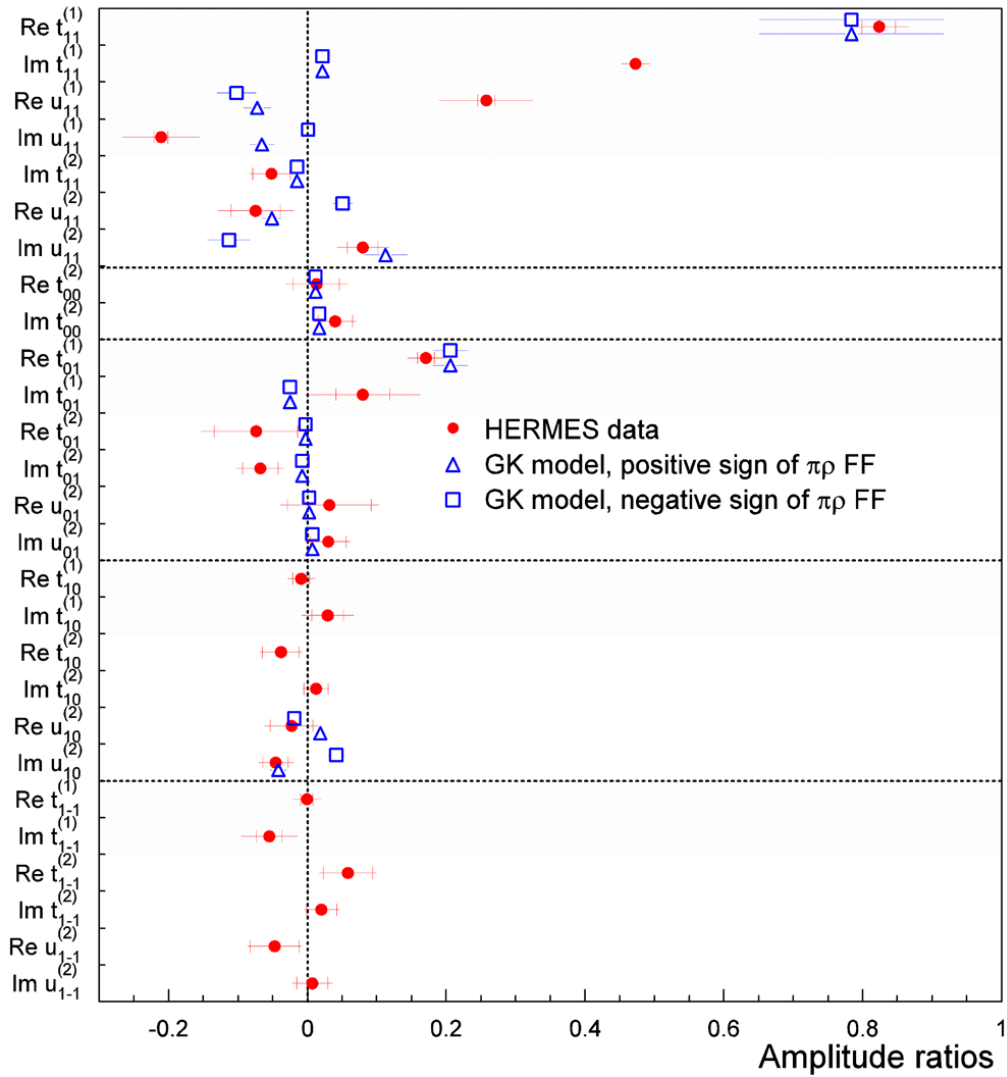


Fig. 1. Comparison of amplitude ratios determined in Ref. [6] to those calculated in the GK model. The *red filled circles* correspond to the extracted amplitude ratios and the *blue open triangles (squares)* represent the result of the GK model calculation using the positive (negative) sign of the $\pi\rho$ transition form factor. The inner (outer) error bars of the red points represent the statistical (total) uncertainty

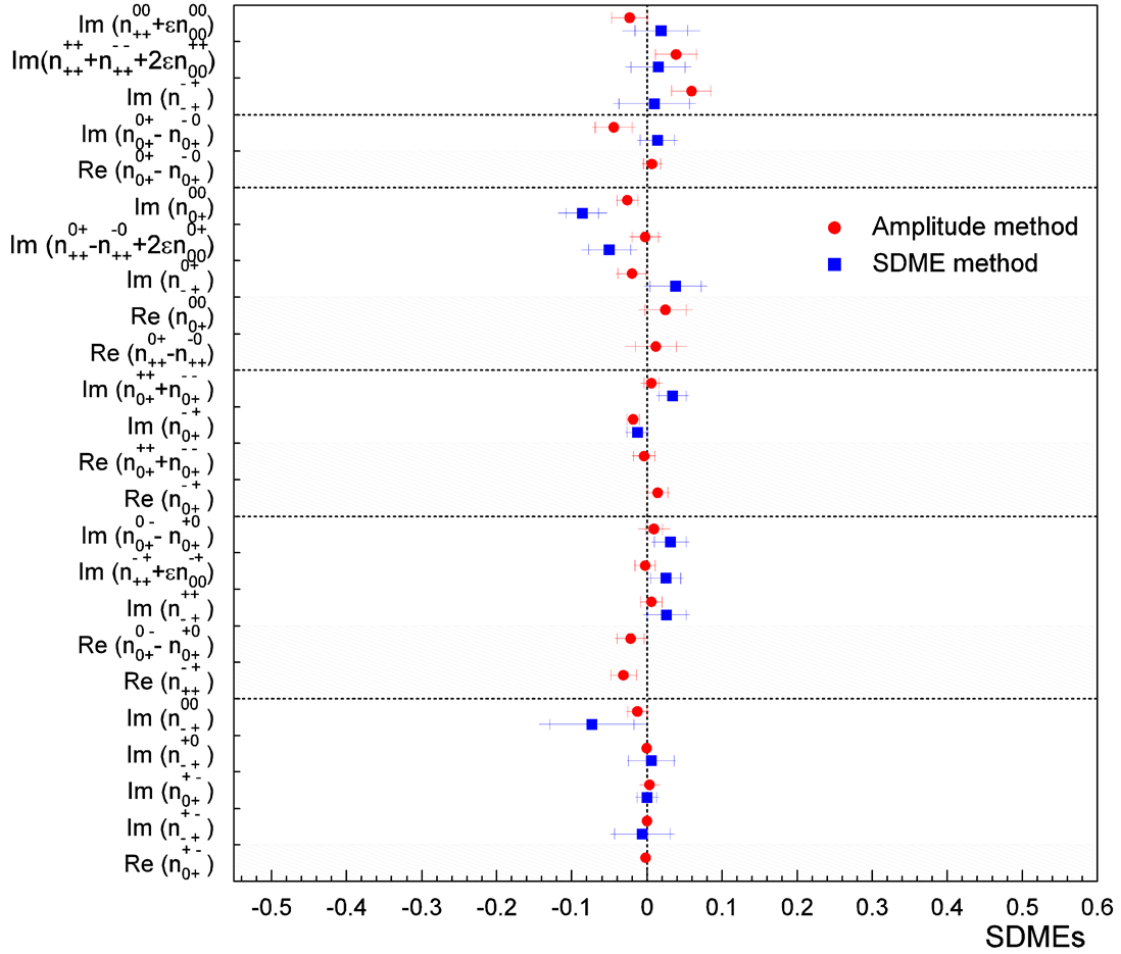


Fig. 2. Comparison of the Diehl SDMEs [7] $n_{\mu\mu'}^{vv'}$ calculated from the helicity-amplitude ratios (*red circles*) and the SDMEs (*blue squares*) directly extracted in Ref. [14] in the entire kinematic region. For the first case, a 25-parameter fit is used. The points in the shaded area show SDMEs that can be obtained only if the beam is longitudinally polarized. The inner (outer) error bars represent the statistical (total) uncertainty

The SDMEs in Figs. 2 and 3 are reordered according to the SDME classes proposed in Refs. [8, 14]. Those SDMEs that can be extracted only from the data taken with a longitudinal polarized lepton beam are shown in shaded areas. Figures 2 and 3 show that for some of the calculated SDMEs $n_{\mu\mu'}^{vv'}$, and $s_{\mu\mu'}^{vv'}$ no published results from work [14] exist, because the beam polarization was not exploited in that analysis. While in Refs. [8] and [14] a total of 53 SDMEs could be extracted, the amplitude method presented here allows for the calculation of 71 SDMEs based on the extraction of 25 parameters. As seen in Figs. 2 and 3, there is reasonable agreement between SDMEs directly extracted in Refs. [8, 14] and those calculated from the HARs in Ref. [6]. The SDMEs which can be obtained with unpolarized targets are not shown in the present paper. But a comparison of the calculated SDMEs $u_{\mu\mu'}^{vv'}$ with those directly extracted from the HERMES data [8] is also performed in Ref. [6] (for the first time in Ref. [5]) and shows reasonable agreement.

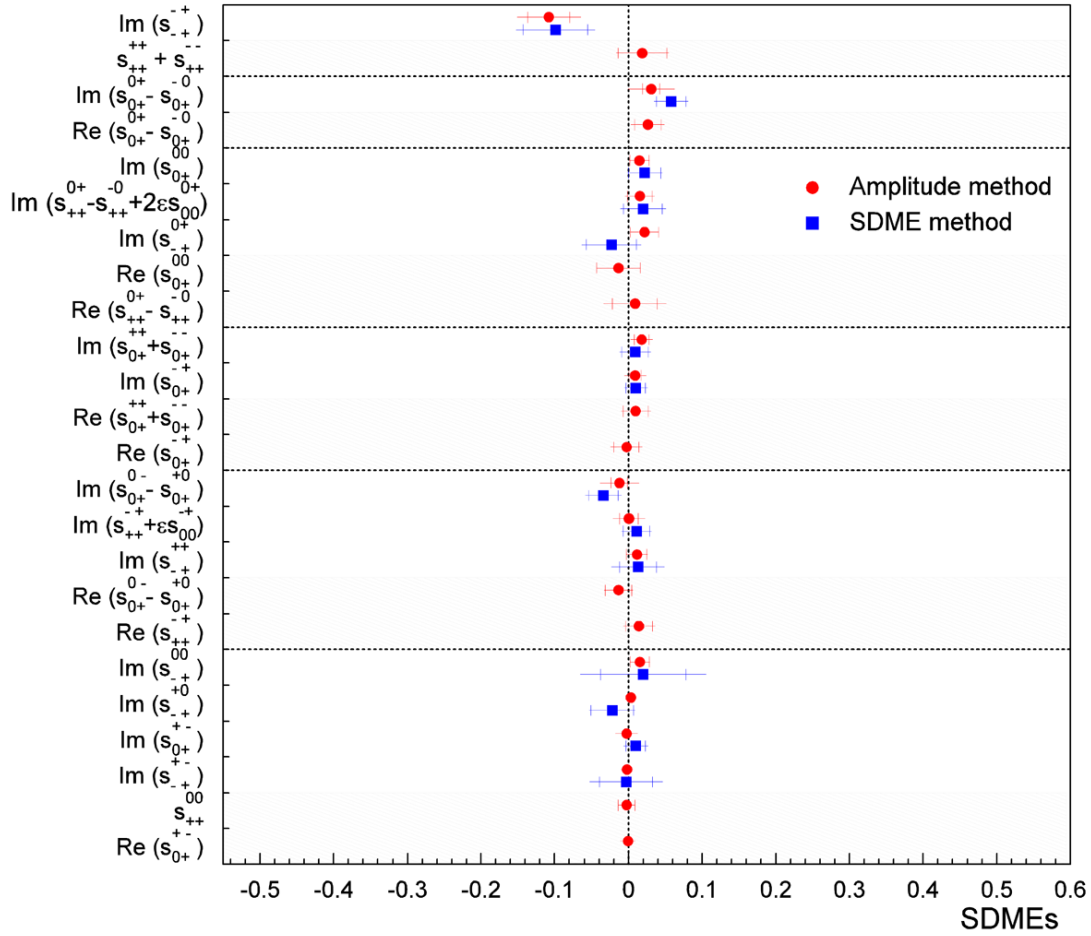


Fig. 3. Comparison of the Diehl SDMEs $s_{\mu\mu'}^{vv'}$ calculated from the helicity-amplitude ratios (*red circles*) and the SDMEs (*blue squares*) directly extracted in Ref. [14]. The meaning of the error bars and the further explanations are the same as for Fig. 2

References

1. M. Diehl, Phys. Rep. **388**, 41 (2003).
2. J.C. Collins, L. Frankfurt, M.S. Strikman, Phys. Rev. D **56**, 2982 (1997).
3. S.V. Goloskokov, P. Kroll, Eur. Phys. J. C **53**, 367 (2008).
4. S.V. Goloskokov, P. Kroll, Eur. Phys. J. A **50**, 146 (2014).
5. HERMES Collaboration, A. Airapetian *et al.*, Eur. Phys. J. C **71**, 1609 (2011).
6. HERMES Collaboration, A. Airapetian *et al.*, Eur. Phys. J. C **77**, 378 (2017).
7. M. Diehl, JHEP **0709**, 064 (2007).
8. HERMES Collaboration, A. Airapetian *et al.*, Eur. Phys. J. C **62**, 659 (2009).
9. HERMES Collaboration, K. Ackerstaff *et al.*, Nucl. Instr. Meth. A **417**, 230 (1998).
10. HERMES Collaboration, N. Akopov *et al.*, Nucl. Instr. Meth. A **479**, 511 (2002).
11. HERMES Collaboration, D.P. Barber *et al.*, Nucl. Instr. Meth. A **329**, 79 (1993).
12. HERMES Collaboration, M. Beckmann *et al.*, Nucl. Instr. Meth. A **479**, 334 (2002).
13. HERMES Collaboration, A. Airapetian *et al.*, Nucl. Instr. Meth. A **540**, 68 (2005).
14. HERMES Collaboration, A. Airapetian *et al.*, Phys. Lett. B **679**, 100 (2009).
15. R. Fruhwirth, Nucl. Instr. Meth. A **262**, 444 (1987).
16. HERMES Collaboration, A. Airapetian *et al.*, Phys. Lett. B **513**, 301 (2001).
17. HERMES Collaboration, A. Airapetian *et al.*, Eur. Phys. J. C **29**, 171 (2003).
18. S.V. Goloskokov, P. Kroll, Eur. Phys. J. C **74**, 2725 (2014).

EXPERIMENT OLYMPUS AT DESY

PNPI participants of the OLYMPUS experiment:

S.L. Belostotski, G.G. Gavrilov, A.A. Izotov, A.Yu. Kisselev, A.G. Krivshich, O.V. Miklukho, Yu.G. Naryshkin, D.O. Veretennikov

1. Introduction

The proton elastic form factor ratio, $\mu G_E/G_M$, measured using the polarization techniques [1], is in a dramatic discrepancy with the ratio obtained using the traditional Rosenbluth technique [2]. One of the hypotheses for the cause of this discrepancy is a contribution to the cross section from the hard two-photon exchange (TPE), which is not included in the standard radiative corrections and which might affect the two measurement techniques differently.

Unfortunately, direct calculations of the TPE diagrams are difficult, and the results contain theoretical uncertainties. As estimations show, the TPE effect on the polarization data is expected to be small, while it may be drastically large in the case of the Rosenbluth technique based on unpolarized cross section measurements.

To address this question, the Olympus experiment was proposed to measure the ratio between the positron–proton and electron–proton elastic scattering cross sections. In the single-photon exchange approximation, this ratio is unity. At the next-to-leading order, the interference of the one-photon and two-photon exchange diagrams changes the sign between the electron and positron scattering, and thus, the ratio may not be equal to unity. Measurements of this ratio (the beam-charge asymmetry) give a possibility to estimate experimentally the contribution of the TPE to the elastic electron or positron scattering. At a fixed primary beam momentum, the two photon exchange effect depends on the lepton scattering angle θ (on the momentum transfer Q^2) or on the virtual photon polarization, $\varepsilon = \left[1 + 2\left(1 + Q^2 / 4M_p^2\right)\tan^2(\theta/2)\right]^{-1}$, where M_p is the proton mass. If the beam momentum is not fixed, the TPE depends both on Q^2 and ε independently.

2. Experiment

The OLYMPUS experiment (Fig. 1) was installed for several months of dedicated data taking at the DORIS electron–positron storage ring at DESY, in Hamburg, Germany. The circulating beams of electrons or positrons passed through an internal hydrogen gas target. The scattered charged leptons and recoiling protons were detected in coincidence over a wide range of scattering angles θ and φ ($12^\circ \leq \theta \leq 75^\circ$, $-15^\circ \leq \varphi \leq 15^\circ$). The hydrogen gas target (an open end tube type) was designed and built at the Massachusetts Institute of Technology (MIT) and installed at the DORIS ring. The MIT BLAST detector used a toroidal magnetic field with a left–right symmetric arrangement of tracking detectors and time of flight scintillators. In addition, new detector systems were designed and built to monitor the luminosity during the experiment. A two-arm telescope mounted at $\theta = 12^\circ$ was conceived, designed and fabricated at the PNPI. It consisted of triple GEM detectors from the Hampton University, two scintillation telescopes with silicon photomultipliers as photodetectors, multi-wire proportional chambers (nine planes, 1 mm spacing) with the PNPI readout electronics. Symmetric Möller–Bhabha (SYMB) calorimeters from Mainz were positioned at a very forward angle of 1.29° . The Bonn group provided the software and hardware for the data acquisition system. The trigger and slow control systems were developed by the MIT. A detailed description of the experiment can be found in Ref. [3].

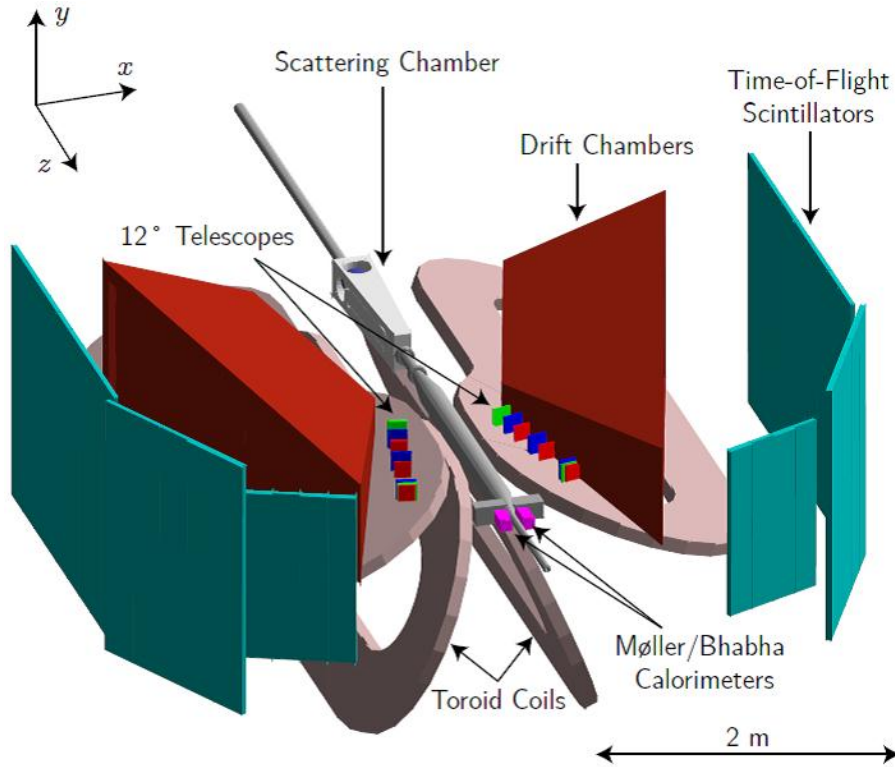


Fig. 1. Schematic view of the OLYMPUS detector

3. Data taking

The OLYMPUS experiment took data in the last running period of the DORIS electron/positron storage ring, before the shutdown. The 2.01 GeV stored beams with up to 65 mA of the current passed through the internal hydrogen gas target with an areal density of $3 \cdot 10^{15}$ atoms/cm². The experiment collected data at a total integrated luminosity of 4.5 fb^{-1} .

The DORIS magnet power supplies were modified to allow the beam species (electrons or positrons) to be changed daily. Upstream and downstream of the target, the beam positions and slopes were carefully monitored for each beam species. The beam intensities were controlled with the help of the mentioned above SYMB calorimeters and the 12° two-arm telescope (Fig. 1). The 12° telescope could serve as a beam monitor under condition that the TPE effects at such a small angle ($Q^2 \approx 0.4 \text{ GeV}^2$) are small (less than 0.5%). In the final analysis, the SYMB monitor was used only for luminosity normalization. The relative luminosity uncertainty for each beam species was $\sim 0.36\%$. With this normalization, the 12° telescope was used for the $R_{2\gamma}$ measurement (Eq. 1) at very small momentum transfers. To a good approximation, the detector system was left–right symmetric and this was used as an additional cross-check in the data analysis.

Most of the data were collected with positive toroid polarity. Unfortunately, the data taking at negative toroid polarity was not possible because of excessive noise rates due to low-energy electrons which were bent away from the beam axis into the drift chambers.

In order to build a reliable Monte Carlo (MC) geometrical file of the detector, a very careful optical survey of all detector component positions was made and the magnetic field was mapped throughout the tracking volume.

4. Monte Carlo model, radiation corrections, and results

A complete MC simulation of the experiment was developed in order to account for the differences between electrons and positrons with respect to radiative effects, changing beam position and energy, the spectrometer acceptance, track reconstruction efficiency, luminosity, and elastic event selection. The ratio reported here is given by

$$R_{2\gamma} = \left[\frac{N_{\text{exp}}(e^+)}{N_{\text{exp}}(e^-)} \right] \bigg/ \left[\frac{N_{\text{MC}}(e^+)}{N_{\text{MC}}(e^-)} \right] = \frac{R_{\text{exp}}}{R_{\text{MC}}}. \quad (1)$$

Here $N_{\text{exp}}(e^\pm)$, $N_{\text{MC}}(e^\pm)$ are the normalized experimental and simulated counts, respectively, for each beam species. A radiative event generator was developed specifically for the OLYMPUS experiment. This generator produced lepton–proton events weighted by several different radiative cross section models. Four prescriptions are presented following Mo–Tsai [4] and Maximon–Tjon [5]. The difference in $R_{2\gamma}$ extracted using the four approaches is as much as 1.5% at low ϵ , indicating that the higher-order effects in radiative corrections are significant and depend on the effective cutoff energy. The corrections are driven by the lepton charge odd corrections: soft TPE and the interference of bremsstrahlung of the lepton and proton. For the OLYMPUS kinematics and the detector configuration, the corrections are about 5–6 % at the lowest ϵ values (highest Q^2), and they are about 1–2% at $\epsilon \approx 1$.

The OLYMPUS results for $R_{2\gamma}$ are presented in Fig. 2. Evaluation of the TPE was performed using the Mo–Tsai [4] prescriptions. The ratio $R_{2\gamma}$ was calculated for all the four prescriptions. The difference between the obtained results is included in the correlated uncertainty (*grey band* in Fig. 2).

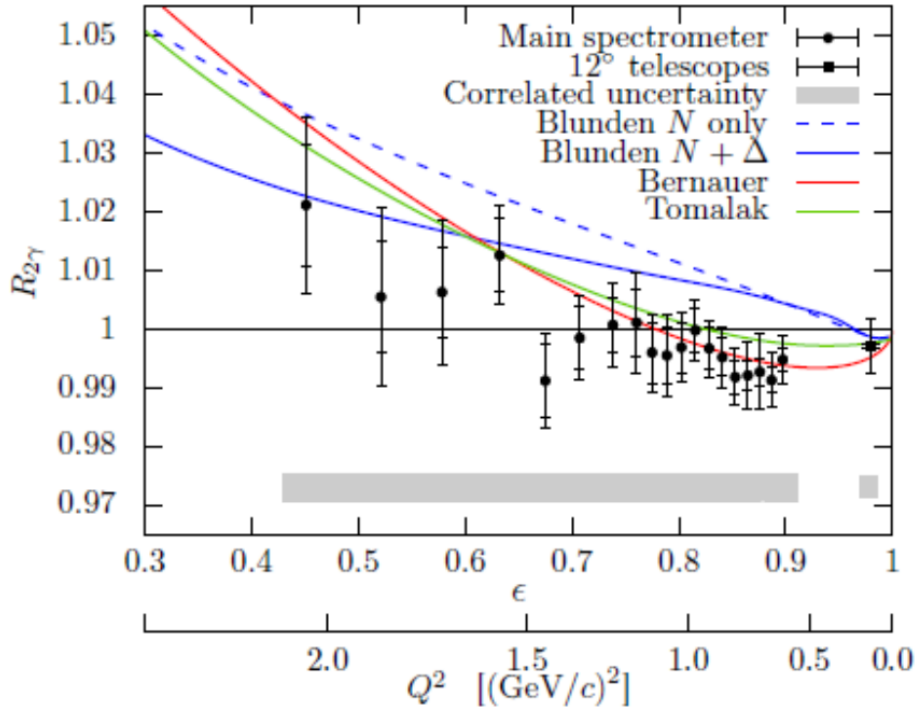


Fig. 2. OLYMPUS result for $R_{2\gamma}$ using the Mo–Tsai [4] prescription for radiative corrections to all orders. The shown uncertainties are statistical (*inner bars*), uncorrelated systematic (added in quadrature, *outer bars*), and correlated systematic (*grey band*). Note that the error in the 12° data point at $\epsilon = 0.978$ is completely dominated by systematic uncertainties

The data shown in Fig. 2 clearly favour a small TPE effect in the explored kinematic domain. The phenomenological prediction of Bernauer suggests that the TPE is causing most of the discrepancy in the form factor ratio in the measured range. One may state that the data practically agree with this prediction (*red curve* in Fig. 2).

The theoretical calculation of Tomalak [7] are similar to the Bernauer prediction. The calculation of Blunden [8] with the nucleon and delta in the intermediate state of the TPE diagrams overshoots the data at all values of Q^2 . To clarify the situation, the size of the TPE at large Q^2 should be determined in future measurements.

A direct comparison of the OLYMPUS data with the results of VEPP-3 [8] and Jefferson Lab [9] is unfortunately not possible as they were obtained in different kinematic domains not overlapping with OLYMPUS. However, the existing sets of data at various Q^2 and ε allow for more theoretical speculations. In order to get conclusive results on the form factor discrepancy, measurements at higher Q^2 -values are urgently needed. A good knowledge of the TPE corrections at small values of Q^2 might be important for determination of the charge proton radius in experiments on electron–proton scattering [10].

References

1. A.J.R. Puckett *et al.*, Phys. Rev. **85**, 045203 (2012).
2. A. Qattan *et al.*, Phys. Rev. Lett. **94**, 142301 (2005).
3. R. Milner *et al.*, Nucl. Instr. Meth. A **741**, 1 (2014).
4. L.W. Mo, Y.-S. Tsai, Rev. Mod. Phys. **41**, 205 (1969).
5. L.C. Maximon, J. A. Tjon, Phys. Rev. C **62**, 054320 (2000).
6. O. Tomalak, M. Vanderhaeghen, Eur. Phys. J. A **51**, 24 (2015).
7. P. Blunden, Priv. Commun. (2016).
8. I.A. Rachek *et al.*, Phys. Rev. Lett. **114**, 062005 (2015).
9. D. Adikaram *et al.*, Phys. Rev. Lett. **114**, 062003 (2015).
10. G. Lee, J.R. Arington, R.J. Hill, Phys. Rev. D **92**, No. 1, 013013 (2015).

The photon tagger analyses the momentum of the Bremsstrahlung electrons by deflecting them in a dipole magnet before detecting them in a hodoscope (Fig. 1, *left panel*). The photon energy is then deduced from the energy conservation, $E_\gamma = E_0 - E$. The photon tagger detects Bremsstrahlung electrons whose energy ranges between 10 and 90% of E_0 with a resolution from 0.16 to 0.62% of E_0 . Figure 1 (*right panel*) shows the time difference between two electrons detected in the same tagger channel. It can be seen that the time resolution of the tagger is about 220 ps, which allows to resolve the 2 ns bunch structure of ELSA. As a consequence, each electron can be assigned to the corresponding bunch. Since the bunch length is known to be equal to 80 ps, the event time is known with a precision of up to 80 ps.

3. The experimental set-up

The BGO–OD detector is formed by coupling the Rugby Ball calorimeter previously used at the GRAAL experiment [5] with the open dipole (OD) magnetic spectrometer. The detector, shown in Fig. 2, can be divided into three parts according to different polar angle coverage. The central part ($155^\circ \leq \theta \leq 25^\circ$) is covered by the Rugby Ball BGO calorimeter, formed by 480 crystals with a photomultiplier tube readout and equipped with sampling analog to digital converters (ADCs). The target (liquid H_2 or D_2 , or solid) sits in the centre of the calorimeter and is surrounded by ancillary detectors (cylindrical multi-wire proportional chambers and scintillator Barrel) for particle tracking and identification. The polar angles between 8 and 25° are covered by a ring of scintillating counters (SciRi) and by multi-gap resistive plate chambers (Daisy) with excellent time resolution. Finally, the forward region is covered by the OD forward spectrometer. Its central part is a 0.45 T large aperture dipole magnet (provided by DESY on permanent loan basis). Tracking is performed by position detectors in front of the magnet (MoMo and Scifi2), both consisting of scintillating fibers, and eight double layer drift chambers (DCs) followed by four ToF scintillating walls behind it. All design of the DCs [6] and of the readout electronics [7] was developed at the PNPI HEPD.

BGO-OD setup

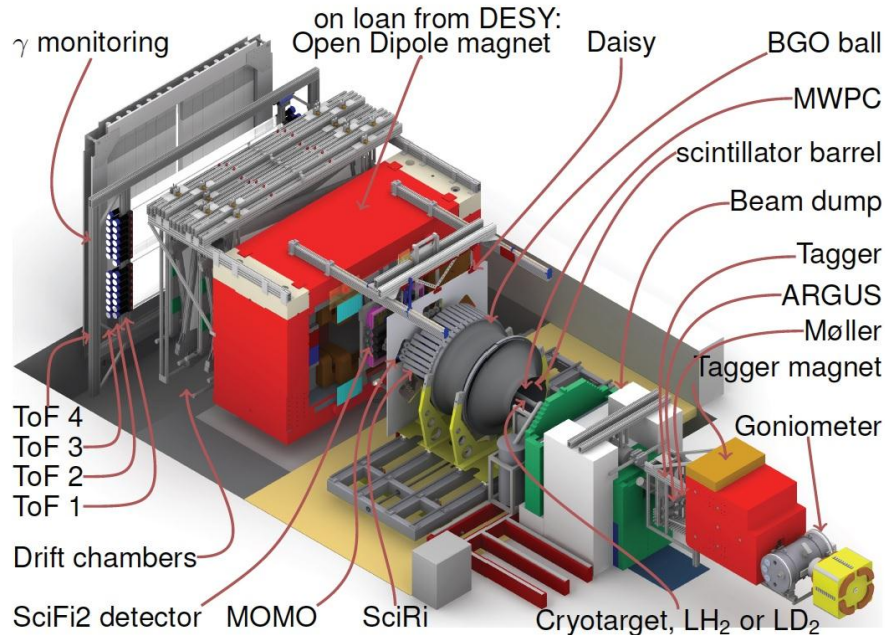


Fig. 2. Schematic view of the BGO–OD experimental set-up. The electron beam enters from the bottom-right corner

The performance of the BGO Rugby Ball is summarized in Fig. 3, where we show the two-photon invariant mass spectrum from a proton target obtained with a kinematical fit and a confidence cut. The π^0 , η , ω , and η' peaks are all clearly visible. The energy calibration is obtained using a ^{22}Na source with the energy peak at 1.275 MeV.

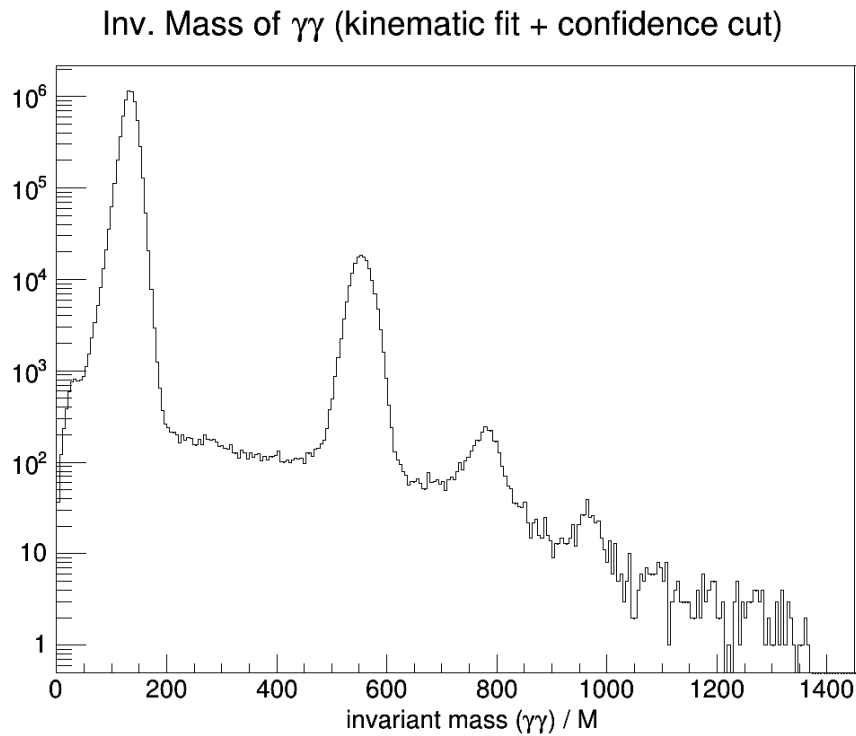


Fig. 3. The two-photon invariant mass from a proton target measured by the Rugby Ball calorimeter

The Rugby Ball can also measure protons [8] and neutrons [9], and by using sampling ADCs with ~ 2 ns time resolution it can also measure K^+ following a method originally developed in Ref. [10]. Positive kaons are stopped within the crystals of the Rugby Ball up to a kinetic energy of approximately 400 MeV. The time resolution allows to distinguish the signal of the stopped K^+ from the signal of the subsequent weak decay $K^+ \rightarrow \mu^+\nu$ (Fig. 4).

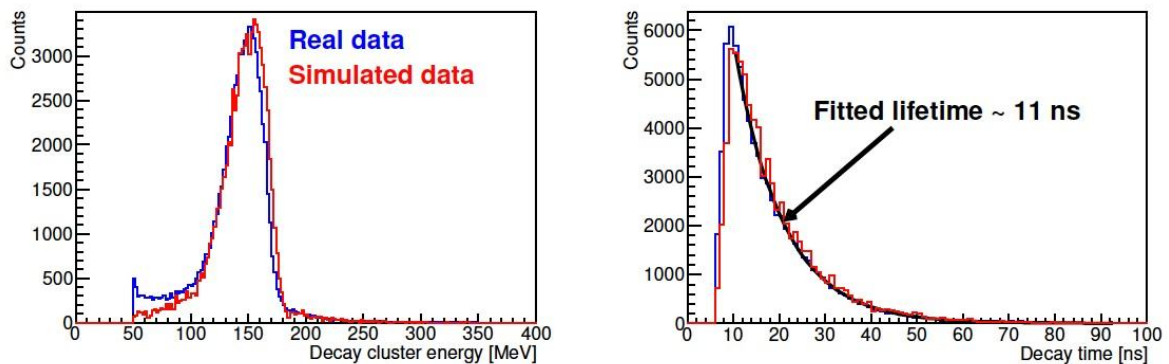


Fig. 4. Energy of the delayed signal from the decay $K^+ \rightarrow \mu^+\nu$; the peak at 153 MeV corresponds to the μ^+ energy deposition from a K^+ decay at rest (left). Reconstructed K^+ lifetime (right)

4. The experimental program

The set-up is ideal for investigation of reactions dominated by t -channel mechanisms due to the acceptance at forward angles with high momentum resolution. The unique combination of excellent calorimetry coupled with high resolution forward tracking is well suited to investigate reaction channels with open strangeness and complicated final states. Strangeness photoproduction off the proton (with final states $K^+\Lambda$, $K^+\Sigma^0$, $K^0\Sigma^+\dots$) will be accessed, and neutral particle identification in the central region helps to determine final states of mixed charge. The cusp-like structure observed by the CBELSA/TAPS Collaboration [11] will be investigated by measuring the differential cross section for the $\gamma p \rightarrow K^0\Sigma^+$ reaction and the beam asymmetry over the K^* threshold region, achieving high statistics by including data of both neutral and charged decays of the K^0 and Σ^+ . The acceptance of the OD forward spectrometer is also ideal to measure data at centre-of-mass angles $\theta_{\text{cm}} \leq 15^\circ$ for K^+Y , where data are scarce and incompatible. The central goal is to disentangle the structure of hyperon excitations, *e. g.*, the $\Lambda(1405)$ or hypothetical Σ^* states of $J^P = 1/2^-$ in the same mass range.

Pseudoscalar and vector meson photoproduction will be studied too, both off the proton and off the neutron, by measuring cross sections and beam asymmetries. Thanks to the high energy resolution for the incoming photon energy provided by the ARGUS hodoscope (see Fig. 2), the beam asymmetry in η photoproduction will be measured at threshold, allowing for a more detailed study of the strong energy dependence observed by the GRAAL Collaboration [5], and at higher energy (up to 1800 MeV) where no experimental data are available yet. The high efficiency of the Rugby Ball for neutron detection will allow the measurements of η and ω off the quasi-free neutron with a liquid D_2 target. Finally, the photoproduction will also be investigated.

5. Preliminary results from the commissioning

Data were taken in 2013 during the commissioning of the detector set-up using both an unpolarized and a linearly polarized photon beam. This section presents an overview of these preliminary results.

Neutral meson reconstruction in the BGO ball. In Figure 5, the invariant mass distribution of two photons in the BGO is shown. The two peaks correspond to the π^0 and the η masses. The energy calibration was based on the 1.27 MeV photons from ^{22}Na sources. The fitted masses are in good agreement with the accepted values. Preliminary measurements of the absolute cross section for π^0 photoproduction off the proton were performed, and the obtained results agree with the SAID partial wave analysis solution within the error limits.

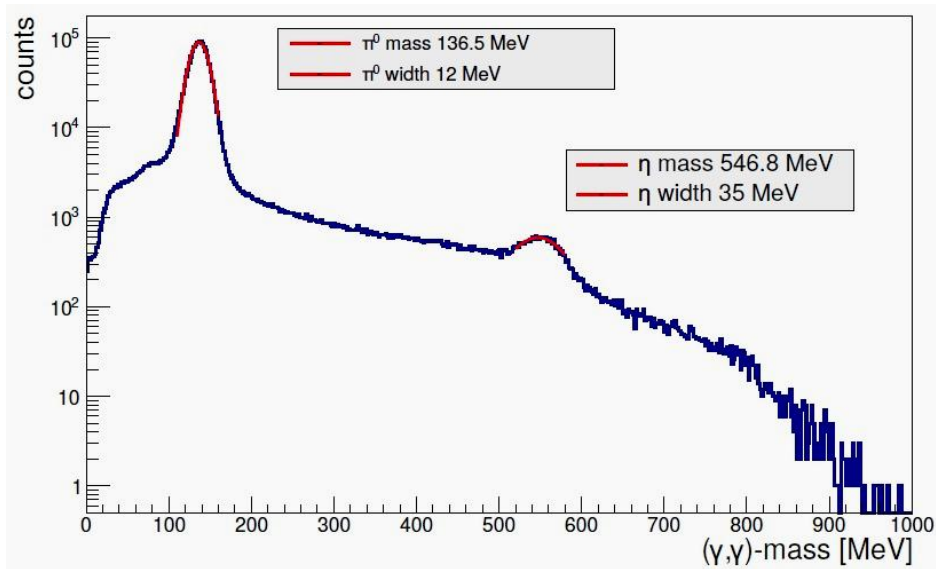


Fig. 5. Invariant mass spectrum of $\gamma\gamma$. Peaks of π^0 and η are visible

First measurements with a linearly polarized photon beam. The use of a diamond radiator produces coherent Bremsstrahlung, resulting in a linearly polarized photon beam if the diamond radiator is properly aligned with respect to the primary electron beam. The alignment is performed through the stonehenge technique [12]. Figure 6 (*left panel*) shows a stonehenge plot of an aligned diamond radiator. Figure 6 (*right panel*) shows an azimuthal distribution of the ratio $N_{\text{pol}}/N_{\text{unpol}}$ in the incoming photon energy range 250–450 MeV.

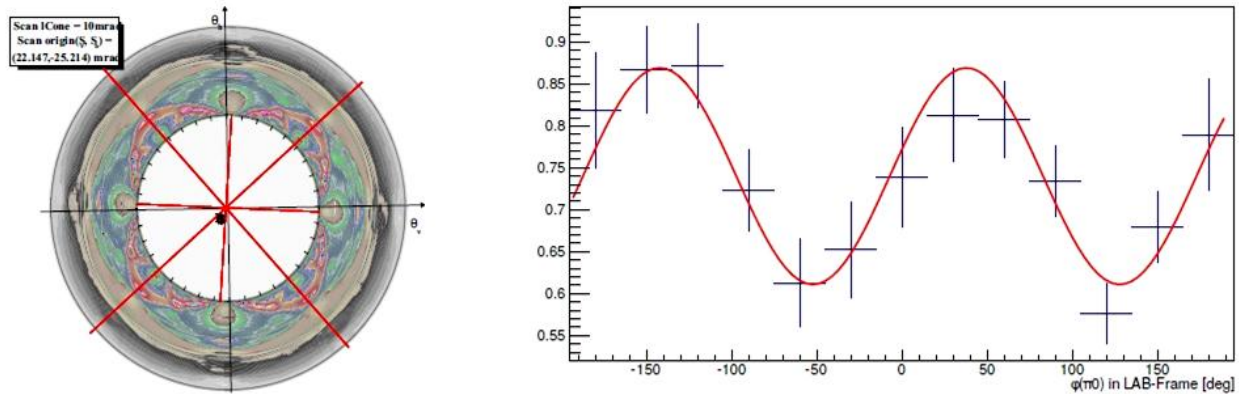


Fig. 6. Stonehenge plot of an already aligned diamond radiator; fourfold symmetry and coherent Bremsstrahlung contribution of the lattice vector are visible (*left*). Azimuthal distribution of the ratio $N_{\text{pol}}/N_{\text{unpol}}$ in the incoming photon energy range 250–400 MeV in the reaction $\gamma p \rightarrow \pi^0 p$: *blue* – data points; *red* – $\cos(2\varphi)$ fit (*right*)

The fourfold symmetry as well as the dominant contribution to the coherent Bremsstrahlung of the lattice vector are visible. Photoproduction of π^0 events is identified, both in the case of a linearly polarized photon beam and for the unpolarized one. The ratio of the number of reconstructed events $N_{\text{pol}}/N_{\text{unpol}}$ is shown in Fig. 6 (*right panel*) for the incoming photon energies $E_\gamma = 250$ –400 MeV as a function of the azimuthal angle φ of the reconstructed π^0 in the laboratory frame. The expected $\cos 2\varphi$ distribution is observed.

Charged particle identification in the forward spectrometer. The magnetic spectrometer is used for charged particle identification for forward angles up to $\theta_{\text{hor}} = 12^\circ$ and $\theta_{\text{vert}} = 8^\circ$. For the momentum reconstruction, a program called GENFIT [13] developed within the PANDA Collaboration is used. The input parameters required by GENFIT are the reconstructed particle tracks, the geometry of the forward spectrometer and the magnetic field of the OD magnet. GENFIT considers multiple scattering and performs automatic energy loss corrections. Presently, a momentum resolution of about 2% has been achieved. This will be improved in the near future using the drift time information from the drift chambers instead of the drift cell hit only. Combining the reconstructed momentum of the detected particles with the time information of the time of flight walls allows charged particles identification by determining the particles velocity. Figure 7 (*left panel*) shows the speed of the charged particles as a function of their momentum. The distributions for π^+ and p are clearly visible.

K^+ identification in the BGO. The K^+ identification in the BGO is performed through the reconstruction of its weak decay $K^+ \rightarrow \mu^+ \nu$. This technique has been already proven and exploited by the A2 Collaboration [10] at MAMI. The missing mass calculated from the K^+ detected in the BGO is shown in Fig. 7 (*right panel*) and both the Λ and the Σ^0 peaks are visible.

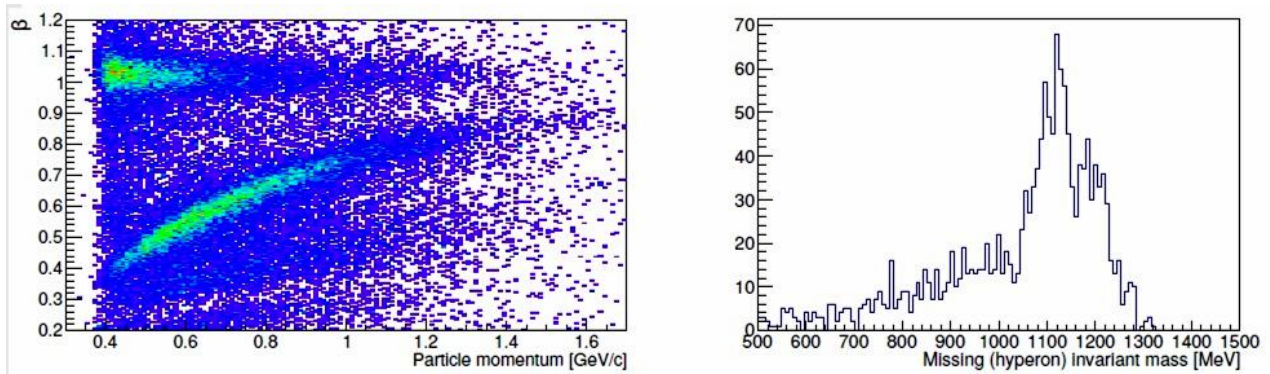


Fig. 7. Speed of charged particles as a function of their momentum; data acquired for the C target (*left*). Missing mass from K^+ detection in the BGO ball (*right*)

6. Conclusion

The BGO–OD experiment is commissioned. The experimental program includes meson photoproduction from proton, deuteron and light nuclei. The BGO–OD experiment is a unique experiment optimized for detection of mixed charged final states. Due to the forward spectrometer, it is well suited for investigation of processes at low momentum transfers. The commissioning is already in an advanced stage but still ongoing. It shows already positive results in neutral and charged meson reconstruction in the BGO ball and the forward spectrometer using an unpolarized and polarized photon beam.

References

1. W. Hillert, *Eur. Phys. J. A* **28**, 139 (2006).
2. P. Levi Sandri *et al.*, *Nucl. Instr. Meth. Phys. Res. A* **370**, 396 (1996).
3. F. Ghio *et al.*, *Nucl. Instr. Meth. Phys. Res. A* **404**, 71 (1996).
4. M. Castoldi *et al.*, *Nucl. Instr. Meth. Phys. Res. A* **403**, 22 (1996).
5. P. Levi Sandri *et al.*, *Eur. Phys. J. A* **51**, 77 (2015).
6. I. Lopatin *et al.*, Production of Drift Chambers and Associated Readout Electronics for the SFB/TR-16/B1 Magnetic Spectrometer. Design Report, PNPI, Gatchina (2008).
7. V. Golovtsov *et al.*, CROS-3B Readout System Drift Chamber Option for RFWU HI. Technical Design, PNPI, Gatchina (25 Nov. 2007).
8. A. Zucchiatti *et al.*, *Nucl. Instr. Meth. A* **321**, 219 (1992).
9. O. Bartalini *et al.*, *Nucl. Instr. Meth. A* **562**, 85 (2006).
10. T.C. Jude, D.I. Glazier, D.P. Watts *et al.*, *Phys. Lett. B* **735**, 112 (2014).
11. R. Ewald *et al.*, *Phys. Lett. B* **713**, 180 (2014).
12. K. Livingston, *Nucl. Instr. Meth. Phys. Res. A* **603**, 205 (2009).
13. C. Hoppner, S. Neubert, B. Ketzer, S. Paul, *Nucl. Instr. Meth. Phys. Res. A* **620**, 518 (2010).

SEARCH FOR NARROW RESONANCES IN πp ELASTIC SCATTERING IN THE EPECUR EXPERIMENT

PNPI participants of the EPECUR experiment:

A.B. Gridnev, V.A. Andreev, N.G. Kozlenko, V.S. Kozlov, A.G. Krivshich, V.A. Kuznetsov,
D.V. Novinsky, V.V. Sumachev, V.I. Tarakanov, V.Yu. Trautman, Ye.A. Filimonov

A major challenge in the domain of hadronic physics is the understanding of states not having the standard qqq structures existing in the traditional constituent quark model. The prediction of an antidecuplet of exotic particles (pentaquarks) within the framework of the chiral soliton model (χ SM) [1] spawned major experimental efforts worldwide. Recently, this interest in pentaquarks has been renewed with the claim of a charmed pentaquark by the LHCb Collaboration [2]. It is an open question whether this newly-discovered state may have its partners at lower masses.

Beginning with the first pentaquark announcement by the LEPS Collaboration [3], there were many reports confirming the observation of the lightest member of the proposed antidecuplet, the $\Theta^+(1538)$ baryon [4]. In 2004, the Particle Data Group (PDG) quoted it as an established three-star particle [5]. Somewhat later, however, most of these results were announced to be statistical fluctuations [4]. Nonetheless, three groups, LEPS [6], DIANA [7], and SVD-2 [8], still insist on this finding. In 2012, a part of the CLAS Collaboration reported a new high-statistics signal which could be associated with the Θ^+ [9]. More recently, however, an experiment at J-PARC found no evidence for this particle [10].

In 2004, a modified SAID partial wave analysis (PWA) of πN scattering data allowed for two P_{11} candidates for the second member of the antidecuplet, the non-strange pentaquark, with masses near 1.68 and 1.73 GeV [11]. To be compatible with the data existing at that time, these candidate states were required to be very narrow and to have a small branching to πN . In this context, the observation of a narrow enhancement at $W \approx 1.68$ GeV in η photoproduction on the neutron (the so-called “neutron anomaly”) appeared to be an important piece of the puzzle. The effect was first observed at GRAAL [12] and then confirmed by the LNS [13], CBELSA/TAPS [14, 15], and A2@MAMI [16] Collaborations. This structure was not seen in the previous measurements of η photoproduction on the proton [17]. Recent precise measurements of the cross section for this reaction at A2@MAMI-C have revealed a narrow dip at the same energy [18]. A narrow resonance-like structure at $W \approx 1.685$ GeV was also observed in the $\gamma p \rightarrow \eta p$ beam asymmetry data from GRAAL [19]. A narrow peak at this energy was found in Compton scattering on the neutron $\gamma n \rightarrow \gamma n$ [20], while neither peak was seen in the $\gamma n \rightarrow \pi^0 n$ cross section [21].

This whole assembly of experimental findings has generated a number of explanations. In line with the pentaquark hypothesis, these may signal a nucleon resonance with unusual properties: a mass $M \approx 1.68$ GeV, a narrow ($\Gamma \leq 25$ MeV) width, strong photoexcitation on the neutron, and a suppressed decay to πN final state [11, 22–25]. The properties of this putative resonance coincide surprisingly well with those expected for the second member of the antidecuplet, the non-strange P_{11} pentaquark [26, 27]. However, contradictory explanations also exist, with several groups explaining the bump in the $\gamma n \rightarrow \eta n$ cross section in terms of

- 1) the interference of well-known and broader resonances [28] or
- 2) the sub-threshold $K\Lambda$ and $K\Sigma$ production (cusp effect) [29].

Therefore, it is of interest to reexamine this problem using elastic πN scattering data.

Much of our knowledge of the baryon resonances was obtained through the analysis of πN scattering. In general, theory predicts only weak couplings of pentaquark states to the elastic πN channel. Therefore, experimental data should be of very high precision. On the other hand, the analysis of such data would have some advantages:

1. The structure of πN amplitude is essentially simpler than that of photoproduction.
2. The πN partial waves are quite well known from phase shift analyses.
3. There is an isospin symmetry in the πN system.

In the years from 2005 to 2013, the EPECUR Collaboration measured $\pi^\pm p \rightarrow \pi^\pm p$ elastic scattering over an energy range of $p_{\text{lab}} = 800\text{--}1300$ MeV/ c and for angles θ_{cm} from 40 to 120° [30]. In total, about

10 000 new data points were obtained. These data have been produced with a momentum resolution of ~ 1 MeV and with $\sim 1\%$ statistical errors.

The $\pi^-p \rightarrow \pi^-p$ data revealed two narrow structures, at $W \approx 1.686$ and at $W \approx 1.720$ GeV, which were not seen in π^+p scattering [31]. This clearly shows that the observed structures appear in the isospin $I = 1/2$ sector only. It is interesting to note that a structure at $W \approx 1.720$ GeV was also recently found in Compton scattering off the proton [32] and η photoproduction off the neutron [33].

In Ref. [31], a preliminary analysis of the data from work [30] was presented, with the finding that these structures could be described by two narrow (with the width of ~ 25 MeV) S_{11} and P_{11} resonances. In this paper, an analysis of the full EPECUR database [30] is presented. Here we attempt to explain the observed structures in terms of both couplings to inelastic channels and resonance contributions. For that purpose, we employ a K -matrix approach based on the effective Lagrangians described in Refs. [34, 35] and applied to both πN scattering and photoproduction in Ref. [36].

It is assumed that the K matrix, as a solution to equations yielding the scattering amplitude, can be described in terms of a sum of the tree-level Feynman diagrams with vertices obtained from an effective Lagrangian. The model includes four-star PDG [37] resonances in the s and u channels and σ , ρ , a_0 , and K^* exchange in the t channel. To describe the high energy tail in π^+p data, the three-star $P_{33}(1900)$ resonance was also included. Two new isospin-1/2 resonances were added, as well, to reproduce the observed structures in the π^-p data, as we describe below. In total, the five-channel analysis took into account elastic, 2π (effective), ηn , $K\Lambda$, and $K\Sigma$ production.

As the main goal of this work was to explore the nature of narrow structures in π^-p elastic scattering, a detailed description of inelastic channels was not attempted. This reduced the number of free parameters, resonance masses and couplings, used in the fits. The employed database included the EPECUR data, the total cross-sections for $\pi^-p \rightarrow \eta n$ [38], and the data for the differential cross sections for $\pi^-p \rightarrow K\Lambda$ and $\pi^-p \rightarrow K\Sigma$ [39]. To achieve the consistency with the data on elastic πN scattering at the energies below the EPECUR data, single-energy solutions from the XP15 [30] PWA were added to the data base (Fig. 1).

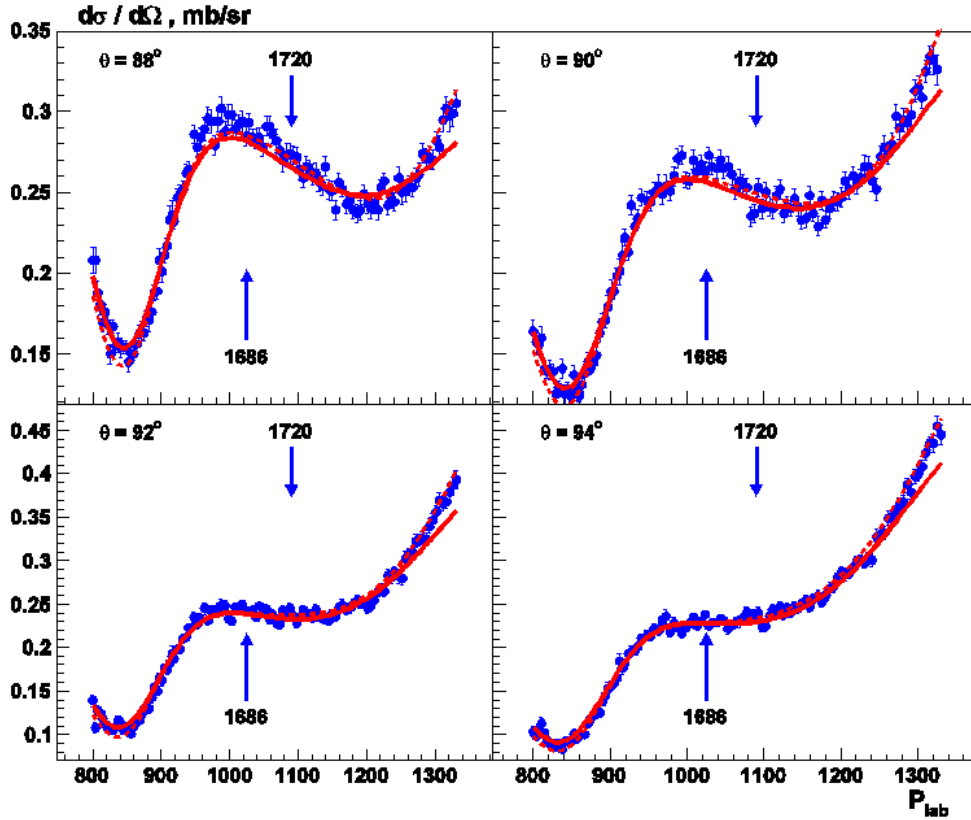


Fig. 1. π^+p elastic scattering. The *solid lines* correspond to the present calculations; the *dotted lines* indicate the XP15 solution

The *XP15* solution was the result of the SAID PWA which included the EPECUR data. This provided a rather good description of the whole data set getting a $\chi^2 \approx 3$ per point. However, a description of the above mentioned sharp structures was absent.

This is clear from Fig. 2, in which the dotted lines correspond to the *XP15* solution. The results of our calculations without any narrow resonances are shown in this figure by the solid lines. It should be noted that the *XP15* parameterization included the inelastic channels $\pi\Delta$, ρN , and ηN , but no $K\Lambda$ or $K\Sigma$ channels.

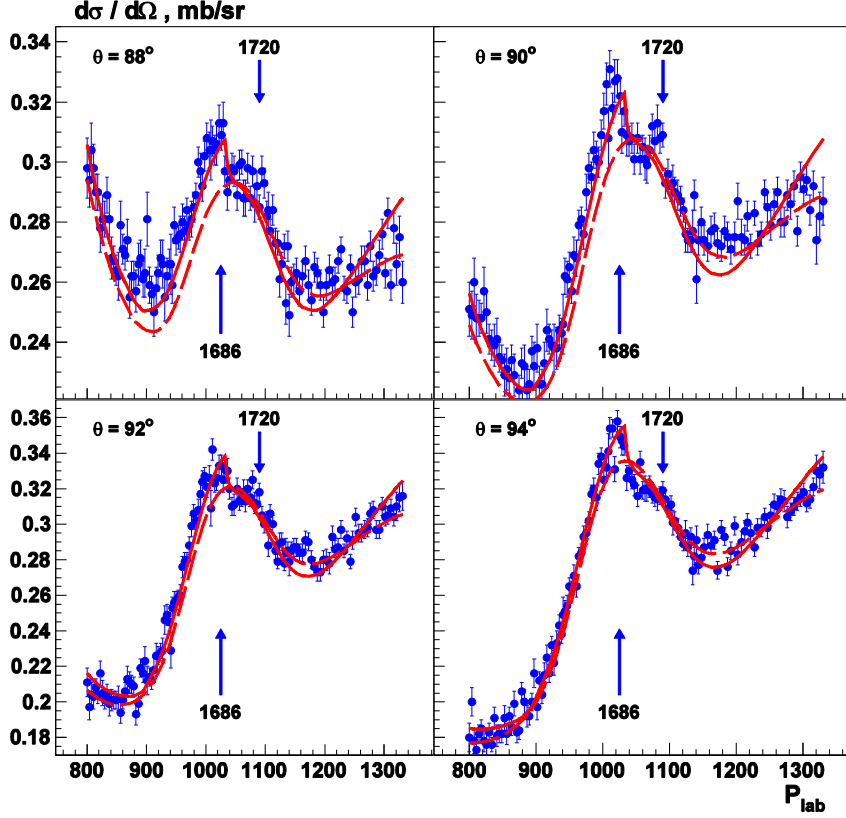


Fig. 2. π^-p elastic scattering. The *solid lines* correspond to the present calculations; the *dotted lines* are the *XP15* solution

Without the inclusion of narrow resonances, the solid lines in Fig. 2 reproduce the rapid variation of the energy dependence seen in the π^-p differential cross section close to the $\pi^-p \rightarrow K\Sigma$ threshold at the angles $\sim 90^\circ$. Such an effect is not seen in the π^+p data. A qualitative explanation of this phenomenon is evident in Fig. 3, in which the energy dependence of the total $\pi p \rightarrow K\Sigma$ cross section for different charged states is shown. One can see that the $\pi^-p \rightarrow K^0\Sigma^0$ and $\pi^-p \rightarrow K^+\Sigma^-$ plots vary rapidly near the threshold $W \approx 1690$ GeV, while the energy dependence of the $\pi^+p \rightarrow K^+\Sigma^+$ reaction is more smooth, and therefore does not generate sharp structures in the π^+p scattering data. Our results for the $\pi p \rightarrow K\Sigma$ total cross section are shown in Fig. 3 by solid lines. The present calculation reproduces these data quite well.

As a next step, two resonances were added in an attempt to improve the fit quality around 90° . Here, the overall χ^2 per datum is not a good parameter to estimate the quality of the fit, as the structure is evident in only ~ 200 data points among 5 000 in total. Thus, the overall χ^2 would be overwhelmed by the quality of the fit to the background behaviour. To compare different fits with additional resonances, χ^2 in the restricted energy interval of $p_{\text{lab}} = 980\text{--}1140$ MeV/c was calculated.

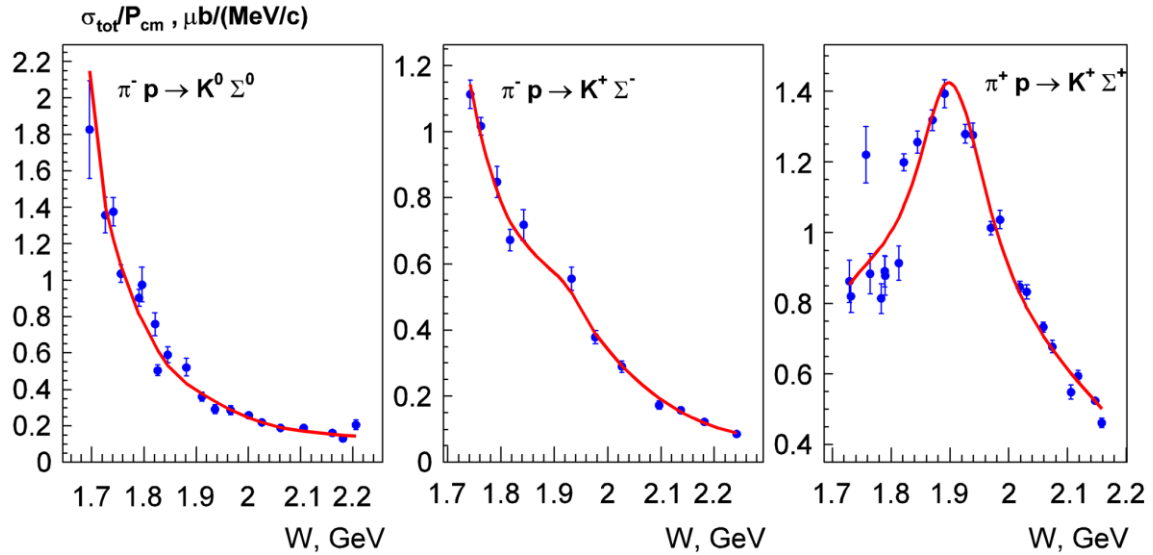


Fig. 3. The total cross section for $\pi p \rightarrow K\Sigma$. The data are from Ref. [39]; the *solid lines* are from the present work

While different quantum numbers for the added resonances were tested, only S_{11} for the first resonance and P_{11} for the second one gave a reasonable χ^2 . The inclusion of these resonances lead to a significant improvement of $\chi^2 \approx 1.5$ as compared with $\chi^2 \approx 2.6$ for the background. The results are shown in Fig. 4 and Table. Both resonances have small widths and small couplings to the elastic πN channel. This is consistent with the predicted properties of the non-strange pentaquark state, the second member of the antidecuplet.

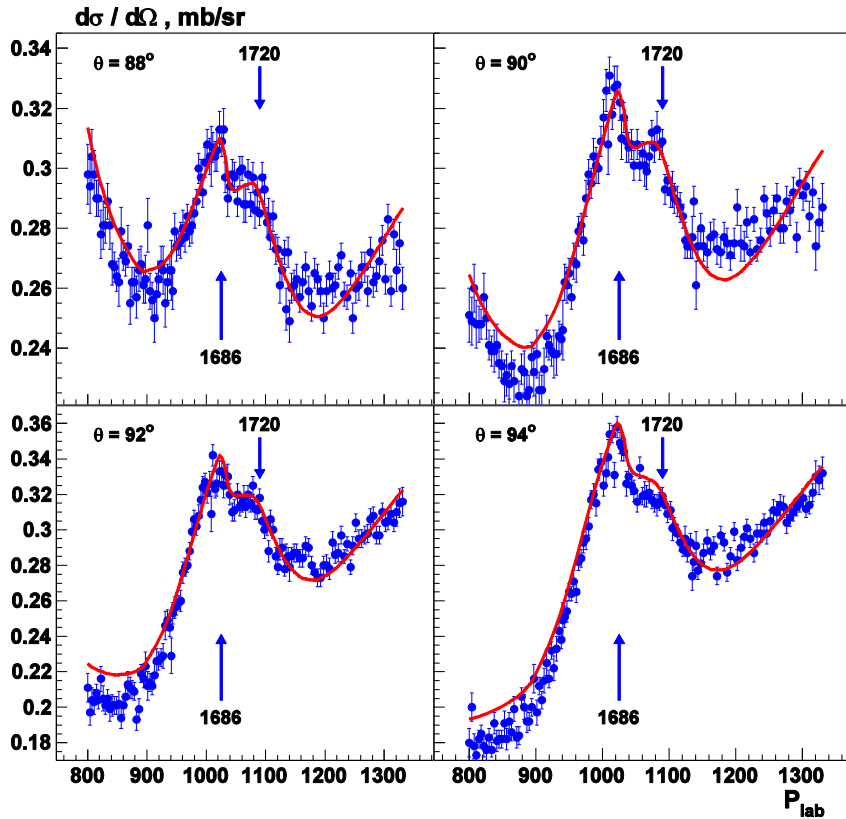


Fig. 4. $\pi^- p$ elastic scattering with the added resonances. The *solid line* corresponds to the present calculation

Table

Resonance parameters

Parameter	S_{11} , MeV	P_{11} , MeV
Mass	1 688	1 724
Γ_{el}	5.0	8.5
$\Gamma_{\eta n}$	2.3	19.8
$\Gamma_{2\pi}$	0.3	7.1
$\Gamma_{K\Lambda}$	10.0	4.8
$\Gamma_{K\Sigma}$	–	4.0
Γ_{tot}	17.6	44.2

Having concentrated on the structure in πN scattering, it is important to see how the added resonances would appear in inelastic channels. In Figure 5, the total cross section for $\pi^- p \rightarrow \eta n$ is presented.

One may see that the data are not in conflict with the resonance contributions, but at the same time they do not prove the existence of the resonances. The dotted line in Fig. 5 gives the S -wave contribution to $\pi^- p \rightarrow \eta n$. As was shown in Ref. [35], the minimum of the S -wave contribution near $p_{lab} \approx 1050$ MeV/c could be explained by interference of the $S_{11}(1535)$ and $S_{11}(1650)$ resonances. Different signs for the coupling constants of the η meson with these resonances were found, in agreement with work [28]. But opposite to these works, the interference does not produce any sharp peak in the $\pi^- p \rightarrow \eta n$ reaction. Moreover, a very small (1%) branching ratio of the $S_{11}(1650)$ resonance to ηn has been found in the present work.

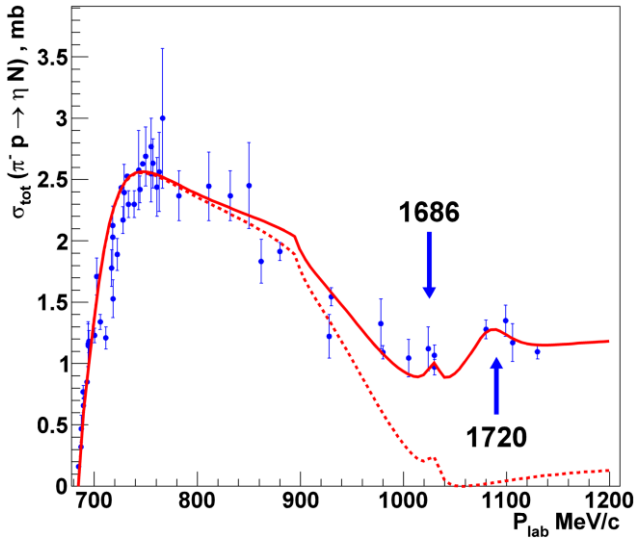


Fig. 5. Comparison of the measured and calculated $\pi p \rightarrow \eta n$ total cross sections. The *solid line* presents the calculations of this work; the *dotted line* indicates the S -wave contribution

We conclude that the two narrow structures observed in elastic $\pi^- p$ scattering can be explained by a combination of threshold effects and two narrow resonances $S_{11}(1686)$ and $P_{11}(1720)$. These contributions are discussed separately below.

Concerning the narrow resonance contributions, narrow structures are also seen in Compton scattering [20] and η photoproduction off the neutron [16]. What is the nature of these structures? The interference of well-known resonances suggests a delicate relation between incoming and outgoing vertexes. It is unlikely that this relation is valid for all three reactions, namely $\pi^- p$ scattering, Compton scattering and η photoproduction. Further work is required before a definitive conclusion can be drawn concerning this possibility.

Another contribution is available *via* the cusp effect, *i. e.* the influence of the closed channels on the incoming amplitude due to the analyticity condition. This element requires further development and remains a hypothesis which requires further detailed verification. It is worth noting that not all threshold

effects result in sizeable cusp effects. For instance, no clear structure is seen in π^-p elastic scattering near the $K\Lambda$ threshold ($p_{\text{lab}} = 900 \text{ MeV}/c$). Finally, in the energy region around 1686 MeV, possible electromagnetic effects must be taken into consideration. Indeed, just below the $K\Sigma$ threshold, a bound atomic-like state of $K^+\Sigma^-$ could be formed. If it exists, this state could in fact be seen in the π^-p and γn reactions only. The existence of these electromagnetic effects could be checked, for example, by measuring the cross sections for two isospin-symmetric reactions $\pi^-p \rightarrow \eta n$ and $\pi^+n \rightarrow \eta p$. Accordingly, the isospin symmetry cross-sections for the reactions should be the same, but the $K^+\Sigma^-$ system would exist for the first reaction only. No such effect exists for a narrow $P_{11}(1724)$, and we consider this resonance which has the nucleon quantum numbers to be the best candidate for the non-strange member of the exotic antidecuplet. New high precision experimental data on $\pi^-p \rightarrow K\Lambda$ and $\pi^-p \rightarrow \eta n$ are needed to achieve a decisive conclusion.

References

1. D. Diakonov, V. Petrov, M. Polyakov, *Z. Phys. A* **359**, 305 (1997).
2. LHCb Collaboration, arXiv:1507.03414 [hep-ex].
3. T. Nakano *et al.*, *Phys. Rev. Lett.* **91**, 012002 (2003).
4. H. Hicks, *Eur. Phys. J. H* **37**, 1 (2012).
5. Particle Data Group, S. Eidelman *et al.*, *Phys. Lett. B* **592**, 1 (2004).
6. T. Nakano *et al.*, *Nucl. Phys. A* **835**, 254 (2010).
7. V. Barmin *et al.*, *Phys. Rev. C* **89**, 045204 (2014).
8. A. Aleev *et al.*, arXiv:0803.3313 [hep-ex].
9. M. Amaryan *et al.*, *Phys. Rev. C* **85**, 035209 (2012).
10. T.N. Takahashi *et al.*, *JPS Conf. Proc.* **8**, 022011 (2015).
11. A. Arndt, Ya.I. Azimov, M.V. Polyakov *et al.*, *Phys. Rev. C* **69**, 035208 (2004).
12. V. Kuznetsov *et al.*, *Phys. Lett. B* **647**, 23 (2007).
13. F. Miyahara *et al.*, *Prog. Theor. Phys. Suppl.* **168**, 90 (2007).
14. I. Jaegle *et al.*, *Phys. Rev. Lett.* **100**, 252002 (2008).
15. I. Jaegle *et al.*, *Eur. Phys. J. A* **47**, 89 (2011).
16. D. Werthmuller *et al.*, *Phys. Rev. C* **90**, 015205 (2014).
17. GRAAL Collaboration, F. Renard *et al.*, *Phys. Lett. B* **528**, (2002) 215.
18. E.F. McNicoll *et al.*, *Phys. Rev. C* **82**, 035208 (2010).
19. V. Kuznetsov, M.V. Polyakov, *JETP Lett.* **88**, 347 (2008).
20. V. Kuznetsov *et al.*, *Phys. Rev. C* **83**, 022201 (2011).
21. M. Dieterle *et al.*, *Phys. Rev. Lett.* **112**, 142001 (2014).
22. Y.I. Azimov, V. Kuznetsov, M.V. Polyakov, I. Strakovsky, *Eur. Phys. J. A* **25**, 325 (2005).
23. A. Fix, L. Tiator, M.V. Polyakov, *Eur. Phys. J. A* **32**, 311 (2007).
24. V. Kuznetsov *et al.*, *JETP Lett.* **106**, 639 (2017).
25. T. Mart, *Phys. Rev. D* **83**, 094015 (2011).
26. M.V. Polyakov, A. Rathke, *Eur. Phys. J. A* **18**, 691 (2003).
27. D. Diakonov, V. Petrov, *Phys. Rev. D* **69**, 094011 (2004).
28. M. Doring, K. Nakayama, *Phys. Lett. B* **683**, 145 (2010).
29. D. Werthmuller, L. Witthauer, D.I. Glazier, B. Krusche, *Phys. Rev. C* **92**, 069801 (2015).
30. I. Alekseev *et al.*, *Phys. Rev. C* **91**, 025205 (2015).
31. A. Gridnev (for EPECUR Collaboration), *PoS Hadron 2013*, 099 (2013).
32. P.F.A. Goudsmit *et al.*, *Nucl. Phys. A* **575**, 673 (1994).
33. Particle Data Group, K.A. Olive *et al.*, *Chin. Phys. C* **38**, 090001 (2014).
34. A.B. Gridnev, N.G. Kozlenko, *Eur. Phys. J. A* **4**, 187 (1999).
35. Particle Data Group, K.A. Olive *et al.*, *Chin. Phys. C* **38**, 090001 (2014).
36. T. Feuster, U. Mosel, *Phys. Rev. C* **59**, 460 (1999).
37. R.A. Arndt *et al.*, *Phys. Rev. C* **69**, 035213 (2004).
38. R.D. Baker *et al.*, *Nucl. Phys. B* **145**, 402 (1978).
39. R.D. Baker *et al.*, *Nucl. Phys. B* **141**, 29 (1978).

MEASUREMENTS OF THE DOUBLE POLARIZATION OBSERVABLES AT A NEUTRAL MESONS PHOTOPRODUCTION IN THE CRYSTAL BARREL EXPERIMENT

PNPI participants of the CB@ELSA Collaboration:

D.E. Bayadilov, Yu.A. Beloglazov, A.B. Gridnev, I.V. Lopatin, D.V. Novinsky, V.V. Sumachev

1. Introduction

Twenty years ago and earlier the experimental base was mostly restricted to pion and kaon induced reactions. However, a significant number of excited states was suspected to have a strongly disfavoured πN coupling [1]. Thus, the baryon resonances photoproduction provided an alternative tool to study nucleon states. The existing facilities at ELSA in Bonn, CLAS at Jefferson Lab, MAMI-C at Mainz and GRAAL at Grenoble (recently) offer possibilities to investigate photoproduction at $E_\gamma > 1$ GeV and to obtain experimental data above the first and second resonance region.

Unambiguous solutions of partial wave analyses (PWA) are generally only possible on the basis of “complete” experiments with regard to the separation of reaction amplitudes. Such experiments depend on linearly and circularly polarized photon beams. The measurement of double polarization observables, inescapable for the “complete” experiment, requires polarized nucleon targets in addition. Eventually, the recoil nucleon polarization needs to be determined as well.

The understanding of the reaction mechanisms is a prerequisite for PWA or dynamical models to disentangle broad and overlapping states. Different final states and concurring (coupled) channels need to be investigated, as well as proton and neutron targets. In addition to polarization, full coverage of the angular and energy range is also essential. Thus, the combination of the Crystal Barrel (CB) [2] and TAPS [3] detectors to form an almost 4π array at the Bonn electron stretcher accelerator ELSA [4] provides an ideal tool for the sketched investigations.

2. Cross section and polarization observables

With the polarized beam and target, in the simplest case of photoproduction of single pseudoscalar mesons the cross section can be written in the form [5]:

$$\begin{aligned} \frac{d\sigma}{d\Omega} = \frac{d\sigma_0}{d\Omega} [1 - P_{\text{lin}}\Sigma \cos 2\Phi + P_x(-P_{\text{lin}}H \sin 2\Phi + P_{\text{circ}}F) - \\ - P_y(-T + P_{\text{lin}}P \cos 2\Phi) - P_z(-P_{\text{lin}}G \sin 2\Phi + P_{\text{circ}}E)], \end{aligned} \quad (1)$$

where σ_0 denotes the unpolarized cross section; $P_{\text{lin}}, P_{\text{circ}}$ – the degree of linear or circular polarization of the incident photon beam, respectively; Φ – the azimuthal orientation of the reaction plane with respect to the plane of linear polarization. The photon direction defines the z axis of a right-handed coordinate frame spanned with the outgoing meson momentum \mathbf{k}_m , *i. e.*, $\mathbf{z} = \mathbf{k}_\gamma/|\mathbf{k}_\gamma|$, $\mathbf{y} = \mathbf{k}_m/|\mathbf{k}_m|$, and $\mathbf{x} = \mathbf{z} \times \mathbf{y}$. P_x, P_y, P_z are the Cartesian components of the target polarization vector in this frame. Once the beam and/or the target are polarized, the polarization observables Σ, H, F, T, P, G , and E are accessible. In particular, Table presents the combinations of beam and target polarizations required for the double polarization measurements.

The polarization observables are the ratios of structure functions and as such are related to the more general case of meson electroproduction. In contrast to a photoproduction experiment, where photon energy and momentum are interrelated, the virtual photon in electroproduction offers the possibility of an independent variation of photon energy and momentum, leading to information on the spatial structure of the hadronic system in addition to the time structure which can be obtained through the spectroscopic information with real photons [6]. If instead of or in addition to target polarization the measurement of nucleon recoil polarization is provided, further double and triple polarization observables can be defined, which are discussed in detail in Ref. [5].

In the sense of the “complete” experiment mentioned in the introduction, it is necessary to determine angular distributions of at least eight quantities. Those must encompass the differential cross section and the single polarization observables Σ and T , as well as the recoil polarization. Furthermore, four double polarization, *i. e.*, beam-target, observables need to be chosen such that the occurrence of discrete ambiguities can be avoided in the analysis of the bilinear forms of the reaction amplitudes [7].

Table
The combinations of beam and target polarizations
required for the double polarization measurements

Observable	Beam	Target
Σ	Linear	–
T	–	Transverse
H	Linear	
F	Circular	
P	Linear	
G	Linear	Longitudinal
E	Circular	

The situation becomes more complicated in the photoproduction of double pseudoscalar [8] and vector mesons. Despite the infeasibility of “complete” experiments with the current techniques in such cases, essential information on the involved reaction mechanisms, in particular on the role of *s*-channel resonances, can be expected from the investigation of single and double polarization observables.

3. Experimental set-up

The experiments are performed at the tagged photon beam of ELSA [4]. Electron beams up to $E_0 = 3.5$ GeV are used to produce unpolarized or polarized bremsstrahlung [9]. Electrons which radiated a photon are momentum analysed by a magnetic dipole tagging spectrometer, thus enabling to assign for each event the photon energy in the range $E = (0.18 \pm 0.92) \cdot E_0$. Photon fluxes of about $2 \cdot 10^7 \text{ s}^{-1}$ are generally used.

Linearly-polarized photons were produced by coherent bremsstrahlung off a diamond crystal [10]. Additional data with an amorphous radiator were taken in order to determine the coherent contributions. The coherent spectrum was extracted by dividing the spectra of the diamond crystal by the amorphous ones. The circularly polarized photons were generated from longitudinally polarized electrons *via* incoherent bremsstrahlung on a thin radiator foil (20 μm Vacoflux 50). The radiator foil was magnetized and allowed for constant monitoring of the electron polarization during data taking with the help of Møller scattering. The electrons polarization was in the range $P_e = 60\text{--}65\%$ and was determined with an uncertainty of 2% [11].

The detector set-up is shown in Fig. 1. The photon beam hits the polarized hydrogen or deuterium target. The polarized target with the “frozen spin” butanol ($\text{C}_4\text{H}_9\text{OH}$) or deuterated butanol ($\text{C}_4\text{D}_9\text{OD}$) [11] was contained within a horizontal $^3\text{He}\text{--}^4\text{He}$ dilution refrigerator. The protons (deuterons) were dynamically polarized in a high magnetic field typically up to 80 or 60%, respectively. The target polarization was measured by a nuclear magnetic resonance (NMR) system with a precision of 1.5–5%. The target was located at the centre of the detector system consisting of two calorimeters (CB and MiniTAPS), which covered the full azimuthal range and a polar angular range from 1 to 156° with respect to the photon beam axis.

A three layer scintillating fiber detector [12], which surrounded the target within the polar angular range from $15\text{--}165^\circ$, was used to determine a point-coordinate for charged particles. Both, charged particles and photons, were detected in the CB detector [13]. Its 1290 individual CsI(Tl) crystals were cylindrically arranged around the target in 23 rings, covering a polar angular range of $30\text{--}168^\circ$. The forward crystals were covered by plastic scintillators, earlier produced at HEPD of PNPI, in front of each crystal to identify charged particles. For photons an energy resolution of $\sigma_{E\gamma}/E\gamma = 2.5\%/\sqrt[4]{E\gamma (\text{GeV})}$ and an angular

resolution of $\sigma_{\theta, \phi} \cong 1.1^\circ$ were obtained. At the end of the photon beam line, a gamma intensity monitor measured the photon flux. Additionally, a thin conversion target with multiple scintillating detectors was used, counting a known fraction of the total flux by exploiting Compton scattering and pair production.

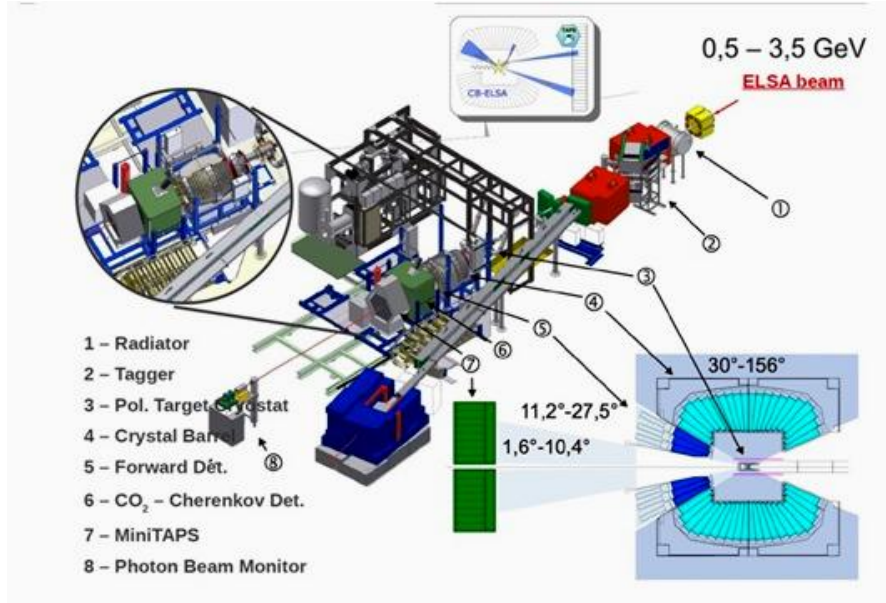


Fig. 1. Set-up of the detector system as described in the text. The photon beam enters from the right up corner

4. Recent results

4.1. η photoproduction off the proton

The η photoproduction is a predestined channel to look for possible resonances with small π - N coupling which might have escaped experimental detection to date. Due to its isoscalarity, the η meson only connects N^* as opposed to Δ^* resonances with the nucleon ground state, which simplifies the observed spectrum considerably beyond the $S_{11}(1535)$ state. The strategy to investigate this at ELSA was threefold. First, differential cross sections were determined over the full angular range across the full nucleon resonance region. Second, as a first step towards the “complete” experiment the photon beam asymmetry was measured at the high-energy tail of the S_{11} resonance and third, “neutron” (deuterium) targets were used in the investigations (see section 4.2 in this paper). The measurement of the reaction $\vec{\gamma}\vec{p} \rightarrow \pi^0 p$ requires linearly-polarized photons and longitudinally-polarized protons. A part of the data was presented earlier in Ref. [14]. In Ref. [15] a detailed account of the extraction of the beam asymmetry Σ and of the double-polarization observable G was given. The resulting asymmetry Σ_B for the full energy range from $E_\gamma = 617$ MeV up to 1325 MeV was compared to the previous measurement of Σ on free protons by the GRAAL Collaboration [16]. A good overall consistency demonstrates that the influence of nucleons bound in nuclei can be controlled.

The cross section for photoproduction of pseudoscalar mesons using linearly-polarized photons on longitudinally-polarized protons can be written as

$$\frac{d\sigma}{d\Omega} = \frac{d\sigma_0}{d\Omega} (1 - P_{\text{lin}}\Sigma \cos 2\varphi_\pi + P_{\text{lin}}P_T G \sin 2\varphi_\pi) \quad (2)$$

with the unpolarized cross section $\frac{d\sigma_0}{d\Omega}$ and the degree of photon (P_{lin}) and proton (P_T) polarization. Two polarization observables, the single-polarization observable Σ , called the beam asymmetry, and the double-polarization observable G , become accessible. To obtain the parameter G , an experiment on a carbon target was needed, which allowed to extract the angle-dependent dilution factor [15].

The data in Fig. 2 are compared with predictions from different PWA models published earlier than the obtained data: with BnGa 2011-02 [17], MAID-2007 [18], JüBo 2013-01 [19], and SAID CM12 [20]. The comparison reveals that at lower energies, the MAID and BnGa analyses can describe the data well, while for the SAID results, a deviation at $\cos\theta \geq 0.4$ becomes apparent. The predictions of JüBo show a similar disagreement as SAID for the two lowest photon energy bins. The largest deviations between the different models can be observed in the higher energy bins ($E > 1\,150$ MeV). These differences most likely occur since the resonance contributions in the fourth resonance region are not well known.

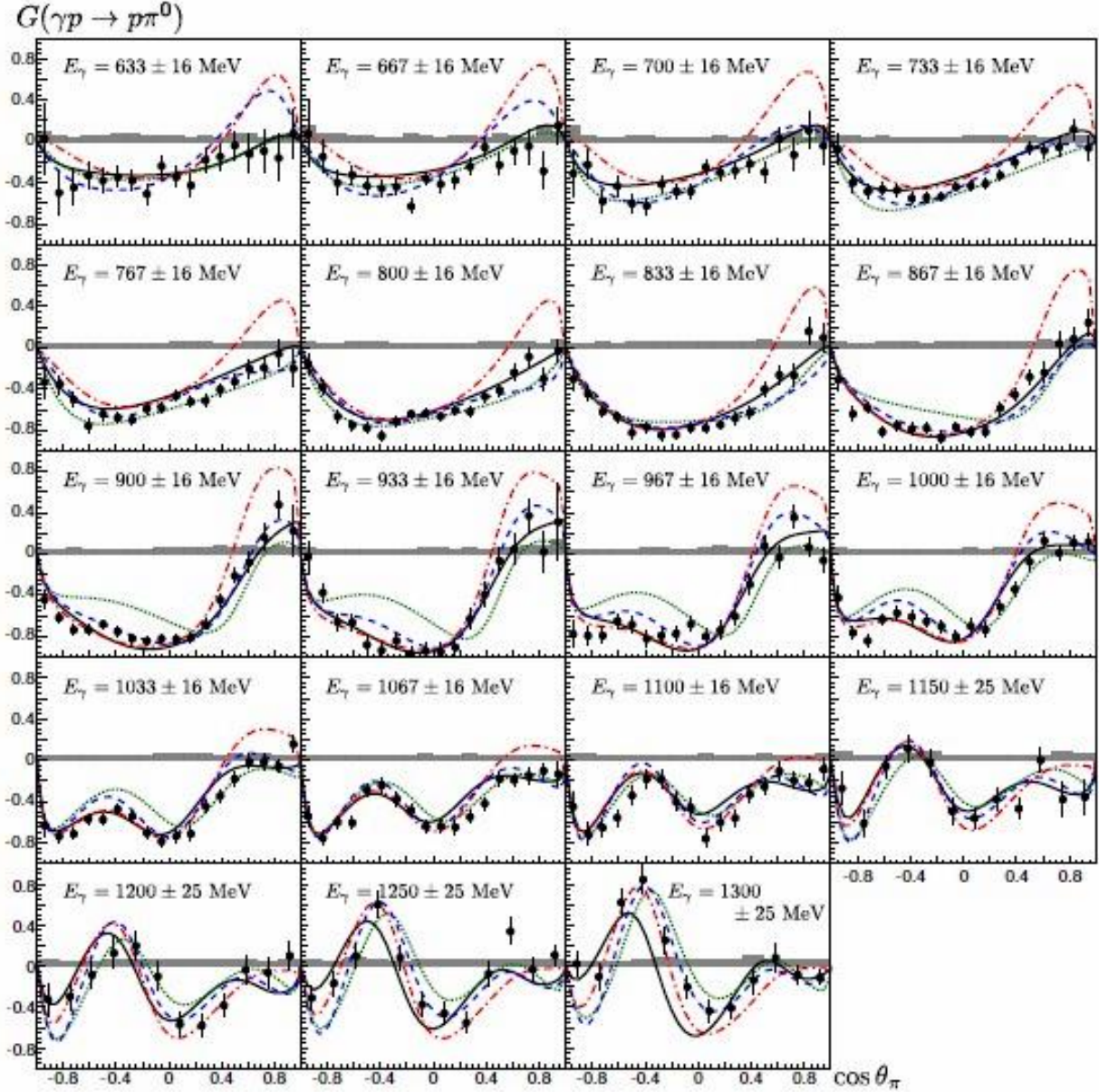


Fig. 2. The double-polarization observable G for all measured photon energies (black dots), compared to PWA predictions: MAID-2007 (green dotted line), SAID CM12 (red dashed-dotted line), JüBo 2013-01 (blue dashed line), and BnGa 2011-02 (black solid line)

4.2. η photoproduction off the neutron

Off the neutron, η -photoproduction had attracted a lot of activity recently. The reason is a rather narrow structure which seemed to exhibit itself in the cross section. Photoproduction of η mesons is a selective reaction due to the isoscalar nature of this meson. Only N^* resonances can decay to the nucleon ground state via η emission, *i. e.*, higher lying Δ states can emit η mesons in decays to $\Delta(1232)\eta$ resulting in an $N\eta\pi$ final state [21].

The double polarization observable E for the reactions $\gamma p \rightarrow \eta p$ and $\gamma n \rightarrow \eta(n)$ is shown in Fig. 3 as a function of the incident photon energy. Apart from a small systematic deviation, the two different analysis versions are in good agreement. The experimental results are compared to model predictions from the BnGa analysis [22] and the MAID model [23]. All models were folded with the Fermi momentum distribution for nucleons bound in deuterium nuclei [24]. The first measurement of the polarization observable E [25] for the neutron was analysed in the semi-inclusive way, *i. e.*, all events without detection of any charged particle were accepted as "neutron participant", while for reactions with "proton participant" detection and identification of the recoil proton was required. The data seem to be in better agreement with the BnGa model solution [22] including an additional narrow P_{11} state than without it. A further investigation should answer this question.

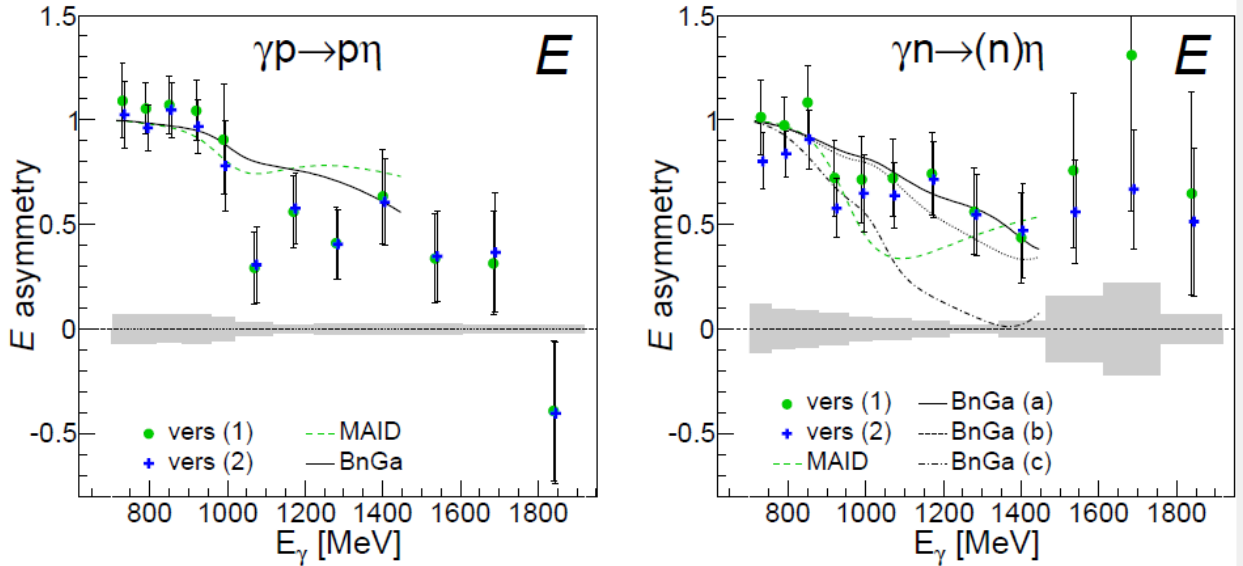


Fig. 3. Double polarization observable E for $\gamma p \rightarrow \eta p$ (left) and $\gamma n \rightarrow \eta(n)$ (right): green dots – analysis version (1) (carbon subtraction); blue crosses – analysis version (2) (normalization to data from unpolarized deuterium target)

5. Conclusion

The excitation spectrum of nucleons is one of the most important testing grounds of our understanding of the strong interaction in the non-perturbative regime. While in the past most experimental information came from hadron induced reactions (such as elastic and inelastic pion scattering), the last two decades saw a huge worldwide effort to study the electromagnetic excitations of baryons with photon induced reactions and with electron scattering. Using the tagged photon beam of ELSA and the combined CB/TAPS set-up, several neutral meson photoproduction channels were investigated. From previous measurements of cross sections and single polarization parameters some unseen states were found. However, to make unambiguous conclusions from PWA or dynamical models, double polarization observables need to be measured as well. Double polarization experiments were established at ELSA, at first by usage of the longitudinally and circularly polarized photon beam in combination with the polarized frozen spin target. The double polarization experiments are expected to answer the question of the existence of at least some of the newly found states.

References

1. S. Capstick, W. Roberts, Phys. Rev. D **49**, 4570 (1994).
2. E. Aker *et al.*, Nucl. Instr. Meth. A **321**, 69 (1992).
3. R. Novotny *et al.*, IEEE Trans. Nucl. Sci. **38**, 378 (1991).
4. W. Hillert, Eur. Phys. J. A **28**, s01, 139 (2006).
5. G. Knöchlein, D. Drechsel, L. Tiator, Z. Phys. A **352**, 327 (1995).
6. V. Burkert, Proc. of the NSTAR'07 (Bonn), Springer-Verlag, 2008, p. 7.
7. W.-T. Chiang, F. Tabakin, Phys. Rev. C **55**, 2054 (1997).
8. W. Roberts, Proc. of the NSTAR'05 (Tallahassee), World Scientific, 2005, p. 138.
9. D. Elsner *et al.*, Eur. Phys. J. A **33**, 147 (2007).
10. CBELSA/TAPS Collaboration, D. Elsner *et al.*, Eur. Phys. J. A **39**, 373 (2009).
11. C. Bradtke *et al.*, Nucl. Instr. Meth. A **436**, 430 (1999).
12. G. Suft *et al.*, Nucl. Instr. Meth. A **538**, 416 (2005).
13. E. Aker *et al.*, Nucl. Instr. Meth. A **321**, 69 (1992).
14. CBELSA/TAPS Collaboration, A. Thiel *et al.*, Phys. Rev. Lett. **109**, 102001 (2012).
15. A. Thiel *et al.*, Eur. Phys. J. A **53**, 8 (2017).
16. GRAAL Collaboration, O. Bartalini *et al.*, Eur. Phys. J. A **26**, 399 (2005).
17. A.V. Anisovich, R. Beck, E. Klempt *et al.*, Eur. Phys. J. A **48**, 15 (2012).
18. D. Drechsel *et al.*, Nucl. Phys. A **645**, 145 (1999); M. Hilt, B.C. Lehnhart, S. Scherer, L. Tiator, Phys. Rev. C **88**, 5, 055207 (2013).
19. D. Rönchen *et al.*, Eur. Phys. J. A **50**, 101 (2014).
20. R.L. Workman, M.W. Paris, W.J. Briscoe, I.I. Strakovsky, Phys. Rev. C **86**, 015202 (2012).
21. A. Käser *et al.*, Phys. Lett. B **748**, 244 (2015).
22. A.V. Anisovich *et al.*, Eur. Phys. J. A **51**, 72 (2015).
23. W.-T. Chiang *et al.*, Nucl. Phys. A **700**, 429 (2002).
24. M. Lacombe *et al.*, Phys. Lett. B **101**, 139 (1981).
25. M. Dieterle *et al.*, Phys. Lett. B **770**, 523 (2017).

SEARCH FOR THE NARROW $N(1685)$ RESONANCE IN $\gamma N \rightarrow \pi\eta N$ REACTIONS

V.A. Kuznetsov, A.B. Gridnev, N.G. Kozlenko, V.V. Sumachev
in the collaboration with Istituto Nazionale di Fisica Nucleare – Sezione di Catania (Italy)
and Dipartimento di Fisica ed Astronomia, Università di Catania (Italy):
F. Mammoliti, F. Tortorici, V. Bellini, V. Brio, G. Russo, M.L. Sperduto, C. Sutura

Understanding of the internal structure of the nucleon is a key task in the domain of hadronic physics. Suggested in the 60th the approximate flavour SU(3) symmetry of quantum chromodynamics led to a remarkably successful classification of low-lying mesons and baryons. Many properties of baryons known at that time were transparently explained by the constituent quark model (CQM) [1] that treats baryons as bound systems of three effective (constituent) quarks. CQM-based calculations predicted a rich spectrum of baryon resonances with widths varying from 80 to 400 MeV. Nevertheless, in spite of significant efforts, many of the predicted resonances still escape from reliable experimental identification (the so-called “missing resonances”).

The chiral soliton model (χ SM) is an alternative picture of baryons. It treats them as space/flavour rotational excitations of a classical object – a soliton of the chiral field. The model predicts the lowest-mass baryon multiplets to be the (8, $1/2^+$) octet and the (10, $3/2^+$) decuplet – exactly as CQM does. χ SM also predicts existence of long-lived exotic particles [2].

Therefore, the search for light-quark exotic states may provide critical benchmarks to examine two different approaches and to establish a connection between them. In this context, the observation of a narrow enhancement at $W \approx 1.68$ GeV in the $\gamma n \rightarrow \eta n$ excitation function (the so-called “neutron anomaly”) at GRAAL, CBELSA/TAPS, LNS, and A2@MAMI-C [3–5] might be quite important. Narrow structures at the same energy were also observed in Compton scattering on the neutron $\gamma n \rightarrow \gamma n$ [6] and in the beam asymmetry in the η photoproduction off the proton $\gamma p \rightarrow \eta p$ [7]. The recent data on the beam asymmetry in the Compton scattering on the proton $\gamma p \rightarrow \gamma p$ [8], the precise data for the $\gamma n \rightarrow \eta n$ [9] and $\pi^- p \rightarrow \pi^- p$ [10] reactions revealed two narrow structures at $W \approx 1.68$ and $W \approx 1.72$ GeV.

The whole complex of experimental observations may signal the existence of one ($N(1685)$) or two ($N(1685)$ and $N(1726)$) narrow nucleon resonances. The properties of $N(1685)$ (if it does exist), namely the isospin $1/2$, strangeness $S = 0$, narrow width ($\Gamma \leq 25$ MeV), strong photoexcitation on the neutron and suppressed decay to the πN final state, do coincide well with those predicted by the χ SM second member of the anti-decuplet of exotic particles [11, 12].

On the other hand, there are alternative interpretations of the “neutron anomaly” in terms of the specific interference of the known wide resonances [13] or as the sub-threshold meson–nucleon production (cusp) [14]. Although being questionable [15], the first assumption is widely discussed in the literature.

The decisive identification of these experimental findings is a challenge for both theory and experiment. In the previous experiments the possible signal of $N(1685)$ was observed in the so-called “formation” reactions in which the incoming particle interacts with the target nucleon and excites resonances. If $N(1685)$ does really exist, its signal should also be seen in multi-particle “production” reactions in which it would manifest itself as a peak in the invariant mass spectra of the final-state products. A possible reaction may be $\gamma N \rightarrow \pi\eta N$.

The photoproduction of $\pi\eta$ pairs on the proton was previously studied at GRAAL [16], CBELSA/TAPS [17], and A2@MAMI-C [18] facilities. The goals of the experiments were to investigate the spectrum of baryon resonances and to constrain theoretical models. The works [16, 17] were restricted only to the $\gamma p \rightarrow \pi^0\eta p$ reaction. The data from Ref. [18] were obtained at photon energies below 1.4 GeV.

In this work, we report on the study of the $\gamma p \rightarrow \pi^0\eta p$, $\gamma p \rightarrow \pi^+\eta n$, $\gamma n \rightarrow \pi^0\eta n$, and $\gamma n \rightarrow \pi^-\eta p$ reactions. Our ultimate goal is to search for a possible signal of $N(1685)$.

The data were collected at the GRAAL facility [19]. The GRAAL highly-polarized beam was produced by means of the back-scattering of the laser light on 6.04 GeV electrons circulating in the storage ring of the European Synchrotron Radiation Facility (Grenoble, France). The GRAAL tagging system provided measurements of the photon energies in the range 0.55–1.5 GeV. The maximum beam intensity and polarization were in the energy range 1.4–1.5 GeV.

Photons from $\eta \rightarrow 2\gamma$ and $\pi^0 \rightarrow 2\gamma$ decays were detected with the BGO ball [20]. This detector covered the range of the polar angles $\theta_{\text{lab}} = 25\text{--}165^\circ$. It made possible to determine the photon energy with the resolution of $3\%/\sqrt{E\gamma(\text{GeV})}$. The angular resolution of the photon detection was $6\text{--}8^\circ$.

The recoil protons and neutrons emitted at forward angles $\theta_{\text{lab}} \leq 25^\circ$ were detected in the assembly of the forward detectors. It consisted of two planar wire chambers, a thin scintillator hodoscope and a lead-scintillator wall [21]. Two latter detectors were located at 3 and 3.3 m behind the target, respectively. They allowed a measurement of the time-of-flight (ToF) of recoiled nucleons with the resolution of ~ 250 ps. Then this quantity was used to retrieve the energies of protons and neutrons. The planar chambers made possible to measure proton angles with the resolution better than 1° . The neutron angles were measured by the lead-scintillator wall which provided about $2\text{--}3^\circ$ resolution.

Charged pions were detected in the BGO ball. Their angular quantities were measured by two cylindrical wire chambers which surrounded the target and provided the angular resolution of $1\text{--}2^\circ$. The pion energies were reconstructed assuming the momentum conservation.

At the first step of the data analysis, η and π^0 mesons were identified by means of the invariant masses of two properly chosen photons. Then the cuts on the proton and η missing masses were applied. The kinematics of the three-body $\gamma N \rightarrow \pi\eta N$ reaction could be considered as a combination of three two-body reactions with one “real” and one “effective” (resonance “ R ”) two-particles in the final state:

$$\gamma N \rightarrow \pi R(\eta N) \rightarrow \pi\eta N, \quad (1)$$

$$\gamma N \rightarrow \eta R(\pi N) \rightarrow \pi\eta N, \quad (2)$$

$$\gamma N \rightarrow NR(\eta\pi) \rightarrow \pi\eta N. \quad (3)$$

At the second stage of the data analysis, the cuts on the coplanarity and on the differences between the missing and invariant masses were applied assuming all three possible kinematic cases were employed. For the selection of $\gamma N \rightarrow \pi\eta N$ events, the π azimuthal angle was compared with the azimuthal angle of the “effective” ηN resonance $R(\eta N)$ (Eq. 1). The missing mass $MM(\gamma\pi)$ of $R(\eta N)$ calculated using the momenta of the incoming photon and the final-state π was compared with the invariant mass of the final-state η and the recoil nucleon N . Then, similar cuts were imposed assuming two other reactions (Eqs. 2, 3).

These cuts eliminated the background which was clearly seen in the initial spectra (for example, in the spectra of η and proton missing masses). To assure the quality of the analysis, our results on the polarized photon beam asymmetry Σ for $\gamma p \rightarrow \pi^0\eta p$ were compared with those published by the CBELSA/TAPS Collaboration [15] (Fig. 1). Both data sets are in good agreement with each other, while our data are more precise at higher energies.

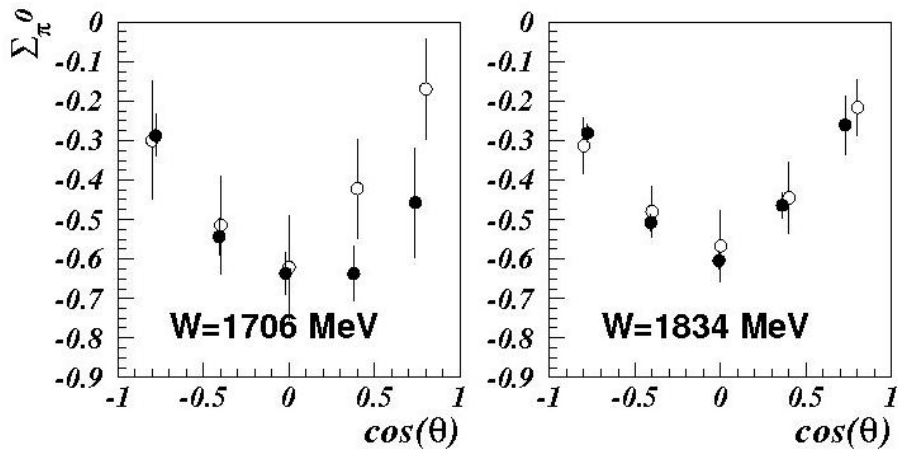


Fig. 1. Beam asymmetry Σ obtained assuming the $\gamma p \rightarrow \pi^0 R(\eta p)$ reaction: *black circles* – the results of this work; *open circles* – the results of the CBELSA/TAPS Collaboration [17]

Given the goal of this work, only the events in the range of the energy of the incoming photon $E_\gamma = 1.4\text{--}1.5$ GeV were selected for further analysis. The lower limit of 1.4 GeV is close to the $\gamma N \rightarrow \pi N(1685)$ threshold. The upper value 1.5 GeV is the limit of the GRAAL beam and it allows to avoid the contribution from higher-lying resonances.

The *left panel* of Fig. 2 shows the Dalitz plot of the invariant mass $IM(\eta N)$ versus the invariant mass $IM(\pi N)$ (the sum of all reactions under study). The events corresponding to $IM(\pi N) \approx 1.2\text{--}1.35$ GeV are major contributors. One may assume that they originate from the $\gamma N \rightarrow \eta \Delta$ production. There is a small narrow enhancement at $IM(\eta N) \approx 1.68$ GeV. This enhancement may signal the resonance $N(1685)$. The corresponding spectrum of the extracted invariant mass $M(\eta N)$ is shown in the *right panel* of Fig. 2.

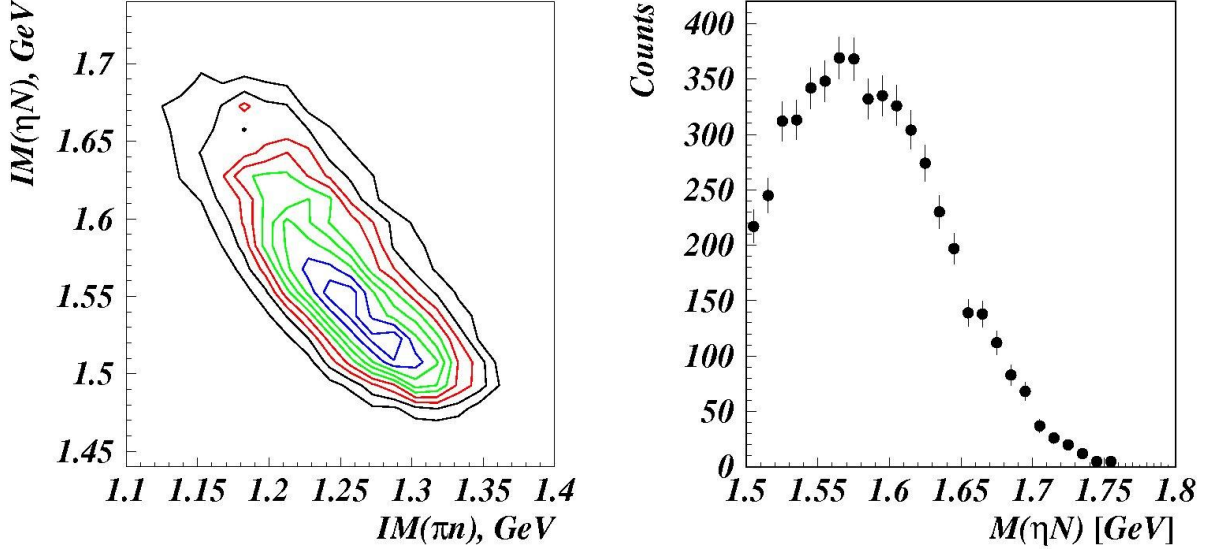


Fig. 2. Bi-dimensional plot of the ηN invariant mass $IM(\eta N)$ versus the πN invariant mass $IM(\pi N)$ in the energy range 1.4–1.5 GeV; sum of all reactions under study (*left*). The corresponding spectrum of the extracted $M(\eta N)$ mass; no cuts on the value of $IM(\pi N)$ are applied (*right*)

To eliminate the contamination of $\gamma N \rightarrow \eta \Delta$ events, further cuts on the invariant mass $1.12 \leq IM(\pi N) \leq 1.22$ GeV and the missing mass $MM(\gamma \eta) \leq 1.22$ GeV were applied to compromise between the overall statistics of the selected events and the rejection of the background. The spectra of the extracted masses $M(\eta N)$ for each reaction are shown in Fig. 3. For the reaction $\gamma p \rightarrow \pi^0 \eta p$ on the free-proton target, $M(\eta p)$ was taken as $[MM(\gamma \pi^0) + IM(\eta p)]/2$. This gave the opportunity to use the most of the information read out from the GRAAL detector and consequently to improve the resolution. In the case of the reaction $\gamma p \rightarrow \pi^+ \eta n$ on the free proton, the energy of π^+ is retrieved from the momentum conservation. That is why a kinematic fit was employed in addition to achieve the best resolution in the $M(\eta n)$ spectrum. For the reactions on the proton and the neutron bound in a deuteron target, the missing masses $MM(\gamma \pi)$ are distorted due to Fermi motion of the target nucleons while the invariant masses $IM(\eta N)$ remain almost unaffected. For these reactions the extracted masses $M(\eta N)$ shown in Fig. 3 were set equal to the corresponding invariant masses $IM(\eta N)$.

All the spectra exhibit enhancements at $M(\eta N) \approx 1.68$ GeV. They are better pronounced and more narrow for the reactions on the free proton (*two upper panels* of Fig. 3). The statistics for these reactions is better because of the available data. In the case of the reactions on the proton and neutron bound in the deuteron, the peaks are wider.

A signal of $N(1685)$ resonance should be seen in both missing mass $MM(\gamma \pi)$ and invariant mass $IM(\eta N)$ spectra. The *left panel* of Fig. 4 shows a bi-dimensional plot of these quantities (the sum of all the reactions). There is a clear enhancement at ~ 1.68 GeV at both axes. The spectrum of the ηN mass (the sum of all reactions under study) reveals a peak-like structure at $W \approx 1.68$ GeV. Being considered in conjunction with high-statistics $\gamma n \rightarrow \eta n$ results [3–12], this structure signals the existence of the $N(1685)$ resonance.

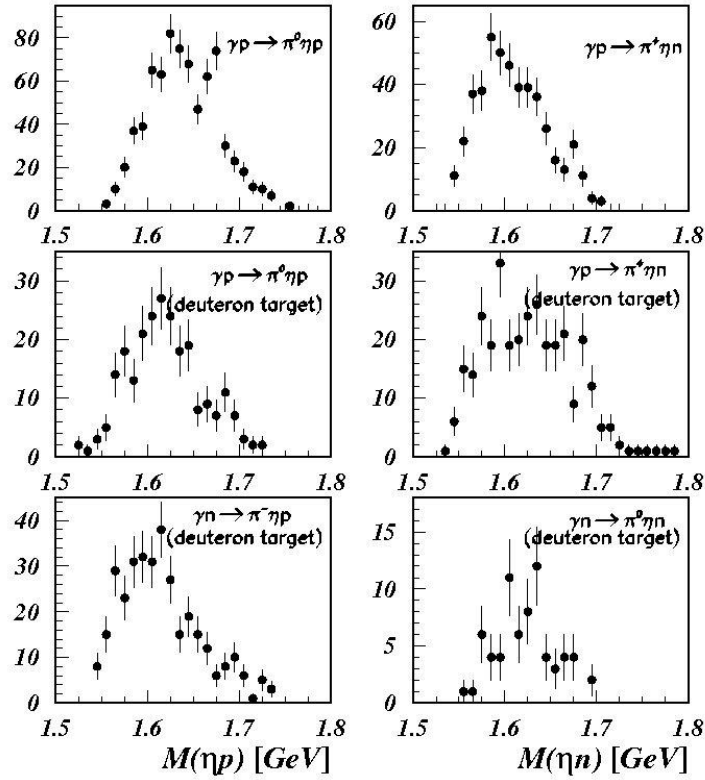


Fig. 3. Spectra of the extracted masses $M(\eta N)$

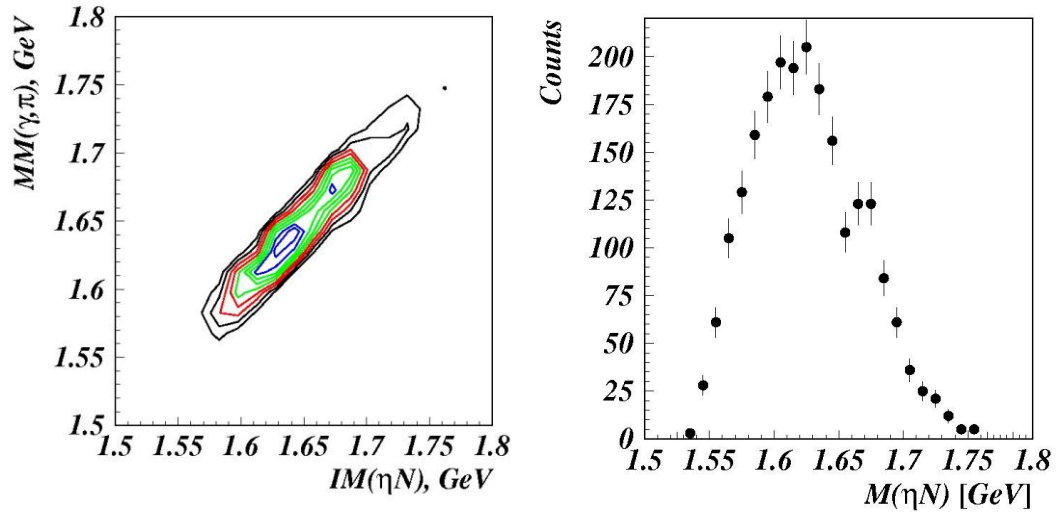


Fig. 4. Bi-dimensional plot of the missing masses $MM(\gamma, \pi)$ vs the invariant masses $IM(\eta N)$ (sum of all channels) with the cut on $IM(\pi N)$ (left). The corresponding spectrum of the extracted mass $M(\eta N)$ (right)

The positions of the peaks in both missing masses $MM(\gamma, \pi)$ and invariant masses $IM(\eta N)$ for each reaction depend on the quality of the calibration of the GRAAL sub-detectors and tagging system. This in particular concerns the forward ToF detectors. A systematic error in the determination of the ToF of the recoil nucleon of ~ 20 ps results in a shift of the peak position by ~ 10 MeV. These errors might be different for recoil protons and recoil neutrons. Other errors originate from the calibration of the tagging system $\Delta E_\gamma = 10$ MeV, from

the threshold effects in the BGO ball, and from the energy losses of the protons during their passage from the target to the detectors. That is why all the spectra were corrected such that the peaks were located at the same average value $M(\eta N) \approx 1.68$ GeV. The deviation of the initial peak positions from this average value did not exceeded 10 MeV.

The sum of the corrected $M(\eta N)$ spectra is shown in Fig. 5. A well pronounced peak at ~ 1.68 GeV is seen. The Gaussian+3-order polynomial (signal – plus background) fit results in the χ -squared value of 23.9/23. The fit by three-order polynomial (background) gives the χ -squared value of 42.6/26. The log likelihood ratio of these two hypotheses $\sqrt{2\ln(L_{s+b}/L_b)}$ corresponds to the confidence level of 4.6σ .

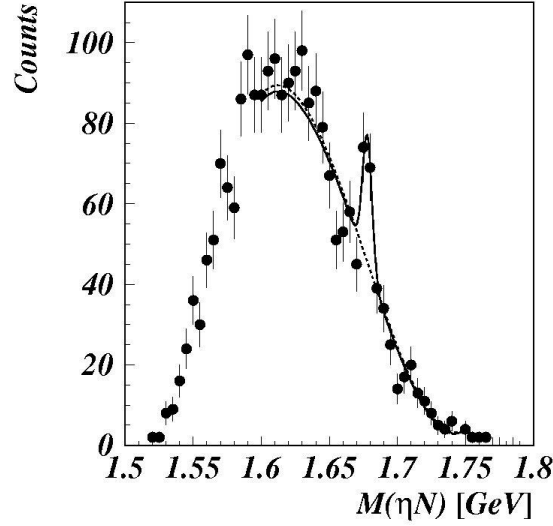


Fig. 5. Spectrum of the extracted $M(\eta N)$ mass (sum of all channels) with corrections

Figure 6 presents the simulated yields of the $\gamma p \rightarrow \pi^0 \eta p$ and $\gamma p \rightarrow \pi^+ \eta n$ reactions obtained by using the same software and cuts as those for the real data shown in Fig. 3. The event generator used in the Monte Carlo included flat cross sections without any narrow resonances. No peaks are seen.

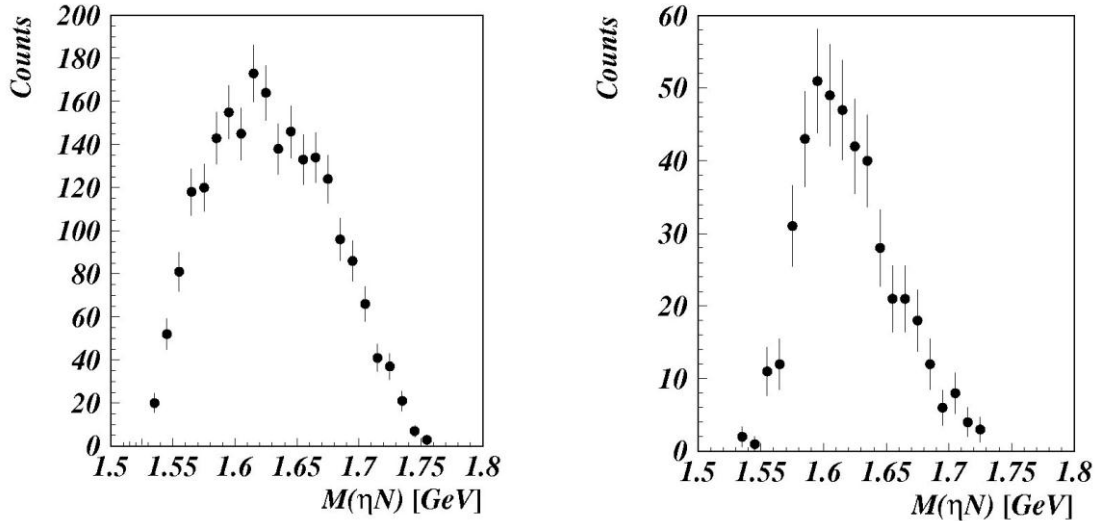


Fig. 6. Simulated spectra of the $M(\eta N)$ invariant masses for the $\gamma p \rightarrow \pi^0 \eta p$ (left) and $\gamma p \rightarrow \pi^+ \eta n$ (right) reactions

Our results support the existence of two narrow resonances, $N^+(1685)$ decaying, in particular, into the ηp final state, and $N^0(1685)$ with one possible decay into ηn (*i. e.* the isospin of the $N(1685)$ resonance is $1/2$). Although the properties of this resonance do coincide well to those expected for the second member of the exotic anti-decuplet [2], its decisive nature determination requires in particular identification of the second structure at $W \approx 1.726$ GeV. It is unclear whether the interference of the known wide resonances [13] or the cusp effect [14] – two other hypotheses under discussion – could explain these results.

Our observation requires confirmations by other groups. It would be interesting to revisit the analysis of the $\gamma p \rightarrow \pi^0 \eta p$ reaction by the CBELSA/TAPS Collaboration [17]. If a similar energy binning ($\Delta E_\gamma = 1.2\text{--}1.45$ GeV) as in Ref. [17] is used in our analysis and no cuts on $IM(\pi^0 p)$ are imposed, no signal of $N(1685)$ is visible. New dedicated experiments at other facilities could provide data with a higher level of quality.

It is our pleasure to thank the staff of the European Synchrotron Radiation Facility for the stable beam operation during the experimental runs. This work was supported by the HEPD of the PNPI and by the Istituto Nazionale di Fisica Nucleare – Section of Catania. Special thanks are to Prof. E. Gutz for providing the data of the CBELSA/TAPS Collaboration.

References

1. S. Capstic, N. Isgur, Phys. Rev. D **34**, 2809 (1986).
2. D. Diakonov, V. Petrov, M.V. Polyakov, Z. Phys. A **359**, 305 (1997).
3. V. Kuznetsov, S. Churikova, G. Gervino *et al.*, Phys. Lett. B **647**, 23 (2007) and references therein.
4. LNS Collaboration, F. Miyahara, J. Kasagi, T. Nakabayashi *et al.*, Prog. Theor. Phys. Suppl. **168**, 90 (2007).
5. A2 Collaboration, L. Witthauer, M. Dieterle, S. Abtet *et al.*, Phys. Rev. C **95**, 055201 (2017).
6. V. Kuznetsov, M.V. Polyakov, V. Bellini *et al.*, Phys. Rev. C **83**, 022201(R) (2011).
7. V. Kuznetsov *et al.*, Acta Phys. Polon. B **39**, 1949 (2008).
8. V. Kuznetsov, F. Mammoliti, V. Bellini *et al.*, Phys. Rev. C **91**, 042201 (2015).
9. D. Werthmiller, L. Witthauer, D.I. Glazier, B. Krusche, Phys. Rev. C **92** 069801 (2015).
10. A. Gridnev, I.G. Alekseev, V.A. Andreev *et al.*, Phys. Rev. C **93** 062201 (2016).
11. M.V. Polyakov, A. Rathke, Eur. Phys. J. A **18**, 691 (2003).
12. Y.I. Azimov, V. Kuznetsov, M.V. Polyakov, I. Strakovsky, Eur. Phys. J. A **25**, 325 (2005); A. Fix, L. Tiator, M.V. Polyakov, Eur. Phys. J. A **32**, 311 (2007); K.S. Choi, S.I. Nam, A. Hosaka, H.C. Kim, Phys. Lett. B **636**, 253 (2006); R. Arndt, Y. Azimov, I. Strakovsky, R. Workman, Phys. Rev. C **69**, 035208 (2004).
13. A.V. Anisovich, E. Klempt, B. Krusche *et al.*, Eur. Phys. J. A **51**, 72 (2015); A.V. Anisovich, V. Burkert, E. Klempt *et al.*, U. Thoma, Eur. Phys. J. A **49**, 67 (2013); V. Shklyar, H. Lenske, U. Mosel, Phys. Lett. B **650**, 172 (2007); R. Shyam, O. Sholten, Phys. Rev. C **78**, 065201 (2008); X.-H. Zhong, Q. Zhao, Phys. Rev. C **84**, 045207 (2011).
14. M. Doring, K. Nakayama, Phys. Lett. B **683**, 145 (2010).
15. V. Kuznetsov, V. Bellini, V. Brio *et al.*, JETP Lett. **105**, 625 (2017).
16. J. Ajaka, O. Bartalini, V. Bellini *et al.*, Phys. Rev. Lett. **100**, 052003 (2008).
17. CBELSA/TAPS Collaboration, E. Gutz, V. Crede, V. Sokhoyan *et al.*, Eur. Phys. J. A **50**, 74 (2014).
18. A2 Collaboration, A. Kaeser, F. Mueller, J. Ahrens *et al.*, Eur. Phys. J. A **52** 272 (2016).
19. GRAAL Collaboration, O. Bartalini, V. Bellini, J.-P. Bocquet *et al.*, Eur. Phys. J. A **26**, 399 (2005).
20. F. Ghio, B. Girolami, M. Capogni *et al.*, Nucl. Instr. Meth. A **404**, 71 (1998).
21. V. Kuznetsov, A. Lapik, S. Churikova *et al.*, Nucl. Instr. Meth. A **487**, 396 (2002).

STUDY OF THE PROTON–PROTON COLLISIONS AT THE BEAM MOMENTUM OF 1 683 MeV/c

K.N. Ermakov, V.A. Nikonov, O.V. Rogachevsky, A.V. Sarantsev, V.V. Sarantsev, S.G. Sherman

1. Introduction

Understanding the proton–proton interaction at low and intermediate energies is an important task of particle physics. At large momentum transfers where the strong coupling is small, the quantum chromodynamic (QCD) calculations can be used efficiently for description of such processes. A large progress was made at low energies, where the effective field approach allowed one to describe processes below the resonance region. However, the region of the intermediate energies and especially the resonance region is much less accessible for theoretical calculations, and phenomenological dynamic models play the leading role here. The data from the nucleon–nucleon (NN) collision reactions form the basis for construction of such models, which in turn have a large range of applications in nuclear and heavy-ion physics.

In the region above the two-pion production threshold and up to 1 GeV, the $NN \rightarrow \pi NN$ reaction is dominated by production of the $\Delta(1232)$ isobar in the intermediate state. It was natural to suggest that such a production is based on the one-pion exchange (OPE) mechanism, and a set of the corresponding models was put forward [1, 2] a rather long time ago. The pion exchange amplitudes are introduced there using certain form factors with the parameters defined from fits to the experimental data. The model of Suslenko *et al.* describes with a reasonable accuracy (up to normalization factors) the differential spectra of the $pp \rightarrow pn\pi^+$ and $pp \rightarrow pp\pi^0$ reactions in the energy region below 1 GeV [1, 3], while the model of Dmitriev *et al.* was applied to the energies over 1 GeV [2]. In a more complicated model based on the one-boson exchange mechanism, the dominant contribution from the $\Delta(1232)$ production is also defined by the OPE: it was found that other boson exchanges contribute around 10% to the total cross section at energies above 1 GeV. However, it should be noted that there are discrepancies in simultaneous description of the measured total cross sections for the $pp \rightarrow pn\pi^+$ and $pp \rightarrow pp\pi^0$ reactions by the OPE model. For example, at the proton momentum of 1 683 MeV/c, the OPE model can reproduce well the measured $pp \rightarrow pn\pi^+$ total cross section with the corresponding choice of the form factor. However, in this case the OPE prediction for the $pp \rightarrow pp\pi^0$ total cross section will be smaller by about 30% than the experimental one (see Ref. [3]).

Moreover, in the region above the incident proton momentum 1.5 GeV/c, other contributions start to play a notable role: for example, the relatively broad Roper resonance is traced in the spectrum. Therefore, for a comprehensive analysis of the data it is necessary to apply an approach beyond the OPE model.

With this purpose, we have performed a partial wave analysis (PWA) of the data on the single-pion production in the framework of the approach based on the work described in Ref. [4]. The result of such an analysis for the lower-energy data measured earlier was reported in Ref. [5].

In analysis [5], several solutions were found which almost equally describe the data. These solutions differ by contributions from the partial waves with high orbital momenta $L > 3$, which were found to be rather unstable in the fit. It is interesting to see which solution is compatible with the new higher energy data of this paper. It is also interesting to compare the result of the PWA with the one predicted by the OPE model.

In this article, we present new data on the elastic and the $pp \rightarrow pn\pi^+$ reactions measured at the proton momentum of 1 683 MeV/c, compare the data with the OPE model calculations, and determine contributions from different partial waves in the combined PWA of the new data and the data measured earlier.

2. Experiment

The description of the experiment performed at the PNPI 1 GeV synchrocyclotron was given in detail in our previous work [6]. The proton beam was formed by three bending magnets and by eight quadrupole lenses. The mean incident proton momentum value was inspected by the kinematics of the elastic scattering events. The accuracy of determination of the incident momentum value and the momentum spread were about 0.5 and 7 MeV/c (FWHM), correspondingly, with perfect Gaussian distributions. A total of $8 \cdot 10^4$ stereoframes were obtained. The frames were double scanned to search for events due to interaction of the incident beam with protons. The double-scanning efficiency was determined to be 99.95%. Approximately $7 \cdot 10^3$ two-prong events were used for the subsequent analysis.

The two-prong events selected in the fiducial volume of the hydrogen bubble chamber were geometrically reconstructed and kinematically fitted to the following reaction hypotheses:

$$p + p \rightarrow p + p, \quad (1)$$

$$p + p \rightarrow p + n + \pi^+, \quad (2)$$

$$p + p \rightarrow p + p + \pi^0, \quad (3)$$

$$p + p \rightarrow d + \pi^+, \quad (4)$$

$$p + p \rightarrow d + \pi^+ + \pi^0. \quad (5)$$

The events identification procedure was also described in details in Ref. [6]. Thus, we list only the most important criteria here:

1. Events with the confidence level higher than 1% were accepted.
2. Events with only one acceptable hypothesis were identified as belonging to this hypothesis.
3. If several versions revealed a good χ^2 value, we used the visual estimation of the bubble density of the track to distinguish between proton (deuteron) and pion.

The total number of the two-prong events which had not passed the reconstruction and fitting procedures was counted to be less than 10%. These unidentified events were apportioned to the fraction of the fitted hypotheses of the accepted events and were used only for the total cross section calculations.

The standard bubble chamber procedure [3] was used to obtain the absolute cross sections for the elastic and pion production reactions. The error in determination of the millibarn-equivalent was found to be about 2%. The cross section values for the inelastic processes together with statistics are listed in Table. Let us remind that the data on the $pp \rightarrow pp\pi^0$ reaction at the same energy were published earlier [6].

Table

Numbers of events and the total cross sections
at the beam momentum of 1 683 MeV/c*

$pp \rightarrow$	Events	σ , mb
Elastic	2 772	23.96 ± 0.57
$pn\pi^+$	2 564	18.97 ± 0.57
$d\pi^+$	57	0.42 ± 0.05
$d\pi^+\pi^0$	7	0.05 ± 0.02

* The total elastic cross section was obtained by interpolation of the differential cross section with the Legendre polynomials. The errors include the statistical errors and the error of the millibarn-equivalent.

The differential cross section for elastic pp scattering measured in the present experiment is shown in Fig. 1 as open squares with statistical errors. The value of the differential cross section for the very forward angle bin is not shown in Fig. 1 due to a notable loss of events with a slow final proton. If the proton momentum is less than 80 MeV/c, the recoil path is too short to be seen in the bubble chamber. The events with the proton momentum less than 200 MeV/c also might be missing during scanning. Since we do not know the real amendment for these angles we excluded the last forward point and show only the angles where the proton momentum is above 200 MeV/c. In Figure 1 we compare our elastic differential cross

section with the data from the EDDA experiment [7] taken at the incident momentum of 1 687.5 MeV/c (*open red circles*).

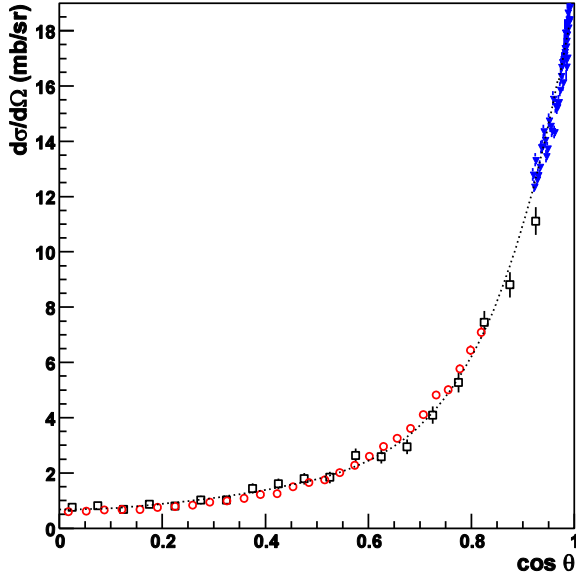


Fig. 1. Elastic differential cross section. The *dotted curve* is the result of the Legendre polynomial fit of our data (*open squares*) restricted by the interval $0 \leq \cos(\theta) \leq 0.95$ and the data from (*blue triangles*) [8]. The *open red circles* show the measurements of the EDDA experiment [7] taken at the incident momentum of 1 687.5 MeV/c

One can see good agreement between our points and the EDDA data, which supports the correctness of our definition of the millibarn-equivalent. To obtain the total elastic cross section, we applied the following procedure. We fitted the differential cross section with a sum of even-order Legendre polynomials $A_n P_n(\cos(\theta))$, $n = 0, 2, 4, \dots$. By examining the flatness of the behaviour of the fit with the decrease of the fitted angular range, we determined the range $0 \leq \cos(\theta) < 0.95$ as the unbiased one. For finding the total elastic cross section, we included in the fit above $\cos(\theta) = 0.95$ the data from Ref. [8] at the incident momentum of 1 685.7 MeV/c, which provide an important constraint for high order polynomials. The result of the fit is shown in Fig. 1 by the dotted curve. The total elastic cross section calculated as $2\pi A_0$ was found to be 23.96 ± 0.57 mb, which is close to the value given in Ref. [9].

3. The $pp \rightarrow pn\pi^+$ reaction and a comparison with the one-pion exchange model

The OPE model [2] describes the single-pion production reactions by four pole diagrams with the π^0 or π^+ exchanges (we would like to express our deep appreciation to the authors of Ref. [1] for their program code). In this model, the intermediate state of the πN -scattering amplitude confines itself to the P_{33} wave only, assuming the leading role of the Δ_{33} resonance.

Figure 2 shows the distributions over the momentum transfer squared, $\Delta^2 = -(p_t - p_f)^2$, where p_t is the four-momentum of the target proton and p_f is the four-momentum of the final proton or neutron in the $pp \rightarrow pn\pi^+$ reaction, correspondingly. The OPE model calculations normalized to the total number of the experimental events is shown by dashed lines, and the shape of the phase volume is shown by dotted lines. One can see that the OPE model describes qualitatively well the Δ^2 distributions in this reaction.

Figure 3 presents centre-of-mass (cms) angular distributions, effective two-particle mass spectra of the final particles and angular distributions in the helicity frame. We would like to point out that the cms angular distributions are symmetrical ones, which is a critical test for the correctness of our event selection. It is seen that the OPE model calculations normalized to the total number of the experimental events reproduce the particle angular distributions in the cms of the reaction and the two-body mass spectra fairly well. However, the angular distributions in the helicity systems show notable deviations from the experimental points.

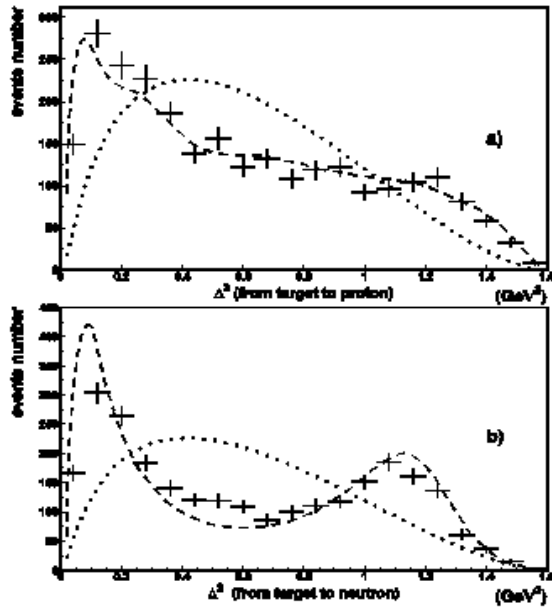


Fig. 2. Four-momentum transfer Δ^2 distribution in the $pp \rightarrow pn\pi^+$ reaction: a – for the momentum transfer to the final proton; b – for the momentum transfer to the neutron. The *dashed* curves are the OPE calculations and the *dotted* curves show the shape of the phase volume

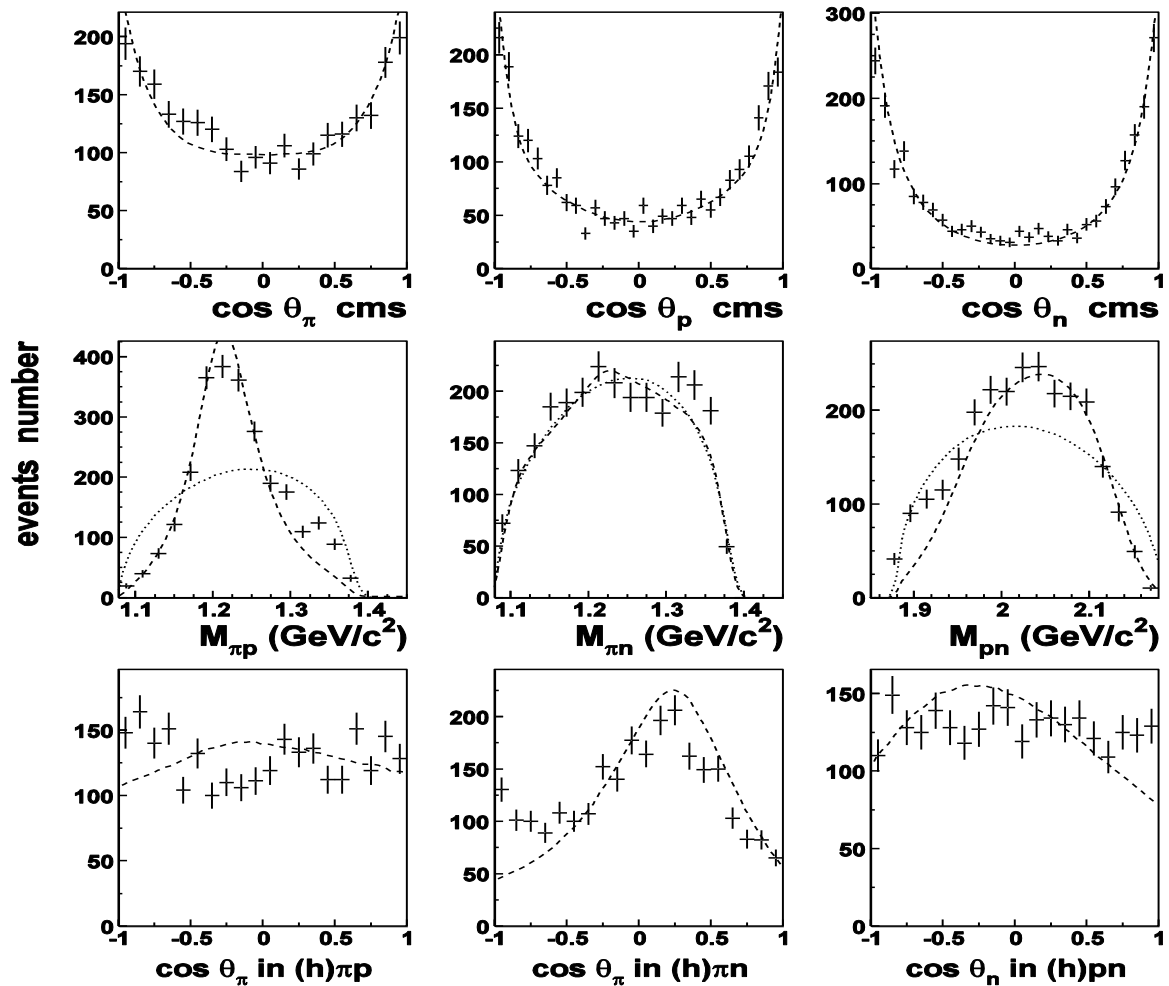


Fig. 3. The $pp \rightarrow pn\pi^+$ data (the crosses with statistical errors): angular distributions of the final particles in the cms of the reaction (*upper*), the effective two-particle mass spectra (*middle*), and angular distributions in the helicity systems (*bottom*). The *dashed* curves show the OPE calculations and the *dotted* curves show the shape of the phase volume

4. Partial-wave analysis results and discussion

To extract the contributions of different partial waves, we applied an event-by-event PWA based on the maximum-likelihood method. The formalism is given in detail in Refs. [4, 10] and is based on the spin-orbital momentum decomposition of the initial and final partial-wave amplitudes. Therefore, it was natural to use the spectroscopic notation $^{2S+1}L_J$ for two-particle partial waves with the intrinsic spin S , the orbital momentum L and the total spin J . For the initial pp system, the states with the total angular momentum $J \leq 4$ and angular momentum $L \leq 5$ between the two protons were taken into account. In the fitting procedure, for the final three-particle system we restricted ourselves to the angular momenta $L \leq 4$ in the system consisting of a two-body subsystem plus a spectator and to the angular momenta $L \leq 2$ in the two-particle systems.

The total amplitude can be written as a sum of partial-wave amplitudes [4, 10]. For description of the energy dependence in the πN system in the intermediate state, we introduced two resonances, $\Delta(1238)P_{33}$ and $N(1440)P_{11}$. For $\Delta(1238)$ we used the relativistic Breit–Wigner formula with the mass and width taken from the Particle Data Group. The Roper state was parameterized using couplings found in the analysis of Ref. [11], where the decay couplings of this state with the πN , $\pi\Delta$, and $N(\pi\pi)_{S\text{-wave}}$ channels were determined. For the description of the final NN interaction we applied a modified scattering-length approximation formula. Details of the partial-wave formalism used can be found in Ref. [12].

We have performed the analysis of the new data starting from our solution obtained in Ref. [5]. This solution was restricted to the partial waves with the total spin J up to 2 and the orbital momentum L up to 3. This solution produces an acceptable description of the lower-energy data but has notable problems in the description of the new data set. For example, χ^2 for the normalized angular distribution of the neutron in the cms of the reaction is equal to 4.49. The solution fails to describe the extreme angles which are mostly sensitive to partial waves with high orbital momentum. Indeed, the solution with $L \leq 5$ and $J \leq 4$ found in Ref. [5] (but only used for the error estimation in that paper) predicts χ^2 to be 1.23. The description of the data with these two solutions is shown in Fig. 4. This provides a strong argument for the presence of higher partial waves at the studied energy. Although the solution with $L \leq 5$ produced a rather good description of the normalized differential cross section, the total cross section predicted by both solutions appeared to be about 10% lower than that given by the data.

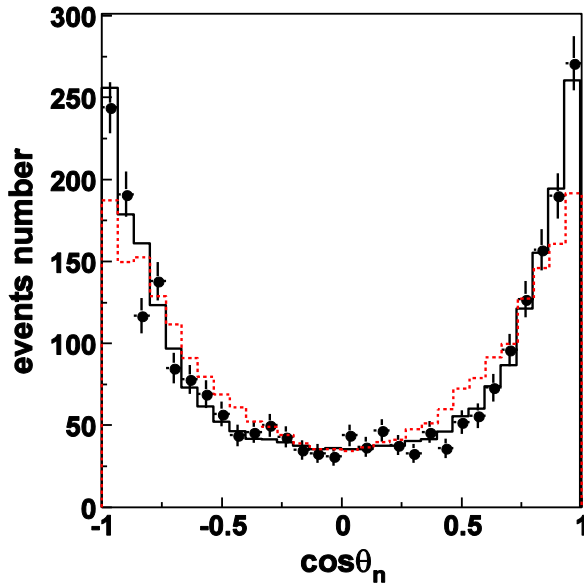


Fig. 4. The neutron angular distribution calculated in the cms of the $pp \rightarrow pn\pi^+$ reaction at 1 683 MeV/c. The data are shown by black circles with statistical errors. The solid (black) histogram shows the prediction of the solution in Ref. [5] where the partial waves up to $L = 5$ were included, and the dotted (red) histogram shows the prediction of the solution in Ref. [5] with L up to 3

Therefore, we used the last solution as a starting point and performed a combined fit of the present data together with the $pp \rightarrow pp\pi^0$ data measured earlier [3, 6, 13] and the $pp \rightarrow pn\pi^+$ data taken at 1 628 and 1 581 MeV/c [5]. In this way, we were able to reproduce both the differential and the total cross sections for all fitted data with good accuracy. It is worth noting that there is no problem to describe simultaneously

the total cross sections for the $pp \rightarrow pn\pi^+$ and $pp \rightarrow pp\pi^0$ reactions in this approach. The result of the PWA is shown in Fig. 5: the histograms correspond to the Monte Carlo events weighted by the differential cross section calculated with the fit parameters. The value of χ^2 for the distributions shown in this picture varies from 0.65 (for the pion angular distribution in the cms of the reaction) to 2.6 (for the π^+p invariant mass). We would like to remind that we used the event-by-event maximum-likelihood analysis and did not fit directly these distributions.

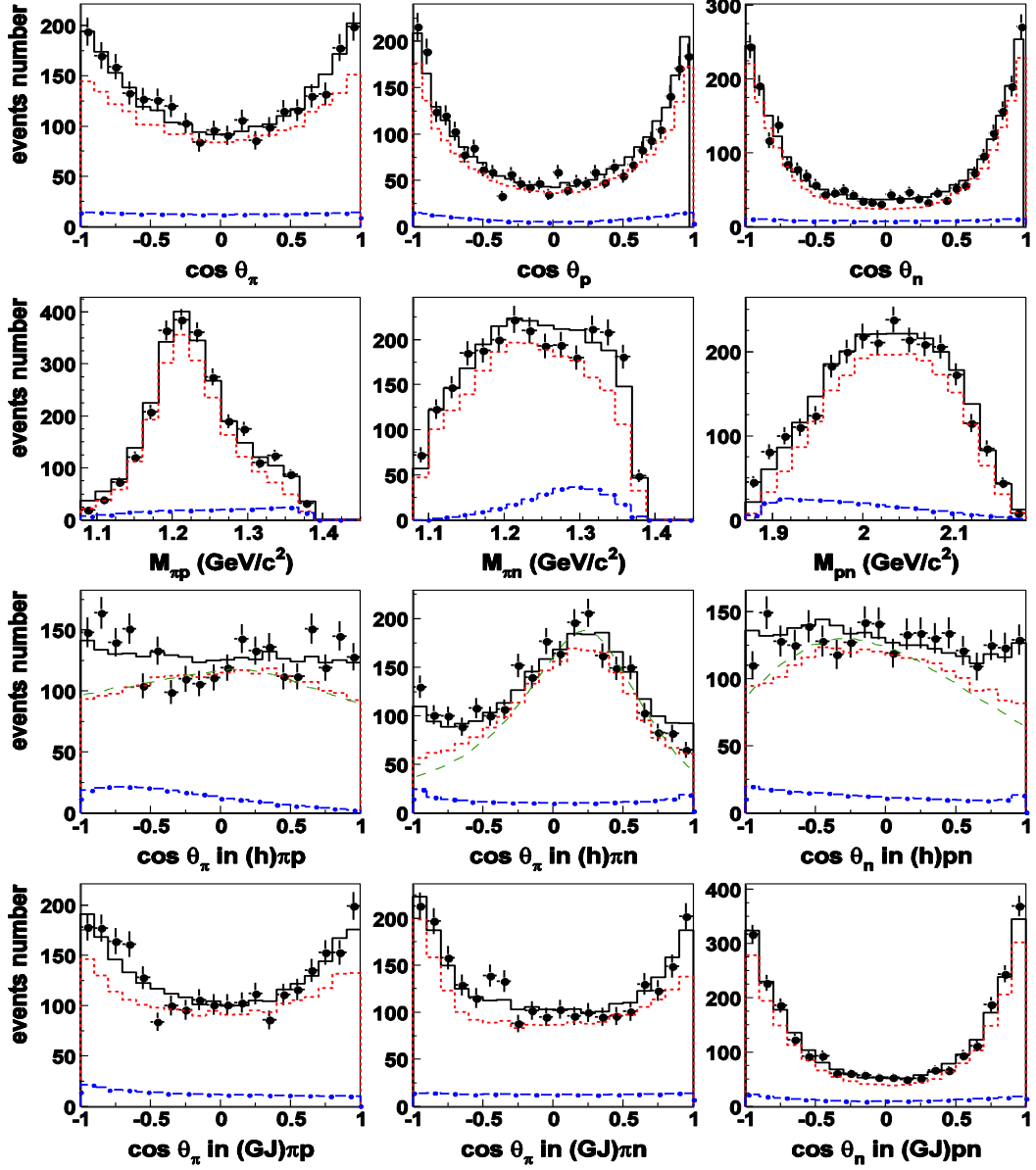


Fig. 5. The $pp \rightarrow pn\pi^+$ data taken at the proton momentum of 1 683 MeV/c with the statistical errors only: *first row* of figures – the angular distributions of the final particles in the cms of the reaction; *second row* – the effective two-particle mass spectra; *third row* – the angular distributions of the final particles in the helicity frame; *fourth row* – the angular distributions of the final particles in the Gottfried–Jackson frame. The solid (*black*) histograms show the result of our partial-wave analysis; the dotted (*red*) and dot-dashed (*blue*) histograms show the contributions from production of the $\Delta(1232)$ and $N(1440)$ intermediate states. The dashed (*green*) curves in the helicity frame show the normalized distributions from the OPE model

The PWA reproduces fairly well the experimental angular distributions in the helicity system, whereas the OPE model does not describe them well. The OPE predictions normalized to the contribution from the $\Delta(1232)$ production calculated using the PWA solution are shown in Fig. 5 with the dashed lines. It is seen that the $\Delta(1232)$ production determined in the PWA and that in the OPE model agree well with each other. This confirms that $\Delta(1232)$ is produced by the OPE mechanism and the deviation of the data from the OPE model is due to production of the Roper state.

The present combined analysis has found the contributions from the leading initial partial waves to be in qualitative agreement with the prediction from the solution reported in Ref. [5]. However, we observe changes for the contributions of the initial partial waves 1D_2 and 3F_2 , which are significantly increased after the fit with the new data. As concerns the partial waves with the total spin $J = 4$, we find a sizeable contribution from 3F_4 . For all initial partial waves, the contribution of channels with the $\Delta(1232)$ production varies from 65 to 100% and only for the 3P_0 wave it is found to be rather small – about 12%. The Roper resonance is produced mostly (in the decreasing order of contributions) from the 3P_2 , 3P_0 , 3P_1 states and (smaller by one order) from 1S_0 .

We have found a notable contribution for the decay of the initial 3P_2 state into the (pn) subsystem 1P_1 with the isospin $I = 0$. To study the stability of the solution we added to the fit partial waves with the total spin J up to 5 decaying into $\Delta(1232)N$. The obtained solution showed some reduction of the contribution from the 3P_0 initial state and increase of the contribution from the 3F_2 state. Taking into account these ambiguities we performed an error analysis of the initial-state contributions to the single-pion production cross sections. For the $pp \rightarrow pn\pi^+$ reaction these contributions are shown in Fig. 6 for three incident momenta.

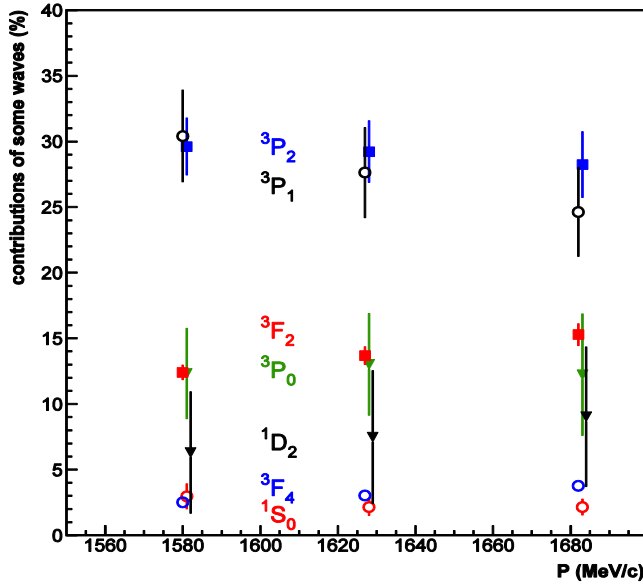


Fig. 6. Contributions (percentages) of the most important waves in the $pp \rightarrow pn\pi^+$ reaction

It is necessary to mention that the present combined analysis defines contributions of the partial waves with smaller errors than those found in Ref. [5]: the unstable contributions from the high spin amplitudes are fixed with the present data. The obtained solution is compatible with the data of the HADES Collaboration on the single-pion production at an energy of 1.25 GeV: including these data in the combined fit does not change the main results of the analysis.

5. Conclusion

The new data on the elastic and $pp \rightarrow pn\pi^+$ reactions taken at the incident proton momentum of 1 683 MeV/c are reported. Including these inelastic data in the combined PWA of the single-pion production reactions leads to a smaller error analysis and therefore to a more precise definition of the partial-wave contributions to the $pp \rightarrow pn\pi^+$ reaction. We observe some changes in specific transition amplitudes as compared to the predictions of the solution in Ref. [5]. As noted earlier in Ref. [3], although the OPE model provides a qualitative description of most differential distributions, it fails to describe simultaneously the total cross section for the $pp \rightarrow pp\pi^0$ and $pp \rightarrow pn\pi^+$ reactions in the investigated energy region. However, our partial wave analysis confirms the dominant role of the $\Delta(1232)$ production defined by the OPE exchange mechanism. The main source of discrepancies between OPE and the experimental data is due to contributions of other intermediate states, in particular of the Roper resonance.

References

1. V.K. Suslenko, I.I. Gaisak, *Yad. Fiz.* **43**, 392 (1986).
2. V. Dmitriev *et al.*, *Nucl. Phys. A* **459**, 503 (1986).
3. V.P. Andreev *et al.*, *Phys. Rev. C* **50**, 15 (1994).
4. A.V. Anisovich *et al.*, *Eur. Phys. J. A* **34**, 129 (2007).
5. K.N. Ermakov *et al.*, *Eur. Phys. J. A* **50**, 98 (2014).
6. V.V. Sarantsev *et al.*, *Eur. Phys. J. A* **21**, 303 (2004).
7. D. Albers *et al.*, *Eur. Phys. J. A* **22**, 125 (2004).
8. A.V. Dobrovolsky *et al.*, *Nucl. Phys. B* **214**, 1 (1987).
9. F. Shimizu *et al.*, *Nucl. Phys. A* **386**, 571 (1982).
10. A.V. Anisovich, A.V. Sarantsev, *Eur. Phys. J. A* **30**, 427 (2006).
11. A.V. Anisovich *et al.*, *Eur. Phys. J. A* **48**, 15 (2012).
12. K.N. Ermakov *et al.*, *Eur. Phys. J. A* **53**, 122 (2017).
13. COSY–TOF Collaboration, S.A. El-Samad *et al.*, *Eur. Phys. J. A* **30**, 443 (2006).

PNPI Participation in the LHC Detectors Upgrade

PNPI IN THE CMS UPGRADE PROGRAM

PNPI participants of the CMS Collaboration:

A.A. Vorobyev, G.E. Gavrilov, V.L. Golovtsov, Yu.M. Ivanov, V.T. Kim, P.M. Levchenko, E.V. Kuznetsova, V.A. Murzin, V.A. Oreshkin, L.A. Schipunov, D.E. Sosnov, V.V. Sulimov, L.N. Uvarov, S.A. Vavilov, S.S. Volkov, An.A. Vorobyev

1. Introduction

The compact muon solenoid (CMS) is a general-purpose detector at the Large Hadron Collider (LHC). It is one of the most ambitious scientific projects designed to investigate a wide range of high energy physics. The recent discovery of the Higgs boson is one of the major CMS achievements. The next step is the search for dark matter candidates and for any manifestation of “physics beyond the Standard Model”. Figure 1 presents a general view of CMS.

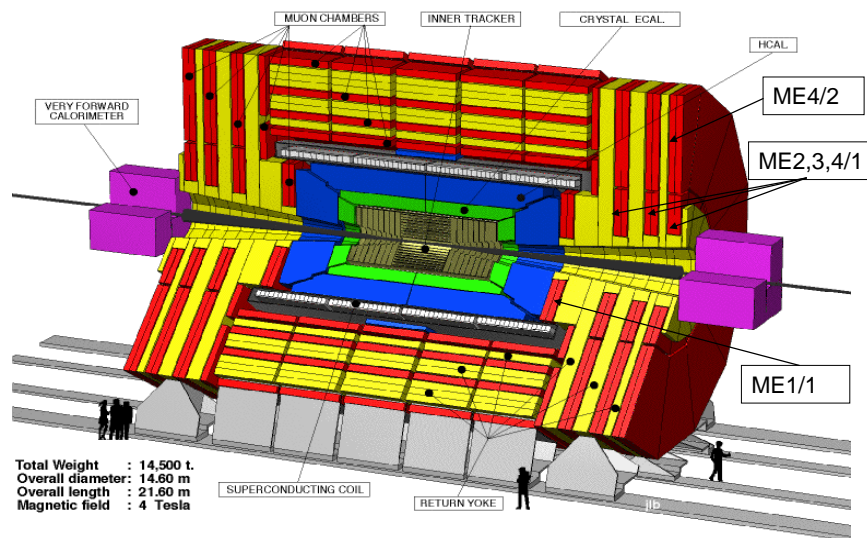


Fig. 1. General view of the CMS detector

Since the beginning of the CMS project, PNPI participated in the design, construction and operation of the endcap muon system (EMU). During the construction phase (2001–2007), 120 six-layer multiwire cathode strip chambers (CSC) were produced at PNPI for the EMU stations ME2, 3, 4/1. Another important contribution was the design and production at PNPI of the 10 000-channel high voltage (HV) supplier for the EMU CSCs, with independent control and regulation of each HV channel. Also, PNPI participated in the design and construction of the track finding processor (TFP), which was an essential part of the EMU trigger system, and in the design and testing of the front-end electronics for the CSCs. Later, in 2011–2013, 76 large CSCs were constructed for the EMU station ME4/2. The production was organized at CERN with active participation of PNPI engineers. Figure 2 shows the PNPI team with one of the CSCs assembled at CERN. In 2014, the ME4/2 chambers were installed into the CMS detector, thus completing construction of the whole EMU system. An additional 2 400-channel HV supplier for the ME4/2 CSCs was produced at PNPI.

PNPI shares responsibility for the maintenance and operation of the EMU system. This system showed very reliable performance during the whole running period (2010–2018). Initially, CMS was designed to operate with an instantaneous luminosity of $1 \cdot 10^{34} \text{ cm}^{-2} \cdot \text{s}^{-1}$. This luminosity was reached already in 2012. By the end of 2018, the peak luminosity was increased to $2 \cdot 10^{34} \text{ cm}^{-2} \cdot \text{s}^{-1}$, and the integrated luminosity reached 200 fb^{-1} .

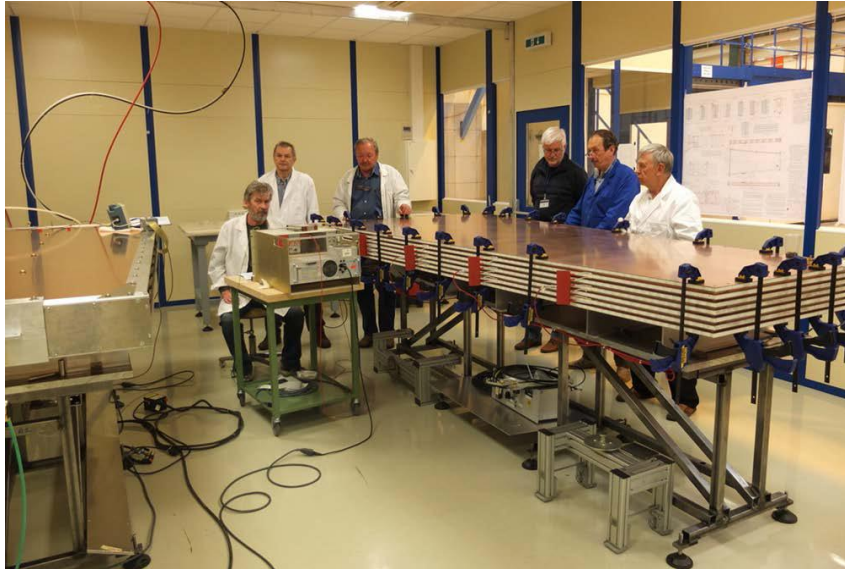


Fig. 2. PNPI engineers played the leading role in assembling and testing the ME4/2 muon chambers at CERN. B. Bochin, An. Vorobyov, V. Golubev, V. Sulimov, S. Getz, V. Tarakanov

During all this period, the gas gain in the CSCs remained practically unchanged. Several CSCs suffered from appearance of the “Malter effect” (uncontrolled self-sustaining discharges) in some sectors of the CSCs. However, this could not influence the CSCs total efficiency due to very high redundancy in construction of these chambers. Each CSC contains six layers of independent chambers. In addition, each layer in most of the CSCs is separated into several (up to five) sectors with independent HV suppliers. Therefore, switching off one sector (by reducing the HV in this sector) does not change noticeably the efficiency of the whole CSC. More critical situation is observed only in the M1/1 station, because of much harder radiation conditions in this region. Also, the M1/1 chambers are not subdivided into HV sectors. As a result, several layers in these chambers were switched off during the running period, to be restored during the Long Shutdown LS2 (2019–2020) by applying a special training procedure.

According to the existing plans for the next 15 years, CMS must be ready to operate after LS2 with the peak luminosity gradually increasing up to $5 \cdot 10^{34} \text{ cm}^{-2} \cdot \text{s}^{-1}$. By the end of 2023, the integrated luminosity should reach 500 fb^{-1} . After LS3 (2024–2025), the luminosity of $5 \cdot 10^{34} \text{ cm}^{-2} \cdot \text{s}^{-1}$ will be maintained during the entire beam fill due to implementation of the luminosity leveling, with the 25 ns bunch spacing. This should allow to use the beam time more efficiently. The goal is to deliver 3000 fb^{-1} of the integrated luminosity. To meet the new requirements, all subsystems of the CMS detector are to be upgraded. The upgrade program was formulated also for the CMS EMU system, though it is not so extensive as in other subsystems. The reliable performance of the CSCs, demonstrated during all previous years, allows to believe that these chambers could operate in the next 15 years and accumulate the integrated luminosity up to 3000 fb^{-1} . The problematic might be only CSCs in the station ME1/1. The decision is to use these CSCs at least until LS3 applying the training procedure to recover the problematic chambers from the Malter effect. Also, these chambers will be equipped with new front-end electronics and will be provided with a new HV system which allows to perform better control for the chamber performance. Additional R&D is foreseen to study the aging processes in the CSCs and the methods of reanimation of the problematic chambers. Also, a possibility should be investigated to replace CF_4 in the CSCs gas mixture with a more ecology-friendly gas. The main efforts will be concentrated on upgrading the readout electronics and the muon trigger system. In addition, there is a plan to modify the 11 000-channel HV system to facilitate the maintenance of this system. PNPI participates in the following items of the CMS EMU upgrade program: upgrade of the HV system, upgrade of the muon trigger, CSC aging studies.

2. Upgrade of the cathode strip chambers high voltage system

The present multi-channel HV system for the CSCs was developed at PNPI in collaboration with the University of Florida (UF), and it was successfully used since the beginning of the CMS experiment. The system has a three-tier structure (Fig. 3). There are eight commercial Matsusada primary HV power supplies ($HV_{\max} = 5\,000\text{ V}$, $I_{\max} = 60\text{ mA}$). They provide the HV power to 50 master boards. Each master board has eight regulated outputs with the 1.5 mA maximum current in each of them. Both the primary HV supplies and the crates with the master boards are located in the USC (underground service cavern, where there is no damage to the electronics circuits due to radiation). The master board outputs are routed to the distribution boards located near the CSCs (on the periphery of the endcap discs). There are two types of the distribution boards: the 30-channel boards serve the ME2/1, ME3/1, ME4/1, ME4/2 chambers (one chamber per board) and the 36-channel boards serve the ME2/1, ME3/1, ME4/1, ME1/2, ME1/3 chambers (two chambers per board). Each distribution board can provide the total current at its outputs up to 1.5 mA (limited by the master board) and the maximum current per channel not exceeding 100 μA . The resolution of current measurements in the individual channels is 100 nA. Table 1 summarizes the quantities of different hardware components in the present UF–PNPI HV system.

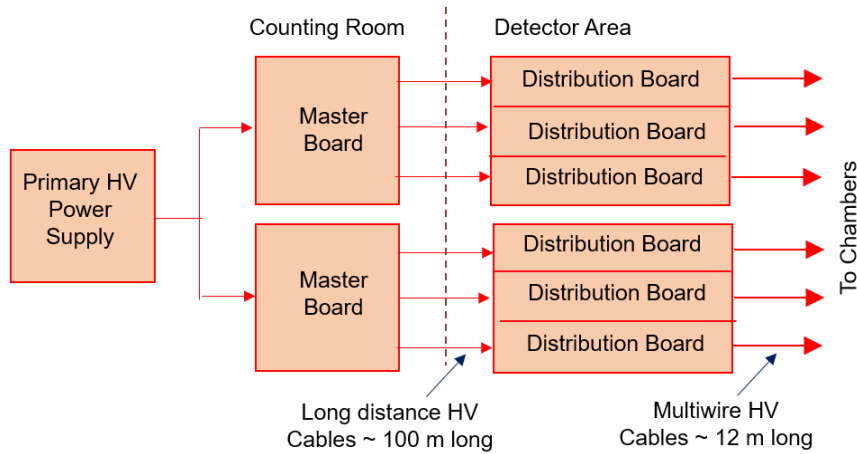


Fig. 3. UF–PNPI high voltage system structure

Table 1

Summary of hardware components in the present UF–PNPI high voltage system

Component	Quantity
Primary HV power supply	8
Master board	50
Distribution board – 30 channels	216
Distribution board – 36 channels	126
Independently regulated and monitored HV distribution channels	11 016

Besides the 11 016-channel UF–PNPI HV system, there is also a commercial 432-channel CAEN HV supplier for the ME1/1 chambers. It has sixteen HV boards (CAEN 1733BP) housed in the USC. Each channel can provide the maximum voltage up to 4 000 V and the maximum current up to 2 mA. Even though the nominal resolution in the current measurements in individual channels is 200 nA, the experience of operating this system shows significant noise in such measurements deteriorating the resolution.

For the future operation of the EMU system, the UF–PNPI HV supplier will be upgraded to have a sufficient margin to handle the current load expected at the LHC with a comfortable safety factor. The CAEN HV supplier serving the ME1/1 chamber must be upgraded to provide more reliable current

measurements needed for reliable detection of the Malter currents, which have already been observed in the ME1/1 chambers and expected to become a more frequent problem at a higher luminosity.

The HV system upgrade plans include the following steps. In the UF–PNPI HV system, the commercial primary HV power suppliers will be withdrawn, and the present master boards will be replaced with thirty eight nine-channel master boards of a new design. Each channel in the upgraded boards will have its own HV power source, capable of outputting voltages from 0 to 4000 V with the maximum current of 2.5 mA. This should be enough even at the ultimate LHC luminosity of $7.5 \cdot 10^{34} \text{ cm}^{-2} \cdot \text{s}^{-1}$. Another advantage of the new HV structure is more simple maintenance and operation of the two-tier system if compared with the three-tier system. The new master boards have been designed and successfully prototyped at PNPI. Figure 4 shows a prototype of the 9-channel master board. The ME1/1 HV subsystem will be absorbed into the total UF–PNPI HV system. For the 432 HV channels of the ME1/1 station we need two upgraded master boards and twelve 36-channel distribution boards of the current design. Besides ensuring reliable current measurements, such a replacement will make the entire CSC HV system homogenous and simpler to operate and maintain. The master and distribution boards for the ME1/1 chamber will be installed in a rack in the USC located near the racks that house the components of the existing UF–PNPI HV system. Table 2 summarized all modules of the upgraded UF–PNPI HV system.



Fig. 4. Nine-channel master board prototype

Table 2

Summary of hardware components in the upgraded UF–PNPI high voltage system

Component	Quantity
Nine-channel master board	52
Distribution board – 30 channels	216
Distribution board – 36 channels	138
Independently regulated and monitored HV distribution channels	11 448

3. Upgrade of the CMS muon trigger

The overall aim of the CMS muon trigger (MT) upgrade is to implement a flexible maintainable system, capable of being adapted to the evolving CMS physics program. The main conceptual changes in the design of the muon trigger are as follows:

- improving the ability to reduce the output data stream due to the quality of track processing without significantly affecting the efficiency,
- using the calorimetric trigger data to implement the tail clip algorithm.

The main technology changes may be summarized as

- the present VME-based electronics is replaced with MicroTCA, the modern telecom standard;
- the system widely uses the latest generation of FPGAs, Xilinx Virtex 7, in a reduced number of common platforms;
- the parallel copper links are replaced with serial optical links, so the link speeds are increased from 1 to 10 Gb/s;
- the look-up memory address field for p_T assignment is increased from 22 to 30 bit.

A schematic of the present MT and the upgraded MT (MTU) systems is shown in Fig. 5. In the present MT, the data of local tracks from the front-end electronics of the drift tubes (DT FE), cathode strip chambers (CSC FE), and resistive plate chambers (RPC FE) are sent to the regional track finder processors (DT TF,

CSC TF), and to the RPC logic board (RPC LB). At this stage, the muon tracks are processed separately in each of the systems, while the CSC and DT processors exchange the data related to their overlap region at $0.8 \leq |\eta| \leq 1.25$. Three regional track finders sort identified muon candidates and transmit them to the global muon trigger (GMT) up to four (CSC TF, DT TF) or eight (RPC LB) candidates every bunch crossing. Each candidate is assigned a p_T and quality code, as well as an (η, ϕ) position in the muon system.

In the upgraded MT, the data from the DT, CSC, and RPC front-end arrive at three upgraded TFPs in parallel, where powerful computing facilities of the modern technology process muon tracks and send the results to the GMT. Separately, the overlap zone is allocated by the overlap TFP (OVL TF), where the data from all three muon subsystems are processed. Also, the calorimetric trigger data (CAL) are implemented for the tail clip algorithm.

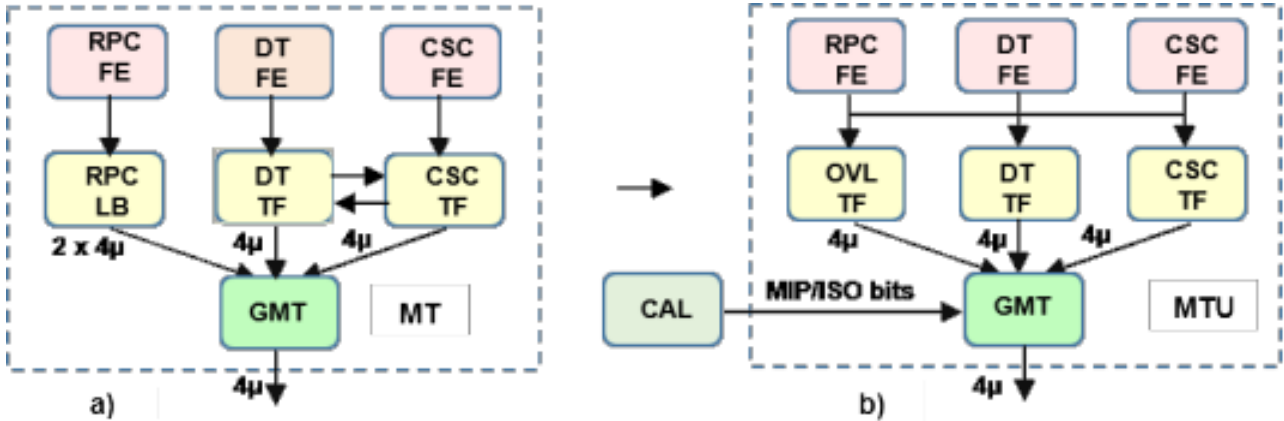


Fig. 5. Muon trigger systems: a – present; b – upgraded

The main element of the upgraded MT system is the TFP, which has a number of characteristics to meet the requirements of the CMS upgrade. The PNPI team is involved in development of the OVL TF elements. The infrastructure for the design and developing of the muon TFP parts has been created at PNPI. It includes a test stand for the electronics based on the MicroTCA standard. This stand can be used for further developments of new electronics systems.

The realization of the CMS MT upgrade program offers a large increase in flexibility of the MT. The address space for p_T assignment will be increased from 30 to 37 bit. The DDR4 memory is suitable for use in the trigger and allows reaching very large memory sizes (64 GB). This increased flexibility is accomplished by using high bandwidth. The use of optical links allows the architecture to be readily changed, while large FPGAs (field-programmable gate array) allow algorithms to evolve as needed. At present, the Firefly optical links at 14 and 26 Gbps with ultrascale FPGA are under tests.

4. Cathode strip chambers aging studies

The general objective of the aging studies is to assess the radiation resistance of the muon chambers (CSC) in view of the planned increase of the integrated luminosity from the present value of 200 up to 3 000 fb^{-1} , with the accumulated charge level reaching 0.4 C per 1 cm of the anode wires. Besides, there is an intention to modify the gas mixture in the CSCs. At present, this gas mixture is 40% Ar + 50% CO_2 + 10% CF_4 . The main purpose to have CF_4 in the gas mixture is to ensure the radiation resistance of the detector. However, CF_4 is considered as a dangerous gas for ecology. It is an extremely stable gas which strongly absorbs infrared radiation at $\sim 8 \mu\text{m}$, and therefore it is capable to influence the greenhouse effect. Today, the CF_4 emission in the CMS detector is quite noticeable. The equivalent of a daily CF_4 emission in the global warming potential units (GWP) for all CSCs is about 12 t of CO_2 , with a lifetime of $\sim 50\,000$ years. Our goal is to consider a possibility either to reduce the amount of CF_4 in the gas mixture

or to replace it with some eco-friendly gas. In both cases, we should guarantee sufficient radiation resistance of the CSCs.

Within this program, two CSC prototypes were manufactured at PNPI for the aging studies. The electric field structure and the construction materials were identical to those in the CSCs operating in the CMS detector. One prototype was filled with the nominal CMS gas mixture 40% Ar + 50% CO₂ + 10% CF₄, while the mixture 37% Ar + 61% CO₂ + 2% CF₄ with the reduced fraction of CF₄ was used in the second prototype. The prototypes were irradiated with an intense β -source ⁹⁰Sr ($E_{\beta} \approx 2.28$ MeV). The ⁹⁰Sr electrons have the energy comparable to the energy of the electrons irradiating the CMS muon tracker.

The control of the signal amplitude stability during the aging run was performed with the help of a ⁵⁵Fe source ($E_{\gamma} = 6$ keV) placed above thin windows in the cathode panels at three control points D, E, and F along the irradiated anode wires. The size of the irradiation zone was ~ 4 cm along the wires. The point E was in the centre of this zone, while the points D and F were at ± 6 cm distance from the point E. The radiation doze was defined as the averaged over the irradiated zone charge collected on 1 cm of the anode wires. This doze was up to 1.36 C/cm for the prototype with the nominal CMS gas mixture and up to 0.39 C/cm for the prototype with the modified gas mixture. The behaviour of the signal amplitudes in terms of the normalized gas gain is shown in Fig. 6. One can see that the gas gain remains stable in all controlled points up to the maximal collected radiation dozes. The dark currents measured during these aging tests did not demonstrate their growth capable to effect the detectors performance. So, according to these local irradiation tests, the reduction by a factor of five of the CF₄ fraction in the gas mixture is acceptable. This conclusion should be confirmed in large area irradiation tests to be carried out at the Gamma Irradiation Facility at CERN.

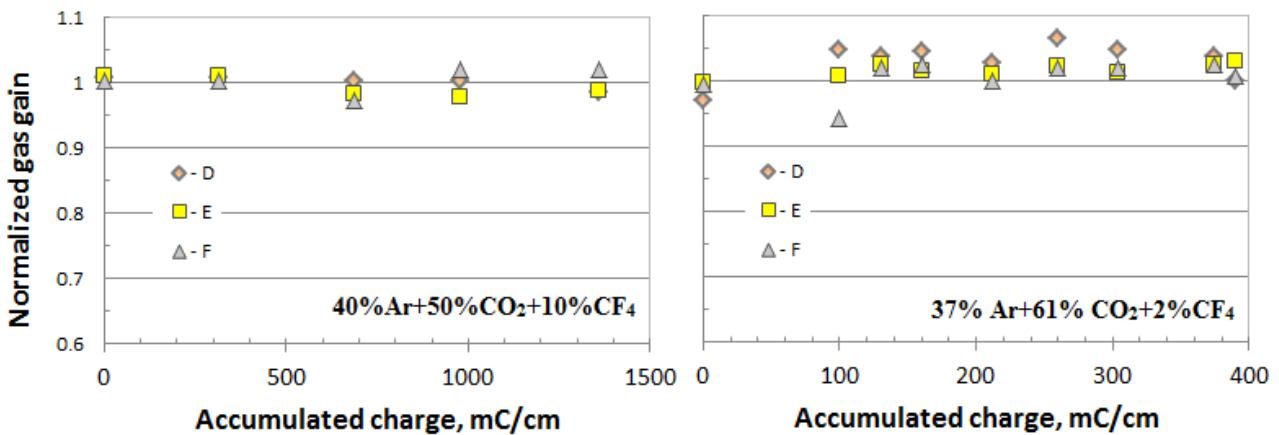


Fig. 6. Dependences of the gas gain on the accumulated charge for two aging runs: with a standard CSC gas mixture (*left panel*) and with a modified gas mixture with five times diminished fraction of CF₄ (*right panel*)

A new promising result was obtained on the way to find a replacement for CF₄. Using a CSC prototype, a new eco-friendly gas mixture 38.8% Ar + 58.2% CO₂ + 3% C₃H₂F₄ was explored. The hydrofluoroolefine (CF₃CH=CHF) has an extremely low GWP: GWP < 1. Figure 7 (*left panel*) shows the measured gas gain in the new gas mixture. Figure 7 (*right panel*) presents the ⁵⁵Fe count rate dependence on the high voltage. The gas gain was evaluated as the ratio of the ⁹⁰Sr current in the gas amplification mode (HV > 1000 V) to the ⁹⁰Sr ionization current at HV ≤ 700 V. Figure 7 (*right panel*) demonstrates the efficiency plateau. A working point for this gas mixture is achieved at HV ≈ 3850 V with the gas gain equal to 5 · 10⁵, both values being consistent with those in the presently operating CMS muon system. That means that the implementation of the new gas mixture would not require any changes in the HV system and in the readout electronics.

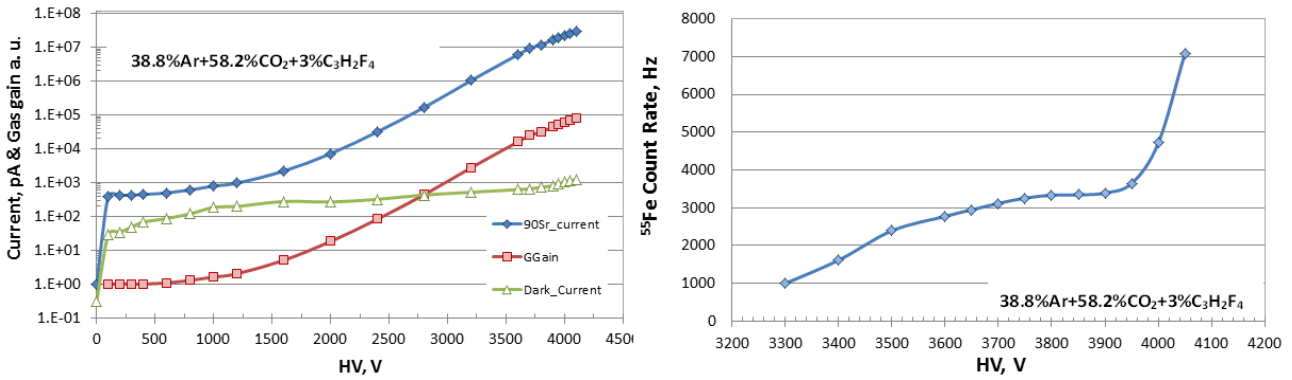


Fig. 7. Gas gain versus the high voltage (*left panel*). ^{55}Fe count rates versus the high voltage (*right panel*). Both measurements were performed with the 38.8% Ar + 58.2% CO_2 + 3% $\text{C}_3\text{H}_2\text{F}_4$ gas mixture

An amplitude spectrum of the ^{55}Fe X-rays measured at $\text{HV} = 3850 \text{ V}$ is shown in Fig. 8 (*left panel*). The position of the 6 keV peak corresponds to the collected charge of 800 fC. Figure 8 (*right panel*) demonstrates the dependence of the gas gain on the fraction of $\text{C}_3\text{H}_2\text{F}_4$ in the gas mixture. It follows from this figure that, in order to be within the limits of the existing CMS HV system ($\text{HV}_{\text{max}} = 4000 \text{ V}$), the fraction of $\text{C}_3\text{H}_2\text{F}_4$ in the gas mixture should not exceed 3%. The next decisive step will be aging tests of the CSCs filled with the 38.8% Ar + 58.2% CO_2 + 3% $\text{C}_3\text{H}_2\text{F}_4$ gas mixture.

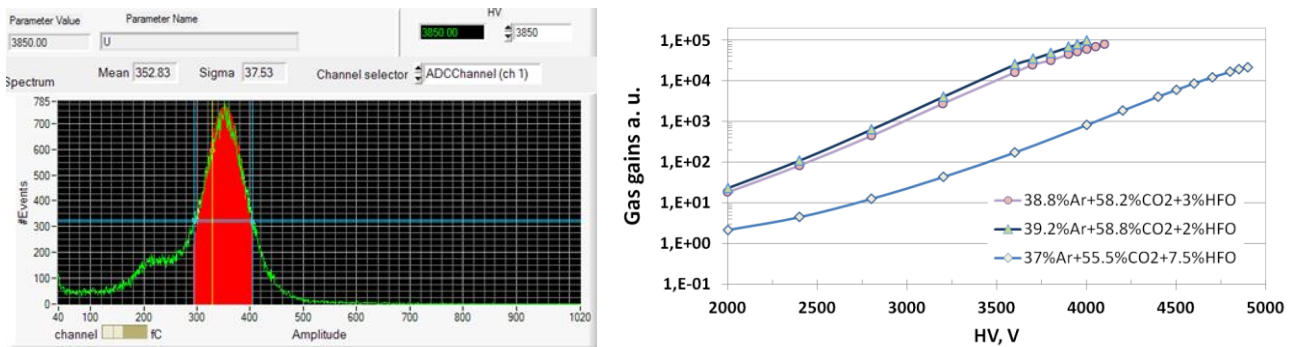


Fig. 8. Amplitude spectrum of ^{55}Fe X-rays ($E_\gamma = 6 \text{ keV}$) measured at $\text{HV} = 3850 \text{ V}$ (*left panel*). Gas gain versus high voltage for different fractions of $\text{C}_3\text{H}_2\text{F}_4$ in the gas mixture (*right panel*)

5. Summary

PNPI has made important contributions to the design and construction of the EMU of the CMS detector and shares responsibility for the EMU maintenance and operation. During the whole running period of the LHC (2010–2018), EMU demonstrated very reliable operation at the luminosity up to $2 \cdot 10^{34} \text{ cm}^{-2} \cdot \text{s}^{-1}$, which exceeds the initially designed value by a factor of two. In fact, EMU proved to be one of the most reliable systems in the CMS detector.

The goal of the EMU upgrade program is to prepare EMU to work for the next 15 years with higher luminosity (up to $7 \cdot 10^{34} \text{ cm}^{-2} \cdot \text{s}^{-1}$). PNPI participates in this program in the following tasks:

- 1) assembling of CSCs for the ME4/2 muon station (completed in 2017),
- 2) upgrade of the muon trigger (completed in 2018),
- 3) upgrade of the high voltage system (to be completed in 2020),
- 4) aging studies of the muon chambers,
- 5) search for a new eco-friendly gas mixture for the muon chambers.

UPGRADE OF THE ATLAS DETECTOR

PNPI participants of the ATLAS Collaboration:

A.E. Basalaev, S.G. Barsov, A.E. Ezhilov, V.T. Grachev, O.L. Fedin, M.P. Levchenko, V.P. Maleev, Yu.G. Naryshkin, S.K. Patrichev, V.A. Schegelsky, V.M. Solovyev

1. Introduction

The Large Hadron Collider (LHC) complex will be upgraded in 2019–2020 (the second Long Shutdown – LS2) to improve some parts of the accelerator complex. These improvements will result in the luminosity increasing to $5 \cdot 10^{34} \text{ cm}^{-2} \cdot \text{s}^{-1}$ (with luminosity leveling) [1]. It is the so-called HL–LHC stage. The integrated luminosity with this ultimate upgrade will be 300 fb^{-1} per year. The ATLAS experiment [2] was designed for a broad physics programme, including the capability of discovering the Higgs boson over a wide mass range and performing searches for the production of heavy particles that would indicate physics beyond the Standard Model (SM), such as supersymmetric particles, as well as searches for other massive objects. In order to take advantage of the improved LHC operation, the ATLAS detector should be upgraded to have better performance at higher luminosity, following the same schedule as the LHC upgrade. Figure 1 shows an approximate timeline for the planned LHC and ATLAS upgrades.

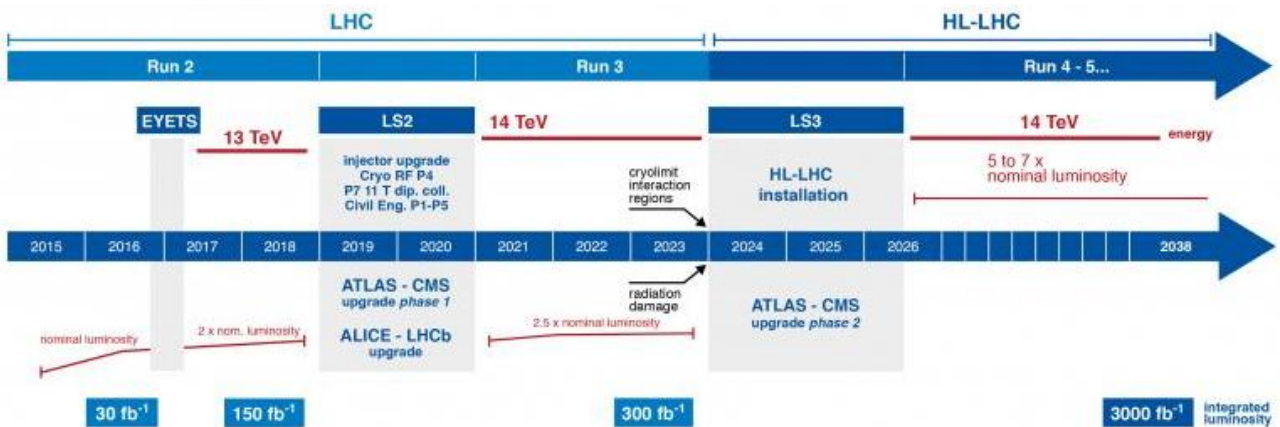


Fig. 1. An approximate timeline for LHC and ATLAS planned upgrades

The main focus of the Phase I ATLAS upgrade (2019–2020) is on the level-1 trigger. The objective is to sharpen the trigger threshold turn-on as well as discriminate against background while maintaining the low transverse momentum (p_T) threshold for single leptons and keeping the level-1 rate at a manageable level.

The upgrades are planned for both the muon and the calorimeter trigger systems, without which the single lepton level-1 triggers would have to be either pre-scaled or p_T threshold increased, resulting in a significant loss of acceptance for many interesting physics processes. The Phase II upgrade of ATLAS includes a full replacement of the central tracking system, as well as major upgrades of the trigger and readout systems.

The discovery of the Higgs boson at a mass of about 125 GeV has engendered detailed studies of the nature of the new boson. Continuing these studies with higher statistics and higher energy will be a major topic for the forthcoming upgraded LHC physics programme [3]. The ATLAS detector will be used to probe new physics beyond the SM – such as the precise measurements of the Higgs coupling to gauge bosons and fermions and studies of Higgs rare decays ($H \rightarrow \mu\mu$, Higgs self-coupling, *etc.*), together with a comparison with the SM expectations. While high luminosity will provide more data, it is essential that the ATLAS detector would still be able to operate in the higher background environment and while maintaining its performance as good as that at lower luminosities.

2. Upgrade of the ATLAS muon spectrometer

The Phase I upgrade of the ATLAS muon spectrometer [4] focuses on the end-cap region. Figure 2 shows a common view of the ATLAS detector with elements of the muon spectrometer pointed out and a cross section of it in the z - y plane. The barrel system covers the η region of $|\eta| < 1.0$, whereas the end-cap system covers the $1.0 < |\eta| < 2.7$ for muon tracking and $1.0 < |\eta| < 2.4$ for the level-1 trigger. The barrel and end-cap systems consist of three stations each, measuring the muon momentum based on the curvature in the ATLAS toroid magnets.

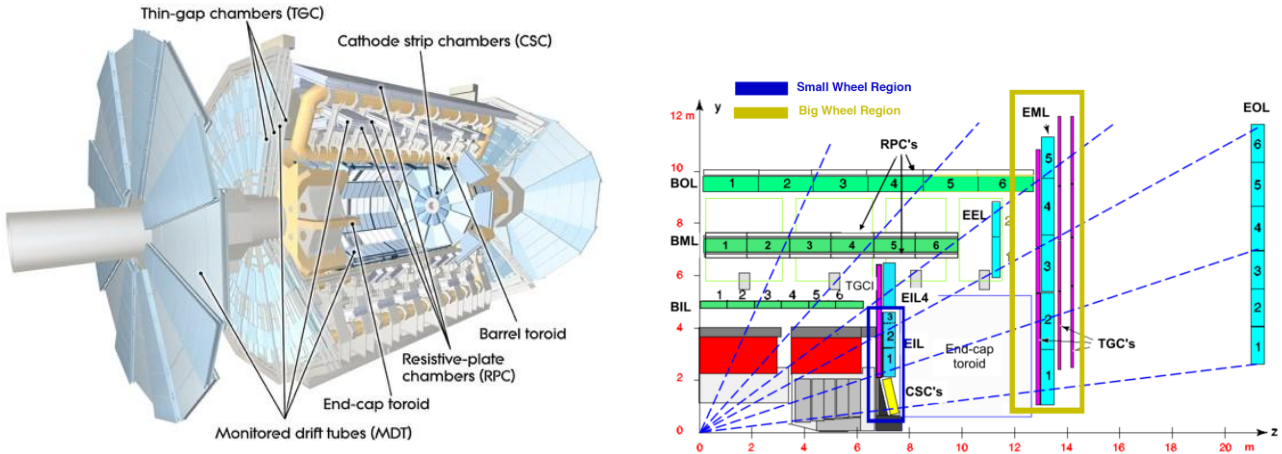


Fig. 2. The ATLAS detector: common view (*left*); the cross section of 1/4 (*right*)

At high luminosity the following two points are of particular importance:

- The performance of the muon tracking chambers (in particular in the end-cap region) degrades with the expected increase of the cavern background rate. An extrapolation from the observed rates at the lower luminosity conditions of the 2012 run to high luminosity and high energy conditions indicates a substantial degradation of the tracking performance, both in terms of efficiency and resolution in the inner end-cap station (at $z = 7$ m), the so-called Small Wheel. Given that the high resolution muon momentum measurement crucially depends on the presence of the measured points at the Small Wheel level (*i. e.* in front of the end-cap toroid magnet), this degradation is detrimental for the performance of the ATLAS detector.
- The level-1 muon trigger in the end-cap region is based on the track segments in the thin gap chambers (TGC) of the middle muon station (endcap muon detector – EM) located after the end-cap toroid magnet. The transverse momentum p_T of the muon is determined by the angle of the segment with respect to the direction pointing to the interaction point. A significant part of the muon trigger rate in the end-caps is background. Low energy particles, mainly protons, generated in the material located between the Small Wheel and the EM station, produce fake triggers by hitting the end-cap trigger chambers at an angle similar to that of real high p_T muons. An analysis of the 2012 data demonstrates that approximately 90% of the muon triggers in the end-caps are fake. As a consequence, the rate of the level-1 muon trigger in the end-cap is eight to nine times higher than that in the barrel region. The TGC of the Small Wheel is currently only used for the measurement of the azimuthal coordinate, complementary to the radial coordinate measured by the monitored drift tubes (MDT).

Both of these two issues represent a serious limitation on the ATLAS performance beyond the design luminosity: a reduced acceptance of good muon tracking and an unacceptable rate of fake high p_T level-1 muon triggers coming from the forward direction. In order to solve the two problems together, ATLAS proposes to replace the present muon Small Wheel with the New Small Wheel (NSW). The NSW is a set of precision tracking and trigger detectors able to work at high rates with an excellent real-time spatial and time resolution. These detectors can provide the muon level-1 trigger system with online track segments of good

angular resolution to confirm that muon tracks originate from the interaction point. In this way the end-cap fake triggers will be considerably reduced. With the proposed NSW the ATLAS muon system will maintain the full acceptance of its excellent muon tracking at the highest LHC luminosities expected. At the same time, the level-1 low p_T (typically $p_T > 20$ GeV) single muon trigger rate will be kept at an acceptable level. The design of the NSW meets the requirement for a very good segment angle resolution of 1 mrad at the level-1 trigger. The background in the NSW high track density environment can be heavily suppressed using this angular resolution. It is also an important step towards a further improvement of the muon level-1 trigger system foreseen in the Phase II upgrade for even higher luminosity. For the Phase II upgrade the level-1 latency will be increased so that more selective triggers from the calorimeter and the new level-1 track trigger as well as the muon system can be applied. The Phase II upgrade will substantially improve the p_T resolution of the level-1 muon trigger, sharpening the threshold turn-on and reducing the contribution from muons of lower p_T below the nominal threshold. This will be achieved by using information of the precision tracking detectors MDT as part of the muon end-cap trigger system and by combining it with the segment angle provided by the NSW.

3. Requirements for the New Small Wheel

The performance of the detector that replaces the current one should be at least as good at high luminosity as that of the current detector at low luminosity. It should, therefore, be able to measure the transverse momentum p_T of passing muons with a precision of 10% for 1 TeV muons in the full pseudorapidity coverage of the Small Wheel (up to $|\eta| = 2.7$). In particular, such a detector should have the following characteristics [5]:

- It has to reconstruct track segments with a position resolution in the bending plane better than 50 μm , to match the performance of the current MDT system. This will ensure that the muon spectrometer has the momentum resolution better than 10% at $p_T \approx 1$ TeV. This performance should not degrade even if a considerable fraction of the detected hits are caused by background particles or if some detector planes are not operational. The required segment position resolution results in a better than 100 μm resolution per plane for the planned four-layer multi-plane detector that may replace the Small Wheel.
- Segment finding efficiency should be better than 97% for muons with p_T greater than 10 GeV (the segment finding efficiency for the current MDT system).
- Efficiencies and resolutions should not degrade at very high momenta (due to δ rays, showers, *etc.*).
- It should measure the second coordinate with a resolution of 1–2 mm to facilitate good linking between the track reconstructed in the muon spectrometer and the track reconstructed in the inner detector for the combined muon reconstruction.

Furthermore, in the lifetime of the detector, detection planes may fail to operate properly, with very limited opportunities for repairing them. Hence, a multi-plane detector is required. Any new detector that might be installed in the place of the current Small Wheel should be operational for the full lifetime of ATLAS.

Performance studies using collision data have shown the presence of unexpectedly high rates of fake triggers in the end-cap region. Figure 3 shows the η distribution of candidates selected by the ATLAS level-1 trigger as muons with at least 10 GeV. The distribution of those candidates that indeed have an offline reconstructed muon track is also shown, together with the muons reconstructed with $p_T > 10$ GeV. More than 80% of the muon trigger rate is from the end-caps ($|\eta| > 1.0$), and most of the triggered objects are not reconstructible offline. Figure 3 also illustrates the tracks for triggering. Tracks C and B are fake tracks and need to be eliminated. Trigger simulations show that selecting muons with $p_T > 20$ GeV at level-1 (L1_MU20) one would get a trigger rate at $\sqrt{s} = 14$ TeV and at an instantaneous luminosity of $3 \cdot 10^{34} \text{ cm}^{-2} \cdot \text{s}^{-1}$ of approximately 60 kHz, to be compared to the total available level-1 rate of 100 kHz.

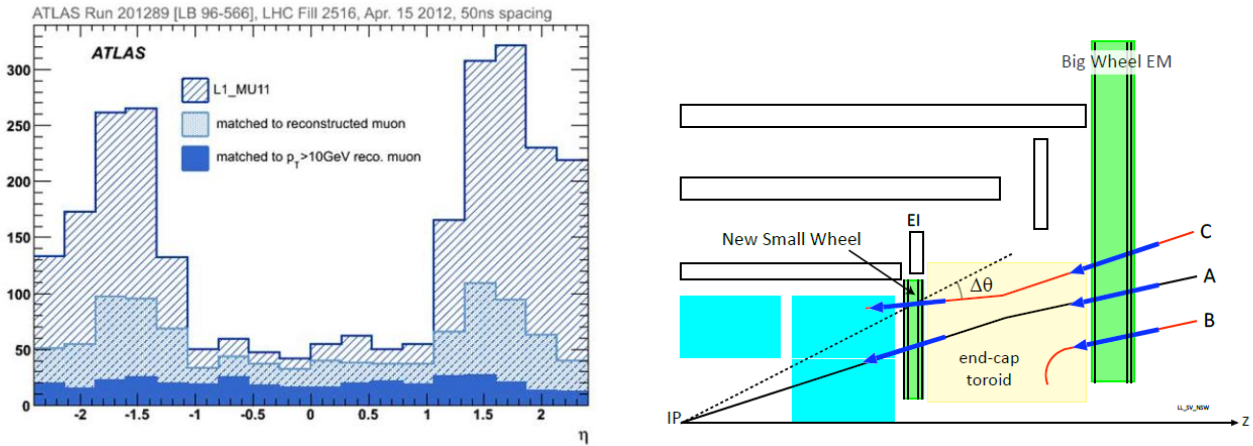


Fig. 3. The rate of the muons (*left*): the L1 trigger rate for $p_T > 11$ GeV (*dashed histo*); the rate of the muons matched to any reconstructed muon (*light blue histo*); the rate of the muons matched to a reconstructed muon with $p_T > 10$ GeV (*deep blue histo*). The illustration of the track for triggering (*right*)

In summary, to reduce the muon level-1 trigger rate to the level of 20 kHz for muons with $p_T > 20$ GeV, the new Small Wheel triggering detector should provide trigger track segments with the following requirements on their quality:

- Track segment information should arrive at the Sector Logic (the muon trigger electronics that combine information from various detectors to provide one or more regions of interest per bunch crossing) not later than 1.088 microsecond after a collision (the current delay of the Big Wheel TGC).
- Track segment reconstruction for triggering should have an angular resolution of 1 mrad (rms) or better.
- Track segments should have a granularity better than 0.04×0.04 in the η - ϕ plane to match the one of the current muon trigger system.
- Track segments should be reconstructed online with high efficiency in the full η coverage of the detector ($1.3 < |\eta| < 2.5$).
- The online track segment reconstruction efficiency should be more than 95%.

4. New Small Wheel layout

The proposed NSW detector system is designed to meet all the requirements above. The NSW consists of 16 detector planes in two multilayers. Each multilayer comprises four small-strip TGC (sTGC) and four Micromegas (MM) [6] detector planes. The sTGC are primarily deployed for triggering given their single bunch crossing identification capability. The detectors are arranged in such a way (sTGC–MM–MM–sTGC) as to maximize the distance between the sTGCs of the two multilayers. As online track hits are reconstructed with a limited precision, the increased distance between the detector multilayers leads to an improved online track segment angle reconstruction resolution. Hence, this detector configuration is optimal for the online track resolution. The MM detectors have exceptional precision tracking capabilities. The choice of eight planes per detector was dictated by the need to provide a robust, fully functional detector system over its whole lifetime. The main issues that have been addressed are operation in a high background environment and detector deterioration with time and their influence on the track segment reconstruction efficiency and resolution. Background neutrons and photons as well as δ rays spoil a number of hits from real tracks. With eight planes per detector, tracks will be reconstructed reliably and with high precision under these conditions. In addition, the NSW is expected to operate for the whole life of the ATLAS experiment. The large number of planes will ensure an appropriate detector performance even if some planes fail to work properly. Access and repair opportunities will be rare and, particularly after LS3, activation issues will severely limit the scope of any possible interventions. Furthermore, it may be required for long-term stability reasons to operate

the detector planes with their high voltage settings lower than is optimal for full efficiency. Eight planes per detector will once more ensure an overall efficiency close to 100% both for online and offline track reconstruction. The two NSW detector technologies also complement each other for their corresponding primary functions. The sTGC may contribute to offline precision tracking, as they are able to measure track hits with a resolution better than 150 μm (depending on the incident track angle). For triggering, experience has shown that redundancy is highly important in the forward direction at high luminosities. The MM detectors will be employed as a trigger in addition to the sTGC to provide improved redundancy, robustness and coverage of the forward trigger.

5. Thin gap chambers

The basic sTGC structure is shown in Fig. 4. It consists of a grid of 50 μm gold-plated tungsten wires with a 1.8 mm pitch, sandwiched between two cathode planes at a distance of 1.4 mm from the wire plane. The cathode planes are made of a mixture of graphite and acrylic resin with a typical surface resistivity of 100 $\text{k}\Omega/\text{cm}^2$ sprayed on a 100 μm thick G-10 plane, behind which there are strips (that run perpendicular to the wires) on one side and pads (covering large rectangular surfaces) on the other side on a 1.6 mm thick printed circuit board with the shielding ground on the opposite side. The strips have a 3.2 mm pitch. The basic detector design for the NSW has two quadruplets 35 cm apart in z . Each quadruplet contains four TGCs, each TGC contains wires, strips, pads and a readout system. The pads are used to produce a 3-out-of-4 coincidence to identify muon tracks roughly pointing to the interaction point. They are also used to define which strips are to be readout to obtain a precise measurement in the bending coordinate for the online muon candidate selection. The azimuthal coordinate, where only about 10 mm precision is needed, is obtained from grouping wires together. The charges of all strips, pads and wires are readout for offline track reconstruction.

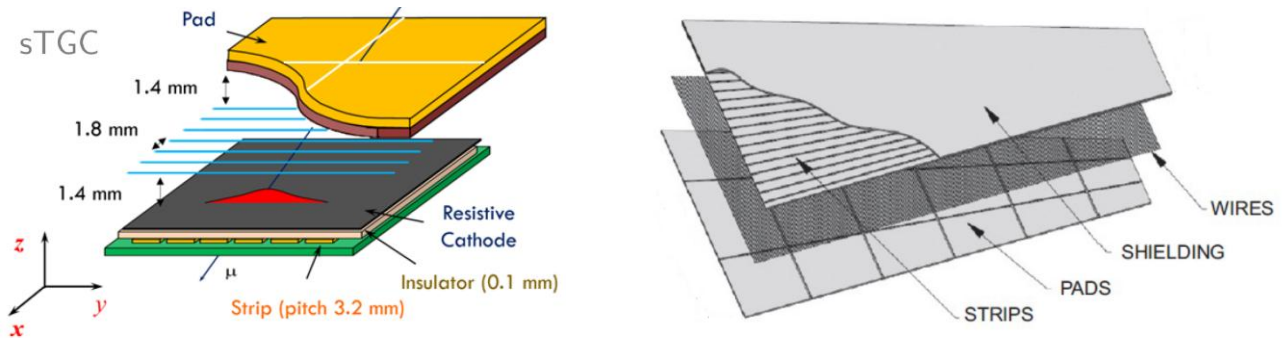


Fig. 4. Internal structure of the sTGC

Beam tests of a full size sTGC prototype were performed in May 2014 at Fermilab [7]. The test utilized a pixel telescope to precisely track the incident point of 32 GeV pions on the sTGC quadruplet and compare it to the measured position in each of the four sTGC detection planes. A moveable x - y table was used to expose different regions of the sTGC detector to the particle beam. The calibration of the electronics, tracking and alignment of the pixel telescope allowed the extraction of the intrinsic sTGC detector resolution of around 60 μm in the best case for perpendicular tracks.

The ATLAS muon end-cap detectors are expected to be exposed to 1 C/cm^2 of the accumulated charge during the 15 years of operation in Run-3 and beyond. Therefore, it is important to study the long term effects of radiation exposure on sTGC detectors. A prototype sTGC measuring 10 cm \times 20 cm was used to test the signal quality after a total accumulated charge of 10 C/cm^2 . This is an equivalent radiation dose to that of 150 LHC years. No signs of ageing were found [8].

The results of these tests are presented in Fig. 5.

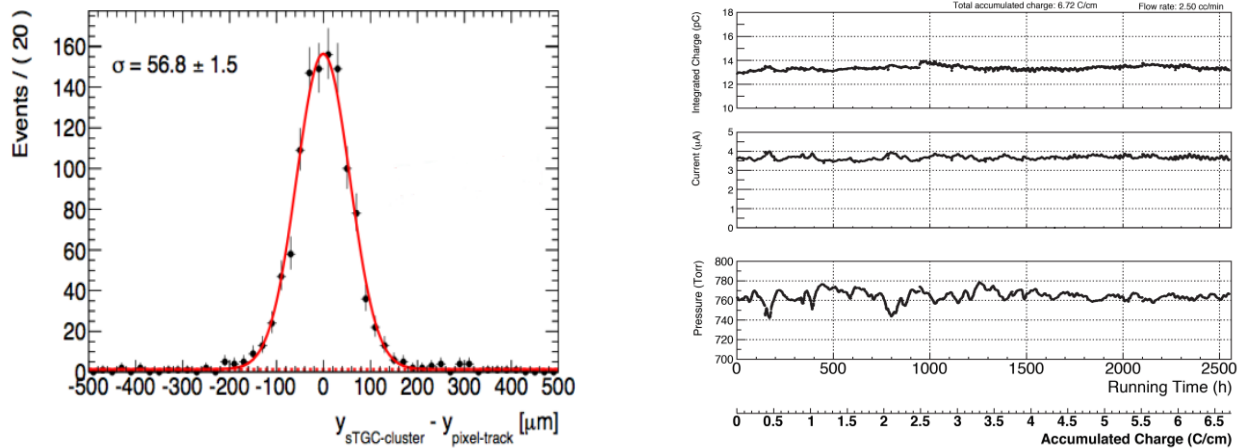


Fig. 5. Spatial resolution of a single sTGC plane measured at the Fermilab test beam in 2014 (*left*). The result of the irradiation test of the sTGC prototype (*right*)

6. Production

To construct the basic quadruplets, five assembly sites were selected – Israel, Canada, China, Chile, and Russia (PNPI). Each site should be equipped with a large set of the required equipment. The basic equipment for constructing and testing the detectors at each production site consists of the following:

- a resistive coating spraying system placed in a well-controlled environment facility with the temperature 25° C and the humidity < 30%;
- a set of 4–5 flat (< 20 μm deviation from flatness) granite tables, with at least one of them in a clean room;
- a vacuum system to be used as part of the granite tables;
- a gas mixing system to test the detectors during various phases of construction;
- a computer controlled winding machine that can apply pre-tension (400 gr) during the winding of the gold-plated tungsten wire on two detectors;
- a number of rotating carriages on which liquid glue can be applied to gas seal the single planes;
- a vertical x – y scanning device to perform an irradiation of single-plane detectors to control their gas amplification uniformity;
- various jiggling devices for precision placement of the planes during assembly;
- a complete set-up to scan the fully constructed quadruplets with cosmic rays, with full readout, to compute local efficiencies and position resolution.

PNPI is responsible for production of the full set (144 single planes) of QL3 quadruplets, which are the biggest ones of the sTGC modules. In 2015–2017, the facility fully equipped with all necessary appointments were built at PNPI. Figure 6 (*left*) presents the sTGC assembly facility at PNPI. The precision granite tables are seen. Figure 6 (*right*) shows the process of the wire soldering on a sTGC plate after winding.

In 2017 pre-production prototype (Module-0) was successfully assembled and tested. Figure 7 presents an assembled Module-0 placed at the X-ray station for testing (*left*) and the result of the testing of that Module-0 (*right*).



Fig. 6. sTGC assembly facility at PNPI (*left*); the soldering of the winded sTGC plate on the winding machine (*right*)

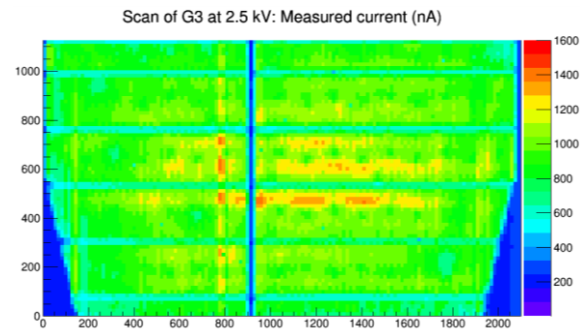
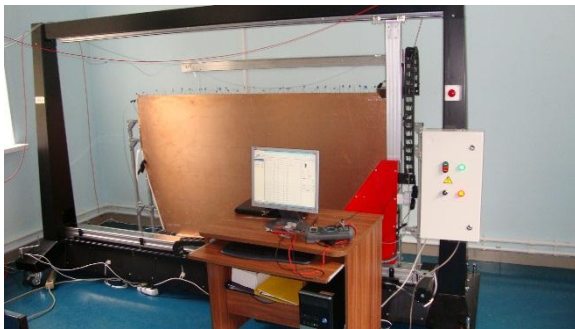


Fig. 7. sTGC Module-0 at the X-ray test station (*left*); the result of the X-ray scanning of the Module-0 (*right*) shows dependence of the current vs position of the X-ray tube

7. Conclusion

The NSW will make significant and necessary improvements to enable triggering and tracking of muons in the forward region of the ATLAS with a reasonable safety margin. It is a crucial upgrade to maintain the ATLAS physics program for Run-3 and beyond.

The sTGC detectors will provide the muon spectrometer with excellent triggering and tracking capabilities. The construction protocol has been validated by test beam measurements on a full-size prototype showing the performance requirements are met.

References

1. L. Rossi, O. Brüning, Tech. Rep. CERN-ATS-2012-236, CERN (2012).
2. ATLAS Collaboration, JINST **3**, S08003 (2008).
3. ATLAS Collaboration, ATL-PHYS-PUB-2012-004, CERN (2012).
4. ATLAS Muon Spectrometer: Technical Design Report. CERN/LHCC/97-22, CERN (1997).
5. ATLAS Collaboration, NSW TDR, CERN-LHCC-2013-006, ATLAS-TDR-020 (2013).
6. G. Iakovidis, JINST **8**, C12007 (2013).
7. A. Abusleme *et al.*, Nucl. Instrum. Meth. A **817**, 85 (2016).
8. M. Gignac *et al.*, PoS ICHEP 2016, 853 (2016).

UPGRADE PROGRAM OF THE LHCb DETECTOR AT THE LARGE HADRON COLLIDER

PNPI participants of the LHCb Collaboration:

B.V. Bochin, N.F. Bondar, A.D. Chubykin, S.A. Gets, V.L. Golovtsov, V.T. Grachev, V.S. Kozlov, S.N. Kotryakhova, Z.G. Kudryashova, O.E. Maev, P.V. Neustroev, E.M. Spiridenkov, V.I. Tarakanov, L.N. Uvarov, S.S. Volkov, A.A. Vorobyev

1. Introduction

The LHCb experiment [1] was designed for precision measurements of CP violation and rare decays of b - and c -flavored hadrons, exploiting unprecedented high rates of the charm and beauty hadrons produced in the forward direction. The experiment is currently operating at a luminosity of $4 \cdot 10^{32} \text{ cm}^{-2} \cdot \text{s}^{-1}$, which is twice the design value but still significantly below what the Large Hadron Collider (LHC) can provide. The limitations are due to the LHCb detector capability to run with high data rates. A scheme of luminosity leveling has been devised where the beams are slightly displaced from head-on collisions and gradually re-centered during the fill as the beam intensity is reduced. This allows the experiment to collect data at a constant luminosity throughout the fill.

The goal of the LHCb upgrade program is to enable the experiment to run at a luminosity of $2 \cdot 10^{33} \text{ cm}^{-2} \cdot \text{s}^{-1}$. Moreover, there will be the radically modernized acquisition system, which should allow to read out data at the rate of 40 MHz into a flexible software-based trigger [2]. All sub-detectors of LHCb will be redesigned to comply with these new operating conditions. This will increase the event yields by a factor of ~ 10 for muonic and by a factor of ~ 20 for hadronic final states.

The LHCb upgrade will take place in the second Long Shutdown (LS2) of the LHC, currently scheduled to begin in December 2018 and will continue in 2024 (LS3) after three-four years of running after LS2. Figure 1 shows a scheme of the upgraded LHCb detector.

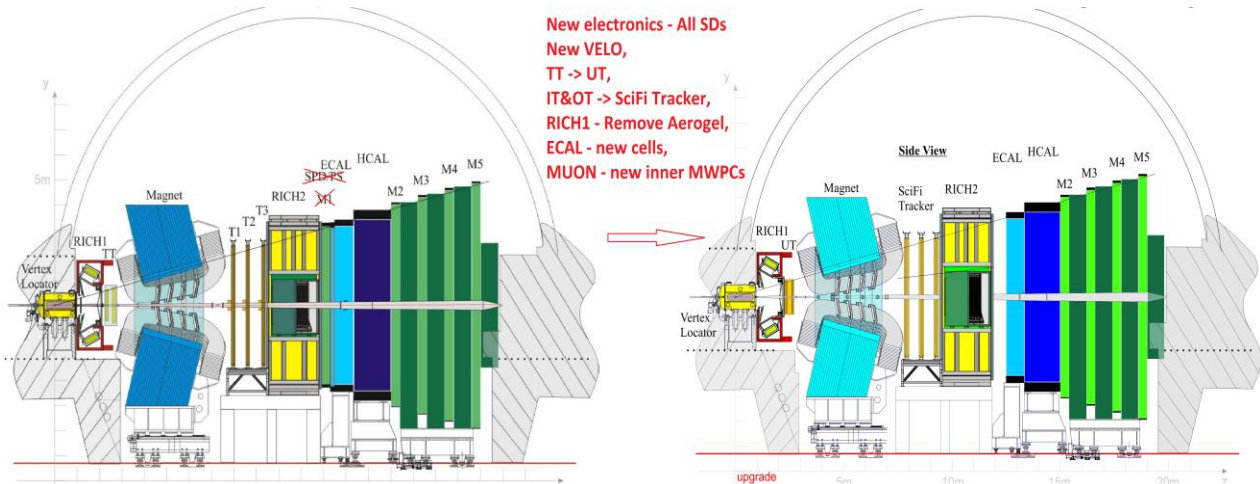


Fig. 1. Side view of the present LHCb detector on the left and after the upgrade on the right

Particularly, all sub-detectors will replace or modify full chains of electronics to be able to accept the 40 MHz data rate (now it is 1 MHz). The vertex locator (VELO) will be replaced by newly designed L-shape modules, that comprise $55 \times 55 \mu\text{m}^2$ pixel sensors with micro channel CO_2 cooling able to sustain ~ 400 Mrad dose accumulated in 10 years. The tracking system presently includes three detectors: tracker turicensis (TT), inner tracker (IT), and outer tracker (OT). It will be replaced with new detectors: upstream tracker (UT), constructed as a silicon strip detector, and SciFi tracker, comprising three planes, each plane made of a stack of round $250 \mu\text{m}$ scintillator fibers.

The particle identification system will be changed much less than the detectors mentioned above [3]. This system includes: the Cherenkov detectors (RICH-1 and RICH-2); the calorimeter system with the pre-

shower (PS), the silicon pad detector (SPD), and the electron (ECAL) and hadron (HCAL) calorimeters; and finally, five muon stations. Both RICHs will use new 64 channel multi anode photomultiplier tube. Additionally, silica aerogel, which is now used as a radiator together with C_4F_{10} , will be removed from RICH-1, and the optics will be improved too. For the calorimeter system two detectors, PS and SPD, will be removed completely. Both are used mostly for suppression in hardware-based low level trigger (L0) and become useless with the new software-based low level trigger (LLT). In addition, ECAL plans to replace the inner cells during LS3 due to expected aging. The first station (M1) of the muon system will be removed because of losing its role in the new LLT due to very high occupancy. The rest four stations remain equipped with the same muon chambers as it is now, except for the replacement of the multi-wire proportional chambers (MWPCs) in very-inner regions in stations M2 and M3 with new high-granularity pad muon chambers to accept very high rates in these regions under upgrade conditions [4].

In the past, PNPI made major contributions into the design and construction of the LHCb muon system. About 600 large MWPCs and a 2000-channel high voltage (HV) supply for the MWPCs were produced at PNPI. The PNPI group plays an important role in the LHCb operation and in the permanent technical support of the muon detector.

The main PNPI responsibility in the LHCb upgrade program is design and production of new high-granularity pad muon chambers for the inner regions in the M2 and M3 muon stations. Also, PNPI should produce about 30 spare MWPCs for the other regions of the muon detector and an additional 2000-channel HV system.

2. LHCb muon detector

The LHCb muon detector [1, 5] consists of five stations (M1–M5) placed along the beam axis. The first station, M1, is located in front of the calorimeters and is important for the p_T measurement at the earliest trigger level; the remaining four stations, M2–M5, are placed behind the hadron calorimeter and are interleaved with the iron walls that act as muon filters. Each station is divided into four regions (R1–R4), as shown in Fig. 2. In total, the muon detector is equipped with 20 types of muon chambers. The MWPCs are used in all regions, except the most irradiated region R1 of the M1 station, where the triple-GEMs (gas electron multipliers) were adopted. The detector comprises 1380 chambers – 1368 MWPCs and 12 GEMs. Each muon chamber installed in the M2–M5 stations consists of four layers of MWPCs (four gaps). The M1 station is equipped with 264 two-gap MWPCs. A summary of the chambers installed in stations M2–M5 is presented in Table 1.

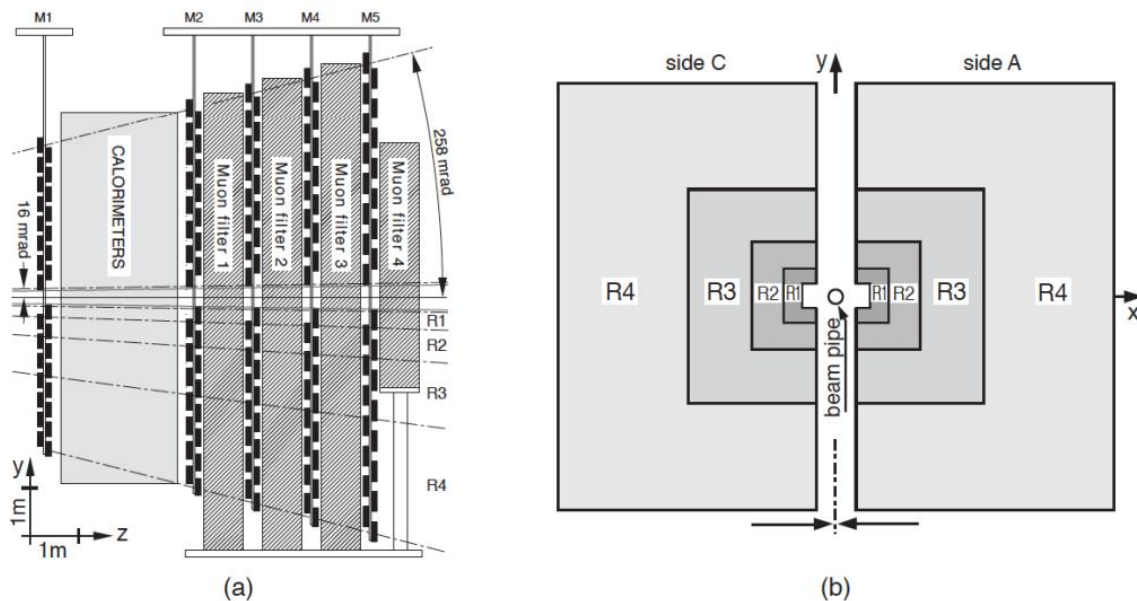


Fig. 2. Side view of the LHCb muon detector (a); layout of a muon station with the four regions R1–R4 (b)

Each chamber gap is independently powered with HV. In total, the muon detector contains 4 944 gaps of 19 different types of MWPCs. The main parameters in all MWPCs are the same: the anode wire planes are centered in a 5 mm gas gap and consist of 30 μm diameter gold-plated tungsten wires with a 2 mm spacing. All MWPCs are filled with an Ar/CO₂/CF₄ (40 : 55 : 5) gas mixture. The gas gain ranges between $4.6 \cdot 10^4$ and $8.8 \cdot 10^4$, depending on the HV settings applied to the chamber gaps.

Table 1

Muon chambers installed in stations M2–M5*

Station	Region	MWPC Quantity	Production site	Sensitive area, mm ²	HV system
M2	R1	12	CERN	30.2 x 24.8	CAEN
M2	R2	24	CERN	60.0 x 25.2	CAEN
M2	R3	48	Italy	120 x 25	PNPI
M2	R4	192	PNPI	120 x 25	PNPI
M3	R1	12	CERN	32.2 x 27.2	CAEN
M3	R2	24	CERN	64.8 x 27.2	CAEN
M3	R3	48	Italy	129.6 x 27	PNPI
M3	R4	192	PNPI	129.6 x 27	PNPI
M4	R1	12	CERN	34.8 x 28.8	CAEN
M4	R2	24	Italy	69.6 x 29.2	CAEN
M4	R3	48	Italy	139.2 x 29	PNPI
M4	R4	192	PNPI	138.6 x 29	PNPI
M5	R1	12	CERN	37.2 x 31.2	CAEN
M5	R2	24	Italy	74.4 x 31.2	CAEN
M5	R3	48	Italy	148.8 x 31	PNPI
M5	R4	192	Italy	148.8 x 30.9	PNPI

* Each muon chamber comprises four layers of MWPCs (four-gaps MWPCs). Each of the 4 416 muon chamber gaps has an individual HV supply channel.

3. Upgrade of the muon detector

The main requirement for the upgraded muon detector is to guarantee a high reconstruction and identification efficiency for muons, while keeping the misidentification of pions and other particles as low as possible, up to luminosities of $2 \cdot 10^{33} \text{ cm}^{-2} \cdot \text{s}^{-1}$. The existing front-end electronics ensures already the readout at 40 MHz *pp*-collision rate provided by the LHC in order to supply information to the current L0-muon trigger. On the other hand, the off-detector readout electronics develops full hit information (position and time) only at the rate of 1 MHz, and it will be replaced by the new modules adopted to the fast communication protocol based on the Gigabit transceiver chip set. This part is already under production.

1. *Spare muon chambers.* One of the important tasks included in the upgrade program is providing the muon detector with enough amount of spare MWPCs for the regions not considered to be renewed in the LS2 and LS3 periods. This is obligatory to guarantee a safely running of the experiment in the next 10 years of the operation. Based on the results of revising the amount and quality of the available spare chambers [6], it was decided to build 54 new spare MWPCs. This work was shared between PNPI and the Italian institutes, with 26 MWPCs to be produced at PNPI. By the end of 2017, all the MWPCs were manufactured and delivered to CERN where they were passing through the final dressing and testing procedures.

2. *High voltage supply for the muon chambers.* The muon stations M2–M4 contain 1 104 four-gaps MWPCs, that is 4 416 gaps in total. Most of the chambers (960 MWPCs) use the multi-channel HV supply

developed and constructed at PNPI. Ideally, each gap should have an individual HV channel. However, in the period of construction of the LHCb detector, PNPI could provide only a 2 000-channel HV supply to feed 3 840 gaps. Therefore, a part of the chambers was connected with the HV supply through a patch panel where one HV-channel provided the voltage for four gaps in parallel. One of the tasks in the LHCb upgrade program was to increase the number of the HV channels. This task was realized during the first Long Shutdown (LS1) in 2012–2013. The PNPI HV system was doubled, which made it possible to supply each of the 3 840 gaps with an individual HV channel. There are also plans to build an additional 600-channel HV system in order to replace the CAEN HV system which is used presently to feed the MWPCs in regions R1 and R2 (576 gaps, see Table 1).

3. *Expected rates in the upgrade conditions.* The main problem in the muon system, arising with the fivefold increased luminosity, is unacceptably high occupancy in the innermost regions M2R1, M2R2, and to some extent in M3R1. As mentioned above, the station M1 will be removed completely because of the very high occupancy. The limiting rate per readout channel is determined by the dead time of the readout electronics (80 ns). Moreover, in the readout scheme presently used in the central regions, the pad size is determined by a coincidence between signals in the anode and the cathode channels (the so called logical pads). Originally, this scheme was accepted to reduce the number of the readout channels. However, in operation at high rates, this scheme has serious disadvantages in comparison with the real cathode pad structure: much larger sizes of the anode and the cathode pads and the increased dead time (the sum of the inefficiencies in the anode and the cathode channels). The acceptable maximal rate per channel in such a scheme is considered to be 1.0 MHz, corresponding to $\sim 10\%$ inefficiency in this channel.

The expected rates at the increased luminosity were measured in a special run with a luminosity of $1 \cdot 10^{33} \text{ cm}^{-2} \cdot \text{s}^{-1}$. Note that in the upgraded LHCb detector, such rates should correspond to the luminosity of $2 \cdot 10^{33} \text{ cm}^{-2} \cdot \text{s}^{-1}$ due to an additional shielding which will be installed around the beam pipe in front of the M2 station and inside the inner part of HCAL. According to simulations, this shielding could reduce the background rates in the region M2R1 by a factor of two. The results of these measurements are presented in Fig. 3.

	Side A		Regions M2R1, M2R2		Side C			Side A		Regions M3R1, M3R2		Side C	
20	302663	374490			401158	271102	20	77566	97227			118352	65080
19	524944	815930			831945	491761	19	148087	316459			311144	139793
18	850038	836838	1575700	1402105	923495	795164	18	211310	220330	785773	668611	281269	207133
17	1370280	2617875			2439212	1304907	17	435607	1010902			1036103	432612
16	1300391	2030252			2317691	1238855	16	372444	744335			958077	345666
15	650499	1076075	1704608	1951677	1043499	840785	15	262900	344181	999767	909640	335410	261077
14	396774	715329			870635	476684	14	131363	271380			313515	124087
13	298870	369692			409313	273128	13	74675	124384			123763	67813

Fig. 3. The measured rates in the anode readout channels at the luminosity of $L = 1 \cdot 10^{33} \text{ cm}^{-2} \cdot \text{s}^{-1}$ in regions M2R1 and M2R2 (*left panel*) and in regions M3R1 and M3R2 (*right panel*). Regions R1 and R2 comprise 12 MWPCs and 24 MWPCs, respectively. The numbers indicate the maximal rate in the anode channels in each chamber. The *red colour* shows the chambers with the rates exceeding 1 MHz/channel

As is seen in Fig. 3, the expected rates exceed the allowable limits, especially in regions M2R1 and M2R2. Therefore, it was decided to replace in these regions the MWPCs with logical pads by the MWPCs with real cathode pads, taking into account the requirement that the external dimensions should repeat the dimensions of the existing chambers. The latter requirement presents some problems, as there is very limited space for the on-board electronics due to the increased number of the readout channels. In the frame of this project, the PNPI team made a design of a high granularity cathode pad MWPC and constructed and tested a prototype of a chamber for the M2R2 region.

4. *Design of high granularity cathode pad MWPCs.* Figure 4 shows the pad structure of the proposed cathode pad MWPCs in comparison with the design of the existing chambers. The readout of the existing chambers in regions M2R1, M2R2, and M3R1 is organized in the following way: the cathode plane is

divided into 64 pads and the anode wires are grouped by forming 48 anode channels. The coincidence between signals from the anode and the cathode pad channels forms 384 or 192 logical channels, depending on the OR-ing of the signals from the cathode pads (see Fig. 4). In the new design, there are 192 pads with the readout from each pad. There is no readout from the anode wires at all. The geometry parameters of the existing and the proposed chambers are given in Table 2.

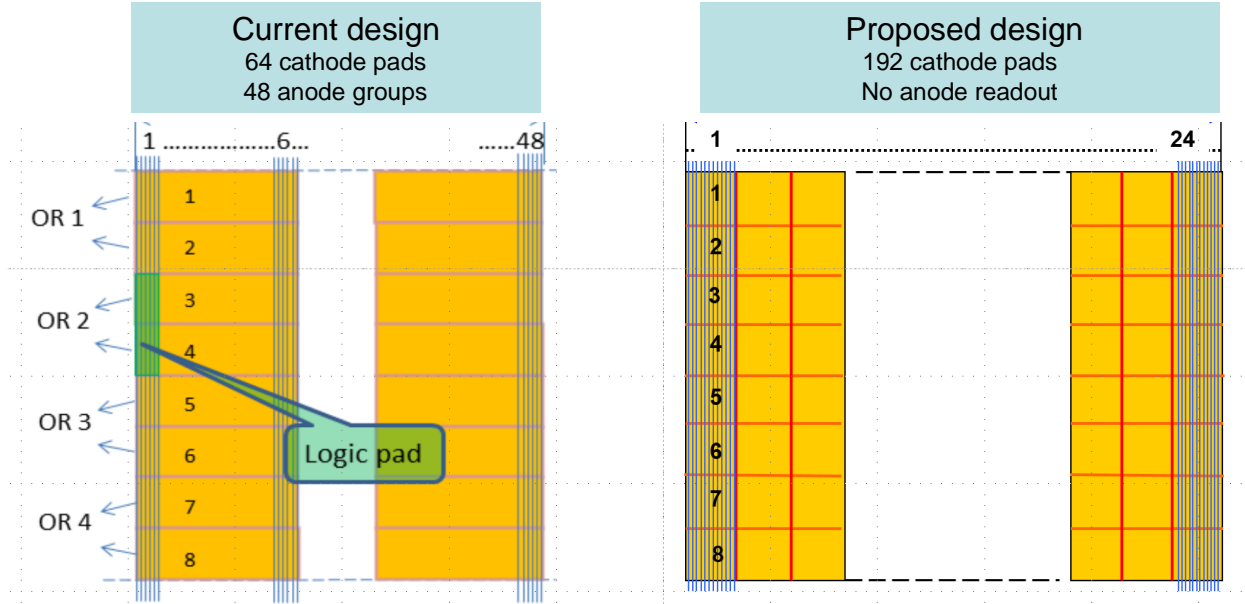


Fig. 4. The pad structure of the existing (left panel) and proposed (right panel) MWPCs for regions M2R1, M2R2, and M3R1

Table 2

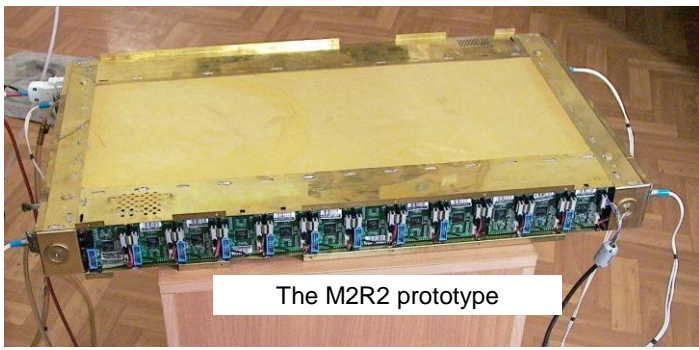
The geometry parameters of the existing and proposed chambers

Region	Sensitive area, mm	Existing chambers					Proposed chambers			
		Cathode pad geometry	Number of pads	Wire pad width, mm	Number of wire pads	Number of logic pads	Cathode pad geometry	Pad size, mm	Number of pads	Cathode plane size, cm
M2R1	308 × 253	8 × 8	64	6.3	48	384	24 × 8	12.8 × 31.6	192	37.5 × 31.3
M2R2	612 × 253	8 × 8	64	12.5	48	192	24 × 8	25.5 × 31.6	192	75 × 31.3
M3R1	332 × 273	8 × 8	64	6.7	48	192	24 × 8	13.8 × 34.1	192	40.5 × 33.7

The size of the cathode pads in the proposed design is by a factor of four smaller than that of the anode pads in the existing chambers. Therefore, we can expect the corresponding reduction (by a factor of four or even more) of the rates per channel, which becomes well below the limiting rate of 1 MHz/channel even at the luminosity of $2 \cdot 10^{33} \text{ cm}^{-2} \cdot \text{s}^{-1}$. An additional advantage of the proposed scheme is the absence of the so called ghost events, typical for the existing scheme with the logical pads in operation at high rates.

5. *Prototype of the high granularity pad chambers for the M2R2 region.* There are several restrictions in design of the new pad chambers coming from the present detector structure. First, the additional readout channels are to be equipped with the existing electronics. Second, all new chambers should be placed geometrically exactly in the positions occupied by the existing chambers. In addition, there will be much higher electrical power dissipation caused by the increased number of the front-end boards from 14 to 24. This means that better cooling should be provided for the inner regions. As an option, we intend to move the power regulators to the periphery of the detector.

A prototype of the new high granularity pad chambers for the M2R2 region was designed and



Anode –cathode distance	2.5 mm
Anode wires spacing	2.5 mm
Anode wire diameter	30 mkm
Cathode pad size	25.5 x 31.6 mm ²
Sensitive area	612 x 253 mm ²
Number of pads	192 pads

Fig. 5. General view and the main geometry parameters of the M2R2 prototype

A special care was taken to reduce the pad-to-pad and pad-to-sinal lines capacitances. This was done by introducing screening strips between the pads and between the signal strips, as it is shown in Fig. 6. Also, the thickness of the cathode plane was increased from 0.8 to 1.6 mm.

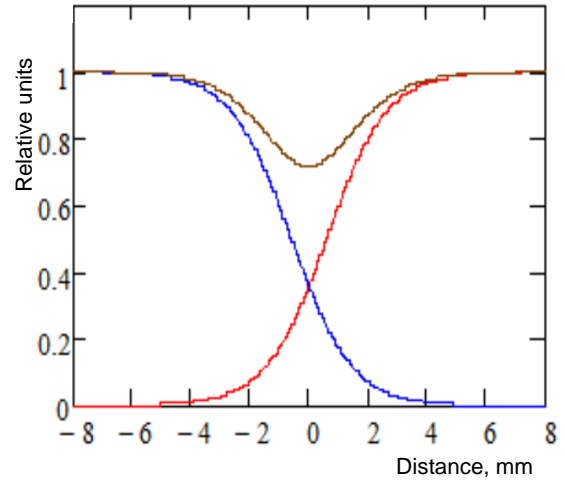
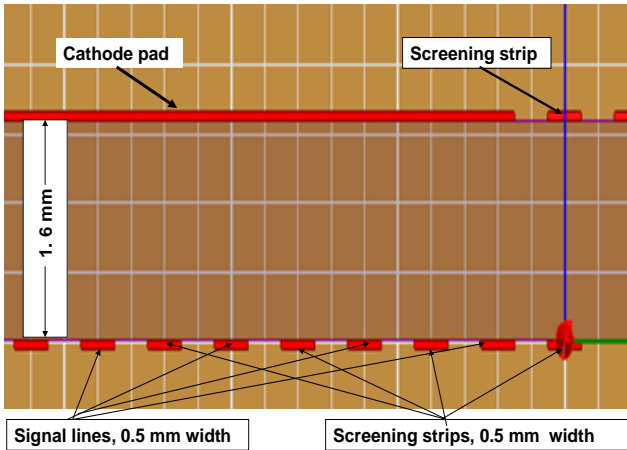


Fig. 6. Scheme of the cathode pads, the signal lines, and the screening strips (*left panel*). The results of the 3D modeling of the signals in the M2R2 prototype (*right panel*). The *red* and *blue* curves present the calculated charges induced on the neighbour pads in function on the distance of the ionization track from the centre of the screening strip in-between the pads. The *black curve* shows the sum of these charges. The dip at $x = 0$ reflects the charge induced on the screening strip

The performance of the M2R2 prototype was simulated using a GARFIELD package to generate the primary ionization data and a 3D simulation “Maxwell” software to establish the charge spatial distribution. One of the goals of this simulation was to compute the probability to trigger a signal on the pads neighbouring to the pad crossed by a particle under working conditions (cross-talk probability). This consideration showed that the main source for the cross-talk is sharing of the induced charge between two neighbouring cathode pads when the ionization track is close to the inter-pad region. For the M2R2 chamber, the cross-talk area was estimated to be ± 2.5 mm from the inter-pad centre (see Fig. 6), which corresponds to the 23% double-cluster probability. As to the cross-talk probability *via* the pad-to-pad and the pad-to-sinal lines capacitances, it was found to be quite low ($\sim 1\%$) for the considered cathode configuration.

In 2016, the M2R2 prototype was tested at a PNPI 1-GeV proton beam. The chamber demonstrated high operational stability. Figure 7 (*left panel*) presents the measured registration efficiency and the time resolution in the mode with all four gaps connected in “OR”. The beam of 1 mm size was set in the centre of

a pad in these measurements. The sharing of the induced charge on the neighbouring pads was measured by displacing the chamber across the beam. The results of this scan are shown in Fig. 7 (*right panel*). These results proved to be in satisfactory agreement with the mentioned above simulation.

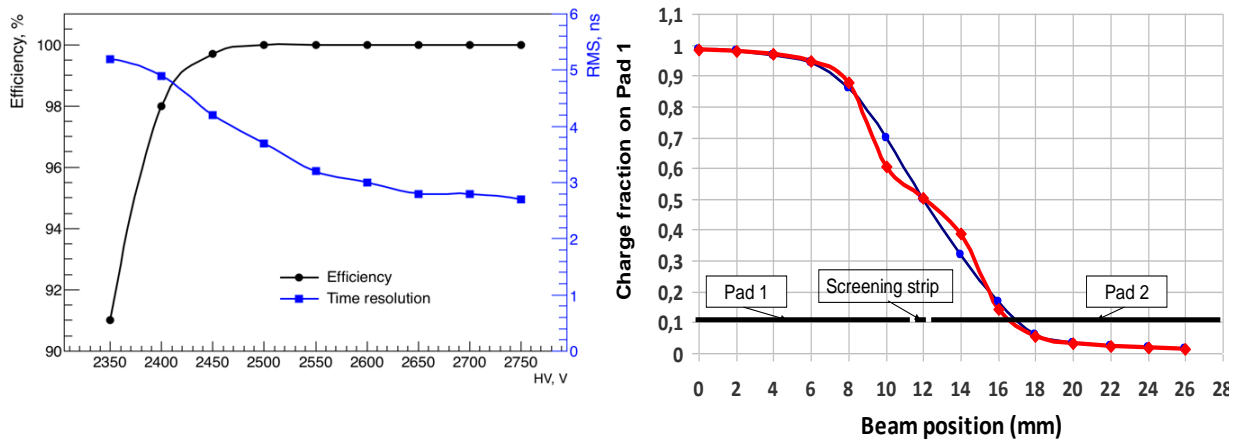


Fig. 7. Results of tests of the M2R2 prototype at a 1-GeV PNPI proton beam. *Left panel* – the registration efficiency in a 25 ns time window and the time resolution measured with four gaps connected in “OR”. *Right panel* – fraction of the charge induced on Pad-1 in function on the beam position relative to the centre of Pad-1 measured with the chamber displacements along the anode wires (*blue line*) and perpendicular to the anode wires (*red curve*)

4. Summary

The goal of the LHCb upgrade program is to enable the experiment to run at a luminosity of $2 \cdot 10^{33} \text{ cm}^{-2} \cdot \text{s}^{-1}$. To achieve this goal, all sub-detectors need essential modernization. The PNPI group is sharing responsibility for performance and modernization of the LHCb muon detector. The main problem arising in the muon detector with the increased luminosity is too high occupancy in the muon chambers in the central regions of Station-2 and Station-3. To solve this problem, the PNPI group suggested to replace the MWPCs in these regions (being used in a “logical pads” option) with specially developed high granularity cathode pad MWPCs. This should allow to reduce the occupancy in the readout channels by a factor of 3 to 4, which would be sufficient to run with the luminosity up to $2 \cdot 10^{33} \text{ cm}^{-2} \cdot \text{s}^{-1}$. An additional advantage of the proposed scheme is absence of the so called ghost events, typical for the existing scheme with the logical pads.

A prototype of the cathode pad MWPCs for the M2R2 region was constructed and successfully tested in the 1-GeV proton beam at PNPI. The LHCb Collaboration accepted the PNPI proposal to build such chambers for the M2R1, M2R2, and M3R1 regions, the work to be done in 2019–2020.

Two more responsibilities of PNPI in the LHCb upgrade program were: production of an additional 2000-channels HV system and production of 26 spare muon chambers for the regions which are not considered to be renewed in the LS2 and LS3 periods. By the end of 2017, both these tasks were completed. The HV system was delivered to CERN and installed into the muon detector system. The spare chambers were delivered to CERN for final dressing and testing procedures.

References

1. A.A. Alves Jr. *et al.*, JINST **3**, S08005 (2008).
2. LHCb Collaboration, LHCb Trigger and Online Upgrade Technical Design Report, CERN-LHCC-2014-016 (2014).
3. LHCb Collaboration, LHCb PID Upgrade Technical Design Report, CERN-LHCC-2013-022 (2013).
4. W. Baldini *et al.*, Pad Chambers for the Consolidation of the Muon Detector, LHCb-INT-2018-009 (2018).
5. LHCb Collaboration, A.A. Alves Jr. *et al.*, JINST **8**, P02022 (2013).
6. M. Anelli *et al.*, Status of Spare Chambers for the LHCb Muon Detector, LHCb-INT-2017-028 (2017).

UPGRADE OF THE ALICE DETECTOR

PNPI participants of the ALICE Collaboration:

V.V. Ivanov, A.V. Khanzadeev, E.L. Kryshen, M.V. Malaev, N.M. Miftakhov, V.N. Nikulin, Yu.G. Riabov, E.V. Roshchin, V.G. Ryabov, V.M. Samsonov, O.P. Tarasenkova, M.B. Zhalov

1. Introduction

ALICE is a general-purpose detector at the CERN Large Hadron Collider (LHC) aimed to study strongly interacting matter using proton–proton, nucleus–nucleus, and proton–nucleus collisions. Initially, it was designed as relatively low-rate detector, but after the Long Stop 2 of the LHC (LS2) the luminosity of the collider is expected to be increased by a factor of 10, and ALICE, as all the LHC detectors, should be upgraded.

In that time, the ALICE will focus on high precision measurements of heavy flavour hadrons, low-momentum quarkonia and low mass dileptons. This physics features a low signal to background ratio and requires large recorded samples of events. The goal is to gain the current statistics by a factor of 100 to the expected statistics in a 10 nb^{-1} integrated luminosity scenario. The measurement strategy is to read all events at the rate of 50 kHz for Pb–Pb (or equivalent 2 MHz event rate for pp collisions) with a minimum bias trigger, or even continuously. The on-line reduction with sophisticated selection criteria can be applied. The new functionality of the readout requires a new data acquisition (DAQ) system.

2. Overview of the ALICE detector upgrades

2.1. Data acquisition upgrade

The ALICE computing upgrade concept consists of transferring all detector data to the computing system. The data will be processed on the fly in parallel with the data collection. Its volume reduction will be performed by processing the data and not by rejecting complete events as do the high-level triggers. The data will be transferred from the detectors either continuously or by using a minimum bias trigger. The raw data will be replaced by the results of the local processing, like cluster finding, thus reducing the data volume.

The data calibration and data on-line reconstruction are performed synchronously with the data taking. At the second stage, the reduced data from all detectors are assembled in the events. In the end, the data will be stored in the grid system and will be available for data analysis.

This strategy will enable to study new classes of processes that do not have signatures that enable traditional triggers (*e. g.* B -meson production).

A dedicated ASIC GBTx has been developed for the DAQ.

2.2. Hardware upgrade

The main subsystems of the ALICE detector after upgrade are shown in Figs. 1 and 2. Some systems – the calorimeters EMCAL (electromagnetic), DCAL (double jet), and PHOS (photon), the transition radiation detector (TRD), the time-of-flight system, the muon tracking, and the muon identifier – will upgrade mostly their readout electronics (both front-end and back-end) to match the new DAQ requirements. The muon identifier will use the new front-end cards with the charge amplification to slow-down the resistive plate chambers (RPC) aging. PHOS will install two more charged particles veto modules.

The time projection chamber (TPC) will upgrade its detection system: the multiwire chambers will be replaced with the GEM-based readout.

The inner tracker system (ITS) and the fast interaction trigger (FIT) (which should overperform the existing T0 and V0 detectors), will be rebuilt from scratch.

A brand-new detector MFT (muon forward tracker) will be included as the vertex detector for the muon spectrometer.

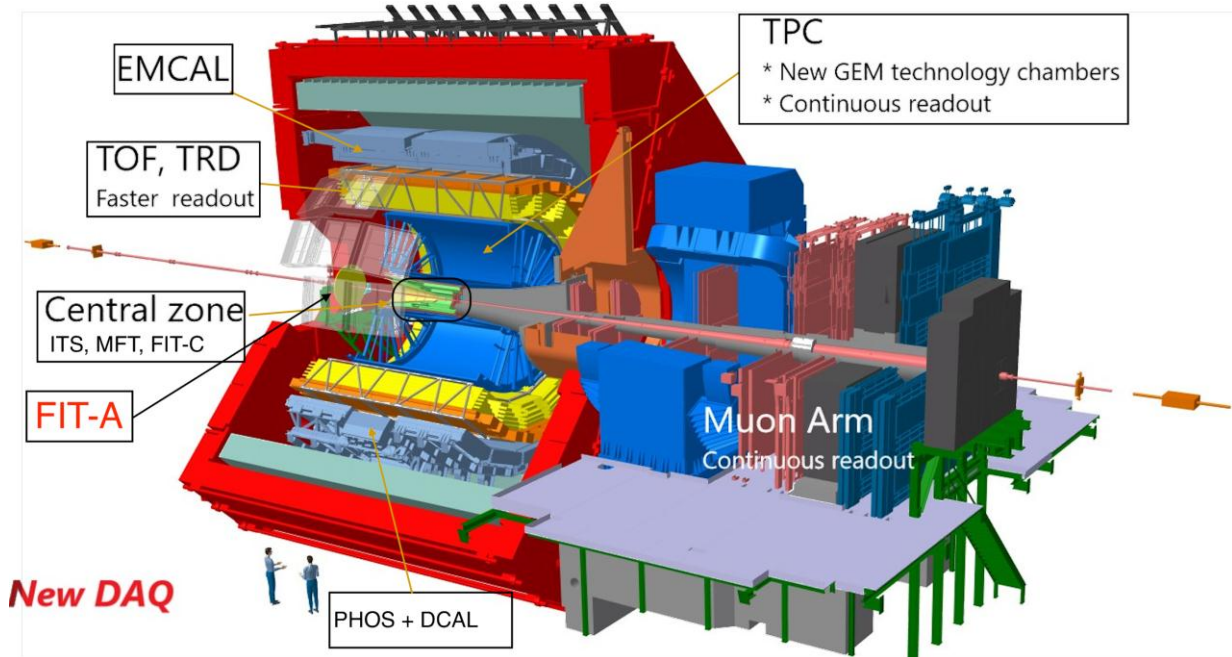


Fig. 1. The ALICE detector after upgrade during LS2. The central zone is presented enlarged in the following figure

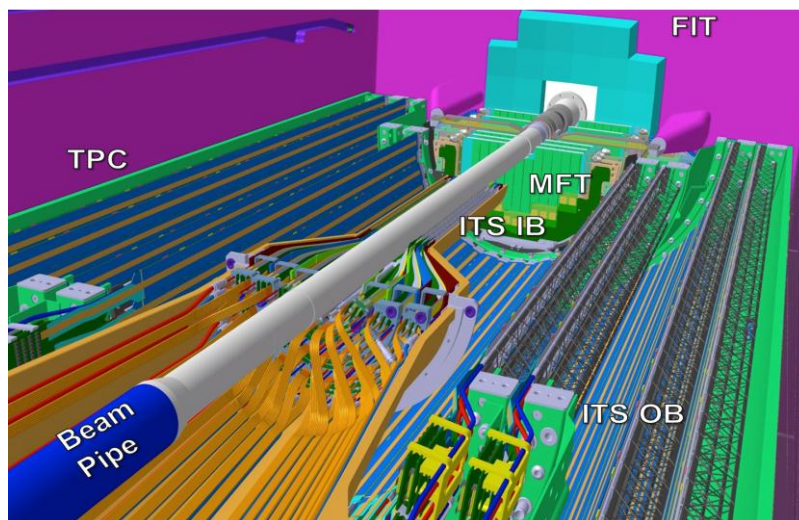


Fig. 2. Enlarged view on the central area of the previous figure: a zone of ALICE inside the TPC. The detectors shown: ITS – inner and outer barrels, the muon forward tracker – MFT, and a C-side part of the fast interaction trigger – FIT-C

2.2.1. Time projection chamber upgrade

Currently, the TPC readout is based on the triggered operation of a multiwire proportional chamber with a gate grid which prevents forming of a spatial charge due to the ion backflow. This charge causes an inefficiency of the chamber and brings to degradation of the vertex resolution from few mm up to one meter. Typically, the gating grid blocks the chamber by the time of about several hundred of microseconds. The intrinsic limitation of the readout rates is a few kHz. The system works well if the interaction and trigger rates are not too high.

The goal for Run-3 is to work at the rate of 50 kHz in case of Pb–Pb collisions, inspecting all tracks. At this rate, an average event spacing is about 20 μ s and therefore an average pileup is about five events. In this situation neither the triggered operation, nor the gating grid would help. The solution is to have

a continuous readout with gas-electron multipliers (GEMs) instead of proportional chambers. The spatial charge caused by the ion backflow could be minimized by highly optimized combination of standard and large pitch foils. This approach solves the problem of stable operation under the LHC Run-3 conditions, making ions at rear GEMs invisible for incoming electrons. The TPC upgrade Production Readiness Review was approved in March 2017, the mass production has been started.

The front-end electronics will be replaced with the new application specific integrated circuit (ASIC) SAMPAs (made with 130 nm TSMS CMOS technology), a common project with the muon spectrometer tracker upgrade. The data stream contains no headers, no markers, just raw values at sampling analog-to-digital converter (ADC) clock. Markers are required to indicate the start of the first ADC channel only. The front-end electronics is still under development, the PRR is scheduled for August 2018. The readout is based on the Gigabit transceiver x ASIC. A special slow control adapter is under development.

2.2.2. Fast interaction trigger

The FIT detector shown in Fig. 3 consists of two Cherenkov quartz radiator arrays coupled with the MCP-PMT sensors (denoted as T0A+ and T0C+) and a segmented scintillator ring V0+. As it was demonstrated during the beam tests, the upgraded T0 will keep excellent intrinsic time resolution ($\sigma \approx 20$ ps). The amplitude resolution of order 25% (full width at half maximum) gives a possibility to use it as a multiplicity monitor.

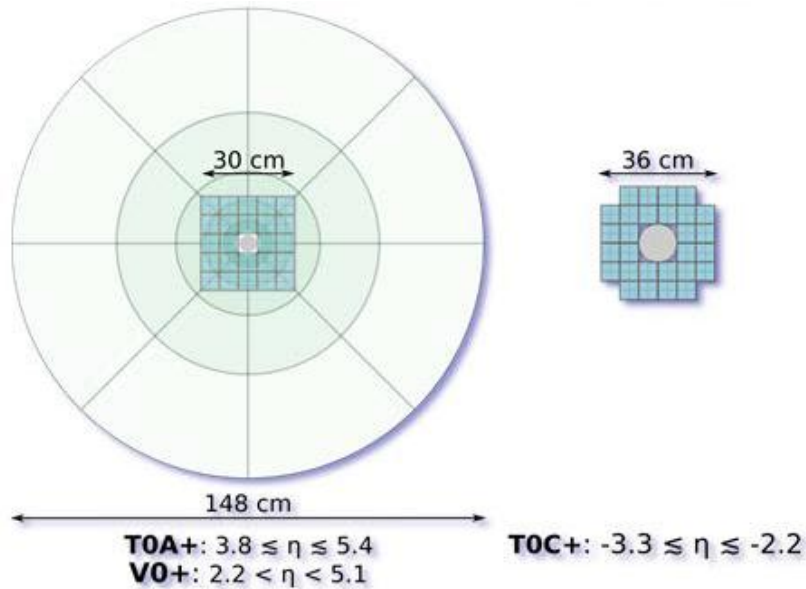


Fig. 3. FIT detectors: T0+ A, V0+ (left), and FIT-C (right)

The larger acceptance improves the detection efficiency of T0 for the pp events from ~ 30 to $\sim 90\%$ ($\sim 95\%$ for multiplicity of $N > 150$). The detector provides high precision time information that triggers the experiment and ensures good particle identification. The detector could be also used as an LHC luminosity monitor, to measure the charged particle multiplicity, and the azimuthal asymmetry. A pair of T0 detectors provides on-line information about the event vertex and allows to eliminate the background from beam-gas interactions.

The V+ detector consists of five rings segmented into eight equal sections. It covers larger acceptance and covers the rapidity gap between the existing ITS and V0. Due to employing of the scintillation counters without the wavelength shifters, it has a compromising time resolution and better ageing properties. The detector is well suited for measurements of the event centrality and event plane measurements.

2.2.3. Inner tracker system

The main detector requirements to preserve the particle inner detector (ID) capabilities for Run-3 include the high tracking efficiency and high resolution at low p_T -values. New ITS will be rebuilt completely to become a low-material, high resolution system. Last, but not least, the design of the new ITS will simplify the maintenance.

The new ITS will have several features aiming to improve the performance for low transverse momenta. The inner barrel will be closer to the beam: its radius will be reduced from 39 to 22 mm. The material budget of each layer will be reduced from $X/X_0 = 1.14$ to 0.3% due to the new sensors of 50 μm thickness and the new design of the supporting structure. The size of the pixels will be reduced from 50×425 to $27 \times 29 \mu\text{m}$. All these modifications will result in an improved vertex resolution, especially for low p_T events.

As for other detectors, a new readout and a new DAQ will be used in order to increase the readout event rate from 1 to 50 kHz and reduce the data size.

3. PNPI in ALICE detector upgrade – muon forward tracker

PNPI joined the ALICE muon spectrometer project from the very beginning, participating in the conception design, production, commissioning, and maintenance of its tracking chambers. The ALICE muon spectrometer consists of the front absorber and tracking and trigger systems. The 4.13-meter-thick absorber reduces the number of particles by two orders of magnitude, the track deviations in the magnetic field give the information about the momentum of the particle, the information in trigger chambers enables (in 600 ns) the fast trigger for transverse momentum of the muon. The inherent drawback of the design is large multiple scattering in the absorber (due to the thickness of about $60 X/X_0$) that does not allow to reconstruct the vertex of the detected event. The MFT is the vertex detector covering the muon spectrometer acceptance. Five planes of silicon pixel sensors will provide a good vertexing.

The reconstruction of the muon production vertex will allow to distinguish prompt particles produced in the nuclear interaction region and heavy unstable hadron decays. The prompt particles provide information about the medium and its evolution dynamics. MFT together with the central part of the detector will make ALICE unique for such kind of studies in a wide rapidity range. In particular, the new MFT detector will provide a possibility to study unreachable before processes and significantly improve previous results. Some examples of the most promising tasks for MFT are the following:

1. Study of the medium influence on the charmonium production including dissociation and regeneration effects. These studies will include reconstruction of J/ψ and $\psi(2C)$ production spectra and determination of the nuclear modification factors in a range up to almost zero transverse momentum.
2. Study of in-medium heavy quark thermalization processes. This will include measurements of the elliptic flow for charm particles up to low transverse momentum ($\sim 1 \text{ GeV}/c$), for beauty particles and prompt charmonium up to zero transvers momentum.
3. Estimation of the density of the produced matter and the mass dependence of parton energy losses in the deconfined medium. This will demand measurements of differential production spectra as a function of the transverse momentum for particles containing b and c quarks.
4. The dramatic improvement of the mass resolution for low mass mesons (from 60 to 15 MeV) should allow a more deep study of the nature of the deconfinement and chiral phase transitions. Such studies will include measurements of the quark–gluon plasma (QGP) thermal radiation and an analysis of low mass vector mesons spectral shape functions for possible modifications due to chiral symmetry restoration.

One can see in Fig. 4 clear modifications in dimuon invariant mass distributions in the charmonium mass region without MFT (*left*) and adding MFT to muon spectrometer (*right*). Though both the signal and the background are affected by the loss of statistics, a significant improvement of the S/B ratio for both J/ψ (*green line*) is reached. Even $\psi(2S)$ becomes visible in the right picture. As it was discussed, prompt charmonium production measurements are good probes of the QGP phase and will help in studies of such competing effects like dissociation due to colour screening of the heavy-quark potential in the deconfined quantum chromodynamic matter and recombination of charm and anti-charm quarks occurring at high densities of charm quarks formed in the initial stages of the collision.

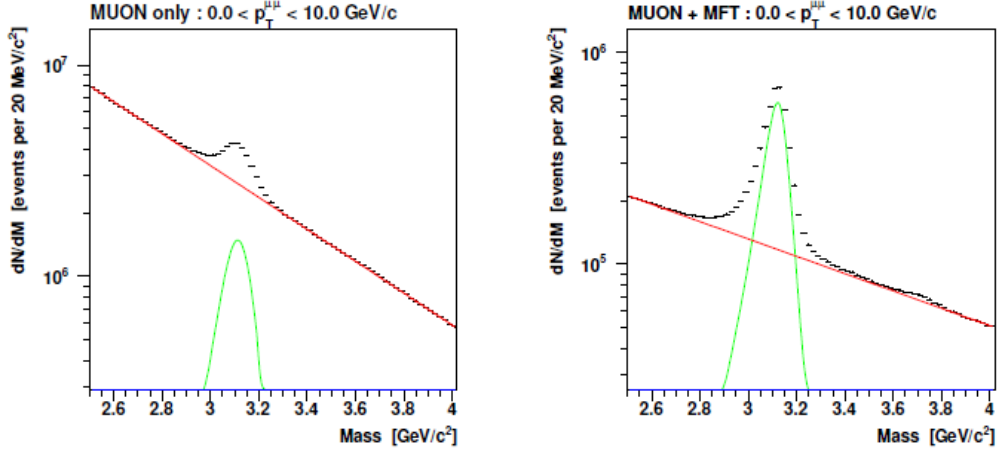


Fig. 4. Dimuon mass distribution in the charmonium region integrated in p_T , for 0–10% Pb–Pb collisions at $\sqrt{s_{NN}} = 5.5$ TeV, normalized to the expected statistics in a 10 nb^{-1} integrated luminosity scenario without the MFT (*left*) and with the MFT (*right*) [1]

Beauty production can be studied by measuring J/ψ from B -hadrons decay. Main contributors are B^+ , B^0 , B_s , and Λ_c . MFT will allow prompt/displaced J/ψ separation down to zero transverse momentum by measuring the pseudo-proper decay time associated to the secondary vertex (Fig. 5, *left*). Furthermore, beauty measurements at forward rapidity *via* displaced J/ψ will complement the measurements at the central rapidity *via* displaced D^0 and J/ψ , and exclusive B reconstruction (Fig. 5, *right*).

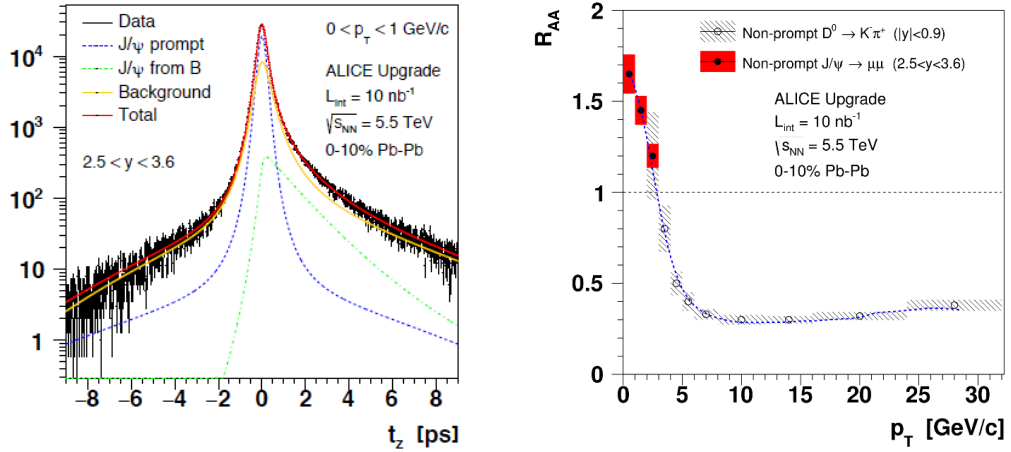


Fig. 5. *Left* – pseudo-proper decay length distributions for the prompt and displaced J/ψ samples, based on the measurement of the transverse distance between the primary and the J/ψ vertices [2]. *Right* – nuclear modification factors (R_{AA}) of beauty mesons measured *via* displaced J/ψ at the forward rapidity including the MFT detector – closed circles [2]; expected R_{AA} for D^0 mesons at the central rapidity – open circles; the expected total uncertainty is shown with filled or dashed area around circles

The MFT design is shown in Fig. 6. It consists of ten half-disks, two detector planes each. 920 silicon sensors are glued to 280 ladders of two to five sensors each. The total sensitive area is 0.4 m^2 . The detector covers the rapidity range of $-3.6 < \eta < -2.45$. A pixel chip ALICE pixel detector (ALPIDE), a common sensor for MFT and ITS, has been developed, its production is expected to be completed in 2018.

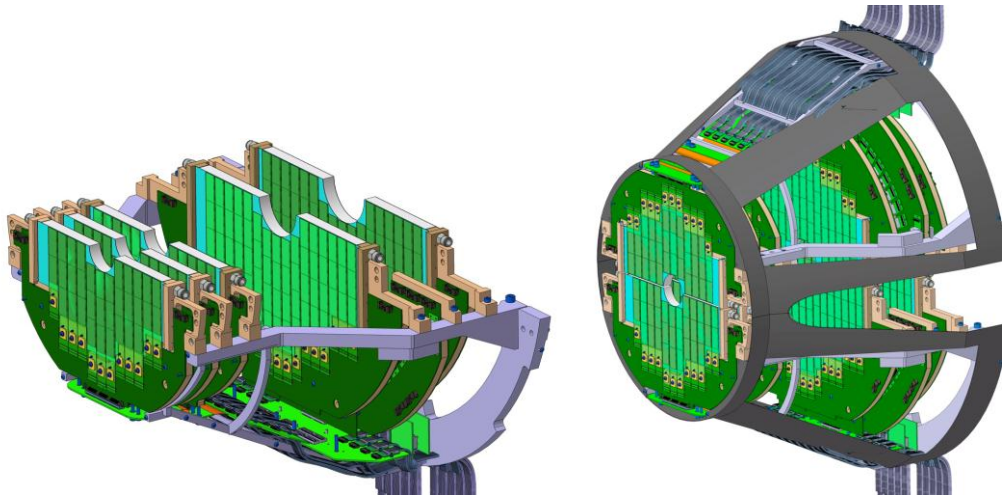


Fig. 6. MFT cone (*right*), consisting of top and bottom half-cones (*left*)

The design of the half-disk is illustrated in Fig. 7. The ladders (ALPIDE chips glued at flexible printed circuit) are glued at the heat exchanger. The precision of the chip position on the ladder and the ladder positioning is about $5\ \mu\text{m}$. The information from the sensors is read out *via* Twinax cables to the dedicated readout crates located at the bottom of the muon spectrometer absorber. Both the sensors and the readout modules should be water-cooled.

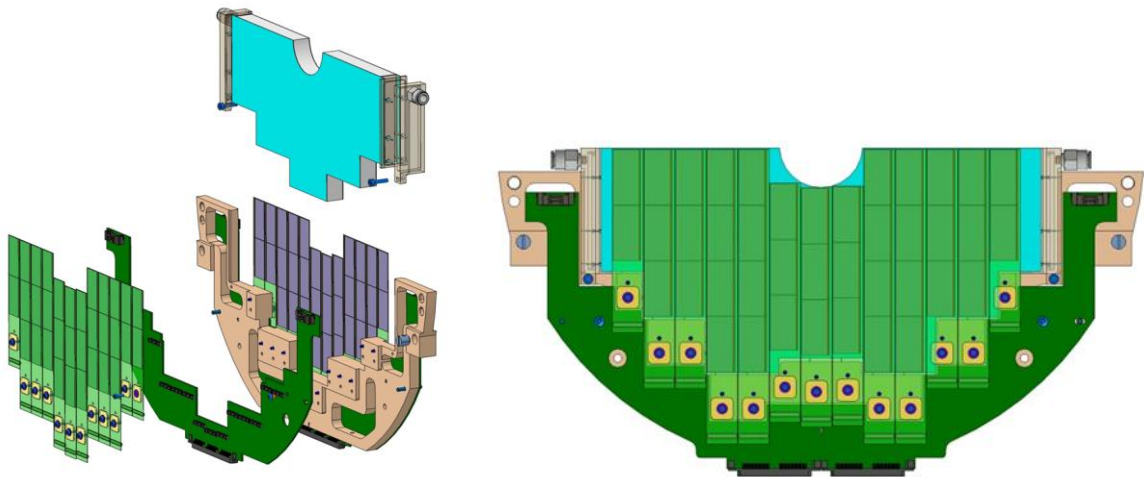


Fig. 7. MFT half-disk design: exploded view (*left*) and assembled (*right*)

The PNPI team participated in R&D works on MFT cooling since 2012. Though we have demonstrated that the air cooling is sufficient for correct operation of the DC–DC converters used, it appeared to be insufficient for sensor cooling. That is why it was decided that the water cooling would be used. The design of the water cooling system was developed together with the CERN detector cooling section of the Engineering Department. It is based on the leakless operation proposed by P. Bonneau in 2002 [3]. The water in the cooling zone is maintained under the pressure smaller than the atmospheric one, so in case of a hole in the cooling pipe the water is not spilling out of the system, instead the air is sucked inside the damaged pipe.

The people from PNPI also participated in the development of the ladder assembling procedure and in the ladder assembling. It is expected that they will participate in the disk assembling and the detector assembling and commissioning.

4. Conclusion

The ALICE detector will be significantly upgraded during the LHC Stop-2 phase in 2019–2020. The new equipment will be produced to be able to work under new LHC beam conditions (the luminosity will be increased by 10 times), that will make possible to study new physics processes and to improve significantly the quality of the experimental data.

The members of the PNPI team work successfully within the MFT Collaboration.

References

1. ALICE Collaboration, Letter of Intent, CERN-LHCC-2013-014 (2013).
2. ALICE Collaboration, Technical Design Report, CERN-LHCC-2015-001 (2015).
3. P. Bonneau, CERN ST/CV Report, <https://detector-cooling.web.cern.ch/detector-cooling/coolingsystems/CoolingSystemWeb/LCSv.2calculations.pdf>



Nuclear and Atomic Physics

SEARCH FOR MUON CATALYZED $d^3\text{He}$ FUSION

PNPI participants of the $^3\text{Hed}\mu$ Collaboration:

V.A. Ganzha, K.A. Ivshin, P.V. Kravchenko, P.A. Kravtsov, E.M. Maev, A.A. Vasilyev,
A.A. Vorobyev, N.I. Voropaev, M.E. Vznuzdaev
in collaboration with Paul Scherrer Institute (Switzerland), University of Washington (USA),
University of Kentucky (USA), Regis University (USA)

1. Introduction

We report here on the results of an experiment aimed at observation of the muon catalyzed $d^3\text{He}$ fusion, which might occur after a negative muon stop in a $\text{D}_2 + ^3\text{He}$ gas mixture. The nuclear fusion reaction



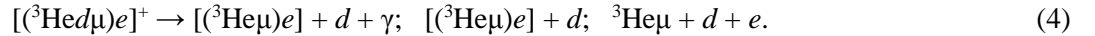
is interesting for various reasons: as a mirror reaction of the $d + t \rightarrow ^4\text{He} + n$ fusion process and as a perspective source of thermonuclear energy. This fusion process was involved in the primordial nucleosynthesis of light elements in the early Universe. For these reasons, it is important to know the cross section for this reaction at low collision energies $E < 10 \text{ keV}$. The phenomenon of muon catalysis of fusion reactions opens an opportunity to study this reaction at practically zero collision energy when fusion occurs in the $^3\text{Hed}\mu$ mesomolecule:



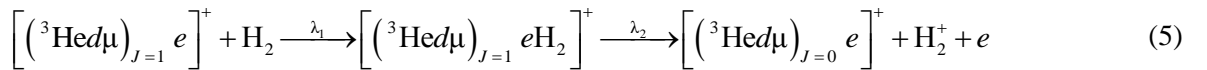
Formation of the $^3\text{Hed}\mu$ molecule occurs in collisions of slow $d\mu$ atoms with ^3He atoms:



This process was first predicted by Y. Aristov *et al.* [1] in 1981 as an intermediate step in the muon transfer from the deuterium mesoatom to the helium atom. This prediction was confirmed in the experiments at PNPI, where the muon transfer rate was measured at room and at low temperatures: $\lambda_{d^3\text{He}} (300 \text{ K}) = (1.24 \pm 0.05) \cdot 10^8 \text{ s}^{-1}$, $\lambda_{d^3\text{He}} (50 \text{ K}) = (2.32 \pm 0.09) \cdot 10^8 \text{ s}^{-1}$, $\lambda_{d^3\text{He}} (39 \text{ K}) = (2.33 \pm 0.16) \cdot 10^8 \text{ s}^{-1}$, in close agreement with the predicted rates. The discovered formation process of the $^3\text{Hed}\mu$ molecules allows to search for the muon catalyzed $d^3\text{He}$ fusion reaction, similar to the muon catalyzed dd and dt fusion reactions. However, a serious complication arises from competition of this fusion reaction with very fast decay of the $^3\text{Hed}\mu$ molecule:



According to the theoretical calculations [2–4], the decay rate is $\lambda_{\text{dec}} \approx 7 \cdot 10^{11} \text{ s}^{-1}$. The nuclear fusion rates $\lambda_f(J)$ in the $^3\text{Hed}\mu$ molecule depend strongly on the value of the molecular angular momentum J . The theoretical predictions are: $\lambda_f(J=0) \approx 2 \cdot 10^5 \text{ s}^{-1}$ and $\lambda_f(J=1) \approx 6.5 \cdot 10^2 \text{ s}^{-1}$ [5, 6]. Unfortunately, about 99% of the initially produced $^3\text{Hed}\mu$ molecules are in the $J=1$ state. However, as it was suggested by L. Menshikov and M. Faifman [7], the transition $(^3\text{Hed}\mu)_{J=1} \rightarrow (^3\text{Hed}\mu)_{J=0}$ is possible in collisions of the $[(^3\text{Hed}\mu)e]^+$ complex with deuterium molecules *via* formation of a large molecular cluster $[(^3\text{Hed}\mu) e\text{D}_2]$ and its decay:



with the formation and the transfer rates of this cluster $\lambda_1 \approx 3 \cdot 10^{13} \varphi \text{ s}^{-1}$ and $\lambda_2 \approx 5 \cdot 10^{11} \text{ s}^{-1}$, respectively, where φ is the H_2 density normalized to the liquid hydrogen density (LHD). Here H_2 stands for D_2 or HD . Such an estimate shows that one can expect quite efficient $(^3\text{Hed}\mu)_{J=1} \rightarrow (^3\text{He} d\mu)_{J=0}$ transfer and, as a consequence, a detectable $^3\text{Hed}\mu$ fusion process. The effective fusion rate λ_f can be defined as

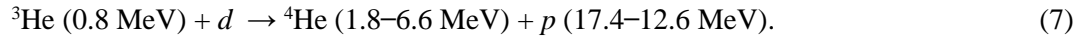
$$\lambda_f = P(J=0) \lambda_f(J=0) + P(J=1) \lambda_f(J=1), \quad (6)$$

where $P(J)$ is population of the ${}^3\text{He}d\mu$ molecule state with the angular momentum J . The population $P(J)$ is defined by the kinetics of formation, decay, transition and fusion in the ${}^3\text{He}d\mu$ molecule.

The first experimental limit on the effective muon catalyzed fusion rate $\lambda_f < 4 \cdot 10^8 \text{ s}^{-1}$ was set at PNPI in 1990 in an experiment with the $\text{D}_2 + {}^3\text{He}$ (5%) gas mixture. Next measurements were carried out in 1996 using the $\text{HD} + {}^3\text{He}$ (5.6%) gas mixture. During a short test run in the intense muon beam at Paul Scherrer Institute (PSI), the upper limit for the ${}^3\text{He}d\mu$ fusion rate was moved down to $\lambda_f < 1.6 \cdot 10^6 \text{ s}^{-1}$. Later in 1997, there was a special physics run at PSI aimed at observation of the muon catalyzed ${}^3\text{He}d$ fusion in the $\text{HD} + {}^3\text{He}$ (5.6%) gas mixture. This experiment resulted with a new upper limit for the effective fusion rate $\lambda_f < 6 \cdot 10^4 \text{ s}^{-1}$ [8].

On the other hand, another collaboration at PSI has undertaken in 1998 a search of the muon catalyzed ${}^3\text{He}d\mu$ fusion in the $\text{D}_2 + {}^3\text{He}$ (5%) gas mixture. The reanalysed results of that experiment were published in 2006 [9]. The authors declared the first observation of this process with the measured effective fusion rates: $\lambda_f = (4.5 + 2.6 / - 2.0) \cdot 10^5 \text{ s}^{-1}$ and $\lambda_f = (6.9 + 3.6 / - 3.0) \cdot 10^5 \text{ s}^{-1}$ at the D_2 density 5.21% and 16.8% of the LHD, correspondingly. Such a fusion rate exceeds by an order of magnitude the upper limit $\lambda_f < 6 \cdot 10^4 \text{ s}^{-1}$ set in our previous experiment. This striking difference might be related with problems of taking into account the background reactions, which could simulate the searched reaction (2). The main background of this type is due to the so-called ${}^3\text{He} + d$ fusion-in-flight. It comes from collisions with D_2 of the ${}^3\text{He}$ (0.8 MeV) nuclei produced in the $dd\mu$ fusion reaction. This background is more important in the $\text{D}_2 + {}^3\text{He}$ gas mixture than in the $\text{HD} + {}^3\text{He}$ gas mixture used in our experiment. On the other hand, the difference between the results of these two experiments might be also due to a possible difference in the formation and transfer rates λ_1 and λ_2 in the $[({}^3\text{He}d\mu)_{J=1}e\text{HD}]^+$ and $[({}^3\text{He}d\mu)_{J=1}e\text{D}_2]^+$ clusters.

Fortunately, the MuSun experiment, presently under way at PSI [10], gives us an excellent possibility to clarify the situation. The main goal of MuSun is to measure the muon capture rate in deuterium. For that, the lifetime of negative muons stopped in ultra clean D_2 gas is measured with high precision (10^{-5}). That requires very high statistics of the detected muon decays. In particular, $1.3 \cdot 10^{10}$ decays of the muons stopped in the sensitive volume of the MuSun active target were registered in Run-8 of this experiment. Besides muons, the active target detects also the products of the reactions initiated by muons, including the products of the ${}^3\text{He} + d$ fusion-in-flight:



Therefore, Run-8 can serve as a high statistical background experiment for an experiment aimed at searches of the muon catalyzed ${}^3\text{He}d\mu$ fusion in the $\text{D}_2 + {}^3\text{He}$ gas mixture.

Having this in mind, the decision was taken by the MuSun Collaboration to perform an additional Run-9 with the active target filled with the $\text{D}_2 + {}^3\text{He}$ (5%) gas mixture, keeping all experimental conditions identical to those in Run-8. The results of these studies are presented below.

2. The MuSun experimental set-up

A principal scheme of the MuSun experiment is shown in Fig. 1. The incoming muons are detected first by a thin scintillator counter μSC and by a wire proportional chamber μPC . Then they pass through a 0.4 mm thick hemispheric beryllium window and stop in the sensitive volume of the time-projection chamber (TPC). The TPC is the key element of the experimental set-up. It is filled with ultrapure protium-depleted deuterium gas at the temperature $T = 31 \text{ K}$ and pressure $P = 5 \text{ bar}$, and it operates as an active target in the ionization grid chamber mode (without gas amplification). Its main goal is to select the muon stops within the fiducial volume of the TPC well isolated from the chamber materials.

The trajectory and the arrival time of the muon decay electrons are measured with two cylindrical wire chambers $e\text{PC1}$, $e\text{PC2}$ and with a double layer scintillator hodoscope $e\text{SC}$ consisting of 32 plastic scintillators. The geometrical acceptance of the electron detector is 70%.

The ionization electrons produced in the TPC drift towards the anode plane in the electric field of 11 kV/cm with the velocity of 5 mm/ μs . The total drift space (the cathode – grid distance) is 72 mm. The anode plane is subdivided into 48 pads making a pad matrix of six pads (horizontal direction X) by eight pads (beam direction Z). The size of the pads is 17.5 mm (X) \times 15.25 mm (Z). About 50% of the muons

passing through the μ SC are stopped within the fiducial volume above the 20 central pads at the distance of more than 1 cm from the cathode and from the grid (Fig. 2).

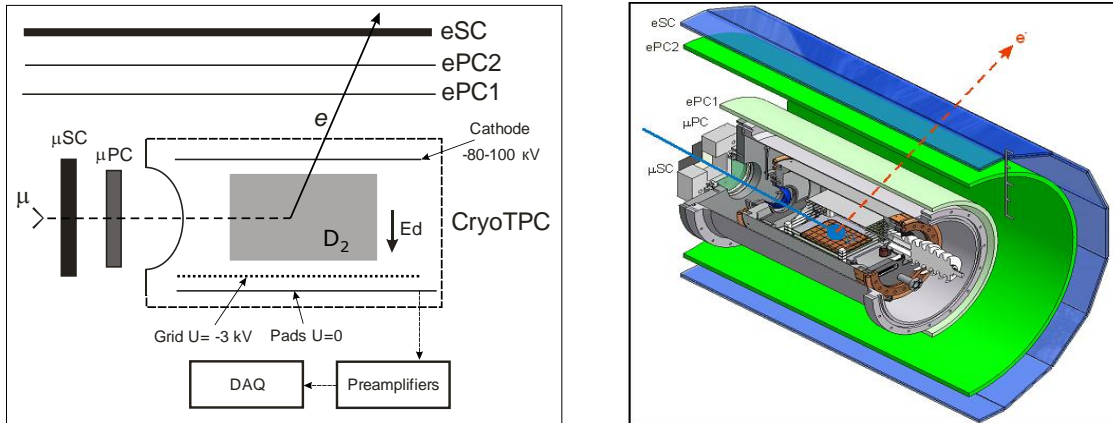


Fig. 1. Principal scheme of the MuSun experiment and schematic view of the MuSun set-up. The TPC is filled with ultrapure protium-depleted deuterium gas at $T \approx 31$ K and $P \approx 5$ bar. The shadowed area shows a fiducial volume with muon stops far enough from all TPC materials

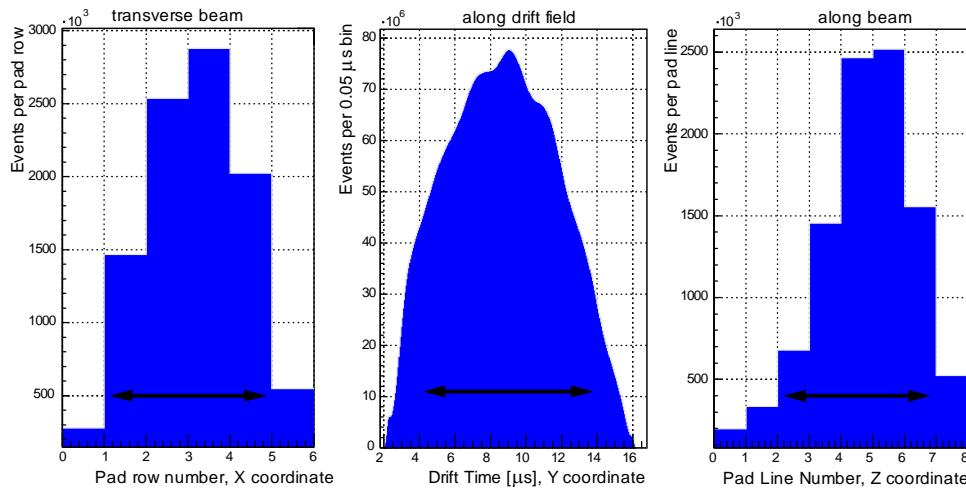


Fig. 2. The measured muon stop distribution inside the TPC sensitive volume. The double arrows show the fiducial volume selected in the present analysis

All anode pads have independent readout channels with fast (100 MHz) analog-to-digital converters (ADCs) allowing to measure the amplitude, the duration, the energy, and the time of appearance of the signals with the amplitude exceeding the 80 keV threshold at any pad in the time window 0–25 μ s after a muon signal is detected by the μ SC counter. The same μ SC signal triggers the “muon-on-request” system, which switches off the muon beam thus excluding arrivals of other muons in the registration time window. The energy resolution (noise) in each channel is around 20 keV (sigma). The TPC measures the ionization produced by the entering TPC muon, determines its trajectory, and selects the 3D muon stop coordinate to be inside the fiducial volume isolated from all TPC materials. Also, the TPC detects products of reactions following the muon stop, including products of the $^3\text{He}d$ fusion.

3. Experimental data and analysis

Table 1 compares the experimental conditions of the TPC in Run-8 and Run-9. The only difference is the gas filling. All other conditions are identical. In both runs, the ultra high gas purity was maintained by continuous operation of a gas purification system.

Table 1

Experimental conditions in Run-8 and in Run-9

Run	Gas filling	Temperature, K	Pressure, bar	D ₂ density, C _d	Gas purity
8	D ₂	31	5	6.5% LHD	$< 2 \cdot 10^{-9}$ (N ₂)
9	D ₂ + 5% ³ He	31	5	6.2% LHD	$< 2 \cdot 10^{-9}$ (N ₂)

Figure 3 shows the scheme of processes initiated by a muon stop in the D₂ + ³He gas mixture. For the goal of this experiment, it is important to know the yield of the ³He μ molecules leading to possible muon catalyzed ³He d fusion and the yield of the ³He (0.82 MeV) nuclei responsible for the main background reaction: ³He + d fusion-in-flight. Both yields can be precisely calculated, as the parameters entering the scheme in Fig. 3 are known with high accuracy [11]. On the other hand, the ³He (0.82 MeV) yield can be determined directly from the experimental data as shown in Fig. 4.

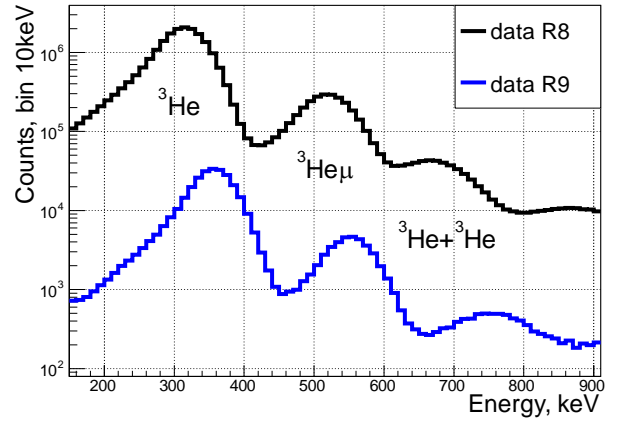
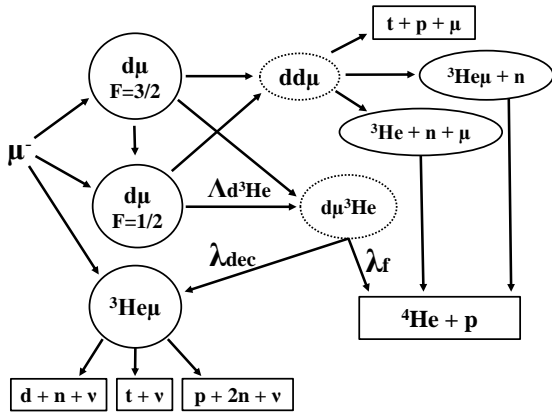


Fig. 3. Scheme of processes initiated by a muon stop in the D₂ + ³He gas mixture (*left*). Energy spectra of the dd fusion events measured in Run-8 and in Run-9 (*right*)

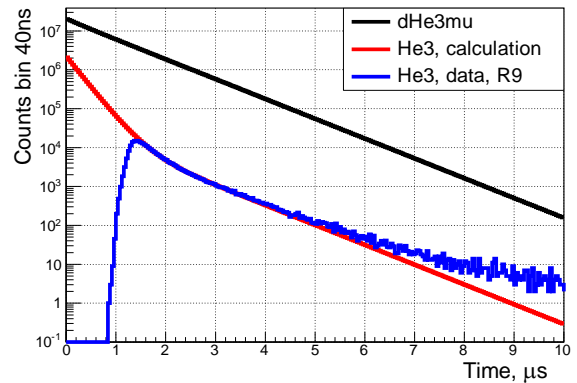
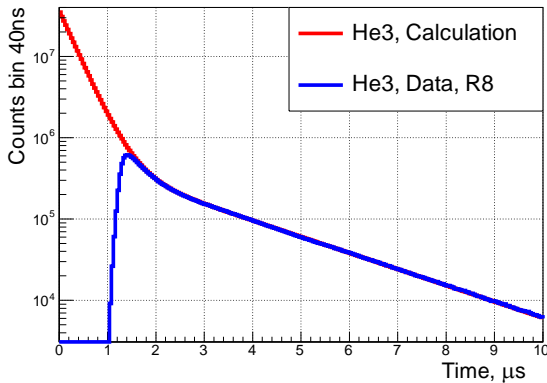


Fig. 4. Time distributions of the $dd \rightarrow {}^3\text{He} + n + \mu$ events in Run-8 (*red line in the left panel*) and in Run-9 (*red line in the right panel*) calculated according to the scheme in Fig. 3 with the kinetics parameters from [11]. Time distributions 74 of the ³He signals separated in time from the muon stop signals measured in Run-8 (*blue line in the left panel*) and in Run-9 (*blue line in the right panel*). The calculated time distribution of the ³He μ molecules (*black line in the right panel*)

The largest peak in the energy spectrum of the dd fusion events shown in Fig. 3 is due to ${}^3\text{He}$ (0.82 MeV) from the $dd \rightarrow {}^3\text{He} + n + \mu$ fusion channel. The next peak is due to ${}^3\text{He}\mu$ (0.82 MeV) from the $dd \rightarrow {}^3\text{He}\mu + n$ fusion channel. Both peaks proved to be shifted from 0.82 MeV to lower energies because of the electron–ion recombination, the effect being larger for doubly charged ${}^3\text{He}^{++}$ ions than for singly charged ${}^3\text{He}\mu^+$ ions. The difference in the ${}^3\text{He}$ peak positions in Run-8 and in Run-9 is because the recombination effect is by 9% lower in the $\text{D}_2 + {}^3\text{He}$ (5%) gas mixture than in pure D_2 gas. The third peak is due to pileup of the ${}^3\text{He}$ signals with the ${}^3\text{He}$ or ${}^3\text{He}\mu$ signals from the next fusion cycle. The weights of the corresponding peaks in Fig. 3 are

$$w({}^3\text{He}) / w({}^3\text{He}\mu) / w({}^3\text{He}^3\text{He}) = 0.842 / 0.125 / 0.033. \quad (8)$$

The fusion-in-flight probabilities for these types of events correlate as

$$F({}^3\text{He}) / F({}^3\text{He}\mu) / F({}^3\text{He}^3\text{He}) = 1.0 / 2.3 / 2. \quad (9)$$

The probability $F({}^3\text{He}\mu)$ is larger than $F({}^3\text{He})$ proportionally to the length R of their tracks: $R({}^3\text{He}) = 0.28$ mm and $R({}^3\text{He}\mu) = 0.64$ mm.

In our analysis, we normalize the number of the fusion-in-flight events to the yield of ${}^3\text{He}$ (0.82 MeV) in the first peak in the spectrum shown in Fig. 3. Note that this yield is measured with the efficiency $\varepsilon({}^3\text{He}) = 0.95$ because of 5% losses in the tail below the low energy cut. The probability $F^*({}^3\text{He})$ to produce a fusion-in-flight event per one ${}^3\text{He}$ (0.82 MeV) signal in the first peak in Fig. 3 is given by the following expression:

$$F^*({}^3\text{He}) = F({}^3\text{He}) [w({}^3\text{He}) + 2.3w({}^3\text{He}\mu) + 2w({}^3\text{He}^3\text{He})] / [w({}^3\text{He}) \varepsilon({}^3\text{He})] = 4.04 \cdot 10^{-5}, \quad (10)$$

where $F({}^3\text{He}) = 2.7 \cdot 10^{-5}$ is the probability to produce a fusion-in-flight event by a ${}^3\text{He}$ (0.82 MeV) particle stopping in the D_2 gas. This probability was calculated using the available ${}^3\text{He} + d$ fusion cross sections in the ${}^3\text{He}$ energy range below 1 MeV [12]. The precision of the calculated value of $F({}^3\text{He})$ is $\sim 5\%$.

The obtained value of $F^*({}^3\text{He})$ can be used to calculate the expected yield of the ${}^3\text{He} + d$ fusion-in-flight events from the measured number of the ${}^3\text{He}$ (0.82 MeV) signals. Figure 4 shows the results of such measurements in Run-8. One can see that after $t = 1.5$ μs the measured ${}^3\text{He}$ distribution proved to be in excellent (without any renormalization) agreement with the distribution calculated on the basis of the kinematics scheme in Fig. 3. The drop below $t = 1.5$ μs is related with overlapping of the ${}^3\text{He}$ signal with the muon stop signal. The averaged value $t^* = 1.28$ μs can be considered as the minimal time between the ${}^3\text{He}$ signal and the muon signal needed for separation of these signals from each other. The total ${}^3\text{He}$ yield (the first peak in Fig. 4) in Run-8 was found to be $N({}^3\text{He}) = 1.283 \cdot 10^7$. Then, the expected yield of the ${}^3\text{He}d$ fusion-in-flight events in the time interval $t \geq 1.28$ μs can be calculated as

$$N({}^4\text{He} + p)_{\text{FinF}} = N({}^3\text{He}) F^*({}^3\text{He}) = 518. \quad (11)$$

Note that the minimal separation time $t^* = 1.28$ μs should be practically the same for the d ${}^3\text{He}$ fusion-in-flight and for the ${}^3\text{He}d\mu$ fusion events. Therefore, we can use this value to calculate the number of the ${}^3\text{He}d\mu$ molecules produced in Run-9 in the time interval $t \geq 1.28$ μs . Similarly to Run-8, Fig. 4 presents the calculated and the measured time distributions of the $dd \rightarrow {}^3\text{He} + n + \mu$ events in Run-9. In addition, it presents the calculated time distribution of the produced ${}^3\text{He}d\mu$ molecules. From these data, we determine the registered number of the ${}^3\text{He}$ particles, $N({}^3\text{He}) = 3.34 \cdot 10^5$, and the number of the ${}^3\text{He}d\mu$ molecules produced at $t \geq 1.28$ μs , $N({}^3\text{He}d\mu) = 1.14 \cdot 10^8$.

The full data set from Run-8 and Run-9 was analysed with the goal to identify the ${}^4\text{He} + p$ events. The muon stops were selected to be inside the TPC fiducial volume (Fig. 2). Also, it was required that the muon stops were accompanied by the muon decay electrons registered in the eSC electron detector in the time window 0–25 μs after the muon stop. The number of thus selected muon stops is $\tilde{N}_\mu = 6.3 \cdot 10^9$ and $\tilde{N}_\mu = 1.0 \cdot 10^9$ for Run-8 and Run-9, respectively. Table 2 summarizes the statistics collected in Run-8 and Run-9 and presents the number of expected fusion-in-flight events calculated according to expression (10).

Table 2

Statistics collected in Run-8 and Run-9*

Run	\tilde{N}_μ	$N(^3\text{He})$	$N(^3\text{He}d\mu)$	$N_{\text{FinF}}(4\pi)$ expected for 4π geometry
8	$6.3 \cdot 10^9$	$1.28 \cdot 10^7$	–	518 ± 26
9	$1.0 \cdot 10^9$	$3.34 \cdot 10^5$	$1.14 \cdot 10^8$	14 ± 0.7

* The number of the selected muon stops \tilde{N}_μ ; the number of the registered ^3He signals $N(^3\text{He})$ (the first peak in the energy spectra in Fig. 3); the number of the produced $^3\text{He}d\mu$ molecules $N(^3\text{He}d\mu)$; and the number of the expected fusion-in-flight events $N_{\text{FinF}}(4\pi)$ in Run-8 and in Run-9 at $t \geq 1.28 \mu\text{s}$.

At the first step, the selection of the candidates for the $^4\text{He} + p$ events was done with the following criteria:

- There should be a signal at the muon stop pad P0 ($E_{P0} \geq 1.0 \text{ meV}$) separated in time from the muon signal and accompanied by two signals at a sequence of two neighbour pads P1 and P2.
-
-

Fig. 5 shows the $^4\text{He} + p$ event. The muon trajectory is shown in the figure. The muon stop on Pad 27 is followed by the signals on Pad 27, Pad 33, and Pad 40. The pads included in the selected muon stop fiducial area are indicated with white colour.

ites for
ng into

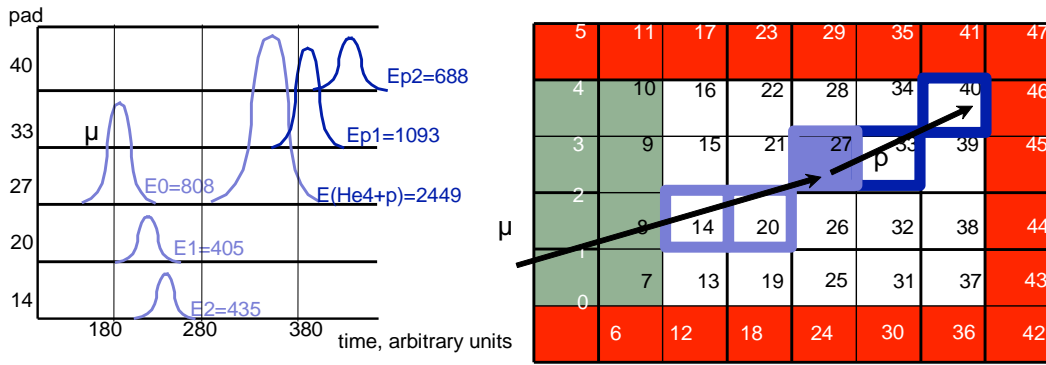


Fig. 5. Flash ADC display of a candidate for the $^4\text{He} + p$ event. It shows a muon trajectory with the muon stop on Pad 27 followed by the signals on Pad 27, Pad 33, and Pad 40. The pads included in the selected muon stop fiducial area are indicated with white colour

The recombination effect reveals itself as a difference between the measured energy of the signal E_{meas} and the real energy of the particle E : $E_{\text{meas}} = E - E_{\text{recomb}}$ (Fig. 6, right). The value of E_{recomb} was determined using the measured signals from the alpha sources, ^{240}Pu ($E_\alpha = 5.156 \text{ MeV}$) and ^{241}Am ($E_\alpha = 5.480 \text{ MeV}$) and from the ^3He (0.82 MeV) peak using for interpolation the following expression:

$$E_{\text{recomb}} = E \left(A\sqrt{\Theta} + B\Theta \right), \quad (12)$$

where $\Theta = Z^2M/E$. Here Z and M are the charge and the mass of the ionizing particle. For Run-9, the fit parameters were found to be $A = (6.26 \pm 0.15) \cdot 10^{-3}$, $B = -(0.0095 \pm 0.0015) \cdot 10^{-3}$. In Run-8, the recombination effect is larger by a factor of 1.09. Figure 6 (left) shows the Monte Carlo (MC) energy spectrum on pad P0 calculated for the $^3\text{He} + d \rightarrow ^4\text{He} + p$ fusion-in-flight events in Run-8 taking into account the recombination effect and the TPC energy resolution. Also shown is the expected energy spectrum for the muon catalyzed $d^3\text{He}$ fusion events in Run-9. Figure 7a presents the energy spectrum on pad P0 of 455 $^4\text{He} + p$ candidates selected in Run-8 according to the above mentioned criteria in the region $E_{P0} \geq 0.85 \text{ MeV}$.

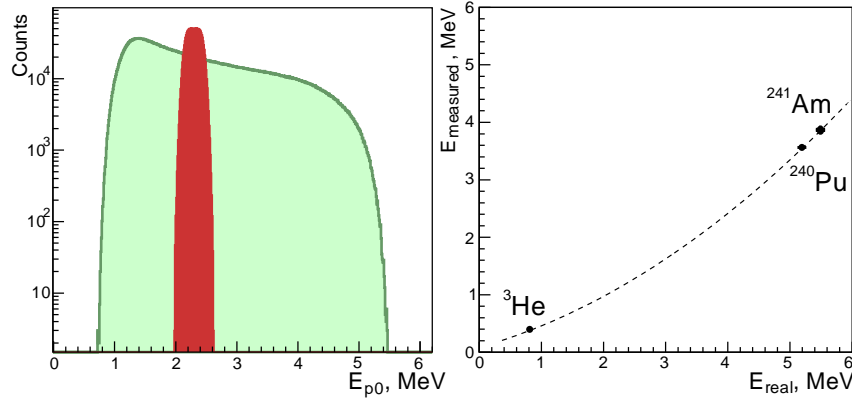


Fig. 6. *Left* – MC energy spectra on pad P0 for the ${}^3\text{He} + d$ fusion-in-flight events in Run-8 (green colour) and for the muon catalyzed $d{}^3\text{He}$ fusion events in Run-9 (red colour). *Right* – the measured energy versus the real energy of the ${}^4\text{He}$ particles in Run-9. The dashed line represents the results of calculations using expression (12) with the parameters $A = 6.26 \cdot 10^{-3}$ and $B = -0.0095 \cdot 10^{-3}$ determined from the fit to the measured ${}^{241}\text{Am}$ and ${}^{240}\text{Pu}$ alpha peak positions and to the ${}^3\text{He}$ (0.82 MeV) peak position

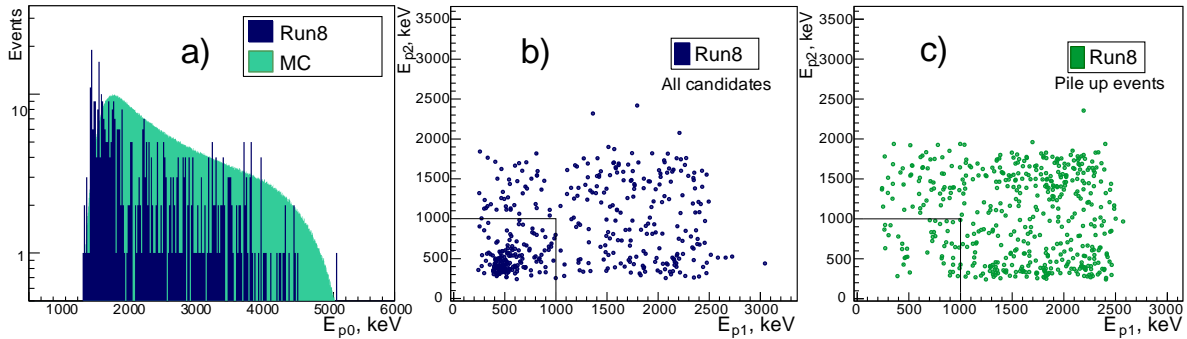


Fig. 7. Energy spectrum on pad P0 of the 455 ${}^4\text{He} + p$ candidates selected in Run-8 (a); energy distribution on pads P1 and P2 of the 455 ${}^4\text{He} + p$ candidates in Run-8 (b); energy distribution of the dd fusion pileup events on pads P1 and P2 (506 events) (c)

The next step includes the analysis of the energy spectra on pads P1 and P2. The range of the 14 MeV protons in the TPC is $R_p = 23$ cm with $dE/dx = 0.35$ MeV/cm. The energy deposited by a proton in the zone of pads P1 and P2 should be around 0.5 MeV. Therefore, we use the region $E_{P1} \leq 1$ MeV, $E_{P2} \leq 1$ MeV for selection of the candidates for the ${}^4\text{He} + p$ events. This resulted in 182 events in Run-8 and 12 events in Run-9.

However, besides the ${}^4\text{He} + p$ events, one can see in Fig. 7b some background with very special distribution ended sharply at $E_{P1} = 2.5$ MeV and at $E_{P2} = 1.8$ MeV. The nature of this background is understood. It is due to piling up of two successive $d\mu d$ fusion reactions:



followed by



or vice versa.

Such events can produce signals on P0 (due to 1.1 MeV ${}^3\text{H}$ and 0.82 MeV ${}^3\text{He}$), on P1 (due to the 3.02 MeV proton with $R_p = 13$ mm), and on P2 (due to scattering of the 2.45 MeV neutron on deuterons). The available in Run-8 experimental data allow to reproduce directly this background by collecting the events with signals on P0 and P1 accompanied by signals on the pads which are not joining the pads P0 and P1. Figure 7c presents the $E_{P1} \times E_{P2}$ plot of such events. To separate the ${}^4\text{He} + p$ events from the dd fusion pileup events, the number of events in the $E_{P1} \times E_{P2}$ plot (Fig. 7c) in the region $E_{P1} \geq 1$ MeV, $E_{P2} \geq 1$ MeV was normalized to the number of events in the corresponding region in Fig. 7b, and the number

of the dd fusion pileup events in the zone $E_{p1} \leq 1$ MeV, $E_{p2} \leq 1$ MeV was determined: $N_{\text{pileup}}(\text{R8}) = 25$. Then the number of the registered d ^3He fusion-in-flight events was obtained: $N_{\text{FinF}}(\text{R8}) = 182 - 25 = 157$. Comparison of this number with the expected number of the $^3\text{He} + d$ fusion-in-flight events gives the registration efficiency of the fusion-in-flight events: $\varepsilon_{\text{FinF}} = (30 \pm 3)\%$. This value is valid also for the registration efficiency of the muon catalyzed d ^3He fusion. The quoted error is determined by the error in the number of the detected fusion-in-flight events and by the error in the calculated probability to produce a fusion-in-flight event by the 0.82 MeV ^3He particle in the D_2 gas.

The considered above two types of events constitute the main background in Run-9 aimed at observation of the muon catalyzed fusion reaction $^3\text{He}d \rightarrow ^4\text{He} + p$. Based on the results obtained in Run-8, we can calculate the expected background in Run-9 using the following expressions:

$$\begin{aligned} N_{\text{FinF}}(\text{R9}) &= N_{\text{FinF}}(\text{R8}) N(^3\text{He})_{\text{R9}} / N(^3\text{He})_{\text{R8}} C_d(\text{R9}) / C_d(\text{R8}), \\ N_{\text{pileup}}(\text{R9}) &= N_{\text{pileup}}(\text{R8}) N(^3\text{He})_{\text{R9}} / N(^3\text{He})_{\text{R8}} P_{\text{pileup}}(\text{R9}) / P_{\text{pileup}}(\text{R8}), \\ N_{\text{bgr}}(\text{R9}) &= N_{\text{FinF}}(\text{R9}) + N_{\text{pileup}}(\text{R9}), \end{aligned} \quad (14)$$

where the ratio of the registered ^3He signals $N(^3\text{He})_{\text{R9}} / N(^3\text{He})_{\text{R8}} = 0.026$; the ratio of the D_2 densities $C_d(\text{R9}) / C_d(\text{R8}) = 0.95$; and the ratio of the dd fusion pileup probabilities $P_{\text{pileup}}(\text{R9}) / P_{\text{pileup}}(\text{R8}) = 0.61$. The calculated in this way background predictions for Run-9 are as follows: $N_{\text{FinF}}(\text{R9}) = 3.87 \pm 0.3$, $N_{\text{pileup}}(\text{R9}) = 0.39 \pm 0.08$, $N_{\text{bgr}}(\text{R9}) = 4.3 \pm 0.4$. The quoted error in $N_{\text{bgr}}(\text{R9})$ is determined mostly by the statistical error in $N_{\text{FinF}}(\text{R8})$.

We can further reduce $N_{\text{bgr}}(\text{R9})$ by cutting the low energy part in the energy spectrum on pad P0 presented in Fig. 7a. The expected position of the signals from the muon catalyzed $^3\text{He}d \rightarrow ^4\text{He} + p$ reaction is above $E_{p0} = 2.4$ MeV (Fig. 7a). Therefore, we can set the low energy cut at the energy up to $E_{p0} = 2.0$ MeV without noticeable decrease in the registration efficiency of the muon catalyzed $^3\text{He}d \rightarrow ^4\text{He} + p$ reaction. Table 3 presents the background predicted for Run-9 for various E_{p0} cuts.

Another source of background in Run-9 might be the breakup reaction $^3\text{He}\mu \rightarrow d + n, p + 2n$. However, the energy deposit on pad P0 being rather small in such events, they could simulate the muon catalyzed $^3\text{He}d \rightarrow ^4\text{He} + p$ fusion events only when piling up with the $dd \rightarrow ^3\text{H} + p$ events. The calculated probability of such process is $0.5 \cdot 10^{-7}$ per muon stop. In addition, it is suppressed by three orders of magnitude to a negligible level by requiring detection of the muon decay electron with the ePC/eSC detectors. Similarly, the muon capture on gas impurities (N_2) could be disregarded, especially taking into account very high purity (10^{-9}) of the D_2 gas in this experiment.

Table 3

Estimation of the number N_{bgr} of the background events*

$E0$ cut, MeV	Run-8			Run-9**			
	N_{tot}	N_{FinF}	N_{pileup}	N_{tot}	N_{FinF}	N_{pileup}	$N_{\text{bgr}} = N_{\text{FinF}} + N_{\text{pileup}}$
1.0	182	157	25	6	3.87 ± 0.31	0.39 ± 0.08	4.3 ± 0.4
1.6	117	93	24	3	2.30 ± 0.23	0.37 ± 0.08	2.7 ± 0.3
2.0	99	77	22	2	1.90 ± 0.22	0.34 ± 0.07	2.2 ± 0.3

* N_{tot} – the total number of selected $^4\text{He} + p$ candidates in Run-8 and Run-9; N_{FinF} – the number of fusion-in-flight events; N_{pileup} – the number of dd fusion pile up events registered in Run-8 and extrapolated to Run-9 for various cuts on the energy deposited on pad P0.

** Background determined from Run-8.

Finally, two candidates for the muon catalyzed $^3\text{He}d$ fusion were registered with the predicted background of 2.2 ± 0.3 events.

Based on this observation, an upper confidence limit for the number of the muon catalyzed $^3\text{He}d$ fusion events was calculated by the method described in Refs. [13, 14] which takes into account the measured background uncertainty: $N_f \leq 3.1$ events at the 90% confidence level (CL). This determines an upper limit for the effective muon catalyzed d ^3He fusion rate:

$$\lambda_f = N_f \lambda_{\text{dec}} / N_{^3\text{Hed}\mu} \varepsilon_f, \quad (15)$$

where $N_{^3\text{Hed}\mu} = 1.14 \cdot 10^8$ is the number of the produced $^3\text{Hed}\mu$ molecules, $\lambda_{\text{dec}} = 7 \cdot 10^{11} \text{ s}^{-1}$ is the decay rate of the $^3\text{Hed}\mu$ molecule, $\varepsilon_f = 0.30$ is the detection efficiency of the ^3Hed fusion events. This gives

$$\lambda_f \leq 6.3 \cdot 10^4 \text{ s}^{-1} \text{ at } 90\% \text{ CL}. \quad (16)$$

4. Conclusion

An upper limit for the rate λ_f of muon catalyzed $d^3\text{He}$ fusion was set in this experiment performed with the $\text{D}_2 + ^3\text{He}$ (5%) gas mixture at 31 K temperature with the gas density $\varphi = 6.5\%$ of the LHD:

$$\lambda_f \leq 6.3 \cdot 10^4 \text{ s}^{-1} \text{ at } 90\% \text{ CL}.$$

An important feature of this experiment was a possibility to determine the level of the background and the registration efficiency using data from the high statistical MuSun experiment performed with pure D_2 gas in the same experimental conditions.

The obtained limit for λ_f is close to that determined in our previous experiment [8] performed with the $\text{HD} + ^3\text{He}$ (5.6%) gas mixture. On the other hand, it disagrees strongly with the rate $\lambda_f \approx 6 \cdot 10^5 \text{ s}^{-1}$ reported in Ref. [9] and thus rules out the statement made in Ref. [9] on observation of the muon catalyzed $d^3\text{He}$ fusion.

Based on the theoretical predictions [2–7], one could expect the rate $\lambda_f \approx 2.5 \cdot 10^4 \text{ s}^{-1}$, which would correspond to observation of 1.3 events in our experiment. Note that this experiment was performed as a supplement to MuSun with only one week running time. In a dedicated experiment with the same set-up, one could increase the sensitivity for detection of the muon catalyzed $d^3\text{He}$ fusion events by an order of magnitude due to several factors. This could be an experiment with the $\text{HD} + 5\% ^3\text{He}$ gas mixture with some modifications of the TPC signals shaping and reduction of the dead time introduced by the “muon on request” system. In this case, the detection efficiency for the muon catalyzed $d^3\text{He}$ fusion events will be increased by a factor of five, while the fusion-in-flight background will be decreased by a factor of four. Therefore, assuming $\lambda_f \approx 2.5 \cdot 10^4 \text{ s}^{-1}$, one could register about 26 muon catalyzed $d^3\text{He}$ fusion events with 8 ± 1 background events in a four weeks running time experiment.

References

1. Y.A. Aristov *et al.*, *Yad. Phys.* **33**, 1066 (1981).
2. Y. Kino, M. Kamimura, *Hyper. Interact.* **82**, 195 (1993).
3. A.V. Kravtsov *et al.*, *Zh. Phys. D* **29**, 49 (1994).
4. S.S. Gershtein, V.V. Gusev, *Hyper. Interact.* **82**, 205 (1993).
5. L.N. Bogdanova, V.I. Korobov, L.I. Ponomarev, *Hyper. Interact.* **118**, 187 (1999).
6. D.I. Abramov, V.V. Gusev, L.I. Ponomarev, *Hyper. Interact.* **119**, 127 (1999).
7. M.P. Faifman, L.I. Men'shikov, *Hyper. Interact.* **119**, 127 (1999).
8. E.M. Maev *et al.*, *Hyper. Interact.* **118**, 171 (1999).
9. V.M. Bystritsky *et al.*, *Eur. Phys. J. D* **38**, 455 (2006).
10. V.A. Ganzha *et al.*, *PNPI. High Energy Physics Division. Main Scientific Activities 2007–2012*, Gatchina, 2013, p. 106.
11. D.V. Balin, V.A. Ganzha, S.M. Kozlov *et al.*, *Phys. Part. Nucl.* **42**, 185 (2011); D.V. Balin, V.A. Ganzha, S.M. Kozlov *et al.* *Part. Nuclei* **42**, 361 (2011).
12. W.E. Kunz, *Phys. Rev.* **97**, 456 (1955); R.M. White, R.W.D. Resler, G.M. Hale, *Tech. Rep. IEAE NDS 177*, Int. Atomic Energy Agency (1997).
13. T.M. Huber *et al.*, *Phys. Rev. D* **41**, 2709 (1990).
14. R.D. Cousins, V.L. Highland, *Nucl. Instrum. Meth. A* **320**, 331 (1992).

PENNING TRAPS IN THE SERVICE OF FUNDAMENTAL PHYSICS: ASTROPHYSICS, NEUTRINO PHYSICS, QUANTUM ELECTRODYNAMICS

PNPI participants of the SHIPTRAP Collaboration:

S.A. Eliseev, S.V. Chenmarev, P.E. Filianin, Yu.I. Gusev, D.A. Nesterenko, Yu.N. Novikov

1. Introduction

Being a versatile tool for exploration of many problems of fundamental physics [1], the Penning trap mass spectrometry (PTMS) allows one to look into many scientific mysteries. The success in the methodology of PTMS targeted to the precision and accuracy allows to cover interests of different fields of physics: from nuclear physics demanding the precision of mass measurements of $\sim 10^{-8}$ towards neutrino physics which needs the precision better than 10^{-9} . The neutrino mass determination should deal with the precision of 10^{-11} .

The PTMS is superior in precision among other methods of mass measurements. At the same time, this method is accurate, *i. e.* reliable, since uses the carbon standard calibration. Another great advantage of PTMS is the highest sensitivity. Trapping a single ion is not only possible but also is desirable because single ion movement is not destroyed by other trapped particles. It is clear that technical requirements for the method are extremely severe, especially for the high homogeneity of the superconductive magnetic field. As a result, there are not many Penning trap systems in the world: three of them are in the USA, one in Canada, and four in Europe. PNPI cooperates with all the European centres and plans to create its own trap system PITRAP at the high-flux reactor PIK in Gatchina.

Over the last two decades, huge efforts have been made in different nuclear centres to improve trap-system parameters taking in mind that improvements in precision in one order of magnitude promise access to new deeper layers of problems in fundamental physics. The most successful was the SHIPTRAP Collaboration at the GSI Helmholtzzentrum für Schwerionenforschung (GSI; Darmstadt) where the increase in precision of at least one order of magnitude was reached. This progress has been achieved due to invention of a conceptually new phase-imaging method of detection of the resonance frequencies of excited ions in the trap [2, 3].

2. Phase-imaging method of ion-detection

The novel phase-imaging method [2, 3] of the ion cyclotron resonance (PI-ICR) is based on the projection of the ion motion onto a position-sensitive detector (MCP detector with a delay line) located on the axis of the measurement trap outside of the magnet (Fig. 1) in order to measure the accumulated phase. We measure the position of spots of ions extracted from the trap without excitation in the trap to determine the central position and with excitations to determine the accumulated phases of magnetron (at the frequency ν_-) and modified cyclotron (at the frequency ν_+) motions. After injection of ions into the measurement trap from the preparation trap, a dipole pulse at ν_- and dipole pulse at ν_z are applied to minimize the coherent component of the magnetron and axial motions, respectively. After this preparation step, the modified cyclotron motion of ions are excited at an arbitrary radius by a dipole pulse at ν_+ . Then the modified cyclotron motion of ions is immediately converted into the magnetron motion by a quadrupole pulse at ν_c . Thus, during the time t before extraction from the trap, ions are accumulating the phase $2\pi\nu_-t = \varphi_- + 2\pi n_-$, where n_- is the number of full revolutions. If the conversion pulse is applied right before extraction of ions from the MT, then during the time t ions are accumulating the phase $2\pi\nu_+t = \varphi_+ + 2\pi n_+$ before the conversion pulse is applied. Since the time t of the phase accumulation is the same in both patterns and $\nu_- + \nu_+ = \nu_c$, the angle

$$\varphi_c = \varphi_- + \varphi_+ = 2\pi\nu_c t - 2\pi(n_- + n_+)$$

allow us to define the cyclotron frequency ν_c . The frequencies ν_- and ν_+ are known with enough accuracy to determine numbers n_- and n_+ . If we place the position of the central spot in the origin, then the difference of

the polar angles of the position of spots α_1 and α_2 (Fig. 2) from pattern 1 and pattern 2, respectively, determines the angle $\varphi_c = \alpha_1 - \alpha_2$. We take the difference between the polar angles, because the magnetron and modified cyclotron motion rotates in opposite directions. Thus, measuring the position of the two spots (magnetron and cyclotron) we determine the angle between two phase spots φ_c and with that the cyclotron frequency ν_c .

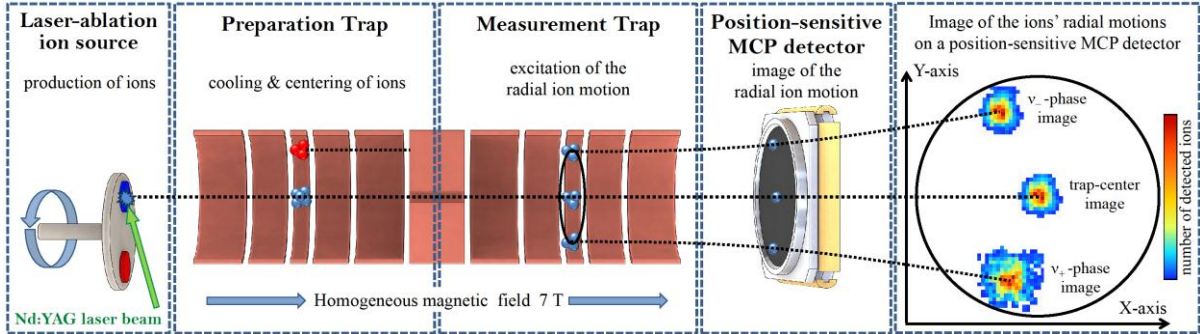


Fig. 1. Schematic of the SHIPTRAP installation in the off-line regime

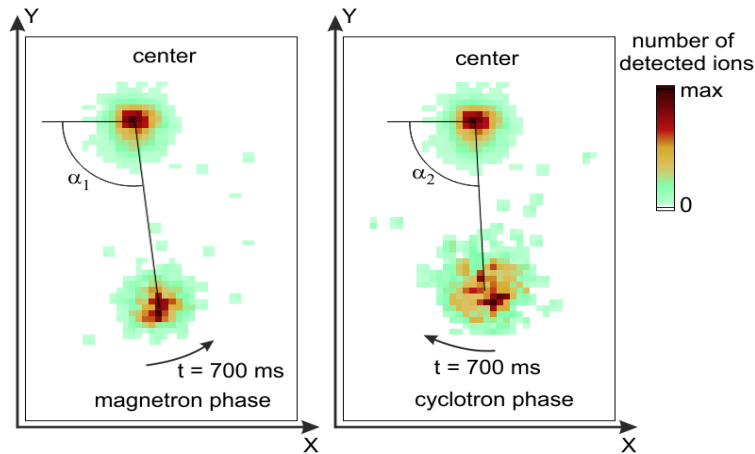


Fig. 2. Illustration of the phase-imaging method

From the cyclotron-frequency ratio for the mother and daughter nuclides the decay Q -value is given as

$$Q = M(\text{moth}) - M(\text{daught}) = [M(\text{daught}) - m_e][\nu_c(\text{daught}+)/\nu_c(\text{moth}+) - 1],$$

where $M(\text{moth})$ and $M(\text{daught})$ are masses of neutral mother and daughter atoms, respectively, index + stands for the ionic state and m_e is the electron mass.

The PI-ICR technique is substantially faster and offers of about 40-fold gain in the resolving power as compared to that in the commonly used time-of-flight ToF-ICR approach. The PI-ICR was firstly employed at SHIPTRAP for measuring of the mass difference of ^{130}Xe and ^{129}Xe atoms. About a three-day measurement of the mass difference is now sufficient to reach the statistical uncertainty of ~ 50 eV, which corresponds to the relative accuracy of about $4 \cdot 10^{-10}$. For comparison, with the ToF-ICR technique a larger uncertainty of ~ 200 eV can be achieved only after a week-run measurement.

3. Low energy transitions. Astrophysical implication

An investigation of modes of some astrophysical processes is based on the abundances of very long-lived nuclides with half-lives comparable with the age of the Universe. However, in stellar conditions, the lifetimes of some of these nuclides can be very different from the earth values. There are two reasons for that. In hot stellar conditions, besides the ground states nuclear excited states in nuclides may also be populated. These excited states can undergo beta-transitions, resulting in a considerable decrease of the effective lifetime. The second factor concerns the decay of these states in highly ionized atoms that influences the transition probabilities, which are especially large for small transition energies. These energies can be measured precisely and, which is of importance, reliably only using Penning traps. Such type of precise direct experiments was started at the SHIPTRAP-facility at GSI in the off-line regime. Precise decay energies for ^{123}Te [4] and ^{187}Re [5] were measured.

The nuclide ^{123}Te may be synthesized only during the *s* process, therefore the knowledge of its “stellar” features is of paramount importance for description of this process itself [6]. The first excited state of ^{123}Te with the 159 keV excitation energy is populated at a typical process temperature of $4 \cdot 10^8$ K with a probability of 2% with respect to the ground state (Fig. 3).

The thermal population of the excited states depends on the energy E^* and the spin value I^* of the excited state in the mother nuclide, on the spin value I of the ground state in the daughter nuclide, and on the temperature T of the environment: $f = (2I^* + 1)/(2I + 1)\exp(-E^*/kT)$. It depends also on the transition energy which includes the mass difference of the neutral ground states. We would like to stress the point that one of important ingredients of the analysis is the energy balance between the ionic ground states of the isobaric nuclides ($^{123}\text{Te}-^{123}\text{Sb}$) which can be derived from the mass difference of the neutral atoms measured directly. Due to opening of an allowed electron capture transition channel, the effective half-life becomes superior over that of the ground state transition for many orders of magnitude (Fig. 4).

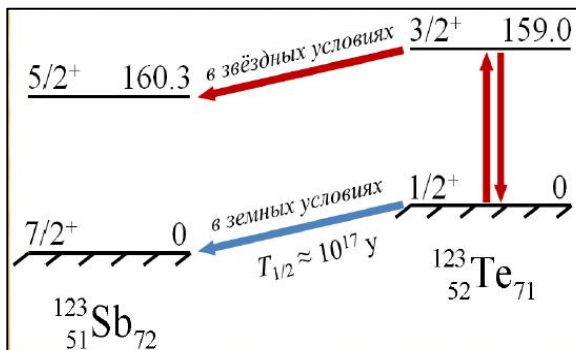


Fig. 3. Opening of a new capture channel from the excited level 159 keV in the hot stellar conditions

The determination of the decay energy Q of ^{123}Te was performed *via* a measurement of the mass difference with the daughter nuclide ^{123}Sb . The measurements of the resonance frequencies, which are in direct connection to the masses, were implemented with utilization of the novel phase imaging method. The result between the neutral ground state transition $Q = 51.912(67)$ keV was used to obtain a picture of the temperature dependence of the effective half-life of ^{123}Te , which showed dramatic, up to 14 orders of magnitude, enhancement in comparison to the earth conditions (Fig. 5).

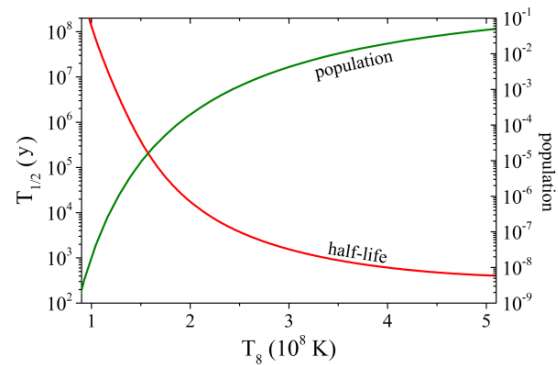


Fig. 4. Dependence of the level population and the half-life of the nuclide ^{123}Te in the stellar conditions

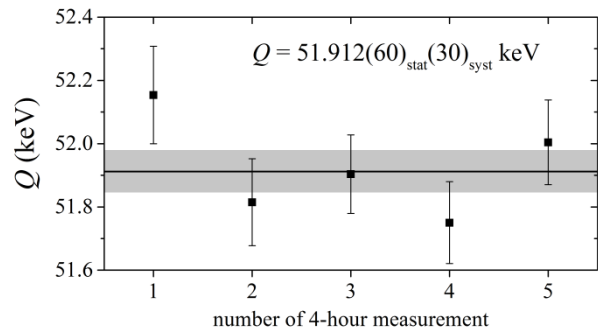


Fig. 5. Q -values for ^{123}Te determined from a series of resonance frequency measurements

Another illustration of astrophysical applications of direct precise mass measurements is a pair $^{187}\text{Re} - ^{187}\text{Os}$. Very small decay energy of ^{187}Re is connected to a very high lifetime which is 43.30(7) Gy for the neutral atoms. This property allowed one to propose for a long time ago a pair of $^{187}\text{Re} - ^{187}\text{Os}$ to be a candidate for the cosmochronology, *i. e.* for the Universe age determination, or simply to be the universe clock. The peculiarity of the 187-isobaric cosmic clock is based on the fact that ^{187}Os is a pure *s*-process nuclide, whereas ^{187}Re is a pure *r*-process product. The nuclide ^{187}Re decays into ^{187}Os whose *s*-component abundance is well investigated. Therefore, subtraction of this component from the total abundance of ^{187}Os gives the radiogenic contribution originating from the *r*-process nucleosynthesis. Hence, the properties of the latter can be reliably derived. This is a unique situation in the whole Periodic table. Possible production of ^{187}Re from the new *s*-process path through an isomer of ^{186}Re showed only less than 1% contribution relative to the abundance of ^{186}Os . Thus, the additional increase of ^{187}Re *via* the *s* process did not make any remarkable change in the chronometry.

Meanwhile, in the hot stellar conditions some of the low excited states of ^{187}Os are in the statistical equilibrium. They can participate in the electron capture process which populates levels in ^{187}Re . The strength of this process depends on the excited states thermal population, which in turn depends on the parameters described above and also on the energy of the transition which includes the mass difference of the neutral ground states. As in the case with $A = 123$ isobars, an important ingredient of the analysis is the energy balance between the ionic ground states of the isobaric nuclides ($^{187}\text{Re} - ^{187}\text{Os}$) which can be derived from the mass difference of these neutral atoms measured directly.

The measurement of the Q -value of ^{187}Re was performed with the Penning trap mass spectrometer SHIPTRAP (see Fig. 1) by direct measurements of the cyclotron frequencies of singly-charged ions $^{187}\text{Re}^+$ and $^{187}\text{Os}^+$. The ions were produced in a laser-ablation ion source by irradiating the corresponding metallic samples of natural Re and Os with a Nd-YAG laser beam. The formed ions were transferred from the ion source through the gas-filled radio-frequency quadrupole into a preparation Penning trap. In the preparation trap, the ions of interest were cooled and centered, remaining unwanted ions were removed. The cyclotron frequencies $\nu_c = qB/(2\pi m)$ of ions with the charge q and mass m in the magnetic field B were measured in the measurement trap with the novel phase-imaging technique developed at SHIPTRAP [2, 3]. To determine cyclotron-frequency ratio $r = \nu_c(^{187}\text{Os}^+)/\nu_c(^{187}\text{Re}^+)$, the measurements with singly charged ions $^{187}\text{Os}^+$ and $^{187}\text{Re}^+$ were performed alternately. The neighbouring measurements of the cyclotron frequency of the reference nuclide, *e. g.*, $^{187}\text{Os}^+$, performed before and after the frequency measurement of $^{187}\text{Re}^+$ were linearly interpolated to the time of the actual measurement of the $^{187}\text{Re}^+$, and the frequency ratio for the two nuclides at the same time was determined. The frequency ratio for a series of such single frequency ratios is the weighted mean. Typically, one series of measurements took 4 h (Fig. 6). The maximum error of the inner and outer uncertainty was taken for the weighted mean frequency ratio. A nonlinear drift of the magnetic field between two neighbouring frequency measurements was negligible. The mass-dependent and residual uncertainties were neglected since we measured ratios of the cyclotron frequencies of the mass doublets. In order to reduce fluctuations of the magnetic field, the temperature in the magnet bore and the pressure in the liquid helium cryostat were stabilized.

We used our measured value $Q = 2492 \pm 32$ keV [5] for assessment of the electron capture (EC) process by ^{187}Os ions in the hot stellar conditions. Some of the low excited states of ^{187}Os can be in the statistical equilibrium and can participate in the EC decay which populates ^{187}Re . Since the atoms in the hot conditions are only in the ionic states (with charge q^+), a possibility of EC depends on the energy balance:

$$Q_\varepsilon = M(^{187}\text{Os}^{q+}) + E^* - B_i - M(^{187}\text{Re}^{q+}) > 0,$$

where B_i is the binding energy of the captured electron; E^* is the energy of the excited state in ^{187}Os . The nuclear recoil energy can be neglected. The Q_ε -value of such an EC decay can be expressed through the masses of the neutral atoms $M(^{187}\text{Os})$ and $M(^{187}\text{Re})$:

$$Q_\varepsilon = M(^{187}\text{Os}) + E^* - B_i - M(^{187}\text{Re}) + (B(\text{Os}) - B(\text{Re})) - (B^{76-q}(\text{Os}) - B^{75-q}(\text{Re})),$$

where $B(\text{Os}) - B(\text{Re}) = 15.31$ keV is the difference between the tabulated total binding energies of electrons in atoms ^{187}Os and ^{187}Re ; $B^{76-q}(\text{Os})$ and $B^{75-q}(\text{Re})$ are the binding energies of $(76-q)$ electrons in the ion $^{187}\text{Os}^{q+}$ and $(75-q)$ electrons in the ion $^{187}\text{Re}^{q+}$, respectively.

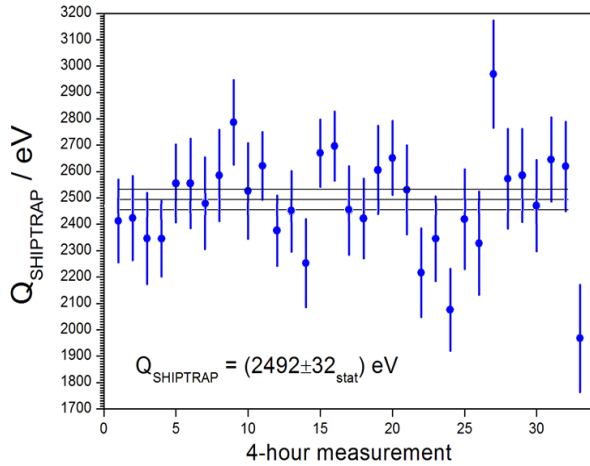


Fig. 6. Q -values for ^{187}Re determined from several series of resonance frequency measurements

One of the low lying states in ^{187}Os is the first excited state with the energy 9.756(19) keV. The EC from this state may energetically appear. The thermal population of this state is 7% when $T \approx 3.4 \cdot 10^7$ K. The energy balance analysis shows that the M -electron capture from this state in the hot stellar conditions can be expected. Meanwhile, there are other excited states in ^{187}Os with energies 187.42(3) and 190.57(6) keV, which can participate in the K -electron capture process. Note that the fractional population of 187.42 and 190.57 keV states with the spin values of 5/2 and 7/2 in the typical conditions of $T = 5.8 \cdot 10^8$ K are quite high (7 and 9%, respectively). As an example, we illustrate the partial M_1 capture from the 9.756(19) keV excited state by the ions Os^{66+} at the temperature $3.4 \cdot 10^7$ K. The energy Q_e for this capture is about 9.5 keV, which manifests a possibility of the EC by the s -process nuclide ^{187}Os towards the r -process nuclide ^{187}Re . Thus, this example with the partial capture shows that the reverse EC from ^{187}Os to ^{187}Re should be taken into account when considering this pair as a cosmochronometer [5].

4. Mass and nature of neutrinos

The neutrino mass is one of the stupendous challenges of modern science. So far, only upper limits on the effective masses of this tiny mysterious particle are known: $2 \text{ eV}/c^2$ for the antineutrino and $225 \text{ eV}/c^2$ for the neutrino. In the near future, a bunch of sophisticated experiments depicted in Fig. 7 will be able to push down both limits to a level of $0.2 \text{ eV}/c^2$. The most impressive is a jump expected for the neutrino mass improvement in the EC sector: three orders of magnitude.

Three experiments on determination of the neutrino mass plan to measure the atomic de-excitation spectrum which occurs after the atomic orbital EC by means of different methods of cryogenic microcalorimetry (CMC). An analytical description of this spectrum allows for determination of the neutrino mass on a sub-eV level, provided the decay energy Q_{EC} is independently and accurately measured with at least 1 eV precision [7].

The most relevant nuclide for such experiments is ^{163}Ho , which disintegrates only *via* EC. It is remarkable that there are no α -, β -, and γ -radiation associated with the decay of its ground state. In addition, a very attractive feature of this unique nuclide is the allowed character of the decay transition and the smallest EC-decay energy ever measured. Quite a large number of experiments measured the Q_{EC} -value with scattered results eventually obtained (Fig. 8). The value determined by CMC is considerably different from that evaluated in the literature (*green line* in Fig. 8). To solve this long-standing puzzle, direct precise measurements of the atomic masses of ^{163}Ho and ^{163}Dy , and thus of the Q_{EC} -value, with PTMS have been reliably performed. To prepare a suitable ^{163}Ho -sample for measurements, a sophisticated procedure was undertaken to first irradiate ^{162}Er with thermal neutrons at the ILL-reactor (Grenoble), then to separate chemically with subsequent mass-separation of the produced ^{163}Ho from the overwhelming amount of other nuclides in the Ho-sample by means of PTMS [8] (Fig. 9).

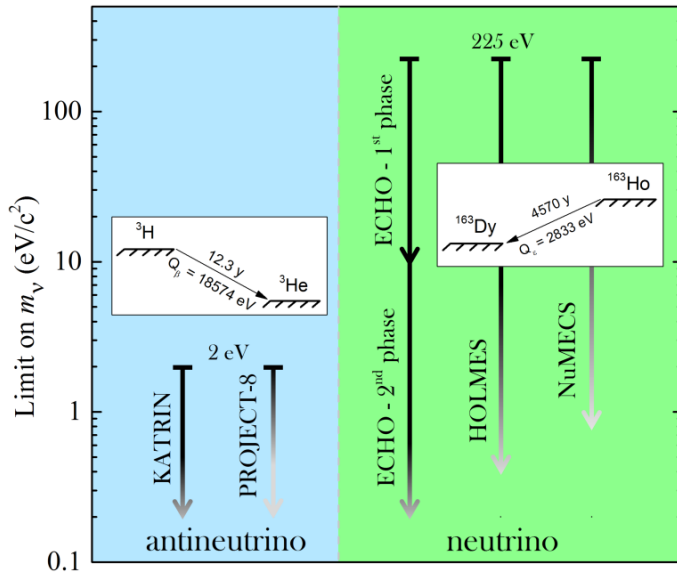


Fig. 7. Different planned projects dedicated to antineutrino (left blue side) and neutrino (right green side) mass determination

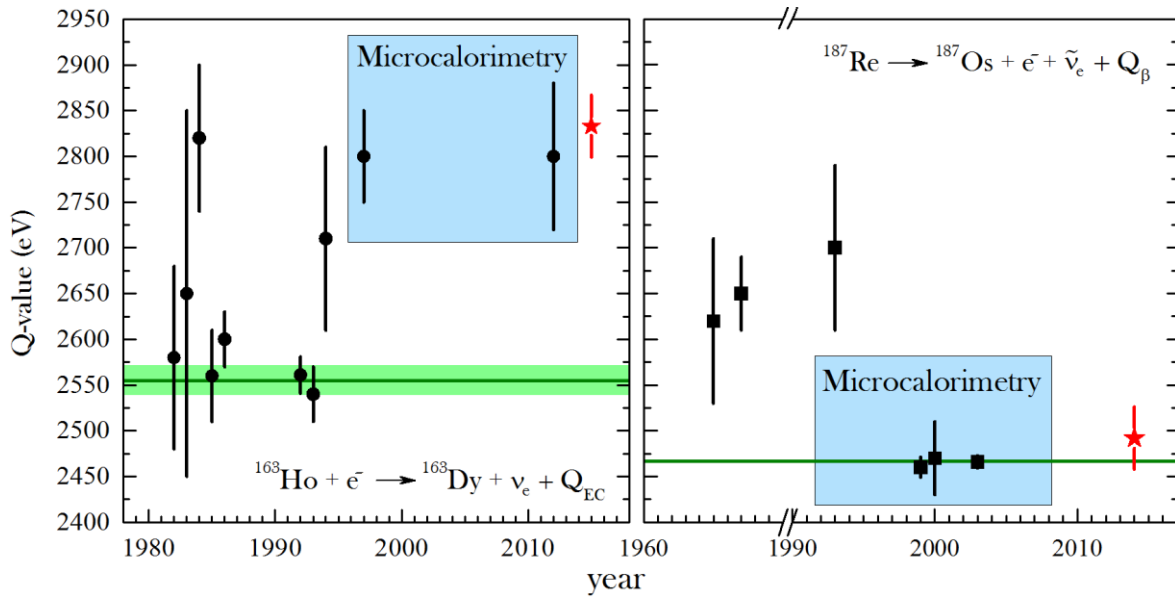


Fig. 8. Collection of the Q -values for ^{163}Ho electron-capture (left) and for ^{187}Re β decay (right). The average data evaluated in the literature are shown by green lines, and measured by PTMS at SHIPTRAP are marked with red stars

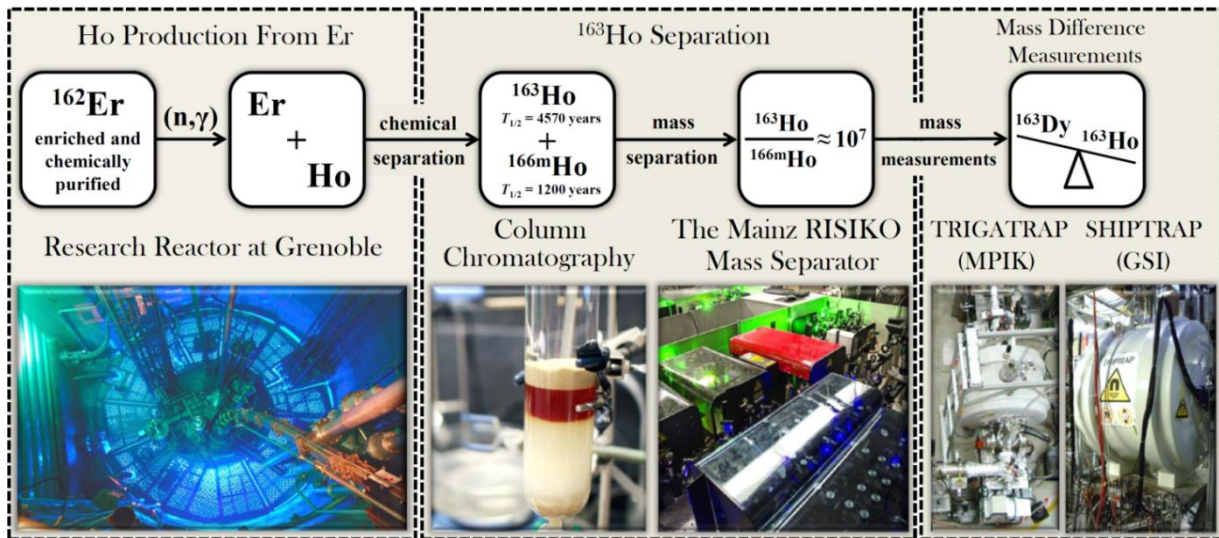


Fig. 9. Steps and mass weighing of the ^{163}Ho – ^{163}Dy difference

Careful and precision measurements of the mass difference with the use of the new method of phase-imaging detection of resonance frequency described above [2, 3] have demonstrated that the CMC Q_{EC} value is correct. PTMS has yielded the Q_{EC} -value of 2 833(34) eV [9] at the SHIPTRAP (see a red cross in Fig. 8), which differs from the evaluated value (in green) by about seven standard deviations. This result means a significant step in the campaign of the neutrino mass measurement, because it opens a door for the possibility to use CMC for the neutrino mass determination with ^{163}Ho on a sub-eV level. It shows that there are no systematic effects inherent in microcalorimetry, which would have a severe impact on the uncertainty of the planned experiments to determine the neutrino mass with this technique.

A goodness of CMC for the reliable Q -value determination was confirmed also by our PTMS-measurements of ^{187}Re – ^{187}Os mass difference [5] (see Fig. 8). The nuclide ^{187}Re may be used for the antineutrino mass determination in addition to the tritium experiment KATRIN.

A joint effort of CMC and high-precision PTMS in investigating the EC process can shed light on another problem of neutrino physics – possible existence of heavy sterile neutrinos with masses from 0.5 to 100 keV/ c^2 . These neutrinos are considered as the warm dark matter candidates (Fig. 10). Sterile neutrinos are expected to perturb the shape of the atomic de-excitation spectrum measured by CMC. This effect should be seen in the ratios of the capture probabilities from different electron orbits [10]. The sensitivity of the ratio values to the contribution of sterile neutrinos strongly depends on how accurately the mass difference between the parent and the daughter nuclides can be measured by PTMS. A determination of the contribution of sterile neutrinos on a level below 1% is feasible and the candidates, besides ^{163}Ho , are the following nuclides: ^{157}Tb , ^{193}Pt , ^{202}Pb , and ^{205}Pb [10, 11].

The detection of the relic neutrinos is another great challenge to modern science which can be solved also with the joint efforts of CMC and PTMS. It was shown in Ref. [12] that if the resonance conditions appear for the capture of relic antineutrinos by nuclei, then a considerable enhancement of the capture rates can be obtained that paves the way towards the experimental identification of relic neutrinos. Calculations and analyses [12] showed that a capture of relic antineutrinos by ^{157}Tb is a suitable case.

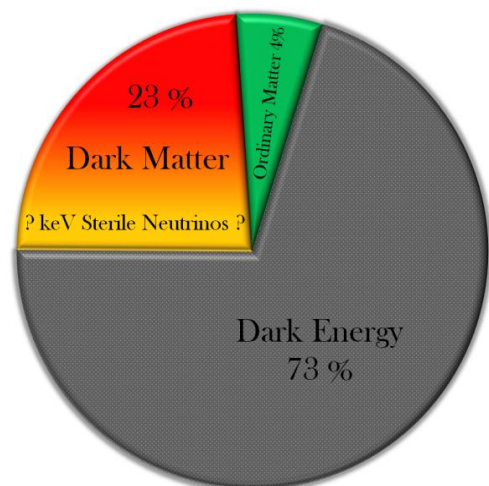


Fig. 10. Matter/energy distribution in Universe with a warm matter sterile neutrino possible contribution

5. Test of quantum electrodynamic predictions for a bound state atomic system

Dominating nuclear effects contributing to isotope shifts typically appear due to differences in nuclear masses, also denoted as nuclear recoil shifts (mass shifts), and by differences in nuclear sizes due to different spatial distributions of the nuclear charge (field shifts). We focus on the isotope dependence of the Zeeman-effect by studying g factors of lithium-like calcium isotopes $^{40}\text{Ca}^{17+}$ and $^{48}\text{Ca}^{17+}$. Featuring on the one hand a 20% mass difference and on the other hand almost identical nuclear charge radii known from experiments, these isotopes provide a unique system across the entire nuclear chart to test the relativistic nuclear recoil shift in presence of a magnetic field. For the experimental determination of the g -factor differences, the mass-values of the tested nuclides should be precisely known.

While the masses of $^{40}\text{Ca}^{17+}$ with a relative mass uncertainty of $\delta m_{\text{ion}}/m_{\text{ion}} = 0.6$ parts per billion (ppb) and also of the electron with $\delta m_e/m_e = 0.03$ ppb are known with sufficient accuracy, the tabulated value of the mass of ^{48}Ca is not adequately precise. High-precision measurements of the ^{48}Ca mass have been performed with the Penning-trap mass spectrometer SHIPTRAP at GSI. The atomic mass of ^{48}Ca was directly determined by measurements of the cyclotron frequency ratio R of the mass doublet of singly charged $^{48}\text{Ca}^+$ ions and $^{12}\text{C}_4^+$ carbon cluster ions. Combining the measured cyclotron frequency ratio $R = 1.00099010175(35)_{\text{stat}} (17)_{\text{syst}}$ ($\delta R/R = 0.39$ ppb) with the known carbon cluster mass $m(^{12}\text{C}_4^+)$ and correcting for the missing electrons and their corresponding binding energies, we obtain the following value for the mass of lithium-like ^{48}Ca :

$$m(^{48}\text{Ca}^{17+}) = 47943204044(19) \text{ u},$$

with

$$\delta m(^{48}\text{Ca})/m(^{48}\text{Ca}) = 0.4 \text{ ppb}.$$

Combining the calcium masses with the experimentally known Larmor to cyclotron frequency ratios, the measured g -factors are $g_{\text{meas}}(^{40}\text{Ca}^{17+}) = 1.99920204055(110)$ with $\delta g/g = 5.6 \cdot 10^{-10}$ and $g_{\text{meas}}(^{48}\text{Ca}^{17+}) = 1.99920202885(80)$ with $\delta g/g = 4.1 \cdot 10^{-10}$ [13]. The experimental g -factor difference turns out to be $\Delta g = 11.70(138) \cdot 10^{-9}$, which agrees with the theoretical value $10.305(27) \cdot 10^{-9}$. It allowed for the first time a direct test of the relativistic interaction of the electron spin with the motile nucleus.

Besides the tests of many-electron quantum electrodynamic (QED) calculations in magnetic fields by considering absolute values of the g factors, the analysis of the measured and predicted g -factor difference between the calcium isotopes deepens our understanding of the interaction between the bound electrons and the nucleus. A further reduction of the mass uncertainties will enable an even more stringent test of the relativistic recoil predictions in the future. The validation of QED calculations is a prerequisite for further fundamental measurements in atomic physics, for example, the determination of the fine structure constant α via g -factor measurements of heavy highly charged ions.

6. Conclusion

Increasing the precision of PTMS approximately by one order of magnitude that pinned down relative mass uncertainty to $4 \cdot 10^{-10}$, has opened new horizons for measurements targeted to the problems of fundamental physics. The most important technical invention was the novel method of detection of ions by their phase imaging on the position sensitive MCP-detector. This direct, precise, accurate, and very sensitive method of mass spectrometry utilized at the SHIPTRAP-facility at the GSI allowed to invade insight in different areas of Science:

1. It allowed to measure very small decay energies of nuclides of astrophysical interest with the result that in the stellar conditions their lifetimes are considerably shorter than the terrestrial ones, which should be taken into account in cosmochronology.
2. The unprecedented accuracy achieved in determination of the decay energy of ^{163}Ho has shown that the microcalorimetric data are correct without any systematic effects inherent in microcalorimetry, that opens a path to use this method for the neutrino mass determination.
3. The precise mass data obtained for ^{48}Ca allowed to test for the first time the relativistic interaction of electrons with the motile nuclei.

Our investigations showed also that PTMS can be successfully attributed to the search for the sterile and relic neutrinos, and can be used to study the relativistic predictions in QED. All in all, it shows that trap physics still holds a big area of creative imagination and ambitious extensions of the current research.

Acknowledgments

This work was performed within the close cooperation of the PNPI authors with the scientists of the SHIPTRAP Collaboration: Max-Planck-Institut für Kernphysik (Germany), GSI Helmholtzzentrum für Schwerionenforschung (Germany), Helmholtz-Institut Mainz and Johannes Gutenberg-Universität (Germany), Saint Petersburg State University (Russia). We would like to thank all our colleagues for very fruitful cooperation.

References

1. K. Blaum, Yu. Novikov, G. Werth, *Contemp. Phys.* **51**, 149 (2010).
2. S. Eliseev, K. Blaum, M. Block *et al.*, *Appl. Phys. B* **114**, 107 (2014).
3. S. Eliseev, K. Blaum, M. Block *et al.* *Phys. Rev. Lett.* **110**, 082501 (2013).
4. P. Filianin *et al.*, *Phys. Lett. B* **758**, 407 (2016).
5. D.A. Nesterenko, S. Eliseev, K. Blaum *et al.*, *Phys. Rev. C* **90**, 042501 (2014).
6. K. Takahashi, K. Blaum, Yu.N. Novikov, *Astroph. J.* **819**, 1 (2016).
7. L. Gastaldo, K. Blaum *et al.*, *Eur. Phys. J. Special Topics* **226**, 1623 (2017).
8. F. Schneider *et al.*, *Eur. Phys. J.* **51**, 89 (2015).
9. S.A. Eliseev, K. Blaum, M. Block *et al.*, *Phys. Rev. Lett.* **115**, 062501-5 (2015).
10. P.E. Filianin, K. Blaum, S.A. Eliseev *et al.*, *J. Phys. G: Nucl. Part. Phys.* **41**, 095004 (2014).
11. R. Adhikari *et al.*, *JCAP* **01**, 025 (2017).
12. J.D. Vergados, Yu.N. Novikov, *J. Phys. G* **41**, 125001 (2014).
13. F. Koehler *et al.*, *Nat. Commun.* **7**, 10246 (2016).

NUCLEAR MATTER DISTRIBUTIONS IN THE CARBON, BERILLIUM, AND BORON ISOTOPES DETERMINED IN MEASUREMENTS WITH THE DETECTOR IKAR AT GSI

G.D. Alkhazov, A.V. Dobrovolsky, A.G. Inglessi, A.V. Khanzadeev, G.A. Korolev,
G.E. Petrov, L.O. Sergeev, A.A. Vorobyev, V.I. Yatsoura

1. Introduction

Recent development of radioactive isotope beam techniques has opened tremendous opportunities to study structure of light unstable nuclei far from the valley of stability. New properties of the nuclear matter were discovered. The weak binding of the last bound nucleons causes formation of a neutron (proton) skin on the surface of a nucleus and formation of a halo, that is a large extension of the matter density distribution beyond the nuclear core. The study of the evolution of sizes and shapes of nuclei in the nuclear chart from the valley of beta stability to the drip-line has become an important direction of investigations in nowadays nuclear physics.

A systematic investigation of a carbon chain will explore the evolution of the nuclear structure with isospin. Information on halo structure in carbon isotopes is rather contradictory. Some nuclei ($^{15,17}\text{C}$) have relatively small separation energies, and a halo structure was observed in these nuclei. A one-neutron halo structure was identified in ^{15}C . The broad parallel momentum distribution of ^{16}C fragments shows no halo structure in ^{17}C . However, the existence of a tail in the density distribution was suggested in a study of the density distribution of ^{17}C in reaction cross section measurements at low energy. Contradictory results were also obtained for ^{16}C . In spite of a relatively large neutron separation energy, $2n$ -halo structure in ^{16}C was suggested to explain a large enhancement in the reaction cross sections. On the other hand, relatively broad momentum distributions of the breakup fragments for ^{16}C were observed.

The proton drip-line nucleus ^8B is considered as the most interesting candidate for the occurrence of a proton halo since it has a very small proton separation energy $S_p = 136.4$ keV. Studies of the proton-rich nuclei ^8B and ^7Be (presumable core for ^8B) are important for both nuclear physics and astrophysics. The ^8B nucleus is produced in the sun through the $^7\text{Be}(p, \gamma)^8\text{B}$ reaction and emits a high energy neutrino. The proton capture rate in ^7Be strongly depends on the ^8B structure. Thus, the size of ^8B and the shape of the proton density distribution at large distances are important for description of the solar neutrino flux. At present, ^8B is considered to be a proton halo nucleus, in spite of the existence of the Coulomb and centrifugal barriers. The main evidence for the proton halo structure in ^8B came from the experiments in which a narrow longitudinal momentum distribution of ^7Be fragments after proton break-up and large one-proton removal cross sections in break-up reactions were measured.

The size and the shape of the radial distribution of the nuclear matter are fundamental properties of nuclei and can be the most convincing evidence for the proton halo structure. The root-mean-square (rms) matter radius R_m of ^8B was deduced in several experiments through measurements of the reaction (interaction) cross section σ_R (σ_I). However, the values for the matter radius determined in these experiments are widely scattered, ranging from 2.38(2) to 2.61(8) fm.

The proton–nucleus elastic scattering at intermediate energies is considered to be one of the best methods to obtain nuclear matter density distributions in stable nuclei. At these energies, the Glauber multiple scattering theory accurately describes the process of elastic scattering and connects the measured differential cross section with the nuclear matter distribution in a rather unambiguous way. In order to study exotic nuclei, it was proposed in PNPI to perform experiments in inverse kinematics using radioactive nuclear beams and the hydrogen active target IKAR. An analysis of the shape of the measured cross sections makes it possible to determine the sizes of the nuclear core and of the halo. The proposed method was successfully used at GSI Helmholtzzentrum für Schwerionenforschung (GSI) at energies around 700 MeV/u to measure absolute differential cross sections for proton elastic scattering in inverse kinematics on the radioactive neutron-rich isotopes ^6He , ^8He , ^8Li , ^9Li , ^{11}Li , ^{12}Be , and ^{14}Be [1–4]. An analysis of the data yielded parameters of the nuclear matter distributions. The elastic $p^4\text{He}$ and $p^6\text{Li}$ differential cross sections were also measured as a consistency check of the experimental method, including the procedure applied for the data analysis [1, 4].

In this paper, we present the first measurement of the absolute differential cross sections for proton elastic scattering on the ^{12}C , ^{15}C , ^{16}C , ^{17}C , ^7Be , and ^8B nuclei in inverse kinematics at an energy of 0.7 GeV/u (Experiment S358). The study of ^{12}C as the $N = Z$ nucleus for which the matter and proton radii are well known was carried out to check the experimental method.

2. Experimental set-up and procedure

The experiment was performed at GSI. A primary ^{22}N beam produced by the UNILAC–SIS accelerator complex was focused on an 8 g/cm² Be production target at the entrance of the fragment separator (FRS). The produced beryllium, boron and carbon ions were separated according to their magnetic rigidity. The contamination from other nuclei was below the 0.1% level. The energy of the secondary beam at the centre of the hydrogen target was ~ 700 MeV/u with an energy spread of 1.3%. The mean energy value was determined with an accuracy of about 0.1%. A schematic view of the experimental layout is shown in Fig. 1.

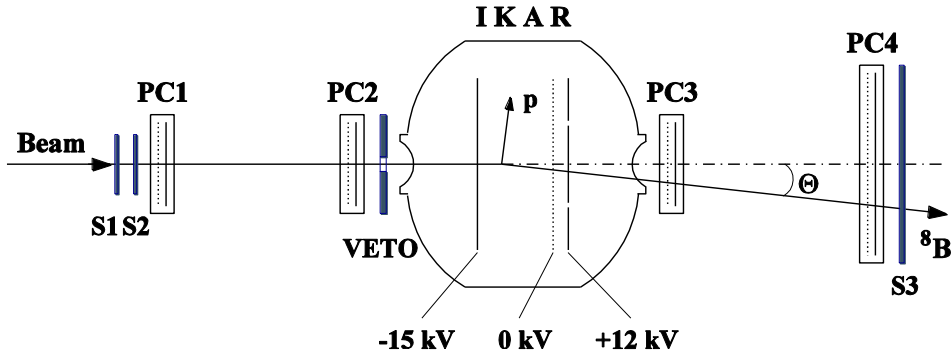


Fig. 1. Schematic view of the experimental set-up for small-angle proton elastic scattering on exotic nuclei in inverse kinematics. The hydrogen-filled ionization chamber IKAR serves simultaneously as a gas target and a detector for recoil protons. For the sake of simplicity only one chamber module of six identical ones is shown. The tracking system consisting of four multi-wire proportional chambers PC1–PC4 determines the scattering angle θ of the projectile. The scintillation counters S1–S3 and VETO are used for beam identification and triggering

The main constituent of the set-up was the active target IKAR filled with pure hydrogen at a pressure of 10 bar, which served simultaneously as a gas target and a recoil proton detector. IKAR was developed at PNPI [5, 6] and was originally used in experiments on small-angle hadron elastic scattering. The chamber consists of six identical modules. The signals from the ionization chamber provide the recoil energy T_R and the z coordinate of the point where the scattering in IKAR occurred. The recoil protons were registered in IKAR in coincidence with the scattered projectile particles. The momentum transfer could be determined either from the measured recoil energy T_R or from the value of the scattering angle θ of the projectiles which was measured by a tracking detector system consisting of two pairs of two-dimensional multi-wire proportional chambers (PC1–PC2 and PC3–PC4), arranged upstream and downstream with respect to IKAR. A set of scintillation counters (S1–S3 and VETO) was used for triggering and identification of the beam particles. For carbon isotopes, the ALADiN magnet and measurements of the coordinate behind the magnet were also used in order to eliminate break-up channels like it was done in our previous experiments [3, 4]. The absolute differential cross section $d\sigma/dt$ was determined using the relation

$$d\sigma/dt = dN / (dtMn\Delta L). \quad (1)$$

Here, dN is the number of elastic proton–nucleus scattering events in the interval dt of the four-momentum transfer squared t ; M is the corresponding number of beam particles impinging on the target; n is the density of the hydrogen nuclei known from the measured gas pressure and temperature; ΔL is the effective target length. The value of t was calculated as $|t| = 2mT_R$, (where m is the mass of the proton) for the low momentum transfers, and from the scattering angle θ of the projectiles for the higher momentum transfers [4]. The differential cross sections $d\sigma/dt$ obtained in the experiment are displayed in Fig. 2 for

the carbon isotopes and in Fig. 3 for ${}^7\text{Be}$ and ${}^8\text{B}$. The indicated energies correspond to the equivalent proton energies in direct kinematics.

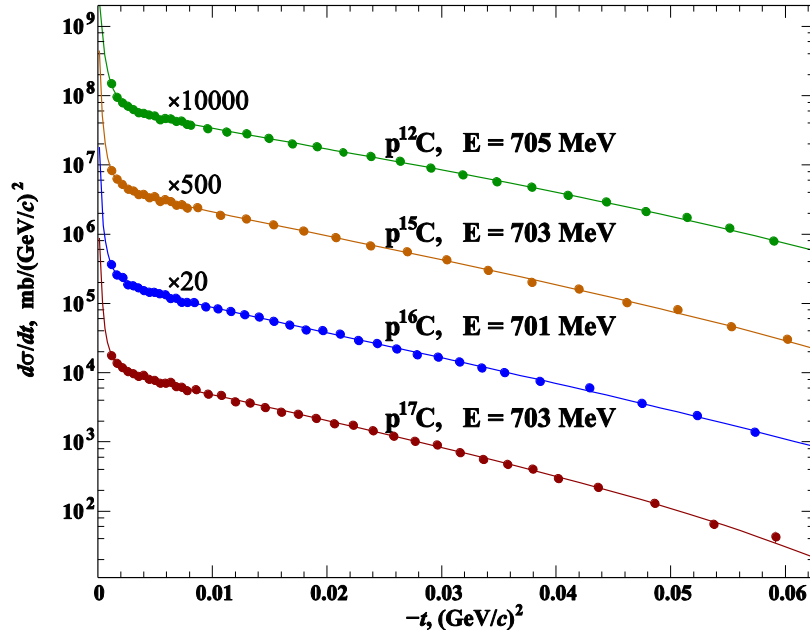


Fig. 2. Absolute differential cross sections for $p^{12, 15, 16, 17}\text{C}$ elastic scattering versus the four-momentum transfer squared. The indicated energy corresponds to the equivalent proton energy for direct kinematics. The plotted error bars denote statistical errors only. The *solid line* represents the cross section calculated by means of the Glauber multiple-scattering theory using a phenomenological matter distribution Gaussian oscillator with fitted parameters

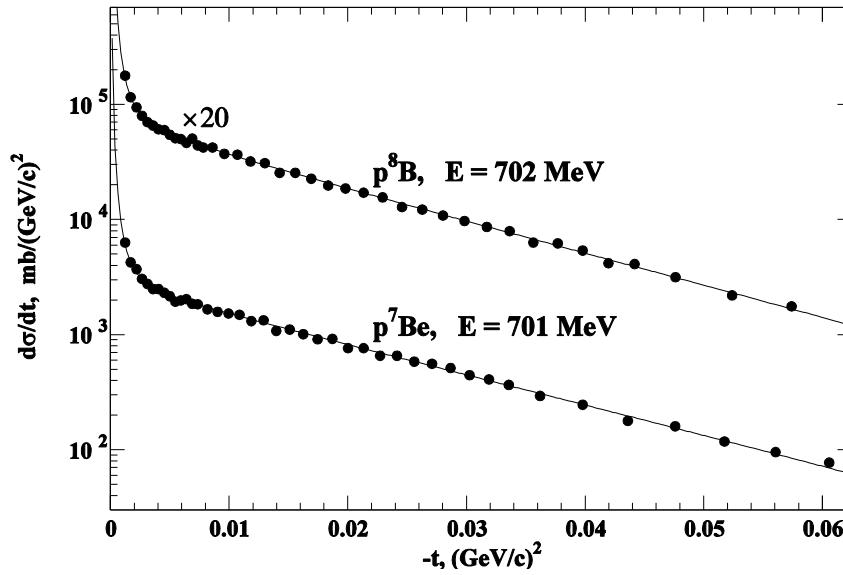


Fig. 3. Absolute differential cross sections for $p^8\text{B}$ and $p^7\text{Be}$ elastic scattering versus the four-momentum transfer squared. The indicated energy corresponds to the equivalent proton energy for direct kinematics. The plotted error bars denote statistical errors only. The *solid line* represents the cross section calculated by means of the Glauber multiple-scattering theory using a phenomenological matter distribution Gaussian oscillator with fitted parameters

3. The data analysis

To establish the nuclear matter density distributions from the measured cross sections, the Glauber multiple scattering theory was applied. Calculations were performed using the basic Glauber formalism for proton–nucleus elastic scattering and taking experimental data on the elementary proton–proton and proton–neutron scattering amplitudes as input. In the analysis of the experimental data, the nuclear many-body density ρ_A was taken as a product of the one-body densities, which were parameterized with different functions. The parameters of these densities were found by fitting the calculated cross sections to the experimental data. Four parameterizations of phenomenological nuclear density distributions were applied, labeled as symmetrized Fermi (SF), Gaussian halo (GH), Gaussian–Gaussian (GG), and Gaussian oscillator (GO). Each of these parameterizations has two free parameters. While the SF and GH parameterizations do not make any difference between the core and halo distributions, the GG and GO parameterizations assume that the nuclei consist of core nucleons and valence nucleons with different spatial distributions. The core distribution is assumed to be a Gaussian one in both the GG and GO parameterizations. The valence nucleon density is described by a Gaussian or a $1p$ shell harmonic oscillator-type distribution within the GG or GO parameterizations, respectively. The free parameters in the GG and GO parameterizations are the rms radii R_c and R_v (R_h) of the core and valence (“halo”) nucleon distributions. It was assumed that the considered nuclei have one (^{15}C , ^{17}C) or two (^{16}C) valence nucleons, ^8B consists of a ^7Be core and a loosely bound valence proton, while ^7Be was considered to consist of a ^4He core and a ^3He “halo”.

4. Results on the matter density distributions and radii

The parameterizations SF and GH applied for ^{12}C allowed us to describe the data equally well and have yielded practically identical values of the matter radius $R_m = 2.37(4)$ fm. For $^{15, 16, 17}\text{C}$, ^7Be , and ^8B good descriptions of the cross sections have been obtained with all the SF, GH, GG, and GO density parameterizations used. The corresponding values of the rms matter radii R_m deduced with all the four parameterizations for these nuclei are close to each other, within rather small errors. The values of R_m , averaged over the results with all density parameterizations and the values of R_c and R_v obtained with the GG and GO density parameterizations are presented in Table. The errors include statistical and systematical uncertainties. The systematical errors in R_m appear due to uncertainties in the absolute normalization of the cross sections, in the t -scale calibration, in the parameters of the elementary proton–nucleon scattering amplitudes, and due to differences in the model density distributions used.

The core and total matter distributions deduced for carbon isotopes are shown in Fig. 4. The core and matter distributions deduced for ^8B by using different parameterizations are compared in Fig. 5 with the matter distribution for ^7Be . All density distributions refer to point-nucleon distributions. Note that the description of the matter density distributions for all the four parameterizations are rather similar in the case of all considered nuclei. All versions also resemble each other in reproducing extended matter distribution in ^{15}C and ^{16}C .

Table

Summary of preliminary results obtained in the present experiment*

Isotope	Composition	R_m , fm	R_c , fm	R_v , fm	$\kappa = R_v/R_c$
^{12}C	–	2.37(4)	–	–	–
^{15}C	$^{14}\text{C} + n$	2.59(5)	2.41(2)	4.36(38)	1.81
^{16}C	$^{14}\text{C} + 2n$	2.72(6)	2.39(6)	4.45(26)	1.86
^{17}C	$^{16}\text{C} + n$	2.66(4)	2.55(2)	3.99(48)	1.56
^7Be	$^4\text{He} + ^3\text{He}$	2.42(4)	1.85(14)	3.00(11)	1.62
^8B	$^7\text{Be} + p$	2.58(6)	2.25(3)	4.24(25)	1.88

* The values R_m , R_c , and R_v denote the rms radii of the matter, core, and valence nucleon(s) distributions, κ is the ratio R_v/R_c .

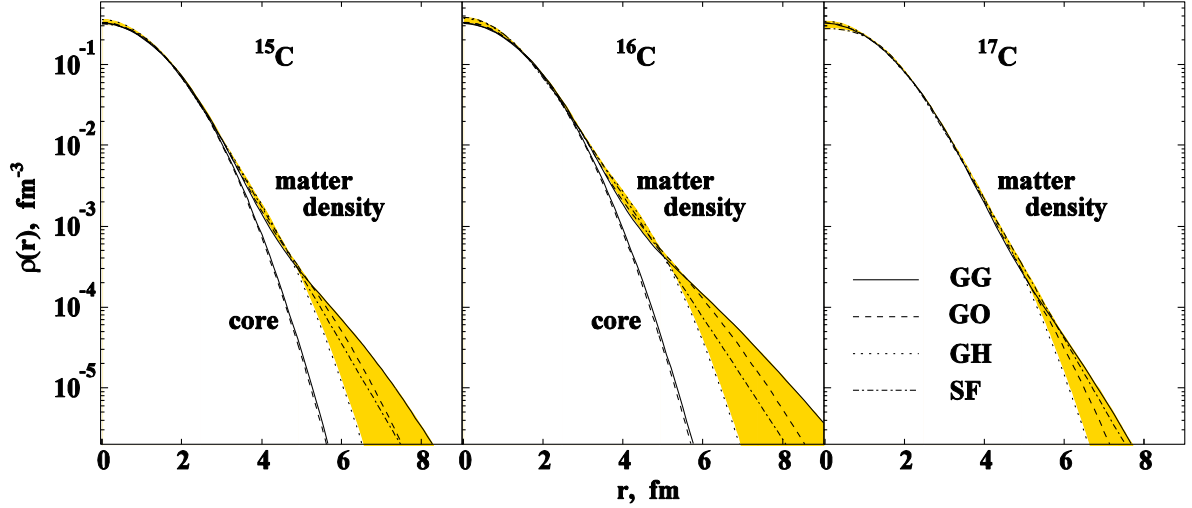


Fig. 4. The core and nuclear point matter distributions deduced for ^{15}C , ^{16}C , and ^{17}C with the GG, GO, GH, and SF parameterizations. The *shaded areas* represent the envelopes of the density variation within the model parameterizations applied, superimposed by the statistical errors. All density distributions are normalized to the number of nucleons

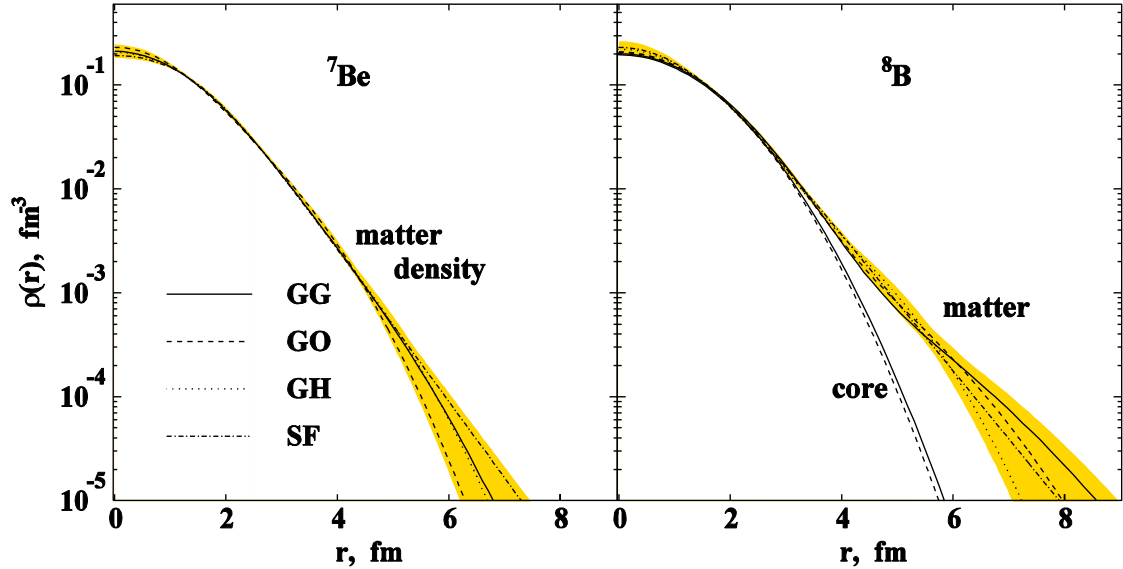


Fig. 5. The core and nuclear point matter distributions deduced for ^8B and ^7Be with the GG, GO, GH, and SF parameterizations. The *shaded areas* represent the envelopes of the density variation within the model parameterizations applied, superimposed by the statistical errors. All density distributions are normalized to the number of nucleons

A criterion for a quantitative assessment of halo nuclei was proposed by Grigorenko *et al.* [7]. The ratio of the valence nucleon to the core nucleon radii $\kappa = R_v/R_c$ is used as a gauge for the halo existence. For light nuclei close to the valley of beta stability, theory predicts typically $\kappa \approx 1.20\text{--}1.25$, while for a halo structure this value can be essentially larger, up to $\kappa > 2$. In the three-cluster model [7] a value of $\kappa = 1.75$ was obtained for ^8B , which can be compared with $\kappa = 1.88(14)$ deduced from the present measurement. In previous experiments on proton elastic scattering with the same method [1, 4] we obtained for the neutron halo nuclei ^6He and ^{12}Be the values of $\kappa = 1.76$ and $\kappa = 1.91$, respectively, the values which are close to those for ^{15}C , ^{16}C , and ^8B in the present experiment. Thus, from our analysis it follows that there are neutron halos in ^{15}C and ^{16}C and there is a proton halo in ^8B . The measured rms nuclear matter radius $R_m = 2.37(4)$ fm for ^{12}C is in good agreement with the value of $R_m = 2.35(2)$ fm, known from measurements of the reaction cross section and with the value of the rms proton radius $R_p = 2.327(2)$ fm determined from the charge radii measured by elastic electron scattering.

5. Discussion

By combining the matter radius R_m deduced in the present work for ${}^7\text{Be}$ with $R_p = 2.507(17)$ fm measured by laser spectroscopy and using the expression

$$AR_m^2 = ZR_p^2 + NR_n^2, \quad (2)$$

where Z and N are the numbers of protons and neutrons; the rms neutron radius for ${}^7\text{Be}$ was determined as $R_n = 2.27 \pm 0.10$ fm. For the thickness of the proton skin $\delta_{pn} = R_p - R_n$, we deduced the value of $\delta_{pn} = 0.23(10)$ fm. Thus, ${}^7\text{Be}$ has a considerable proton skin.

In some theoretical studies, the nucleon structure of ${}^8\text{B}$ was treated as a three-cluster system. In particular, the theoretical description of ${}^8\text{B}$ in Ref. [7] utilizes a (${}^4\text{He} + {}^3\text{He} + p$) three-body model with explicit inclusion of the binary (${}^7\text{Be} + p$) channel. The model describes the bulk properties of ${}^8\text{B}$ well and predicts a value of $R_m = 2.59$ fm in agreement with our result $R_m = 2.58(6)$ fm. An important finding of this model is that the presence of a loosely bound proton leads to a contraction of the ${}^7\text{Be}$ cluster inside ${}^8\text{B}$. Indeed, according to our measurements, the deduced ${}^7\text{Be}$ core of the ${}^8\text{B}$ nucleus $R_c = 2.25(3)$ fm is essentially smaller than the ${}^7\text{Be}$ matter radius $R_m = 2.42(4)$ fm. Assuming that for ${}^8\text{B}$ the rms radius of the neutron distribution R_n equals the core radius R_c and using expression (2) we obtain the rms radius of the proton distribution as $R_p = 2.76 \pm 0.09$ fm. In Figure 6 the value of R_p measured in the present work for ${}^8\text{B}$ is compared with the values of R_p derived for other boron isotopes. The values for the proton radii for the stable ${}^{10}\text{B}$ and ${}^{11}\text{B}$ are known from electron and π^+ scattering measurements and from muonic atoms X -rays studies. The values R_p for the neutron-rich boron isotopes ${}^{12-17}\text{B}$ were recently determined from charge-changing cross section measurements at GSI. The ${}^8\text{B}$ proton radius is fairly larger than the ones for the stable boron isotopes. This observation supports the concept of a halo structure in ${}^8\text{B}$. Taking into account the relation between the point proton and the charge radius of a nucleus, the ${}^8\text{B}$ charge radius is deduced to be $R_{ch} = 2.89 \pm 0.09$ fm.

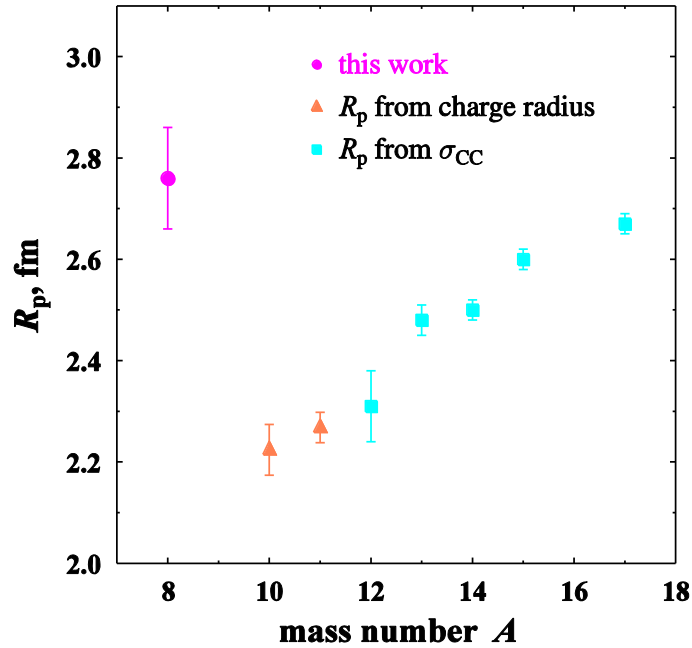


Fig. 6. Experimental values of the proton radii R_p for the boron isotopes. The *filled circle* for ${}^8\text{B}$ is the result of the present work. The *filled triangles* for ${}^{10}\text{B}$ and ${}^{11}\text{B}$ are proton radii determined from the measured charge radii. The *filled squares* for ${}^{12-17}\text{B}$ are the proton radii extracted from the charge-changing cross sections through a Glauber model analysis with harmonic oscillator densities

Finally, for the thickness of the proton skin $\delta_{pn} = R_p - R_n$ for ${}^8\text{B}$ we obtain a value of $\delta_{pn} = 0.51(9)$ fm. This value seems to be the largest one among the measured values for proton-rich nuclei.

6. Conclusion

In the present work we used a method developed by PNPI–GSI Collaboration of small angle proton–nucleus elastic scattering in inverse kinematics to determine nuclear density distributions of the carbon isotopes ^{12}C , ^{15}C , ^{16}C , ^{17}C , and proton-rich ^7Be and ^8B . The absolute differential cross sections for proton elastic scattering were measured in the range $0.001 \leq |t| \leq 0.06$ (GeV/c)² of the four-momentum transfer squared. The cross sections were determined using secondary beams from GSI fragment separator at the energy of ~ 700 MeV/u. The hydrogen-filled ionization chamber IKAR served simultaneously as a hydrogen target and a recoil-proton detector.

The nuclear matter radii and radial matter distributions have been determined with the aid of the Glauber multiple-scattering theory. In the analysis, four phenomenological density distributions were used, each of these parameterizations has two free parameters. For all investigated nuclei good descriptions of the cross sections were obtained with all the density parameterizations used. Our measurements confirm existence of a halo structure in ^{15}C and ^{16}C . In ^{17}C a halo structure was not found in spite of small neutron separation energy $S_n = 0.728$ MeV. The measured value of $R_m = 2.66(4)$ fm is essentially smaller than the previously known value. The value of $R_m = 2.42(4)$ fm deduced for ^7Be is larger than the matter radii obtained in previous experiments based on measurements of total interaction and reaction cross sections. On the other hand, our value of R_m is in perfect agreement with most theoretical predictions. Similar descriptions of the matter density distributions were obtained for all four parameterizations including GG and GO, which suggest two-cluster structure ($^4\text{He} + ^3\text{He}$) of ^7Be .

The matter density distributions of the proton-rich ^8B nucleus which has also important astrophysical implications, are very close for all the parameterizations used and demonstrate an extended form. In the case of GG and GO parameterizations, the deduced rms halo radius $R_h = 4.24(25)$ fm is 1.88 times larger than the rms core radius $R_c = 2.25(3)$ fm, thus giving clear evidence for a halo structure. In the three-body model Grigorenko *et al.* [7] predicted a contraction of the ^7Be cluster inside ^8B . Our measurement supports this finding. Assuming that for ^8B the rms radius of the neutron distribution is equal to the core radius R_c , we have deduced the rms radius of the proton distribution as $R_p = 2.76(9)$ fm. This value is in agreement with theoretical calculations and is significantly larger than the R_p values for the neighbouring successive boron isotopes confirming the existence of a halo in ^8B . The ^8B proton radius R_p and the corresponding charge radius $R_{ch} = 2.89(9)$ fm are determined experimentally for the first time. The proton halo in ^8B is the largest one measured up to now.

Experiment S358 was performed by the IKAR Collaboration: G.D. Alkhazov, A.V. Dobrovolsky, A.G. Inglessi, A.V. Khanzadeev, G.A. Korolev, G.E. Petrov, L.O. Sergeev, A.A. Vorobyev, V.I. Yatsoura – PNPI; P. Egelhof, A. Estradé, I. Dillmann, F. Farinon, H. Geissel, S. Ilieva, Y. Ke, O.A. Kiselev, J. Kurcewicz, X.C. Le, Yu.A. Litvinov, A. Prochazka, C. Scheidenberger, H. Simon, M. Takechi, S. Tang, V. Volkov, H. Weick – GSI.

References

1. G.D. Alkhazov, A.V. Dobrovolsky, P. Egelhof *et al.*, Nucl. Phys. A **712**, 265 (2002).
2. S.R. Neumaier, G.D. Alkhazov, M.N. Andronenko *et al.*, Nucl. Phys. A **712**, 246 (2002).
3. A.V. Dobrovolsky, G.D. Alkhazov, M.N. Andronenko *et al.*, Nucl. Phys. A **766**, 1 (2006).
4. S. Ilieva, F. Aksouh, G.D. Alkhazov *et al.*, Nucl. Phys. A **875**, 8 (2012).
5. A.A. Vorobyov, G.A. Korolev, V.A. Schegelsky *et al.*, Nucl. Instr. Meth. **119**, 509 (1974).
6. A.A. Vorobyov, Yu.S. Grigorev, Yu.K. Zalite *et al.*, Exp. Tech. **24**, 1127 (1982).
7. L.V. Grigorenko *et al.*, Phys. Rev. C **57**, 2099(R) (1998).

ONSET OF DEFORMATION IN NEUTRON-DEFICIENT Bi ISOTOPES

A.E. Barzakh, D.V. Fedorov, V.S. Ivanov, P.L. Molkanov, F.V. Moroz,
S.Yu. Orlov, V.N. Panteleev, M.D. Seliverstov, Yu.M. Volkov

1. Introduction

Understanding the shape evolution and shape coexistence in atomic nuclei is one of the greatest challenges faced by theories of nuclear structure [1]. The neutron-deficient isotopes near $Z = 82$ exhibit the richest manifestation of the shape evolution and shape coexistence phenomena. The behaviour of the ground and isomeric states shape differs markedly for different Z in this region. While in the Hg isotopic chain ($Z = 80$) a jump-like odd-even shape staggering was observed at $N < 106$ [2], for Po nuclei ($Z = 84$) an early onset and gradual increase of deformation was found at $N < 113$ [3]. At the same time, the neutron-deficient Pb and Tl nuclei ($Z = 82, 81$) remain essentially spherical up to and beyond the neutron mid-shell at $N = 104$ [4–6].

Investigations of the neutron-deficient Bi isotopes ($Z = 83$) play an important role in the understanding of the shape evolution and shape coexistence phenomena in this region of the nuclide chart. These isotopes reveal, along with the near spherical ground states, the presence of oblate and prolate structures resulting from the occupancy of $\pi i_{13/2}$ and $\pi s_{1/2}$ orbitals (*e. g.*, see Ref. [7] and references therein).

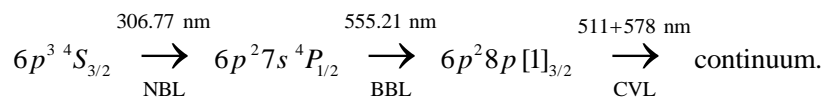
The Bi isotopic chain is intermediate between the Pb ($Z = 82$) and Po ($Z = 84$) chains with different shape evolution patterns. On the other hand, the Tl and Bi isotopic chains are “mirror” in respect to the filled proton shell ($Z = 82$). However, in contrast to Tl isotopes with their nearly spherical ground states down to $N = 98$ [6], in neutron deficient Bi isotopes there are some indications on possible structural changes in their ground states below $N = 110$ – 108 (see Ref. [7] for even- N isotopes and Ref. [8] for odd- N isotopes). In particular, in work [9] the binding energies of the $9/2^-$ ground states in Bi were compared with the results of simplified shell-model calculations. These calculations agree well with the experimental data until $A = 191$ ($N = 108$), where a small deviation is discernible. This deviation was related to the onset of deformation [9].

Observables that give a model-independent information on the nuclear shape are the charge radius changes determined by the atomic spectroscopy *via* isotope shift (IS) measurements. Besides, the atomic spectroscopy gives information on the nuclear electromagnetic moments *via* hyperfine structure (hfs) measurements. So far, atomic spectroscopy measurements for a restricted set of bismuth isotopes $^{202-213}\text{Bi}$ [10] have been performed. It is important to perform systematic IS/hfs measurements for the Bi isotopic chain, especially at $N < 111$ ($A < 194$), where the structural change in the adjacent Po isotopic chain was found [3] and the onset of deformation for the Bi ground states was suggested [9].

2. Experimental details

The method of the resonance laser photoionization in a laser ion source (see Refs. [11, 12] and references therein) for bismuth IS/hfs measurements was used. All measurements were carried out at the laser-nuclear complex [13] of the IRIS (investigation of radioactive isotopes at the synchrocyclotron) facility working on-line with a 1-GeV proton beam of the Petersburg Nuclear Physics Institute synchrocyclotron.

The radioactive Bi isotopes under study were produced in spallation reactions by 1-GeV protons in a high density uranium monocarbide target [14] with the thickness of $40 \text{ g} \cdot \text{cm}^{-2}$. The spallation products diffused out of the high temperature target as neutral atoms into the hot cavity of the ion source. Laser beams were introduced into this cavity to perform three-step resonance ionization of Bi atoms *via* the following scheme [12]:



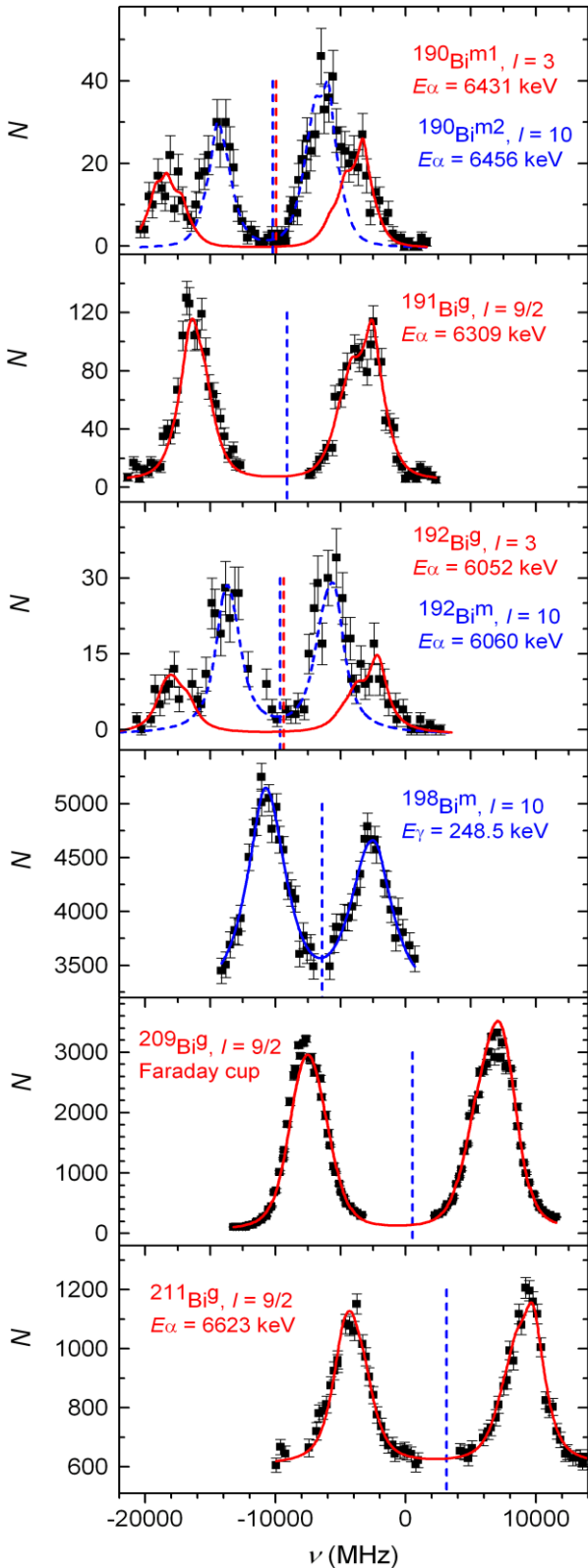


Fig. 1. The hfs spectra of the selected Bi isotopes: *full lines* are the results of fitting with the Voigt profiles; *vertical dashed lines* mark the centre of gravity of the corresponding hfs

A narrowband scanning dye laser (NBL; linewidth of 700 MHz) on the first step was tuned to the 306.77 nm transition. At the second step, a beam of a broadband laser (BBL; linewidth of 60 GHz) was used. A copper-vapor laser (CVL) beam ionized bismuth atoms from the level of 50594.59 cm^{-1} into continuum. For a detailed description of the laser set-up see Ref. [13].

After selective laser photoionization, the radioactive Bi ions were extracted and accelerated to 30 keV, mass separated and directed to the counting station placed at the tape station at the exit of the mass-separator. The photo-ion current was measured *via* detection of characteristic β - γ and/or α decays of the isotopes in question as a function of the scanned laser frequency of the first excitation step. The experimental spectra represent the dependence of the photo-ion current on the scanned laser frequency (Fig. 1).

3. Results

The position of the hyperfine components on the spectrum of the isotope with atomic number A is determined by the well-known formulas with four free parameters: the isotope shift relative to the stable ^{209}Bi ($\delta_{VA, 209}$), the magnetic hfs constants (a and a') for the first ($6p^3 4S_{3/2}$) and the second ($6p^2 7s 4P_{1/2}$) excitation levels, and the electric quadrupole hfs constant (b) for the first level (the b constant for the second level is equal to zero since the electronic spin of this level is $J = 1/2$). These hfs constants are proportional to the nuclear magnetic (μ) and electric quadrupole (Q) moments, respectively.

Experimental data were fitted by the Voigt profile. In the fitting procedure, the ratio a'/a was fixed in accordance with its value for ^{205}Bi : $\rho^{205} = a(6p^2 7s 4P_{1/2}, ^{205}\text{Bi})/a(6p^3 4S_{3/2}, ^{205}\text{Bi}) = -11.137(29)$ [10]. The change of ρ^A with the change of the atomic number is determined by the hyperfine structure anomaly [15]. It was estimated that this change is less than 2%. Correspondingly in the fitting procedure we used $\rho^A = -11.1(2)$. The 2% uncertainty of ρ induces a systematic error in the deduced values of the a -constants.

Due to the limited resolution and low electronic spins for the atomic levels involved, the nuclear spins for the investigated isotopes/isomers were not determined in our experiments. The spins were fixed (Table 1) in accordance with the adopted assignments based on the α - β -decay systematics. Some of them were substantiated by the magnetic moments analysis

in the present work (see Sec. 4.1). The ordering of the long-lived states in ^{190}Bi is unknown, thus they are denoted by “ $m1$ ” and “ $m2$ ” in the present work. For isotopes with $I \neq 9/2$ only the upper limit for the b constants was deduced from the experimental spectra ($|b| < 1.2$ GHz).

In Table 1, the experimental values of the a and b constants and isotope shifts for the investigated Bi isotopes are presented. The systematic errors in the a -constants due to ρ indeterminacy are shown in the curly brackets. The isotope shift and a -constant values for the comparatively long-lived $^{212}, ^{213}\text{Bi}$ isotopes, measured in the present work, agree in the limits of uncertainties with the more precise data obtained by the off-line gas cell method [10] (see Table 1). This agreement testifies to the correctness of the applied fitting procedure.

Table 1
Isotope shifts and magnetic hfs-constants for Bi isotopes studied in the present work

A	I	$\delta\nu_{A, 209}$, MHz	$a(^4S_{3/2})$, MHz*	$b(^4S_{3/2})$, MHz
189	(9/2)	-19 900(1100)	-405(30) {8}	–
190 $m1$	(3)	-21 020(470)	-631(15) {12}	–
190 $m2$	(10)	-21 550(260)	-117(6) {2}	–
191	(9/2)	-19 370(230)	-400(5) {8}	-1 130(550)
192	(3)	-19 690(330)	-682(28) {14}	–
192 m	(10)	-20 210(240)	-116(6) {2}	–
193	(9/2)	-18 280(160)	-406(6) {8}	-1 360(280)
193 m	(1/2)	-15 230(190)	-1 468(13)	–
194	(3)	-18 190(520)	-683(16) {14}	–
194 m	(10)	-18 450(340)	-121(5) {2}	–
195	(9/2)	-16 880(280)	-420(6) {8}	-1 030(380)
195 m	(1/2)	-13 750(230)	-1 503(8) {30}	–
197	(9/2)	-14 900(330)	-426(9) {8}	-1 001(600)
197 m	(1/2)	-11 280(410)	-1 573(30)	–
198 m	(10)	-14 220(220)	-120(4) {2}	–
211	9/2	5 450(170)	-417(3) {8}	-410(200)
212	1	7 760(100)**	-156(19)**	–
		7 620(240)	-168(13) {3}	–
213	9/2	10 507(24)**	-399.3(18)**	–
		10 630(230)	-397(8) {8}	–

* The errors in the parentheses reflect only the statistical experimental uncertainties. The systematic errors stemming from the uncertainty of the a -constants ratio ρ are given in the curly brackets.

** Reference [10].

3.1. Magnetic moments

The nuclear magnetic moment μ_A of the isotope with the atomic number A is connected with the hfs constant a_A by the following relation:

$$\mu_A = \mu_{209} \frac{I_A}{I_{209}} \frac{a_A(^4S_{3/2})}{a_{209}(^4S_{3/2})}. \quad (1)$$

In this relation, the hfs anomaly (hfa) for the atomic level with an electronic configuration without an unpaired s electron ($6p^3$) is neglected. For the stable ^{209}Bi , the following reference values were used: $a_{209}(^4S_{3/2}) = -446.937(1)$ MHz [10], $\mu_{209} = 4.1103(5)$ μ_N [16]. The magnetic moments calculated using Eq. (1)

are presented in Table 2. The systematic errors stemming from the indeterminacy of the a -constants ratio ρ , are shown in the curly brackets.

Table 2

Magnetic moments, changes in the mean-square charge radii and the mean-square deformation for the Bi isotopes studied in the present work

A	I	$\mu(\mu_N)^*$	$Q_s(\text{b})$	$\delta\langle r^2 \rangle_{A, 209}, \text{fm}^{2**}$	$ \beta_{\text{DM}} ^{***}$
189	(9/2)	3.72(28) {7}	–	–0.792(44) {55}	0.19(2)
190 m 1	(3)	3.869(92) {77}	–	–0.839(19) {59}	0.16(2)
190 m 2	(10)	2.40(12) {5}	–	–0.860(10) {60}	0.16(2)
191	(9/2)	3.680(48) {70}	–	–0.772(9) {54}	0.17(2)
192	(3)	4.18(17) {8}	–	–0.786(13) {55}	0.14(2)
192 m	(10)	2.37(12) {5}	–	–0.807(10) {56}	0.14(2)
193	(9/2)	3.734(59) {75}	–1.88(38)	–0.729(7) {51}	0.14(2)
193 m	(1/2)	1.500(14) {30}	–	–0.606(8) {42}	0.17(1)
194	(3)	4.186(99) {84}	–	–0.727(21) {51}	0.12(3)
194 m	(10)	2.47(11) {5}	–	–0.737(14) {52}	0.12(2)
195	(9/2)	3.862(56) {77}	–1.42(52)	–0.674(11) {47}	0.12(2)
195 m	(1/2)	1.536(8) {31}	–	–0.548(9) {38}	0.16(1)
197	(9/2)	3.918(80) {78}	–	–0.596(13) {42}	0.10(2)
197 m	(1/2)	1.607(31) {32}	–1.38(83)	–0.449(17) {31}	0.15(1)
198 m	(10)	2.444(87) {49}	–	–0.568(9) {40}	0.09(2)
211	9/2	3.838(32) {77}	–0.57(28)	0.219(7) {15}	0.11(1)

* The errors in the parentheses reflect only the statistical experimental uncertainties. The systematic errors stemming from the uncertainty in the a -constants ratio ρ are given in the curly brackets.

** The errors in the parentheses reflect only the statistical experimental uncertainties. The systematic errors, stemming from the uncertainty in the F and M factors, are given in the curly brackets.

*** The errors take into account the statistical and systematic uncertainties in $\delta\langle r^2 \rangle_{A, 209}$.

3.2. Changes in the mean square charge radii

The changes in the mean-square charge radii $\delta\langle r^2 \rangle_{A, A'}$ can be deduced from the measured isotope shift $\delta\nu^{A, A'}$ using the well-known relations:

$$\delta\nu^{A, A'} = \delta\nu_F^{A, A'} + \delta\nu_M^{A, A'}; \quad \delta\nu_F^{A, A'} = F\delta\langle r^2 \rangle_{A, A'}; \quad \delta\nu_M^{A, A'} = \frac{M(A - A')}{AA'}, \quad (2)$$

where $\delta\nu_F^{A, A'}$ and $\delta\nu_M^{A, A'}$ are the field and mass shifts; F is the electronic factor; $M = M^{\text{NMS}} + M^{\text{SMS}}$; M^{NMS} and M^{SMS} are the normal mass shift (NMS) and specific mass shift (SMS) constants, respectively. There are no atomic calculations of the SMS and the F -factor for the 306.77 nm transition in Bi. The F -factor was estimated using the systematics of $\delta\langle r^2 \rangle$ for the isotope pairs with $N = 126, 124$ and $124, 122$ for different elements in the Pb-region: $F(\text{Bi}; 306.77 \text{ nm}) = 24.8(17) \text{ GHz/fm}^2$ [17]. The SMS is usually small for this type of transition ($p \rightarrow s$), and one can assume that $M = (1 \pm 2)M^{\text{NMS}}$ (cf. similar relations for analogous transitions in adjacent atoms). The values of $\delta\langle r^2 \rangle$ for Bi isotopes calculated with Eq. (2) are presented in Table 2. In Figure 2, the changes in the mean-square charge radii $\delta\langle r^2 \rangle_{A, 209}$ for Bi nuclei are shown.

It is generally acknowledged that the main isotopic trend of the $\delta\langle r^2 \rangle$ is described by the droplet model (DM) (see Ref. [18] and references therein). Deviations from the DM-trend can be attributed to the development of the mean-square quadrupole deformation:

$$\langle r^2 \rangle = \langle r^2 \rangle_{\text{DM}} \left(1 + \frac{5}{4\pi} \langle \beta_{\text{DM}}^2 \rangle \right), \quad (3)$$

where $\langle r^2 \rangle_{\text{DM}}$ is the mean square charge radius calculated by the DM with zero deformation. The values of $|\beta_{\text{DM}}| \equiv \langle \beta_{\text{DM}}^2 \rangle^{1/2}$ were calculated using Eq. (3) and the experimental values of $\delta \langle r^2 \rangle$ with the DM-parameters taken from Ref. [18] and setting $|\beta_{\text{DM}}|(^{209}\text{Bi}) = |\beta_{\text{DM}}|(^{208}\text{Pb}) = 0.055$ [19]. These values are presented in Table 2. Figure 2 shows the DM $\delta \langle r^2 \rangle$ lines with constant mean-square deformations to provide an insight into the development of the deformation in the Bi isotopic chain.

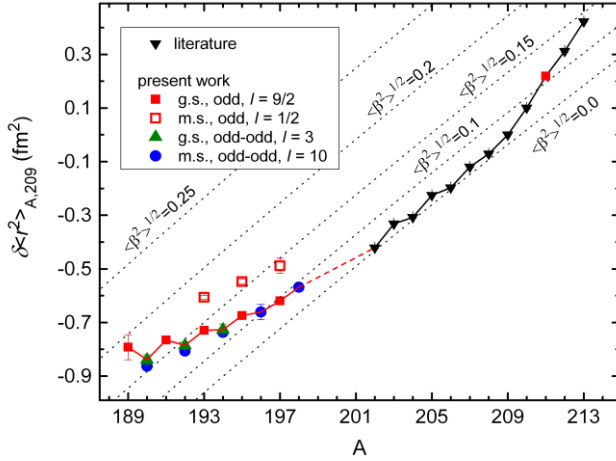


Fig. 2. Changes in the mean-square charge radii for Bi isotopes: *downward triangles* – literature data [10]; *stars* – present work, ground states ($I^\pi = 9/2^-$); *circles* – present work, states with $I^\pi = 10^-$; *upward triangles* – present work, states with $I^\pi = 3^-$. Only experimental errors are shown. *Dotted lines* represent the droplet model prediction with different mean-square deformations

4. Discussion

4.1. Magnetic moments

The magnetic moments for the ground and isomeric states in the Bi and Tl isotopes with the spin $I = 9/2$ are compared in Fig. 3. The magnetic moments of the $^{197, 195, 193, 191, 189}\text{Bi}$ ground states with $I = 9/2$ follow a linearly-decreasing A dependence, approaching more closely the Schmidt value ($\mu_{\text{Schmidt}} = 2.6 \mu_N$) when going away from the closed shell. Within the limits of errors they coincide with the magnetic moments of the isotonic Tl nuclei. It should be noted that the nuclear states with the same spin in Tl and Bi have different nature: $\pi h_{9/2}$ state is normal for Bi and an intruder [$1p-2h$] for Tl nuclei; $\pi s_{1/2}$ state is an intruder [$2p-1h$] for Bi and normal for Tl nuclei.

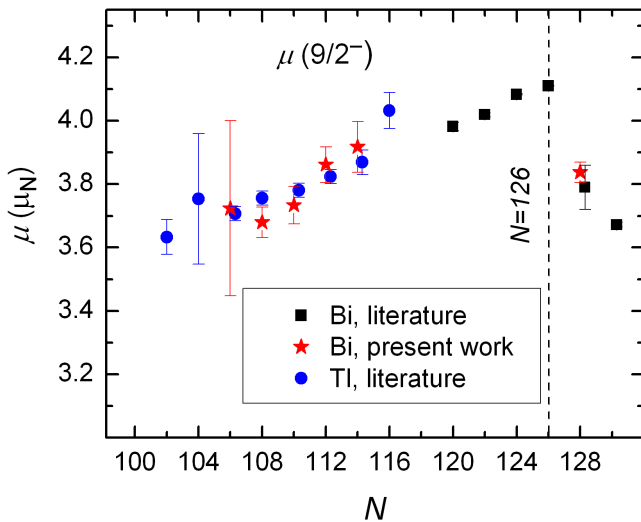


Fig. 3. Magnetic moments for Bi and Tl isotopes with the spin $I = 9/2$: *full stars* – Bi, present work; *squares* – Bi [10]; *circles* – Tl [5, 6, 15]

The discussion of the magnetic moments of the odd-odd Bi isotopes will be guided by comparisons with estimates from the additivity relation to obtain information on the underlying configuration. According to the additivity relation, the magnetic moment of a two-particle state $|i_p i_n I\rangle$ in an odd-odd nucleus can be calculated from the following formula:

$$\mu_{\text{add}} = \frac{I}{2} \left(\frac{\mu_p}{i_p} + \frac{\mu_n}{i_n} \right) + \frac{I}{2} \left(\frac{\mu_p}{i_p} - \frac{\mu_n}{i_n} \right) \frac{i_p(i_p+1) - i_n(i_n+1)}{I(I+1)}, \quad (4)$$

where i_p and i_n are the proton and neutron single-particle angular momenta; μ_p and μ_n are the single-particle magnetic moments. For the latter values, the known magnetic moments of the adjacent odd- A nuclei can be used. The isomers with $I^\pi = 10^-$ were found in all odd-odd Bi nuclei from $N = 125$ to at least $N = 105$ with the assigned configuration $[\pi 1h_{9/2} \times \nu 1i_{13/2}]_{10^-}$.

The magnetic moments for the heavy odd-odd Bi isomers ($N = 119-125$) agree fairly well with the results of calculations by the additivity relation for this configuration, when μ_p from the magnetic moments of the adjacent odd- A Bi isotopes ($I = 9/2$) and μ_n from the magnetic moments of the adjacent odd- A Pb isotopes ($I = 13/2$) are exploited. However, this prescription does not work for the neutron deficient $^{190, 192, 194}\text{Bi}_{107, 109, 111}$ isomers with $I = 10$ (Fig. 4). The agreement with the experiment may be restored by using for μ_n the magnetic moments of the Po 13/2-isomers with the appropriate deformation [3]. Accordingly, in the μ_{add} calculations we adopted $\mu_n(^{194}\text{Bi}) = \mu(^{199}\text{Po}; I = 13/2)$ and $\mu_n(^{190}\text{Bi}) = \mu(^{195}\text{Po}; I = 13/2)$, taking into account the proximity of the mean-square deformations for the corresponding Bi and Po nuclei. Thus, the description of the magnetic moments of $^{194, 192, 190}\text{Bi}$ ($I = 10$) in the framework of the additivity relation becomes possible only when the dependence of $\mu(I = 13/2)$ on the deformation observed in the Po nuclei is taken into account. This may be regarded as an indication on the possible proximity of the structure of the considered odd-odd Bi nuclei to that of the corresponding odd- A Po nuclei rather than to the structure of the odd- A Pb nuclei with the same neutron numbers. It should be reminded that the latter are usually considered as spherical nuclei, whereas the former were consistently described as the mixture of spherical and deformed configurations [3].

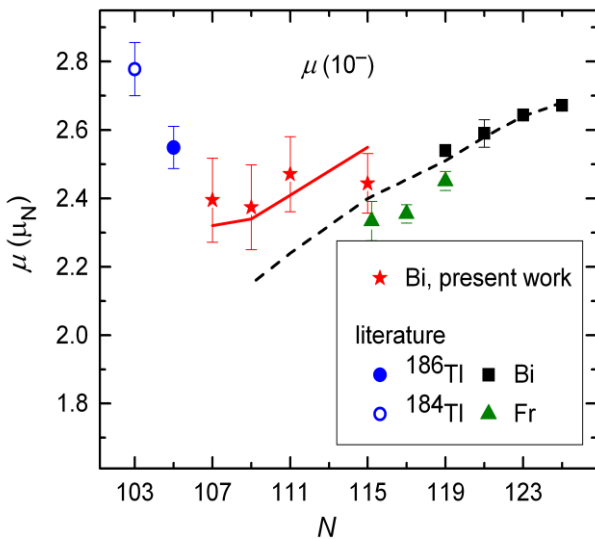


Fig. 4. Magnetic moments for Bi, Fr, and Tl isotopes with the spin $I = 10$: stars – Bi, present work; squares – Bi [10]; triangles – Fr [20]; filled circle – ^{186}Tl [5]; empty circle – ^{184}Tl [6]. The calculations by the additivity relation [Eq. (4)]: dashed line – with the μ_n values from the experimental magnetic moments of the adjacent odd- A Pb nuclei; solid line – with the μ_n values from the experimental magnetic moments for Po nuclei with the appropriate deformation (see the text)

A similar analysis of the magnetic moments of the long-lived low-spin states in $^{190, 192, 194}\text{Bi}_{107, 109, 111}$ also indicates the presence of deformation in the corresponding isotopes and a possible proximity of the structure of the considered odd-odd Bi nuclei to that of the corresponding odd- A Po isotopes (Fig. 5 and Ref. [21]).

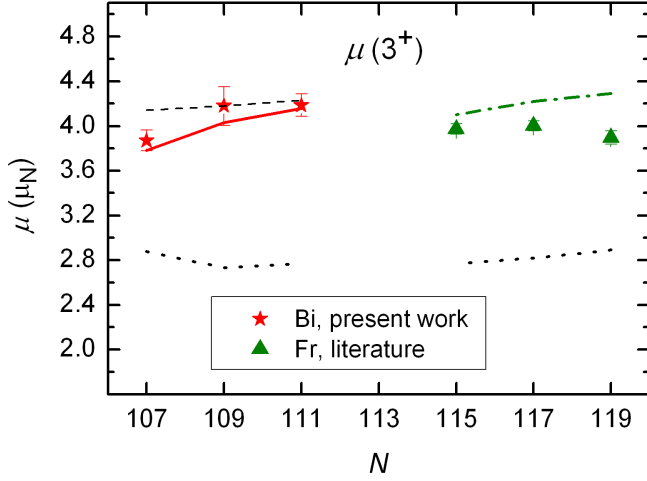


Fig. 5. Magnetic moments for Bi and Fr isotopes with $I = 3$: stars – Bi, present paper; triangles – Fr [20]. The calculation by the additivity relation [Eq. (4)]: dotted lines – the configuration $[\pi 1h_{9/2} \times \nu 1f_{5/2}]$ with the μ_n values from the magnetic moments of the adjacent odd-A Po nuclei [3]; dot-dashed line – the configuration $[\pi 1h_{9/2} \times \nu 1p_{3/2}]$ with the μ_n values from the magnetic moments of the adjacent odd-A Po nuclei [3]; dashed line – the configuration $[\pi 1h_{9/2} \times \nu 1p_{3/2}]$ with the μ_n values from the magnetic moments of the adjacent odd-A Pb nuclei [4]; solid line – the configuration $[\pi 1h_{9/2} \times \nu 1p_{3/2}]$ with the μ_n values from the magnetic moments for Po nuclei with the appropriate deformation

4.2. Changes in the mean-square charge radii

When we compare different isotopic chains in the Pb-region, in order to avoid indeterminacy of the electronic factors we use the relative values of $\delta\langle r^2 \rangle$: $\delta\langle r^2 \rangle_{N, 126} / \delta\langle r^2 \rangle_{124, 122} = \delta\nu_{N, 126}^F / \delta\nu_{124, 122}^F$.

Figures 6a (even- N) and 6b (odd- N) show the relative $\delta\langle r^2 \rangle$ values for the lead, polonium, and bismuth nuclei. For Pb and Po nuclei the IS-data from Refs. [4] and [3] were used, respectively. For the odd- N nuclei, the data for the states with the odd neutron in the same shell ($\nu i_{13/2}$) are displayed.

The bismuth relative radii follow the Pb-trend until $N = 111$ and markedly deviate from this trend at $N < 111$ both for even- N and odd- N nuclei. At the same time, the deviation from the Pb radii-trend for the odd-neutron Bi isotopes is evidently smaller than that for the even-neutron Bi isotopes (see Fig. 6b). This leads to a pronounced odd-even effect (see Fig. 2). It was shown previously that the thallium radii perfectly follow the Pb-trend even beyond the mid-shell (until $N = 98$; see Ref. [6]), whereas the polonium radii display a substantial deviation, which was interpreted as the onset of deformation at $N < 113$ (Ref. [3] and Fig. 6). One can conclude that the change of deformation for even-neutron Bi isotopes is “intermediate” between the changes for ^{82}Pb and ^{84}Po .

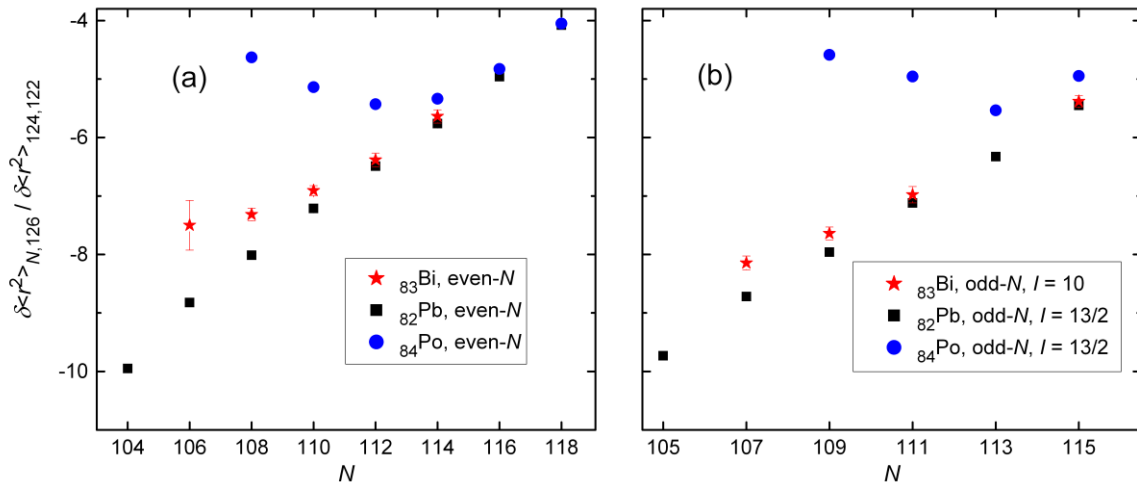


Fig. 6. Relative values of $\delta\langle r^2 \rangle$ for the Pb and Bi nuclei: a – even- N ground states, stars – Bi nuclei (present paper), squares – Pb nuclei [4], circles – Po nuclei [3]; b – odd- N nuclei, Po and Pb isomers with $I = 13/2$ (configuration $\nu i_{13/2}$), Bi isomers with $I = 10$ (configuration $[\pi h_{9/2} \times \nu i_{13/2}]$)

This conclusion is supported by our analysis of the magnetic moments of odd-odd Bi isotopes (see Section 4.1). Thus, the radii evolution (*i. e.*, the shape evolution) in the Bi and Tl isotopic chains differs from each other, although these chains are “mirror” in respect to the filled proton shell ($Z = 82$).

It is worth to note that the recent shell-model calculations indicate a spherical Bi ground state down to ^{193}Bi while the discrepancy between theory and experiment in the lighter isotopes was attributed to the onset of deformation [9]. Some structural changes between ^{193}Bi and ^{191}Bi were also pointed to in Refs. [7, 8]. These assumptions are supported by our analysis of the radii and magnetic moments.

One can see (Fig. 2) that the intruder Bi isomers ($I = 1/2$) have larger radii (deformation) than the corresponding ground states ($A = 193, 195, 197$). Thus, the commonly adopted shape-coexistence interpretation of these Bi isomers is confirmed. This picture is quite similar to that for Tl $9/2^-$ isomers [5, 6]. In Figure 7, the isomer shifts for Bi and Tl intruder isomers are compared. The isomer shift for Bi intruder isomers is constant for $N = 110$ – 114 and corresponds to a small increase of deformation ($\delta(|\beta|) = 0.03$ – 0.05 ; see Table 2) in comparison with the ground state. The Tl intruder isomer shift is also nearly constant at $N = 110$ – 116 and its value is close to that for Bi isomers (see Fig. 7).

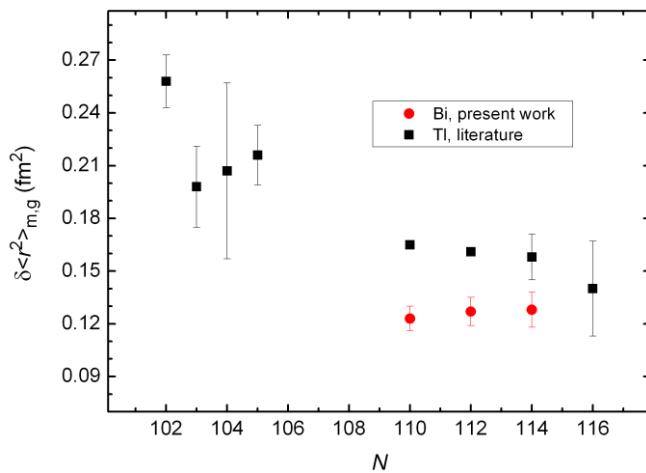


Fig. 7. Isomer shift between the intruder and normal states: *squares* – Tl nuclei [5, 6]; *circles* – Bi nuclei, present work. Only the statistical errors are shown

5. Conclusion

The hfs parameters and the isotope shifts have been measured for the bismuth isotopes ($A = 189, 190m1, 190m2, 191, 192, 192m, 193, 193m, 194, 194m, 195, 195m, 197, 197m, 198m, 213$) using the 306.77 nm atomic transition. For the Bi nuclei, a marked deviation from the isotopic trend of $\delta\langle r^2 \rangle$ in lead and thallium isotopic chains has been demonstrated at $N < 111$. This deviation is interpreted as an indication of the onset of the quadrupole deformation. The deformation evolution for ^{83}Bi isotopes has been found to be “intermediate” between that for the ^{82}Pb and ^{84}Po isotopic chains. An analysis of the magnetic moments for odd-odd Bi isotopes ($I = 3, 10$) also points to a possible increase of deformation at $N < 111$. The difference in the charge radii connected with the difference in the mean square deformation for the ground ($9/2^-$) and intruder isomeric ($1/2^+$) states of odd- A neutron deficient Bi nuclei ($A = 193, 196, 197$), is demonstrated. The corresponding isomer shift is constant and close to the intruder isomer shift in the isotonic Tl nuclei.

The presented results for Bi isotopes have been published in Refs. [17, 21].

References

1. K. Heyde, J.L. Wood, *Rev. Mod. Phys.* **83**, 1467 (2011).
2. G. Ulm *et al.*, *Zh. Phys. A* **325**, 247 (1986).
3. T.E. Cocolios, M.D. Seliverstov *et al.*, *Phys. Rev. Lett.* **106**, 052503 (2011); M.D. Seliverstov *et al.*, *Phys. Rev. C* **89**, 034323 (2014).
4. H. De Witte, D. Fedorov *et al.*, *Phys. Rev. Lett.* **98**, 112502 (2007); M.D. Seliverstov *et al.*, *Eur. Phys. J. A* **41**, 315 (2009).
5. A.E. Barzakh *et al.*, *Phys. Rev. C* **88**, 024315 (2013).
6. A.E. Barzakh *et al.*, *C* **95**, 014324 (2017).
7. A.N. Andreyev *et al.*, *Phys. Rev. C* **69**, 054308 (2004).
8. A.N. Andreyev *et al.*, *Eur. Phys. J. A* **18**, 39 (2003).
9. A. Hürstel *et al.*, *Eur. Phys. J. A* **15**, 329 (2002).
10. M.R. Pearson *et al.*, *J. Phys. G* **26**, 1829 (2000).
11. G.D. Alkhazov *et al.*, *Nucl. Instrum. Meth. B* **69**, 517 (1992).
12. V.N. Fedosseev *et al.*, *Rev. Sci. Instrum.* **83**, 02A903 (2012).
13. A.E. Barzakh *et al.*, *Rev. Sci. Instrum.* **83**, 02B306 (2012).
14. V.N. Panteleev *et al.*, *Eur. Phys. J. A* **42**, 495 (2009).
15. A.E. Barzakh *et al.*, *Phys. Rev. C* **86**, 014311 (2012).
16. Y. Ting, D. Williams, *Phys. Rev.* **89**, 595 (1953); T. Baştuğ, B. Fricke, M. Finkbeiner, W.R. Johnson, *Zh. Phys. D* **37**, 281 (1996).
17. A.E. Barzakh *et al.*, *Phys. Rev. C* **94**, 024334 (2016).
18. D. Berdichevsky, F. Tondeur, *Zh. Phys. A* **322**, 141 (1985).
19. S. Raman, C.W. Nestor Jr., P. Tikkanen, *Atom. Data Nucl. Data Tabl.* **78**, 1 (2001).
20. A. Voss *et al.*, *Phys. Rev. C* **91**, 044307 (2015); K.M. Lynch *et al.*, *Phys. Rev. X* **4**, 011055 (2014).
21. A.E. Barzakh *et al.*, *Phys. Rev. C* **95**, 044324 (2017).

SHAPE COEXISTENCE IN THE LEAD REGION VIA α - AND β -DECAY STUDIES WITH THE APPLICATION OF THE LASER ION SOURCE

A.E. Barzakh, D.V. Fedorov, P.L. Molkanov, M.D. Seliverstov
and IS511 Collaboration

1. Introduction

The region of neutron-deficient nuclei in the vicinity of the proton shell-gap at $Z = 82$ and neutron mid-shell at $N = 104$ exhibits conceivably the most extensive manifestation of shape coexistence, whereby a nucleus shows several distinct types of deformation at low energy. The coexistence of different deformations in the neutron-deficient isotopes in the lead region has been well established by using different techniques: from optical pumping and laser spectroscopy, to in-beam and decay spectroscopy [1]. However, in order to fully characterize the underlying link between collective features and their microscopic origin it is necessary to complete the experimental information on the yrast and non-yrast states with not only energies, but also branching rates, lifetimes, static and transitional moments. Recent experiments, such as Coulomb excitation of radioactive isotopes, lifetime measurements, α - and β -decay studies and laser-spectroscopy studies are pursuing these goals.

The experiments were performed at CERN/ISOLDE and are a part of systematic α -, β -fission, β -delayed fission and laser spectroscopy studies of neutron-deficient thallium isotopes. Partial decay schemes were established for $^{179, 180, 182, 184}\text{Tl}$. Many new γ and α lines, excited levels and nuclear properties relevant for the shape coexistence studies in the lead region were determined [2–7]. The most important findings are presented in this paper.

2. Experimental details

The Tl radioactive ions were produced by 1.4 GeV proton-induced spallation in a $50 \text{ g} \cdot \text{cm}^{-2} \text{UC}_x$ target followed by surface and resonant laser ionization. Laser ionization ensures production of pure Tl-nuclei sources due to high selectivity of the resonance ionization.

The ions were subsequently extracted from the ion source, accelerated to 50 keV and separated with the mass separator. As a result, a high-purity beam of Tl isotopes was obtained. The thallium beam was implanted on one of ten carbon foils, $20 \mu\text{g} \cdot \text{cm}^{-2}$ thick, set on a rotatable wheel inside a vacuum chamber. By rotating the wheel every 40–50 s, the irradiated foil was moved to the decay position and the next foil moved to the implantation position. Two silicon detectors were placed in close geometry at the implantation point, covering a solid angle of 24% of 4π . An annular detector having an active area of 450 mm^2 and thickness $300 \mu\text{m}$, placed upstream the foil, has a central hole of 8 mm so that the ion beam was passing through this hole before being implanted into the foil. A circular detector with an active area of 300 mm^2 and thickness of $300 \mu\text{m}$ was placed behind the foil. Two extra circular Si detectors, $300 \mu\text{m}$ thick and 300 mm^2 , were placed at the decay position.

The Si detectors were used for detection of electrons, positrons, and α particles. The γ rays following the de-excitation of the levels fed in the daughter nuclei were detected by two individual HPGe detectors placed outside the vacuum chamber at 0 and 90° with respect to the direction of the incoming beam. The α , β , and γ decays of the involved isotopes and isomers feeds levels in daughter nuclei which are characterized through β - γ , e - γ , α - γ , and γ - γ coincidence studies.

In the case of ^{184}Tl , a narrow-band laser approach was used to enhance the production of the higher-spin isomers. By tuning the first excitation step frequency of the laser to selectively enhance the production of the $I = (10^-)$ state, an isomerically purified beam was produced. This became possible due to a marked difference in hyperfine structures (hfs) of different ^{184}Tl isomers (Fig. 1).

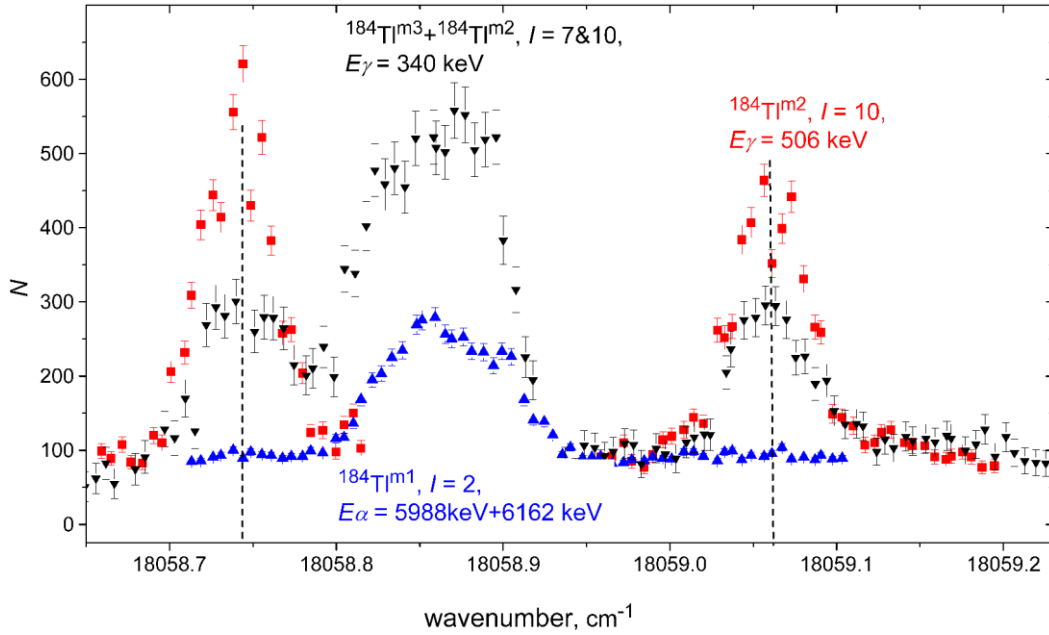


Fig. 1. Hyperfine structures of three long-lived states in ^{184}Tl . The intensity of the 506 keV (red squares), 340 keV (black downward triangles), 5 988 and 6 162 keV (blue upward triangles) γ and α lines as a function of the first excitation step laser wavenumber (before frequency doubling) are shown. The vertical dashed lines indicate the wave numbers to which the first step narrowband laser was tuned to in order to enhance the production of the $I = (10^-)$ state

3. Alpha-decay branching ratio for $^{182}\text{Tl}^{\text{Is}}$

In accordance with the results of the α -decay study of ^{186}Bi [8], clear evidence was found for the presence of two isomeric states in ^{182}Tl from our β - and α -decay studies [5, 6]. The hfs patterns for different α and γ lines in the ^{182}Tl decay spectra, obtained in narrowband laser scans, strongly support this observation [9]. We used the results of two fittings of the ^{182}Tl hfs for estimation of the absolute value of the α -decay branching ratio b_α . Let N_E denotes the sum of the counts in the α line with the energy E at the fixed frequencies of the narrow-band scanning laser near the first maximum of the observed hfs: 18 058.794,

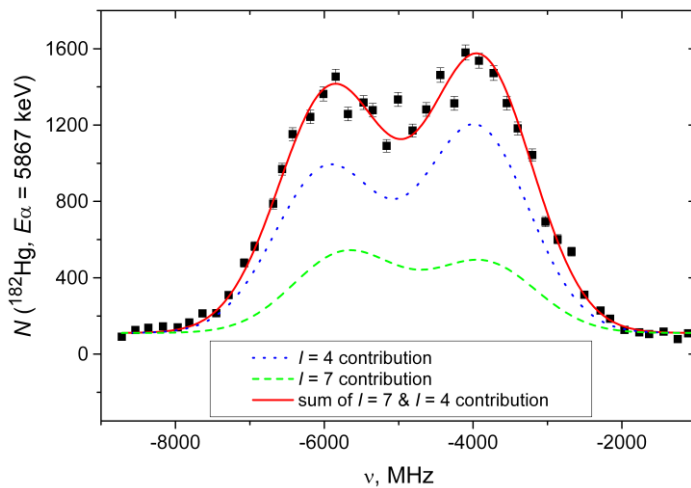


Fig. 2. Two-hfs fit of the hfs produced by 5 868-keV α line

18 058.800, 18 058.805, 18 058.811 cm^{-1} . To determine the α -decay branching, we compared N_E for the most intensive $^{182}\text{Tl}^{\text{Is}}$ α -line (6 046 keV) and the most intensive ^{182}Hg α -line (5 867 keV): $N_{6\,046} = 228(15)$, $N_{5\,867} = 5\,318(73)$. Taking into account the relative intensities of the observed ^{182}Tl α -decay lines [5] and assuming that possible weak unobserved ^{182}Tl α lines give less than 10% of the total α intensity, one obtains $N_\alpha(^{182}\text{Tl}^{\text{Is}}) = 556(64)$, where $N_\alpha(^{182}\text{Tl}^{\text{Is}})$ is the total number of $^{182}\text{Tl}^{\text{Is}}$ α decays with the narrowband laser at the chosen frequencies. With the known $b_\alpha(^{182}\text{Hg}) = 13.8(9)\%$ N_{dec} , the total number of ^{182}Hg decays, may be determined from $N_{5\,867}$: $N_{\text{dec}}(^{182}\text{Hg}) = 38\,900(2\,600)$.

However, ^{182}Hg is produced by the decay of both ^{182}Tl isomers. Decomposing the 5 867-hfs spectrum by the two-hfs procedure (Fig. 2), the number of decays of the ^{182}Hg nuclei produced in the only low-spin isomer β decay, $N_{\text{Is dec}}$, is determined:

$N_{\text{is dec}}(^{182}\text{Hg}) = 26\,600(12\,400)$. The total number of $^{182}\text{Tl}^{\text{ls}}$ β decays, $N_{\beta}(^{182}\text{Tl}^{\text{ls}})$, is equal to the number of ^{182}Hg nuclei produced by $^{182}\text{Tl}^{\text{ls}}$ β decay, $N_{\text{is}}(^{182}\text{Hg})$. The latter value is easily determined from $N_{\text{is dec}}(^{182}\text{Hg})$ taking into account the lifetimes of the nuclei involved and the time of the activity collection t_{sc} : $T_{1/2}(^{182}\text{Hg}) = 10.83(6)$ s, $T_{1/2}(^{182}\text{Tl}^{\text{ls}}) = 1.9(1)$ s [5], $t_{\text{sc}} = 42$ s.

The result, $N_{\text{is}}(^{182}\text{Hg}) = 44\,800(20\,900)$, gives the final value for the sought-for α -branching: $b_{\alpha}(^{182}\text{Tl}^{\text{ls}}) = N_{\alpha}(^{182}\text{Tl}^{\text{ls}})/(N_{\alpha}(^{182}\text{Tl}^{\text{ls}}) + N_{\text{is}}(^{182}\text{Hg})) = 1.2(6)\%$. The main part of the error stems from the two-hfs fitting procedure. Correspondingly, the absolute values of the reduced widths δ_{α}^2 for the observed $^{182}\text{Tl}^{\text{ls}}$ α lines have been calculated using the Rasmussen approach [10]. They are shown in Table.

Table

Alpha-decay energies and reduced widths of α decays for ^{180}Tl and low-spin states in the neighbouring odd-odd Tl isotopes*

^{178}Tl [2]		^{180}Tl [7]		^{182}Tl		^{184}Tl [5]	
E_{α} , keV	δ_{α}^2 , keV	E_{α} , keV	δ_{α}^2 , keV	E_{α} , keV	δ_{α}^2 , keV	E_{α} , keV	δ_{α}^2 , keV
6 862(10)	0.30(15)	6 553(7)	0.16(11)	6 406	0.043(25)	6 161	0.57(6)
6 693(10)	13.0(17)	6 354(7)	2.9(19)	6 360(6)	0.048(28)	5 988(12)	2.4(4)
6 595(10)	10.2(24)	6 348(7)	0.27(18)	6 165(6)	1.13(66)	5 964(12)	–
–	–	6 245(7)	4.9(33)	6 046(5)	5.8(34)	5 810(12)	0.9(1)
–	–	6 199(7)	5.2(35)	5 962(5)	6.0(35)	5 748(12)	< 0.09

* Only five highest-energy decays are shown for ^{180}Tl .

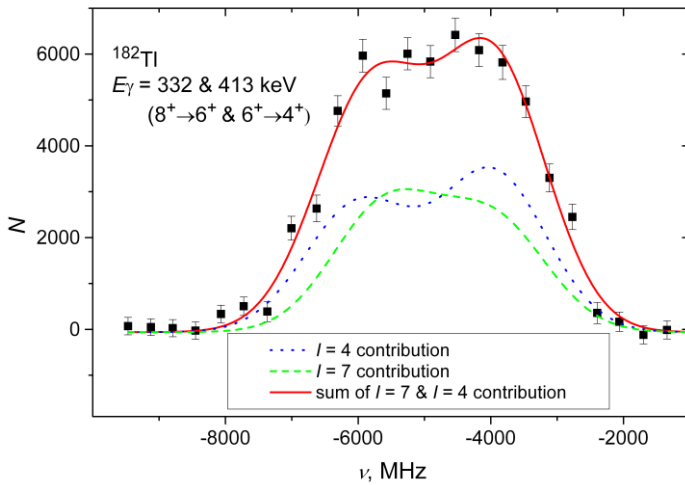


Fig. 3. Two-hfs fit of the hfs produced by 332- and 413-keV γ line

found in our β -decay study [6]. At the same time, the relative contribution of the low-spin isomer to the 413- and 332-hfs is found to be near 50% (by the two-hfs fitting, see Fig. 3). Thus, the existence of (still unobserved) internal decay ($4^- \rightarrow 7^+$) seems to be rather plausible, although a firm conclusion is impossible at the present level of accuracy.

It is worth noting that the same two-hfs fitting testifies to the noticeable low-spin contribution in the 413- and 332-hfs ($8^+ \rightarrow 6^+$ and $6^+ \rightarrow 4^+$ transitions in ^{182}Hg ; Fig. 3). Accordingly, with the spin assignment (4^-) for the low-spin isomer [9], the contribution of the low-spin isomer to the 413- and 332-hfs may be explained either by the existence of internal transition from the low-spin isomer to the high-spin isomer (ground state in this case), or by the side-feeding of the 8^+ and 6^+ levels in ^{182}Hg from the higher lying low-spin states which may be directly fed from the 4^- parent state. (The presence of both mechanisms cannot be excluded either.) No intensive γ line from ^{182}Tl β -decay ending at the 8^+ level was

4. Reduced width of thallium α decays

In the course of our experiments, the fine-structure in α decays of all studied Tl nuclei was explored, and the corresponding energies, branching ratios and half-lives were measured. In particular, the reduced α decay width for the ground state to ground state decay of ^{179}Tl unambiguously testifies to its unhindered nature: $\delta_\alpha^2(^{179}\text{Tl}; \text{g. s. to g. s.}) = 50(3)$ keV. A completely another picture was observed in odd-odd Tl isotopes.

For ^{180}Tl , all transitions have $\delta_\alpha^2 > 5$ keV (Fig. 4), which means they are hindered compared to the unhindered decays of neighbouring odd isotopes. When compared with the reduced width for ^{179}Tl , the δ_α^2 value for the highest-energy transition of ^{180}Tl (6 553 keV) yields a hindrance factor of ~ 400 . We ruled out the population of a high-spin isomer in ^{176}Au (with the suggested configuration of $[\pi_{11/2}-(h_{11/2}) \otimes \nu_{7/2}-(h_{9/2}f_{7/2})]_{8,9+}$) based on the absence of α - γ coincidences from its decay. Further, as no isomeric α decay was observed in ^{180}Tl , this 6 553-keV α transition is assigned as connecting the ^{180}Tl g. s. and ^{176}Au low-spin states. Thus, we rule out the previously suggested configuration of $[\pi_{1/2}+(s_{1/2}) \otimes \nu_{7/2}-(h_{9/2}f_{7/2})]_{3,4-}$ for $^{176}\text{Au}^{\text{ls}}$, as it would not be in agreement with the deduced hindrance factor of ~ 400 . This earlier suggested dominant configuration of the $^{176}\text{Au}^{\text{ls}}$ overlaps to a large extent with the g. s. configuration of ^{180}Tl proposed by the laser-spectroscopy studies [9]. Therefore, the α decay between these two configurations would be quasiunhindered. However, our recent laser-spectroscopy measurement and the extracted magnetic moment suggest a different configuration of $[\pi d_{3/2} \otimes \nu f_{7/2}]$, $I^\pi = (4,5-)$ and a spherical shape for $^{176}\text{Au}^{\text{ls}}$. This configuration means that both proton and neutron have to change orbitals ($\pi s_{1/2} \rightarrow \pi d_{3/2}$ and $\nu h_{9/2} \rightarrow \nu f_{7/2}$), which is likely a reason for the strongly hindered 6 553-keV α decay between the states.

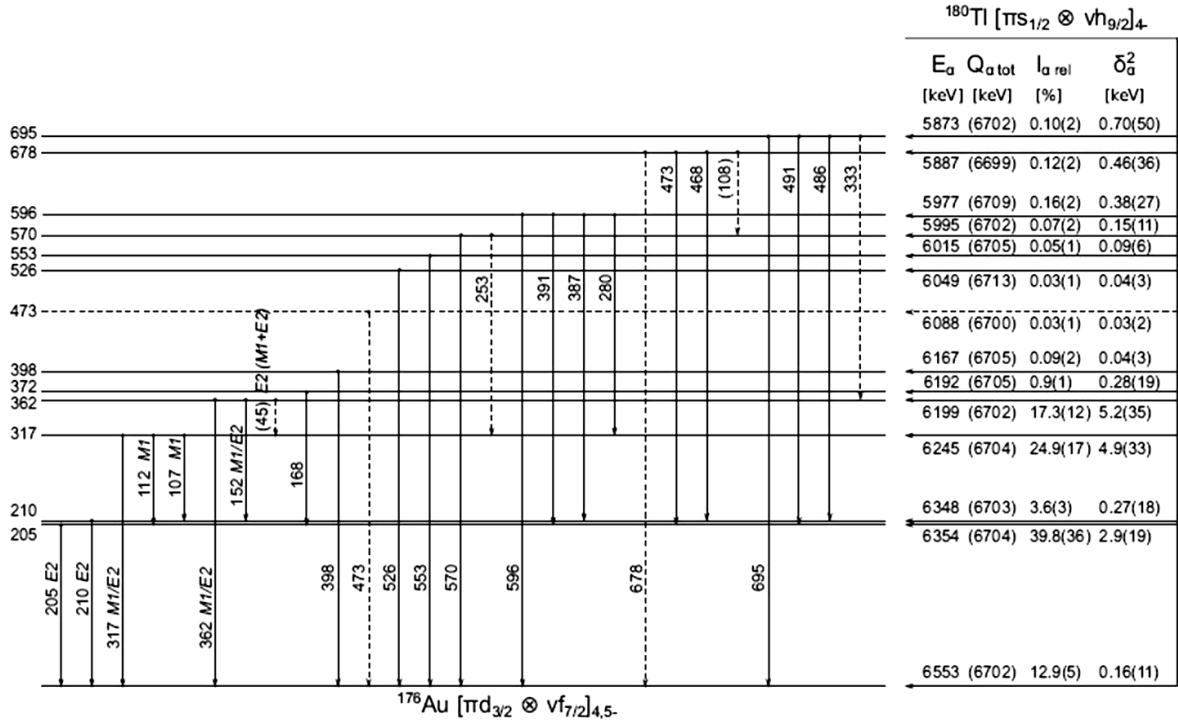


Fig. 4. Proposed α -decay scheme of ^{180}Tl . Tentative levels and transitions are denoted by *dashed lines*. Transitions with energies in brackets were not observed, but they were placed into decay scheme based on indirect evidence

The systematics of δ_α^2 values for α decays of low-spin states in odd-odd thallium isotopes $^{178, 180, 182, 184}\text{Tl}$ are shown in Table. All decays are hindered, although two decays of ^{178}Tl are hindered only moderately. Overall, the transitions in these isotopes can be divided into three groups according to their δ_α^2 values.

Decays in the first group have δ_α^2 of a few keV (with the exception of ^{178}Tl with the values around 10 keV), the values in the second group are $0.1 < \delta_\alpha^2 < 1$ keV, and in the third group δ_α^2 are smaller than 0.1 keV. The highest-energy α decay for each isotope is strongly hindered, with the values of $\delta_\alpha^2 < 0.6$ keV, which emphasizes that in all four cases the structures of the parent and daughter states are significantly different.

5. Intruder isomer in ^{184}Tl

The decay of the (10^-) isomeric state in ^{184}Tl was studied. The half-life was deduced as $T_{1/2} = 47.1(7)$ ms and its IT decay measured. The precisely determined excitation energy of this state (506.1(1) keV) extends the $(10^-) \rightarrow (7^+)$ energy systematics beyond the neutron midshell and confirms the parabolic behaviour as a function of the neutron number. From the half-life value and branching ratios, the retardation factors of the depopulating $E3$ and $M2$ transitions were determined and compared with the retardation factors in the neighbouring odd-mass and even-mass thallium isotopes. Combined with the information on the published reduced widths of the α decay of $^{187-192}\text{Bi}$ populating levels in daughter nuclei $^{183-188}\text{Tl}$, a confirmation of the proton $1p-2h$ intruder character of the (10^-) isomer and an interpretation of the levels in ^{184}Tl fed in the isomeric decay in terms of $[\pi 3s_{1/2} \otimes \nu 1i_{13/2}]$ and $[\pi d_{3/2} \otimes \nu 1i_{13/2}]$ could be obtained. It is worth noting that the proton intruder interpretation of the (10^-) isomer is supported by the results of the isotopic shift/hfs structure measurements in the same series of experiments [9].

6. Shape coexistence studies in $^{182, 184}\text{Hg}$ via the β decay of $^{182, 184}\text{Tl}$

The low-lying excited states in $^{182, 184}\text{Hg}$ were investigated following the β decay of $^{182, 184}\text{Tl}$. In the case of ^{184}Tl , the narrow-band laser spectroscopy was used to disentangle the decay of both isomers. The decay schemes of these nuclei were extended and revised based on high quality γ - γ coincidence data (see the decay scheme of two isomers of ^{184}Tl in Fig. 5).

The detailed level scheme of the lowest energy states in $^{182, 184}\text{Hg}$ and the precise description of their decay properties (energy of the transitions, intensity and conversion coefficients), which were achieved in this analysis, provide crucial information for the re-evaluation of the $^{182, 184}\text{Hg}$ Coulomb excitation study performed at REX-ISOLDE with the Miniball set-up.

In ^{182}Hg , a precise energy of 335(1) keV for the 0_2^+ state was measured together with its feeding from a tentatively proposed 2_3^+ state at 973 keV. Large conversion coefficients for the $2_2^+ \rightarrow 2_1^+$ transition in $^{182, 184}\text{Hg}$ were measured to be 7.2(13) and 14.2(36), respectively, giving evidence for a strong $E0$ component.

The updated systematics of the lowest positive-parity states in the even-even $^{180, 182, 184, 186}\text{Hg}$ is shown in Fig. 6. With the precise determination of the energy of the 0_2^+ state in ^{182}Hg , the energy systematics of the 0_1^+ , 0_2^+ , 2_1^+ , 2_2^+ , and 4_1^+ becomes completed. The identification of the 973 keV level in ^{182}Hg completes the systematics of a level present in the four nuclei with a specific decay pattern, only feeding the 0_2^+ , 2_1^+ levels, while no transition to the ground state is observed. This leads to a suggestion that it might be the (2^+) band-head of the γ -vibrational band built on top of the 0_2^+ deformed state.

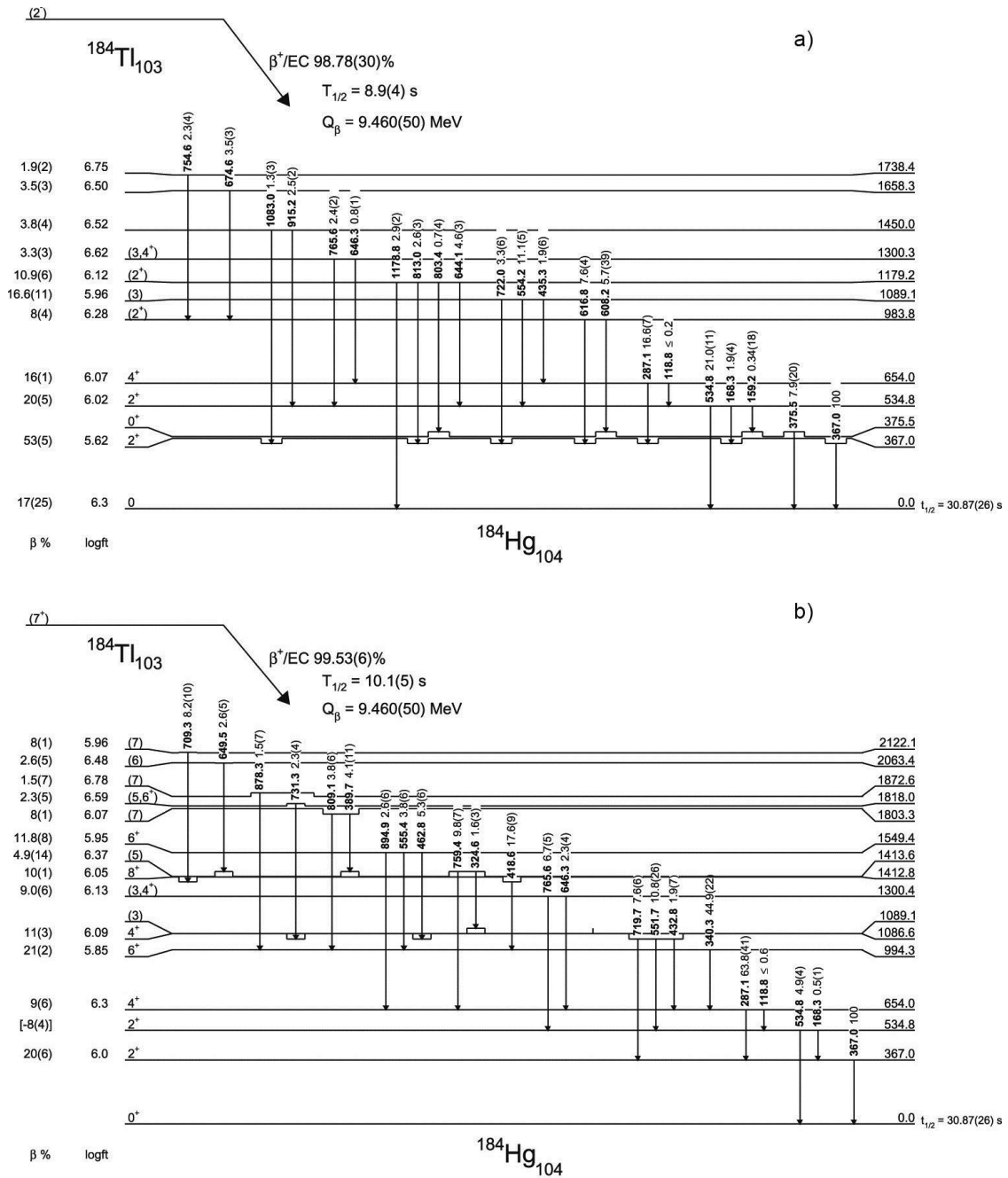


Fig. 5. Decay scheme of the (2^-) (a) and (7^+) (b) β -decaying states in ^{184}Tl

CHANGES IN MEAN-SQUARED CHARGE RADII AND MAGNETIC MOMENTS OF NEUTRON DEFICIENT Tl ISOTOPES MEASURED BY IN-SOURCE LASER SPECTROSCOPY

A.E. Barzakh, D.V. Fedorov, V.S. Ivanov, P.L. Molkanov, F.V. Moroz,
S.Yu. Orlov, V.N. Panteleev, M.D. Seliverstov, Yu.M. Volkov
and IS511 Collaboration

1. Introduction

The region of the neutron-deficient isotopes near the proton shell closure at $Z = 82$ has drawn considerable interest as it exhibits a clear manifestation of shape coexistence in nuclei [1]. Isotope/isomer shift and hyperfine splitting data obtained by laser spectroscopy are of primary importance in these studies. Along with shape coexistence, a pronounced shape staggering was observed in this region of the nuclide chart for the neutron-deficient Hg isotopes [2]. At the same time, odd- A and even- A Pb isotopes remain nearly spherical down to ^{181}Pb ($N = 99$) [3].

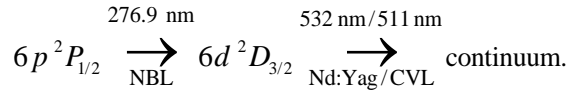
The Tl ($Z = 81$) isotopic chain is intermediate between the Pb ($Z = 82$) and Hg ($Z = 80$) chains, therefore it is important to perform systematic isotope shift (IS) and hyperfine structure (hfs) measurements with the aim to assess the possible effects of shape coexistence. Prior to our work, laser spectroscopic studies of Tl nuclei were limited to $A = 186\text{--}208$ [4]. It was shown that the charge radii of the Tl ground states follow the trend found previously for isotonic (spherical) Pb nuclei down to ^{186}Tl ($N = 105$). Thus, the previous laser spectroscopic investigations ended before the neutron midshell ($N = 104$), where the most pronounced shape staggering or shape transition effects are expected. It is of importance to continue these studies beyond the midshell.

In the spherical shell-model approach, the spin-parity of $I^\pi = 1/2^+$ for the ground states of all presently known odd- A Tl isotopes can be understood as being due to the “normal” $\pi 3s_{1/2}$ orbital. The so-called proton “intruder” excited states with $I^\pi = 9/2^-$, involving one-particle-two hole $\pi(1p-2h)$ excitations to the $\pi 1h_{9/2}$ orbital above the $Z = 82$ shell closure, are also well known down to ^{181}Tl [1]. Alternatively, within the deformed mean-field approach, the $I^\pi = 9/2^-$ states can be interpreted as oblatelly-deformed, in contrast to the spherical ground states with $I^\pi = 1/2^+$. This interpretation was supported by the isotope/isomer shift measurements which provided evidence for the marked difference between the radii for the ground and isomeric (intruder) states in the odd- A $^{187\text{--}193}\text{Tl}$ [4]. This difference was explained by the corresponding change in quadrupole deformation. In the odd-odd Tl isotopes, the coupling of both normal $\pi 3s_{1/2}$ and intruder $\pi 1h_{9/2}$ orbitals with valence neutrons from several shells should be considered. In particular, long-lived high-spin intruder states of, presumably, $[\pi 1h_{9/2} \times \nu 1i_{13/2}]$ origin, are well-known in the odd-odd $^{184\text{--}200}\text{Tl}$ isotopes, their tentative spin-parity assignments are based on decay spectroscopy experiments [5]. It is of importance to continue the laser spectroscopic study of the Tl isotopic chain to check whether the large isomer shift preserves for the lighter ($A < 187$) and heavier ($A > 193$) odd Tl isotopes and whether it exists for intruder-based states in odd-odd Tl isotopes.

The IS and hsf investigation, presented in this paper, is a part of a coordinated experimental campaign at the ISOLDE (CERN) and IRIS (PNPI) facilities aimed at laser spectroscopy studies of neutron-deficient thallium isotopes. The main results were published in Refs. [6–8].

2. Experimental details

The experiments were performed at the ISOLDE facility (CERN) and the IRIS mass-separator (PNPI). The radioactive Tl isotopes under study were produced in spallation reactions by a proton beam in a uranium target. The spallation products diffused out of the high temperature target as neutral atoms into the cavity of the resonance ionization laser ion source. Laser beams were introduced into the same cavity through a quartz window to provide resonance ionization of the atoms under investigation. A detailed description of the experimental set-up is presented in Refs. [9, 10]. The laser set-up was arranged to provide a two-step resonance ionization of Tl atoms *via* the following scheme:



The excitation from the atomic ground state $6p^2P_{1/2}$ to an intermediate electronic state $6d^2D_{3/2}$ (36117.9 cm^{-1}) was performed by a frequency-doubled narrow-band tunable dye laser (NBL) beam at 276.9 nm with a linewidth of about 0.8 GHz (before frequency doubling). Pumping of the dye laser and subsequent ionization of the excited thallium atoms were accomplished by 532-nm output of a 10 kHz Edgewave Nd:YAG laser (at ISOLDE) or 511-nm beam of copper-vapor laser (CVL; at IRIS). After selective laser photoionization in the hot cavity, the radioactive thallium ions were extracted and accelerated, mass separated and directed to the counting stations. The photo-ion current was measured *via* the detection of characteristic β - γ and/or α decays of the isotopes in question.

Figure 1 shows examples of the hfs spectra for several thallium isotopes, in which the dependence of their counting rate is plotted as a function of the frequency of the scanned narrow-band laser. In some cases, to increase statistics for the hfs spectra, alpha decays of daughter products (Hg, Pt, and Au, after β and α decay) were also used.

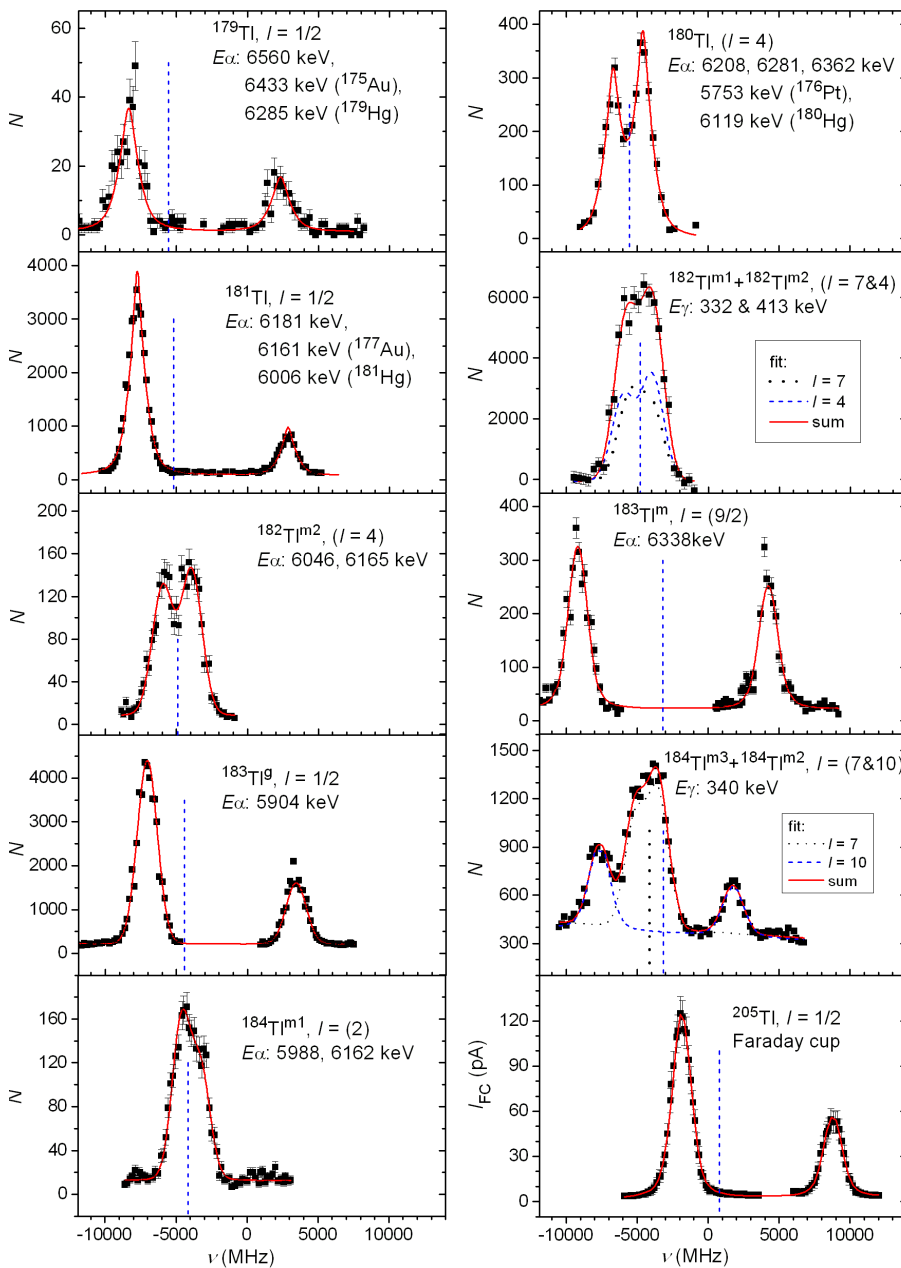


Fig. 1. The hfs spectra of selected Tl isotopes. In the insets, the spin of the corresponding nuclide and the energies of the γ - or α -decay lines used for the photo-ion current monitoring are shown: *full lines* are the results of fitting with the Voigt profiles; *vertical dashed lines* mark the centre of gravity of the corresponding hfs

3. Results

The positions of the hyperfine components as a function of the scanning laser frequency are determined by the well-known formulas:

$$\nu^{F,F'} = \nu_0 + \Delta\nu^{F'} - \Delta\nu^F,$$

where ν_0 is the position of the centre of gravity of the hfs, the prime symbol denotes the upper level of the atomic transition, and

$$\Delta\nu^F = a \frac{K}{2} + b \frac{0.75K(K+1) - I(I+1)J(J+1)}{2(2I-1)(2J-1)IJ}, \quad (1)$$

where $K = F(F+1) - I(I+1) - J(J+1)$; F is the total angular momentum of the atomic level; a and b are the magnetic dipole and electric quadrupole hyperfine coupling constants, respectively. These constants are proportional to the nuclear magnetic dipole (μ) and electric quadrupole (Q_s) moments, correspondingly.

Experimental hfs spectra were fitted by the Voigt profile. The ratio a'/a was fixed in accordance with its value for the stable isotope ^{205}Tl : $a(6d^2D_{3/2}, ^{205}\text{Tl})/a(6p^2P_{1/2}, ^{205}\text{Tl}) = -0.002013(19)$ [11]. In the fitting procedure, the nuclear spin should be fixed. Spins $I = 1/2$ for the ground states in $^{179}, ^{181}, ^{183}, ^{185}\text{Tl}$ were determined by the hfs patterns analysis (see Sec. 3.1). For other Tl nuclei tentative spin assignments, based on α - and β -decay systematics (Table 1), were used. Some of them were substantiated by the magnetic moments analysis in the present work (see Sec. 4.1). The ordering of the long-lived states in $^{182}, ^{184}\text{Tl}$ is unknown, therefore, they are denoted by “ $m1$ ”, “ $m2$ ”, and “ $m3$ ” in the present work. For the ground state of ^{180}Tl , a tentative assignment $I = (4, 5)$ was proposed on the basis of our β -decay study [12]. Correspondingly, both options were used in the ^{180}Tl -hfs fitting (see Table 1).

Table 1

Measurement results: isotope shifts, magnetic hfs constants, magnetic moments, and changes in mean-square charge radii for Tl nuclei

A	I	$\delta\nu_{205, A}$, MHz	$a(6p^2P_{1/2})$, MHz	$\mu(\mu_N)$	$\delta\langle r^2 \rangle_{205, A}$, fm ²
197 <i>m</i>	(9/2)	-2 790(250)	5 900(77)	4.032(57)	-0.271(26) {19}
195 <i>m</i>	(9/2)	-3 330(110)	5 634(55)	3.869(39)	-0.324(11) {23}
186 <i>m</i>	(10)	-7 350(220)	1 670(40)	2.549(62)	-0.719(23) {50}
185 <i>m</i>	(9/2)	-7 480(280)	5 470(300)	3.75(21)	-0.731(29) {51}
185 <i>g</i>	1/2	-9 500(400)	20 910(500)	1.607(38)	-0.938(41) {66}
184 <i>m1</i>	(2)	-9 930(320)	1 045(110)	0.321(36)	-0.979(32) {69}
184 <i>m2</i>	(7)	-9 890(240)	399(18)	0.428(22)	-0.976(24) {68}
184 <i>m3</i>	(10)	-7 960(210)	1 820(50)	2.778(78)	-0.777(20) {54}
183 <i>m</i>	(9/2)	-7 960(160)	5 268(80)	3.619(62)	-0.775(15) {54}
183 <i>g</i>	1/2	-10 460(160)	20 868(90)	1.603(8)	-1.033(15) {72}
182 <i>m1</i>	(4)	-11 340(180)	-900(50)	-0.549(33)	-1.120(18) {78}
182 <i>m2</i>	(7)	-11 370(310)	508(90)	0.54(10)	-1.123(30) {78}
181	1/2	-11 890(160)	21 321(180)	1.638(14)	-1.174(16) {82}
180 ($I = 4$)	(4)	-12 680(220)	-919(34)	-0.564(23)	-1.254(22) {88}
180 ($I = 5$)	(5)	-12 730(220)	-755(30)	-	-
179	1/2	-12 900(290)	21 310(200)	1.637(16)	-1.274(29) {89}

3.1. Magnetic moments

Due to the low electronic spin ($J = 1/2$) of the atomic ground state in thallium, the nuclear spins for the investigated nuclei cannot be determined by counting of the hyperfine components. On the other hand, the nuclear spin determines the amplitude ratio of the two observed hyperfine components. In the case of the odd- A $^{179, 181, 183, 185}\text{Tl}$ ground states, the hfs may be fairly well fitted only with an assumption of $I = 1/2$. As an example, in Fig. 2 the fittings with the nuclear spin assumptions of $I = 1/2$ and $3/2$ are compared. This comparison demonstrates a strong preference for the former value. Thus, the nuclear spin $I = 1/2$ was unambiguously determined for $^{179, 181, 183, 185}\text{Tl}^g$ in our experiment.

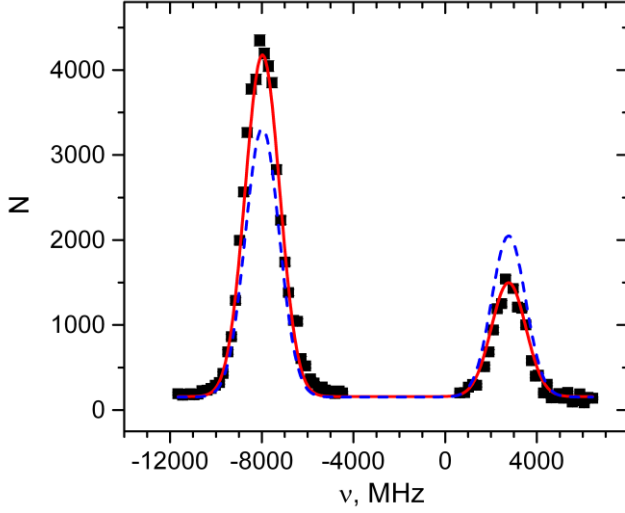


Fig. 2. Hyperfine structure spectrum of $^{181}\text{Tl}^g$: *full line* represents fitting with $I = 1/2$; *dashed line* represents fitting with $I = 3/2$

For evaluation of the magnetic moments, the following relation was used:

$$\mu_A = \mu_{A_0} \frac{I_A}{I_{A_0}} \frac{a_A(6p^2P_{1/2})}{a_{A_0}(6p^2P_{1/2})} \left[1 + {}^{A_0}\Delta^A(6p^2P_{1/2}) \right], \quad (2)$$

where ${}^{A_0}\Delta^A(nl)$ is the hfs anomaly (hfa) (see Ref. [6] and references therein).

It was shown in Ref. [6], that the relativistic ‘‘coupled-cluster’’ approach [13] describes experimental data for the hfa in thallium fairly well. This approach was used for estimation of the hfa for Tl isotopes and for magnetic moments evaluation. In Table 1, the magnetic moments of the Tl isotopes corrected by the estimated (small) hfa are presented.

3.2. Changes in mean square charge radii

The changes in the mean-square charge radii $\delta\langle r^2 \rangle^{A,A'}$ were deduced from the measured isotope shifts $\delta\nu^{A,A'}$ using the relations:

$$\delta\nu^{A,A'} = F_\nu \lambda^{A,A'} + M_\nu \frac{A - A'}{AA'}, \quad (3)$$

where $M_\nu = M_\nu^{\text{NMS}} + M_\nu^{\text{SMS}}$ and $M_\nu^{\text{NMS}} = \frac{\nu}{(m_p/m_e)}$; $\lambda^{A,A'} = K(Z)\delta\langle r^2 \rangle^{A,A'}$; ν is the transition frequency;

M_ν^{NMS} and M_ν^{SMS} are normal mass shift (NMS) and specific mass shift (SMS) constants, respectively, and $K(Z)$ takes into account the contribution of the higher order radii moments in $\lambda^{A,A'}$.

The values $F_{535 \text{ nm}} = -18.0 \text{ GHz} \cdot \text{fm}^{-2}$ and $M_{535 \text{ nm}}^{\text{SMS}} = 0 \text{ GHz} \cdot \text{amu}$ were used in Ref. [14] in a combined analysis of the optical, muonic atom, and electron scattering data in a model-independent way. The contribution of the higher order radii moments was also determined in this analysis: $K(81) = 0.938$. These values of $F_{535 \text{ nm}}$, $M_{535 \text{ nm}}$, and $K(81)$ were used in a King-plot procedure [7] to determine atomic F and M constants for the 276.9 nm transition: $F_{276.9 \text{ nm}} = 10.38 \text{ GHz} \cdot \text{fm}^{-2}$ and $M_{276.9 \text{ nm}} = 701 \text{ GHz} \cdot \text{amu}$. Scale uncertainty due to F and M indeterminacy can be estimated as 7%. In Table 1, the values of $\delta\langle r^2 \rangle_{205, A}$ deduced from the IS data by Eq. 3 with the atomic constants for 276.9 nm transition, are presented. The errors in round brackets reflect only the statistical IS uncertainties; the systematic errors which stem from the scaling uncertainty of the electronic factor and the specific mass shift are given in curly brackets.

Figure 3 shows the changes in the mean-square charge radii $\delta\langle r^2 \rangle_{205, A}$ of the Tl nuclei. It is generally acknowledged that the main isotopic trend of the $\delta\langle r^2 \rangle$ values is described by the droplet model (DM) (see Ref. [15] and references therein). Deviations from the DM-trend can be attributed to the development of the mean-square quadrupole deformation according to the expression:

$$\langle r^2 \rangle = \langle r^2 \rangle_{\text{DM}} \left(1 + \frac{5}{4\pi} \langle \beta_{\text{DM}}^2 \rangle \right), \quad (4)$$

where $\langle r^2 \rangle_{\text{DM}}$ is the mean-square charge radius calculated by the DM with zero deformation. In Figure 3, the lines of $\delta\langle r^2 \rangle$ calculated with the DM-parameters from work [15] and a constant mean-square deformation (setting $\langle \beta^2 \rangle^{1/2}(^{205}\text{Tl}) = \langle \beta^2 \rangle^{1/2}(^{204}\text{Hg}) = 0.069$ [16]) are also shown to provide insight into the development of the deformation across the Tl isotopic chain.

4. Discussion

4.1. Magnetic moments

Figure 4a shows the magnetic moments for Tl isotopes with $I = 1/2$. Despite rather large errors for $^{195, 187, 185}\text{Tl}$, the measured magnetic moments clearly follow a parabolic A dependence with a minimum near $A = 191$. While full understanding of the observed behaviour needs further theoretical work, it is intriguing that this behaviour follows the “typical” parabolic trend of the intruder states energy in the lead and neighbouring nuclei (see Ref. [17] and references therein). In contrast to the parabolic behaviour of the $\mu(1/2^+, \text{Tl}^g)$ values, the magnetic moments of the Tl intruder isomers with $I = (9/2)$ follow a linearly-decreasing A dependence (Fig. 4b), approaching more closely the Schmidt value ($\mu_{\text{Schmidt}} = 2.6\mu_N$) when going away from the closed shell.

In Ref. [12], a tentative spin-parity assignment of $I^\pi(^{180}\text{Tl}^g) = (4^-, 5^-)$ was proposed, with the most probable configuration of $[\pi 3s_{1/2} \times \nu 1h_{9/2}]$. Apart from the β/α -decay pattern arguments, the configuration assignment in Ref. [12] was based on the expected complete depletion of the $1i_{13/2}$ neutron shell below ^{181}Tl ($N = 100$), with the $1h_{9/2}$ (or possibly, $2f_{7/2}$) neutron orbital starting to play a role in the lightest Tl isotopes with $N < 100$.

We investigated the inferences on the possible spin and configuration of ^{180}Tl which can be drawn from the magnetic moment values determined in the present work. Following the discussion above, we will consider two possible configurations $[\pi 3s_{1/2} \times \nu 2f_{7/2}]_4^-$ and $[\pi 3s_{1/2} \times \nu 1h_{9/2}]_4^-, 5^-$, which can both explain the proposed spin $I^\pi(^{180}\text{Tl}^g) = (4^-)$, while only the latter can explain $I^\pi(^{180}\text{Tl}^g) = (5^-)$.

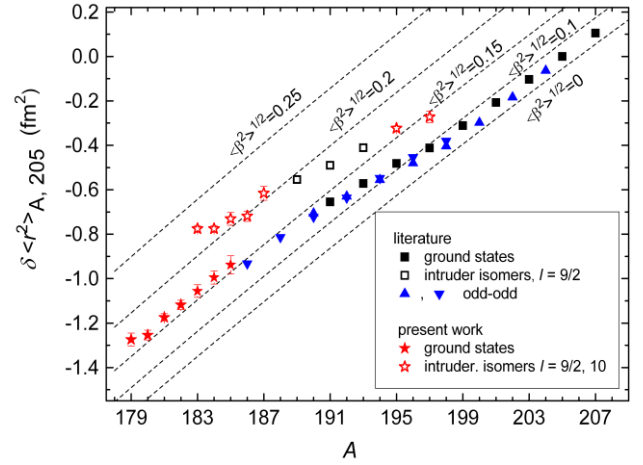


Fig. 3. Isotopic dependence of the changes in the mean-square charge radii for the Tl isotopes: stars – present work; squares – literature data [4]; dashed lines – the DM prediction with different constant mean-square deformations

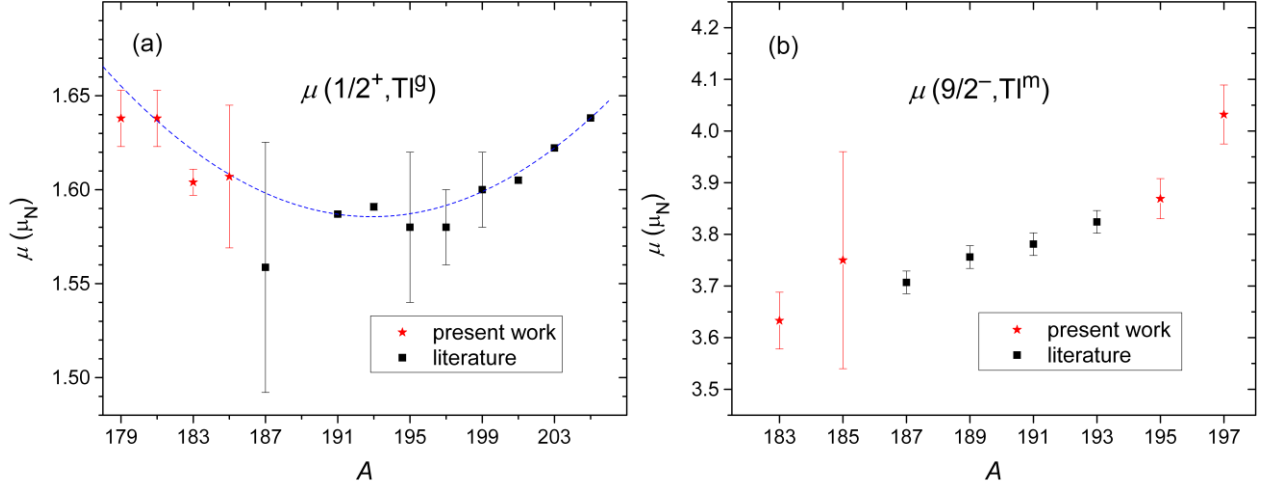


Fig. 4. Magnetic moments: a – Tl^g ($I = 1/2$); b – Tl^m ($I = 9/2$) nuclei. *Squares* – literature data (see Ref. [4] and references therein); *stars* – present work; *dashed curve* – a parabolic fit

According to the additivity relation, the magnetic moment of a two-particle state $|i_p i_n I\rangle$ in an odd-odd nucleus can be calculated using the following formula:

$$\mu_{\text{add}} = \frac{I}{2} \left(\frac{\mu_p}{i_p} + \frac{\mu_n}{i_n} \right) + \frac{I}{2} \left(\frac{\mu_p}{i_p} - \frac{\mu_n}{i_n} \right) \frac{i_p(i_p+1) - i_n(i_n+1)}{I(I+1)}, \quad (5)$$

where i_p and i_n are the proton and neutron single-particle angular moments; μ_p and μ_n are the single-particle magnetic moments. For the latter values, the known magnetic moments of the adjacent odd- A nuclei can be used. As there are no experimental data for the magnetic moment of the $1h_{9/2}$ neutron state (*e. g.*, for ^{181}Pb), the $\mu_n(\nu 1h_{9/2})$ was calculated by the standard single-particle formula with the commonly adopted renormalization of the neutron g -factors for the lead region [18]: $\mu_n(\nu 1h_{9/2}) = 0.74 \mu_N$.

In Table 2, the $\mu(^{180}\text{Tl}^g)$ values calculated by Eq. (5) with different spin and configuration assumptions are compared with the experimental values. Only the $[\pi 3s_{1/2} \times \nu 1h_{9/2}]_{4^-}$ configuration matches the observed negative experimental value, while other variants can be rejected as they do not reproduce the negative sign of the magnetic moment. Thus, this comparison strongly supports $I^\pi(^{180}\text{Tl}^g) = (4^-)$ assignment with the dominant configuration $[\pi 3s_{1/2} \times \nu 1h_{9/2}]$.

Table 2

Comparison of the experimental magnetic moments μ_{exp} for $^{180}\text{Tl}^g$ obtained with different spin and configuration assumptions, with magnetic moments μ_{add} calculated by the additivity relation

Configuration	Spin	$\mu_{\text{add}}(\mu_N)$	$\mu_{\text{exp}}(\mu_N)$
$\pi 3s_{1/2} \times \nu 1h_{9/2}$	4	-0.58	-0.564(23)
$\pi 3s_{1/2} \times \nu 1h_{9/2}$	5	2.38	-0.579(24)
$\pi 3s_{1/2} \times \nu 2f_{7/2}$	4	0.70	-0.564(23)

In Ref. [19], a (7^+) assignment for the ^{182}Tl parent state with a half-life of 3.1(10) s was proposed. In the α -decay study of ^{186}Bi [20], evidence was found for the presence of two (ls and hs – low-spin and high-spin,) long-lived states in ^{182}Tl .

The hfs patterns for different α and γ lines in the ^{182}Tl decay spectra, obtained in narrow-band laser scans, strongly support the presence of two long-lived states in ^{182}Tl . This is seen, *e. g.*, in Fig. 5, which shows that the hfs pattern of the $8^+ \rightarrow 6^+$ (413 keV) and $6^+ \rightarrow 4^+$ (332 keV) transitions in ^{182}Hg as a function of the laser frequency is distinctly different from the pattern of the $2^+ \rightarrow 0^+$ (351 keV) transition.

From the analysis of the hfs patterns for different γ lines, one can conclude that the ls-hfs represents two not fully resolved peaks with a clear dip in the centre, whereas the hs-hfs represents one broad flat-topped peak. In our β -decay study of the same data set [21], the noticeable population of the 4_1^+ ($E^* = 612$ keV) and 4_2^+ ($E^* = 1124$ keV) states in the daughter ^{182}Hg was observed along with the previously found 6^+ and 8^+ feeding [19]. This also points to the presence of two long-lived states in ^{182}Tl : high-spin (presumably, 7^+) and low-spin (presumably, $I = 3, 4, 5$).

In our dedicated α -decay study of ^{182}Tl , several ^{182}Tl α -decay lines were observed [22]: $E_\alpha = 5962, 6046, 6165, 6406,$ and 6360 keV. Remarkably, 6165 -hfs and 6046 -hfs patterns practically coincide with the hfs-pattern of ^{180}Tl . Correspondingly, one can suppose that in these cases the contribution of the hs-hfs is negligible. The similarity of the hfs patterns of the low-spin ^{182}Tl isomer (6165 - and 6046 -hfs's) and of ^{180}Tl suggests that the same $[\pi 3s_{1/2} \times \nu 1h_{9/2}]_4^-$ configuration is involved in both cases. The (7^+) spin and parity assignment for the high-spin isomer in ^{182}Tl is compatible with the corresponding assignment for one of the long-lived states in the heavier isotopes $^{186-204}\text{Tl}$. These tentative spin assignments were used in the fitting procedure.

The presence of two strongly overlapping hfs in the laser scans demands the application of a ‘‘two-hfs’’ fitting model which takes into account a possible mixture of two sets of hyperfine components. All hyperfine spectra produced for different α or γ lines, could be consistently fitted by this two-hfs fitting model. The resulting magnetic moment for the presumed 7^+ state, $\mu(7^+, ^{182}\text{Tl}^{m2}) = 0.54(10) \mu_N$, follows the general trend of magnetic moments of the states with the same spin in the heavier Tl nuclei. The magnetic moment of the presumed 4^- state, $\mu(4^-, ^{182}\text{Tl}^{m1}) = -0.549(33) \mu_N$, coincides within the experimental uncertainties with the magnetic moment of $^{180}\text{Tl}^g$ with the same (presumed) configuration and spin.

The application of the additivity relation for magnetic moments of the other odd-odd Tl nuclei enables us to confirm their leading configuration assignments and spins: $[\pi 3s_{1/2} \times \nu 1i_{13/2}]_{7^+}$ for $^{184}\text{Tl}^{m2}$; $[\pi 1h_{9/2} \times \nu 1i_{13/2}]_{10^-}$ for $^{184}\text{Tl}^{m3}$ and $^{186}\text{Tl}^m$ (see details in Refs. [7, 8]).

4.2. Changes in mean-square charge radii

In contrast to the mercury isotopic chain, where the strong odd-even staggering in the charge radii was found at $N < 106$ [2], no such an effect is observed for the thallium isotopes ground states (see Fig. 3). These states preserve their near spherical shape beyond the neutron mid-shell ($A < 186$). The similar smooth behavior of $\delta\langle r^2 \rangle$, testifying the persistence of the near spherical shape, was previously observed in the $^{182-208}\text{Pb}$ isotopes ($N = 100-126$) [3].

To compare different isotopic chains in the Pb-region we use a relative value of $\delta\langle r^2 \rangle$: $\delta\langle r^2 \rangle_{N,126} / \delta\langle r^2 \rangle_{124,122} = \delta\nu_{N,126}^F / \delta\nu_{124,122}^F$, thus avoiding indeterminacy of the electronic factors. Figure 6 shows the relative changes in $\delta\langle r^2 \rangle$ for the lead and thallium nuclei. It is clearly seen that the Tl radii perfectly follow the pattern of the Pb radii above and below the midshell at $N = 104$. Thus, the behaviour of the thallium nuclei is clearly different from the lighter- Z elements Hg ($Z = 80$) and Au ($Z = 79$), in which a well-known pronounced deviation from sphericity was found.

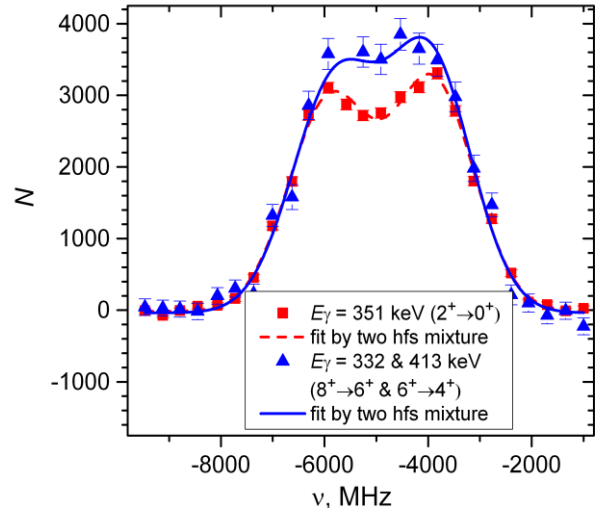


Fig. 5. Hyperfine structure pattern for different γ lines in the ^{182}Tl β decay: *squares* – $E_\gamma = 351$ keV; *triangles* – $E_\gamma = 413$ and 332 keV; *solid and dashed lines* – fits by a two hfs mixture with different percentage of the low- and high-spin hfs contribution

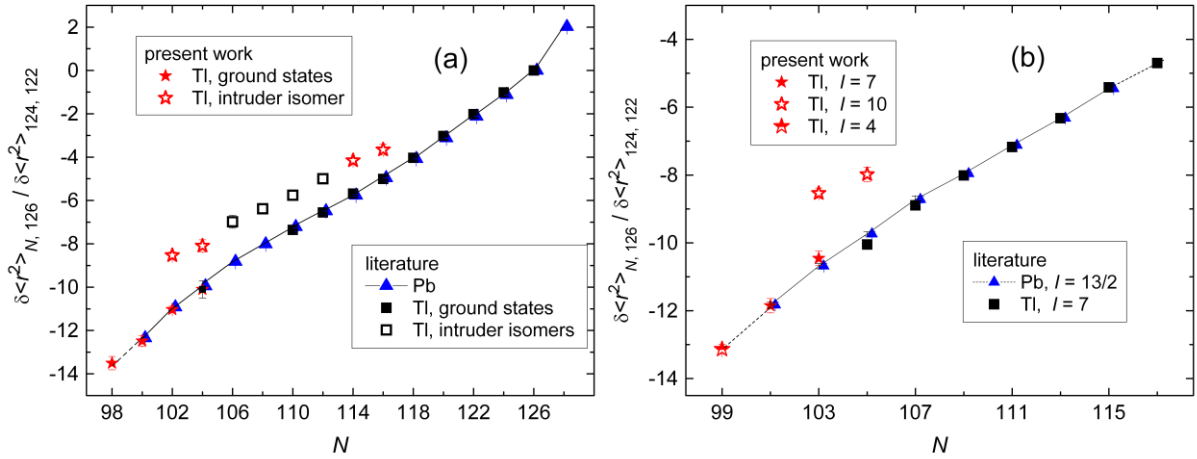


Fig. 6. Relative changes in $\delta\langle r^2 \rangle$ for the even-neutron (a) and odd-neutron (b) thallium and lead nuclei. Literature data: *triangles* – Pb [3]; *full squares* – Tl (ground states) [4]; *hollow squares* – Tl (intruder isomers) [4]. Present work: *full stars* – Tl (ground states); *hollow star* – Tl (intruder isomer); *semihollow star* – ^{180}Tl

Previously, a large IS between the ground ($\pi 3s_{1/2}$) and isomeric (intruder, $\pi 1h_{9/2}$) states in $^{191, 193}\text{Tl}$ was found [4]. This shift was attributed to the increase of deformation for intruder isomers in comparison with the ground states. The same conclusion may be drawn for $^{183, 185, 195, 197}\text{Tl}^m$ studied in the present work. An unexpected growth of the IS relative to the heavier odd- A Tl nuclei was observed for $^{185, 183}\text{Tl}$. In ^{183}Tl with the $h_{9/2}$ proton intruder configuration, two bands were interpreted as weakly deformed oblate and strongly deformed prolate structures [1]. The observed growth of the IS when going from $A = 191$ to $A = 183$ may be explained by the increased mixing between these weakly deformed oblate and strongly deformed prolate structures.

For the first time, a large IS for the odd-odd Tl intruder isomer was found in $^{186, 184}\text{Tl}$. The IS in $^{186, 184}\text{Tl}$ is similar to that in odd- A Tl nuclei and may be interpreted in a similar way as the result of the increase of deformation in the corresponding intruder isomers (see Fig. 3). This supports the shape-coexistence interpretation for these odd-odd nuclei [5].

5. Conclusion

Hfs structure parameters and IS have been measured for the neutron deficient thallium isotopes ($A = 179\text{--}195, 197$) using the 276.9 nm atomic transition.

From the analysis of the hfs, spins for $^{179, 181, 183, 185}\text{Tl}^g$ have been determined as $I = 1/2$. Magnetic moments and changes in the nuclear mean-square charge radii have been deduced. The magnetic moments of $^{179, 181, 183}\text{Tl}^g$ ($I = 1/2$) and $^{183}\text{Tl}^m$ [$I = (9/2)$] follow the parabolic and linear trends for the heavier Tl nuclei with the same spins, correspondingly. A detailed analysis of the hfs patterns produced by different α and γ lines following the decay of ^{182}Tl confirms the existence of a low-spin isomer in ^{182}Tl .

The charge radii of the $^{179\text{--}184}\text{Tl}$ ground states follow the trend found previously for isotonic (spherical) lead nuclei. A significant difference in charge radii for ground and isomeric (intruder, $9/2^-$ and 10^-) states of $^{183\text{--}186, 195, 197}\text{Tl}$ is observed. The larger charge radii for the isomers suggest a larger deformation of these isomers compared to the ground states. An unexpected growth of the isomer shift for $^{183, 185}\text{Tl}$ points to the possible prolate–oblate mixture.

References

1. K. Heyde, J.L. Wood, Phys. Scr. **91**, 083008 (2016).
2. G. Ulm *et al.*, Zh. Phys. A **325**, 247 (1986).
3. M.D. Seliverstov *et al.*, Eur. Phys. J. A **41**, 315 (2009).
4. W. Lauth *et al.*, Phys. Rev. Lett. **68**, 1675 (1992); J.A. Bounds *et al.*, Phys. Rev. C **36**, 2560 (1987); R. Menges *et al.*, Z. Phys. A **341**, 475 (1992); H.A. Schuessler, E.C. Benck, F. Buchinger, H.K. Carter, Nucl. Instrum. Meth. A **352**, 583 (1995).
5. A.J. Kreiner *et al.*, Phys. Rev. Lett. **47**, 1709 (1981); M. Huyse *et al.*, Phys. Lett. B **201**, 293 (1988); P. Van Duppen *et al.*, Nucl. Phys. A **529**, 268 (1991); A.N. Andreyev *et al.*, Eur. Phys. J. A **18**, 39 (2003).
6. A.E. Barzakh *et al.*, Phys. Rev. C **86**, 014311 (2012).
7. A.E. Barzakh *et al.*, Phys. Rev. C **88**, 024315 (2013).
8. A.E. Barzakh *et al.*, Phys. Rev. C **95**, 014324 (2017).
9. A.E. Barzakh *et al.*, Rev. Sci. Instrum. **83**, 02B306 (2012).
10. M.D. Seliverstov *et al.*, Phys. Rev. C **89**, 034323 (2014).
11. G. Hermann, G. Lasnitschka, D. Spengler, Zh. Phys. D **28**, 127 (1993).
12. J. Elseviers... A. Barzakh *et al.*, Phys. Rev. C **84**, 034307 (2011).
13. A.-M. Mårtensson-Pendrill, Phys. Rev. Lett. **74**, 2184 (1995).
14. G. Fricke, K. Heilig, *Nuclear Charge Radii*, Springer, Berlin, 2004.
15. D. Berdichevsky, F. Tondeur, Zh. Phys. A **322**, 141 (1985).
16. B. Pritychenko, M. Birch, B. Singh, M. Horoi, Atom. Data Nucl. Data Tables **107**, 1 (2016).
17. A.N. Andreyev *et al.*, Phys. Rev. C **80**, 024302 (2009).
18. S. Nagamiya, T. Yamazaki, Phys. Rev. C **4**, 1961 (1971).
19. A. Bouljedri *et al.*, Zh. Phys. A **339**, 311 (1991).
20. A.N. Andreyev *et al.*, Eur. Phys. J. A **18**, 55 (2003).
21. E. Rapisarda, A. Barzakh *et al.*, J. Phys. G: Nucl. Part. Phys. **44**, 074001 (2017).
22. C. Van Beveren, A. Barzakh *et al.*, J. Phys. G **43**, 025102 (2016).

STUDY OF NUCLEON CORRELATIONS IN NUCLEI BY THE (p, p') INELASTIC REACTION AT 1 GeV

O.V. Miklukho, V.A. Andreev, A.A. Izotov, A.Yu. Kisselev, N.G. Kozlenko,
A.N. Prokofiev, A.V. Shvedchikov, S.I. Trush, A.A. Zhdanov

1. Introduction

The study of the nuclear structure using a 1-GeV proton beam in high resolution experiments is traditional at the PNPI synchrocyclotron. In the first experiments done about 45 years ago, the nuclear matter distributions were investigated and the neutron density parameters were extracted using the Glauber diffraction scattering model [1]. Later high precision experiments were performed on $(p, 2p)$ and (p, pn) reactions studying in details proton and neutron shells in nuclei [2].

The polarization was also measured in high resolution proton diffraction scattering [3]. The deuteron structure at small distances was studied in $(p, 2p)$ quasielastic scattering with the polarization measured using the low momentum arm of the two-arm magnetic spectrometer [4]. New experiments were developed due to an upgrade of this spectrometer equipped with polarimeters in each arm. At first, the spin-orbital structure of the ${}^6\text{Li}$ and ${}^7\text{Li}$ nuclei was studied by measuring the effective polarization of nuclear protons [5, 6]. Later the goal of these investigations was shifted to an important question of how the free nucleon scattering amplitude is modified in the nuclear matter. First experiments were jointly done in collaboration with the group of physicists from the Research Center for Nuclear Physics (Japan) [7, 8]. Due to a new fast readout electronics CROS-3 developed at the PNPI for the two-arm magnetic spectrometer, the polarization experiments were performed [9, 10], in which the spin-correlation parameters of the reaction with nuclei were measured as well.

Herein we report results of new inclusive experiments, which were recently done using the high-energy arm of the two-arm magnetic spectrometer.

2. Motivation of the experiments

This work is a part of the experimental program in the framework of which the effects from scattering off nucleon associations (nucleon correlations – NCs) in nuclei were studied with the 1-GeV proton beam at the synchrocyclotron of the PNPI [10–15]. These effects were also investigated in other experiments by various nuclear reactions (*e. g.*, in Ref. [14]).

In exclusive experiments [10], an essential difference in the polarization of two secondary protons from the $(p, 2p)$ reaction on nuclei was found. This effect may be explained as due to scattering on the NCs of the protons registered in the low-energy arm of the two-arm magnetic spectrometer.

In our first inclusive experiment [11], a growth of the polarization with the final proton momentum K in the (p, p') inelastic reaction with the ${}^{40}\text{Ca}$ nucleus at the scattering angle of 21° was observed. At the value of K corresponding to the kinematics of the quasielastic scattering on a ${}^4\text{He}$ -like nucleon cluster inside of the calcium nucleus, the polarization turned out to be close to that as in free elastic $p^4\text{He}$ scattering.

In new inclusive experiments [12–15], we studied in details the inelastic (p, p') reaction with different nuclei with a better statistics accuracy. The polarization P of the secondary proton and the differential cross section $\sigma^{\text{incl}} = d^2\sigma/(d\Omega dK)$ of the reaction were measured as a function of the scattered proton momentum K in narrow intervals of K ($\sim 10 \text{ MeV}/c$).

3. Experimental method and reaction kinematics

The general layout of the experimental set-up for investigating (p, p') reaction with nuclei is presented in Fig. 1 [13]. The secondary protons from the reaction under investigation were detected by means of the magnetic spectrometer MAP equipped with a polarimeter based on multiwire proportional chambers and a carbon analyzer. The spectrometer was installed at the angle of 21° with respect to the direction of the proton beam. Its momentum resolution for this scattering angle could be estimated by the width

of the clearly separated 2^+ excited level in the reaction with the carbon nucleus (Fig. 2), and it was about ± 2.5 MeV/c.

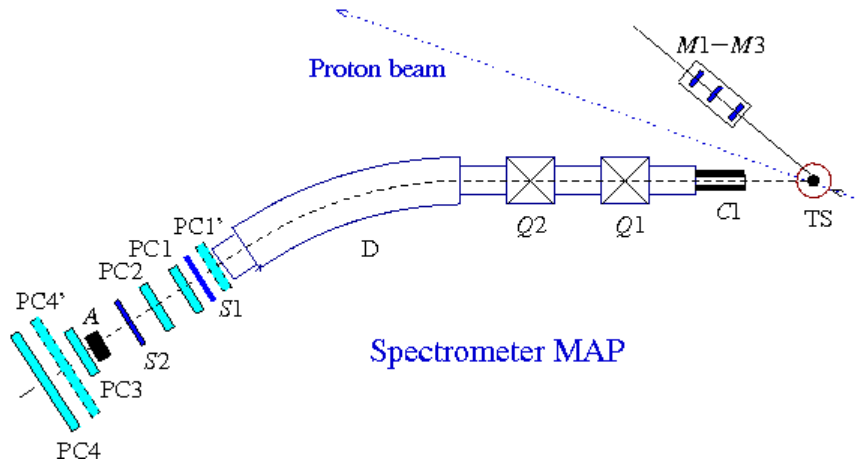


Fig. 1. The experimental set-up: TS – target of the magnetic spectrometer; Q1, Q2 – magnetic quadrupoles; D – dipole magnet; C1 – collimator; S1, S2, and M1–M3 – scintillation counters; PC1–PC4, PC1', PC4', A – proportional chambers and the carbon analyzer of the MAP polarimeter

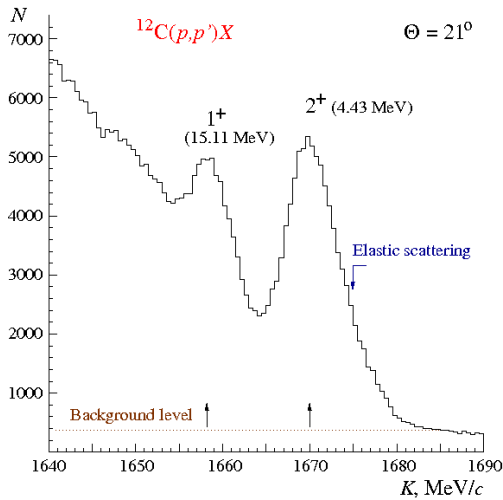


Fig. 2. Momentum distribution in the $^{12}\text{C}(p, p')X$ reaction at the scattering angle of $\Theta = 21^\circ$ [13]

The reaction differential cross sections were determined at different momentum settings of the spectrometer using information from the proportional chamber PC2-X. The polarization of the secondary protons was defined by the azimuthal angular asymmetry of their scattering off the carbon analyzer. The analyzing power of the MAP polarimeter was calibrated on the basis of the polarization data obtained for elastic pp scattering in the present experiment. In order to carry out the calibration over a wide range of the scattered proton energies, polarization measurements were performed with polyethylene (CH_2) and carbon (C) targets for various angular and proper momentum settings of the spectrometer. The found values of the pp polarization were compared with the predictions of the phase-shift analysis. A correction to the analyzing power of the polarimeter was introduced thereupon [13].

We performed measurements in a wide range of the scattered proton momentum K covering the pN quasielastic peak with its maximum at $K = K_{pN} \approx 1480$ MeV/c and in a high momentum region ($K > 1530$ MeV/c) up to the momentum (K_L) corresponding to the excited level of the nucleus under investigation. At $K > K_{pN}$, the quasielastic pNC scattering off the NCs is kinematically more preferable since NCs are more massive than the nucleon. In this region, the four-momentum transfer Q remains almost invariable (~ 600 MeV/c). Consequently, the Bjorken variable $x_B = Q^2/2mv$ is actually determined only by the value of the K momentum. The momentum interval between K_{pN} and K_L covers a range of $x_B = 1-4$.

The momentum $K_N^{\min}(\Theta)$ is the minimum momentum which a nuclear nucleon should have in order to scatter a beam proton with the final momentum K . This momentum is a monotonically increasing function of K . The dashed vertical line in Fig. 3 at $K = K_C \approx 1575$ MeV/c separates the K momentum region where the $K_N^{\min}(21^\circ)$ momentum is larger than the Fermi momentum k_F for the carbon nucleus (~ 220 MeV/c) [14]. In the range $K > K_C$, a contribution from scattering off the uncorrelated nuclear nucleons is essentially suppressed [12].

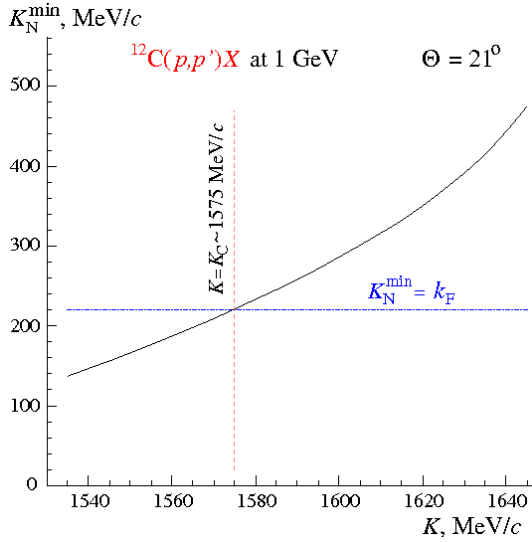


Fig. 3. The K_N^{\min} momentum versus the scattered proton momentum K . The *solid curve* is the averaged estimation of K_N^{\min} for the carbon nucleus [14]. The momenta K_N^{\min} , k_F , and K_C , the *dashed vertical* and *dash-dotted horizontal* lines are defined in the text

4. Experimental data and observations

In Figure 4, the secondary proton polarization (*blue squares*) and the cross sections (*circles*) of the (p, p') inelastic reaction with the ^{12}C nucleus are presented as a function of the scattered proton momentum K [13]. The left and right vertical axes refer to the polarization and the scattering cross section, respectively. The dashed curve is the result of the polarization calculation in the framework of the spin-dependent distorted wave impulse approximation (DWIA) taking into account the relativistic distortion of the nucleon spinor in the nuclear medium DWIA* [10]. In the calculations, the known THREEDEE code was used.

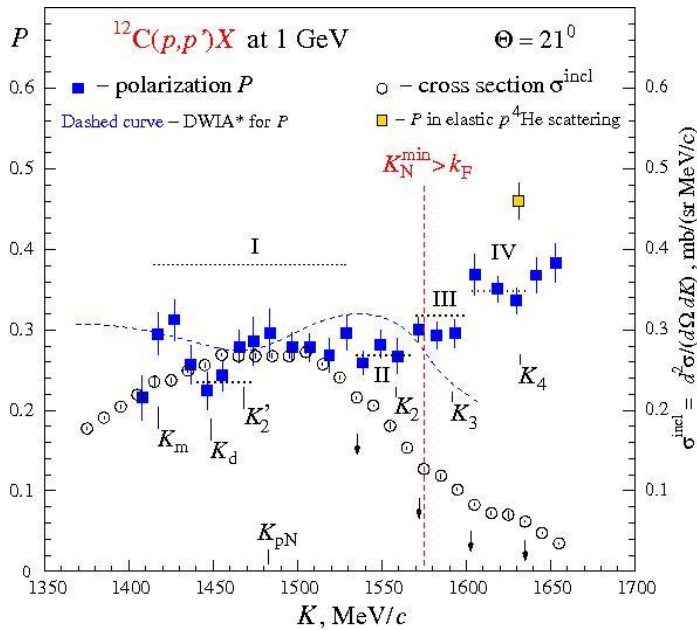


Fig. 4. Polarization (*blue squares*) and cross section (*circles*) of the $^{12}\text{C}(p, p')X$ reaction at the angle of $\Theta = 21^\circ$ versus the scattered proton momentum K [13]. The *gold square* is the polarization in free elastic $p^4\text{He}$ scattering [8]. Momentum intervals I–IV and the corresponding *dotted-line segments*, the momenta K_m , K_d , K_2 , K_3 , K_4 , K_N^{\min} , k_F , the *dashed curve* and the *dashed vertical line* (see also Fig. 3) are defined in the text

At the K momentum larger than the momentum corresponding to the maximum of the quasielastic pN peak ($K_{pN} \approx 1480$ MeV/ c), it is possible to distinguish the momentum intervals indicated by the dotted-line segments and marked with the Roman numerals II (1 535–1 570 MeV/ c), III (1 570–1 600 MeV/ c), and IV (1 600–1 635 MeV/ c). The signs on which these intervals were allocated are as follows:

1. The polarization within each interval practically does not change and grows from interval II to interval IV.
2. The beginning of each interval corresponds to slowing down of the scattering cross section (indicated by an arrow) which may be due to scattering by a heavier NC.

We suppose that intervals II, III, and IV correspond to elastic scattering in the nuclear medium on two-, three-, and four-nucleon correlations. Note that a high-momentum region, just above range IV, possibly corresponds to quasielastic scattering off the residual nucleus X from the reaction under investigation.

To verify the last assumption, we calculated the momenta K_2 , K_3 , and K_4 corresponding to the quasielastic maxima in the scattering on these correlations (see Fig. 4). In the kinematical calculations, we assumed:

- 1) the nucleon correlation does not move;
- 2) the NC mass is equal to the mass of the real light nucleus with a simple structure like ${}^2\text{H}$, ${}^3\text{He}$ (${}^3\text{H}$), and ${}^4\text{He}$;
- 3) the residual nuclei (X) in the $A(p, p')X$ reaction are in the ground state.

One can see that the momenta K_2 , K_3 , and K_4 are within the momentum intervals II, III, and IV, respectively. This is so in the inclusive case where the NC mass is smaller (because of the in-medium modification [10]) than the mass of the corresponding free light nucleus. A decrease of about 10% in the NC masses reduces the momenta K_2 , K_3 (K_3^*), and K_4 by about 12, 8, and 6 MeV/ c , respectively. Note that for the ${}^{12}\text{C}$ data the K_3 and K_3^* momenta corresponding to the scattering off the ${}^3\text{He}$ and ${}^3\text{H}$ nuclei are virtually identical.

We suppose that the width of each momentum interval is determined by the NC movement in the transverse direction with respect to the proton beam. The horizontal angular acceptance of the elastic scattering on a moving four-nucleon cluster ($\sim 4.5^\circ$) is significantly larger than that of the scattering on a motionless correlation ($\sim 1^\circ$). This enables us to observe the angular distribution of the polarization P_{IV} for the scattering on a ${}^4\text{He}$ -like nucleon cluster within the fourth momentum range. We expected to see a close to homogeneous distribution of the polarization, as it was observed in the free elastic $p^4\text{He}$ scattering shown in Fig. 5 [8].

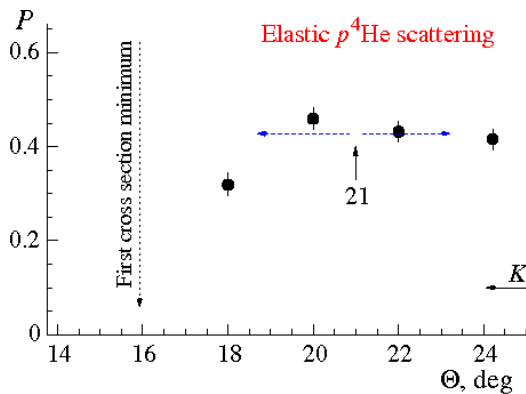


Fig. 5. Angular dependence of the polarization in elastic $p^4\text{He}$ scattering at 1 GeV [8]. The *dashed horizontal arrows* are defined in the text

Two horizontal oppositely directed arrows in Fig. 5 indicate the angular range corresponding to the effective acceptance seen in the inclusive reaction in momentum interval IV.

Note that the polarization (P_{IV}) in interval IV is smaller than that ($P_{4\text{He}}$) in the free elastic $p^4\text{He}$ scattering (*gold square*) [8]. This can be due to the in-medium modification of the proton interaction with the four-nucleon cluster. The relative decrease of the polarization in the nuclear medium is about 20%. We see approximately the same polarization decrease for the scattering on the uncorrelated nuclear nucleons

when we compare the polarizations P_{DWIA} and P_{DWIA^*} calculated without account and with account of the nuclear medium effect [13].

In region I (indicated in Fig. 4 by a *dotted-line segment*) around the momentum K_{pN} , a contribution from multistep processes of nucleon knockout from the nucleus can be rather sizeable [16]. The outgoing proton momentum in these processes is lower than that in the one-step (p, p') reaction under investigation. The two-step nucleon knockout process decreases the polarization at the momentum K smaller than K_m (see Fig. 4). A similar effect is also observed in the analyzing power measured at Los Alamos Meson Physics Facility at 0.8 GeV [16]. We see a dip in the polarization in the range of K around the momentum K_d (for all the investigated nuclei). This dip in the polarization may be due to inelastic scattering by a two-nucleon short-range correlation [17] resulting in its decay into two nucleons [18]. The polarization in this process, as well as in the in-medium elastic scattering off the correlation in range II, can be essentially smaller than that in the in-medium elastic scattering off the uncorrelated nuclear nucleons. In the short range correlation approach [19], two nucleons belonging to the two-nucleon correlation have oppositely directed momenta of nearly equal magnitude close to the Fermi momentum (~ 250 MeV/c, corresponding to the nucleon kinetic energy ~ 35 MeV). The momentum K_2' (Fig. 4) was obtained using a kinematical program at the excitation energy (~ 70 MeV) of the residual nucleus ($X = {}^{10}\text{B}$) equal to the total kinetic energy of the nucleons in the motionless NC. The K_2' momentum is shifted with respect to the momentum K_2 (for interval II) toward lower values of K . The momentum range (marked by the *dotted-line segment*) covering the momentum K_2' is caused by the NC motion.

Figure 6 presents the data obtained for the inelastic ${}^{40}\text{Ca}(p, p')X$ reaction [13]. All designations in the figure are the same as in Fig. 4. For the calcium nucleus we determined the aforementioned momentum intervals II (1 545–1 575 MeV/c), III (1 575–1 610 MeV/c), and IV (1 610–1 645 MeV/c).

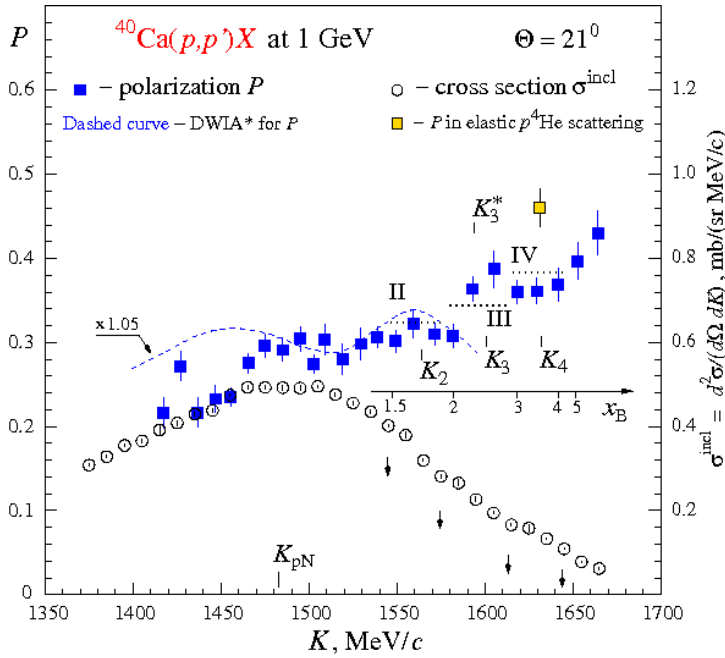


Fig. 6. Polarization (blue squares) and cross section (circles) of the ${}^{40}\text{Ca}(p, p')X$ reaction at the angle of $\Theta = 21^\circ$ versus the scattered proton momentum K [13]. The gold square is the polarization in free elastic $p^4\text{He}$ scattering [8]. Momentum intervals II–IV and the corresponding *dotted-line segments*, the momenta K_{pN} and K_2, K_3, K_3^*, K_4 , and the *dashed curve* are defined in the text. An additional axis to indicate the Bjorken variable x_B is also given

Below we perform a comparison with the carbon data:

1. The beginning of each interval for the ${}^{40}\text{Ca}$ nucleus is shifted with respect to that for the ${}^{12}\text{C}$ nucleus by about 5 to 10 MeV/c toward higher values. The investigation of the ${}^{56}\text{Fe}$ nucleus showed that this effect is not related to a bigger mass of the calcium nucleus [15].

2. The polarization in interval III for the calcium data increases with K unlike the polarization in the scattering off the ${}^{12}\text{C}$ nucleus. It is possible that this is due to a dispersion effect because of a noticeable difference (~ 7 MeV/c) between the momenta K_3 and K_3^* corresponding to the in-medium elastic scattering on the ${}^3\text{He}$ and ${}^3\text{H}$ nuclei (the spectrometer momentum resolution was about 2.5 MeV/c). It is also assumed that the polarization in the elastic scattering on the ${}^3\text{He}$ nucleus is bigger than that on the tritium nucleus [13].

In this case, when K is higher than K_3^* , the scattering on the ${}^3\text{He}$ nucleus dominates and the averaged polarization has the maximum value. In the region where K is smaller than K_3^* (within momentum interval III), the processes of scattering off these three-nucleon correlations are mixed and the averaged polarization decreases.

3. The polarizations in interval IV (P_{IV}) in the scattering on the calcium and carbon nuclei are nearly identical [$P_{IV}(\text{Ca}) = 0.363 \pm 0.009$, $P_{IV}(\text{C}) = 0.348 \pm 0.010$].

In Figures 7 and 8, the secondary proton polarizations in the (p, p') reaction with the ${}^{56}\text{Fe}$ and ${}^{28}\text{Si}$ nuclei are presented [15]. The appropriate cross sections of the reactions were published in Refs. [14, 15]. The *dashed blue curve* and *dashed red line* correspond to the results of calculations for the reaction with the carbon nucleus (see Fig. 4).

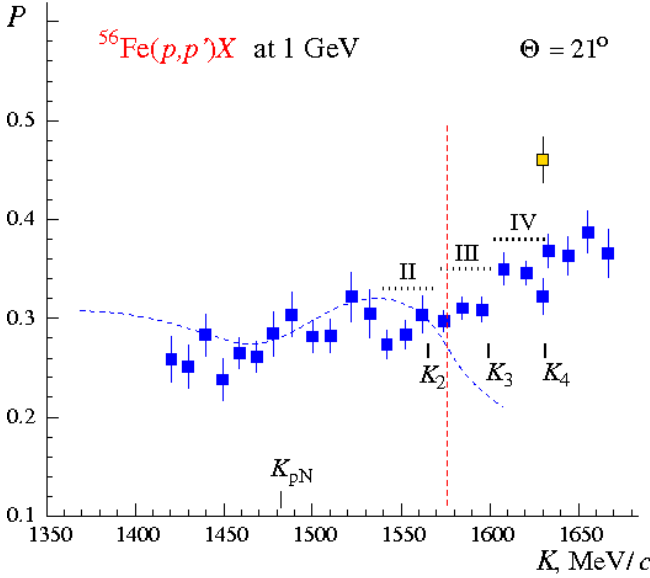


Fig. 7. Polarization in the ${}^{56}\text{Fe}(p, p')X$ reaction [15]. All designations are the same as in Fig. 4

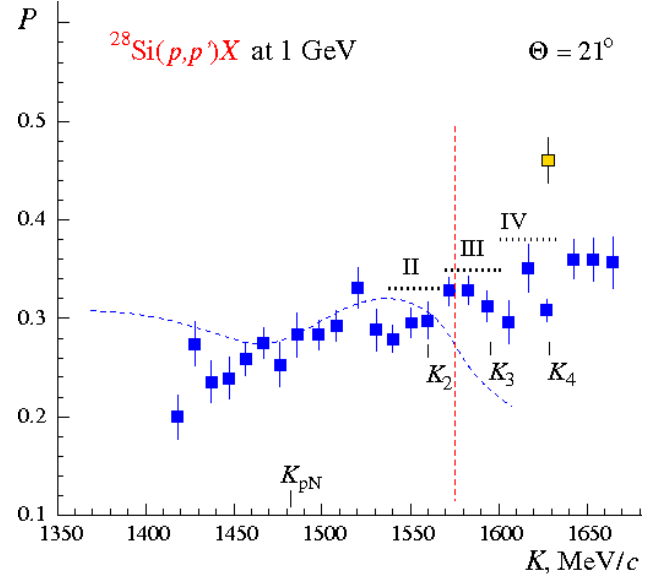


Fig. 8. Polarization in the ${}^{28}\text{Si}(p, p')X$ reaction [15]. All designations are the same as in Fig. 4

Main observations are below:

1. On the whole, a similar polarization structure in the inelastic scattering off the ${}^{28}\text{Si}$ and ${}^{56}\text{Fe}$ nuclei is observed as in the carbon and calcium data.
2. The structure momentum intervals II, III, and IV for the ${}^{28}\text{Si}$ and ${}^{56}\text{Fe}$ nuclei coincide with the analogous intervals for the ${}^{12}\text{C}$ nucleus.
3. The polarization (P_{IV}) in interval IV for the ${}^{28}\text{Si}$ nucleus is noticeably inhomogeneous [15].
4. The measured polarization values of P_{IV} in the middle of the momentum interval IV in the reaction with the ${}^{12}\text{C}$, ${}^{28}\text{Si}$, ${}^{40}\text{Ca}$, and ${}^{56}\text{Fe}$ nuclei are almost the same [$P_{IV}(\text{C}) = 0.351 \pm 0.016$, $P_{IV}(\text{Si}) = 0.351 \pm 0.024$, $P_{IV}(\text{Ca}) = 0.361 \pm 0.015$, $P_{IV}(\text{Fe}) = 0.346 \pm 0.012$].

In Figure 9, the scattering cross section ratios for the (p, p') reaction with the ${}^{56}\text{Fe}$ and ${}^{12}\text{C}$ nuclei $\eta(\text{Fe}/\text{C})$, with the ${}^{56}\text{Fe}$ and ${}^{28}\text{Si}$ nuclei $\eta(\text{Fe}/\text{Si})$, and with the ${}^{56}\text{Fe}$ and ${}^{40}\text{Ca}$ nuclei $\eta(\text{Fe}/\text{Ca})$ are presented [14].

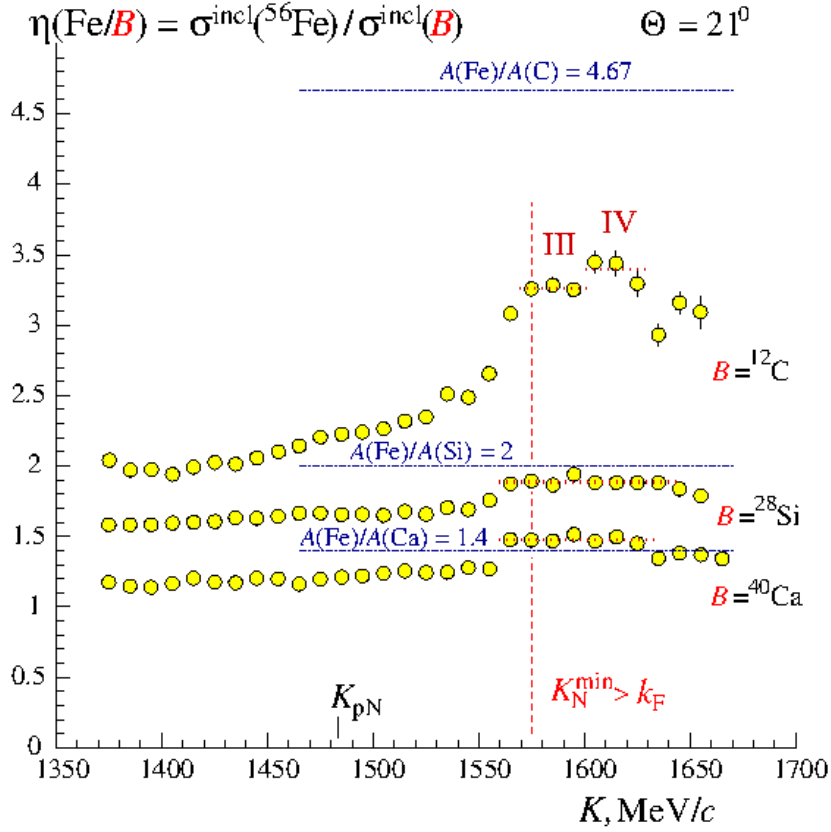


Fig. 9. Scattering cross section ratios $\eta(\text{Fe}/B)$ (circles), where B corresponds to the ^{12}C , ^{28}Si , or ^{40}Ca nucleus, versus the scattered proton momentum K [14]. The dashed vertical line represents the same as in Figs. 3, 4. The dash-dotted horizontal lines correspond to the ratios of the appropriate atomic numbers A of the nuclei under investigation. The dotted-line segments cover intervals III, IV, and 1 560–1 635 MeV/c. These intervals and the momenta K_N^{min} , k_F , and K_{pN} are defined in the text

Main observations are below:

1. We see a step-function behaviour of the scattering cross section ratio $\eta(\text{Fe}/\text{C})$ in the region of K from 1 560 to 1 630 MeV/c covering momentum intervals III and IV indicated by the dotted-line segments. Within the intervals a value of the $\eta(\text{Fe}/\text{C})$ ratio does not depend substantially on K (*i. e.*, scaling is observed). These intervals coincide with the analogues intervals in the polarization and cross section data for the carbon nucleus (see Fig. 4), which are presumably due to the in-medium elastic scattering off three- and four-nucleon correlations [13]. According to the Jefferson Lab (e, e') experiment [19], the observation of such steps in the cross section ratio is a crucial test of the dominance of inclusive electron scattering on the short-range nucleon correlations, and the steps are due to the average nucleon density in the iron nucleus to be larger than that in the carbon nucleus [14].

2. The scaling of the cross section ratios $\eta(\text{Fe}/\text{Si})$ and $\eta(\text{Fe}/\text{Ca})$ are observed in the mentioned above region of K . We do not see any steps in these ratios. It is possible that the average nucleon density in the nuclei ^{28}Si , ^{40}Ca , and ^{56}Fe is the same [14]. It is interesting that the values of these ratios are close (within the systematic errors of their determination) to those of the atomic number ratios $A(\text{Fe}/\text{Si})$ and $A(\text{Fe}/\text{Ca})$ (indicated by the dash-dotted line segments).

5. Conclusion

A structure in the polarization and cross section of the (p, p') inelastic reaction with the nuclei ^{12}C , ^{28}Si , ^{40}Ca , and ^{56}Fe at 1 GeV and the laboratory scattering angle of $\Theta = 21^\circ$ has been observed. This structure can be related to the in-medium elastic scattering on nucleon correlations in the nuclei.

The scaling of the scattering cross section ratios off the nuclei under investigation (a value of the ratio is independent of the secondary proton momentum K) has been observed in the high momentum range of $K = 1.560\text{--}1.635$ MeV/ c .

List of participants of the present work

G.M. Amalsky, G.E. Gavrilov, D.S. Ilyin, A.A. Izotov, A.Yu. Kisselev, N.G. Kozlenko, P.V. Kravchenko, M.P. Levchenko, D.A. Maysuzenko, O.V. Miklukho, V.A. Murzin, V.I. Murzin, D.V. Novinsky, A.N. Prokofiev, A.V. Shvedchikov, S.I. Trush and A.A. Zhdanov

Acknowledgments

We are grateful to the staff of the PNPI 1-GeV proton accelerator for the stable beam operation and to A.A. Vorobyov and S.L. Belostotski for their support and fruitful discussions.

References

1. G.D. Alkhazov, S.L. Belostotski, A.A. Vorobyov, Phys. Rept. **42**, 89 (1978).
2. A.A. Vorobyov, Yu.V. Dotsenko, *PNPI Research Report 1971–1996 (HEPD)*, 1998, p. 172.
3. G.D. Alkhazov *et al.*, Phys. Lett. B **90**, 364 (1980).
4. N.P. Aleshin *et al.*, Nucl. Phys. A **568**, 809 (1994).
5. O.V. Miklukho *et al.*, Phys. Atom. Nucl. **63**, 824 (2000).
6. O.V. Miklukho *et al.*, Nucl. Phys. A **683**, 145 (2001).
7. V.A. Andreev *et al.*, Phys. Rev. C **69**, 024604 (2004).
8. O.V. Miklukho *et al.*, Phys. Atom. Nucl. **69**, 474 (2006).
9. O.V. Miklukho *et al.*, Phys. Atom. Nucl., **73**, 1 (2010).
10. O.V. Miklukho *et al.*, Phys. Atom. Nucl. **76**, 871 (2013).
11. O.V. Miklukho *et al.*, e-Print: arXiv:1103.6113v1 [nucl-ex] (2011).
12. O.V. Miklukho *et al.*, JETP Letters **102**, 11 (2015).
13. O.V. Miklukho *et al.*, Phys. Atom. Nucl. **80**, 299 (2017).
14. O.V. Miklukho *et al.*, JETP Letters **106**, 69 (2017).
15. O.V. Miklukho *et al.*, Phys. Atom. Nucl. **81**, Iss. 3, 320 (2018).
16. R.D. Smith and S.J. Wallace, Phys. Rev. C **32**, 1654 (1985).
17. D.I. Blokhintsev, Sov. Phys. JETP **6**, 995 (1958).
18. O.V. Miklukho *et al.*, J. Phys.: Conf. Ser. **938**, 012013 (2018).
19. K.S. Egiyan *et al.*, Phys. Rev. Lett. **96**, 082501 (2006).

SENSITIVITY OF REACTION CROSS SECTIONS TO HALO NUCLEUS DENSITY DISTRIBUTIONS

G.D. Alkhazov, V.V. Sarantsev

1. Introduction

Reaction cross sections σ_R serve as one of the main sources of information on sizes of exotic halo nuclei. The root mean square (rms) matter radius R_m of an exotic nucleus is determined by comparing the experimental reaction cross section for nucleus–nucleus scattering involving the nucleus of interest with theoretical model predictions. At the same time, the reaction cross sections depend not only on the rms nuclear matter radius, but also to some extent on the radial shape of the studied nucleus. Bush with coauthors [1] investigated the sensitivity of reaction cross sections to ^{11}Li density distributions, and they concluded that ^{11}Li -target cross sections at fixed rms matter radii retain a substantial sensitivity to higher radial moments of the assumed ^{11}Li density distribution, which is quite different for light and heavy targets. According to their consideration, reaction cross sections for nucleus–nucleus scattering are significantly more sensitive to the matter density at the nuclear periphery than those for nucleus–proton scattering. Therefore, measuring reaction cross sections for nucleus–nucleus and nucleus–proton scattering one can determine the rms nuclear matter radius and obtain information on the radial shape of the studied nucleus. However, calculations of cross sections in Ref. [1] were performed using the Glauber theory in the optical limit approximation, which as is well known noticeably overestimates nucleus–nucleus reaction cross sections, especially for the case of halo nuclei. For this reason, it is not clear whether the conclusion of Bush *et al.* that nucleus–nucleus cross sections are more sensitive to the nuclear periphery than nucleus–proton cross sections reflects the real physical case, or this conclusion was made due to the optical approximation to the Glauber theory used in their calculations.

In the present work, we investigate the sensitivity of reaction cross sections to the shape of the nuclear matter distribution by performing calculations of reaction cross sections for scattering of the halo nuclei ^6He , ^{11}Li , and ^{19}C on different nuclear targets at the energy of 0.8 GeV/u.

2. Cross section calculations

The reaction cross section σ_R for nucleus–nucleus scattering is defined as the difference between the total cross section σ_{tot} and the integral elastic cross section σ_{el} :

$$\sigma_R = \sigma_{\text{tot}} - \sigma_{\text{el}}. \quad (1)$$

Here σ_{tot} and σ_{el} can be calculated as

$$\sigma_{\text{tot}} = (4\pi/k) \text{Im} |F_{\text{el}}(0)| \quad (2)$$

and

$$\sigma_{\text{el}} = (2\pi/k^2) \int |F_{\text{el}}(\mathbf{q})|^2 q dq, \quad (3)$$

where $F_{\text{el}}(\mathbf{q})$ is the amplitude of elastic nucleus–nucleus scattering; k is the value of the wave vector of the incident nucleus; \mathbf{q} is the momentum transfer. In the given paper the amplitude $F_{\text{el}}(\mathbf{q})$ was calculated using the Glauber theory within the “rigid target” approximation, that is, at first the amplitude of scattering of one nucleon on the nuclear target was calculated, and then this amplitude was used in the calculations of the cross sections for scattering of an exotic nucleus consisting of several nucleons. As was shown in Ref. [2], the reaction cross sections for scattering of exotic nuclei on nuclear targets calculated within the rigid target approximation are very close to those calculated with the exact Glauber formula. In the calculations, a spin-independent isospin-averaged amplitude of the free nucleon–nucleon (NN) scattering was employed, the traditional high-energy parametrization of this amplitude and the corresponding profile function

$$\gamma(\mathbf{b}) = \sigma_{NN} (1 - i \epsilon_{NN}) \exp(-\mathbf{b}^2 / 2\beta_{NN}) / (4\pi\beta_{NN}) \quad (4)$$

being taken with the same parameters as in Ref. [1]. The ratio of the real to imaginary part ϵ_{NN} of the NN scattering amplitude has very little influence on the calculated value of σ_R , and this parameter was set to zero. (Within the optical-limit approximation, σ_R does not depend on ϵ_{NN} at all.) As in Ref. [1], we did not take the nucleon correlations into account. In more detail, the procedure of the calculations is described in work [3].

3. Density distributions

In the present calculations it was assumed that the ${}^6\text{He}$, ${}^{11}\text{Li}$, and ${}^{19}\text{C}$ nuclei consist of a nuclear core of 4, 9, and 18 nucleons, correspondingly, the number of halo neutrons being correspondingly two, two, and one. The many-body densities in the target nuclei were presented as products of one-body target densities $\rho_t(\mathbf{r})$, while the many-body densities in the halo nuclei were presented as products of one-body core densities $\rho_c(\mathbf{r})$ and halo densities $\rho_h(\mathbf{r})$, where \mathbf{r} is the nucleon radius vector. As in Ref. [1], the matter density distributions in the core were described by Gaussian distributions

$$\rho_c(\mathbf{r}) = (3/2\pi R_c^2)^{3/2} \exp(-3\mathbf{r}^2/2R_c^2), \quad (5)$$

whereas the density distributions in the halo were described by a $1p$ -shell harmonic oscillator-type function

$$\rho_h(\mathbf{r}) = (5/3)(5/2\pi R_h^2)^{3/2} (\mathbf{r}/R_h)^2 \exp(-5\mathbf{r}^2/2R_h^2). \quad (6)$$

Here, R_c and R_h are the rms radii of the core and halo matter density distributions.

Calculations with the halo density distributions containing long density ‘‘tails’’ (to be discussed later) were also performed. We used the matter density distributions in the target nuclei ${}^4\text{He}$, ${}^{12}\text{C}$, ${}^{28}\text{Si}$, ${}^{58}\text{Ni}$, and ${}^{208}\text{Pb}$ the same as those in Ref. [4].

4. Results and discussion

At first, using the Glauber formulas in the optical limit approximation we repeated the calculations of Bush *et al.* [1] of the reaction cross sections σ_R for scattering of ${}^{11}\text{Li}$ on protons and nuclear targets ${}^{12}\text{C}$ and ${}^{208}\text{Pb}$ at several fixed ${}^{11}\text{Li}$ rms matter radii R_m with different ratios R_h/R_c . The calculated cross sections are shown in Fig. 1 versus the ratio $\epsilon = \langle r^4 \rangle / \langle r^2 \rangle^2$. The results of our calculations are practically the same as those in Ref. [1]. (A small difference between the cross sections calculated in our study and in Ref. [1] is evidently due to slightly different target nuclear matter distributions used in the calculations.) In addition to the nuclear targets ${}^{12}\text{C}$ and ${}^{208}\text{Pb}$, considered by Bush *et al.*, we also performed calculations for the ${}^4\text{He}$ target. It is seen that the dependence of σ_R upon ϵ is essentially different for light and heavy targets. According to work [1], these results indicate that reaction cross sections for heavy targets have higher sensitivity to valence nucleons of exotic nuclei than that for light targets.

Then, we repeated similar calculations using the Glauber theory within the rigid target approximation (Fig. 2). The cross sections calculated in the rigid target approximation are somewhat different from those calculated in the optical limit approximation. At the same time, for the given R_m values, the variations of the cross sections as a function of ϵ are more or less similar in both cases. With ϵ increasing, the reaction cross sections σ_R for light targets (protons and ${}^4\text{He}$) decrease, while for heavy targets (${}^{208}\text{Pb}$) they increase. For ${}^{11}\text{Li} + {}^{12}\text{C}$ scattering, the cross section calculated in the optical limit approximation increases by a few percent with ϵ increasing, while the cross section calculated in the rigid target approximation is almost constant, the variation of σ_R with ϵ being very small.

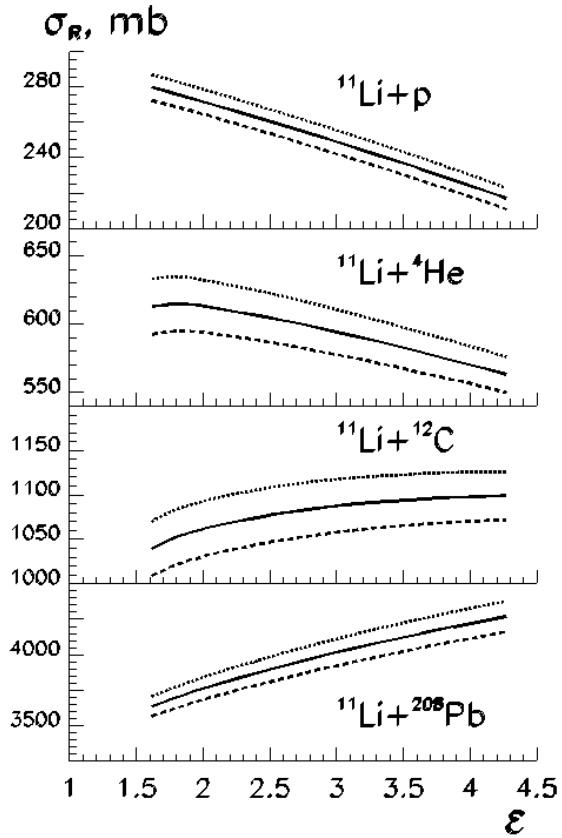


Fig. 1. Variation of the reaction cross sections σ_R with $\varepsilon = \langle r^4 \rangle / \langle r \rangle^2$ at fixed total rms matter radii R_m of ^{11}Li equal to 2.9 (dashed lines), 3.0 (solid lines), and 3.1 fm (dotted lines). The cross sections σ_R are calculated in the optical limit approximation to the Glauber theory for scattering of ^{11}Li on the hydrogen, ^4He , ^{12}C , and ^{208}Pb targets

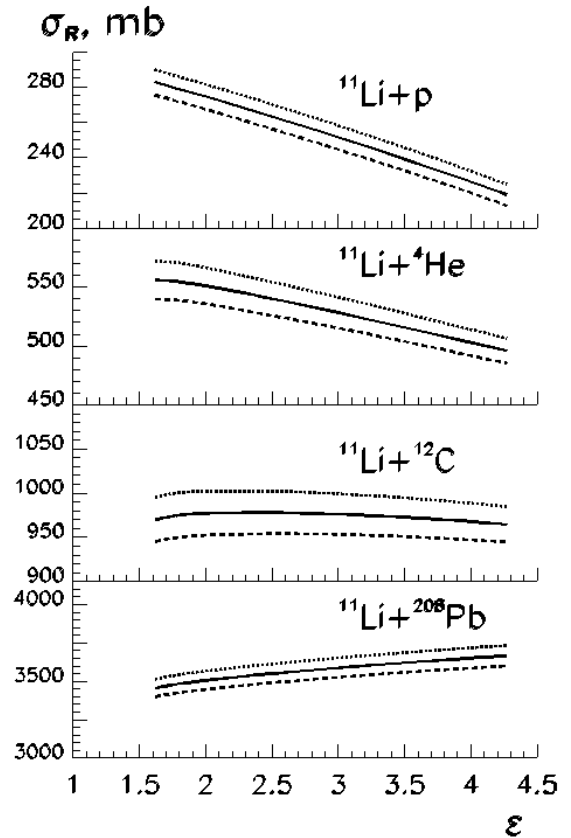


Fig. 2. Variation of the reaction cross sections σ_R with ε . The same as in Fig. 1 for the cross sections calculated in the rigid target approximation

We also carried out calculations of the reaction cross sections σ_R for scattering of the halo nuclei ^6He and ^{19}C on protons and the nuclear targets ^4He , ^{12}C , and ^{28}Si . As compared to ^{11}Li , the considered nuclei ^6He and ^{19}C have different relative amount of halo neutrons. The results of the calculations (Figs. 3 and 4) show that here also with ε increasing the cross sections σ_R decrease in the case of light target nuclei (protons and ^4He), while they increase for a heavier nucleus ^{28}Si .

The performed calculations confirm the conclusions of Bush *et al.* that the cross sections σ_R at fixed rms radii of halo nuclei retain a significant sensitivity to higher radial moments of the nuclear density, which is different for light and heavy targets. This means that information about the rms radius can only be meaningfully extracted from the measured cross section if some form is assumed for the radial density distribution of the studied nucleus. At the same time, analysing reaction cross sections measured for several nuclear targets of different size one can assess the rms nuclear matter radius more precisely and also get information on the radial shape of the studied nucleus. (Note that in the case of heavy targets the Coulomb dissociation of the exotic nuclei should be also taken into account.)

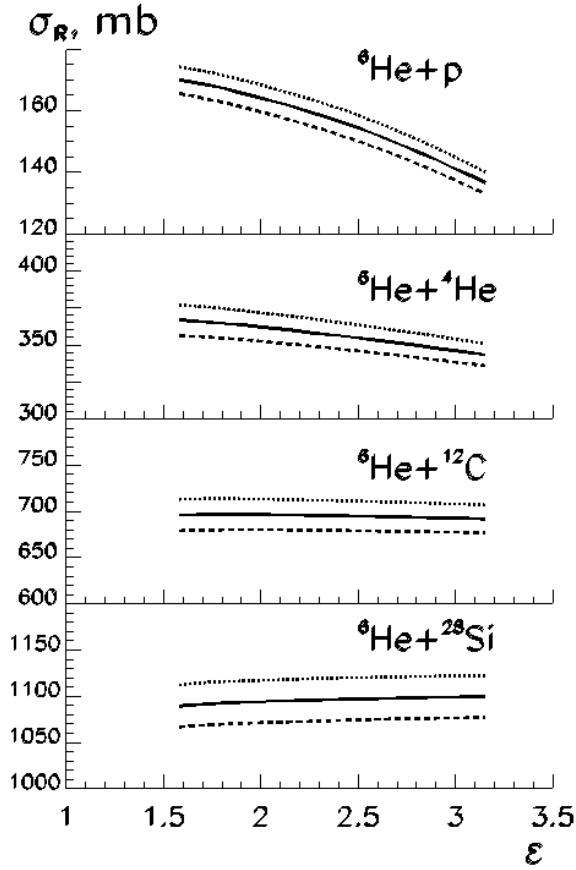


Fig. 3. Variation of the reaction cross sections σ_R with $\varepsilon = \langle r^4 \rangle / \langle r \rangle^2$ at fixed total rms matter radii R_m of ${}^6\text{He}$ equal to 2.4 (dashed lines), 2.5 (solid lines), and 2.6 fm (dotted lines). The cross sections are calculated in the rigid target approximation for scattering of ${}^6\text{He}$ on the hydrogen, ${}^4\text{He}$, ${}^{12}\text{C}$, and ${}^{28}\text{Si}$ targets

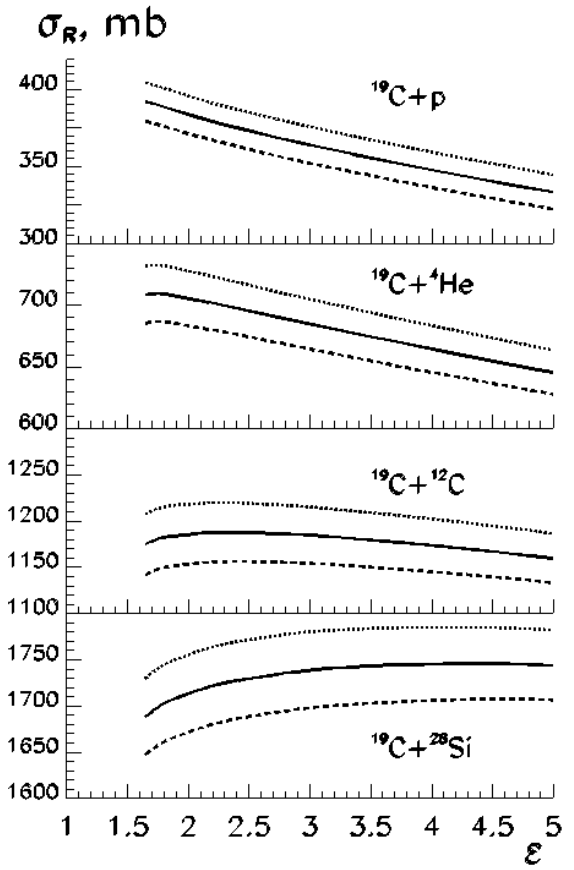


Fig. 4. Variation of the reaction cross sections σ_R with $\varepsilon = \langle r^4 \rangle / \langle r \rangle^2$ at fixed total rms matter radii R_m of ${}^{19}\text{C}$ equal to 3.0 (dashed lines), 3.1 (solid lines), and 3.2 fm (dotted lines). The cross sections are calculated in the rigid target approximation for scattering of ${}^{19}\text{C}$ on the hydrogen, ${}^4\text{He}$, ${}^{12}\text{C}$, and ${}^{28}\text{Si}$ targets

Equation (6) with $R_h > R_c$ can describe an extended nucleon distribution of valence nucleons. However, this distribution at large distances from the nuclear centre decreases with the radius r increasing faster than it is predicted by theory. According to Refs. [5, 6], in addition to the main halo component which can be described to a first approximation by Eq. (6), the halo in exotic nuclei with low binding energy contains also a long density “tail”, which decreases exponentially with the radius r increasing (Figs. 5, 6). Though such a density tail contains a small amount of matter (of the order of 1%), it can produce a noticeable effect on the total rms nuclear matter radius. Due to smallness of the density tails, it can be expected that the sensitivity of the reaction cross sections σ_R to the density tails is relatively poor. In the present study we investigate the sensitivity of reaction cross sections to the density tails by performing calculations of σ_R using model nuclear density distributions with a tail and without it. We performed calculations of σ_R for scattering of ${}^6\text{He}$ and ${}^{11}\text{Li}$ on protons and several nuclear targets. The nuclear density distributions in ${}^6\text{He}$ and ${}^{11}\text{Li}$ used in the calculations are shown in Figs. 5 and 6.

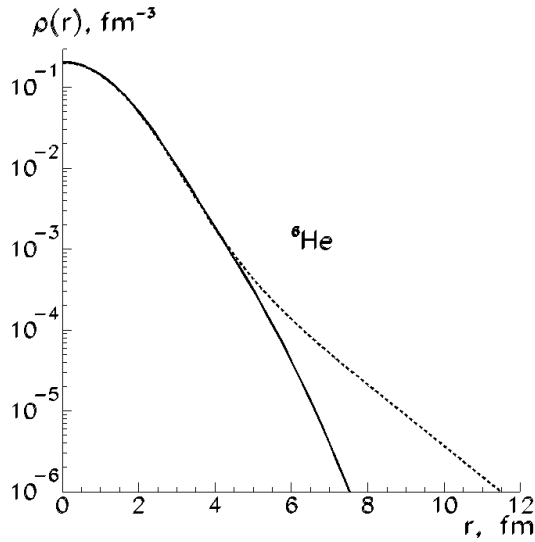


Fig. 5. The nuclear matter density distribution in ${}^6\text{He}$ (applied in the cross-section calculations) without a density tail (*solid curve*, $R_c = 1.95$ fm, $R_h = 2.88$ fm, $R_m = 2.30$ fm) and with a density tail (*dashed curve*, see the text)

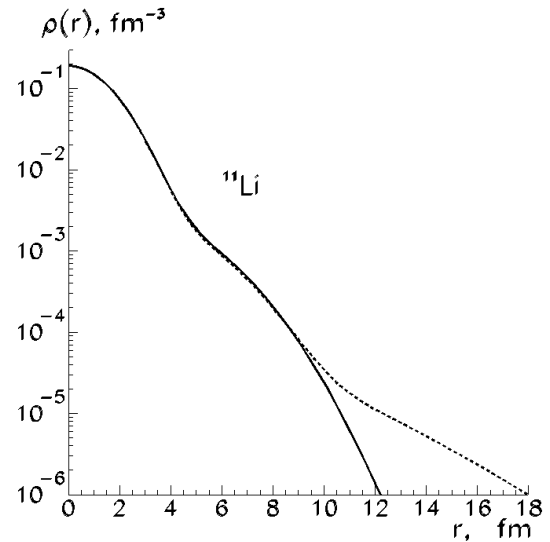


Fig. 6. The nuclear matter density distribution in ${}^{11}\text{Li}$ (applied in the cross-section calculations) without a density tail (*solid curve*, $R_c = 2.30$ fm, $R_h = 5.86$ fm, $R_m = 3.37$ fm) and with a density tail (*dashed curve*, see the text)

The solid curves in these figures show the density distributions without a tail with the following parameters: $R_c = 1.95$ fm, $R_h = 2.88$ fm, $R_m = 2.30$ fm for ${}^6\text{He}$, and $R_c = 2.30$ fm, $R_h = 5.86$ fm, $R_m = 3.37$ fm for ${}^{11}\text{Li}$. The dashed curves show the same distributions including the tails corresponding to the theoretical density distributions FC of Ref. [5] and P2 of Ref. [6]. Inclusion of these tails increases the rms matter radii R_m by 0.20 fm and 0.26 fm, correspondingly in ${}^6\text{He}$ and ${}^{11}\text{Li}$. The Table presents the relative increase $\Delta\sigma_R/\sigma_R$ of the calculated reaction cross sections when the density tails are taken into account. For comparison, we also show the relative increase $\Delta\sigma'_R/\sigma_R$ of the cross sections calculated without density tails, but with the increased halo radii R_h so that the total rms matter radii R_m are larger by 0.20 fm and 0.26 fm, correspondingly in ${}^6\text{He}$ and ${}^{11}\text{Li}$.

Table

Relative increases of the calculated cross sections when the density tails are taken into account and when the halo radii are increased

Interacting	$\Delta\sigma_R/\sigma_R$, %	$\Delta\sigma'_R/\sigma_R$, %
${}^6\text{He} + p$	1.8	3.9
${}^6\text{He} + {}^4\text{He}$	2.9	4.8
${}^6\text{He} + {}^{12}\text{C}$	3.6	4.6
${}^6\text{He} + {}^{28}\text{Si}$	3.6	4.2
${}^6\text{He} + {}^{58}\text{Ni}$	3.5	4.0
${}^{11}\text{Li} + p$	0.4	1.4
${}^{11}\text{Li} + {}^4\text{He}$	1.1	3.1
${}^{11}\text{Li} + {}^{12}\text{C}$	2.2	5.2
${}^{11}\text{Li} + {}^{28}\text{Si}$	3.3	6.1
${}^{11}\text{Li} + {}^{58}\text{Ni}$	4.1	6.5

It is seen that the sensitivity of the reaction cross sections σ_R for nucleus–proton scattering to the density tails is rather poor, especially when the tail is long but contains small amount of nuclear matter, as in the case of ${}^{11}\text{Li}$. At the same time, the sensitivity of σ_R to the density tails is more sizeable in the case of nucleus–nucleus scattering for middle-weight nuclear targets (${}^{28}\text{Si}$, ${}^{58}\text{Ni}$). In all the cases, the values of $\Delta\sigma_R/\sigma_R$

are smaller than those of $\Delta\sigma'_R/\sigma_R$. This means that taking the density tails into account in the analyses of the reaction cross sections σ_R is important in order to deduce accurate values of the rms matter radii of the studied nuclei.

5. Conclusion

We have performed calculations of the reaction cross sections σ_R for nucleus–nucleus and nucleus–proton scattering assuming different model density distributions of the considered halo nuclei. The calculations were performed within the rigid target approximation to the Glauber theory, which is more accurate than the optical limit approximation used in previous calculations by Bush *et al.* [1]. Though the results of our calculations differ quantitatively from Ref. [1], they are in qualitative agreement with the conclusion of Bush *et al.* that the reaction cross sections for nucleus–nucleus scattering are more sensitive to the matter density at the nuclear periphery than those for nucleus–proton scattering. For all the considered cases, the calculated reaction cross sections σ_R for nucleus–nucleus scattering depend not only on the rms matter radius of the studied exotic nucleus but also on the shape of its matter distribution. However, for the case of the ^{12}C target this dependence is rather weak, the value of σ_R depending basically on the rms nuclear matter radius. Analysing the reaction cross sections for nucleus–proton and nucleus–nucleus scattering for light and middle-weight target nuclei it is possible to determine the rms matter radius of the exotic nucleus and to obtain information on the shape of its matter distribution. Our considerations also have shown that to deduce accurately the nuclear matter radius from the measured reaction cross sections it is important to take into account long matter density tails of the exotic nuclei at the nuclear far periphery.

References

1. M.P. Bush, J.S. Al-Khalili, J.A. Tostevin, R.C. Johnson, Phys. Rev. C **53**, 3009 (1996).
2. G.D. Alkhazov, A.A. Lobodenko, Yad. Fiz. **70**, 98 (2007) [Phys. At. Nucl. **70**, 93 (2007)].
3. G.D. Alkhazov, V.V. Sarantsev, Yad. Fiz. **77**, 960 (2014) [Phys. At. Nucl. **77**, 912 (2014)].
4. G.D. Alkhazov, V.V. Sarantsev, Yad. Fiz. **75**, 1624 (2012) [Phys. At. Nucl. **75**, 1544 (2012)].
5. J.S. Al-Khalili, J.A. Tostevin, Phys. Rev. C **57**, 1846 (1998).
6. I.J. Thompson, M.V. Zhukov, Phys. Rev. C **49**, 1904 (1994).

TAKING INTO ACCOUNT THE CENTRE-OF-MASS CORRELATIONS IN THE CROSS SECTIONS FOR ELASTIC SCATTERING OF INTERMEDIATE ENERGY PROTONS ON THE EXOTIC NUCLEI ${}^6\text{He}$ AND ${}^8\text{He}$

G.D. Alkhazov, V.V. Sarantsev

1. Introduction

Proton–nucleus elastic scattering at intermediate energy is an efficient means of studying the nuclear spatial structure. Several experiments were performed in which the cross sections for proton elastic scattering on light exotic nuclei were measured in inverse kinematics at GSI Helmholtzzentrum für Schwerionenforschung (GSI) at an energy of ~ 700 MeV/u at small momentum transfers up to $|t| = 0.05$ (GeV/c) 2 , where t is the four-momentum transfer squared. The cross sections were measured with the help of the hydrogen-filled ionization chamber IKAR, which served simultaneously as a gas target and a detector of the recoil protons. In particular, the $p{}^6\text{He}$ and $p{}^8\text{He}$ cross sections were measured [1].

The measured cross sections were analysed in the framework of the Glauber multiple-scattering theory, and the root mean square (rms) radii of the nuclear total matter R_m , the nuclear core R_c , and the neutron halo R_h were deduced for ${}^6\text{He}$ and ${}^8\text{He}$. Later, the $p{}^6\text{He}$ and $p{}^8\text{He}$ cross sections for elastic scattering were measured [2] practically at the same energy at higher momentum transfers up to $|t| = 0.225$ (GeV/c) 2 using an experimental set-up with a liquid hydrogen target. The new experimental data at higher values of $|t|$ in combination with the cross sections [1] measured at low $|t|$ -values allow, in principle, to determine the ${}^6\text{He}$ and ${}^8\text{He}$ nuclear radii R_c , R_h , and R_m with better accuracy [3]. The many-body density distributions of ${}^6\text{He}$ and ${}^8\text{He}$ used in the calculations [3] of the cross sections were represented as products of one-body densities. The effect of the centre-of-mass (CM) correlations in the calculated amplitude of the proton–nucleus elastic scattering $F_A(\mathbf{q})$, where \mathbf{q} is the momentum transfer, was taken into account by multiplying the amplitude $F_A(\mathbf{q})$ with a CM correction factor $H(\mathbf{q})_{\text{CM}} = \exp[\mathbf{q}^2 R_m^2 / 6(A - 1)]$, where A is the total number of nucleons in the nucleus. Such a procedure of taking the CM correlations into account is exact when all one-body densities are Gaussian distributions with the same radial parameter, so that the total matter distribution is also a Gaussian one. However, in the case of halo nuclei, such as ${}^6\text{He}$ and ${}^8\text{He}$, the total matter distribution is significantly different from a Gaussian one, and a question arises how accurate is the approach of taking the CM correlations into account with the mentioned correction factor $H(\mathbf{q})_{\text{CM}}$. In the present paper, to answer this question and to see how big the effect of the CM correlations is in the $p{}^6\text{He}$ and $p{}^8\text{He}$ cross sections, we have calculated these cross sections neglecting the CM correlations, taking them into account exactly, and using the approximate method with the correction factor $H(\mathbf{q})_{\text{CM}}$.

2. Basic formulas

In the calculations of the proton–nucleus elastic scattering amplitude $F_A(\mathbf{q})$ we use the Glauber formula and a spin-independent amplitude of the free proton–nucleon (pN) scattering with the traditional high-energy parametrization of this amplitude and the corresponding profile-function

$$\gamma(\mathbf{b}) = \sigma_{pN} (1 - i \varepsilon_{pN}) \exp(-\mathbf{b}^2 / 2\beta_{pN}) / (4\pi\beta_{pN}), \quad (1)$$

where \mathbf{b} is the impact-parameter vector; σ_{pN} is the total cross section for the pN interaction; β_{pN} is the pN amplitude slope parameter; ε_{pN} is the ratio of the real to imaginary parts of the pN scattering amplitude.

We describe the core and halo distributions in the ${}^6\text{He}$ and ${}^8\text{He}$ nuclei by Gaussians. In this case the CM correlations can be taken into account exactly in a simple way as described below. We assume that the core of ${}^6\text{He}$ and ${}^8\text{He}$ consists of a four-nucleon cluster with the size R_c^* the same as that of the ${}^4\text{He}$ nucleus ($R_c^* = 1.46$ fm). This cluster experiences some motion around the CM of the nucleus so that the effective core size R_c is larger than R_c^* . Similarly, the effective halo size R_h is larger than the size R_h^* of the halo cluster (two neutrons in ${}^6\text{He}$ and four neutrons in ${}^8\text{He}$) in its CM system.

It is easy to show that

$$R_h^* = [R_h^2 - (A_c/A_h)^2 (R_c^2 - R_c^{*2})]^{1/2}, \quad (2)$$

where A_c and A_h are correspondingly the numbers of the core and halo nucleons.

We calculate the proton–nucleus scattering amplitude $F_A(\mathbf{q})$ using the following equations:

$$F_A(\mathbf{q}) = (ik/2\pi) \exp(\mathbf{q}^2 d^2/2A) \int d^2b \exp(i\mathbf{q}\mathbf{b}) \{1 - [1 - \Gamma_c(\mathbf{b})][1 - \Gamma_h(\mathbf{b})]\} \quad (3)$$

with

$$\Gamma_c(\mathbf{b}) = (2\pi ik)^{-1/2} \int d^2q \exp(-\mathbf{q}^2 d^2/2A_c) F_c^*(\mathbf{q}) \exp(-i\mathbf{q}\mathbf{b}) \quad (4)$$

and

$$\Gamma_h(\mathbf{b}) = (2\pi ik)^{-1/2} \int d^2q \exp(-\mathbf{q}^2 d^2/2A_h) F_h^*(\mathbf{q}) \exp(-i\mathbf{q}\mathbf{b}), \quad (5)$$

where $F_c^*(\mathbf{q})$ and $F_h^*(\mathbf{q})$ are the amplitudes of proton elastic scattering on the core and halo clusters, calculated by the Glauber formula with the CM correction factors

$$H_c^*(\mathbf{q}) = \exp[\mathbf{q}^2 R_c^{*2}/6(A_c - 1)] \quad (6)$$

and

$$H_h^*(\mathbf{q}) = \exp[\mathbf{q}^2 R_h^{*2}/6(A_h - 1)] \quad (7)$$

correspondingly for $F_c^*(\mathbf{q})$ and $F_h^*(\mathbf{q})$. The radial parameter d , used in the calculations, is equal to

$$d = [(AA_c/3A_h) (R_c^2 - R_c^{*2})]^{1/2}. \quad (8)$$

In more detail the procedure of the calculations is described in Ref. [4].

3. Results of calculations

We have calculated the cross sections for proton elastic scattering on the nuclei ${}^6\text{He}$ and ${}^8\text{He}$ correspondingly at the energies 717 and 674 MeV in the momentum transfer range $0 < |t| < 0.30$ (GeV/c)². The values of the rms radii R_c and R_h of the ${}^6\text{He}$ and ${}^8\text{He}$ nuclei and the input parameters σ_{pN} , β_{pN} , and ε_{pN} of the proton–nucleon scattering amplitudes were taken from Ref. [3]:

$$R_c = 1.96 \text{ fm}, R_h = 3.30 \text{ fm for } {}^6\text{He};$$

$$R_c = 1.81 \text{ fm}, R_h = 3.12 \text{ fm for } {}^8\text{He};$$

$$\sigma_{pp} = 44.6 \text{ mb}, \beta_{pp} = 0.20 \text{ fm}^2, \varepsilon_{pp} = 0.069;$$

$\sigma_{pn} = 37.7 \text{ mb}, \beta_{pn} = 0.24 \text{ fm}^2, \varepsilon_{pn} = -0.307$ for the proton–proton (pp) and proton–neutron (pn) interaction in the case of $p{}^6\text{He}$ scattering, and

$$\sigma_{pp} = 41.9 \text{ mb}, \beta_{pp} = 0.20 \text{ fm}^2, \varepsilon_{pp} = 0.129;$$

$$\sigma_{pn} = 37.4 \text{ mb}, \beta_{pn} = 0.24 \text{ fm}^2, \varepsilon_{pn} = -0.283$$
 for the pp and pn interaction in the case of $p{}^8\text{He}$ scattering.

The internal size of the core R_c^* in these nuclei was assumed to be $R_c^* = 1.46$ fm. The Coulomb interaction was taken into account as usual. The results of the calculations are presented in Figure.

The *dotted*, *dashed*, and *solid curves* correspond respectively to the calculations where the CM correlations were neglected, included with the approximate correction factor $H(\mathbf{q})_{\text{CM}}$, and taken into account exactly as has been described above. Note that in these three calculations the same nuclear one-body density distribution was used:

$$\rho_A(\mathbf{r}) = [A_c(3/2\pi R_c^2)^{3/2} \exp(-3\mathbf{r}^2/2R_c^2) + A_h(3/2\pi R_h^2)^{3/2} \exp(-3\mathbf{r}^2/2R_h^2)]/A. \quad (9)$$

So the difference between the results of these calculations is due to neglect or different account of the CM correlations. The experimental cross sections are also shown in the figures: the *hollow circles* – the data of Ref. [1], the *solid squares* – the data of Ref. [2].

As it is seen in the figures, the effect of the CM correlations in the calculated cross sections at $0 < |t| < 0.10$ (GeV/c)² is rather small and in a first approximation can be neglected. At $|t| > 0.10$ (GeV/c)², especially in the region of the first diffraction minimum and the second diffraction maximum, the effect of the CM correlations is rather sizeable. We also see that at high momentum transfers the approximate

approach to taking the CM correlations into account results in a significant overestimation of the cross sections as compared with the exact calculations.

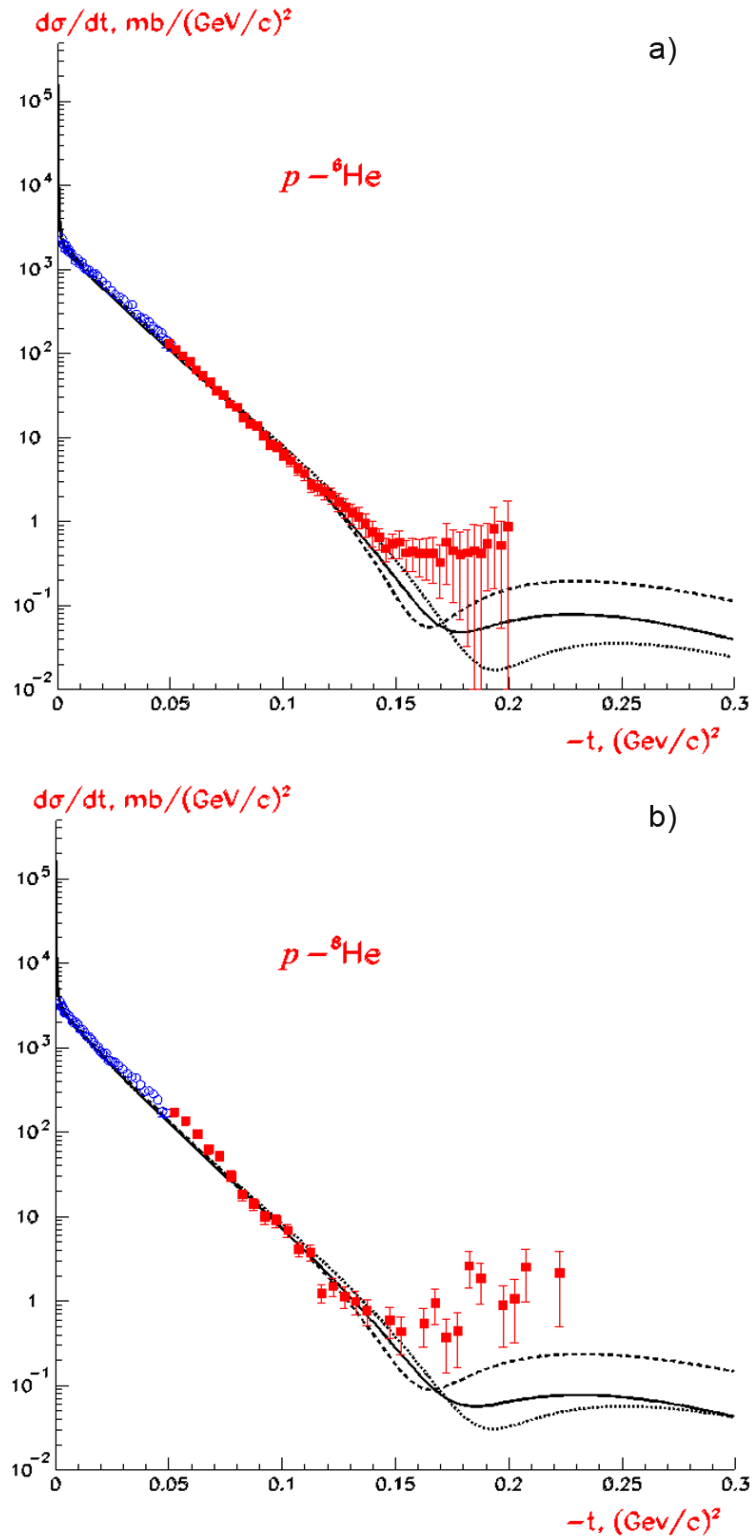


Fig. Cross sections for proton elastic scattering on the ${}^6\text{He}$ nuclei at an energy: a – of 717 MeV; b – 674 MeV. *Hollow circles* – data of Ref. [1]; *solid squares* – data of Ref. [2]. *Dotted, dashed, and solid curves* correspond respectively to the cross sections calculated without taking the CM correlations into account, with the CM correlations taken into account using the approximate correction factor $H(\mathbf{q})_{\text{CM}}$, and with the CM correlations taken into account exactly

The calculated cross sections at $|t| > 0.13 \text{ (GeV}/c)^2$ are smaller than the experimental ones. The behaviour of the calculated cross sections at high values of $|t|$ is governed mainly by the size of the nuclear core and its radial shape. So, varying the core size and its shape, in principle, it is possible to fit the calculated cross sections to the data. However, in the present paper we did not try to perform such a fit. We note that the experimental cross sections of Ref. [2] have rather large uncertainties at $|t| > 0.15 \text{ (GeV}/c)^2$. In order to get more precise sizes of the cores of the studied nuclei and to get information on the radial shapes of the cores, new experimental data of better quality at high $|t|$ -values, and new theoretical analyses with accurate accounts of the CM nucleon correlations are needed.

4. Conclusion

We have shown that the effect of the CM correlations in the cross sections for intermediate-energy proton elastic scattering on light exotic nuclei at high momentum transfers is rather sizeable, and it is important to take it accurately into account. We have also shown that an approximate account of the CM correlations with the correction factor $H(\mathbf{q})_{\text{CM}}$ is not justified since it results in a significant overestimation of the calculated cross sections at high $|t|$ -values.

References

1. S.R. Neumaier, G.D. Alkhazov, M.N. Andronenko *et al.*, Nucl. Phys. A **712**, 247 (2002).
2. O.A. Kiselev, F. Aksouh, A. Bleibe *et al.*, Nucl. Intr. Meth. Phys. Res., Sect. A **641**, 72 (2011).
3. L.X. Chung, O.A. Kiselev, D.T. Khoa, P. Egelhof, Phys. Rev. C **92**, 034608 (2015).
4. G.D. Alkhazov, V.V. Sarantsev, Yad. Fiz. **80**, 613 (2017).

μSR INVESTIGATIONS AT THE PNPI

S.G. Barsov, A.L. Getalov, E.N. Komarov, S.A. Kotov, G.V. Shcherbakov, S.I. Vorob'ev

1. Introduction

The magnetic properties of the nanostructured CoFe_2O_4 ferrofluid and the manganites EuMn_2O_5 and $\text{Eu}_{0.8}\text{Ce}_{0.2}\text{Mn}_2\text{O}_5$ have been investigated making use of the μSR method. The study of these samples was carried out with the μSR set-up and the polarized muon beam with the average momentum $p = 90 \text{ MeV}/c$, the momentum spread $\Delta p/p = 0.02$ (full width at half maximum) and the longitudinal polarization $P_\mu \approx 0.90\text{--}0.95$ of the PNPI synchrocyclotron [1, 2]. The μSR set-up allowed to vary the temperature of the samples over a range of 10–300 K and to apply external magnetic field up to 1.5 kOe.

Time μSR -spectra were obtained by measurements of the count rate of the decay positrons. Their time spectrum can be expressed as

$$N(t) = N_0 \exp(-t/\tau_\mu) [1 + a_0 G(t)] + B. \quad (1)$$

Here N_0 is the normalization constant; t is the time interval between the detected positron and the moment of the muon stop; τ_μ is the muon lifetime; a_0 is the total asymmetry of the angular distribution of the decay positrons; B is the accidental background. The value a_0 is independent of the temperature and the external magnetic field, but it depends on the set-up geometry. The value a_0 can be determined in the paramagnetic state of the sample. The relaxation function $G(t)$ depends on magnetic properties of the sample and its parameters are determined from the analysis of the precession spectra of the magnetic moment of the muon in the local internal field of the sample. Usually, the relaxation function $G(t)$ can be represented in the factorized form $G(t) = G_d(t) G_{st}(t)$, where $G_d(t) = \exp(-\lambda t)$ is the dynamic relaxation function with the relaxation rate λ and $G_{st}(t)$ is the static one. The dynamic function $G_d(t)$ describes the influence of slow space fluctuations of the magnetic field in the process of degrading and thermalization of the muon in the sample. The function $G_{st}(t)$ is responsible for fast space fluctuations of the magnetic field of the sample near the places of the muon localization. The last ones take place only in the ordered state. When approaching the paramagnetic phase, the function $G_{st}(t)$ degenerates: $G_{st}(t) \rightarrow 1$.

2. Ferrofluid with CoFe_2O_4 nanoparticles

The nanostructured materials have important practical applications, and their study is of considerable interest [3]. Among them there are ferrofluids in which the magnetic nanoparticles are distributed in nonmagnetic medium. To prevent sticking of nanoparticles, one uses a special surface active substance.

We have studied a ferrofluid with the concentration of the CoFe_2O_4 nanoparticles of 3% [4]. It was a suspension of the nanodispersed cobalt ferrite CoFe_2O_4 in water. The mean size of the nanoparticles was 8.5 nm. The sample was packed into a cylindrical copper cell of 80 mm in diameter, 10 mm thick; its axis was parallel to the muon beam direction. The measurements were performed in the temperature range of 26–300 K at different cooling conditions: in the field cooled (FC) mode the sample was cooled in the magnet field, whereas the zero field cooled (ZFC) mode the sample was cooled with the magnetic field switched off, and then the magnetic field was switched on.

The precession of the muon spin was described by the relaxation function $G(t) = a \exp(-\lambda t) \cos(\Omega t)$ with the frequency Ω and the relaxation rate λ . The amplitude a in the sample was compared with that in the copper sample at the room temperature, for which the asymmetry was equal to $a = 0.308 \pm 0.003$ in the transverse magnetic field 525 Oe. In the carried out experiments, the muonium contribution to the total asymmetry could not be observed because of the high precession frequency of the muonium magnetic moment and the limited time resolution of the registration system.

In the FC mode, the magnetic moments of nanoparticles are ordered in the external magnetic field. As a result, the value of the magnetic field in the sample differs from the external one. In the ZFC mode, the magnetic moments of nanoparticles are frozen in random directions and the mean magnetic field from the nanoparticles is equal to zero. It leads to a difference in the muon spin precession frequencies in

the FC and ZFC modes at low temperatures (Fig. 1). Of course, when the temperature increases, the ordering of the magnetic moments is destroyed and the ZFC-frequency approaches to the FC frequency.

It should be noted that at low temperatures the precession frequency in the ZFC-mode coincidences with that in the Cu target at the room temperature. Taking into account the average values of the muon spin precession frequencies within the temperature range 30–250 K for the FC measurements and within 26–175 K for the ZFC ones, it can be found that the magnetization of nanoparticles generates an additional magnetic field

$$H = [\omega(\text{ZFC}) - \omega(\text{FC})]/\gamma_\mu = 4.7 \pm 0.2 \text{ Oe}, \quad (2)$$

where $\gamma_\mu = 0.01355 \text{ Oe/MHz}$ is the gyromagnetic ratio for a muon.

The Fourier analysis of the μSR data shows also that the magnetic field in the sample differs from the external one not only in the magnitude, but also in its spread (Fig. 2).

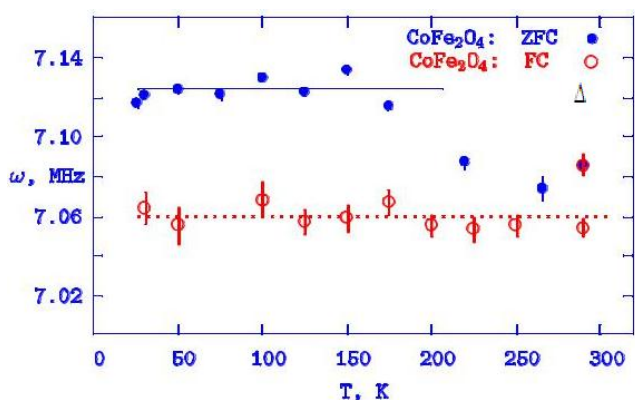


Fig. 1. The temperature dependence of the frequency of the muon spin precession in a sample measured in the magnetic field $H = 525 \text{ Oe}$ in the FC and ZFC modes; Δ – the result of the measurement on the Cu target

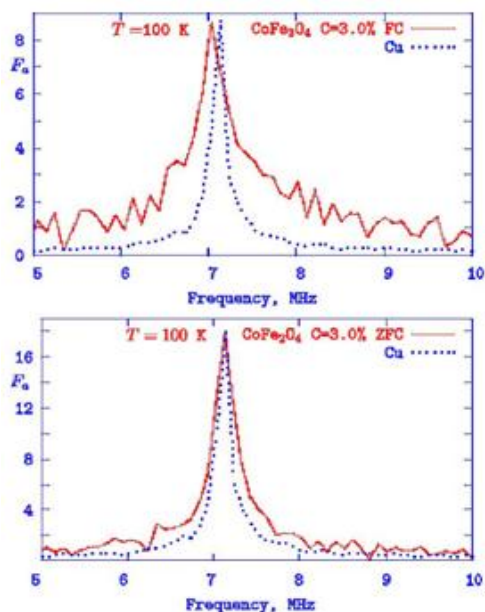


Fig. 2. The results of the Fourier transformation of the spectra for the Cu target and for the sample measured in the magnetic field $H = 525 \text{ Oe}$ at 100 K in the FC and ZFC modes

3. Manganites

RMnO_3 and RMn_2O_5 (R – the rare-earth ion) are promising materials for creation of devices for operating electric and magnetic signals. For practical applications they should have sufficiently high ($\geq 200 \text{ K}$) and similar temperatures of the magnetic and ferroelectric transitions. One of the ways to get such a material is to dope the base structure of a sample with another rare-earth ion.

We have carried out a comparative study of the magnetic properties of the EuMn_2O_5 (EMO) and $\text{Eu}_{0.8}\text{Ce}_{0.2}\text{Mn}_2\text{O}_5$ (ECMO) ceramic compounds in the zero external magnetic field in the temperature range from 15 to 300 K [5, 6]. The obtained μSR time spectra were used to derive the temperature dependences of the relaxation parameters of the muon polarization, the precession frequencies of its spin in the internal magnetic field of the samples and the partial contributions of different precession modes to the total asymmetry of the muon decay.

The ceramic cylindrical samples, 30 mm in diameter and 12 mm thick, were fabricated by the solid-phase synthesis technology. Their structure (the space group Pbam) was determined by an X-ray diffraction study which confirmed that they have the single-phase structure. The sizes of the ceramic grains were several tens of microns.

The measurements were performed in three modes of cooling (heating) of the samples. The first mode (Run-1) involved cooling of the sample from the temperature $T \approx 290$ K to $T = 41$ K with stops at intermediate temperature points with intervals of $\Delta T \approx 5\text{--}10$ K, where the data were collected for two hours in the temperature stabilization mode. Then the sample was cooled quite rapidly (within 1 h) from 41 to 15 K; after this the sample was stepwise heated to the final temperature $T = 41$ K (with steps of $\Delta T \approx 2.5$ K), the data being collected at each intermediate stabilized temperature point. This mode was applied to both samples. The second mode (Run-2) involved fast (within 1 h) cooling from $T = 290$ K to $T = 15$ K and subsequent heating with stops at the given temperatures for data collection (for 6 h) at each temperature. This mode was applied only to the ECMO sample. The third mode (Run-3) included fast cooling (within 1 h) of the sample to a temperature of about 70 K and then subsequent stepwise cooling to $T = 15$ K with steps of $\Delta T = 5$ K and stops at the given temperatures for data collection (for 2 h) at each temperature. Next, the sample was heated from the temperature $T = 17.5$ K to the final temperature $T \approx 75$ K with stops at intermediate temperatures with steps $\Delta T = 5$ K for data collection (for 2 h at each temperature). Mode Run-3 was applied only to the ECMO sample.

The μ SR time spectra were described by expression (1). The magnitude and the time structure of the background of the random coincidences were determined by processing the initial segment of the time spectrum preceding the muon stop in the sample. The asymmetry a_b and the relaxation rate λ_b for each sample were extracted by processing the time spectra recorded in an external magnetic field at the temperature of the samples below the Neel temperature $T < T_N$ (thus the contribution of the construction elements of the set-up was determined): $a_b \approx 0.02$ and $\lambda_b = 0.02$ for both samples. The total asymmetry above the Neel temperature was $a_F = a_s + a_b \approx 0.3$; it was obtained as the amplitude of the muon spin precession in the external magnetic field (at $T > T_N$). In the paramagnetic region the asymmetry of the muon decay $a_s = a_F - a_b$ is equal to a_0 . The observed residual asymmetry a_s can depend on the temperature if additional channels of the loss of the muon polarization takes place.

During the data processing of the experimental spectra one used the expression

$$G_d(t) = \exp(-\lambda t) \quad (3)$$

for the dynamic relaxation function which describes the average spatial fluctuations of the internal magnetic fields in the sample at large distances (of about the muon diffusion length) and the expression

$$G_{st}(t) = \sum a_i [1/3 + 2/3 \cos(\Omega_i t) \exp(-\Delta_i t)] \quad (4)$$

for the static relaxation function of the isotropic magnetic. Here a_i are the partial amplitudes of the observed muon spin precession frequencies $\Omega_i = 2\pi F_i$ in the local internal magnetic fields. The static relaxation dispersions Δ_i depend on fluctuations of these fields near the points of the muon localization in the sample. In the limiting case of the paramagnetic state, $G_{st}(t) = 1$.

Figures 3 and 4 show the normalized residual asymmetry a_s/a_0 (a_0 – the residual asymmetry in the paramagnetic region) and the relaxation rate λ for the ECMO and EMO samples in the mode Run-1. The jump of the value a_s/a_0 and the maximum of the relaxation rate λ correspond to the temperature of establishment of the long-range magnetic order $T_N \approx 45$ K for the EMO sample [6] and $T_N \approx 42.5$ K for the ECMO sample. Thus, the polarization loss $\sim 20\%$ takes place ($a_s/a_0 < 1/3$). We also have found that below the temperature T_N for both EMO and ECMO samples the relaxation rate and the polarization loss appear to be similar at any cooling mode.

The polarization loss is due to fast depolarization of some muons in the time interval shorter than 9 ns (the dead time of the registration system). Fast depolarization occurs because of formation of $\text{Mn}^{4+}\text{--Mn}^{4+} + \text{Mu}$ ferromagnetic complexes (the muonium Mu is the μ^+e^- bound state). These complexes appear owing to the spin–spin interaction of a muon μ^+ with the polarized e_g -electrons involved in the double exchange process in $\text{Mn}^{3+}\text{--Mn}^{4+}$ ferromagnetic pairs. Such ion pairs in EMO exist in the basic antiferromagnetic matrix along the b axis (at $T < T_N$) and in the regions of the phase separation (existing in a wide temperature interval 5–300 K [7, 8]). An additional channel of formation of $\text{Mn}^{3+}\text{--Mn}^{4+}$ ferromagnetic pairs exists in the ECMO sample because the electron doping increases the volume with the phase separation. However, the doping simultaneously partially destroys the charge order along the b axis at $T < T_N$, reducing

the number of such pairs in the basic antiferromagnetic matrix. As a result, the polarization losses in EMO and ECMO at $T < T_N$ are almost identical.

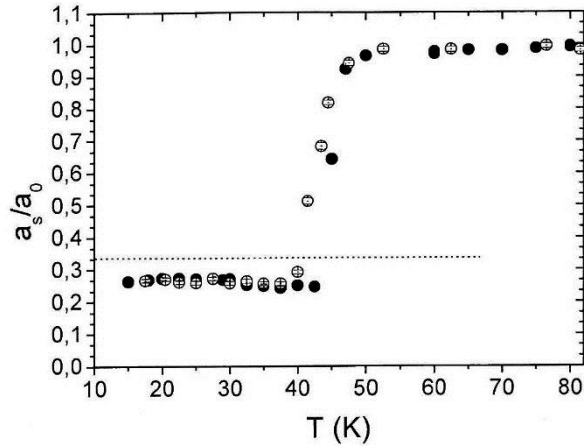


Fig. 3. The temperature dependence of the normalized residual asymmetry for the ECMO (*open circles*) and EMO (*closed circles*) samples in the Run-1 mode; *horizontal dotted straight line* – the $a_s/a_0 = 1/3$ level

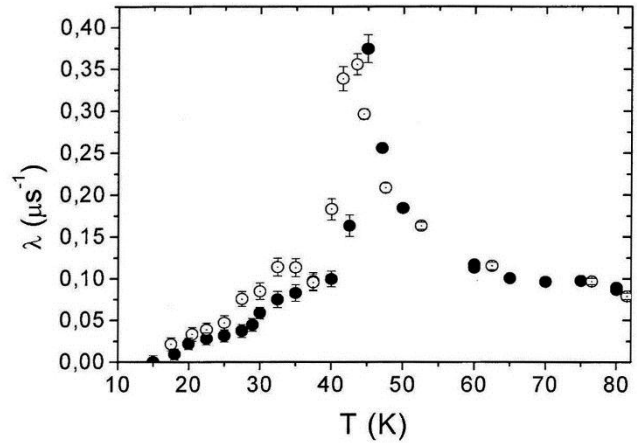


Fig. 4. The temperature dependence of the relaxation rate of the polarization of muons stopped in the ECMO (*open circles*) and EMO (*closed circles*) samples in the Run-1 mode

The temperature behaviour of the relaxation rate λ for the ECMO sample is demonstrated in Fig. 5 in three modes of cooling (heating). Only for the mode Run-2 the additional dynamic term $a_{s2}G_{d2} = a_{s2} \exp(-\lambda_2 t)$ is necessary to describe the experimental time spectra in the temperature range 25–40 K:

$$N_e(t) = N_0 \exp(-t/\tau_\mu) [1 + a_s G_d(t) + a_{s2} G_{d2}(t) + a_b G_b(t)] + B, \quad (5)$$

where a_{s2} and λ_2 are the partial asymmetry and the relaxation rate of the additional depolarization channel (and $\lambda \rightarrow \lambda_1$). As it is seen in Fig. 6, the relaxation rate λ_2 is an order of magnitude higher than the relaxation rate λ_1 . Thus, the ordered antiferromagnetic and disordered paramagnetic phases coexist in the temperature range under consideration.

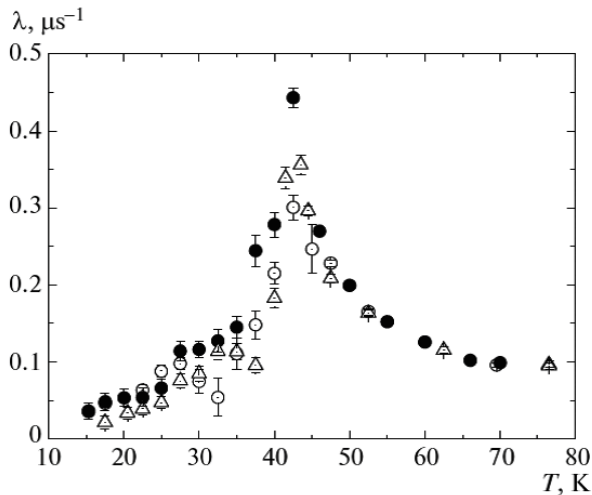


Fig. 5. The temperature dependence of the relaxation rate of the polarization of muons stopped in the ECMO sample in different modes: *triangles* – Run-1; *open circles* – Run-2; *closed circles* – Run-3

The temperature dependence of the normalized total residual asymmetry a_s/a_0 is shown in Fig. 7. It should be noted that in the range 25–40 K this value is equal to $a_s/a_0 + 1/3 a_{s2}/a_0$ (the total residual polarization of the muon is $3a_s/a_0 + a_{s2}/a_0$).

A significant difference of the temperature behaviour of the relaxation function of the EMO and ECMO samples in the range under consideration (25–40 K) may be caused due to different procedures of cooling

(heating) of the samples: the point of the phase transition $T_N = 42.5$ K was passed slowly in the modes Run-1 and Run-3, but it was passed rapidly in the mode Run-2.

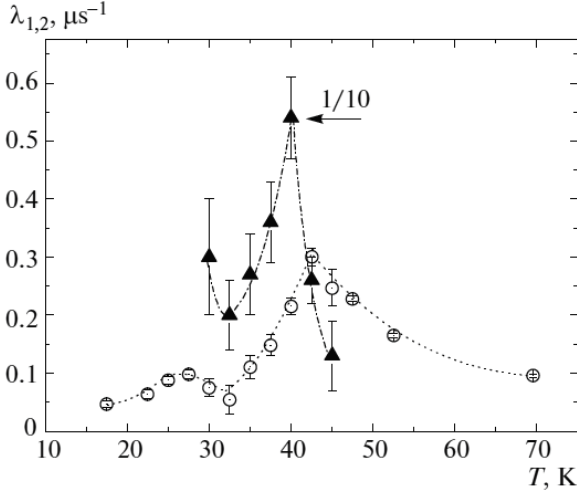


Fig. 6. The effect of separation of the ECMO sample in the relaxation rates of muon polarization in the Run-2 mode: *open circles* – the slowly relaxing component (λ_1); *triangles* – the rapidly relaxing component ($\lambda_2/10$ is plotted)

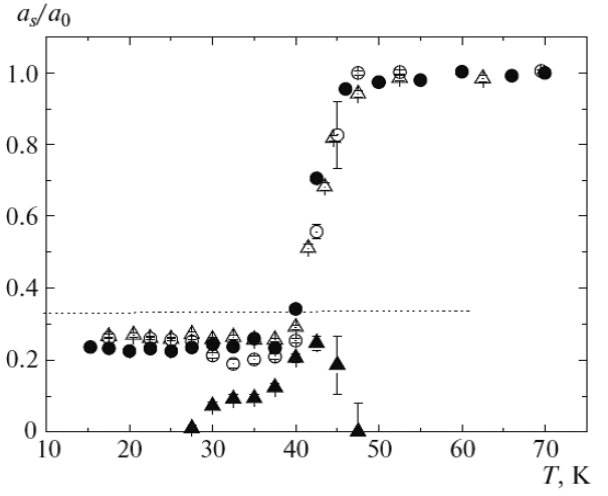


Fig. 7. The temperature dependences of the normalized residual asymmetry in the ECMO sample in different modes: *open triangles* – Run-1; *closed circles* – Run-3; *open circles* – Run-2, the slowly relaxed component; *closed circles* – the fast relaxed component; *dotted horizontal straight line* – the $a_s/a_0 = 1/3$ level

According to Refs. [7, 8], a high conductivity is conserved in the regions of the phase separation at low temperatures at the fast cooling in contrast with the slow one (the mode of the temperature variation in Refs. [7, 8] corresponded to the mode Run-2 of our work). Besides, the regions of the phase separation in ECMO below $T = 35$ K have a form of the 1D superlattices with the alternating conducting ferromagnetic and insulating layers [9, 10]. The conducting ferromagnetic layers are the layers with the 2D electron gas where the de Haas–van Alfvén oscillations were observed at the temperatures $T < 30$ – 35 K [7, 8]. The fast relaxation regions can be referred to the layers with the 2D electron gas, as the high density of free electrons in such layers should enhance the relaxation of the muon polarization owing to fast multiple recharging: $\mu^+ + e^- \rightarrow \text{Mu} \rightarrow \mu^+ + e^- \rightarrow \text{Mu} \rightarrow \dots$. The muon depolarization increases strongly because of scattering of free carriers from the muonium. Such an effect in the EMO sample should be much weaker [11, 12].

As far as the static part of the G function is concerned, it contains two different contributions which correspond to two types of localization spots of the muons. The precession frequencies F_1 and F_2 of the muon spin depend on the internal magnetic field of a sample and their temperature behaviour is shown in Fig. 8 for the ECMO sample in the Run-2 mode. The frequency F_1 does not depend on the temperature up to $T \approx 30$ K. The temperature dependence of the frequency F_2 follows the Curie–Weiss law $F_2 \sim (1 - T/T_N)^\beta$, where $T_N = 42.5$ K and $\beta = 0.29 \pm 0.02$, however the exponent β differs noticeably from the value $\beta = 0.39 \pm 0.01$, which was determined in Ref. [6] for the EMO sample and which is characteristic for the Heisenberg antiferromagnetics.

The weights of the frequency contributions and their frequency spreads are approximately identical in the temperature range 30–40 K ($a_1/a_0 \approx a_2/a_0$, $\Delta_1 \approx \Delta_2$). However, they are noticeable different below 30 K (Figs. 9 and 10). The doping of the sample enhances the frustration of the antiferromagnetic order in the initial matrix in the ECMO sample as compared to the EMO one. As a result, the critical exponents for the muon spin precession frequencies are different for the ECMO and EMO samples. The frequency F_1 refers to the limited regions of the phase separation (1D superlattices), where the dynamically equilibrium state is due to a balance of a number of interactions (the double exchange, the Jahn–Teller interaction and the Coulomb repulsion) and almost does not depend on the temperature below 30–35 K.

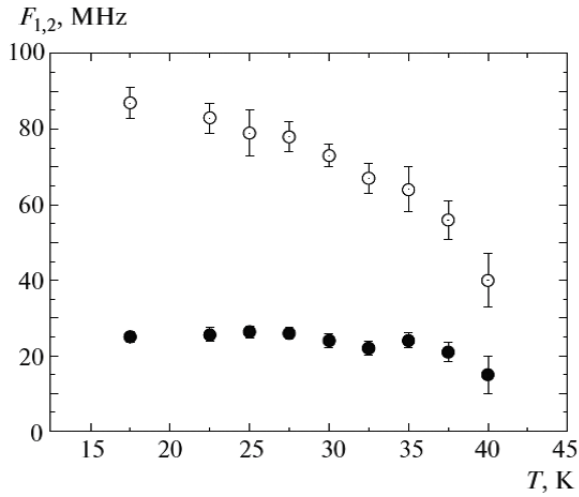


Fig. 8. The temperature dependences of the two observed precession frequencies F_1 (closed circles) and F_2 (open circles) of the muon spin for the ECMO sample in the Run-2 mode

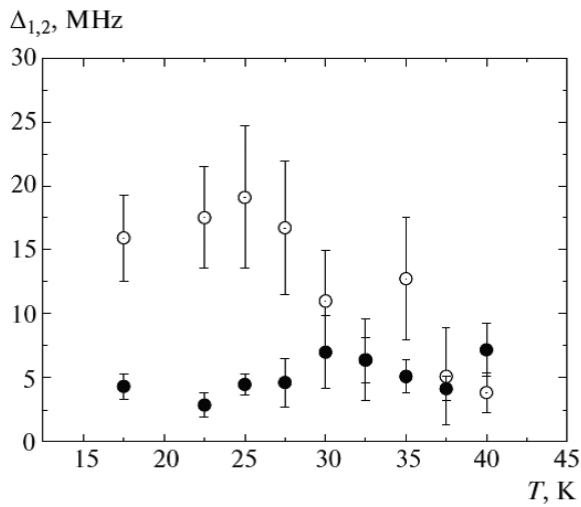


Fig. 9. The temperature dependence of the frequency spreads Δ_1 (closed circles) and Δ_2 (open circles) for two observed muon spin precession frequencies in the ECMO sample measured in the Run-2 mode

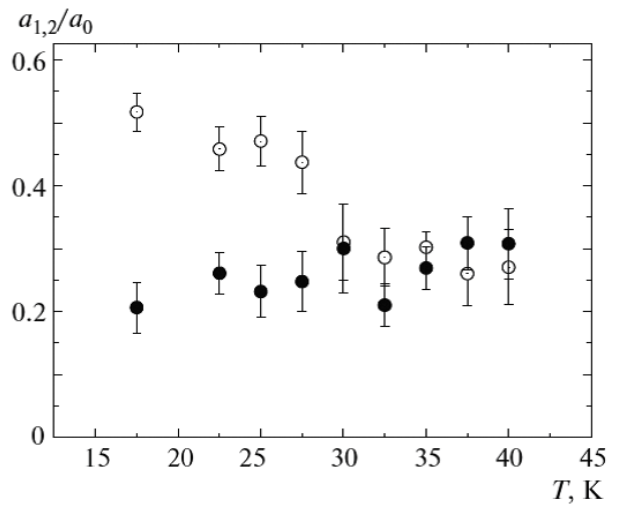


Fig. 10. The temperature dependence of the normalized amplitudes a_1/a_0 (closed circles) and a_2/a_0 (open circles) of the muon spin precession frequencies for the ECMO sample measured in the Run-2 mode

In this temperature range, there is a difference as in the values of a_1 and a_2 , so in the values of Δ_1 and Δ_2 (see Figs. 9 and 10). This may be attributed to a change of the phase state near 30 K. Indeed, it was found that the intensities of the ferromagnetic resonances from the layers of the 1D superlattices in the doped crystal decrease sharply when approaching the temperature $T = 30$ K [9, 10] and the magnetoresistance changes the sign [8]. Such behaviour is due to variation of the charge carrier density in the layers of the superlattices when changing the type of the prevailing conductivity from the tunneling to the hopping one.

References

1. S.G. Barsov, S.I. Vorob'ev, V.P. Koptev *et al.*, *Instrum. Exp. Tech.* **50**, 750–756 (2007).
2. S.G. Barsov, S.I. Vorob'ev, V.P. Koptev *et al.*, Preprint PNPI-2738, Gatchina (2007).
3. B.M. Berkovski, V.P. Medvedev, M.S. Krakov, *Magnetic Fluids*, Oxford Univ. Press, Oxford, 1993 [Khimiya, Moscow, 1989].
4. T.N. Mamedov, D.S. Andrievskii, M. Balasoiu *et al.*, *JOAM* **17**, 1086 (2015).
5. S.I. Vorob'ev, D.S. Andrievskii, S.G. Barsov *et al.*, *JETP Lett.* **150**, 1170 (2016).
6. S.I. Vorob'ev, E.I. Golovenchits, V.P. Koptev *et al.*, *JETP Lett.* **91**, 512 (2010).
7. V.A. Sanina, E.I. Golovenchits, V.G. Zalesskii *et al.*, *Phys. Rev. B* **80**, 224401 (2009).
8. V.A. Sanina, E.I. Golovenchits, V.G. Zalesskii *et al.*, *J. Phys.: Condens. Matter* **23**, 456003(2011).
9. E.I. Golovenchits, V.A. Sanina, V.G. Zalesskii, *JETP Lett.* **95**, 386 (2012).
10. V.A. Sanina, E.I. Golovenchits, V.G. Zalesskii, *J. Phys.: Condens. Matter* **24**, 346002 (2012).
11. V.P. Smilga, Yu.M. Belousov, *The Muon Method in Science*, Nauka, Moscow, 1991 [Nova Science, NY, 1984].
12. S.I. Vorob'ev, D.S. Andrievskii, S.G. Barsov *et al.*, *JEPT* **123**, 1017 (2016).

New Projects

PROJECT FOR PRECISION MEASUREMENT OF THE PROTON CHARGE RADIUS IN AN ELECTRON–PROTON SCATTERING EXPERIMENT

A.A. Vorobyev, A.A. Vasilyev, S.L. Belostotsky, B.V. Bochyn, A.A. Dzyuba, G.E. Gavrilov,
V.T. Grachev, K.A. Ivshin, A.G. Inglessi, P.V. Kravchenko, P.A. Kravtsov, E.M. Maev,
S.M. Mikirtychanz, P.V. Neustroev, G.E. Petrov, N.R. Sagidova, A.N. Solovyev, I.N. Solovyev,
E.M. Spiridenkov, V.A. Trofimov, M.E. Vznuzdaev

in collaboration with Institute for Nuclear Physics, University of Mainz (Germany), Joint Institute
for Nuclear Research (Russia), GSI Helmholtzzentrum für Schwerionenforschung (Germany),
William and Mary College (USA), Mount Allison University (Canada),
University of Regina (Canada), Saint Mary’s University (Canada)

1. Introduction

This project is motivated by the striking discrepancy (4%) between precise measurements of the proton charge rms-radius $R_p = \langle R_{pE}^2 \rangle^{1/2}$ in the muonic hydrogen (μH atoms) Lamb shift experiments performed at Paul Scherrer Institute by the CREMA Collaboration ($R_p = 0.84184(87)$ fm [1], $R_p = 0.84087(39)$ fm [2]) and the radius determined in the electron–proton (ep) elastic scattering experiments: $R_p = 0.879(5)_{\text{stat}}(6)_{\text{sys}}$ fm, A1 Collaboration at Mainz [3], and $R_p = 0.875(10)$ fm, Thomas Jefferson National Accelerator Facility (Jefferson Lab) [4].

The “proton radius puzzle” is widely discussed in the scientific community. Various reasons for the observed discrepancy are under discussion, including possible existence of an exotic particle coupling differently to electrons and muons (physics beyond the Standard Model). It is generally agreed that new ep elastic scattering experiments are needed to resolve this puzzle.

In the ep elastic scattering experiments, the proton charge radius is extracted from the slope of the electric form factor at the momentum transfer squared $Q^2 \rightarrow 0$. The A1 Collaboration at Mainz Microtron (MAMI) obtained the most accurate data set on ep scattering consisting of more than 1 400 points in the momentum transfer range of $0.004 \text{ GeV}^2 \leq Q^2 \leq 1 \text{ GeV}^2$, and the result of this measurement proved to be now in strong disagreement with the values determined in the muonic hydrogen Lamb shift experiments. A similar result was obtained in the ep scattering experiments performed at the Jefferson Lab.

However, these results are under discussion at present. The problem is that the available experimental data in the low Q^2 region are not sufficient for precision extraction of the proton radius. Therefore, extrapolation from higher Q^2 regions is used, and the result becomes dependent on the assumed Q^2 shape of the proton form factors. This was demonstrated in some recent analyses of the A1 experimental data [5].

Another problem might be related to application of the radiative corrections to the measured differential cross sections. In all previous ep scattering experiments, the differential cross sections were determined by measuring the angular distribution of the scattered electrons selected by momentum with magnetic spectrometers. In this case, the radiative corrections are quite large ($\sim 10\%$), depending on the selection procedure of the scattered electrons. The radiative corrections are Q^2 dependent and they may influence the extracted value of the proton radius. In principle, the level of the introduced radiative corrections could be controlled by the absolute measurements of the differential cross sections. However, no such measurements exist until today. In this context, new high-precision data on ep scattering in the low Q^2 region, including absolute measurements of the differential cross sections, are highly desired.

The first new generation ep scattering experiment aimed at precision measurement of the proton radius is the PRad experiment at Jefferson Lab [6]. In this experiment, the electron scattering on a hydrogen gas jet-like target will be studied in the Q^2 range from $2 \cdot 10^{-4}$ to $8 \cdot 10^{-2} \text{ GeV}^2$ at 1.1- and 2.2-GeV beam energies. The angle and the energy of the scattered electron are detected with a forward tracker and a forward calorimeter. The estimated radiative corrections will be at the level of 15%. The elastic ep scattering cross sections will be normalized to the simultaneously measured Møller scattering cross section. The PRad experiment started taking data in 2016. The goal is to reach a sub-percent precision in R_p .

The experiment described in this project will use an innovative method allowing for detection of recoil protons and scattered electrons at low Q^2 with high accuracy and resolution, thus leading to a completely

new approach for extraction of the proton radius. The goal is to measure the ep differential cross sections in the Q^2 range from 0.001 to 0.04 GeV^2 with 0.1% relative and 0.2% absolute precision and to determine the proton radius with a sub-percent precision. An important advantage of the applied method is considerably lower radiative corrections inherent to the recoil proton method controlled, in addition, by the absolute measurement of the differential cross sections.

The experiment will be performed at the Mainz electron accelerator MAMI. This accelerator can provide an electron beam with practically ideal for this experiment parameters, as it was demonstrated in a special test run in September 2017. The proposal was approved by the MAMI Program Advisory Committee, and a special Agreement aimed at realization of this experiment was signed between PNPI and Institute for Nuclear Physics (Mainz).

2. Experimental overview

The ep elastic scattering differential cross section at high electron energies is given by the following expression:

$$\frac{d\sigma}{dt} = \frac{\pi\alpha^2}{t^2} \left\{ G_E^2 \left[\frac{(4M + t/\varepsilon_e)^2}{4M^2 - t} + \frac{t}{\varepsilon_e^2} \right] - \frac{t}{4M^2} G_M^2 \left[\frac{(4M + t/\varepsilon_e)^2}{4M^2 - t} - \frac{t}{\varepsilon_e^2} \right] \right\}, \quad (1)$$

where $\alpha = 1/137$; ε_e – the initial total electron energy; M – the proton mass; $t = -Q^2 = -2MT_R$; T_R – the recoil proton energy; G_E – the electric form factor; G_M – the magnetic form factor. At low Q^2 , the form factors G_E and G_M can be represented by the power series expansions:

$$G_{EM}(Q^2)/G_{EM}(0) = 1 - \langle R_p^2 \rangle Q^2/6 + \langle R_p^4 \rangle Q^4/120 - \langle R_p^6 \rangle Q^6/5040 + \dots \quad (2)$$

Here R_p stands for R_{pE} or R_{pM} – the proton charge and magnetic radii, respectively. The proton charge radius can be determined from the slope of the electric form factor G_E at $Q^2 \rightarrow 0$. An example of $d\sigma/dt$ in the small Q^2 region is shown in Fig. 1.

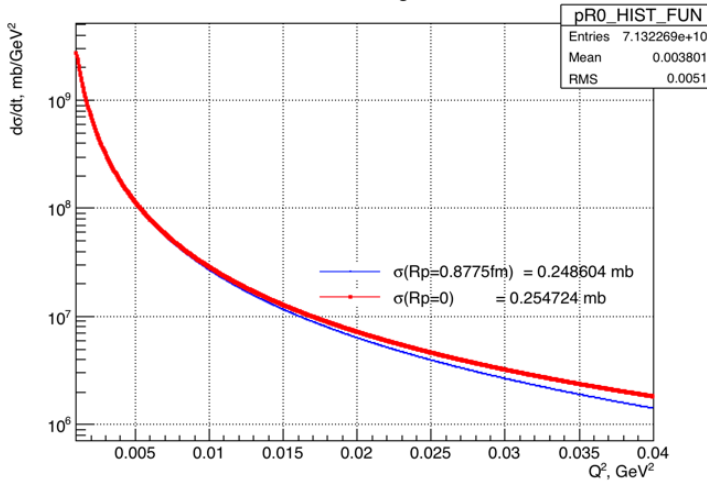


Fig. 1. Differential cross section for ep elastic scattering at $\varepsilon_e = 720$ MeV calculated for $R_p = 0$ and for $R_p = 0.8775$ fm following from a modified dipole form factor

The differential cross sections will be measured for $\varepsilon_e = 720$ MeV in the Q^2 range from 0.001 to 0.04 GeV^2 . The sensitivity of $d\sigma/dt$ to the proton radius in this Q^2 range is rather low, as it is demonstrated in Fig. 2. The cross sections corresponding to $R_p = 0.88$ and $R_p = 0.84$ fm differ only by 1.3% at $Q^2 = 0.02$ GeV^2 . That means that at least 0.2% precision in measurements of $d\sigma/dt$ is needed to distinguish reliably between these two options. In this experiment, the differential cross sections will be measured with 0.1% relative and 0.2% absolute precision.

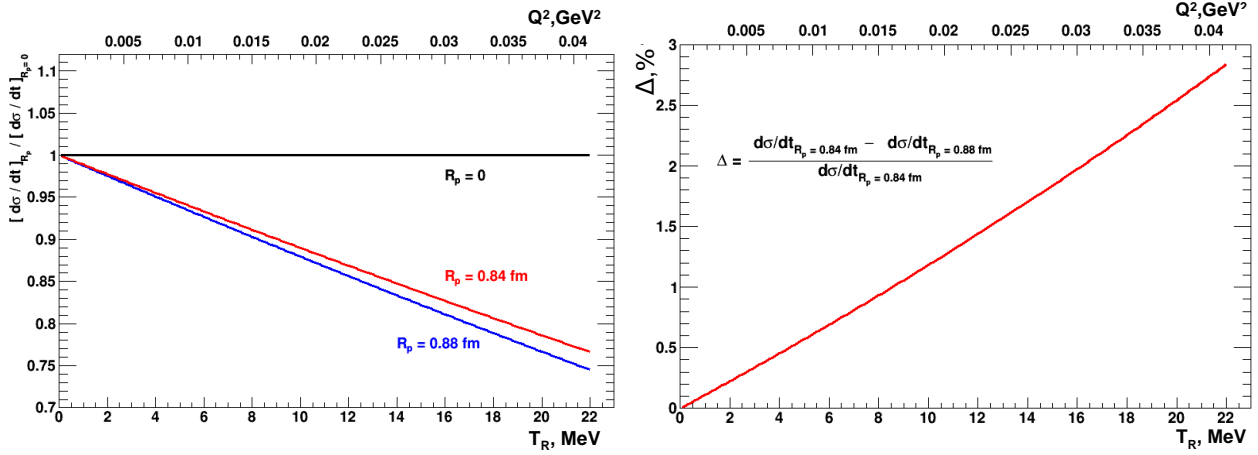


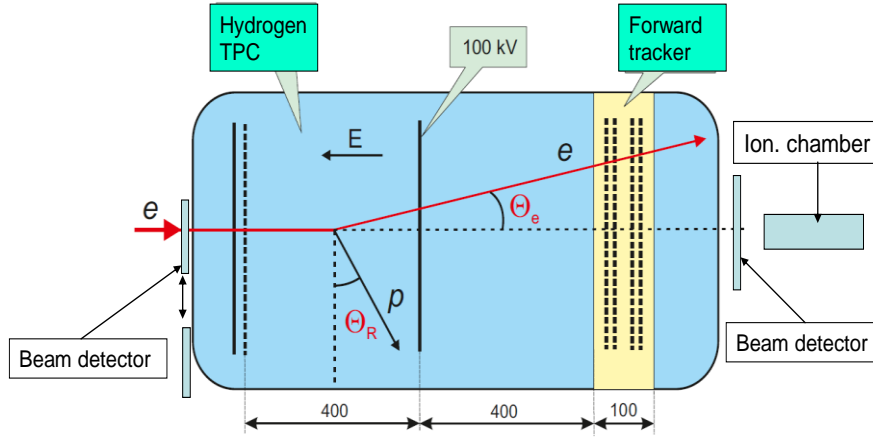
Fig. 2. Ratio of $d\sigma/dt$ calculated for two different values of R_p to that calculated for the point-like proton (*left panel*); difference between the ep differential cross sections corresponding to $R_p = 0.84$ and $R_p = 0.88$ fm (*right panel*)

3. Experimental method

An active hydrogen target – a time projection chamber (TPC) detecting recoil protons will be used in combination with a high precision forward tracker (FT) detecting the scattered electrons. The hydrogen TPC was first developed at PNPI, and it was used in several experiments [7–9] including experiments WA9 and NA8 at CERN for studies of small-angle πp and pp scattering at high energies. A new advanced version of the hydrogen TPC will be used in this experiment.

Figure 3 shows a schematic view of the proposed experimental set-up. It consists of a hydrogen TPC with a multiwire proportional chamber (MWPC) based FT and a beam monitoring system. The TPC operates in the ionization mode (no gas amplification). It allows to measure the recoil proton energy T_R , the recoil proton angle θ_R , and the Z coordinate of the vertex Z_V . The cathode–grid distance (drift space) is $400.00 \text{ mm} \pm 40 \text{ }\mu\text{m}$. The anode–grid distance is 10 mm. Grid: 100 μm wires with 1 mm wire spacing. The anode is subdivided into a central pad (10 mm diameter) surrounded by seven rings (40 mm width each) plus an outer ring (15 mm width). The anode outer diameter is 600 mm (Fig. 4). The TPC will operate at two gas pressures, 20 and 4 bar, with the maximal energy of the protons stopped in the TPC sensitive volume 10 and 4 MeV, respectively. For higher proton energies, the TPC measures the energy deposited in the sensitive volume (for example, 5 for 20 MeV protons at 20 bar H_2) and the angle. Also, there is a possibility to use the CH_4 gas filling. In this case the maximal energy of the protons stopped inside the TPC is 22 MeV (see Fig. 4).

The FT is designed for high absolute precision in measuring the X and Y coordinates of the electron track relative to the beam line. Also, it measures the arrival times of the scattered electrons. The FT acceptance is from 4 to 460 mrad, which provides full coverage of the θ_e distribution corresponding to the selected Q^2 range at the electron beam energy 500–720 MeV (see Fig. 4). The FT consists of two pairs of cathode strip chambers (CSC): X_1/Y_1 and X_2/Y_2 . Each chamber is a symmetric MWPC with a 3.0 mm gap between the cathode and the anode planes. The size of the chamber is $600 \times 600 \text{ mm}^2$. The readout is from both cathode planes. The anode wire plane contains 30 μm wires spaced by 3 mm. Both cathode planes are made of 50 μm wires wound with 0.5 mm step. The cathode wires are orthogonal to the anode wires in one cathode plane and inclined by 45° in the other cathode plane. The wires in the inclined cathode plane are grouped into 10 mm strips. The key element of the CSC is the cathode plane with orthogonal cathode-to-anode wires. It determines the absolute measurements of the coordinate along the anode wire. In this plane, 2.5 mm strips are formed by joining together five wires. Using the centre-of-gravity method, the coordinate of each detected track is determined with $\sim 30 \text{ }\mu\text{m}$ resolution.



Measured quantities:

Recoil energy T_R $-t = \frac{4\epsilon_e^2 \sin^2 \frac{\vartheta}{2}}{1 + \frac{2\epsilon_e}{M} \sin^2 \frac{\vartheta}{2}}$

Recoil angle Θ_R

Vertex Z coordinate

Electron scattering angle θ_e $-t = 2MT_R$

Fig. 3. Schematic view of the combined TPC&FT detectors

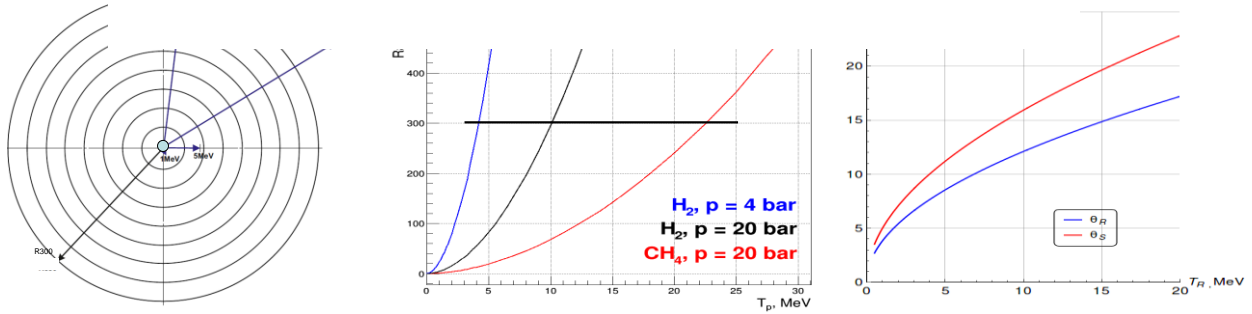


Fig. 4. TPC anode structure: a 10 mm in diameter circle surrounded by eight rings (*left panel*); proton range-energy plots for H_2 gas (20 and 4 bar) and for CH_4 (20 bar) (*central panel*); scattering electron and recoil proton angles θ_e and θ_R in function of the recoil proton energy for 500 MeV electrons (*right panel*)

The CSC strip plane is fabricated in such a way that it provides the absolute linear scale with $\sim 0.02\%$ precision. The FT and TPC are assembled in a common vessel in separated volumes. The TPC operates with ultraclean hydrogen at up to 20 bar gas pressure, while the $Ar + 2\% CH_4$ gas mixture is used in the FT at the gas pressure equalized with that in the TPC. The gas purity and pressure will be maintained by special gas circulation/purification systems. The gas gain in the MWPCs varies from 10^3 to 10^4 for 20 and 4 bar pressure, respectively. There is a dead zone in the centres of the CSCs (20 mm in diameter) to reduce the sensitivity to the electron beam crossing the CSCs. This is done by electrolytically depositing an additional gold layer on the anode wire in this spot. Note that some sensitivity still remains, and it will be used in the detector alignment procedure.

The beam detectors have several functions:

- 1) tracing the beam line and control for beam stability,
- 2) measuring the arrival times of the beam electrons,
- 3) absolute counting of the beam electrons for determination of the absolute cross section.

The first of these functions is provided by the pixel detectors, which were successfully tested in the 2017 test run ($3 \times 3 \text{ mm}^2$ size, $80 \times 100 \text{ }\mu\text{m}^2$ pixels). The second and the third functions will be realized with two fast scintillator detectors placed downstream of the TPC&FT detector. Also, a high-pressure ionization chamber will be used for the beam current control and for evaluation of the pile-up correction in the absolute

counting of the beam rate by the SC detectors (the beam rate will be around 2 MHz). The upstream beam detectors (SC detectors and pixels) will be used only for calibration purposes, and they will be in the out-of-beam position during the physics runs in order to reduce the amount of material in the beam line. The beam enters the TPC through a 400 μm Be window.

With this system, the integrated beam rate will be measured with 0.1% absolute precision. The beam parameters are presented in Table 1.

Table 1
Parameters of the electron beam planned to use in this experiment

Parameter	Value
Beam energy	720 MeV
Beam energy resolution	< 20 keV (1σ)
Absolute beam energy precision	± 150 keV (1σ)
Beam intensity (main run)	$2 \cdot 10^6$ e/s
Beam intensity for calibration	10^4 e/s and 10^3 e/s
Beam divergency	≤ 0.5 mrad (1σ)
Beam size	≤ 0.2 mm (1σ)
Duty factor	100%

The gas pressure in the TPC will be measured with 0.01% absolute precision. The temperature of the detector body will be maintained constant at 298 K with a special thermo-stabilization system, and it will be measured with 0.015% absolute precision. This determines the proton density with 0.025% absolute precision. The electron drift velocity W in the TPC will be measured directly in this experiment with precision 0.01%. The maximal drift time is ~ 90 μs . The gas target length is determined from the measured difference between the maximal and minimal arrival times of the TPC signals in the chosen drift space, $L_{\text{tag}} = (t_{\text{R max}} - t_{\text{R min}}) W$. The expected precision in determination of L_{tag} is 0.02% for $L_{\text{tag}} = 35$ cm. Note that thus selected hydrogen gas target is separated from the grid and from the cathode, therefore there are no wall effects in the measurements.

Recoil energy (T_{R}), angle (θ_{R}), and arrival time (t_{R}) resolution. The anode channels will be equipped with low-noise preamplifiers with the noise at the level of 20 keV (σ). The beam induced noise is essential only at the central pad where it is expected to be around 80 keV for the main run conditions (20 bar hydrogen, 2 MHz beam rate). The expected recoil arrival time resolution is 40 ns. The recoil angle will be determined by the difference in arrival times of the signals from the neighbour pads (possible for proton ranges exceeding 60 mm). The recoil angular resolution will be from 15 to 10 mrad.

Vertex position and resolution. The Z coordinate of the vertex Z_{V} is determined by the drift time t_{R} and the drift velocity W with ± 100 μm absolute precision. The X_{V} and Y_{V} coordinates are distributed around the central values $X_{\text{V}} = 0$ and $Y_{\text{V}} = 0$ determined by the beam position along the TPC axis, the deviations being caused by the beam size (~ 200 μm), beam divergence (~ 0.5 mrad), and the Coulomb scattering (~ 0.5 mrad).

Angle θ_e of scattered electrons, absolute value, and resolution. The angle θ_e of a scattered electron is determined by the vertex coordinate Z_{V} and the $X1/Y1$ coordinates in the FT with the resolution ~ 1 mrad (beam divergence and Coulomb scattering).

The centre-of-gravity of the θ_e distribution corresponding to a selected recoil energy T_{R} is measured with 0.02% precision determined mainly by the absolute precision in measurements of the $X1/Y1$ coordinates.

4. Measurement procedure

The ep differential cross section is determined by the transfer momentum and is practically independent of the electron energy at $\varepsilon_e \geq 500$ MeV in the considered low Q^2 region. The transfer momentum $-t = Q^2$ can be determined either by the recoil proton energy T_R or by the electron scattering angle θ_e . The advantage of the T_R method is determination of the transfer momentum independently of the electron energy ε_e :

$$-t = 2MT_R. \quad (3)$$

Therefore, measuring the transfer momentum by the T_R method, we avoid the influence of the beam energy losses before the ep collision (as well as the initial beam energy spread) on the measured $d\sigma/dt$. This is especially important for the ep scattering because of the radiation losses of the electrons in the materials upstream of the ep collision point. On the contrary, the transfer momentum determined *via* the electron scattering angle θ_e depends on ε_e :

$$-t = \frac{4\varepsilon_e^2 \sin^2 \frac{\theta_e}{2}}{1 + \frac{2\varepsilon_e}{M} \sin^2 \frac{\theta_e}{2}}. \quad (4)$$

A possible tail in ε_e results in a tail in the measured Q^2 distribution (Fig. 5) and thus disturbs the $d\sigma/dt$ measurement. On the other hand, the θ_e scale can be fabricated with high absolute precision. This allows to perform a precise T_R scale calibration using the measured θ_e - T_R correlation plot. We call this procedure as self-calibration of the T_R scale as it does not require any special measurements and can be performed using the full set of the collected experimental data. This is an essential point of our experimental method. The electron scattering angle is measured with 0.02% precision which allows to calibrate the T_R scale with 0.04% relative precision. Furthermore, the absolute energy of the 720 MeV electron beam is known with 0.02% precision. This means that the T_R scale can be calibrated with 0.08% absolute precision.

Another advantage of the recoil method is relatively small radiative corrections to the measured value of $d\sigma/dt$. Figure 5 (*left panel*) shows the main diagrams of the radiative processes in the ep scattering. In the previous experiments, where the transfer momentum was determined by measuring the angle and the momentum of the scattered electron, the main contributions to the radiative corrections came from diagrams v2, r1, and r2. On the contrary, they cancel each other almost exactly when the transfer momentum is determined by the recoil energy T_R (under condition that there are no cuts introduced in the scattered electron distributions). Figure 5 (*right panel*) demonstrates the radiative tail in the θ_e distribution corresponding to a selected recoil energy around $T_R = 5$ MeV. This tail is within the acceptance of the forward detector. In the analysis, when calculating $d\sigma/dt$, it can be included into the total number of events corresponding to the selected ΔT_R , while the transfer momentum (used for the T_R scale calibration) is determined by the peak position ($\theta_{e \max}$) in the θ_e distribution. The remaining radiative corrections can be calculated with rather high accuracy. Moreover, they can be controlled by the absolute measurements of $d\sigma/dt$ planned in this experiment.

Elimination of the background reactions. The T_R - θ_e , T_R - θ_R , and θ_R - θ_e correlations can be used to eliminate the backgrounds. As an example, Fig. 6 demonstrates these correlation plots calculated for the ep elastic scattering and for the background reaction $ep \rightarrow ep\pi^0$ for 720 MeV electrons. One can see that the elastic scattering can be well separated from the background.

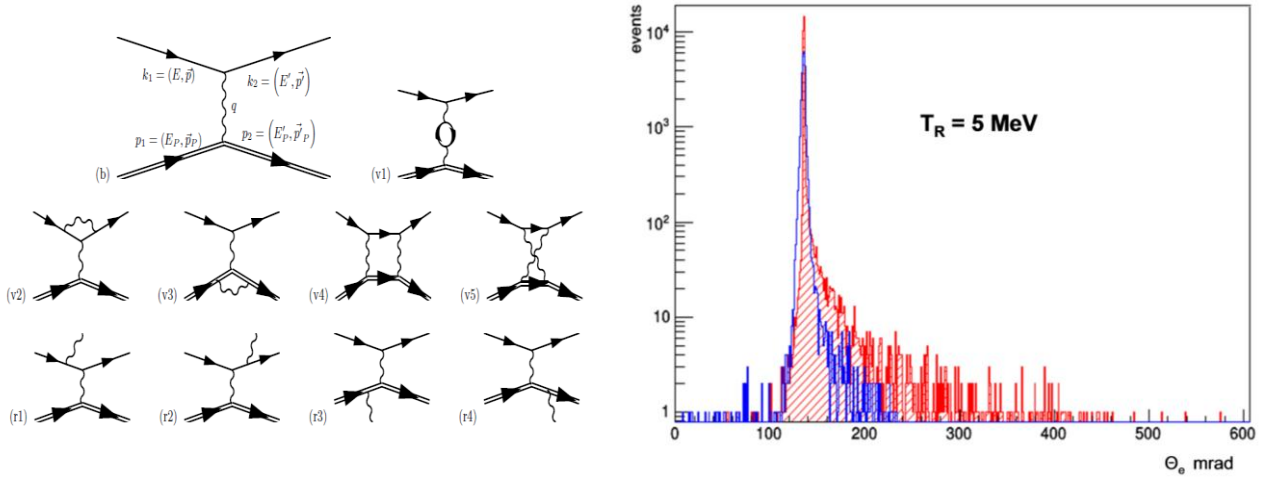


Fig. 5. Left panel – main diagrams for radiative processes in ep elastic scattering. Right panel – angular distribution of 720 MeV electrons after ep collisions calculated with the ESEPP generator taking into account all radiative corrections – red colour. This distribution corresponds to the selected recoil energy around $T_R = 5$ MeV. For comparison, the angular distribution of the electrons due to multiple Coulomb scattering is shown in blue colour

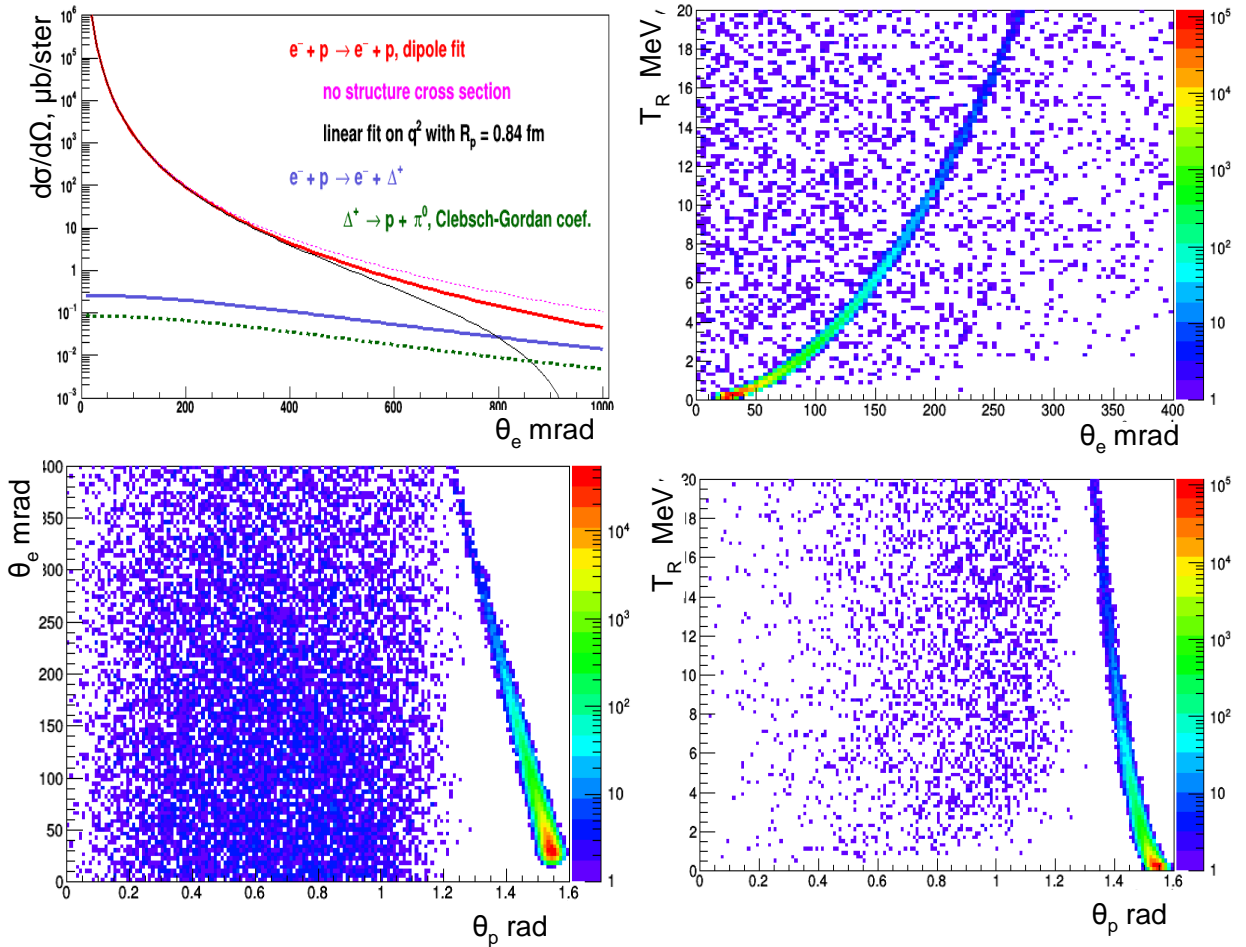


Fig. 6. The T_R - θ_e (upper right), T_R - θ_p (bottom right), and θ_R - θ_e (bottom left) correlation plots calculated for elastic ep scattering and for the background reaction $ep \rightarrow ep\pi^0$ at $\epsilon_e = 720$ MeV. Also shown are the differential cross sections for elastic and inelastic ep scattering (upper left). Note that θ_p in these plots corresponds to $90^\circ - \theta_R$

Trigger and acquisition. An adjustable combination of signals from the TPC anodes exceeding some threshold values will be used for triggering the readout system (the TPC self-triggering mode). This is the most safe and effective triggering option. The expected trigger rate will be around 50 Hz. The acquisition system will provide continuous data flow without introducing any dead time. After receiving a trigger signal, the information from all detectors which appeared in a 100 μs time interval before the arrival of the trigger is readout from the pipeline and sent to data acquisition (DAQ). The efficiency in detection of the ep events triggered by the TPC should be close to 100% in the measured t range.

Selection of true ep collisions. The trigger is a recoil signal ($T_R \geq 0.3$ MeV) detected in the TPC at the time t_R . The maximum drift time in the TPC is 100 μs . Therefore, any beam electron appearing in the TPC in the time interval $t_R - 100 \mu\text{s} \leq t \leq t_R$ should be considered as a candidate for the recoil parent particle. The electron beam intensity is $2 \cdot 10^6$ e/s. This means that the average number of the ep candidates at this stage is 200. The selection of the true ep scattering event is needed for finding the correct Z_V coordinate of the ep collision vertex. This selection will be done in the off-line analysis applying the following criteria. First, the requirement of a track detected in the FT (outside the 2 cm central dead area) in the 100 μs time window before arrival of the trigger signal will reduce the number of the ep candidates by a factor of 40. The remaining candidates with arrival times t_i correspond to different coordinates of the ep vertex: $Z_i = W(t_R - t_i)$ where W is the drift velocity. Tracing back the electron trajectory determined by the FT1 and FT2 planes, one can determine the Z_{back} coordinate and compare it with Z_i . According to MC simulations, after this selection less than one false candidate in average remains per one true ep event. Finally, the $\theta_e - T_R$ correlation provides a powerful background rejection. Together with the previous selection steps, this allows to select the true ep events on a high confidence level with $\sim 100\%$ detection efficiency.

Statistics and beam time. The statistical error in the measured proton radius was estimated by simulation of $7 \cdot 10^7$ ep scattering events in the Q^2 -range from 0.001 to 0.04 GeV^2 (integrated luminosity $2.81 \cdot 10^8$ mb^{-1}). Such a number of events could be collected during 45 days of continuous running in the $2 \cdot 10^6$ e/s beam with the TPC operating at 20 bar with 35 cm target length ($3.6 \cdot 10^{22}$ p/cm^2). For this analysis, $d\sigma/dt$ was generated assuming $G_M(Q^2) = \mu_p G_E(Q^2)$, where μ_p is the proton magnetic moment. Both form factors were represented by a modified dipole form factor corresponding to a fixed value of $R_{pE} = R_{pM} = \langle R_p^2 \rangle^{1/2} = 0.8775$ fm:

$$G(Q^2) / G(0) = (1 + Q^2/0.6068)^{-2}. \quad (5)$$

The generated $d\sigma/dt$ was fitted using $d\sigma/dt_{\text{fit}}$ with the form factors represented by a power series expansion:

$$G(Q^2) / G(0) = A \left(1 + \sum_{n=1}^{n_{\text{max}}} C_n Q^{2n} \right), \quad (6)$$

where $C_n = (-1)^n \langle R_p^{2n} \rangle / (2n + 1)! (0.1973)^{2n}$. Here Q^{2n} and $\langle R_p^{2n} \rangle$ are expressed in GeV^{2n} and in fm^{2n} , respectively. The parameters A , $\langle R_p^2 \rangle$, and $\langle R_p^4 \rangle$ were the fitting parameters. The parameter $\langle R_p^6 \rangle$ was fixed to various values to study the sensitivity of the extracted R_p to this parameter. Also, it could be used as an additional free parameter in the fits. Figure 7 (*left panel*) presents the results of the fit performed without the Q^6 term in expression (6), that is for $\langle R_p^6 \rangle = 0$. A similar analysis was done with 100 times higher statistics to estimate a possible systematic bias which could be related with neglecting the Q^6 and higher terms in the power series expansion of the fit function. The results are presented in Fig. 7 (*right panel*).

As it follows from Fig. 7 (*left panel*), the statistical error in determination of $R_2 = \langle R_p^2 \rangle$ is $0.0072/0.7700 = 0.93\%$, which corresponds to a 0.47% error in determination of R_p . The systematic bias shown in Fig. 7 (*right panel*) is $\Delta R_2 = 0.7681 - 0.7700 = -0.0019$ fm^2 . This corresponds to a 0.12% systematic bias in measurement of R_p (± 0.001 fm).

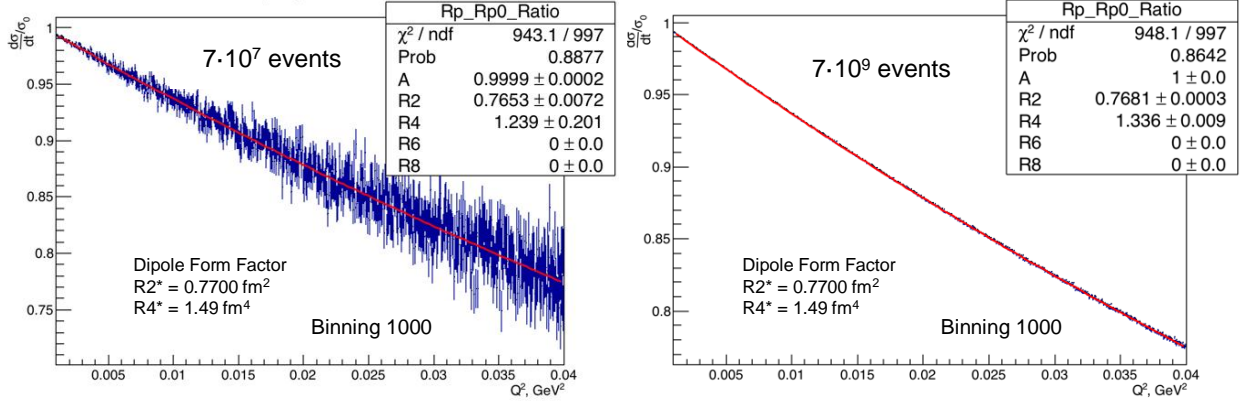


Fig. 7. Fitting of the ratio $R = d\sigma/dt (R_p = 0.8775 \text{ fm}) / d\sigma/dt (R_p = 0)$ in the Q^2 range $0.001 \text{ GeV}^2 \leq Q^2 \leq 0.04 \text{ GeV}^2$. The cross section $d\sigma/dt$ was generated with the electric and magnetic form factors represented by Eq. (5). The fit function $G(Q^2)_{\text{fit}} / G(0)$ was taken as a power series expansion (6) with $n_{\text{max}} = 2$, ($\langle R_p^6 \rangle = 0$). *Left panel* – fit to $d\sigma/dt$ generated with the statistics foreseen for this experiment, $7 \cdot 10^7$ events. *Right panel* – a similar fit with 100 times higher statistics, $7 \cdot 10^9$ events. R2, R4, R6, R8 stand for $\langle R_p^2 \rangle$, $\langle R_p^4 \rangle$, $\langle R_p^6 \rangle$, $\langle R_p^8 \rangle$, respectively. In terms of the power series expansion, the dipole form factor used in this analysis corresponds to $\langle R_p^2 \rangle = 0.7700 \text{ fm}^2$, $\langle R_p^4 \rangle = 1.49 \text{ fm}^4$, $\langle R_p^6 \rangle = 5.3 \text{ fm}^6$

This consideration shows that, if the proton form factor could be represented by the dipole form factor, the Q^6 term can be neglected in the fit function without noticeable influence on the measured proton radius. However, previous analyses of the existing ep scattering data showed that contributions of the higher terms of the power series expansion of the proton form factor may be considerably larger than those in the dipole form factor. In particular, J. Bernauer [5, 10] has obtained the following results from the analysis of the A1 experiment data using a tenth order power series expansion of the proton form factor:

$$\langle R_p^2 \rangle = 0.774(8) \text{ fm}^2, \langle R_p^4 \rangle = 2.59(19)(04) \text{ fm}^4, \langle R_p^6 \rangle = 30(7.6)(12.6) \text{ fm}^6, \langle R_p^8 \rangle = 372 \text{ fm}^8.$$

Based on these results, we have analysed the sensitivity of the extracted value of the proton radius R_p to variations of $\langle R_p^4 \rangle$ from 2.4 to 2.8 fm^4 and $\langle R_p^6 \rangle$ from 11 to 41 fm^6 in the generated $d\sigma/dt$ with the form factors represented by the power series expansion (6) with fixed values of $\langle R_p^2 \rangle = 0.7700 \text{ fm}^2$ and $\langle R_p^8 \rangle = 372 \text{ fm}^8$. Similarly, the fit function $d\sigma/dt_{\text{fit}}$ contained the form factors parametrized by the power series expansion with A, $\langle R_p^2 \rangle$, and $\langle R_p^4 \rangle$ used as free parameters, and $\langle R_p^6 \rangle$ as a variable fixed parameter. It was shown that, with the $\langle R_p^6 \rangle$ value fixed around 26 fm^6 , the above mentioned variations of $\langle R_p^4 \rangle$ and $\langle R_p^6 \rangle$ in the simulated $d\sigma/dt$ resulted in $\pm 0.0025 \text{ fm}$ systematic bias in the value of the proton radius R_p extracted with the statistical error of $\pm 0.0041 \text{ fm}$.

Fits with four free parameters (A, $\langle R_p^2 \rangle$, $\langle R_p^4 \rangle$, and $\langle R_p^6 \rangle$) allow to extract the proton radius with very low systematic bias ($\leq 0.001 \text{ fm}$) but with larger statistical errors ($\pm 0.0085 \text{ fm}$).

5. Summary of systematic errors

Table 2 summarizes the expected systematic errors in various components critical for measurements of the relative and absolute differential ep elastic scattering cross sections in the Q^2 -range from 0.001 to 0.04 GeV^2 with 0.1 and 0.2% precision, respectively.

Table 2

Summary of systematic errors expected in the proposed experiment

No.	Parameter	Systematic error, %	Comment
1	Drift velocity, $W1$	0.01	–
2	High voltage, HV	0.01	–
3	Temperature, K	0.015	–
4	Pressure, P	0.01	–
5	H ₂ density, ρ_p	0.025	Sum of errors 3 and 4
6	Target length, L_{tag}	0.02	–
7	Number of protons in target, N_p	0.045	Sum of errors 5 and 6
8	Number of beam electrons, N_e	0.05	Beam detector counts corrected for pileups
9	Detection efficiency of ep events	0.05	–
10	Electron beam energy, ϵ_e	0.02	–
11	Electron scattering angle, θ_e	0.02	–
12	t -scale calibration, T_R relative	0.04	Follows from error 11
13	t -scale calibration, T_R absolute	0.08	Follows from the sum of errors 11 and 10
14	$d\sigma/dt$, relative	0.1	0.08% from error 12
15	$d\sigma/dt$, absolute	0.2	0.16% from error 13 plus errors 7–9

6. Conclusion

This project is designed for measurements of differential cross sections for the electron–proton elastic scattering in the transfer momentum region $0.001 \text{ GeV}^2 \leq Q^2 \leq 0.04 \text{ GeV}^2$ with 0.1% relative and 0.2% absolute precision. The experimental method is based on measurements of the energy of the recoiled proton and the angle of the scattered electron. One of the advantages of this method is relatively low radiative corrections to the measured cross sections. These measurements should allow to extract the proton charge radius with a sub-percent precision that could be decisive for solving the “proton radius puzzle”. The experiment will be performed in the 720-MeV electron beam of the Mainz electron accelerator MAMI.

References

1. R. Pohl *et al.*, Nature **466**, 213 (2010).
2. A. Antognini *et al.*, Science **339**, 417 (2013).
3. J.C. Bernauer *et al.*, Phys. Rev. Lett. **105**, 242001 (2010).
4. X. Zhan *et al.*, Phys. Lett. B **705**, 59 (2014).
5. I. Sick, D. Trautmann, Phys. Rev. C **95**, 012501 (2017).
6. H. Gao, C. Peng, EPJ Web Conf. **113**, 03007 (2016).
7. J.P. Burq *et al.*, Nucl. Phys. B **217**, 285 (1983).
8. A.V. Dobrovolsky *et al.*, Nucl. Phys. A **766**, 1 (2006).
9. V.A. Andreev *et al.*, Phys. Rev. Lett. **110**, 022504 (2013).
10. J.C. Bernauer, *Ph. D. Theses*, University of Mainz, 2010.

SHiP: SEARCH FOR HIDDEN PARTICLES

PNPI participants of the SHiP Collaboration:

V.T. Kim, E.V. Kuznetsova, O.L. Fedin, G.E. Gavrilov, V.L. Golovtsov, N.V. Gruzinskiy,
V.P. Maleev, S.A. Nasybulin, L.N. Uvarov, V.I. Yatsyura

1. Introduction

SHiP (search for hidden particles) is a newly proposed experiment [1] aimed at exploring the domain of very weakly interacting particles, which can, in particular, be constituents of the dark matter of the Universe, and studying the properties of tau neutrinos. It is designed to be installed downstream of a new beam-dump facility at the Super Proton Synchrotron (SPS). The CERN SPS and PS experiments Committee (SPSC) completed in 2016 a review of the SHiP Technical and Physics Proposal [2–4], and it recommended that the SHiP Collaboration would proceed towards preparing a comprehensive design report, which would provide input into the next update of the European Strategy for Particle Physics in 2019/2020.

Why is the SHiP physics program so timely and attractive? By now we have observed all particles of the Standard Model (SM), however it is clear that the SM is not the ultimate theory. Some yet unknown particles or interactions are required to explain a number of observed phenomena in particle physics, astrophysics and cosmology, the so-called beyond the Standard Model (BSM) problems, such as dark matter, neutrino masses and oscillations, baryon asymmetry, and the expansion of the universe.

While these phenomena are well-established observationally, they give no indication about the energy scale of new physics. The analysis of new Large Hadron Collider (LHC) data collected at 13 TeV will soon have directly probed the TeV scale for new particles with couplings at $O(\%)$ level. The experimental efforts in flavour physics and searches for charged lepton flavour violation and electric dipole moments will continue the quest for specific flavour symmetries to complement direct exploration of the TeV scale.

However, it is possible that we have not observed some of the hidden particles responsible for the BSM problems due to their extremely feeble interactions, rather than due to their heavy masses. Even in the scenarios in which BSM physics is related to high-mass scales, many models contain degrees of freedom with suppressed couplings that stay relevant at much lower energies.

Given the small couplings and mixings, and hence typically long lifetimes, these particles of the hidden sector (HS) have not been significantly constrained by previous experiments, and the reach of current experiments is limited by both luminosity and acceptance. Hence the search for low-mass BSM physics should also be pursued at the intensity frontier, along with expanding the energy frontier.

SHiP is designed to give access to a large class of interesting models with HS particles. It has the discovery potential for the major observational puzzles of modern particle physics and cosmology, and can explore some of the models down to their natural “bottom line”. SHiP also has a unique potential to test lepton flavour universality by comparing interactions of muon and tau neutrinos.

2. SHiP experimental set-up

Despite an active program of searches for HS particles in many experiments, SHiP remains a unique dedicated experiment capable of reconstructing the decay vertex of an HS particle, measuring its invariant mass and providing particle identification of the decay products in an environment of extremely low background. Moreover, SHiP is also optimised to search for light dark matter (LDM) through scattering signatures and for tau neutrino physics.

After the technical proposal (TP) [2, 3] the SHiP design went through a significant re-optimisation phase. Figure 1 shows the layout of the re-optimised SHiP detector. While the overall set-up of the detector remains unchanged, the geometry and the detector composition has been significantly modified, and technological studies and test beams have brought maturity to the design. SHiP consists of a proton target, followed by a hadron stopper and an active muon shield [5] that sweeps muons produced in the beam dump out of acceptance. Since the TP, the target has been extended from ten to twelve interaction lengths in order to reduce the hadronic shower leakage. Studies were made to minimise the distance between the target and the SHiP

spectrometers to improve the acceptance of the spectrometers, and to reduce the weight and cost of the muon shield. A significant improvement was achieved by starting the first section of the muon shield within the hadron stopper by integrating a coil which magnetises the iron shielding blocks.

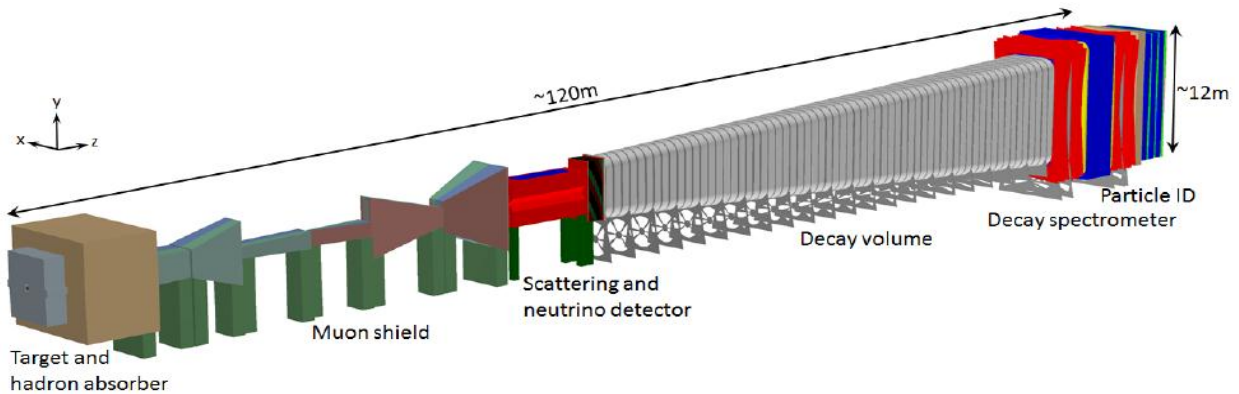


Fig. 1. Overview of the SHiP experiment

The SHiP detector itself incorporates two complementary devices, the scattering and neutrino detector (SND), and the HS spectrometer. The SND will search for LDM scattering and perform neutrino physics. It is made of an emulsion spectrometer located inside a single long magnet with a field above 1.2 T in the entire volume, and a muon identification system. The emulsion spectrometer is a hybrid detector consisting of alternating layers of an absorber, nuclear emulsion films and fast electronic trackers. The absorber mass totals ~ 10 t.

The HS decay spectrometer aims at measuring the visible decays of HS particles by reconstructing their decay vertices in a 50 m long decay volume. In order to eliminate the background from neutrinos interacting in the decay volume, it is maintained at a pressure of $O(10^{-3})$ bar. To maximise the sensitivity to HS particles, the muon shield was shortened in combination with changing the shape of the decay volume from an elliptic cylinder to a pyramidal frustum. The decay volume is followed by a large spectrometer with a rectangular acceptance of 5 m in width and 10 m in height.

The main element of the HS decay detector is the spectrometer straw tracker (SST) designed to accurately reconstruct the decay vertex, the mass, and the impact parameter of the hidden particle trajectory at the proton target. The main change since the TP is the removal of the straw veto station that was located 5 m into the decay volume, and the increase of the straw diameter from 10 to 20 mm. Also, all tracker stations upstream and downstream of the magnet have now the same dimensions to ease construction and to reduce cost. The spectrometer dipole magnet is still based on a warm magnet with a fiducial aperture of 5×10 m² and a field integral of ~ 0.5 Tm, but the coil and the fitting of the coil have been updated in order to accommodate the rectangular vacuum tank of the spectrometer section.

A set of calorimeters and muon detectors provide particle identification [2], which is essential in discriminating between a very wide range of HS models. For the TP, the electromagnetic calorimeter (ECAL) was optimised to provide electron identification and π^0 reconstruction. It has now been decided to extend the ECAL requirements to include reconstruction of axion-like-particles (ALP) decaying to the two photon final state that is the unique way to discriminate between an ALP and a dark photon or a dark scalar. The current version of ECAL, called SplitCal, is a longitudinally segmented lead sampling calorimeter consisting of two parts, which are mechanically separated in the longitudinal direction. Each part is equipped with high spatial resolution layers in order to provide pointing with a resolution of ~ 5 mrad for photons originating from ALP decays. The longitudinal layer segmentation of SplitCal also improves the electron/hadron separation. This opens the possibility to remove the hadron calorimeter detector without compromising the particle ID (PID) performance, and only leaves the absorber for the purpose of muon filtering.

The muon system consists of four stations interleaved by three muon filters. The ECAL converter material and the muon filters provide sufficient material budget to stop low momenta muons, such that the last muon

station is reached only by muons with momenta exceeding $5.3 \text{ GeV}/c$. Since the TP, the muon system considers a new technology based on scintillating tiles with direct silicon photomultipliers readout. This option provides better time resolution and is more robust against hit rate variations.

Since the key feature of the HS decay spectrometer design is to ensure efficient suppression of various backgrounds, the tracking and particle identification are complemented by a dedicated timing detector with $\sim 100 \text{ ps}$ resolution to provide a measure of time coincidence, in order to reject combinatorial backgrounds. The decay volume is instrumented by the surround background tagger (SBT), whose purpose is to detect neutrino and muon inelastic interactions in the vacuum vessel walls which may produce long-lived neutral particles decaying in the decay volume and mimicking the HS signal events. Similarly, tagging of interactions in the upstream material of the muon identification system of the SND is provided by the associated detector layers.

The muon shield and the SHiP detector systems are housed in an $\sim 120 \text{ m}$ long underground experimental hall at a depth of $\sim 15 \text{ m}$. To minimise the background induced by the flux of muons and neutrinos interacting with material in the vicinity of the detector, no infrastructure systems are located on the sides of the detector, and the hall is 20 m wide along its entire length.

3. Hidden sector decay spectrometer

The HS decay spectrometer consists of a large vacuum vessel, the surround background tagger, the spectrometer straw tracker, together with the large spectrometer magnet with a total field integral of about 0.5 Tm , the timing detector (TD), the electromagnetic calorimeter and the downstream muon system.

The decay spectrometer has to perform precise measurements of charged particles and photons originating from decay vertices of hidden particles in the decay volume, measure their momenta, and provide PID information. Moreover, the decay spectrometer has to ensure a redundant background suppression using timing and track information from the TD and the SST, vetoing criteria from the upstream muon system of the SND and the SBT, and PID by the calorimeter and the muon systems.

The principal features and main parameters of the HS decay spectrometer subdetectors are implemented in FairShip, SHiP software framework based on FairRoot [2, 3, 5–7]. These parameters have been used in the simulation studies of the HS decay spectrometer performance. Specific proof-of-principle tests of prototypes have been undertaken in order to demonstrate that the expected detector performance can be achieved.

The purpose of the spectrometer straw tracker, a key element of the HS decay detector, is to measure track parameters and momentum of charged particles with high efficiency and accurate enough to reconstruct decays of hidden particles, and to reject background events. The precision of the extrapolated position of the tracks must be well matched with the segmentation of the TD such that the high accuracy of the associated track time can be used to remove combinatorial background. The invariant mass, the vertex quality, the timing, the matching to background veto taggers, and the pointing to the production target are crucial tools for rejecting background.

The spectrometer consists of a large aperture dipole magnet and two tracking telescopes, one on each side of the magnet and each composed of two tracking stations. The four stations are identical with a nominal acceptance of 5 m in X and 10 m in Y , and are based on ultrathin straw drift tubes oriented horizontally. Each station contains four views, in a $Y-U-V-Y$ arrangement, where U and V are stereo views with straws rotated by a small angle $\pm\theta_{\text{stereo}}$ around the z -axis with respect to the y -measuring straws.

As has been already mentioned, the main change since the TP [2, 3] is the increase of the straw diameter D from 10 to 20 mm [6]. This change is motivated by the refined background rate simulations which confirm that for $D = 20 \text{ mm}$ the rate per straw remains modest ($< 7 \text{ kHz}$ in the hottest straw).

Tools for producing 20 mm straws have been developed and several prototype straws, using as before a $36 \mu\text{m}$ thick polyethylene terephthalate film coated with 50 nm Cu and 20 nm Au , have been produced with no new difficulty encountered compared to the fabrication of the original 10 mm straws. Several straws of 20 mm diameter and 5 m length were fabricated. The rupture over-pressure was measured on ten samples of 50 cm length and was found to be around 4.4 bar , as expected. This is considered a sufficient margin for operating the straws at a pressure of about 1 bar in vacuum. The torsion of 5 m long straws, cemented on one

side and pressurised to 1 bar over-pressure, was measured. A rotation of 38° was found at the free end. A torque of about 0.076 Nm was needed to cancel the rotation. A 2 m long $D = 20$ mm straw was fabricated and its performance as a MIP detector was characterised in a test run with beam in the SPS north area as a function of the wire offset at nominal conditions (~ 1.05 bar pressure, 70% Ar – 30% CO₂). First results indicate that a straw hit resolution of 120 μm is achievable with high hit efficiency over most of the straw diameter, independently of the wire offset. The drift time spectra for different wire offsets are being analysed, and methods to extract the local wire offset from the distinctive features of the spectra are being investigated. Alignment studies for the full detector, using Monte Carlo (MC) simulations, are being started, which should allow us to define the geometrical constraints for the mechanical engineering design.

A preliminary conceptual design of the vacuum enclosure is being worked out which foresees a vacuum chamber with rectangular cross section, longitudinally extending over the whole spectrometer length, and providing four rectangular openings on the top side. These openings are used to insert the tracker station frames, fully equipped, into the vacuum volume. In this concept, the vacuum enclosure is decoupled from the mechanical structures of the detector. Front-end electronics are located inside the vacuum and require active cooling.

4. Proton beam and experimental facility

At the CERN SPS, the optimal experimental conditions for SHiP are obtained with a proton beam energy of around 400 GeV. The SHiP operational scenario implies returning to full exploitation of the capacity of the SPS (Fig. 2). The request for the proton yield is based on a similar fraction of beam time as the past CERN Neutrinos to Gran Sasso program. A nominal beam intensity of $4 \cdot 10^{13}$ protons on target per spill is assumed for the design of the experimental facility (Fig. 3) and the detector (Fig. 4). In the baseline scenario for SHiP, the beam sharing delivers an annual yield of $4 \cdot 10^{19}$ protons to the beam dump facility and a total of 10^{19} to the other physics programs at the CERN North Area, while respecting the beam delivery required by the HL–LHC. The physics sensitivities are based on acquiring a total of $2 \cdot 10^{20}$ protons on target, which may thus be achieved in five years of nominal operation.

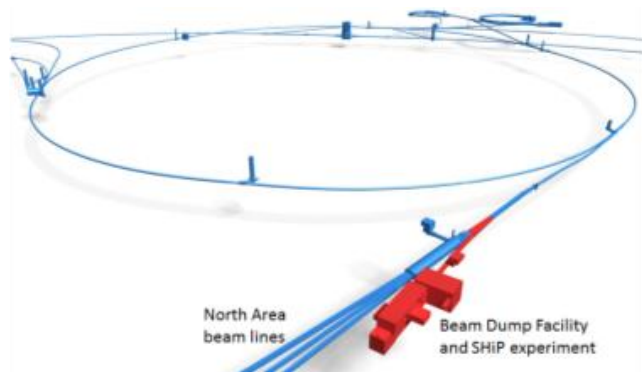


Fig. 2. Overview of the CERN injector complex indicating the location of the new SPS beam dump facility designed to house the SHiP experiment

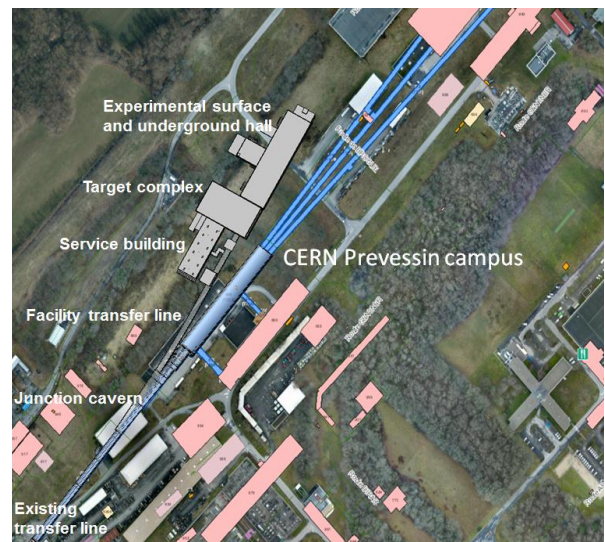


Fig. 3. Overview of new surface and underground structures for the beam dump facility. The beam-axis is at a depth of about 10 m which allows trenching the entire complex from the surface

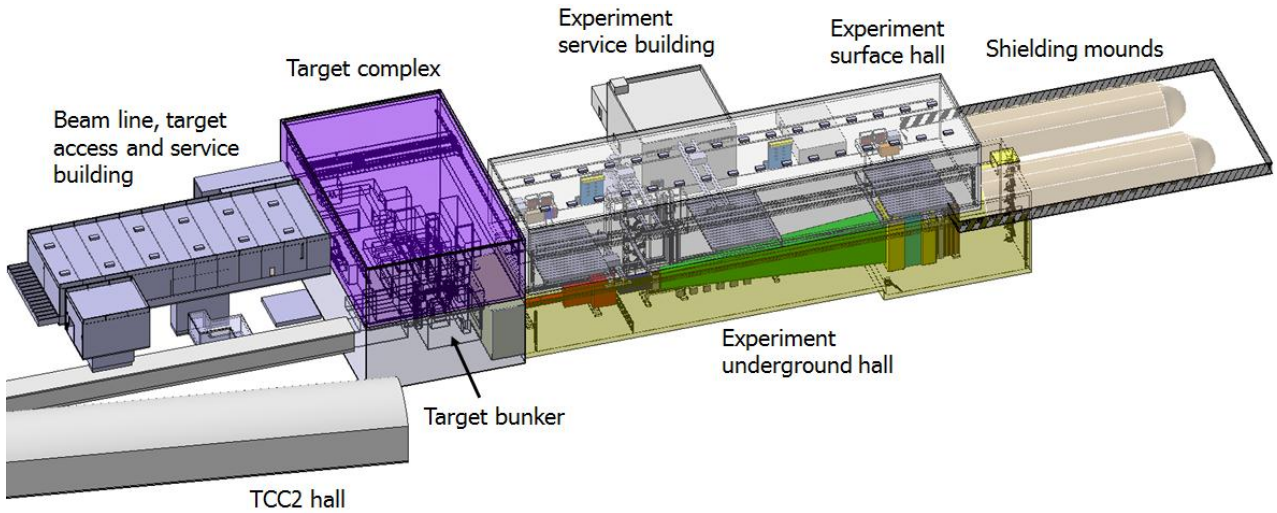


Fig. 4. Overview of the experimental area at the beam dump facility

5. SHiP physics performance

The physics performance of the SHiP experiment is anchored in the emphasis on an extremely efficient and redundant background suppression, and a detector which is sensitive to as many decay modes as possible to ensure a model independent search for hidden particles. A set of common benchmark models is used below to illustrate the physics performance to HS particle decays and to LDM, including the neutrino physics performance.

5.1. Hidden sector particle decays

All benchmark HS models predict a signature with an isolated vertex in the HS spectrometer. Hence, HS signal candidates are required to form an isolated vertex in the fiducial volume. For fully reconstructed signal decays, where all particles coming from the decaying hidden particle are reconstructed in the spectrometer, it is required that the impact parameter (IP) to the target is less than 10 cm. This selection cut is very powerful in rejecting all background sources. Partially reconstructed final states (with one or more missing particles, *e. g.* $N \rightarrow \mu^+ \mu^- \nu$) point back more loosely to the target. These final states are therefore more challenging to discriminate from the background. The signal candidates are required to have $IP < 250$ cm and, in addition, no associated activity in the SBT.

The background to the searches for hidden particles includes three main classes: neutrino and muon induced backgrounds resulting from inelastic interactions in the material of the detector and the cavern walls, and combinatorial muon background resulting from residual muons reconstructed as charged tracks in the SHiP decay spectrometer. As it was demonstrated in the SHiP TP [2, 3], backgrounds originating from cosmic muons can be reduced to a negligible level.

Large samples of neutrino and muon inelastic backgrounds, corresponding to about ten years and five years of SHiP nominal operation, respectively, have been generated using FairShip, forcing all produced neutrinos and muons to interact with the material. The interaction points were distributed along the neutrino and muon trajectories, with weights according to the material density along the tracks.

While the background rejection and signal sensitivities presented here rely on linear cuts, multivariate techniques can be expected to further improve the performance of the final experiment. The expected background to the HS particle search at 90% CL for $2 \cdot 10^{20}$ protons on target is quite small: < 1 event from neutrino background and $< 6 \cdot 10^{-2}$ events from muon background.

All signal sensitivities are obtained using the FairShip simulation framework [2, 4, 6, 7]. The 90% confidence region is defined as the region in the parameter space where on average $N_{\text{events}}^- \geq 2.3$ reconstructed

signal events are expected in the whole mass range, corresponding to a discovery threshold with an expected background level of 0.1 events.

5.2. Heavy neutral leptons

The neutrino portal consists of adding to the SM new gauge-singlet fermions – heavy neutral leptons (HNLs). Phenomenologically, HNLs are massive Majorana particles with mass M_N that possess “neutrino-like” interactions with W and Z bosons (the interaction with the Higgs boson does not play a role in our analysis and will be ignored). The interaction strength is suppressed as compared to that of ordinary neutrinos by flavour-dependent factors (known as mixing angles) $U_\alpha \ll 1$ ($\alpha = \{e, \mu, \tau\}$).

The dominant production channels for HNLs in the SHiP experiment occur through weak decays of flavoured mesons. For HNLs with masses $M \leq 500 \text{ MeV}/c^2$ kaon decays are the dominant production channel. While $O(10^{20})$ kaons are expected at SHiP, most of them are stopped in the target or hadron stopper before decaying. As a consequence, only HNLs originating from charm and beauty mesons are included in the estimation of the sensitivity below. Figure 5 shows the production rates of HNLs used in this analysis.

The production of HNLs through the decay of charm mesons dominates for HNL masses greater than the kaon masses. For HNL masses greater than charm meson masses, decays of beauty mesons are responsible for the production of HNLs at SHiP, as shown in Fig. 5. For masses $M_N \geq 3 \text{ GeV}/c^2$ the contribution of B_c may become important and even dominant.

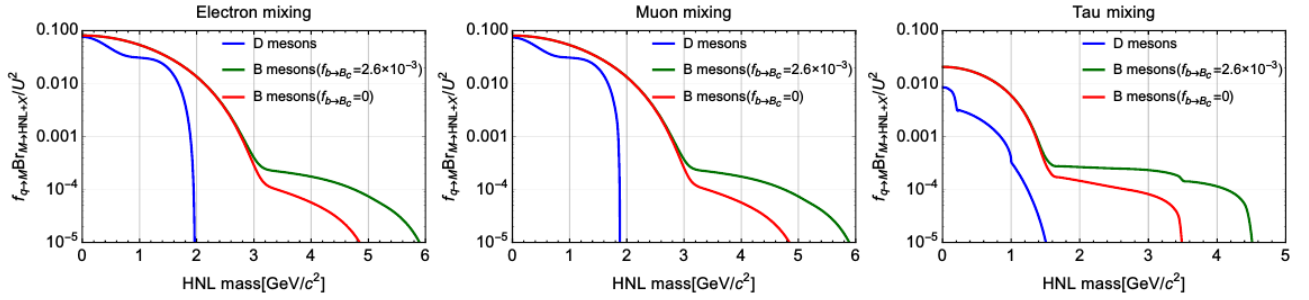


Fig. 5. Meson fragmentation fraction times branching fraction of meson decays to heavy neutral leptons as a function of the HNL mass. Contributions from D and B mesons are shown. To demonstrate the influence of B_c mesons, two cases are shown: the B_c fragmentation fraction at SHiP energies equal to that at the LHC energies: $f(b \rightarrow B_c) = 2.6 \cdot 10^{-3}$ (maximal contribution), and $f(b \rightarrow B_c) = 0$

The fraction of B_c mesons among all beauty mesons (*i. e.* the fragmentation fraction $f(b \rightarrow B_c)$) at SHiP energies is unknown. Given this uncertainty, two estimates were provided:

- Assuming that $f(b \rightarrow B_c)$ is the same as that at the LHC energies, $f(b \rightarrow B_c) = 2.6 \cdot 10^{-3}$.
- Assuming that $f(b \rightarrow B_c) = 0$.

The main decay channels of HNLs treated in this study are considered in Refs. [4, 7]. Signal events were simulated through FairShip for various masses and mixing angles U_i^2 with SM electron, muon, and tau neutrinos as input parameters. The sensitivity to various HNL benchmark models is estimated by applying the reconstruction and selection criteria [2, 4, 6, 7] for partially reconstructed final states.

When estimating the contribution from HNLs produced through decays of B_c mesons, the angular distribution of B_c mesons is taken to be the same as that of B^+ mesons, based on comparisons performed with the BCVEGPY and FONLL packages. The energy distribution is obtained by re-scaling the energy distribution of the B^+ meson to account for the mass difference with the B_c .

Figure 6 presents the sensitivity curve for HNLs, with the benchmark assumption that the ratio between the three HNL mixing angles corresponds to $U_e^2 : U_\mu^2 : U_\tau^2 = 0 : 1 : 0$. For completeness, both the conservative curves for the case $f(b \rightarrow B_c) = 0$, and the optimistic ones with $f(b \rightarrow B_c) = 2.6 \cdot 10^{-3}$ are shown in all sensitivity plots.

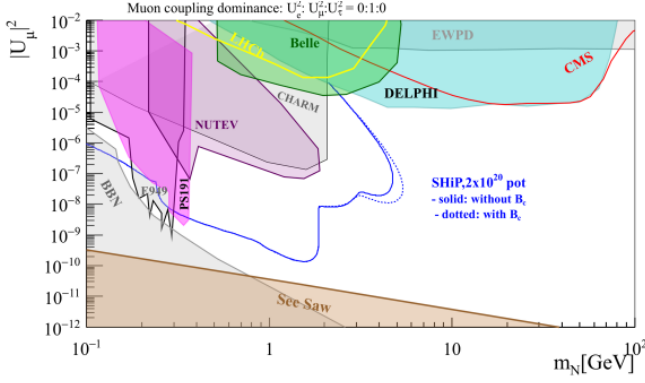


Fig. 6. Sensitivity curve for HNLs, with the benchmark assumption that the ratio between the three HNL mixing angles corresponds to $U_e^2 : U_\mu^2 : U_\tau^2 = 0 : 1 : 0$

5.3. Dark scalars

The scalar portal couples a gauge-singlet scalar S to the gauge invariant combination $H^\dagger H$ made of the SM Higgs doublet.

Further details on the phenomenology of the scalar portal are provided in Refs. [4, 7]. Dark scalars are produced from decays of kaons and B^\pm mesons [4, 7]. However, as discussed for the HNLs, kaons are mainly absorbed in the hadron absorber in SHiP, and here only the production *via* B mesons is considered.

The hadronic decay width of these scalars S is subject to large uncertainties for masses $M_S \approx 1 \text{ GeV}/c^2$, where neither chiral perturbation theory nor perturbative quantum chromodynamics (QCD) can provide reliable results.

The SHiP sensitivity is calculated within the FairShip simulation framework that allows us to apply the reconstruction and selection criteria described in Refs. [2, 6]. In contrast to the neutrino portal, the contribution of the dark scalar production through B_c -meson decays is negligible, thus there is no need to assess the B_c contributions to the sensitivity. The sensitivity of the SHiP experiment to dark scalars is shown in Fig. 7.

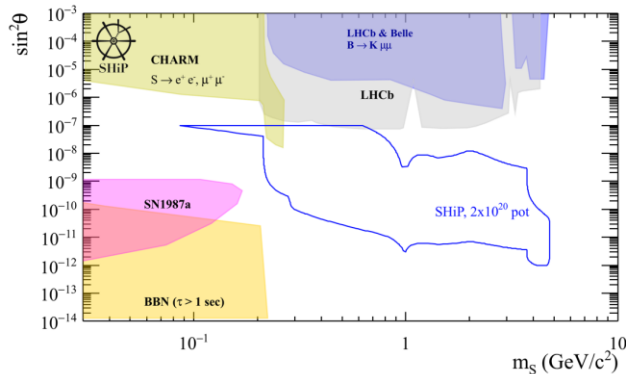


Fig. 7. Sensitivity of the SHiP experiment to dark scalars. Only the contribution from B mesons is taken into account

5.4. Dark photons

The minimal dark photon (DP) model considers the addition of a $U(1)$ gauge group to the SM, whose gauge boson is a vector field called the DP. A kinetic mixing between the DP and the SM $U(1)$ gauge bosons is allowed [7], with a reduced strength parameterized by a coupling ϵ , also called the kinetic mixing parameter. In its simplest form, the knowledge of the mass of the DP m_{DP} and the kinetic mixing parameter ϵ is enough to characterise the model and calculate the production cross section and decay properties (Fig. 8). Different mechanisms are possible for the production of such new particles at a fixed-target experiment. Three different modes are investigated for estimating the sensitivity of the SHiP detector (see Fig. 6) considering only the primary proton–proton interactions: initial proton bremsstrahlung, quark–antiquark annihilation, and meson decays (the cascade production, which is included for HNL and dark scalar, is ignored here).

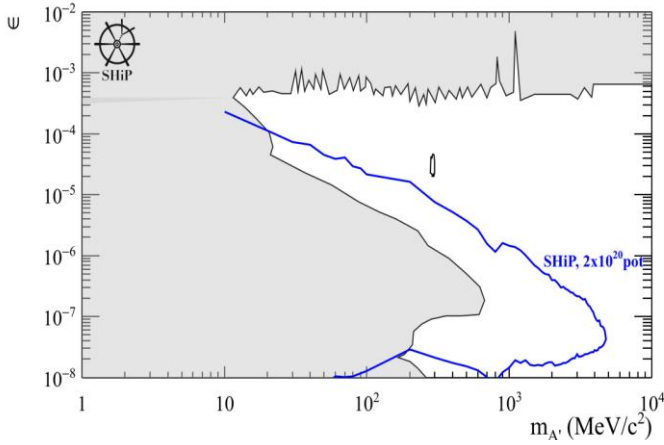


Fig. 8. Expected 90% exclusion region as a function of the dark photon mass and of the kinetic mixing parameter ϵ , for the three production modes studied

DP with masses below $0.9 \text{ GeV}/c^2$ can mix with photons from neutral meson decays (π^0 , η , ω , η'), that are produced in non-diffractive interactions. The PYTHIA 8.2 MC generator is used to obtain an estimate of the neutral meson production rate. For an incident beam momentum of $400 \text{ GeV}/c$ on fixed-target protons, the non-diffractive interactions represent 60% of the total proton–proton interactions. Branching ratios of mesons to dark photons are calculated according to Refs. [2, 7].

The proton–proton interaction can also lead to DP emission *via* a bremsstrahlung process, dominant for DP masses in the range $0.4\text{--}1.3 \text{ GeV}/c^2$. An approach identical to that of Refs. [2, 7] is followed to parameterize the probability density function for producing DPs with a given momentum and angle to the beam-line, and calculate the total production rate. Above this threshold, the dominant production mechanism happens through quark–quark annihilation into the DP. This process is simulated using the generic implementation of a resonance that couples both to SM fermion pairs and hidden particles as implemented in PYTHIA 8.2 under the “HiddenValley” Z' model [2, 7]. The native cross section from PYTHIA 8.2 is used for the normalization of the process.

5.5. Axion-like particles

Pseudo Nambu–Goldstone bosons can arise from spontaneously broken symmetries at high energies. A prime example is the axion introduced to solve the strong CP problem in QCD with mass $\sim 10^{-5} \text{ eV}$. The SHiP experiment is not sensitive to QCD axions, however other pseudoscalar particles can feature very similarly to axions but with larger masses. These hypothetical particles are known as axion-like particles (ALPs). Two cases were considered: the coupling of ALPs with photons and with fermions.

The ALPs coupling to fermions have an analogous production mechanism to that of dark scalars. The sensitivity for ALPs coupling to fermions, compared to previous experiments is shown in Fig. 9.

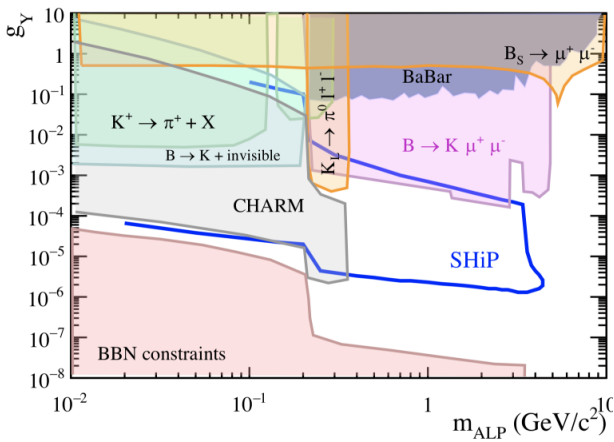


Fig. 9. SHiP sensitivity to axion-like particles coupling to fermions

5.6. Physics with neutrinos

The neutrino fluxes produced at the beam dump were estimated with FairShip, including the contribution from cascade production in the target. The number of charged-current (CC) deep-inelastic interactions in the neutrino target is evaluated by convoluting the generated neutrino spectrum with the cross section provided by GENIE. The distance of the scattering spectrometer from the downstream end of the proton target, as well as the compact transverse area of the emulsion target, reduce the flux to about 2 and 1% for electron and muon neutrinos, respectively. The acceptance for the ν_τ component amounts to $\sim 4\%$.

The nuclear emulsion technology combined with the information provided by the muon identification system makes it possible to identify the three different neutrino flavours in the SND. The neutrino flavour is determined through the flavour of the primary charged lepton produced in neutrino charged-current interactions. The lepton identification is also used to classify the tracks produced in the τ decay and therefore to identify the τ decay channel. In addition, the target magnetisation will allow for the first time to distinguish between ν_τ from anti- ν_τ . The available statistics will allow to test the lepton flavour violation in the neutrino sector. Also, with a few thousand ν_τ CC interactions in the scattering and neutrino spectrometer, the SHiP experiment can significantly constrain the ν_τ magnetic moment.

6. Project plan and cost

All sub-systems of SHiP have undertaken genuine programs of prototyping to validate their performance with beam tests of small scale prototypes. The results have been used in the simulation of the expected physics performance.

The next level of prototyping is ongoing and consists in the preparation of larger-scale prototypes aiming to measure their global performance in beam tests in 2021 and confirm the manufacturing techniques. This ensures validating the detector concepts in time for the technical design reports in 2022, and also serves as the basis for the cost and planning of the experiment. The engineering of the muon shield and the straw tracker, and the design of the calorimeter with the required angular resolution for the $ALP \rightarrow \gamma\gamma$ reconstruction, are considered to be particularly challenging projects.

The proposed schedule for both the SHiP experiment and the beam dump facility is largely driven by the CERN long-term accelerator schedule and the unique opportunity to fully exploit the current SPS in the LHC Run-4 and Run-5. At the same time it respects the technical constraints and the operating schedule of the CERN beam facilities during the construction. The civil engineering required for the beam dump facility is an important driver of the time to completion. The global time-line is shown in Fig. 10. It has been elaborated in collaboration with the Beam Dump Facility Working Group.

Accelerator schedule	2015	2016	2017	2018	2019	2020	2021	2022	2023	2024	2025	2026	2027
LHC		Run 2			LS2		Run 3			LS3		Run 4	
SPS											SPS stop	NA stop	
SHiP / BDF	Comprehensive design & 1st prototyping				Design and prototyping			Production / Construction / Installation					
Milestones	TP				CDS	ESPF		TDR	PRR				CwB

Fig. 10. Global project schedule for the beam dump facility and the SHiP detector. CDS, TDR, PRR mark the submission of the comprehensive design study report, submission of technical design reports and production readiness reviews for the SHiP detector, and CwB marks commissioning with beam

The schedule requires preparation of final prototypes and the TDRs for the detector by the end of 2022. The schedule foresees three years for the continued detector R&D, prototyping, and validation. With the past three years of comprehensive design study, and first prototypes of all subsystems already constructed and tested, this amount of time is considered sufficient with margins for financial delays. It is estimated that the detector production will require two to three years, and that the detector assembly and installation, including infrastructure, will require another two years. Most of the experimental facility can be constructed in parallel to operating all of the current beam facilities. However, to minimize the impact on the availability of beam in the CERN North Area during the connection of the facility to the existing beam line, and to fully profit from

the operation of the accelerators in the LHC Run-4, the last phase of civil engineering and installation of the facility and the SHiP detector is planned for the Long Shutdown 3, allowing commissioning and starting data taking early in Run-4.

A class 3 cost, about 59 million swiss francs estimate for the SHiP detector based on a detailed breakdown of each item in the conceptual design of the detector, was prepared for the TP [2, 3]. A new cost estimate is in preparation for the comprehensive design study report, which will be submitted in the second half of 2019. It is expected that the cost will remain within the uncertainty of the TP cost estimate.

7. The SHiP Collaboration

The SHiP Expression of Interest was submitted to SPSC in October 2013 [1]. This was followed by the TP submitted to the SPSC in April 2015 [2]. The SHiP TP was successfully reviewed by the SPSC and the CERN RB up to March 2016, with a recommendation to prepare a comprehensive design study report by 2019.

SHiP is currently a collaboration of 53 institutes and 4 associated institutes, in total representing 18 countries, CERN and JINR.

PNPI joined the SHiP project in 2014 since preparation of the SHiP TP [2]. PNPI team is involved in R&D of the SST, a key system of the SHiP experiment. Now PNPI scientists and engineers are busy with the SHiP comprehensive design study phase. In particular, they are taking part in SST optimisation of signal and background reconstruction, straw tube production R&D, SST gas system, and developing a conceptual design of the SST digital electronic readout for 18 000 channels.

8. Conclusion

The intensity frontier greatly complements the search for new physics at the LHC. In accordance with the recommendations of the last update of the European Strategy for Particle Physics, a multi-range experimental program is being actively developed all over the world. Major improvements and new results are expected during the next decade in neutrino and flavour physics, proton-decay experiments and measurements of the electric dipole moments. CERN will be well-positioned to make a unique contribution to exploration of the hidden-particle sector with the SHiP experiment at the SPS.

References

1. W. Bonivento *et al.*, arXiv:1310.1762.
2. SHiP Collaboration, M. Anelli *et al.*, Tech. Rep. CERN-SPSC-2015-016, SPSC-P-350 (2015), arXiv:1504.04956.
3. SHiP Collaboration, M. Anelli *et al.*, Tech. Rep. CERN-SPSC-2015-040, SPSC-P-350-ADD-2 (2015).
4. S. Alekhin *et al.*, Rep. Prog. Phys. **79**, 124201 (2016), arXiv:1504.04855.
5. SHiP Collaboration, A. Akmete *et al.*, JINST **12**, P05011 (2017).
6. SHiP Collaboration, C. Ahdida *et al.*, arXiv:1810.06880.
7. SHiP Collaboration, C. Ahdida *et al.*, arXiv:1811.00930.

PROJECT IRINA AT THE REACTOR PIK

V.N. Panteleev, A.E. Barzakh, L.Kh. Batist, D.V. Fedorov, V.S. Ivanov,
V.V. Lukashevich, P.L. Molkanov, M.D. Seliverstov

1. Introduction

The investigation of neutron-deficient and neutron-rich exotic nuclei at the edge of proton and neutron stability with ISOL (isotope separator on-line) methods is of great importance for many goals: for low energy nuclear physics studies, as nearly all information about the nuclear structure and nuclear state characteristics has been obtained by experiments at ISOL facilities; for astrophysics, where ideas about the creation of chemical elements in the universe and the evolution of stars can be tested experimentally by the interaction of a radioactive nuclear beam with a hydrogen target; for solid state physics, where the radioactive ion implantation is used to investigate material properties; and for modern medicine as well, providing a fast and harmless disease diagnostics and therapy.

Presently, about twenty ISOL facilities operate over the world, and new ones are constructed and projected to be built in the following decade. At the PNPI, the ISOL installation IRIS (investigation of radioactive isotopes at the synchrocyclotron) [1, 2] is operating for more than forty years. In systematic investigations carried out by the Short-Lived Nuclei Laboratory based on this facility, more than 300 nuclides were obtained and studied (17 of them were produced and investigated for the first time). For this long period, many new approaches and methods of production and investigation of short-lived isotopes were developed and applied at the IRIS facility. A decisive factor for efficient investigation of the nuclei very close to the stability border is the isobar purity of the isotopes under study. To provide isotope selective ionization of a range of elements, the resonance laser ionization in a hot cavity was applied [3, 4]. This method was developed and successfully used for the first time at the IRIS facility. It makes possible to get isobarically pure radioactive isotope beams of a large number of chemical elements.

The utilization of 1-GeV protons as projectile particles allows to produce mainly neutron-deficient nuclei, making use of different type of targets. There is a possibility to produce neutron-rich isotopes as well in the fission reaction of 1-GeV protons with ^{238}U . For this purpose, a high density uranium carbide target was developed and successfully used for production of neutron-rich isotopes of Ag, Cd, In, Sn, and others [5]. This target has demonstrated very good characteristics during prolonged (three months) on-line tests at a high working temperature (2 000–2 100 °C). Nevertheless, despite the rather successful utilization of the proton accelerator method [6, 7] for production of neutron-rich isotope, the use of a high flux of thermal neutrons from reactors allows to considerably increase the production yields of isotopes with a large neutron excess [8, 9]. In this case the target material containing ^{235}U should be used.

According to preliminary calculations, the yield of ^{132}Sn (double-magic, far from β stability), considered as a reference nuclide for ISOL facilities, at the neutron beam of the reactor PIK (thermal neutron flux of $3 \cdot 10^{13} \text{ cm}^{-2} \cdot \text{s}^{-1}$, target – 4 g of ^{235}U) can be of about 10^{11} particles per second. The operating ISOL systems IRIS (PNPI) and ISOLDE (CERN) are able to provide 10^7 and 10^8 of ^{132}Sn nuclides per second, correspondingly. The maximum yield of this isotope at the perspective ISOL installation SPIRAL-2 (GANIL, France) will not exceed 10^9 nuclides per second. At present, at PNPI (Gatchina), the project IRINA (investigation of radioactive isotopes with neutron facility) [9] of an ISOL installation for the high intensity exotic neutron-rich isotope production at thermal neutrons of the high flux reactor PIK is being developed.

The IRINA facility will provide the most intensive beams of neutron-rich nuclei in the world. A very important direction of the studies of neutron-rich exotic nuclei at the IRINA facility is the measurement of the ground state properties of short-lived nuclei (spins, mean square charge radii, electromagnetic moments, *etc.*), making use the method of the resonant laser spectroscopy in a laser ion source. Such a possibility is of great importance for the traditional area of the laser-nuclear spectroscopy application – for the isotope shift (IS) and hyperfine splitting (hfs) measurements. Mean square charge radii, spins and electromagnetic moments can be evaluated from these experimental data. It is planned also to build at one of the beam lines of the IRINA facility a system of Penning traps for precise mass measurements of nuclei lying extremely far from the β -stability line. With the high production efficiency of neutron rich nuclides at the IRINA facility,

we can get a chance to investigate very interesting areas of nuclei with anomalously short life-times. Additionally, there is a plan to construct a special ion beam of the IRINA mass-separator for production of high purity isotopes with rather long life-times, which can be utilized for solid-state physics and for nuclear medicine purposes. The use of the high-flux neutron reactors for these purposes looks very promising.

2. IRINA facility project

A schematic view of the IRINA set-up with the laser ionization complex in the experimental hall of horizontal channels of the reactor PIK is presented in Fig. 1. One of the main parts of IRINA is an isotope mass-separator. A target-ion source device of the mass-separator is placed inside the reactor channel HEC (horizontal experimental channel) 5-5' on the thermal neutron flux of $(3-5) \cdot 10^{13} \text{ cm}^{-2} \cdot \text{s}^{-1}$. This neutron flux irradiates the target material and heats it up to 2200–2400 °C. The power emission as a result of about 10^{14} fissions per second in the 4 g of ^{235}U (90% enrichment) target is close to 3 kW. As the planned target position is about 0.9 m from the central point of the channel HEC 5-5', there is a principal possibility to increase the neutron flux through the target by almost one order of magnitude. But in that case a very serious problem with a power dissipation of about 30 kW should be solved.

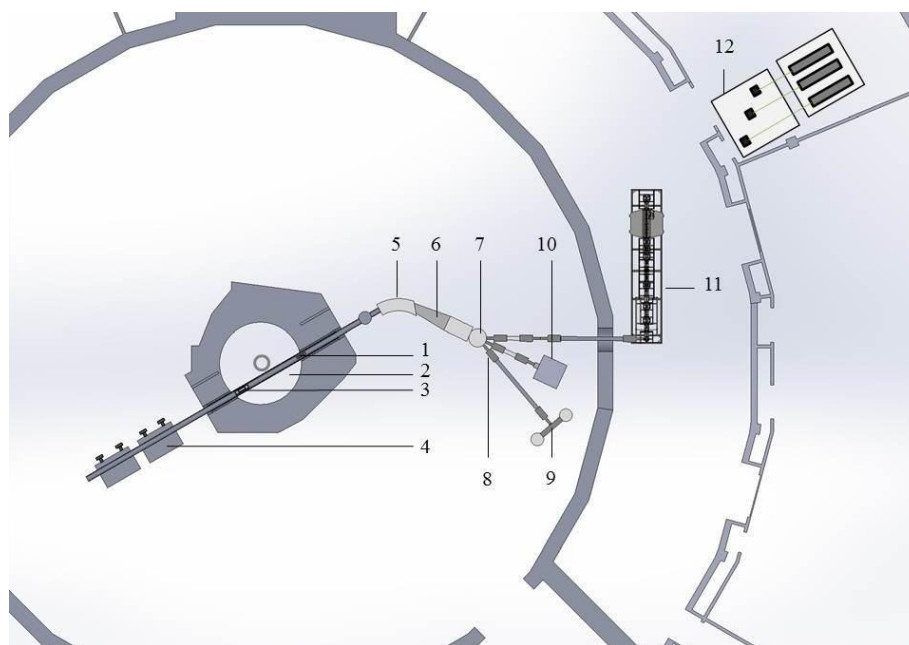


Fig. 1. Layout of the IRINA facility at the experimental hall of the PIK reactor: 1 – ion beam focusing system; 2 – water tank of the reactor; 3 – ion source-target unit; 4 – hot cells; 5 – mass-separator magnet; 6 – collector chamber; 7 – switchyard; 8 – ion beam lines; 9 – tape moving system; 10 – neutron detector; 11 – system of Penning traps; 12 – laser installation

The IRINA facility functioning at the thermal neutron beam of the reactor PIK can be described as follows. Fission products (atoms of neutron-rich isotopes) are thermally released at a high temperature (2200–2400 °C) from the target material and due to diffusion and effusion processes reach the ion source cavity. The produced ions are extracted from the ion source and accelerated by extraction–acceleration electrical field and are formed into a beam with a divergence of about $2 \cdot 10^{-2}$ rad. After that, the ion beam passing the focusing lens is transferred into a parallel one. The formed parallel beam enters into the mass-separator magnet normally to the magnetic field lines and is focused in the vertical and horizontal planes. The ion beam cross-section in the focal plane of the mass-separator magnet is about 1 mm (in the vertical plane) and 1.5 mm (in the horizontal plane). The central trajectory curvature in the magnetic field is equal to $R = 1500$ mm and provides the distance between the neighbour masses equal to $D = R/A$, mm (A is a mass number). For instance, for $A = 100$ the dispersion will be $D \approx 15$ mm. The mass range in the focal plane

is $\pm 15\%$ of the central mass (the mass in the centre of the focal plane). For example, the mass range in the tin region is from the mass number 110 to 150.

The mass-separated ion beams are transported from the collector chamber to the bending and beam distribution chamber – the vacuum chamber with two cylindrical capacitors bending the ion beam at $+30^\circ$ and -30° from the unbent central beam trajectory. The selected ion beams are directed to the experimental hall with the ion guide systems. Focusing triplets of electrostatic lenses are installed along the ion beam lines to focus the ion beam to detection posts of the experimental set-up. The ion beam cross-sections in the implantation point is about $2 \times 2 \text{ mm}^2$. The vacuum system should provide the air pressure of about $(2-4) \cdot 10^{-6} \text{ mbar}$ in all parts of the mass-separator. The ion beam transmission from the ion source to the detection posts should be in the range of 60–90% (depending on the type of the ion source and on the beam focusing quality).

All ion beam lines are connected to the corresponding experimental set-ups. The first ion guide will be supplied with an ion trap for high precision mass measurements (detection post 2 in Fig. 1). Using the ion trap system, where a Penning trap is used for the mass measurement, it is possible, as has already been shown, to obtain the mass determination accuracy of $\delta m/m \approx 1 \cdot 10^{-7}$ even for half-lives as short as a few hundred milliseconds.

A neutron 4π detector for registration of delayed neutrons will be installed on the second ion guide (detection post 1 in Fig. 1). A fast tape station with α , β , and γ detectors for identification and investigation of rare isotopes will be placed at the third ion guide. All the detection posts, the tape station and the mass-separator will be controlled with a mainframe computer.

3. Target-ion source unit development for the IRINA facility

As a prototype of the combined target-ion source for the IRINA mass-separator, the target construction developed at the IRIS facility will be used as an effective high-temperature target unit for on-line production of short-lived radioactive isotopes. The construction of the target unit allows to avoid cold spots usually arising in the target-ion source assemblies in the places of connections of the target with the transfer tube and the transfer tube with the ion source. The peculiarity of the developed target unit is the absence of the ion source [10] since the ionization process occurs in the target volume itself. This allows to avoid an additional time delay due to atoms travel inside the transfer tube and the ion source. This target construction could be especially useful for production of short-lived isotopes of elements with a long sticking time, such as isotopes of Co, Ni, Sn, and other hard volatile elements. The only difference will be the change of the tantalum foils to the mono carbide of ^{235}U of a high density as a target material. The use of a tungsten container instead of a traditional tantalum one allows to rise the target working temperature up to 2500°C , thereby decreasing the delay time for nuclides produced in the target and hence increasing the yield of short-lived isotopes. A high temperature of the target material and the absence of cold spots in the target volume are crucial for effective production of isotopes of many refractory elements delayed in the target volume in the effusion process.

A schematic diagram in Fig. 2 shows the high-temperature ionizing target which was used for off-line and on-line tests at the IRIS facility. The target container was made of a very tightly rolled multi-layer tungsten foil and had a wall thickness of 0.2–0.3 mm. From both sides it was closed by tantalum plugs with holes to extract the ions (*right*) and to introduce the laser beam (*left*) into the target volume. The dimensions and geometry of the integrated target-ion source used for off-line and on-line tests were the following: the length – 45 mm; the outer tungsten container diameter – 12 mm; the inner tantalum cylinder diameter – 10 mm; the ion extraction hole diameter – 1.5 mm; the diameter of the hole for the laser beam – 2 mm.

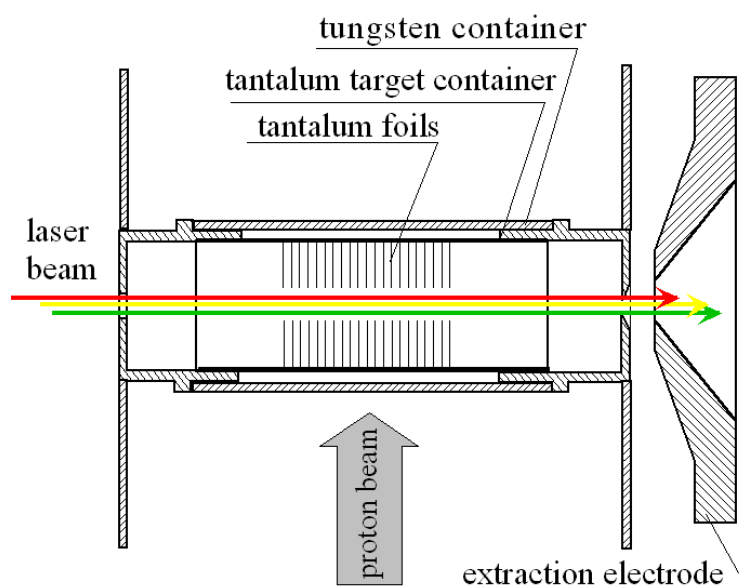


Fig. 2. Scheme of the high-temperature ionising target used in the course of off-line and on-line experiments. The target temperature was varied in the interval 2 000–2 500 °C

The diameter of the axial hole in the tantalum foils for the laser beam was 3 mm. For the resonance laser ionization tests, three laser beams from the IRIS laser installation [8] brought together were introduced into the target container through the hole in the left tantalum plug and directed along the target central axis.

4. Target material investigation for the IRINA facility

During the latest thirty years, at the ISOL facilities there was a trend of developing fast uranium carbide targets for on-line production of rare nuclides. Since the beginning, a growing interest in the development of uranium carbide targets was stimulated by the study of exotic neutron-rich nuclei far from the line of stability produced in fission reactions of ^{238}U by high-energy protons. In addition, these targets allow to produce a wide range of neutron-deficient heavy nuclei by means of fragmentation and spallation reactions. Presently, an increasing request for targets containing large fractions of ^{238}U has been enhanced by new projects concerning ISOL facilities with intensive proton beams as projectile particles. At the IRINA facility, as it was pointed above, 4 g of ^{235}U (90% enrichment) in the form of the uranium mono carbide will be exposed by a beam of thermal neutrons. As the physical and chemical properties of the target material do not depend on the particular uranium isotope used in the target, preliminary target tests were carried out at the proton beam of the IRIS facility with the targets containing ^{238}UC of a high density. The targets for the IRINA facility will be prepared from the identical target material containing a highly enriched ^{235}U . For the targets we used a special uranium carbide with the density of 11 g/cm³, that is rather close to its theoretical monocrystal value (13.6 g/cm³) [7]. In order to measure their characteristics, long term tests of about three months were carried out at the IRIS facility. The yields and delay times were obtained, which demonstrated reproducibility of the relevant values after three month heating of the target at the temperature 2 000–2 100 °C. In Figure 3, the photos of the discs and the surface structure of the utilized uranium carbide target material are shown.

In Figure 4, a comparison of the production efficiencies of francium isotopes with half-lives in the interval 0.005–1 000 s from the IRIS and ISOLDE uranium carbide targets are presented. In the graph, in the vertical axis the values of the production efficiency and in the horizontal axis the inverted values of the half-life period are plotted.

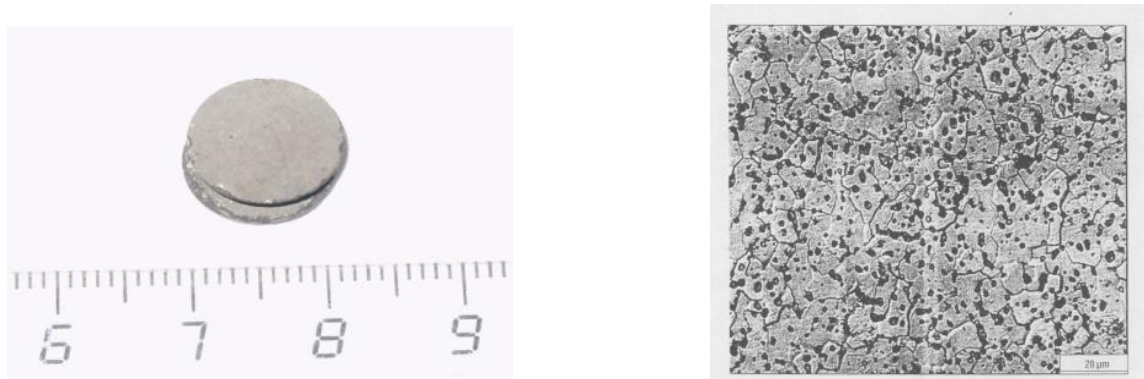


Fig. 3. Photos of the discs (*left*) and the surface structure of the uranium carbide target material with the 1 000 times of microscope magnification (*right*) are presented

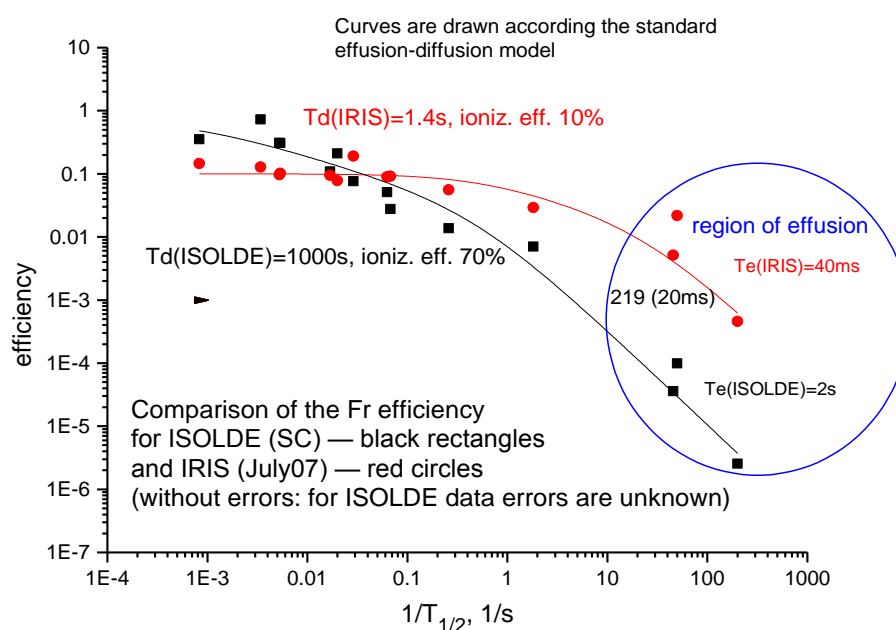


Fig. 4. Production efficiencies of francium isotopes with half-lives in the interval 0.005–1 000 s from the IRIS and ISOLDE uranium carbide targets: *abscissa axis* – the inverted values of the half-life $T_{1/2}$; *ordinate axis* – the values of the production efficiency

As we can see in Fig. 4, the delay characteristics of the IRIS mono carbide high density target (diffusion and effusion delay times) are much shorter than similar characteristics of the ISOLDE uranium carbide target. The IRIS target gives two orders of magnitude higher yields for short-lived francium isotopes in the millisecond region of isotope half-lives. Additionally, in a series of off-line and on-line experiments carried out at the IRIS facility, it was demonstrated that the target can be maintained for more than 2 400 h at a temperature of about 2 100 °C without appreciable changes in its main characteristics. This result is very important, as the developed target will be utilized at the reactor beam during the reactor working cycle, which is about one month period. Another important result is good reproducibility of the yields and release times of the investigated nuclides for a long period of the target maintenance. Thus, at present we consider this target with the described target material as a good prototype of the designed target unit for the IRINA facility.

5. Outline of the physical program at IRINA

In Figure 5, the expected production rates for different isotopic chains with the IRINA ^{235}U target are presented. In our experiments at ISOLDE and IRIS, it was shown that IS/hfs measurements with the laser ion source are possible at the production rate as low as 10^{-1} – 1.0 s^{-1} . Taking into account possible decay losses, one may consider the isotopes with the expected production rate larger than 1 – 10 s^{-1} as probable objects of investigations. Below in Fig. 5, the isotopes with the corresponding production rates are considered as “accessible at IRINA”.

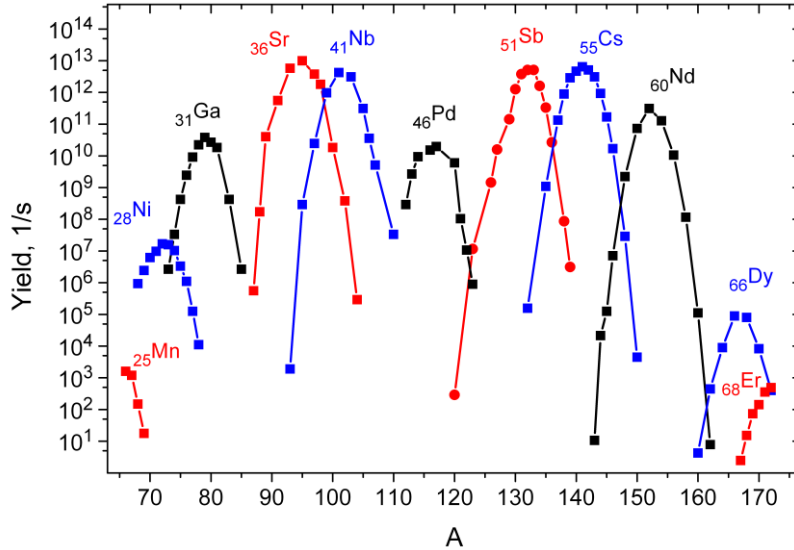


Fig. 5. Estimated production rates for several isotopic chains in the target of the IRINA installation

The following trends in the scientific activities of the Short-Lived Nuclei Laboratory at IRINA are the most interesting and important.

5.1. Astrophysical applications

Neutron-rich nuclei with $Z = 25$ – 68 accessible at IRINA, provide the nuclear characteristics which are very valuable for the models of astrophysical processes ($T_{1/2}$, mass, βn -decay branching, *etc.*). Due to the extremely low production rate, the investigation of these nuclides should be carried out against the background of isobars with the production rates by some order of magnitude higher than that for the isotopes under study. Hence, the isobaric selectivity obtained by using a laser ion source becomes crucial. Such exotic nuclei as $^{144, 145}\text{Te}$, ^{142}Sb , ^{140}Sn , and ^{129}Ag near the r -process path are expected to be accessible at IRINA. Especially interesting are the so called r -process waiting points, ^{129}Ag , ^{128}Pd , ^{78}Ni , with the yet unknown βn -decay branching and possible long-lived isomers. The following isotopes important for astrophysics are also expected to be accessible: ^{95}Se , at the production rate $\sim 10^2\text{ s}^{-1}$, $^{98}\text{Br} \sim 10^3\text{ s}^{-1}$, $^{101}\text{Kr} \sim 10^4\text{ s}^{-1}$, $^{103}\text{Rb} \sim 10^5\text{ s}^{-1}$, $^{106}\text{Sr} \sim 10^3\text{ s}^{-1}$, and $^{109}\text{Y} \sim 10^3\text{ s}^{-1}$.

5.2. Shell evolution far from stability

The problem of shell evolution for the far from stability nuclides has the fundamental significance. Recently obtained data point to the change of the magic number values for exotic nuclei (^{24}O , ^{54}Ca , ^{32}Mg , ^{42}Si , *etc.*). This leads to a considerable revision of the magic-number concept itself. A new magic number at $N = 90$ is predicted for Sn (and, possibly, for Sb) isotopes. These isotopes will be achievable at IRINA.

Detailed nuclear-spectroscopic investigations of the shell evolution far from stability are of primary importance. Apart from the change of the magic numbers, the shell quenching and the shell swap occur, for

example, in the Cu chain. There are some indications that such phenomena might be explained by introducing $3N$ forces. At IRINA, we will be able to check the existence of the same phenomena near $Z = 50$ and to continue investigations near $Z = 28$ (Cu, Ga...).

5.3. Laser spectroscopy

We are going to continue measurements of the ground state properties of short-lived nuclei (spins, changes in the mean-square charge radii, the electromagnetic moments, *etc.*) by the laser spectroscopy at IRINA. Similar experiments for neutron-deficient nuclides were successfully realized by our team at the IRIS and ISOLDE facilities.

One of the most interesting objects of the laser-nuclear spectroscopy is the study of the shell-closure effect in the mean-square charge radii of the far from β -stability nuclides, *i. e.* the kink in the mean square charge radius isotopic dependency at the neutron

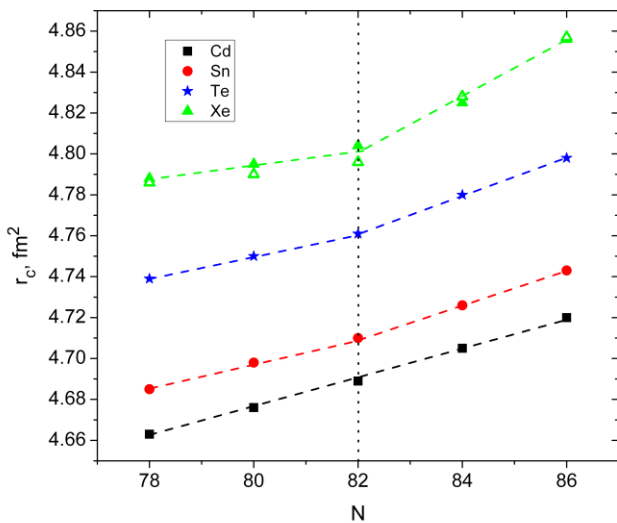


Fig. 6. Prediction of the disappearance of the shell effect in radii at $N = 82$

magic number. The relativistic mean field approach predicts the disappearance of the shell effect for Ni (at $N = 50$) and Cd and Sn (at $N = 82$; Fig. 6) [11]. At IRINA, we will be able to study these isotopic chains to check the theory predictions (^{28}Ni up to $N = 52$; ^{30}Zn up to $N = 56$; ^{32}Ge up to $N = 57$; ^{48}Cd up to $N = 86$; ^{49}In up to $N = 87$; ^{50}Sn up to $N = 89$; ^{51}Sb up to $N = 90$; ^{52}Te up to $N = 92$).

Information on the magnetic moments in the corresponding isotopic chains is of importance for shell evolution studies (*cf.* discussion in Ref. [12]).

The laser spectroscopy is also a powerful tool for investigations of the shape evolution and shape coexistence. The corresponding phenomena are known (or expected) near $N = 60$ (Ru, Se, Br, Kr...) and in some other regions. This field of research is one of the most challenging for nuclear theory. At IRINA, the corresponding isotopes will be accessible.

5.4. Example of a proposal for a possible experiment at IRINA

The Sb isotopic chain may be considered as a possible object of investigation. An analysis of the expected production rate (Fig. 7) shows that the mass range $A = 120$ – 141 ($N = 69$ – 90) will be accessible for measurements. An efficient ionization scheme (Fig. 8) for Sb atoms has been found. During such experiments, single particle states near $N = 82$ can be explored, the presence of the shell effect in the radii and magnetic moments at $N = 82$ will be checked and the corresponding parameters will be determined to reveal a possible Z dependence of the shell effect, the hypothesis about the new $N = 90$ magic number will be tested, the relevant properties of the r -process nuclides $^{140, 141}\text{Sb}$ are expected to be determined, the shell-evolution effects will be searched, *etc.*

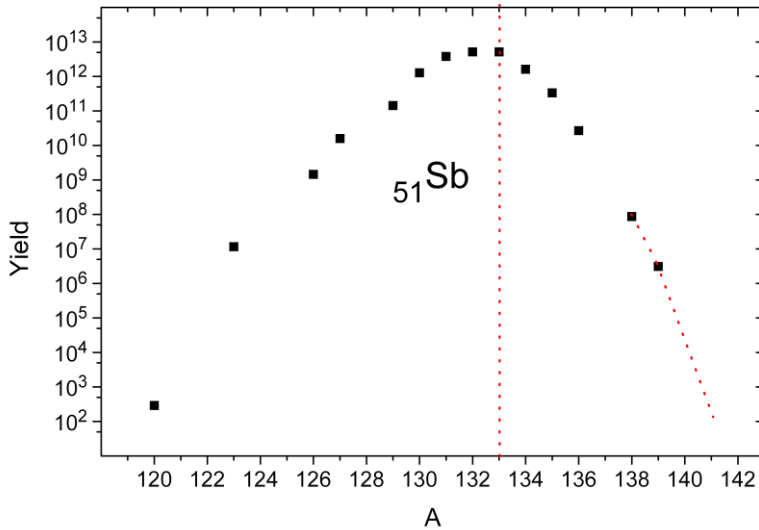


Fig. 7. Estimated production rates for the Sb isotopic chain at the IRINA installation

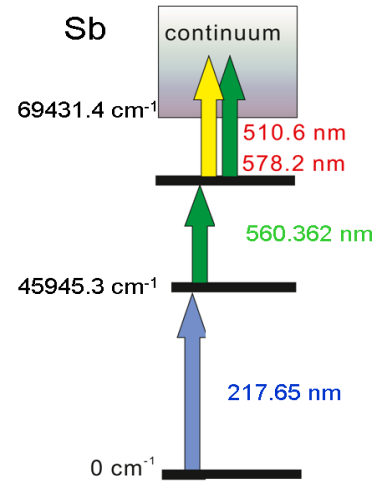


Fig. 8. Ionization scheme for the Sb isotopes

6. Conclusion

The project IRINA at the reactor PIK opens up new opportunities for production and research of neutron rich nuclei. It will be able to compete with and in some cases to surpass the current and projected ISOL installations. The combination of the mass-separator with the laser resonance ionization facility enables one to overcome the inevitable difficulties in these investigations due to a low production rate of most exotic nuclei. The Penning trap technique will allow to measure with a very high precision a large survey of the mass surface of extremely neutron rich nuclei far from the β -stability region.

References

1. E.Ye. Berlovich *et al.*, *Izv. Akad. Nauk SSSR, Ser. Fiz.* **40**, 2036 (1976).
2. V.N. Panteleev *et al.*, *Rev. Sci. Instrum.* **73** (2), 738 (2002).
3. G.D. Alkhazov *et al.*, *Nucl. Instrum. Meth. A* **306**, 400 (1991).
4. A.E. Barzakh *et al.*, *Rev. Sci. Instrum.* **83**, 02B306 (2012).
5. A. Andrighetto *et al.*, *Nucl. Instrum. Meth. Phys. Res. B* **204**, 267 (2003).
6. H.L. Ravn, *et al.*, *Nucl. Instrum. Meth. B* **70**, 107 (1992).
7. V.N. Panteleev *et al.*, *Nucl. Instrum. Meth. Phys. Res. B* **240**, 888 (2005).
8. J.A. Pinston, *et al.*, *Nucl. Instrum. Meth. Phys. Res. B* **126**, 22 (1997).
9. V.N. Panteleev *et al.*, *PNPI. High Energy Physics Division. Main Scientific Activities 2007–2012*, Gatchina, 2013, pp. 274–277.
10. V.N. Panteleev *et al.*, *Eur. Phys. J. A* **26**, 147 (2005).
11. S.E. Agbemava, A.V. Afanasjev, D. Ray, P. Ring, *Phys. Rev. C* **89**, 054320 (2014); Supplemental Material at <http://link.aps.org/supplemental/10.1103/PhysRevC.89.054320>
12. K.T. Flanagan *et al.*, *Phys. Rev. Lett.* **103**, 142501 (2009); U. Köster *et al.*, *Phys. Rev. C* **84**, 034320 (2011).

PITRAP PROJECT AT THE PIK REACTOR

Yu.I. Gusev, V.S. Gusel'nikov, S.V. Chenmarev, S.A. Eliseev, P.E. Filyanin, T.V. Koneva, D.A. Nesterenko, Yu.N. Novikov, A.W. Popov, D. Simonovski

1. Introduction

The advancement of fundamental nuclear physics requires the study of the properties of nuclides far from the β -stability line. This exploration started about 50 years ago and manifested as a goal of the study of the structure of asymmetric (in terms of the nucleon composition) nuclides. These studies have now acquired special interest, because the methods for obtaining and studying nuclides make it possible to reach the borders encompassing the nuclides that participate directly in different explosive astrophysical processes. The success in experiments with nuclides with an exotic proton/neutron composition depends on the intensity of the primary beam, as well as the sensitivity of the measuring set-up. The PIK reactor is a high-flux facility [1], and for this reason it is a powerful producer of such exotic nuclides. A Penning ion trap is an ultrasensitive apparatus capable of operating with a single ion. The combination of PIK and a Penning ion trap provides a unique possibility for studying exotic nuclei. Penning ion traps are widely used to solve different physical problems [2]. The Penning ion-trap systems ISOLTRAP (CERN), SHIPTRAP (Germany), JYFLTRAP (Finland), LEBIT (USA), and TITAN (Canada) operate in combination with particle accelerators and are intended for direct measurements of the mass of radionuclides. The TRIGATRAP (Germany) set-up includes Penning traps placed in a secondary beam of a reactor. The PITRAP-project proposed at the PNPI incorporates many years of experience gained by the authors of the present project on some of the set-ups listed above.

2. Physical problems

The primary block of problems of the plan involves direct on-line high-precision measurements of the mass of exotic short-lived nuclides, whose beams can be obtained by irradiating internal or external targets in the PIK reactor. It is expected that the high productivity will make it possible to cover wide regions of the nuclide map and obtain unique information with the nuclear-physical and astrophysical content.

Exotic nuclei play an important role in different astrophysical processes, which encompass a nuclide mass region far from the valley of stability. For fast neutron capture (r process) the density distribution of neutron-excess isotopes having N and $N + 1$ neutrons is expressed by the relation [3]

$$\log \frac{n(Z, N+1)}{n(Z, N)} = \log n_n - 34.07 - \frac{3}{2} \log T_9 + \frac{5.04}{T_9} S_n,$$

where $n(Z, N)$ is the density of nuclei with Z protons and N neutrons; n_n is the density of neutrons; T_9 is the temperature, 10^9 K; S_n is the neutron separation energy, MeV. This equation relates the astrophysical parameters (neutron density and temperature of the stellar medium) and the nuclear parameter – the separation energy of a neutron in nuclei, which depends on the mass difference of the nuclei. The latter quantity determines the path of the process under prescribed astrophysical conditions. For this reason, the nuclide mass becomes the key quantity that sets the path of the r process. It is important to know the true “nuclide path” of this process in order to determine the parameters characterizing the explosion of a star. The mass of nuclides in the initial and middle regions of the r process at $N = 50$ and $N = 82$, which are important for determining and studying the starting path of this astrophysical process, can be measured at the PIK reactor [1].

The mass of a nucleus, which is directly related with the total binding energy of nucleons, is one of the fundamental characteristics reflecting the sum of all nucleonic interactions in a nucleus. The behaviour of the separation energy of two neutrons S_{2n} and two protons S_{2p} makes it possible to investigate the shell structure of nuclei. The measurement of nuclear masses in long isotopic and isotonic chains makes it possible to study the fine structure of the mass shell and to determine its singularities more accurately in order to

extract information on the nuclear structure and the existence of closed shells and new magic numbers. An important question in direct measurements of the nuclear mass in the study of the nuclear structure is the possibility to resolve the isomeric and ground states by energy. For example, in Ref. [4] the mass doublet ^{164}Er – ^{164}Dy with the mass difference $Q = 25.07(12)$ keV was resolved by the method of octupole excitation in a Penning trap; the attained resolution was about $2 \cdot 10^7$. A new method of phase determination of the cyclotron frequency, which makes it possible to reach a higher resolution, was also adopted in the SHIPTRAP set-up [5]. These methods can be used in PITRAP to study the isomeric states of nuclides. A large volume of new information on the masses of nuclides that can be obtained in a PITRAP will allow to improve the parameterization of the empirical mass formulas with the further possibility of using them directly to predict even more exotic regions of nuclides.

Another block of problems is associated with high-precision off-line measurements of stable or long-lived radionuclides. These nuclides can be produced by irradiating targets in the PIK reactor. The measurements can be performed in a trap independently of the operation of the reactor. High-precision measurements of the masses of stable and long-lived nuclides open up an entire strata of problems in fundamental physics ranging from neutrino physics to cosmochronology. One such problem is the search for candidate nuclides on neutrinoless double-electron capture. Such a search requires measuring the mass difference of stable nuclides with an error ≤ 100 eV. These measurements allow us to detect the energy degeneracy of the parent and daughter atomic states which leads to a resonance in the probability of neutrinoless double-electron capture, backed by the law of nonconservation of the lepton number and the Majorana type neutrino [6]. Another direction of the research related to the determination of the neutrino mass involves the use of the long-lived nuclides ^{157}Tb , ^{163}Ho , and ^{202}Pb produced in the PIK reactor in neutron capture reactions for precise measurements of their decay and determination of the neutrino mass in combination with the results of measurements of the atomic de-excitation following the orbital electron capture by means of cryogenic microcalorimetry [7].

3. Production and transportation of exotic nuclei

The nuclides formed by irradiation of targets in the PIK reactor can be extracted by several methods:

- 1) using a system for transportation of fission products in a gas stream outside of the reactor core by means of aerosols followed by ionization of atoms and delivery of ions into a trap (similar to TRIGATRAP [8]),
- 2) using a “cold target” in the area of the reactor core in combination with the IGISOL-type mass separation [9],
- 3) using a “hot target” together with the IRINA mass separator [10].

Two alternative variants (1) and (3) are examined in the present work.

The planned arrangement of PITRAP in the PIK reactor complex is shown in Fig. 1. A capillary with the carrier gas and aerosols delivering the reaction products is connected to the chamber where a skimmer, an ion source, and extracting electrodes are located. If the IRINA separator is used, an ion-optical channel is placed in this location. The magnet which turns the ion beam into the PITRAP channel and also performs the selection by mass is located farther.

The nuclide production rate with unknown or poorly studied masses is presented in Table in cold and hot target variants. The thermal neutron flux is taken to be $I_n = 3 \cdot 10^{13} \text{ cm}^{-2} \cdot \text{s}^{-1}$ in both cases. The variant with a cold target is supposed to be used in combination with a gas stream. In this case the target consists of a ^{235}U metal foil with thickness 20 mg/cm^2 and area 150 cm^2 ; the target mass is 2 g. The power release in the target is approximately 1.5 kW. The target is cooled by water circulating in a closed loop.

A hot target is used in the variant with the mass separator [10]. It consists of ^{235}U carbide in the form of a cylinder. The target mass in terms of uranium is 4 g, the effective area is 5.1 cm^2 , and the working temperature is 2300–2600 K. It is evident from Table that the productivity of the two types of targets is approximately the same.

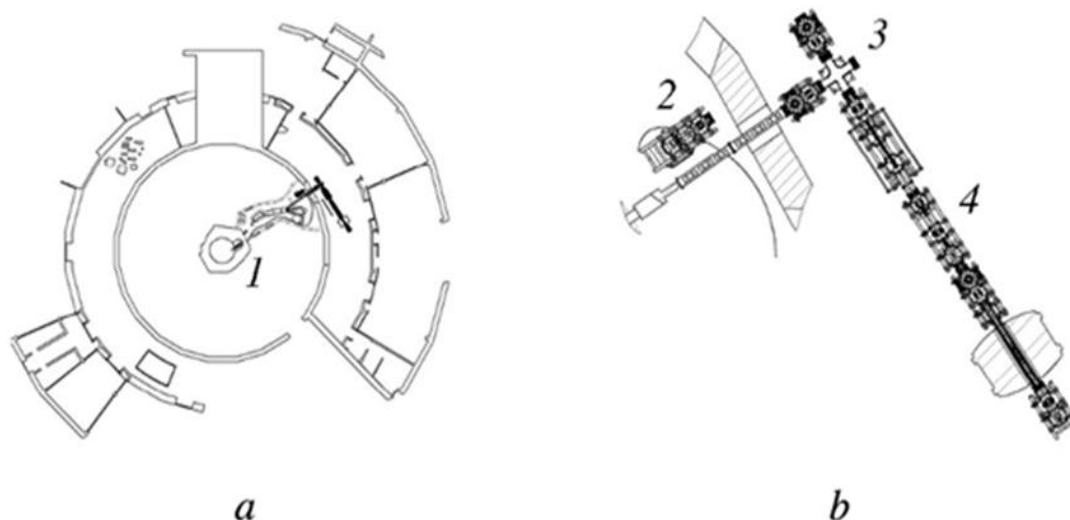


Fig. 1. Arrangement of the set-up in the measuring room of the PIK reactor facility (a); in enlarged view, the part pertaining to PITRAP (b): 1 – reactor core; 2 – extracting electrodes; 3 – magnet; 4 – PITRAP channel

Table

Isotope expected yields from cold and hot targets in the PIK reactor

Nuclide	Z	$T_{1/2}$, ms [11]	Yield per fission	Production rate, s^{-1}	
				cold target	hot target
^{74}Ni	28	680(\pm 120)	$5.0 \cdot 10^{-8}$	$5.4 \cdot 10^6$	$7.5 \cdot 10^6$
^{78}Cu	29	335(\pm 11)	$8.3 \cdot 10^{-8}$	$9.0 \cdot 10^6$	$1.2 \cdot 10^7$
^{80}Zn	30	550(\pm 11)	$3.6 \cdot 10^{-6}$	$3.9 \cdot 10^8$	$5.4 \cdot 10^8$
^{84}Ga	31	85(\pm 10)	$1.7 \cdot 10^{-7}$	$1.8 \cdot 10^7$	$2.6 \cdot 10^7$
^{85}Ge	32	540(\pm 50)	$2.4 \cdot 10^{-5}$	$2.6 \cdot 10^9$	$3.6 \cdot 10^9$
^{87}As	33	610(\pm 120)	$1.1 \cdot 10^{-4}$	$1.2 \cdot 10^{10}$	$1.7 \cdot 10^{10}$
^{91}Se	34	270(\pm 50)	$6.9 \cdot 10^{-6}$	$7.5 \cdot 10^8$	$1.0 \cdot 10^9$
^{93}Br	35	102(\pm 10)	$1.9 \cdot 10^{-5}$	$2.1 \cdot 10^9$	$2.9 \cdot 10^9$
^{95}Kr	36	114(3)	10^{-4}	$1.1 \cdot 10^{10}$	$1.5 \cdot 10^{10}$
^{100}Rb	37	48(\pm 3)	$3.9 \cdot 10^{-8}$	$4.2 \cdot 10^6$	$5.9 \cdot 10^6$
^{102}Sr	38	69(\pm 6)	$4.8 \cdot 10^{-7}$	$5.2 \cdot 10^7$	$7.2 \cdot 10^7$
^{102}Y	39	298(\pm 9)	$1.1 \cdot 10^{-4}$	$1.2 \cdot 10^{10}$	$1.7 \cdot 10^{10}$
^{130}Cd	48	162(\pm 7)	$7.3 \cdot 10^{-6}$	$7.9 \cdot 10^8$	$1.1 \cdot 10^9$
^{133}In	49	165(\pm 3)	$3.1 \cdot 10^{-6}$	$3.3 \cdot 10^8$	$4.7 \cdot 10^8$
^{134}Sn	50	1 050(\pm 11)	$1.3 \cdot 10^{-4}$	$1.4 \cdot 10^{10}$	$2.0 \cdot 10^{10}$
^{136}Sb	51	923(\pm 14)	$2.1 \cdot 10^{-3}$	$2.3 \cdot 10^{11}$	$3.2 \cdot 10^{11}$
^{138}Te	52	1 400(\pm 400)	$9.4 \cdot 10^{-4}$	10^{11}	$1.4 \cdot 10^{11}$
^{141}I	53	430(\pm 20)	$2.1 \cdot 10^{-4}$	$2.3 \cdot 10^{10}$	$3.2 \cdot 10^{10}$
^{145}Xe	54	188(\pm 4)	$3.7 \cdot 10^{-6}$	$4.0 \cdot 10^8$	$5.6 \cdot 10^8$
^{148}Cs	55	146(\pm 6)	$1.6 \cdot 10^{-7}$	$1.7 \cdot 10^7$	$2.4 \cdot 10^7$
^{150}Ba	56	300	$5.9 \cdot 10^{-7}$	$6.4 \cdot 10^7$	$8.9 \cdot 10^7$
^{150}La	57	510(\pm 30)	$1.1 \cdot 10^{-4}$	$1.2 \cdot 10^{10}$	$1.7 \cdot 10^{10}$

A method similar to the one implemented in the TRIGATRAP set-up [8] for transportation of the products outside of the reactor core can be used in the PITRAP project [12]. The fission products in the chamber holding a target in the form of ^{235}U metal foil with a thickness of about 10 μm and a nickel coating will be thermalized in a buffer gas, for example, in helium at a pressure of 0.2–0.3 MPa. Then they are secured to aerosol particles, for example, KCl, PbCl_2 , CO_2 , and C_2H_4 , and extracted through a capillary tube with an inner diameter equal to about 1 mm. Aerosols deliver the reaction products together with the carrier gas within a flexible capillary several meters long to a unit with a source of ions. The gas stream passes through a differentially evacuated skimmer system, where up to 90% of the carrier gas is separated and pumped out with a Roots pump. Upon leaving the capillary, the stream diverges into a cone, whose aperture will be larger for a lighter carrier gas than for aerosol particles carrying fission products, and the skimmer “cuts out” this small cone. Next, the aerosol particles with the nuclides of interest enter the tungsten ionization tube, whose temperature reaches 2300 K, where ionization occurs. Then the ions are extracted and accelerated by the subsequent electrodes. The expected efficiency of the removal of the isotopes through the capillary up to the ion source is 50–70%. The ionization efficiency depends on the type of the ion source as well as on the particular isotope and can vary from 0.1 to 10%. The details of this method can be found in Ref. [12].

The second proposed variant uses a massive hot target [10]. It is proposed that the target material in the form of ^{235}U carbide with the mass of 4 g in a graphite capsule is placed in a hermetic rhenium or tungsten container in the horizontal channel of the reactor. The entire assembly is located in an evacuated volume cooled by distilled water. In the working regime with the neutron flux intensity $3 \cdot 10^{13} \text{ cm}^{-2} \cdot \text{s}^{-1}$ through the target its temperature should not exceed 2500 K at the melting temperature of the target substance of about 2800 K. The ion source (the surface ionization variant) consists of a tungsten tube, heated to 2600 K either by direct current or by electron bombardment. In the case of ionization by electron impact, a variant of a plasma ion source, specially developed for the operating conditions in an intense neutron flux, will be used. The mass-separator system has been designed for the accelerating voltage to 50 kV. The collector chamber is followed by a chamber for separating the ion beams where three turning cylindrical condensers are supposed to be located followed by three ion channels equipped with focusing electrostatic quadrupole lenses for transportation of three mass-separated ion beams into the experimental low-background room. The dimensions of the ion beam are about $2 \times 2 \text{ mm}^2$ at the locations where the ion channels are connected with experimental facilities. The transmission of the beam from the ion source to the experimental facilities is supposed to be 60–90%. The vacuum in the entire system of the mass separator must be no worse than $(2\text{--}4) \cdot 10^{-4} \text{ Pa}$. One ion channel will be connected with the turning magnet (unit 3 in Fig. 1) for deflecting the ion beam to PITRAP.

4. PITRAP set-up

The proposed variant of PITRAP is displayed in Fig. 2. After the ion source magnet (1) turns the ion beams by 90° ; the ions are directed into the deceleration section in front of a gas-filled radio frequency quadrupole, where they are moderated and focused. Cooling and accumulation of ions occurs in the gas-filled radio frequency quadrupole (2). Next, a group of ions enters a pulse cavity, where their potential is reduced to the required value and directed into the time-of-flight (ToF) mass-analyzer (3), which can operate as a mass-spectrometer for fast measurement of the ion mass or as a mass-separator for additional purification of the ion beam by removal of undesirable impurities. Next, a group of ions in the operating regime of a ToF mass-separator is transported toward a system of Penning traps, located in the superconducting magnet (4), for precision mass measurement. An ion source for test measurements or experiments in the off-line regime can be located in front of the turning magnet (1). The ions obtained in them can be deflected by quadrupole deflectors and focused into the system of Penning traps.

The moderated beam of ions is fed into the radio-frequency quadrupole filled with a buffer gas (helium) at $\sim 1 \text{ Pa}$ pressure. The radio-frequency quadrupole consists of four segmented rods to which a radio-frequency voltage is applied in order to keep the ions in the radial plane. A constant voltage can also be applied to the segments of rods in order to form an electric field along the axis of the system, having the minimum potential in the region of the penultimate segments. Colliding with molecules of the buffer

gas, the ions lose kinetic energy and accumulate at the minimum of the potential. Thus, a group of ions, which after reduction of the potential on the last segments of the rods is extracted from the radio-frequency quadrupole, is formed. Most of the elements of the radio-frequency quadrupole are supposed to be arranged on a high-voltage platform surrounded by a mesh (see (2) in Fig. 2) The longitudinal emittance of a 2.5 keV beam after the quadrupole will be $10 \text{ eV} \cdot \mu\text{s}$ and the transverse emittance $\sim 10 \pi \cdot \text{mm} \cdot \text{mrad}$. The cooling time in the gas-filled radio-frequency quadrupole is about 10 ms. The potential of the effluxing group of ions is lowered by means of a pulsed change of their potential energy in the pulse cavity, comprising a tube on which the voltage is switched as the group of ions flies through it.

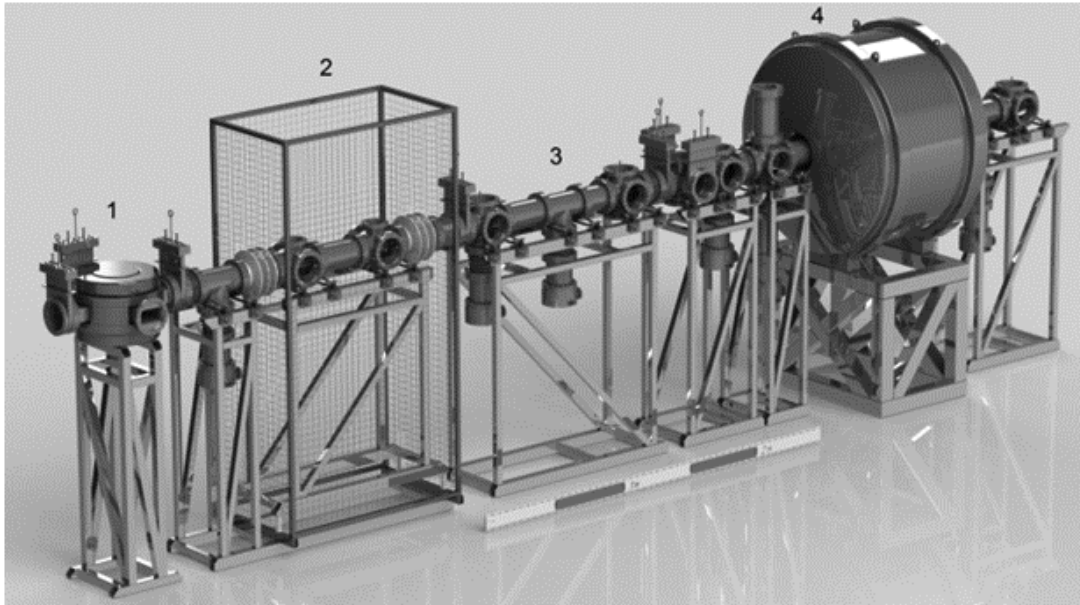


Fig. 2. Model of the measuring facility based on a Penning ion-trap: 1 – magnet; 2 – gas-filled radio frequency quadrupole; 3 – time-of-flight mass-analyzer; 4 – superconducting magnet

5. Time-of-flight mass-analyzer and Penning traps system

After the pulse cavity, the group of ions is directed toward the ToF mass-analyzer, which consists of two electrostatic mirrors separated by a 460-mm long field-free drift space (see (3) in Fig. 2) [10, 13]. The electrostatic mirrors are in an antiparallel arrangement, making it possible to repeatedly reflect the group of ions thereby increasing their path length.

The ToF t_i of an ion on one and the same path depends on its mass-to-charge ratio $t_i \propto v_i^{-1} \propto (m_i/q_i)^{1/2}$, where v_i is the ion velocity, q_i its charge, and m_i its mass. Thus, groups of ions with different mass can be separated in time at the detector if the time between them is larger than the width of their proper signals. The resolution of the mass-analyzer with the optimized voltage on the electrodes reaches $2 \cdot 10^5$. The ToF mass-analyzer can be used to determine the composition of the ion beam and for fast measurement of the ion mass.

After the ToF mass-analyzer, the ions are transported by means of electrostatic lenses and deflectors to the Penning traps (see (4) in Fig. 2). It is proposed that a variant with two cylindrical traps arranged in one tube of a superconducting magnet (7 T; analog of the SHIPTRAP set-up [14]) be used. Two centres of the greatest uniformity of the magnetic field, which are determined by the magnet, correspond to the centres of the traps. The first preparatory trap, intended for mass-selective cooling of the ions in the buffer gas, is filled with helium at the working pressure $\sim 10^{-4}$ Pa. It permits separation of ions with a definite charge-to-mass ratio. The second trap, intended for high-precision mass measurements, is evacuated to high vacuum 10^{-6} – 10^{-7} Pa. A 1.5 mm in diameter diaphragm separates the traps. They are evacuated by separate turbo pumps arranged along both sides of the magnet. It is planned to use the ToF ion cyclotron resonance method [15], as well as the phase method of determining the cyclotron frequency [5].

6. Conclusion

The record intensity of the neutron flux of the PIK reactor at PNPI in combination with the ion trap technique of high sensitivity and precision opens up prospects for multifunctional studies in different areas of science. The proposed design, which includes two Penning ion traps in tandem, is considered for their use on-line with secondary beams, as well as off-line for studies of fission products and products of neutron capture reactions. The first variant is of the greatest interest for studying exotic neutron-rich nuclides with direct measurement of their mass for determining the true path of a fast multiple-neutron capture process in astrophysics. This r process is assumed to be responsible for creation of chemical elements in nature. Its “nuclide” path can be determined uniquely in a ground-based laboratory only by precise measurement of masses of large regions of exotic nuclides. Possibilities for using ion traps in the interests of atomic and neutrino physics by means of high-precision measurements of the mass difference of long-lived and stable isotopes of chemical elements open up in the off-line measurement regime. The technical working up of the design takes account of this multifaceted nature of the problems. The design of PITRAP was developed using years of experience gained in working with different ion traps in foreign laboratories. This experience will also be helpful for developing the first Penning ion trap for fundamental physics exploration in our country. The technical design project is presented in Ref. [16].

We are grateful to A.A. Vorobiev for stimulating the work on the Penning ion trap design at PNPI. We are also grateful to K. Blaum (Max Planck Institut für Kernphysik in Heidelberg) and M. Block (GSI Helmholtzzentrum für Schwerionenforschung – FAIR in Darmstadt) for their interest in the project and for fruitful discussions. We thank A.A. Vasil’ev, V.F. Ezhov, A.N. Erykalov, K.A. Konoplev, V.N. Panteleev and V.V. Fedorov for a discussion of the possibilities of practical implementation of the project.

References

1. K.A. Konoplev, *Main Scientific Results of PNPI in 2000–2004*, Gatchina, 2005, pp. 18–23.
2. K. Blaum, Yu. Novikov, G. Werth, *Contemp. Phys.* **51**, No. 2, 149 (2010).
3. E. Burbidge, G. Burbidge, W. Fowler, F. Hoyle, *Rev. Mod. Phys.* **29**, 547 (1957).
4. S. Eliseev, C. Roux, K. Blaum *et al.*, *Phys. Rev. Lett.* **107**, 152501 (2011).
5. S. Eliseev, C. Roux, K. Blaum *et al.*, *Phys. Rev. Lett.* **110**, 082501 (2013).
6. S. Eliseev, Yu. Novikov, K. Blaum *et al.*, *J. Phys. G: Nucl. Part. Phys.* **39**, 124003 (2012).
7. H.-J. Kluge, Yu. Novikov, *Nucl. Phys. News* **17**, No. 4, 48–50 (2007).
8. J. Ketelaer, J. Krämer, D. Beck *et al.*, *Nucl. Instrum. Meth. A* **594**, 162 (2008).
9. A.G. Dernjatın, K.A. Mezilev, Yu.N. Novikov, A.W. Popov, *Projects Planned at the Reactor PIK on 1991–1995*. PNPI, Abstracts (1991).
10. V. Panteleev, A. Barzakh, D. Fedorov *et al.*, *PNPI. High Energy Physics Division. Main Scientific Activities 2007–2012*, Gatchina, 2013, pp. 274–277.
11. G.G. Audi, F. Kondev, M. Wang *et al.*, *Chinese Phys. C* **41**, No. 3, 030001 (2017).
12. D. Simonovski, Yu.I. Gusev, Yu.N. Novikov *et al.*, *At. Energy* **125**, 338 (2018).
13. R. Wolf, D. Beck, K. Blaum *et al.*, *Nucl. Instrum. Meth. A* **686**, 82 (2012).
14. M. Block, D. Ackermann, K. Blaum *et al.*, *Eur. Phys. J. D* **45**, 39 (2007).
15. M. König, G. Bollen, H. Kluge *et al.*, *Int. J. Mass Spectrom. Ion Proc.* **142**, 95 (1995).
16. Yu.N. Novikov, Yu.I. Gusev, S.A. Eliseev *et al.* Report No. F-310. B.P. Konstantinov NRC “Kurchatov Institute” – PNPI, Gatchina, 2016.

NEUTRINO OSCILLOMETRY AND PROPOSAL OF THE OMNIBUS EXPERIMENT

Yu.N. Novikov, M.V. Smirnov

in collaboration with K.K. Loo, W.H. Trzaska, J.D. Vergados, M. Wurm

1. Introduction

A statement that neutrino oscillates, *i. e.* changes its flavour during its spread in space, was made in the experiments which observed the “appearance” or “disappearance” of the effects caused by neutrinos at the place of the detector. As a matter of fact, this statement was based on the observation of results triggered by oscillations. At the same time, the full oscillation curve, *i. e.* point-by-point flavour appearance and disappearance, was never observed. The most precise and unambiguous way to measure neutrino oscillations would be to determine changes in the flux of the given flavour of neutrinos over the entire oscillation length. Since the oscillation length is inversely proportional to the neutrino mass squared difference, its proper observation would require a detector of a few hundred or thousand kilometers in length if used with the present or proposed “active flavour” neutrino beams, or one should observe the high energy cosmic neutrinos! As this is unrealistic, all beam experiments aiming at active neutrino oscillations consider just a single or at most two point measurements.

The discovery of neutrino oscillations, being one of the greatest triumphs of physics, cannot answer many questions on the neutrino properties: How large is the neutrino absolute mass value? What can we say on the neutrino mass hierarchy? Are neutrinos Dirac or Majorana particles? Is the total lepton number conserved? Could we expect *CP* as well as *CPT* violation in the lepton sector? How many, if any, sterile neutrinos are there, *etc.* The answers to these questions will, perhaps, be given in future challenging experimental and theoretical investigations.

Determination of the phase of the *CP* violation in the leptonic sector was the main goal of the two largest and most ambitious neutrino experiments proposed so far: Large Apparatus studying Grand Unification and Neutrino Astrophysics (LAGUNA) – Long Baseline Neutrino Oscillation (LBNO) in Europe and Deep Underground Neutrino Experiment (DUNE) – Long Baseline Neutrino Facility (LBNF) in the USA. Discovery of the *CPT* violation in the neutrino sector would be of even more fundamental importance, but there are currently no coordinated plans to search for it. Equally significant would be verification of the sterile neutrino hypothesis and, if it is confirmed, determination of the relevant oscillation parameters.

It was shown by the Russian–Finnish–German team [1] that both the *CPT* and *CP* violation together with the search for sterile neutrinos can be probed in one do-it-all experiment. Such OMNIBUS experiment can be utilized only by the so called neutrino oscillometry with preferably large liquid scintillator detectors (like LENA [2], JUNO [3], or RENO-50 [4]).

2. Neutrino oscillometry

The name “oscillometry” was firstly introduced in Ref. [5]. It means the observation of both neutrino flavour appearance and disappearance in one experiment within the dimensions of a single detector. The oscillometric approach was elaborated later in detail in Refs. [6–8].

The method is based on the following four pillars: 1) small neutrino energy, 2) big dimensions (length) of the detector, 3) strong neutrino source, 4) well-known and controlled background.

1. It is a well-known fact that the oscillation length scales linearly with the neutrino/antineutrino energy. For instance, in the well-known case of the mixing angle θ_{13} , the formula may be reduced to a very simple form: $L_{13} \text{ (m)} \approx E_\nu \text{ (keV)}$. It means that 300 keV neutrinos have the oscillation length of only about 300 m. This example shows that even for active neutrinos a large detector with good sensitivity at low energies would be able to register a significant part of the oscillation curve instead of performing measurements only at the near and far locations, as it is the case for the proposed long- and mid-baseline oscillation experiments.

2. Of the three main technologies proposed for giant neutrino observatories – water Cherenkov, liquid argon time projection chamber (TPC), and liquid scintillator (LSc) – only the LSc technology due to the low threshold for electron neutrino elastic scattering has the required sensitivity in the sub-MeV range.

JUNO [4], scheduled for commissioning in 2020, will have 20 kton fiducial mass and 34.5 m diameter while the proposed detector LENA [3] aims at 50 kton inside of a 100 m long cylinder with the radius of 14 m. RENO-50 [5] proposes a 30 m diameter, 30 m high cylinder.

3. Successful applications of the neutrino oscillometry require energy selection and a well-defined source position. For these reasons, the experiment cannot rely on natural neutrino sources such as the Sun, the Earth or cosmic neutrinos. Also, the use of nuclear power reactors is excluded, as it would not allow to reach the required accuracy in determination of the oscillation parameters. The best alternatives are provided by man-made, high-intensity β -decaying radioactive sources emitting electron neutrinos and antineutrinos in the energy range of about 1 MeV. The ^{51}Cr nuclide is a most suitable source of practically monoenergetic electron neutrinos. It decays with $T_{1/2} = 27.7$ days *via* electron capture. The monochromatic ~ 750 -keV neutrinos come from the 90.1% branching ratio to the ground state of ^{51}V . The expected activity at the start can be of the order of 300 PBq. The main measure is the neutrino elastic scattering on the electrons of the target. For the electron antineutrinos there are no monoenergetic sources but the continuous antineutrino spectrum characteristic of the β decay gives an additional advantage using the inverse β decay – the “golden” detection channel, which is very suitable for the LSc. In this case, the favorite choice is the ^{144}Ce – ^{144}Pr mother–daughter combination providing detectable neutrinos with energies in the 1.8–3 MeV bin accounting for 48.5% of the emitted electron antineutrinos. The half-life of the source is determined by ^{144}Ce with $T_{1/2} = 258$ days. The daughter nucleus decays with $T_{1/2} = 17$ min. The expected activity at the start of the measurement is around 4.6 PBq.

4. All possible sources of the background for this approach should be investigated carefully. The level of the background should be minimized as much as possible.

The existence of sterile neutrinos was proposed to explain anomalies in short-baseline accelerator experiments as well as in gallium-based solar neutrino experiments. Anomalies were also reported in the reactor neutrino spectra at short distances. There is still no solid evidence for the existence of sterile neutrinos. One of the anticipated features of sterile neutrinos should be a very short oscillation length ($L_{14} \approx 1$ m) as compared to the known active neutrino flavours. This makes sterile neutrinos very well suited for oscillometric studies. If the length of the detector L is much larger than the oscillation length L_{14} , then many patterns of the oscillation curve can be observed. As, for instance, if the neutrino source (^{51}Cr) is installed on the top of a long detector, the recoil electrons from the neutrino scattering will be detected when the neutrino flavour is associated with the electron neutrino. The signals from the electron will be strongly damped along the length of the detector when the flavour is changed. This behaviour of the oscillometry curve was investigated in Ref. [6]. The advantage of the use of long detectors with $L \gg L_{14}, L_{15} \dots$ is that the mixed oscillometry curves for many possible sterile neutrino schemes can be decomposed.

3. Proposed OMNIBUS experiment

If the *CPT* principle is strictly conserved, the oscillation of neutrinos and antineutrinos of a given flavour would be described by identical mixing angles and mass-squared differences. Precise measurements of these values both for electron neutrinos and antineutrinos will be the key outcome of the proposed experiment.

Multiple oscillation patterns within the active volume of the detector in the proposed experiment would indicate the existence of sterile neutrinos. Lack of such patterns would allow us to set new stringent limits for the existence of right-handed neutrinos, but it would also exclude the possibility to probe the *CPT* violation. The main goal of the proposed experiment is to measure and compare oscillation parameters obtained for electron neutrinos (^{51}Cr source) and electron antineutrinos (^{144}Ce – ^{144}Pr). If there are differences, the *CPT* symmetry has been clearly violated. However, if no differences are observed, the opposite conclusion cannot be derived, as there are many other ways to break that symmetry. In fact, most current theories concerning *CPT* violation do not anticipate particle/antiparticle mass asymmetries [9]. Nevertheless, this is exactly the point that we propose to verify. It is also worthwhile to notice that finding asymmetry in the survival probability between electron neutrinos and antineutrinos would indicate not only the *CPT* violation, but also the *CP* violation [1].

Investigation details are described in Ref. [1]. We have considered two scenarios: 1) placing of a strong radioactive source in the centre of JUNO [4] – a spherical detector, 2) placing of a source on the top of

LENA [3] – a cylindrical detector (Fig. 1). While the first option is the best as far as detection efficiency and symmetry are concerned, the second is considerably easier to realize, as the integrity of the LSc tank does not have to be compromised. Actually, the variant of a cylindrical detector with the source outside of the active volume is a simplification of the spherical case using hemisphere as a sensitive volume. A big advantage of the cylindrical detector is the possibility to install neutrino and antineutrino sources on the top and bottom of the long cylinder, correspondingly, for the simultaneous measurements.

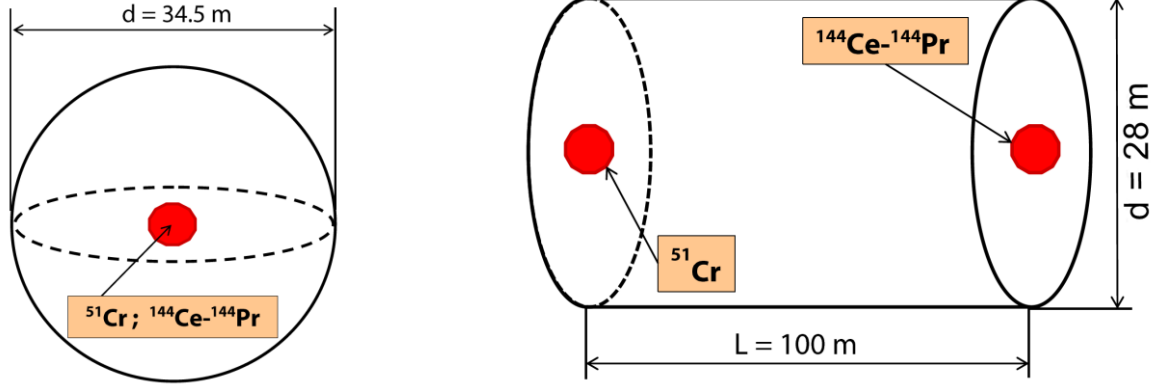


Fig. 1. Experimental geometries: the source is located in the centre of a spherical detector (*left panel*); the source is located on the top of a tall, cylindrical detector (*right panel*). The dimensions and other key parameters were taken from the specifications provided for JUNO and LENA

The proposed experiment will be sensitive to two of the new oscillation parameters associated with the sterile neutrinos (for the most probable scenario $3 + 1$): θ_{ee} and Δm_{41}^2 . The accuracy of the amplitude measurements is limited by statistical fluctuations of the event rate. For that reasons, also the extracted θ_{ee} will be known, though with a relatively poor accuracy. We expect to observe up to 10 oscillation minima (for neutrinos) and 3 (for antineutrinos). Since Δm_{41}^2 corresponds to the frequency of the oscillation curve, we can measure it more precisely than the mixing angle. Thus, in the current research the sensitivity is associated only with Δm_{41}^2 . It allows to search for anomalies indicated as the mass asymmetry between neutrino and antineutrino. Our analysis is based on a comparison of two event spectra: with oscillation of sterile neutrinos and without oscillations. The ratio of these spectra should give us the probability function. The confidence level was obtained on the basis of minimization of the probability function as a fit-function of two parameters (θ_{ee} and Δm_{41}^2). A Gaussian distribution for errors of oscillation parameters was assumed. The impact of the background was taken into account in calculations. This analysis was implemented using the ROOT package MINUIT 2.

Figure 2 illustrates the expected event spectrum from neutrino and antineutrino sources including statistical fluctuations in the JUNO detector.

At the present stage, we have limited the phase space of oscillation parameters used for the calculations to the immediate vicinity of the values indicated by the current global fit: $\Delta m_{41}^2 = 1 \text{ eV}^2$ and $\sin^2(2\theta_{ee}) = 0.1$. For the mass parameter, the range is from 0.4 to 5.0 eV^2 . For the $\sin^2(2\theta_{ee})$ we have used two fixed values: 0.1 and 0.05. The calculations were made for two detector geometries: a sphere (JUNO) with the source in the centre (*left panels* of Fig. 3), and a cylinder (LENA) with the source on the top (*right panels* of Fig. 3). The active volumes were a sphere with $R = 17.25 \text{ m}$ for JUNO and a semi-sphere with $R = 14 \text{ m}$ for LENA. In the case of JUNO, the energy resolution of 3% for 1 MeV and position resolution of 9 cm (neutrino) and 4.5 cm (antineutrino) were assumed. For LENA, 6.1% for 1 MeV, 10 cm (neutrino), and 4.5 cm (antineutrino) were used, respectively.

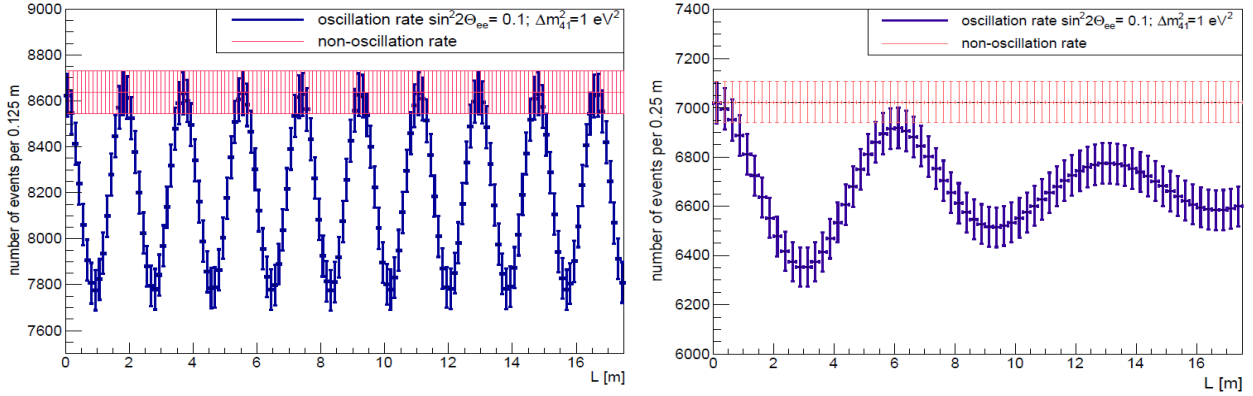


Fig. 2. The expected event rate in the JUNO detector [1]: the total rate for the ^{51}Cr source, time of measurement is 55 days (*left panel*); the total rate for the ^{144}Ce - ^{144}Pr source, time of measurement is 300 days (*right panel*)

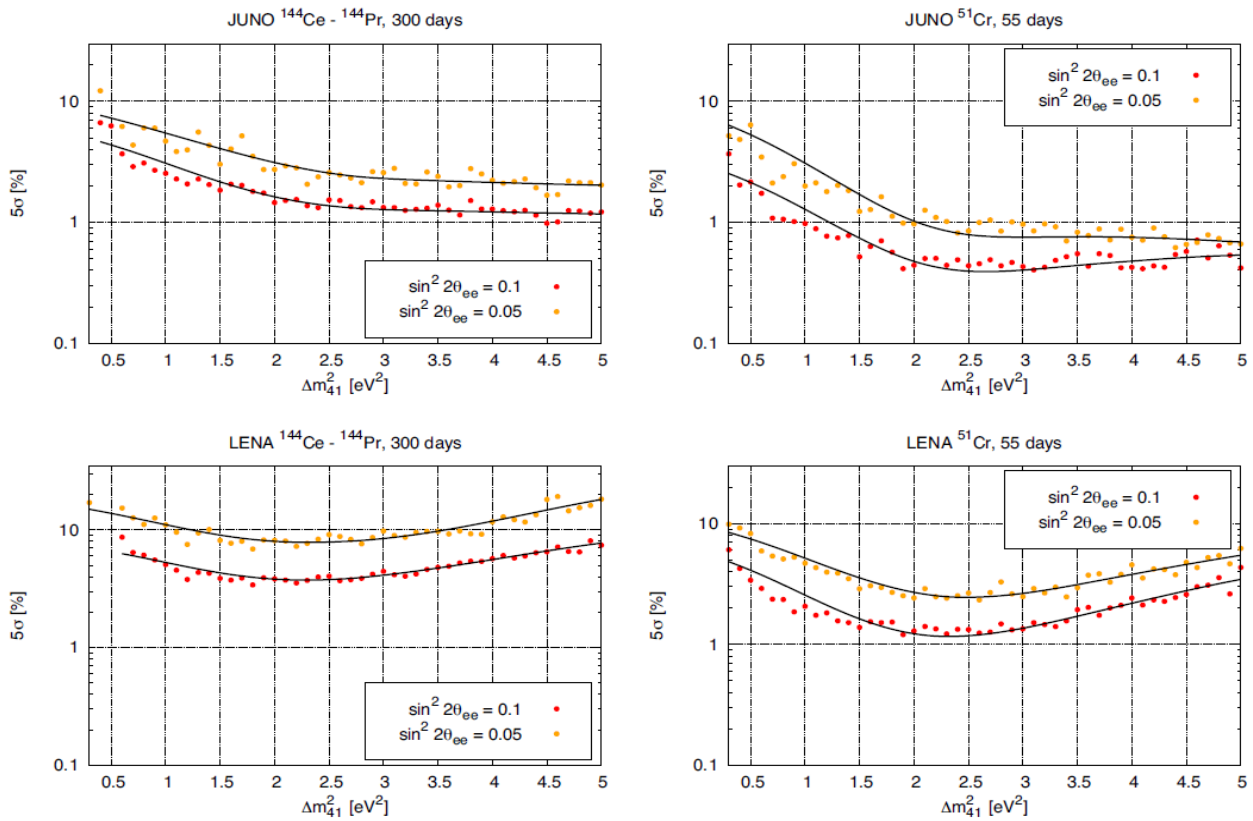


Fig. 3. Outcome of the simulations showing the sensitivity to extract Δm^2_{41} at 5σ confidence level with respect to the true value of the Δm^2 for two different values of the mixing angle

The simulations were done for two radioactive sources. The top panels summarize the results with ^{144}Ce - ^{144}Pr source. The simulated exposition lasts 300 days and assumes 4.6 PBq activity at the start. The two bottom panels show the outcome of the simulations for the ^{51}Cr source. The exposition is 55 days and the activity at the start is 300 PBq.

4. Conclusions

In view of the ongoing and planned experiments, it is expected that within a few years the existence of the sterile neutrinos will be clarified. Especially relevant would be the outcome of the proposed Borexino SOX experiment [10] as it would use, albeit on a considerably smaller scale, the same sources and the same detection method. Clearly, if the sterile neutrinos do exist, the OMNIBUS experiment would be of a fundamental importance for the study of their properties and the physics behind it. The cost of such an experiment would be relatively modest and it would not compromise the main research goals proposed for the new large-scale liquid scintillator detectors. For that reason, even if Borexino SOX would yield a negative result, it would be still worthwhile to perform oscillometric measurements on a large scale using detectors like JUNO, LENA, or RENO-50.

Our results show that in a favorable case (^{51}Cr) one may expect the sensitivity of a few units per-mille. In Ce-Pr source, the sensitivity is just over one percent. It may not be sufficient to detect subtle effects but it would provide an independent probe in the search for the symmetry violations in the leptonic sector.

In any case, the OMNIBUS approach of one do-it-all experiment should be considered already during the planning and construction stage of JUNO and other giant installations.

References

1. M. Smirnov, K. Loo, Yu. Novikov *et al.*, Nucl. Phys. B **90**, 104 (2015).
2. M. Wurm *et al.*, Astropart. Phys. **35**, 685 (2012).
3. F. An *et al.*, J. Phys. G: Nucl. Part. Phys. **43**, 030401 (2016).
4. S. Kim, arXiv.org/pdf/1412.2199.
5. J.D. Vergados, Yu.N. Novikov, Nucl. Phys. B **839**, 1 (2010).
6. Yu. Novikov *et al.*, arXiv:1110.2983.
7. J. Vergados, Y. Giomataris, Yu. Novikov, Nucl. Phys. B **854**, 54 (2012).
8. K. Loo *et al.*, J. Phys.: Conf. Ser. **375**, 042053 (2012).
9. O. Greenberg, Phys. Rev. Lett. **89**, 231602 (2002).
10. G. Bellini *et al.*, JHEP **1308**, 038 (2013).

DOUBLE POLARIZED d - d -FUSION EXPERIMENT

PNPI participants of the POLFUSION Collaboration:

V.D. Fotyev, K.A. Ivshin, E.N. Komarov, L.M. Kotchenda, P.V. Kravchenko, P.A. Kravtsov, S.G. Sherman, A.N. Soloviev, I.N. Soloviev, V.A. Trofimov, A.A. Vasilyev, M.E. Vznuzdaev

1. Introduction

Due to limited supplies of fossil fuels and to a decrease in production of the nuclear waste, thermonuclear fusion reactors are envisaged to replace the fission reactors besides the use of the regenerative energy conversion. The principal aspects of the thermonuclear fusion problem include: 1) understanding the nuclear physics aspects of fundamental fusion reactions at low energies, 2) confinement of the hot and dense plasma, 3) extraction of energy from the plasma. The standard candidates for the fusion fuel are the hydrogen isotopes (the hydrogen, deuterium, tritium) and the light isotope of helium, ^3He . As an input to the realization of the fusion reactors, one needs the nuclear interaction cross sections of light nuclei. The same cross sections enter the analysis of energy production in the stellar interior and the primordial nucleosynthesis at early stages of the Big Bang.

The cross sections of nuclear interactions of light nuclei were extensively studied, but still not all of them are well known. This is especially true for the spin sector, although the spin effects in few-body reactions are large. Here we cite just three classical examples:

1. In the nucleon–nucleon system the bound state, the deuteron, exists only in the spin-triplet channel. The spin-singlet scattering length has an opposite sign and is about four times larger in magnitude than the spin-triplet scattering length.

2. A strong resonance exists in the n - ^3He scattering cross section in the spin-singlet channel. The strong spin-singlet absorption enables an almost 100% spin filtering of neutrons with an excellent transmission rate of 50% with the use of a polarized ^3He [1]. This technique has become one of the methods to generate intense polarized neutron beams [2].

3. The amplitudes of the important fusion reactions $\text{D} + ^3\text{H} \rightarrow n + ^4\text{He}$, $\text{D} + ^3\text{He} \rightarrow p + ^4\text{He}$ are dominated by the S -wave $I^P = 3/2^+$ resonance. Such a resonance greatly simplifies the treatment of double-polarization effects: the numbers of the magnetic substates, four for $I = 3/2$ and two for $I = 1/2$, imply that in an unpolarized plasma only 2/3 of nuclei undergo the fusion. Alternatively, the full polarization of the deuteron and ^3He would enhance the fusion cross section by 50%. Such a strong polarization effect has been confirmed experimentally to a good accuracy [3].

Based on the scrutiny of the available experimental data on the d - d interaction, as early as in 1969 Ad'yasevich and Fomenko suggested a possibility of polarization enhancement of the D - D fusion rate by a factor of two [4]. The first proposal by the Kurchatov Institute group on the experimental study of the polarization coefficients in double-polarized $\vec{d}(\vec{d}, p)t$ and $\vec{d}(\vec{d}, n)^3\text{He}$ collisions in vacuum dates back to 1976 [5]. The proposal was not pursued as at that time polarized atomic and ion beams of adequate intensity were not available.

A substantial step forward was made in 1982 in a theoretical study of the depolarization of nuclei in a magnetically confined plasma [6]. The principal conclusion was that the depolarization time greatly exceeds the fusion reaction time. Presently, it is considered feasible to confine ^3He with the nuclear polarization reaching 55% and to inject neutral deuterium with the nuclear polarization of about 55%. An estimated enhancement of the fusion yield is 15%. A corresponding experiment at the DIII-D tokamak at San Diego is planned [7]. In the case the polarization retention is confirmed, it is planned to perform investigations with polarized tritium, which would offer improved prospects of ignition in the International Thermonuclear Experimental Reactor program and possible important cost savings. An alternative approach to the experimental confirmation of the polarization persistence in a fusion process was suggested at Orsay [8]. It was proposed to look for nuclear reactions in the plasma generated by a petawatt laser hitting a polarized frozen hydrogen/deuterium target. Detecting the final state gammas and neutrons, one would have an experimental access to polarization effects in the reactions $p + \text{D} \rightarrow ^3\text{He} + \gamma$ and $\text{D} + \text{D} \rightarrow ^3\text{He} + n$

by measuring the angular distributions relative to the quantization axis – the direction of the magnetic holding field.

2. Polarization phenomena in few-body systems: theory and experiment

A comprehensive review of experimental data on polarization phenomena in few-body interactions relevant to polarized fusion and of theoretical approaches to the problem has recently been published [3]. As we already emphasized above, on the one hand the strong dominance of the $3/2^+$ resonance mechanism tremendously simplifies the theoretical consideration of the single- and double-polarized D–T and D– ^3He fusion. On the other hand, polarization effects in the d – d fusion remain an entirely open issue.

When thinking of the theoretical approaches, one should bear in mind that hitherto there are no direct experimental data on the fundamental neutron–neutron interaction and the existing experimental determinations of the neutron–neutron scattering length are contradictory. A consistent theory of three- and four-nucleon forces is as yet lacking, although a certain progress has been made in the framework of the effective field theories [9]. Referring to the mentioned review for details and references, we recall that tedious numerical solutions of the Faddeev–Yakubovsky equations in the three-body p – d and n – d channels, based on the realistic potentials with allowance for the Coulomb interactions, do provide a satisfactory description of the experimental data. However, when it comes to a spin observable – the analyzing power A_y – there is a persistent 20 to 30% disagreement between the theory and experiment. Such a disagreement extends to a four-body system. The calculations give a correct trend of the angular dependence of A_y in elastic p – ^3He scattering, but the predicted analyzing power is by some 30% smaller than the experimental one. Some attribute these failures of the theory to poorly known three-nucleon forces. The existing database on polarized D–D interactions is restricted to the single-spin observables [3]. Again, the calculations do reproduce gross features of the angular dependence of the vector and tensor analyzing powers, but not their absolute values. Besides, the model dependence of the theoretical results exceeds the experimental errors. Of course, the theoretical analysis is greatly complicated by Coulomb effects, which are particularly strong at low energies – a complete solution of the Faddeev–Yakubovsky equations for the four-body channel is as yet lacking. In contrast to the S -wave dominated D–T fusion, a treatment of the D–D fusion is further complicated by a large contribution from the P and D waves in the entrance channel, which persists even at very low energy of 3 keV. The presence of these partial waves suggests rather strong polarization correlations exceeding those in the polarized D–T fusion.

On the theory side, one of the hopes for the progress is linked to possible incorporation of the nucleon–nucleon amplitudes from the effective field-theory analysis into the resonating group method (RGM). An obvious advantage of the RGM, based on the variational approach, is that Coulomb effects can be taken into account much easier than with the Faddeev–Yakubovsky technique. Here one recalls that in the three-body channel with the same input interaction the results from the RGM are consistent with the Faddeev–Yakubovsky results to one percent accuracy. A full merging of the RGM and the effective field theory approach, a speciality of the theory group of the Institut für Kernphysik of Forschungszentrum Jülich, would require implementation of the supercomputer codes and could well take up to five years. The theoretical predictions then could be compared with the experimental data to be obtained for the polarization correlations in the D–D interaction.

The reactions $\vec{d} + \vec{t}$ and $\vec{d} + ^3\vec{\text{He}}$ with polarized initial particles have been fairly well investigated [3]. At the same time, the spin-correlation components of the basic fusion reaction $\vec{d} + \vec{d}$, which is always present in the thermonuclear reactor with the energy range of 10–100 keV, have not been measured experimentally yet. When using polarized fuel in a thermonuclear reactor, two spin combinations, with parallel and antiparallel deuteron-spin orientations, are to be considered. Thermonuclear deuteron fusion reaction proceeds through two channels: $\vec{d} + \vec{d} \rightarrow ^3\text{He} + n$ and $\vec{d} + \vec{d} \rightarrow t + p$. Theoretical predictions for the ratio of the reaction cross section with parallel deuteron spin orientation $\sigma_{1,1}$ to the unpolarized cross section σ_0 , defined as quintet suppression factor (QSF), exhibit a very strong model dependence and are quite contradictory (Fig. 1). Here $\text{QSF} = 1$ means that polarization of the initial particles does not affect the total

reaction cross section. Figure 1 features the results of calculations making use of various models. Significant scattering of the theoretical results illustrates a strong demand for the measurement of this ratio.

According to the variety of theoretical predictions, the planned measurements without polarization and with parallel deuteron spin orientation will provide answers to three questions:

1. Is it possible to increase the D–D cross section by parallel deuteron spin orientation by a factor up to 2.5? This would raise the energy yield at the same input plasma density.

2. Is it possible to modify the ratio of proton to neutron production favouring the first process? Neutrons are an unwelcome product of the fusion reactions in thermonuclear power reactors since they have large penetrating power. Therefore, a possible suppression of the neutron channel is extremely desirable to reduce the radioactive waste and increase the lifetime of the blanket.

3. Is it possible to modify the angular distribution in the neutron emission by the use of polarized fuel? This is an important issue for the shielding of the reactor, since the neutron flux is one of the main factors destroying the reactor walls and blankets, and it necessitates special shielding. Concentration of the neutron flux in the predefined directions or planes helps to considerably reduce this danger and build the shield at dedicated locations.

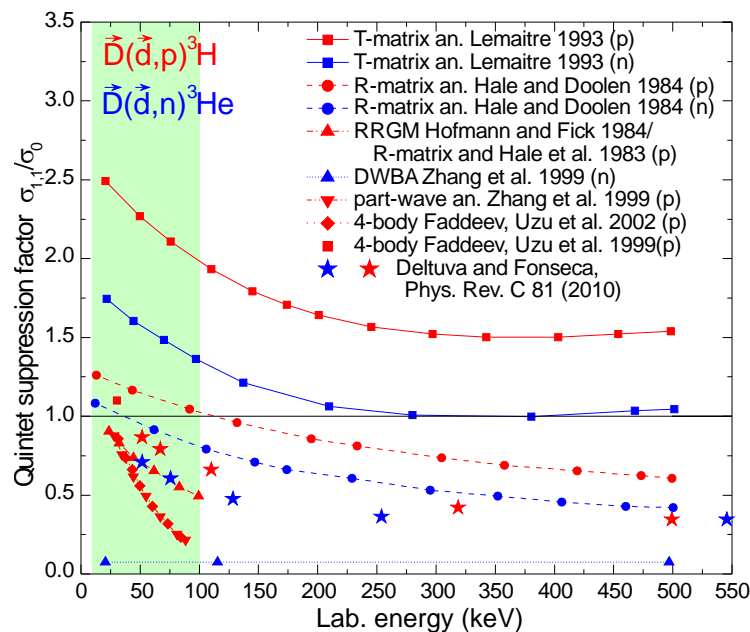


Fig. 1. Theoretical predictions of the quintet suppression factor

A direct experimental measurement of the differential D–D fusion cross section with parallel spin orientation may demonstrate the advantage of using polarized fuel in future fusion reactors. On the nuclear physics side, the principal objectives of the present program are the measurements of the asymmetry of the differential cross sections, determination of the total cross-section change for the polarized initial particles, and measurement of the spin-correlation factors $C_{z,z}$ and $C_{zz,zz}$ for investigation of the quintet suppression factor.

3. Experimental set-up

The spin-correlation coefficients for the interaction of polarized 10 to 100 keV deuterons are to be determined by measuring the angular distributions of the ejectiles in the reactions $\vec{d} + \vec{d} \rightarrow {}^3\text{He} + n$ and $\vec{d} + \vec{d} \rightarrow t + p$.

Due to a very low energy of the initial particles, their penetrating power is exceedingly small – less than a micrometer in a solid target. Therefore, the d – d interaction will be studied with crossing beams of polarized

atoms from a polarized atomic beam source (ABS) and polarized deuterons from a polarized ion source as it is shown in the scheme of Fig. 2. The polarized ABS is based on the source from the University of Ferrara that was previously used in Indiana University Cyclotron Facility (IUCF) [10]. It delivers a beam of deuterium atoms of the requested nuclear vector or tensor polarization and energies of about 0.1 eV. The intensity of the beam of $4 \cdot 10^{16}$ atoms/s, achieved at the IUCF, is sufficient for measurements of a low cross-section of the fusion reaction.

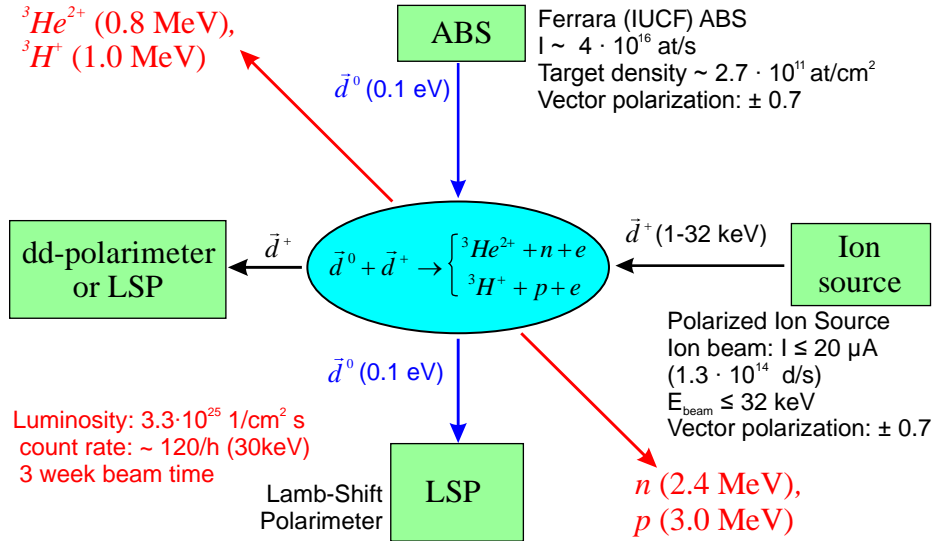


Fig. 2. Layout of the experiment

The atomic deuterium beam from the ABS is crossed by the beam of the polarized deuterons from the polarized ion source – POLIS. This source is based on the injector equipment [11] of the cyclotron at the Kernfysisch Versneller Instituut (KVI) of Rijksuniversiteit Groningen, the Netherlands. Nowadays the KVI scientific program has switched from light to heavy ions. The light-ion source has become available, and presently it is at our disposal. This source is capable of producing an ion beam of 20 mA and energies up to 35 keV. The current project requires a substantial upgrade of this source to increase the beam energy up to 100 keV. This energy is required to combine new experimental results with the existing data available for energies around 100 keV and higher. Such an overlap is essential for a crosscheck with other data. A new electron cyclotron resonance (ECR) ionizer was designed, capable to increase the ion energy up to 100 keV.

The use of the polarized atomic and ion beams requires the knowledge of their nuclear polarization. Instruments are necessary for the tuning of the polarized sources and for the constant monitoring as well. It is planned to use two polarimeters in the experiment, 1) a Lamb-shift polarimeter (LSP) and 2) a nuclear-reaction polarimeter.

The LSP allows more precise polarization measurements. More effort, however, is needed for its operation. Therefore, before the beginning of a data-production run it is used to tune first the ABS and the ion source. Then it is positioned as shown in Fig. 2 and is used to control the ABS-beam polarization from time to time in short measurements of 2 s. The polarization of the ion beam is permanently monitored by the $d-d$ polarimeter. It contains a $0.5 \mu\text{m}$ titanium foil with unpolarized deuterium, implanted before the measurement by the ion beam. During the experimental run, the angular distribution of the ejectiles from the $d-d$ reaction is measured continuously with nine semiconductor detectors, positioned at appropriate angles around the titanium foil.

One of the crucial tasks of the experiment is the detection of the fusion-reaction ejectiles, *i. e.*, protons, tritium ions, and ${}^3\text{He}$ ions (neutrons are not detected in this experiment). Typical prospective count rates are 120 events per hour for 30 keV ions. Therefore, the detector system should have low background and noise to distinguish these rare events. The solution of this task might be simplified by two aspects:

1. Due to the relatively large Q values, all reaction products have energies essentially higher than the initial deuterons. The latter have an energy up to 100 keV, while the energy of the reaction products is in the range 0.8–3 MeV. Since the semiconductor detectors are energy-sensitive devices, they are used to identify the reaction products by their energy. The background caused by scattered electrons and deuterons can be discriminated against the ejectile spectra. The background contribution by the cosmic radiation and the radioactivity of the construction material should be investigated.

2. We investigate the two-particles reaction (two incident particles and two products) with well defined particle energies. Consequently, the particle identification by the energy will be reliable.

The main goal of the experiment is to measure the angular distributions of the reaction products. Therefore, the detector system should cover the whole range of emission angles. Ideally it has to cover the 4π solid angle around the $d-d$ interaction volume with a typical angular resolution of $10-15^\circ$ for a reliable comparison with theoretical calculations of the differential cross-section. A magnet system, providing the holding field for the polarization maintenance in the $d-d$ interaction volume, was designed with permanent magnet elements. It provides a uniform magnetic field of the required strength (up to 320 G) in the beam interaction area. The direction of the magnetic field can be varied in a wide range according to the experimental requirements.

The detector system (Fig. 3) is made as a cubic structure with the inner surface covered with 576 Hamamatsu S3590 silicon PIN diodes. The sides of the cube are produced by the printed circuit board technology and are used as a supporting structure for the diodes, and for the routing the detector signals as well. The sides of the detector are wired to the connectors at the upper flange of the vacuum chamber. A special readout electronic module ASF48 has been designed and produced for the detector data acquisition. Each module contains 48 charge-sensitive channels. The module provides continuous and simultaneous measurement in all 48 channels with six eight-channel pipeline the analog-to-digital converters (ADC's). The signal in every channel is registered automatically in case of exceeding the amplitude trigger threshold and is sent to the readout computer. The time of the signal is also recorded by the trigger actuation with 10 ns accuracy. The sampling frequency of the ADC is 65 MHz.

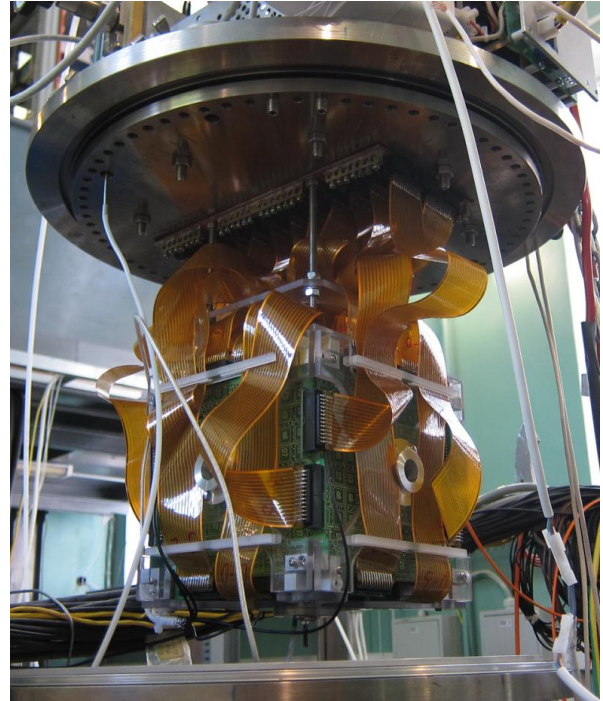


Fig. 3. Detector system of the PolFusion experiment

4. Test measurements and software development

An unpolarized experiment with an ion beam and a solid target was carried out in order to check the detector system and the readout electronics. The target foil was made of deuterated polymethylmetacrylate and installed in the detector chamber at the outlet of the ion source, surrounded by a test set-up of eight semiconducting detectors.

The target was exposed to the ion beam of 10 mA and 15 keV energy. The amplitude spectra obtained in this experiment show three distinct peaks of the deuterium fusion products, namely 0.8-MeV $^3\text{He}^{2+}$, 1-MeV tritium, and 3-MeV protons (Fig. 4). A successful registration of the $d-d$ fusion reaction products confirms the proper selection of the detector elements and good performance of the readout electronics.

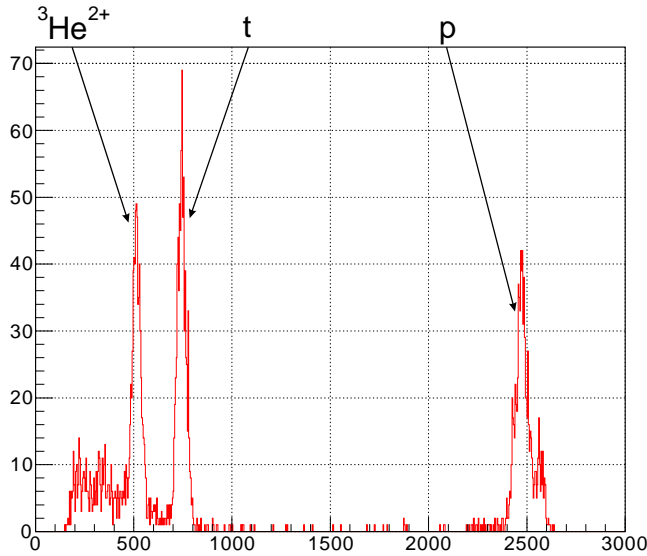


Fig. 4. Typical ion spectra of first detector tests with unpolarized $d-d$ fusion reactions at 15 keV. The protons (3 MeV), tritons (1 MeV), and ${}^3\text{He}^{2+}$ ions (0.8 MeV) can be clearly identified with the PIN diodes

A mathematical algorithm was developed for experimental data analysis. It describes reactions of two particles with spin 1 in the initial state. Analytical formulae were obtained using partial wave expansion for the calculation of all observables of the reactions $\vec{d} + \vec{d} \rightarrow {}^3\text{He} + n$ and $\vec{d} + \vec{d} \rightarrow t + p$. The complete set of the matrix elements was evaluated in an explicit form for the S , P , and D waves at low energies.

Analytical equations were developed for the $d-d$ -reaction cross-section for any arbitrary polarization of the beam and the target using mean values of the polarization operators of the density matrix of the initial state. This enables simulation of the experimental observables using the set of partial amplitudes.

The existing experimental data for the $d-d$ fusion reaction at low energy were collected and analysed, including the results of unpolarized and partially polarized measurements performed in the years 1956–2006 with solid and gas targets. A minimization algorithm was developed for the calculation of partial amplitudes from experimental data, making use of the collected data set and analytical functions obtained in partial wave expansion in the complete spin of two-particle system representation.

A software has been developed for calculations of the experimental observables. This software will be used for evaluation of the total and differential cross-section, analyzing powers, correlation coefficients, and polarization transfer coefficients.

5. $D-d$ and $d-d$ fusion reaction

With the present set-up, the planned nuclear $d-d$ fusion measurements are to be performed with the crossed polarized atomic D beam from the ABS (energy about 0.1 eV) and the polarized 20 to 100 keV ionic d beam from the ion source. With decreasing the centre-of-mass energy, the electron-shielding effect is increasing. The non-zero probability to find the s electron in the range of the deuteron reduces the Coulomb repulsion between the deuterons. Therefore, in the $D-d$ interaction at energies below 20 keV, the reaction cross section gets enlarged compared with that in the double-ionic $d-d$ reaction encountered in a fusion reactor with highly ionized reaction partners. The electron screening effect, also important in astrophysical fusion, was confirmed with unpolarized deuterons [12]. With the present set-up and a future extension to store unpolarized or even polarized D atoms, the unpolarized data might be extended to single or even double polarized effects, including a polarized electron, with the use of the polarized ionic d beam of energies below 10 keV.

References

1. R.M. Moon, T. Riste, W.C. Koehler, *Phys. Rev. A* **181**, 920 (1969).
2. T.E. Chupp *et al.*, *Nucl. Instrum. Meth. A* **574**, 500 (2007).
3. H. Paetz gen. Schieck, *Eur. Phys. J. A* **44**, 321 (2010).
4. B.P. Adyasevich, D.E. Fomenko, *Sov. J. Nucl. Phys. No. 9*, 167 (1969).
5. B. Adjasevich, V. Antonenko. Preprint IEA-2704, Moscow (1976).
6. R.M. Kulsrud, H.P. Furth, E.J. Valeo, M. Goldhaber, *Phys. Rev. Lett.* **49**, 1248 (1982).
7. A. Honig, A. Sandorfi, in *Proc. of the 17th Int. Spin Phys. Symp.* AIP Conf. Proc. **915**, 1010 (2007).
8. J.-P. Didelez, C. Deutsch, *EPJ Web of Conf.* **3**, 04018 (2010).
9. E. Epelbaum, *Progr. Part. Nucl. Phys.* **57**, 654 (2006).
10. T. Wise *et al.*, *Nucl. Instrum. Meth. A* **336**, 410 (1993).
11. H.R. Kremers *et al.*, *Nucl. Instrum. Meth. A* **536**, 329 (2005).
12. F. Raiola *et al.*, *Eur. Phys. J. A* **13**, 377 (2002).

PNPI IN THE CBM PROJECT AT FAIR: RING CHERENKOV AND MUON CHAMBER SUBSYSTEMS OF THE CBM DETECTOR

PNPI participants: V.V. Baublis, V.V. Ivanov, A.V. Khanzadeev, L.M. Kochenda, B.G. Komkov, P.A. Kravtsov, E.L. Kryshen, L.G. Kudin, N.M. Miftakhov, V.N. Nikulin, Yu.G. Riabov, E.V. Roschin, G.V. Rybakov, V.M. Samsonov, O.P. Tarasenkova, D.V. Tyts, M.E. Vznuzdaev, M.B. Zhalov

1. Introduction: the CBM experiment

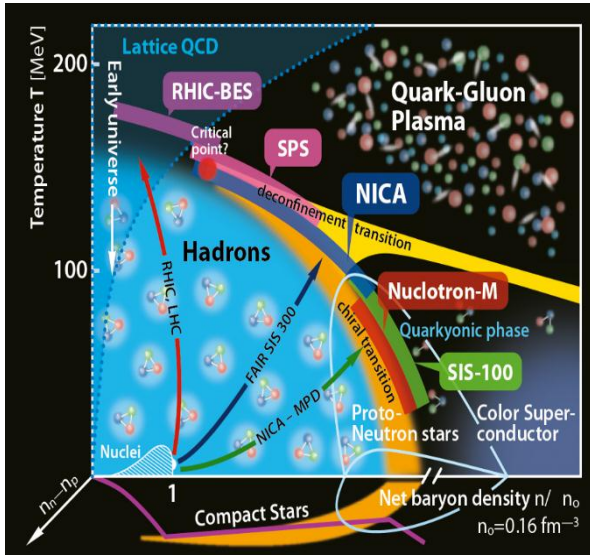


Fig. 1. Sketch of the phase diagram of strongly interacting matter [1]

Heavy ion collision experiments at relativistic energies create extreme states of strongly interacting matter and enable their investigation in the laboratory. Figure 1 illustrates the conjectured phases of strongly interacting matter and their boundaries in a diagram of temperature versus net baryon density [1]. The compressed barionic matter (CBM) experiment [2] is designed to study the high-density nuclear matter created in heavy ion collisions at Facility for Antiproton and Ion Research (FAIR), which is currently under construction in GSI Helmholtzzentrum für Schwerionenforschung (GSI, Germany). The CBM experiment is intended to operate in full energy range of FAIR synchrotron SIS300. While SIS300 provides a long term prospective, it has been decided that the CBM, approved as one of the four main pillars of the modularized start version [3], should start at SIS100, which is a pre-accelerator of SIS300. This study is complementary to the activities at the top Relativistic Heavy Ion Collider (RHIC) energy and at the Large Hadron Collider (LHC), which

investigate deconfined quantum chromodynamic (QCD) matter at the highest available energy densities, but vanishing baryon matter density.

In heavy-ion collisions at beam energies up to 11(14) A GeV for Au(Ca) available at SIS100, model calculations predict the creation of a strongly interacting QCD matter at extreme values of density, similar to neutron star core densities. This makes it possible to explore the QCD phase diagram in the region of high net-baryon densities, to study the equation of state, to search for phase transitions, chiral symmetry restoration, and exotic forms of (strange) QCD matter with a dedicated experiment focusing mainly at the following observables:

- *Multi-strange hyperons.* The yields and phase-space distributions of multi-strange hyperons (Ξ , Ω) are particularly promising tools to study the properties and the degrees of freedom of the QCD matter at high densities and a possible transition to the quarkyonic matter. The production of multi-strange hyperons is expected to be enhanced at high densities, and their yield to be sensitive to both the strangeness content and the baryon density reached in the fireball. The production of antihyperons, on the other hand, is strongly suppressed in a baryon-dense environment. This constraint would be relaxed in case of a quark–gluon plasma (QGP). Because of the very low yield, systematic measurements of antihyperons production will be possible only with the CBM experiment with its high rate capability.

- *Fluctuations and the critical point.* The observable to detect critical behaviour, as expected in the vicinity of the QCD critical point, are event-by-event fluctuations of the conserved quantities. No conclusive indications for criticality have yet been observed. It should be noted that not only the location of the critical point is unknown, but it is either unclear how close to this point the system has to pass so that such a critical behavior could be observed.

- *Vector mesons.* An observable consequence of the restoration of the chiral symmetry would be a modification of hadron properties inside nuclei, or in the hot and dense matter. Short-lived vector mesons,

in particular the ρ meson, decay inside the fireball and thus preserve their state in the decay kinematics. The leptons, not strongly interacting, leave the reaction zone undisturbed and thus carry the information on the vector meson properties. Of similar interest is the dilepton mass region between the ϕ and J/ψ mesons, since here no hadronic sources contribute directly. Thus, the lepton pairs in this mass region are the results of direct radiation from the hot collision zone. Their transverse mass spectrum gives access to the apparent temperature of the medium.

- *Charm.* Hadrons containing charm quarks are very promising diagnostic probes of hot and dense nuclear matter. Because of their large mass, charm quarks cannot be thermally produced in nucleus–nucleus reactions, but are formed in the initial stage by first chance collisions of the participating nucleons. If the produced medium is the partonic one, the formation of charmonium states is suppressed by Debye screening, and the charm quarks finally coalesce with light quarks to form hadrons with open charm. This “anomalous” suppression of the J/ψ yield relative to the muon pairs from Drell–Yan processes was observed by the NA50 Collaboration in central Pb + Pb collisions at 158 A GeV [4], providing one of the strongest arguments for a QGP formation at the top Super Proton Synchrotron (SPS) energy [5]. It is therefore natural to look for disappearance of this signal at lower collision energies, where the energy density is not sufficient to create a QGP.

The CBM detector, designed as a multi-purpose device, will measure the collective behaviour of hadrons, together with rare diagnostic probes such as multi-strange hyperons, charmed particles and vector mesons decaying into lepton pairs with unprecedented precision and statistics. Most of these particles will be studied for the first time in the FAIR energy range. In order to achieve the required precision, the measurements should be performed at the reaction rates up to 10 MHz. This requires very fast and radiation hard detectors, a novel data read-out and analysis concept including free streaming front-end electronics, and a high-performance computing cluster for online event selection.

The CBM experimental set-up depicted in Fig. 2 comprises the following components:

- large aperture superconducting dipole magnet;
- micro vertex detector consisting of four layers of silicon monolithic active pixel sensors;
- silicon tracking system based on double-sided silicon micro-strip sensors arranged in eight stations inside a dipole magnet;
- time-of-flight wall based on multi-gap resistive plate chambers with low-resistivity glass;
- ring imaging Cherenkov (RICH) detector for electron identification;
- transition radiation detector (TRD) for pion suppression, particle tracking, and identification using specific energy loss;
- muon chamber (MUCH) system for muon identification;
- electromagnetic calorimeter for measurements of photons;
- projectile spectator detector for event characterization.

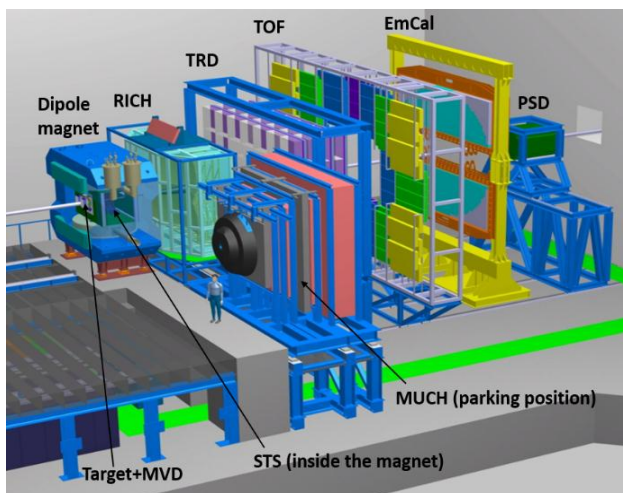


Fig. 2. The CBM experimental set-up. The CBM detector components are described in the text. For muon measurements RICH will be exchanged by MUCH which is shown in a parking position to the right of the beam axis

According to the final decision on the sharing between the institutes-participants of the collaboration of the tasks to create the start version of the CBM detector, PNPI contributes in building of the RICH and MUCH detectors with the following:

- the MUCH detector mechanics including superstructure,
- the RICH detector mechanics,
- the gas supply systems for both detectors.

2. Muon chamber detector

The MUCH detector [6] comprises six absorbers, the first one made of carbon and the rest of iron, and six tracking stations. Each tracking station consists of three layers of chambers located in the air gap between the absorber segments. The total number of detector chambers is 18 (three behind each absorber). The total absorber length amounts to 265 cm divided into 60 cm carbon and (20 + 20 + 30 + 35 + 100) cm of iron, which is equivalent to 13.5λ , where λ is the hadronic interaction length. An additional lead shielding is used

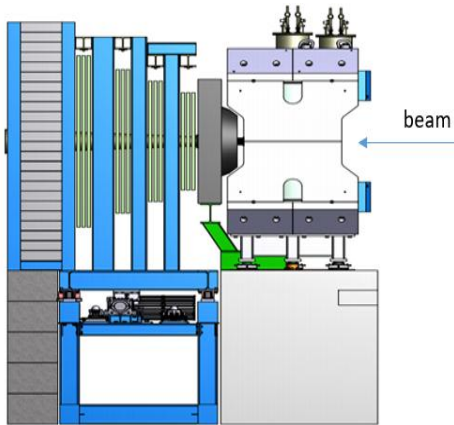


Fig. 3. Schematic view of MUCH SIS100-B layout. It consists of four tracking stations and five absorbers with the total absorber thickness of 265 cm

around the beam pipe. This geometry can be used for identification both of charmonium and low mass vector mesons at the top FAIR energy. The angular acceptance of the detector spans from ~ 5 to 25° . Apart from the SIS-300 configuration, MUCH will be taking data in the start version of FAIR at SIS100. Two start versions of MUCH at CBM called SIS100-A and SIS100-B were optimized. SIS100-A will consist of three absorber layers of the same total absorber thickness as for SIS-300 and three tracking stations with the last station to be used for the muon trigger. This configuration is for J/ψ measurements only. The detectors to be used for the first stations are GEM-chambers filled with Argon based gas mixture as the active medium. The R&D considered different types of detector technology. Based on the progress of the R&D by the time when SIS100 will start to deliver a beam, it is planned to extend the SIS100-A version by including two more tracking stations to the SIS100-B version (shown in Fig. 3). This configuration has been found suitable even for measurements of low-mass vector mesons from Au + Au collisions at 8 A GeV.

2.1. Muon chamber mechanics

The MUCH detector in the dimuon mode of operation should be as close to the target as possible to avoid pions decaying to muons, which enhance the dimuon background. It is planned that MUCH and RICH will occupy the same place at the beam on alternative basis. As RICH is a relatively lightweight device, the CBM 30-ton crane available in the cave can easily handle it. An estimated weight of MUCH is greater than 300 t; therefore it can be handled by the crane in pieces only. The absorber segments and the tracking stations are to be mounted together and fixed on a platform that can have a possibility of movement to a parking position for quick switch to operation in the dielectron mode.

Each tracking chamber is composed of two half-chambers that are mechanically independent with their own frames. The half-chambers will hang with movable mechanisms on individual rails attached to the transverse beams and in turn to the superstructure. Therefore, there is possibility to pull out a separate half-chamber and to get access for repairing or individual service.

An intensive work on conceptual design of the MUCH mechanics has been done to this date. Real design work is currently underway.

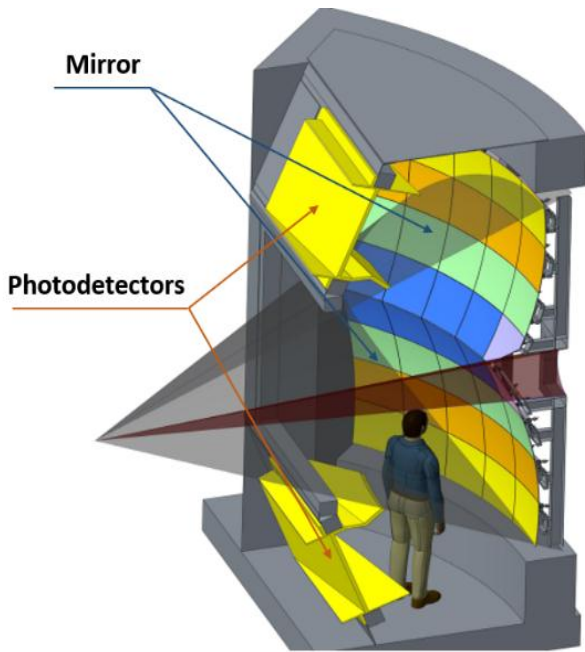


Fig. 5. Schematic view of the RICH layout

The RICH detector will provide identification of electrons and suppression of pions in the momentum range below 10 GeV/c. The gaseous RICH detector will be built in a standard projective geometry with a focusing mirror and a photon detector. CO₂ with a pion threshold for Cherenkov radiation of 4.65 GeV/c will serve as a radiator gas. The detector, as it shown in Fig. 2, will be located behind the dipole magnet about 1.8 m downstream of the target.

Focusing of the emitted Cherenkov light is achieved by a large, multi-segmented spherical mirror system of 13 m² (two half mirrors above/below the beam pipe) with the curvature radius of 3 m (Fig. 5). Glass mirror tiles (~ 40 × 40 cm², 6 mm thick) with Al + MgF₂ reflective coating (reflectivity 85% over a large wavelength range) will be used.

The photon detection system covers a total active area of 2.4 m². Multi-anode photomultipliers (Hamamatsu H12700) with UV-transparent windows will be used, matching well the transmission range of CO₂ (the transmission cut-off is at 180 nm). The use of a wavelength shifting coating applied on the

photomultiplier tube (PMT) window is considered to further increase the UV efficiency. The readout pixel size is 6 × 6 mm², leading to a total of 55 k readout channels.

The residual magnetic field affects the operation of the photomultipliers. In order to move the photon detectors to the region with smaller magnetic fields, the mirror focusing system was tilted. Unfortunately, such a slope leads to deterioration of the detector performance (the shape of the rings begins to deviate from the circle, and this reduces the ring finding efficiency). After intensive simulations and calculations, the optimum tilt angle of the optical system (about 10°) was chosen. But in this case, to reduce the magnetic field at the photo cathodes to the value of 1–2 mT, additional iron shielding boxes around the photon detectors are required.

For complex verification of the selected components, a full scale prototype of the RICH detector was built [8] and successfully tested during three test sessions in a test beam at CERN. The tests showed that 22 photons are registered per electron ring. About a hundred rings are seen in central Au + Au collisions at 25 A GeV beam energy due to the large material budget in front of the RICH detector. Nevertheless, due to high granularity and high number of photons per ring, the pion suppression larger than 100 is expected to be achieved according to simulations.

3.1. Ring imaging Cherenkov mechanics

The RICH detector will have a size of about 2 × 5 × 6 m (length × height × width). It will share its location with the MUCH detector, both being used alternately with a typical change period of once a year. The mechanical construction of RICH must therefore allow for an easy movability of the RICH detector as a whole either by crane or by rails.

The acceptance of the RICH detector covers a range of scattering angles up to 35° in the horizontal ($x-z$) plane and up to 25° in the vertical ($y-z$) plane with respect to the nominal target position. The gas radiator length (measured from the entrance window to the mirror surface) is 1.70 m (the overall length is approximately 2 m). The remaining space behind is reserved for the mirrors, their mounts and support frames.

3.1.1. Focusing mirror system

Each of two halves of the RICH mirror plane is split into 40 rectangular segments (tiles) with four rows of ten tiles each (Fig. 6). Four types of tiles with different sizes are used. This splitting scheme allows for reasonable size of the glass mirror tiles and provides acceptable gaps of 3–4 mm between the tiles.

Since the RICH detector will be installed right behind the magnet, the mirror supporting frame will be inside the acceptance of the downstream detectors. Therefore, we have additional requirements for the mirror supporting structure mechanical design. On the one hand, the structure should provide the stability of the optical system, even during transportation with the crane. On the other hand, the structure should be radiation-transparent to prevent the influence on the operation of the detectors installed behind RICH. To solve this problem, intensive simulations and calculations were carried out for about ten different versions of the mirror supporting frame design. As a result, the most promising option with the so-called pillar, carrying two rows of mirror tiles, was proposed (Fig. 7d). In this version, a three-point (tripod) mount concept was chosen for the mirror mount geometry (Fig. 7a) with three mount points on the mirror forming an equal-sided triangle. This tripod version allows for maximum deviations at the mirror edges up to 5 μm , thus the mounting scheme permits to compensate the gravitational deformation of the tile. The proposed mount leg structure (Fig. 7b) allows to orient each individual mirror tile to ensure good optical convergence and focusing quality of the combined mirror system. Three adjustable mirror mounts provide the link between an individual tile and the aluminium frame supporting the tiles. Each supporting frame, keeping two individual tiles (schematically presented in Fig. 7c), is attached to a vertical pillar. The pillars (six pillars in total) are fixed in a rigid frame. Figure 7d presents a schematic design of the mirror support system.

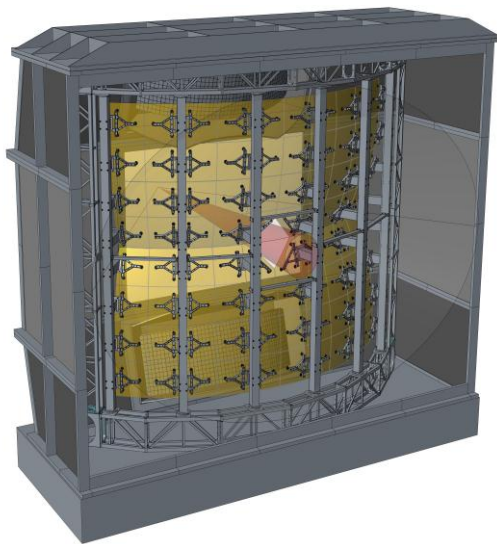


Fig. 6. Schematic view of the RICH mirror system

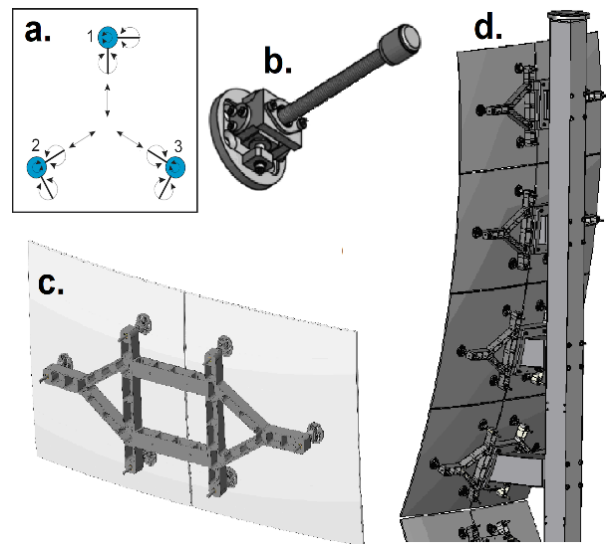


Fig. 7. Mirror support system: a – scheme of three-point mirror mount concept; b – adjustable mirror mount; c – design of the supporting frame for two tiles; d – pillar structure, containing two rows of mirror tiles

For a complete test of the pillar version it was decided to construct a prototype with two pillars. A detailed design of the prototype has been elaborated (Fig. 8.). With this prototype we can develop the assembly technology, test different pillar designs and different materials, check the geometry (gaps), an provide the strength tests, mechanical response (shaking, acceleration) tests, check the structure behaviour in time, to work out the assembly methods and the procedure of adjustment. At present, the prototype is in the production stage.

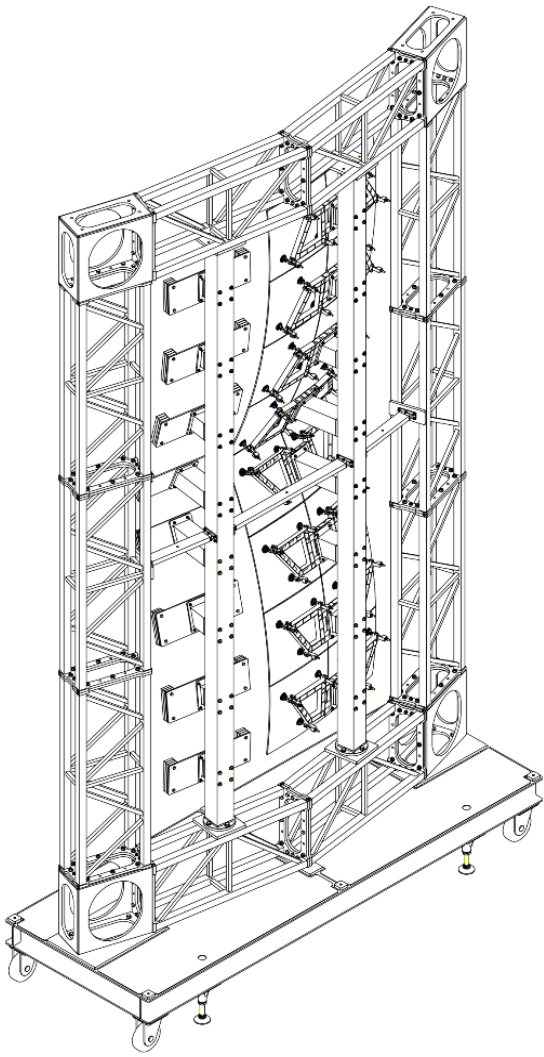


Fig. 8. Mirror supporting frame prototype

3.1.2. Gas box

The design of the gas box is based on solutions tested with the full scale prototype [8] and contains a reinforced frame covered with rigid panels on all sides (see Fig. 6). It should provide a gas-tight and light-tight enclosure for the CO₂ radiator volume and provide mechanical support for the focusing mirror system inside, as well as mounting flanges for two photon detectors and their magnetic shield. The position and orientation of these flanges define the exact detector position, and their design should be specified in compliance with the team responsible for building the photon detectors. The gas box also contains the beam pipe as an integral part, the vacuum inside it should be on the level of 10⁻⁴ mbar. A reinforced construction of the gas box is needed to allow the movement of the detector with the crane. The design enables disassembly of the gas box for transportation in a standard container. A part of one of the side panels can be dismantled for installation of the mirror supporting frame. The front and rear panels can also be removed to have an access to the supporting frame and the photon detectors. The front and rear panels are made of a Kapton foil with a thickness of 200 μm. Alternatively, a 2 mm plastic sheet may be used for the rear panel. The corresponding parts of the frame will have structures to support the beam pipe.

3.2. Ring imaging Cherenkov gas system

The design of the RICH gas system is very similar to that of MUCH (see Section 2.2) with one difference – for RICH we need one-component gas only. The purifying and drying systems should be able to keep the water and oxygen content at the maximum level of a few ppm. Both systems need capabilities for regeneration. The gas system should be

adaptable in case if different radiator gases are to be used in the future. The temperature, pressure, oxygen, and water content will be monitored in the CBM slow control system. Such a system was produced to supply the full-scale RICH prototype with CO₂ and was tested at the CERN beam facility [8]. During the test experiment, the system showed high stability of the differential gas pressure at work in the recirculation mode and high efficiency of the gas dryer and purifier. In general, the gas system provided stable operation and reliable control of all required gas parameters.

4. Conclusion

The CBM experiment at the future FAIR complex will investigate the phase diagram of strongly interacting matter at high baryon density and moderate temperatures. The fireball created in the nucleus–nucleus collision passes several stages of evolution, where different types of particles can be produced. As leptons and photons are not affected by hadronic final state interactions, they provide an opportunity to look into the fireball at different stages of its evolution. Two subsystems of the CBM detector, RICH, and MUCH, which are built with participation of PNPI, are directed at detection of leptons.

A unique combination of the accelerator that provides a high-intensity heavy-ion beam with a state-of-the-art high-rate experiment based on innovative detectors and computer technology offers optimal conditions for a research program with significant potential for discovering the fundamental properties of the QCD matter.

References

1. T. Ablyazimov *et al.*, *Eur. Phys. J. A* **53**, No. 3, 60 (2017).
2. *The CBM Physics Book*, eds. B. Friman *et al.*, *Lect. Notes Phys.* **814**, 980 (2011).
3. Fair Green Paper: The Modularized Start Version,
http://www.fair-center.de/fileadmin/fair/publications_FAIR/FAIR_GreenPaper_2009.pdf
4. NA50 Collaboration, B. Alessandro *et al.*, *Eur. Phys. J. C* **39**, 335 (2005).
5. CERN Press Release, 10 Febr., 2000,
<http://press.web.cern.ch/press-releases/2000/02/new-state-matter-created-cern>
6. The CBM Collaboration, Technical Design Report for the CBM Muon Chambers, GSI-2015-02580 (2015), <http://repository.gsi.de/record/161297>
7. CBM Collaboration, Technical Design Report for the CBM Ring Imaging Cerenkov Detector, GSI Report 2013-4 (June 2013), <http://repository.gsi.de/record/65526>
8. J. Adamczewski-Musch *et al.*, *Nucl. Instrum. Meth. A* **845**, 434 (2017).

EXPERIMENT PANDA AT GSI

PNPI participants of the PANDA experiment:

S.L. Belostotski, A.A. Izotov, S.I. Manaenkov, O.V. Miklukho, D.O. Veretennikov, A.A. Zhdanov

1. Introduction. Physics potential of the PANDA experiment

The PANDA experiment will perform precise studies of $\bar{p}p$ annihilations and reactions of \bar{p} with nucleons of heavier nuclear targets [1]. It will benefit from \bar{p} beams of unprecedented quality which will be provided by the high energy storage ring (HESR). The accelerator HESR is under construction now at GSI Helmholtzzentrum für Schwerionenforschung (GSI, Darmstadt, Germany).

The Ring will operate in the momentum range from 1.5 to 15 GeV/ c . In a high momentum resolution mode (HR) of HESR, the relative momentum spread of the beam is reduced to $5 \cdot 10^{-5}$ with 10^{10} circulating antiprotons at the peak luminosity of $2 \cdot 10^{31} \text{ cm}^{-2} \cdot \text{s}^{-1}$. In a high luminosity (HL) mode, the peak luminosity reaches $2 \cdot 10^{32} \text{ cm}^{-2} \cdot \text{s}^{-1}$ at the same target density. The relative momentum spread in this regime is expected to be about 10^{-4} . The HR and HL modes are established to meet the challenging requirements of the PANDA experimental program.

The main experimental subject matters of the PANDA program were widely presented, discussed and commonly approved by the international physical community [1–4]. The PANDA experiment plans to exploit an extraordinary physics potential of the projected high quality \bar{p} beams with unprecedented momentum resolution. Precise measurements of all states below and above the open charm threshold is of great importance for quantum chromodynamics (QCD). All charmonium states can be formed directly in $\bar{p}p$ annihilation in the invariant mass range $2.25 < M(\bar{p}p) < 5.46 \text{ GeV}$. At full luminosity, PANDA will be able to collect several thousand $\bar{c}c$ states per day. By means of beam momentum scans, it will be possible to measure masses with accuracies of the order of 100 keV and widths to 10%, or better. The latter is crucially important for theoretical analyses.

Search for pure gluonic excitations and exotic hadron states is another interesting topics. This is one of the main challenges of the modern hadron physics. A full description of future PANDA experimental activities can be found in Ref. [4].

2. The PANDA spectrometer

The PANDA experiment is designed to achieve the 4π solid angle coverage, high resolution for tracking, good particle identification, high precision calorimetry. A high rate capability is planned with a versatile readout and a very good event selection. A detailed description of the PANDA detector can be found in Ref. [5]. The \bar{p} beam interacts with a cluster or pellet hydrogen target, or with a deuterium or heavy nucleus target. The detector is composed of two magnetic spectrometers: the target spectrometer (TS), based on a superconducting solenoid magnet and the forward spectrometer (FS) based on a dipole magnet. The TS is designed to provide the 4π solid angle coverage around the interaction point, while the FS is used to cover small polar angles in the forward region. The PANDA spectrometer comprises a variety of sub-detectors dedicated to measure tracks of produced particles, their energy deposit, Cherenkov light and timing. The most important characteristics of the PANDA spectrometer are listed below:

- possibility of mass scans with the resolution of 100 keV,
- event rate capability of $2 \cdot 10^7 \text{ s}^{-1}$,
- practically 4π acceptance with high detection efficiency,
- momentum resolution of 0.01,
- event start time reconstruction at picosecond level (off-line),
- good enough secondary vertex resolution (*e. g.* for D -meson decay reconstruction),
- excellent particle identification,
- wide range of photon detection (from 1 MeV to 10 GeV).

In this article, timing measurements are of particular interest. Timing information is foreseen in several PANDA sub-detectors (*e. g.*, barrel detection of internally reflected Cherenkov light (DIRC) or forward ring imaging Cherenkov (FRICH)). The high time resolution at the picosecond level will be provided for the PANDA experiment with two dedicated time-of-flight (ToF) detectors: the barrel ToF (BToF) in the TS and the forward ToF (FToF) wall in the FS. A side view of the PANDA spectrometer is shown in Fig. 1.

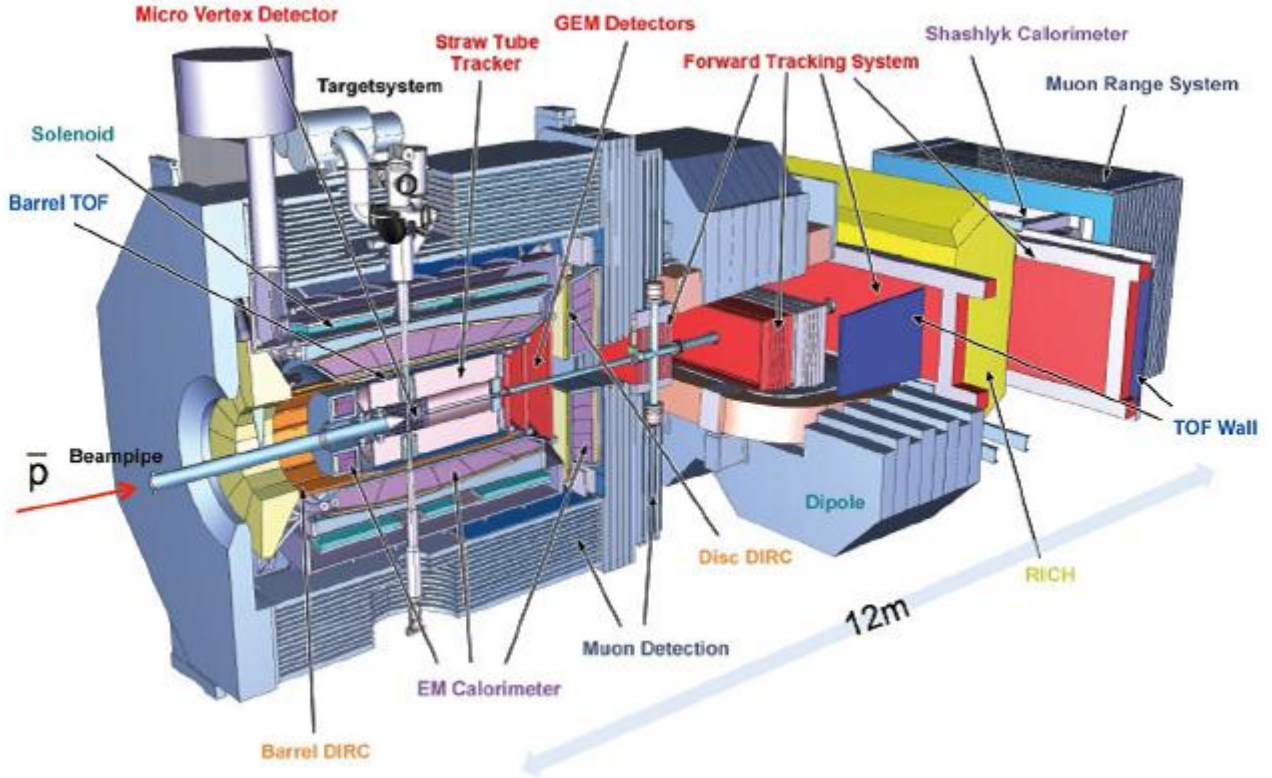


Fig. 1. Side view of the PANDA spectrometer with the target spectrometer (*left*), and the forward spectrometer starting with the dipole magnet centre (*right*). The \bar{p} beam enters from the left. The parts of the ToF wall inside the dipole are not included in the present design

3. The forward time-of-flight wall functions

3.1. Particle identification of low momentum hadrons

One important function of the FToF wall is to measure the ToF of forward particles emitted within the FS acceptance under laboratory angles below 5° and 10° in the vertical and horizontal directions, respectively. The FToF scintillation wall is assumed to be positioned at 7.5 m downstream of the PANDA target behind the FS dipole and PANDA FRICH detector (see Fig. 1). It has a large sensitive area: 560 cm (width) by 140 cm (height). In the off line analysis of the FToF wall data, the information on the particle momentum and track length provided by the dipole forward tracking (FT) system is used. With this information, the FToF wall should identify the hadrons (pions, kaons, protons, and their antiparticles) by the ToF criterion. As Monte Carlo (MC) analysis shows, a reliable proton–kaon and kaon–pion separation is possible at the momenta below 4.3 and 3 GeV, respectively, provided that the time resolution of the FToF detector is better than 100 ps. Note that this low momentum range is typically below the FRICH thresholds where there is no guarantee for the hadron detection with a high efficiency. No dedicated start counter in the interaction point area is foreseen for the PANDA detector. Similar to the HADES experiment at GSI [6], the ToF information is assumed to be obtained by using the time correlations between the responses (time

stamps) of two or more scintillation counters of the FToF wall. Besides, the combined information of the FToF wall and BToF can be used in many cases.

3.2. Determination of the event start T_0

As mentioned above, no dedicated start counter is assumed in the PANDA spectrometer. On the other hand, the determination of the antiproton-target interaction time stamp (event start) T_0 is one of the crucial points for the data analysis. The time stamp of a particle detected with a FToF wall counter may be used for a rough on-line determination of T_0 . The ToF for a relativistic particle from the interaction point to the FToF wall position is about $25 + \Delta$ ns where Δ is a relatively small additional time-variation depending on the sort of the particle, its scattering angle and momentum analysed with the help of the FS. Thus, for the momenta higher than 1 GeV, Δ is typically less than 20 ns, which defines a precision of the on-line T_0 measurement. T_0 can be determined much more precisely if a FToF wall particle hit is independently identified, *e. g.*, with FRICH or forward Shashlyk calorimeter, or forward muon range system, and the particle track is reconstructed by the FT system. Thus, if the particle is identified (say with the help of the FRICH), then the corresponding time stamps in the scintillation wall would give T_0 at a picosecond level.

3.3. Providing information on energy deposition

The energy deposition of the particles detected with the FToF wall is estimated to vary from 5 to 50 MeV. Once using the amplitude correction in timing measurements, this information is automatically available and can be extracted from the data for the analysis.

4. The forward time-of-flight wall design

The main technical requirements for the FToF wall design are summarized below:

- the time resolution should be better than 100 ps,
- the FToF wall is positioned at 7.5 m downstream of the target,
- in order to fully cover the FS acceptance, the sensitive area of the scintillation wall should be 5.6 m (width) by 1.4 m (height),
- the scintillation wall should withstand a high counting rate corresponding to the maximal luminosity of the PANDA experiment,
- the dynamic range of the detector should cover all possible variations of energy deposition in the scintillators.

The technical requirements above can be satisfied using commercially available components. The detector is modularized to be built of scintillation counters assembled of plastic scintillation slabs with good timing characteristics (*e. g.*, Bicron 408) and the fast photomultiplier tube (PMT) readout. The counters are assembled at 7.5 m downstream of the target, forming a wall with a sensitive area according to the technical conditions. The wall consists of 66 scintillation counters: 20 counters in the central part and 46 counters in the side parts (23 counters on each side). The height of all plastic scintillator slabs is 140 cm, and their thickness is 2.5 cm, while the width of the slabs is 5 and 10 cm for the central and side parts, respectively. Each scintillator is coupled on both ends with fast PMTs. The Hamamatsu PMT R4998 (1") and R2083 (2"), for the slabs of 5 and 10 cm width are planned to be used, respectively.

The R4998 and R2083 Hamamatsu tubes were tested by us during a long period in the process of prototyping together with some other PMTs. The performance of the Hamamatsu PMT was found to be the best. The light guides made of plexiglas are of the truncated cone (fish tail) configuration with different dimensions for the PMT of 1" or 2" diameter. In the central part of the wall, a rectangular hole (size: 20 cm by 20 cm) through which the beam pipe passes is left open. The hole is somewhat displaced off the exact centre because of deflection of the circulating beam by the PANDA dipole. The readout electronics is based on the FPGA system with four TRB-3 platforms and 18 PADIWA4 front-end interface modules [7–9]. The supporting frame of the FToF detector is positioned on a rail. An option to roll out the system to the service position is foreseen.

4.1. Prototyping

All the photodetectors used for prototyping were preliminary tested at the PNPI test station using electrons from β decay of a radioactive source ^{90}Sr . After a correction for the time walk and the readout electronics contribution, the time resolution noticeably better than 100 ps (about 40–50 ps) was achieved for the Hamamatsu R4998 and R2083 PMTs. Tests with large scintillators were performed using a 1-GeV proton beam of the PNPI synchrocyclotron and a 2-GeV proton beam from the COSY accelerator in Juelich. The most detailed tests were made in the PNPI with the help of the MAP magnetic spectrometer, which selected 920-MeV secondary protons elastically scattered off a hydrogen target. The scintillation counter prototypes were placed in the focal plane of the spectrometer (Fig. 2). The counter was mounted on a movable platform equipped with remotely controlled electric motors. Measurements were carried out at 14 positions of the slab moving along the horizontal axis perpendicular to the spectrometer axis.

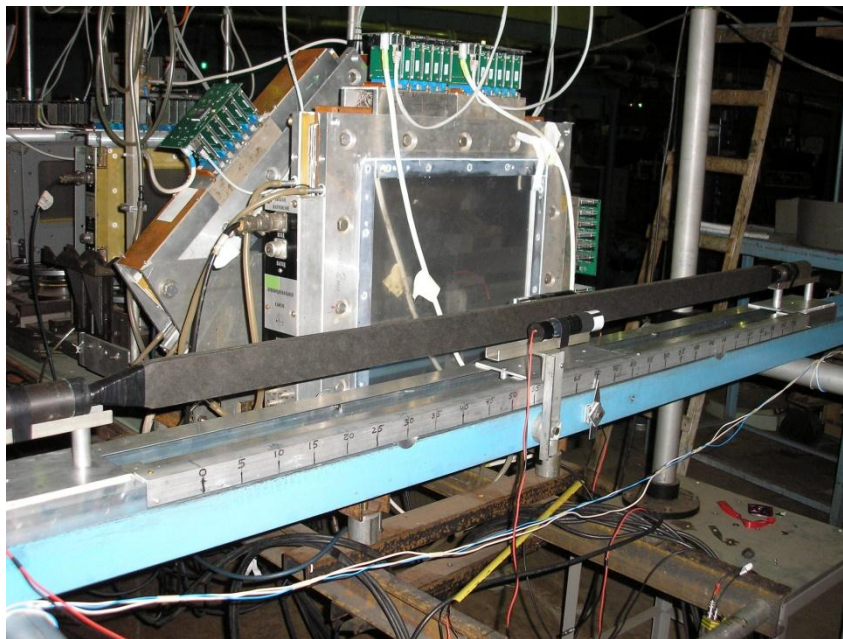


Fig. 2. A prototype of the scintillation counter placed on a movable platform in the focal plane of the MAP spectrometer

The momentum resolution was about 1%. The hit position on the slab was determined with 1 mm precision using tracking chambers. Depending on the hit position, the raw time resolution σ varied from 140 to 230 ps for a PMT at each end of the plastic scintillator. After applying (off-line) the amplitude and hit position corrections the resolution σ of 60–70 ps, was obtained. Here σ is the weighted mean of both end PMTs: $1/\sigma^2 = 1/\sigma_{\text{PMT1}}^2 + 1/\sigma_{\text{PMT2}}^2$. It is important that the variation of σ with the hit position on the slab was found to be small.

4.2. Monte Carlo simulation

A number of MC studies were performed in order to validate the detector design. It has been shown that the overall counting rate in the central part of the FToF wall will not exceed 2 MHz at the maximal luminosity ($2 \cdot 10^{32} \text{ cm}^{-2} \cdot \text{s}^{-1}$), which determines the detector granularity. One should remember that the latter must be compromised with the detector cost.

The main source of background is intensive production of neutral pions with consecutive $\pi^0 \rightarrow 2\gamma$ decay and production of the e^+e^- pairs in the spectrometer materials. This background depends strongly on the electron (positron) momentum. It stays below 10^5 s^{-1} at the lepton momenta smaller than 2 GeV. It drops down to negligible values at higher lepton momenta.

At the 10-GeV \bar{p} beam, the multiple hit probability in the FToF wall is almost 50% and the probability of FToF · BToF coincidences is about 40%. These numbers are essential for the efficiency of the ToF analysis. It has been shown that the intensive anti-Lambda hyperon peak is autonomously reconstructed with the FToF wall which can be additionally used for the detector tuning and calibration.

5. Conclusion

The project of the scintillation wall (FToF wall) which plays an important role in the hadron particle identification (PID) and determination of the event start in the PANDA experiment has been here briefly presented. The FToF wall was proposed and designed by the PNPI group. The PNPI is responsible for the final tests and construction of this detector. A description of the FToF wall in detail can be found in the FToF wall technical design report [10], which is presently under consideration by the Facility for Antiproton and Ion Research administration.

References

1. M. Kotulla *et al.*, Strong Interaction Studies with Antiprotons. Letter of Intent for PANDA (2004).
2. N. Brambilla, U.-G. Meissner, arXiv:1512.03299.
3. B. Singh, Nucl. Phys. A **954**, 323 (2016).
4. M.F.M. Lutz *et al.*, Physics Performance Report for PANDA: Strong Interaction Studies with Antiprotons (2009).
5. M. Kotulla *et al.*, Technical Progress Report for PANDA: Strong Interaction Studies with Antiprotons (2005).
6. G. Agakishiev *et al.*, Eur. Phys. J. A **41**, 243 (2009).
7. A. Neiser *et al.*, JINST **8**, C12043 (2013).
8. I. Froehlich *et al.*, in *Proc. of 10th Conf., ICATPP 2007, Como, Italy, 8–12 Oct., 2007*, 973 (2008).
9. F. Gonnella, V. Kozhuharov, M. Raggi, Nucl. Instrum. Meth. A **791**, 16 (2015).
10. PANDA Collaboration, S. Belostotski *et al.*, Technical Design Report for PANDA Forward Time of Flight Detector (FToF Wall) (2018),
https://panda.gsi.de/system/files/user_uploads/admin/RE-TDR-2016-004.pdf

PNPI IN THE R³B PROJECT AT FAIR

PNPI participants of the R³B experiment:

G.D. Alkhazov, V.A. Andreev, D.V. Balin, L.Kh. Batist, A.V. Dobrovolsky, V.L. Golovtsov, D.S. Ilyin, A.G. Inglessi, A.V. Khanzadeev, G.A. Korolev, A.G. Krivshich, E.M. Maev, D.A. Maysuzenko, A.V. Nadtochiy, G.E. Petrov, V.V. Sarantsev, N.Yu. Shvetsova, L.N. Uvarov, S.S. Volkov, V.I. Yatsoura, A.A. Zhdanov

1. Introduction

A versatile reaction set-up R³B with high efficiency, acceptance, and resolution for kinematically complete measurements of reactions with high-energy radioactive beams [1] is under construction at GSI Helmholtzzentrum für Schwerionenforschung (GSI, Darmstadt). R³B is a part of the NuSTAR project. The R³B set-up (Fig. 1) will be located at the focal plane of the high-energy branch of the Super-FRS. The experimental configuration is based on the concept similar to the existing LAND reaction set-up at GSI introducing substantial improvements with respect to resolution and an extended detection scheme, which comprises additional detection of light recoil particles and a high-resolution fragment spectrometer. The set-up is adapted to the highest beam energies (corresponding to 20 Tm magnetic rigidity) provided by the Super-FRS capitalizing on the highest possible transmission of secondary beams. The experimental set-up is suitable for a wide variety of scattering experiments, *i. e.*, such as heavy-ion induced electromagnetic excitation, knockout and breakup reactions, or light-ion elastic, inelastic, and quasi-free scattering in inverse kinematics, thus enabling a broad physics program with rare-isotope beams to be performed. The R³B program will focus on the most exotic short-lived nuclei, which cannot be stored and cooled efficiently, and on reactions with large-momentum transfers allowing the use of thick targets.

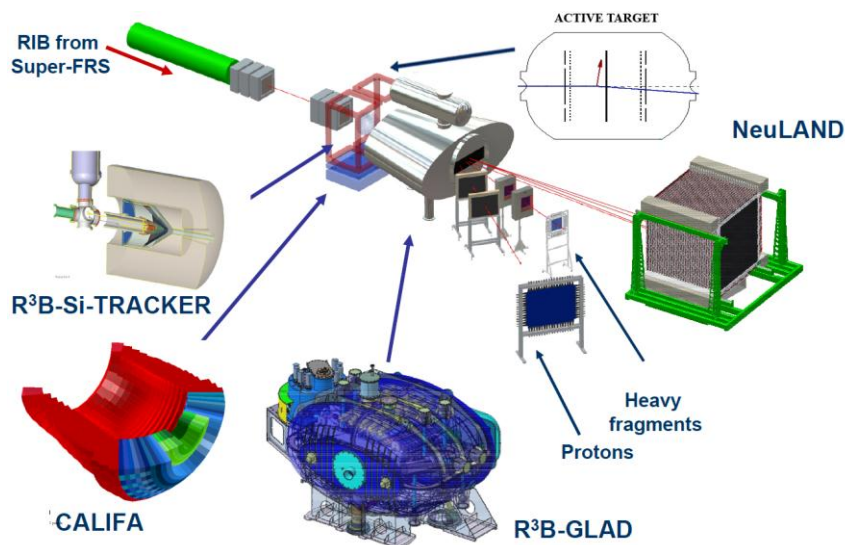


Fig. 1. The R³B detector set-up with its main components: the silicon tracker R³B–Si-TRACKER, the calorimeter CALIFA, the active target detector ACTAF, the dipole magnet R³B–GLAD, the protons and heavy fragments detectors, the neutron time-of-flight spectrometer NeuLAND

The incoming secondary beams are tracked and identified on an event-by-event basis. Measurements of the magnetic rigidity $B\rho$ (position measurement at the dispersive focus in the Super-FRS), time-of-flight (ToF), and energy loss ΔE provide unique isotope identification and momentum determination. After the secondary target, the kinematically forward focused projectile residues are again identified and momentum analysed. The large gap of the dipole provides a free cone of ± 80 mrad for the neutrons, which are detected in forward direction by a new large area neutron detector (NeuLAND). The target is surrounded by a γ -ray spectrometer. For elastic, inelastic and quasi-free scattering experiments or charge-exchange

reactions, liquid hydrogen or frozen hydrogen targets are considered. Recoiling protons and neutrons are detected by a Si-strip array and plastic scintillators, respectively. For measurements at low momentum transfers, the use of an active target is foreseen. For most of the experiments envisaged, a high-efficiency total-absorption spectrometer (cooled CsI or NaI) is the optimum solution, which is also used to measure the energy of recoiling protons. For specific experiments requiring ultimate energy resolution for γ detection, the germanium spectrometer AGATA might be used alternatively.

High beam energies, in the range of a few hundred MeV/u, allow a quantitative description of the reaction mechanisms, while also having experimental merits, such as the possibility of using relatively thick targets (in the order of 1 g/cm²). Moreover, due to the kinematical forward focusing full-acceptance measurements are feasible with moderately sized detectors. This makes it possible to gain nuclear-structure information from reaction studies even with very low beam intensities, as low as about 1 ion/s. R³B will cover experimental reaction studies with exotic nuclei far off stability, with emphasis on nuclear structure and dynamics. Astrophysical aspects and technical applications will be also concerned. A survey of reaction types and associated physics goals that can be achieved is given in Table.

Table

Reaction types with high-energy beams measurable with R³B and corresponding achievable information

Reaction type	Physics goals
Knockout	Shell structure, valence-nucleon wave functions, many-particle decay channels, unbound states, nuclear resonances beyond the drip lines
Quasi-free scattering	Single-particle spectral functions, shell-occupation probabilities, nucleon–nucleon correlations, cluster structures
Total-absorption measurements	Nuclear matter radii, halo, and skin structures
Elastic p scattering	Nuclear matter densities, halo, and skin structures
Heavy-ion induced electromagnetic excitation	Low-lying transition strength, single-particle structure, astrophysical S factor, soft coherent modes, low-lying resonances in the continuum, giant dipole (quadrupole) strength
Charge-exchange reactions	Gamow–Teller strength, soft excitation modes, spin-dipole resonance, neutron skin thickness
Fission	Shell structure, dynamical properties
Spallation	Reaction mechanism, astrophysics, applications: nuclear-waste transmutation, neutron spallation sources
Projectile fragmentation and multifragmentation	Equation-of-state, thermal instabilities, structural phenomena in excited nuclei, γ spectroscopy of exotic nuclei

PNPI physicists participate in the R³B project in construction of the high voltage (HV) system for the detector NeuLAND, the proton detector PAS for tracking protons and other light charged particles behind the R³B dipole magnet, and the active target (targets) for fair ACTAF for detection of low-energy recoil particles, as well as in the physics program when the R³B set-up starts to collect data.

NeuLAND is the next-generation high-energy neutron detector (200 to 1 000 MeV) designed for R³B, which meets all requirements defined by the ambitious physics program proposed for the R³B facility. NeuLAND features a high detection efficiency, a high resolution, and a large multi-neutron-hit resolving power. This is achieved by a highly granular design of plastic scintillators, avoiding insensitive converter material. The detector will consist of 3 000 individual sub-modules with a size of $5 \times 5 \times 250$ cm³, arranged in 30 double planes with 100 submodules providing an active face size of 250×250 cm² and a total depth of 3 m. NeuLAND can be divided into two detectors for special applications and will be placed at different distances from the target, in order to meet specific experimental demands. The main design goals of NeuLAND comprise a one-neutron detection efficiency above 95% in a wide energy range and a full

acceptance corresponding to an angular coverage of 80 mrad. The desired resolutions for momenta and thus the excitation energies lead to the required spatial resolutions of ~ 1.5 cm and to the time resolution of ~ 150 ps for the standard distance between the detector and the target of 15.5 m. When placed at a distance of 35 m, an excitation-energy resolution of better than 20 keV will be reached for an excitation energy of 100 keV above threshold for a beam energy of 600 A MeV. Apart from the excellent energy resolution, NeuLAND has an enhanced multineutron recognition capability with an efficiency of up to 60% for reconstructed four-neutron events.

2. High voltage system for NeuLAND

In 2012, PNPI physicists presented to GSI a proposal for designing and manufacturing a HV distribution system (HVDS) for 6 000 photomultipliers of the spectrometer NeuLAND.

The principle of operation of the proposed HVDS is individual down-regulation of the output voltage of a primary HV power supply for each photomultiplier tube (PMT), Fig. 2. The advantages of this proposal are the following:

1. The HV value from a primary power supply (PS) unit is individually down-regulated and then distributed to each PMT.

2. The HV value is generated locally at the PMT base, the control levels and voltage and current monitoring values being delivered to/from the PMT *via* an analog interface.

3. The HV value is generated the same way as above, but digital-to-analog converters (DAC) and analog-to-digital converters (ADCs) are located on each PMT base as well.

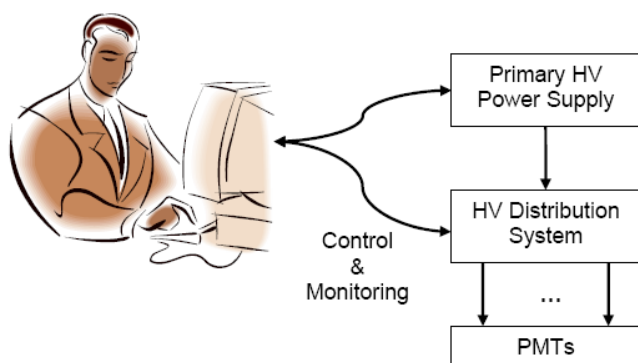


Fig. 2. HVDS for NeuLAND

The host computer controls HV settings of the primary PS and each out of 6 000 down-regulators of the HVDS. It also monitors the actual HV applied to each PMT and the current drawn by it. All control and monitoring operations are executed over Ethernet. Each PMT consumes 0.3 mA of current, a primary HV PS rated at 1 A can feed up to 3 000 PMTs, or one half of the NeuLAND detector. The proposed HVDS details are shown in Fig. 3.

Each PMT is powered from an output of a separate regulator Reg_XX, where XX is a channel number spanning from 01 to 50. Fifty regulators reside at a 50-channel distributor board (DB50). Only 4 DB50s are needed for a double plane of scintillator bars (containing 100 scintillator bars), with 2 DB50s sitting at each top corner of the double-plane frame. A single primary HV PS rated at 1 A can feed up to 15 double planes or up to 60 DB50s.

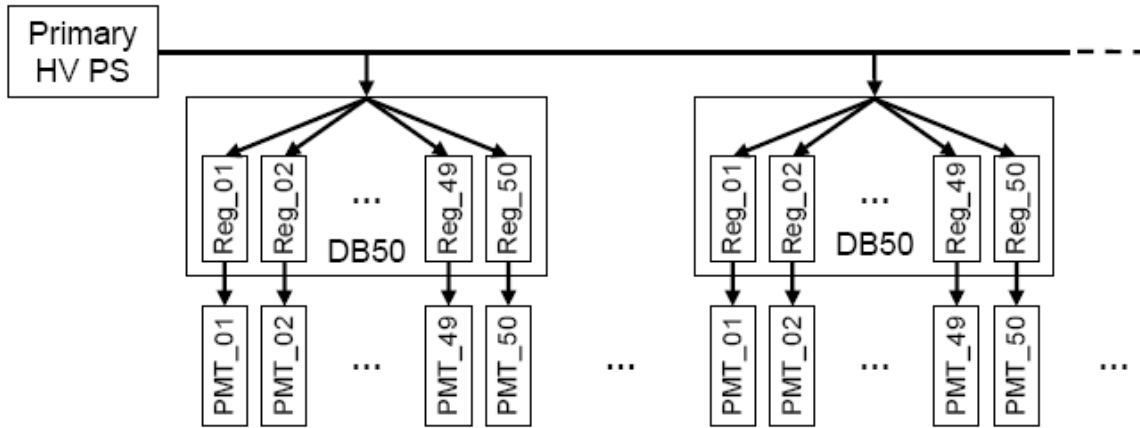


Fig. 3. HV distribution from a primary HV power supply

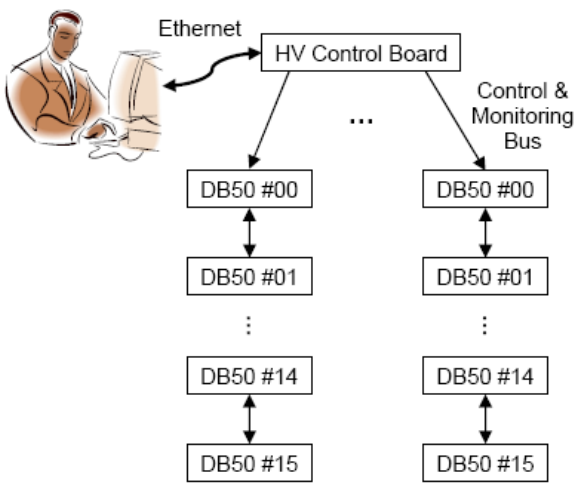


Fig. 4. HVDS control and monitoring

A host computer uses Ethernet to connect to the HV control board (HVCB) (Fig. 4). The HVCB features four outputs with RJ-45s for connecting control and monitoring buses (CMB). Each CMB is capable to control and monitor up to 16 DB50s. The HVCB serves up to 64 DB50s, which translates to 3 200 PMTs. The CMB is implemented as a Cat 5 network cable with four pairs of wires. Two pairs are used for downloading HV settings and two pairs – for receiving voltage and current monitoring data. Each DB50 has a pair of RJ-45s connected to the same bus. To add a new DB50 to the already existing bus, the user just needs to add a jumper cable from the last DB50 in the chain to a new one. Plugging in the CMB terminator in the last DB50 is optional and depends on the overall CMB length. The DB50 has a switch that sets its address (from 00 to 15 in decimal or from 0×0 to $0 \times F$ in hex). Of course, all DB50s on the same CMB should carry exclusive

addresses. The HVCB carries an field-programmable gate array (FPGA) that keeps the control and monitoring data for each HV regulator. There is also a sequencer that continuously updates control values in regulators and scans them for monitoring data.

The output voltage is regulated from 0 to 1 600 V by a 10-bit DAC. The voltage is monitored by a 10-bit ADC for the same range. The current is monitored by a 10-bit ADC with a 1 nA resolution. The maximum output current into load is 0.5 μ A. The system comes with a software package to perform control, monitoring and calibration tasks.

The production of the HV system was started in 2014. By the end of 2017, the HV system for 3 000 channels was fabricated. The completion of the HV system production (of 6 000 channels) is planned in 2019.

3. Proton arm spectrometer for the R³B set-up at FAIR

The tracking detectors for R³B are designed to be used in a wide variety of experiments with the R³B set-up, where beams of unstable nuclei up to 1 GeV/u formed by the Super-FRS at Facility for Antiproton and Ion Research (FAIR) impinge on a secondary target, the reaction products being magnetically analysed with the superconducting magnet GLAD (GSI large-acceptance dipole). For multi-particle final states, the invariant mass is obtained from the momenta and relative angles of the outgoing particles.

Protons emitted in flight from excited fragments are bent in the dipole magnet GLAD and tracked using the dedicated proton arm spectrometer (PAS) that is placed inside of a large vacuum chamber.

A thick plastic scintillator wall, which is placed behind the PAS after the vacuum exit window of the GLAD magnet, will be used for timing, triggering and particle identification. It consists of vertically placed paddles read out by photomultiplier tubes covering the size of $2.7 \times 1.2 \text{ m}^2$.

The PAS project was proposed by PNPI physicists and it received approvals of both the German (the expert council of the FAIR megaproject) and Russian parties (the expert council of the State Atomic Energy Corporation “Rosatom”). The proposed project is basically different from that considered previously by the R³B Collaboration [2]. The complex of following fundamental problems should be solved in the course of realization of the project:

1. The tracking detector that previously registered X and Y coordinates of protons in one plane, *i. e.* in other words, it represented a hodoscope, now it will be a proton spectrometer (telescope), which registers the coordinates of the proton tracks at several points along the beam, providing a high angular resolution (better than 10 mrad).

2. The detector aperture is increased from $500 \times 500 \text{ mm}^2$ to $2300 \times 1100 \text{ mm}^2$, the number of information recording channels is increased up to 2000.

3. The PAS will be installed inside the vacuum chamber behind the GLAD dipole magnet. To ensure reliable operation of PAS under vacuum conditions and simultaneously achieve the required operating characteristics in a confined space in the vacuum chamber, the proton arm spectrometer will be based on straw-tube technology.

4. The spatial resolution of a single straw tube should be better than $200 \mu\text{m}$. Two-track resolution of PAS of time-correlated pair events should be less than 10 mm.

5. The resistance of straw tubes (mylar/kapton and thin-walled aluminum) to radiation damage while working in intense and complex-composition radiation fields (protons, light, and heavy ions) should be studied.

The PAS detector will contain a small amount of material ($X/X_0 \approx 0.05\%$ per tube) having a long length (up to 2.5 m). The layout and space position of the PAS detectors inside the GLAD vacuum chamber is shown in Fig. 5. PAS will consist of four straw-tube walls (STW), two pairs detecting either horizontal or vertical positions of particles. The PAS cover an active area that fully matches the geometrical acceptance given by the gap of the GLAD dipole magnet of $\pm 80 \text{ mrad}$, thus providing a full coverage of the available solid angle behind the magnet to detect the emitted protons. The geometry and the operational parameters of the STWs are optimized to detect minimum-ionizing particles with an efficiency higher than 95% and a spatial resolution of $\sigma_{x,y} \leq 200 \mu\text{m}$.

The angular resolution of a single STW is about 10 mrad. Evidently, the total angular resolution is improved by using multiple planes separated by some distance. With this geometry, the angular resolution in the dispersive

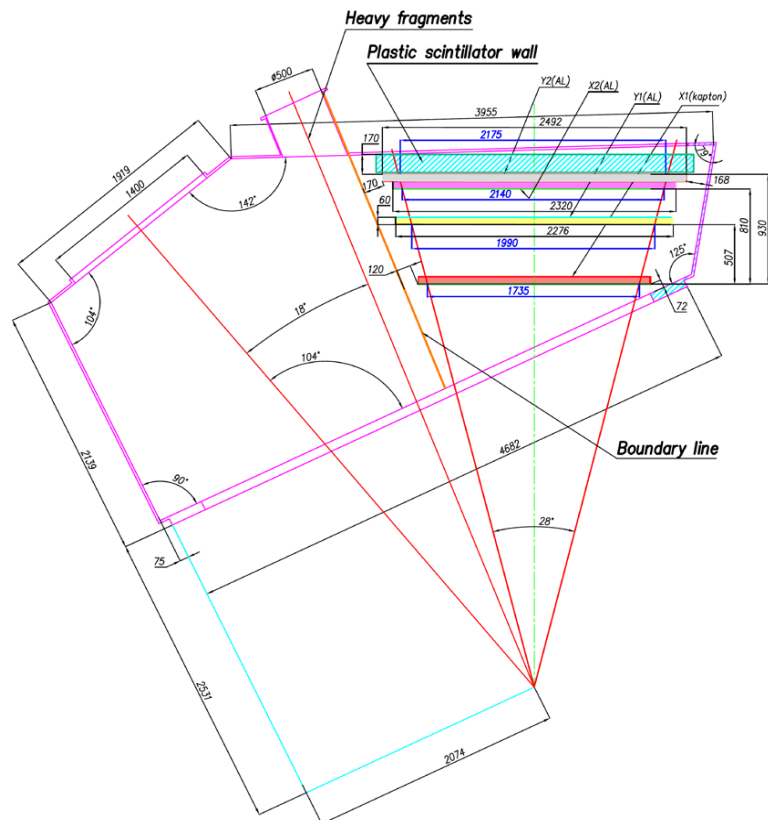


Fig. 5. Layout of PAS detectors in the GLAD vacuum chamber. The violet color line shows the boundaries of the vacuum volume

direction is about 0.3 mrad, significantly smaller than the typical angular straggling that a 500–1 000 MeV energy proton suffers while passing the first plane.

The first STW (X_1) is made of thin-walled kapton (or mylar) tubes. The kapton is chosen as the basic material for the straw cathodes because of its good mechanical properties, small amount of material, and resistance to radiation damage. This high transparency allows less shadowing on the following detectors and background-free tracking.

The other three STWs (Y_1 , X_2 , Y_2) are made of aluminum tubes with a wall thickness of about 300 μm . Their diameter is 10 mm. Although the angular straggling caused by these tubes is significantly larger compared to the thin kapton tubes, their influence in the dispersive angular measurement is small since they are located near the end of the track. Aluminum tubes are used in order to minimize the total leakage of the gas into the vacuum volume and to constrain the total cost of the array.

To facilitate access to PAS, the PAS detector is placed on a movable platform inside the large vacuum chamber behind GLAD. The electronic front-end readout cards, the gas system, the high- and low-voltage PS, and other services of PAS are arranged at the detector and the mechanical frame structures.

Each STW of the PAS will consist of three layers of straw tubes filled with a gas mixture at the overpressure of about 1 bar. The tubes are glued together, each layer being shifted by one tube radius with respect to the previous layer. Then, for an orthogonal proton track, a lower detection efficiency close to the tube wall is always combined with high efficiency in the centre of the straw in the following (staggered) layer. Also, the track's left/right ambiguity from the wire can be disentangled in the next layer.

The straw tubes under the overpressure of the gas mixture (1–2 atm) in vacuum can be seen as this basic technology. This will ensure the required cylindrical shape of each tube and allows to build a self-sustaining detector design that does not require special strong supporting outer frames. On the other hand, the overpressure results in serious problems that should be solved during implementation of this project. The problems include:

1. A possible instability of operation of each of the straw tubes (caused by a change in their length and diameter, and as a consequence a change in the tension of the anode wires) can result in structural deformations of a group of several hundreds of straw tubes combined together that form the STW- X_1 detector station and, as a consequence, a serious deterioration of the detector operating characteristics.

2. Different diffusion rate of the working gas components through the tube mylar (kapton) walls.

The 25 μm -diameter gold-plated tungsten anode wire is stretched by a weight of 70 g and placed in the copper pins (0.1 mm holes). At such a wire tension, the calculated gravitational sag for Y_1 and Y_2 should be smaller than 30 μm , which is below the projected spatial resolution of 200 μm .

The granularity (tube diameter) of 10 mm and the straws precise alignment allows a continuous tracking with a few hits per track, which is important in order to resolve complex track patterns. The position accuracy of the mounted STW relative to the precision alignment marks in the end angles of the PAS mechanical frame should be better than 100 μm . Due to the close packaging of the glued straws in a module with a precise tube-to-tube distance, the deviations in the position of a single straw is less than 100 μm . The overall mechanical precision in the X – Y plane will be below 200 μm .

Straw tubes are proportional counters that are used as drift chambers with the corresponding structure of the electric field inside. The PAS straws will be operated in the proportional mode. The drift time information can be converted to distance R from the particle track position to the anode wire by using the so-called X – T relation obtained from calibration experiments. The ideal gas mixture will present a linear X – T relation over the entire distance R in the straw. The optimal choice of the working gas mixture is still to be determined.

The straw tubes will work in intense radiation fields of complex composition (protons and heavy ions). The detector will detect not only protons with energies $E_p = 500$ –1 000 MeV, but also the background of light and heavy ions. Dedicated studies of radiation resistance of the detector will allow to optimize the detector radiation resistance at the design and examination stage and will ensure the maximum lifetime of the detector in experiments.

The four STWs of the PAS consist of about 2 000 channels. The front-end electronics are placed in vacuum close to the straw-tube detectors for optimum performance in terms of noise. The electronics

consists of two types of signal processing boards – DA16 and DD32 – and of a communication board DC2K for threshold control on the individual channel bases.

For the read-out of the STW signals, a time-to-digital converter (TDC) with $\sigma_t \leq 500$ ps time resolution will be used. The TDC will accept low-voltage differential signals (LVDS) directly from the discriminator. The TDC modules must be fully compatible with the R³B DAQ standards. The PAS TDCs will run an internal clock for time measurement, which will be synchronized with a distributed clock signal (*e. g.* 100 MHz) from the R³B DAQ.

The PAS electronics will normally run with an external trigger provided by the R³B DAQ. However, for testing and commissioning, the PAS electronics should also be able to run in stand-alone mode. For this, an additional input for a reference signal (start counter) should also be foreseen.

The PAS electronics provides: the preamp/shaper peaking time – 10 ns; the digitizing rate – up to 1 000 MHz; the trigger rate, max – 25 kHz; the trigger latency, max – 100 μ s; the data flow, max – 750 kB/s.

4. Active targets

In the R³B project, the implementation of an active target ACTAF is proposed mainly for two types of experiments:

1. Investigation of direct reactions where only recoil particles and beam-like particles need to be detected, for example, the elastic scattering of nuclei on protons at low momentum transfers in inverse kinematics and charge-exchange reactions.

2. Investigation of direct reactions where, besides the recoil and projectile particles, also γ -rays are detected in coincidence, for example, inelastic scattering of nuclei on helium nuclei in the region of the giant resonances in inverse kinematics.

These tasks differ in their general set-up and particularly in registration of recoiled particles in the active target. Investigation of elastic scattering requires measurements of the energy of the recoiled particles in a relatively large dynamic range, as well as of their angle. In the study of inelastic scattering, not only the recoiled particle will be detected, but also the γ quanta will be registered by the external detector CALIFA. So, ACTAF will be placed in this case inside of this detector, and therefore the dimensions of this detector are limited. We have proposed to build two active targets (ACTAF1 and ACTAF2), well adapted to the demands of the different experiments to be performed (in the beginning, the names of these targets were ACTAR1 and ACTAR2). These detectors will be designed and constructed for studies of elastic and inelastic scattering of light to heavy nuclei on protons and helium targets. The ionization chamber ACTAF1 has a diameter of ~ 1 m, it is filled with pure hydrogen at the pressure of up to 20 bar. It will be used for studying proton–nucleus elastic scattering in inverse kinematics. The chamber ACTAF2 has a diameter of 0.4 m, it is filled with helium at a pressure up to 10 bar. ACTAF2 will be placed inside the γ spectrometer CALIFA and will be used for the investigation of inelastic scattering of exotic nuclei on helium nuclei in coincidence with γ rays in order to study giant resonances. The operating principle and the design of the ACTAF chambers are similar to those of the IKAR hydrogen-filled ionization chamber used at GSI since 1993 in experiments on proton–nucleus scattering in inverse kinematics with beams of light nuclei up to ¹⁷C [3]. As distinct from IKAR, the anodes of ACTAF are segmented, which allows one to determine the azimuthal angle of the scattered recoil particle, to determine the range of the recoil particles and to reduce background from δ electrons. For details of the construction of active targets ACTAF1 and ACTAF2 see the “Technical Report for the Design, Construction and Commissioning of the Active Target for FAIR (ACTAF) for the R³B Experiment” [4].

PNPI physicists have fabricated a prototype of the active target ACTAF2 (Figs. 6, 7) for studying inelastic ⁴He-nucleus scattering in inverse kinematics. During 2012–2013 the prototype of the chamber ACTAF2 was constructed and prepared for testing in GSI ion beams. In 2014–2017, three test experiments were performed at the GSI and MAMI (Mainz) accelerator facilities aiming to check the functionality of the detector ACTAF. The first test experiment was performed at the GSI accelerator facility in 2014 [5]. A beam of ⁵⁸Ni ions with an energy of ~ 700 MeV/u passed through the chamber. The chamber was filled with a helium–hydrogen (10%) mixture at several gas pressures (2.5 and 10 bar) for evaluation of optimal

conditions for registration of recoiled particles with different energy. Hydrogen was added to helium in order to increase the gas breakdown strength, as pure helium does not allow the necessary high voltage.

The anode planes of the ACTAF prototype are designed so that the beam of heavy ions would pass across the central anode of 20 mm diameter and possibly the first ring-shaped anode of 40 mm outer diameter. The beam diameter was expected to be less than 40 mm. All other anodes around the central anode and the first ring-shaped one are segmented. The total number of segmented anodes is 66. The construction of the ACTAF multi-segmented anode plane gives the possibility to distinguish different types of recoil particles (p , d , t , ^3He , and ^4He) using the correlation between the energy deposit and the range of the recoil particles. The signals from all anodes are read out independently by the electronics including preamplifiers, amplifiers and fast 14 bit Flash-ADCs (FADs). In the test experiment, along with the information from the ionization chamber, the data from other detectors of the whole set-up were recorded. The general start of the readout system was triggered by the beam scintillator detector. The information from all FADCs was recorded if a sufficiently large pulse (more than 0.45 MeV) was present at least at one of the segmented anodes. The energy calibration was performed using a precise pulser and an ^{241}Am α -source. The ^{58}Ni beam intensity was ~ 5 kHz. The energy resolution in this experiment was estimated to be 20 keV (rms). This value was similar to the one obtained with a pulse generator, demonstrating a relatively small influence on the energy resolution of δ electrons emitted by heavy projectiles. The test experiment in 2014 was the first implementation of an active target of this type having a beam of ions heavier than carbon.

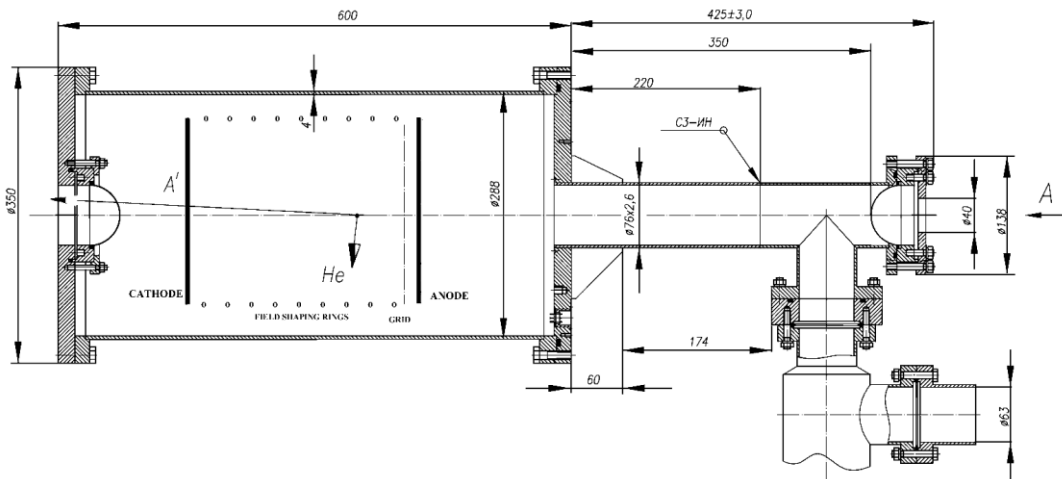


Fig. 6. Schematic side view of the ACTAF2 prototype

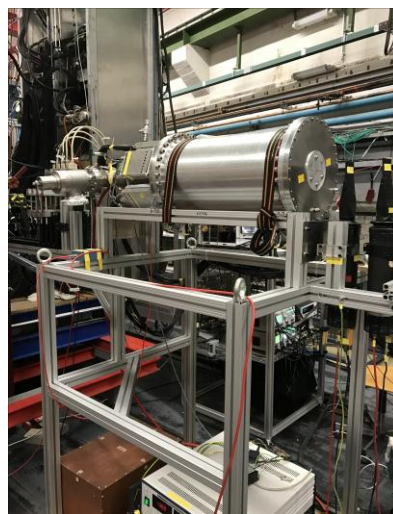


Fig. 7. ACTAF2 prototype in the experimental hall of the accelerator MAMI

During 2016–2017, next test experiments were performed at GSI (with a beam of ^{124}Xe ions with an energy of ~ 600 MeV/u) and at the MAMI (Mainz) electron accelerator with the purpose to continue detail checks of the functionality of the ACTAF2 prototype. Figure 7 shows the ACTAF2 prototype in the experimental hall of the MAMI accelerator. The intensity of the electron beam with the energy of 720 MeV was changed from 10 kHz up to 2 MHz. The filling gas was He + 4% N₂ at 10 bar. Figure 8 shows the geometry of the ACTAF2 prototype anode and signals on the fired anode segments from one of the recoil α -particles. The experimental data obtained in these three test experiments with the ACTAF2 prototype proved the possibility of registration of different types of recoil particles with low energies (0.4 MeV) and the efficiency close to 100%, the energy resolution being 20–30 keV.

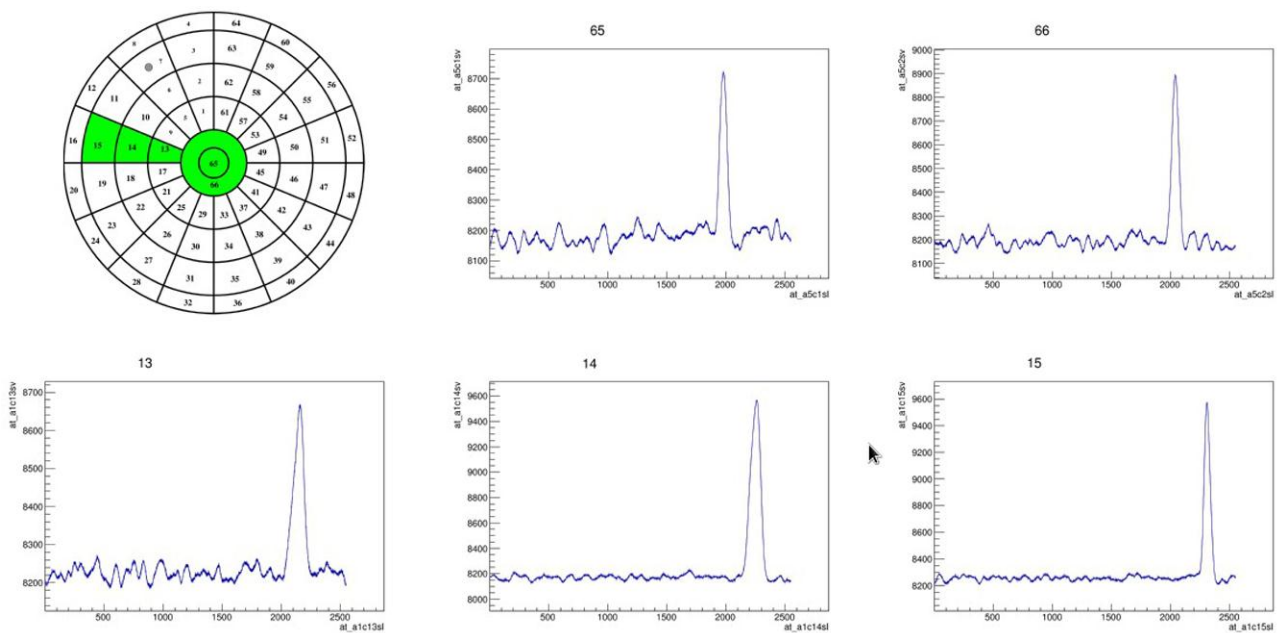


Fig. 8. Segmented anode of ACTAF2 and signals from a recoil α particle on the fired anode segments (marked by *green*)

5. Concluding remarks

The experiment R³B at FAIR is devoted to the study of the nuclear structure of exotic nuclei using a universal experimental set-up with high efficiency, acceptance, and resolution for kinematically complete measurements of reactions with high-energy radioactive beams. PNPI physicists plan to participate in construction of this set-up by fabricating the high-voltage system for the NeuLAND detector, by designing and building the proton tracking detector PAS for measuring coordinates and angles of protons and light nuclei emitted in nuclear reactions, and the active targets ACTAF1 for studying elastic proton–nucleus scattering (in inverse kinematics) and ACTAF2 for studying inelastic ^4He -nucleus scattering.

The experiment R³B will be a unique facility providing the capability for kinematically complete measurements of reactions with relativistic heavy-ion beams of short-lived nuclei up to about 1 A GeV. The experimental results which will be obtained with the R³B set-up are expected to be very important for theory of the nuclear structure and nuclear reactions, and for solving open questions of modern astrophysics.

References

1. GSI. A Next Generation Experimental Setup for Studies of Reactions with Relativistic Radioactive Beams, <http://www.gsi.de/r3b>
2. Technical Report for the Design, Construction and Commissioning of the Tracking Detectors for R³B (2014), https://edms.cern.ch/ui/file/1865815/2/TDR_R3B_TrackingDetectors_public.pdf
3. G.D. Alkhazov, A.A. Vorobyov, A.V. Dobrovolsky *et al.*, *Yad. Fiz.* **78**, 411 (2015).
4. Technical Report for the Design, Construction and Commissioning of the Active Target for FAIR (ACTAF) for the R³B Experiment (2016), https://edms.cern.ch/ui/file/1816116/1/TDR_R3B_ACTAF_public.pdf
5. G.D. Alkhazov *et al.*, GSI Scientific Report 2014, GSI, 2015, p. 191.

Methodical and Applied Research

UNIVERSAL PROTON AND NEUTRON CENTRE FOR RADIATION RESISTANCE OF AVIONIC SPACE ELECTRONICS AND OTHER APPLICATIONS AT THE 1-GeV SYNCHROCYCLOTRON IN PNPI

D.A. Amerkanov, S.A. Artamonov, E.M. Ivanov, J.S. Lebedeva, G.F. Mikheev, G.A. Riabov, O.A. Shcherbakov, A.S. Vorobyev
in collaboration with the Branch of JSC “United Rocket and Space Corporation” – “Institute of Space Device Engineering” (Russia): P.A. Chubunov, V.S. Anashin, L.R. Bakirov, A.E. Koziukov

1. Introduction

The proton synchrocyclotron SC-1000 with the proton energy of 1 GeV and intensity of the extracted proton beam of 1 μ A [1] is one of the basic installations of the PNPI. It was commissioned in 1970 and was significantly modernized during its exploitation. The experimental complex of the SC-1000 is used for investigations in the fields of elementary particle physics, atomic nuclear structure and mechanisms of nuclear reactions, solid state physics, and for purposes of applied physics and nuclear medicine. Radiation resistance testing of electronics is conducted at the SC-1000 during more than two decades. A sharp growth of the needs in the accelerated single-event effect testing of electronic components and systems intended for avionic/space and other applications has led to a development of new test facilities at high-energy accelerators, which are used as powerful sources of protons and neutrons.

In the present report, a short description is presented of the proton (IS SC-1000 and IS OP-1000) and neutron (IS NP/GNEIS) test facilities developed at the PNPI in collaboration with the Branch of JSC “United Rocket and Space Corporation” – “Institute of Space Device Engineering” (Branch of JSC “URSC”– “ISDE”), a Head Organization of the Roscosmos Interagency Testing Centre. A unique conjunction of proton beams with variable energy 60–1 000 MeV and a neutron beam with a broad energy range (1–1 000 MeV) spectrum enables to perform complex testing of semiconductor electronic devices at the SC-1000 within a single testing cycle.

2. Proton test facilities

At present, two of three proton beam lines of the SC-1000 are used for radiation testing of electronics. The IS SC-1000 test facility has a fixed proton energy of 1 000 MeV and is located in the P2 beam line. At the IS OP-1000 facility located at the P3 beam line, the proton energy can be varied from 1 000 MeV down to 60 MeV by means of a system of copper degraders (absorbers) of variable thickness from 73 mm (at 900 MeV) to 530 mm (at 60 MeV) [2]. A scheme of the proton beams and irradiation workstations placed in the experimental room, as well as a photo of the degrader system located in the SC-1000 main room are shown in Fig. 1. The parameters of both proton test facilities are given in Table 1.

An adjustment of the proton beam profile is carried out roughly by means of quadrupole lenses whereas for final tuning a 2m-long steel collimator with 20 mm aperture is used. All irradiations are carried out at open air and room temperature. Both proton and neutron beam lines are equipped with a remotely controlled system intended for positioning the device under test and heating it in the 20–125 °C temperature range.

Parameters of the proton beam at the outlet of the copper absorber of variable thickness were evaluated by means of the GEANT4 code calculation. The energy distribution of the initial proton beam was supposed to be of a Gaussian type with the parameters of 1 000 and 3.84 MeV for the proton energy and standard deviation, respectively. The results of GEANT4 calculations are given in Table 2 and Fig. 2. Both incoming and outgoing proton beam parameters were verified experimentally by means of ToF-measurements carried out using the microstructure of the proton beam (~ 73 ns between proton micropulses).

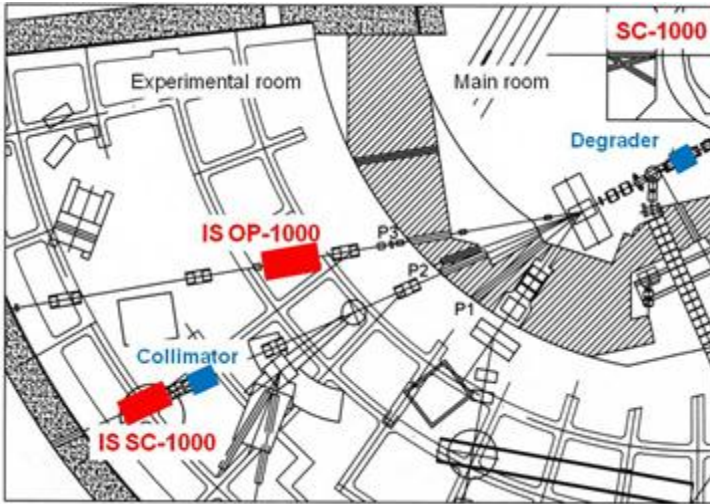


Fig. 1. Scheme of the proton beam lines: P2 – protons with the energy of 1 000 MeV; P3 – protons with the energy variable from 1 000 to 60 MeV (*left*); device for remote variation of the absorber length and of the proton energy (*right*)

Table 1

Parameters of the proton test facilities

Parameter	IS SC-1000	IS OP-1000
Irradiation conditions	Atmosphere	Atmosphere
Particle	Protons	Protons
Energy, MeV	1 000	60–1 000
Flux, $p/cm^2 \cdot s$	10^5 – 10^8	10^5 – 10^8
Irradiation area, mm	$\varnothing \geq 25$	$\varnothing \geq 25$
Uniformity, %	≤ 10	≤ 10
Status	In operation (since 1998)	In operation (since 2015)

Table 2

Parameters of the proton beam after transmission through the copper absorber (GEANT4 calculation)

Proton energy, MeV	Standard deviation, MeV	Absorber thickness, mm	Absorber transmission, %
62.1	28.20	530.5	1.6
100.09	24.63	521.2	2.3
197.93	15.77	490.8	3.4
300.21	12.12	448.7	5.4
399.12	10.24	398.0	8.4
499.24	8.92	340.9	13.5
601.03	7.89	279	22.0
699.88	7.01	213.1	35.6
800.18	6.13	144.3	56
899.85	5.13	73.11	82.1

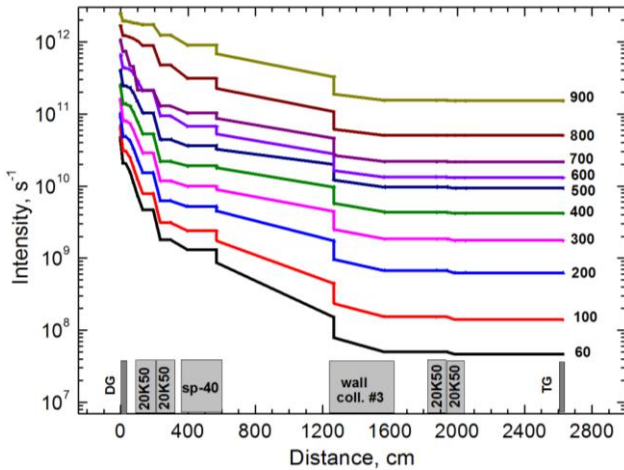


Fig. 2. Dynamics of protons losses at different energies along the beam line P3: DG – absorber; 20K50 – quadrupole; SP-40 – bending magnet; wall, coll. #3 – a wall with the collimator #3 between the main and experimental room of the accelerator; TG – target

The beam diagnostics is carried out using a set of standard tools which includes: 1) a thin scintillator screen coupled with a CCD-sensor for rapid evaluation of the beam profile image, 2) a 2D-moving Se-stripe-type beam profile meter, 3) a double-section ionization chamber for “on-line” control of the proton intensity (fluence), 4) an Al-foil activation technique in conjunction with a high-resolution HPG-detector as an absolute “off-line” monitor of the proton fluence.

3. Neutron test facility

The IS NP/GNEIS test facility is operated since 2010 at the neutron ToF-spectrometer GNEIS [3, 4]. Its main feature is a spallation source with the neutron spectrum resembling that of terrestrial neutrons in the energy range of 1–1 000 MeV. The water-cooled lead target located inside the accelerator vacuum chamber (Fig. 3) produces short 10 ns pulses of fast neutrons with a repetition rate of 45–50 Hz and an average intensity up to $3 \cdot 10^{14} n \cdot s^{-1}$. The IS NP/GNEIS test facility is located inside the GNEIS building on the neutron beam No. 5, which has the following parameters:

- neutron energy range: 1–1 000 MeV,
- neutron flux: $4 \cdot 10^5 \text{ cm}^{-2} \cdot \text{s}^{-1}$ (at 36 m flight path),
- beam diameter: 50–100 mm (at 36 m flight path),
- uniformity of the beam profile plateau: $\pm 10\%$.

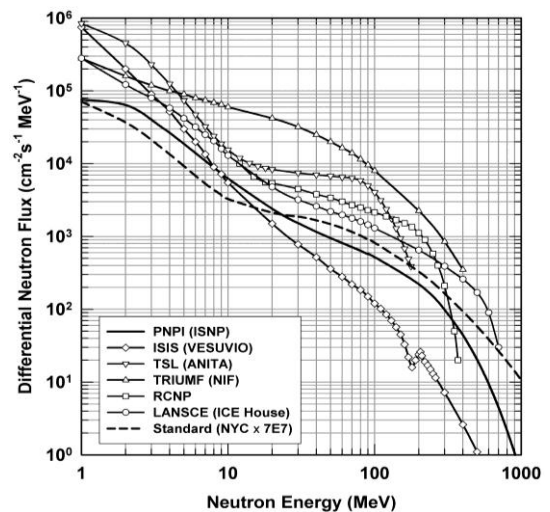
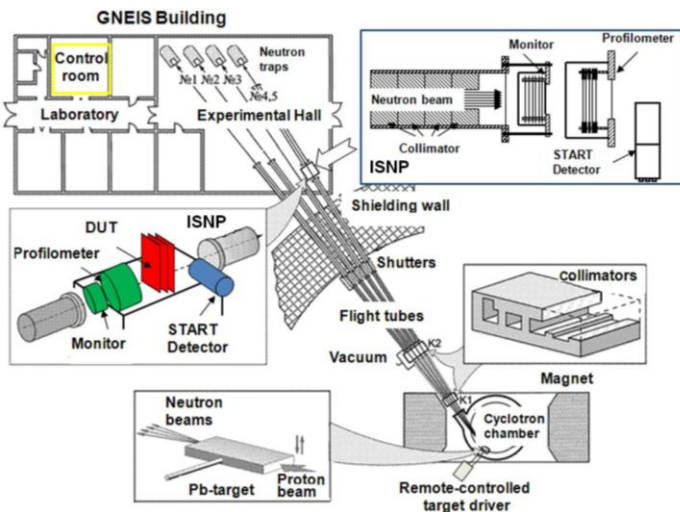


Fig. 3. General layout of the neutron time-of-flight spectrometer GNEIS and IS NP test facility (left); neutron spectrum $F_{IS NP}(E)$ of the IS NP/GNEIS facility in comparison with the standard terrestrial neutron spectrum and spectra of other world-class test facilities (right)

The neutron flux of $4 \cdot 10^5 \text{ cm}^{-2} \cdot \text{s}^{-1}$ is an integral over the neutron spectrum in the energy range 1–1 000 MeV. It corresponds to the maximum value of $3 \mu\text{A}$ of the internal average proton beam current. The neutron flux and the shape of the neutron spectrum are measured using a neutron monitor and the ToF-technique (Fig. 4). The neutron monitor is a fast parallel-plate ionization chamber which contains two targets of ^{235}U and ^{238}U . The neutron fission cross sections of these nuclei are the recommended standards in the energy range 1–200 MeV. The neutron beam profile is measured by means of a multiwire proportional chamber (MWPC) – a two-coordinate position sensitive MWPC used for registration of fission fragments from the ^{235}U target deposited on the MWPC's cathode [5].

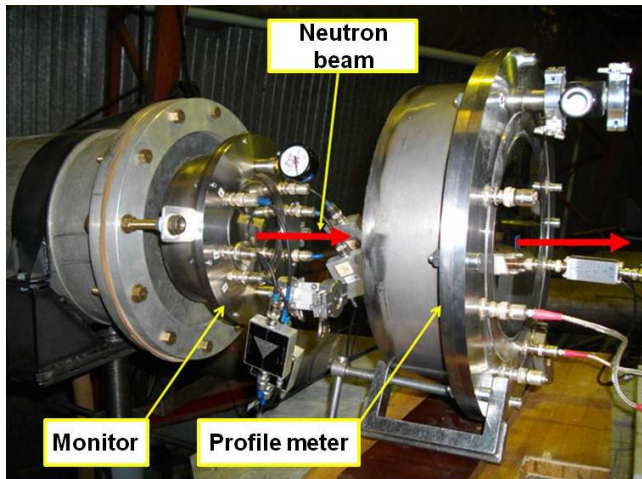


Fig. 4. Neutron monitor and a profile meter MWPC

The neutron spectrum $F_{\text{IS NP}}(E)$ is shown in Fig. 3 together with the JEDEC standard terrestrial neutron spectrum from JESD89A referenced to New York City and multiplied by a scaling factor $7 \cdot 10^7$, as well as the neutron spectra of leading test facilities. Both the shape of the neutron flux and neutron intensity demonstrates that the IS NP/GNEIS is successfully competing with other first-grade test facilities with the atmospheric-like neutron spectrum. The SC-1000 possesses a potential to increase the neutron intensity. A new irradiation station located at a distance of 5–6 m from the neutron-production target operated on the extracted proton beam enables to increase the neutron flux at least by 10 times. Simultaneously, irradiation of bulky equipment is possible.

4. Conclusion

A versatile complex of test facilities has been developed at the SC-1000 accelerator of the PNPI. At present, a growing number of Russian research organizations specialized in radiation testing of the electronics conduct their research on the proton and neutron beams under direct agreements with the PNPI or with the Branch of JSC “URSC”–“ISDE”.

Acknowledgment

The authors express their sincere gratitude to all colleagues from the PNPI who participated in the development of the radiation test facilities at the SC-1000 synchrocyclotron.

References

1. N.K. Abrosimov *et al.*, Zh. Tekhn. Fiz. **41**, 1769 (1971).
2. S.A. Artamonov *et al.*, Phys. Part. Nucl. Lett. **14**, No. 1, 188 (2017).
3. N.K. Abrosimov *et al.*, Nucl. Instr. Meth. A **242**, 121 (1985).
4. N.K. Abrosimov *et al.*, Instr. Exp. Tech. **53**, 469 (2010).
5. O.A. Shcherbakov *et al.*, IEEE Trans. Nucl. Sci. **63**, 2152 (2016).

NUMERICAL SIMULATION AND OPTIMIZATION OF THE VARIABLE ENERGY 60–1 000 MeV PROTON BEAMS AT THE PNPI SYNCHROCYCLOTRON FOR TESTING THE RADIATION RESISTANCE OF ELECTRONICS USED FOR NEEDS OF AVIATION AND SPACECRAFT

S.A. Artamonov, D.A. Amerkanov, E.M. Ivanov, G.I. Gorkin, G.A. Riabov, V.A. Tonkikh

1. Introduction

The synchrocyclotron (SC-1000) at PNPI accelerates protons to a fixed energy of 1 000 MeV with an intensity of the extracted beam of 1 μ A. The accelerator has an extensive network of proton and π - and μ -meson beams, and a neutron beam [1]. However, to solve a number of problems of fundamental nuclear physics and a variety of applications, there is a need for beams of protons with lower energy. It is desirable to have proton beams of variable energy, which are concentrated in one system. The main method of producing such beams is to decelerate a primary beam by using the mechanism of ionization losses in the material, *i. e.* on the basis of using a degrader. At the time, this method was applied in the Joint Institute of Nuclear Research [2] to obtain a medical beam with 200 MeV from a primary beam of 680 MeV, and, for example, for formation of a beam with variable energy in the cyclotron medical centre, the United States [3].

At PNPI this method was also used previously in experiments to study the elastic pp scattering in the energy range 500–1 000 MeV [4] and in measuring the cross sections of a whole group of nuclei [5]. For these purposes, a beam with variable energy from 200 to 1 000 MeV with a relatively small intensity of 10^5 – 10^6 s⁻¹ was developed and implemented [6]. However, many accelerators are used at present not only for solving scientific problems. More and more of their operating time is devoted to practical purposes.

The proton therapy at the SC-1000 with a beam energy of 1 000 MeV (the Gatchina method) gives very good results, but its application is limited to a fairly narrow range of diseases [7]. Therefore, in PNPI a possibility of forming a proton beam with the energy of 140–230 MeV for treatment of patients with oncological diseases of internal organs based on the effect of the Bragg peak was additionally investigated [8]. During the execution of works [4–6, 8], the simplest design of a degrader, which was a set of cylindrical copper disks 80 mm in diameter installed in the guide housing close to each other, was used. The degrader was located close to the output window of the accelerator; its length could be changed manually to produce the required energy.

Recently, a new applied problem has emerged. For successful operation of aviation and space technique in conditions of radiation, radiation-resistant electronics are required. A universal centre for testing electronic components (EC) for the needs of aviation and cosmonautics is being created at the accelerator SC-1000 PNPI jointly with the research Institute of Space Instrumentation. One of the main tools of such tests is the proton beam of variable energy. However, for multiple radiation tests of electronic components, it is necessary to have fast tunable beams with wider energy ranges than the previous ones – \sim 60, 100, 200, 300, 400, 500, 600, 700, 800, 900, and 1 000 MeV, and with a whole set of preassigned properties. In particular, for radiation tests, a higher beam current with a flux density of 10^8 cm⁻² · s⁻¹ and 10% homogeneity area of the beam of at least 25 mm in diameter is needed; it is necessary also to provide a possibility of temperature changes of the test object from +25 to +125 °C. For realization of all these conditions, it is necessary to build a degrader whose length can be changed remotely. Moreover, it is necessary to determine the material from which it is possible to produce the degrader and develop its automated construction. This will allow for each experiment the necessary value of the beam energy to be installed easily and safely, and to reduce significantly the dose load on the staff and unproductive consumption of the accelerator working time. The degrader is preferably positioned as close as possible to the focusing lens to increase the beam intensity at low energies. A complete computer control for the magnetic elements of the designed line should be fulfilled. A permanent test stand to work on the beams with the specified parameters should be built. Ultimately, the process of irradiation of electronic components should be maximally automated.

Time-consuming calculations for each required value of the beam energy were needed to implement such an ambitious program. With the software package GEANT4 [9], Monte Carlo (MC) simulations were performed of the passage of protons with an energy of 1 000 MeV with the desired properties, reflecting

the experimental parameters of the beam through the degraders of copper and tungsten, and the lengths of the degraders for each energy $\sim 60, 100, 200, 300, 400, 500, 600, 700, 800, 900, 1\,000$ MeV were determined. For the specified set of energies, the parameters of the beams which passed through the copper degrader were calculated. The data were used as the input data for the MESON [10] and OPTIMUM [11] programs, which allowed us to trace the trajectory of each proton in the channel, optimize the beam parameters, and determine the optimal modes of all magnetic elements of the line. Thus, the main calculated parameters for each beam, such as intensity, energy heterogeneity, beam sizes, and the homogeneity of its spatial distribution have been obtained.

2. SC-1000 accelerator and the beam lines with variable energy

The intensity of the extracted proton beam with an energy of 1 000 MeV at the SC-1000 can be varied from 10^6 to $6 \cdot 10^{12} \text{ s}^{-1}$, and the beam diameter in the focus can be from 5 to 500 mm in the beam lines P2 (medical beam) and P3 (IRIS beam). The versatility of the synchrocyclotron of PNPI is due to the well-developed system of primary and secondary beams, which is shown in Fig. 1 in Ref. [12], where, in particular, the old layout of the equipment placement is presented: degrader, collimators, the parting magnet, two doublets of quadrupole lenses (ML1 and ML2), and the experimental set-up [4, 5] in the direction P3.

For radiation tests of electronic components, it is necessary to have beams of variable energy with the maximum intensity, especially for low values of energy. It is possible to increase the intensity of such beams without significant reworking of the existing line due to proximity of the degrader to the focusing lenses in the main hall of the accelerator. For this purpose, the degrader should be designed to fit into the gap of ~ 90 cm.

Therefore, it was decided to form a new beam of protons of variable energy $\sim 60, 100, 200, 300, 400, 500, 600, 700, 800, 900$ MeV on the current direction of P3 (1 000 MeV – on the current direction of P2). The alteration of the line is reduced mainly to designing and manufacturing of a new degrader with remote control, located at a new position of this line (see Fig. 1 in Ref. [12]). Three collimators 1, 2, and 3, limiting the size and divergence of the beam, two doublets of quadrupole lenses, and the SP-40 bending magnet remain the same. The total length of the line will be ~ 26 m.

3. Modeling with the GEANT4 software program

One of the most common and widely used codes for calculations of passage of particles through matter, based on the MC method, is the GEANT4 program [9]. In the present work, using this program we generated before the degrader a beam of protons (a few million trajectories) extracted from some vacuum volume of the accelerator line. It was assumed that the beam had a Gaussian form with the parameters $\sigma_x = \sigma_z = 0.64$ cm (x, z are the cross sizes) and the energy of 1 000 MeV ($\sigma_E = 3.84$ MeV), which correspond to the experimental results. Here σ is the standard deviation.

In the simulation of the passage of the beam through the degrader, the set of physical interactions (Physics List) describing the electromagnetic processes, Emstandard_opt3, was applied. The energy loss due to ionization, formation of δ electrons, multiple scattering, Compton scattering, bremsstrahlung, the photoelectric effect, the pair production, and e^+e^- annihilation were taken into account. All hadron interactions (elastic scattering, formation of mesons, decays of particles, excitation of nuclei and emission of photons, nuclear fission, neutron capture, and nuclei disintegration) were also linked up. The interactions described by the class G4InelasticProcess are of special interest in the field of hadronic interactions. Three models for inelastic interactions are provided in the package GEANT4. This is the algorithm GHEISHA, which was also implemented in the previous version of the GEANT3 [13], and the algorithms Bertini cascade and Binary cascade.

3.1. Determination of the material and length of the copper and tungsten alloy degraders

It was assumed in all calculations that the degrader is fabricated in the form of a cylinder 80 mm in diameter either of copper with the density $\rho_m = 8.88 \text{ g/cm}^3$ or of the alloy of powders: tungsten (T) of 97.50, nickel (N) of 1.75, and iron (I) of 0.75% (TNI) with a density of $\rho_w = 18.6 \text{ g/cm}^3$.

The length of the degrader for obtaining protons with necessary energy E_i was defined as the difference of the proton ranges, $L_D = R_0 - R_i$, where R_0 is the range of protons with the initial energy $E_0 = 1000 \text{ MeV}$ and R_i the range of protons with the energy E_i .

Choosing a degrader made of copper, its degrader length L_{Dm} can be determined using this simple formula. In the case a degrader is made of an alloy of tungsten–nickel–iron powders, the length L_{Dw} of the TNI degrader can be determined also by the same formula.

Table 1 in Ref. [12] presents estimation results for a variant of the degrader made of the alloy of the TNI powders. It also shows for comparison the values of the mean ranges of protons of different energies obtained by the calculations using the well-known SRIM program [14]. It follows from Table 1 in Ref. [12] that the error in the calculation of the length of the degrader L_{Dw} according to the SRIM and GEANT4 for the entire range of energies reaches $\Delta L \approx 2\%$. The length of the degrader, calculated with SRIM, for all values of energies is larger than that determined using the code GEANT4. The experience of previous calculations [6] indicates that the difference of $\Delta L \approx 2\%$ can lead to significant inaccuracies in determination of the given values of energy.

An analysis of the calculation results shows that, taking into account modern possibilities in the manufacture of details by the powder metallurgy method, for each value of the energy, a degrader of the desired length from the TNI alloy can be formed on the basis of a combination of 13 base discs with the diameter of 80 mm. The disks should have the following thickness: 100, 100, 50, 50, 20, 20, 10, 5, 2, 2, 1, 0.5, and 0.3 mm. It was clarified in the process of developing the degrader that the production of the discs made of the TNI alloy with a specified density $\rho_w = 18.6 \text{ g/cm}^3$ is possible in principle, but only with the use of a quite complex and expensive technology. It was therefore decided, together with the degrader from the TNI alloy, to consider the case where the traditional copper is selected as the material of the degrader. This required new calculations to find the design of the degrader and its collimator made of copper.

The final lengths of the degrader made of copper with the density $\rho_m = 8.88 \text{ g/cm}^3$, obtained on the basis of calculations using the SRIM, GEANT3, and GEANT4 for different values of energies are presented in Ref. [12] in Table 2. The calculations showed that the technical implementation of the stacked degrader made of copper with $\rho_m = 8.8 \text{ g/cm}^3$ is quite possible using 11 base disks 80 mm in diameter of the following thicknesses: 200, 150, 100, 50, 20, 20, 10, 5, 2, 2, and 1 mm.

3.2. Beams of variable energy after the copper degrader

In the calculations using the GEANT4 for protons which passed the degrader, the coordinates, the momentum, and the energy of each proton were registered at its output plane, and these parameters were recorded in a separate file for each required level of the beam energy for further multiple analyses. In additional files, information about primary protons (which did not experience inelastic interactions in the degrader) and secondary particles (products of inelastic interactions) was recorded.

The total energy distributions of the protons for different energy values at the exit of the degrader are presented in Ref. [12] in Fig. 2. Table 3 in Ref. [12] presents important results of the calculations for the entire range of energies: a_E – the mathematical expectation of the beam energy; σ_E – the standard deviation; P – the value of the momentum, and the value I/I_0 – the efficiency of the passage of the beam through the degrader in percentage of the intensity of the original beam. These results demonstrate that the magnitudes of the required energies are determined in the calculations reasonably well.

4. Modeling beams of variable energy in the P3 transportation path

One of the objectives of the present work is to calculate and optimize parameters of the beam of a variable energy for tests of radiation resistance of electronic components and to determine optimal operation modes of the magnetic elements of the beam line for all required values of energy. The degrader is a source of particles obtained using the GEANT4 software with a set of parameters that are, for further purposes, the input data for the programs MESON [10] and OPTIMUM [11].

4.1. Methods and algorithms for calculations of the transport channel

The optimized transport channel of the beam P3 consists of two doublets of lenses, a deflection magnet, and a collimator in the wall between the main and experimental halls. The focusing gradients of the magnetic fields in the lenses for obtaining a beam with the maximum intensity and minimum width of the momentum distribution on the target are varied in the optimization. The distance between the lenses in the doublets is not varied because the P3 channel is also used for other purposes.

The MESON program allows us to calculate the parameters of the primary and secondary particle beams by the MC method, which consists of modeling a large number of trajectories of particles passing the given magneto-optical system. The particles of the beam at the entrance to the magneto-optical system are defined in a separate file that contains information about the number of tracks for which the calculation is performed and the parameters characterizing the given particle: the coordinates and the vector components of the momentum, the module of the momentum, and the energy. The file is generated in a special way by the GEANT4 program. The trajectories in free gaps and in the magnetic lenses are calculated by usual formulas [15].

Along with a relatively simple task of the trajectory calculations in the given structure of the tract, the problem of optimizing its parameters should be solved [16]. The optimization problem combines two parts: 1) calculation of the parameters of the beam and 2) the algorithm for searching the optimum. Both of these tasks can be efficiently solved by the MC method.

4.2. Effect of the collimator after degrader on the beam parameters

To improve the beam parameters it was set in the calculations that the new collimator made of copper with the density $\rho_m = 8.88 \text{ g/cm}^3$ would be located after the degrader. Based on the available practical possibilities for the placement, the collimator was chosen with a length of 132 mm. It was assumed in the calculations that the radius of the hole in the collimator could be varied from $R = 1 \text{ cm}$ to $R = 5 \text{ cm}$. An analysis of the calculation results shows (see Fig. 3 in Ref. [12]) that the collimator strongly influences the amount of losses for all energy values in the considered range of variation of the radius of the hole.

4.3. Optimal alternation of the polarities of the lenses and the losses during the passage of the transport channel P3

It is commonly accepted that in the channels with a magnet deflecting the beam in the horizontal plane, the polarity of the first doublet HD–HF (horizontal defocusing–horizontal focusing) is chosen to get a small size of the beam after the magnet in the plane of its deflection. This representation was set in the initial calculations with the optimization of the parameters. However, further optimization calculations of the parameters of the channel revealed that the alternation of the polarities HF–HD for the two doublet lenses 20K50 gave for the specific geometry of the considered channel a higher intensity at the end of the path than the opposite polarities. Figure 2 in Ref. [17] presents a typical calculated change of the number of protons with the energy 60–900 MeV after the passage of the transport channel. The results of the optimization show that for all energies there is a significant decrease of the number of protons in the main hall of the accelerator, *i. e.* at the initial part of the tract. This is due to the fact that after the degrader and collimator the emittance of the beam is substantially larger than the acceptance of the channel. A similar situation is

observed with the passage of the proton beam through the deflecting magnet SP-40 and the holes in the wall between the main and the experimental halls, which is a natural collimator with a hole diameter of 110 mm.

4.4. Optimization of the size of the beam for different energies

The optimal gradients of the magnetic fields in the lenses for all values of energies, achieving their maximum possible intensity with the minimum width of the momentum distribution at a target with a diameter of $d = 5$ cm, are presented in Fig. 5 of Ref. [12].

The optimal parameters of beams of different energies with the same diameter $d = 5$ cm of the target are presented in Table 1.

Table 1

Estimated parameters of beams of different energies at the end of the path for the same diameter of the target $d = 5$ cm*

E_i , MeV, desired	E_i , MeV, calculated	I , s ⁻¹	$\Delta P/P$, %	σ_x , cm	σ_z , cm	Homogeneity 10%	
						x , mm	z , mm
60	62.1	$1.53 \cdot 10^7$	14.9	3.00	1.41	25.9	14.5
100	100.1	$4.60 \cdot 10^7$	12.2	3.63	1.37	35.2	14.7
200	197.9	$2.06 \cdot 10^8$	7.93	2.46	1.37	25.3	17.2
300	300.2	$5.87 \cdot 10^8$	4.70	2.48	1.44	24.0	19.0
400	399.1	$1.39 \cdot 10^9$	3.29	2.26	1.44	24.4	21.0
500	499.2	$3.13 \cdot 10^9$	2.49	2.27	1.38	23.3	21.5
600	601.0	$4.33 \cdot 10^9$	1.96	1.26	1.41	13.6	16.3
700	699.9	$7.23 \cdot 10^9$	1.51	0.86	1.51	12.0	27.0
800	800.2	$1.67 \cdot 10^{10}$	1.27	0.69	1.55	11.3	27.0
900	899.8	$5.10 \cdot 10^{10}$	0.98	0.57	1.48	11.7	19.7

* Here ΔP is the full width of the momentum distribution of the beam at the half-maximum (FWHM).

The table results indicate that the requirement of 10% uniformity of beams with the dimension of ≥ 25 mm simultaneously for the two transverse coordinates x and z directions cannot be satisfied with the target of the diameter $d = 5$ cm for all values of energies. Therefore, more research is needed to obtain the necessary transverse beam sizes for the complete set of energies.

For this purpose, the optimization calculations were performed for different possible target diameters from $d = 5$ cm to $d = 18$ cm while maintaining the number of particles that reached the target. The information about the shape of the beam is given by the standard deviations σ_x and σ_z calculated by the specified method for each desired value of the energy.

Figure 6 of Ref. [12] shows how the optimized values of the standard deviations σ_x and σ_z depend on the diameter of the target for the energies of $\sim 60, 100, 200,$ and 300 MeV. It is seen that for all these energies the standard deviation σ_x is a slowly varying function of d , while σ_z has a not predictable behaviour with increase of d .

The values of the gradients of the magnetic fields in the quadrupole lenses of the experimental hall for all values of the energies realizing their maximum possible intensity with the minimum width of the momentum distributions on the targets with the optimal diameters are presented in Fig. 8 of Ref. [12]. The calculation results for all energies are summed in Table 2.

Table 2

Estimated parameters of beams of different energies at the end of the path for the optimal diameters of the target

d_{opt} , cm	E_i , MeV, calculated	σ_x , cm	σ_z , cm	Homogeneity 10%	
				x , mm	z , mm
15	62.1	2.88	2.84	27.8	27.0
18	100.1	3.40	3.53	31.5	33.9
15	197.9	2.62	3.14	28.1	28.1
18	300.2	3.18	3.41	30.8	30.5
15	399.1	3.01	2.44	35.7	34.0
13	499.2	2.46	2.64	27.3	32.9
15	601.0	2.82	2.71	30.5	34.9
13	699.9	2.49	2.43	31.2	34.0
9	800.2	1.45	1.81	27.1	29.8
11	899.8	2.71	1.78	34.9	30.8

5. Conclusion

At the SC-1000 PNPI, together with the research Institute of Space Instrumentation, a universal centre for testing the electronic component base for aviation and space has been built.

For a successful implementation of this task, careful and time-consuming calculations for each required value of the beam energy were done. Simulations of the passage of protons with an energy of 1 000 MeV through copper and tungsten degraders were performed by the MC method using the GEANT4 software package [9]. As a result, the lengths of these degraders providing the required energies ~ 60, 100, 200, 300, 400, 500, 600, 700, 800, 900, and 1 000 MeV were determined. For the desired set of the energies, by selecting the copper degrader, the parameters of each beam which passed the degrader were calculated. The data were used as the input data for the MESON [10] and OPTIMUM [11] programs, which allowed us to trace the trajectory of each proton in the beam transport line, to choose the optimum size of the collimator of the degrader, to optimize the beam parameters in the channel, and to determine the optimal modes of all the magnetic elements of the tract. The main parameters of each beam, such as the intensity, the energy heterogeneity, the beam sizes, and the homogeneity of its spatial distribution were calculated. The calculations showed a possibility to form beams of protons in the energy range 1 000–62 MeV with the density of the intensity at the place of exposure from $1 \cdot 10^9$ to $6 \cdot 10^5 \text{ cm}^{-2} \cdot \text{s}^{-1}$ with the 10% homogeneity area in intensity within a diameter of no less than 25 mm. A copper degrader with a remote change of its length and with a fully automated control system was designed and built. This system allows the necessary value of the beam energy to be installed easily and safely, and it allows one to significantly reduce the dose load on the staff and unproductive consumption of the accelerator working time in each experiment. The degrader was placed as close as possible to the focusing lens channel P3, which resulted in an increase of the beam intensity at low energies. A complete computer control of the magnetic elements of the line was implemented.

In conclusion, it should be emphasized that at the SC-1000 radiation tests of electronic components can be carried out not only in proton beams of variable energy 62–900 and 1 000 MeV, but in the neutron beam with a spectrum similar to the atmosphere neutron spectrum [18]. Thus, the synchrocyclotron PNPI is the only accelerator in Russia where extensive radiation tests of electronic components can be conducted in proton beams in the energy range of 60–900 and 1 000 MeV and in a neutron beam with energies 1–1 000 MeV.

References

1. N.K. Abrosimov, S.P. Dmitriev, V.A. Eliseev *et al.*, in *Proc. of the 7th All-Union Workshop on Charged Particle Accelerators, Dubna, 14–16 Oct., 1980*, **2**, 75–79 (1981).
2. V.P. Dzhelepov, V.I. Komarov, O.V. Savchenko, *Med. Radiol.* **4**, 54 (1969).
3. E.W. Cascio, J.M. Sisterson, J.B. Flanz, M.S. Wagner, in *Proc. of the IEEE Radiation Effects Data Workshop, 21–25 July, 2003* (IEEE, Piscataway, NJ, 2003).
4. A.A. Vorobyev, A.S. Denisov, Yu.K. Zalite, G.A. Korolev *et al.*, Preprint PhTI-430 (1972).
5. A.A. Kotov, L.A. Vaishnena, V.G. Vovchenko *et al.*, *Phys. Rev. C* **74**, 034605 (2006).
6. N.K. Abrosimov, E.M. Ivanov, Yu.T. Mironov *et al.*, *VANT, Ser. Phys. Rad. Vozdeistv. Radioelektron. Appar.*, No. 4, 43 (2003).
7. N.K. Abrossimon, Yu.A. Gavrikov, E.M. Ivanov *et al.*, *J. Phys.: Conf. Ser.* **41**, 424 (2006).
8. N.K. Abrosimov, E.M. Ivanov, G.A. Ryabov, M.G. Tverskoy, Preprint PNPI-2805 (2009).
9. GEANT4 a Simulation Toolkit, <http://geant4.cern.ch/>
10. N.K. Abrosimov, V.A. Volchenkov, G.A. Ryabov, in *Proc. of the 4th All-Union Workshop on Charged Particle Accelerators*, **1**, 258–261 (1975).
11. N.K. Abrosimov, V.A. Volchenkov, G.A. Ryabov, in *Proc. of the 6th All-Union Workshop on Charged Particle Accelerators*, **2**, 175–177 (1979).
12. S.A. Artamonov, E.M. Ivanov, N.A. Ivanov *et al.*, *Phys. Part. Nucl. Lett.*, **14**, No. 1, 188 (2017), DOI 10.1134/S1547477117010046.
13. ROOT. Data Analysis Framework, <http://root.cern.ch/installing-geant3>
14. SRIM – the Stopping and Range of Ions in Matter, <http://srim.org>
15. G. Vol'nik, *Optics of Charged Particles*, Energoatomizdat, St. Petersburg, 1992.
16. D.M. Kuz'menkov, V.I. Chernetskii, *Algorithms and Programs of Random Search*, Zinatne, Riga, 1969, p. 145.
17. S.A. Artamonov, D.A. Amerkanov, E.M. Ivanov *et al.*, in *Proc. of XXV Russian Particle Accelerator Conf. (RuPAC 2016), St. Petersburg, 21–25 Nov., 2016*, pp. 105–107.
18. O.A. Sherbakov, A.S. Vorobyev, A.M. Gagarski *et al.*, in *Proc. of Int. Conf. on Radiation Effects on Components and Systems (RADECS-2015), Moscow, 14–18 Sept., 2015*, p. 40.

MAGNETIC FIELD OF THE 40–80 MeV H⁻ ISOCHRONOUS CYCLOTRON AT GATCHINA. EXPERIMENTS AND 3D CALCULATIONS

S.A. Artamonov, D.A. Amerkanov, G.I. Gorkin, V.P. Gres, E.M. Ivanov, G.A. Riabov

1. Introduction

The isochronous cyclotron C-80 which is now started up at the PNPI is planned to be used as for applied physics program – for production of medicine isotopes, for therapy of eye melanoma and surface forms of cancer, for radiation resistance tests of electronic components – as well as for fundamental research in nuclear physics, solid state physics and biology. Here we present the final parameters of the magnetic field distribution of the new H⁻ isochronous cyclotron and results of 3D computer calculations and experimental measurements.

The magnet and the magnetic system are the most important and expensive parts of the cyclotron, and a considerable attention was paid to their design. The magnetic field of the cyclotron C-80 should meet several requirements. The magnetic field rigidity at the final orbit must reach $Br = 13.2$ kGs · m, which corresponds to 80-MeV energy of the proton beam. For insuring the isochronism, the magnetic field averaged over the azimuth when going from the centre of the magnet to the final orbit should increase by ~8.5%. The azimuthal variation of the magnetic field should provide the vertical and horizontal transversal focusing. Some room should be left for a high frequency system: the gap between the shims should be wider than 160 mm. In distinction from a standard cyclotron, there is an additional and essential requirement for an H⁻ machine – to keep H⁻ losses due to dissociation less than some percent. Acceleration of H⁻ ions has obvious advantages: a possibility for 100 % extraction of the beam with high intensity and variable energy. On the other hand, it requires a special source of H⁻ ions, high vacuum, and what is most important, the magnetic field strength in the magnet sector should not exceed in our case 16.8 kGs to prevent H⁻ electromagnetic dissociation.

2. General description

A few years ago, as a first approximation, the magnetic structure of the cyclotron was designed on the basis of 2D calculations by using the POISSON program and measurements on two small models [1, 2]. The geometry and the key parameters of the magnetic system for the cyclotron were selected. It was supposed that the height of each of the sectors would be equal to 90 mm, and during further optimization it was not changed. For obtaining the required isochronism, the height of the correction sector shims was varied. The initial height of these shims was selected equal to 20 mm. Besides, in the course of the optimization, a special constrained condition was imposed. It was required that the amplitude of the main fourth field harmonic should not exceed ~3 000 Gs, and the field near the extraction radius $r \approx 90$ cm should be $B \leq 16 800$ Gs. To reduce H⁻ dissociation losses, a magnetic structure of C-80 with high spiral angles was proposed. Under these conditions, the H⁻ dissociation should be below 5% [3]. For these purposes, additional valley shims were introduced into the magnetic system, and their geometrical parameters were also varied. Thus, the formation of the demanded isochronous field was carried out only by changing the iron shims geometry without using correction coils. For an improvement of the accelerated beam orbits centering and reducing lower magnetic field harmonics (1, 2, 3), four pairs of azimuthal correcting coils were installed between the sectors at the radii 85–1 025 mm.

The extraction of the beam of variable energy 40–80 MeV in the H⁻ isochronous C-80 cyclotron is performed without variation of the magnetic field but by changing the radial position of the stripping foil.

The major unit of the cyclotron, its electromagnet, was designed using the model of the magnet of the PNPI SC-1000 synchrocyclotron (SP-72). This electromagnet has a traditional design with an E-shaped magnet yoke and a pole of 2.05 m in diameter. The system to move upward the magnet upper part (the half-yoke) was worn-out and outdated. Therefore, it was replaced with four pairs of ball bearings and screws equipped with servomechanisms and position sensors. The maximum height of the half-yoke lifting is about 600 mm, the setting accuracy is better than 50 μm.

Main parameters of the C-80 magnetic structure are presented in Table.

Table

Main magnet parameters

Parameter	Value
Pole diameter	2.05 m
Valley gap	386 mm
Hill gap (min)	163 mm
Number of sectors	4
Spiral angle (max)	65°
Field in the centre	1.352 T
Flutter (max)	0.025
Ampere-turns	$3.4 \cdot 10^5$
Power	120 kW
Weight	250 t

3. 3D optimization

The main parameters of the cyclotron magnetic system were refined and optimized by computer simulations with the 3D MERMAID code [4, 5], and the dynamics simulations were performed with the code in Ref. [6]. The main peculiarities and modifications of the preliminary design can be formulated as follows.

The detailed 3D geometry of the magnet yoke, of the sectors (four pairs), sector shims (17 correction shims in each sector), and the valley shims, the coils, and the external boundaries was introduced in the computer model. Because of a big angular extension of the spiral sectors in C-80, it was necessary to use in the calculations a half of the magnet with the corresponding symmetry boundary conditions. The external boundary of the area where the calculations were performed was chosen rather far to get rid of its influence on the magnetic field in the working region and to determine correctly the fringe field. The fringe field was taken into account for correct calculations of the extraction beam optics. Thus, for the description of the magnetic structure of C-80 using the MERMAID program, about 20.5 million direct prisms were required, which allowed to reach the necessary precision of 10^{-3} – 10^{-4} in the calculations of the magnetic field.

The nonlinear magnetic properties of the used electro technical steels (three types) were taken into account. To increase the vertical focusing in the central region, the zero and low spiral sectors were prolonged from the radius of 27 cm to the radius of 40 cm.

In the preliminary version of the magnet structure, four valley shims in each valley were used to provide isochronisms on the last radii. To cut down the number of the valley shims from four to one, the azimuthal width of the sectors was expanded by ~ 20 mm from the radius of 70 cm to the final radius of 102.5 cm. Under these conditions, the H^- dissociation is below 3 % [5].

Only the 3D field calculations made possible to perform the central region design taking into account the axial injection system geometry and the design of the magnetic field bump for the beam focusing at the first turns.

4. Main results

At the final stage of the magnetic field formation, the computer calculations and the magnetic field measurements were performed in parallel. The magnetic field in the full scale magnet was measured using a system based on twenty nuclear magnetic resonance calibrated Hall probes and an automated coordinate system, which could position probes in the cylindrical coordinate system with an accuracy of 0.1 mm along the radius at each azimuthal angle (with steps 0.5, 1, 1.5, 2, or 2.5°) at the radii from zero up to 100 cm (with steps 0.5, 1, 1.5, 2, or 2.5 cm). The total measurement accuracy was about 0.02%. The time of the magnet

topography measurements on the super period was $\sim 6\text{--}8$ h and on the periodicity element was about 2 h. The local field defects were corrected by using iron shims. The necessary shim thickness was estimated by 3D calculations. Disagreements between the computer predicted and the measured fields did not exceed some Gs.

The final field distribution (Fig. 1) was reached by selection of the thickness of the 17 types of the iron sector shims in every sector and selection of the thickness of the valley shims by using the trial-and-error method.

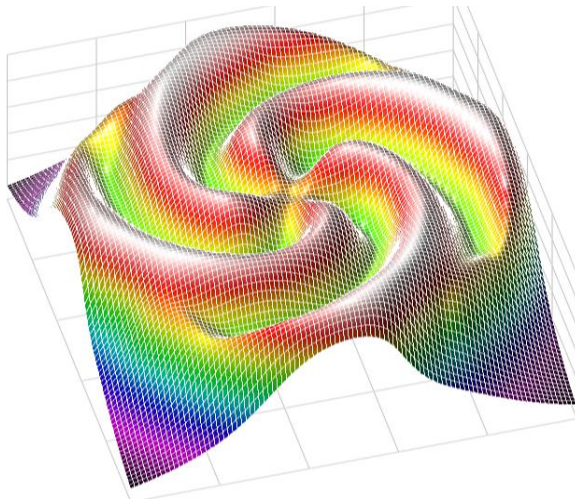


Fig. 1. Final magnetic field distribution

As a result, the magnetic field was obtained which provided the beam acceleration from the radius of ~ 15 mm up to the radius of ~ 90 cm.

We remind that in the working magnet gap four pairs of sectors with high spirality angles were placed. Coils for the correction of the average magnetic field were not used in the cyclotron C-80. For improvement of the accelerated beam orbits centering, four pairs of azimuthal correcting coils between the sectors were installed at the radii 85–1 025 mm.

The comparison of the measured average magnetic field and its isochronous value is shown in Fig. 2.

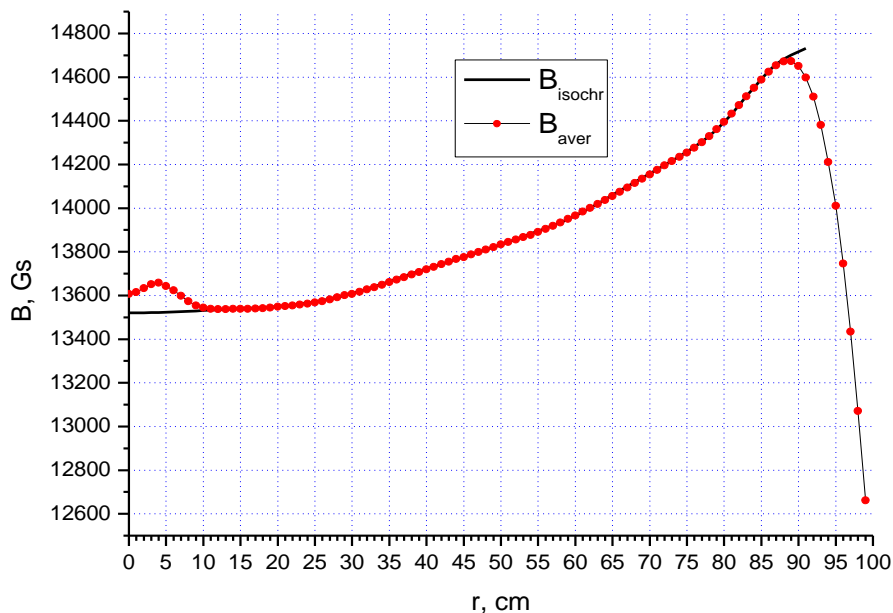


Fig. 2. Comparison of the measured magnetic field B_{aver} and the isochronous field B_{isochr}

The isochronism of the magnetic field was provided with the accuracy of 2–5 Gs. The difference between the measured magnetic field and the isochronous cyclotron field is presented in Fig. 3.

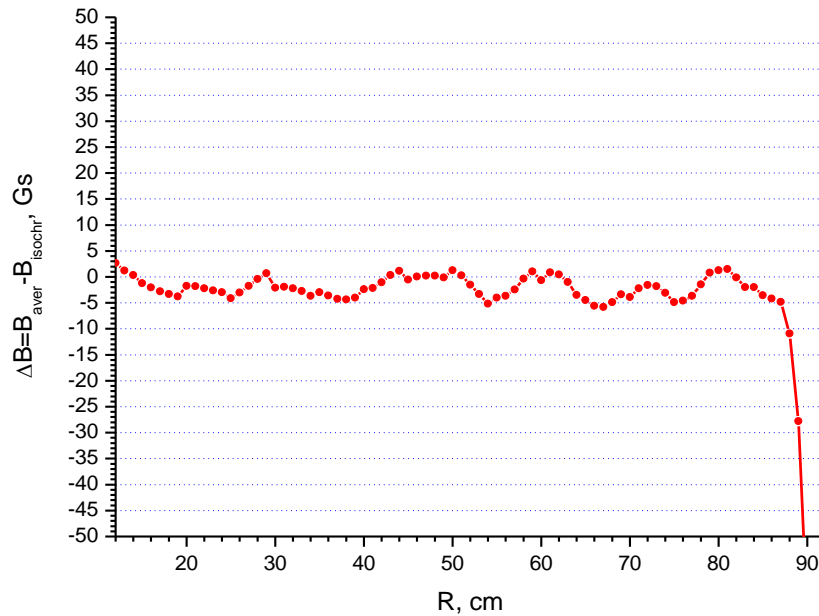


Fig. 3. Difference between the measured magnetic field and the isochronous cyclotron field

The measured harmonics of the magnetic field versus the radius are shown in Fig. 4. It is seen that at the interface of the direct sector with its spiral part, there is a significant decrease of the main harmonic A_4 . Near the extraction radii, a growth of the harmonic A_{12} is observed, which hinders the drop of the harmonic A_4 .

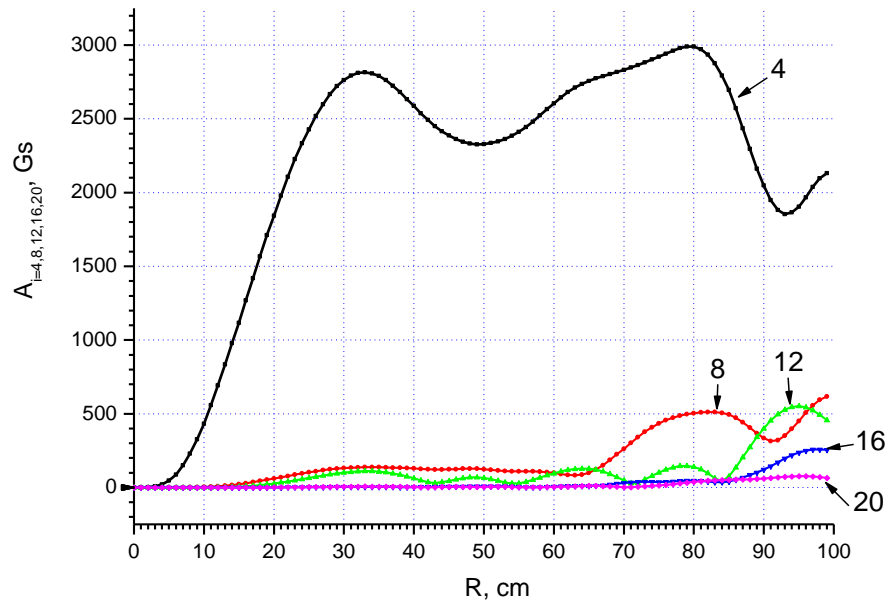


Fig. 4. Measured harmonics (4, 8, 12, 16, and 20) of the magnetic field versus the radius

A special attention was paid to reduce the lower harmonics (Fig. 5). The most dangerous harmonics A_1 , A_2 , A_3 lead to strong distortions of the accelerated orbits. After considerable efforts in our case, the first harmonic on the last radii did not exceed 10–12 Gs.

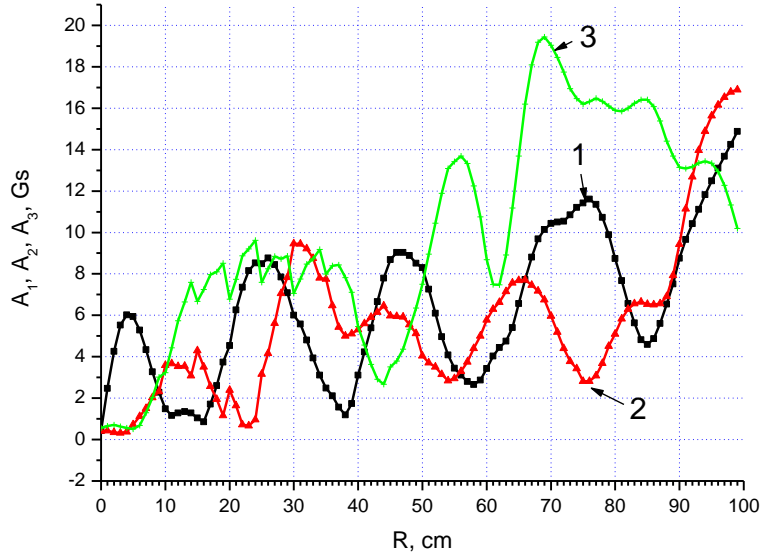


Fig. 5. Measured lower harmonics of the magnetic field versus the radius

The first and second harmonics of the magnetic field perturbations have an essential influence on the radial motion of the beam in C-80. The amplitude of the first harmonic is determined by inaccuracies in production and assembling of the cyclotron magnet. The amplitude of the second harmonic at the last radii is less than 8 Gs.

The nature of the action of these harmonics on the beam dynamics is various. The amplitude of the first harmonic noticeably affects the coherent radial oscillations of the beam, since betatron frequency ν_r in the entire acceleration region is close to 1.

The gradient of the increase of the amplitude of the second harmonic is the driving term of the parametric resonance $2\nu_r = 2$. In principle, this resonance can lead to an increase of free radial incoherent oscillations of the ions and also to a growth of the radial emittance. The effective force of this resonance depends on specific conditions: the value of the gradient, how far the working point is located from the resonance, and the duration of the resonance action.

The first, second, and third harmonics can be compensated only by harmonic coils. In the every valley A, B, C, and D there are four types of the correction coils I, II, III, IV (Fig. 6). The magnetic fields of these four harmonic coils was measured and examined. These coils are used to decrease the lower harmonics A_1, A_2, A_3 of the cyclotron magnetic field. The contributions of the harmonic coils magnetic fields into the measured average field of the cyclotron are presented in Fig. 7.

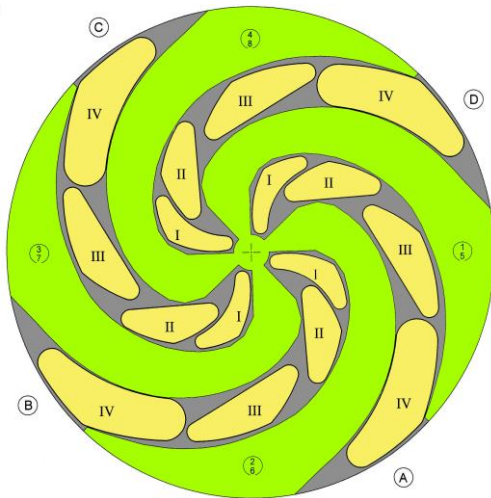


Fig. 6. Top view of the pole tip of C-80

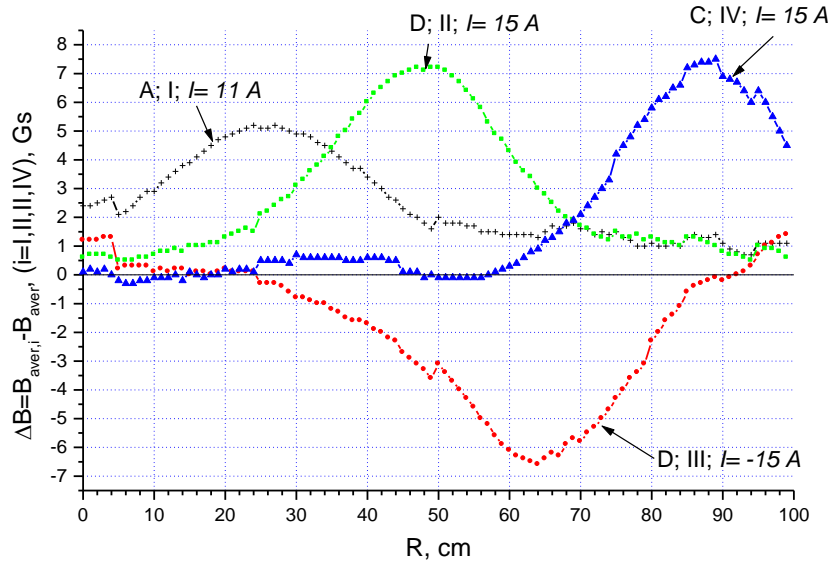


Fig. 7. Contributions of the harmonic coil magnetic fields into the measured average field of the cyclotron

The nominal currents in the harmonic coils were selected as follows: I – $I = \pm 25$ A, II – $I = \pm 25$ A, III – $I = \pm 25$ A, IV – $I = \pm 42$ A.

The measured magnetic field allows the vertical and horizontal focusing (Fig. 8) and the isochronism in the acceleration region [7].

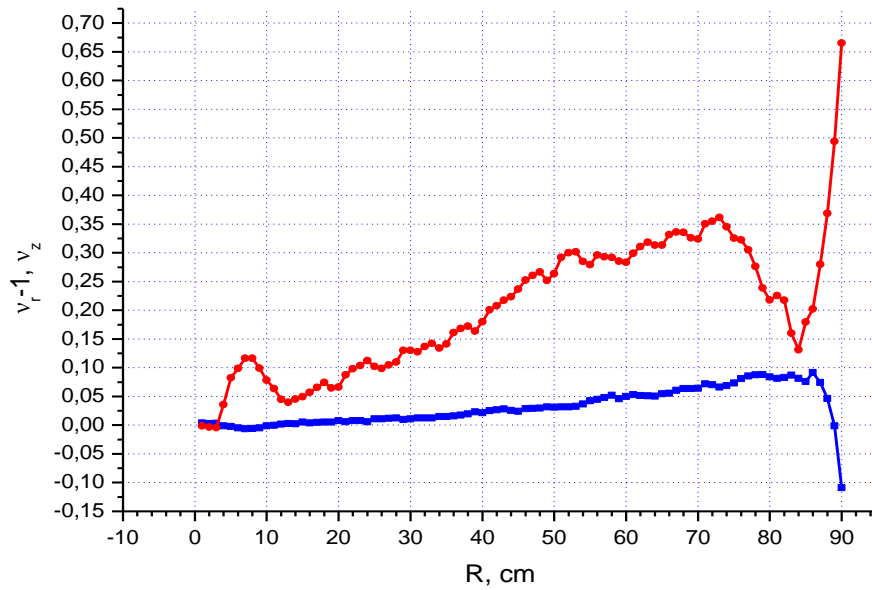


Fig. 8. Frequency of free oscillations v_r (blue) and v_z (red) versus the average radius of the orbit

A special attention was paid to avoid dangerous resonances. Detailed dynamics simulations were performed to be sure that the resonances which are crossed during the acceleration do not cause a significant harmful effect on the beam. The number of ion turns in C-80 is expected to be about 400.

5. Conclusion

Results of the final magnetic field distribution of the 80 MeV H^- isochronous cyclotron at Gatchina are presented. Main features and problems are connected with applying the high spirality magnetic structure for acceleration of H^- ions. The formed structure permits to accelerate H^- ions up to an energy 80 MeV using a rather small two-meter magnet, the beam losses due to the ion dissociation being less than 3%. As far as H^- cyclotron operates at the fixed magnetic field, the necessary field distribution was obtained by using iron correction shims only. To obtain the necessary field distribution, 3D-computer calculations and successive magnetic measurements were very helpful.

At the present time, all cyclotron systems are installed and tested. In June 2016, a physical start-up of the C-80 cyclotron system was realized. Works were carried out in the pulse mode at low currents of the accelerated beam to exclude strong activation of the equipment to make possible a safe continuation of works in the cyclotron vacuum chamber, with the components of the beam transport system, *etc.* The design parameters of the cyclotron were obtained in November 2016.

References

1. N.K. Abrossimov, S.A. Artamonov, V.A. Eliseev, G.A. Riabov, in *Proc. of the Second Int. Workshop: Beam Dynamics & Optimization – BDO, St. Petersburg, 1995*, pp. 7–15.
2. N.K. Abrossimov, S.A. Artamonov, V.A. Eliseev, G.A. Riabov, in *Proc. of the XV Int. Conf. on Cyclotron and Their Application, Caen, France, 1998*, pp. 518–521.
3. N.K. Abrossimov, S.A. Artamonov, V.A. Eliseev, G.A. Riabov, *PNPI Research Report 1994–1995*, Gatchina, 1996, pp. 275–278.
4. S.N. Andrianov, S.A. Artamonov, A.N. Dubrovin, V.A. Eliseev, *Vestnik SPbSU*, Ser. **10**, Iss. 3, 12 (2008).
5. S.A. Artamonov, E.M. Ivanov, G.A. Riabov, N.A. Chernov. in *Proc. of RuPAC 2012, St. Petersburg, 2012*, WEPPC015, pp. 475–477.
6. S.N. Andrianov, S.A. Artamonov, *Vestnik SPbSU*, Ser. **10**, Iss. 2, 3 (2009).
7. S.A. Artamonov *et al.*, in *Proc. of XX Int. Conf. Beam Dynamics & Optimization, BDO-2014, St. Petersburg, 2014*, pp. 18–19.

HIGH EFFICIENCY STRIPPING EXTRACTION IN THE 80-MeV H⁻ ISOCHRONOUS CYCLOTRON AT PNPI

S.A. Artamonov, A.N. Chernov, E.M. Ivanov, G.A. Riabov, V.A. Tonkikh

1. Introduction

The start up of a new high intensity isochronous cyclotron with the design beam energy from 40 up to 80 MeV and beam current of 100 μ A was announced in November 2016. The cyclotron is intended for production of high quality medicine isotopes, organization of eye melanoma treatment facility, treatment of surface forms of cancer and radiation resistance tests of the electronics for the aviation and space research [1].

The H⁻ cyclotron has the advantage that the high intensity internal beam can be extracted from the acceleration chamber with practically 100% efficiency by transformation of H⁻ ions into H⁺ ions by using a thin foil. The extraction system consists of a probe with a stripping foil, an extraction window in the vacuum chamber and two aligning magnets to match the extracted beam with the beam transport line. The beam optics calculations in the measured magnetic field make it possible to find the optimal relative position of the extraction system elements as well the parameters of the extracted beam with the energy 40–80 MeV. At present, the beam is extracted from the chamber with the efficiency about 100% and there is good agreement with the optic calculations.

The external view of the cyclotron and the first part of the beam transport line are presented in Fig. 1. Basic parameters of the cyclotron are summarized in Table 1.



Fig. 1. The external view of the C-80 cyclotron and the beginning line of the transport line

Table 1

Characteristics of the C-80 cyclotron

Parameter	Value
Magnet	
Pole diameter	2.05 m
Valley gap	386 mm
Hill gap (min)	163 mm
Number of sectors	4
Spiral angle (max)	65°
Magnetic field in the centre	1.352 T
Flatter (max)	0.025
Extraction radius	0.65–0.90 m
Extracted beams	
Energy	40–80 MeV
Method	Stripping

A 3D sketch of the cyclotron and the extraction system are presented in Fig. 2. A schematic view of the extraction system is presented in Fig. 3.

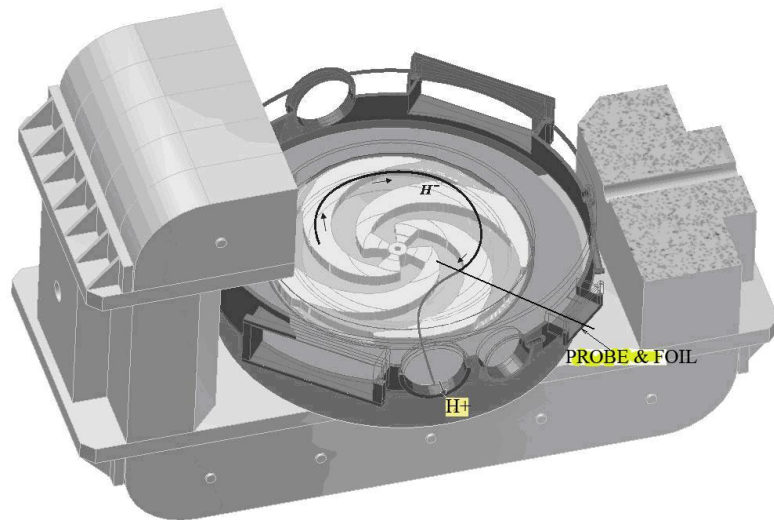


Fig. 2. 3D sketch of the C-80 cyclotron and the extraction system

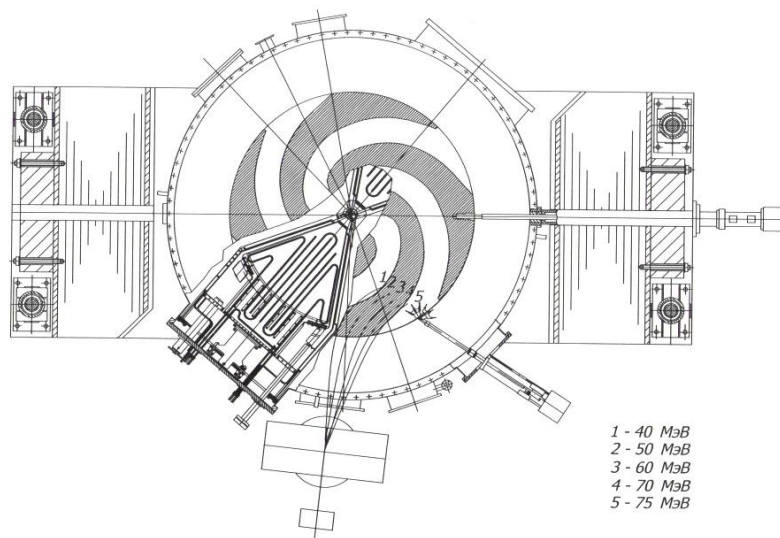


Fig. 3. Schematic view of the extraction system of the C-80 cyclotron

2. Magnetic field

To design the extraction system, it is necessary to know the magnetic field as in the acceleration region, so on the edges. For that reason, the residual magnetic field was measured up to the radius of 230 cm.

The C-80 cyclotron has some specific features in the magnetic structure. As can be seen from Table 1, the magnetic structure with very low flatter and very high spiral angles (up to 65°) is used in the cyclotron. Such a structure makes it possible to decrease the magnetic field in the hill region to avoid beam losses due to electro-dissociation of H^- ions. As a result, it permits acceleration of H^- ions up to an energy of 80 MeV using a magnet with the pole diameter of 2 m and keeping the beam losses below 3%. A detailed description of the magnetic structure can be found in RUPAC-2014 report [2]. The final magnetic field of the C-80 cyclotron is presented in Fig. 4.

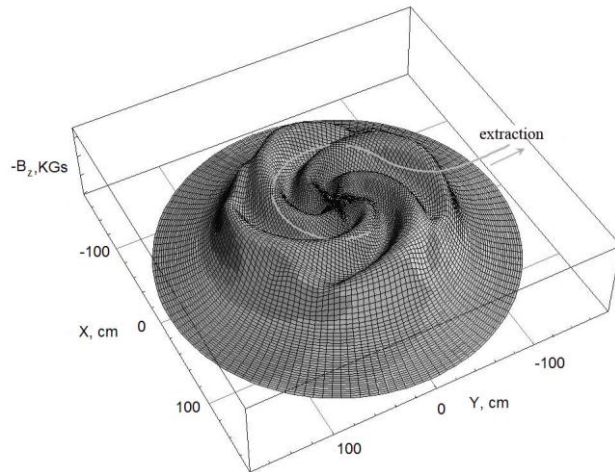


Fig. 4. Magnetic field of the C-80 cyclotron

3. Reference trajectories

One of the problems in designing of the extraction system is to determine the relative positions of the stripping foil and the extraction window in the vacuum chamber. As a first approximation, the positions of the foil and the window were estimated on the basis of simulated closed orbits in the calculated magnetic field. The particle trajectories started from the closed orbits. It was necessary to provide that the particles of different energies pass through the extraction window and enter the entrance of the aligning magnet. This was achieved by varying the stripper position along the radius and azimuth. Trajectories of the extracted particles are shown in Fig. 5.

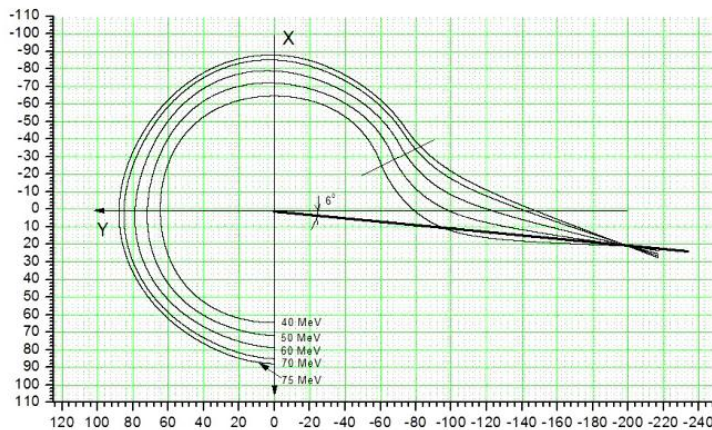


Fig. 5. Trajectories of the extracted particles

As a result of these calculations, it was established that the full energy in a range from 40 up to 80 MeV can be obtained when the stripper foil is moved along a nearly straight line in the coordinate system shown in Fig. 5 (the line equation is $y = 0.88857x - 36.27$). The maximal deviation from the straight line does not exceed a few centimeters.

An original stripper probe with three stripper foils was designed for the C-80 cyclotron. The probe can be moved along the straight line, and in addition each foil can move along the azimuth by 5 cm. As a result, it permits to obtain the whole energy range by moving the probe along the straight line. The reference trajectory calculations made possible to estimate the main parameters of the extraction system: the position of the extraction window in the vacuum chamber, the position and movement ranges of the stripper foil, the arrival points of particles with different energies at the aligning magnet entrance, the direction of the extracted beam and the necessary angle range for the aligning magnet. The direction of the extracted beam is $\sim 6^\circ$ with respect to the longitudinal axis of the cyclotron magnet as it is shown in Fig. 5. The deviation angle in the aligning magnet is varied from 15° up to -4° .

4. Beam optics calculation

Besides the reference trajectory, it was necessary to determine the size and divergence of the beam near the reference trajectory to design the beam transport line.

The computer simulations [3] were used to determine both the reference trajectory and the beam optics. In the linear approximation, the movements in the vertical and horizontal planes are independent, and the beam behaviour can be described by two independent phase ellipses. The starting ellipse size at the stripper in the vertical plane is defined assuming that the maximum beam size in the cyclotron is about 6 mm. The divergence and orientation of the ellipse in the phase space of the vertical plane repeat these parameters of the matched with the magnetic structure ellipse at the radius and azimuth of the stripper. The beam spot at the stripper is supposed to be 3 mm in the horizontal plane and the divergence and orientation of the phase space ellipse corresponds to the matched ellipse. An example of evolution of the phase ellipses in the extraction process for 70-MeV beam is shown in Fig. 6.

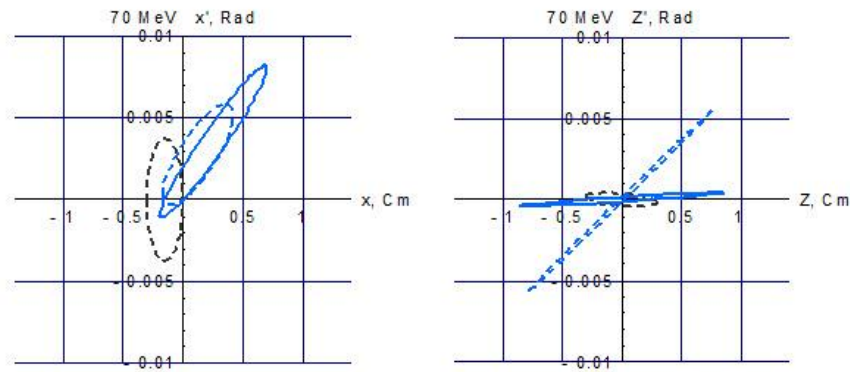


Fig. 6. Phase ellipses for 70-MeV beam in the extraction process: the *black dotted line* corresponds to the stripper position; the *blue dotted line* corresponds to the entrance of the aligning magnet and the *blue solid line* corresponds to the exit of the magnet

Figure 7 shows the evolution of the beam envelopes from the stripper foil up to the exit of the aligning magnet for the 70-MeV beam. After the stripper foil, the beam is exposed to defocusing forces in the horizontal and vertical planes.

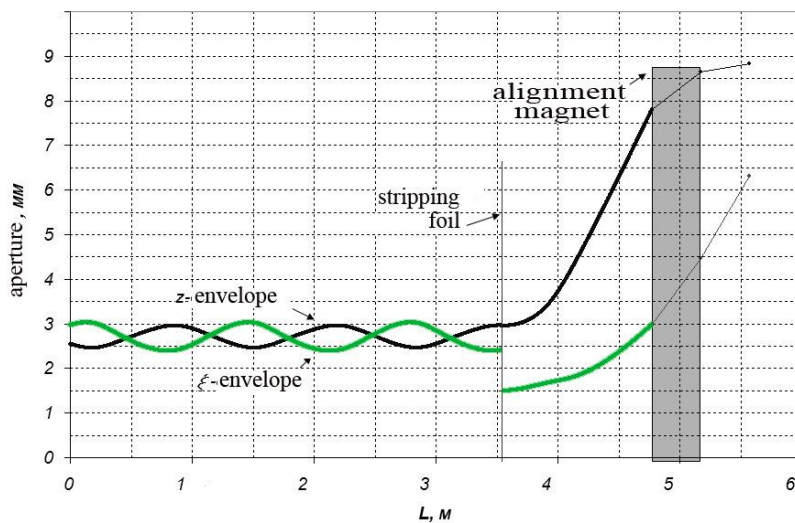


Fig. 7. Transformation of the beam envelopes in the extraction process

The calculated parameters of the beam ellipses at the aligning magnet are presented in Table 2.

Table 2

Twiss beam ellipse parameters at the alignment magnet entrance*

$T, \text{ MeV}$	40		70	
	ξ	z	ξ	z
α	-1.793	-5.079	-3.562	-3.123
$\beta, \text{ mm/mrad}$	5.801	5.010	3.559	62.220
$\gamma, \text{ mrad/mm}$	0.727	5.348	3.845	0.173
$\varepsilon, \text{ mm} \cdot \text{ mrad}$	5.4	3.8	5.6	1.2
$D, \text{ cm}$	105		51	
$D^1, \text{ rad}$	1.03		0.52	

* For details see Ref. [3].

5. Trajectory calculations in the experimentally measured magnetic field

At the final stage, 500 particle trajectories were calculated with random start conditions in the experimentally measured magnetic field map from the inflector exit up to the entrance of the aligning magnet. These calculations confirmed to a great extent the previous results for the positions of the stripper foil and the extraction window, the direction of the extracted beam and the beam parameters. In addition, it was found that the beam spot in the horizontal plane on the stripper foil is 3 mm, as it was assumed in the previous calculations. The energy uncertainty is about 1%. Furthermore, it was found that the internal beam quality strongly depends on the cyclotron tuning, in particular on the central optics tuning, and on the first and third harmonics of the magnetic field. It is interesting to note that the second and fifth harmonics have no effect on the beam emittance.

6. Experiment

The physical start up of the C-80 cyclotron was in summer of 2016. The design beam parameters were achieved in November 2016. The extracted beam was obtained in the energy range from 40 up to 78 MeV. The extraction efficiency estimated as a ratio of the current on the first in beam line Faraday cup and the current on the internal probe was 80–100%. The beam was directed into the beam line, which position was defined from computer simulations. The beam energy could be changed by moving the stripper probe along the calculated line. The results of computer simulations were confirmed by experiment.

Optimization of the beam line and the tuning of the cyclotron regime are planned for the near future.

Acknowledgment

In conclusion, we would like to thank colleagues Yu.N. Gavrish, V.G. Mudrolyubov, and A.V. Galchuk from D.V. Efremov Scientific Research Institute of Electrophysical Apparatus for useful discussions and assistance in some calculations.

References

1. Yu.N. Gavrish *et al.*, in *Proc. of XXV Russ. Particle Accelerator Conf. (RuPAC 2016), St. Petersburg, 21–25 Nov., 2016*, TUCASH04, pp. 176–178.
2. S.A. Artamonov *et al.*, in *Proc. of XX Int. Conf. Beam Dynamics & Optimization, BDO-2014, St. Petersburg, 30 June – 04 July, 2014*, pp. 18–19.
3. N.K. Abrossimov *et al.*, Preprint PNPI-2851 (2010).
4. N.K. Abrossimov *et al.*, Preprint PNPI-2858 (2011).

DEVELOPMENT OF NEW METHODS FOR PRODUCTION OF MEDICAL RADIONUCLIDES AT THE RADIOISOTOPE COMPLEX RIC-80

V.N. Pantelev, A.E. Barzakh, L.Kh. Batist, D.V. Fedorov, V.S. Ivanov, S.A. Krotov, P.L. Molkanov, S.Yu. Orlov, M.D. Seliverstov, Yu.M. Volkov

1. Introduction

The development of nuclear physics experimental methods combined with the use of high current cyclotrons and very sensitive detectors provide very good opportunities for a completely new direction in medical diagnostics and therapies of various diseases. The nuclear medicine technologies used for diagnostics and therapy are based on the employment of artificially produced radioactive isotopes with specific properties. In this paper, the new installation RIC-80 (radioactive isotopes at cyclotron C-80) [1, 2] is shortly discussed, which is being constructed presently at the beam of a new C-80 cyclotron [3]. The RIC-80 project includes the construction of three target stations, one of them is the station coupled with a mass-separator. It is planned to produce the most widely used medical radioisotopes. These are $^{64,67}\text{Cu}$, ^{68}Ge , ^{82}Sr , ^{111}In , $^{123,124}\text{I}$, $^{223,224}\text{Ra}$, and others, which are under discussion at present as perspective radionuclides for diagnostics and therapy. The mass-separator method will make it possible to produce very pure beams of some radioisotopes.

In this paper, the results on the development of a new method [4] of a high temperature separation of radioisotopes ^{82}Sr and ^{67}Cu and others from different kind of target materials are presented. The production of radionuclides that decay with emission of positrons, allowing their use for positron emission tomography (PET), is very important for diagnostics of different diseases. The isotope-generator ^{82}Sr , which is utilized for PET diagnostics of heart and brain diseases, is one of the most needed radionuclides for PET diagnostics over the world.

The radioisotope ^{67}Cu is regarded now as one of very promising radionuclides for the cancer therapy using monoclonal antibodies. A high demand in radiopharmaceuticals on the base of ^{67}Cu requires new efficient methods for its production, which are actively developed at accelerators.

2. The RIC-80 installation

The main parameters of the new built C-80 cyclotron are the following: the proton beam energy can be varied in the interval 40–80 MeV, and the beam intensity is planned to be up to 200 μA . The cyclotron is intended mainly for production of a wide spectrum of medical radionuclides for diagnostics and therapy. A photograph of the C-80 external beam line with three proton beam lines to the target stations is presented in Fig. 1. The proton beam line is directed from the ground floor to the cellar, where it can be deflected and focused to one of three target stations. The mass-separator with its target station [2] will allow for production of separated beams of medical radionuclides of a high purity implanted into the corresponding collectors from which they can be easily extracted. The target stations will be equipped with special devices to transfer the highly radioactive targets into protection containers, so that they can be transported safely to special storage places, or to hot cells for the after-treatment and corresponding preparations for pharmaceuticals. As it was pointed out previously, the C-80 gives a possibility to obtain sources of a high activity practically for a whole list of radionuclides produced at accelerators.

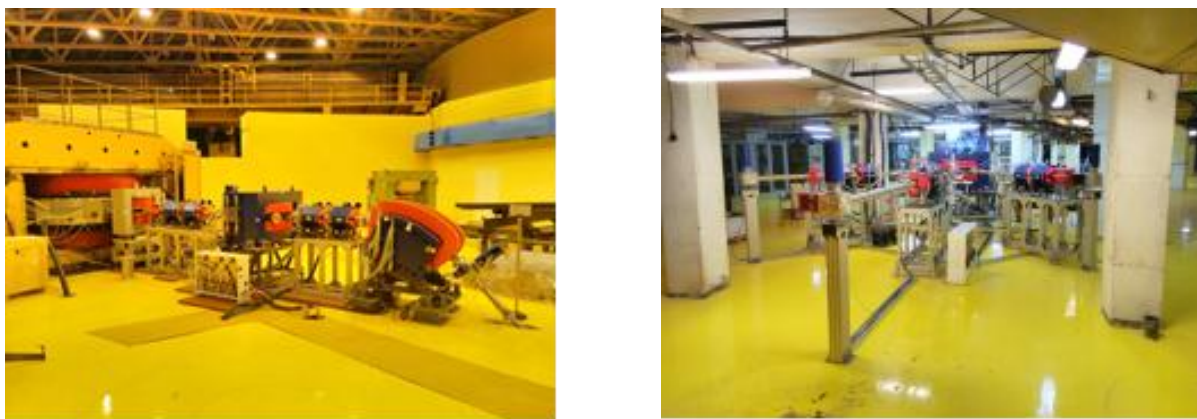


Fig. 1. Cyclotron C-80 (ground floor) with three proton beam lines to the target stations (in the cellar)

3. ^{82}Sr production and extraction from RbCl target material

In the experimental tests for production of ^{82}Sr , the powder of RbCl was used as a target material. The radionuclide ^{82}Sr with a half-life $T_{1/2} = 25.55$ days is a generator for its daughter isotope ^{82}Rb ($T_{1/2} = 1.25$ min), which is widely used in PET diagnostics. For separation of the target material and the produced strontium isotopes, a new developed high temperature method was utilized [4].

After irradiation by a 1-GeV proton beam at the PNPI synchrocyclotron, the RbCl powder was placed into a vessel manufactured from stainless steel, which was put into a Ta–W oven heated by direct current. The powder was heated slowly in a high vacuum to a temperature of 900 °C to be evaporated into a separate volume specially constructed to minimize losses of the irradiated material in the process of its evaporation. At that temperature, the process of complete evaporation of the target material of one gram mass takes about one hour. To control the evaporation process, the γ spectrum of the vessel with the irradiated RbCl was measured at regular intervals [5]. Additionally, after each heating the vessel was weighed to control the mass of the evaporated material. In Figures 2 and 3 a part of γ spectra of the irradiated sample of rubidium chloride is presented. They were measured with a high purity germanium detector. The γ line of the energy 552 keV belongs to the decay of ^{83}Rb with the half-life 86.2 days and its decreasing indicates the efficiency of the target material evaporation. The γ line of the energy 776 keV belongs to the decay of ^{82}Rb with the half-life 1.27 min, which is the daughter isotope of ^{82}Sr , and its decreasing indicates the strontium radionuclide evaporation. In Figure 2, the spectrum of the vessel with the irradiated RbCl before heating is shown by squares. The spectrum after one hour vessel heating at a temperature of 500 °C is shown by circles. In Figure 3, the spectra after heating at a temperature 500 °C (*red dots*) and at a temperature 900 °C (*green dots*) are compared.

As one can see in Fig. 2, heating of the irradiated sample at a temperature 500 °C for one hour does not give any effect on the target material evaporation. The same result was obtained by weighing the sample before and after its heating at 500 °C. At the same time, Fig. 3 shows that after the vessel with the RbCl was heated up to 900 °C, the target material was evaporated completely with almost hundred percent conservation of strontium. The fact of complete evaporation of the irradiated target material was confirmed by weighing the sample before and after its heating at 900 °C. Finally, the conserved radioactive Sr atoms can be evaporated from the vessel at a higher temperature, or it can be washed out by a small amount of an acid solution.

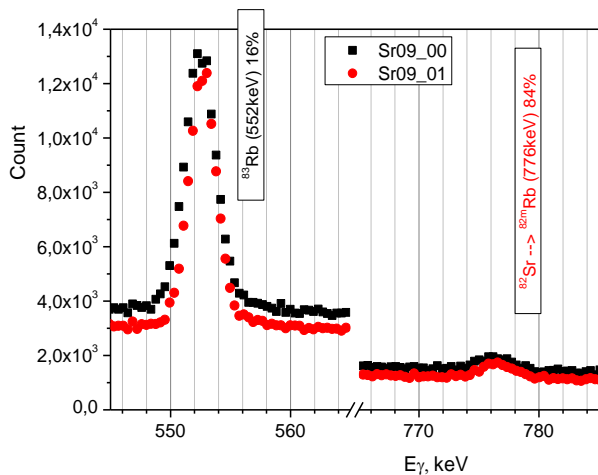


Fig. 2. On the left – the spectrum of the vessel with the irradiated RbCl before heating is shown by squares; the spectrum after one hour vessel heating at a temperature 500 °C is shown by circles. On the right – the vessel with the irradiated RbCl powder after one hour vessel heating at a temperature 500 °C is shown [5]. The RbCl white powder is seen in the vessel

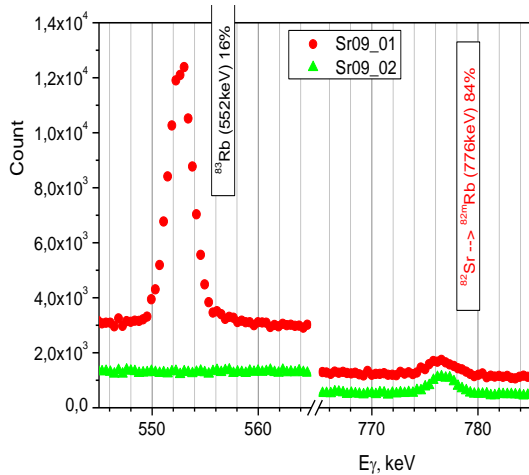


Fig. 3. On the left – the spectrum of the vessel with the irradiated RbCl after its heating at a temperature 500 °C (red dots) and the spectrum after one hour vessel heating at a temperature 900 °C (green dots). On the right – the vessel after one hour heating at a temperature 900 °C [5]. It is seen that practically all RbCl powder was evaporate

Therefore, as one can see in Figs. 2 and 3, the separation of strontium isotopes can be performed in a few stages of evaporation of the target material and the produced species by heating the target in a high vacuum at different temperatures. To separate strontium from the rubidium chloride target, the target heating was started at a low temperature 500–900 °C to evaporate the target material RbCl which is considerably higher volatile than strontium atoms. After that, strontium was selectively extracted by washing of internal vessel volume with the HCl solution. Another way of extraction of strontium was to use the niobium or tantalum vessel, which was heated up to 1 700 °C after the target material was evaporated at 900 °C. The evaporated strontium atoms were directed to the collector cooled by floating water. The carried out experiments have demonstrated the efficiency of the target material separation higher than 99.9%. The efficiency of the strontium radionuclide extraction was about 95%.

4. Experiment description and results of ^{67}Cu and other radionuclide extraction from irradiated target materials

In the experimental tests for production of ^{67}Cu , natural metallic Zn was used as a target material. The radionuclide ^{67}Cu with a half-life 2.57 days is considered as a very perspective radioisotope for therapy of some kinds of malignant tumours. For separation of the target material and the produced ^{67}Cu radionuclide, the new so called “dry” high temperature method, similar to the one of strontium isotope extraction was utilized. After irradiation by the 1-GeV proton beam at the PNPI synchrocyclotron, metallic zinc was placed into a vessel manufactured from tantalum, which was put into a Ta–W oven heated by direct current. In a high vacuum, the irradiated zinc was heated slowly up to the temperature 700 °C to be evaporated into a separate volume specially constructed to minimize losses of the irradiated material in the process of its evaporation. The process of complete evaporation of the target material of one gram mass (at the temperature of 700 °C) took about one hour. To control the evaporation process, the γ spectrum of the vessel with the irradiated zinc was measured before and after the heating process. Additionally, the vessel after its heating was weighed to control the mass of the evaporated material. In Figures 4a and 4b, a part of the γ spectra of the irradiated sample of zinc is presented [6]. The γ line of the energy 1115 keV belongs to the decay of ^{65}Zn with a half-life 244.3 days, and its disappearance indicates the efficiency of the target material evaporation. The fact of complete evaporation of the irradiated zinc target material was confirmed by weighing the sample before and after its heating at 700 °C. The γ line of the energy 185 keV belongs to the decay of ^{67}Cu ($T_{1/2} = 2.57$ days), which is the produced required radioisotope. The spectrum of the vessel with the irradiated Zn before heating is shown in Fig. 4a by *blue dots*. The spectrum after one hour vessel heating at a temperature 700 °C is shown by *red dots*.

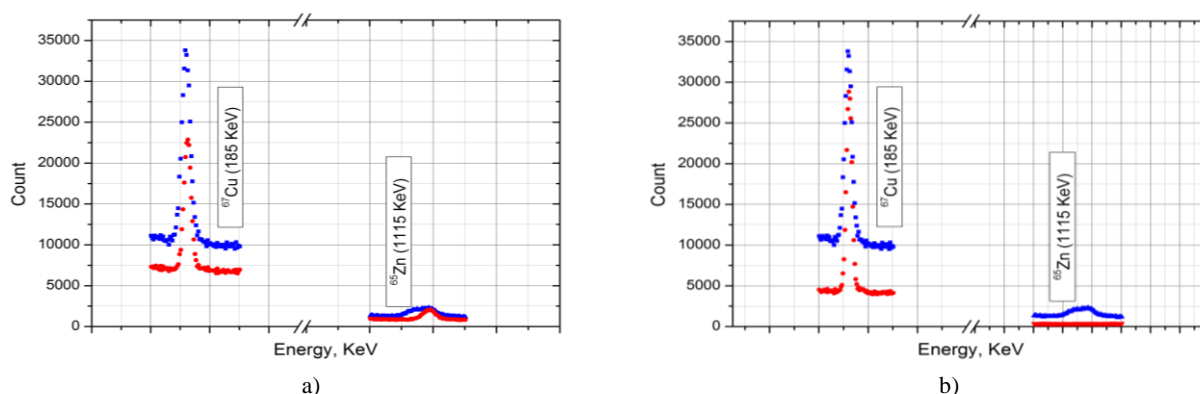


Fig. 4. The spectrum of the vessel with the irradiated Zn before heating is shown by *blue dots*; the spectrum after one hour vessel heating at a temperature 700 °C is shown by *red dots* (a). The spectrum of the evaporated copper atoms collected at the cold finger cooled by floating water after the vessel heating at a temperature 1460 °C for two hours is shown by *red dots*; for comparison, the spectrum of the vessel with the irradiated Zn before heating is shown by *blue dots* (b)

As one can see, after heating the target material was completely evaporated. It was confirmed by weighing the vessel before and after heating as well. At the same time, the radioactive atoms of copper, having considerably higher boiling point (2562 °C), remained in the vessel. Also, the presence of the γ line of the energy 1120 keV of ^{46}Sc ($T_{1/2} = 83.8$ days) at the spectrum measured after the target material evaporation (Fig. 4a) demonstrates that atoms of scandium which is a rather hard volatile element (boiling point at 2830 °C) do not evaporate from the target vessel at a temperature of 700 °C. The spectrum of the evaporated copper atoms collected at the cold finger cooled by floating water after heating the vessel at a temperature 1460 °C for two hours is shown in Fig. 4b by *red dots*. For comparison, the spectrum of the vessel with the irradiated Zn before heating is also shown (*blue dots*). Therefore, as one can see in Figs. 4a and 4b, for separation of the copper radionuclides and the zinc target material, there should be two stages: the first one is slow evaporation of the target material at a temperature about 700 °C; and the second one is evaporation of the produced copper species by heating the target at a temperature 1460 °C. The first

experiments carried out demonstrated the efficiency of the target material separation better than 99%. The efficiency of the copper radionuclide extraction and collection was about 90%.

In Figure 5, a slightly different part of the γ spectrum of the irradiated sample of zinc is presented. The γ lines of the energy 1 115 and 1 120 keV belong as in the previous spectra to the decay of ^{65}Zn and ^{46}Sc , whereas the γ lines of the energy 1 039 and 1 099 keV are from the decay of ^{66}Cu , which is a daughter isotope of ^{66}Ni , and from the decay of ^{59}Fe . The irradiated Zn spectrum is shown before heating (*blue dots*) and after two hours heating at a temperature 700 °C (*red dots*). As one can see in Fig. 6, the target material (zinc) was fully evaporated from the heated vessel. The fact of complete evaporation of the irradiated zinc target material was confirmed by weighing the sample before and after its heating. At the same time, the radioactive atoms of Ni, Fe, and Sc, having considerably higher boiling points than the target material (Ni – 2 562 °C, Fe – 2 861 °C, Sc – 2 830 °C), remained in the vessel. The boiling point of the target material Zn is 907 °C. These measurements demonstrate that separation of the target material and the produced radioisotope may be very efficient, if the target material and the produced species have considerably different boiling points. This method of separation of the target material, when the required nuclides do not escape from the target vessel can be used only for production of relatively long-lived radionuclides, as the process of evaporation of the target material may take some hours.

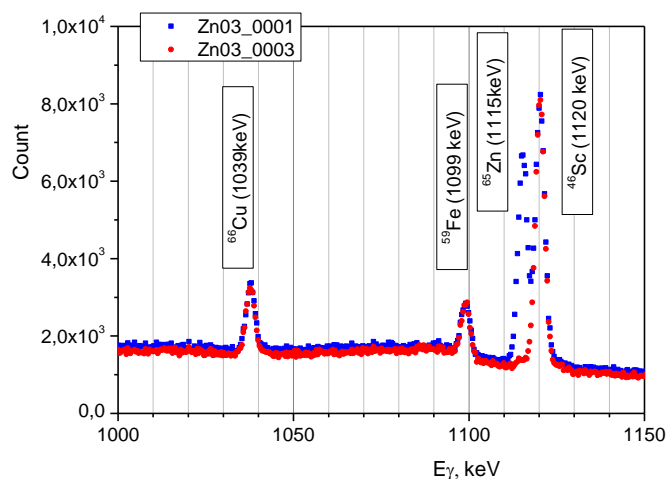


Fig. 5. The irradiated Zn spectrum before heating (*blue dots*) and after two hours heating at a temperature 700 °C (*red dots*)

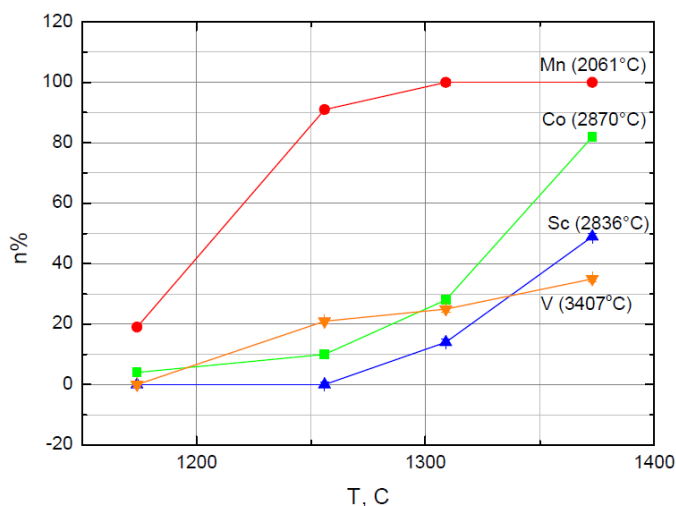


Fig. 6. The evaporated fractions of different radionuclides produced by nuclear reactions in the copper target material and evaporated from it at different temperatures [6]. In the right side in brackets, the boiling points of the evaporated species are presented

Similar experiments were carried out with copper as irradiated target material [6]. A metallic copper sample of natural abundance was heated slowly in the tantalum capsule up to the temperature of 1500 °C. The mass of the evaporated target material was controlled by weighing the sample after each step of its heating. The evaporated amount of the radioactive species was controlled by measurements of their γ -lines integral counts after each step of heating at the defined temperature. In Figure 6, the fractions of atoms of different radioactive isotopes produced by nuclear reactions in the copper target material and evaporated from it at different temperatures are shown. The evaporated fraction is given by the following equation:

$$n = [(N_1 - N_2)/N_1] \cdot 100\%,$$

where N_1 is the appropriate γ -line integral count before heating; N_2 is the same γ -line integral count after heating at the defined temperature.

As one can see in Fig. 6, the evaporated fraction of the radionuclides produced in the measured temperature interval is in good correlation with their boiling point. This makes it possible to rather effectively separate the radionuclides having considerably different boiling points, for example, to separate the radionuclide Mn from Sc or from V.

5. Conclusion

At PNPI, a high current cyclotron C-80 with the energy of extracted proton beam of 40–80 MeV and the current up to 200 μ A has been put into operation lately. One of the main goals of C-80 is production of a large number of medical radio nuclides for diagnostics and therapy. At the present time, the construction of the radioisotope complex RIC-80 at the beam of C-80 is carried out. A peculiarity of the proposed radioisotope facility is the use of the mass-separator with the target-ion source device as one of three target stations for on-line and semi on-line production of a high purity separated radio isotopes. An important part of the work was devoted to the developments of targets for the new project RIC-80. The tested target materials will be used to manufacture real target prototypes for the RIC-80 radioisotope complex. The R@D of new high temperature methods of separation of the produced radionuclides ^{82}Sr and ^{67}Cu from the rubidium and zinc irradiated targets was carried out. As it was demonstrated, the new developed high temperature method can be expanded for production of other medical radionuclides. The following stage of the work will be construction of the target unit prototype with the amount of the target material of 40–60 g, which is required for effective medical radionuclide production at the RIC-80.

References

1. V.N. Panteleev *et al.*, *PNPI. High Energy Physics Division. Main Scientific Activities 2007–2012*, Gatchina, 2013, p. 278, http://hepd.pnpi.spb.ru/hepd/articles/PNPI_2007-2012.pdf
2. V.N. Panteleev *et al.*, *Rev. Sci. Instrum.* **86**, 123510 (2015).
3. S.A. Artamonov *et al.*, *PNPI. High Energy Physics Division. Main Scientific Activities 2007–2012*, Gatchina, 2013, p. 332, http://hepd.pnpi.spb.ru/hepd/articles/PNPI_2007-2012.pdf
4. V.N. Panteleev, Russ. Patent for Invention No. 2598089, The Production Method of Radionuclide Strontium-82, 30 Aug., 2016.
5. V.N. Panteleev *et al.*, *Rad. Applic.* **1**, No. 2, 95 (2016).
6. V.N. Panteleev, A.E. Barzakh, L.Kh. Batist *et al.*, *RAD Conf. Proc.* **2**, 43 (2017).

ULTRACOLD NEUTRON DETECTOR

A.G. Krivshich, V.A. Andreev, A.V. Vasiljev, E.A. Ivanov, D.S. Ilyin, A.P. Serebrov

1. Introduction

The problem of the neutron lifetime refinement is related with such important issues of particle physics and cosmology as verification of the Standard Model and the model of nucleosynthesis in the early stages of formation of our universe. By present, the highest accuracy of the neutron lifetime measurements has been achieved by the PNPI group [1, 2]: $t_n = 878.5 \pm 0.8$ s.

The aim of a new experiment is to still further improve the measurement accuracy to the level of 0.2 s. A new spectrometer has been developed to achieve this goal. It is based on the method of ultracold neutron (UCN) storage in a large gravitational trap (UCN source – PF2/MAM) at the Institute Laue–Langevin (ILL, Grenoble, France) [1].

The main spectrometer components were optimized: the volume of the trap was increased by more than a factor of 5, neutron losses on the walls of the trap were reduced due to a new hydrogen-free coatings, the working temperature was lowered down to 80–100 K, and the vacuum was improved to the level of 10^{-7} mbar.

An important part of the spectrometer is the UCN detector which was designed by the Track Detector Department HEPD (PNPI) in collaboration with the Neutron Physics Laboratory of the Neutron Research Division (PNPI).

2. Detector system

The UCN detector is the key unit of the spectrometer, whose working stability determines the accuracy of neutron counting during experimental runs and consequently determines also the accuracy of the neutron lifetime measurement. On this basis, the detector should meet the following requirements:

1. A high UCN detection efficiency, which requires a correct choice of the composition of the working gas mixture in order to reduce primary ionization charge losses in the detector gas volume in the vicinity of the cathode, as well as minimization of neutron losses in the entrance window.
2. Low noise level and low sensitivity to the background.
3. Reliability and long-term neutron counting stability, which is achieved by reduction of the gas leakage and by long-term maintenance of the working gas purity through proper selection of the materials used for the detector construction.

2.1. Detector construction

The design of the gas-filled detector is based on six independent proportional counters (cells), which are placed in a single gas volume. This guarantees that the gas mixture properties are identical in each proportional counter. This constructional concept has already proven itself well in previous experiments.

All counters have the cross-section of 48×46 mm² (height \times width), the Au–W anode wire diameter is 25 μ m. The lengths of the counters are optimized to cover the maximum detection area (Fig. 1). The respective counter lengths are 165 mm (1 and 6), 252 mm (2 and 5), and 287 mm (3 and 4). These counters are combined in two independent counting channels according to the scheme: 1, 3, 5 and 2, 4, 6.

The entrance window of 290 mm in diameter is made of a thin 100 μ m aluminum foil in order to minimize UCN losses. The force acting on the foil at the working conditions is about 6.5 kN. Therefore, a special stainless steel grid is placed in front of the foil to support it from the neutron guide side (vacuum). The optimal pressure of the gas mixture is 1 bar (abs.).



Fig. 1. UCN detector parts: 1 – the upper part of the detector with the entrance window (the grid supporting the entrance foil is seen); 2 – the bottom part of the detector with six proportional counters; 3 – assembled UCN detector, shown from its back side (two preamplifiers and a gas manometer are seen)

2.2. Optimization of the electric field structure

The structure of the electric field within each of the proportional counters was optimized in order to minimize a negative impact of the detector design on the measured amplitude spectra.

1. Compared to the previous prototype, the design of the detector was changed to remove the drift space with non-uniform electric field that is located near the entrance window (Fig. 2).

2. The construction of the cathodes was optimized to provide a symmetrical structure of the electric field in the transverse direction of each anode wire.

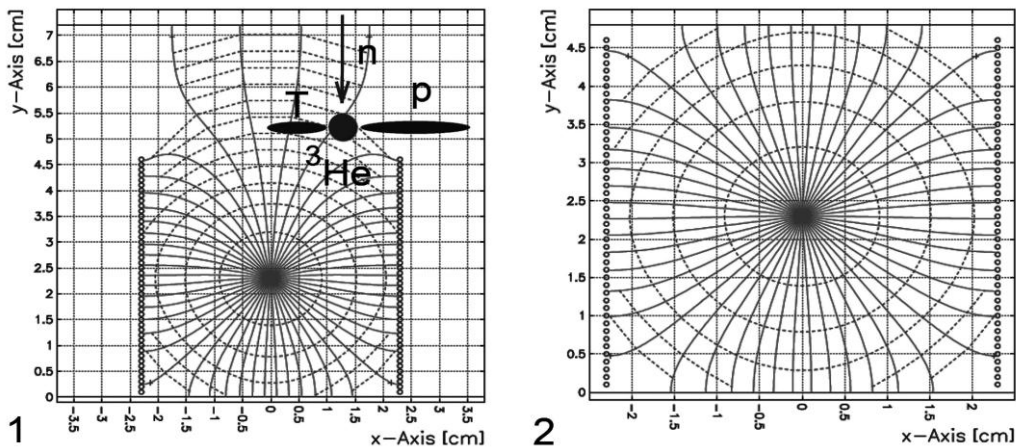


Fig. 2. The structure of the electric field and the timing diagrams in a cell calculated with GARFIELD [3] for a gas mixture 30 mbar ^3He + 970 mbar CF_4 and an anode voltage of 2 kV: 1 – prototype cell; 2 – improved cell. The *solid lines* are the drift lines of electrons; the *dotted lines* are the electron time contours in time steps of 0.1 μs

The measures taken greatly improved the detector characteristics:

1) a high uniformity of the gas gain along the anode wires was achieved and the maximal fluctuations did not exceed $\pm 4\%$;

2) cross-talks between neighboring cells (counters) caused by ingress of parts of the proton–tritium tracks that trigger two independent events with smaller amplitudes were practically excluded (Fig. 2);

3) the maximum time required to collect the ions formed in a gas avalanche was reduced by more than a factor 8, thus not exceeding $10^4 \mu\text{s}$.

2.3. Principle of ultracold neutron registration

The neutrons are detected through the nuclear reaction ${}^3\text{He} + n \rightarrow p + T + 764 \text{ keV}$. Since the reaction cross-section is inversely proportional to the neutron velocity v , one obtains $\sigma_{\text{UCN}} = \sigma(1.8 \text{ \AA})v(1.8 \text{ \AA})/v_{\text{UCN}}$, where $\sigma(1.8 \text{ \AA}) = 5333 \text{ b}$; $v(1.8 \text{ \AA}) = 2200 \text{ m/s}$; $v_{\text{UCN}} = 8 \text{ m/s}$; $\sigma_{\text{UCN}} \approx 1.5 \cdot 10^6 \text{ b}$.

In accordance with the momentum conservation law, the particles acquire kinetic energies $E(p) = 573 \text{ keV}$ and $E(T) = 191 \text{ keV}$, respectively. They are emitted in opposite directions from the point of interaction and produce primary ionization charges. The centre of gravity (c. g.) of this charge cloud is shifted relative to the interaction point by a distance $R_{\text{sph}} = 0.35R(p)$, where $R(p)$ is the proton range. So, the c. g. of charges are placed on a spheroid surface of radius R_{sph} for all neutrons absorbed at the same point.

2.4. Detector efficiency and the “wall” effect

The key factor in achieving an effective rejection of the background from the “neutron” events is to minimize the “wall” effect [4], which is associated with a partial loss of the primary ionization charge near the cathode walls. The largest contribution comes from the tracks which are formed near the entrance window (Fig. 3).

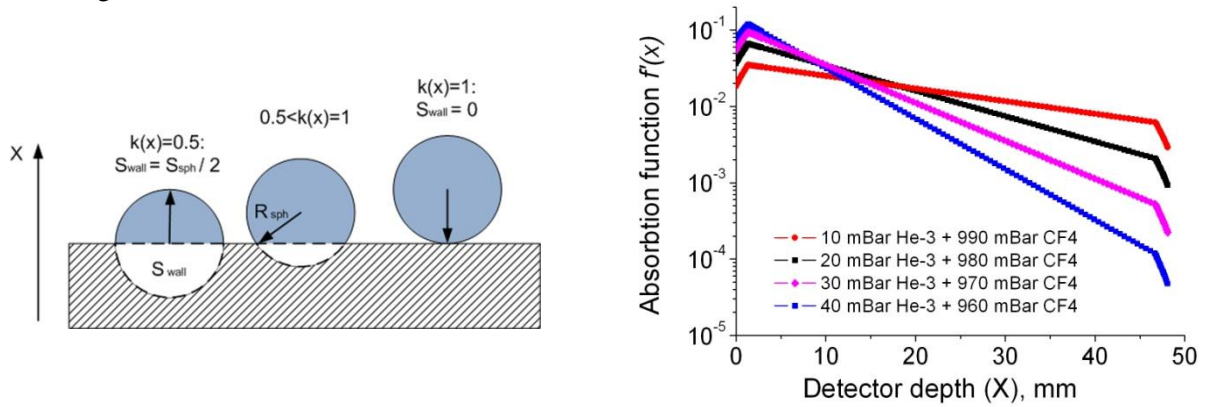


Fig. 3. The influence of the “wall” effect: the illustration for explaining the calculation of the correction factor $k(x)$ (left); the function $f'(x)$ for various compositions of the gas mixture (right)

The degree of influence of the “wall” effect is determined by two main factors: 1) the probability function $f(x)$ of the UCN absorption which depends on the partial pressure of ${}^3\text{He}$; 2) the ranges of protons and tritons in the gas mixture, which are determined by the partial pressure of the stop-gas CF_4 or Ar.

The ranges of the particles were calculated with the SRIM program [5]. The results for Ar and CF_4 are $R_{\text{sph}}(\text{CF}_4) \approx 1.5/P \text{ [mm/bar]}$ and $R_{\text{sph}}(\text{Ar}) \approx 3.8/P \text{ [mm/bar]}$, where P is the absolute gas pressure in bar.

The UCN absorption efficiency $\varepsilon(L)$ and the probability function of absorption $f'(x)$ are:

$$\varepsilon(L) = \int_0^L f'(x) dx,$$

$$f'(x) = f(x)k(x), \quad f(x) = n\sigma e^{-n\sigma x}, \quad k(x) = 1 - S_{\text{wall}}/S_{\text{sph}},$$

where $L = 48 \text{ mm}$ is the detector thickness; n is the concentration of ${}^3\text{He}$; σ is the cross-section for the reaction ${}^3\text{He}(n, p)T$, and $k(x)$ is a correction factor accounting for the “wall” effect (front and back walls of the cell in the x direction). S_{wall} is the area of the circle segment with $r = R_{\text{sph}}$ truncated by the cathode wall, S_{sph} is the area of the full circle, and x is the coordinate along the beam direction (from the window to the back), as indicated in Fig. 3.

The correction factor $k(x)$ varies from 0.5 to 1. So, there are a few cases: 1) $k = 1$ for complete p - T tracks, 2) $0.5 < k < 1$ for truncated tracks, 3) $k = 0.5$ when the absorption point of the neutron (the centre of the spheroid) coincides with the wall surface. Events with $k < 0.5$ are not taken into account.

The “wall” effect value W of the cell takes into account all walls: $W = (1 - S/S_0)$, where

$$S_0 = \int_{X_{\min}}^{X_{\max}} \int_{Y_{\min}}^{Y_{\max}} f(x) dx dy$$

is the “effective” area of the cell ($X_{\min} = Y_{\min} = 0$ mm, $X_{\max} = 48$ mm, $Y_{\max} = 46$ mm) and

$$S_0 = \int_{X_{\min}}^{X_{\max}} \int_{Y_{\min}}^{Y_{\max}} f'(x)k(x) dx dy$$

is the “effective” area of the cell including wall effect corrections (front, back, and side walls of the cell), and $k(y)$ is the correction factor in the direction perpendicular to the x -axis and accounts for the side walls of the cell. The results of the calculations are shown in Fig. 4.

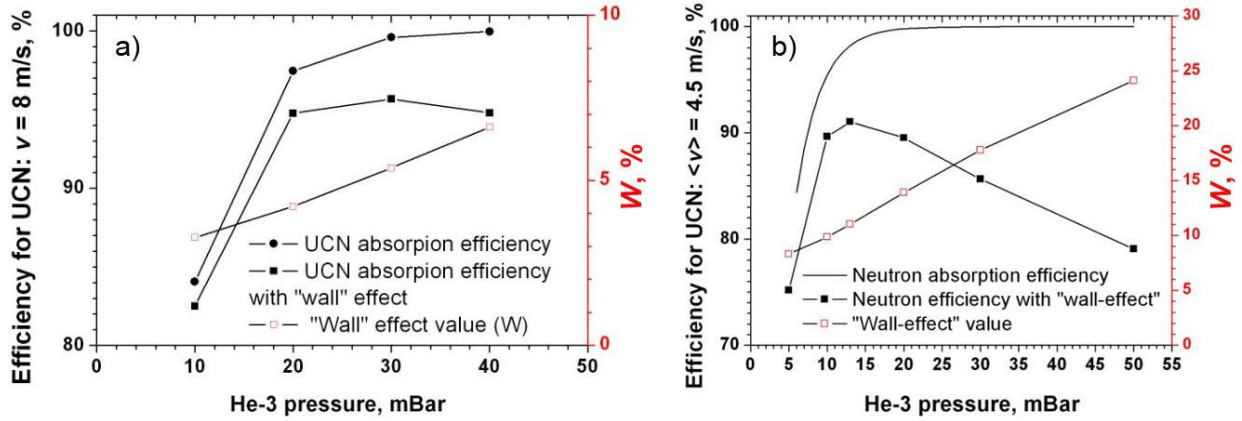


Fig. 4. Calculated efficiency and the “wall” effect value W versus the partial pressure of ^3He in the gas mixture: a – for the UCN velocity $v = 8$ m/s and the gas mixture $^3\text{He}\text{-CF}_4$; b – for the average UCN velocity $v = 4.5$ m/s in the UCN spectrometer at the ILL and the gas mixture $^3\text{He}\text{-Ar}\text{-CO}_2$. W is the fraction of truncated tracks in %

2.5. Choice of the gas mixture

The gas mixtures were carefully selected to minimize the “wall” effect and to achieve the maximal UCN efficiency.

For the initially planned UCN velocity $v = 8$ m/s, we choose the gas mixture $^3\text{He}\text{-CF}_4$ which is conventional for thermal neutron detectors. For this gas mixture, the optimal pressure of ^3He is 30 mbar (see Fig. 4a). The maximal efficiency $\epsilon_{\text{UCN}} \approx 95\%$ and a small “wall” effect value $W \approx 5.5\%$ were achieved for that ^3He pressure. The partial pressure of CF_4 was 1 030 mbar, limited by the maximum operational pressure (see Section 3.1).

The final composition of the gas mixture was optimized during detector tests under real experimental conditions. The real mean UCN velocity was $\langle v \rangle = 4.5 \pm 1.0$ m/s. For this case, the initial choice of the ^3He pressure 30 mbar was not optimal (see Fig. 4b), since the “wall” effect value $W \approx 17\%$ was high and the UCN efficiency $\epsilon_{\text{UCN}} \approx 85\%$ was relatively low.

Therefore, the ^3He pressure was reduced to 13 mbar to achieve the maximal efficiency $\epsilon_{\text{UCN}} \approx 91\%$ and to minimize the value of W down to $W \approx 11\%$. To reduce the operating voltage and consequently the high-voltage noise, the finally selected working gas mixture was 13 mbar ^3He + 1 060 mbar Ar + 20 mbar CO_2 .

3. Detector tests

3.1. Lab tests (PNPI, Russia)

The detector was successfully tested both at the PNPI lab with a Pu–Be source and as a part of the UCN spectrometer at the PF2/MAM beam port of the ILL high-flux reactor in Grenoble. In particular, the gas gain non-uniformity along the anode wire was confined to be $\pm 4\%$ for all cells, and the amplitude spectra were the same for both channels. An amplitude resolution $\Delta E/E = 6\text{--}15\%$ (full width at half maximum) was obtained in the operating range of the anode high voltage $HV = 1.7\text{--}1.9\text{ kV}$.

3.2. Reactor tests (ILL, France)

The detector was installed at the UCN spectrometer at the HFR reactor in Grenoble. As mentioned before, the mean UCN velocity at the PF2/MAM beam port was $v = 4.5 \pm 1.0\text{ m/s}$. The initial measurements with a $^3\text{He}\text{--CF}_4$ gas mixture showed a significant number of “neutron” events with incomplete ionization tracks – low-amplitude tails in the amplitude spectra (Fig. 5a).

The impact of low-amplitude events on the amplitude spectra was significantly reduced by optimization of the gas mixture composition, as can be clearly seen in Fig. 5b from the counting rate reduction at the tritium energy level.

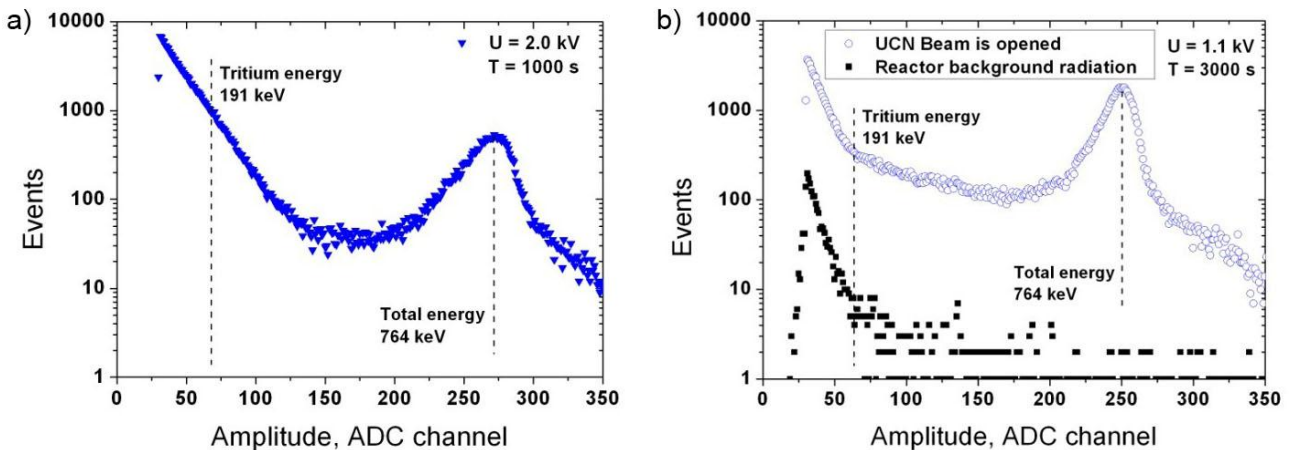


Fig. 5. Amplitude spectra obtained with the second counting channel of the detector at the UCN spectrometer at the HFR reactor with the thermal power 30 MW: a – for the $^3\text{He}\text{--CF}_4$ gas mixture (UCN irradiation); b – for the working gas mixture $^3\text{He}\text{--Ar}\text{--CO}_2$ (UCN and reactor background irradiation). Tritium and total reaction energy levels are indicated by *dotted lines*

Indeed, the gas mixture optimization improved the shape of the amplitude spectra, allowing for a more effective background rejection because a smaller number of “neutron” events were lost after amplitude discrimination.

4. Conclusion

The UCN detector has been designed and successfully tested. Currently it is used at the UCN spectrometer at the ILL Grenoble.

It has been shown that the influence of the “wall” effect on the structure of the UCN amplitude spectrum manifests itself in an additional continuous spectrum from background up to the total energy peak $E_0 = 764\text{ keV}$.

The negative impact of this effect offers a difficulty in rejecting background events from “neutron” events, since a significant number of such events have incomplete ionization tracks and, as a result, have low amplitudes.

This work was performed at the PNPI under a support of the Russian Science Foundation, the project No. 14-22-00105.

References

1. A. Serebrov *et al.*, J. Tech. Phys. **83**, No. 11, 136 (2013).
2. A. Serebrov *et al.*, Phys. Rev. C **78**, 035505 (2008).
3. R. Veenhof, Garfield – Simulation of Gaseous Detectors, <http://consult.cern.ch/writeup/garfield>
4. R. Batchelor *et al.*, Rev. Sci. Instrum. **26**, 1037 (1955).
5. J. Ziegler, Srim – the Stopping and Range of Ions in Matter, <http://www.srim.org/>

UNIVERSITY OF FLORIDA–PNPI HIGH VOLTAGE SYSTEM IN THE CMS ENDCAP MUON DETECTOR

S.S. Volkov, S.V. Bondarev, V.L. Golovtsov, N.B. Isaev, E.M. Orischin, L.O. Sergeev, L.N. Uvarov

The design and construction of the University of Florida (UF) – PNPI high voltage system (HVS) was performed in collaboration with specialists of the UF [1] for three detecting stations ME1/2, ME1/3, ME2, ME3, and ME4 of each of the two endcaps in the CMS endcap muon system (EMU) [2]. In total, there are 234 cathode strip chambers (CSC) per each endcap as it is shown in Fig. 1. The detecting stations are divided into two regions each: ME1/2 and ME1/3, ME2, 3, 4/1 and ME2, 3, 4/2. At present, there are 468 six-plane CSC. Each plane should be provided with a high voltage (HV) line. Moreover, the HV line in each layer is subdivided into several segments (Fig. 2). Five segments are in the chambers ME2/2, ME3/2, ME4/2, and 3 segments are in all other chambers.

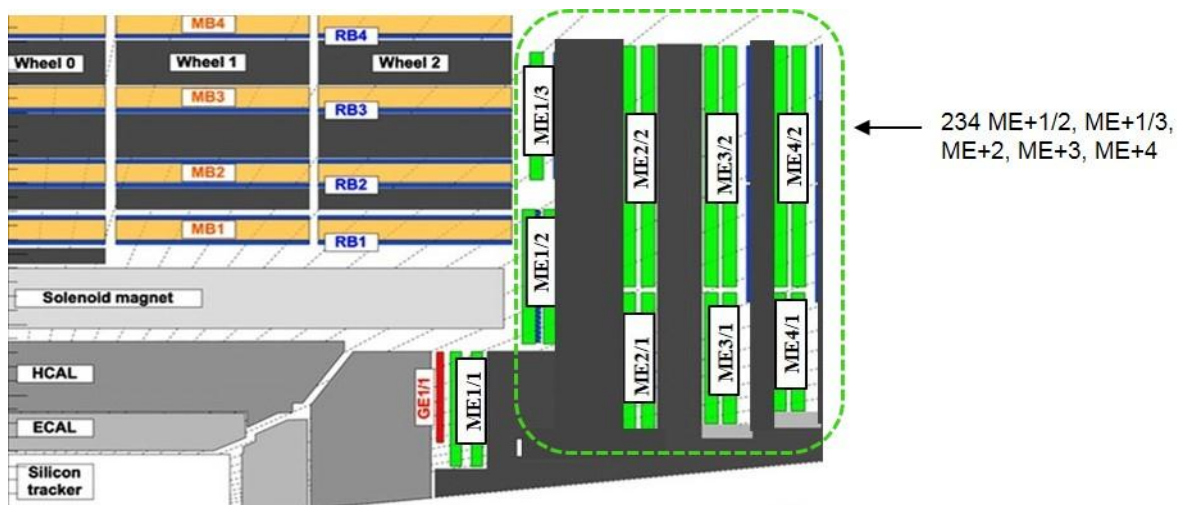


Fig. 1. Structure of the CMS endcap muon system

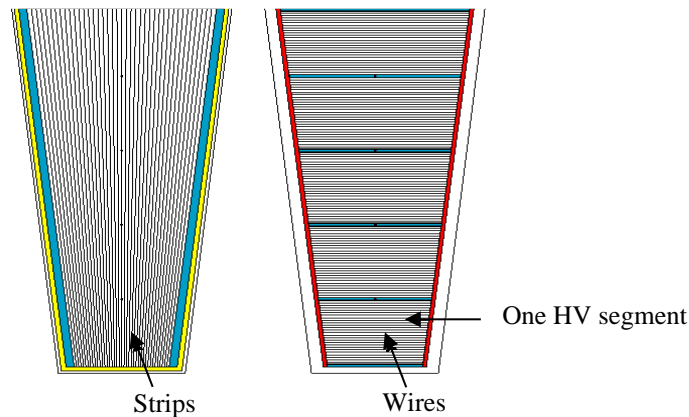


Fig. 2. Structure of the CSC with five HV segments

The main purpose of the HVS is to provide high voltage for the CMS endcap CSCs. CSC features that affect the HVS design are the following:

- small HV segments and high tolerance to HV failures,
- the same working voltage with small variation from segment to segment,
- a problematic segment can be fixed by reducing voltage or disconnecting from HV,

- precise consumption current for each segment,
- detects discharges and leaks.

Figure 3 shows the overall hierarchical structure of the HV distribution in the HVS.

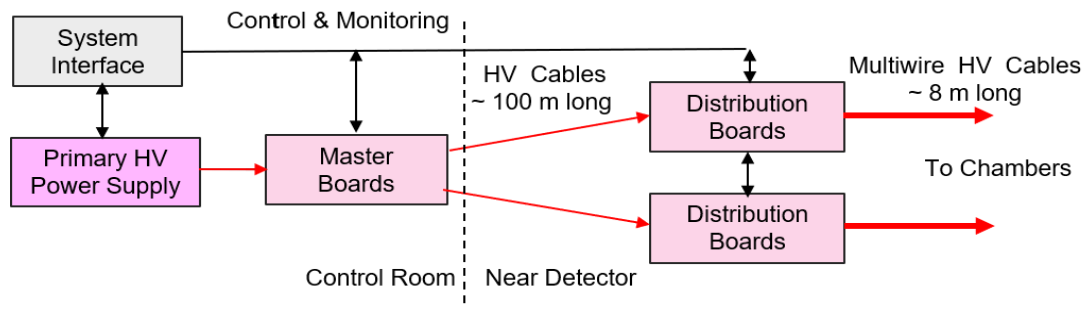


Fig. 3. HVS distribution structure

The custom-made HVS has a three-tier structure. There are eight commercial Matsusada primary HV power supplies (PHVPS). They provide the HV power to 50 master boards, each of which has eight regulated outputs. Both the PHVPS and the crates with the master boards are located in underground service cavern (USC). The master board outputs are routed to the distribution boards located near CSCs (on the periphery of the endcap discs). There are two types of distribution boards: 216 30-channel boards serve ME2/2, ME3/2, ME4/2 chambers (one chamber per board); 126 36-channel boards serve ME2/1, ME3/1, ME4/1, ME1/2, ME1/3 chambers (two chambers per board). The system interface consists of a control computer and control boards, which provide control and monitoring operation for each channel of the HVS. Table 1 summarizes the quantities of different hardware components in the HVS.

Table 1

Summary of hardware components in the HVS

Component	Quantity
Primary high voltage power supply	8
Control computers	2
Low voltage power supplies	2
Control boards	4
Master boards	50
Distribution boards, 30 channels	216
Distribution boards, 36 channels	126
Independently regulated and monitored distribution channels	11 016

There are eight PHVPSs in the system. All of them are located in the control room. Each of these modules supplies high voltage to one of eight partitions of the HVS. PHVPS is a commercially available module, manufactured by Matsusada Precision with the following parameters:

- AU-5P60-LF(U) HV power supply, 5 000 V / 60 mA;
- GP-HV-L(U) control interface;
- RS-232C module for control interface.

The master boards are located in the control room, and they receive HV generated by PHVPS and distribute it to its eight outputs. Each output is independent and capable of

- regulate voltage from 0 to 4 000 V,
- deliver up to 1.5 mA of current into the load,
- voltage measurement from 0 to 4 000 V,
- current measurement from 0 to 1.5 mA,
- over-voltage and over-current protection with programmable threshold.

The distribution boards are located in underground experimental cavern (UXC), in racks near the discs, to minimize the length of the cables that deliver voltage from them to all chambers. Each distributor board receives high voltage from the master board *via* very long cable and distributes it to its 30 or 36 outputs. Each output of a distribution board is independent and capable of

- regulate voltage up to 1 000 V down from maximum voltage supplied from the master board output,
- deliver up to 100 mA of current into the load,
- voltage measurement from 0 to 4 000 V,
- current measurement from 0 to 100 mA,
- over-voltage and over-current protection with programmable thresholds and timeouts.

Each distribution board output provides power for one HV segment of a CSC.

Two computers control the entire HVS. Both computers are located in USC. Figure 4 shows the software structure and control interfaces of the HVS. The software was designed and maintained by specialists of the UF.

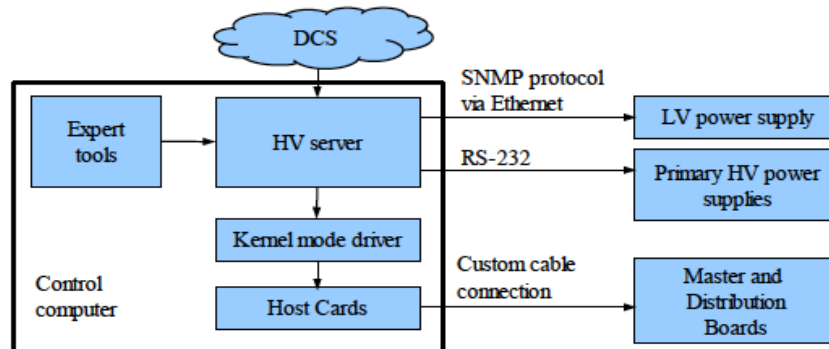


Fig. 4. Software structure and control interfaces of the HVS

The HV server is based on the distributed information management (DIM) system [3] and performs the following tasks:

- receives high-level commands from detector control system graphical user interface or from expert tools;
- decodes these commands; passes the corresponding parameters to the kernel mode driver, the PHVPS and the low voltage power supply (LVPS);
- reads out and publishes the monitoring information from all master and distribution boards, the PHVPS and the LVPS.

The main purpose of the kernel mode driver is to provide control and monitoring of the master and distribution boards in real time:

- over-current and over-voltage trips,
- voltage ramp-up and ramp-down,
- pre- and post-trip data logging for future analysis.

There are several standalone expert tools that can be run on the HVS control computer. They provide control of one or multiple components of the system including:

- displaying voltages, currents, voltage and current trip levels and timeouts, states of all channels of the selected component;
- setting any of the above parameters using simple command-line interface;
- each channel calibration for voltage setting, voltage, and current sensors;
- trip profile analysing in case of overcurrent or overvoltage.

As a result, the HVS has a developed hardware and software basis to provide stable operation for a number of years. Table 2 shows the number of channel and board failures by years. Elevated failures in 2009 are due to the replacement operation of the batch of resistors with unstable parameters. Elevated failures in 2014 are due to the system upgrade with new boards installation for ME4/2.

Table 2

HVS channel and board failures

Year	Distribution board – 36		Distribution board – 30		Master board	
	Single channel	Board	Single channel	Board	Single channel	Board
2009	23	1	30	2	3	1
2010	11	1	4	0	0	0
2011	4	16	6	1	1	1
2012	4	1	2	1	0	0
2013	0	0	0	0	0	0
2014	0	1	6	6	2	1
2015	2	0	0	0	2	1

Figure 5 shows the voltage calibration stability in time during one year. The drift is negligible. The voltage calibrations are now tested periodically for all channels.

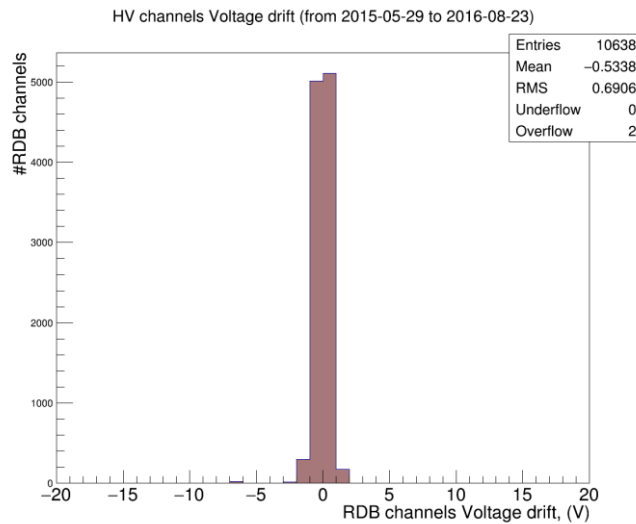


Fig. 5. HVS high voltage channels drift in time

References

1. A.A. Vorobyov *et al.*, *PNPI. High Energy Physics Division. Main Scientific Activities 2002–2006*, Gatchina, 2007, pp. 26–34.
2. A.A. Vorobyov *et al.*, *PNPI. High Energy Physics Division. Main Scientific Activities 2007–2012*, Gatchina, 2013, p. 27.
3. DCS Users Manual, <https://twiki.cern.ch/twiki/bin/view/CMS/CSCOperationsDCS>

NONINVASIVE METHOD OF RECOVERY OF GAS PARTICLE DETECTORS UNDER OPERATION IN HIGH-INTENSITY FIELDS OF RADIATION

V.A. Andreev, G.E. Gavrilov, A.G. Krivshich, D.A. Maisuzenko, A.A. Fetisov, N.Yu. Shvetsova

1. Introduction

Here we describe a method of noninvasive recovery of gas-discharge detectors, which have been degraded due to operation in intense radiation fields. The proposed techniques are based on the plasma-chemical reactions, which occur during the detector training in the gas discharge that is generated in a special gas mixture. It has been shown that the method of plasma-chemical etching in a gas discharge increases the detector lifetime in several times.

Usually, aging effects result in a surface degradation of both the anode and cathode electrodes, which occur in different forms. The first one is the anode type of aging. First of all, it is associated with silicon deposits formed on the surface of the anode wires. The source of these deposits are structural materials and elements of the gas supply system of the detector [1]. These effects are manifested even with small accumulated charges in the range of 0.1–1.0 C/cm of the anode wire length. If there would be no silicon contamination in the detector, it could operate at higher doses with the accumulated charge exceeding 1 C/cm. In that case, the main mechanism of aging would be swelling of the wire caused by chemical interaction of the oxygen which is coming from the gas avalanche with the tungsten which is the main material of the anode wire [2].

The second type of aging is the cathode aging. It is associated with formation of dielectric films at the cathode, which usually cause the Malter effect (ME) [3, 4] – spontaneous self-sustained current in the detector initiated by electron emission from the cathode surface through dielectric films formed at the cathode.

The explanations of these mechanisms can be considered in terms of plasma chemistry. Different types of chemical radicals and ions are produced in the gas avalanche near the anode wire. They can cause plasma chemical reactions. Polymers and other chemical compounds resulting from these reactions may deposit on the surface of the detector electrodes and due to interaction with the electrode materials may form even new chemically different substances.

A noninvasive method of cleaning the cathode and anode wire surface from organic compounds, silicon, and tungsten compositions (swelling effects) has been developed at PNPI. It is based on the plasma-chemical etching reactions which are used in the microelectronics production. Recovery of the main technical characteristics of the detector after its aging without disassembling and repairing is actual for many physical experiments, since the development of a detector operating with an accumulated charge of about 10–20 C/cm is still a problem.

2. Malter effect at the cathode

For recovery of multiwire proportional chambers (MWPC) of the muon tracker in the LHCb experiment at the Large Hadron Collider from the ME, the 40% Ar + 55% CO₂ + 5% CF₄ working gas mixture with added 2% of oxygen was tested. The oxygen radicals and ozone produced in the gas discharge plasma near the wire interact efficiently with organic and silicon films at the cathode, forming volatile compounds, which are removed in the process of gas flushing [5, 6]. Figure 1 shows the Malter current as a function of MWPC training time. The ME current on a level of 25 μA was ignited by ⁹⁰Sr β-source irradiation at a voltage of 2 600–2 700 V and maintained by increasing the voltage step by step up to the maximum value 2 850 V; the ME current decreases as the formations at the cathode are removed. As one can see, during four hours of MWPC training in the gas mixture with 2% oxygen, the ME nearly vanished. In contradictory to this, the current remained virtually constant even after six hours of MWPC training in the working gas mixture. This method was used to recover four MWPC units, which could not be recovered by training in the working gas mixture.

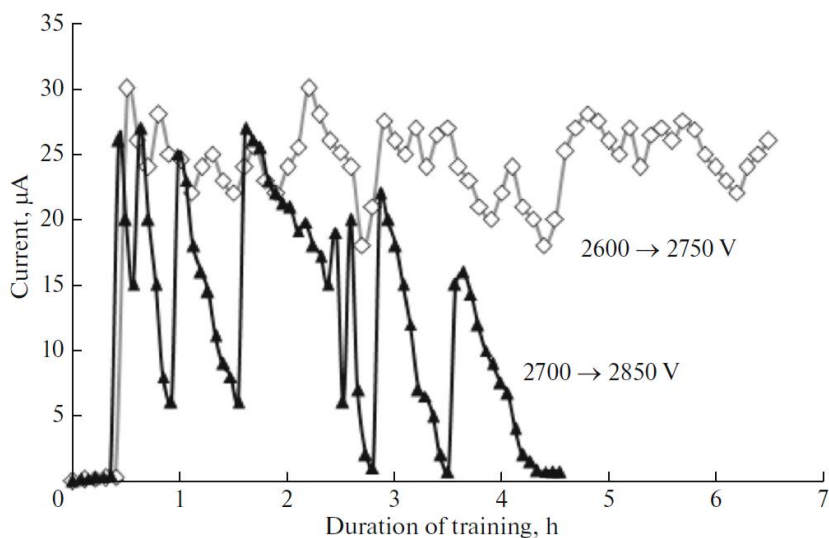


Fig. 1. Malter current in a MWPC during recovery: \diamond – training in the working gas mixture; \blacktriangle – gas mixture with 2% O_2 added

3. Anode wire recovery

The etching of various types of formations on the anode wire surface took place in the gas-discharge plasma that is generated in the 80% CF_4 + 20% CO_2 gas mixture near the anode wire with a negative potential. The basis of the process is the plasma-chemical etching by fluoride active radicals both silicon and tungsten containing compounds in the gas discharge in the vicinity of the anode wire.

In the course of the wire recovery, the damaged region is irradiated by a ^{55}Fe source. X-ray photons with an energy of 5.9 keV maintain ionization in the gas-discharge plasma and provide desorption of the etching products [7–9]. The etching efficiency of silicon and tungsten formations was studied with the use of proportional straw counters.

The experimental results of the straw recovery from silicon formations are shown in Fig. 2. The diameter of the anode wire in the straw was 50 μm , the diameter of the cathode-polyamide tube with deposited carbon was 4 mm. The straw aging effects were studied in a gas mixture of 60% Ar + 30% CO_2 + 10% CF_4 . This straw was irradiated by a ^{90}Sr β source with a total intensity of about 15 MHz. The anode wire was aged three times in a silicon-contaminated gas mixture until the amplitude was reduced by $\sim 35\%$, and each time the anode wire recovered in the 80% CF_4 + 20% CO_2 gas mixture.

Figure 2a shows the wire surface pictures from the scanning microscope and the X-ray fluorescence analysis spectra (SEM/XEM) of the wire surface before and after three “aging–recovery” cycles. As one can see, the wire diameter has increased from 50 to 59 μm (18%). Intensive peaks of silicon and oxygen are observed on the anode wire surface.

Figure 2b shows the gas amplification factor (GAF) behaviour as a function of the accumulated charge. In order to be sure that the recovery effect exists for silicon polluted anode wires, two independent straws were aged and recovered. Each of them was subjected to this procedure three times. The obtained results were very similar (see Figs. 2a and 2b), which confirmed the effectiveness of the proposed method.

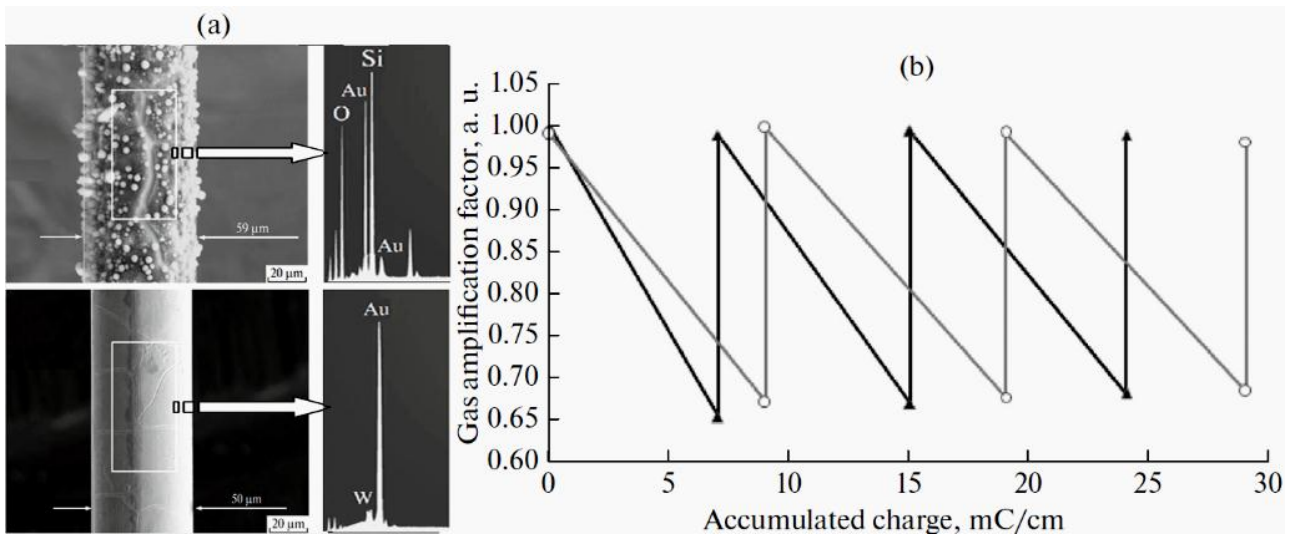


Fig. 2. Results of a SEM/XEM examination of the surface of an aged anode wire (*upper part*) and of a wire recovered by the etching procedure (*lower part*); on the *right side* – results of a XEM spectra analysis of the wire surface are shown (a). GAF as a function of the accumulated charge during multiple recovery of two counters (b): \blacktriangle – straw-1; \circ – straw-2; *slanting lines* – the GAF reduction during irradiation; *vertical lines* – the GAF recovery during etching

For achieving the anode swelling effect, a clean gas system was used. In order to be sure that the recovery effect exists for swelled anode wires, two independent series of measurements were performed, for each of them the aging-recovery cycles were repeated three times. The obtained results were very similar (Figs. 3a and 3b). In the first series, straws were irradiated until the signal amplitude dropped down by $\sim 6\%$, and in the second series, it dropped down by $\sim 3\%$ [10]. The results of measurements are shown in Fig. 3. Figure 3a shows a SEM/XEM analysis of the anode wire surface. A film of tungsten-oxide compound is clearly observed on the gold coating of the wire. Figure 3b shows the GAF behaviour as a function of the accumulated charge.

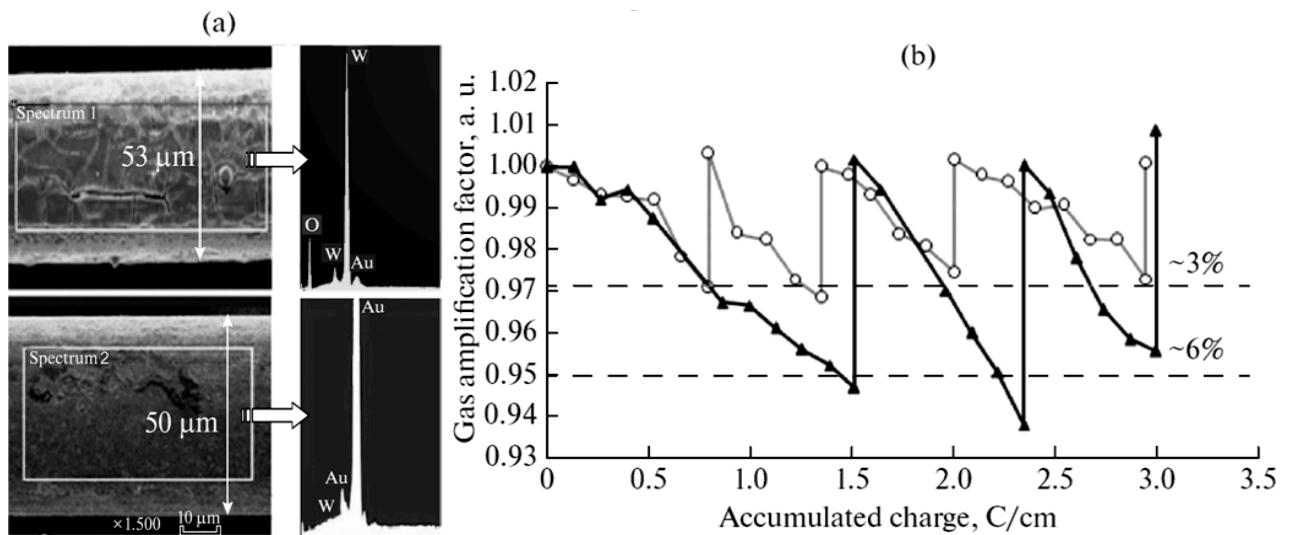


Fig. 3. Results of a SEM/XEM examination of the surface of an aged wire (*upper part*) and of a wire aged and three times cleaned (*lower part*); on the *right side* there are results of a XEM spectra analysis of the wire surface measured in a rectangular area indicated by a white line on the *left side* (a). GAF as a function of the accumulated charge during multiple recovery of counters (b): \blacktriangle – straw-1; \circ – straw-2 [10]

4. Conclusion

Application of the proposed method of the plasma-chemical etching in a gas discharge to recover the aged gas-discharge detectors increases the detector lifetime by several times. This method of recovery has a universal character and can be a suitable solution to the problem of detectors aging in future experiments.

References

1. M. Capeans, Nucl. Instr. Meth. Phys. Res. A **515**, 73 (2003).
2. T. Ferguson, G. Gavrilo, V. Gratchev *et al.*, Nucl. Instrum. Meth. Phys. Res. A **515**, 266 (2003).
3. L. Malter, Phys. Rev. **50**, 48 (1936).
4. J. Va'vra, Nucl. Instrum. Meth. Phys. Res. A **515**, 1 (2003).
5. F.I. Grigor'ev, *Plasma-Chemical and Ion-Chemical Etching in Microelectronic Technology, Textbook*, Mosk. Gos. Univ., Elektron. Mat., Moscow, 2003 [in Russian].
6. A.M. Boyarsky, Nucl. Instrum. Meth. Phys. Res. A **604**, 573 (2009).
7. V.P. Zhuze, B.V. Kurchatov, Physik. Z. Sowjetunion **2**, 453 (1932).
8. S. Belostotski, S. Frullani *et al.*, Nucl. Instrum. Meth. Phys. Res. A **591**, 353 (2008).
9. G.E. Gavrilo, V.M. Vakhtel, A.G. Krivshich *et al.*, Preprint PNPI-2983, Gatchina (2015).
10. G.E. Gavrilo, D.A. Aksenov, R. Conti *et al.*, Nucl. Instrum. Meth. Phys. Res. A **694**, 167 (2012).

RECOVERY OF GAS DISCHARGE DETECTORS FROM MALTER EFFECT

G.E. Gavrilov, E.V. Kuznetsova, O.E. Maev, D.A. Maysuzenko, S.A. Nasybulin

1. Introduction

Aging or degradation of operating characteristics of gas discharge detectors remains a real problem in modern high energy physics experiments with high radiation background levels. According to results of numerous studies [1, 2], very often aging of gaseous detectors is caused by residual contamination of silicon compounds in the working gas mixture. Silicon is the most widespread element which is regularly registered in analyses of precipitates formed on electrode surfaces. The working gas mixture can be contaminated by a gas circulation pump, gas system connections, and fiberglass electrodes of the detector.

Polymerization reactions take place near the wire in the gas discharge plasma, and the formed polymers precipitate on the surface of anode wires as well as on cathode planes, causing degradation of operation characteristics of the detector. The presence of dielectric polymer films on the conducting metal cathode surface (wires or plane) as a rule results in appearance of a self-sustained secondary emission current, the so-called Malter effect (ME) [3, 4]. This current is the result of accumulation of a positive electric charge on a thin ($< 1 \mu\text{m}$) film during the operation of the chamber. Depending on the charge value and the thickness of the dielectric film, the resulting electric field may become sufficient to cause spontaneous secondary electron emission-from the cathode.

For gas discharge detectors, the ME is the most devastating of all secondary electron emission effects. It appears when formation of the electric charge is not compensated by a leakage current from the film surface. Multi-wire proportional chambers (MWPC) operating in a high radiation environment may demonstrate a self-sustained current reaching up to 30–50 μA . The ME results in an increased noise rate, in trips of the high-voltage supply system due to high currents exceeding the usual safe limits, and in the accelerated aging of anode wires around the zone of ME occurrence.

A number of MWPCs operated by the LHCb experiment at the Large Hadron Collider (LHC) demonstrate appearance of the ME. In this work, a noninvasive recovery method of quick and efficient ME current suppression is described. This approach was successfully applied to problematic chambers of the LHCb muon detector and brought them back to a nominal operation. Recovery of gas discharge detectors from aging without disassembling and repair is topical for many modern experiments and often is a challenging task.

2. Curing Malter effect in multi-wire proportional chambers in presence of CF_4

The ME is well known to experimentalists for many years. In some cases it can be cured by adding up of 0.2% of water vapour or 2–3% of various alcohols to the working gas mixture [2, 5]. Molecules of water and alcohol stop the polymerization processes in the gas mixture and precipitation on the cathode surface, and rapidly increase its conductivity. However, these additives cannot be applied to all types of MWPCs. Water vapours deposited on the surface of electrodes and insulators cause micro-sparks, and alcohol vapours, being solvents, cause deformation and swelling of dielectric elements of the detector construction [5].

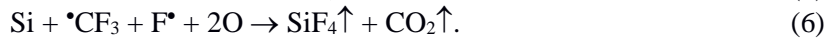
Because of the above limitations, neither water nor alcohol vapours were considered for eliminating the ME in MWPCs of the muon detector at the LHCb experiment. At the same time, the presence of CF_4 in the working gas mixture of the muon detector (40% Ar + 55% CO_2 + 5% CF_4) allows one to cure the ME without using potentially dangerous admixtures.

CF_4 is often added to MWPC gas mixtures to prevent chamber aging caused by silicon deposits on anode wires [1, 6]. Moreover, CF_4 is widely used in microelectronics and microelectromechanical device production for plasma etching of Si, SiO_2 , and, in presence of oxygen, of various polymer materials [7–11]. Fluorine radicals produced in plasma react with silicon and polymers, resulting in the surface etching by forming volatile products.

In proportional chambers, the most intensive formation of free radicals takes place around anode wires, where the electric field reaches $20\text{--}200 \text{ kV} \cdot \text{cm}^{-1}$. Electron impact dissociation of CF_4 molecules at the electron energy of about $E_e \approx 3\text{--}5 \text{ eV}$ occurs with formation of the following chemically active radicals [7, 8]:



$\bullet\text{CF}_3$, $\bullet\text{CF}_2$, and F^\bullet radicals produced in plasma-chemical reactions (1–3) efficiently react with different silicon formations. Volatile molecules (CO_2 , O_2 , and SiF_4) formed in etching reactions (4–6) are easily removed from the detector volume with the gas flow:



To recover MWPCs from the ME caused by silicon or organic films on the cathode surface, the corresponding depositions should be etched. However, near the cathodes, which are located at a distance of several millimeters from the anode wires, the concentration of fluorine radicals is low. Therefore, the recovery procedure often requires a relatively long time.

3. Recovery procedure developed for the muon detector of the LHCb experiment

The muon detector consists of 1368 modules of 19 different types covering a total area of 435 m^2 . Despite different dimensions, each module has the same internal geometry and consists of four or two MWPC gaps, A, B, C, and D, as shown in Fig. 1. Cathode electrodes of the MWPCs are made of FR-4 fiberglass plates with two-sided $35 \mu\text{m}$ thick copper coating. Cathode plates of adjacent gaps are separated by honeycomb panels or rigid polyurethane foam which provide precise gap alignment over the whole chamber area. The general parameters of all MWPCs are the same: the anode planes are centered inside 5 mm gas gaps and are formed from $30 \mu\text{m}$ diameter gold-plated tungsten wires stretched with 2 mm steps. All MWPCs are filled with the $40\% \text{ Ar} + 55\% \text{ CO}_2 + 5\% \text{ CF}_4$ working gas mixture. The operation gas gain ranges between $4.6 \cdot 10^4$ and $8.8 \cdot 10^4$, depending on the high voltage settings. Each MWPC gap has an independent high-voltage channel. The gas mixture is supplied into the gaps sequentially, as is shown in Fig. 1.

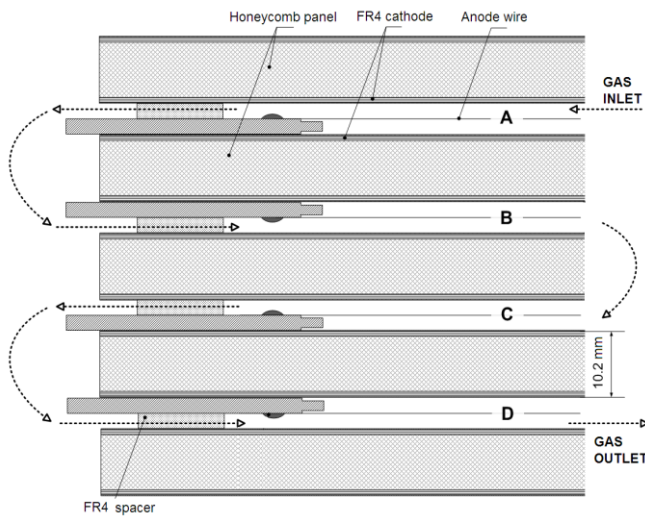


Fig. 1. Cross section of the LHCb muon chamber

Since the beginning of the LHCb operation, up to 17% of the muon detector modules experienced operation problems caused by the ME. In average, about 100 MWPC gaps suffer every year from high Malter currents and the concomitant high voltage trips. Nevertheless, all those problematic modules were successfully recovered *in situ*, under the nominal LHC beam conditions by means of a long-term high voltage training with the working gas mixture.

The gaps affected by the ME were trained during data taking. To increase concentration of fluorine radicals, *i. e.* to make the training more efficient, a sufficiently high Malter current should be supported in the damaged zone.

The training session starts with a slightly increased high voltage which provokes a rapid appearance of the Malter current from the problematic region. Usually the initial voltage values do not exceed 20–30 V above the nominal working point. During the training, the high voltage is varied to support the current at the level of $\sim 40 \mu\text{A}$.

A MWPC is considered to be restored when the current at the operating voltage reaches the nominal value corresponding to the LHC beam conditions (100–200 nA), and, when the beam drops, the current in the chamber also drops to zero. The duration of the training procedure for restoring a single ME spot in the proportional chamber may vary from one week to several months. A typical MWPC recovery under the high voltage training is demonstrated in Fig. 2. The bottom plot shows a history of changes of the high voltage which supported a reasonable level of the Malter current during the training procedure (*top plot*). As a result of the training, the self-sustained current dropped down to zero, and the nominal beam current ($I_{\text{nom}} \approx 140 \text{ nA}$) was obtained at the working voltage ($V_{\text{nom}} = 2600 \text{ V}$). The total duration of the presented recovery procedure is rather short – five days. On a statistical basis, the results of the training procedure are very positive – more than 90% of the MWPC suffered from the ME were restored to their normal behaviour.

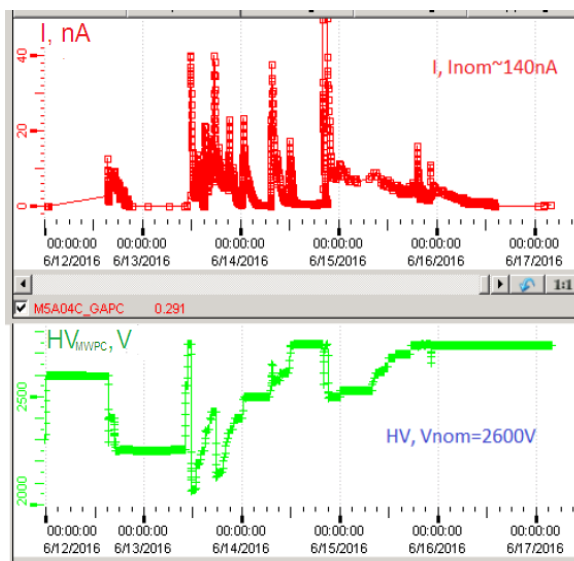
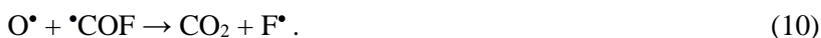


Fig. 2. Typical recovery procedure from the ME at the beam

With all the success of this method, the long duration of the training procedure greatly complicates the possibilities of its application. That is why it was proposed to use an oxygen admixture during the training procedure in order to accelerate the chamber recovery.

4. Gas composition for accelerated recovery from the Malter effect

Various studies of silicon dry etching processes showed that the etching rate in the $\text{CF}_4\text{-O}_2$ mixture is significantly higher than that in the pure CF_4 plasma [7–10, 12]. Oxygen radicals promote formation of $\cdot\text{COF}_x$, which quickly dissociates in collisions with surrounding electrons and atoms (see Eqs. (7–10)), and indirectly increase the number of fluorine radicals in the gas discharge plasma:



The highest silicon etch rate is obtained in the $\text{CF}_4\text{-O}_2$ mixtures with the oxygen content from 10 to 30% [7–10]. Moreover, oxygen plays a significant role in polymer film dry etching with $\text{CF}_4\text{-O}_2$ mixtures [11] and may even be sufficient in some cases for dielectric deposition cleaning in the pure O_2 plasma [13].

Kinetics of chemical reactions in MWPC gas discharges may significantly differ from reactions rates in industrial reactors due to different plasma nature, gas pressure and electric field configuration. In MWPCs, the electric field varies from $E \approx 5\text{--}6 \text{ kV} \cdot \text{cm}^{-1}$ on the cathode surface up to $E \approx 150\text{--}200 \text{ kV} \cdot \text{cm}^{-1}$ on the anode wire. In industrial etching set-ups, the electric field is uniform and amounts to $10\text{--}50 \text{ kV} \cdot \text{cm}^{-1}$, and a silicon wafer (to be etched) is placed in the plasma rich of active radicals. In proportional chambers, radicals are produced close to the anodes, which are separated from the cathodes with several millimeters of a low field region. Moreover, gas-discharge detectors usually operate with gas mixtures at the atmospheric pressure, which is several orders of magnitude higher than the pressure in industrial plasma reactors.

Nevertheless, even though the molecules and radicals in MWPCs have significantly smaller mean free path between electron collisions ($\sim 1 \mu\text{m}$), the average electron energy (5–10 eV) is quite similar for both proportional chambers and reactors [14]. This makes possible to use dry etching chemical models in qualitative predictions for chemical processes in MWPCs.

Reactions of oxygen impact dissociation and excitation significant at this electron energy range are given below. The oxygen radical production in dissociative electron attachment by O_2 molecules (Eq. (11)) happens already at the electron energies ~ 5 eV, while, for example, the CO_2 electron impact dissociation starts only at ~ 13 eV [15]. Both, the atomic oxygen, O^* , and the excited molecular oxygen $^*\text{O}_2$, formed in collisions with electrons (Eq. 12), are chemically aggressive:



The atomic oxygen O^* interacts with O_2 molecules forming ozone:



The excited ozone molecule, O_3^* , loses the excess energy through interaction with the plasma. The ground state ozone, O_3 , can participate in processes of plasma chemistry etching on the cathode surface or recombines with free oxygen radicals:



In contrast to the plasma reactor case, the O_2 content in the MWPC working gas mixture should be strongly limited due to the high oxygen electron attachment coefficient. Oxygen reduces the electron density in the discharge plasma, which results in reduction of the charge amplification. Therefore, to keep the gas gain at the level sufficient for the recovery process, the oxygen content should be optimized.

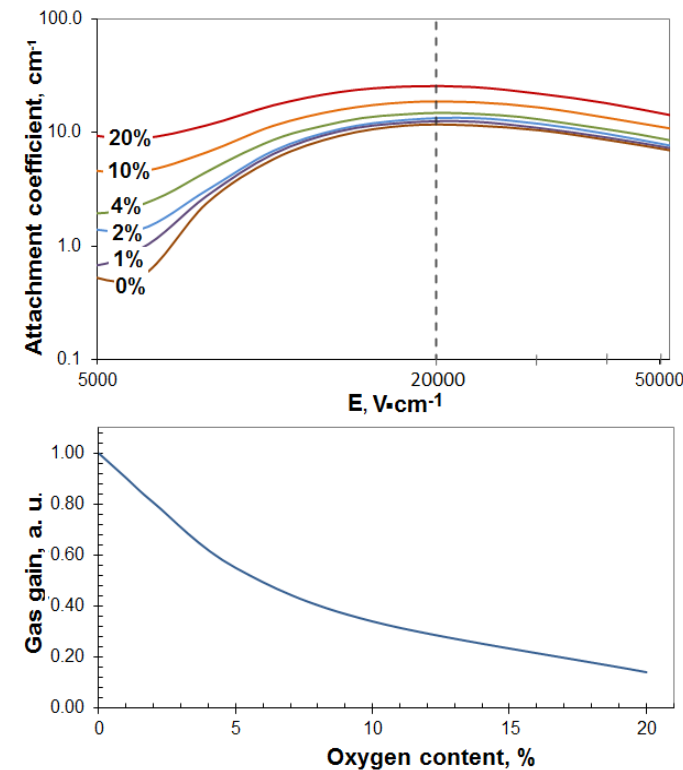


Fig. 3. Electron attachment coefficient as a function of the electric field strength (*top*); the gas gain as a function of the oxygen content (*bottom*)

Figure 3 (*top*) shows that for 1–4% of the O_2 content the electron attachment coefficient increases substantially only in the drift region, especially near the cathode surface, where the electric field strength is about $6000 \text{ kV}\cdot\text{cm}^{-1}$. When the oxygen content exceeds 10%, a noticeable electron attachment occurs throughout the whole drift path and in the avalanche region. As a result, the MWPC gas gain at the operation voltage drops by more than 60%, as can be seen in Fig. 3 (*bottom*).

Under such conditions, the charging of a dielectric deposit film on the cathode surface will be slowed down, which reduces the Malter current. A too small current cannot support an effective etching process. According to the GARFIELD predictions, to compensate for such a gain reduction, the high voltage should

be increased up to 3 000 V, that is above the safe operation range. Therefore, the oxygen content in the gas mixture used for the recovery procedure is a compromise between the acceleration of training and the voltage increase needed to compensate for the gas gain drop caused by the presence of oxygen.

5. Accelerated recovery of muon multi-wire proportional chambers with the gas mixture containing oxygen

To test the ME suppressing procedure with an oxygen-containing gas mixture, four modules of the muon detector were chosen. These modules were removed from the experimental set-up because of high ME currents impeding their proper operation and due to multiple fails of the standard recovery procedure with the nominal working gas mixture.

Localization of the ME zones on cathodes of the damaged MWPC gaps were performed with a collimated ^{90}Sr ($E_{\beta} = 2.28$ MeV) β source. The Malter currents ignited by the source were hundred times larger than the ionization current. As a result of thorough scans performed for each of the four MWPC of every module, seven ME zones were identified.

The recovery training with an oxygenated gas mixture was performed for each of those zones. The ^{90}Sr β source irradiated the recovering area to ignite and to support the Malter currents. The training was identical to the one described in Section 3. Supporting a few tens microampere current during the training resulted in the accelerated recovery of all ME zones. The recovery procedure is based on the plasma-chemical etching of silicon and organic compounds by fluoride, oxygen active radicals and ozone produced in the gas discharge. Volatile compounds formed during the etching were removed in the process of gas flushing [4].

Figure 4 shows the currents caused by the ME as a function of the training time for the nominal 40% Ar + 55% CO₂ + 5% CF₄ gas mixture (*red rhombuses*) and for the nominal gas mixture enriched with two percent oxygen (*blue circles*). An initial Malter current of 25 μA was ignited by the ^{90}Sr β source at the voltage of 2 600–2 700 V and was maintained by increasing the voltage in 50 V steps. The ME current decreases as the dielectric film is being removed from the cathode surface. The total time required to recover the ME zone in the case of the oxygen-containing mixture was around 4 h. However, with the nominal working mixture the Malter current stays constant even after more than 6 h [4].

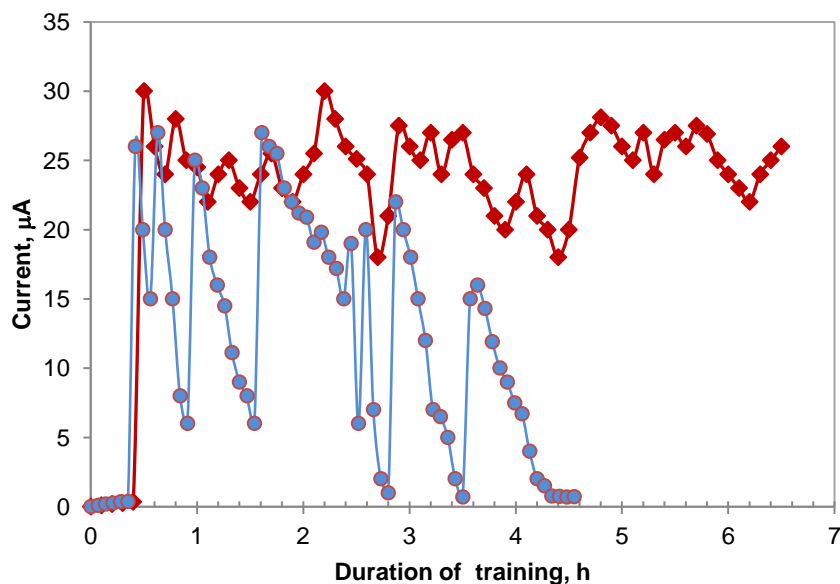


Fig. 4. Current in the MWPC during the ME suppression training

6. Conclusion

- Adding of oxygen to the Ar–CO₂–CF₄ gas mixture allow us to speed up the ME suppression training hundreds of times.
- The given technique allows several times to increase the durability of the MWPC operation in the field of intensive irradiation.
- The non-invasive character of the recovery technique makes it actual for many experiments where the detectors operate with the gas mixtures containing CO₂ and CF₄.

References

1. M. Capeans, Nucl. Instrum. Meth. Phys. Res. A **515**, 73 (2003).
2. S. Belostotski *et al.*, Nucl. Instrum. Meth. Phys. Res. A **591**, 353 (2008).
3. L. Malter, Phys. Rev. **50**, 48 (1936).
4. G.E. Gavrilov *et al.*, Phys. Elem. Particles Atom. Nucl. **49**, No. 1, 33 (2018).
5. J. Va'vra, Nucl. Instrum. Meth. Phys. Res. A **515**, 1 (2003).
6. G.E. Gavrilov, V.M. Vakhtel *et al.*, Phys. Atom. Nucl. **80**, No. 9, 1 (2017).
7. J.W. Coburn, *Plasma Etching and Reactive Ion Etching*, Am. Vacuum Soc., New York, 1982.
8. K.R. Ryan, I.C. Plumb, Plasma Chem. Plasma Process. **6**, Iss. 3, 205 (1986).
9. Yu.N. Grigoryev, A.G. Gorobchuk, Comput. Technol. **8**, No. 2, 53 (2003).
10. F.I. Grigoryev, *Plasma-Chemical and Ion-Chemical Etching in Microelectronics Technology, Textbook*, Mosc. Gos. Univ., Elektron. Mat., Moscow, 2003 [in Russian].
11. M.D. Koretsky, J.A. Reimer, J. Appl. Phys., **72**, No. 11, 5081 (1992).
12. C.J. Mogab, A.C. Adams, D.L. Flamm, J. Appl. Phys. **49**, 3796 (1978).
13. Boeing Aerospace Research & Engineering Div., Active Cleaning Technique for Removing Contamination from Optical Surface in Space, Final Report D180-17610-1, Contract NAS8-26385, Siettle, Washington, 98124, Aug. 1973.
14. J. Va'vra, Nucl. Instrum. Meth. Phys. Res. A **252**, 547 (1986).
15. J.W. McConkey, C.P. Malone, P.V. Johnson *et al.*, Phys. Rep. **466**, 1 (2008).

CONTENTS

PREFACE	3
STATUS OF THE ACCELERATOR FACILITIES AT PNPI	
50 YEARS OF THE PNPI SYNCHROCYCLOTRON SC-1000 S.A. Artamonov, E.M. Ivanov, G.F. Mikheev, G.A. Riabov, G.D. Alkhazov	6
STATUS OF THE PNPI H ⁻ ISOCHRONOUS CYCLOTRON C-80 D.A. Amerkanov, S.A. Artamonov, E.M. Ivanov, G.F. Mikheev, G.A. Riabov, V.A. Tonkikh, V.I. Yurchenko	15
ELEMENTARY PARTICLES PHYSICS	
SELECTED PHYSICS RESULTS FROM THE CMS EXPERIMENT AT THE LARGE HADRON COLLIDER	
A.A. Vorobyev, V.T. Kim, Yu.M. Ivanov, V.L. Golovtsov, E.V. Kuznetsova, P.M. Levchenko, V.A. Murzin, V.A. Oreshkin, L.A. Shchipunov, I.B. Smirnov, D.E. Sosnov, V.V. Sulimov, L.N. Uvarov, S.A. Vavilov, S.S. Volkov, An.A. Vorobyev	22
EXPERIMENT ATLAS AT THE LARGE HADRON COLLIDER A.E. Basalaev, A.E. Ezhilov, O.L. Fedin, M.P. Levchenko, V.P. Maleev, Yu.G. Naryshkin, V.A. Schegelsky, V.M. Solovyev	32
EXPERIMENT LHCb AT THE LARGE HADRON COLLIDER G.D. Alkhazov, N.F. Bondar, A.D. Chubykin, A.A. Dzyuba, S.N. Kotryakhova, O.E. Maev, N.R. Sagidova, Yu.A. Shcheglov, A.A. Vorobyev	40
OVERVIEW OF ALICE RESULTS Ya.A. Berdnikov, V.V. Ivanov, A.V. Khanzadeev, E.L. Kryshen, M.V. Malaev, V.N. Nikulin, Yu.G. Riabov, V.G. Ryabov, V.M. Samsonov, M.B. Zhalov	49
HIGGS BOSON PROPERTIES STUDIED IN ATLAS AND CMS EXPERIMENTS O.L. Fedin, A.E. Ezhilov, V.T. Grachev, M.P. Levchenko, V.P. Maleev, I.G. Naryshkin, V.A. Schegelsky, V.M. Solovyev; A.A. Vorobyev, V.T. Kim, Y.M. Ivanov, V.L. Golovtsov, E.V. Kuznetsova, P.M. Levchenko, V.A. Murzin, V.A. Oreshkin, I.B. Smirnov, V.V. Sulimov, L.N. Uvarov, S.A. Vavilov, An.A. Vorobyev	58
DIJETS WITH LARGE RAPIDITY SEPARATION AT CMS A.A. Vorobyev, Yu.M. Ivanov, V.T. Kim, A.Yu. Egorov, V.L. Golovtsov, E.V. Kuznetsova, P.M. Levchenko, V.A. Murzin, V.A. Oreshkin, I.B. Smirnov, D.E. Sosnov, V.V. Sulimov, L.N. Uvarov, S.A. Vavilov	67
THE ELECTROWEAK Z-BOSON PRODUCTION WITH TWO ASSOCIATED JETS IN THE CMS EXPERIMENT AT THE LARGE HADRON COLLIDER ENERGIES 7, 8, AND 13 TeV A.A. Vorobyev, B.V. Bochyn, S.A. Gets, V.L. Golovtsov, Yu.M. Ivanov, V.T. Kim, E.V. Kuznetsova, P.M. Levchenko, V.A. Murzin, V.A. Oreshkin, L.A. Schipunov, I.B. Smirnov, V.V. Sulimov, V.I. Tarakanov, L.N. Uvarov, S.A. Vavilov, S.S. Volkov, An.A. Vorobyev	72

MEASUREMENTS OF THE ANGULAR COEFFICIENTS IN Z-BOSON EVENTS USING ELECTRON AND MUON PAIRS FROM THE DATA TAKEN AT $\sqrt{s} = 8$ TeV WITH THE ATLAS DETECTOR A.E. Basalaev, A.E. Ezhilov, O.L. Fedin, V.T. Grachev, M.P. Levchenko, V.P. Maleev, Yu.G. Naryshkin, V.A. Schegelsky, V.M. Solovyev	75
SEARCH FOR DARK MATTER PARTICLES PRODUCED IN ASSOCIATION WITH A Z BOSON AT THE ATLAS DETECTOR A.E. Basalaev, A.E. Ezhilov, O.L. Fedin, V.T. Grachev, M.P. Levchenko, V.P. Maleev, Yu.G. Naryshkin, V.A. Schegelsky, V.M. Solovyev	82
SEARCH FOR A NEW HEAVY GAUGE BOSON RESONANCE WITH THE ATLAS DETECTOR A.E. Basalaev, A.E. Ezhilov, O.L. Fedin, V.T. Grachev, M.P. Levchenko, V.P. Maleev, Yu.G. Naryshkin, V.A. Schegelsky, V.M. Solovyev	88
STUDY OF THE BOSE–EINSTEIN CORRELATIONS AT THE ATLAS DETECTOR V.A. Schegelsky, M.G. Ryskin	94
STUDY OF RARE DECAYS OF B^0 AND B_s^0 MESONS IN THE LHCb EXPERIMENT G.D. Alkhazov, N.F. Bondar, A.D. Chubykin, A.A. Dzyuba, S.N. Kotryakhova, O.E. Maev, Yu.A. Shcheglov, N.R. Sagidova, A.A. Vorobyev	100
DISCOVERY OF NEW HEAVY CHARM BARYONS IN THE LHCb EXPERIMENT G.D. Alkhazov, N.F. Bondar, A.D. Chubykin, A.A. Dzyuba, S.N. Kotryakhova, O.E. Maev, N.R. Sagidova, Yu.A. Shcheglov, A.A. Vorobyev	106
PRODUCTION OF SHORT-LIVED HADRONIC RESONANCES IN Pb–Pb COLLISIONS AT $\sqrt{s_{NN}} = 2.76$ AND 5 TeV MEASURED BY THE ALICE EXPERIMENT AT THE LARGE HADRON COLLIDER Ya.A. Berdnikov, V.V. Ivanov, A.V. Khanzadeev, E.L. Kryshen, M.V. Malaev, V.N. Nikulin, Yu.G. Riabov, V.G. Ryabov, V.M. Samsonov, M.B. Zhalov	112
LOW- x GLUON DENSITY IN NUCLEI FROM EXCLUSIVE CHARMONIUM PHOTOPRODUCTION IN ULTRAPERIPHERAL ION COLLISIONS AT THE LARGE HADRON COLLIDER V.A. Guzey, E.L. Kryshen, M.V. Zhalov	118
COLLIMATION OF THE LARGE HADRON COLLIDER BEAMS WITH CRYSTALS Yu.M. Ivanov, A.S. Denisov, Yu.A. Gavrikov, B.L. Gorshkov, M.A. Koznov, L.P. Lapina, L.G. Malyarenko, V.I. Murzin, L.F. Pavlova, V.V. Skorobogatov, L.A. Vaishnene	124
EXPERIMENT D0: RECENT RESULTS AND JETS WITH LARGE RAPIDITY SEPARATION G.D. Alkhazov, V.T. Kim, A.A. Lobodenko, P.V. Neustroev, G.Z. Obrant, V.A. Oreshkin, Yu.A. Shcheglov, L.N. Uvarov, S.L. Uvarov	134
HIGH-ENERGY ASYMPTOTIC QUANTUM CHROMODYNAMIC EFFECTS AT COLLIDERS V.T. Kim	146
STUDY OF THE QUARK–GLUON PLASMA PROPERTIES BY PHENIX V.V. Baublis, D.A. Ivanishchev, A.V. Khanzadeev, B.G. Komkov, D.O. Kotov, M.V. Malaev, V.G. Riabov, Yu.G. Riabov, V.M. Samsonov	154

JET QUENCHING IN ASYMMETRIC HEAVY-ION COLLISIONS (Cu + Au, $\sqrt{s_{NN}} = 200$ GeV) MEASURED BY THE PHENIX EXPERIMENT AT RELATIVISTIC HEAVY ION COLLIDER V.V. Baublis, D.A. Ivanishchev, A.V. Khanzadeev, B.G. Komkov, D.O. Kotov, M.V. Malaev, V.G. Riabov, Yu.G. Riabov, V.M. Samsonov	162
HELICITY AMPLITUDE RATIOS FOR EXCLUSIVE ρ^0 -MESON ELECTROPRODUCTION ON TRANSVERSELY POLARIZED PROTONS S.L. Belostotski, G.E. Gavrilov, A.A. Izotov, A.Yu. Kisselev, P.V. Kravchenko, S.I. Manaenkov, Yu.G. Naryshkin, D.O. Veretennikov, V.V. Vikhrov	167
EXPERIMENT OLYMPUS AT DESY S.L. Belostotski, G.G. Gavrilov, A.A. Izotov, A.Yu. Kisselev, A.G. Krivshich, O.V. Miklukho, Yu.G. Naryshkin, D.O. Veretennikov	173
COMMISSIONING AND FIRST RESULTS OF THE BGO-OD EXPERIMENT AT ELSA D.E. Bayadilov, A.B. Gridnev, I.V. Lopatin, D.V. Novinskiy, A.M. Stugelev, V.V. Sumachev, V.I. Tarakanov	177
SEARCH FOR NARROW RESONANCES IN πp ELASTIC SCATTERING IN THE EPECUR EXPERIMENT A.B. Gridnev, V.A. Andreev, N.G. Kozlenko, V.S. Kozlov, A.G. Krivshich, V.A. Kuznetsov, D.V. Novinsky, V.V. Sumachev, V.I. Tarakanov, V.Yu. Trautman, Ye.A. Filimonov	183
MEASUREMENTS OF THE DOUBLE POLARIZATION OBSERVABLES AT A NEUTRAL MESONS PHOTOPRODUCTION IN THE CRYSTAL BARREL EXPERIMENT D.E. Bayadilov, Yu.A. Beloglazov, A.B. Gridnev, I.V. Lopatin, D.V. Novinsky, V.V. Sumachev	189
SEARCH FOR THE NARROW $N(1685)$ RESONANCE IN $\gamma N \rightarrow \pi \eta N$ REACTIONS V.A. Kuznetsov, A.B. Gridnev, N.G. Kozlenko, V.V. Sumachev	195
STUDY OF THE PROTON-PROTON COLLISIONS AT THE BEAM MOMENTUM OF 1 683 MeV/c K.N. Ermakov, V.A. Nikonov, O.V. Rogachevsky, A.V. Sarantsev, V.V. Sarantsev, S.G.Sherman ...	201
PNPI PARTICIPATION IN THE LHC DETECTORS UPGRADE	
PNPI IN THE CMS UPGRADE PROGRAM A.A. Vorobyev, G.E. Gavrilov, V.L. Golovtsov, Yu.M.Ivanov, V.T. Kim, P.M. Levchenko, E.V. Kuznetsova, V.A. Murzin, V.A. Oreshkin, L.A. Schipunov, D.E. Sosnov, V.V. Sulimov, L.N. Uvarov, S.A. Vavilov, S.S. Volkov, An.A. Vorobyev	210
UPGRADE OF THE ATLAS DETECTOR A.E. Basalaev, S.G. Barsov, A.E. Ezhilov, V.T. Grachev, O.L. Fedin, M.P. Levchenko, V.P. Maleev, Yu.G. Naryshkin, S.K. Patrichev, V.A. Schegelsky, V.M. Solovyev	217
UPGRADE PROGRAM OF THE LHCb DETECTOR AT THE LARGE HADRON COLLIDER B.V. Bochyn, N.F. Bondar, A.D. Chubykin, S.A. Gets, V.L. Golovtsov, V.T. Grachev, V.S. Kozlov, S.N. Kotryakhova, Z.G. Kudryashova, O.E. Maev, P.V. Neustroev, E.M. Spiridenkov, V.I. Tarakanov, L.N. Uvarov, S.S. Volkov, A.A. Vorobyev	224

UPGRADE OF THE ALICE DETECTOR V.V. Ivanov, A.V. Khanzadeev, E.L. Kryshen, M.V. Malaev, N.M. Miftakhov, V.N. Nikulin, Yu.G. Riabov, E.V. Roshchin, V.G. Ryabov, V.M. Samsonov, O.P. Tarasenkova, M.B. Zhalov	232
---	-----

NUCLEAR AND ATOMIC PHYSICS

SEARCH FOR MUON CATALYZED $d^3\text{He}$ FUSION V.A. Ganzha, K.A. Ivshin, P.V. Kravchenko, P.A. Kravtsov, E.M. Maev, A.A. Vasilyev, A.A. Vorobyev, N.I. Voropaev, M.E. Vznuzdaev	240
PENNING TRAPS IN THE SERVICE OF FUNDAMENTAL PHYSICS: ASTROPHYSICS, NEUTRINO PHYSICS, QUANTUM ELECTRODYNAMICS S.A. Eliseev, S.V. Chenmarev, P.E. Filianin, Yu.I. Gusev, D.A. Nesterenko, Yu.N. Novikov	249
NUCLEAR MATTER DISTRIBUTIONS IN THE CARBON, BERILLIUM, AND BORON ISOTOPES DETERMINED IN MEASUREMENTS WITH THE DETECTOR IKAR AT GSI G.D. Alkhazov, A.V. Dobrovolsky, A.G. Inglessi, A.V. Khanzadeev, G.A. Korolev, G.E. Petrov, L.O. Sergeev, A.A. Vorobyev, V.I. Yatsoura	258
ONSET OF DEFORMATION IN NEUTRON-DEFICIENT Bi ISOTOPES A.E. Barzakh, D.V. Fedorov, V.S. Ivanov, P.L. Molkanov, F.V. Moroz, S.Yu. Orlov, V.N. Pantelev, M.D. Seliverstov, Yu.M. Volkov	265
SHAPE COEXISTENCE IN THE LEAD REGION <i>VIA</i> α - AND β -DECAY STUDIES WITH THE APPLICATION OF THE LASER ION SOURCE A.E. Barzakh, D.V. Fedorov, P.L. Molkanov, M.D. Seliverstov	274
CHANGES IN MEAN-SQUARED CHARGE RADII AND MAGNETIC MOMENTS OF NEUTRON DEFICIENT Tl ISOTOPES MEASURED BY IN-SOURCE LASER SPECTROSCOPY A.E. Barzakh, D.V. Fedorov, V.S. Ivanov, P.L. Molkanov, F.V. Moroz, S.Yu. Orlov, V.N. Pantelev, M.D. Seliverstov, Yu.M. Volkov	281
STUDY OF NUCLEON CORRELATIONS IN NUCLEI BY THE (p, p') INELASTIC REACTION AT 1 GeV O.V. Miklukho, V.A. Andreev, A.A. Izotov, A. Yu. Kisselev, N.G. Kozlenko, A.N. Prokofiev, A.V. Shvedchikov, S.I. Trush, A.A. Zhdanov	290
SENSITIVITY OF REACTION CROSS SECTIONS TO HALO NUCLEUS DENSITY DISTRIBUTIONS G.D. Alkhazov, V.V. Sarantsev	298
TAKING INTO ACCOUNT THE CENTRE-OF-MASS CORRELATIONS IN THE CROSS SECTIONS FOR ELASTIC SCATTERING OF INTERMEDIATE ENERGY PROTONS ON THE EXOTIC NUCLEI ^6He AND ^8He G.D. Alkhazov, V.V. Sarantsev	304
μSR INVESTIGATIONS AT THE PNPI S.G. Barsov, A.L. Getalov, E.N. Komarov, S.A. Kotov, G.V. Shcherbakov, S.I. Vorob'ev	308

NEW PROJECTS

PROJECT FOR PRECISION MEASUREMENT OF THE PROTON CHARGE RADIUS IN AN ELECTRON-PROTON SCATTERING EXPERIMENT

A.A. Vorobyev, A.A. Vasilyev, S.L. Belostotsky, B.V. Bochin, A.A. Dzyuba, G.E. Gavrilov,
V.T. Grachev, K.A. Ivshin, A.G. Inglessi, P.V. Kravchenko, P.A. Kravtsov, E.M. Maev,
S.M. Mikirtychanz, P.V. Neustroev, G.E. Petrov, N.R. Sagidova, A.N. Solovyev, I.N. Solovyev,
E.M. Spiridenkov, V.A. Trofimov, M.E. Vznuzdaev 316

SHiP: SEARCH FOR HIDDEN PARTICLES

V.T. Kim, E.V. Kuznetsova, O.L. Fedin, G.E. Gavrilov, V.L. Golovtsov, N.V. Gruzinskiy,
V.P. Maleev, S.A. Nasybulin, L.N. Uvarov, V.I. Yatsyura 326

PROJECT IRINA AT THE REACTOR PIK

V.N. Pantelev, A.E. Barzakh, L.Kh. Batist, D.V. Fedorov, V.S. Ivanov, V.V. Lukashevich,
P.L. Molkanov, M.D. Seliverstov 336

PITRAP PROJECT AT THE PIK REACTOR

Yu.I. Gusev, V.S. Gusel'nikov, S.V. Chenmarev, S.A. Eliseev, P.E. Filyanin, T.V. Koneva,
D.A. Nesterenko, Yu.N. Novikov, A.W. Popov, D. Simonovski 344

NEUTRINO OSCILLOMETRY AND PROPOSAL OF THE OMNIBUS EXPERIMENT

Yu.N. Novikov, M.V. Smirnov 350

DOUBLE POLARIZED $d-d$ -FUSION EXPERIMENT

V.D. Fotyev, K.A. Ivshin, E.N. Komarov, L.M. Kotchenda, P.V. Kravchenko, P.A. Kravtsov,
S.G. Sherman, A.N. Soloviev, I.N. Soloviev, V.A. Trofimov, A.A. Vasilyev, M.E. Vznuzdaev 355

PNPI IN THE CBM PROJECT AT FAIR: RING CHERENKOV AND MUON CHAMBER SUBSYSTEMS OF THE CBM DETECTOR

V.V. Baublis, V.V. Ivanov, A.V. Khanzadeev, L.M. Kochenda, B.G. Komkov, P.A. Kravtsov,
E.L. Kryshen, L.G. Kudin, N.M. Miftakhov, V.N. Nikulin, Yu.G. Riabov, E.V. Roschin,
G.V. Rybakov, V.M. Samsonov, O.P. Tarasenkova, D.V. Tyts, M.E. Vznuzdaev, M.B. Zhalov 362

EXPERIMENT PANDA AT GSI

S.L. Belostotski, A.A. Izotov, S.I. Manaenkov, O.V. Miklukho, D.O. Veretennikov, A.A. Zhdanov 370

PNPI IN THE R³B PROJECT AT FAIR

G.D. Alkhazov, V.A. Andreev, D.V. Balin, L.Kh. Batist, A.V. Dobrovolsky, V.L. Golovtsov,
D.S. Ilyin, A.G. Inglessi, A.V. Khanzadeev, G.A. Korolev, A.G. Krivshich, E.M. Maev,
D.A. Maysuzenko, A.V. Nadtochiy, G.E. Petrov, V.V. Sarantsev, N.Yu. Shvetsova, L.N. Uvarov,
S.S. Volkov, V.I. Yatsoura, A.A. Zhdanov 375

METHODICAL AND APPLIED RESEARCH

UNIVERSAL PROTON AND NEUTRON CENTRE FOR RADIATION RESISTANCE OF AVIONIC SPACE ELECTRONICS AND OTHER APPLICATIONS AT THE 1-GeV SYNCHROCYCLOTRON IN PNPI

D.A. Amerkanov, S.A. Artamonov, E.M. Ivanov, J.S. Lebedeva, G.F. Mikheev, G.A. Riabov,
O.A. Shcherbakov, A.S. Vorobyev 386

NUMERICAL SIMULATION AND OPTIMIZATION OF THE VARIABLE ENERGY 60–1 000 MeV PROTON BEAMS AT THE PNPI SYNCHROCYCLOTRON FOR TESTING THE RADIATION RESISTANCE OF ELECTRONICS USED FOR NEEDS OF AVIATION AND SPACECRAFT S.A. Artamonov, D.A. Amerkanov, E.M. Ivanov, G.I. Gorkin, G.A. Riabov, V.A. Tonkikh	390
MAGNETIC FIELD OF THE 40–80 MeV H ⁻ ISOCHRONOUS CYCLOTRON AT GATCHINA. EXPERIMENTS AND 3D CALCULATIONS S.A. Artamonov, D.A. Amerkanov, G.I. Gorkin, V.P. Gres, E.M. Ivanov, G.A. Riabov	397
HIGH EFFICIENCY STRIPPING EXTRACTION IN THE 80-MeV H ⁻ ISOCHRONOUS CYCLOTRON AT PNPI S.A. Artamonov, A.N. Chernov, E.M. Ivanov, G.A. Riabov, V.A. Tonkikh	404
DEVELOPMENT OF NEW METHODS FOR PRODUCTION OF MEDICAL RADIONUCLIDES AT THE RADIOISOTOPE COMPLEX RIC-80 V.N. Panteleev, A.E. Barzakh, L.Kh. Batist, D.V. Fedorov, V.S. Ivanov, S.A. Krotov, P.L. Molkanov, S.Yu. Orlov, M.D. Seliverstov, Yu.M. Volkov	409
ULTRACOLD NEUTRON DETECTOR A.G. Krivshich, V.A. Andreev, A.V. Vasiljev, E.A. Ivanov, D.S. Ilyin, A.P. Serebrov	415
UNIVERSITY OF FLORIDA–PNPI HIGH VOLTAGE SYSTEM IN THE CMS ENDCAP MUON DETECTOR S.S. Volkov, S.V. Bondarev, V.L. Golovtsov, N.B. Isaev, E.M. Orischin, L.O. Sergeev, L.N. Uvarov	421
NONINVASIVE METHOD OF RECOVERY OF GAS PARTICLE DETECTORS UNDER OPERATION IN HIGH-INTENSITY FIELDS OF RADIATION V.A. Andreev, G.E. Gavrilov, A.G. Krivshich, D.A. Maisuzenko, A.A. Fetisov, N.Yu. Shvetsova	425
RECOVERY OF GAS DISCHARGE DETECTORS FROM MALTER EFFECT G.E. Gavrilov, E.V. Kuznetsova, O.E. Maev, D.A. Maysuzenko, S.A. Nasybulin	429
CONTENTS	435

High Energy Physics Division MAIN SCIENTIFIC ACTIVITIES 2013–2018

Отпечатано в издательско-полиграфическом отделе
НИЦ «Курчатовский институт» – ПИЯФ
на Konica Minolta bizhub PRO C1060L

188300, Гатчина Ленинградской обл., мкр. Орлова роща, д. 1
Зак. 500, тир. 80, уч.-изд. л. 54; 19.11.2019 г.